cells

Special Issue Reprint

New Advances in Lens Biology and Pathology

Edited by
Frank J. Lovicu

mdpi.com/journal/cells

MDPI

New Advances in Lens Biology and Pathology

New Advances in Lens Biology and Pathology

Guest Editor

Frank J. Lovicu

MDPI

Basel • Beijing • Wuhan • Barcelona • Belgrade • Novi Sad • Cluj • Manchester

Guest Editor
Frank J. Lovicu
School of Medical Sciences
Save Sight Institute
University of Sydney
Sydney, NSW
Australia

Editorial Office
MDPI AG
Grosspeteranlage 5
4052 Basel, Switzerland

This is a reprint of the Special Issue, published open access by the journal *Cells* (ISSN 2073-4409), freely accessible at: https://www.mdpi.com/journal/cells/special_issues/Lens_Biology.

For citation purposes, cite each article independently as indicated on the article page online and as indicated below:

Lastname, A.A.; Lastname, B.B. Article Title. *Journal Name* **Year**, *Volume Number*, Page Range.

ISBN 978-3-7258-8487-2 (Hbk)
ISBN 978-3-7258-8488-9 (PDF)
https://doi.org/10.3390/books978-3-7258-8488-9

© 2026 by the authors. Articles in this reprint are Open Access and distributed under the Creative Commons Attribution (CC BY) license. The reprint as a whole is distributed by MDPI under the terms and conditions of the Creative Commons Attribution-NonCommercial-NoDerivs (CC BY-NC-ND) license (https://creativecommons.org/licenses/by-nc-nd/4.0/).

Contents

About the Editor . . . . . **vii**

Preface . . . . . **ix**

Aleš Cvekl and Michael John Camerino
Generation of Lens Progenitor Cells and Lentoid Bodies from Pluripotent Stem Cells: Novel Tools for Human Lens Development and Ocular Disease Etiology
Reprinted from: *Cells* **2022**, *11*, 3516, https://doi.org/10.3390/cells11213516 . . . . . **1**

Eri Kubo, Shinsuke Shibata, Teppei Shibata, Hiroshi Sasaki and Dhirendra P. Singh
Role of Decorin in the Lens and Ocular Diseases
Reprinted from: *Cells* **2023**, *12*, 74, https://doi.org/10.3390/cells12010074 . . . . . **43**

Zongbo Wei, Pasley Gordon, Caili Hao, Jingru Huangfu, Emily Fan, Xiang Zhang, et al.
Aged Lens Epithelial Cells Suppress Proliferation and Epithelial–Mesenchymal Transition-Relevance for Posterior Capsule Opacification
Reprinted from: *Cells* **2022**, *11*, 2001, https://doi.org/10.3390/cells11132001 . . . . . **61**

Caterina Sellitto, Leping Li and Thomas W. White
Double Deletion of PI3K and PTEN Modifies Lens Postnatal Growth and Homeostasis
Reprinted from: *Cells* **2022**, *11*, 2708, https://doi.org/10.3390/cells11172708 . . . . . **80**

Oscar Jara, Peter J. Minogue, Viviana M. Berthoud and Eric C. Beyer
Levels and Modifications of Both Lens Fiber Cell Connexins Are Affected in Connexin Mutant Mice
Reprinted from: *Cells* **2022**, *11*, 2786, https://doi.org/10.3390/cells11182786 . . . . . **93**

Michael P. Vu and Catherine Cheng
Mapping the Universe of Eph Receptor and Ephrin Ligand Transcripts in Epithelial and Fiber Cells of the Eye Lens
Reprinted from: *Cells* **2022**, *11*, 3291, https://doi.org/10.3390/cells11203291 . . . . . **106**

Samuel G. Novo, Adam P. Faranda, Mahbubul H. Shihan, Yan Wang, Ananya Garg and Melinda K. Duncan
The Immediate Early Response of Lens Epithelial Cells to Lens Injury
Reprinted from: *Cells* **2022**, *11*, 3456, https://doi.org/10.3390/cells11213456 . . . . . **118**

Morgan D. Basta, A. Sue Menko and Janice L. Walker
PI3K Isoform-Specific Regulation of Leader and Follower Cell Function for Collective Migration and Proliferation in Response to Injury
Reprinted from: *Cells* **2022**, *11*, 3515, https://doi.org/10.3390/cells11213515 . . . . . **146**

Kevin L. Schey, Zhen Wang, Kristie L. Rose and David M. G. Anderson
Imaging Cataract-Specific Peptides in Human Lenses
Reprinted from: *Cells* **2022**, *11*, 4042, https://doi.org/10.3390/cells11244042 . . . . . **162**

Lisa Brennan, M. Joseph Costello, J. Fielding Hejtmancik, A. Sue Menko, S. Amer Riazuddin, Alan Shiels and Marc Kantorow
Autophagy Requirements for Eye Lens Differentiation and Transparency
Reprinted from: *Cells* **2023**, *12*, 475, https://doi.org/10.3390/cells12030475 . . . . . **175**

Jacquelyn Gerhart and Mindy George-Weinstein
Myo/Nog Cells: The Jekylls and Hydes of the Lens
Reprinted from: *Cells* **2023**, *12*, 1725, https://doi.org/10.3390/cells12131725 . . . . . **196**

Anil Upreti, Stephanie L. Padula, Jared A. Tangeman, Brad D. Wagner, Michael J. O'Connell, Tycho J. Jaquish, et al.
Lens Epithelial Explants Treated with Vitreous Humor Undergo Alterations in Chromatin Landscape with Concurrent Activation of Genes Associated with Fiber Cell Differentiation and Innate Immune Response
Reprinted from: *Cells* **2023**, *12*, 501, https://doi.org/10.3390/cells12030501 . . . . . **214**

Mary Flokis and Frank J. Lovicu
FGF-2 Differentially Regulates Lens Epithelial Cell Behaviour during TGF-β-Induced EMT
Reprinted from: *Cells* **2023**, *12*, 827, https://doi.org/10.3390/cells12060827 . . . . . **242**

Archana D. Siddam, Matthieu Duot, Sarah Y. Coomson, Deepti Anand, Sandeep Aryal, Bailey A. T. Weatherbee, et al.
High-Throughput Transcriptomics of *Celf1* Conditional Knockout Lens Identifies Downstream Networks Linked to Cataract Pathology
Reprinted from: *Cells* **2023**, *12*, 1070, https://doi.org/10.3390/cells12071070 . . . . . **262**

Tayler F. L. Wishart and Frank J. Lovicu
Spatiotemporal Localisation of Heparan Sulphate Proteoglycans throughout Mouse Lens Morphogenesis
Reprinted from: *Cells* **2023**, *12*, 1364, https://doi.org/10.3390/cells12101364 . . . . . **283**

Miguel Jarrin, Alexia A. Kalligeraki, Alice Uwineza, Chris S. Cawood, Adrian P. Brown, Edward N. Ward, et al.
Independent Membrane Binding Properties of the Caspase Generated Fragments of the Beaded Filament Structural Protein 1 (BFSP1) Involves an Amphipathic Helix
Reprinted from: *Cells* **2023**, *12*, 1580, https://doi.org/10.3390/cells12121580 . . . . . **303**

Matthieu Duot, Roselyne Viel, Justine Viet, Catherine Le Goff-Gaillard, Luc Paillard, Salil A. Lachke, et al.
Eye Lens Organoids Made Simple: Characterization of a New Three-Dimensional Organoid Model for Lens Development and Pathology
Reprinted from: *Cells* **2023**, *12*, 2478, https://doi.org/10.3390/cells12202478 . . . . . **322**

Kineret Taler, Nour Zatari, Mohammad Iqbal Lone, Shahar Rotem-Bamberger and Adi Inbal
Identification of Small Molecules for Prevention of Lens Epithelium-Derived Cataract Using Zebrafish
Reprinted from: *Cells* **2023**, *12*, 2540, https://doi.org/10.3390/cells12212540 . . . . . **346**

Jiawen Xiang, Anthony J. Pompetti, Adam P. Faranda, Yan Wang, Samuel G. Novo, David Wan-Cheng Li and Melinda K. Duncan
ATF4 May Be Essential for Adaption of the Ocular Lens to Its Avascular Environment
Reprinted from: *Cells* **2023**, *12*, 2636, https://doi.org/10.3390/cells12222636 . . . . . **362**

Pandi Saranya, Madhu Shekhar, Aravind Haripriya, Veerappan Muthukkaruppan and Chidambaranathan Gowri Priya
Towards the Identification and Characterization of Putative Adult Human Lens Epithelial Stem Cells
Reprinted from: *Cells* **2023**, *12*, 2727, https://doi.org/10.3390/cells12232727 . . . . . **389**

About the Editor

Frank J. Lovicu

Frank J. Lovicu is the Head of the Cataract and Lens Research Laboratory and is a teaching academic, holding a professorship at the School of Medical Sciences, and the Save Sight Institute at The University of Sydney, Sydney, NSW 2006, Australia. His research is primarily directed at understanding the molecular and cellular mechanisms governing the behavior of eye lens cells during health, aging, and disease, with interests in eye lens development and morphogenesis, cataract formation and prevention, growth factor signaling and lens regeneration. Professor Lovicu is actively involved in national and international professional organisations within vision research and ophthalmology. He is the current President of the International Society for Eye Research (ISER, 2025–2027) and past Vice-president and Fellow of the Association for Research in Vision and Ophthalmology (ARVO, 2025–2026).

Preface

In this Special Issue for *Cells*, contributions in the form of original research articles, reviews, or shorter perspective articles on all aspects related to the theme of "Advances in Lens Biology and Pathology" were solicited. Expert articles describing mechanistic, functional, cellular, biochemical, or general aspects of lens biology and pathology were submitted on topics including but not limited to Growth Factor signaling, in vitro and in vivo models, the extracellular matrix, fibrosis, bioimaging, translational medicine, lens physiology, developmental processes, cell behavior, gene expression, cataract, lens proliferation and/or fiber differentiation, EMT, and lens morphogenesis.

Frank J. Lovicu
Guest Editor

cells

MDPI

Review

Generation of Lens Progenitor Cells and Lentoid Bodies from Pluripotent Stem Cells: Novel Tools for Human Lens Development and Ocular Disease Etiology

Aleš Cvekl [1,2,*] and Michael John Camerino [1,2]

[1] Departments Ophthalmology and Visual Sciences, Albert Einstein College of Medicine, Bronx, NY 10461, USA
[2] Department of Genetics, Albert Einstein College of Medicine, Bronx, NY 10461, USA
* Correspondence: ales.cvekl@einsteinmed.edu; Tel.: +1-718-430-3217; Fax: +1-718-430-8778

Abstract: In vitro differentiation of human pluripotent stem cells (hPSCs) into specialized tissues and organs represents a powerful approach to gain insight into those cellular and molecular mechanisms regulating human development. Although normal embryonic eye development is a complex process, generation of ocular organoids and specific ocular tissues from pluripotent stem cells has provided invaluable insights into the formation of lineage-committed progenitor cell populations, signal transduction pathways, and self-organization principles. This review provides a comprehensive summary of recent advances in generation of adenohypophyseal, olfactory, and lens placodes, lens progenitor cells and three-dimensional (3D) primitive lenses, "lentoid bodies", and "micro-lenses". These cells are produced alone or "community-grown" with other ocular tissues. Lentoid bodies/micro-lenses generated from human patients carrying mutations in crystallin genes demonstrate proof-of-principle that these cells are suitable for mechanistic studies of cataractogenesis. Taken together, current and emerging advanced in vitro differentiation methods pave the road to understand molecular mechanisms of cataract formation caused by the entire spectrum of mutations in DNA-binding regulatory genes, such as PAX6, SOX2, FOXE3, MAF, PITX3, and HSF4, individual crystallins, and other genes such as BFSP1, BFSP2, EPHA2, GJA3, GJA8, LIM2, MIP, and TDRD7 represented in human cataract patients.

Keywords: cranial placodes; crystallins; de-nucleation; differentiation; gene expression; lens progenitor cells; lentoid bodies; optic cup; pluripotent stem cells; PAX6; self-organization

1. Introduction

The original discovery of embryonic stem (ES) cells and their in vitro cultures triggered new research avenues that transformed both basic and translational research towards better understanding of mammalian embryonic development and human diseases [1,2]. The promise of this field was further boosted by the discovery of nuclear reprograming methods to generate induced pluripotent stem (iPS) cells from mature somatic cells. Over two decades of research using cultured human, monkey, and mouse ES/iPS cells demonstrated their ability to differentiate into a full spectrum of common lineage progenitors and a variety of terminally differentiated cells that exhibit similar morphological, functional, and molecular signatures of individual tissues or even organs [3–6]. Here, we call organoids in vitro-generated 3D structures from differentiating pluripotent stem cells to individual tissues and organs that exhibit realistic microanatomy compared to their natural counterparts [7]. It has been shown earlier that it is possible to mechanically dissociate cells from chicken organs, such as kidney, liver, and skin, followed by their reconstitution through self-sorting and reaggregation [8]. Experiments conducted during the last 20 years further demonstrated that tissue-progenitor cells can self-organize through cell sorting and exchange of signals into spatially organized mini-tissues and organs [7]. Remarkably, it is now even possible to reconstruct "synthetic" in vitro ~E8.5 mouse embryos

derived from three ES-derived cell populations capable to complete gastrulation and early organogenesis [9,10].

Elaborate methods of genome engineering, currently driven by CRISPR-Cas9 technologies [11,12], allow efficient generation of a range of mutations, gene expression reporters, and production of fusion proteins with a variety of fluorescent tags to be tracked even at single-molecule levels [13]. These methods can dissect precise molecular mechanisms specific to any mRNA, ncRNA, and protein of interest. In 2006–2007, the breakthrough discoveries of cellular reprogramming that established mouse- [6] and human-induced [14] pluripotent stem (iPS) cells for the first time now allow routine generations of patient-specific iPS cells carrying defined disease-causing mutations and their corrected version [15–17].

Eye development is an intriguing and challenging system to apply pluripotent stem cell technologies to address numerous gaps in our understanding of both the mechanisms of human eye development, eye diseases, and the development of new cell- and drug-based therapies [18–20]. Although traditional vertebrate models of eye development established a comprehensive foundation for our understanding of cellular and molecular mechanisms of eye formation, there are several unique features of the human eye (see below) and its underlying gene regulatory networks (GRNs) that can now be modeled using human cells.

Despite these advances, multiple experimental challenges remain to be addressed in the emerging field of 3D eye tissue/organoid engineering. Lessons from normal embryonic eye development continue to serve as invaluable resources for these experiments. In the application stage of these in vitro models, it is important to consider that mutations in individual genes, especially those encoding regulatory proteins, may impact the whole eye, selected ocular tissues, or just an individual tissue, e.g., the lens, cornea, cones, rods, or retinal pigmented epithelium (RPE). Mechanistically, these mutations can act cell-autonomously, non-cell-autonomously, or via a combination of these mechanisms [21–25].

Ocular lens development is a classical model for a highly orchestrated formation of committed lens progenitor cells originating from a transient population of cells at the border between the neuroectoderm and naïve ectoderm, the anterior pre-placodal region [26–28]. This inverted U-shape morphogenetic zone gives rise to three types of distinct structures, including a single anterior pituitary placode and more posteriorly, two symmetric pairs of olfactory and lens placodes [27,29] (Figure 1A).

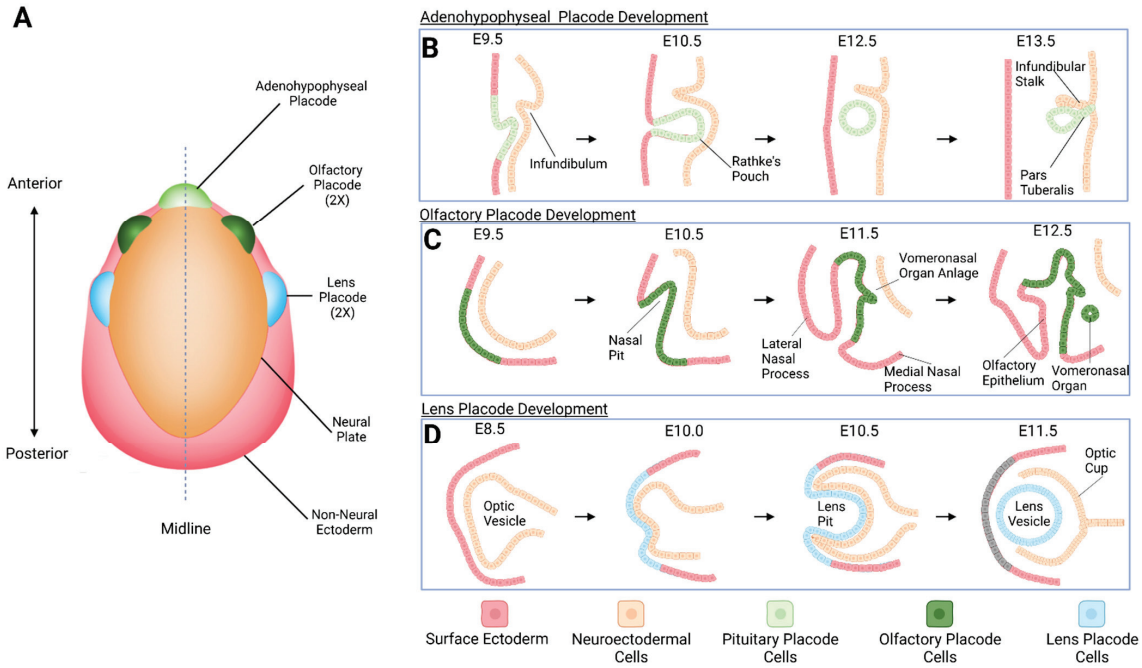

Figure 1. Formation of three anterior cranial placodes during mid-stage mouse embryogenesis. (**A**) Highly schematic visualization of future location of adenohypophyseal, olfactory, and lens placodes

relative to the neural tube and its anterior/posterior patterning at the E8.0 mouse embryo. Regarding the eye and lens formation, note that the eye field is already formed within the anterior subregion of the neural plate [30] (not shown), and undergoes its symmetric division, later forming a symmetric pair of optic vesicles (see panel D). (**B**) Adenohypophyseal (pituitary) gland development from E9.5 via Rathke's pouch [31] to E13.5, forming the infundibular stalk and the pars tuberalis [32]. (**C**) Olfactory placode development from E9.5 to E12.5, forming the vomeronasal organ [33]. (**D**) Lens placode development from E8.5 to E11.5, forming the lens vesicle [34]. The prospective corneal epithelium formed after the separation of the lens vesicle from the surface ectoderm is highlighted in gray. Note that for simplification, neural crest cells including periocular mesenchymal cells are not shown, but they are generally located in the space between the neuroectoderm and surface ectoderm. For additional details, see https://syllabus.med.unc.edu/ for ultrastructural images of mouse eye development between these stages.

The formation of both lens and olfactory placodes requires temporally regulated BMP signaling [35–37]. In addition, FGF signaling in lens progenitor cell formation prevents the formation of the alternate epidermal cell fate [36]. Nevertheless, given the complexity of FGF signaling at the neural plate/neural fold stage [30,38], there is no single or combined gene loss-of-function experiments including individual FGF receptors, FGFs, and other components of this pathway that abrogate lens placode formation. A subsequent reciprocal invagination of the non-neurogenic lens placode and neuroectoderm-derived optic vesicle generates the earliest 3D eye primordium, comprised of the lens vesicle and optic cup [28,30,34]. These eye primordia are surrounded by periocular mesenchymal cells, required subsequently for anterior segment morphogenesis [39–44] and covered by the surface ectoderm, giving rise to the corneal epithelium [45]. At its anterior portion, the polarized lens vesicle is patterned by gradients of BMP, FGF, IGF, PDGF, and Wnt growth factors. Spatially regulated expression of these growth factor receptors [46–49] subsequently forms the monolayer of the epithelium. The posterior portion of the lens vesicle undergoes cell cycle-exit coupled differentiation regulated by complex interactions between BMP, FGF, and PDGF signaling [50–53] to generate the primary lens fiber cells. The proliferation of epithelial cells generates new cells at the lens equator and their subsequent differentiation generates secondary lens fibers.

The three hallmark features of lens fiber cell differentiation include: (a) robust transcription, translation, and accumulation of crystallin proteins required for lens transparency and light refraction [54,55], (b) formation of elaborate organization of lens membranes and lens fiber cell cytoskeleton coupled to extensive cellular elongation [56–61], and (c) highly organized degradation of all subcellular organelles, culminating with lens fiber cell denucleation in maturing lens fiber cells, to generate the "organelle-free zone" (OFZ) [62–64]. The fully maturated lens fibers exhibit interdigitated "ball-and-socket" junctions [65,66]. The abundant junctions between individual lens fibers implicates that enucleated lens fibers function as a syncytium with respect of free movement of small molecules [67,68]. The lens growth process was quantitatively analyzed in the murine model from the onset of secondary lens fiber cell differentiation to the end of the lifespan [69,70]. These complex processes underlying lens fiber cell maturation [71] must be at least partially recapitulated during in vitro generation of lentoid bodies as well as during the formation of lenses together with retinal tissues.

Why are human eye organoid models derived from differentiated pluripotent stem cells so important? Human eyes evolved far more complex vision and intricate functional anatomy compared to the rodent models used in the laboratory research. Humans employ diurnal vision while rodents rely on rod photoreceptors and nocturnal vision. The human eye contains a unique anatomical structure called the macula and its central portion, the fovea, rich in cone photoreceptors [72,73]. The morphogenetic processes underlying cone-dominant foveal development can be only partially inferred from other model organisms (e.g., 13-line ground squirrels, chameleons, and other reptiles) [74–76]. The human eye can

accommodate lenses to both near-sight focus and over a distance of several hundreds of meters. Consequently, human lenses are much softer, and two γ-crystallin genes in rodents, Cryge and Crygf (mouse chromosome 1), mutated into a pair of human pseudogenes located on the syntenic region of human chromosome 2 [34] likely contributing to this phenomenon through the overall reduction of γ-crystallin proteins in the lens nucleus. Finally, in vitro generation of artificial human tissues can address the scarcity of authentic ocular tissues, allowing for expansion of more in-depth human biochemical studies and other analyses.

Here, we examine the formation of lens progenitor cells and subsequent generation of lentoid bodies to study human lens development and model cataract formation and lens pathology. We organize different experimental procedures into groups with shared features and outcomes. In Section 2, we include a pioneering study using mouse ES cells to generate whole eyes published in 2003. Section 3 is focused on eye-independent formation of lentoid bodies and 3D-formation of optic cups to illustrate the general self-organization principles introduced above. Induction of cranial placodes in multiple systems is used to illustrate the function of regulatory genes and signaling pathways required for normal lens morphogenesis (Section 4). Advanced systems to generate 3D lentoid bodies based on cell-sorting principles are included in Section 5. In Section 6, we discuss modeling of cataract and other human ocular diseases using pluripotent cell differentiation, genome engineering, and application of unbiased multi-omics methods for analyses. Finally, Section 7 provides a summary of current challenges in tissue engineering to form ideal lenses and eye-like structures and the future direction of this fascinating research.

2. Prologue (2002–2003)

Mouse ES cells were first derived from the inner cell mass of the early embryos in 1981 [1,77]. Subsequently, generation and initial characterization of human ES cells followed in 1998 [2]. Early pioneering studies have shown differentiation of human and mouse ES cells into a representative number of mature cells such as dopamine neurons [78], motor neurons [79], and RPE cells [80].

Early research on lens differentiation has demonstrated that in vitro-cultured lens epithelial cells can be differentiated into primitive 3D lens-like structures, termed "lentoid bodies" [81–91]. Lentoid bodies are comprised from aggregated cells all expressing crystallin proteins and some cells exhibit elongated morphology. Importantly, some of these studies directly showed that lentoid bodies are both transparent and refract light. Hence, these early studies supported the general concept of self-organization [7,92] in 3D-cultures (see Section 6 for details) as a foundation of contemporary tissue engineering.

Interestingly, lentoid body-like structures were also found in vivo in embryos of diverse model vertebrates as the result of spontaneous or engineered mutations in genes involved in lens morphogenesis [93–97] or via ectopic expression of the lens regulatory gene Six3 in medaka fish [98] and Pax6 in frogs [99]. An elegant study has shown that lens formation can be restored in Rax-depleted mouse embryos through the elimination of β-catenin expression, a major player of the canonical Wnt signaling, in the head surface ectoderm [100]. Trans-differentiation of RPE cells into lentoid bodies also illustrates that primitive lens formation is not required to be inside of the optic cup [81,101,102]. Lens regeneration from the dorsal iris in newts is another example of developmental plasticity [103]. Taken together, these studies demonstrated lens formation under various abnormal conditions. It was just a matter of time to detect lenses in early attempts to "spontaneously" differentiate pluripotent stem cells into various ectoderm-derived tissues.

The first pioneering studies of in vitro formation of lens and retinal cells from mouse pluripotent stem cells indeed generated remarkable outputs [104,105]. The first system used 129/SV mouse ES cells in the absence of any feeder cells and leukemia inhibitory factor to generate embryonic bodies [104]. A subsequent treatment with 5 and 50 nM of retinoic acid (RA) promoted formation of the optic vesicle, lens, and retina, as well as other

cell types in 20 days of cultures; however, these cells were only visualized via rudimentary histology and without detection of any cell-specific protein markers.

The other system employed the PA6 stromal cells derived from C57/Bl6 mice as a feeder layer required for differentiation as they produce neural-inducing factors [106,107]. The aggregated colonies of cells were observed at day seven of cultures, and, two days later, globular structures including weakly pigmented RPE-like cells were detected [105]. More complex eye-like structures, including primitive lenses validated by studies of crystallin gene expression, were found as early as at day 11, around the time when mid-gestation mouse embryos generate the lens vesicles and early optic cups. Addition of bFGF/FGF2 further improved induction of eye-like structures. The presence of PA6 feeder cells was critical and the use of bFGF could not replace them. Finally, this study demonstrated that the use of Pax6−/− ES cells did not produce any of these structures using nearly 3000 early cell colonies generated from the mutated cells. As expected, Pax6+/− ES cells retained this ability [105]. Taken together, this single study demonstrated for the first time a "proof-of-principle" that complex 3D eye structures can be generated in vitro without any sophisticated procedures and unusual time constraints.

In parallel, cynomolgus monkey ES cells were grown on PA6 stromal cells as a source of differentiation factors plated on gelatin-coated dishes [108]. Lentoid bodies were detected from day 14–16 of cultures and analyzed up to day 53. FGF2 was tested at concentrations of 2, 4, and 8 ng/mL and improved the yield of lentoid bodies [108]. It is of interest that the "parental" protocol generates pigmented epithelial cells and dopaminergic neurons [109].

Nevertheless, these three initial studies were underappreciated as iPS cell technologies emerged later in 2006. The generation of iPS cells via cellular reprogramming was a game changer in the field of pluripotent stem cell differentiation [6] as it bypassed the use of human early embryonic materials, facilitated generation of iPS cells from both normal individuals and patients with specific genetic abnormalities, leading to diseases [14], allows correction of the genetic defect(s), and facilitates large-scale generation of interesting mutations using isogenic iPS cells (see Section 6.2 for details). In addition, dynamic visualization of the formation of the optic cup using fluorescent proteins was also employed much later in 2011 [110,111]. Finally, in 2001, another important study showed that Matrigel can replace feeder cells to grow and expand ES cells [112]. The extracellular matrix known as Matrigel is isolated from mouse Engelbreth–Holm–Swarm teratocarcinoma cells that secrete excess basement membrane-type extracellular matrix (ECM) instead of cartilaginous matrix proteins [113]. Biochemical data show that Matrigel is a gelatinous mixture of collagen IV, laminin, proteoglycans, entactin, and other growth factors [114] that also promotes differentiation of various cell types [115], including lens cells [116].

3. Independent Formation of Lentoid Bodies and Optic Cups (2010–2016)

A specific goal to generate in vitro lens progenitor cells and lentoid bodies has been achieved primarily through lessons taken from lens developmental biology [35,36,46,117–120], including the role of ECM proteins [116,121–125]. The Matrigel-based three-stage procedure (Figure 2A) is based on neuroectoderm formation via Noggin (stage 1).

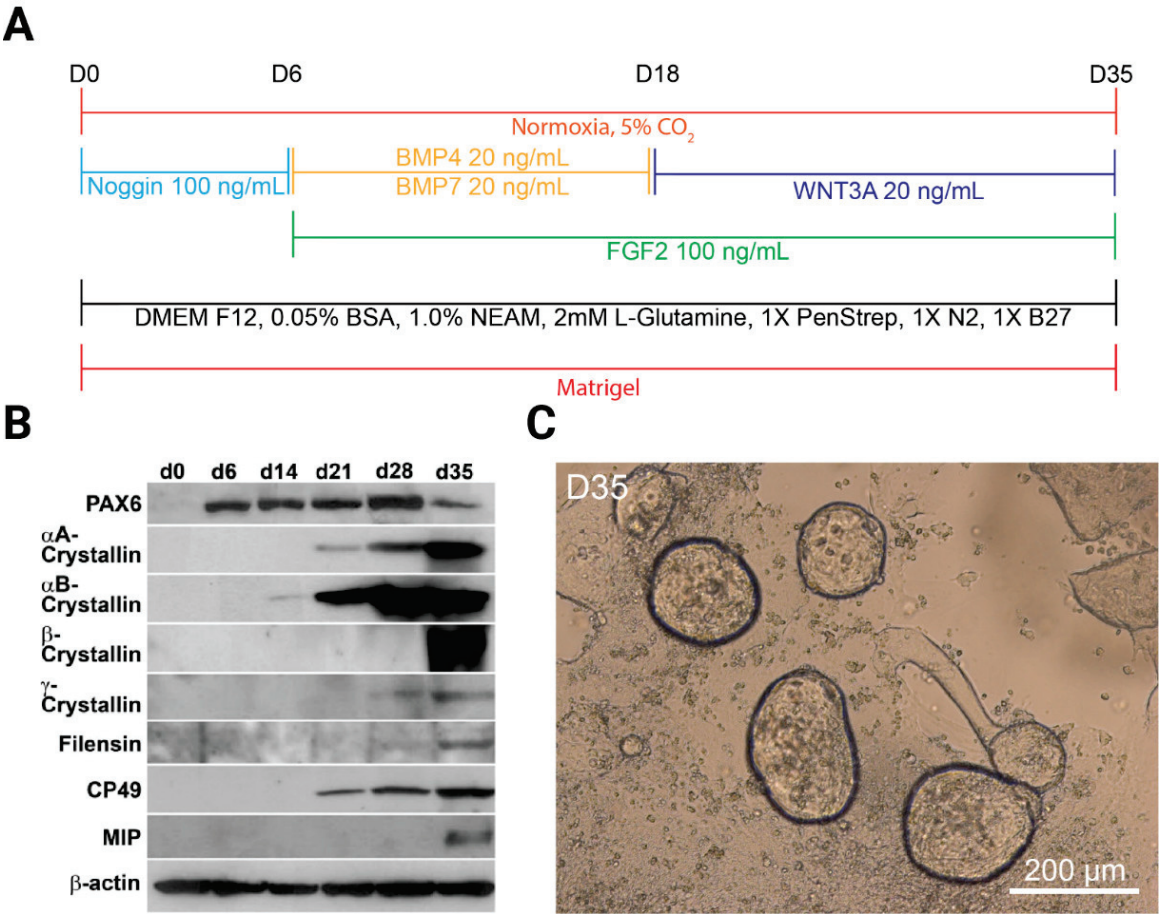

Figure 2. Summary of three-stage procedure to generate human lentoid bodies. (**A**) Lentoid bodies were differentiated over a 35-day period on Matrigel using specific concentrations of Noggin, BMP4, BMP7, FGF2, and WNT3A at the time points shown. Additional components and their concentrations of the basal medium are also shown [125]. (**B**) Western blot analysis shows expression of key lens markers PAX6, αA-, αB-, β-, and γ-crystallins, filensin (BFSP1), CP49 (BFSP2), and MIP (AQP0). Expression of β-actin was used as a loading control [125]. (**C**) Brightfield image of lentoid bodies produced at day 35 of differentiation.

Stage 1 was followed by activation of BMP and FGF signaling by BMP4, BMP7, and FGF2 to generate lens progenitor cells (stage 2) and completed by FGF2 with or without Wnt3a stimulation of lens fiber cell differentiation to generate 3D lentoid bodies (stage 3) using human H1 ES cells (WiCell) [126]. Matrigel (see above) was particularly selected as the major lens capsule core structural proteins are laminin [122] and collagen IV [121], together with smaller quantities of nidogen [123] and perlecan [125]. Lens progenitor cells were identified via expression of transcription factors PAX6, SIX3, and SOX2 and the onset of αB-crystallin (CRYAB) expression (Figure 2B). Lentoid body formation peaked by day 29, producing over 100 lentoid bodies per cm^2. The lentoid bodies (day 35) were analyzed by scanning and transmission electron microscopy, immunofluorescence, and Western immunoblotting. The cells forming lentoid bodies expressed high levels of crystallins; however, enucleated lens fibers were rarely detected at day 35 of the cultures [126]. This timing could be a consequence of the fact that normal lens fiber cell de-nucleation in humans occurs much later, as primary lens fibers are formed at seven weeks of gestation. Taken together, this three-stage protocol from 2010 recapitulates three phases of normal lens formation, i.e., formation of neuroectoderm and surrounding naïve ectoderm, emergence of lens progenitor cells, and their transition into crystallin protein-expressing cells.

Using this protocol, age-related cataract patients were used as a source of lens epithelial cells to be reprogrammed into iPS cells via lentiviral transduction of Oct4, Sox2, Klf4, and c-Myc "Yamanaka factors" [6]. The individual human iPS cells were subsequently used to remake the "normal" lens cells and lentoid bodies [127,128] using the three-step protocol [126].

A different approach was based on the ability of Pax6 and Six3 to induce ectopic lenses (see above). Pax6 or Six3 expression vectors were used to transduce human and mouse ES cells grown on inactivated mouse embryonic fibroblast feeders, including engineered mouse cells expressing green fluorescent protein under the control of the Pax6 lens-specific promoter/enhancer in 2014 [129]. Interestingly, lens markers were expressed by cells close to the transduced cells, suggesting that these cells adopt a lens fate by a non-cell-autonomous mechanism [129]. Cell aggregates expressing γA-cystallin proteins were already found at day 7 following their transition into lentoid bodies analyzed at day 30. Both the lens epithelial cell marker transcription factor Foxe3 and fiber cell abundant transcription factor Prox1, RNA-binding protein Tdrd7, α- and β-crystallins were expressed in the mouse ES cell-derived lentoid bodies [129].

In another study, mouse iPS cells from fetal fibroblasts were generated from transgenic mice in which the αA-crystallin promoter [130] was linked to the tdTomato fluorescent reporter gene [131]. The non-viral reprogramming was conducted using a "Sleeping Beauty" multi-cistronic transposon system including mouse Oct4, Sox2, Klf4, and c-Myc cDNAs separated by sequences coding for the self-cleaving 2A peptides [132]. Three cell lines (NTERA-2, P19, and control STO cells) were evaluated as feeder cells, while no individual growth factors were tested. Human NTERA-2 cells are committed neuroectodermal cells and mouse P19 cells are known to differentiate into all three germ layers. The first tdTomato-positive cells were found around day 28 of cultures using NTERA-2 and P19 feeder cells. Some of these cells organized themselves into lentoid bodies analyzed at day 45 for light refraction [131]. Note that normal mouse lens morphogenesis, defined by the formation of OFZ, is completed around E18.5. Thus, the feeder cells likely express suboptimal concentrations and/or combinations of factors that promote lens cell fates and lentoid bodies.

Three of the four mentioned studies [126,129,131] have independently concluded that relatively simple cell culture conditions generate 3D lentoid bodies analyzed in detail between 5 and 7 weeks of cultures. Engineering of cells with fluorescent reporters provides advantages for rapid screening of the differentiating cells [129,131]. Nevertheless, no systematic analyses of cell fate decisions towards the lens and its alternatives as well unbiased analysis of all cell populations present on the dish and their dynamic changes during the individual stages of the three-stage protocol [126,127] or both single-stage protocols were conducted [129,131].

Regarding contemporary eye research (2011–2012), parallel studies generated 3D optic cups from ES/iPS cells using Matrigel and a few distinct small-molecule drugs without any lenses within their concave openings [110,133]. These studies highlighted the concept of self-organization (see Sections 1, 5.2 and 7 for additional information) as the mechanistic foundation explaining in vitro formation of 3D biological structures [7]. For comparisons, the procedures to generate retinal and eye organoids of various complexity [105,110,111,126,129,131,134–162] are listed in Table 1, as they are important for human eye disease modeling (see Section 6).

Table 1. A representative list of human ES/iPS differentiation methods to generate the entire spectrum of ocular cell types.

Tissue(s)	Cells	Differentiation Procedures, Outcomes, and References	Growth Factors/Small Molecules *
Whole eye-like structures	mESCs	PA6 feeder cell system, self-organizing ocular-like structures including RPE, lens, neural retina [105]	**None**
Whole eye-like structures	hiPSCs	Self-formed ectodermal autonomous multi-zone (SEAM) protocol using highly specific LN211E8 laminin matrix, self-organizing ocular-like structures including RPE, lens, neural retina, and cornea [134]	**Noggin, SB431542, FGF2,** KGF, Y27632
Whole eye-like structures	hiPSCs	2-step method to obtain self-organized multizone ocular progenitor cells (mzOPCs) on Matrigel → isolated 3D-suspension culture producing RPE, neuroretina, cornea-like structures with less frequent clusters of lens cells [135]	**Noggin, DKK1 IGF1, FGF2** followed by IGF1 and ATRA, completed by IGF1 and ATRA (cornea) or IGF1 and T3 (photoreceptors and RPE)
Lens progenitor cells and lentoid bodies/micro-lenses	hESCs, hiPSCs	3-stage protocol on Matrigel, self-organizing lens progenitors and lentoid bodies [126], "fried egg" modification [136], ROR1-based cell sorting [137], and large-scale use [138]	**Noggin, BMP4, BMP7, FGF2, WNT3A**
Lens and other placodes	hESCs hiPSCs	Dual-SMAD inhibition (dSMADi) using Matrigel, self-organizing anterior pituitary, trigeminal, and lens placodes [140–142]	**SB431542, Noggin, SHH, SU5402, FGF2**, FGF8, BMP2, BMP4
Lens and other placodes, lentoid bodies	hESCs	Matrigel-grown cells in insulin-transferrin-selenium (ITS) serum-free medium, HGFR (c-MET), and CD44 sorting to isolate proliferative lens epithelium populations [143]	**None**
Pre-placodal ectoderm, lens placodes, and early lens spheres	hESCs	Adherent culture on Matrigel differentiated into pre-placodal progenitors able to produce lens placode, pituitary, and other precursors [144]	**Noggin, SB431542, BMP4, bovine vitreous humor**, FGF2, 6-BIO (GSK3β inhibitor), dorsomorphin (AMPK inhibitor), **LDN193189, cyclopamine** (SHH inhibitor), RA, purmorphamine (Smo receptor agonist)
Lens progenitor cells and lentoid bodies	mESCs hESCs	Transfection and transduction of *Pax6* and *Six3* induced differentiation of lens progenitor cells grown on mouse embryonic fibroblast feeder cells [129]	**None**
Lens progenitor cells and lentoid bodies	miPSCs	Engineered miPSCs with Cryaa/tdTomato reporter were grown on NTERA-2 and P19 feeder cells [131]	**None**
RPCs and optic cups	mESCs hESCs	Self-organizing optic cups, retinal progenitors, neural retina in Matrigel suspension culture [110,111]	Y27632, IWR1e, SAG, CHIR99021
RPCs (floating retinas)	hESCs	Retinal organoids formed from floating cysts suspended in Matrigel [145,146]	Y27632
RPC and photoreceptors	hiPSCs	Self-organizing suspension culture system that generates retinal cups with all major retinal cell types [147]	RA
Neural retina and RPE	hESCs	Generation of retinal organoids with increased efficiency using IGF-1 signaling [148]	IGF1

Table 1. *Cont.*

Tissue(s)	Cells	Differentiation Procedures, Outcomes, and References	Growth Factors/Small Molecules *
RGCs	hESCs	Generation of transplantable retinal ganglion cells in Matrigel culture [149,150]	Forskolin, IDE2, DAPT, dorsomorphin, nicotinamide
Cone photoreceptors	hESCs	Generation of M- and S-opsin-positive cones with outer segment-like structures in Matrigel culture [151]	Noggin, DKK1, IGF1, DAND5/COCO, FGF2
RPE	hiPSCs	Efficient generation of RPE cells by chemically defined conditions using a triphasic protocol [152]	LDN193189, SB431452, CKI-7, IGF1
RPE	hiPSCs	RPE cells generated by an unbiased differentiation approach using high-throughput compound screen and hiPSC-based RPE reporter assay [153]	Chetomin, nicotinamide
Corneal epithelium	hiPSCs	Biphasic culture method using CnT-30 media that transitions from suspension to adherent culture generating corneal epithelium [154]	SB505124, IWP-2, FGF2
Corneal epithelium	hiPSCs	4-stage protocol transitioning from suspension to adherent culture using supplemented hormonal epithelial medium and small drug ROCK inhibitor, Y27632 [155]	Y27632
Corneal epithelium	hiPSCs	Biphasic culture method using CnT-30 media that transitions from Matrigel- to Collagen-IV-coated plates [156]	BMP4, Trans-RA, EGF, SB505124, IWP-2, LDN193189, Y27632, SB431542
Corneal endothelium	hiPSCs	Corneal endothelium cells generated using TGF-β inhibitor and GSK-3 inhibitor cultured on laminin-521 [157]	LDN193189, SB431542, CHIR99021, RA
Corneal limbus	hiPSCs	Corneal limbal progenitors derived using Panserin 801 medium supplemented with BMP4 cultured on fibronectin and laminin [154,158]	BMP4
Trabecular meshwork	miPSCs	Induction of trabecular meshwork (TM) cells using miPSCs cocultured with human trabecular meshwork (TM) cells [159]	None
Trabecular meshwork	miPSCs	Induction of TM cells using miPSCs using media conditioned by human TM cells [160]	None
Trabecular meshwork	miPSCs	Two-step induction of TM cells through verification of neural crest cell intermediary stage grown in TM cell-conditioned media [161]	Y27632
Periocular mesenchyme	hESCs	Periocular mesenchymal cells generated from hESCs using TGF-β and WNT signaling inhibition [162]	SB431542, ATRA, IWP-2

* Growth factors/small molecules listed here were used towards the lens cells and lentoid bodies (**bold font**, see Table 3 for details). Other factors evaluated (alone or in combinations) in the systems for other purposes are shown to illustrate the range and spectrum of currently known possible treatments of eye organoids. Abbreviations/codes: All-trans retinoic acid, ATRA; GSK3 inhibitor, CHIR99021; CKI-7, casein kinase 1 inhibitor; DAN domain BMP antagonist family member 5 DAND5 (COCO), γ-secretase inhibitor, DAPT; epidermal growth factor, EGF; small-molecule inhibitor of Wnt signaling, IWP-2; Wnt/β-catenin signaling inhibitor, IWR1e; fibroblast growth factor 7, FGF7 (also known as keratinocyte growth factor, KGF); Rho kinase inhibitor, Y27632; SAG, hedgehog pathway activator of SMO receptor; GSK3α/β inhibitor, 6-BIO; inhibitor of TGF-β receptors, SB505124; triiodothyronine, T3.

4. Complex Differentiation Procedures: Induction of Cranial Placodes and Parallel Formation of Lenses Together with Other Ocular Tissues

Although generation of isolated lentoid bodies alone is an important model system with inherited limitations, some of which are described above, production of lens cells together with other ocular tissues ("community-grown" lenses) should provide additional opportunities for research focused on mechanistic aspects of early lens development and eye tissue engineering. This section will thus provide background and accomplishments of the field to generate in vitro adenohypophyseal, olfactory, and lens anterior cranial placodes, normally produced during late stages of mammalian gastrulation.

Early lens development originates from cells located at the border between the anterior neural plate and surface ectoderm, called the anterior pre-placodal region [27,28,33,34,163–165]. The common Pax6$^+$ cells emerging in the pre-placodal region give rise to three cranial placodes, including the non-neurogenic adenohypophyseal/anterior pituitary placode, neurogenic olfactory, and non-neurogenic lens placodes (Figure 1B–D). Thus, it was of interest for both the lens research field and the basic science questions regarding growth factor-directed differentiation of ES and iPS cells towards neuroectoderm [166] to directly examine the formation of all early placodal progenitors [140–143]. Other studies probed formation of more posterior optic placodes [167] and SOX10$^+$ neural crest cells [142,168,169].

4.1. Dual-SMAD Inhibition and Generation of Placodal Precursors

It has been shown earlier that neuronal cells are induced via concomitant inhibition of BMP and TGF-β, Activin, and Nodal signaling by Noggin and small drug SB431542 (see Table 3), called dual-SMAD inhibition (dSMADi), using Matrigel-coated dishes [166]. De-repression of endogenous BMP signaling that follows the initial generation of neuronal cells, typically after day 3 of cultures (Figure 3), results in robust generation of over 70% of placodal precursor cells marked by expression of SIX1, DLX3, and EYA1 (Table 2) by day 11 of the cultures [140].

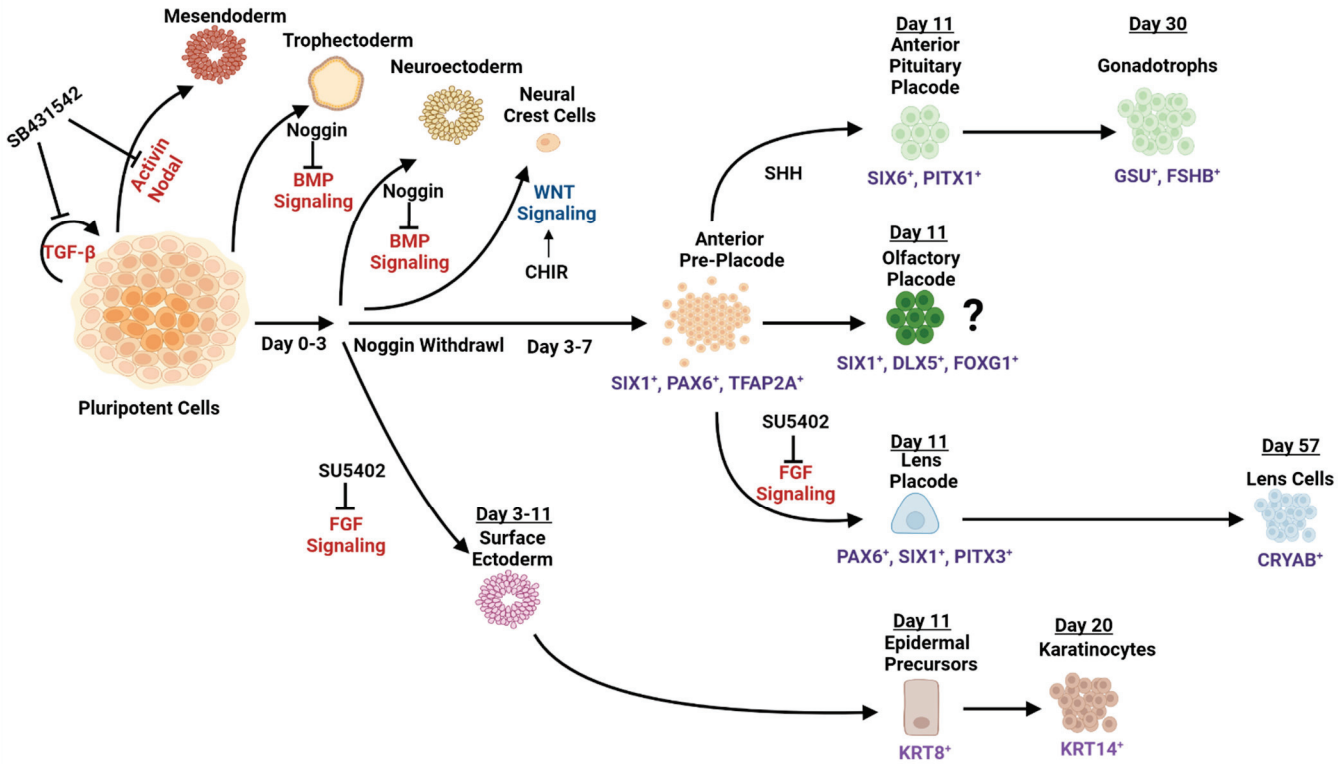

Figure 3. A summary model of the generation of anterior placodes from hPSCs using the dSMADi-based procedures. The diagram illustrates multiple cell fate decisions of the pluripotent stem cells,

including those following Noggin- and SB431542-mediated phase of inhibition and TGF-β, Activin, and Nodal signaling inhibition [139]. Formation of anterior pre-placodal cell fate commitment can be subsequently induced through BMP activation. In contrast, epidermal precursors can be generated through surface ectoderm induction mediated by FGF inhibition. The anterior pre-placodal cells can generate anterior pituitary placodal cells through activation of SHH signaling to produce gonadotrops at day 30 of the cultures [139]. Note that these cells treated subsequently by FGF8, BMP2, and both factors together generate hormone-producing cells analyzed at day 60 [140]. The olfactory placodal cell fate pathway analysis was limited to identification of a few cell markers, SIX1, DLX5, and FOXG1, and is marked (?) accordingly. Addition of BMP4 between days 7 and 11 increased the expression of lens lineage-specific transcription factors PAX6 and PITX3. Lens placodal cells were enriched through inhibition of FGF signaling by SU5402 at day 7, followed by analyses of lens placode markers PAX6, SIX3, and PITX3 and subsequent formation of αB-crystallin-expressing cells analyzed at day 57 [139].

Regarding lens placodal cell fate (Table 2), re-analysis of data shows increased expressions of transcription factors GATA3 [170] and TFAP2A [171] at days 7 and 11 of the cultures, respectively. At day 11, the cultures also increased the expression of ALDH1A3 and ALDH1A1, both found in the early mouse pre-placodal cells (Table 2). Use of the specific inhibitor of FGF signaling SU5402 (Table 3) blocked placodal cell formation and promoted the formation of surface ectoderm marked by high levels of keratin 14 (KRT14) expression (Figure 3). Increased concentrations of BMP4 also suppressed placodal cells while formation of putative trophectoderm cells increased.

Table 2. Marker genes expressed during the formation of lens and olfactory placodes.

Region	Stage	Genes Expressed [33,163–165]
aPPR	E8–8.5	Dlx2, Dlx5, Foxg1, Otx2, Six1, Six4
Lens/olfactory	E8.5–8.75	Aldh1a1, Aldh1a3, Gata3, Pax6, Six1, Six3
Lens	E9–E9.5	Aldh1a1, Aldh1a3, Cryab, Eno1, FoxE3, Gata3, Has2, Lama1, Mab21l1, Maf, Mafb, Prox1, ROR1, Six3, Sox2
Olfactory	E9–E9.5	Aldh1a3, Dlx6, Dmrt4, Emx2, Ebf2, Fgf8, Foxd4, Ngn1, Pax6, Six1, Six4, Sox2, Sox3

Table 3. Growth factors and small-molecule drugs used in lens progenitor cell and lentoid bodies' formation.

Growth Factor or Inhibitor	Structure, Function, and References	Application in Generation of Lens Progenitor Cells and Lentoid Bodies
Noggin	BMP inhibitor (232 aa, 25.7 kDa), adopts a cysteine-knot fold tertiary structure to form a homodimer that binds BMP homodimer to form a ring-like structure that prevents BMPs to interact with their receptors in a reversible manner [171], binds BMP2, 4–7, 13, and 14	Required for neuroectoderm induction [125,139,165]
FGF2	Heparin-binding protein family (288 aa, 30.7 kDa), globular structure comprised of β-strands, α-helices, and two turns, binds receptors FGFR1–4 [172]	Formation of lens progenitors [125], lentoid bodies' differentiation [135,136]
BMP4	SMAD signaling activator (408 aa, 46.5 kDa), homodimers bind type 1 receptors BMPRIA and type 2 BMPR2. Once these three molecules are bound together, BMPR2 phosphorylates and activates BMPR1A [48]	Epidermal induction, averts neural cell fate; formation of lens progenitors [125] and pre-placodal cells [139]

Table 3. *Cont.*

Growth Factor or Inhibitor	Structure, Function, and References	Application in Generation of Lens Progenitor Cells and Lentoid Bodies
BMP7	SMAD signaling activator (431 aa, 49.3 kDa), homodimers bind type 1 ACVR1 (ALK2) and BMPRIB (ALK6), and type 2 receptor ACVR2A [173,174]	Used to generate lens progenitor cells and lentoid bodies [125]
WNT3A	β-catenin-dependent Wnt signaling activator (352 aa, 39.4 kDa), binds receptors Frizzled, LRP5, and LRP6 signaling complex [175]	Improves FGF2-dependent lentoid body formation [125]
DKK1	β-catenin-dependent Wnt inhibitor (266 aa, 28.7 kDa), binds via C-terminal Cys-rich domain co-receptor LRP6 via a tandem of β-propeller regions [176]	Formation of the presumptive lens ectoderm in SEAM [133]
IGF-1	Secreted insulin-like growth hormone (195 aa, 21.8 kDa), binds to the α-subunit of IGF1R receptor and integrin complexes ITGAV:ITGB3 and ITGA6:ITGB4 [177]	Promotes formation of 3D primitive ocular-like structures that contain primitive lenses [178]
SB431542	SMAD signaling inhibitor drug derived from benzamide (MW: 384), inhibits type 1 receptors TGFBRI (ALK5), ACVR1B (ALK4), and ACVR1C (ALK7) [179]	Neuroectoderm induction (dSMADi) [139,165]
SU5402	Pyrrole-3-propanoic acid derivative (MW: 296), inhibits tyrosine kinase receptors VEGFR2, FGFR1, and PDGFRβ [180]	Disrupts placode induction and triggers epidermal cell fate and later promotes lens cell formation [139]
LDN193189	Pyrazolol and pyrimidine derivative of quinoline (MW: 406.5), inhibits type 1 ACVR1 (ALK2), BMPR1A (ALK3), and BMPR1B (ALK6) receptors [181]	"Transitional" BMP inhibition by this drug favors expression of PAX6, while BMP4 added later strongly induces lens placodal cells [143]
Cyclopamine	Steroidal alkaloid (MW: 411.6) with a high affinity for cell surface membrane protein Smoothened (SMO), a G-protein-coupled receptor (class F) which works downstream of Sonic hedgehog (SHH) 12-pass transmembrane protein receptor Patched (PTC) [182–184]	Inhibition of SHH signaling by this drug boosts FOXE3 and CRYAA expression [143]

Four cell lineages were characterized in detail in this pioneering study, including anterior pituitary, lens placodes, and neurogenic trigeminal sensory neuron placodes (not shown in Figure 3), as well as the ectoderm pathway. Purified placodal cells can be subsequently differentiated by a combinatorial action of Sonic hedgehog (SHH), FGF8, and FGF10 into pituitary-like cells at day 30 of the cultures [140], and subsequently into three groups of hormone-secreting pituitary cells by FGF8 or BMP2 alone, or by a combination of FGF8 and BMP2 [141]. The procedure did not show any data on the olfactory placode; nevertheless, the authors stated that FGF8 increased ASCL1 [140]. In fact, multiple genes found in the olfactory placodes (Table 2), including ALDH1A1, GATA3, FOXG1, and SIX1, were induced between days 5 and 11, as shown by their transcriptomic and/or protein analyses. Addition of BMP4 at days 7–11 increased the expression of lens lineage-specific transcription factors PAX6 and PITX3. Surprisingly, use of SU5042 (see Table 3) at days 7–11 of cultures also promoted expression of both these genes, culminating in detection of αB-crystallin (CRYAB)-positive cells at day 57 (Figure 3).

4.2. Alternate Methods to Generate Multiple Placodal Progenitors

Two additional independent studies also examined the formation of multiple placodal progenitors, including lens cells (Table 1), using human H9 ES cells grown on

Matrigel [143,144]. The undifferentiated human ES cells were first dissociated into single cells and grown on Matrigel in the presence of standard human ES cell medium supplemented with 8 ng/mL of FGF2 and Rho kinase inhibitor Y27632, that was removed 24 h after the passage [144]. After day 2 or 3, three different media were used to direct differentiation towards neural and neural crest, pre-placodal ectoderm, and epidermis. Serum-free medium promoted the expression of both early (SIX1, GATA3, and TFAP2A) and advanced (SIX1, EYA1, EYA2, and DACH1) pre-placodal markers (Table 2), regulators of lineage-specific transcription. Addition of 20 ng/mL of BMP4 promoted placodal formation. In contrast, Noggin (300 ng/mL) reduced the expression of these markers and the number of $SIX1^+$ cells [144]. Interestingly, transitional addition of the drug inhibitor of BMP signaling LDN193189 (Table 3) increased the expression of PAX6 and the number of $PAX6^+$ cells increased 7-fold, with 90% of them co-expressing both PAX6 and SIX1 and PAX6 and DLX5 transcription factors. Prolonged cultures in serum-free conditions expressed high levels of PAX6 and FOXE3 but no αA-crystallin (CRYAA) expression was found. Addition of 20 ng/mL of BMP4 induced the expression of αA-crystallin proteins [144]. Next, bovine vitreous humor was used as a source of natural factors, promoting lens differentiation [185]. While primitive spheres of lens cells were found, no signs of lens fiber cell differentiation were observed, pointing to differences between in vitro-generated lens cells and primary lens cell cultures. The data further showed expression of two corneal markers, keratins KRT3 and KRT15, implicating induction of corneal epithelial cells. Finally, SHH signaling was examined via the inhibitor cyclopamine (Table 3) and the SMO receptor agonist purmorphamine. As expected from earlier studies [41,186], inhibition of SHH increased the expression of FOXE3 and CRYAA, while addition of purmorphamine abolished the expression of lens markers and increased the expression of oral ectoderm marker transcription factors PITX1 and PITX3 [144].

A parallel study of the formation of cranial placodes from the neural plate border employed fluorescence-activated cell sorting (FACS) to analyze proportions of lens cells within the cultures [143]. For the positive selection of lens cells grown in serum-free medium (Table 1), the hepatocyte growth factor receptor (HGFR, also known as c-MET) was used, while p75, HNK1, and CD15 were used for the negative selection. More advanced cell cultures showed expression of the hyalouran receptor CD44, which is expressed in cortical lens fibers [187]. Quantitative analyses showed very small percentages (<1%) of putative lens cells as both these receptors are also expressed in many different cell types. The small fraction of $p75^-$, $HGFR^+$, HNK^-, $CD44^+$, and $CD15^-$ cells generated lentoid bodies within 10 days, analyzed by the expression of CRYAA, BFSP1, and MIP genes [143].

4.3. Placodal Cells and Their Quantities

The three studies discussed above demonstrate that cell fate choices in differentiated pluripotent stem cells generally recapitulate normal embryonic development; however, their specific outcome is dictated by an intricate complexity of cell fate decisions governed by temporally and spatially controlled canonical signal transduction pathways, in the case of anterior neuronal development and its nearby border region, the BMP, FGF, and SHH signaling pathways [188]. While olfactory placode formation is a major component of these processes during normal embryogenesis (Figure 1), the above studies provided very little insights into this pathway. Nevertheless, a recent study employed human iPS cells (WiCell) grown on Matrigel using serum-free ITS medium (see above), which generates olfactory placodal cells [189]. Inhibition of BMP signaling via LDN193189 (Table 3) promoted the expression of genes encoding transcription factors DLX5, EMX2, and POU2F1 and blocking the expression of FOXE3. Additional growth factors tested for olfactory placodal cells included FGF8, TGF-α, and SB431542, and Wnt signaling inhibitors [189]. Taken together, lens cells are generated by these "universal" systems at much smaller quantities (<1%) compared to the 41% of $PAX6^+$ and $CRYAA^+$ cells generated by the 3-stage protocol [126]. A possible interpretation of these efficiencies may be related to the model in which lens cell fate specification is the ground state for other anterior placodes [190].

5. Advanced Procedures to Generate Lentoid Bodies

5.1. Cell Sorting and Isolation Prior to Cell Differentiation

Two advanced methods further explored efficient generation of lentoid bodies via manual dissection of cell aggregates [136] or cell surface-driven isolation of lens progenitor cells [137]. Using the three-stage lens differentiation protocol [126], the mechanical isolation of cell aggregates both increased the efficiency and reduced the time taken for the formation lentoid bodies. This 2017 protocol was coined as the "fried egg" method due to the selection of colonies that formed dense clusters of differentiating cells surrounded by support cells. These "fried egg"-like colonies were characterized as a dense center of E-cadherin-positive cells surrounded by a monolayer of E-cadherin-negative cells, where differentiation of lentoid bodies would occur from the center.

After Noggin treatment for six days, cells with epithelial-like morphology around the periphery of the colonies were mechanically isolated, re-seeded, and cultured under the three-stage differentiation conditions. By day 11, colonies that have formed "fried egg"-like structures were further differentiated. At day 14, immature lentoid bodies began to form. These immature lentoid bodies were characterized by loss of expression of the lens epithelial marker FOXE3 when compared to the surrounding support cells. Cells were then differentiated in the presence of FGF2 and WNT3A. By day 25, mature lentoid bodies expressed αA-, αB-, β-, and γ-crystallin proteins [136].

An important finding during the development of this method was the effect of cell-seeding density and colony size on the efficiency of lentoid body formation. Optimal seeding density was ~40 colonies per 35 mm culture dish containing ~50 cells per colony, which yielded the largest size and number of lentoid bodies. Higher seeding densities either reduced the number of "fried egg" colony formations or created colonies that had "multiple fried egg" structures that did not produce lentoid bodies [136]. Transcriptome profiling of lentoid bodies generated from the "fried egg" method show a >96% overlap in differentially expressed genes (DEGs) when comparing iPSC- vs. hESC-derived culture systems with a 95% quantitatively similar transcriptome profile (within 2 standard deviations) [136].

Importantly, proteome changes of lentoid bodies generated from the "fried egg" using both 25- and 35-day cultures revealed little to no change in proteome when compared to P0.5 mouse lens epithelial and fiber cell proteomes [136], reaching concordance levels of >93% and >92%, respectively [191]. When compared with E14.5 mouse lens epithelial and fiber proteomes, 25- and 35-day cultures showed 89% and 90% overlapping of lens proteins, respectively [192]. More than 5000 proteins not reported earlier [193] were expressed in lentoid bodies [191]. Hence, the authors proposed that non-lens-associated proteins are from a mixed population of lens-associated cells that support lentoid body differentiation and maturation [191].

In a parallel study, cell sorting of lens epithelial cells based on the expression of the receptor tyrosine kinase-like orphan receptor 1 (ROR1) surface marker was accomplished in 2018 [137]. ROR1 was identified from previous lens microarray data as a potential cell surface marker for lens epithelial cells [194]. Further analyses found enriched expression of ROR1 in E14 mouse lenses and during the second stage of the original three-stage procedure. In addition to the magnetic-activated sorting (MACS) step, this method increased the Noggin concentration from 100 to 500 ng/mL and included 10 mM of SB431542 (Table 3) in stage 1 (Figure 2). Stage 3 was also modified by reducing the concentration of FGF2 to 10 ng/mL. Collectively, these conditions optimized the previous "naïve" protocol via selective proliferation of the $ROR1^+$ cell population [137].

Hence, for the first time, this modified protocol allows for the large-scale purification of lens epithelial cells from human pluripotent stem cells [137]. Prior to this method, lentoid bodies were generated spontaneously with random shape, size, and a heterogeneous population of cells. This process was scaled using forced aggregation of $ROR1^+$ cells into ~100 μm aggregates at a density of 1200 aggregates per well of a 24-well plate. Cell aggregates were cultured for three weeks in the presence of both FGF2 (100 ng/mL) and WNT3A (20 ng/mL). After only three weeks, lentoid bodies exhibited a remarkable

refractive and light-focusing capability. Interestingly, the light transmittance quality of lentoid bodies was associated with changes in α-, β-, and γ-crystallin expression levels. Particularly, α- and β-crystallins were most abundant in lentoid bodies that focused light. Bulk RNA-seq data and analysis of DEGs also revealed expression of lens-specific integrins, laminins, and collagens that indicate the formation of the lens capsule. Evidence of lens capsule formation was also seen under ultra-structural analysis via transmission electron microscopy [137]. This method can generate tens-of-millions of human lens epithelial-like cells [139]. The analyses included unbiased single-cell RNA-seq (scRNA-seq) and mass spectrometry combined with light and electron microscopy, including microscopical evidence for the formation of gap junctions between fiber-like cells, general reduction of subcellular organelles, and early stages of de-nucleation. Additional analysis of the scRNA-seq data obtained from ROR1$^+$ lens epithelial cells was reported elsewhere [195].

Taken together, concerted efforts from multiple directions established diverse experimental models to generate lens progenitor cells at different efficiencies. High-yielding lens systems have the power of generating 3D lentoid bodies and micro-lenses of different complexity, while low-yielding systems of lens progenitor cell formation are highly relevant to study cell fate decisions that mimic the formation of the anterior pre-placodal ectoderm and cell signaling processes underlying the formation of non-neurogenic adenohypophyseal and lens and neurogenic olfactory placodes.

5.2. Complex Cell Cultures Generating "Byproduct" Lens Cells

Three-dimensional-laminated neural retinal organoids can be produced from human H9 ES cells in a minimal medium containing neural supplements B27 and N2 [196]. Low-attachment bacteriological dishes were used. A follow-up study in 2015 found that addition of IGF-1 (Table 3) at 5 ng/mL until day 37 and at 10 ng/mL in basal knockout serum-free medium (until day 90) stimulates production of bi-layered optic cups with maturing photoreceptor cells, though most of the organoids had reverse laminar organization (Table 1) [179]. Interestingly, clusters of lens-like cells were found in these cultures and immunofluorescence data exist for lens proteins PAX6, SOX1, CRYAA, and CRYAB. Some of these cells did not generate positive nuclear staining, indicating active de-nucleation processes. In addition, emergence of corneal epithelium-like cells was visualized by keratin 19 (CK19) [179].

Another system, called "self-formed ectodermal autonomous multi-zone" (SEAM), was developed in 2016 from a collection of human iPS cells from the RIKEN Bio Source Center using StemFit medium and LN511E8 isoform laminin-coated dishes (Table 1) [134]. These cells spontaneously form multiple primordia comprised of four concentric zones, 1–4, that were characterized by a collection of specific protein markers to identify different cell types in analogy with the human eyeball. For example, PAX6 was expressed in the inner zones 1–3, while the most outer zones 3 and 4 expressed surface ectoderm transcription factor TP63 and epithelial surface E-cadherin [134]. In the most inner zone 1, neural cell-specific transcription factors SOX2 and SOX6 and β3-tubulin (TUBB3) are expressed. Zone 2 expressed optic vesicle and neural crest cell transcription factors RAX and SOX10, respectively. At the margin of zones 2 and 3, αA-crystallin (CRYAA)-positive lens-like cells formed after four weeks of culture. Zone 3 is comprised from the future cells forming the ocular surface epithelium marked by PAX6, TP63, E-cadherin, and keratins K14 and K18 [134]. It was shown later that the 211 isoform of the E8 fragment of laminin (LN211E8) used as ECM promotes generation of dense hiPSC cell colonies due to actomyosin contraction. In turn, this leads to cell density-dependent YAP inactivation and subsequent retinal differentiation in the colony centers [197].

Consistent with earlier studies, the authors found that BMP signaling inhibitors (Table 3) Noggin and small-molecule LDN193189 block the formation of zone 3 and SB431542 disrupts the standard multi-zone formation, respectively [134]. No additional data on lens cells are available as the follow-up experiments focused on modeling of corneal development; nevertheless, several possible treatments and cell enrichments exist based

on the procedures summarized above. Both individual treatments and a range of concentrations, and their combinations, should be empirically tested during and after the basic 28-day SEAM protocol.

Finally, a two-step procedure to obtain self-organized multizone ocular progenitor cells (mzOPCs) on Matrigel was optimized to form 3D retinal, corneal, RPE, and multi-ocular organoids (Table 1) in 2021 [135]. While solid progress was accomplished towards these systems, lens cell formation was documented only via sparse detection of γ-crystallin-positive "lentoid cell clusters".

5.3. General Lessons from In Vitro Lens Cell Formation Studies in Diverse Pluripotent Cell Cultures

The lens-generating differentiation procedures used a wide range of experimental conditions (see Table 1, top nine procedures). Matrigel and a laminin variant (LN211E8) were employed as ECM proteins, and PA6, NTERA-2, P19, and embryonic fibroblast cells were used as feeders and/or inducers of differentiation (see above). The emerging common denominator between these procedures is the generation of neuroectodermal cells that are most likely a default stage of the normal ectoderm [198]. Termination of Noggin and dSMADi "deterministic" stages allow the cultured cells to exit this default mode and promote the emergence of new common progenitor lineages, including anterior placode progenitors. The subsequent steps of individual cultures differ from no growth factors/drugs added, to single (e.g., BMP4, IGF-1, and SU5402) and multiple combinatorial treatments (e.g., BMP4, BMP7, and FGF2, see Figure 2). Although no procedure quantitatively analyzed parallel formation of lens cells and other cell types, their variable outcomes reflect the heterogeneity of the presumptive transitional populations of biased, specified, and determined cell types and their responses to activation of TGF-β/BMP [48] and activation or repression of FGF/MAPK [49] signal transduction pathways. We propose that variable expression of multiple individual BMP and TGFβ type 1 and type 2 receptors and FGFR1-4 dimers and their particular sensitivities to the growth factors and/or their antagonists or agonists present on the cell surface modulate the outcomes towards each desired cell type, i.e., adenohypophyseal, olfactory, and lens placodes, as well as more posterior otic placodes [167]. In any case, the individual specified and determined placodal cells undergo migration and spontaneously self-organize into cell-homogenous clusters, from which more complex structures, such as the lentoid bodies/micro-lenses, ultimately emerge.

These cell culture models should help to resolve remaining questions regarding the cell fate determination of the individual placodal cells [188]. Chicken embryonic cell manipulations suggest that the lens program dominates early following placodal progenitor cell diversification [190], while other studies support the model of common lens/olfactory progenitors [36]. A paradox exists between the role of FGF2 and the SU5402 inhibitor of FGFR1 (Table 3) to generate lens cells in the three-stage [126,136,137] and dSMADi [140] protocols, respectively. Is it possible that the expression levels of individual FGFR2, FGFR3, and FGFR4 receptor proteins and their affinities to the prevalent FGF1, FGF2, FGF3, FGF8, FGF15, and FGF24 compensate for the selective block of FGFR1? Both these questions can be addressed via scRNA-sequencing and identification of transient populations of cells and determining their developmental trajectories and specific cell surface receptors, cell adhesion molecules, and ECM proteins required for their self-organization [199].

Finally, four treatments in combination with other growth factors offer improvements for the generation of lentoid bodies described above (see Sections 3–5). Early studies of IGF-1 [124,200] suggest use of this growth factor (Table 3) beyond what has been already accomplished [179]. In addition, RA is a powerful morphogen during normal lens development, crystallin gene expression, and lens regeneration [104,201–206]. Early studies in 1988 have shown that in vitro pulsatile delivery of platelet-derived growth factor (PDGF) dramatically increased rat lens growth in serum-free conditions [207]. PDGF is a dimeric glycoprotein and a potent mitogen binding a tyrosine kinase cell surface receptor PDGFR and cross-talks with both FGF/MAPK and phosphatidylinositol 3-kinase (PI3K)

signaling [53]. PI3K signaling is necessary for avian lens fiber cell differentiation and survival [208]. Importantly, a recent 2022 study of drug-mediated inhibition of PI3K signaling demonstrated that this pathway activates autophagy and generation of lens OFZ [209].

6. 3D-Eye Organoids: Experimental Challenges and In Vitro Modeling of Human Ocular Diseases

Significant progress has been made in the generation and molecular characterization of diverse systems, leading to the formation of lens progenitor cells and both isolated and "community-grown" lentoid bodies, as described above. Nevertheless, this field is poised for major advancements to produce the "next generation" of lens and eye organoids to more precisely model human eye development and diseases, provided that more accurate experimental conditions are established. To achieve these goals, we need to consider unique features of normal lens morphogenesis and current bioengineering tools.

During the formation of the lens vesicle and optic cup, the posterior portion of the lens interacts with a transient hyaloid vascular system, leaving the optic cup via its transient opening, the optic cup fissure [28,30,210–212]. This system, called tunica vasculosa lentis, is regulated by VEGF-A [213,214], transcriptional co-activator Cited2 [215], and cyclin-dependent kinase inhibitor 2a, Cdkn2a (other names: Arf and p16Ink4a) [216,217]. During the formation of primary lens fibers and closure of the optic fissure (E13.5–E14.5), this vascular system retrogresses and disappears, and the cavity between the lens and the retina is filled by the transparent vitreous humor gel [218]. Consequently, the anterior aqueous and posterior humors are the only source of oxygen for the lens [219–222]. Low levels of oxygen contained in the aqueous humor combined with the consumption of oxygen by the mitochondria-containing lens epithelial cells at the surface of the lens contribute to the overall low-oxygen environment at the lens surface [221,222]. Studies on interior lens oxygen levels revealed a 20-fold decrease in oxygen levels from the anterior surface of the lens to the equatorial region [221]. Consistent with this hypoxic environment, depletion of the basic helix-loop-helix transcription factor Hif1α in the mouse lens results in disrupted lens growth and ultimate degeneration [223]. Hif1α is the key regulator allowing cells to function in hypoxic conditions via blocking their ubiquitination [224,225]. When stabilized in hypoxia, its target genes promote survival in low-oxygen conditions. Most recent lens studies provide additional insights into these processes via detailed studies of Hif1α and batteries of its regulated genes, including direct regulation of mitophagy regulatory gene encoding BCl2-interacting protein-3-like protein Bnip3l by Hif1α [64,226,227].

Lens physiology is dramatically affected by degradation of mitochondria via mitophagy regulated by BCL2-interacting protein 3-like (Bnip3l, Nix) [228] as a prerequisite of the OFZ formation [62,63,229]. Thus, the majority of the lens requires anaerobic glycolysis, while oxidative phosphorylation is limited to outer regions of the lens fiber cell compartment [230,231]. In addition, the posterior vitreous contains a lower concentration of oxygen compared to the anterior aqueous humor chamber [232]. Finally, it is well-established that normal lens development and postnatal growth are regulated predominantly by BMP, FGF/MAPK, and Wnt signaling pathways [28,46,48,49,233]. Evidence exists that individual growth factors and their receptors are not evenly expressed along the lens vesicle and optic cup [27,35,234–237]. Taken together, lens physiology evolved very complex temporal and spatial regulation of key processes linked to its precise metabolic requirements as oxidative stress-caused damage to the lens proteins is detrimental to its transparency [238–242]. Thus, lens physiology under hypoxia represents an important parameter to be considered for the next generation of lentoid bodies.

6.1. Tissue Engineering and "Next-Generation" Eye Organoids

The next-generation lentoid bodies can be both grown isolated and as "community-grown" structures. Although current advanced procedures generate isolated lentoid bodies with some enucleated cells [136,137], these procedures are performed under normal oxygen concentrations. Thus, the next logical step is to perform "late" stages of their differen-

tiation in incubators, mimicking hypoxic conditions, testing a gradual reduction within ~10 days of culture or a stepwise reduction to 2–3 different lower concentrations, followed by their detailed morphological analyses. However, these procedures may not be suitable for community-grown lentoid bodies as other tissues require a normal oxygen concentration and some moderate hypoxia gradients are generated if the lens-like structures are surrounded by a mass of retinal cells.

The advanced differentiating lentoid bodies, classified by their size, shape, and transparency, can be transferred into Matrigel wells with variable levels (e.g., 1–5 mm levels of Matrigel) or scaffolds from various neutral materials (agarose) that contain a cluster of micropatterned elliptically shaped wells to support further growth of individual "reseeded" lentoid bodies. Various multi-compartmental biomaterial scaffolds are being developed and tested for 3D-cultures of pluripotent stem cells [243,244]. Physical properties such as biomaterial stiffness, crosslinking capacity, and density can aid cellular differentiation, especially if individual growth and differentiation factors are supplied with the biomaterials [244–246]. A more advanced approach is to design scaffolds that contain 50–100 ng/mL of FGF2 and the cell culture medium will contain only lower FGF2 concentrations (e.g., 5 ng/mL) to support growth and survival of the lens epithelium. A higher FGF2 concentration at the bottom of the well should promote lens fiber cell differentiation [247]. Gradients of BMP2 and FGF2 were already used in sub-micron polystyrene fibers and evaluated in myocyte differentiation [248]. More recent examples are printed collagen/chitosan scaffolds with stable FGF2-STAB [249]. An alternative to Matrigel is to prepare proteins from bovine lens capsules at a large scale or to model capsule protein composition using ECM proteins collagen IV, laminin, and smaller amounts of nidogen and perlecan [250,251]. Additional proteins to include are various heparane sulfate proteoglycans as they bind FGF1 and FGF2 [252,253] as well as entactin [254].

Another possibility is to mechanically insert lentoid bodies into the optic cups, initially grown individually. Most likely, the optimal approach would be to print "elastic" scaffolds to mimic the optic cup shape and transfer optic cups from floating cultures and allow them appropriate time to adjust to these microenvironments. Following their adaptation, individual lentoid bodies would be "transplanted" and covered by a biodegradable sheet to assure their smooth adoptions by the individual optic cups.

The original method to produce whole eyes [105] can also be tested using human pluripotent stem cells. Next, genome engineering by CRISPR-Cas9 can generate fluorescently labeled fusion proteins such as VSX2-GFP and CRYAA-dTomato to visualize retinal and lens cells, respectively. This double-labeling will aid in the identification of appropriate organoids for long-term cultures. All these tissue-engineering approaches may be needed to establish optimized procedures to produce "dream" lentoid bodies with nearly perfect morphology, including lens sutures as the zones of discontinuity [255].

6.2. Advantages of Modeling Human Embryonic Lens Development

The formation of adenohypophyseal, olfactory, and lens placodal cells described above (see Section 4, Figures 1 and 3) is the first direct demonstration of generating anterior pre-placodal ectoderm using a human model, while prior studies employed chicken [36,190,256–258], frog [259], and zebrafish cells [260,261]. This model of neural induction and neural plate border was recently re-examined. Interestingly, the chick "pre-border" cells were found comparable with mouse ES cell transcriptomic signatures [262]. Detailed analyses of scRNA-seq analysis of mid-gestation mouse embryos [263–265] identified trajectories leading to the individual placodes; nevertheless, the spatial information on cell heterogeneity around the neural plate is still missing. Thus, sorting of pre-placodal cells, visualization of cell migration, and placode aggregation can be modeled using engineered pluripotent stem cells coupled with analysis and direct visualization of individual cells and their clusters.

An impressive number of mouse in vivo models exists that probe cell cycle-coupled differentiation of lens fiber cells using loss-of-function [235,266–270] and

gain-of-function [271–275] models. Nevertheless, a number of open questions remain to be addressed that require large-scale protein purifications and analyses of protein–protein complexes and their post-translational modifications at different stages of the cell cycle, e.g., to probe formation of E2F-pRb [275,276], Pax6-pRb complexes [277,278], and interactions between FGF receptors, other membrane proteins, and their intracellular components [53,235,279–288]. Although dramatic progress with ChIP-seq methods using CUT&RUN, recently implemented in chicken lens studies [226], requires smaller number of cells, genome-wide analysis of lens chromatin occupancy by multiple DNA-binding transcription factors regulating these processes, including p53 [266], Gata3 [289], Hey1 [269], Prox1 [289,290], and Rbpj [291–293], can now be performed in parallel with analyses of modified histones and histone variants in chromatin isolated from micro-dissected lenses. For example, loss-of-function of CBP and EP300 histone acetyltransferases disrupts mouse lens placode morphogenesis [294]; however, apart from Pax6, the transcription factors recruiting these enzymes remain mostly unknown in the lens. In addition, we have very limited knowledge on genome localization of nuclear effectors of BMP and FGF signaling in the lens, including transcription factors such as c-Jun, Etv1, Etv4, Etv5, Smad1/5/8, and Smad4. Thus, the requirement for millions of early cells to prepare chromatin can be met using human lentoid bodies. While the in vitro models of lens differentiation described above have limitations and require improvements (see Section 6.1), even current procedures can be scaled up and coupled with cell cycle synchronization and FACS protocols to prepare materials for unbiased multi-omics analyses.

Likewise, determining the individual roles of BPMs, FGFs, their receptors, and nuclear effectors of these signal transduction pathways requires additional studies [28,48,49]. Fluorescent reporter pluripotent stem cells can be engineered using targeted insertions into genes of particular interest, such as transcription and growth factors, to assure that the engineering does not disrupt their normal function. Use of small-molecule inhibitors and/or agonists beyond those listed in Table 3 can be used to modulate their activities and downstream effects on lens cell differentiation [51,52,295,296].

The generation of OFZ is regulated by hypoxia and likely, many other aspects of in vivo lens fiber cell differentiation require hypoxic conditions. It is now feasible to control these levels in the incubator and take full advantage of engineered cell lines to express diverse fluorescent tags and monitor their expression. A recent example is the development of three reporters in single-human iPS cells to tag regulatory genes that control retinal cell differentiation stepwise [297]. Regarding the mechanisms governing OFZ formation, one can simultaneously visualize mitochondria using the mitochondria-targeting sequence "mito" from subunit VIII of human cytochrome c oxidase coupled with GFP [298] and other proteins (mCherry-Mito-7) [299], or the nuclear compartment via core histone protein H2B and lamin B1 fusion proteins. Given the similarities and differences between lens fiber cell de-nucleation [300] and erythrocyte enucleation [301], lens studies can be inspired by pluripotent stem cell cultures that produce human enucleated red blood cells [302].

An increasing number of -omics data exist on the human eye transcriptome [303–307] and proteome [308], including the lens and retinal RNA datasets [146,308] and protein data [309–313]. More data will be available via the NIH-sponsored Human Biomolecular Atlas Program [314]. Any of these data are useful for comparative analyses of lentoid bodies with authentic human lenses. These methods are also useful in the development of standardized quantitative protocols, including integrated epigenetic analyses, to optimize sources of cells for iPS cell procedures [315].

6.3. Modeling of Human Early-Onset Congenital Ocular Diseases and Cataracts

There are numerous challenges to understand human congenital eye diseases (Table 4) that affect the lens due to the scarcity of authentic tissues and anatomical and aging differences between humans and mammalian models, such as mice and rats [316]. Cataract remains a leading progressive disease causing blindness worldwide [139]. Many promising drug candidates tested in rodent model diseases fail in human models and clinical test-

ing [317]. Nevertheless, there are many similarities in aging of primate and rodent lenses that demonstrate functional overlaps between different mammalian models [318].

Table 4. Examples of model transcription factors (TFs) and their roles in lens development.

Name	Structure and Function	Representative Human Protein Mutations for Future Studies
PAX6	Paired domain (4–132 aa) and homeodomain (210–269 aa) TF (422/436 aa, 46/48 kDa). Regulates all stages of lens morphogenesis through its expression in lens precursor, progenitor, lens epithelium, and lens fiber cells [21,23,319–321]	Nonsense mutations: R203X, R240X, R317X, and R353X; missense mutations: G18W, R26G, G64V, R128C, and R242T [322–332]
TFAP2A	Non-canonical AP-2-type DNA-binding helix-span-helix and dimerization domain (280–410 aa) TF (437 aa, 52 kDa). Regulates separation of the lens vesicle from the surface ectoderm and maintenance of lens epithelium [171,333,334]	Missense mutation: H384Y [335]
FOXE3	Forkhead domain (71–165 aa) TF (319 aa, 33 kDa). Required for lens epithelium morphogenesis and lens formation [336,337]	Missense mutations: A96T, R120P, and T124M [338]
PITX3	Homeodomain (62–121 aa) TF (302 aa, 31.8 kDa). Deletion in mouse Pitx3 promoter causes aphakia (absence of the lens) via degeneration of the lens vesicle [339–341]	Nonsense C240X [342], missense S13N and G219fs mutations [343]. Frameshift Ser192Alafs* 117 mutation [344]
MAF	Basic motif (288–313 aa) and leucine zipper (316–337 aa) bZIP TF (373 aa, 38.5 kDa), binds to DNA as homo- or hetero-dimers. Required for lens fiber cell elongation and crystallin gene expression [295,345–349]	Missense mutations: G273N, R294W, C305W [350], R288P [351], and S270T [352]
HSF4	Helix-turn-helix DNA-binding domain (17–121 aa) and two leucine zipper oligomerization domains to form a triple-coiled-coil trimeric structure on DNA of this TF (492 aa, 53 kDa). Abnormal lens fiber cell differentiation and disrupted de-nucleation [353], binding to αB- [354] and γ-crystallin promoters [353], regulation of DNase IIβ expression [355,356], and other lens-specific genes [357]	Missense mutations: K64E [358], R116H [359], and Homozygous splice mutation of intron 12 (c.1327 + 4A > G) [360]

Table 4 shows examples, background, and rationale for systematic studies of transcription factors PAX6, FOXE3, TFAP2A, PITX3, MAF, and HSF4 and their individual mutations causing lens developmental abnormalities and early-onset congenital cataracts. In addition, the microphthalmia-anophthalmia-coloboma (MAC) syndrome [361–364] is caused by disruption of functionally diverse genes such as OTX2 [364,365], PAX6 [335,336], SOX2 [366], FOXE3 [342], and MAB21L1 [367,368].

The human lens organoid systems are particularly interesting for analyses of congenital cataracts caused by mutations in the main lens structural proteins, e.g., crystallins, MIP/aquaporin 0, gap junction, and cytoskeletal proteins [369,370] (Table 5), as well as key lens-specific transcription factors upstream of crystallin and other lens-specific genes described above (Table 4). The in vitro cataract models discussed here must be directly compared to authentic human cataractous lenses probed by a range of ultramicroscopic [371–373] and proteomics [374–378] methods. Generation of mutants primarily for lens/cataract research often finds broader applications to study other eye and central nervous system diseases. For example, mutations in rat Cryba1 affect normal function of RPE and this can be extrapolated into the pathology of human age-related macular degeneration [379,380]. Regarding aging as the major factor in cataract development, current models use genome engineering to induce premature aging through cellular senescence and other mechanisms such as via progerin-induced aging [381], and many organoid cultures are long-lived, such as retinal organoids grown for over 6–9 months [146,147,382]. This approach would be applicable for the modification of lens epithelial cells to disrupt

their support of the lens fiber cell compartment. In contrast, a proof-of-principle exists that partial nuclear reprograming by Oct4/Pou5f1, Sox2, and Klf4 of retinal ganglion cells (RGCs) of a mouse model of glaucoma can reverse ageing clocks [383] and can be tested with the lens epithelial cells as well.

Table 5. Examples of mutated cataract genes encoding lens structural proteins and their current/future models in lentoid bodies.

Gene/Protein	Structure and Function	Representative Human Protein Mutations in Ongoing and Future Studies
CRYAA/HSPB4	αA-crystallin (173 aa, 19.9 kDa). Small heat-shock-like protein (52–164 aa), molecular chaperone-like activities. Both α-crystallins form heterogeneous multimeric assemblies between 16 to over 50 subunits and represent about 35% of lens soluble proteins [384,385]	R49C [386] and R116C [387] missense mutations, single amino acid deletion p.117delR [388], 174Sext * 41 and 174Gext * 41 mutations in the stop codon following 41 aa extension [389]
CRYAB/HSPB5	αB-crystallin (175 aa, 20.2 kDa). Small heat-shock-like protein (56–164 aa), molecular chaperone-like activities (see above for CRYAA).	G154S, R157H, and A171T missense mutations cause cataract and heart defects [390]
CRYBA1	βA1/A3-crystallin (215 and 198 aa, 25.2 and 23 kDa). The β/γ-crystallins originated from gene duplication of an ancestral gene encoding two domain proteins. Each domain consists of four β-strands, forming a "Greek key" structural motif [391–393]	Splice mutation c.215 + 1G > A [394], G91del mutation of 3 bps [395]
CRYBB1	βB1-crystallin (252 aa, 28 kDa) [392–394]	Missense S129R mutation [396]
CRYBB2	βB2-crystallin (205 aa, 23.4 kDa) [392–394]	Missense P24T/iPS cells [138] and nonsense Q155X [397]
CRYGC	γC-crystallin (174 aa, 20.9 kDa) [392–394]	G129C missense mutation causing nuclear cataract [398]
CRYGD	γD-crystallin (174 aa, 20.8 kDa) [392–394]	R36C mutation causes microcrystals within the lens [399], W43R [400], and Q155X/iPS cells [138]
MIP/AQP0	Lens fiber major intrinsic protein/water channel (aquaporin 0), six transmembrane passes, C-terminal region binds BFSP1 (263 aa, 28.1 kDa) [401,402]	Missense E134G and T138R [403,404] mutations.
LIM2/MP19	Lens-specific membrane protein (173 aa, 19.7 kDa) involved in organization of cell junctions and receptor for calmodulin, four transmembrane domains [405,406]	Missense G78D [407] and R130C [408,409] mutations.
GJA8/connexin 50	Gap junction protein alpha 8 (433 aa, 48.2 kDa) in lens fibers. N-terminal intramembrane domain followed by three transmembrane domains and C-terminal extracellular domain [410–412].	Missense mutations in second transmembrane domain P88S [413] and P88Q [414].
GJA3/connexin 43	Gap junction protein alpha 3 (435 aa, 47.4 kDa); four N-terminal transmembrane domains, four types of dimers: homomeric, heterotypic homomeric, heterotypic heteromeric, and heteromeric [415,416].	P32L missense mutation in the first transmembrane domain [417], T19M [418].
EPHA2	EPH-receptor A2 single-pass transmembrane protein with C-terminal tyrosine kinase domain, ephrin ligand binding, cysteine-rich EGF-like domain, and two fibronectin III-type repeats binding in the N-terminal extracellular domain (976 aa, 130 kDa) [419].	Missense G668D in kinase domain [420], R175C in N-terminal ligand-binding domain [421], splice-site mutation c.2826 − 9G > A [422].

Table 5. *Cont.*

Gene/Protein	Structure and Function	Representative Human Protein Mutations in Ongoing and Future Studies
BFSP1/filensin/CP115	Lens-specific intermediate filament protein (665 aa, 74.5 kDa). Head (1–40 aa), intermediate filament rod (40–320 aa) [59].	Splicing mutation: c.625 + 3A > G [423]; iPS cells with double heterozygous mutations Glu269Lys in BFSP1 and L125P in RHO gene [424].
BFSP2/phakinin/CP49	Lens-specific intermediate filament protein (415 aa, 46 kDa). Head (2–114 aa), intermediate filament rod (104–415 aa) [59].	ΔE233 [425].
TDRD7	RNA-binding protein (1098 aa, 123.5 kDa), two Tudor domains (513–570 and 703–760 aa) [426].	V618del in-frame deletion of 3 bps [426].

Use of human lenses generated from iPS cells to examine molecular mechanisms of cataract formation and their hierarchical structure is already in progress [427]. Treatments of micro-lenses by small drugs indeed affect their transparency and focusing range [137]. Exposure of lentoid bodies to hydrogen peroxide triggers protein aggregation and their opacification [428]. Importantly, two patient-specific iPS cell lines carrying missense and nonsense mutations in CRYBB2 and CRYGD genes (see Table 5), respectively, were reported in 2021 to produce lentoid bodies, followed by detailed morphological and molecular studies [138]. The results nicely demonstrate that lentoid bodies can serve as outstanding models to study protein aggregation and solubility and employ drugs for potential treatments [429–432].

An important issue is to consider advantages and limitations of using patient-derived iPS vs. isogenic iPS cell lines. Patient-derived iPS cells offer detailed clinical background and phenotypic variability of the inherited mutation. It is necessary to correct the mutation, either heterozygous, homozygous, or compound heterozygous, to produce a pair of cell lines or generate a similar "reference" line from the closest normal relative. If the patient carries a heterozygous mutation, generation of a homozygous mutation represents an additional experimental procedure. These comparative models of two or three iPS cells to generate differentiated cells are instrumental to understand functions of missense and nonsense as well as non-coding mutations such as those affecting splicing, such as in PAX6 [433–435], and promoter polymorphism, such as in the αB-crystallin (CRYAB) [436]. To analyze mechanisms of the mutation, it is important to compare it to other mutations that affect the same functional subdomain of the protein. The appropriate patients may not be locally available. In contrast, generation of isogenic iPS cell lines in the laboratory readily produces both hetero- and homo-zygous mutations, and two or more mutations are produced in the same genetic background. In addition, mutations in two or more genes working in the same pathway can be generated. Thus, this approach can expand the repertoire of scientific questions such as complex aging mechanisms to be addressed with these experimental models.

It has been shown earlier that the source of adult cells for reprogramming and generation of iPS cells influences their capacities to be differentiated into specific tissues through their "epigenetic memory" [319,437,438]. The first iPS cells tested for lentoid bodies' formation were derived from lens epithelial cells collected during age-related cataract surgery of a 56-year-old and three additional individuals, and normal human fibroblasts and H9 ES were used for comparison [127]. Later, normal kidney fibroblasts collected from urine were used [136]. Additional reprograming procedures and primary cells should be tested to determine if there are any differentiation variabilities and produce "standard" protocols for lentoid bodies [139].

Epigenetic regulatory mechanisms are not just important to choose the optimal source of human adult cells and specific reprogramming methods but also serve as important processes underlying cellular differentiation and maintenance of the cell-type

memory [439–441]. Thus, analyses of DNA methylation and chromatin landscape, pioneered in chicken [227,442] and mouse lenses [443], pave the road for similar studies of human lens cell formation and differentiation using the in vitro procedures. The availability of specific "epigenetic drugs" to pharmacologically target specific enzymes and proteins in charge of individual epigenetic mechanisms provides new tools for future lens research, such as ATP-dependent chromatin remodeling enzymes, DNA methyltransferases and Tet demethylases, histone acetyltransferases and deacetylases, and histone methyltransferases and demethylases. The examples include ATP-dependent chromatin remodeling enzymes Brg1 (Smarca4) [316] and Snf2h (Smarca5) [360], DNA methyltransferases Dnmt1, Dnmt3a, and Dnmt3b [444], histone acetyltransferases EP300 and CBP [295], as well as regulatory subunit Ncoa6 [445] and Znhit1 [446] of the histone methyltransferase MLL3/4 and ATP-dependent SRCAP chromatin remodeling complexes, respectively, which were already examined through loss-of-function studies in the murine lenses.

7. Conclusions and Future Research Directions

Despite the current limitations and drawbacks, studies of other organoids have shown that self-organization principles coupled with creative tissue engineering can overcome major obstacles to generate both individual 3D lentoid bodies and primitive eyes comprised of the cornea, lens, and retina [133]. Obviously, the long-term goal of this field is to move from the current micro- and meso-scale into the macroscale order that is needed not only for basic research but for translational applications [5]. Sections 6.1–6.3 discuss specific examples of questions related to normal human lens development, generation of most advanced lentoid bodies, and various cataract models, respectively. The translational applications include high-throughput testing of candidate anti-cataract drugs as well as testing of drug toxicity within both general and eye-focused clinical trials. There are already studies published in recent years to demonstrate the feasibility of these goals [137–139,428,432].

Research on human aging revealed "protective" variants of several genes responsible for longevity [447,448]. It is known that a small fraction of the population does not form age-onset cataracts even in the ninth decade of life [449]. Thus, these individuals would be an excellent source of cells for reprograming and generation of lens organoids to uncover the protective mechanisms using assays such as oxidative stress analyzed by unbiased multi-omics.

In addition to the multi-omics approaches analyzing the chromatin landscape, gene expression, and proteomes in lens cells described above, recent studies (2017–2022) demonstrate the power of metabolomics analyses and different common and gene-specific cataract mechanisms [450–454].

The eye organoids are excellent examples of tissue–tissue coupling, including biomechanical and bioelectrical interactions, vascularization, innervation, host–microbiome interactions, as well as circadian clock entrainment [5,455]. The ocular lens further represents a system with an intricate and compartmentalized microcirculation system and different basic metabolisms, external biomechanical properties, and most importantly, transparency and light refraction [456]. There are challenges of how to mimic these functions; nevertheless, the existing and expanding tool warehouse provides an integrated framework to adapt synergistic engineering modalities to reconstruct all these components in next-generation lentoid bodies, e.g., "bioengineered 3D lenses" or "light-focusing human micro-lenses" [427], and complex eye organoids [5].

One of these challenges relates to the precise 3D lens shape and its control via a combination of processes governing lens growth, optic, and mechanical stretching to generate a gradient refractive index underlying physiological lens function [457] that may not be possible without complex tissue engineering to mimic functionally active lens ciliary muscles and zonules [458,459].

To illustrate the range of options in tissue bioengineering, these recent pioneering studies within the eye research require further attention. Human iPS cell-generated trabecular meshwork cells, normally of mesenchymal origin, cultured on epoxy-based biologically,

fully compatible SU-8 microfabricated scaffolds, show expected morphology, ECM deposition, and physiological responses to dexamethasone treatment [460,461]. Other examples are development of the Bruch's membrane-mimetic substrate to grow RPE cells using 3D printing technology to model various retinal degenerations [462], generation of clinical-grade patches of human RPE cells from iPS cells using biodegradable scaffolds [152], and use of low-fibril density thin-collagen vitrigels as 3D scaffolds [463] to improve maturation of human RPE [464]. Finally, a recent study established lacrimal gland organoids from minced murine and diagnostic human lacrimal glands treated by a combination of growth factors and small-molecule drugs [465]. These experiments demonstrate additional opportunities of how to employ primary cells in the eye organoid research.

Organ-on-a-chip technology applied to vision research remains in its infancy [466]. This biomedical engineering research platform is a multi-channel 3D microfluidic cell culture system to grow artificial organs of various complexity to mimic as many physiological parameters as possible of the normal organ, its vasculature, nutritional regimens, growth factor flow, and mechanical forces [467,468], with some features already applied to retinal [469,470] and corneal [471] research. A general challenge of these studies is the sustainability of the long-term cultures. We estimate that the bioengineered 3D lenses should reach sizes within the 2–10 mm scale within 12–16 weeks.

Taken together, the research on lens and eye organoids is poised for new breakthrough discoveries through collaborations between lens and vision researchers with experts in tissue engineering and bioprinting, individual multi-omics methods, genome engineering, high-throughput methods of drug screening, and other related disciplines. Experimental challenges remain in the ambitious goal to produce in vitro-generated macroscale human lenses with as close as possible morphology and size compared to authentic human embryonic and adult lenses, as current lentoid bodies and micro-lenses only partially meet these requirements. In parallel, efforts to generate 3D human eyes are not far away given the rapid pace of earlier transformative discoveries summarized in this review.

Author Contributions: Writing—original draft preparation, A.C. and M.J.C.; writing—review and editing, A.C. and M.J.C.; visualization, M.J.C. All authors have read and agreed to the published version of the manuscript.

Funding: NIH grants R01 EY012200 and R01 EY014237.

Acknowledgments: This article is dedicated to a special issue "New Advances in Lens Biology and Pathology" organized by Frank Lovicu. We thank Marc Kantorow, Tim Plageman, and Hynek Wichterle for critical reading of the manuscript. Figures were created with BioRender.com.

Conflicts of Interest: The authors declare no conflict of interest.

Abbreviations

Base pairs, bp; bone morphogenic protein, BMP; differentially expressed genes, DEGs; dual-SMAD inhibition, dSMADi; embryonic stem, ES; extracellular matrix, ECM; fluorescent-activated cell sorting, FACS; fibroblast growth factor, FGF; gene regulatory networks, GRNs; human pluripotent stem cells, hPSCs; induced pluripotent stem, iPS; magnetic-activated cell sorting, MACS; mouse-induced pluripotent stem cells, miPSCs; multizone ocular progenitor cells, mzOPCs; organelle-free zone, OFZ; phosphatidylinositol 3-kinase, PI3K; platelet-derived growth factor, PDGF; retinal ganglion cells, RGCs; retinal pigmented epithelium, RPE; retinoic acid, RA; self-formed ectodermal autonomous multi-zone, SEAM; single-cell RNA-sequencing, scRNA-seq; sonic hedgehog, SHH; three-dimensional, 3D; trabecular meshwork, TM.

References

1. Evans, M.J.; Kaufman, M.H. Establishment in culture of pluripotential cells from mouse embryos. *Nature* **1981**, *292*, 154–156. [CrossRef] [PubMed]
2. Thomson, J.A.; Itskovitz-Eldor, J.; Shapiro, S.S.; Waknitz, M.A.; Swiergiel, J.J.; Marshall, V.S.; Jones, J.M. Embryonic stem cell lines derived from human blastocysts. *Science* **1998**, *282*, 1145–1147. [CrossRef] [PubMed]

3. Clevers, H. Modeling Development and Disease with Organoids. *Cell* **2016**, *165*, 1586–1597. [CrossRef]
4. Li, R.; Zhong, C.; Yu, Y.; Liu, H.; Sakurai, M.; Yu, L.; Min, Z.; Shi, L.; Wei, Y.; Takahashi, Y.; et al. Generation of Blastocyst-like Structures from Mouse Embryonic and Adult Cell Cultures. *Cell* **2019**, *179*, 687–702.e618. [CrossRef]
5. Shao, Y.; Fu, J. Engineering multiscale structural orders for high-fidelity embryoids and organoids. *Cell Stem Cell* **2022**, *29*, 722–743. [CrossRef]
6. Takahashi, K.; Yamanaka, S. Induction of pluripotent stem cells from mouse embryonic and adult fibroblast cultures by defined factors. *Cell* **2006**, *126*, 663–676. [CrossRef]
7. Lancaster, M.A.; Knoblich, J.A. Generation of cerebral organoids from human pluripotent stem cells. *Nat. Protoc.* **2014**, *9*, 2329–2340. [CrossRef]
8. Weiss, P.; Taylor, A.C. Reconstitution of complete organs from single-cell suspensions of chick embryos in advanced stages of differentiation. *Proc. Natl. Acad. Sci. USA* **1960**, *46*, 1177–1185. [CrossRef]
9. Amadei, G.; Handford, C.E.; Qiu, C.; De Jonghe, J.; Greenfeld, H.; Tran, M.; Martin, B.K.; Chen, D.-Y.; Aguilera-Castrejon, A.; Hanna, J.H.; et al. Synthetic embryos complete gastrulation to neurulation and organogenesis. *Nature* **2022**, *610*, 143–153. [CrossRef]
10. Tarazi, S.; Aguilera-Castrejon, A.; Joubran, C.; Ghanem, N.; Ashouokhi, S.; Roncato, F.; Wildschutz, E.; Haddad, M.; Oldak, B.; Gomez-Cesar, E.; et al. Post-gastrulation synthetic embryos generated ex utero from mouse naive ESCs. *Cell* **2022**, *185*, 3290–3306.e3225. [CrossRef]
11. Doudna, J.A.; Charpentier, E. The new frontier of genome engineering with CRISPR-Cas9. *Science* **2014**, *346*, 1258096. [CrossRef] [PubMed]
12. Jiang, F.; Doudna, J.A. CRISPR-Cas9 structures and mechanisms. *Annu. Rev. Biophys.* **2017**, *46*, 505–529. [CrossRef] [PubMed]
13. Vera, M.; Biswas, J.; Senecal, A.; Singer, R.H.; Park, H.Y. Single-Cell and Single-Molecule Analysis of Gene Expression Regulation. *Annu. Rev. Genet.* **2016**, *50*, 267–291. [CrossRef] [PubMed]
14. Takahashi, K.; Tanabe, K.; Ohnuki, M.; Narita, M.; Ichisaka, T.; Tomoda, K.; Yamanaka, S. Induction of pluripotent stem cells from adult human fibroblasts by defined factors. *Cell* **2007**, *131*, 861–872. [CrossRef] [PubMed]
15. Kiskinis, E.; Eggan, K. Progress toward the clinical application of patient-specific pluripotent stem cells. *J. Clin. Investig.* **2010**, *120*, 51–59. [CrossRef]
16. Wiley, L.A.; Burnight, E.R.; Songstad, A.E.; Drack, A.V.; Mullins, R.F.; Stone, E.M.; Tucker, B.A. Patient-specific induced pluripotent stem cells (iPSCs) for the study and treatment of retinal degenerative diseases. *Prog. Retin. Eye Res.* **2015**, *44*, 15–35. [CrossRef]
17. Sances, S.; Bruijn, L.I.; Chandran, S.; Eggan, K.; Ho, R.; Klim, J.R.; Livesey, M.R.; Lowry, E.; Macklis, J.D.; Rushton, D. Modeling ALS with motor neurons derived from human induced pluripotent stem cells. *Nat. Neurosci.* **2016**, *19*, 542–553. [CrossRef]
18. Thompson, D.A.; Ali, R.R.; Banin, E.; Branham, K.E.; Flannery, J.G.; Gamm, D.M.; Hauswirth, W.W.; Heckenlively, J.R.; Iannaccone, A.; Jayasundera, K.T. Advancing therapeutic strategies for inherited retinal degeneration: Recommendations from the Monaciano Symposium. *Investig. Ophthalmol. Vis. Sci.* **2015**, *56*, 918–931. [CrossRef]
19. Ludwig, A.L.; Gamm, D.M. Outer Retinal Cell Replacement: Putting the Pieces Together. *Transl. Vis. Sci. Technol.* **2021**, *10*, 15. [CrossRef]
20. Bharti, K.; den Hollander, A.I.; Lakkaraju, A.; Sinha, D.; Williams, D.; Finnemann, S.C.; Rickman, C.B.; Malek, G.; D'Amore, P.A. Cell culture models to study retinal pigment epithelium-related pathogenesis in age-related macular degeneration. *Exp. Eye Res.* **2022**, *222*, 109170. [CrossRef]
21. Collinson, J.M.; Quinn, J.C.; Buchanan, M.A.; Kaufman, M.H.; Wedden, S.E.; West, J.D.; Hill, R.E. Primary defects in the lens underlie complex anterior segment abnormalities of the Pax6 heterozygous eye. *Proc. Natl. Acad. Sci. USA* **2001**, *98*, 9688–9693. [CrossRef]
22. Bassett, E.A.; Pontoriero, G.F.; Feng, W.; Marquardt, T.; Fini, M.E.; Williams, T.; West-Mays, J.A. Conditional deletion of activating protein 2α (AP-2α) in the developing retina demonstrates non-cell-autonomous roles for AP-2α in optic cup development. *Mol. Cell Biol.* **2007**, *27*, 7497–7510. [CrossRef]
23. Klimova, L.; Kozmik, Z. Stage-dependent requirement of neuroretinal Pax6 for lens and retina development. *Development* **2014**, *141*, 1292–1302. [CrossRef]
24. Rausch, R.L.; Libby, R.T.; Kiernan, A.E. Ciliary margin-derived BMP4 does not have a major role in ocular development. *PLoS ONE* **2018**, *13*, e0197048. [CrossRef]
25. Ibad, R.T.; Mazhar, B.; Vincent, C.; Bernard, C.; Dégardin, J.; Simonutti, M.; Lamonerie, T.; Di Nardo, A.A.; Prochiantz, A.; Moya, K.L. OTX2 non-cell autonomous activity regulates inner retinal function. *eNeuro* **2020**, *7*. [CrossRef]
26. Grainger, R.M. Embryonic lens induction: Shedding light on vertebrate tissue determination. *Trends Genet.* **1992**, *8*, 349–355. [CrossRef]
27. Gunhaga, L. The lens: A classical model of embryonic induction providing new insights into cell determination in early development. *Philos. Trans. R. Soc. Lond. B Biol. Sci.* **2011**, *366*, 1193–1203. [CrossRef]
28. Cvekl, A.; Zhang, X. Signaling and Gene Regulatory Networks in Mammalian Lens Development. *Trends Genet.* **2017**, *33*, 677–702. [CrossRef]
29. Bhattacharyya, S.; Bronner-Fraser, M. Hierarchy of regulatory events in sensory placode development. *Curr. Opin. Genet. Dev.* **2004**, *14*, 520–526. [CrossRef] [PubMed]

30. Diacou, R.; Nandigrami, P.; Fiser, A.; Liu, W.; Ashery-Padan, R.; Cvekl, A. Cell fate decisions, transcription factors and signaling during early retinal development. *Prog. Retin. Eye Res.* **2022**, *91*, 101093. [CrossRef]
31. Takuma, N.; Sheng, H.Z.; Furuta, Y.; Ward, J.M.; Sharma, K.; Hogan, B.; Pfaff, S.L.; Westphal, H.; Kimura, S.; Mahon, K.A. Formation of Rathke's pouch requires dual induction from the diencephalon. *Development* **1998**, *125*, 4835–4840. [CrossRef] [PubMed]
32. Rizzoti, K. Genetic regulation of murine pituitary development. *J. Mol. Endocrinol.* **2015**, *54*, R55–R73. [CrossRef] [PubMed]
33. Schlosser, G. Induction and specification of cranial placodes. *Dev. Biol.* **2006**, *294*, 303–351. [CrossRef] [PubMed]
34. Cvekl, A.; Ashery-Padan, R. The cellular and molecular mechanisms of vertebrate lens development. *Development* **2014**, *141*, 4432–4447. [CrossRef]
35. Furuta, Y.; Hogan, B.L. BMP4 is essential for lens induction in the mouse embryo. *Genes Dev.* **1998**, *12*, 3764–3775. [CrossRef]
36. Sjödal, M.; Edlund, T.; Gunhaga, L. Time of Exposure to BMP Signals Plays a Key Role in the Specification of the Olfactory and Lens Placodes Ex Vivo. *Dev. Cell* **2007**, *13*, 141–149. [CrossRef]
37. Huang, J.; Liu, Y.; Filas, B.; Gunhaga, L.; Beebe, D.C. Negative and positive auto-regulation of BMP expression in early eye development. *Dev. Biol.* **2015**, *407*, 256–264. [CrossRef]
38. Turner, N.; Grose, R. Fibroblast growth factor signalling: From development to cancer. *Nat. Rev. Cancer* **2010**, *10*, 116–129. [CrossRef] [PubMed]
39. Cvekl, A.; Tamm, E.R. Anterior eye development and ocular mesenchyme: New insights from mouse models and human diseases. *Bioessays* **2004**, *26*, 374–386. [CrossRef]
40. Gage, P.J.; Zacharias, A.L. Signaling "cross-talk" is integrated by transcription factors in the development of the anterior segment in the eye. *Dev. Dyn.* **2009**, *238*, 2149–2162. [CrossRef]
41. Kerr, C.L.; Huang, J.; Williams, T.; West-Mays, J.A. Activation of the hedgehog signaling pathway in the developing lens stimulates ectopic FoxE3 expression and disruption in fiber cell differentiation. *Investig. Ophthalmol. Vis. Sci.* **2012**, *53*, 3316–3330. [CrossRef] [PubMed]
42. Walker, H.; Akula, M.; West-Mays, J.A. Corneal development: Role of the periocular mesenchyme and bi-directional signaling. *Exp. Eye Res.* **2020**, *201*, 108231. [CrossRef] [PubMed]
43. Weigele, J.; Bohnsack, B.L. Genetics underlying the interactions between neural crest cells and eye development. *J. Dev. Biol.* **2020**, *8*, 26. [CrossRef] [PubMed]
44. Duester, G. Towards a Better Vision of Retinoic Acid Signaling during Eye Development. *Cells* **2022**, *11*, 322. [CrossRef]
45. Lwigale, P.Y. Corneal development: Different cells from a common progenitor. *Prog. Mol. Biol. Transl. Sci.* **2015**, *134*, 43–59. [CrossRef]
46. Lovicu, F.; McAvoy, J. Growth factor regulation of lens development. *Dev. Biol.* **2005**, *280*, 1–14. [CrossRef]
47. Lovicu, F.; McAvoy, J.; De Iongh, R. Understanding the role of growth factors in embryonic development: Insights from the lens. *Philos. Trans. R. Soc. Lond. B Biol. Sci.* **2011**, *366*, 1204–1218. [CrossRef]
48. Shu, D.Y.; Lovicu, F.J. Insights into Bone Morphogenetic Protein—(BMP-) Signaling in Ocular Lens Biology and Pathology. *Cells* **2021**, *10*, 2604. [CrossRef]
49. Makrides, N.; Wang, Q.; Tao, C.; Schwartz, S.; Zhang, X. Jack of all trades, master of each: The diversity of fibroblast growth factor signalling in eye development. *Open Biol.* **2022**, *12*, 210265. [CrossRef]
50. Boswell, B.A.; Overbeek, P.A.; Musil, L.S. Essential role of BMPs in FGF-induced secondary lens fiber differentiation. *Dev. Biol.* **2008**, *324*, 202–212. [CrossRef]
51. Jarrin, M.; Pandit, T.; Gunhaga, L. A balance of FGF and BMP signals regulates cell cycle exit and Equarin expression in lens cells. *Mol. Biol. Cell* **2012**, *23*, 3266–3274. [CrossRef] [PubMed]
52. Boswell, B.A.; Musil, L.S. Synergistic interaction between the fibroblast growth factor and bone morphogenetic protein signaling pathways in lens cells. *Mol. Biol. Cell* **2015**, *26*, 2561. [CrossRef] [PubMed]
53. Li, H.; Mao, Y.; Bouaziz, M.; Yu, H.; Qu, X.; Wang, F.; Feng, G.-S.; Shawber, C.; Zhang, X. Lens differentiation is controlled by the balance between PDGF and FGF signaling. *PLoS Biol.* **2019**, *17*, e3000133. [CrossRef]
54. Donaldson, P.; Kistler, J.; Mathias, R.T. Molecular solutions to mammalian lens transparency. *Physiology* **2001**, *16*, 118–123. [CrossRef] [PubMed]
55. Cvekl, A.; Eliscovich, C. Crystallin gene expression: Insights from studies of transcriptional bursting. *Exp. Eye Res.* **2021**, *207*, 108564. [CrossRef] [PubMed]
56. Rao, P.V.; Maddala, R. The role of the lens actin cytoskeleton in fiber cell elongation and differentiation. *Semin. Cell. Dev. Biol.* **2006**, *17*, 698–711. [CrossRef] [PubMed]
57. Gong, X.; Cheng, C.; Xia, C.-h. Connexins in lens development and cataractogenesis. *J. Memb. Biol.* **2007**, *218*, 9–12. [CrossRef]
58. FitzGerald, P.G. Lens intermediate filaments. *Exp. Eye Res.* **2009**, *88*, 165–172. [CrossRef]
59. Song, S.; Landsbury, A.; Dahm, R.; Liu, Y.; Zhang, Q.; Quinlan, R.A. Functions of the intermediate filament cytoskeleton in the eye lens. *J. Clin. Investig.* **2009**, *119*, 1837–1848. [CrossRef]
60. Beyer, E.C.; Berthoud, V.M. Connexin hemichannels in the lens. *Front. Physiol.* **2014**, *5*, 20. [CrossRef]
61. Cheng, C.; Nowak, R.B.; Fowler, V.M. The lens actin filament cytoskeleton: Diverse structures for complex functions. *Exp. Eye Res.* **2017**, *156*, 58–71. [CrossRef] [PubMed]

62. Bassnett, S. On the mechanism of organelle degradation in the vertebrate lens. *Exp. Eye Res.* **2009**, *88*, 133–139. [CrossRef] [PubMed]
63. Rowan, S.; Chang, M.-L.; Reznikov, N.; Taylor, A. Disassembly of the lens fiber cell nucleus to create a clear lens: The p27 descent. *Exp. Eye Res.* **2017**, *156*, 72–78. [CrossRef] [PubMed]
64. Brennan, L.; Disatham, J.; Kantorow, M. Hypoxia regulates the degradation of non-nuclear organelles during lens differentiation through activation of HIF1a. *Exp. Eye Res.* **2020**, *198*, 108129. [CrossRef]
65. Kuszak, J.; Alcala, J.; Maisel, H. The surface morphology of embryonic and adult chick lens-fiber cells. *Am. J. Anat.* **1980**, *159*, 395–410. [CrossRef]
66. Willekens, B.; Vrensen, G. The three-dimensional organization of lens fibers in the rhesus monkey. *Graefes Arch. Clin. Exp. Ophthalmol.* **1982**, *219*, 112–120. [CrossRef]
67. Rae, J.; Bartling, C.; Rae, J.; Mathias, R. Dye transfer between cells of the lens. *J. Memb. Biol.* **1996**, *150*, 89–103. [CrossRef]
68. Shi, Y.; Barton, K.; De Maria, A.; Petrash, J.M.; Shiels, A.; Bassnett, S. The stratified syncytium of the vertebrate lens. *J. Cell Sci.* **2009**, *122*, 1607–1615. [CrossRef]
69. Šikić, H.; Shi, Y.; Lubura, S.; Bassnett, S. A stochastic model of eye lens growth. *J. Theor. Biol.* **2015**, *376*, 15–31. [CrossRef]
70. Šikić, H.; Shi, Y.; Lubura, S.; Bassnett, S. A full lifespan model of vertebrate lens growth. *R. Soc. Open Sci.* **2017**, *4*, 160695. [CrossRef]
71. Bassnett, S.; Beebe, D.C. Development of the Ocular Lens: Lens Fiber Differentiation. Lovicu, F.J., Robinson, M.L., Eds.; Cambridge University Press: Cambridge, UK, 2004; pp. 214–244.
72. Provis, J.M.; Dubis, A.M.; Maddess, T.; Carroll, J. Adaptation of the central retina for high acuity vision: Cones, the fovea and the avascular zone. *Prog. Retin. Eye Res.* **2013**, *35*, 63–81. [CrossRef] [PubMed]
73. Bringmann, A.; Syrbe, S.; Görner, K.; Kacza, J.; Francke, M.; Wiedemann, P.; Reichenbach, A. The primate fovea: Structure, function and development. *Prog. Retin. Eye Res.* **2018**, *66*, 49–84. [CrossRef] [PubMed]
74. Sannan, N.S.; Shan, X.; Gregory-Evans, K.; Kusumi, K.; Gregory-Evans, C.Y. Anolis carolinensis as a model to understand the molecular and cellular basis of foveal development. *Exp. Eye Res.* **2018**, *173*, 138–147. [CrossRef] [PubMed]
75. Sajdak, B.S.; Bell, B.A.; Lewis, T.R.; Luna, G.; Cornwell, G.S.; Fisher, S.K.; Merriman, D.K.; Carroll, J. Assessment of outer retinal remodeling in the hibernating 13-lined ground squirrel. *Investig. Ophthalmol. Vis. Sci.* **2018**, *59*, 2538–2547. [CrossRef] [PubMed]
76. Rasys, A.M.; Pau, S.H.; Irwin, K.E.; Luo, S.; Kim, H.Q.; Wahle, M.A.; Trainor, P.A.; Menke, D.B.; Lauderdale, J.D. Ocular elongation and retraction in foveated reptiles. *Dev. Dynam.* **2021**, *250*, 1584–1599. [CrossRef]
77. Martin, G.R. Isolation of a pluripotent cell line from early mouse embryos cultured in medium conditioned by teratocarcinoma stem cells. *Proc. Natl. Acad. Sci. USA* **1981**, *78*, 7634–7638. [CrossRef]
78. Kim, J.-H.; Auerbach, J.M.; Rodríguez-Gómez, J.A.; Velasco, I.; Gavin, D.; Lumelsky, N.; Lee, S.-H.; Nguyen, J.; Sánchez-Pernaute, R.; Bankiewicz, K. Dopamine neurons derived from embryonic stem cells function in an animal model of Parkinson's disease. *Nature* **2002**, *418*, 50–56. [CrossRef]
79. Wichterle, H.; Lieberam, I.; Porter, J.A.; Jessell, T.M. Directed differentiation of embryonic stem cells into motor neurons. *Cell* **2002**, *110*, 385–397. [CrossRef]
80. Klimanskaya, I.; Hipp, J.; Rezai, K.A.; West, M.; Atala, A.; Lanza, R. **Derivation** and comparative assessment of retinal pigment epithelium from human embryonic stem cells using transcriptomics. *Clon. Stem Cells* **2004**, *6*, 217–245. [CrossRef]
81. Eguchi, G.; Okada, T. Differentiation of lens tissue from the progeny of chick retinal pigment cells cultured in vitro: A demonstration of a switch of cell types in clonal cell culture. *Proc. Natl. Acad. Sci. USA* **1973**, *70*, 1495–1499. [CrossRef]
82. Chader, G.J.; Masterson, E.; Goldman, A. Tissue culture of chick embryonic choroidal cells: Cell aggregation and pigment accumulation. *Adv. Exp. Med. Biol.* **1982**, *158*, 307–320. [CrossRef] [PubMed]
83. Reddy, V.; Lin, L.-R.; Arita, T.; Zigler, J., Jr.; Huang, Q. Crystallins and their synthesis in human lens epithelial cells in tissue culture. *Exp. Eye Res.* **1988**, *47*, 465–478. [CrossRef]
84. Kidd, G.L.; Reddan, J.R.; Russell, P. Differentiation and angiogenic growth factor message in two mammalian lens epithelial cell lines. *Differentiation* **1994**, *56*, 67–74. [CrossRef] [PubMed]
85. Ibaraki, N.; Lin, L.-R.; Reddy, V.N. Effects of growth factors on proliferation and differentiation in human lens epithelial cells in early subculture. *Investig. Ophthalmol. Vis. Sci.* **1995**, *36*, 2304–2312.
86. Ibaraki, N.; Lin, L.-R.; Reddy, V.N. A Study of Growth Factor Receptors in Human Lens Epithelial Cells and their Relationship to Fiber Differentiation. *Exp. Eye Res.* **1996**, *63*, 683–692. [CrossRef]
87. Wagner, L.M.; Takemoto, D.J. Protein kinase Cα and γ in N/N 1003A rabbit lens epithelial cell differentiation. *Mol. Vis.* **2001**, *7*, 57–62.
88. Nagineni, C.N.; Bhat, S.P. Lens fiber cell differentiation and expression of crystallins in Co-cultures of human fetal lens epithelial cells and fibroblasts. *Exp. Eye Res.* **1992**, *54*, 193–200. [CrossRef]
89. O'Connor, M.D.; McAvoy, J.W. In vitro generation of functional lens-like structures with relevance to age-related nuclear cataract. *Investig. Ophthalmol. Vis. Sci.* **2007**, *48*, 1245–1252. [CrossRef]
90. Wu, G.; Glickstein, S.; Liu, W.; Fujita, T.; Li, W.; Yang, Q.; Duvoisin, R.; Wan, Y. The anaphase-promoting complex coordinates initiation of lens differentiation. *Mol. Biol. Cell* **2007**, *18*, 1018–1029. [CrossRef]
91. West-Mays, J.A.; Pino, G.; Lovicu, F.J. Development and use of the lens epithelial explant system to study lens differentiation and cataractogenesis. *Prog. Retin. Eye Res.* **2010**, *29*, 135–143. [CrossRef]

92. Simon, C.S.; Hadjantonakis, A.K.; Schröter, C. Making lineage decisions with biological noise: Lessons from the early mouse embryo. *Dev. Biol.* **2018**, *7*, e319. [CrossRef] [PubMed]
93. Kondoh, H.; Uchikawa, M.; Yoda, H.; Takeda, H.; Furutani-Seiki, M.; Karlstrom, R.O. Zebrafish mutations in Gli-mediated hedgehog signaling lead to lens transdifferentiation from the adenohypophysis anlage. *Mech. Dev.* **2000**, *96*, 165–174. [CrossRef]
94. Kondoh, H.; Uchikawa, M.; Kamachi, Y. Interplay of Pax6 and SOX2 in lens development as a paradigm of genetic switch mechanisms for cell differentiation. *Int. J. Dev. Biol.* **2004**, *48*, 819–827. [CrossRef] [PubMed]
95. Smith, A.N.; Miller, L.-A.D.; Song, N.; Taketo, M.M.; Lang, R.A. The duality of β-catenin function: A requirement in lens morphogenesis and signaling suppression of lens fate in periocular ectoderm. *Dev. Biol.* **2005**, *285*, 477–489. [CrossRef] [PubMed]
96. Kreslova, J.; Machon, O.; Ruzickova, J.; Lachova, J.; Wawrousek, E.F.; Kemler, R.; Krauss, S.; Piatigorsky, J.; Kozmik, Z. Abnormal lens morphogenesis and ectopic lens formation in the absence of β-catenin function. *Genesis* **2007**, *45*, 157–168. [CrossRef]
97. Lewis, K.E.; Drossopoulou, G.; Paton, I.R.; Morrice, D.R.; Robertson, K.E.; Burt, D.W.; Ingham, P.W.; Tickle, C. Expression of ptc and gli genes in talpid3 suggests bifurcation in Shh pathway. *Development* **1999**, *126*, 2397–2407. [CrossRef]
98. Oliver, G.; Loosli, F.; Köster, R.; Wittbrodt, J.; Gruss, P. Ectopic lens induction in fish in response to the murine homeobox gene Six3. *Mech. Dev.* **1996**, *60*, 233–239. [CrossRef]
99. Altmann, C.R.; Chow, R.L.; Lang, R.A.; Hemmati-Brivanlou, A. Lens Induction by Pax-6 in Xenopus laevis. *Dev. Biol.* **1997**, *185*, 119–123. [CrossRef]
100. Swindell, E.C.; Liu, C.; Shah, R.; Smith, A.N.; Lang, R.A.; Jamrich, M. Eye formation in the absence of retina. *Dev. Biol.* **2008**, *322*, 56. [CrossRef]
101. Mochii, M.; Mazaki, Y.; Mizuno, N.; Hayashi, H.; Eguchi, G. Role of Mitf in differentiation and transdifferentiation of chicken pigmented epithelial cell. *Dev. Biol.* **1998**, *193*, 47–62. [CrossRef]
102. Matsuo, T.; Takabatake, M.; Matsuo, N. The effects of growth factors on multicellular spheroids formed by chick embryonic retinal cells. *Acta Med. Okayama* **1997**, *51*, 251–260. [CrossRef] [PubMed]
103. Suetsugu-Maki, R.; Maki, N.; Nakamura, K.; Sumanas, S.; Zhu, J.; Rio-Tsonis, D.; Tsonis, P.A. Lens regeneration in axolotl: New evidence of developmental plasticity. *BMC Biol.* **2012**, *10*, 1–8. [CrossRef] [PubMed]
104. Kawamorita, M.; Suzuki, C.; Saito, G.; Sato, T.; Sato, K. In vitro differentiation of mouse embryonic stem cells after activation by retinoic acid. *Hum. Cell* **2002**, *15*, 178–182. [CrossRef]
105. Hirano, M.; Yamamoto, A.; Yoshimura, N.; Tokunaga, T.; Motohashi, T.; Ishizaki, K.; Yoshida, H.; Okazaki, K.; Yamazaki, H.; Hayashi, S.; et al. Generation of structures formed by lens and retinal cells differentiating from embryonic stem cells. *Dev. Dyn.* **2003**, *228*, 664–671. [CrossRef]
106. Sasai, Y. Generation of dopaminergic neurons from embryonic stem cells. *J. Neurol.* **2002**, *249* (Suppl. S2), Ii41–Ii44. [CrossRef]
107. Yamazoe, H.; Iwata, H. Efficient generation of dopaminergic neurons from mouse embryonic stem cells enclosed in hollow fibers. *Biomaterials* **2006**, *27*, 4871–4880. [CrossRef] [PubMed]
108. Ooto, S.; Haruta, M.; Honda, Y.; Kawasaki, H.; Sasai, Y.; Takahashi, M. Induction of the differentiation of lentoids from primate embryonic stem cells. *Investig. Ophthalmol. Vis. Sci.* **2003**, *44*, 2689–2693. [CrossRef]
109. Kawasaki, H.; Suemori, H.; Mizuseki, K.; Watanabe, K.; Urano, F.; Ichinose, H.; Haruta, M.; Takahashi, M.; Yoshikawa, K.; Nishikawa, S.; et al. Generation of dopaminergic neurons and pigmented epithelia from primate ES cells by stromal cell-derived inducing activity. *Proc. Natl. Acad. Sci. USA* **2002**, *99*, 1580–1585. [CrossRef]
110. Eiraku, M.; Takata, N.; Ishibashi, H.; Kawada, M.; Sakakura, E.; Okuda, S.; Sekiguchi, K.; Adachi, T.; Sasai, Y. Self-organizing optic-cup morphogenesis in three-dimensional culture. *Nature* **2011**, *472*, 51–56. [CrossRef]
111. Nakano, T.; Ando, S.; Takata, N.; Kawada, M.; Muguruma, K.; Sekiguchi, K.; Saito, K.; Yonemura, S.; Eiraku, M.; Sasai, Y. Self-formation of optic cups and storable stratified neural retina from human ESCs. *Cell Stem Cell* **2012**, *10*, 771–785. [CrossRef]
112. Xu, C.; Inokuma, M.S.; Denham, J.; Golds, K.; Kundu, P.; Gold, J.D.; Carpenter, M.K. Feeder-free growth of undifferentiated human embryonic stem cells. *Nat. Biotechnol.* **2001**, *19*, 971–974. [CrossRef] [PubMed]
113. Orkin, R.W.; Gehron, P.; McGoodwin, E.B.; Martin, G.R.; Valentine, T.; Swarm, R. A murine tumor producing a matrix of basement membrane. *J. Exp. Med.* **1977**, *145*, 204–220. [CrossRef] [PubMed]
114. Hughes, C.; Ma, B.; Lajoie, G.A. *De novo sequencing methods in proteomics. Proteome Bioinformatics*; Springer: Berlin/Heidelberg, Germany, 2010; pp. 105–121.
115. Kleinman, H.K.; Martin, G.R. Matrigel: Basement membrane matrix with biological activity. *Proc. Semin. Canc. Biol.* **2005**, *15*, 378–386. [CrossRef] [PubMed]
116. Blakely, E.A.; Bjornstad, K.A.; Chang, P.Y.; McNamara, M.P.; Chang, E.; Aragon, G.; Lin, S.P.; Lui, G.; Polansky, J.R. Growth and differentiation of human lens epithelial cells in vitro on matrix. *Investig. Ophthalmol. Vis. Sci.* **2000**, *41*, 3898–3907.
117. McAvoy, J.W.; Chamberlain, C.G. Fibroblast growth factor (FGF) induces different responses in lens epithelial cells depending on its concentration. *Development* **1989**, *107*, 221–228. [CrossRef]
118. Wawersik, S.; Purcell, P.; Rauchman, M.; Dudley, A.T.; Robertson, E.J.; Maas, R. BMP7 acts in murine lens placode development. *Dev. Biol.* **1999**, *207*, 176–188. [CrossRef]
119. Stump, R.J.; Ang, S.; Chen, Y.; von Bahr, T.; Lovicu, F.J.; Pinson, K.; de Iongh, R.U.; Yamaguchi, T.P.; Sassoon, D.A.; McAvoy, J.W. A role for Wnt/beta-catenin signaling in lens epithelial differentiation. *Dev. Biol.* **2003**, *259*, 48–61. [CrossRef]
120. Chen, Y.; Stump, R.J.; Lovicu, F.J.; Shimono, A.; McAvoy, J.W. Wnt signaling is required for organization of the lens fiber cell cytoskeleton and development of lens three-dimensional architecture. *Dev. Biol.* **2008**, *324*, 161–176. [CrossRef]

121. Brinker, J.M.; Pegg, M.T.; Howard, P.S.; Kefalides, N.A. Immunochemical characterization of type IV procollagen from anterior lens capsule. *Coll. Relat. Res.* **1985**, *5*, 233–244. [CrossRef]
122. Kohno, T.; Sorgente, N.; Ishibashi, T.; Goodnight, R.; Ryan, S.J. Immunofluorescent studies of fibronectin and laminin in the human eye. *Investig. Ophthalmol. Vis. Sci.* **1987**, *28*, 506–514.
123. Dong, L.; Chen, Y.; Lewis, M.; Hsieh, J.C.; Reing, J.; Chaillet, J.R.; Howell, C.Y.; Melhem, M.; Inoue, S.; Kuszak, J.R.; et al. Neurologic defects and selective disruption of basement membranes in mice lacking entactin-1/nidogen-1. *Lab. Investig.* **2002**, *82*, 1617–1630. [CrossRef] [PubMed]
124. Walker, J.L.; Zhang, L.; Zhou, J.; Woolkalis, M.J.; Menko, A.S. Role for α6 integrin during lens development: Evidence for signaling through IGF-1R and ERK. *Dev. Dyn.* **2002**, *223*, 273–284. [CrossRef] [PubMed]
125. Rossi, M.; Morita, H.; Sormunen, R.; Airenne, S.; Kreivi, M.; Wang, L.; Fukai, N.; Olsen, B.R.; Tryggvason, K.; Soininen, R. Heparan sulfate chains of perlecan are indispensable in the lens capsule but not in the kidney. *EMBO J.* **2003**, *22*, 236–245. [CrossRef] [PubMed]
126. Yang, C.; Yang, Y.; Brennan, L.; Bouhassira, E.E.; Kantorow, M.; Cvekl, A. Efficient generation of lens progenitor cells and lentoid bodies from human embryonic stem cells in chemically defined conditions. *FASEB J.* **2010**, *24*, 3274–3283. [CrossRef] [PubMed]
127. Qiu, X.; Yang, J.; Liu, T.; Jiang, Y.; Le, Q.; Lu, Y. Efficient generation of lens progenitor cells from cataract patient–specific induced pluripotent stem cells. *PLoS ONE* **2012**, *7*, e32612. [CrossRef] [PubMed]
128. Li, D.; Qiu, X.; Yang, J.; Liu, T.; Luo, Y.; Lu, Y. Generation of Human Lens Epithelial-Like Cells from Patient-Specific Induced Pluripotent Stem Cells. *J. Cell Physiol.* **2016**, *231*, 2555–2562. [CrossRef]
129. Anchan, R.M.; Lachke, S.A.; Gerami-Naini, B.; Lindsey, J.; Ng, N.; Naber, C.; Nickerson, M.; Cavallesco, R.; Rowan, S.; Eaton, J.L.; et al. Pax6- and Six3-mediated induction of lens cell fate in mouse and human ES cells. *PLoS ONE* **2014**, *9*, e115106. [CrossRef]
130. Yang, Y.; Stopka, T.; Golestaneh, N.; Wang, Y.; Wu, K.; Li, A.; Chauhan, B.K.; Gao, C.Y.; Cveklová, K.; Duncan, M.K.; et al. Regulation of αA-crystallin via Pax6, c-Maf, CREB and a broad domain of lens-specific chromatin. *EMBO J.* **2006**, *25*, 2107–2118. [CrossRef]
131. Anand, T.; Talluri, T.R.; Kumar, D.; Garrels, W.; Mukherjee, A.; Debowski, K.; Behr, R.; Kues, W.A. Differentiation of induced pluripotent stem cells to lentoid bodies expressing a lens cell-specific fluorescent reporter. *PLoS ONE* **2016**, *11*, e0157570. [CrossRef]
132. Grabundzija, I.; Wang, J.; Sebe, A.; Erdei, Z.; Kajdi, R.; Devaraj, A.; Steinemann, D.; Szuhai, K.; Stein, U.; Cantz, T.; et al. Sleeping Beauty transposon-based system for cellular reprogramming and targeted gene insertion in induced pluripotent stem cells. *Nucleic Acids Res.* **2012**, *41*, 1829–1847. [CrossRef]
133. Sasai, Y.; Eiraku, M.; Suga, H. In vitro organogenesis in three dimensions: Self-organising stem cells. *Development* **2012**, *139*, 4111–4121. [CrossRef] [PubMed]
134. Hayashi, R.; Ishikawa, Y.; Sasamoto, Y.; Katori, R.; Nomura, N.; Ichikawa, T.; Araki, S.; Soma, T.; Kawasaki, S.; Sekiguchi, K.; et al. Co-ordinated ocular development from human iPS cells and recovery of corneal function. *Nature* **2016**, *531*, 376–380. [CrossRef] [PubMed]
135. Isla-Magrané, H.; Veiga, A.; García-Arumí, J.; Duarri, A. Multiocular organoids from human induced pluripotent stem cells displayed retinal, corneal, and retinal pigment epithelium lineages. *Stem Cell Res. Ther.* **2021**, *12*, 581. [CrossRef]
136. Fu, Q.; Qin, Z.; Jin, X.; Zhang, L.; Chen, Z.; He, J.; Ji, J.; Yao, K. Generation of Functional Lentoid Bodies from Human Induced Pluripotent Stem Cells Derived From Urinary Cells. *Investig. Ophthalmol. Vis. Sci.* **2017**, *58*, 517–527. [CrossRef] [PubMed]
137. Murphy, P.; Kabir, M.H.; Srivastava, T.; Mason, M.E.; Dewi, C.U.; Lim, S.; Yang, A.; Djordjevic, D.; Killingsworth, M.C.; Ho, J.W.K.; et al. Light-focusing human micro-lenses generated from pluripotent stem cells model lens development and drug-induced cataract in vitro. *Development* **2018**, *145*, dev155838. [CrossRef] [PubMed]
138. Lyu, D.; Zhang, L.; Qin, Z.; Ni, S.; Li, J.; Lu, B.; Hao, S.; Tang, Q.; Yin, H.; Chen, Z.; et al. Modeling congenital cataract in vitro using patient-specific induced pluripotent stem cells. *NPJ Regen. Med.* **2021**, *6*, 60. [CrossRef] [PubMed]
139. Dewi, C.U.; Mason, M.; Cohen-Hyams, T.; Killingsworth, M.C.; Harman, D.G.; Gnanasambandapillai, V.; Liyanage, L.; O'Connor, M.D. A simplified method for producing human lens epithelial cells and light-focusing micro-lenses from pluripotent stem cells. *Exp. Eye Res.* **2021**, *202*, 108317. [CrossRef]
140. Dincer, Z.; Piao, J.; Niu, L.; Ganat, Y.; Kriks, S.; Zimmer, B.; Shi, S.H.; Tabar, V.; Studer, L. Specification of functional cranial placode derivatives from human pluripotent stem cells. *Cell Rep.* **2013**, *5*, 1387–1402. [CrossRef]
141. Zimmer, B.; Piao, J.; Ramnarine, K.; Tomishima, M.J.; Tabar, V.; Studer, L. Derivation of diverse hormone-releasing pituitary cells from human pluripotent stem cells. *Stem Cell Reps.* **2016**, *6*, 858–872. [CrossRef]
142. Tchieu, J.; Zimmer, B.; Fattahi, F.; Amin, S.; Zeltner, N.; Chen, S.; Studer, L. A modular platform for differentiation of human PSCs into all major ectodermal lineages. *Cell Stem Cell* **2017**, *21*, 399–410.e397. [CrossRef]
143. Mengarelli, I.; Barberi, T. Derivation of multiple cranial tissues and isolation of lens epithelium-like cells from human embryonic stem cells. *Stem Cells Transl. Med.* **2013**, *2*, 94–106. [CrossRef] [PubMed]
144. Leung, A.W.; Kent Morest, D.; Li, J.Y. Differential BMP signaling controls formation and differentiation of multipotent preplacodal ectoderm progenitors from human embryonic stem cells. *Dev. Biol.* **2013**, *379*, 208–220. [CrossRef] [PubMed]
145. Lowe, A.; Harris, R.; Bhansali, P.; Cvekl, A.; Liu, W. Intercellular Adhesion-Dependent Cell Survival and ROCK-Regulated Actomyosin-Driven Forces Mediate Self-Formation of a Retinal Organoid. *Stem Cell Reps.* **2016**, *6*, 743–756. [CrossRef] [PubMed]

146. Kim, S.; Lowe, A.; Dharmat, R.; Lee, S.; Owen, L.A.; Wang, J.; Shakoor, A.; Li, Y.; Morgan, D.J.; Hejazi, A.A. Generation, transcriptome profiling, and functional validation of cone-rich human retinal organoids. *Proc. Natl. Acad. Sci. USA* **2019**, *116*, 10824–10833. [CrossRef]
147. Zhong, X.; Gutierrez, C.; Xue, T.; Hampton, C.; Vergara, M.N.; Cao, L.-H.; Peters, A.; Park, T.S.; Zambidis, E.T.; Meyer, J.S. Generation of three-dimensional retinal tissue with functional photoreceptors from human iPSCs. *Nat. Commun.* **2014**, *5*, 4047. [CrossRef]
148. Amirpour, N.; Karamali, F.; Rabiee, F.; Rezaei, L.; Esfandiari, E.; Razavi, S.; Dehghani, A.; Razmju, H.; Nasr-Esfahani, M.H.; Baharvand, H. Differentiation of Human Embryonic Stem Cell–Derived Retinal Progenitors into Retinal Cells by Sonic Hedgehog and/or Retinal Pigmented Epithelium and Transplantation into the Subretinal Space of Sodium Iodate–Injected Rabbits. *Stem Cells Dev.* **2011**, *21*, 42–53. [CrossRef]
149. Sluch, V.M.; Chamling, X.; Liu, M.M.; Berlinicke, C.A.; Cheng, J.; Mitchell, K.L.; Welsbie, D.S.; Zack, D.J. Enhanced Stem Cell Differentiation and Immunopurification of Genome Engineered Human Retinal Ganglion Cells. *Stem Cells Transl. Med.* **2017**, *6*, 1972–1986. [CrossRef]
150. Zhang, X.; Tenerelli, K.; Wu, S.; Xia, X.; Yokota, S.; Sun, C.; Galvao, J.; Venugopalan, P.; Li, C.; Madaan, A. Cell transplantation of retinal ganglion cells derived from hESCs. *Restor. Neurol. Neurosci.* **2020**, *38*, 131–140. [CrossRef]
151. Zhou, S.; Flamier, A.; Abdouh, M.; Tétreault, N.; Barabino, A.; Wadhwa, S.; Bernier, G. Differentiation of human embryonic stem cells into cone photoreceptors through simultaneous inhibition of BMP, TGFβ and Wnt signaling. *Development* **2015**, *142*, 3294–3306. [CrossRef]
152. Sharma, R.; Khristov, V.; Rising, A.; Jha, B.S.; Dejene, R.; Hotaling, N.; Li, Y.; Stoddard, J.; Stankewicz, C.; Wan, Q.; et al. Clinical-grade stem cell–derived retinal pigment epithelium patch rescues retinal degeneration in rodents and pigs. *Sci. Transl. Med.* **2019**, *11*, eaat5580. [CrossRef]
153. Maruotti, J.; Sripathi, S.R.; Bharti, K.; Fuller, J.; Wahlin, K.J.; Ranganathan, V.; Sluch, V.M.; Berlinicke, C.A.; Davis, J.; Kim, C.; et al. Small-molecule–directed, efficient generation of retinal pigment epithelium from human pluripotent stem cells. *Proc. Natl. Acad. Sci. USA* **2015**, *112*, 10950–10955. [CrossRef]
154. Mikhailova, A.; Ilmarinen, T.; Uusitalo, H.; Skottman, H. Small-Molecule Induction Promotes Corneal Epithelial Cell Differentiation from Human Induced Pluripotent Stem Cells. *Stem Cell Reps.* **2014**, *2*, 219–231. [CrossRef] [PubMed]
155. He, J.; Ou, S.; Ren, J.; Sun, H.; He, X.; Zhao, Z.; Wu, H.; Qu, Y.; Liu, T.; Jeyalatha, V.; et al. Tissue engineered corneal epithelium derived from clinical-grade human embryonic stem cells. *Ocul. Surf.* **2020**, *18*, 672–680. [CrossRef] [PubMed]
156. Kamarudin, T.A.; Bojic, S.; Collin, J.; Yu, M.; Alharthi, S.; Buck, H.; Shortt, A.; Armstrong, L.; Figueiredo, F.C.; Lako, M. Differences in the Activity of Endogenous Bone Morphogenetic Protein Signaling Impact on the Ability of Induced Pluripotent Stem Cells to Differentiate to Corneal Epithelial-Like Cells. *Stem Cells* **2018**, *36*, 337–348. [CrossRef] [PubMed]
157. Grönroos, P.; Ilmarinen, T.; Skottman, H. Directed differentiation of human pluripotent stem cells towards corneal endothelial-like cells under defined conditions. *Cells* **2021**, *10*, 331. [CrossRef]
158. Lee, H.S.; Mok, J.; Joo, C.-K. Bone Morphogenetic Protein 4 (BMP4) Enhances the Differentiation of Human Induced Pluripotent Stem Cells into Limbal Progenitor Cells. *Curr. Issues Mol. Biol.* **2021**, *43*, 2124–2134. [CrossRef]
159. Ding, Q.J.; Zhu, W.; Cook, A.C.; Anfinson, K.R.; Tucker, B.A.; Kuehn, M.H. Induction of trabecular meshwork cells from induced pluripotent stem cells. *Investig. Ophthalmol. Vis. Sci.* **2014**, *55*, 7065–7072. [CrossRef]
160. Sui, S.; Yu, H.; Wang, X.; Wang, W.; Yang, X.; Pan, X.; Zhou, Q.; Xin, C.; Du, R.; Wu, S.; et al. iPSC-Derived Trabecular Meshwork Cells Stimulate Endogenous TM Cell Division Through Gap Junction in a Mouse Model of Glaucoma. *Investig. Ophthalmol. Vis. Sci.* **2021**, *62*, 28. [CrossRef]
161. Kumar, A.; Cheng, T.; Song, W.; Cheuk, B.; Yang, E.; Yang, L.; Xie, Y.; Du, Y. Two-step induction of trabecular meshwork cells from induced pluripotent stem cells for glaucoma. *Biochem. Biophys. Res. Commun.* **2020**, *529*, 411–417. [CrossRef]
162. Lovatt, M.; Yam, G.H.; Peh, G.S.; Colman, A.; Dunn, N.R.; Mehta, J.S. Directed differentiation of periocular mesenchyme from human embryonic stem cells. *Differentiation* **2018**, *99*, 62–69. [CrossRef]
163. Baker, C.V.H.; Bronner-Fraser, M. Vertebrate Cranial Placodes I. Embryonic Induction. *Dev. Biol.* **2001**, *232*, 1–61. [CrossRef] [PubMed]
164. Saint-Jeannet, J.P.; Moody, S.A. Establishing the pre-placodal region and breaking it into placodes with distinct identities. *Dev. Biol.* **2014**, *389*, 13–27. [CrossRef] [PubMed]
165. Streit, A. Specification of sensory placode progenitors: Signals and transcription factor networks. *Int. J. Dev. Biol.* **2018**, *62*, 195–205. [CrossRef] [PubMed]
166. Chambers, S.M.; Fasano, C.A.; Papapetrou, E.P.; Tomishima, M.; Sadelain, M.; Studer, L. Highly efficient neural conversion of human ES and iPS cells by dual inhibition of SMAD signaling. *Nat. Biotechnol.* **2009**, *27*, 275–280. [CrossRef] [PubMed]
167. Koehler, K.R.; Mikosz, A.M.; Molosh, A.I.; Patel, D.; Hashino, E. Generation of inner ear sensory epithelia from pluripotent stem cells in 3D culture. *Nature* **2013**, *500*, 217–221. [CrossRef]
168. Lee, G.; Chambers, S.M.; Tomishima, M.J.; Studer, L. Derivation of neural crest cells from human pluripotent stem cells. *Nat. Protoc.* **2010**, *5*, 688–701. [CrossRef]
169. Mica, Y.; Lee, G.; Chambers, S.M.; Tomishima, M.J.; Studer, L. Modeling neural crest induction, melanocyte specification, and disease-related pigmentation defects in hESCs and patient-specific iPSCs. *Cell Reps.* **2013**, *3*, 1140–1152. [CrossRef]

170. Martynova, E.; Bouchard, M.; Musil, L.S.; Cvekl, A. Identification of novel Gata3 distal enhancers active in mouse embryonic lens. *Dev. Dyn.* **2018**, *247*, 1186–1198. [CrossRef]
171. Pontoriero, G.F.; Deschamps, P.; Ashery-Padan, R.; Wong, R.; Yang, Y.; Zavadil, J.; Cvekl, A.; Sullivan, S.; Williams, T.; West-Mays, J.A. Cell autonomous roles for AP-2α in lens vesicle separation and maintenance of the lens epithelial cell phenotype. *Dev. Dyn.* **2008**, *237*, 602–617. [CrossRef]
172. Groppe, J.; Greenwald, J.; Wiater, E.; Rodriguez-Leon, J.; Economides, A.N.; Kwiatkowski, W.; Affolter, M.; Vale, W.W.; Belmonte, J.C.I.; Choe, S. Structural basis of BMP signalling inhibition by the cystine knot protein Noggin. *Nature* **2002**, *420*, 636–642. [CrossRef]
173. Plotnikov, A.N.; Hubbard, S.R.; Schlessinger, J.; Mohammadi, M. Crystal structures of two FGF-FGFR complexes reveal the determinants of ligand-receptor specificity. *Cell* **2000**, *101*, 413–424. [CrossRef]
174. Mehler, M.F.; Mabie, P.C.; Zhang, D.; Kessler, J.A. Bone morphogenetic proteins in the nervous system. *Trends Neurosci.* **1997**, *20*, 309–317. [CrossRef]
175. Greenwald, J.; Groppe, J.; Gray, P.; Wiater, E.; Kwiatkowski, W.; Vale, W.; Choe, S. The BMP7/ActRII extracellular domain complex provides new insights into the cooperative nature of receptor assembly. *Mol. Cell* **2003**, *11*, 605–617. [CrossRef]
176. Hirai, H.; Matoba, K.; Mihara, E.; Arimori, T.; Takagi, J. Crystal structure of a mammalian Wnt–frizzled complex. *Nat. Struct. Mol. Biol.* **2019**, *26*, 372–379. [CrossRef] [PubMed]
177. Ahn, V.E.; Chu, M.L.-H.; Choi, H.-J.; Tran, D.; Abo, A.; Weis, W.I. Structural basis of Wnt signaling inhibition by Dickkopf binding to LRP5/6. *Dev. Cell* **2011**, *21*, 862–873. [CrossRef]
178. Xu, Y.; Kong, G.K.-W.; Menting, J.G.; Margetts, M.B.; Delaine, C.A.; Jenkin, L.M.; Kiselyov, V.V.; De Meyts, P.; Forbes, B.E.; Lawrence, M.C. How ligand binds to the type 1 insulin-like growth factor receptor. *Nat. Commun.* **2018**, *9*, 821. [CrossRef]
179. Mellough, C.B.; Collin, J.; Khazim, M.; White, K.; Sernagor, E.; Steel, D.H.; Lako, M. IGF-1 Signaling Plays an Important Role in the Formation of Three-Dimensional Laminated Neural Retina and Other Ocular Structures from Human Embryonic Stem Cells. *Stem Cells* **2015**, *33*, 2416–2430. [CrossRef]
180. Watabe, T.; Miyazono, K. Roles of TGF-β family signaling in stem cell renewal and differentiation. *Cell Res.* **2009**, *19*, 103–115. [CrossRef]
181. Mohammadi, M.; McMahon, G.; Sun, L.; Tang, C.; Hirth, P.; Yeh, B.K.; Hubbard, S.R.; Schlessinger, J. Structures of the tyrosine kinase domain of fibroblast growth factor receptor in complex with inhibitors. *Science* **1997**, *276*, 955–960. [CrossRef]
182. Williams, E.; Bullock, A.N. Structural basis for the potent and selective binding of LDN-212854 to the BMP receptor kinase ALK2. *Bone* **2018**, *109*, 251–258. [CrossRef]
183. Taipale, J.; Cooper, M.K.; Maiti, T.; Beachy, P.A. Patched acts catalytically to suppress the activity of Smoothened. *Nature* **2002**, *418*, 892–896. [CrossRef] [PubMed]
184. Rohatgi, R.; Scott, M.P. Patching the gaps in Hedgehog signalling. *Nat. Cell Biol.* **2007**, *9*, 1005–1009. [CrossRef] [PubMed]
185. Schulz, M.W.; Chamberlain, C.G.; de Iongh, R.U.; McAvoy, J.W. Acidic and basic FGF in ocular media and lens: Implications for lens polarity and growth patterns. *Development* **1993**, *118*, 117–126. [CrossRef]
186. Zilinski, C.A.; Shah, R.; Lane, M.E.; Jamrich, M. Modulation of zebrafish pitx3 expression in the primordia of the pituitary, lens, olfactory epithelium and cranial ganglia by hedgehog and nodal signaling. *Genesis* **2005**, *41*, 33–40. [CrossRef] [PubMed]
187. Desai, V.D.; Wang, Y.; Simirskii, V.N.; Duncan, M.K. CD44 expression is developmentally regulated in the mouse lens and increases in the lens epithelium after injury. *Differentiation* **2010**, *79*, 111–119. [CrossRef] [PubMed]
188. Conti, E.; Harschnitz, O. Human stem cell models to study placode development, function and pathology. *Development* **2022**, *149*, dev200831. [CrossRef] [PubMed]
189. Bricker, R.L.; Bhaskar, U.; Titone, R.; Carless, M.A.; Barberi, T. A molecular analysis of neural olfactory placode differentiation in human pluripotent stem cells. *Stem Cells Dev.* **2022**, *31*, 507–520. [CrossRef]
190. Bailey, A.P.; Bhattacharyya, S.; Bronner-Fraser, M.; Streit, A. Lens specification is the ground state of all sensory placodes, from which FGF promotes olfactory identity. *Dev. Cell* **2006**, *11*, 505–517. [CrossRef]
191. Ali, M.; Kabir, F.; Raskar, S.; Renuse, S.; Na, C.H.; Delannoy, M.; Khan, S.Y.; Riazuddin, S.A. Generation and proteome profiling of PBMC-originated, iPSC-derived lentoid bodies. *Stem Cell Res.* **2020**, *46*, 101813. [CrossRef]
192. Aryal, S.; Viet, J.; Weatherbee, B.A.; Siddam, A.D.; Hernandez, F.G.; Gautier-Courteille, C.; Paillard, L.; Lachke, S.A. The cataract-linked RNA-binding protein Celf1 post-transcriptionally controls the spatiotemporal expression of the key homeodomain transcription factors Pax6 and Prox1 in lens development. *Hum. Genet.* **2020**, *139*, 1541–1554. [CrossRef]
193. Zhao, Y.; Wilmarth, P.A.; Cheng, C.; Limi, S.; Fowler, V.M.; Zheng, D.; David, L.L.; Cvekl, A. Proteome-transcriptome analysis and proteome remodeling in mouse lens epithelium and fibers. *Exp. Eye Res.* **2019**, *179*, 32–46. [CrossRef] [PubMed]
194. Hawse, J.R.; Hejtmancik, J.F.; Horwitz, J.; Kantorow, M. Identification and functional clustering of global gene expression differences between age-related cataract and clear human lenses and aged human lenses. *Exp. Eye Res.* **2004**, *79*, 935–940. [CrossRef] [PubMed]
195. Shparberg, R.; Dewi, C.U.; Gnanasambandapillai, V.; Liyanage, L.; O'Connor, M.D. Single cell RNA-sequencing data generated from human pluripotent stem cell-derived lens epithelial cells. *Data Brief* **2021**, *34*, 106657. [CrossRef] [PubMed]
196. Mellough, C.B.; Sernagor, E.; Moreno-Gimeno, I.; Steel, D.H.; Lako, M. Efficient stage-specific differentiation of human pluripotent stem cells toward retinal photoreceptor cells. *Stem Cells* **2012**, *30*, 673–686. [CrossRef] [PubMed]

197. Shibata, S.; Hayashi, R.; Okubo, T.; Kudo, Y.; Katayama, T.; Ishikawa, Y.; Toga, J.; Yagi, E.; Honma, Y.; Quantock, A.J. Selective laminin-directed differentiation of human induced pluripotent stem cells into distinct ocular lineages. *Cell Reps.* **2018**, *25*, 1668–1679.e5. [CrossRef]
198. Argelaguet, R.; Clark, S.J.; Mohammed, H.; Stapel, L.C.; Krueger, C.; Kapourani, C.-A.; Imaz-Rosshandler, I.; Lohoff, T.; Xiang, Y.; Hanna, C.W. Multi-omics profiling of mouse gastrulation at single-cell resolution. *Nature* **2019**, *576*, 487–491. [CrossRef]
199. Cherry, C.; Maestas, D.R.; Han, J.; Andorko, J.I.; Cahan, P.; Fertig, E.J.; Garmire, L.X.; Elisseeff, J.H. Computational reconstruction of the signalling networks surrounding implanted biomaterials from single-cell transcriptomics. *Nat. Biomed. Eng.* **2021**, *5*, 1228–1238. [CrossRef]
200. Richardson, N.A.; Chamberlain, C.G.; McAvoy, J.W. IGF-1 enhancement of FGF-induced lens fiber differentiation in rats of different ages. *Investig. Ophthalmol. Vis. Sci.* **1993**, *34*, 3303–3312.
201. Gopal-Srivastava, R.; Cvekl, A.; Piatigorsky, J. Involvement of retinoic acid/retinoid receptors in the regulation of murine αB-crystallin/small heat shock protein gene expression in the lens. *J. Biol. Chem.* **1998**, *273*, 17954–17961. [CrossRef]
202. Enwright, J.F., 3rd; Grainger, R.M. Altered retinoid signaling in the heads of small eye mouse embryos. *Dev. Biol.* **2000**, *221*, 10–22. [CrossRef]
203. Králová, J.; Czerny, T.; Španielová, H.; Ratajová, V.; Kozmik, Z. Complex regulatory element within the γE-and γF-crystallin enhancers mediates Pax6 regulation and is required for induction by retinoic acid. *Gene* **2002**, *286*, 271–282. [CrossRef]
204. Grogg, M.W.; Call, M.K.; Okamoto, M.; Vergara, M.N.; Rio-Tsonis, D.; Tsonis, P.A. BMP inhibition-driven regulation of six-3 underlies induction of newt lens regeneration. *Nature* **2005**, *438*, 858–862. [CrossRef] [PubMed]
205. Thomas, A.G.; Henry, J.J. Retinoic acid regulation by CYP26 in vertebrate lens regeneration. *Dev. Biol.* **2014**, *386*, 291–301. [CrossRef]
206. Smith, J.N.; Walker, H.M.; Thompson, H.; Collinson, J.M.; Vargesson, N.; Erskine, L. Lens-regulated retinoic acid signalling controls expansion of the developing eye. *Development* **2018**, *145*, dev167171. [CrossRef] [PubMed]
207. Brewitt, B.; Clark, J.I. Growth and Transparency in the Lens, an Epithelial Tissue, Stimulated by Pulses of PDGF. *Science* **1988**, *242*, 777–779. [CrossRef] [PubMed]
208. Weber, G.F.; Menko, A.S. Phosphatidylinositol 3-Kinase Is Necessary for Lens Fiber Cell Differentiation and Survival. *Investig. Ophthalmol. Vis. Sci.* **2006**, *47*, 4490–4499. [CrossRef]
209. Gheyas, R.; Ortega-Alvarez, R.; Chauss, D.; Kantorow, M.; Menko, A.S. Suppression of PI3K signaling is linked to autophagy activation and the spatiotemporal induction of the lens organelle free zone. *Exp. Cell Res.* **2022**, *412*, 113043. [CrossRef]
210. Saint-Geniez, M.; D'Amore, P.A. Development and pathology of the hyaloid, choroidal and retinal vasculature. *Int. J. Dev. Biol.* **2004**, *48*, 1045–1058. [CrossRef]
211. Zigler, J.S., Jr.; Valapala, M.; Shang, P.; Hose, S.; Goldberg, M.F.; Sinha, D. βA3/A1-crystallin and persistent fetal vasculature (PFV) disease of the eye. *Biochim. Biophys. Acta* **2016**, *1860*, 287–298. [CrossRef]
212. Lutty, G.A.; McLeod, D.S. Development of the hyaloid, choroidal and retinal vasculatures in the fetal human eye. *Prog. Retin. Eye Res.* **2018**, *62*, 58–76. [CrossRef]
213. Shui, Y.-B.; Wang, X.; Hu, J.S.; Wang, S.-P.; Garcia, C.M.; Potts, J.D.; Sharma, Y.; Beebe, D.C. Vascular Endothelial Growth Factor Expression and Signaling in the Lens. *Investig. Ophthalmol. Vis. Sci.* **2003**, *44*, 3911–3919. [CrossRef]
214. Garcia, C.M.; Shui, Y.-B.; Kamath, M.; DeVillar, J.; Johnson, R.S.; Gerber, H.-P.; Ferrara, N.; Robinson, M.L.; Beebe, D.C. The function of VEGF-A in lens development: Formation of the hyaloid capillary network and protection against transient nuclear cataracts. *Exp. Eye Res.* **2009**, *88*, 270–276. [CrossRef]
215. Chen, Y.; Doughman, Y.-Q.; Gu, S.; Jarrell, A.; Aota, S.-I.; Cvekl, A.; Watanabe, M.; Dunwoodie, S.L.; Johnson, R.S.; van Heyningen, V.; et al. Cited2 is required for the proper formation of the hyaloid vasculature and for lens morphogenesis. *Development* **2008**, *135*, 2939–2948. [CrossRef]
216. McKeller, R.N.; Fowler, J.L.; Cunningham, J.J.; Warner, N.; Smeyne, R.J.; Zindy, F.; Skapek, S.X. The Arf tumor suppressor gene promotes hyaloid vascular regression during mouse eye development. *Proc. Natl. Acad. Sci. USA* **2002**, *99*, 3848–3853. [CrossRef]
217. Zheng, Y.; Devitt, C.; Liu, J.; Mei, J.; Skapek, S.X. A distant, cis-acting enhancer drives induction of Arf by Tgfβ in the developing eye. *Dev. Biol.* **2013**, *380*, 49–57. [CrossRef]
218. Beebe, D.C. Maintaining transparency: A review of the developmental physiology and pathophysiology of two avascular tissues. *Proc. Semin. Cell Dev. Biol.* **2008**, *19*, 125–133. [CrossRef] [PubMed]
219. Shestopalov, V.I.; Bassnett, S. Expression of autofluorescent proteins reveals a novel protein permeable pathway between cells in the lens core. *J. Cell Sci.* **2000**, *113*, 1913–1921. [CrossRef] [PubMed]
220. Bassnett, S.; McNulty, R. The effect of elevated intraocular oxygen on organelle degradation in the embryonic chicken lens. *J. Exp. Biol.* **2003**, *206*, 4353–4361. [CrossRef]
221. McNulty, R.; Wang, H.; Mathias, R.T.; Ortwerth, B.J.; Truscott, R.J.W.; Bassnett, S. Regulation of tissue oxygen levels in the mammalian lens. *J. Physiol.* **2004**, *559*, 883–898. [CrossRef] [PubMed]
222. Beebe, D.C.; Shui, Y.-B.; Siegfried, C.J.; Holekamp, N.M.; Bai, F. Preserve the (intraocular) environment: The importance of maintaining normal oxygen gradients in the eye. *Jpn. J. Ophthalmol.* **2014**, *58*, 225–231. [CrossRef]
223. Shui, Y.-B.; Beebe, D.C. Age-dependent control of lens growth by hypoxia. *Investig. Ophthalmol. Vis. Sci.* **2008**, *49*, 1023–1029. [CrossRef]
224. Kaelin, W.G., Jr. Proline hydroxylation and gene expression. *Annu. Rev. Biochem.* **2005**, *74*, 115. [CrossRef] [PubMed]

225. Semenza, G.L. Hypoxia-inducible factors in physiology and medicine. *Cell* **2012**, *148*, 399–408. [CrossRef] [PubMed]
226. Disatham, J.; Brennan, L.; Chauss, D.; Kantorow, J.; Afzali, B.; Kantorow, M. A functional map of genomic HIF1α-DNA complexes in the eye lens revealed through multiomics analysis. *BMC Genom.* **2021**, *22*, 497. [CrossRef]
227. Disatham, J.; Brennan, L.; Jiao, X.; Ma, Z.; Hejtmancik, J.F.; Kantorow, M. Changes in DNA methylation hallmark alterations in chromatin accessibility and gene expression for eye lens differentiation. *Epigenetics Chromatin* **2022**, *15*, 8. [CrossRef]
228. Brennan, L.A.; McGreal-Estrada, R.; Logan, C.M.; Cvekl, A.; Menko, A.S.; Kantorow, M. BNIP3L/NIX is required for elimination of mitochondria, endoplasmic reticulum and Golgi apparatus during eye lens organelle-free zone formation. *Exp. Eye Res.* **2018**, *174*, 173–184. [CrossRef] [PubMed]
229. Brennan, L.; Disatham, J.; Kantorow, M. Mechanisms of organelle elimination for lens development and differentiation. *Exp. Eye Res.* **2021**, *209*, 108682. [CrossRef] [PubMed]
230. Hockwin, O.; Blum, G.; Korte, I.; Murata, T.; Radetzki, W.; Rast, F. Studies on the citric acid cycle and its portion of glucose breakdown by calf and bovine lenses in vitro. *Ophthal. Res.* **1971**, *2*, 143–148. [CrossRef]
231. van Heyningen, R.; Linklater, J. The metabolism of the bovine lens in air and nitrogen. *Exp. Eye Res.* **1975**, *20*, 393–396. [CrossRef]
232. Sakaue, H.; Negi, A.; Honda, Y. Comparative study of vitreous oxygen tension in human and rabbit eyes. *Investig. Ophthal. Vis. Sci.* **1989**, *30*, 1933–1937.
233. Griep, A.E. Cell cycle regulation in the developing lens. *Semin. Cell Dev. Biol.* **2006**, *17*, 686–697. [CrossRef]
234. Faber, S.C.; Robinson, M.L.; Makarenkova, H.P.; Lang, R.A. Bmp signaling is required for development of primary lens fiber cells. *Development* **2002**, *129*, 3727–3737. [CrossRef] [PubMed]
235. Garcia, C.M.; Yu, K.; Zhao, H.; Ashery-Padan, R.; Ornitz, D.M.; Robinson, M.L.; Beebe, D.C. Signaling through FGF receptor-2 is required for lens cell survival and for withdrawal from the cell cycle during lens fiber cell differentiation. *Dev. Dyn.* **2005**, *233*, 516–527. [CrossRef] [PubMed]
236. Zhao, H.; Yang, T.; Madakashira, B.P.; Thiels, C.A.; Bechtle, C.A.; Garcia, C.M.; Zhang, H.; Yu, K.; Ornitz, D.M.; Beebe, D.C. Fibroblast growth factor receptor signaling is essential for lens fiber cell differentiation. *Dev. Biol.* **2008**, *318*, 276–288. [CrossRef] [PubMed]
237. Pandit, T.; Jidigam, V.K.; Patthey, C.; Gunhaga, L. Neural retina identity is specified by lens-derived BMP signals. *Development* **2015**, *142*, 1850–1859. [CrossRef]
238. Mathias, R.; Rae, J.; Baldo, G. Physiological properties of the normal lens. *Physiol. Rev.* **1997**, *77*, 21–50. [CrossRef]
239. Mathias, R.T.; White, T.W.; Gong, X. Lens gap junctions in growth, differentiation, and homeostasis. *Physiol. Rev.* **2010**, *90*, 179–206. [CrossRef]
240. Truscott, R.J.; Friedrich, M.G. The etiology of human age-related cataract. Proteins don't last forever. *Biochim. Biophys. Acta* **2016**, *1860*, 192–198. [CrossRef]
241. Lim, J.C.; Umapathy, A.; Grey, A.C.; Vaghefi, E.; Donaldson, P.J. Novel roles for the lens in preserving overall ocular health. *Exp. Eye Res.* **2017**, *156*, 117–123. [CrossRef]
242. Schey, K.L.; Petrova, R.S.; Gletten, R.B.; Donaldson, P.J. The Role of Aquaporins in Ocular Lens Homeostasis. *Int. J. Mol. Sci.* **2017**, *18*, 2693. [CrossRef]
243. Derby, B. Printing and prototyping of tissues and scaffolds. *Science* **2012**, *338*, 921–926. [CrossRef] [PubMed]
244. McMurtrey, R.J. Multi-compartmental biomaterial scaffolds for patterning neural tissue organoids in models of neurodevelopment and tissue regeneration. *J. Tissue Eng.* **2016**, *7*, 2041731416671926. [CrossRef] [PubMed]
245. Bittner, S.M.; Guo, J.L.; Mikos, A.G. Spatiotemporal control of growth factors in three-dimensional printed scaffolds. *Bioprinting* **2018**, *12*, e00032. [CrossRef] [PubMed]
246. Marchini, A.; Gelain, F. Synthetic scaffolds for 3D cell cultures and organoids: Applications in regenerative medicine. *Crit. Rev. Biotechnol.* **2022**, *42*, 468–486. [CrossRef]
247. Wu, W.; Tholozan, F.M.; Goldberg, M.W.; Bowen, L.; Wu, J.; Quinlan, R.A. A gradient of matrix-bound FGF-2 and perlecan is available to lens epithelial cells. *Exp. Eye Res.* **2014**, *120*, 10–14. [CrossRef]
248. Ker, E.D.; Nain, A.S.; Weiss, L.E.; Wang, J.; Suhan, J.; Amon, C.H.; Campbell, P.G. Bioprinting of growth factors onto aligned sub-micron fibrous scaffolds for simultaneous control of cell differentiation and alignment. *Biomaterials* **2011**, *32*, 8097–8107. [CrossRef]
249. Vojtová, L.; Pavliňáková, V.; Muchová, J.; Kacvinská, K.; Brtníková, J.; Knoz, M.; Lipový, B.; Faldyna, M.; Göpfert, E.; Holoubek, J. Healing and angiogenic properties of collagen/chitosan scaffolds enriched with hyperstable FGF2-STAB® protein: In vitro, ex ovo and in vivo comprehensive evaluation. *Biomedicines* **2021**, *9*, 590. [CrossRef]
250. Danysh, B.P.; Duncan, M.K. The lens capsule. *Exp. Eye Res.* **2009**, *88*, 151–164. [CrossRef]
251. DeDreu, J.; Walker, J.L.; Menko, A.S. Dynamics of the lens basement membrane capsule and its interaction with connective tissue-like extracapsular matrix proteins. *Matrix Biol.* **2021**, *96*, 18–46. [CrossRef]
252. Schulz, M.W.; Chamberlain, C.G.; McAvoy, J.W. Binding of FGF-1 and FGF-2 to heparan sulphate proteoglycans of the mammalian lens capsule. *Growth Factors* **1997**, *14*, 1–13. [CrossRef]
253. Wishart, T.F.; Flokis, M.; Shu, D.Y.; Das, S.J.; Lovicu, F.J. Hallmarks of lens aging and cataractogenesis. *Exp. Eye Res.* **2021**, *210*, 108709. [CrossRef] [PubMed]
254. Cammarata, P.R.; Cantu-Crouch, D.; Oakford, L.; Morrill, A. Macromolecular organization of bovine lens capsule. *Tissue Cell* **1986**, *18*, 83–97. [CrossRef]

255. Kuszak, J.R.; Zoltoski, R.K.; Tiedemann, C.E. Development of lens sutures. *Int. J. Dev. Biol.* **2004**, *48*, 889–902. [CrossRef] [PubMed]
256. Bhattacharyya, S.; Bailey, A.P.; Bronner-Fraser, M.; Streit, A. Segregation of lens and olfactory precursors from a common territory: Cell sorting and reciprocity of Dlx5 and Pax6 expression. *Dev. Biol.* **2004**, *271*, 403–414. [CrossRef]
257. Litsiou, A.; Hanson, S.; Streit, A. A balance of FGF, BMP and WNT signalling positions the future placode territory in the head. *Development* **2005**, *132*, 4051–4062. [CrossRef]
258. Bhattacharyya, S.; Bronner, M.E. Clonal analyses in the anterior pre-placodal region: Implications for the early lineage bias of placodal progenitors. *Int. J. Dev. Biol.* **2013**, *57*, 753. [CrossRef]
259. Pieper, M.; Eagleson, G.W.; Wosniok, W.; Schlosser, G. Origin and segregation of cranial placodes in Xenopus laevis. *Dev. Biol.* **2011**, *360*, 257–275. [CrossRef]
260. Whitlock, K.E.; Westerfield, M. The olfactory placodes of the zebrafish form by convergence of cellular fields at the edge of the neural plate. *Development* **2000**, *127*, 3645–3653. [CrossRef]
261. Dutta, S.; Dietrich, J.-E.; Aspöck, G.; Burdine, R.D.; Schier, A.; Westerfield, M.; Varga, Z.M. Pitx3 defines an equivalence domain for lens and anterior pituitary placode. *Development* **2005**, *132*, 1579–1590. [CrossRef]
262. Trevers, K.E.; Prajapati, R.S.; Hintze, M.; Stower, M.J.; Strobl, A.C.; Tambalo, M.; Ranganathan, R.; Moncaut, N.; Khan, M.A.; Stern, C.D. Neural induction by the node and placode induction by head mesoderm share an initial state resembling neural plate border and ES cells. *Proc. Natl. Acad. Sci. USA* **2018**, *115*, 355–360. [CrossRef]
263. Peng, G.; Suo, S.; Chen, J.; Chen, W.; Liu, C.; Yu, F.; Wang, R.; Chen, S.; Sun, N.; Cui, G. Spatial transcriptome for the molecular annotation of lineage fates and cell identity in mid-gastrula mouse embryo. *Dev. Cell* **2016**, *36*, 681–697. [CrossRef] [PubMed]
264. Peng, G.; Suo, S.; Cui, G.; Yu, F.; Wang, R.; Chen, J.; Chen, S.; Liu, Z.; Chen, G.; Qian, Y. Molecular architecture of lineage allocation and tissue organization in early mouse embryo. *Nature* **2019**, *572*, 528–532. [CrossRef] [PubMed]
265. Pijuan-Sala, B.; Wilson, N.K.; Xia, J.; Hou, X.; Hannah, R.L.; Kinston, S.; Calero-Nieto, F.J.; Poirion, O.; Preissl, S.; Liu, F. Single-cell chromatin accessibility maps reveal regulatory programs driving early mouse organogenesis. *Nat. Cell Biol.* **2020**, *22*, 487–497. [CrossRef]
266. Morgenbesser, S.D.; Williams, B.O.; Jacks, T.; DePinho, R.A. p53-dependent apoptosis produced by Rb-deficiency in the developing mouse lens. *Nature* **1994**, *371*, 72–74. [CrossRef] [PubMed]
267. Zhang, P.; Liégeois, N.J.; Wong, C.; Finegold, M.; Hou, H.; Thompson, J.C.; Silverman, A.; Harper, J.W.; DePinho, R.A.; Elledge, S.J. Altered cell differentiation and proliferation in mice lacking p57KIP2 indicates a role in Beckwith–Wiedemann syndrome. *Nature* **1997**, *387*, 151–158. [CrossRef]
268. Zhang, P.; Wong, C.; DePinho, R.A.; Harper, J.W.; Elledge, S.J. Cooperation between the Cdk inhibitors p27KIP1 and p57KIP2 in the control of tissue growth and development. *Genes Dev.* **1998**, *12*, 3162–3167. [CrossRef]
269. Jia, J.; Lin, M.; Zhang, L.; York, J.P.; Zhang, P. The Notch signaling pathway controls the size of the ocular lens by directly suppressing $p57^{Kip2}$ expression. *Mol. Cell Biol.* **2007**, *27*, 7236–7247. [CrossRef]
270. Chaffee, B.R.; Hoang, T.V.; Leonard, M.R.; Bruney, D.G.; Wagner, B.D.; Dowd, J.R.; Leone, G.; Ostrowski, M.C.; Robinson, M.L. FGFR and PTEN signaling interact during lens development to regulate cell survival. *Dev. Biol.* **2016**, *410*, 150–163. [CrossRef]
271. Pan, H.; Griep, A.E. Altered cell cycle regulation in the lens of HPV-16 E6 or E7 transgenic mice: Implications for tumor suppressor gene function in development. *Genes Dev.* **1994**, *8*, 1285–1299. [CrossRef]
272. Morgenbesser, S.D.; Schreiber-Agus, N.; Bidder, M.; Mahon, K.A.; Overbeek, P.A.; Horner, J.; DePinho, R.A. Contrasting roles for c-Myc and L-Myc in the regulation of cellular growth and differentiation in vivo. *EMBO J.* **1995**, *14*, 743–756. [CrossRef]
273. Lovicu, F.J.; Overbeek, P.A. Overlapping effects of different members of the FGF family on lens fiber differentiation in transgenic mice. *Development* **1998**, *125*, 3365–3377. [CrossRef]
274. Nguyen, M.M.; Nguyen, M.L.; Caruana, G.; Bernstein, A.; Lambert, P.F.; Griep, A.E. Requirement of PDZ-containing proteins for cell cycle regulation and differentiation in the mouse lens epithelium. *Mol. Cell Biol.* **2003**, *23*, 8970–8981. [CrossRef]
275. Chen, Q.; Liang, D.; Yang, T.; Leone, G.; Overbeek, P.A. Distinct capacities of individual E2Fs to induce cell cycle re-entry in postmitotic lens fiber cells of transgenic mice. *Dev. Neurosci.* **2004**, *26*, 435–445. [CrossRef] [PubMed]
276. Saavedra, H.I.; Wu, L.; de Bruin, A.; Timmers, C.; Rosol, T.J.; Weinstein, M.; Robinson, M.L.; Leone, G. Specificity of E2F1, E2F2, and E2F3 in mediating phenotypes induced by loss of Rb. *Cell Growth Differ.* **2002**, *13*, 215–225. [PubMed]
277. Cvekl, A.; Kashanchi, F.; Brady, J.N.; Piatigorsky, J. Pax-6 interactions with TATA-box-binding protein and retinoblastoma protein. *Investig. Ophthalmol. Vis. Sci.* **1999**, *40*, 1343–1350.
278. Cvekl, A.; Yang, Y.; Chauhan, B.K.; Cveklova, K. Regulation of gene expression by Pax6 in ocular cells: A case of tissue-preferred expression of crystallins in lens. *Int. J. Dev. Biol.* **2004**, *48*, 829. [CrossRef]
279. Gotoh, N.; Ito, M.; Yamamoto, S.; Yoshino, I.; Song, N.; Wang, Y.; Lax, I.; Schlessinger, J.; Shibuya, M.; Lang, R.A. Tyrosine phosphorylation sites on FRS2alpha responsible for Shp2 recruitment are critical for induction of lens and retina. *Proc. Natl. Acad. Sci. USA* **2004**, *101*, 17144–17149. [CrossRef]
280. Pan, Y.; Woodbury, A.; Esko, J.D.; Grobe, K.; Zhang, X. Heparan sulfate biosynthetic gene Ndst1 is required for FGF signaling in early lens development. *Development* **2006**, *133*, 4933–4944. [CrossRef]
281. Rivera, C.; Yamben, I.F.; Shatadal, S.; Waldof, M.; Robinson, M.L.; Griep, A.E. Cell-autonomous requirements for Dlg-1 for lens epithelial cell structure and fiber cell morphogenesis. *Dev. Dyn.* **2009**, *238*, 2292–2308. [CrossRef]

282. Newitt, P.; Boros, J.; Madakashira, B.P.; Robinson, M.L.; Reneker, L.W.; McAvoy, J.W.; Lovicu, F.J. Sef is a negative regulator of fiber cell differentiation in the ocular lens. *Differentiation* **2010**, *80*, 53–67. [CrossRef]
283. Qu, X.; Hertzler, K.; Pan, Y.; Grobe, K.; Robinson, M.L.; Zhang, X. Genetic epistasis between heparan sulfate and FGF–Ras signaling controls lens development. *Dev. Biol.* **2011**, *355*, 12–20. [CrossRef] [PubMed]
284. Dawes, L.J.; Sugiyama, Y.; Tanedo, A.S.; Lovicu, F.J.; McAvoy, J.W. Wnt-frizzled signaling is part of an FGF-induced cascade that promotes lens fiber differentiation. *Investig. Ophthalmol. Vis. Sci.* **2013**, *54*, 1582–1590. [CrossRef] [PubMed]
285. Lee, S.; Shatadal, S.; Griep, A.E. Dlg-1 interacts with and regulates the activities of fibroblast growth factor receptors and EphA2 in the mouse lens. *Investig. Ophthalmol. Vis. Sci.* **2016**, *57*, 707–718. [CrossRef] [PubMed]
286. Collins, T.N.; Mao, Y.; Li, H.; Bouaziz, M.; Hong, A.; Feng, G.-S.; Wang, F.; Quilliam, L.A.; Chen, L.; Park, T. Crk proteins transduce FGF signaling to promote lens fiber cell elongation. *eLIFE* **2018**, *7*, e32586. [CrossRef]
287. Zhao, G.; Bailey, C.G.; Feng, Y.; Rasko, J.; Lovicu, F.J. Negative regulation of lens fiber cell differentiation by RTK antagonists Spry and Spred. *Exp. Eye Res.* **2018**, *170*, 148–159. [CrossRef]
288. Wishart, T.F.; Lovicu, F.J. An Atlas of Heparan Sulfate Proteoglycans in the Postnatal Rat Lens. *Investig. Ophthalmol. Vis. Sci.* **2021**, *62*, 5. [CrossRef]
289. Martynova, E.; Zhao, Y.; Xie, Q.; Zheng, D.; Cvekl, A. Transcriptomic analysis and novel insights into lens fibre cell differentiation regulated by Gata3. *Open Biol.* **2019**, *9*, 190220. [CrossRef]
290. Audette, D.S.; Anand, D.; So, T.; Rubenstein, T.B.; Lachke, S.A.; Lovicu, F.J.; Duncan, M.K. Prox1 and fibroblast growth factor receptors form a novel regulatory loop controlling lens fiber differentiation and gene expression. *Development* **2016**, *143*, 318–328. [CrossRef]
291. Rowan, S.; Conley, K.W.; Le, T.T.; Donner, A.L.; Maas, R.L.; Brown, N.L. Notch signaling regulates growth and differentiation in the mammalian lens. *Dev. Biol.* **2008**, *321*, 111–122. [CrossRef]
292. Le, T.T.; Conley, K.W.; Mead, T.J.; Rowan, S.; Yutzey, K.E.; Brown, N.L. Requirements for Jag1-Rbpj mediated Notch signaling during early mouse lens development. *Dev. Dyn.* **2012**, *241*, 493–504. [CrossRef]
293. Saravanamuthu, S.S.; Le, T.T.; Gao, C.Y.; Cojocaru, R.I.; Pandiyan, P.; Liu, C.; Zhang, J.; Zelenka, P.S.; Brown, N.L. Conditional ablation of the Notch2 receptor in the ocular lens. *Dev. Biol.* **2012**, *362*, 219–229. [CrossRef] [PubMed]
294. Wolf, L.; Harrison, W.; Huang, J.; Xie, Q.; Xiao, N.; Sun, J.; Kong, L.; Lachke, S.A.; Kuracha, M.R.; Govindarajan, V.; et al. Histone posttranslational modifications and cell fate determination: Lens induction requires the lysine acetyltransferases CBP and p300. *Nucleic Acids Res.* **2013**, *41*, 10199–10214. [CrossRef] [PubMed]
295. Xie, Q.; McGreal, R.; Harris, R.; Gao, C.Y.; Liu, W.; Reneker, L.W.; Musil, L.S.; Cvekl, A. Regulation of c-Maf and αA-Crystallin in Ocular Lens by Fibroblast Growth Factor Signaling. *J. Biol. Chem.* **2016**, *291*, 3947–3958. [CrossRef] [PubMed]
296. Dawes, L.J.; Shelley, E.J.; McAvoy, J.W.; Lovicu, F.J. A role for Hippo/YAP-signaling in FGF-induced lens epithelial cell proliferation and fibre differentiation. *Exp. Eye Res.* **2018**, *169*, 122–133. [CrossRef] [PubMed]
297. Lam, P.T.; Gutierrez, C.; Del Rio-Tsonis, K.; Robinson, M.L. Generation of a retina reporter hiPSC line to label progenitor, ganglion, and photoreceptor cell types. *Transl. Vis. Sci. Technol.* **2020**, *9*, 21. [CrossRef] [PubMed]
298. Rizzuto, R.; Brini, M.; Pizzo, P.; Murgia, M.; Pozzan, T. Chimeric green fluorescent protein as a tool for visualizing subcellular organelles in living cells. *Curr. Biol.* **1995**, *5*, 635–642. [CrossRef]
299. Olenych, S.G.; Claxton, N.S.; Ottenberg, G.K.; Davidson, M.W. The Fluorescent Protein Color Palette. *Curr. Prot. Cell Biol.* **2007**, *36*, 21.25.21–21.25.34. [CrossRef]
300. Limi, S.; Senecal, A.; Coleman, R.; Lopez-Jones, M.; Guo, P.; Polumbo, C.; Singer, R.H.; Skoultchi, A.I.; Cvekl, A. Transcriptional burst fraction and size dynamics during lens fiber cell differentiation and detailed insights into the denucleation process. *J. Biol. Chem.* **2018**, *293*, 13176–13190. [CrossRef]
301. Zhao, B.; Mei, Y.; Schipma, M.J.; Roth, E.W.; Bleher, R.; Rappoport, J.Z.; Wickrema, A.; Yang, J.; Ji, P. Nuclear condensation during mouse erythropoiesis requires caspase-3-mediated nuclear opening. *Dev. Cell* **2016**, *36*, 498–510. [CrossRef]
302. Olivier, E.N.; Zhang, S.; Yan, Z.; Suzuka, S.; Roberts, K.; Wang, K.; Bouhassira, E.E. PSC-RED and MNC-RED: Albumin-free and low-transferrin robust erythroid differentiation protocols to produce human enucleated red blood cells. *Exp. Hematol.* **2019**, *75*, 31–52.e15. [CrossRef]
303. Carnes, M.U.; Allingham, R.R.; Ashley-Koch, A.; Hauser, M.A. Transcriptome analysis of adult and fetal trabecular meshwork, cornea, and ciliary body tissues by RNA sequencing. *Exp. Eye Res.* **2018**, *167*, 91–99. [CrossRef] [PubMed]
304. van Zyl, T.; Yan, W.; McAdams, A.M.; Monavarfeshani, A.; Hageman, G.S.; Sanes, J.R. Cell atlas of the human ocular anterior segment: Tissue-specific and shared cell types. *Proc. Natl. Acad. Sci. USA* **2022**, *119*, e2200914119. [CrossRef] [PubMed]
305. Wolf, J.; Boneva, S.; Schlecht, A.; Lapp, T.; Auw-Haedrich, C.; Lagrèze, W.; Agostini, H.; Reinhard, T.; Schlunck, G.; Lange, C. The Human Eye Transcriptome Atlas: A searchable comparative transcriptome database for healthy and diseased human eye tissue. *Genomics* **2022**, *114*, 110286. [CrossRef] [PubMed]
306. Wolf, J.; Lapp, T.; Reinhard, T.; Agostini, H.; Schlunck, G.; Lange, C. Web-based gene expression analysis-paving the way to decode healthy and diseased ocular tissue. *Ophthalmologie* **2022**, 1–7. [CrossRef] [PubMed]
307. Ahmad, M.T.; Zhang, P.; Dufresne, C.; Ferrucci, L.; Semba, R.D. The human eye proteome project: Updates on an emerging proteome. *Proteomics* **2018**, *18*, 1700394. [CrossRef]
308. Sheng, W.; Lu, Y.; Mei, F.; Wang, N.; Liu, Z.-Z.; Han, Y.-Y.; Wang, H.-T.; Zou, S.; Xu, H.; Zhang, X. Effect of Resveratrol on Sirtuins, OPA1, and Fis1 Expression in Adult Zebrafish Retina. *Investig. Ophthalmol. Vis. Sci.* **2018**, *59*, 4542–4551. [CrossRef]

309. Lampi, K.J.; Ma, Z.; Hanson, S.R.; Azuma, M.; Shih, M.; Shearer, T.R.; Smith, D.L.; Smith, J.B.; David, L.L. Age-related changes in human lens crystallins identified by two-dimensional electrophoresis and mass spectrometry. *Exp. Eye Res.* **1998**, *67*, 31–43. [CrossRef]
310. Wilmarth, P.; Tanner, S.; Dasari, S.; Nagalla, S.; Riviere, M.; Bafna, V.; Pevzner, P.; David, L. Age-related changes in human crystallins determined from comparative analysis of post-translational modifications in young and aged lens: Does deamidation contribute to crystallin insolubility? *J. Proteome Res.* **2006**, *5*, 2554–2566. [CrossRef]
311. Wang, Z.; Han, J.; David, L.L.; Schey, K.L. Proteomics and Phosphoproteomics Analysis of Human Lens Fiber Cell Membranes. *Investig. Ophthalmol. Vis. Sci.* **2013**, *54*, 1135–1143. [CrossRef]
312. Wenke, J.L.; McDonald, W.H.; Schey, K.L. Spatially directed proteomics of the human lens outer cortex reveals an intermediate filament switch associated with the remodeling zone. *Investig. Ophthalmol. Vis. Sci.* **2016**, *57*, 4108–4114. [CrossRef]
313. Friedrich, M.G.; Wang, Z.; Schey, K.L.; Truscott, R.J. Spontaneous protein–protein crosslinking at glutamine and glutamic acid residues in long-lived proteins. *Biochem. J.* **2021**, *478*, 327–339. [CrossRef] [PubMed]
314. Snyder, M.P.; Lin, S.; Posgai, A.; Atkinson, M.; Regev, A.; Rood, J.; Rozenblatt-Rosen, O.; Gaffney, L.; Hupalowska, A.; Satija, R.; et al. The human body at cellular resolution: The NIH Human Biomolecular Atlas Program. *Nature* **2019**, *574*, 187–192. [CrossRef]
315. Hiler, D.; Chen, X.; Hazen, J.; Kupriyanov, S.; Carroll, P.A.; Qu, C.; Xu, B.; Johnson, D.; Griffiths, L.; Frase, S. Quantification of retinogenesis in 3D cultures reveals epigenetic memory and higher efficiency in iPSCs derived from rod photoreceptors. *Cell Stem Cell* **2015**, *17*, 101–115. [CrossRef]
316. Eintracht, J.; Toms, M.; Moosajee, M. The use of induced pluripotent stem cells as a model for developmental eye disorders. *Front. Cell Neurosci.* **2020**, *14*, 265. [CrossRef] [PubMed]
317. Breslin, S.; O'Driscoll, L. Three-dimensional cell culture: The missing link in drug discovery. *Drug Discov. Today* **2013**, *18*, 240–249. [CrossRef] [PubMed]
318. Cheng, C.; Parreno, J.; Nowak, R.B.; Biswas, S.K.; Wang, K.; Hoshino, M.; Uesugi, K.; Yagi, N.; Moncaster, J.A.; Lo, W.-K. Age-related changes in eye lens biomechanics, morphology, refractive index and transparency. *Aging* **2019**, *11*, 12497. [CrossRef]
319. Hogan, B.L.; Hirst, E.M.; Horsburgh, G.; Hetherington, C.M. Small eye (Sey): A mouse model for the genetic analysis of craniofacial abnormalities. *Development* **1988**, *103*, 115–119. [CrossRef]
320. Quinn, J.C.; West, J.D.; Hill, R.E. Multiple functions for Pax6 in mouse eye and nasal development. *Genes Dev.* **1996**, *10*, 435–446. [CrossRef]
321. Ashery-Padan, R.; Marquardt, T.; Zhou, X.; Gruss, P. Pax6 activity in the lens primordium is required for lens formation and for correct placement of a single retina in the eye. *Genes Dev.* **2000**, *14*, 2701–2711. [CrossRef]
322. Chauhan, B.K.; Yang, Y.; Cveklová, K.; Cvekl, A. Functional interactions between alternatively spliced forms of Pax6 in crystallin gene regulation and in haploinsufficiency. *Nucleic Acids Res.* **2004**, *32*, 1696–1709. [CrossRef]
323. Xie, Q.; Ung, D.; Khafizov, K.; Fiser, A.; Cvekl, A. Gene regulation by PAX6: Structural-functional correlations of missense mutants and transcriptional control of Trpm3/miR-204. *Mol. Vis.* **2014**, *20*, 270–282. [PubMed]
324. Glaser, T.; Jepeal, L.; Edwards, J.G.; Young, S.R.; Favor, J.; Maas, R.L. PAX6 gene dosage effect in a family with congenital cataracts, aniridia, anophthalmia and central nervous system defects. *Nat. Genet.* **1994**, *7*, 463–471. [CrossRef] [PubMed]
325. Yamaguchi, Y.; Sawada, J.I.; Yamada, M.; Handa, H.; Azuma, N. Autoregulation of Pax6 transcriptional activation by two distinct DNA-binding subdomains of the paired domain. *Genes Cells* **1997**, *2*, 255–261. [CrossRef] [PubMed]
326. Wolf, M.T.; Lorenz, B.; Winterpacht, A.; Drechsler, M.; Schumacher, V.; Royer-Pokora, B.; Blankenagel, A.; Zabel, B.; Wildhardt, G. Ten novel mutations found in aniridia. *Hum. Mut.* **1998**, *12*, 304–313. [CrossRef]
327. Hanson, I.M.; Fletcher, J.M.; Jordan, T.; Brown, A.; Taylor, D.; Adams, R.J.; Punnett, H.H.; van Heyningen, V. Mutations at the PAX6 locus are found in heterogeneous anterior segment malformations including Peters' anomaly. *Nat. Genet.* **1994**, *6*, 168–173. [CrossRef]
328. Hanson, I.; Churchill, A.; Love, J.; Axton, R.; Moore, T.; Clarke, M.; Meire, F.; van Heyningen, V. Missense Mutations in the Most Ancient Residues of the PAX6 Paired Domain Underlie a Spectrum of Human Congenital Eye Malformations. *Hum. Mol. Genet.* **1999**, *8*, 165–172. [CrossRef]
329. Kondo-Saitoh, A.; Matsumoto, N.; Sasaki, T.; Egashira, M.; Saitoh, A.; Yamada, K.; Niikawa, N.; Amemiya, T. Two nonsense mutations of PAX6 in two Japanese aniridia families: Case report and review of the literature. *Eur. J. Ophthalmol.* **2000**, *10*, 167–172. [CrossRef]
330. D'Elia, A.V.; Puppin, C.; Pellizzari, L.; Pianta, A.; Bregant, E.; Lonigro, R.; Tell, G.; Fogolari, F.; van Heyningen, V.; Damante, G. Molecular analysis of a human PAX6 homeobox mutant. *Eur. J. Hum. Genet.* **2006**, *14*, 744–751. [CrossRef]
331. Hingorani, M.; Hanson, I.; van Heyningen, V. Aniridia. *Eur. J. Hum. Genet.* **2012**, *20*, 1011–1017. [CrossRef]
332. Cunha, D.L.; Arno, G.; Corton, M.; Moosajee, M. The Spectrum of PAX6 Mutations and Genotype-Phenotype Correlations in the Eye. *Genes* **2019**, *10*, 1050. [CrossRef]
333. West-Mays, J.A.; Zhang, J.; Nottoli, T.; Hagopian-Donaldson, S.; Libby, D.; Strissel, K.J.; Williams, T. AP-2αTranscription Factor Is Required for Early Morphogenesis of the Lens Vesicle. *Dev. Biol.* **1999**, *206*, 46–62. [CrossRef] [PubMed]
334. Kerr, C.L.; Zaveri, M.A.; Robinson, M.L.; Williams, T.; West-Mays, J.A. AP-2α is required after lens vesicle formation to maintain lens integrity. *Dev. Dyn.* **2014**, *243*, 1298–1309. [CrossRef] [PubMed]
335. Dumitrescu, A.V.; Milunsky, J.M.; Longmuir, S.Q.; Drack, A.V. A family with branchio-oculo-facial syndrome with primarily ocular involvement associated with mutation of the TFAP2A gene. *Ophthal. Genet.* **2012**, *33*, 100–106. [CrossRef] [PubMed]

336. Blixt, Å.; Mahlapuu, M.; Aitola, M.; Pelto-Huikko, M.; Enerbäck, S.; Carlsson, P. A forkhead gene, FoxE3, is essential for lens epithelial proliferation and closure of the lens vesicle. *Genes Dev.* **2000**, *14*, 245–254. [CrossRef]
337. Medina-Martinez, O.; Brownell, I.; Amaya-Manzanares, F.; Hu, Q.; Behringer, R.R.; Jamrich, M. Severe defects in proliferation and differentiation of lens cells in Foxe3 null mice. *Mol. Cell Biol.* **2005**, *25*, 8854–8863. [CrossRef]
338. Reis, L.M.; Sorokina, E.A.; Dudakova, L.; Moravikova, J.; Skalicka, P.; Malinka, F.; Seese, S.E.; Thompson, S.; Bardakjian, T.; Capasso, J. Comprehensive phenotypic and functional analysis of dominant and recessive FOXE3 alleles in ocular developmental disorders. *Hum. Mol. Genet.* **2021**, *30*, 1591–1606. [CrossRef]
339. Semina, E.V.; Murray, J.C.; Reiter, R.; Hrstka, R.F.; Graw, J. Deletion in the promoter region and altered expression of Pitx3 homeobox gene in aphakia mice. *Hum. Mol. Genet.* **2000**, *9*, 1575–1585. [CrossRef]
340. Medina-Martinez, O.; Shah, R.; Jamrich, M. Pitx3 controls multiple aspects of lens development. *Dev. Dyn.* **2009**, *238*, 2193–2201. [CrossRef]
341. Wada, K.; Matsushima, Y.; Tada, T.; Hasegawa, S.; Obara, Y.; Yoshizawa, Y.; Takahashi, G.; Hiai, H.; Shimanuki, M.; Suzuki, S. Expression of truncated PITX3 in the developing lens leads to microphthalmia and aphakia in mice. *PLoS ONE* **2014**, *9*, e111432. [CrossRef]
342. Valleix, S.; Niel, F.; Nedelec, B.; Algros, M.-P.; Schwartz, C.; Delbosc, B.; Delpech, M.; Kantelip, B. Homozygous nonsense mutation in the FOXE3 gene as a cause of congenital primary aphakia in humans. *Am. J. Hum. Genet.* **2006**, *79*, 358–364. [CrossRef]
343. Sakazume, S.; Sorokina, E.; Iwamoto, Y.; Semina, E.V. Functional analysis of human mutations in homeodomain transcription factor PITX3. *BMC Mol. Biol.* **2007**, *8*, 84. [CrossRef] [PubMed]
344. Verdin, H.; Sorokina, E.A.; Meire, F.; Casteels, I.; de Ravel, T.; Semina, E.V.; De Baere, E. Novel and recurrent PITX3 mutations in Belgian families with autosomal dominant congenital cataract and anterior segment dysgenesis have similar phenotypic and functional characteristics. *Orphanet J. Rare Dis.* **2014**, *9*, 26. [CrossRef] [PubMed]
345. Kim, J.I.; Li, T.; Ho, I.-C.; Grusby, M.J.; Glimcher, L.H. Requirement for the c-Maf transcription factor in crystallin gene regulation and lens development. *Proc. Natl. Acad. Sci. USA* **1999**, *96*, 3781–3785. [CrossRef] [PubMed]
346. Kawauchi, S.; Takahashi, S.; Nakajima, O.; Ogino, H.; Morita, M.; Nishizawa, M.; Yasuda, K.; Yamamoto, M. Regulation of lens fiber cell differentiation by transcription factor c-Maf. *J. Biol. Chem.* **1999**, *274*, 19254–19260. [CrossRef]
347. Ring, B.Z.; Cordes, S.P.; Overbeek, P.A.; Barsh, G.S. Regulation of mouse lens fiber cell development and differentiation by the Maf gene. *Development* **2000**, *127*, 307–317. [CrossRef]
348. Rajaram, N.; Kerppola, T.K. Synergistic transcription activation by Maf and Sox and their subnuclear localization are disrupted by a mutation in Maf that causes cataract. *Mol. Cell Biol.* **2004**, *24*, 5694–5709. [CrossRef]
349. Xie, Q.; Cvekl, A. The orchestration of mammalian tissue morphogenesis through a series of coherent feed-forward loops. *J. Biol. Chem.* **2011**, *286*, 43259–43271. [CrossRef]
350. Ma, A.S.; Grigg, J.R.; Ho, G.; Prokudin, I.; Farnsworth, E.; Holman, K.; Cheng, A.; Billson, F.A.; Martin, F.; Fraser, C.; et al. Sporadic and Familial Congenital Cataracts: Mutational Spectrum and New Diagnoses Using Next-Generation Sequencing. *Hum. Mut.* **2016**, *37*, 371–384. [CrossRef]
351. Jamieson, R.; Munier, F.; Balmer, A.; Farrar, N.; Perveen, R.; Black, G. Pulverulent cataract with variably associated microcornea and iris coloboma in a MAF mutation family. *Br. J. Ophthalmol.* **2003**, *87*, 411–412. [CrossRef]
352. Dudakova, L.; Stranecky, V.; Ulmanova, O.; Hlavova, E.; Trková, M.; Vincent, A.L.; Liskova, P. Segregation of a novel p.(Ser270Tyr) MAF mutation and p.(Tyr56∗) CRYGD variant in a family with dominantly inherited congenital cataracts. *Mol. Biol. Reps.* **2017**, *44*, 435–440. [CrossRef]
353. Fujimoto, M.; Izu, H.; Seki, K.; Fukuda, K.; Nishida, T.; Yamada, S.i.; Kato, K.; Yonemura, S.; Inouye, S.; Nakai, A. HSF4 is required for normal cell growth and differentiation during mouse lens development. *EMBO J.* **2004**, *23*, 4297–4306. [CrossRef] [PubMed]
354. Somasundaram, T.; Bhat, S.P. Developmentally dictated expression of heat shock factors: Exclusive expression of HSF4 in the postnatal lens and its specific interaction with αB-crystallin heat shock promoter. *J. Biol. Chem.* **2004**, *279*, 44497–44503. [CrossRef] [PubMed]
355. Cui, X.; Wang, L.; Zhang, J.; Du, R.; Liao, S.; Li, D.; Li, C.; Ke, T.; Li, D.W.-C.; Huang, H. HSF4 regulates DLAD expression and promotes lens de-nucleation. *Biochim. Biophys. Acta* **2013**, *1832*, 1167–1172. [CrossRef]
356. He, S.; Limi, S.; McGreal, R.S.; Xie, Q.; Brennan, L.A.; Kantorow, W.L.; Kokavec, J.; Majumdar, R.; Hou Jr, H.; Edelmann, W. Chromatin remodeling enzyme Snf2h regulates embryonic lens differentiation and denucleation. *Development* **2016**, *143*, 1937–1947. [CrossRef]
357. He, S.; Pirity, M.K.; Wang, W.-L.; Wolf, L.; Chauhan, B.K.; Cveklova, K.; Tamm, E.R.; Ashery-Padan, R.; Metzger, D.; Nakai, A. Chromatin remodeling enzyme Brg1 is required for mouse lens fiber cell terminal differentiation and its denucleation. *Epigenetics Chromatin* **2010**, *3*, 21. [CrossRef] [PubMed]
358. Berry, V.; Pontikos, N.; Moore, A.; Ionides, A.C.W.; Plagnol, V.; Cheetham, M.E.; Michaelides, M. A novel missense mutation in HSF4 causes autosomal-dominant congenital lamellar cataract in a British family. *Nature* **2018**, *32*, 806–812. [CrossRef] [PubMed]
359. Jing, Z.; Gangalum, R.K.; Bhat, A.M.; Nagaoka, Y.; Jiang, M.; Bhat, S.P. HSF 4 Mutation p. Arg116 H is Found in Age-Related Cataracts and in Normal Populations Produces Childhood Lamellar Cataract in Transgenic Mice. *Hum. Mut.* **2014**, *35*, 1068–1071. [CrossRef]

360. Smaoui, N.; Beltaief, O.; BenHamed, S.; M'Rad, R.; Maazoul, F.; Ouertani, A.; Chaabouni, H.; Hejtmancik, J.F. A Homozygous Splice Mutation in the HSF4 Gene Is Associated with an Autosomal Recessive Congenital Cataract. *Investig. Ophthalmol. Vis. Sci.* **2004**, *45*, 2716–2721. [CrossRef]
361. Williamson, K.A.; FitzPatrick, D.R. The genetic architecture of microphthalmia, anophthalmia and coloboma. *Eur. J. Med. Genet.* **2014**, *57*, 369–380. [CrossRef]
362. Reis, L.M.; Semina, E.V. Conserved genetic pathways associated with microphthalmia, anophthalmia, and coloboma. *Birth Defects Res. C Embryo Today* **2015**, *105*, 96–113. [CrossRef]
363. Deml, B.; Reis, L.M.; Lemyre, E.; Clark, R.D.; Kariminejad, A.; Semina, E.V. Novel mutations in PAX6, OTX2 and NDP in anophthalmia, microphthalmia and coloboma. *Eur. J. Hum. Genet.* **2016**, *24*, 535–541. [CrossRef] [PubMed]
364. Harding, P.; Moosajee, M. The molecular basis of human anophthalmia and microphthalmia. *J. Dev. Biol.* **2019**, *7*, 16. [CrossRef] [PubMed]
365. Ragge, N.K.; Brown, A.G.; Poloschek, C.M.; Lorenz, B.; Henderson, R.A.; Clarke, M.P.; Russell-Eggitt, I.; Fielder, A.; Gerrelli, D.; Martinez-Barbera, J.P. Heterozygous mutations of OTX2 cause severe ocular malformations. *Am. J. Hum. Genet.* **2005**, *76*, 1008–1022. [CrossRef] [PubMed]
366. Yonova-Doing, E.; Zhao, W.; Igo, R.P.; Wang, C.; Sundaresan, P.; Lee, K.E.; Jun, G.R.; Alves, A.C.; Chai, X.; Chan, A.S. Common variants in SOX-2 and congenital cataract genes contribute to age-related nuclear cataract. *Commun. Biol.* **2020**, *3*, 755. [CrossRef]
367. Seese, S.E.; Reis, L.M.; Deml, B.; Griffith, C.; Reich, A.; Jamieson, R.V.; Semina, E.V. Identification of missense MAB21L1 variants in microphthalmia and aniridia. *Hum. Mut.* **2021**, *42*, 877–890. [CrossRef]
368. Xiao, Y.; Xiang, J.W.; Gao, Q.; Bai, Y.Y.; Huang, Z.X.; Hu, X.H.; Wang, L.; Li, D.W. MAB21L1 promotes survival of lens epithelial cells through control of αB-crystallin and ATR/CHK1/p53 pathway. *Aging* **2022**, *14*, 6128–6148. [CrossRef]
369. Shiels, A.; Hejtmancik, J.F. Biology of Inherited Cataracts and Opportunities for Treatment. *Ann. Rev. Vis. Sci.* **2019**, *5*, 123–149. [CrossRef]
370. Shiels, A.; Hejtmancik, J.F. Inherited cataracts: Genetic mechanisms and pathways new and old. *Exp. Eye Res.* **2021**, *209*, 108662. [CrossRef]
371. Al-Ghoul, K.; Lane, C.; Taylor, V.; Fowle, W.; Costello, M. Distribution and type of morphological damage in human nuclear age-related cataracts. *Exp. Eye Res.* **1996**, *62*, 237–252. [CrossRef]
372. Al-Ghoul, K.J.; Nordgren, R.K.; Kuszak, A.J.; Freel, C.D.; Costello, M.J.; Kuszak, J.R. Structural evidence of human nuclear fiber compaction as a function of ageing and cataractogenesis. *Exp. Eye Res.* **2001**, *72*, 199–214. [CrossRef]
373. Vrensen, G.F.; Otto, C.; Lenferink, A.; Liszka, B.; Montenegro, G.A.; Barraquer, R.I.; Michael, R. Protein profiles in cortical and nuclear regions of aged human donor lenses: A confocal Raman microspectroscopic and imaging study. *Exp. Eye Res.* **2016**, *145*, 100–109. [CrossRef] [PubMed]
374. Sweeney, M.H.; Truscott, R.J. An impediment to glutathione diffusion in older normal human lenses: A possible precondition for nuclear cataract. *Exp. Eye Res.* **1998**, *67*, 587–595. [CrossRef] [PubMed]
375. Su, S.P.; Song, X.; Xavier, D.; Aquilina, J.A. Age-related cleavages of crystallins in human lens cortical fiber cells generate a plethora of endogenous peptides and high molecular weight complexes. *Proteins* **2015**, *83*, 1878–1886. [CrossRef] [PubMed]
376. Zhou, H.Y.; Yan, H.; Wang, L.L.; Yan, W.J.; Shui, Y.B.; Beebe, D.C. Quantitative proteomics analysis by iTRAQ in human nuclear cataracts of different ages and normal lens nuclei. *Proteom. Clin. Appl.* **2015**, *9*, 776–786. [CrossRef]
377. Wang, Z.; Friedrich, M.G.; Truscott, R.J.; Schey, K.L. Cleavage C-terminal to Asp leads to covalent crosslinking of long-lived human proteins. *Biochim. Biophys. Acta* **2019**, *1867*, 831–839. [CrossRef]
378. Duindam, J.J.; Vrensen, G.F.; Otto, C.; Greve, J. Cholesterol, phospholipid, and protein changes in focal opacities in the human eye lens. *Investig. Ophthalmol. Vis. Sci.* **1998**, *39*, 94–103.
379. Valapala, M.; Wilson, C.; Hose, S.; Bhutto, I.A.; Grebe, R.; Dong, A.; Greenbaum, S.; Gu, L.; Sengupta, S.; Cano, M. Lysosomal-mediated waste clearance in retinal pigment epithelial cells is regulated by CRYBA1/βA3/A1-crystallin via V-ATPase-MTORC1 signaling. *Autophagy* **2014**, *10*, 480–496. [CrossRef]
380. Ghosh, S.; Shang, P.; Terasaki, H.; Stepicheva, N.; Hose, S.; Yazdankhah, M.; Weiss, J.; Sakamoto, T.; Bhutto, I.A.; Xia, S. A role for βA3/A1-crystallin in type 2 EMT of RPE cells occurring in dry age-related macular degeneration. *Investig. Ophthalmol. Vis. Sci.* **2018**, *59*, AMD104–AMD113. [CrossRef]
381. Miller, J.D.; Ganat, Y.M.; Kishinevsky, S.; Bowman, R.L.; Liu, B.; Tu, E.Y.; Mandal, P.K.; Vera, E.; Shim, J.-w.; Kriks, S. Human iPSC-based modeling of late-onset disease via progerin-induced aging. *Cell Stem Cell* **2013**, *13*, 691–705. [CrossRef]
382. Sridhar, A.; Hoshino, A.; Finkbeiner, C.R.; Chitsazan, A.; Dai, L.; Haugan, A.K.; Eschenbacher, K.M.; Jackson, D.L.; Trapnell, C.; Bermingham-McDonogh, O. Single-cell transcriptomic comparison of human fetal retina, hPSC-derived retinal organoids, and long-term retinal cultures. *Cell Reps.* **2020**, *30*, 1644–1659. e1644. [CrossRef]
383. Lu, Y.; Brommer, B.; Tian, X.; Krishnan, A.; Meer, M.; Wang, C.; Vera, D.L.; Zeng, Q.; Yu, D.; Bonkowski, M.S.; et al. Reprogramming to recover youthful epigenetic information and restore vision. *Nature* **2020**, *588*, 124–129. [CrossRef] [PubMed]
384. Horwitz, J. Alpha-crystallin. *Exp. Eye Res.* **2003**, *76*, 145–153. [CrossRef]
385. Sprague-Piercy, M.A.; Rocha, M.A.; Kwok, A.O.; Martin, R.W. α-Crystallins in the vertebrate eye lens: Complex oligomers and molecular chaperones. *Ann. Rev. Phys. Chem.* **2021**, *72*, 143–163. [CrossRef] [PubMed]
386. Mackay, D.S.; Andley, U.P.; Shiels, A. Cell death triggered by a novel mutation in the αA-crystallin gene underlies autosomal dominant cataract linked to chromosome 21q. *Eur. J. Hum. Genet.* **2003**, *11*, 784–793. [CrossRef]

387. Litt, M.; Kramer, P.; LaMorticella, D.M.; Murphey, W.; Lovrien, E.W.; Weleber, R.G. Autosomal Dominant Congenital Cataract Associated with a Missense Mutation in the Human Alpha Crystallin Gene CRYAA. *Hum. Mol. Genet.* **1998**, *7*, 471–474. [CrossRef]
388. Kong, X.D.; Liu, N.; Shi, H.R.; Dong, J.M.; Zhao, Z.H.; Liu, J.; Li-Ling, J.; Yang, Y.X. A novel 3-base pair deletion of the CRYAA gene identified in a large Chinese pedigree featuring autosomal dominant congenital perinuclear cataract. *Genet. Mol. Res.* **2015**, *14*, 426–432. [CrossRef]
389. Marakhonov, A.V.; Voskresenskaya, A.A.; Ballesta, M.J.; Konovalov, F.A.; Vasilyeva, T.A.; Blanco-Kelly, F.; Pozdeyeva, N.A.; Kadyshev, V.V.; López-González, V.; Guillen, E.; et al. Expanding the phenotype of CRYAA nucleotide variants to a complex presentation of anterior segment dysgenesis. *Orphanet. J. Rare Di.S* **2020**, *15*, 207. [CrossRef]
390. Gerasimovich, E.S.; Strelkov, S.V.; Gusev, N.B. Some properties of three αB-crystallin mutants carrying point substitutions in the C-terminal domain and associated with congenital diseases. *Biochimie* **2017**, *142*, 168–178. [CrossRef]
391. Slingsby, C.; Wistow, G.J.; Clark, A.R. Evolution of crystallins for a role in the vertebrate eye lens. *Protein Sci.* **2013**, *22*, 367–380. [CrossRef]
392. Serebryany, E.; King, J.A. The βγ-crystallins: Native state stability and pathways to aggregation. *Prog. Biophys. Mol. Biol.* **2014**, *115*, 32–41. [CrossRef]
393. Lampi, K.J.; Wilmarth, P.A.; Murray, M.R.; David, L.L. Lens β-crystallins: The role of deamidation and related modifications in aging and cataract. *Prog. Biophys. Mol. Biol.* **2014**, *115*, 21–31. [CrossRef] [PubMed]
394. Ma, Z.; Yao, W.; Chan, C.-C.; Kannabiran, C.; Wawrousek, E.; Hejtmancik, J.F. Human βA3/A1-crystallin splicing mutation causes cataracts by activating the unfolded protein response and inducing apoptosis in differentiating lens fiber cells. *Biochim. Et Biophys. Acta Mol. Basis Dis.* **2016**, *1862*, 1214–1227. [CrossRef]
395. Reddy, M.A.; Bateman, O.A.; Chakarova, C.; Ferris, J.; Berry, V.; Lomas, E.; Sarra, R.; Smith, M.A.; Moore, A.T.; Bhattacharya, S.S.; et al. Characterization of the G91del CRYBA1/3-crystallin protein: A cause of human inherited cataract. *Hum. Mol. Genet.* **2004**, *13*, 945–953. [CrossRef] [PubMed]
396. Wang, K.J.; Wang, S.; Cao, N.-Q.; Yan, Y.-B.; Zhu, S.Q. A novel mutation in CRYBB1 associated with congenital cataract-microcornea syndrome: The p.Ser129Arg mutation destabilizes the βB1/βA3-crystallin heteromer but not the βB1-crystallin homomer. *Hum. Mut.* **2011**, *32*, E2050–E2060. [CrossRef] [PubMed]
397. Litt, M.; Carrero-Valenzuela, R.; LaMorticella, D.M.; Schultz, D.W.; Mitchell, T.N.; Kramer, P.; Maumenee, I.H. Autosomal Dominant Cerulean Cataract Is Associated with a Chain Termination Mutation in the Human β-Crystallin Gene CRYBB2. *Hum. Mol. Genet.* **1997**, *6*, 665–668. [CrossRef] [PubMed]
398. Li, X.-Q.; Cai, H.-C.; Zhou, S.-Y.; Yang, J.-H.; Xi, Y.-B.; Gao, X.-B.; Zhao, W.-J.; Li, P.; Zhao, G.-Y.; Tong, Y.; et al. A novel mutation impairing the tertiary structure and stability of γC-crystallin (CRYGC) leads to cataract formation in humans and zebrafish lens. *Hum. Mut.* **2012**, *33*, 391–401. [CrossRef]
399. Kmoch, S.; Brynda, J.; Asfaw, B.; Bezouška, K.; Novák, P.; Řezáčová, P.; Ondrová, L.; Filipec, M.; Sedláček, J.; Elleder, M. Link between a novel human γD-crystallin allele and a unique cataract phenotype explained by protein crystallography. *Hum. Mol. Genet.* **2000**, *9*, 1779–1786. [CrossRef]
400. Wang, B.; Yu, C.; Xi, Y.-B.; Cai, H.-C.; Wang, J.; Zhou, S.; Zhou, S.; Wu, Y.; Yan, Y.-B.; Ma, X.; et al. A novel CRYGD mutation (p.Trp43Arg) causing autosomal dominant congenital cataract in a Chinese family. *Hum. Mut.* **2011**, *32*, E1939–E1947. [CrossRef]
401. Mulders, S.M.; Preston, G.M.; Deen, P.M.; Guggino, W.B.; van Os, C.H.; Agre, P. Water channel properties of major intrinsic protein of lens. *J. Biol. Chem.* **1995**, *270*, 9010–9016. [CrossRef]
402. Shiels, A.; Bassnett, S. Mutations in the founder of the MIP gene family underlie cataract development in the mouse. *Nat. Genet.* **1996**, *12*, 212–215. [CrossRef]
403. Francis, P.; Chung, J.-J.; Yasui, M.; Berry, V.; Moore, A.; Wyatt, M.K.; Wistow, G.; Bhattacharya, S.S.; Agre, P. Functional impairment of lens aquaporin in two families with dominantly inherited cataracts. *Hum. Mol. Genet.* **2000**, *9*, 2329–2334. [CrossRef] [PubMed]
404. Berry, V.; Francis, P.; Kaushal, S.; Moore, A.; Bhattacharya, S. Missense mutations in MIP underlie autosomal dominant 'polymorphic'and lamellar cataracts linked to 12q. *Nat. Genet.* **2000**, *25*, 15–17. [CrossRef] [PubMed]
405. Shiels, A.; King, J.M.; Mackay, D.S.; Bassnett, S. Refractive defects and cataracts in mice lacking lens intrinsic membrane protein-2. *Investig. Ophthalmol. Vis. Sci.* **2007**, *48*, 500–508. [CrossRef] [PubMed]
406. Shi, Y.; De Maria, A.B.; Wang, H.; Mathias, R.T.; FitzGerald, P.G.; Bassnett, S. Further analysis of the lens phenotype in Lim2-deficient mice. *Investig. Ophthalmol. Vis. Sci.* **2011**, *52*, 7332–7339. [CrossRef] [PubMed]
407. Irum, B.; Khan, S.Y.; Ali, M.; Kaul, H.; Kabir, F.; Rauf, B.; Fatima, F.; Nadeem, R.; Khan, A.O.; Al Obaisi, S. Mutation in LIM2 is responsible for autosomal recessive congenital cataracts. *PLoS ONE* **2016**, *11*, e0162620. [CrossRef]
408. Berry, V.; Fujinami, K.; Mochizuki, K.; Iwata, T.; Pontikos, N.; Quinlan, R.A.; Michaelides, M. A recurrent variant in LIM2 causes an isolated congenital sutural/lamellar cataract in a Japanese family. *Ophthalmic Genet.* **2022**, 1–5. [CrossRef]
409. Berry, V.; Pontikos, N.; Dudakova, L.; Moore, A.T.; Quinlan, R.; Liskova, P.; Michaelides, M. A novel missense mutation in LIM2 causing isolated autosomal dominant congenital cataract. *Ophthalmic Genet.* **2020**, *41*, 131–134. [CrossRef]
410. Wang, E.; Geng, A.; Maniar, A.M.; Mui, B.W.; Gong, X. Connexin 50 regulates surface ball-and-socket structures and fiber cell organization. *Investig. Ophthalmol. Vis. Sci.* **2016**, *57*, 3039–3046. [CrossRef]
411. Flores, J.A.; Haddad, B.G.; Dolan, K.A.; Myers, J.B.; Yoshioka, C.C.; Copperman, J.; Zuckerman, D.M.; Reichow, S.L. Connexin-46/50 in a dynamic lipid environment resolved by CryoEM at 1.9 Å. *Nat. Commun.* **2020**, *11*, 4331. [CrossRef]

412. Minogue, P.J.; Tong, J.-J.; Wichmann, K.; Mysliwiec, H.; Ebihara, L.; Beyer, E.C.; Berthoud, V.M. Cataract-linked serine mutations in the gap junction protein connexin50 expose a sorting signal that promotes its lysosomal degradation. *J. Biol. Chem.* **2022**, *298*, 101673. [CrossRef]
413. Berthoud, V.M.; Minogue, P.J.; Guo, J.; Williamson, E.K.; Xu, X.; Ebihara, L.; Beyer, E.C. Loss of function and impaired degradation of a cataract-associated mutant connexin50. *Eur. J. Cell Biol.* **2003**, *82*, 209–221. [CrossRef]
414. Vanita, V.; Singh, J.R.; Singh, D.; Varon, R.; Sperling, K. A novel mutation in GJA8 associated with jellyfish-like cataract in a family of Indian origin. *Mol. Vis.* **2008**, *14*, 323. [PubMed]
415. Myers, J.B.; Haddad, B.G.; O'Neill, S.E.; Chorev, D.S.; Yoshioka, C.C.; Robinson, C.V.; Zuckerman, D.M.; Reichow, S.L. Structure of native lens connexin 46/50 intercellular channels by cryo-EM. *Nature* **2018**, *564*, 372–377. [CrossRef] [PubMed]
416. Berthoud, V.M.; Montegna, E.A.; Atal, N.; Aithal, N.H.; Brink, P.R.; Beyer, E.C. Heteromeric connexons formed by the lens connexins, connexin43 and connexin56. *Eur. J. Cell Biol.* **2001**, *80*, 11–19. [CrossRef] [PubMed]
417. Jiang, H.; Jin, Y.; Bu, L.; Zhang, W.; Liu, J.; Cui, B.; Kong, X.; Hu, L. A novel mutation in GJA3 (connexin46) for autosomal dominant congenital nuclear pulverulent cataract. *Mol. Vis.* **2003**, *9*, 579–583.
418. Santhiya, S.T.; Kumar, G.S.; Sudhakar, P.; Gupta, N.; Klopp, N.; Illig, T.; Söker, T.; Groth, M.; Platzer, M.; Gopinath, P.M.; et al. Molecular analysis of cataract families in India: New mutations in the CRYBB2 and GJA3 genes and rare polymorphisms. *Mol. Vis.* **2010**, *16*, 1837–1847.
419. Zhou, Y.; Bennett, T.M.; Ruzycki, P.A.; Shiels, A. Mutation of the EPHA2 tyrosine-kinase domain dysregulates cell pattern formation and cytoskeletal gene expression in the lens. *Cells* **2021**, *10*, 2606. [CrossRef]
420. Zhai, Y.; Zhu, S.; Li, J.; Yao, K. A novel human congenital cataract mutation in EPHA2 kinase domain (p. G668D) alters receptor stability and function. *Investig. Ophthalmol. Vis. Sci.* **2019**, *60*, 4717–4726. [CrossRef]
421. Bennett, T.M.; M'Hamdi, O.; Hejtmancik, J.F.; Shiels, A. Germ-line and somatic EPHA2 coding variants in lens aging and cataract. *PLoS ONE* **2017**, *12*, e0189881. [CrossRef]
422. Berry, V.; Pontikos, N.; Albarca-Aguilera, M.; Plagnol, V.; Massouras, A.; Prescott, D.; Moore, A.T.; Arno, G.; Cheetham, M.E.; Michaelides, M. A recurrent splice-site mutation in EPHA2 causing congenital posterior nuclear cataract. *Ophthalmic Genet.* **2018**, *39*, 236–241. [CrossRef]
423. Zhai, Y.; Li, J.; Yu, W.; Zhu, S.; Yu, Y.; Wu, M.; Sun, G.; Gong, X.; Yao, K. Targeted exome sequencing of congenital cataracts related genes: Broadening the mutation spectrum and genotype–phenotype correlations in 27 Chinese Han families. *Sci. Reps.* **2017**, *7*, 1219. [CrossRef] [PubMed]
424. Chen, F.; Wang, T.; Yang, Y.; Huang, Z.; Dong, Y.; Zhang, R.; Chen, J.; Zhou, Q. Generation of an induced pluripotent stem cell line (SYSUSCi001-A) from a congenital cataract patient carrying heterozygous mutations in BFSP1 and RHO. *Stem Cell Res.* **2022**, *59*, 102644. [CrossRef] [PubMed]
425. Jakobs, P.M.; Hess, J.F.; FitzGerald, P.G.; Kramer, P.; Weleber, R.G.; Litt, M. Autosomal-dominant congenital cataract associated with a deletion mutation in the human beaded filament protein gene BFSP2. *Am. J. Hum. Genet.* **2000**, *66*, 1432–1436. [CrossRef] [PubMed]
426. Lachke, S.A.; Alkuraya, F.S.; Kneeland, S.C.; Ohn, T.; Aboukhalil, A.; Howell, G.R.; Saadi, I.; Cavallesco, R.; Yue, Y.; Tsai, A.C. Mutations in the RNA granule component TDRD7 cause cataract and glaucoma. *Science* **2011**, *331*, 1571–1576. [CrossRef]
427. Dewi, C.U.; O'Connor, M.D. Use of human pluripotent stem cells to define initiating molecular mechanisms of cataract for anti-cataract drug discovery. *Cells* **2019**, *8*, 1269. [CrossRef]
428. Qin, Z.; Zhang, L.; Lyu, D.; Li, J.; Tang, Q.; Yin, H.; Chen, Z.; Yao, K.; Fu, Q. Opacification of lentoid bodies derived from human induced pluripotent stem cells is accelerated by hydrogen peroxide and involves protein aggregation. *J. Cell Physiol.* **2019**, *234*, 23750–23762. [CrossRef]
429. Makley, L.N.; McMenimen, K.A.; DeVree, B.T.; Goldman, J.W.; McGlasson, B.N.; Rajagopal, P.; Dunyak, B.M.; McQuade, T.J.; Thompson, A.D.; Sunahara, R. Pharmacological chaperone for α-crystallin partially restores transparency in cataract models. *Science* **2015**, *350*, 674–677. [CrossRef]
430. Daszynski, D.M.; Santhoshkumar, P.; Phadte, A.S.; Sharma, K.K.; Zhong, H.A.; Lou, M.F.; Kador, P.F. Failure of oxysterols such as lanosterol to restore lens clarity from cataracts. *Sci. Reps.* **2019**, *9*, 8459. [CrossRef]
431. Molnar, K.S.; Dunyak, B.M.; Su, B.; Izrayelit, Y.; McGlasson-Naumann, B.; Hamilton, P.D.; Qian, M.; Covey, D.F.; Gestwicki, J.E.; Makley, L.N. Mechanism of action of VP1-001 in cryAB (R120G)-associated and age-related cataracts. *Investig. Ophthalmol. Vis. Sci.* **2019**, *60*, 3320–3331. [CrossRef]
432. Zhang, L.; Qin, Z.; Lyu, D.; Lu, B.; Chen, Z.; Fu, Q.; Yao, K. Postponement of the opacification of lentoid bodies derived from human induced pluripotent stem cells after lanosterol treatment-the first use of the lens aging model in vitro in cataract drug screening. *Front. Pharmacol.* **2022**, *13*, 959978. [CrossRef]
433. Filatova, A.Y.; Vasilyeva, T.A.; Marakhonov, A.V.; Voskresenskaya, A.A.; Zinchenko, R.A.; Skoblov, M.Y. Functional reassessment of PAX6 single nucleotide variants by in vitro splicing assay. *Eur. J. Hum. Genet.* **2019**, *27*, 488–493. [CrossRef] [PubMed]
434. Moravikova, J.; Kozmik, Z.; Hlavata, L.; Putzova, M.; Skalicka, P.; Michaelides, M.; Malinka, F.; Dudakova, L.; Liskova, P. Phenotype Variability in Czech Patients Carrying PAX6 Disease-Causing Variants. *Folia Biol.* **2020**, *66*, 123–132.
435. Tarilonte, M.; Ramos, P.; Moya, J.; Fernandez-Sanz, G.; Blanco-Kelly, F.; Swafiri, S.T.; Villaverde, C.; Romero, R.; Tamayo, A.; Gener, B. Activation of cryptic donor splice sites by non-coding and coding PAX6 variants contributes to congenital aniridia. *J. Med. Genet.* **2022**, *59*, 428–437. [CrossRef] [PubMed]

436. Stoevring, B.; Frederiksen, J.L.; Christiansen, M. CRYAB promoter polymorphisms: Influence on multiple sclerosis susceptibility and clinical presentation. *Clin. Chim. Acta* **2007**, *375*, 57–62. [CrossRef] [PubMed]
437. Kim, K.; Wen, B.; Ng, K.; Zhao, R.; Cahan, P.; Kim, J.; Aryee, M.; Ji, H.; Ehrlich, L.; Yabuuchi, A. Epigenetic memory in induced pluripotent stem cells. *Nature* **2010**, *467*, 285–290. [CrossRef]
438. Bar-Nur, O.; Russ, H.A.; Efrat, S.; Benvenisty, N. Epigenetic memory and preferential lineage-specific differentiation in induced pluripotent stem cells derived from human pancreatic islet beta cells. *Cell Stem Cell* **2011**, *9*, 17–23. [CrossRef]
439. Kadauke, S.; Blobel, G.A. Mitotic bookmarking by transcription factors. *Epigenetics Chromatin* **2013**, *6*, 6. [CrossRef]
440. Bellec, M.; Radulescu, O.; Lagha, M. Remembering the past: Mitotic bookmarking in a developing embryo. *Curr. Opin. Syst. Biol.* **2018**, *11*, 41–49. [CrossRef]
441. Palozola, K.C.; Lerner, J.; Zaret, K.S. A changing paradigm of transcriptional memory propagation through mitosis. *Nat. Rev. Mol. Cell Biol.* **2019**, *20*, 55–64. [CrossRef]
442. Disatham, J.; Chauss, D.; Gheyas, R.; Brennan, L.; Blanco, D.; Daley, L.; Menko, A.S.; Kantorow, M. Lens differentiation is characterized by stage-specific changes in chromatin accessibility correlating with differentiation state-specific gene expression. *Dev. Biol.* **2019**, *453*, 86–104. [CrossRef]
443. Zhao, Y.; Zheng, D.; Cvekl, A. Profiling of chromatin accessibility and identification of general cis-regulatory mechanisms that control two ocular lens differentiation pathways. *Epigenetics Chromatin* **2019**, *12*, 27. [CrossRef] [PubMed]
444. Hoang, T.V.; Horowitz, E.R.; Chaffee, B.R.; Qi, P.; Flake, R.E.; Bruney, D.G.; Rasor, B.J.; Rosalez, S.E.; Wagner, B.D.; Robinson, M.L. Lens development requires DNMT1 but takes place normally in the absence of both DNMT3A and DNMT3B activity. *Epigenetics* **2017**, *12*, 27–40. [CrossRef] [PubMed]
445. Wang, W.-L.; Li, Q.; Xu, J.; Cvekl, A. Lens fiber cell differentiation and denucleation are disrupted through expression of the N-terminal nuclear receptor box of NCOA6 and result in p53-dependent and p53-independent apoptosis. *Mol. Biol. Cell* **2010**, *21*, 2453–2468. [CrossRef] [PubMed]
446. Lu, J.; An, J.; Wang, J.; Cao, X.; Cao, Y.; Huang, C.; Jiao, S.; Yan, D.; Lin, X.; Zhou, X. Znhit1 Regulates p21Cip1 to Control Mouse Lens Differentiation. *Investig. Ophthalmol. Vis. Sci.* **2022**, *63*, 18. [CrossRef]
447. Atzmon, G.; Rincon, M.; Schechter, C.B.; Shuldiner, A.R.; Lipton, R.B.; Bergman, A.; Barzilai, N. Lipoprotein Genotype and Conserved Pathway for Exceptional Longevity in Humans. *PLoS Biol.* **2006**, *4*, e113. [CrossRef]
448. Lin, J.-R.; Sin-Chan, P.; Napolioni, V.; Torres, G.G.; Mitra, J.; Zhang, Q.; Jabalameli, M.R.; Wang, Z.; Nguyen, N.; Gao, T.; et al. Rare genetic coding variants associated with human longevity and protection against age-related diseases. *Nat. Aging* **2021**, *1*, 783–794. [CrossRef]
449. Willcox, D.C.; Willcox, B.J.; Wang, N.-C.; He, Q.; Rosenbaum, M.; Suzuki, M. Life at the Extreme Limit: Phenotypic Characteristics of Supercentenarians in Okinawa. *J. Gerontol.* **2008**, *63*, 1201–1208. [CrossRef]
450. Nye-Wood, M.G.; Spraggins, J.M.; Caprioli, R.M.; Schey, K.L.; Donaldson, P.J.; Grey, A.C. Spatial distributions of glutathione and its endogenous conjugates in normal bovine lens and a model of lens aging. *Exp. Eye Res.* **2017**, *154*, 70–78. [CrossRef]
451. Yanshole, V.V.; Yanshole, L.V.; Snytnikova, O.A.; Tsentalovich, Y.P. Quantitative metabolomic analysis of changes in the lens and aqueous humor under development of age-related nuclear cataract. *Metabolomics* **2019**, *15*, 29. [CrossRef]
452. Frankfater, C.; Bozeman, S.L.; Hsu, F.-F.; Andley, U.P. Alpha-crystallin mutations alter lens metabolites in mouse models of human cataracts. *PLoS ONE* **2020**, *15*, e0238081. [CrossRef]
453. Khan, S.Y.; Ali, M.; Kabir, F.; Na, C.H.; Delannoy, M.; Ma, Y.; Qiu, C.; Costello, M.J.; Hejtmancik, J.F.; Riazuddin, S.A. The role of FYCO1-dependent autophagy in lens fiber cell differentiation. *Autophagy* **2022**, *18*, 2198–2215. [CrossRef] [PubMed]
454. Serebryany, E.; Chowdhury, S.; Woods, C.N.; Thorn, D.C.; Watson, N.E.; McClelland, A.A.; Klevit, R.E.; Shakhnovich, E.I. A native chemical chaperone in the human eye lens. *eLife* **2022**, *11*, e76923. [CrossRef] [PubMed]
455. Mikos, A.G.; Herring, S.W.; Ochareon, P.; Elisseeff, J.; Lu, H.H.; Kandel, R.; Schoen, F.J.; Toner, M.; Mooney, D.; Atala, A. Engineering complex tissues. *Tissue Eng.* **2006**, *12*, 3307–3339. [CrossRef] [PubMed]
456. Quinlan, R.A.; Clark, J.I. Insights into the Biochemical and Biophysical Mechanisms Mediating the Longevity of the Transparent Optics of the Eye Lens. *J. Biol. Chem.* **2022**, 102537. [CrossRef]
457. Pierscionek, B.K.; Regini, J.W. The gradient index lens of the eye: An opto-biological synchrony. *Prog. Retin. Eye Res.* **2012**, *31*, 332–349. [CrossRef]
458. Bassnett, S.; Shi, Y.; Vrensen, G.F.J.M. Biological glass: Structural determinants of eye lens transparency. *Philos. Trans. R. Soc. Lond. B. Biol. Sci.* **2011**, *366*, 1250–1264. [CrossRef]
459. Jaimes-Nájera, A.; Gómez-Correa, J.; Coello, V.; Pierscionek, B.; Chavez-Cerda, S. Single function crystalline lens capable of mimicking ciliary body accommodation. *Biomed. Opt. Express* **2020**, *11*, 3699–3716. [CrossRef]
460. Torrejon, K.Y.; Pu, D.; Bergkvist, M.; Danias, J.; Sharfstein, S.T.; Xie, Y. Recreating a human trabecular meshwork outflow system on microfabricated porous structures. *Biotechnol. Bioeng.* **2013**, *110*, 3205–3218. [CrossRef]
461. Tian, Y.I.; Zhang, X.; Torrejon, K.; Danias, J.; Gindina, S.; Nayyar, A.; Du, Y.; Xie, Y. A bioengineering approach to Schlemm's canal-like stem cell differentiation for in vitro glaucoma drug screening. *Acta. Biomater.* **2020**, *105*, 203–213. [CrossRef]
462. Kim, J.; Park, J.Y.; Kong, J.S.; Lee, H.; Won, J.Y.; Cho, D.W. Development of 3D Printed Bruch's Membrane-Mimetic Substance for the Maturation of Retinal Pigment Epithelial Cells. *Int. J. Mol. Sci.* **2021**, *22*, 1095. [CrossRef]
463. Takezawa, T.; Ozaki, K.; Nitani, A.; Takabayashi, C.; Shimo-Oka, T. Collagen vitrigel: A novel scaffold that can facilitate a three-dimensional culture for reconstructing organoids. *Cell Transplant.* **2004**, *13*, 463–474. [CrossRef] [PubMed]

464. Wang, X.; Maruotti, J.; Majumdar, S.; Roman, J.; Mao, H.Q.; Zack, D.J.; Elisseeff, J.H. Collagen vitrigels with low-fibril density enhance human embryonic stem cell-derived retinal pigment epithelial cell maturation. *J. Tissue Eng. Regen. Med.* **2018**, *12*, 821–829. [CrossRef] [PubMed]
465. Bannier-Hélaouët, M.; Post, Y.; Korving, J.; Bustos, M.T.; Gehart, H.; Begthel, H.; Bar-Ephraim, Y.E.; van der Vaart, J.; Kalmann, R.; Imhoff, S.M. Exploring the human lacrimal gland using organoids and single-cell sequencing. *Cell Stem Cell* **2021**, *28*, 1221–1232. e1227. [CrossRef] [PubMed]
466. O'Hara-Wright, M.; Gonzalez-Cordero, A. Retinal organoids: A window into human retinal development. *Development* **2020**, *147*, dev189746. [CrossRef]
467. Brassard, J.A.; Lutolf, M.P. Engineering stem cell self-organization to build better organoids. *Cell Stem Cell* **2019**, *24*, 860–876. [CrossRef]
468. Garreta, E.; Kamm, R.D.; Chuva de Sousa Lopes, S.M.; Lancaster, M.A.; Weiss, R.; Trepat, X.; Hyun, I.; Montserrat, N. Rethinking organoid technology through bioengineering. *Nat. Mater.* **2021**, *20*, 145–155. [CrossRef]
469. Achberger, K.; Probst, C.; Haderspeck, J.; Bolz, S.; Rogal, J.; Chuchuy, J.; Nikolova, M.; Cora, V.; Antkowiak, L.; Haq, W.; et al. Merging organoid and organ-on-a-chip technology to generate complex multi-layer tissue models in a human retina-on-a-chip platform. *eLife* **2019**, *8*, e46188. [CrossRef]
470. Xue, Y.; Seiler, M.J.; Tang, W.C.; Wang, J.Y.; Delgado, J.; McLelland, B.T.; Nistor, G.; Keirstead, H.S.; Browne, A.W. Retinal organoids on-a-chip: A micro-millifluidic bioreactor for long-term organoid maintenance. *Lab Chip* **2021**, *21*, 3361–3377. [CrossRef]
471. Puleo, C.M.; Ambrose, W.M.; Takezawa, T.; Elisseeff, J.; Wang, T.-H. Integration and application of vitrified collagen in multilayered microfluidic devices for corneal microtissue culture. *Lab Chip* **2009**, *9*, 3221–3227. [CrossRef]

cells

MDPI

Review

Role of Decorin in the Lens and Ocular Diseases

Eri Kubo [1,*], Shinsuke Shibata [1], Teppei Shibata [1], Hiroshi Sasaki [1] and Dhirendra P. Singh [2]

[1] Department of Ophthalmology, Kanazawa Medical University, Kanazawa 920-0293, Ishikawa, Japan
[2] Department of Ophthalmology, University of Nebraska Medical Center, Omaha, NE 68198, USA
* Correspondence: kuboe@kanazawa-med.ac.jp; Tel.: +81-76-286-2211 (ext. 3412); Fax: +81-76-286-1010

Abstract: Decorin is an archetypal member of the small leucine-rich proteoglycan gene family and is involved in various biological functions and many signaling networks, interacting with extracellular matrix (ECM) components, growth factors, and receptor tyrosine kinases. Decorin also modulates the growth factors, cell proliferation, migration, and angiogenesis. It has been reported to be involved in many ischemic and fibrotic eye diseases, such as congenital stromal dystrophy of the cornea, anterior subcapsular fibrosis of the lens, proliferative vitreoretinopathy, et al. Furthermore, recent evidence supports its role in secondary posterior capsule opacification (PCO) after cataract surgery. The expression of decorin mRNA in lens epithelial cells in vitro was found to decrease upon transforming growth factor (TGF)-β-2 addition and increase upon fibroblast growth factor (FGF)-2 addition. Wound healing of the injured lens in mice transgenic for lens-specific human decorin was promoted by inhibiting myofibroblastic changes. Decorin may be associated with epithelial–mesenchymal transition and PCO development in the lens. Gene therapy and decorin administration have the potential to serve as excellent therapeutic approaches for modifying impaired wound healing, PCO, and other eye diseases related to fibrosis and angiogenesis. In this review, we present findings regarding the roles of decorin in the lens and ocular diseases.

Keywords: decorin; posterior capsule opacification; fibrotic diseses; TGF-β2; FGF-2

1. Introduction

Decorin (DCN) belongs to a growing family of class I small leucine-rich proteoglycan proteins (SLRPs) that consist of a single glycosaminoglycan side chain (GAG), including a core protein containing leucine-rich repeats (LRR) with a molecular weight of approximately 42 kDa [1]. Decorin is mainly synthesized by fibroblasts, stressed vascular endothelial cells, and smooth muscle cells. It is widely distributed in the stromal tissues and is expressed and secreted in various connective tissues, including the skin, bone, cartilage, ligaments, breast and vessel walls, and eyeballs, and in body fluids such as the plasma, aqueous humor, and vitreous humor [1–14]. Decorin is the main component of the extracellular matrix (ECM), together with collagen fibrils, and acts as a bridging molecule between type I and type VI collagen [15–17]. Decorin also regulates various cellular processes, including the ECM remodeling, fibrosis, cell proliferation, migration, differentiation, wound healing, autophagy, and angiogenesis. It also has essential inhibitory roles in inflammation, fibrotic disorders, and tumors [3,6,18–26]. Decorin interacts with and modulates multiple growth factors and signaling pathways, such as the transforming growth factor (TGF)-β pathway, fibroblast growth factor (FGF), platelet-derived growth factor (PDGF), and cellular communication network factor 2/connective tissue growth factor (CCN2/CTGF). Moreover, it directly blocks various receptor tyrosine kinase (RTK) family proteins, such as the epidermal growth factor receptor (EGFR), Erb4, and its other family members, insulin-like growth factor-I receptor (IGF-IR), vascular endothelial growth factor receptor 2 (VEGFR2) and the hepatocyte growth factor receptor 1 (HGFR1), and Toll-like receptors (TLRs) binding to multiple binds multiple cell surface receptors [4,5,26–28]. Decorin also acts as a reservoir for several different growth factors, sequestering signaling

molecules in the ECM [29]. Thus, it is well known that decorin evokes potent tumor repression and wound-healing properties.

Here, we review the current knowledge of the role of decorin in the lens and ocular diseases. We hypothesize that decorin plays an important regulatory role in inhibiting ocular inflammatory and fibroblastic responses.

2. Structure and Function of Decorin

The structural and putative functional features of decorin are shown in Figure 1. The mature decorin molecule consists of a globular core protein and a covalently- linked GAG chain [30]. The primary translation product of human decorin is 359 amino acids long and can be divided into four functional domains (Figure 1) [30]. Domain I contains the initial 16-amino-acid long signal peptide directing the nascent protein to the rough endo plasmic reticulum, which is absent in the mature decorin protein [31]. Domain II contains 14 amino acid propeptide residues, regulating the attachment of GAGs composed of either dermatan or chondroitin sulfate [31]. GAG interacts with thrombospondins (Thbs), other GAGs, cytokines, and growth factors, such as TNF (tumor necrosis factor)-α and FGF1, 2, 7, and 8, regulating cell growth, wound healing, axon regeneration, and neural stem cell proliferation [32,33]. Decorin GAG may also inhibit blood coagulation by interacting with heparin cofactor II [34].

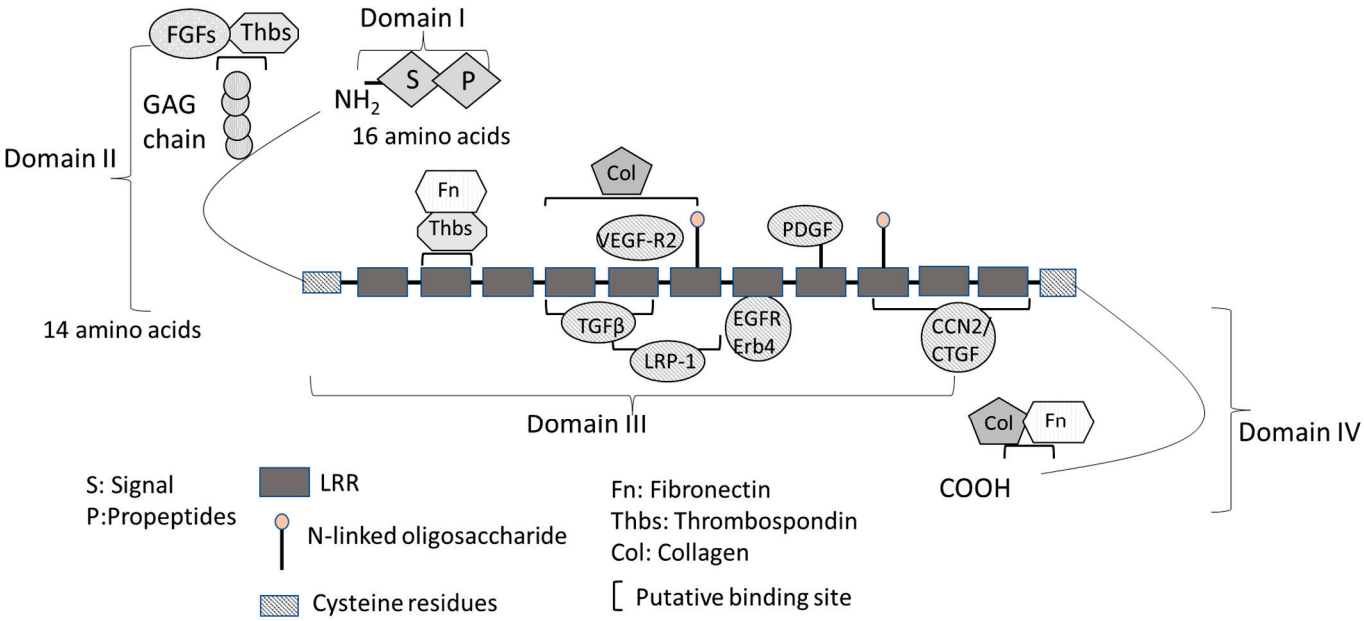

Figure 1. Structural and putative functional features of the decorin (DCN) molecule. Mammalian decorin contains core proteins and a glycosaminoglycan (GAG) side chain attached to a serine residue near the N terminus. Four domains of core proteins (I–IV) of DCN are shown. In domain I, the initial 16-amino-acid long signal peptide directs the incipient core protein to the rough endoplasmic reticulum and is cleaved via the co-translational pathway. In domain II, the propeptide is composed of 14 amino acids and regulates the attachment of the GAG chain. The protein core consists of tandem leucine-rich repeats (LRRs) flanking cysteine-rich disulfide domains. Twelve LRRs in domain III comprise the major central domain. Most decorin ligands share an interface with decorin at its core protein, an important hub for the extracellular matrix, cell surface receptors, and growth factors. Decorin has a high-affinity binding site for collagen (Col) at LRRs 4–6 and a low-affinity site at the C-terminus. The binding sites of TGF-β isoforms are LRR4 and LRR5 at the decorin core protein in domain II. The LRR7 domain binds to EGFR and ErB4 and activates the MAPK pathway. Decorin interacts with multiple growth factor signaling pathways. The carboxyl terminus domain and binding sites for fibronectin Fn and collagen Col can be found in domain IV.

Domain III is the most important domain of decorin and has a major regulatory role by interacting with different signaling molecules [30]. Domain III consists of twelve tan-dem LRRs flanked by conserved cysteine (Cys)-rich domains and is important for its biological function. Decorin has a high-affinity binding site for collagen at LRRs 4–6 and a low-affinity site at the C-terminus for interacting with multiple collagen molecules simultaneously [31]. Decorin is also involved in the regulation of collagen fibrillogenesis. Mutant mice with a targeted disruption of the decorin gene ($Dcn^{-/-}$) have fragile skin with abnormal collagen architecture in the dermis and reduced tensile strength, and showed a delay in epidermal and dermal wound healing [6,35,36]. Decorin has two binding sites for TGF-β isoforms at LRR4 and LRR5 with varying affinity in its core protein domain III, thus regulating TGF-β/ECM interactions (Figure 1) [37]. Decorin binds with high affinity to all isoforms of the TGF-β family and neutralizes their interaction with pro-fibrotic receptors [20]. LDL receptor-related protein 1 (LRP-1), an endocytic receptor for decorin involved in mediating TGF-β-dependent signaling, binds LRR5 and LRR6 [38–40]. CCN2/CTGF is an matricellular protein which that bridges the functional divide division between structural macromolecules and growth factors, which regulates regulating many cellular functions including cell adhesion, matrix production, structural remodeling, angiogenesis, and cell proliferation, fibrosis, and differentiation [41]. CCN2/CTGF binds and induces growth factors (e.g., TGF-β and VEGF, thereby regulating their functions) and ECM proteins [41]. CCN2/CTGF also binds to LRR10-12, stimulating decorin and repressing the activity of important cytokines [42,43]. The LRR7 domain binds to EGFR and ErB4 and activates the mitogen-activated protein kinase (MAPK) pathway [44]. The LRR5 domain binds directly to VEGFR2 at a site that partially overlaps with the canonical binding site for VEGF-A [45]. Domain IV, the carboxyl terminus domain, contains binding sites for collagen fibrils and fibronectin (Fn) [30].

Although they are do not act as binding ligands for decorin, proteases play an important role in the decorin interaction network. These proteases primarily include matrix metalloproteinases (MMP) 2, 3, and 7 [46–48]. MMP2, MMP3, and MMP7 induce the deg-radation of decorin, which is digested into fragments via interactions with its protein core [49]. This digestion of decorin allows the release of TGF-β1 [49]. MMP2 and MMP9 also activate TGF-β2 [50,51]. Thus, a single decorin molecule could simultaneously sequester multiple important mediators of cell growth and antagonize several signaling pathways crucial for fibrotic diseases.

3. Interaction between Decorin and TGF-β

TGF-β is considered a potent and ubiquitous multifunctional cytokine involved in wound repair, proliferation, migration, apoptosis, differentiation, and fibrosis, including a pleiotropic effect in immune response [52,53]. The expressions of TGF-β is increased in almost all fibrotic diseases involving all organ systems, including ocular diseases [54–60]. Three isoforms of TGF-β exist: TGFβ1, TGFβ2, and TGFβ3. They are secreted by many types of cells and are involved in a wide range of actions, including the promotion of cell differentiation, promotion or inhibition of cell proliferation, induction of ECM production, immunosuppression, and increase in mitochondrial reactive oxygen species (ROS) production [59]. TGF-β is also considered a potent immunosuppressive cytokine and is considered a target for immunotherapy to suppresses tissue rejection and prolong corneal allograft survival after penetrating keratoplasty [53,61]. The intracellular signaling of the TGF-β family is regulated by Smads. TGF-β signaling through the canonical Smad pathway has been well-described for its regulation of multiple target genes, including fibrosis inducible genes [60]. Smad2 and Smad3 are the two major downstream regulators, while Smad7 serves as a negative feedback regulator of the TGF-β/Smad pathway [62]. The canonical TGF-β signaling pathway involves ligand-receptor complex formation, the activation of kinase domains within the cell membrane receptors and its subsequent phosphorylation cascade, and the activation of intracellular signaling downstream of Smad-2/3 [63], which are transcriptional regulators that accumulate in the nucleus. Thus, Smad-2/3 both transmit sig-

nals into the nucleus and regulate gene transcription by binding to Smad-binding elements present in the promoters of their target genes [63,64]. This phenomenon has been demonstrated in several cell types in vitro and in vivo [40,48,49]. Besides Smad pathways, other non-canonical pathways of TGF-β signaling, including the MAPK, phosphatidylinositol-3-kinase (PI3K), and Rho-like GTPase pathways, are also crucial for the effect of TGF-β on different pathways [65–67]. These non-canonical path-ways of TGF-β signaling indirectly regulate gene transcription in the nucleus as activators of Smad-dependent pathways [52]. Moreover, TGF-β upregulates epithelial–mesenchymal transition (EMT) related genes, such as fibronectin, α-smooth muscle actin (αSMA), and tropomyo-sin (Tpm) [7,68–70]. Decorin regulates the Smad pathway by interacting with LRP1, an endocytic receptor for decorin [44]. In addition, decorin can bind to TGF-β and inhibit the binding of TGF-β ligands to their receptors. The bound complex formation with decorin prevents the binding of TGF-β to its receptor, repressing its activity [30].

Many previous studies have confirmed the regulatory role of decorin for TGF-β activity [71,72]. Our and other previous studies have demonstrated that TGF-β regulates gene transcription, and some genes, including the decorin gene, contain putative TGF-β-negative cis-acting elements (TIE) [73–78]. The promoter of decorin is divided into two main regions: a proximal promoter at 188 bp and a distal promoter at ~800 bp (Figure 2). The proximal promoter contains two functional TATA and CAAT boxes [79]. This region also contains two TNF-α-responsive elements (TNFRE) that mediate the TNF-α-induced transcriptional repression of the decorin gene [80]. The proximal promoter region also contains an activator protein 1 (AP1) binding site, a dual regulator of decorin gene expression repression by TNF-α and induction by interleukin-1 (NF/IL-1) [81]. The distal promoter of decorin has many homologous cis-acting factors, including AP1, AP5, and nuclear factor κ-light-chain-enhancer of activated B cells (NF-κB), several direct repeat factors, and a TIE [79]. It has been reported that the TIE at position −685 of the promoter region of the decorin gene exon Ib is a transcriptional silencer [76–78]. This TIE has been found in various protease gene sequences that are downregulated by TGF-β and could inhibit decorin gene transcription [78]. Supporting this regulatory mechanism, we reported that decorin expression was downregulated in lens epithelial cells (LECs) and rabbit articular chondrocytes after the addition of TGF-β2 [7,82]. On the other hand, the expression of decorin was reported to be upregulated in mesangial cells and rat liver cells, and after treatment with TGF-β [83]. These results show that the molecular mechanisms for decorin induction may differ among cell types and that many aspects of the underlying regulatory mechanisms are still currently unknown.

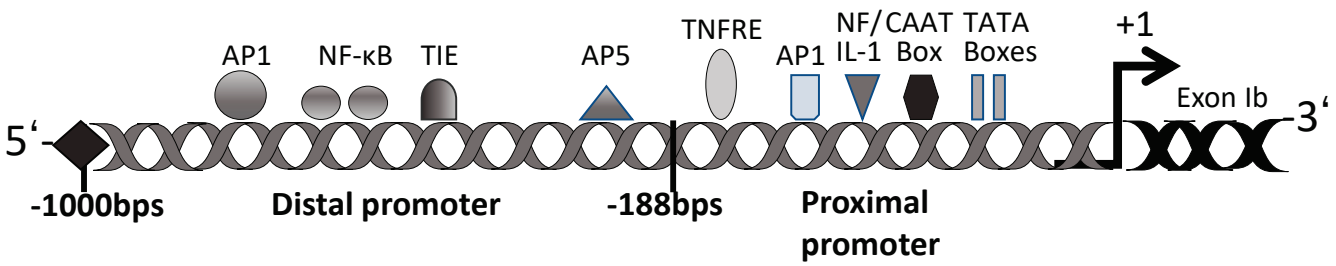

Figure 2. Schematic representation of the human decorin promoter. Consensus sequences for cis-regulatory elements are labeled.

The ocular tissues in the eyes are susceptible to fibrotic diseases, such as primary an-terior subcapsular fibrosis (ASF) in cataracts, secondary posterior capsule opacification (PCO) after cataract surgery, scarring in the cornea and conjunctiva , primary open-angle glaucoma (POAG), age-related macular degeneration (AMD), proliferative diabetic retinopathy (PDR), and proliferative vitreoretinopathy (PVR) [2,57,84–89]. TGF-β signaling is involved in the pathogenesis of fibrotic eye diseases, impairing the quality of vision and intra- and extra-ocular homeostasis [2,57,84–89]. Physiologically, TGF-β is mainly pro-

duced in the ciliary epithelium, LECs, and retinal pigment epithelial cells (RPEs) as a la-tent, inactive form of mature TGF-β [90–93]. TGF-β2 was also detected in human tears [94]. TGF-β2 levels change in the aqueous humor during the clinical course of various ophthalmic diseases. For example, changes in TGF-β2 levels in the eyes of patients with PVR could cause post-retinal detachment and retinal fibrosis. In addition, TGF-β2 concentrations in the vitreous fluid increase as retinal fibrosis progresses [95]. Levels of total and active TGF-β2 are higher in cataract patients with diabetic retinopathy, neovascular glaucoma, and POAG than in cataract patients without these ocular diseases [96–99]. Altered decorin expression is also associated with several fibrotic eye diseases, including congenital stromal dystrophy of the cornea [100,101], corneal wound healing [102], PCO [2,7], glaucoma [10,88], and PVR [103]. Thus, interactions between decorin and TGF-β may be involved in the pathogenesis of ocular diseases that involve fibrotic changes.

4. Distribution of Decorin in the Eye

Decorin is mainly localized to the connective tissue and extracellular matrix and primarily involves collagen fiber formation. In the eyes, decorin is expressed in all ocular tissues such as the corneal stroma, conjunctival stroma, trabecular meshwork, lens, and in all layers of the retina, optic nerve, and sclera. It is secreted in the tears, aqueous humor, and vitreous humor [1,2,7,9,13,14,88,103,104]. Decorin is typically synthesized and se-creted by fibroblasts, maintaining the balance of ECM homeostasis [105]. However, epithelial and endothelial cells can also synthesize decorin [105]. Recent work has shown that decorin expression is conisderably upregulated in LECs during PCO and pseudoexfoliation glaucoma (PXG), in the aqueous humor of subjects in PDR [2,7,9,106], and in the vitreous humor of patients with rhegmatogenous retinal detachment and PVR [103,107]. On the other hand, decorin protein levels were also markedly decreased in the aqueous and vitreous humor in patients with POAG [88]. We previously reported that the protein level of decorin was not altered in the aqueous humor and LECs with aging when we compared the grade and type of lens opacity using human anterior lens capsule samples obtained during cataract surgery [7]. The expression of decorin is modulated by various cytokines and can reduce inflammation and fibrosis. Therefore, the altered expression levels of decorin in eye diseases suggest that it may play a role in modulating the ECM and cellular and microvascular integrity.

5. The Role of Decorin in the Lens

No drug has been discovered to treat or prevent cataracts; thus, the only current treatment for cataracts is surgery. In modern cataract surgery, a lens capsular bag is produced after the aspiration and removal of the lens contents, consisting of a portion of the anterior and the entire posterior and intraocular lens (IOL) inserted into the lens capsule. However, after several years post-operation, patients may develop opacity in the lens posterior capsule. Due to PCO, visual function is impaired; this is referred to as "after-cataracts" [86]. Months to years after cataract surgery, fibroblast-like differentiation, EMT, and the formation of a regenerating lens (called Elschnig pearls) may develop, leading to clouding and shrinkage of the lens capsule [86,108]. EMT results in an increased cell motility and ECM accumulation in LECs and has also been reported to be implicated in cell invasion, wound healing, and fibrosis [57,109]. After cataract surgery, transdifferentiation of LECs into fibroblast-like cells is induced in residual LECs, expressing high levels of fibronectin, procollagen, Tpm, and αSMA, resembling the wound healing process [68,69,86,108].

Aberrant TGF-β signaling plays a central role in the pathobiology of human ASF in the lens [57,110–112] and PCO [68,69,108,113,114]. As with TGF-β, the biological effects of FGF2 on the development of PCO may be either detrimental or beneficial since FGF2 stim-ulates LEC proliferation and mitosis and collagen synthesis but reduces the expression of αSMA [115–117]. FGF2 stimulates lens fiber differentiation in a dose-dependent manner [118,119] and activates LEC mitosis, increasing collagen formation [120]. The concentra-tion of FGF2 increases in the LECs after cataract surgery [121]. Aberrant TGF-β2

signaling also promotes LEC migration, proliferation, stress fiber formation, and EMT, inducing the appearance of αSMA-positive myofibroblasts, which is modulated by FGF2 [68].

There are only a few reports on the role of decorin in the lens and its involvement in lens-related diseases. Under normal physiological conditions, the expression of decorin in LECs is low; however, the mRNA levels of decorin are increased in human LEC tissues (HLECs) with ASF obtained during cataract surgery [2]. Our recent study revealed that decorin may play a significant role in PCO and wound healing in the lens [7]. The expression of many genes related to the ECM, including decorin, collagen, and fibronectin, were upregulated in LECs obtained from a mouse PCO model using a microarray-based approach after extracapsular clear lens extraction (ECLE) [7]. Increased expression of decorin during EMT was confirmed in both rat and mouse PCO models via real-time quantitative PCR and Western blotting, suggesting that decorin is related to the cell proliferation, differentiation, fibrosis, and EMT of LECs observed in ASF and PCO [7]. Therefore, we ana-lyzed the interaction of decorin with TGF-β and FGF2 in the lens. In cultured mouse LECs (MLECs) and HLECs, the expression of decorin mRNA levels increased in response to FGF2 and decreased in response to TGFβ-2 [7]. Similar to our report, reduced expressions of decorin protein and mRNA after TGF-β treatment have been observed in many cell types, including fibroblasts [122,123]. It has been reported that the decorin gene contains TIE as a transcriptional silencer [76–78]. Thus, the addition of TGF-β may transcriptionally inhibit the expression of decorin in cultured LECs.

On the other hand, the mechanisms underlying the transcriptional regulation of decorin by FGF have not been elucidated, and the effect of FGF2 on the expression of decorin differed among various cell types [124–127]. Previous studies reported that decorin is secreted from skin fibroblasts and binds to FGF2 and FGF-7 in the human wound fluids collected within 24 h of surgery, activating cellular proliferation through the activation of the MAPK pathway [128,129]. Thus, the interaction of FGF2 and decorin may induce cell proliferation in PCO tissues. hDCN overexpression in HLECs suppressed TGF-β-induced Tpm1 upregulation [7]. Tpms are known as proteins that stabilize F-actin filaments, regulating the dynamic and structural properties of these filaments by controlling their interactions with actin binding proteins [130,131]. In our previous study, we observed that *Tpm1* and *Tpm2* are involved in regulating EMT and stabilizing actin stress fibers [68]. Both *Tpm1* and *Tpm2* are induced by TGFβ-2 during EMT in LECs and have been used as EMT markers in lens cells [68,132]. Thus, the overexpression of decorin in the lens may suppress TGFβ-mediated EMT. Moreover, FGF2 also acts as an antagonist of TGF-β-mediated EMT [68]. We reported that *Tpm1* and *Tpm2* expression was repressed after adding FGF2 to cultured MLECs and HLECs [133]. In a previous in vivo functional study, the extent of decorin binding to TGF-β inhibits hepatic fibrosis [20]. In other words, there is a complex relationship between decorin and TGF-β in that TGF-β can mutually repress decorin gene expression in fibroblasts and LECs. This suggests that a complex feedback loop exists between these two factors to maintain cellular homeostasis after surgery and during wound healing (Figure 3).

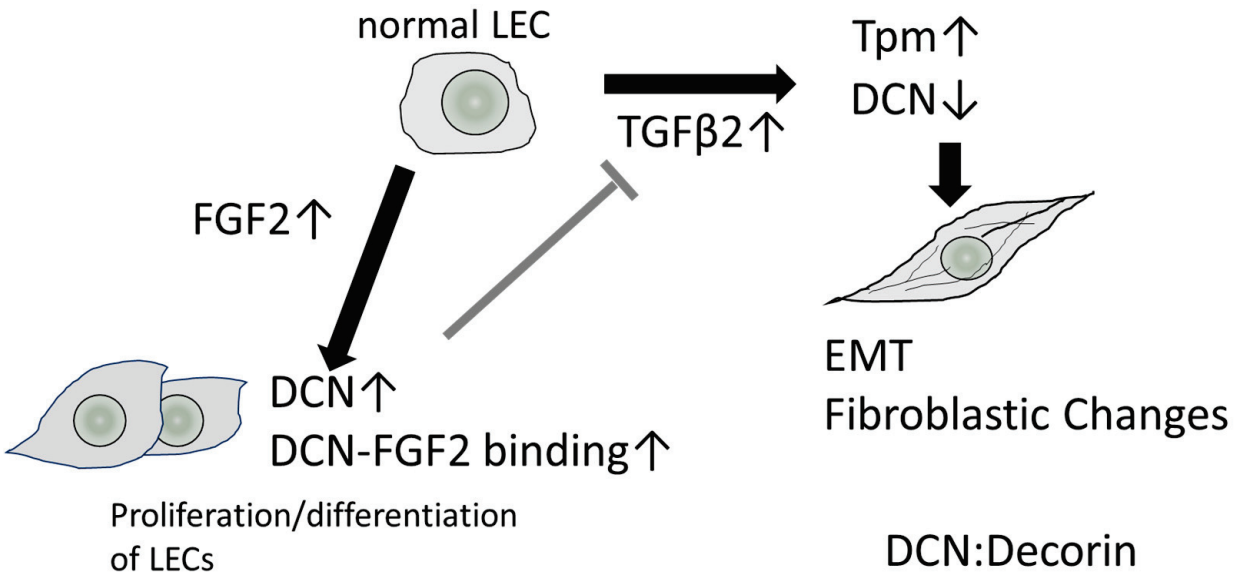

Figure 3. Schematic representation of the role of decorin (DCN) in the LECs. FGF2 induces the expression of DCN, but its mechanism is unclear. FGF2 binds to the GAG chain of DCN enhancing the activity of FGF2 and potentially promoting LEC proliferation and differentiation. Higher levels of DCN bind to TGF-β and inhibit its activity. On the other hand, TGF-β binds to the promoter of DCN and represses decorin expression, possibly promoting EMT and fibrosis. Increased expression of decorin inhibits the expression of Tpm1 and Tpm2 and may promote normal cell growth and wound healing. DCN, decorin; LECs, lens epithelial cells; FGF2, fibroblast growth factor 2; GAG, glycosamino-glycan; TGF-β, transforming growth factor-β; EMT, epithelial–mesenchymal transition.

In a human PCO model using capsular bags from donor eyes that received an IOL, the levels of MMP2 and MMP9 were transiently elevated [134]. Additionally, pro-MMP2 and pro-MMP9 levels were increased and sustained upon treatment with active TGF-β2 [134]. Furthermore, the levels of pro-form MMP2 and MMP9 and active MMP2 were in-creased in the bathing media upon treatment with TGF-β in an organ-cultured lens from a rat ASF model [135]. In addition, the broad-spectrum MMP inhibitor GM6001 and a specific MMP2/9 inhibitor suppressed the TGF-β induced-ASF [135]. From these studies, we speculate that decorin may be cleaved by MMPs in ASF and PCO and accelerate the acti-vation and release of TGF-β.

In the context of wound healing [6], it has been suggested that decorin interacts by localizing TGF-β, FGF2, and EGF close to the receptor. In the pathogenesis of PCO and other fibrotic eye diseases, decorin expression may be upregulated by FGF2, suppressing EMT and inducing normal cell proliferation and differentiation in LECs (Figure 3). We previously established a mouse PCO model with injury-induced EMT and fibrosis in the lens capsule to analyze the effect of decorin overexpression in wound healing in the lens using lens-specific human decorin conditional transgenic mice (*hDCN*-Tg) [7,133]. To examine the effect of decorin over-expression on the eye lens in vivo, we generated lens-specific *hDCN*-Tg using a plasmid in which Pax6-human αA-crystallin composite promoter (CPV14) [136] drives *hDCN* cDNA, as described in our previous study [7]. When the anterior capsule was injured via needle puncture, LECs differentiated into fibroblasts during the healing process via epithelial-myoblastic transition (EMyoT) [94,95] and transformed into αSMA-positive myofibroblasts. Wound healing was enhanced and fibrosis was suppressed after lens injury in *hDCN*-Tg mice compared with those in the wild-type (WT) [7]. It has been reported that cutaneous excisional wound healing in decorin-deficient mice ($Dcn^{-/-}$) was delayed compared with that in WT ($Dcn^{+/+}$) controls [6]. Thus, it is clear that the overexpression and addition of decorin may serve as an excellent therapeutic approach for improving wound healing and PCO. Moreover, the lenses of *hDCN*-Tg mice were clear and did not show any phenotypic abnormalities, such as abnormal arrangement or swelling of lens

fibers and cell loss or abnormal growth of LECs through 48 weeks of age (Figure 4). Hence, decorin does not adversely affect the normal development and differentiation of the mouse lens.

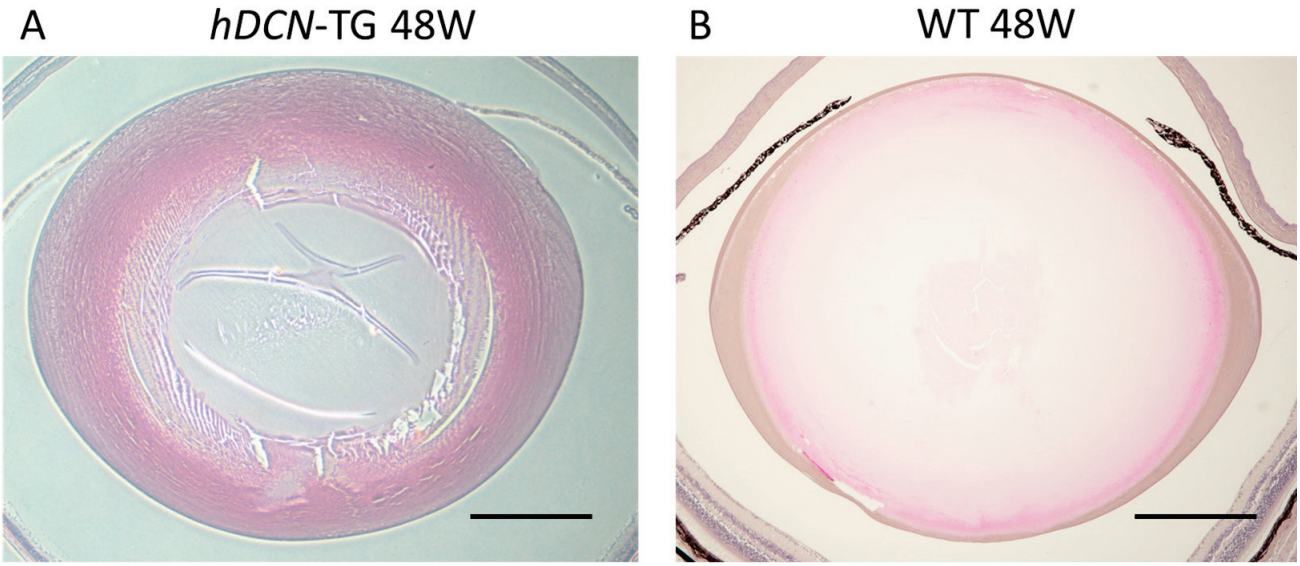

Figure 4. Histochemical analysis of lenses in 48-week-old (W) *hDCN*-Tg mice. Adult lenses in 48 W *hDCN*-Tg animals (**A**) did not show lens fiber damage and pathological changes and did not differ from those in WT mice (**B**). Overexpression of *hDCN* did not affect the histological changes in lens devel-opment. Scale bar = 200 μm.

In another study on the lens, decorin was found to inhibit high glucose-induced ROS production and apoptosis by reducing the induction of p22phox and phospho-p38 in a cultured human LEC cell line [137]. It was also reported that decorin could increase the levels of endogenous antioxidants, such as glutathione peroxidase and superoxide dis-mutase (SOD), and decrease the levels of tissue malondialdehyde, nitric oxide, and caspase-3 in the rat cerebrum after post-traumatic brain injuries [138]. Furthermore, decorin could protect retinal pigment epithelial (RPE) cells from H2O2-induced oxidative stress and apoptosis by promoting autophagy [11]. Furthermore, ROS induces the secretion and activation of TGF-β1 and is essential for TGF-β-mediated myofibroblast differentiation under different pathological conditions in various cells [56,139–141]. TGF-β also increases intracellular ROS content in different cell types, including LECs and trabecular meshwork (TM) cells by downregulating the expression of antioxidant-related genes, including *SOD*, *catalase*, *glutaredoxin*, and *lens epithelium-derived growth factor (LEDGF)* [139,142–144]. This redox imbalance is an important contributor to the pathophysiological effects of TGF-β, including fibrosis [145]. Thus, decorin may work as an antioxidant and anti-TGFβ1 agent and maintain redox balance in lens tissues.

6. The Role of Decorin in Other Eye Diseases

6.1. Cornea

There are many reports on the role and function of decorin in the cornea. Decorin was first identified in the chicken cornea [146]. In humans, mutations in the decorin gene could cause congenital stromal corneal dystrophy (CSCD) when truncated decorin binds to collagen, resulting in aggregation in the stroma [100,147]. CSCD is the only human disease associated with mutations in decorin. CSCD is a rare autosomal dominant disorder characterized by small opacities found throughout the stroma [100,148]. Decorin is believed to inhibit corneal neovascularization under normal physiological conditions and is expected to maintain avascularity in the cornea [29]. The overexpression of decorin in cultured human corneal fibroblasts inhibited the TGF-β-induced expression of fibrogenic ECM

genes such as fibronectin; alpha collagen type-I, -III, and -IV; and αSMA, a known EMT marker. In addition, the overexpression of decorin via tissue-targeted adeno-associated virus (AAV) 5-mediated delivery of the Decorin (*Dcn*) gene reduced corneal fibrosis caused by photorefractive keratectomy and corneal neovascularization in rabbits in vivo [149,150]. In addition, AAV5–*Dcn* gene delivery in the rabbit cornea revealed that it is safe and non-toxic to the eye in vivo during the 6-month follow-up period [151]. Thus, decorin plays a significant role in maintaining corneal transparency.

Decorin has also been reported to have therapeutic applications for various diseases of the cornea. For example, sustained topical delivery of a fluid gel eye drop containing human decorin to the cornea promoted wound healing and reduced corneal scarring and opacity in a murine model of pseudomonas-induced keratitis [152]. Furthermore, topical decorin treatment also promoted corneal epithelial nerve regeneration after corneal abrasion injury using Cx3cr1-deficient mice spontaneously lacking resident corneal epithelial dendritic cells [153]. From these results, it was hypothesized that decorin induces corneal nerve regeneration through the activation of dendritic cells [153]. Thus, decorin gene therapy or the optical administration of decorin has a high potential for treating corneal fibrotic and angiogenic diseases.

6.2. Glaucoma

Intraocular pressure (IOP) is the cardinal modifiable important risk factor for the on-set and progression of glaucoma [154,155]. TM and Schlemm's canal provide the major route for the outflow of the aqueous humor from the anterior segment of the eye and are responsible for the raised IOP associated with POAG due to increased outflow resistance [156]. Here, the TM exhibits marked contractile properties, and TM contraction is associ-ated with reduced aqueous humor drainage through the outflow system [157]. Decorin has extenisve anti-fibrotic effects in glaucoma. The aqueous level of decorin was found to be decreased in eyes with glaucoma compared with non-glaucomatous eyes [88]. Moreo-ver, it has been reported that soluble decorin attenuated the generation and expression of typical downstream target genes, such as *CCN2/CTGF*, *Fn*, and *Col IV*, in human TM cells by TGF-β2. The negative reciprocal regulation of decorin and TGF-β was also observed, confirming the dramatic downregulation of decorin in the canonical outflow pathway of patients with POAG [14]. Expression of decorin mRNA was also decreased in the endo-thelial cells of the Schlemm canal derived from glaucomatous patients [158]. Intracameral injection of human recombinant decorin considerably reduced fibrosis in the TM and IOP and inhibited retinal ganglion cell loss in a rodent model of TM fibrosis via repeated in-tracameral injection of TGF-β [8]. Thus, decorin may be useful in developing an effective therapy for eyes with ocular hypertension and POAG associated with the fibrosis of the TM.

In POAG, the disturbed ECM metabolism and ECM remodeling are observed in the human optic nerve (ON) head, which is particularly obvious in the lamina cribrosa (LC) layer [159]. The remodeling processes in the ON head of glaucomatous patients are ac-companied by a disruption of the homeostatic balance of growth factors such as TGF-β [160]. In oligonucleotide microarray analysis using cultured LC cells from POAG human donors, expression of decorin was decreased [159]. In decorin-deficient mice, it was re-ported that an increase in IOP and a loss of ON axons [14] as well as a dramatic upreg-ulation of CTGF/CCN2, TGF-β-1, and TGF-β-2 were found [161]. In ON astrocytes, decorin negativery regulated TGF-β and CTGF/CCN2 [161]. Thus, the downregulation of decorin in the glaucomatous Schlemm canal endothelial cells, LC cells, and optic nerve head may affect the progression of POAG. The treatment of decorin may attenuate the remodeling process in the ON head observed during the progression of glaucoma and may reduce IOP.

Furthermore, in patients with uncontrolled glaucoma with progressive visual field loss due to glaucoma medication, IOP reduction by glaucoma surgery may be necessary. Glaucoma filtration surgery is a useful technique in reducing the IOP. Although this tech-

nique immediately reduces IOP, the long-term effect is often eclipsed by the postoperative wound-healing process [162–164]. After glaucoma filtration treatments, the subconjunctival injection of decorin in rabbits showed markedly reduced conjunctival scarring and maintained lower IOP levels [165]. Thus, the application of decorin can inhibit the obstruction of the fistula, which in turn inhibits fibroproliferative processes in fibroblasts from Tenon's capsule and the episclera after filtration surgery [165].

The protein expression of decorin was also found to be increased in LECs of patients with PXG compared with those with pseudoexfoliation syndrome [106]. Simultaneously, TGFβ1 and FGF2 expression is elevated in the LECs of patients with PXG [106,166]. Thus, through the protein interaction networks of TGF-β and FGF2 that induce ECM remodeling, decorin may play a potential role in PXG and may be used as a novel therapeutic target for glaucoma.

6.3. Retinal Diseases

SLRPs are crucial in many important biological functions involved in the mainte-nance of retinal homeostasis [13]. Decorin localizes in all layers of the human retina, in-cluding the RPE, Bruch's membrane, choroidal stroma, and choroidal blood vessel walls [12]. A key step in PDR is neo-vascularization, beginning with the activation of the angio-genic switch after ischemic changes. Wet AMD is characterized by the so-called angio-genesis choroidal neovascularization or retinal aingiomatous proliferation [167]. Decorin is a key regulator for angiogenic responses by acting as an inhibitor for multiple RTKs and suppressing VEGFR through various mechanisms in choroid-retinal endothelial cells [26,168]. Moreover, many reports have demonstrated the anti-angiogenic effects of decorin in the retina [168,169]. A decreased expression of decorin has been reported in the retina of animal models of ischemic disease in the retinal vessels, such as oxygen-induced retinopathy in rats [170,171]. In another study, decorin treatment in rats with oxygen-induced retinopathy inhibited retinal neovascularization by reducing neovascular endothelial cell proliferation and the immunoreactivity of VEGF and TNF-α in the retina [172]. Additionally, intravitreal injection of decorin extensively suppressed VEGF and TNF-α expression and inhibited TGF-β expression in the RPE-choroid complex in a mouse model of laser-induced choroidal neovascularization, a model of AMD [169]. Thus, the administration of decorin into the eyes may inhibit VEGF-induced retinal diseases related to angiogenesis. Moreover, PVR is a complex process involving cell proliferation and ECM remodeling [173]. TGF-β is over-expressed in the vitreous humor of patients with PVR and PDR [55]. TGF-β is also presumed to be involved in the contraction of proliferative membranes and subretinal strands in PVR [174]. In an experimental model of rabbit traumatic PVR, intravitreal injection of decorin during vitrectomy reduced the development of fibrosis and tractional retinal detachment [175]. Therefore, decorin is also expected to prevent or regress neovascularization, EMT, and fibrosis in ischemic retinal diseases such as retinopathy of prematurity, proliferative DR, PVR, retinal detachment, and AMD as a TGF-β antagonist [9,11,107,168,172,175].

7. Summary

In summary, decorin can neutralize several important mediators of fibrosis and angiogenesis in the eyes. Decorin has been shown to have anti-fibrotic effects in various an-imal models of eye diseases, and no toxicity has been reported in these studies. Decorin regulates the activity of multiple growth factors, receptor tyrosine kinases, and extracellu-lar matrix components. Although preclinical studies have been conducted, decorin has not yet been clinically applied as a drug due to its short half-life in circulation and diffi-culty in mass production since high doses are required for effective treatment. In the future, it is expected that GAG-unbound decorin core proteins, which are easier to create, will be produced in large quantities for use in pharmaceuticals [27,176]. Therefore, decorin is expected to be clinically used in the treatment of various ocular diseases needing adjuvant peptide therapies, including PCO, due to its anti-fibrotic, anti-inflammatory, anti-angiogenic, and

antioxidant effects by affecting several growth factor pathways in the eyes. Hence, the development of effective intraocular delivery methods for decorin is warranted.

Author Contributions: E.K. wrote the manuscript. H.S. and S.S. guided the planning. D.P.S. wrote the review manuscript. T.S. and D.P.S. critically amended the manuscript. All authors have read and agreed to the published version of the manuscript.

Funding: This work was supported by a grant provided by the JSPS Grants-in-Aid for Scientific Research C 23592588 (to S.S.), the National Eye Institute, National Institute of Health [grant number EY024589, (to D.P.S.); and Bridge Grant, UNMC (to D.P.S.).

Institutional Review Board Statement: Not applicable.

Informed Consent Statement: Not applicable.

Data Availability Statement: Not applicable.

Conflicts of Interest: The authors declare no conflict of interest.

References

1. Mohan, R.R.; Tovey, J.C.; Gupta, R.; Sharma, A.; Tandon, A. Decorin biology, expression, function and therapy in the cornea. *Curr. Mol. Med.* **2011**, *11*, 110–128. [CrossRef] [PubMed]
2. Azuma, N.; Hara, T.; Hara, T. Extracellular matrix of opacified anterior capsule after endocapsular cataract surgery. *Graefes Arch. Clin. Exp. Ophthalmol.* **1998**, *236*, 531–536. [CrossRef] [PubMed]
3. Hu, X.; Villodre, E.S.; Larson, R.; Rahal, O.M.; Wang, X.; Gong, Y.; Song, J.; Krishnamurthy, S.; Ueno, N.T.; Tripathy, D.; et al. Decorin-mediated suppression of tumorigenesis, invasion, and metastasis in inflammatory breast cancer. *Commun. Biol.* **2021**, *4*, 72. [CrossRef] [PubMed]
4. Iozzo, R.V. Matrix proteoglycans: From molecular design to cellular function. *Annu. Rev. Biochem.* **1998**, *67*, 609–652. [CrossRef] [PubMed]
5. Iozzo, R.V.; Schaefer, L. Proteoglycans in health and disease: Novel regulatory signaling mechanisms evoked by the small leucine-rich proteoglycans. *FEBS J.* **2010**, *277*, 3864–3875. [CrossRef] [PubMed]
6. Jarvelainen, H.; Puolakkainen, P.; Pakkanen, S.; Brown, E.L.; Hook, M.; Iozzo, R.V.; Sage, E.H.; Wight, T.N. A role for decorin in cutaneous wound healing and angiogenesis. *Wound Repair Regen.* **2006**, *14*, 443–452. [CrossRef]
7. Shibata, S.; Shibata, N.; Ohtsuka, S.; Yoshitomi, Y.; Kiyokawa, E.; Yonekura, H.; Singh, D.P.; Sasaki, H.; Kubo, E. Role of decorin in posterior capsule opacification and eye lens development. *Cells* **2021**, *10*, 863. [CrossRef]
8. Hill, L.J.; Mead, B.; Blanch, R.J.; Ahmed, Z.; De Cogan, F.; Morgan-Warren, P.J.; Mohamed, S.; Leadbeater, W.; Scott, R.A.; Berry, M.; et al. Decorin reduces intraocular pressure and retinal ganglion cell loss in rodents through fibrolysis of the scarred trabecular meshwork. *Investig. Ophthalmol. Vis. Sci.* **2015**, *56*, 3743–3757. [CrossRef]
9. Low, S.W.Y.; Vaidya, T.; Gadde, S.G.K.; Mochi, T.B.; Kumar, D.; Kassem, I.S.; Costakos, D.M.; Ahmad, B.; Sethu, S.; Ghosh, A.; et al. Decorin concentrations in aqueous humor of patients with diabetic retinopathy. *Life* **2021**, *11*, 1421. [CrossRef]
10. Oruc, Y.; Keser, S.; Yusufoglu, E.; Celik, F.; Sahin, I.; Yardim, M.; Aydin, S. Decorin, tenascin C, total antioxidant, and total oxidant level changes in patients with pseudoexfoliation syndrome. *J. Ophthalmol.* **2018**, *2018*, 7459496. [CrossRef]
11. Xie, X.; Li, D.; Cui, Y.; Xie, T.; Cai, J.; Yao, Y. Decorin protects retinal pigment epithelium cells from oxidative stress and apoptosis via AMPK-mTOR-regulated autophagy. *Oxid. Med. Cell. Longev.* **2022**, *2022*, 3955748. [CrossRef] [PubMed]
12. Keenan, T.D.; Clark, S.J.; Unwin, R.D.; Ridge, L.A.; Day, A.J.; Bishop, P.N. Mapping the differential distribution of proteoglycan core proteins in the adult human retina, choroid, and sclera. *Investig. Ophthalmol. Vis. Sci.* **2012**, *53*, 7528–7538. [CrossRef] [PubMed]
13. Low, S.W.Y.; Connor, T.B.; Kassem, I.S.; Costakos, D.M.; Chaurasia, S.S. Small leucine-rich proteoglycans (SLRPs) in the retina. *Int. J. Mol. Sci.* **2021**, *22*, 7293. [CrossRef] [PubMed]
14. Schneider, M.; Pawlak, R.; Weber, G.R.; Dillinger, A.E.; Kuespert, S.; Iozzo, R.V.; Quigley, H.A.; Ohlmann, A.; Tamm, E.R.; Fuchshofer, R. A novel ocular function for decorin in the aqueous humor outflow. *Matrix Biol.* **2021**, *97*, 1–19. [CrossRef]
15. Vogel, K.G.; Paulsson, M.; Heinegard, D. Specific inhibition of type I and type II collagen fibrillogenesis by the small proteoglycan of tendon. *Biochem. J.* **1984**, *223*, 587–597. [CrossRef]
16. Nareyeck, G.; Seidler, D.G.; Troyer, D.; Rauterberg, J.; Kresse, H.; Schonherr, E. Differential interactions of decorin and decorin mutants with type I and type VI collagens. *Eur. J. Biochem.* **2004**, *271*, 3389–3398. [CrossRef]
17. Ruhland, C.; Schonherr, E.; Robenek, H.; Hansen, U.; Iozzo, R.V.; Bruckner, P.; Seidler, D.G. The glycosaminoglycan chain of decorin plays an important role in collagen fibril formation at the early stages of fibrillogenesis. *FEBS J.* **2007**, *274*, 4246–4255. [CrossRef]
18. Neill, T.; Schaefer, L.; Iozzo, R.V. Decorin: A guardian from the Matrix. *Am. J. Pathol.* **2012**, *181*, 380–387. [CrossRef]

19. Merline, R.; Moreth, K.; Beckmann, J.; Nastase, M.V.; Zeng-Brouwers, J.; Tralhao, J.G.; Lemarchand, P.; Pfeilschifter, J.; Schaefer, R.M.; Iozzo, R.V.; et al. Signaling by the matrix proteoglycan decorin controls inflammation and cancer through PDCD4 and MicroRNA-21. *Sci. Signal.* **2011**, *4*, ra75. [CrossRef]
20. Baghy, K.; Iozzo, R.V.; Kovalszky, I. Decorin-TGFbeta axis in hepatic fibrosis and cirrhosis. *J. Histochem. Cytochem.* **2012**, *60*, 262–268. [CrossRef]
21. Bi, X.; Pohl, N.M.; Qian, Z.; Yang, G.R.; Gou, Y.; Guzman, G.; Kajdacsy-Balla, A.; Iozzo, R.V.; Yang, W. Decorin-mediated inhibition of colorectal cancer growth and migration is associated with E-cadherin *in vitro* and in mice. *Carcinogenesis* **2012**, *33*, 326–330. [CrossRef] [PubMed]
22. Iozzo, R.V.; Sanderson, R.D. Proteoglycans in cancer biology, tumour microenvironment and angiogenesis. *J. Cell. Mol. Med.* **2011**, *15*, 1013–1031. [CrossRef] [PubMed]
23. Gubbiotti, M.A.; Neill, T.; Frey, H.; Schaefer, L.; Iozzo, R.V. Decorin is an autophagy-inducible proteoglycan and is required for proper in vivo autophagy. *Matrix Biol.* **2015**, *48*, 14–25. [CrossRef] [PubMed]
24. Chen, S.; Young, M.F.; Chakravarti, S.; Birk, D.E. Interclass small leucine-rich repeat proteoglycan interactions regulate collagen fibrillogenesis and corneal stromal assembly. *Matrix Biol.* **2014**, *35*, 103–111. [CrossRef]
25. Santra, M.; Eichstetter, I.; Iozzo, R.V. An anti-oncogenic role for decorin. Down-regulation of ErbB2 leads to growth suppression and cytodifferentiation of mammary carcinoma cells. *J. Biol. Chem.* **2000**, *275*, 35153–35161. [CrossRef]
26. Csordas, G.; Santra, M.; Reed, C.C.; Eichstetter, I.; McQuillan, D.J.; Gross, D.; Nugent, M.A.; Hajnoczky, G.; Iozzo, R.V. Sustained down-regulation of the epidermal growth factor receptor by decorin. A mechanism for controlling tumor growth in vivo. *J. Biol. Chem.* **2000**, *275*, 32879–32887. [CrossRef]
27. Jarvinen, T.A.; Prince, S. Decorin: A growth factor antagonist for tumor growth inhibition. *BioMed Res. Int.* **2015**, *2015*, 654765. [CrossRef]
28. Schaefer, L.; Schaefer, R.M. Proteoglycans: From structural compounds to signaling molecules. *Cell Tissue Res.* **2010**, *339*, 237–246. [CrossRef]
29. Gubbiotti, M.A.; Vallet, S.D.; Ricard-Blum, S.; Iozzo, R.V. Decorin interacting network: A comprehensive analysis of decorin-binding partners and their versatile functions. *Matrix Biol.* **2016**, *55*, 7–21. [CrossRef]
30. Stander, M.; Naumann, U.; Wick, W.; Weller, M. Transforming growth factor-beta and p-21: Multiple molecular targets of decorin-mediated suppression of neoplastic growth. *Cell Tissue Res.* **1999**, *296*, 221–227. [CrossRef]
31. Chen, S.; Birk, D.E. Focus on molecules: Decorin. *Exp. Eye Res.* **2011**, *92*, 444–445. [CrossRef] [PubMed]
32. Schulz, M.W.; Chamberlain, C.G.; McAvoy, J.W. Binding of FGF-1 and FGF-2 to heparan sulphate proteoglycans of the mammalian lens capsule. *Growth Factors* **1997**, *14*, 1–13. [CrossRef] [PubMed]
33. Seidler, D.G.; Dreier, R. Decorin and its galactosaminoglycan chain: Extracellular regulator of cellular function? *IUBMB Life* **2008**, *60*, 729–733. [CrossRef] [PubMed]
34. Hocking, A.M.; Shinomura, T.; McQuillan, D.J. Leucine-rich repeat glycoproteins of the extracellular Matrix. *Matrix Biol.* **1998**, *17*, 1–19. [CrossRef] [PubMed]
35. Danielson, K.G.; Baribault, H.; Holmes, D.F.; Graham, H.; Kadler, K.E.; Iozzo, R.V. Targeted disruption of decorin leads to abnormal collagen fibril morphology and skin fragility. *J. Cell Biol.* **1997**, *136*, 729–743. [CrossRef]
36. Dunkman, A.A.; Buckley, M.R.; Mienaltowski, M.J.; Adams, S.M.; Thomas, S.J.; Satchell, L.; Kumar, A.; Pathmanathan, L.; Beason, D.P.; Iozzo, R.V.; et al. Decorin expression is important for age-related changes in tendon structure and mechanical properties. *Matrix Biol.* **2013**, *32*, 3–13. [CrossRef]
37. Takeuchi, Y.; Kodama, Y.; Matsumoto, T. Bone matrix decorin binds transforming growth factor-beta and enhances its bioactivity. *J. Biol. Chem.* **1994**, *269*, 32634–32638. [CrossRef]
38. Brandan, E.; Retamal, C.; Cabello-Verrugio, C.; Marzolo, M.P. The low density lipoprotein receptor-related protein functions as an endocytic receptor for decorin. *J. Biol. Chem.* **2006**, *281*, 31562–31571. [CrossRef]
39. Cabello-Verrugio, C.; Brandan, E. A novel modulatory mechanism of transforming growth factor-beta signaling through decorin and LRP-1. *J. Biol. Chem.* **2007**, *282*, 18842–18850. [CrossRef]
40. Cabello-Verrugio, C.; Santander, C.; Cofre, C.; Acuna, M.J.; Melo, F.; Brandan, E. The internal region leucine-rich repeat 6 of decorin interacts with low density lipoprotein receptor-related protein-1, modulates transforming growth factor (TGF)-beta-dependent signaling, and inhibits TGF-beta-dependent fibrotic response in skeletal muscles. *J. Biol. Chem.* **2012**, *287*, 6773–6787. [CrossRef]
41. Ungvari, Z.; Valcarcel-Ares, M.N.; Tarantini, S.; Yabluchanskiy, A.; Fulop, G.A.; Kiss, T.; Csiszar, A. Connective tissue growth factor (CTGF) in age-related vascular pathologies. *Geroscience* **2017**, *39*, 491–498. [CrossRef] [PubMed]
42. Lipson, K.E.; Wong, C.; Teng, Y.; Spong, S. CTGF is a central mediator of tissue remodeling and fibrosis and its inhibition can reverse the process of fibrosis. *Fibrogenesis Tissue Repair* **2012**, *5*, S24. [CrossRef] [PubMed]
43. Vial, C.; Gutierrez, J.; Santander, C.; Cabrera, D.; Brandan, E. Decorin interacts with connective tissue growth factor (CTGF)/CCN2 by LRR12 inhibiting its biological activity. *J. Biol. Chem.* **2011**, *286*, 24242–24252. [CrossRef] [PubMed]
44. Schaefer, L.; Iozzo, R.V. Biological functions of the small leucine-rich proteoglycans: From genetics to signal transduction. *J. Biol. Chem.* **2008**, *283*, 21305–21309. [CrossRef]

45. Khan, G.A.; Girish, G.V.; Lala, N.; Di Guglielmo, G.M.; Lala, P.K. Decorin is a novel VEGFR-2-binding antagonist for the human extravillous trophoblast. *Mol. Endocrinol.* **2011**, *25*, 1431–1443. [CrossRef]
46. Rohani, M.G.; Parks, W.C. Matrix remodeling by MMPs during wound repair. *Matrix Biol.* **2015**, *44–46*, 113–121. [CrossRef]
47. Itoh, Y. Membrane-type matrix metalloproteinases: Their functions and regulations. *Matrix Biol.* **2015**, *44–46*, 207–223. [CrossRef]
48. Deryugina, E.I.; Quigley, J.P. Tumor angiogenesis: MMP-mediated induction of intravasation- and metastasis-sustaining neovasculature. *Matrix Biol.* **2015**, *44–46*, 94–112. [CrossRef]
49. Imai, K.; Hiramatsu, A.; Fukushima, D.; Pierschbacher, M.D.; Okada, Y. Degradation of decorin by matrix metalloproteinases: Identification of the cleavage sites, kinetic analyses and transforming growth factor-beta1 release. *Biochem. J.* **1997**, *322 Pt 3*, 809–814. [CrossRef]
50. Yu, Q.; Stamenkovic, I. Cell surface-localized matrix metalloproteinase-9 proteolytically activates TGF-beta and promotes tumor invasion and angiogenesis. *Genes Dev.* **2000**, *14*, 163–176. [CrossRef]
51. Dallas, S.L.; Rosser, J.L.; Mundy, G.R.; Bonewald, L.F. Proteolysis of latent transforming growth factor-beta (TGF-beta)-binding protein-1 by osteoclasts. A cellular mechanism for release of TGF-beta from bone Matrix. *J. Biol. Chem* **2002**, *277*, 21352–21360. [CrossRef] [PubMed]
52. Tandon, A.; Tovey, J.C.; Sharma, A.; Gupta, R.; Mohan, R.R. Role of transforming growth factor Beta in corneal function, biology and pathology. *Curr. Mol. Med.* **2010**, *10*, 565–578. [CrossRef] [PubMed]
53. Li, M.O.; Wan, Y.Y.; Sanjabi, S.; Robertson, A.K.; Flavell, R.A. Transforming growth factor-beta regulation of immune responses. *Annu. Rev. Immunol.* **2006**, *24*, 99–146. [CrossRef] [PubMed]
54. Hales, A.M.; Schulz, M.W.; Chamberlain, C.G.; McAvoy, J.W. TGF-beta 1 induces lens cells to accumulate alpha-smooth muscle actin, a marker for subcapsular cataracts. *Curr. Eye Res.* **1994**, *13*, 885–890. [CrossRef] [PubMed]
55. Kita, T.; Hata, Y.; Kano, K.; Miura, M.; Nakao, S.; Noda, Y.; Shimokawa, H.; Ishibashi, T. Transforming growth factor-beta2 and connective tissue growth factor in proliferative vitreoretinal diseases: Possible involvement of hyalocytes and therapeutic potential of Rho kinase inhibitor. *Diabetes* **2007**, *56*, 231–238. [CrossRef]
56. Liu, R.M.; Desai, L.P. Reciprocal regulation of TGF-beta and reactive oxygen species: A perverse cycle for fibrosis. *Redox Biol.* **2015**, *6*, 565–577. [CrossRef]
57. Lovicu, F.J.; Schulz, M.W.; Hales, A.M.; Vincent, L.N.; Overbeek, P.A.; Chamberlain, C.G.; McAvoy, J.W. TGFbeta induces morphological and molecular changes similar to human anterior subcapsular cataract. *Br. J. Ophthalmol.* **2002**, *86*, 220–226. [CrossRef]
58. Broekelmann, T.J.; Limper, A.H.; Colby, T.V.; McDonald, J.A. Transforming growth factor beta 1 is present at sites of extracellular matrix gene expression in human pulmonary fibrosis. *Proc. Natl. Acad. Sci. USA* **1991**, *88*, 6642–6646. [CrossRef]
59. Massague, J. The transforming growth factor-beta family. *Annu. Rev. Cell Biol.* **1990**, *6*, 597–641. [CrossRef]
60. Ask, K.; Bonniaud, P.; Maass, K.; Eickelberg, O.; Margetts, P.J.; Warburton, D.; Groffen, J.; Gauldie, J.; Kolb, M. Progressive pulmonary fibrosis is mediated by TGF-beta isoform 1 but not TGF-beta3. *Int. J. Biochem. Cell Biol.* **2008**, *40*, 484–495. [CrossRef]
61. Zhou, L.; Zhu, X.; Tan, J.; Wang, J.; Xing, Y. Effect of recombinant adeno-associated virus mediated transforming growth factor-beta1 on corneal allograft survival after high-risk penetrating keratoplasty. *Transpl. Immunol.* **2013**, *28*, 164–169. [CrossRef] [PubMed]
62. Hu, H.H.; Chen, D.Q.; Wang, Y.N.; Feng, Y.L.; Cao, G.; Vaziri, N.D.; Zhao, Y.Y. New insights into TGF-beta/Smad signaling in tissue fibrosis. *Chem. Biol. Interact.* **2018**, *292*, 76–83. [CrossRef] [PubMed]
63. Massague, J.; Seoane, J.; Wotton, D. Smad transcription factors. *Genes Dev.* **2005**, *19*, 2783–2810. [CrossRef] [PubMed]
64. Schmierer, B.; Hill, C.S. TGFbeta-SMAD signal transduction: Molecular specificity and functional flexibility. *Nat. Rev. Mol. Cell Biol.* **2007**, *8*, 970–982. [CrossRef]
65. Yu, L.; Hebert, M.C.; Zhang, Y.E. TGF-beta receptor-activated p38 MAP kinase mediates Smad-independent TGF-beta responses. *EMBO J.* **2002**, *21*, 3749–3759. [CrossRef]
66. Stratton, R.; Rajkumar, V.; Ponticos, M.; Nichols, B.; Shiwen, X.; Black, C.M.; Abraham, D.J.; Leask, A. Prostacyclin derivatives prevent the fibrotic response to TGF-beta by inhibiting the Ras/MEK/ERK pathway. *FASEB J.* **2002**, *16*, 1949–1951. [CrossRef]
67. Biernacka, A.; Dobaczewski, M.; Frangogiannis, N.G. TGF-beta signaling in fibrosis. *Growth Factors* **2011**, *29*, 196–202. [CrossRef]
68. Kubo, E.; Shibata, S.; Shibata, T.; Kiyokawa, E.; Sasaki, H.; Singh, D.P. FGF2 antagonizes aberrant TGFbeta regulation of tropomyosin: Role for posterior capsule opacity. *J. Cell. Mol. Med.* **2017**, *21*, 916–928. [CrossRef]
69. Kubo, E.; Shibata, T.; Singh, D.P.; Sasaki, H. Roles of TGF beta and FGF signals in the lens: Tropomyosin regulation for posterior capsule cpacity. *Int. J. Mol. Sci.* **2018**, *19*, 3093. [CrossRef]
70. Kurosaka, D.; Kato, K.; Nagamoto, T.; Negishi, K. Growth factors influence contractility and alpha-smooth muscle actin expression in bovine lens epithelial cells. *Investig. Ophthalmol. Vis. Sci.* **1995**, *36*, 1701–1708.
71. Yamaguchi, Y.; Mann, D.M.; Ruoslahti, E. Negative regulation of transforming growth factor-beta by the proteoglycan decorin. *Nature* **1990**, *346*, 281–284. [CrossRef] [PubMed]
72. Ruoslahti, E.; Yamaguchi, Y. Proteoglycans as modulators of growth factor activities. *Cell* **1991**, *64*, 867–869. [CrossRef] [PubMed]
73. Kerr, L.D.; Miller, D.B.; Matrisian, L.M. TGF-beta 1 inhibition of transin/stromelysin gene expression is mediated through a Fos binding sequence. *Cell* **1990**, *61*, 267–278. [CrossRef] [PubMed]

74. White, L.A.; Mitchell, T.I.; Brinckerhoff, C.E. Transforming growth factor beta inhibitory element in the rabbit matrix metalloproteinase-1 (collagenase-1) gene functions as a repressor of constitutive transcription. *Biochim. Biophys. Acta* **2000**, *1490*, 259–268. [CrossRef]
75. Sharma, P.; Fatma, N.; Kubo, E.; Shinohara, T.; Chylack, L.T., Jr.; Singh, D.P. Lens epithelium-derived growth factor relieves transforming growth factor-beta1-induced transcription repression of heat shock proteins in human lens epithelial cells. *J. Biol. Chem.* **2003**, *278*, 20037–20046. [CrossRef]
76. Danielson, K.G.; Siracusa, L.D.; Donovan, P.J.; Iozzo, R.V. Decorin, epiphycan, and lumican genes are closely linked on murine Chromosome 10 and are deleted in lethal steel mutants. *Mamm. Genome* **1999**, *10*, 201–203. [CrossRef] [PubMed]
77. Demoor-Fossard, M.; Galera, P.; Santra, M.; Iozzo, R.V.; Pujol, J.P.; Redini, F. A composite element binding the vitamin D receptor and the retinoic X receptor alpha mediates the transforming growth factor-beta inhibition of decorin gene expression in articular chondrocytes. *J. Biol. Chem.* **2001**, *276*, 36983–36992. [CrossRef] [PubMed]
78. Iozzo, R.V.; Cohen, I. Altered proteoglycan gene expression and the tumor stroma. *Experientia* **1993**, *49*, 447–455. [CrossRef]
79. Iozzo, R.V.; Moscatello, D.K.; McQuillan, D.J.; Eichstetter, I. Decorin is a biological ligand for the epidermal growth factor receptor. *J. Biol. Chem.* **1999**, *274*, 4489–4492. [CrossRef]
80. Mauviel, A.; Santra, M.; Chen, Y.Q.; Uitto, J.; Iozzo, R.V. Transcriptional regulation of decorin gene expression. Induction by quiescence and repression by tumor necrosis factor-alpha. *J. Biol. Chem.* **1995**, *270*, 11692–11700. [CrossRef]
81. Mauviel, A.; Korang, K.; Santra, M.; Tewari, D.; Uitto, J.; Iozzo, R.V. Identification of a bimodal regulatory element encompassing a canonical AP-1 binding site in the proximal promoter region of the human decorin gene. *J. Biol. Chem.* **1996**, *271*, 24824–24829. [CrossRef] [PubMed]
82. Demoor-Fossard, M.; Redini, F.; Boittin, M.; Pujol, J.P. Expression of decorin and biglycan by rabbit articular chondrocytes. Effects of cytokines and phenotypic modulation. *Biochim. Biophys. Acta* **1998**, *1398*, 179–191. [CrossRef] [PubMed]
83. Border, W.A.; Okuda, S.; Languino, L.R.; Ruoslahti, E. Transforming growth factor-beta regulates production of proteoglycans by mesangial cells. *Kidney. Int.* **1990**, *37*, 689–695. [CrossRef] [PubMed]
84. Shu, D.Y.; Lovicu, F.J. Myofibroblast transdifferentiation: The dark force in ocular wound healing and fibrosis. *Prog. Retin. Eye Res.* **2017**, *60*, 44–65. [CrossRef] [PubMed]
85. Lois, N.; Taylor, J.; McKinnon, A.D.; Smith, G.C.; van't Hof, R.; Forrester, J.V. Effect of TGF-beta2 and anti-TGF-beta2 antibody in a new in vivo rodent model of posterior capsule opacification. *Investig. Ophthalmol. Vis. Sci.* **2005**, *46*, 4260–4266. [CrossRef]
86. McDonnell, P.J.; Rowen, S.L.; Glaser, B.M.; Sato, M. Posterior capsule opacification. An in vitro model. *Arch. Ophthalmol.* **1985**, *103*, 1378–1381. [CrossRef]
87. Nikhalashree, S.; George, R.; Shantha, B.; Lingam, V.; Vidya, W.; Panday, M.; Sulochana, K.N.; Coral, K. Detection of proteins associated with extracellular matrix regulation in the aqueous humour of patients with primary glaucoma. *Curr. Eye Res.* **2019**, *44*, 1018–1025. [CrossRef]
88. NikhalaShree, S.; Karthikkeyan, G.; George, R.; Shantha, B.; Vijaya, L.; Ratra, V.; Sulochana, K.N.; Coral, K. Lowered decorin with aberrant extracellular matrix remodeling in aqueous humor and tenon's tissue from primary glaucoma patients. *Investig. Ophthalmol. Vis. Sci.* **2019**, *60*, 4661–4669. [CrossRef]
89. Guerin, C.J.; Hu, L.; Scicli, G.; Scicli, A.G. Transforming growth factor beta in experimentally detached retina and periretinal membranes. *Exp. Eye Res.* **2001**, *73*, 753–764. [CrossRef]
90. Jampel, H.D.; Roche, N.; Stark, W.J.; Roberts, A.B. Transforming growth factor-beta in human aqueous humor. *Curr. Eye Res.* **1990**, *9*, 963–969. [CrossRef]
91. Wallentin, N.; Wickstrom, K.; Lundberg, C. Effect of cataract surgery on aqueous TGF-beta and lens epithelial cell proliferation. *Investig. Ophthalmol. Vis. Sci.* **1998**, *39*, 1410–1418.
92. Hu, D.N.; McCormick, S.A.; Lin, A.Y.; Lin, J.Y. TGF-beta2 inhibits growth of uveal melanocytes at physiological concentrations. *Exp. Eye Res.* **1998**, *67*, 143–150. [CrossRef] [PubMed]
93. Hirsch, L.; Nazari, H.; Sreekumar, P.G.; Kannan, R.; Dustin, L.; Zhu, D.; Barron, E.; Hinton, D.R. TGF-beta2 secretion from RPE decreases with polarization and becomes apically oriented. *Cytokine* **2015**, *71*, 394–396. [CrossRef] [PubMed]
94. Kokawa, N.; Sotozono, C.; Nishida, K.; Kinoshita, S. High total TGF-beta 2 levels in normal human tears. *Curr. Eye. Res.* **1996**, *15*, 341–343. [CrossRef]
95. Connor, T.B., Jr.; Roberts, A.B.; Sporn, M.B.; Danielpour, D.; Dart, L.L.; Michels, R.G.; de Bustros, S.; Enger, C.; Kato, H.; Lansing, M.; et al. Correlation of fibrosis and transforming growth factor-beta type 2 levels in the eye. *J. Clin. Investig.* **1989**, *83*, 1661–1666. [CrossRef]
96. Fuchshofer, R.; Tamm, E.R. The role of TGF-beta in the pathogenesis of primary open-angle glaucoma. *Cell Tissue Res.* **2012**, *347*, 279–290. [CrossRef]
97. Igarashi, N.; Honjo, M.; Asaoka, R.; Kurano, M.; Yatomi, Y.; Igarashi, K.; Miyata, K.; Kaburaki, T.; Aihara, M. Aqueous autotaxin and TGF-betas are promising diagnostic biomarkers for distinguishing open-angle glaucoma subtypes. *Sci. Rep.* **2021**, *11*, 1408. [CrossRef]
98. Saucedo, L.; Pfister, I.B.; Zandi, S.; Gerhardt, C.; Garweg, J.G. Ocular TGF-beta, matrix metalloproteinases, and TIMP-1 increase with the development and progression of diabetic retinopathy in Type 2 diabetes mellitus. *Mediat. Inflamm.* **2021**, *2021*, 9811361. [CrossRef]

99. Yu, X.B.; Sun, X.H.; Dahan, E.; Guo, W.Y.; Qian, S.H.; Meng, F.R.; Song, Y.L.; Simon, G.J. Increased levels of transforming growth factor-betal and -beta2 in the aqueous humor of patients with neovascular glaucoma. *Ophthalmic Surg. Lasers Imaging* **2007**, *38*, 6–14. [CrossRef]
100. Bredrup, C.; Knappskog, P.M.; Majewski, J.; Rodahl, E.; Boman, H. Congenital stromal dystrophy of the cornea caused by a mutation in the decorin gene. *Investig. Ophthalmol. Vis. Sci.* **2005**, *46*, 420–426. [CrossRef]
101. Rodahl, E.; Van Ginderdeuren, R.; Knappskog, P.M.; Bredrup, C.; Boman, H. A second decorin frame shift mutation in a family with congenital stromal corneal dystrophy. *Am. J. Ophthalmol.* **2006**, *142*, 520–521. [CrossRef] [PubMed]
102. Gupta, S.; Buyank, F.; Sinha, N.R.; Grant, D.G.; Sinha, P.R.; Iozzo, R.V.; Chaurasia, S.S.; Mohan, R.R. Decorin regulates collagen fibrillogenesis during corneal wound healing in mouse in vivo. *Exp. Eye Res.* **2022**, *216*, 108933. [CrossRef] [PubMed]
103. Begum, G.; O'Neill, J.; Chaudhary, R.; Blachford, K.; Snead, D.R.J.; Berry, M.; Scott, R.A.H.; Logan, A.; Blanch, R.J. Altered decorin biology in proliferative vitreoretinopathy: A mechanistic and cohort study. *Investig. Ophthalmol. Vis. Sci.* **2018**, *59*, 4929–4936. [CrossRef] [PubMed]
104. Al-Beshri, A.S.; Edward, D.P.; Haiti, K.A.; Craven, E.R. Overhanging-dissecting blebs: Immunohistochemical characterization. *J. Glaucoma* **2018**, *27*, 450–454. [CrossRef] [PubMed]
105. Kinsella, M.G.; Bressler, S.L.; Wight, T.N. The regulated synthesis of versican, decorin, and biglycan: Extracellular matrix proteoglycans that influence cellular phenotype. *Crit. Rev. Eukaryot. Gene Expr.* **2004**, *14*, 203–234. [CrossRef]
106. Sahay, P.; Chakraborty, M.; Rao, A. Global and comparative proteome signatures in the lens capsule, trabecular meshwork, and iris of patients with pseudoexfoliation glaucoma. *Front. Mol. Biosci.* **2022**, *9*, 877250. [CrossRef]
107. Abdullatif, A.M.; Macky, T.A.; Abdullatif, M.M.; Nassar, K.; Grisanti, S.; Mortada, H.A.; Soliman, M.M. Intravitreal decorin preventing proliferative vitreoretinopathy in perforating injuries: A pilot study. *Graefes Arch. Clin. Exp. Ophthalmol.* **2018**, *256*, 2473–2481. [CrossRef]
108. Wormstone, I.M. Posterior capsule opacification: A cell biological perspective. *Exp. Eye Res.* **2002**, *74*, 337–347. [CrossRef]
109. Marcantonio, J.M.; Syam, P.P.; Liu, C.S.; Duncan, G. Epithelial transdifferentiation and cataract in the human lens. *Exp. Eye Res.* **2003**, *77*, 339–346. [CrossRef]
110. de Iongh, R.U.; Lovicu, F.J.; Overbeek, P.A.; Schneider, M.D.; Joya, J.; Hardeman, E.D.; McAvoy, J.W. Requirement for TGFbeta receptor signaling during terminal lens fiber differentiation. *Development* **2001**, *128*, 3995–4010. [CrossRef]
111. de Iongh, R.U.; Wederell, E.; Lovicu, F.J.; McAvoy, J.W. Transforming growth factor-beta-induced epithelial-mesenchymal transition in the lens: A model for cataract formation. *Cells Tissues Organs* **2005**, *179*, 43–55. [CrossRef] [PubMed]
112. Lee, E.H.; Seomun, Y.; Hwang, K.H.; Kim, J.E.; Kim, I.S.; Kim, J.H.; Joo, C.K. Overexpression of the transforming growth factor-beta-inducible gene betaig-h3 in anterior polar cataracts. *Investig. Ophthalmol. Vis. Sci.* **2000**, *41*, 1840–1845.
113. Saika, S.; Miyamoto, T.; Ishida, I.; Shirai, K.; Ohnishi, Y.; Ooshima, A.; McAvoy, J.W. TGFbeta-Smad signalling in postoperative human lens epithelial cells. *Br. J. Ophthalmol.* **2002**, *86*, 1428–1433. [CrossRef] [PubMed]
114. Medvedovic, M.; Tomlinson, C.R.; Call, M.K.; Grogg, M.; Tsonis, P.A. Gene expression and discovery during lens regeneration in mouse: Regulation of epithelial to mesenchymal transition and lens differentiation. *Mol. Vis.* **2006**, *12*, 422–440.
115. Hayashi, N.; Kato, H.; Kiyosawa, T.; Hayashi, H.; Oshima, K.; Yamaoka, M. [The change in immunohistochemical localization of basic fibroblast growth factor (b-FGF) around the lens capsule after extracapsular extraction]. *Nihon Ganka Gakkai Zasshi* **1991**, *95*, 621–624.
116. Lovicu, F.J.; McAvoy, J.W. Localization of acidic fibroblast growth factor, basic fibroblast growth factor, and heparan sulphate proteoglycan in rat lens: Implications for lens polarity and growth patterns. *Investig. Ophthalmol. Vis. Sci.* **1993**, *34*, 3355–3365.
117. Meacock, W.R.; Spalton, D.J.; Stanford, M.R. Role of cytokines in the pathogenesis of posterior capsule opacification. *Br. J. Ophthalmol.* **2000**, *84*, 332–336. [CrossRef]
118. Chamberlain, C.G.; McAvoy, J.W. Induction of lens fibre differentiation by acidic and basic fibroblast growth factor (FGF). *Growth Factors* **1989**, *1*, 125–134. [CrossRef]
119. McAvoy, J.W.; Chamberlain, C.G. Fibroblast growth factor (FGF) induces different responses in lens epithelial cells depending on its concentration. *Development* **1989**, *107*, 221–228. [CrossRef]
120. Nishi, O.; Nishi, K.; Fujiwara, T.; Shirasawa, E.; Ohmoto, Y. Effects of the cytokines on the proliferation of and collagen synthesis by human cataract lens epithelial cells. *Br. J. Ophthalmol.* **1996**, *80*, 63–68. [CrossRef]
121. Wormstone, I.M.; Del Rio-Tsonis, K.; McMahon, G.; Tamiya, S.; Davies, P.D.; Marcantonio, J.M.; Duncan, G. FGF: An autocrine regulator of human lens cell growth independent of added stimuli. *Investig. Ophthalmol. Vis. Sci.* **2001**, *42*, 1305–1311.
122. Kahari, V.M.; Larjava, H.; Uitto, J. Differential regulation of extracellular matrix proteoglycan (PG) gene expression. Transforming growth factor-beta 1 up-regulates biglycan (PGI), and versican (large fibroblast PG) but down-regulates decorin (PGII) mRNA levels in human fibroblasts in culture. *J. Biol. Chem.* **1991**, *266*, 10608–10615. [PubMed]
123. Vuorio, T.; Kahari, V.M.; Black, C.; Vuorio, E. Expression of osteonectin, decorin, and transforming growth factor-beta 1 genes in fibroblasts cultured from patients with systemic sclerosis and morphea. *J. Rheumatol.* **1991**, *18*, 247–251. [PubMed]
124. Shu, C.; Smith, S.M.; Little, C.B.; Melrose, J. Use of FGF-2 and FGF-18 to direct bone marrow stromal stem cells to chondrogenic and osteogenic lineages. *Future Sci. OA* **2016**, *2*, FSO142. [CrossRef]

125. Tan, E.M.; Hoffren, J.; Rouda, S.; Greenbaum, S.; Fox, J.W.t.; Moore, J.H., Jr.; Dodge, G.R. Decorin, versican, and biglycan gene expression by keloid and normal dermal fibroblasts: Differential regulation by basic fibroblast growth factor. *Exp. Cell Res.* **1993**, *209*, 200–207. [CrossRef]
126. Wang, S.C.; Lin, C.T.; Nie, D.B.; Ouyang, H.S. The effect of basic fibroblast growth factor on the gene expression of decorin by periodontal ligament fibroblasts in culture. *Hua Xi Kou Qiang Yi Xue Za Zhi* **2008**, *26*, 352–354.
127. Sonal, D. Prevention of IGF-1 and TGFbeta stimulated type II collagen and decorin expression by bFGF and identification of IGF-1 mRNA transcripts in articular chondrocytes. *Matrix Biol.* **2001**, *20*, 233–242. [CrossRef]
128. Trowbridge, J.M.; Rudisill, J.A.; Ron, D.; Gallo, R.L. Dermatan sulfate binds and potentiates activity of keratinocyte growth factor (FGF-7). *J. Biol. Chem* **2002**, *277*, 42815–42820. [CrossRef]
129. Penc, S.F.; Pomahac, B.; Winkler, T.; Dorschner, R.A.; Eriksson, E.; Herndon, M.; Gallo, R.L. Dermatan sulfate released after injury is a potent promoter of fibroblast growth factor-2 function. *J. Biol. Chem.* **1998**, *273*, 28116–28121. [CrossRef]
130. Gunning, P. Emerging issues for tropomyosin structure, regulation, function and pathology. *Adv. Exp. Med. Biol.* **2008**, *644*, 293–298.
131. Gunning, P.W.; Schevzov, G.; Kee, A.J.; Hardeman, E.C. Tropomyosin isoforms: Divining rods for actin cytoskeleton function. *Trends Cell Biol.* **2005**, *15*, 333–341. [CrossRef] [PubMed]
132. Shu, D.Y.; Lovicu, F.J. Enhanced EGF receptor-signaling potentiates TGFbeta-induced lens epithelial-mesenchymal transition. *Exp. Eye Res.* **2019**, *185*, 107693. [CrossRef] [PubMed]
133. Shibata, T.; Shibata, S.; Ishigaki, Y.; Kiyokawa, E.; Ikawa, M.; Singh, D.P.; Sasaki, H.; Kubo, E. Tropomyosin 2 heterozygous knockout in mice using CRISPR-Cas9 system displays the inhibition of injury-induced epithelial-mesenchymal transition, and lens opacity. *Mech. Ageing Dev.* **2018**, *171*, 24–30. [CrossRef] [PubMed]
134. Wormstone, I.M.; Tamiya, S.; Anderson, I.; Duncan, G. TGF-beta2-induced matrix modification and cell transdifferentiation in the human lens capsular bag. *Investig. Ophthalmol. Vis. Sci.* **2002**, *43*, 2301–2308.
135. Dwivedi, D.J.; Pino, G.; Banh, A.; Nathu, Z.; Howchin, D.; Margetts, P.; Sivak, J.G.; West-Mays, J.A. Matrix metalloproteinase inhibitors suppress transforming growth factor-beta-induced subcapsular cataract formation. *Am. J. Pathol.* **2006**, *168*, 69–79. [CrossRef]
136. Zhao, H.; Yang, Y.; Rizo, C.M.; Overbeek, P.A.; Robinson, M.L. Insertion of a Pax6 consensus binding site into the alphaA-crystallin promoter acts as a lens epithelial cell enhancer in transgenic mice. *Investig. Ophthalmol. Vis. Sci.* **2004**, *45*, 1930–1939. [CrossRef]
137. Du, S.; Shao, J.; Xie, D.; Zhang, F. Decorin inhibits glucose-induced lens epithelial cell apoptosis via suppressing p22phox-p38 MAPK signaling pathway. *PLoS ONE* **2020**, *15*, e0224251. [CrossRef]
138. Ozay, R.; Turkoglu, E.; Gurer, B.; Dolgun, H.; Evirgen, O.; Erguder, B.I.; Hayirli, N.; Gurses, L.; Sekerci, Z.; Yilmaz, E.R. Does Decorin Protect Neuronal Tissue via Its Antioxidant and Antiinflammatory Activity from Traumatic Brain Injury? An Experimental Study. *World Neurosurg.* **2017**, *97*, 407–415. [CrossRef]
139. Fatma, N.; Kubo, E.; Sharma, P.; Beier, D.R.; Singh, D.P. Impaired homeostasis and phenotypic abnormalities in Prdx6$^{-/-}$ mice lens epithelial cells by reactive oxygen species: Increased expression and activation of TGFbeta. *Cell Death Differ.* **2005**, *12*, 734–750. [CrossRef]
140. Bondi, C.D.; Manickam, N.; Lee, D.Y.; Block, K.; Gorin, Y.; Abboud, H.E.; Barnes, J.L. NAD(P)H oxidase mediates TGF-beta1-induced activation of kidney myofibroblasts. *J. Am. Soc. Nephrol.* **2010**, *21*, 93–102. [CrossRef]
141. Fatma, N.; Kubo, E.; Toris, C.B.; Stamer, W.D.; Camras, C.B.; Singh, D.P. PRDX6 attenuates oxidative stress- and TGFbeta-induced abnormalities of human trabecular meshwork cells. *Free Radic. Res.* **2009**, *43*, 783–795. [CrossRef] [PubMed]
142. Ohba, M.; Shibanuma, M.; Kuroki, T.; Nose, K. Production of hydrogen peroxide by transforming growth factor-beta 1 and its involvement in induction of egr-1 in mouse osteoblastic cells. *J. Cell Biol.* **1994**, *126*, 1079–1088. [CrossRef] [PubMed]
143. Herrera, B.; Murillo, M.M.; Alvarez-Barrientos, A.; Beltran, J.; Fernandez, M.; Fabregat, I. Source of early reactive oxygen species in the apoptosis induced by transforming growth factor-beta in fetal rat hepatocytes. *Free Radic. Biol. Med.* **2004**, *36*, 16–26. [CrossRef] [PubMed]
144. Herrera, B.; Alvarez, A.M.; Sanchez, A.; Fernandez, M.; Roncero, C.; Benito, M.; Fabregat, I. Reactive oxygen species (ROS) mediates the mitochondrial-dependent apoptosis induced by transforming growth factor (beta) in fetal hepatocytes. *FASEB J.* **2001**, *15*, 741–751. [CrossRef] [PubMed]
145. Weidinger, A.; Kozlov, A.V. Biological Activities of Reactive Oxygen and Nitrogen Species: Oxidative Stress versus Signal Transduction. *Biomolecules* **2015**, *5*, 472–484. [CrossRef]
146. Blochberger, T.C.; Cornuet, P.K.; Hassell, J.R. Isolation and partial characterization of lumican and decorin from adult chicken corneas. A keratan sulfate-containing isoform of decorin is developmentally regulated. *J. Biol. Chem* **1992**, *267*, 20613–20619. [CrossRef]
147. Kamma-Lorger, C.S.; Pinali, C.; Martinez, J.C.; Harris, J.; Young, R.D.; Bredrup, C.; Crosas, E.; Malfois, M.; Rodahl, E.; Meek, K.M.; et al. Role of decorin core protein in collagen organisation in congenital stromal corneal dystrophy (CSCD). *PLoS ONE* **2016**, *11*, e0147948. [CrossRef]
148. Bredrup, C.; Stang, E.; Bruland, O.; Palka, B.P.; Young, R.D.; Haavik, J.; Knappskog, P.M.; Rodahl, E. Decorin accumulation contributes to the stromal opacities found in congenital stromal corneal dystrophy. *Investig. Ophthalmol. Vis. Sci.* **2010**, *51*, 5578–5582. [CrossRef]

149. Mohan, R.R.; Tandon, A.; Sharma, A.; Cowden, J.W.; Tovey, J.C. Significant inhibition of corneal scarring in vivo with tissue-selective, targeted AAV5 decorin gene therapy. *Investig. Ophthalmol. Vis. Sci.* **2011**, *52*, 4833–4841. [CrossRef]
150. Mohan, R.R.; Tovey, J.C.; Sharma, A.; Schultz, G.S.; Cowden, J.W.; Tandon, A. Targeted decorin gene therapy delivered with adeno-associated virus effectively retards corneal neovascularization in vivo. *PLoS ONE* **2011**, *6*, e26432. [CrossRef]
151. Mohan, R.R.; Balne, P.K.; Muayad, M.S.; Tripathi, R.; Sinha, N.R.; Gupta, S.; An, J.A.; Sinha, P.R.; Hesemann, N.P. Six-Month In Vivo Safety Profiling of Topical Ocular AAV5-Decorin Gene Transfer. *Transl. Vis. Sci. Technol.* **2021**, *10*, 5. [CrossRef] [PubMed]
152. Hill, L.J.; Moakes, R.J.A.; Vareechon, C.; Butt, G.; Ng, A.; Brock, K.; Chouhan, G.; Vincent, R.C.; Abbondante, S.; Williams, R.L.; et al. Sustained release of decorin to the surface of the eye enables scarless corneal regeneration. *NPJ Regen. Med.* **2018**, *3*, 23. [CrossRef] [PubMed]
153. Wu, M.; Downie, L.E.; Grover, L.M.; Moakes, R.J.A.; Rauz, S.; Logan, A.; Jiao, H.; Hill, L.J.; Chinnery, H.R. The neuroregenerative effects of topical decorin on the injured mouse cornea. *J. Neuroinflamm.* **2020**, *17*, 142. [CrossRef] [PubMed]
154. Collaborative Normal-Tension Glaucoma Study Group. The effectiveness of intraocular pressure reduction in the treatment of normal-tension glaucoma. *Am. J. Ophthalmol.* **1998**, *126*, 498–505. [CrossRef]
155. Collaborative Normal-Tension Glaucoma Study Group. Comparison of glaucomatous progression between untreated patients with normal-tension glaucoma and patients with therapeutically reduced intraocular pressures. *Am. J. Ophthalmol.* **1998**, *126*, 487–497. [CrossRef]
156. Moses, R.A. The effect of intraocular pressure on resistance to outflow. *Surv. Ophthalmol.* **1977**, *22*, 88–100. [CrossRef]
157. Wiederholt, M. Direct involvement of trabecular meshwork in the regulation of aqueous humor outflow. *Curr. Opin. Ophthalmol.* **1998**, *9*, 46–49. [CrossRef]
158. Overby, D.R.; Zhou, E.H.; Vargas-Pinto, R.; Pedrigi, R.M.; Fuchshofer, R.; Braakman, S.T.; Gupta, R.; Perkumas, K.M.; Sherwood, J.M.; Vahabikashi, A.; et al. Altered mechanobiology of Schlemm's canal endothelial cells in glaucoma. *Proc. Natl. Acad. Sci. USA* **2014**, *111*, 13876–13881. [CrossRef]
159. Kirwan, R.P.; Wordinger, R.J.; Clark, A.F.; O'Brien, C.J. Differential global and extra-cellular matrix focused gene expression patterns between normal and glaucomatous human lamina cribrosa cells. *Mol. Vis.* **2009**, *15*, 76–88.
160. Pena, J.D.; Taylor, A.W.; Ricard, C.S.; Vidal, I.; Hernandez, M.R. Transforming growth factor beta isoforms in human optic nerve heads. *Br. J. Ophthalmol.* **1999**, *83*, 209–218. [CrossRef]
161. Schneider, M.; Dillinger, A.E.; Ohlmann, A.; Iozzo, R.V.; Fuchshofer, R. Decorin-an antagonist of TGF-beta in astrocytes of the optic nerve. *Int. J. Mol. Sci.* **2021**, *22*, 7660. [CrossRef] [PubMed]
162. Addicks, E.M.; Quigley, H.A.; Green, W.R.; Robin, A.L. Histologic characteristics of filtering blebs in glaucomatous eyes. *Arch. Ophthalmol.* **1983**, *101*, 795–798. [CrossRef] [PubMed]
163. Jampel, H.D.; Morrison, J.; Vocci, M.; Quigley, H. Identification of fibrin/fibrinogen in glaucoma filtration surgery wounds. *Ophthalmic Surg. Lasers Imaging Retin.* **1988**, *19*, 576–579. [CrossRef]
164. Jampel, H.D.; McGuigan, L.J.; Dunkelberger, G.R.; L'Hernault, N.L.; Quigley, H.A. Cellular proliferation after experimental glaucoma filtration surgery. *Arch. Ophthalmol.* **1988**, *106*, 89–94. [CrossRef] [PubMed]
165. Grisanti, S.; Szurman, P.; Warga, M.; Kaczmarek, R.; Ziemssen, F.; Tatar, O.; Bartz-Schmidt, K.U. Decorin modulates wound healing in experimental glaucoma filtration surgery: A pilot study. *Investig. Ophthalmol. Vis. Sci.* **2005**, *46*, 191–196. [CrossRef]
166. Sahay, P.; Reddy, S.; Prusty, B.K.; Modak, R.; Rao, A. TGFbeta1, MMPs and cytokines profiles in ocular surface: Possible tear biomarkers for pseudoexfoliation. *PLoS ONE* **2021**, *16*, e0249759. [CrossRef]
167. Rattner, A.; Nathans, J. Macular degeneration: Recent advances and therapeutic opportunities. *Nat. Rev. Neurosci.* **2006**, *7*, 860–872. [CrossRef]
168. Du, S.; Wang, S.; Wu, Q.; Hu, J.; Li, T. Decorin inhibits angiogenic potential of choroid-retinal endothelial cells by downregulating hypoxia-induced Met, Rac1, HIF-1alpha and VEGF expression in cocultured retinal pigment epithelial cells. *Exp. Eye Res.* **2013**, *116*, 151–160. [CrossRef]
169. Wang, X.; Ma, W.; Han, S.; Meng, Z.; Zhao, L.; Yin, Y.; Wang, Y.; Li, J. TGF-beta participates choroid neovascularization through Smad2/3-VEGF/TNF-alpha signaling in mice with Laser-induced wet age-related macular degeneration. *Sci. Rep.* **2017**, *7*, 9672. [CrossRef]
170. Lee, N.E.; Park, Y.J.; Chung, I.Y.; Seo, S.W.; Park, J.M.; Yoo, J.M.; Song, J.K. Gene expression changes in a rat model of oxygen-induced retinopathy. *Korean J. Ophthalmol.* **2011**, *25*, 42–47. [CrossRef]
171. Park, Y.J.; Kim, Y.H.; Choi, W.S.; Chung, I.Y.; Yoo, J.M. Treatment with triamcinolone acetonide prevents decreased retinal levels of decorin in a rat model of oxygen-induced retinopathy. *Curr. Eye Res.* **2010**, *35*, 657–663. [CrossRef] [PubMed]
172. Duran, G.L.S.; Balbaba, M.; Colakoglu, N.; Bulmus, O.; Ulas, F.; Eroksuz, Y. Effect of Decorin and Bevacizumab on oxygen-induced retinopathy in rat models: A comparative study. *Indian J. Ophthalmol.* **2021**, *69*, 369–373. [CrossRef]
173. Ryan, S.J. The pathophysiology of proliferative vitreoretinopathy in its management. *Am. J. Ophthalmol.* **1985**, *100*, 188–193. [CrossRef] [PubMed]
174. Winkler, J.; Hoerauf, H. TGF-ss and RPE-derived cells in taut subretinal strands from patients with proliferative vitreoretinopathy. *Eur. J. Ophthalmol.* **2011**, *21*, 422–426. [CrossRef]

175. Nassar, K.; Luke, J.; Luke, M.; Kamal, M.; Abd El-Nabi, E.; Soliman, M.; Rohrbach, M.; Grisanti, S. The novel use of decorin in prevention of the development of proliferative vitreoretinopathy (PVR). *Graefes Arch. Clin. Exp. Ophthalmol.* **2011**, *249*, 1649–1660. [CrossRef]
176. Jarvinen, T.A. Design of target-seeking antifibrotic compounds. *Methods Enzymol.* **2012**, *509*, 243–261. [CrossRef]

Disclaimer/Publisher's Note: The statements, opinions and data contained in all publications are solely those of the individual author(s) and contributor(s) and not of MDPI and/or the editor(s). MDPI and/or the editor(s) disclaim responsibility for any injury to people or property resulting from any ideas, methods, instructions or products referred to in the content.

cells

MDPI

Article

Aged Lens Epithelial Cells Suppress Proliferation and Epithelial–Mesenchymal Transition-Relevance for Posterior Capsule Opacification

Zongbo Wei [1,†], Pasley Gordon [2,†], Caili Hao [1,†], Jingru Huangfu [1], Emily Fan [3], Xiang Zhang [4], Hong Yan [5] and Xingjun Fan [1,*]

[1] Department of Cellular Biology and Anatomy, Medical College of Georgia at Augusta University, 1460 Laney Walker Blvd., CB Building, Room CB1119, Augusta, GA 30912, USA; zowei@augusta.edu (Z.W.); chao@augusta.edu (C.H.); jhuangfu@augusta.edu (J.H.)
[2] Department of Ophthalmology, Medical College of Georgia at Augusta University, Augusta, GA 30912, USA; pagordon@augusta.edu
[3] Lakeside High School at Columbia County, Evans, GA 30809, USA; emilyfan3140@gmail.com
[4] Genomics, Epigenomics and Sequencing Core, Department of Environmental and Public Health Sciences, University of Cincinnati, Cincinnati, OH 45221, USA; zhanx5@ucmail.uc.edu
[5] Xi'an Fourth Hospital, Xi'an Jiaotong University, Xi'an 710049, China; yan2128ts@med.nwu.edu.cn
* Correspondence: xfan@augusta.edu
† These authors contributed equally to this work.

Abstract: Posterior capsule opacification (PCO) is a frequent complication after cataract surgery, and advanced PCO requires YAG laser (Nd: YAG) capsulotomy, which often gives rise to more complications. Lens epithelial cell (LEC) proliferation and transformation (i.e., epithelial–mesenchymal transition (EMT)) are two critical elements in PCO initiation and progression pathogenesis. While PCO marginally impacts aged cataract surgery patients, PCO incidences are exceptionally high in infants and children undergoing cataract surgery. The gene expression of lens epithelial cell aging and its role in the discrepancy of PCO prevalence between young and older people have not been fully studied. Here, we conducted a comprehensive differentially expressed gene (DEG) analysis of a cell aging model by comparing the early and late passage FHL124 lens epithelial cells (LECs). *In vitro*, TGFβ2, cell treatment, and *in vivo* mouse cataract surgical models were used to validate our findings. We found that aged LECs decelerated rates of cell proliferation accompanied by dysregulation of cellular immune response and cell stress response. Surprisingly, we found that LECs systematically downregulated epithelial–mesenchymal transition (EMT)-promoting genes. The protein expression of several EMT hallmark genes, e.g., fibronectin, αSMA, and cadherin 11, were gradually decreased during LECs aging. We then confirmed these findings in vitro and found that aged LECs markedly alleviated TGFβ2-mediated EMT. Importantly, we explicitly confirmed the *in vitro* findings from the *in vivo* mouse cataract surgery studies. We propose that both the high proliferation rate and EMT-enriched young LECs phenotypic characteristics contribute to unusually high PCO incidence in infants and children.

Keywords: cataracts; posterior capsule opacification; PCO; epithelial–mesenchymal transition; EMT; aging; cataract surgery; lens

1. Introduction

According to the World Health Organization (WHO), at least 94 million people worldwide have cataracts, a leading cause of blindness. Most cataracts are related to aging, referred to as age-related cataracts (ANC). In addition, an estimated 200,000 children worldwide are blinded due to congenital or developmental cataracts, and an estimated 20,000 to 40,000 newborns each year carry congenital cataracts [1]. Currently, cataract surgery is the only treatment option for the disease. Approximately 4 million and 28 million cataract

surgical procedures are performed annually in the US and worldwide, respectively. Despite a well-established surgical procedure, posterior capsule opacification (PCO) is a frequent complication after cataract surgery, also known as a secondary cataract. If PCO sufficiently reduces vision, patients must undergo a YAG laser (Nd: YAG) capsulotomy to remove PCO tissue and restore a clear line of sight. In addition to added healthcare costs for cataract patients, Nd: YAG capsulotomy is often associated with other complications, such as increasing transient intraocular pressure, lens subluxation and dislocation, retinal detachment and lens pitting, exacerbation of local endophthalmitis, and free-floating fragments [2].

The prevalence of PCO is closely associated with patient age, surgical techniques, the surgeon's experience, and the materials and design of the intraocular lens (IOL). The PCO incidence rate is exceptionally high for infants and young children when the posterior capsule is retained during the surgery. Basti et al. [3] found a 43.7% PCO rate at the 11-month follow-up of 87 extracapsular cataract extraction with IOL implantation (ECCE+IOL) patients between 2 and 4 years of age. Knight-Nanan et al. [4] found a 95.8% PCO occurrence at the 2-year follow-up of 24 ECCE plus IOL implantation eyes of patients ranging from 4 weeks to 12 years old. Clinical studies found close to 100% PCO incidence rates in pediatric cataract surgeries via ECCE plus IOL implantation [5–7]. For this reason, primary posterior capsulotomy and anterior vitrectomy are now routine surgical strategies in pediatric cataract surgery [8].

The PCO incidence is much lower in adult cataract patients after surgery. Several large-size retrospective cohort studies have examined the prevalence of PCO while comparing the impact of IOL material and design on PCO formation. Ursell et al. [9] assessed a 3-year incidence of Nd: YAG capsulotomy and PCO among 52,162 eyes from 39,324 patients aged 65 and older with cataract surgery with IOL implantation made from different materials. The Nd: YAG capsulotomy incidence rate was between 2.4% and 10.9%, and the PCO rate was between 4.7% and 14.8%. In a separate study, a 5-year follow-up of electronic record examinations of 20,763 eyes from 16,595 patients aged 65 and older who had cataract surgery with single-piece IOL implantation revealed a 7.1–22.6% PCO incidence rate [10]. It is worth noting that elevated PCO incidence rates were found in patients younger than 60 years from a retrospective cohort study that examined the record of 10,044 eye surgeries [11].

PCO originates from residual lens epithelial cells (LECs) after cataract surgery, which will eventually deposit at the posterior capsule through survival, proliferation, migration, and transformation [12]. LEC proliferation and transformation are two critical components in PCO initiation and progression. Continuous proliferation and sometimes hyperproliferation is vital to LEC survival, and newly proliferated LECs can expand and migrate toward the posterior capsule [13,14]. LEC transformation is considered a critical process that alters the LEC phenotype by acquiring mesenchymal-like functions, a more invasive type. The epithelial–mesenchymal transition (EMT) is believed to be the primary mechanism driving LEC transformation [15–17].

Due to the nature of the disease, the need for cataract surgery primarily impacts either the very young or elderly population. The discrepancy in PCO incidences between young and aged people raises an essential question of how LECs respond to wound healing originating from similar surgical procedures and how LEC transformation impacts PCO progression at different ages. Currently, a commonly accepted explanation is that young lens epithelial cells are more proliferative than aged LECs since it has been well documented that cell division rates decrease with age [18,19]. However, PCO formation is widely believed to result from complex and multifactorial processes. The actual mechanisms responsible for the discrepancy in PCO prevalence between young and aged groups remain unknown. The present study discovered that aged LECs not only decelerate proliferation but also suppress epithelial–mesenchymal transition (EMT) based on a comprehensive comparative transcriptomic analysis of our established LEC aging model. We then confirmed the in vitro findings using the *in vivo* mouse cataract surgery model.

2. Methods

2.1. Reagents

All chemicals used were of analytical reagent grade. Milli-Q water was used for the preparation of standards and reagents. DAPI (23018) was purchased from Biotium (Fremont, CA, USA). Hoechst33342 (H3570) was purchased from Thermo Fisher Scientific (Waltham, MA, USA). Antibody to fibronectin (P1H11) was obtained from the Developmental Studies Hybridoma Bank (DSHB, Iowa City, IA, USA). Fibronectin (Ab268020) and tenascin C (ab108930) antibodies were purchased from Abcam (Cambridge, MA, USA). αSMA antibody (F3777) was purchased from Millipore-Sigma (St. Louis, MO, USA). N-cadherin antibody (14215) was purchased from Cell Signaling Technology (Danvers, MA, USA). Cadherin-11 antibody (368702) was purchased from BioLegend (San Diego, CA, USA). ZO-1 (40-2200) and GAPDH (PA1-987) antibodies were purchased from Thermo Fisher Scientific. The Cell Counting Kit-8 assay kit (HY-K0301) was purchased from MedChem Express (Monmouth Junction, NJ, USA). All other chemicals were obtained from Sigma-Aldrich and Thermo Fisher Scientific.

2.2. Cell Culture and Lens Epithelial Cell Aging Model

The human lens epithelial cell line, FHL124 cells [20], established by Prof. John Reddan at Oakland University, was supplied by Prof. Michael Wormstone at the University of East Anglia, UK, and was grown in MEM with 5% FBS and 100 U/mL of penicillin and streptomycin at 35 °C in a humidified 5% CO_2 incubator.

The FHL124 cell cellular aging model was established following our previous study, [21]. In brief, FHL124 cells were continuously cultured and split when cells reached 80% confluence. For early passage (young) FHL124 cells, the doubling time is around two days; for late passage (old) FHL124 cells, the doubling time is around 3–4 days.

2.3. Animals

All animal experiments were performed by procedures approved by the Augusta University Animal Care and Use Committee and conformed to the ARVO Statement for the Use of Animals in Ophthalmic and Vision Research. Animals were housed under a diurnal lighting condition and allowed free access to food and water. C57BL/6J mice at 2 and 20 months were purchased from the National Institute of Aging (NIA) aged rodent colonies.

2.4. Cell Proliferation Assay

The rate of cell proliferation was determined by colorimetric assay using the Cell Counting Kit-8 assay following the manufacturer's instructions. In brief, 2000 cells per well were placed in a 96-well-plate, and cell division was measured every 24 h for seven days. At each time point, 10 μL of CCK-8 solution was added to each well, and cells were incubated at 35 °C for 1.5 h before recording the absorbance at 450 nm. The cell-free medium served as the blank.

2.5. RNAseq and Data Analysis

For the RNAseq study, we used passage 15 (P15) and 42 (P42) FHL124 cells. The next-generation deep sequencing was carried out by the Genomics, Epigenomics, and Sequencing Core at the University of Cincinnati with a similar procedure as our previous study [22]. Three biological replicates of each passage were sequenced (n = 3). The RNA quality control, polyRNA enrichment, and library preparation were described in our previous study [21]. The library was indexed and amplified under 11 PCR cycle numbers. After library Bioanalyzer QC analysis and quantification via real-time PCR (NEBNext Library Quant Kit, NEB), the proportionally pooled libraries were sequenced using a NextSeq 550 sequencer (Illumina, San Diego, CA, USA). Under the sequencing setting of single read 1 × 85 bp, about 25 million pass filter reads per sample were generated.

The deep sequencing data were processed using Partek Flow. Unaligned reads were trimmed based on a PHRED quality score with a minimal read >25 nt. Trimmed reads

were aligned to the latest human genome assembly hg19 using a STAR aligner. Aligned reads were quantitatively aligned to Ensembl Transcripts release 100. Raw counts were further filtered and normalized to transcripts per million (TPM). Deferentially expressed genes (DEGs) and pairwise comparison of p15 and p42 were extrapolated and normalized using a negative binomial model in DESeq2. The significantly DEGs between groups were expressed as fold change or $\log_2$ fold change with p-value < 0.05 and false discovery rate (FDR < 0.05). RNAseq data are deposited in the Gene Expression Omnibus (GEO) database under accession number GSE184422.

The FVB/N mouse lens epithelium deep sequencing data [23] were obtained from NCBI's Sequence Read Archive (SRA accession number: SRP040480), CD1 mouse lens epithelium deep sequence data [24] were obtained from GEO (accession number: GSE113887), and C57BL/6 mouse epithelium deep sequence data [25] were obtained from GEO (accession number: GSE166619). All raw sequencing data with fastq format were analyzed and normalized through Partek Flow using the same calculation and normalization method as that of FHL124 cells.

2.6. Gene Set Enrichment Analysis (GSEA)

GSEA is a powerful gene enrichment tool developed by a joint project of UC San Diego and Broad Institute using a pre-ranked gene database based on the fold changes of all gene expression profiles in contrast to taking only significant DEGs [26]. P42 and P15 passage gene sets were analyzed for the Molecular Signature Database (MSigDB 7.4). To identify the most relevant biological processes, we only selected the nominal p-value below 0.05, a false discovery rate less than 15%, and a normalized enrichment score (NES) > 1.40 or <-1.30. The resulting normalized enrichment scores (NESs) were then used to create heatmaps, and enriched genes were further analyzed based on their relative expression via transcript per million (TPM).

2.7. TGFβ2 Treatment

Cells at different passages were seeded in 35 mm culture dishes at a density of 1.0×10^5 cells/dish 16 h before treatment. Cell medium was then replaced with freshly prepared medium with or without 10 ng/mL TGFβ2. Then, 24 h after treatment, cells were washed three times with cold PBS before being harvested for immunoblot assay.

2.8. Cell Immunofluorescence Staining

FHL124 cells were seeded on a 35 mm round glass coverslip at a density of 3×10^4/mL in a 24-well plate. After about 16 h, cells were fixed by 4% PFA at RT for 15 min. Except for ZO-1 staining, a membrane protein, fixed cells were treated with 0.5% TritonX-100 for 10 min at RT to permeabilize the cell membrane. Subsequently, coverslips were incubated with 5% normal goat serum for 30 min at RT to block non-specific background. Coverslips were incubated with appropriate primary antibodies at 4 °C overnight in a humidified chamber. Following 3×5 min PBST (PBS with 0.1% Tween 20) wash, coverslips were incubated with a fluorescent conjugated secondary antibody at RT for 1 h. After 3×5 min PBST rinse, coverslips were mounted with a mounting medium and subjected to confocal microscopy.

2.9. Mouse Cataract Surgery

Mice at 2 months and 20 months of age were used in this study. Mice were anesthetized with a ketamine-xylazine before surgery. A detailed surgical procedure was described in our previous study [27]. For each mouse, left eye surgery was performed on day 1. On day 5, right eye cataract surgery was performed, and the mouse was euthanized immediately after surgery to harvest both eyes so that the right eye served as a control. Eye drops containing 0.3% of ofloxacin were applied once immediately after surgery. The harvested eyes were fixed in 4% paraformaldehyde fixative for 24 h and then subjected to paraffin embedding and sectioning.

2.10. Immunofluorescence Staining of Paraffin Sections

Before the antigen retrieval, sections were deparaffined and rehydrated by xylene, series gradient ethanol, and PBS. For αSMA and FN1 staining, sodium citrate antigen retrieval buffer (10 mM sodium citrate, 0.05% Tween 20, pH 6.0) was used. In contrast, TE antigen retrieval buffer (10 mM Tris base, 1 mM EDTA solution, 0.05% Tween 20, pH 9.0) was used for tenascin C staining. Sections were immersed into a proper antigen retrieval buffer and processed by the Epitope Retrieval Steamer Set (IW-1102) from IHC World (Woodstock, MD, USA) for 20 min. After 10 min cooling times at RT, slides were washed 2 × 5 min with PBS. Tissues were then permeabilized by incubating with 0.5% Triton-X-100 for 10 min at RT. Tissue slides were then blocked by 5% goat serum for 30 min at RT before being stained with an anti-αSMA antibody (1:500, F3777, Sigma-Aldrich), anti-fibronectin antibody (1:200, Ab268020, Abcam), and anti-tenascin C antibody (1:500, Ab108930, Abcam) at 4 °C overnight. The next day, sections were washed 3 × 5 min with PBST before being incubated with proper secondary antibody conjugated with fluorescent dye at RT for 1 h. After a 3 × 5 min wash with PBST, the sections were mounted with a mounting medium and ready for confocal microscopy.

2.11. Confocal Microscopy

All images were captured by a Leica STELLARIS confocal microscopy (Leica) and analyzed by LAS-X software.

2.12. Immunoblot Assay

Immunoblot assays were performed as previously described by [27]. In brief, the protein concentration from the supernatant was measured by protein bicinchoninic acid (BCA) assay (Thermo Fisher Scientific). Equal amounts of protein were subjected to appropriate SDS-PAGE gel electrophoresis and transferred to a 0.45 μm pore PVDF membrane. Detection was done using the ECL Western blotting detection system.

2.13. Statistics

All values are expressed as mean ± SD. In short, one-way ANOVA with Tukey's honest post hoc analysis and 2-way ANOVA with Holm–Šídák's multiple-comparisons test were computed using SPSS and GraphPad 9 software. Significance was considered at $p < 0.05$.

3. Results

3.1. FHL124 Is a Suitable Human Lens Epithelial Cell Line for Aging Study

Aiming to understand the role of gene expression in the discrepancy of PCO incidence rates between young and older adults, we performed a comparative transcriptome analysis of FHL124 human lens epithelial cells between their early passage (P15) and late passage (P42). FHL124 cells are spontaneously grown out of human lens epithelial cell lines without artificial immortalization that share 99.5% homology with native human lens epithelium [28,29]. Continuous cell division is an ideal cellular aging model for studying LEC aging. We have found that this in vitro cellular aging model closely resembles the *in vivo* situation [21]. FHL124 cells reached their senescence around passage 55 (P55) [21], and for this study, we performed all our assays before passage 50 (P50) to avoid a complete senescence state. To further validate the FHL124 cells' LEC characteristics at both early and late passages, we compared the top 500 most expressed genes between FHL124 cells and three strains (FVB/N, age p0 [23]; CD1, age p0.5 [24]; and C57BL/6, age 3 months [25]) of mouse lens epithelium under the same transcript normalization method. There are 245 genes shared between three strains of mouse lens epithelium. Notably, 179 over 245 genes (70.4%) also sit in the top 500 most expressed genes in FHL124 cells at P15 and P42 (Figure 1A). All the shared genes are listed in Table S1. Furthermore, we also surveyed the pro-LEC gene expression profile of P15 and P42 passage FHL124 cells. From 300 lens top-enriched genes ranked by iSyTE [30], we found that 246 genes (82%) were expressed,

and 161 genes (54%) were significantly expressed (top 1000 most expressed genes) in FHL124 cells at both passage 15 and 42. Several prominent lens epithelial cell-associated genes, such as CRYAB, PAX6, HSPB1, ANTXR1, ANXA1, S100A6, SPARC, and EZR, were highly expressed in both P15 and P42 passage FHL124 cells (Figure 1B). Although we found that several of these genes had significant changes in their expression between early and late passages, their overall expression levels were abundant in both passages. Conversely, we compared several lens fiber cell markers and their expression in P15 and P42 passage FHL124 cells. As shown in Figure 1C, almost no detectable expression of CRYGC, MIP, PGAM2, CRYBA4, GJE1, PLA3G7, CRYGA, and CRYGB was found in early and late passage FHL124 cells. These results suggest that FHL124 cells closely resemble the lens epithelium and are suitable for lens biology and aging studies.

3.2. Aging Induces Substantial Gene Expression Changes in Lens Epithelial Cells

Over 27,000 transcripts were normalized and compared between P42 and P15 (Figure 2A, heatmap; Figure S1A, volcano plot; and Figure S1B, principal component analysis (PCA)). We found that 454 differentially expressed genes (DEGs) were upregulated, and 526 were downregulated for more than 2-fold with both a *p*-value and false discovery rate (FDR) of less than 0.05 when comparing P42 with P15 passage FHL124 cells, respectively (Figure 2B). To evaluate the status of cell senescence at P42, we performed a differential expression analysis of genes that either induce (n = 133) or inhibit (n = 108) cell senescence according to the database of cell senescence genes from the human aging genomic resource (https://genomics.senescence.info, accessed on 12 October 2021). As shown in Figure S2A–E, most cell senescence induction and inhibition genes showed no significant changes in P42 compared with P15 FHL124 cells. For example, in the case of several key cell senescence-inducing genes, e.g., p53 (~1.10 up), p16 (cyclin-dependent kinase inhibitor 2A, CDKN2A, ~1.38 up), 53BP1 (tumor protein p53 binding protein 1, TP53BP1, ~1.18 dn), and laminB1 (LMNB1, ~1.14 dn), and several essential cell senescence inhibition genes, e.g., CDK1 (cyclin-dependent kinase 1, ~1.13 up), and MYC (MYC proto-oncogene, ~1.51 dn), their expressions were mildly up- or downregulated in P42 compared with P15 passage FHL124 cells. However, we did observe several cell senescence induction genes significantly downregulated in P42LECs compared with P15, such as CDKN1C (cell cycle inhibitor cyclin-dependent kinase inhibitor 1C, ~6.96 dn). In contrast, some cell senescence induction genes were significantly upregulated, such as p21 (cyclin-dependent kinase inhibitor 1A, CDKN1A, ~5.35 up). These results suggest that FHL124 cells at passage 42 have undergone age-induced transition but have yet to reach the senescence stage.

3.3. Aging Decelerates Proliferation in Lens Epithelial Cells

To better understand these differentially expressed genes during the cell aging process, we conducted a comprehensive pathway analysis using the MSigDB canonical pathway (gene set enrichment analysis, GSEA). As shown in Figure 2C, a 13-hallmark gene set with a nominal *p*-value below 0.05 and FDR q-value less than 5% was significantly enriched in the late passage (P42) FHL124 cells. These enriched pathways heavily pointed to a dysregulation of the immune response, such as inflammatory (n = 200), TNFα signaling via NFκB (n = 199), IFγ response (n = 198), and allograft rejection (n = 195). This was followed by cell stress response pathways, e.g., apoptosis (n = 160), xenobiotic metabolism (n = 196), the reactive oxygen species (ROS) pathway (n = 49), and oxidative phosphorylation (n = 200). In addition, upregulated KRAS signaling (n = 199) and the p53 pathway (n = 196) were significantly enriched in aged LECs. As shown in Figure 2D, a seven-hallmark gene set with a nominal *p*-value below 0.05 and a false discovery rate (FDR) q-value less than 15% was significantly enriched in the early passage (P15) FHL124 cells. These enriched pathways include upregulated cholesterol homeostasis (n = 73), unfolded protein response (UPR) (n = 107), epithelial–mesenchymal transition (EMT) (n = 196), hedgehog signaling (n = 36), hypoxia (n = 196), mTORC1 signaling (n = 196), and downregulated UV response (n = 142).

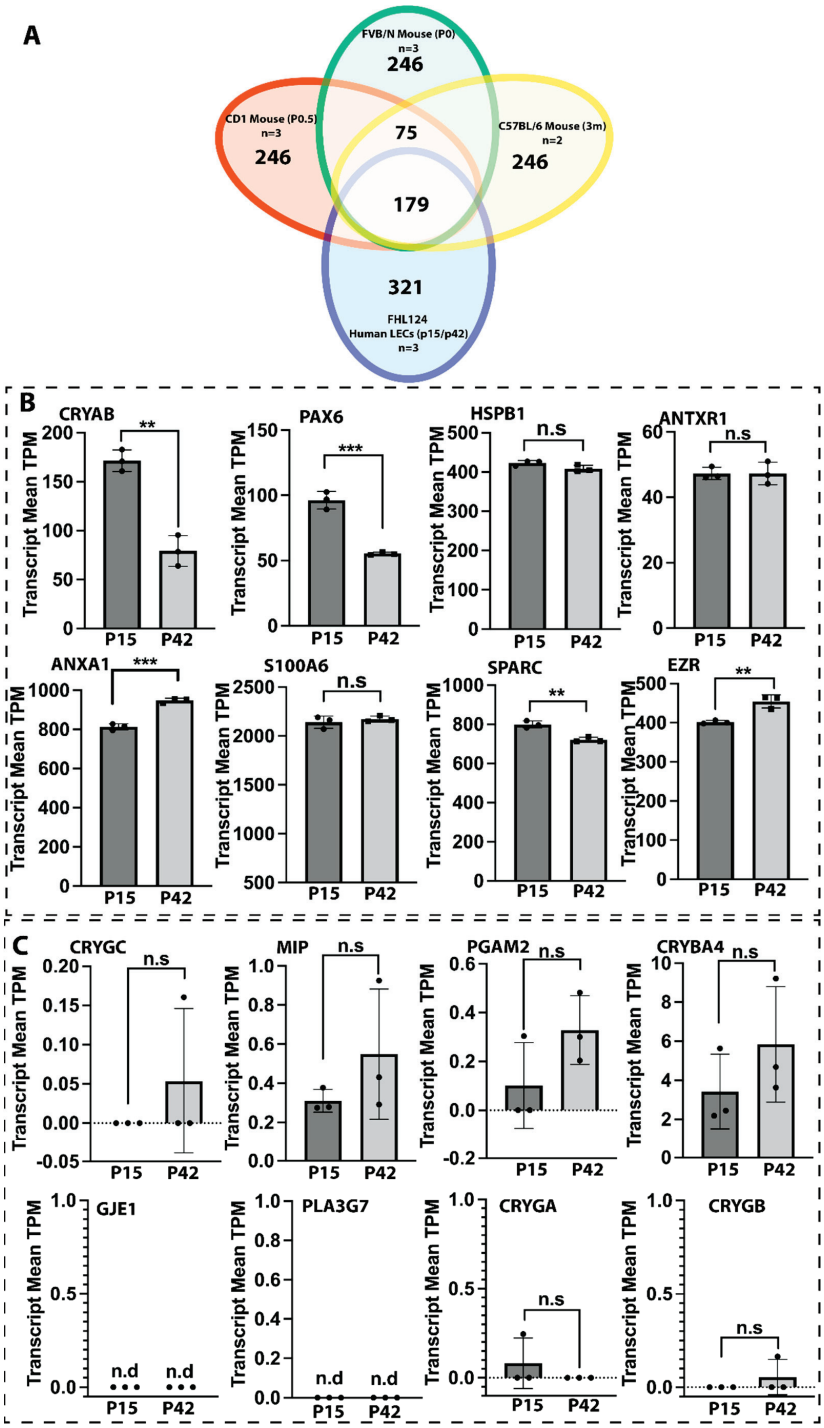

Figure 1. Normalized pro-LEC and pro-fiber cell gene expression in P15 and P42 FHL124 cells. (**A**) Shared and distinct top 500 most expressed genes between mouse lens epithelium and the human FHL124 LECs. (**B**) Pro-LEC gene transcript means count measured as transcript per million (TPM). (**C**) Pro-fiber gene transcript means count measured as transcript per million (TPM). Results are expressed as mean ± SD and were analyzed using Student's t-test. Only $p < 0.05$ is considered significant. * < 0.05, ** < 0.01, *** < 0.001, **** < 0.0001; n.s, not significant; n.d, not detectable.

These enriched pathways suggest that young LECs maintain vital cell survival and proliferative signaling, e.g., cholesterol homeostasis, hedgehog signaling, and mTORC1 signaling. At the same time, aged LECs adapt their cellular pathways to cope with elevated stress, e.g., ROS and apoptosis. To compare the cell proliferation rate between young

and aged FHL124 cells, we performed cell proliferation analysis by Cell Counting Kit-8 (CCK-8). As demonstrated in Figure 2E, the doubling time of passage 26 (P26) FHL124 cells was around two days, while the time for passage 48 (P48) FHL124 cells was around four days. These results indicate that aged lens epithelial cells significantly decelerate cell proliferation. Also, continued cell division with a doubling time of fewer than five days further confirmed that the late passage cells we used had not yet reached cell senescence.

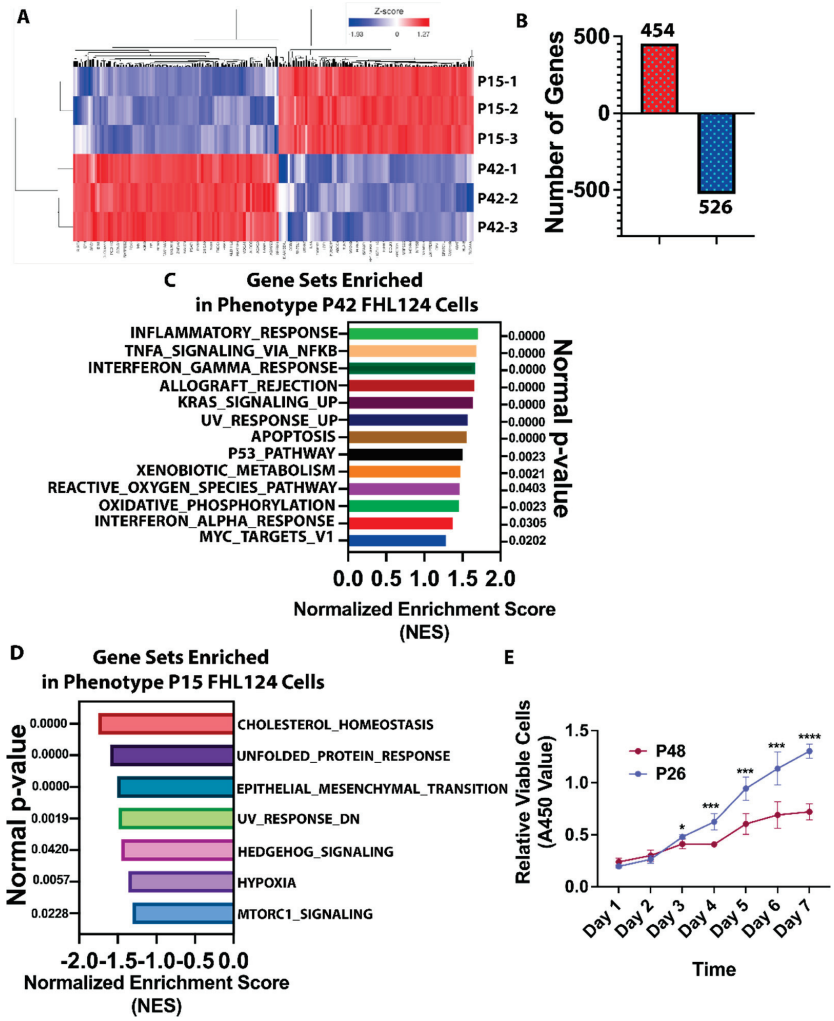

Figure 2. Aging alters LEC gene expression and decelerates LECs' proliferation. Passage 15 (n = 3) and passage 42 (n = 3) FHL124 cells were used for RNAseq, and normalized transcriptomes were comparatively analyzed between P42 and P15 cells. (**A**) RNAseq heatmap showing the top 1000 genes differentially expressed in passage 42 and passage 15 FHL124 cells. (**B**) When comparing P42 to P15, differential gene expression (DGE) analysis revealed that 454 genes were upregulated, and 526 genes were downregulated more than 2-fold with both *p*-value and false discovery rate (FDR) less than 0.05. (**C**) GSEA (gene set enrichment analysis) identified 13 top-ranked pathways enriched in P42 passage FHL124 cells with a nominal *p*-value less than 0.05 and FDR below 5%. The pathways were ranked by normalized enrichment score (NES). (**D**) GSEA using MSigDB canonical pathway identified 7 top-ranked pathways enriched in P15 passage FHL124 cells with a nominal *p*-value less than 0.05 and FDR below 15%. The pathways were ranked by normalized enrichment score (NES). (**E**) Seven-day cell proliferation curve of both P26 and P48 passage FHL124 cells was assayed by CCK8 (n = 8 at each data point). Results in E are expressed as mean ± SD and were analyzed using 2-way ANOVA with Holm–Šídák's multiple-comparisons test. Only $p < 0.05$ is considered significant. * < 0.05, ** < 0.01, *** < 0.001, **** < 0.0001.

3.4. Aged Lens Epithelial Cells Suppress Epithelial–Mesenchymal Transition (EMT)

Most surprisingly, epithelial-mesenchymal-transition (EMT) was significantly enriched in young FHL124 lens epithelial cells with a nominal *p*-value less than 0.0001 and a 3.7% FDR q-value (Figure 3A). To gain a full picture of this cellular process, we performed a differential analysis of the 334 top-ranking genes selected from pathway enrichment analysis [26,31], the pan-cancer web-based EMTome portal [32], and Ingenuity Pathway Analysis (IPA, Qiagen). These genes have been shown to positively affect or induce the EMT process. Intriguingly, aged LECs showed more than a 2-fold downregulation of 110 of these 334 genes (Figure 3B–G). P42 LECs saw mild downregulation (less than 2-fold) of 107 out of 334 genes compared with P15 (Figure 3B–G). Only 55 out of 334 genes were upregulated more than 2-fold in P42 LECs compared with P15, and 72 out of 334 genes were slightly upregulated (less than 2-fold) in P42 LECs relative to P15 (Figure 3B–G). These significantly downregulated genes included several transcription factors, such as ZFPM2 (12.75-fold dn), MAF (11.24-fold dn), LEF1(7.94-fold dn), MYB (9.50-fold dn), ELF3 (8.38-fold dn), IRF6 (5.66-fold dn), and SOX2 (3.43-fold dn). We saw that the expression of a large number of genes related to the extracellular matrix was significantly downregulated in aged LECs, including fibulin 1(FBLN1, 33.63-fold dn), biglycan (BGN, 11.70-fold dn), ADAM metallopeptidase domain 23 (ADAM23, 10.45-fold dn), extracellular matrix protein 2 (ECM2, 5.28-fold dn), type III collagen (COL3A1, 5.84-fold dn), type VIII collagen (COL8A2, 4.17-fold dn), and fibronectin (FN1, 4.64-fold dn). We also noticed that the expression of several cell adhesion molecules was significantly downregulated (more than 2-fold) in P42 LECs compared with P15, including several cadherin family genes, e.g., cadherin 11 (CDH11, 50.04-fold dn) and cadherin 6 (CDH6, 46.59-fold dn), and integrins, e.g., subunit alpha 4 (ITGA4, 10.23-fold dn) and subunit beta 5 (ITGB5, 2.12-fold dn). In addition to fibronectin and collagens, the EMT hallmark gene, alpha-smooth muscle actin (αSMA), was significantly downregulated (4-fold) in P42 passage FHL124 cells compared with P15 LECs. We also observed significant (albeit less than 2-fold) downregulation of vimentin (VIM, 1.77-fold dn, $p < 0.05$)) and tenascin C (TNC, 1.25-fold dn, $p < 0.05$). Overall, these results demonstrated that systemic EMT-promoting genes were significantly downregulated in aged LECs.

3.5. Lens Epithelial Cells Gradually Decrease αSMA and Fibronectin Expression in Aging

Inspired by the surprise findings above, we decided to titrate the protein expression of several EMT hallmark genes in increased cell passages of FHL124 lens epithelial cells. αSMA and fibronectin (FN1), two classic EMT markers, and ZO-1 (TJP1), a cell tight junction marker, were tested. Figure 4A shows the relative mRNA ratios between P42 and P15 FHL124 cells. Both αSMA and fibronectin were significantly downregulated, while ZO1 was only mildly downregulated. We continuously cultured FH124 cells from passage 17 (P17) to passage 48 (P48). As shown in Figure 4B, αSMA and fibronectin protein expression gradually decreased with increased cell passages, and a significant decline of αSMA and fibronectin expression was seen around passage 31 (P31) as contrasted with passage 17 (P17) (Figure 4C,D).

Since the ZO-1 antibody we obtained was only suitable for immunocytochemistry (ICC), we also performed immunofluorescence (IF) staining of FHL124 cells at their early, middle, and late passages. Figure 4E–H (αSMA), Figure 4I–L (fibronectin), and Figure 4M–P (ZO-1) depict IF and statistical data based on the relative fluorescence intensity of αSMA, fibronectin, and ZO-1, respectively. A profound decline of immunofluorescence intensity was seen in higher passage FHL124 cells for both αSMA and fibronectin staining. There was no remarkable difference in ZO-1 expression between early, middle, and late passage cells. These results strongly support the RNAseq results, which indicate that aged lens epithelial cells suppress the EMT process.

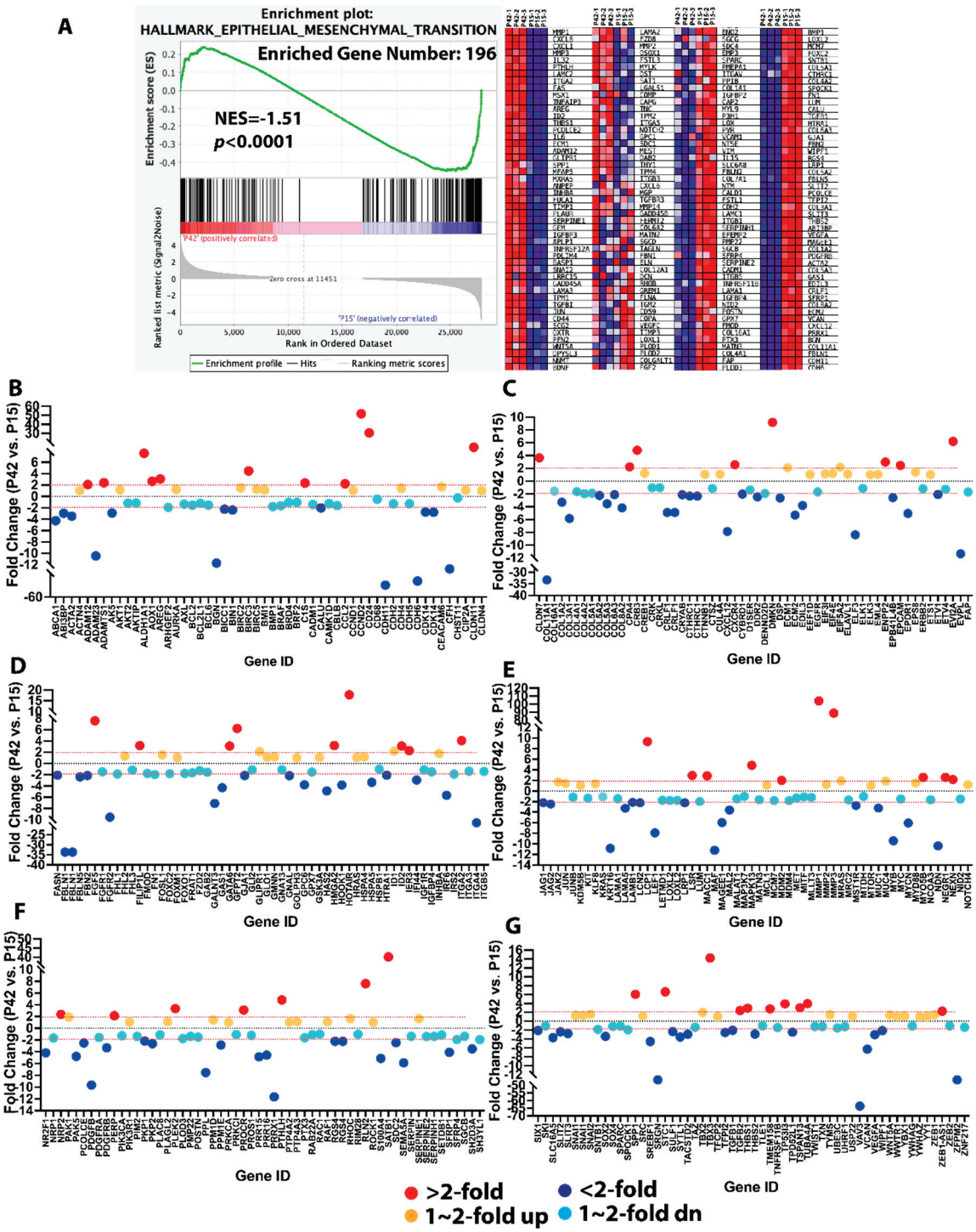

Figure 3. Aged LECs systematically downregulate EMT-promoting genes. (**A**) GSEA (gene set enrichment analysis) revealed that EMT is a major pathway enriched in P15 FHL124 cells with a nominal *p*-value < 0.0001, FDR = 0.037, and NES = −1.51. The left panel is the enrichment plot, and the right panel is the heatmap of 196 differentially expressed genes (DEGs) between P15 and P42 passage FHL124 cells enriched by GSEA. (**B**–**G**) DEGs analysis of 334 top-ranking EMT-promoting genes in P42 and P15 passage FHL124 cells. Gene expression is expressed as fold change between P42 and P15 passage FHL124 cells. Red dot: >2-fold upregulated; orange dot: >1 but <2-fold upregulated; dark blue dot: >2-fold downregulated; light blue dot: >1 but <2-fold downregulated.

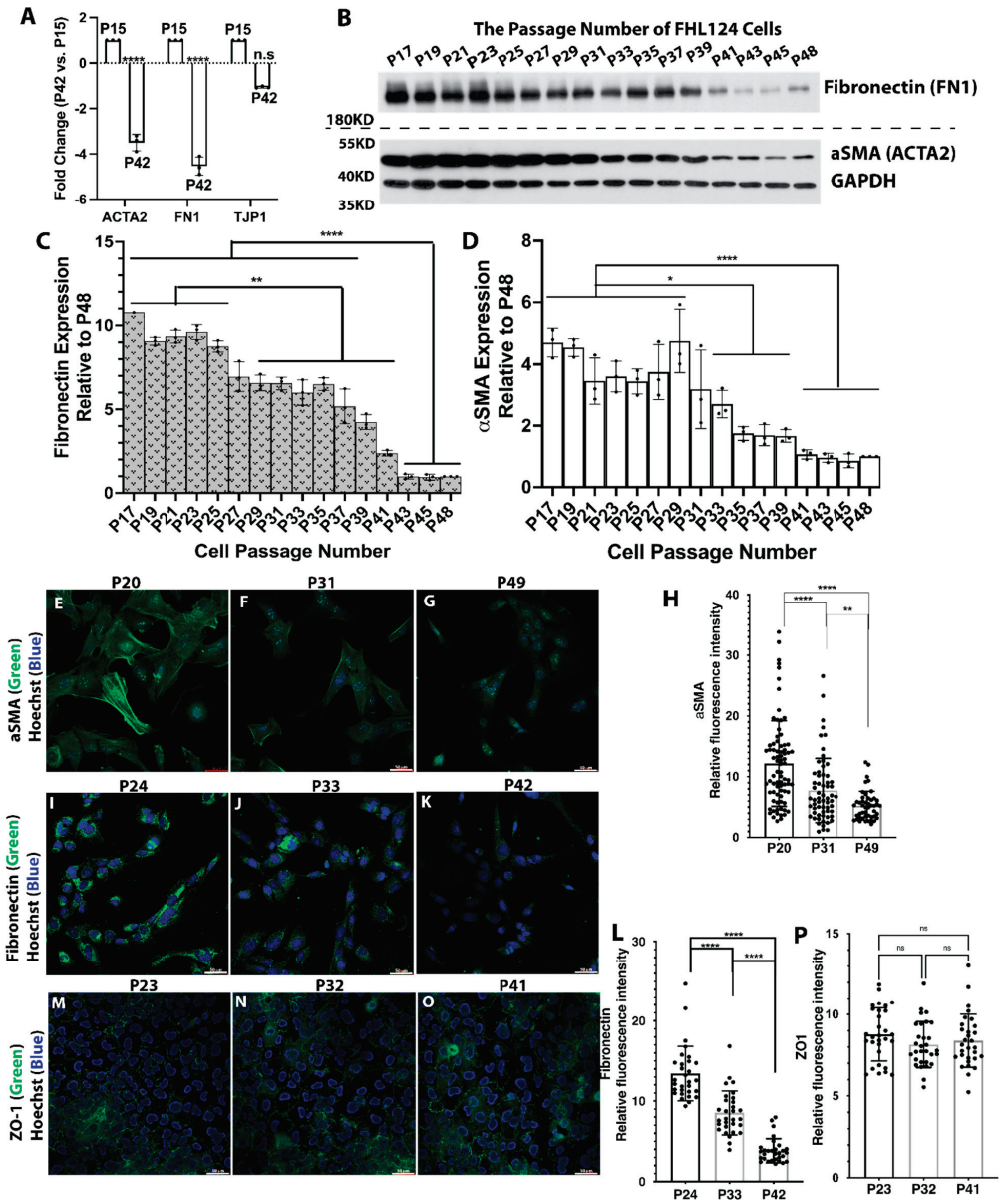

Figure 4. Fibronectin and αSMA protein expression gradually decreased in LECs aging. (**A**) Relative mRNA expression of fibronectin and αSMA between P42 and P15 passage FHL124 cells. Data are expressed as fold change relative to P15. (**B**) Fibronectin and αSMA protein levels from passage 17 to passage 48 FHL124 cells (n = 3). GAPDH serves as a loading control. (**C**) Semi-quantitative results of fibronectin expression from immunoblot (**B**) (n = 3). (**D**) Semi-quantitative results of αSMA expression from immunoblot (**B**) (n = 3). (**E**–**P**) immunofluorescence staining of fibronectin, αSMA, and ZO-1 protein expression in early, middle, and late passage LECs. (**E**–**G**) αSMA IF: αSMA (green), nuclei (blue) by Hoechst 33342. (**E**) Passage 20. (**F**) Passage 31. (**G**) Passage 49. (**I**–**K**) Fibronectin IF: fibronectin (green), nuclei (blue). (**I**) Passage 24. (**J**) Passage 33. (**K**) Passage 42. (**M**–**O**) ZO-1 IF: ZO-1 (green), nuclei (blue). (**M**) Passage 23. (**N**) Passage 32. (**O**) Passage 41. (**H**) Quantitative results of αSMA protein expression based on fluorescence intensity. Fluorescence intensity from 50 cells was measured. (**L**) Quantitative results of fibronectin protein expression based on fluorescence intensity. Fluorescence intensity from 50 cells was measured. (**P**) Quantitative results of ZO-1 protein expression based on fluorescence intensity. Fluorescence intensity from 50 cells was measured. Results are expressed as mean ± SD and were analyzed using one-way ANOVA with Tukey's multiple comparisons test. Only $p < 0.05$ is considered significant. * < 0.05, ** < 0.01, *** < 0.001, **** < 0.0001; n.s, not significant.

The most altered genes from early to late passage FHL124 cells were cadherin 11 (CDH11) followed by cadherin 6 (CDH6), with each downregulated around 50-fold and 45-fold in P42 LECs compared with P15, respectively. Figure S3A shows common cadherin genes, including E-cadherin (CDH1) and N-cadherin (CDH2). The former is an indicator of epithelial cell integrity, and the latter is an indicator of cell transformation, i.e., EMT. In addition to CDH11 and CDH6, we also found several cadherin family genes that were significantly downregulated, including cadherin 3, 8, 15, 18, and 26. However, when we compared the relative intracellular mRNA levels, extremely low mRNA levels of E-cadherin were seen in both early and late passage FHL124 cells. For reference, cell tight junction gene ZO-1 expression levels were around 280-fold compared to E-cadherin (Figure S3B). CDH8, 15, 18, and 26 were also barely detectable. N-cadherin was the most dominant cadherin gene expressed in FHL124 cells, followed by CDH11 and CDH6 (Figure S3B). Interestingly, there were no remarkable changes in N-cadherin mRNA levels between P42 and P15 FHL124 cells (Figure S3A).

We confirmed the above findings at the protein level by titrating N-cadherin and CDH11 with increased cell passages. As shown in Figure S3C,D with increased cell division from passage 17 to passage 48, no remarkable N-cadherin protein expression changes were seen across 31 cell passages. In contrast, a gradual decline of CDH11 expression was seen in FHL124 cells, and a profound reduction of CDH11 protein expression was observed after passage 33 (Figure S3C,D).

3.6. High Passage Lens Epithelial Cells Are Less Sensitive to TGFβ2-Mediated EMT

TGFβ is one of the most potent EMT inducers, and TGFβ-induced EMT is a well-recognized mechanism in the PCO initiation and progression [15,33]. To test young and aged LECs' response to TGF-mediated EMT signaling, we treated young (passage 14, P14) and aged (passage 45, P45) FHL124 cells with 10 ng/mL TGFβ2 for 24 h. As shown in Figure 5A–C, without TGFβ2 stimulation, the baseline expression of cadherin 11 (CDH11), αSMA, and fibronectin was significantly lower in passage 45 FHL124 cells compared with passage 14. There was a mild decrease in tenascin C (TNC) expression, and no noticeable expression changes were seen in N-cadherin (CDH2) when comparing P45 with P14 FHL124 cells. After 24 h TGFβ2 treatment, significantly increased tenascin C (TNC), cadherin 11 (CDH11), αSMA, fibronectin, and N-cadherin (CDH2) were seen in P14 FHL124 cells compared with non-treated P14 cells. Although we found that fibronectin and N-cadherin expression was significantly higher in TGFβ2 treated P45 cells compared with non-treated P45 cells, we did not see a remarkable increase of tenascin C and cadherin 11 expression in TGFβ2 treated P45 cells compared with non-treated P45 cells (Figure 5A–C). αSMA expression was only detectable after a long time of exposure in P45 FHL124 cells with and without TGFβ2 treatment (Figure 5A). Importantly, the levels of these EMT markers were markedly decreased in TGFβ2 treated P45 compared with TGFβ2 treated P14 FHL124 cells (Figure 5A–C). Overall, these results demonstrate that aged lens epithelial cells mitigate TGFβ2-induced EMT signaling.

3.7. Aged Mice Alleviate Lens Epithelial Cell EMT Signaling after Cataract Surgery

The substantial evidence above was based on the cellular aging model study, and an obvious question is whether this is also happening in the *in vivo* situation. To test this, we used the mouse cataract surgery model. We performed mouse cataract surgery on 2- and 20-month-old mice and determined the EMT signaling five days after surgery. Mice were immediately euthanized and processed after cataract surgery to serve as a control. As shown in Figure 6A,B (2 mos) and Figure 6E,F (20 mos) of the control group, a stronger αSMA staining signal was seen in 2-month-old mouse lens epithelium compared with 20- month-old mouse lens epithelium. Semi-quantitative data indicated that epithelium αSMA levels were significantly higher in 2-month-old mice than 20-month-old mice (Figure 6I). There was a drastic increase in αSMA in 2-month-old lens capsules five days after surgery. αSMA-positive cells were not only seen clustering around the anterior capsule

but also along with the posterior capsule (Figure 6C,D). We did observe αSMA-positive staining cells 5 days after cataract surgery in 20-month-old mice, but it was markedly lower than in two-month-old surgery mice (Figure 6G–I). Similar results were seen in fibronectin immunostaining. Baseline fibronectin was considerably higher in 2-month-old mouse epithelium than 20-month-old mouse epithelium (Figure 6J,K (2 mos) and Figure 6N,O (20 mos), Figure 6R), and cataract surgery substantially increased fibronectin expression in both 2-month-old and 20-month-old mice. However, levels of fibronectin in 2-month-old surgery mice were significantly higher than in 20-month-old surgery mice (Figure 6L,M (2 mos), Figure 6P,Q (20 mos), Figure 6R). Tenascin C was barely detectable in control lens epithelium from both 2- and 20-month-old mice, and a remarkable elevation of tenascin C expression was seen five days after cataract surgery (Figure S4). Significantly higher levels of tenascin C were seen in 2-month-old lens capsules than 20-month-old lens capsules (Figure S4). These results strongly suggest that aged lens epithelial cells suppress EMT signaling in *in vivo* conditions mimicking cataract surgical procedures.

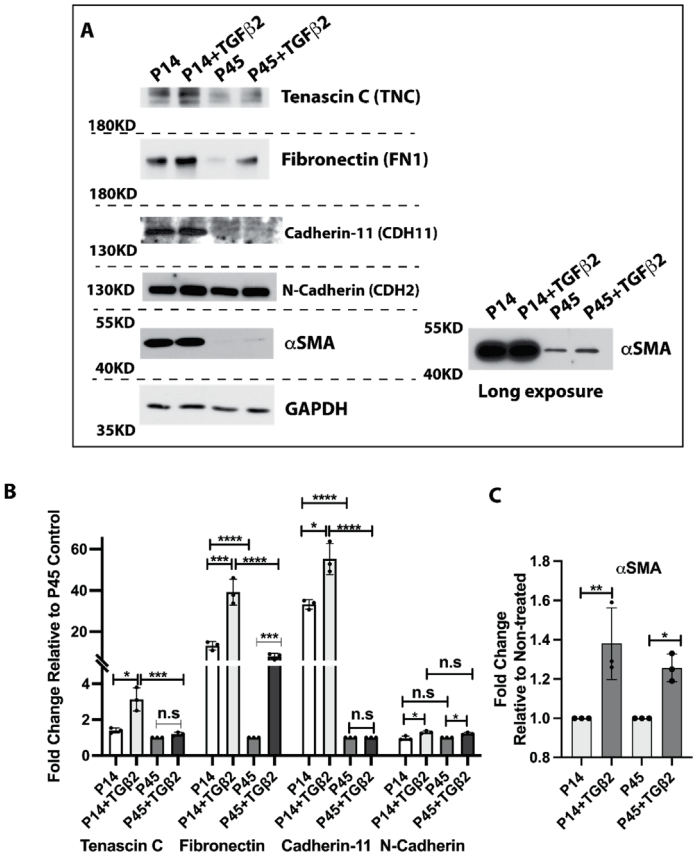

Figure 5. Aged LECs mitigate TGFβ2-mediated EMT. Passage 14 and 45 FHL124 cells were treated with 10 ng/mL TGFβ2 for 24 h. (**A**) Protein levels of fibronectin, cadherin 11, tenascin C, N-cadherin, and αSMA were determined by immunoblot assay of both P14 and P45 passage FHL124 cells with and without TGFβ2 treatment. A long exposure image of αSMA was included to measure αSMA expression in P45 passage cells. (**B**) Semi-quantitative results of tenascin C, fibronectin, cadherin 11, and N-cadherin protein expression. Data are expressed as fold change relative to P45 non-treated cells (control). (**C**) Semi-quantitative results of αSMA protein expression. Data are expressed as fold change relative to non-treated cells of the same passage. (**B**,**C**) Results are expressed as mean ± SD and were analyzed using one-way ANOVA with Tukey's multiple comparisons test. Only $p < 0.05$ is considered significant. * < 0.05, ** < 0.01, *** < 0.001, **** < 0.0001; n.s, not significant.

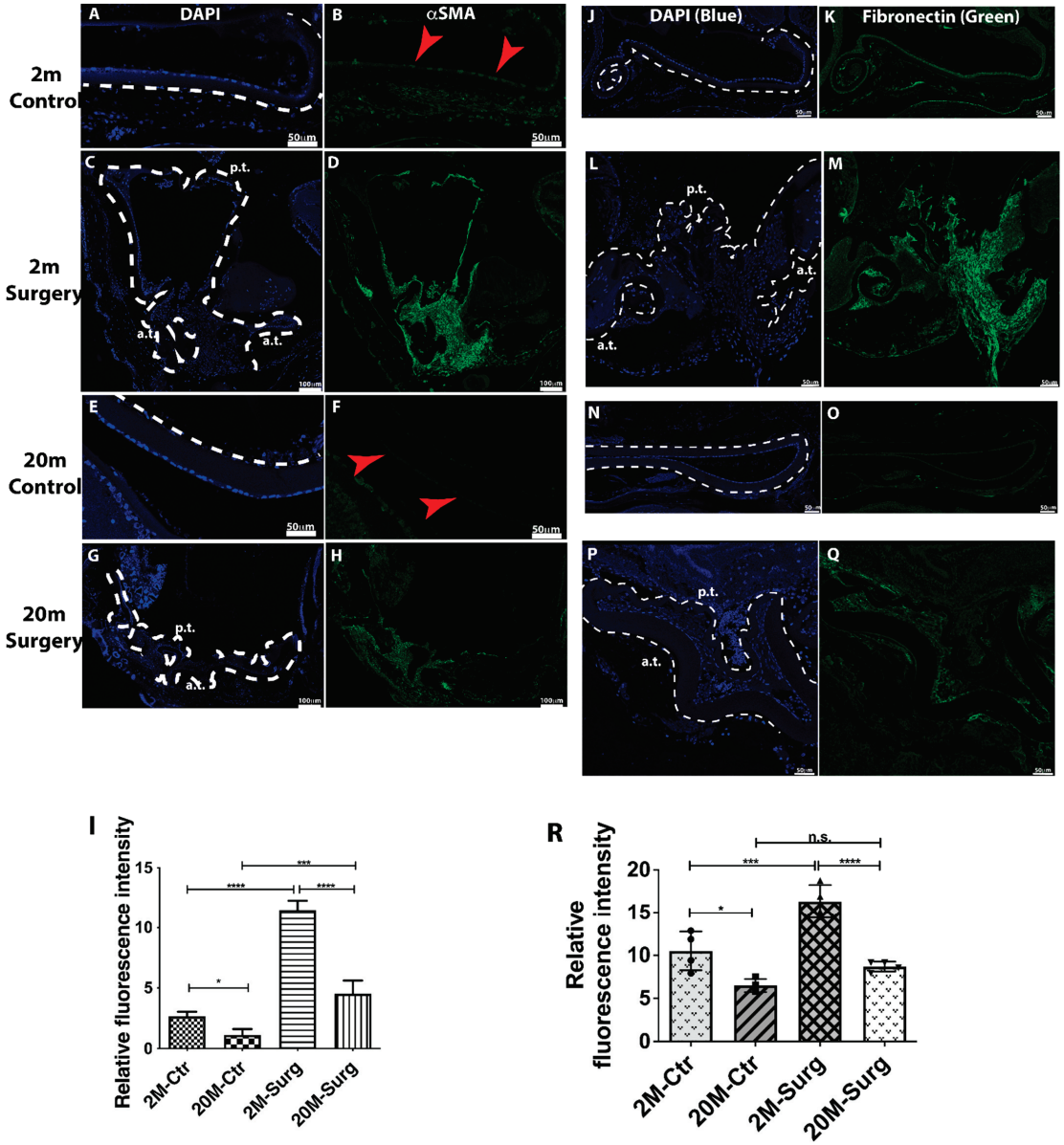

Figure 6. αSMA and fibronectin protein expression in 2- and 20-month-old mouse lens capsules after cataract surgery. (**A**,**C**,**E**,**G**) Cell nucleus staining by DAPI is shown in blue. (**B**,**D**,**F**,**H**) αSMA antibody staining is shown in green. (**A**) Two-month control, DAPI. (**B**) Two-month control, αSMA. (**C**) Two-month surgery, DAPI. (**D**) Two-month surgery, αSMA. (**E**) Twenty-month control, DAPI. (**F**) Twenty-month control, αSMA. (**G**) Twenty-month surgery, DAPI. (**H**) Twenty-month surgery, αSMA. (**I**) Quantitative results of αSMA protein expression based on fluorescence intensity (n = 4). (**J**,**L**,**N**,**P**) Cell nucleus stain by DAPI is shown in blue. (**K**,**M**,**O**,**Q**) Fibronectin antibody stain is shown in green. (**J**) Two-month control, DAPI. (**K**) Two-month control, fibronectin. (**L**) Two-month surgery, DAPI. (**M**) Two-month surgery, fibronectin. (N) Twenty-month control, DAPI. (**O**) Twenty- month control, fibronectin. (**P**) Twenty-month surgery, DAPI. (**Q**) Twenty-month surgery, fibronectin. (**R**) Quantitative results of fibronectin protein expression based on fluorescence intensity (n = 4). Results are expressed as mean ± SD and were analyzed using one-way ANOVA with Tukey's multiple comparisons test. Only $p < 0.05$ is considered significant. * < 0.05, ** < 0.01, *** < 0.001, **** < 0.0001; n.s., not significant.

4. Discussion

A profound difference in the PCO incidences between young and aged cataract surgery patients implies that there must be some fundamental differences between young and old

lens epithelial cells or the surrounding environment. Consequently, these differences provide an excellent point of entry to studying mechanisms of PCO formation. The present study focuses on the lens epithelial cells' age-related changes by conducting a comprehensive comparative transcriptomic analysis between young and aged LECs. We found that aged LECs not only decelerated rates of cell proliferation but also suppressed LEC EMT through systemically downregulating EMT-promoting genes. These findings were confirmed in the in vitro TGFβ2-mediated EMT signaling and the *in vivo* mouse cataract surgery model studies.

There was some debate regarding which aging model we should choose for this study, i.e., lens epithelium isolated from collected human lenses at young and old age versus an in vitro cellular aging model. We believed that LECs harvested from intact human lenses might not sufficiently reflect the actual cell growth conditions after cataract surgery. LECs within an entire lens are enclosed by the lens capsule, and the LECs' apical side faces lens fibers, a relatively sealed environment. On the contrary, the apical side of residual LECs on the lens capsule after cataract surgery faces a continuously circulating aqueous humor, a relatively open environment. After cataract surgery, LECs on the lens capsule from either young or aged patients will first adapt to an opened growth condition closer to the *in vitro* cell culture scenario. However, we did see very similar age-related gene expression changes between our cell culture model and the recent aging mouse epithelium transcriptome study [25], such as upregulated immune response and cellular stress responses. Collecting LECs from cataract surgery donors would be more problematic because donors' cataract surgeries were often done years ago, and LECs may already be situated in various PCO stages. FHL124 cells are spontaneously grown out of the lens epithelial cell line without any additional immortalization. It is an ideal cell suitable for a cellular aging model to study LEC aging. In fact, even several immortalized mouse lens epithelial cell lines were found to have high homology to the lens epithelium [34]. However, the in vitro cultured LECs may significantly alter some gene expressions compared with lens epithelium since the 5% FBS used in the culture medium is different from the physiological condition. One key example is that FHL124 cells have higher αSMA endogenous expression levels than human epithelium, but we expect their age-related behavior and adaptation would be similar. Importantly, we have demonstrated that the FHL124 cellular aging model closely resembles the *in vivo* situation [21]. Furthermore, in vitro cellular aging culture models are widely used and well-received in aging studies [35–37]. In the present study, conclusions drawn from the in vitro FHL124 cellular aging study agree with the *in vivo* mouse cataract surgery study.

The present study yielded well-anticipated results that aged LECs decelerate cell proliferation rates. Pathway and gene enrichment analysis indicate that either cell survival or cell proliferation promoting pathways are enriched in young LECs, such as the hedgehog signaling [38], the UPR pathway [39], and the MTORC1 signaling [40]. In contrast, cell apoptosis and cell stress response pathways, such as ROS and oxidative phosphorylation pathways [41], are enriched in aged LECs. For this study, we used FHL124 cells at least five passages ahead of the complete cell senescence [21], and this was primarily confirmed based on cell doubling times. However, although most senescent genes remained unchanged, we did observe some cell senescent genes that were up- or downregulated to promote cell senescence. These changes suggest that aged LECs at passage 42 or so are in the transition stage of acquiring a senescence-like phenotype. In fact, deregulation in immune response, upregulated cytokines, and immune modulators in aged LECs likely result from senescence-associated secretory phenotype (SASP), a well-known cell senescence phenotype [42]. Declined cell proliferation in the lens epithelium is also supported by work from both human and rodent studies. Li et al. [43] found that the proliferative capacity of LECs in old mice was decreased significantly compared with LECs from young mice. Using the human capsular bag culture model, Wormstone et al. [19] found much higher LEC proliferation rates on lens capsules from donors aged <40 years compared with >60 years. In a follow-up study, Dawes et al. [44] demonstrated that the intracellular signaling might

be responsible for high cell proliferation in the young lens capsule rather than secreted cytokines in the medium. Our present study supports the notion that systemic regulatory pathways in young and aged LECs determine the rates of cell division. However, the impact of cytokines from the medium and cell growth environment in LEC transformation, i.e., EMT, remains to be clarified.

The present study also yielded a surprise finding that aged LECs systemically downregulated signaling pathways to suppress EMT. An EMT suppressive behavior in aged LECs is contrary to epithelial or endothelial cells from many tissues that have been shown to acquire EMT characteristics during aging, which adversely cause organ fibrosis via altering epithelial or endothelial cell phenotypic properties and depositing extracellular matrix (ECM). This includes kidney, cardiac, and idiopathic pulmonary fibrosis [45–49]. We found that hundreds of EMT-promoting genes, including several key EMT markers, such as fibronectin and αSMA, were significantly downregulated. Importantly, we demonstrated that FHL124 cells mitigate TGFβ2-mediated EMT signaling at their higher passages. Furthermore, we have explicitly confirmed our in vitro findings through *in vivo* mouse cataract surgery studies. Several EMT hallmark genes, including fibronectin, αSMA, and tenascin C, are markedly increased in mouse lens capsules at 2 months compared with 20 months after cataract surgery. In addition, substantially decreased baseline fibronectin and αSMA expression from 2-month-old to 20-month-old mouse lens epithelium agrees with our in vitro cellular aging model study. We also had another surprise finding that a well-known cell adhesion molecule, E-cadherin (CDH1), is barely expressed in FHL124 cells from RNAseq. We could not detect E-cadherin protein with a widely used commercial antibody. N-cadherin (CDH2), on the other hand, is abundantly expressed in FHL124 cells but does not alter with age and has only a mild TGFβ2-mediated response. Interestingly, cadherin 11 (CDH11), an emerging gene marker and a top-ranked EMT gene [32,50–52], is moderately expressed in young FHL124 cells and demonstrates an age-related decline in FHL124 cells. Along with the positive TGFβ2-mediated response, we believe CDH11 may be used as a sensitive EMT marker for LECs. Unfortunately, several commercially available CDH11 antibodies we tested in this study only work for the Western blot, and antibodies capable of immunohistology are urgently needed.

The present study suggests that not only do rapid proliferative LECs at a young age lead to increased PCO incidence, but pro-EMT characteristics of young LECs may also inevitably accelerate PCO progression. Conversely, slow LEC division and systematic EMT suppression in aged lenses collaboratively slow PCO initiation and progression. Downregulation of a wide scale of pro-EMT genes, from young to aged LECs, also implies a significant challenge in preventing PCO development, especially in infant and children cataract patients. This is most likely because complex and multifactorial pathways are involved in the pathogenesis of PCO formation. Future studies are needed to dissect these pathways and multi-pathway crosstalk, which will significantly increase the identification of therapeutic targets. For that purpose, we believe the database established in the present study may serve as a valuable resource. However, we are aware that this study focuses solely on the LECs' gene expression shift during aging. The microenvironment after cataract surgery and its impact on PCO initiation and progression remain to be elucidated.

Taken all together, our present study implicates that the discrepancy of rates of PCO incidence between young and aged cataract surgery patients results at least from both cellular proliferation capacity and pro-EMT characteristics. Unravelling these players will help us gain a significant insight that can assist in identifying therapeutic targets.

Supplementary Materials: The following supporting information can be downloaded at: https://www.mdpi.com/article/10.3390/cells11132001/s1, Table S1. Common and distinct genes in human FHL124 LECs vs. three mouse lens epithelium in their top 500 most expressed genes; Figure S1. RNAseq data analysis summary. (A) volcano plot comparing P42 to Pl 5 FHL 124 cells. (B) Principal component analysis (PCA); Figure S2. DEGs analysis of cell senescence genes. Figure S3. Cadherin 11 (CDH11) is an EMT marker for LECs. (A) RNAseq data of cell adhesion cadherin family molecules. Data are expressed as fold change of P42 vs. Pl 5 passage FHL 124 cells. Dark blue dot:

>2-fold downregulated; light blue dot: >1 but <2-fold downregulated; orange dot: >1 but <2-fold upregulated. (B) The relative mRNA levels of selected cadherin genes are measured by normalized mean count of transcripts per million (TPM). ZO-1 (TJP1) serves as a reference cell junction gene. (C) N-cadherin and CDH11 protein expression determined by immunoblot. GAPDH serves as a loading control. (D) Semi-quantitative results of N-cadherin and CDH11 protein levels in FHL 124 cells at various passages. Results are expressed as mean ± SD and were analyzed using one-way ANOVA with Tu key's multiple comparisons test. Only $p < 0.05$ is considered significant. * $p < 0.05$, ** $p < 0.01$, *** $p < 0.001$, **** $p < 0.0001$, n.s, not significant; Figure S4. Tenascin C protein expression in 2- and 20-months old mouse lens capsules after cataract surgery. (A,C,E,G) cell nucleus staining by DAPI is shown in blue. (B,D,F,H) Tenascin C antibody staining is shown in green. (A) 2 months control, DAPI.(B) 2 months control, Tenascin C. (C) 2 months surgery, DAPI. (D) 2 months surgery, Tenascin C. (E) 20 months control, DAPI. (F) 20 months control, Tenascin C. (G) 20 months surgery, DAPI. (H) 20 months surgery, Tenascin C. (I) Quantitative results of Tenascin C protein expression based on fluorescence intensity (n = 4). Results are expressed as mean± SD and were analyzed using one-way ANOVA with Tu key's multiple comparisons test. Only $p < 0.05$ is considered signi cant. * $p < 0.05$, ** $p < 0.01$, *** $p < 0.001$, **** $p < 0.0001$, ns. not significant.

Author Contributions: Conceptualization, X.F.; methodology, Z.W., P.G., C.H., J.H., X.Z. and X.F.; software, E.F., X.Z. and X.F.; validation, Z.W., P.G., C.H. and X.F.; formal analysis, Z.W., P.G., C.H., H.Y. and X.F.; investigation, Z.W., P.G., C.H., J.H. and E.F.; resources, H.Y.; data curation, Z.W., P.G., C.H., J.H., X.Z. and X.F.; writing—original draft preparation, X.F.; writing—review and editing, Z.W., P.G. and E.F.; visualization, E.F. and X.F.; supervision, X.F.; project administration, X.F.; funding acquisition, X.F. All authors have read and agreed to the published version of the manuscript.

Funding: This research was funded by the National Eye Institute, grant EY028158(XF), the James Fickel Alzheimer's Disease Research Fund (XF), and the National Eye Institute, Center Core Grant for Vision Research (P30EY031631) at Augusta University.

Institutional Review Board Statement: The study was conducted in accordance with the Declaration of Helsinki and approved by the Institutional Review Board of Augusta University (protocol code 2018-0980 and date of 23 September 2021).

Informed Consent Statement: Not applicable.

Data Availability Statement: RNAseq data are deposited in the Gene Expression Omnibus (GEO) database under accession number GSE184422. The authors will provide a detailed description of methods and original data upon request.

Acknowledgments: We are very grateful to Michael Wormstone at the University of East Anglia, UK, for providing the mouse lens epithelial cell line. We are very grateful to Rachel Cui at Augusta University Cell Imaging Core for helping in microscopy image collections.

Conflicts of Interest: The authors declare no conflict of interest.

References

1. Foster, A.; Gilbert, C.; Rahi, J. Epidemiology of cataract in childhood: A global perspective. *J. Cataract. Refract. Surg.* **1997**, *23* (Suppl. S1), 601–604. [CrossRef]
2. Vella, M.; Wickremasinghe, S.; Gupta, N.; Andreou, P.; Sinha, A. YAG laser capsulotomy, an unusual complication. *Eye* **2004**, *18*, 193. [CrossRef] [PubMed]
3. Basti, S.; Ravishankar, U.; Gupta, S. Results of a prospective evaluation of three methods of management of pediatric cataracts. *Ophthalmology* **1996**, *103*, 713–720. [CrossRef]
4. Knight-Nanan, D.; O'Keefe, M.; Bowell, R. Outcome and complications of intraocular lenses in children with cataract. *J. Cataract. Refract. Surg.* **1996**, *22*, 730–736. [CrossRef]
5. Koch, D.D.; Kohnen, T. Retrospective comparison of techniques to prevent secondary cataract formation after posterior chamber intraocular lens implantation in infants and children. *J. Cataract. Refract. Surg.* **1997**, *23* (Suppl. S1), 657–663. [CrossRef]
6. Vasavada, A.; Chauhan, H. Intraocular lens implantation in infants with congenital cataracts. *J. Cataract. Refract. Surg.* **1994**, *20*, 592–598. [CrossRef]
7. O'Keefe, M.; Fenton, S.; Lanigan, B. Visual outcomes and complications of posterior chamber intraocular lens implantation in the first year of life. *J. Cataract. Refract. Surg.* **2001**, *27*, 2006–2011. [CrossRef]
8. Vasavada, A.R.; Praveen, M.R.; Tassignon, M.J.; Shah, S.K.; Vasavada, V.A.; Vasavada, V.A.; Van Looveren, J.; De Veuster, I.; Trivedi, R.H. Posterior capsule management in congenital cataract surgery. *J. Cataract. Refract. Surg.* **2011**, *37*, 173–193. [CrossRef]

9. Ursell, P.G.; Dhariwal, M.; Majirska, K.; Ender, F.; Kalson-Ray, S.; Venerus, A.; Miglio, C.; Bouchet, C. Three-year incidence of Nd:YAG capsulotomy and posterior capsule opacification and its relationship to monofocal acrylic IOL biomaterial: A UK Real World Evidence study. *Eye* **2018**, *32*, 1579–1589. [CrossRef]
10. Ursell, P.G.; Dhariwal, M.; O'Boyle, D.; Khan, J.; Venerus, A. 5 year incidence of YAG capsulotomy and PCO after cataract surgery with single-piece monofocal intraocular lenses: A real-world evidence study of 20,763 eyes. *Eye* **2020**, *34*, 960–968. [CrossRef]
11. Lindholm, J.M.; Laine, I.; Tuuminen, R. Five-Year Cumulative Incidence and Risk Factors of Nd:YAG Capsulotomy in 10 044 Hydrophobic Acrylic 1-Piece and 3-Piece Intraocular Lenses. *Am. J. Ophthalmol.* **2019**, *200*, 218–223. [CrossRef] [PubMed]
12. Wormstone, I.M. Posterior capsule opacification: A cell biological perspective. *Exp. Eye Res.* **2002**, *74*, 337–347. [CrossRef] [PubMed]
13. Wormstone, I.M.; Wormstone, Y.M.; Smith, A.J.O.; Eldred, J.A. Posterior capsule opacification: What's in the bag? *Prog. Retin. Eye Res.* **2021**, *82*, 100905. [CrossRef]
14. Walker, J.L.; Wolff, I.M.; Zhang, L.; Menko, A.S. Activation of SRC kinases signals induction of posterior capsule opacification. *Investig. Ophthalmol. Vis. Sci.* **2007**, *48*, 2214–2223. [CrossRef]
15. Taiyab, A.; Holms, J.; West-Mays, J.A. beta-Catenin/Smad3 Interaction Regulates Transforming Growth Factor-beta-Induced Epithelial to Mesenchymal Transition in the Lens. *Int. J. Mol. Sci.* **2019**, *20*, 78. [CrossRef] [PubMed]
16. Shu, D.Y.; Lovicu, F.J. Enhanced EGF receptor-signaling potentiates TGFbeta-induced lens epithelial-mesenchymal transition. *Exp. Eye Res.* **2019**, *185*, 107693. [CrossRef] [PubMed]
17. Shihan, M.H.; Kanwar, M.; Wang, Y.; Jackson, E.E.; Faranda, A.P.; Duncan, M.K. Fibronectin has multifunctional roles in posterior capsular opacification (PCO). *Matrix Biol.* **2020**, *90*, 79–108. [CrossRef]
18. Tomasetti, C.; Poling, J.; Roberts, N.J.; London, N.R., Jr.; Pittman, M.E.; Haffner, M.C.; Rizzo, A.; Baras, A.; Karim, B.; Kim, A.; et al. Cell division rates decrease with age, providing a potential explanation for the age-dependent deceleration in cancer incidence. *Proc. Natl. Acad. Sci. USA* **2019**, *116*, 20482–20488. [CrossRef]
19. Wormstone, I.M.; Liu, C.S.; Rakic, J.M.; Marcantonio, J.M.; Vrensen, G.F.; Duncan, G. Human lens epithelial cell proliferation in a protein-free medium. *Investig. Ophthalmol. Vis. Sci.* **1997**, *38*, 396–404.
20. Reddan, J.R.; Lindemann, C.B.; Hitt, A.L.; Bagchi, M.; Raphtis, E.M.; Pena, J.T.; Dziedzic, D.C. Generation of two non-transfected human lens cell lines. *Investig. Ophthalmol. Vis. Sci.* **1999**, *40*, S970.
21. Wei, Z.; Hao, C.; Huangfu, J.; Srinivasagan, R.; Zhang, X.; Fan, X. Aging lens epithelium is susceptible to ferroptosis. *Free Radic. Biol. Med.* **2021**, *167*, 94–108. [CrossRef] [PubMed]
22. Whitson, J.A.; Zhang, X.; Medvedovic, M.; Chen, J.; Wei, Z.; Monnier, V.M.; Fan, X. Transcriptome of the GSH-Depleted Lens Reveals Changes in Detoxification and EMT Signaling Genes, Transport Systems, and Lipid Homeostasis. *Investig. Ophthalmol. Vis. Sci.* **2017**, *58*, 2666–2684. [CrossRef]
23. Hoang, T.V.; Kumar, P.K.; Sutharzan, S.; Tsonis, P.A.; Liang, C.; Robinson, M.L. Comparative transcriptome analysis of epithelial and fiber cells in newborn mouse lenses with RNA sequencing. *Mol. Vis.* **2014**, *20*, 1491–1517. [PubMed]
24. Zhao, Y.; Zheng, D.; Cvekl, A. A comprehensive spatial-temporal transcriptomic analysis of differentiating nascent mouse lens epithelial and fiber cells. *Exp. Eye Res.* **2018**, *175*, 56–72. [CrossRef] [PubMed]
25. Faranda, A.P.; Shihan, M.H.; Wang, Y.; Duncan, M.K. The aging mouse lens transcriptome. *Exp. Eye Res.* **2021**, *209*, 108663. [CrossRef] [PubMed]
26. Subramanian, A.; Tamayo, P.; Mootha, V.K.; Mukherjee, S.; Ebert, B.L.; Gillette, M.A.; Paulovich, A.; Pomeroy, S.L.; Golub, T.R.; Lander, E.S.; et al. Gene set enrichment analysis: A knowledge-based approach for interpreting genome-wide expression profiles. *Proc. Natl. Acad. Sci. USA* **2005**, *102*, 15545–15550. [CrossRef] [PubMed]
27. Wei, Z.; Caty, J.; Whitson, J.; Zhang, A.D.; Srinivasagan, R.; Kavanagh, T.J.; Yan, H.; Fan, X. Reduced Glutathione Level Promotes Epithelial-Mesenchymal Transition in Lens Epithelial Cells via a Wnt/beta-Catenin-Mediated Pathway: Relevance for Cataract Therapy. *Am. J. Pathol.* **2017**, *187*, 2399–2412. [CrossRef]
28. Eldred, J.A.; Hodgkinson, L.M.; Dawes, L.J.; Reddan, J.R.; Edwards, D.R.; Wormstone, I.M. MMP2 activity is critical for TGFbeta2-induced matrix contraction–implications for fibrosis. *Investig. Ophthalmol. Vis. Sci.* **2012**, *53*, 4085–4098. [CrossRef]
29. Wormstone, I.M.; Tamiya, S.; Eldred, J.A.; Lazaridis, K.; Chantry, A.; Reddan, J.R.; Anderson, I.; Duncan, G. Characterisation of TGF-beta2 signalling and function in a human lens cell line. *Exp. Eye Res.* **2004**, *78*, 705–714. [CrossRef]
30. Lachke, S.A.; Ho, J.W.; Kryukov, G.V.; O'Connell, D.J.; Aboukhalil, A.; Bulyk, M.L.; Park, P.J.; Maas, R.L. iSyTE: Integrated Systems Tool for Eye gene discovery. *Investig. Ophthalmol. Vis. Sci.* **2012**, *53*, 1617–1627. [CrossRef]
31. Mootha, V.K.; Lindgren, C.M.; Eriksson, K.F.; Subramanian, A.; Sihag, S.; Lehar, J.; Puigserver, P.; Carlsson, E.; Ridderstrale, M.; Laurila, E.; et al. PGC-1alpha-responsive genes involved in oxidative phosphorylation are coordinately downregulated in human diabetes. *Nat. Genet.* **2003**, *34*, 267–273. [CrossRef] [PubMed]
32. Vasaikar, S.V.; Deshmukh, A.P.; den Hollander, P.; Addanki, S.; Kuburich, N.A.; Kudaravalli, S.; Joseph, R.; Chang, J.T.; Soundararajan, R.; Mani, S.A. EMTome: A resource for pan-cancer analysis of epithelial-mesenchymal transition genes and signatures. *Br. J. Cancer* **2021**, *124*, 259–269. [CrossRef] [PubMed]
33. Das, S.J.; Wishart, T.F.L.; Jandeleit-Dahm, K.; Lovicu, F.J. Nox4-mediated ROS production is involved, but not essential for TGFbeta-induced lens EMT leading to cataract. *Exp. Eye Res.* **2020**, *192*, 107918. [CrossRef]

34. Terrell, A.M.; Anand, D.; Smith, S.F.; Dang, C.A.; Waters, S.M.; Pathania, M.; Beebe, D.C.; Lachke, S.A. Molecular characterization of mouse lens epithelial cell lines and their suitability to study RNA granules and cataract associated genes. *Exp. Eye Res.* **2015**, *131*, 42–55. [CrossRef]
35. Bigagli, E.; Luceri, C.; Scartabelli, T.; Dolara, P.; Casamenti, F.; Pellegrini-Giampietro, D.E.; Giovannelli, L. Long-term Neuroglial Cocultures as a Brain Aging Model: Hallmarks of Senescence, MicroRNA Expression Profiles, and Comparison with In Vivo Models. *J. Gerontol. A Biol. Sci. Med. Sci.* **2016**, *71*, 50–60. [CrossRef]
36. Campisi, J. From cells to organisms: Can we learn about aging from cells in culture? *Exp. Gerontol.* **2001**, *36*, 607–618. [CrossRef]
37. Marko Bunc, S.M.H.; Jose, M.P.; Julijana, K.; Orlu, M. Characterisation of an In Vitro Aged Cell Culture Model. *Farmacia* **2019**, *67*, 240–247. [CrossRef]
38. Hsu, Y.C.; Li, L.; Fuchs, E. Transit-amplifying cells orchestrate stem cell activity and tissue regeneration. *Cell* **2014**, *157*, 935–949. [CrossRef]
39. Hetz, C. The unfolded protein response: Controlling cell fate decisions under ER stress and beyond. *Nat. Rev. Mol. Cell Biol.* **2012**, *13*, 89–102. [CrossRef]
40. Saxton, R.A.; Sabatini, D.M. mTOR Signaling in Growth, Metabolism, and Disease. *Cell* **2017**, *168*, 960–976. [CrossRef]
41. Liguori, I.; Russo, G.; Curcio, F.; Bulli, G.; Aran, L.; Della-Morte, D.; Gargiulo, G.; Testa, G.; Cacciatore, F.; Bonaduce, D.; et al. Oxidative stress, aging, and diseases. *Clin. Interv. Aging* **2018**, *13*, 757–772. [CrossRef] [PubMed]
42. Childs, B.G.; Gluscevic, M.; Baker, D.J.; Laberge, R.M.; Marquess, D.; Dananberg, J.; van Deursen, J.M. Senescent cells: An emerging target for diseases of ageing. *Nat. Rev. Drug Discov.* **2017**, *16*, 718–735. [CrossRef] [PubMed]
43. Li, Y.; Yan, Q.; Wolf, N.S. Long-term caloric restriction delays age-related decline in proliferation capacity of murine lens epithelial cells in vitro and in vivo. *Investig. Ophthalmol. Vis. Sci.* **1997**, *38*, 100–107.
44. Dawes, L.J.; Duncan, G.; Wormstone, I.M. Age-related differences in signaling efficiency of human lens cells underpin differential wound healing response rates following cataract surgery. *Investig. Ophthalmol. Vis. Sci.* **2013**, *54*, 333–342. [CrossRef]
45. Imran, S.A.M.; Yazid, M.D.; Idrus, R.B.H.; Maarof, M.; Nordin, A.; Razali, R.A.; Lokanathan, Y. Is There an Interconnection between Epithelial-Mesenchymal Transition (EMT) and Telomere Shortening in Aging? *Int. J. Mol. Sci.* **2021**, *22*, 3888. [CrossRef]
46. Santos, F.; Moreira, C.; Nobrega-Pereira, S.; Bernardes de Jesus, B. New Insights into the Role of Epithelial(-)Mesenchymal Transition during Aging. *Int. J. Mol. Sci.* **2019**, *20*, 891. [CrossRef]
47. Liu, Y. New insights into epithelial-mesenchymal transition in kidney fibrosis. *J. Am. Soc. Nephrol.* **2010**, *21*, 212–222. [CrossRef]
48. Olive, M.; Harten, I.; Mitchell, R.; Beers, J.K.; Djabali, K.; Cao, K.; Erdos, M.R.; Blair, C.; Funke, B.; Smoot, L.; et al. Cardiovascular pathology in Hutchinson-Gilford progeria: Correlation with the vascular pathology of aging. *Arter. Thromb. Vasc. Biol.* **2010**, *30*, 2301–2309. [CrossRef]
49. Chilosi, M.; Poletti, V.; Zamo, A.; Lestani, M.; Montagna, L.; Piccoli, P.; Pedron, S.; Bertaso, M.; Scarpa, A.; Murer, B.; et al. Aberrant Wnt/beta-catenin pathway activation in idiopathic pulmonary fibrosis. *Am. J. Pathol.* **2003**, *162*, 1495–1502. [CrossRef]
50. Chen, X.; Xiang, H.; Yu, S.; Lu, Y.; Wu, T. Research progress in the role and mechanism of Cadherin-11 in different diseases. *J. Cancer* **2021**, *12*, 1190–1199. [CrossRef]
51. Kaur, H.; Phillips-Mason, P.J.; Burden-Gulley, S.M.; Kerstetter-Fogle, A.E.; Basilion, J.P.; Sloan, A.E.; Brady-Kalnay, S.M. Cadherin-11, a marker of the mesenchymal phenotype, regulates glioblastoma cell migration and survival in vivo. *Mol. Cancer Res.* **2012**, *10*, 293–304. [CrossRef] [PubMed]
52. Tsang, E.S.; Topham, J.T.; Karasinska, J.M.; Lee, M.K.C.; Williamson, L.M.; Mendis, S.; Denroche, R.E.; Jang, G.H.; Kalloger, S.E.; Moore, R.A.; et al. Delving into Early-onset Pancreatic Ductal Adenocarcinoma: How Does Age Fit In? *Clin. Cancer Res.* **2021**, *27*, 246–254. [CrossRef] [PubMed]

cells

MDPI

Article

Double Deletion of PI3K and PTEN Modifies Lens Postnatal Growth and Homeostasis

Caterina Sellitto, Leping Li and Thomas W. White *

Department of Physiology & Biophysics, Stony Brook University School of Medicine, Stony Brook, NY 11794, USA

* Correspondence: thomas.white@stonybrook.edu; Tel.: +1-631-444-9683

Abstract: We have previously shown that the conditional deletion of either the p110α catalytic subunit of phosphatidylinositol 3-kinase (PI3K), or its opposing phosphatase, phosphatase and tensin homolog (PTEN), had distinct effects on lens growth and homeostasis. The deletion of p110α reduced the levels of phosphorylated Akt and equatorial epithelial cell proliferation, and resulted in smaller transparent lenses in adult mice. The deletion of PTEN increased levels of phosphorylated Akt, altered lens sodium transport, and caused lens rupture and cataract. Here, we have generated conditional p110α/PTEN double-knockout mice, and evaluated epithelial cell proliferation and lens homeostasis. The double deletion of p110α and PTEN rescued the defect in lens size seen after the single knockout of p110α, but accelerated the lens rupture phenotype seen in PTEN single-knockout mice. Levels of phosphorylated Akt in double-knockout lenses were significantly higher than in wild-type lenses, but not as elevated as those reported for PTEN single-knockout lenses. These results showed that the double deletion of the p110α catalytic subunit of PI3K and its opposing phosphatase, PTEN, exacerbated the rupture defect seen in the single PTEN knockout and alleviated the growth defect observed in the single p110α knockout. Thus, the integrity of the PI3K signaling pathway was absolutely essential for proper lens homeostasis, but not for lens growth.

Keywords: mouse; lens; knockout; PTEN; PI3K; Akt

1. Introduction

Class I phosphoinositide 3-kinases (PI3Ks) are lipid kinases that phosphorylate the 3′-hydroxyl group of phosphatidylinositol-(4,5) P_2 following the activation of cell surface receptors. In turn, the phosphatidylinositol-(3,4,5)P_3 (PIP_3) generated goes on to activate additional signaling pathways that regulate cell growth, proliferation, motility, and survival [1]. Class IA PI3Ks are heterodimers composed of an 85 kD regulatory subunit and a 110 kD catalytic subunit. The p110α catalytic subunit is widely expressed, and responds to input from receptor tyrosine kinases [2]. PI3K generates PIP_3, which leads to the activation of the Akt signaling pathway [3–6]. Mutations in the gene encoding p110α are often linked to cancer, highlighting the importance of the PI3K signaling cascade in cell proliferation and survival [1]. Phosphatase and tensin homolog (PTEN) is a widely expressed lipid phosphatase that antagonizes PI3K signaling [7,8]. PTEN dephosphorylates PIP_3 generated by PI3K and negatively regulates Akt activity [3,9]. The interplay between PTEN, PI3K, and Akt controls numerous cellular processes in many organs, including the ocular lens [10–14].

The anterior surface of the lens is covered by a monolayer of epithelial cells, which differentiate into fiber cells at the equator and fill the lens core [15]. Epithelial cell proliferation drives the growth of the lens, and primarily occurs in a band of cells near the equator called the germinative zone [16–18]. Lens development and growth are influenced by growth factor signaling. For example, fibroblast growth factors (FGFs) and fibroblast growth factor receptors (FGFRs) regulate lens induction, epithelial cell proliferation, and fiber differentiation [19–21]. Once activated by FGFs, FGFRs stimulate the mitogen-activated protein kinase

(MAPK) and PI3K–Akt intracellular signaling pathways [10,22,23]. Genetic dissection experiments have illuminated the roles of many components of the MAPK pathway in the lens [24–30]. In contrast, the roles played by PI3K, Akt, and PTEN in these processes are less well characterized. One recent study examined the effects of the lens-specific knockout of p110α [13]. The loss of p110α substantially reduced phosphorylated Akt levels and caused a reduction in the number of proliferating lens epithelial cells present in the germinative zone on postnatal day 0 (P0), resulting in significantly reduced lens size throughout life. Two additional studies reported the consequences of the lens-specific deletion of PTEN, the lipid phosphatase that antagonizes PI3K [7,8]. In both studies, the levels of phosphorylated Akt were significantly elevated following the loss of PTEN, with different consequences related to the developmental timing of lens-specific knockout [14,31]. The loss of PTEN at the lens placode stage rescued a cell death phenotype caused by the knockout of the FGFR2 [31]. The knockout of PTEN at the lens vesicle stage reduced Na^+/K^+-ATPase activity, which caused the intracellular hydrostatic pressure to increase, leading to lens swelling and rupture [14].

Here, we have generated and characterized a conditional double-knockout mouse lacking both p110α and PTEN in the lens using a Cre recombinase active at the lens vesicle stage [32]. We evaluated the epithelial cell proliferation on P0, levels of phosphorylated Akt, lens growth, and lens homeostasis. We found that the double deletion of p110α and PTEN rescued the deficits in germinative zone proliferation and lens growth seen after the single knockout of p110α [13], but exacerbated the lens rupture phenotype seen in PTEN single-knockout mice [14]. The levels of phosphorylated Akt in double-knockout lenses were elevated 4.5-fold compared to wild-type lenses. These results document that the double deletion of p110α and PTEN alleviated the proliferation and growth deficits, and exacerbated the lens rupture defects seen in the respective single knockouts.

2. Materials and Methods

2.1. Generation of Knockout Mice

All animal use was approved by the Stony Brook University Institutional Animal Care and Use Committee. Mice with lens-specific conditional knockouts of the p110α catalytic subunit of PI3K [13], or PTEN [14], were interbred to obtain double-knockout animals (p110α/PTEN dKO). Briefly, p110α homozygous floxed [33] and PTEN homozygous floxed mice [34] were interbred with heterozygous MLR10-Cre mice [32]. Genotypes were verified by a PCR of tail DNA as previously described [13,14]. Due to the mixed genetic background that resulted from the interbreeding of three different strains of original mice, littermate controls were used for all experiments. All animals used for breeding had homozygous floxed alleles for both PTEN and p110α, while one member of the breeding pair carried a heterozygous copy of the MLR10-Cre transgene. The resulting litters contained one half of the animals with no Cre (wild-type controls) and one half with the double knockout of PTEN and p110α (dKOs). No backcrossing of animals was performed. Some authors have reported spurious Cre-mediated lens and eye phenotypes that were not dependent on the deleted gene of interest [35]. We have twice published studies using the MLR10-Cre mice where no lens phenotype was observed following the successful knockout of floxed alleles for both Cx43 [36] and the p110β catalytic subunit of PI3K [13], and we feel that this is not an issue in the present study. No differences in phenotype were observed between male and female knockout mice.

2.2. Lens Growth Analysis and Photography

Littermate mice from birth to 24 weeks of age were euthanized by CO_2 inhalation. Their eyes were removed and transferred to a tissue culture dish filled with 37 °C Tyrode solution on a prewarmed stage. Lenses were surgically removed and photographed using a SZX16 dissecting microscope attached to a digital camera (Olympus, Waltham, MA, USA). The diameters of lenses were measured from images and lens volume was calculated assuming a spherical shape. The incidence of lens rupture was also recorded [13,14,37].

2.3. Western Blotting

Lenses were surgically removed from dissected eyes and placed in Tyrode solution. Lens capsules were separated from the fiber cells of the lens using fine forceps, heat denatured in 2 × sample buffer, and then electrophoretically separated on SDS–PAGE gels. After being transferred to nitrocellulose membranes, western blots were probed with antibodies against PI3K p110α (rabbit monoclonal, Cell Signaling Technology, Danvers, MA, USA), antibodies against PTEN (rabbit monoclonal, Cell Signaling Technology, Danvers, MA, USA), antibodies against serine 473 phospho-Akt (mouse monoclonal, Cell Signaling Technology, Danvers, MA, USA), or antibodies against total AKT1/2/3 (rabbit polyclonal, Santa Cruz Biotechnology, Dallas, TX, USA). Peroxidase-conjugated goat anti-rabbit (Jackson ImmunoResearch, West Grove, PA, USA), or sheep anti-mouse (GE Healthcare, Pittsburgh, PA, USA) secondary antibodies were used to facilitate ECL detection. NIH ImageJ software (version 1.49v, http://imagej.nih.gov, USA, accessed on 22 August 2022) [38] was used to determine band densities from three independent blots.

2.4. 5-Ethynyl-2′-deoxyuridine (EdU) Staining

Postnatal day 0 (P0) mice were subcutaneously injected with 50 μg/gm EdU (Click-iT, Thermo Fisher Scientific, Waltham, MA, USA) and returned to their mothers for 2 h. Then, lenses were dissected and fixed in a 4% formaldehyde in PBS for 1 h and photographed. The permeabilization of fixed lenses and Click-iT staining were performed according to manufacturer's instructions and previously published protocols [13,39]. Z-stacks of fluorescent images were acquired on an Axiovert 200 M microscope (Zeiss, Thornwood, NY, USA) and processed using ImageJ (version 1.49v, http://imagej.nih.gov, USA, accessed on 22 August 2022). For line-scan analysis, the flattened fluorescent image of EdU staining was manually thresholded in ImageJ (version 1.49v, http://imagej.nih.gov, USA, accessed on 22 August 2022), and the plot profile function was used in ImageJ to measure fluorescent intensity across the lens diameter as previously described [13].

2.5. Histology

Eyes from postnatal day 7 mice were dissected and fixed in 4% formaldehyde in phosphate-buffered saline (PBS) for 18 to 22 h at room temperature. After fixation, eyes were rinsed with PBS, dehydrated through a series of increasing ethanol concentrations and then embedded in paraffin. 2–3 μm sections were cut using a diamond knife and deparaffinized, before being stained with hematoxylin–eosin as previously described [13,14]. Histological sections were observed on a BX51 microscope and photographed with a DP72 digital camera (Olympus, Waltham, MA, USA).

2.6. Statistics

Data are presented as the mean ± SD, or SEM, as described in each figure. Statistical significance was determined using one-way ANOVA, or the two sample *t*-test in the Origin 2020 (64-bit) SR1software program (OriginLab Corporation, Northampton, MA, USA). p values that were less than 0.05 were considered significant.

3. Results

3.1. Lens-Specific Double Deletion of p110α and PTEN Caused Accelerated Cataract and Lens Rupture

Mice with homozygous floxed p110α and PTEN alleles [33,34] were interbred with MLR10-Cre transgenic mice [32] to obtain lens-specific conditional double-knockout animals. MLR10-Cre mice express Cre recombinase in both the lens epithelium and fiber cells starting at the lens vesicle stage. Lenses isolated from homozygous floxed p110α/PTEN animals lacking the MLR10-Cre transgene (i.e., wild-type) remained transparent and intact at all ages examined (Figure 1a–c). In contrast, lenses dissected between 1 and 12 weeks of age from homozygous floxed p110α/PTEN animals expressing the MLR10-Cre transgene (i.e., p110α/PTEN dKO) showed a progressive pathology (Figure 1d–i). This phenotype

was similar to that reported for the single PTEN KO lenses [14], but with an altered time course. At 1 week of age, the majority of p110α/PTEN dKO lenses (Figure 1d) appeared clear and of normal size. Only 23% of p110α/PTEN dKO lenses showed a ring of cortical vacuoles (Figure 1g) as previously reported for 80% of the single PTEN KO lenses at this age. At 5 weeks of age, only 5% of p110α/PTEN dKO lenses showed opacities dispersed throughout the outer lens cortex (Figure 1e,h), compared to 71% of single PTEN KO lenses at this age. By 12 weeks of age, 72% of p110α/PTEN dKO lenses had ruptured, leaving behind cortical fragments and a dense nuclear cataract (Figure 1f,i), compared to only 9% rupture for single PTEN KOs at this time point. Lenses that had not ruptured were noticeably larger than wild-type controls, and contained diffuse opacities. Thus, the double deletion of p110α and PTEN in the lens reduced the vacuole number, but accelerated the rupture phenotype described in single PTEN knockout mice [14].

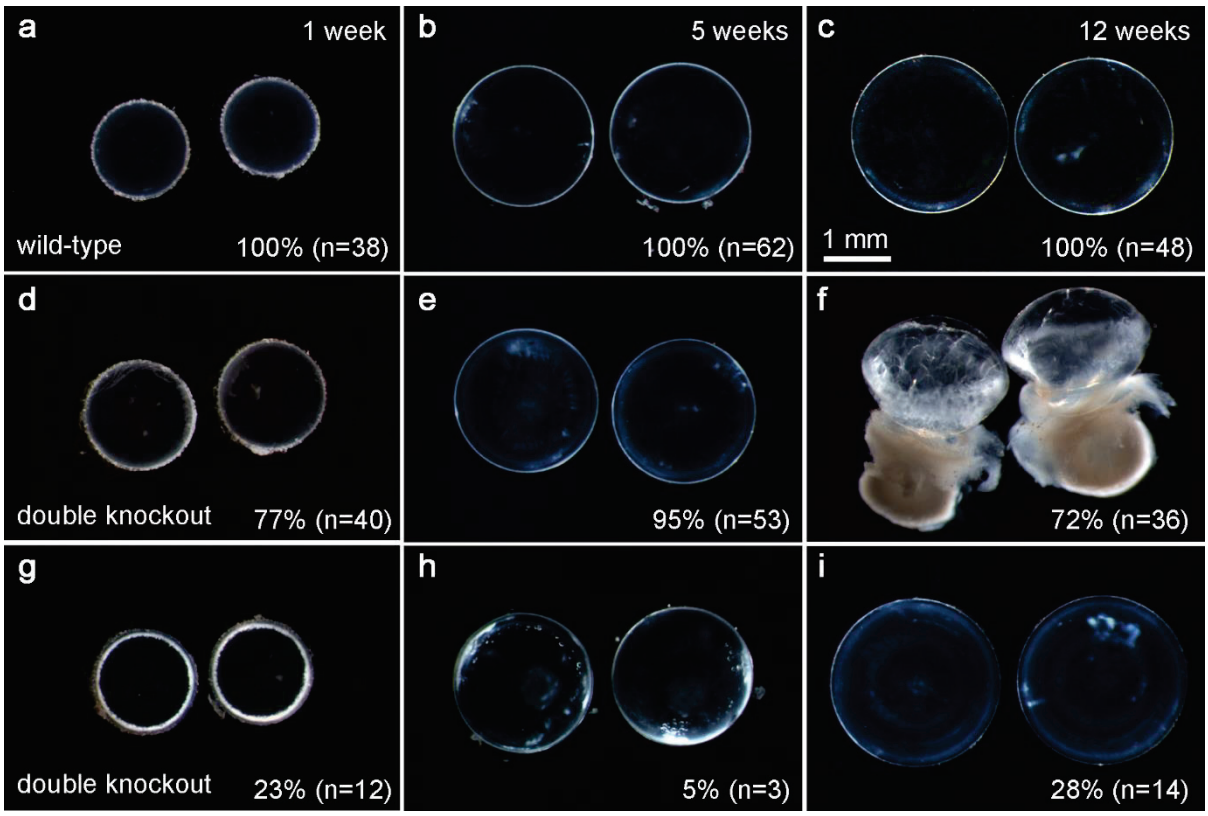

Figure 1. p110α/PTEN dKO mice develop cataract and lens rupture. Lenses dissected from wild-type (**a**–**c**) and p110α/PTEN double-knockout (**d**–**i**) mice are shown at 1, 5, and 12 weeks of age. Wild-type lenses (**a**–**c**) were transparent and intact at all ages studied. dKO lenses displayed a phenotype similar to single PTEN KO lenses [14], but with an altered time course. At 1 week, the majority of dKO lenses (**d**) appeared clear and of normal size when compared to WT (**a**). Only 23% of dKO lenses showed a ring of cortical vacuoles (**g**) as previously reported for 80% of single PTEN KO lenses at this age. At 5 weeks, only 5% of dKO lenses showed dispersed vacuoles (**h**), compared to 71% of single PTEN KO lenses at this age. At 12 weeks, 72% of dKO lenses had ruptured (**f**), compared to only 9% rupture for single PTEN KOs. The dense opaque material in panel f is the cataractous lens core. At 1 and 5 weeks, dKO lenses were of normal size (**d**,**e**,**g**,**h**), in contrast to single p110α KO lenses [13] which were significantly smaller than wild-type at all postnatal ages. n = number of lenses.

3.2. Double Knockout of p110α and PTEN Increased Lens Volume and Accelerated Lens Rupture

Changes in lens size and integrity were quantified over time by dissecting and photographing lenses from Postnatal day 0 (P0), P2, and 1, 5, and 12 week-old age-matched p110α/PTEN double homozygous floxed littermate animals, with or without the MLR10-Cre transgene. Single p110α and PTEN knockout lenses were also analyzed for comparison

to the p110α/PTEN dKO animals. Lens diameters were measured and used to calculate volumes assuming spherical geometry [13,14,37]. As shown in Figure 2a, the effect of p110α/PTEN dKO on lens size developed slowly, with no significant differences in volume compared to wild-type observed between P0 and 1 week of age. In contrast, a 7% increase in lens volume in p110α/PTEN dKO lenses developed between 1 and 5 weeks when compared to wild-type ($p < 0.05$, Student's *t*-test), which grew to a 22% volume increase by 12 weeks in the reduced number of intact dKO lenses still available at that age ($p < 0.05$). As previously reported [13,14], p110α single KO lenses were significantly smaller than wild-type at all postnatal ages studied, and PTEN single KO lenses showed a volume increase comparable to the p110α/PTEN dKOs. The overall eye size, as expressed by eye mass, was also similar between wild-type and p110α/PTEN dKOs animals (Figure 2b). This contrasted with the significantly decreased eye size previously reported for p110α single KO animals [13]. We further recorded the frequency of lens rupture between P0 and 24 weeks for wild-type and p110α/PTEN dKO littermate animals, and compared these data with the rupture frequency observed in single p110α and PTEN KOs. Wild-type, or single p110α KO, lenses never exhibited lens rupture in the time period examined, while 22% of p110α/PTEN dKO lenses had ruptured by 8 weeks, which increased to a 100% incidence of rupture at 24 weeks (Figure 2c). In contrast, only 9% of single PTEN KO lenses had ruptured by 12 weeks, and 19% of PTEN KO lenses were still intact at 24 weeks of age. These data suggested that although the activity of p110α alone was required by the lens to grow to a normal lens volume [13], further removal of PTEN in p110α/PTEN dKO lenses alleviated this growth deficit. They also showed that although the loss of PTEN alone resulted in a loss of lens ionic homeostasis and ultimate lens rupture [14], the further removal of p110α in p110α/PTEN dKO lenses greatly accelerated this loss of lens homeostasis.

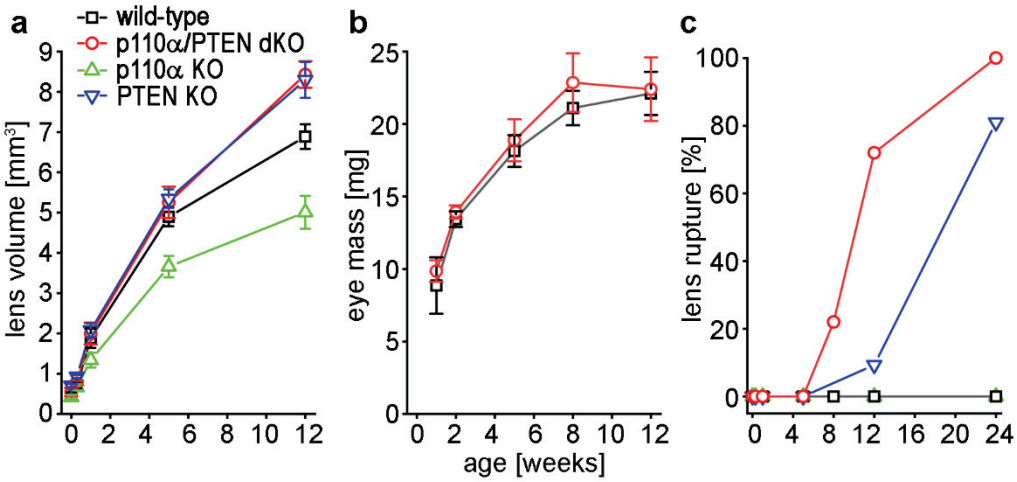

Figure 2. Double deletion of p110α/PTEN eliminated the growth defect of single p110α KO mice, and accelerated the rupture phenotype of single PTEN KO animals. (**a**) Diameters of lenses dissected from WT, p110α KO, PTEN KO and p110α/PTEN dKO mice at P0, P2, and 1, 5, or 12 weeks of age were used to calculate lens volume. The volumes of dKO lenses were similar to single PTEN KO lenses [14] at all ages. In contrast, the reduced lens volume reported for single p110α KO lenses [13] was absent. (**b**) Eye mass was not increased in dKO lenses when compared to WT. (**c**) The incidence of lens rupture versus age for WT, p110α KO, PTEN KO, and p110α/PTEN dKO mice at P0, P2, and 1, 5, 8, 12, and 24 weeks. Lens rupture was accelerated in dKO animals compared to single PTEN KO mice. No rupture was observed in wild-type or single p110α KO lenses. Data are plotted as mean ± SD. See Table S1 for a detailed breakdown of the number of lenses (4–64) analyzed per genotype per time point. See Table S2 for statistical comparison of dKO versus wild-type lens and eye growth per time point.

3.3. Double Knockout of p110α and PTEN Increased Levels of Phospho-Akt

To confirm the absence of p110α and PTEN proteins, and determine how downstream Akt signaling was effected in dKO lenses, epithelial cell extracts were probed by western

blot (Figure 3a–d). Wild-type epithelial cells expressed both the p110α catalytic subunit of PI3K and its opposing phosphatase PTEN, which were completely absent from epithelial cells isolated from the dKO mice. Consistent with the presence of additional active PI3K isoforms in the lens [13,40] and PTEN's antagonistic role toward PI3K signaling, the levels of phosphorylated Akt were elevated in p110α/PTEN dKO epithelial cells compared to wild-type. As expected, total Akt levels were not affected by p110α/PTEN double deletion. The quantitation of band densities (Figure 3e,f) showed no significant differences in levels of total Akt between wild-type and p110α/PTEN dKO epithelial cells ($p > 0.05$). In contrast, the levels of phospho-Akt were elevated approximately ~4.5-fold in p110α/PTEN dKO epithelial cells ($p < 0.05$). Full size images of replicate blots are shown in Figure S1. These data confirm that the loss of PTEN antagonism of PI3K activity resulted in elevated levels of phospho-Akt in p110α/PTEN dKO lenses, and further suggest that the absence of the growth defect observed in single p110α KOs may have been due to the restoration of elevated phospho-Akt levels in the dKO mice.

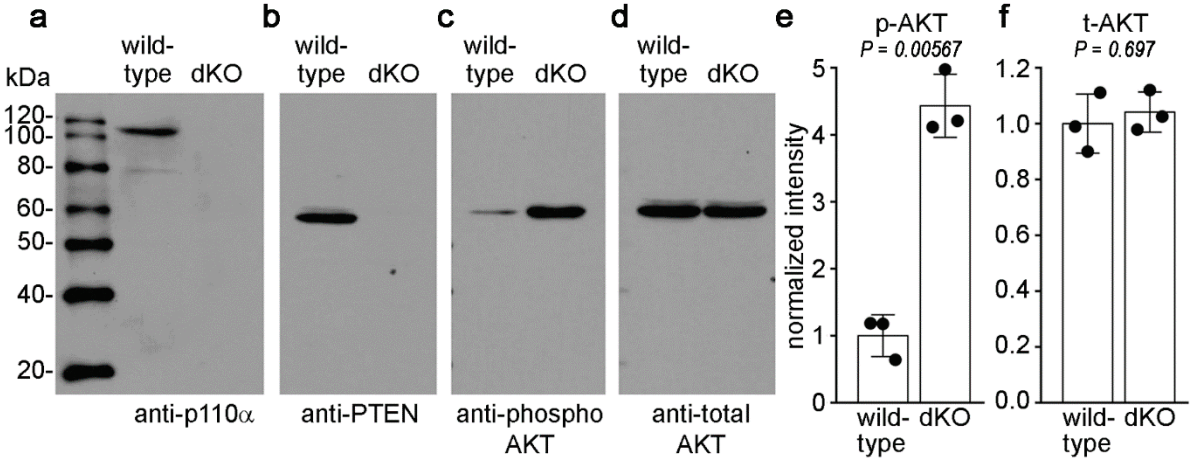

Figure 3. Double deletion of p110α/PTEN increased levels of phospho-AKT. Lens capsules with attached epithelial cells were isolated from 3 week old WT or dKO lenses, and used for western blots. Blots were probed with antibodies against p110α, PTEN, phospho, or total AKT. Both p110α (**a**) and PTEN (**b**) proteins failed to be detected in dKO lenses. (**c**) As previously reported for single PTEN KO lenses [14], phospho-AKT (p-AKT) levels were elevated in dKO lenses. (**d**) Total AKT (t-AKT) levels were the same in wild-type and dKO lenses. Quantitation of band intensities showed a ~4.5-fold increase in p-AKT levels in dKO lenses (**e**, $p < 0.05$, two sample *t*-test), and no significant differences in t-AKT levels between wild-type and dKO mice (**f**, $p > 0.05$ two sample *t*-test). Raw data are plotted as filled circles, bars represent the mean ± SD, n = 3.

3.4. Double Knockout of p110α and PTEN Eliminated the Postnatal Proliferation Defect Present in Single p110α Knockout Lenses

We have previously shown that the pattern of mitosis in p110α single KO lenses was significantly altered on P0, with the most prominent feature being a reduction in cell division in a band of cells known as the equatorial germinative zone of the lens epithelium [13]. To examine the effect of the double knockout of p110α/PTEN on postnatal mitosis, lenses from wild-type, single p110α and PTEN KO, or p110α/PTEN dKO mice were labeled with EdU on P0 (Figure 4). Wild-type, PTEN KO, and p110α/PTEN dKO lenses all displayed similar patterns of robust EdU labeling, with the highest level of fluorescence in the germinative zone near the lens equator as previously reported [13,41,42]. In contrast, single p110α KO lenses lacked the ring of increased labeling near the equatorial germinative zone, and showed a more homogeneous pattern of EdU incorporation as previously described [13]. The mean values of the line scans of fluorescent intensity taken along the lens diameter confirmed this change in mitotic pattern between EdU-labeled images from p110α KO and p110α/PTEN dKO lenses on P0. Wild-type, PTEN KO, and

p110α/PTEN dKO lenses all had clear peaks of EdU fluorescent intensity near the equator. In contrast, p110α knockout lenses lacked the equatorial peaks, and had maximum values of fluorescence that ranged from 45% to 49% lower than either the wild-type, PTEN KO, or p110α/PTEN dKO lenses on average. Overlaying the average p110α KO trace onto that of the p110α/PTEN dKO lenses (Figure 4q) clearly showed that the lens equatorial proliferation peaks were recovered in the dKO animals.

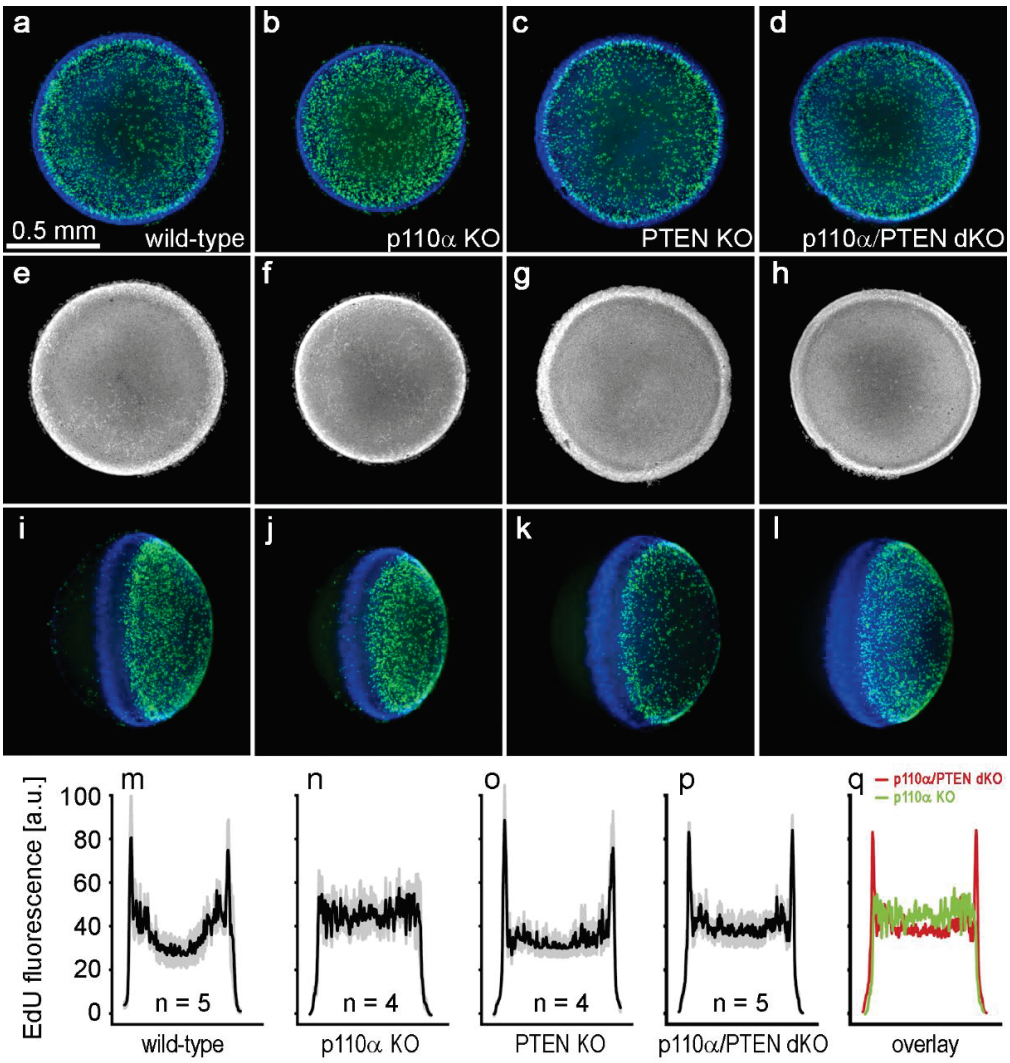

Figure 4. Double p110α/PTEN knockouts lacked the postnatal proliferation defect of single p110α knockout lenses. Postnatal day 0 lenses from wild type (**a**,**e**,**i**), single p110α KO (**b**,**f**,**j**), single PTEN KO (**c**,**g**,**k**), and p110α/PTEN dKO (**d**,**h**,**i**) mice were stained with EdU (green, **a**–**d**, **i**–**l**) and Hoechst (blue, **a**–**d**, **i**–**l**, or gray, **e**–**h**). Z-stack images were generated looking onto the epithelial surface (**a**–**d**), or onto the lens edge (**i**–**l**). Grayscale images of Hoechst-stained nuclei were also displayed to verify the overall integrity of the lens epithelium (**e**–**h**). EdU labeling showed that the distribution of proliferating cells in the p110α/PTEN dKO lenses was similar to that of wild-type, or single PTEN KO lenses, with the highest signal in the equatorial germinative zone. Plots of mean values of line scans (black lines, ± the SEM gray bars) of EdU fluorescence taken along the lens diameter (**m**–**q**) confirmed that the p110α/PTEN dKO lenses had recovered peak proliferation in the equatorial germinative zone, which was greatly reduced from single p110α KO lenses [13]. n = 4–5 lenses per genotype.

Higher power views of EdU fluorescence confirmed that equatorial germinative zone proliferation was restored in p110α/PTEN dKO lenses (Figure 5). A quantitative analysis of the peak EdU fluorescent signal detected in the germinative zone showed a 1.8-fold

increase in p110α/PTEN dKO lenses compared to p110α single KOs ($p < 0.05$). There was no significant difference in peak EdU signal between the dKOs and PTEN single KOs, or wild-type lenses ($p > 0.05$). These data suggest that the significant reduction in lens volume, caused by a transient loss of proliferating epithelial cells in the germinative zone on P0 in single p110α KO lenses [13], was alleviated by the further removal of PTEN in p110α/PTEN dKO lenses.

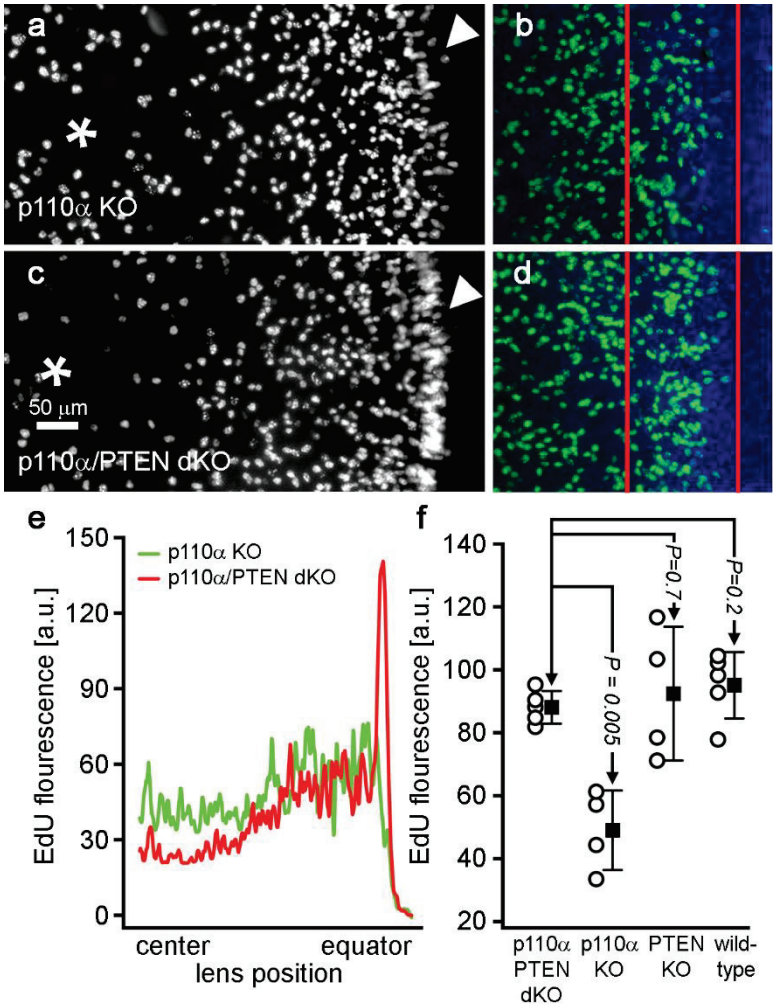

Figure 5. Germinative zone proliferation in double p110α/PTEN knockouts was significantly increased compared to single p110α knockout lenses. (**a**–**d**) Higher magnification views of postnatal day 0 lenses from single p110α KO (**a**,**b**) and p110α/PTEN dKO (**c**,**d**) looking onto the epithelial surface (**a**,**c**, EdU fluorescence alone), or onto the lens edge (**b**,**d**, EdU green, DAPI, blue). EdU-labeled cells are visibly increased in the germinative zone of p110α/PTEN dKOs in both views (white arrowheads in a and c, red lines in b and d). (**e**) Line scans of the entire field of view in panels a and c confirmed the increase in EdU fluorescence in the equatorial germinative zone in dKO lenses. (**f**) Plots of mean values of peak EdU fluorescence (open circles are raw data, filled squares are means ± the SD) showed a significant increase ($p < 0.05$) in p110α/PTEN dKOs compared to p110α KOs. There were no significant differences between p110α/PTEN dKOs and PTEN KO, or wild-type lenses ($p > 0.5$, two sample *t*-test). The center of the lens is indicated by an * in panels a and c. n = 4–5 lenses per genotype.

3.5. Double Deletion of p110α/PTEN Produced Histological Abnormalities in the Equatorial Region of the Lens

To examine the histology of p110α/PTEN dKO lenses, we dissected eyes from littermate mouse pups on postnatal day 7, sectioned them, and stained with hematoxylin and eosin (Figure 6). Sagittal sections through the central region of wild-type lenses showed a normal appearance, whereas p110α/PTEN dKO lenses displayed small vacuoles in the

equatorial cortex. Despite the presence of vacuoles, fiber cell differentiation appeared to proceed normally in dKO mice. Vacuoles have been reported in other mouse lens cataract models [14,26,27,43], and consistent with these reports, we observed an increase in the number of vacuoles in the dKO compared to wild-type. Histological abnormalities were not observed following the single knockout of p110α [13], unlike single PTEN KO lenses which showed more extensive vacuole formation at earlier ages than P7 [14]. Thus, the double deletion of p110α/PTEN from the lens resulted in milder histological defects in the lens cortex that appeared developmentally later than those observed in single PTEN KOs.

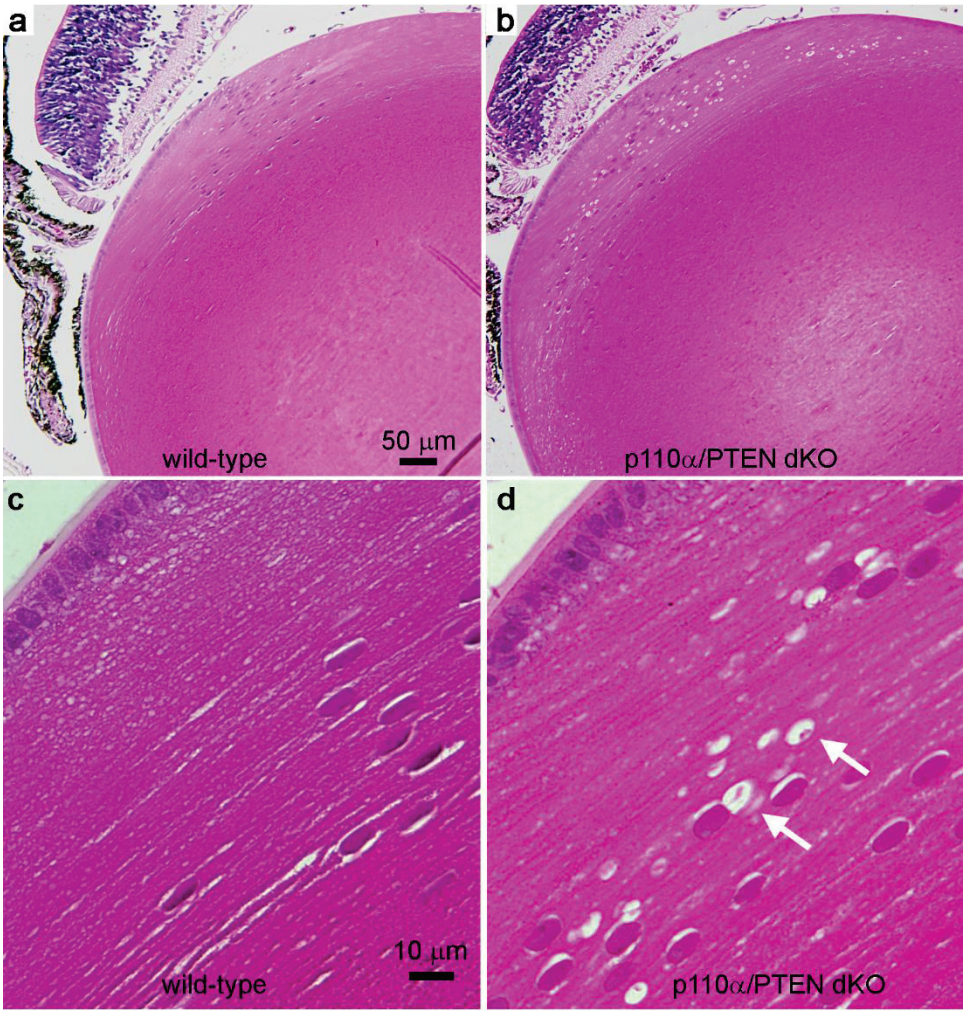

Figure 6. Postnatal day 7 lenses were fixed, embedded in paraffin, sectioned, and stained with hematoxylin and eosin. (**a**) Sagittal sections through the central region of wild-type lenses showed a normal appearance. (**b**) p110α/PTEN dKO lenses had numerous small vacuoles in the cortical region. (**c**) Higher power view of the cortex region of the wild-type lens shown in panel a. Higher power view of the cortex region of the p110α/PTEN dKO lens in panel b, showing the location of small vacuoles in the cortical fiber cells (white arrows). (**a**,**b**) Bar = 50 μm. (**c**,**d**) Bar = 10 μm.

4. Discussion

We have generated p110α/PTEN double-knockout mice with the goal of improving our understanding of the integration of PI3K and PTEN signaling with the normal physiology and pathophysiology of the lens. The double deletion of p110α and PTEN produced a phenotype with features distinct from both of the respective single knockouts. The proliferation defect and smaller size of p110α KO lenses [13] was rescued by the further removal of PTEN in the dKO. In contrast, the rupture phenotype observed in PTEN KO lenses [14] remained, although the time course over which it developed was different.

Vacuoles, which appeared as early as P2 in PTEN single Kos, were not visibly apparent before 1 week of age in the dKO. The rupture phenotype, on the other hand, was both accelerated and more penetrant. Phospho-Akt, which was reduced in p110α KO lenses, was elevated in both the PTEN KO and dKO.

Mouse lens growth undergoes a transition during the first postnatal week, the period where we previously reported a significant reduction in the number of dividing epithelial cells in p110α KO lenses [13]. Throughout embryonic development, the lens diameter grows linearly and its volume increases in an exponential manner [44,45]. Shortly after birth, the growth of the lens becomes oscillatory in a way corresponding to the epithelial cell cycle that can be reproduced in organ culture with the pulsatile administration of growth factors [46,47]. In the single p110α KO lenses, peak epithelial cell proliferation in the germinative zone transiently vanished at P0, despite being clearly present on E17 and P2 [13]. Lenses from p110α/PTEN dKOs maintained peak epithelial cell proliferation in the germinative zone at P0, and had elevated levels of phospho-Akt. These data show that the embryonic constant growth and the postnatal pulsatile growth mechanisms both produce maximum cell division in the germinative zone in the absence of p110α. However, the transition period between these mechanisms was sensitive to the loss of p110α activity alone, but not to the double deletion of p110a/PTEN. This suggests that elevated levels of phospho-Akt, whether generated through the activity of p110α, or the loss of PTEN, were required to maintain germinative zone proliferation during the transition between lens growth modes. The precise mechanism whereby Akt activity is required for the preservation of normal germinative zone proliferation around P0 would be a good subject for future studies.

The loss of the antagonism of PI3K signaling in single PTEN KO lenses increased the activation of Akt, and reduced Na^+/K^+-ATPase activity within the epithelial cells [14]. This caused a reduction in the normal sodium and water efflux mediated by the lens circulation [48,49], resulting in an increased intracellular hydrostatic pressure and ultimately lens rupture. The single PTEN lens KO phenotype initially displayed the formation of a ring of densely packed cortical vacuoles in neonatal mice that could be eliminated by in utero treatment with an Akt inhibitor [14]. Vacuole formation in the p110a/PTEN dKO was greatly reduced at both 1 week and 5 weeks of age, which was correlated with an overall reduction in the elevation of phospho-Akt levels in the p110a/PTEN dKO (4.5 times higher than wild-type control) compared to the PTEN KO (12 times higher than wild-type control). Thus, the reduced vacuole formation in the p110α/PTEN dKOs may have resulted from a failure to reach a sufficient threshold of Akt activation at the lens equator to disrupt cellular structure. Paradoxically, lens rupture in the p110α/PTEN dKO was greatly accelerated compared to the single PTEN KO, despite the fact that vacuole formation preceded lens rupture by several weeks. We have not directly measured the lens hydrostatic pressure in p110α/PTEN dKO lenses, and this would likely be difficult to achieve due to the high incidence of lens rupture. Since increased hydrostatic pressure is also known to be an Akt-dependent phenomenon [14,50,51], it is possible that differential levels of Akt activation are responsible for the accelerated rate of lens rupture in the p110α/PTEN dKO lenses. The elucidation of the precise signaling cascades that regulate lens hydrostatic pressure, including PI3K, PTEN, and Akt, will require further investigation.

Although this initial characterization of p110α/PTEN double-knockout lenses has elucidated several interesting findings, there remain a number of unanswered questions. Will the findings from this mouse model be relevant to human ocular health, or other vertebrate lenses? How are lens vacuoles initially produced, and why are they less abundant in the dKO than the PTEN single knockout? In addition to changes in phosphorylated Akt, what other downstream signaling molecules have their activity modulated by the combined loss of PI3K and PTEN? A better understanding of the relationship(s) between lens growth, the formation of lens vacuoles, changes in lens hydrostatic pressure, lens rupture, and the signaling cascades regulated by PI3K, Akt and PTEN will require additional experimentation.

We have examined PI3K/PTEN signaling in the lens using an in vivo methodology involving mice with multiple gene knockouts. PI3K/PTEN signaling critically regulates the activity of a broad network of lens ion channels and transporters, including connexins, TRP channels, and the Na^+/K^+-ATPase [14,50–52]. Future studies could examine mice with deletions of these transport proteins in conjunction with PI3K and/or PTEN knockout to further elucidate the mechanisms whereby this signaling cascade influences lens development and homeostasis. The systemic regulation of membrane channel/transporter activity by PI3K/PTEN has emerged as a novel homeostatic mechanism across many cell types and tissues. For example, the down regulation of PI3K signaling prolonged the QT interval of the cardiac action potential by affecting multiple ion channels, potentially explaining why some tyrosine kinase inhibitors in clinical use as anti-cancer therapies lead to an increased risk of arrhythmias, as with long QT syndrome [53,54]. In the central nervous system, the altered PTEN regulation of channels involved with synaptic transmission may explain abnormal social and cognitive behaviors observed in humans with PTEN hamartoma tumor syndrome (PHTS) and other neurological syndromes such as autism spectrum disorders [55,56]. In the initial segment of the epididymal epithelium, the targeted deletion of PTEN altered ion channel and transporter activity, resulting in reduced male fertility [57]. The loss of PTEN in thyroid cancer cells resulted in the altered plasma membrane expression of SLC2A1, and increased glucose uptake [58]. In a similar manner, PTEN has been linked to the altered activity of glucose transport, the ABCG2 transporter, and the glutamate aspartate transporter in other cell types [59–61].

Taken together, these observations suggest that PI3K/PTEN signaling may broadly participate in the regulation of the activity of diverse channels and transporters in many tissues, and that the loss of this regulation may contribute to a variety of developmental defects and disease states. Further study on how lens channels and PI3K/PTEN signaling work together to maintain clarity, preserve integrity, and regulate postnatal mitosis could provide broad insights into the regulation of channel/transport activity in many other tissues.

Supplementary Materials: The following are available online at https://www.mdpi.com/article/10.3390/cells11172708/s1, Figure S1: Original Images for Blots, Table S1: Number of lenses analyzed per age and genotype for Figure 2. Table S2: Statistical comparison of lens and eye growth between wild-type and p110α/PTEN dKO mice.

Author Contributions: Conceptualization, C.S. and T.W.W.; methodology, C.S., L.L. and T.W.W.; formal analysis, C.S., L.L. and T.W.W.; investigation, C.S. and L.L.; data curation, C.S., L.L. and T.W.W.; writing—original draft preparation, C.S. and T.W.W.; writing—review and editing, C.S., L.L. and T.W.W.; project administration, T.W.W.; funding acquisition, T.W.W. All authors have read and agreed to the published version of the manuscript.

Funding: This research was funded by National Institutes of Health, grant number EY026911.

Institutional Review Board Statement: Animal use was approved by the Stony Brook University Institutional Animal Care and Use Committee (IACUC 252607_AR001).

Informed Consent Statement: Not applicable.

Data Availability Statement: The data presented in this study are contained within the article or supplementary material.

Acknowledgments: We thank Howard Luan for assistance with genotyping.

Conflicts of Interest: The authors declare no conflict of interest.

References

1. Ilic, N.; Roberts, T.M. Comparing the roles of the p110alpha and p110beta isoforms of PI3K in signaling and cancer. *Curr. Top. Microbiol. Immunol.* **2010**, *347*, 55–77. [CrossRef] [PubMed]
2. Vanhaesebroeck, B.; Guillermet-Guibert, J.; Graupera, M.; Bilanges, B. The emerging mechanisms of isoform-specific PI3K signalling. *Nat. Rev. Mol. Cell Biol.* **2010**, *11*, 329–341. [CrossRef] [PubMed]
3. Cantley, L.C. The phosphoinositide 3-kinase pathway. *Science* **2002**, *296*, 1655–1657. [CrossRef]

4. Engelman, J.A.; Luo, J.; Cantley, L.C. The evolution of phosphatidylinositol 3-kinases as regulators of growth and metabolism. *Nat. Rev. Genet.* **2006**, *7*, 606–619. [CrossRef]
5. Fruman, D.A.; Meyers, R.E.; Cantley, L.C. Phosphoinositide kinases. *Annu. Rev. Biochem.* **1998**, *67*, 481–507. [CrossRef]
6. Hawkins, P.T.; Anderson, K.E.; Davidson, K.; Stephens, L.R. Signalling through Class I PI3Ks in mammalian cells. *Biochem. Soc. Trans.* **2006**, *34*, 647–662. [CrossRef]
7. Cantley, L.C.; Neel, B.G. New insights into tumor suppression: PTEN suppresses tumor formation by restraining the phosphoinositide 3-kinase/AKT pathway. *Proc. Natl. Acad. Sci. USA* **1999**, *96*, 4240–4245. [CrossRef]
8. Waite, K.A.; Eng, C. Protean PTEN: Form and function. *Am. J. Hum. Genet.* **2002**, *70*, 829–844. [CrossRef]
9. Sarbassov, D.D.; Ali, S.M.; Sabatini, D.M. Growing roles for the mTOR pathway. *Curr. Opin. Cell Biol.* **2005**, *17*, 596–603. [CrossRef]
10. Martinez, G.; de Iongh, R.U. The lens epithelium in ocular health and disease. *Int. J. Biochem. Cell Biol.* **2010**, *42*, 1945–1963. [CrossRef]
11. Teo, Z.L.; McQueen-Miscamble, L.; Turner, K.; Martinez, G.; Madakashira, B.; Dedhar, S.; Robinson, M.L.; de Iongh, R.U. Integrin linked kinase (ILK) is required for lens epithelial cell survival, proliferation and differentiation. *Exp. Eye Res.* **2014**, *121*, 130–142. [CrossRef]
12. Weber, G.F.; Menko, A.S. Phosphatidylinositol 3-kinase is necessary for lens fiber cell differentiation and survival. *Investig. Ophthalmol. Vis. Sci.* **2006**, *47*, 4490–4499. [CrossRef]
13. Sellitto, C.; Li, L.; Vaghefi, E.; Donaldson, P.J.; Lin, R.Z.; White, T.W. The Phosphoinosotide 3-Kinase Catalytic Subunit p110alpha is Required for Normal Lens Growth. *Investig. Ophthalmol. Vis. Sci.* **2016**, *57*, 3145–3151. [CrossRef]
14. Sellitto, C.; Li, L.; Gao, J.; Robinson, M.L.; Lin, R.Z.; Mathias, R.T.; White, T.W. AKT activation promotes PTEN hamartoma tumor syndrome-associated cataract development. *J. Clin. Investig.* **2013**, *123*, 5401–5409. [CrossRef]
15. Piatigorsky, J. Lens differentiation in vertebrates. A review of cellular and molecular features. *Differentiation* **1981**, *19*, 134–153. [CrossRef]
16. McAvoy, J.W.; Chamberlain, C.G.; de Iongh, R.U.; Hales, A.M.; Lovicu, F.J. Lens development. *Eye* **1999**, *13 (Pt. 3b)*, 425–437. [CrossRef]
17. McAvoy, J.W. Cell division, cell elongation and the co-ordination of crystallin gene expression during lens morphogenesis in the rat. *J. Embryol. Exp. Morphol.* **1978**, *45*, 271–281. [CrossRef]
18. Sikic, H.; Shi, Y.; Lubura, S.; Bassnett, S. A stochastic model of eye lens growth. *J. Theor. Biol.* **2015**, *376*, 15–31. [CrossRef]
19. Lovicu, F.J.; McAvoy, J.W. FGF-induced lens cell proliferation and differentiation is dependent on MAPK (ERK1/2) signalling. *Development* **2001**, *128*, 5075–5084. [CrossRef]
20. Garcia, C.M.; Yu, K.; Zhao, H.; Ashery-Padan, R.; Ornitz, D.M.; Robinson, M.L.; Beebe, D.C. Signaling through FGF receptor-2 is required for lens cell survival and for withdrawal from the cell cycle during lens fiber cell differentiation. *Dev. Dyn.* **2005**, *233*, 516–527. [CrossRef]
21. Robinson, M.L. An essential role for FGF receptor signaling in lens development. *Semin. Cell Dev. Biol.* **2006**, *17*, 726–740. [CrossRef] [PubMed]
22. Wang, Q.; Stump, R.; McAvoy, J.W.; Lovicu, F.J. MAPK/ERK1/2 and PI3-kinase signalling pathways are required for vitreous-induced lens fibre cell differentiation. *Exp. Eye Res.* **2009**, *88*, 293–306. [CrossRef] [PubMed]
23. Iyengar, L.; Patkunanathan, B.; Lynch, O.T.; McAvoy, J.W.; Rasko, J.E.; Lovicu, F.J. Aqueous humour- and growth factor-induced lens cell proliferation is dependent on MAPK/ERK1/2 and Akt/PI3-K signalling. *Exp. Eye Res.* **2006**, *83*, 667–678. [CrossRef]
24. Xie, L.; Overbeek, P.A.; Reneker, L.W. Ras signaling is essential for lens cell proliferation and lens growth during development. *Dev. Biol.* **2006**, *298*, 403–414. [CrossRef] [PubMed]
25. Upadhya, D.; Ogata, M.; Reneker, L.W. MAPK1 is required for establishing the pattern of cell proliferation and for cell survival during lens development. *Development* **2013**, *140*, 1573–1582. [CrossRef]
26. Gong, X.; Wang, X.; Han, J.; Niesman, I.; Huang, Q.; Horwitz, J. Development of cataractous macrophthalmia in mice expressing an active MEK1 in the lens. *Investig. Ophthalmol. Vis. Sci.* **2001**, *42*, 539–548.
27. Shakespeare, T.I.; Sellitto, C.; Li, L.; Rubinos, C.; Gong, X.; Srinivas, M.; White, T.W. Interaction between Connexin50 and mitogen-activated protein kinase signaling in lens homeostasis. *Mol. Biol. Cell.* **2009**, *20*, 2582–2592. [CrossRef]
28. Le, A.C.; Musil, L.S. A novel role for FGF and extracellular signal-regulated kinase in gap junction-mediated intercellular communication in the lens. *J. Cell Biol.* **2001**, *154*, 197–216. [CrossRef]
29. Le, A.C.; Musil, L.S. FGF signaling in chick lens development. *Dev. Biol.* **2001**, *233*, 394–411. [CrossRef]
30. Iyengar, L.; Wang, Q.; Rasko, J.E.; McAvoy, J.W.; Lovicu, F.J. Duration of ERK1/2 phosphorylation induced by FGF or ocular media determines lens cell fate. *Differentiation* **2007**, *75*, 662–668. [CrossRef]
31. Chaffee, B.R.; Hoang, T.V.; Leonard, M.R.; Bruney, D.G.; Wagner, B.D.; Dowd, J.R.; Leone, G.; Ostrowski, M.C.; Robinson, M.L. FGFR and PTEN signaling interact during lens development to regulate cell survival. *Dev. Biol.* **2016**, *410*, 150–163. [CrossRef] [PubMed]
32. Zhao, H.; Yang, Y.; Rizo, C.M.; Overbeek, P.A.; Robinson, M.L. Insertion of a Pax6 consensus binding site into the alphaA-crystallin promoter acts as a lens epithelial cell enhancer in transgenic mice. *Investig. Ophthalmol. Vis. Sci.* **2004**, *45*, 1930–1939.
33. Lu, Z.; Jiang, Y.P.; Wang, W.; Xu, X.H.; Mathias, R.T.; Entcheva, E.; Ballou, L.M.; Cohen, I.S.; Lin, R.Z. Loss of cardiac phosphoinositide 3-kinase p110 alpha results in contractile dysfunction. *Circulation* **2009**, *120*, 318–325. [CrossRef]

34. Suzuki, A.; Yamaguchi, M.T.; Ohteki, T.; Sasaki, T.; Kaisho, T.; Kimura, Y.; Yoshida, R.; Wakeham, A.; Higuchi, T.; Fukumoto, M.; et al. T cell-specific loss of Pten leads to defects in central and peripheral tolerance. *Immunity* **2001**, *14*, 523–534. [PubMed]
35. Lam, P.T.; Padula, S.L.; Hoang, T.V.; Poth, J.E.; Liu, L.; Liang, C.; LeFever, A.S.; Wallace, L.M.; Ashery-Padan, R.; Riggs, P.K.; et al. Considerations for the use of Cre recombinase for conditional gene deletion in the mouse lens. *Hum. Genom.* **2019**, *13*, 10. [CrossRef]
36. DeRosa, A.M.; Mese, G.; Li, L.; Sellitto, C.; Brink, P.R.; Gong, X.; White, T.W. The cataract causing Cx50-S50P mutant inhibits Cx43 and intercellular communication in the lens epithelium. *Exp. Cell Res.* **2009**, *315*, 1063–1075. [CrossRef]
37. White, T.W.; Goodenough, D.A.; Paul, D.L. Targeted ablation of connexin50 in mice results in microphthalmia and zonular pulverulent cataracts. *J. Cell Biol.* **1998**, *143*, 815–825.
38. Schneider, C.A.; Rasband, W.S.; Eliceiri, K.W. NIH Image to ImageJ: 25 years of image analysis. *Nat. Methods* **2012**, *9*, 671–675.
39. Wiley, L.A.; Shui, Y.B.; Beebe, D.C. Visualizing lens epithelial cell proliferation in whole lenses. *Mol. Vis.* **2010**, *16*, 1253–1259.
40. Hoang, T.V.; Kumar, P.K.; Sutharzan, S.; Tsonis, P.A.; Liang, C.; Robinson, M.L. Comparative transcriptome analysis of epithelial and fiber cells in newborn mouse lenses with RNA sequencing. *Mol. Vis.* **2014**, *20*, 1491–1517.
41. Shi, Y.; De Maria, A.; Lubura, S.; Sikic, H.; Bassnett, S. The penny pusher: A cellular model of lens growth. *Investig. Ophthalmol. Vis. Sci.* **2015**, *56*, 799–809. [CrossRef] [PubMed]
42. Harding, C.V.; Hughes, W.L.; Bond, V.P.; Schork, P. Autoradiographic localization of tritiated thymidine in wholemount preparations of lens epithelium. *Arch. Ophthalmol.* **1960**, *63*, 58–65. [CrossRef] [PubMed]
43. Graw, J. Mouse models of congenital cataract. *Eye* **1999**, *13 (Pt. 3b)*, 438–444. [CrossRef]
44. Foster, F.S.; Zhang, M.; Duckett, A.S.; Cucevic, V.; Pavlin, C.J. In vivo imaging of embryonic development in the mouse eye by ultrasound biomicroscopy. *Invest. Ophthalmol. Vis. Sci.* **2003**, *44*, 2361–2366. [CrossRef] [PubMed]
45. Mu, J.; Slevin, J.C.; Qu, D.; McCormick, S.; Adamson, S.L. In vivo quantification of embryonic and placental growth during gestation in mice using micro-ultrasound. *Reprod. Biol. Endocrinol.* **2008**, *6*, 34. [CrossRef] [PubMed]
46. Brewitt, B.; Clark, J.I. Growth and transparency in the lens, an epithelial tissue, stimulated by pulses of PDGF. *Science* **1988**, *242*, 777–779. [CrossRef]
47. Brewitt, B.; Teller, D.C.; Clark, J.I. Periods of oscillatory growth in developing ocular lens correspond with cell cycle times. *J. Cell Physiol.* **1992**, *150*, 586–592. [CrossRef]
48. Giannone, A.A.; Li, L.; Sellitto, C.; White, T.W. Physiological Mechanisms Regulating Lens Transport. *Front. Physiol.* **2021**, *12*, 818649. [CrossRef]
49. Mathias, R.T.; Kistler, J.; Donaldson, P. The lens circulation. *J. Membr. Biol.* **2007**, *216*, 1–16. [CrossRef]
50. Gao, J.; Sun, X.; White, T.W.; Delamere, N.A.; Mathias, R.T. Feedback Regulation of Intracellular Hydrostatic Pressure in Surface Cells of the Lens. *Biophys. J.* **2015**, *109*, 1830–1839. [CrossRef]
51. Delamere, N.A.; Shahidullah, M.; Mathias, R.T.; Gao, J.; Sun, X.; Sellitto, C.; White, T.W. Signaling Between TRPV1/TRPV4 and Intracellular Hydrostatic Pressure in the Mouse Lens. *Investig. Ophthalmol. Vis. Sci.* **2020**, *61*, 58. [CrossRef]
52. Chen, Y.; Gao, J.; Li, L.; Sellitto, C.; Mathias, R.T.; Donaldson, P.J.; White, T.W. The Ciliary Muscle and Zonules of Zinn Modulate Lens Intracellular Hydrostatic Pressure Through Transient Receptor Potential Vanilloid Channels. *Investig. Ophthalmol. Vis. Sci.* **2019**, *60*, 4416–4424. [CrossRef]
53. Lu, Z.; Wu, C.Y.; Jiang, Y.P.; Ballou, L.M.; Clausen, C.; Cohen, I.S.; Lin, R.Z. Suppression of phosphoinositide 3-kinase signaling and alteration of multiple ion currents in drug-induced long QT syndrome. *Sci. Transl. Med.* **2012**, *4*, 131ra150. [CrossRef] [PubMed]
54. Wan, X.; Dennis, A.T.; Obejero-Paz, C.; Overholt, J.L.; Heredia-Moya, J.; Kirk, K.L.; Ficker, E. Oxidative inactivation of the lipid phosphatase phosphatase and tensin homolog on chromosome ten (PTEN) as a novel mechanism of acquired long QT syndrome. *J. Biol. Chem.* **2011**, *286*, 2843–2852. [CrossRef]
55. Takeuchi, K.; Gertner, M.J.; Zhou, J.; Parada, L.F.; Bennett, M.V.; Zukin, R.S. Dysregulation of synaptic plasticity precedes appearance of morphological defects in a Pten conditional knockout mouse model of autism. *Proc. Natl. Acad. Sci. USA* **2013**. [CrossRef]
56. Weston, M.C.; Chen, H.; Swann, J.W. Multiple roles for mammalian target of rapamycin signaling in both glutamatergic and GABAergic synaptic transmission. *J. Neurosci.* **2012**, *32*, 11441–11452. [CrossRef] [PubMed]
57. Xu, B.; Turner, S.D.; Hinton, B.T. Alteration of transporter activities in the epididymides of infertile initial segment-specific Pten knockout mice. *Biol. Reprod.* **2018**, *99*, 536–545. [CrossRef]
58. Morani, F.; Phadngam, S.; Follo, C.; Titone, R.; Aimaretti, G.; Galetto, A.; Alabiso, O.; Isidoro, C. PTEN regulates plasma membrane expression of glucose transporter 1 and glucose uptake in thyroid cancer cells. *J. Mol. Endocrinol.* **2014**, *53*, 247–258. [CrossRef]
59. Tang, X.; Powelka, A.M.; Soriano, N.A.; Czech, M.P.; Guilherme, A. PTEN, but not SHIP2, suppresses insulin signaling through the phosphatidylinositol 3-kinase/Akt pathway in 3T3-L1 adipocytes. *J. Biol. Chem.* **2005**, *280*, 22523–22529. [CrossRef]
60. Huang, F.F.; Zhang, L.; Wu, D.S.; Yuan, X.Y.; Yu, Y.H.; Zhao, X.L.; Chen, F.P.; Zeng, H. PTEN regulates BCRP/ABCG2 and the side population through the PI3K/Akt pathway in chronic myeloid leukemia. *PLoS ONE* **2014**, *9*, e88298. [CrossRef]
61. Huang, Z.; Hu, Z.; Xie, P.; Liu, Q. Tyrosine-mutated AAV2-mediated shRNA silencing of PTEN promotes axon regeneration of adult optic nerve. *PLoS ONE* **2017**, *12*, e0174096. [CrossRef]

cells

MDPI

Article

Levels and Modifications of Both Lens Fiber Cell Connexins Are Affected in Connexin Mutant Mice

Oscar Jara, Peter J. Minogue, Viviana M. Berthoud and Eric C. Beyer *

Department of Pediatrics, University of Chicago, Chicago, IL 60637, USA
* Correspondence: ecbeyer@uchicago.edu

Abstract: In the lens, cell homeostasis and transparency are supported by intercellular communication facilitated by the channels formed of connexin46 (Cx46) and connexin50 (Cx50). Mutations of these connexins are linked to inherited cataracts. We studied the levels and the variations in electrophoretic mobilities of the immunoreactive Cx46 and Cx50 bands between 1 and 21 days after birth in the lenses of wild-type mice and homozygous animals from two different mouse models of connexin-linked cataracts (Cx46fs380 and Cx50D47A). In Cx50D47A mice, the expression of the mutant Cx50 reduced the normal phosphorylation of the co-expressed wild-type Cx46. In both models, levels of the mutant connexin and the co-expressed wild-type connexin decayed more rapidly than in wild-type mice but with different time courses. In the Cx46fs380 mice, modeling suggested that Cx50 degradation could be explained by the mixing of mutant Cx46 with wild-type Cx50. However, in Cx50D47A mice, similar modeling suggested that mixing alone could not explain the decrease in Cx46 levels. These data highlight the complex influences between two connexin proteins expressed in the same cell, some of which occur through direct mixing, while others occur indirectly, as in Cx50D47A mice, where the expression of the mutant connexin causes endoplasmic reticulum stress and impaired differentiation.

Keywords: connexin; cataracts; lens; connexin50; connexin46

1. Introduction

Communication between cells is a critical process in all tissues within the body. Direct intercellular communication is facilitated by the passage of ions and small molecules through the channels contained in gap junctions. A gap junction channel is formed by the docking of two hemichannels (one in the plasma membrane of each of the apposing cells) that each contain six subunit proteins called connexins (reviewed in [1]). The connexins form a closely related family with 21 different members expressed in humans and 20 in mice [2,3]. Although an intercellular channel can be formed by one connexin subtype, many cells express more than one connexin subtype, allowing for the formation of channels containing combinations of different connexin subtypes.

The lens is a transparent and avascular organ formed by epithelial and fiber cells. During development, epithelial cells in the equatorial region differentiate into fiber cells, a process that involves cell elongation and the loss of the organelles. Gap junctions and the intercellular communication that they support are critical for the survival of the lens and the maintenance of transparency because they are key components of the internal circulation of water and ions that supports lens homeostasis [4]. While most studies have focused on the importance of gap junctions for normal physiology and the development of disease, the lens is also an excellent system to study the cell biology and biochemistry of the connexin proteins under normal (physiological) and pathological conditions. The fiber cells that comprise the bulk of the lens predominantly express two connexins, connexin46 (Cx46) and connexin50 (Cx50). At least some of the gap junction hemichannels contain both connexins [5,6]. Therefore, the lens is also an excellent system with which to study interactions between co-expressed connexins.

Mutations in the genes encoding Cx46 and Cx50 cause cataracts [7]. We have been studying two mouse models that mimic human congenital cataracts, one expressing a frameshift mutation in Cx46 (Cx46fs380) [8] and the other expressing a missense mutation in Cx50 (Cx50D47A) [9]. In both models, gap junction-mediated fiber cell coupling is reduced (when studied at 2–3 months of age) and cataracts develop through calcium accumulation and precipitation [10–12]. However, the timing of cataract development is different between these mouse models. In both homozygous and heterozygous Cx50D47A mice, lens opacities are detectable at 1 month of age. In contrast, in Cx46fs380 mice, opacities are not observed until about 2 months in homozygotes and 4 months (or later) in heterozygotes. At any given age, the cataracts are more severe in Cx50D47A mice than in Cx46fs380 mice. While the sizes of the lenses are similar in wild-type and Cx46fs380 mice, differentiation and growth are impaired in Cx50D47A mutant lenses. Interestingly, even though only one connexin carries a mutation, the levels of both Cx46 and Cx50 are severely reduced in heterozygous and homozygous of both mouse lines [8–10,12].

Most of our previous quantitative studies of connexin abundance in lenses of the connexin mutant mice were performed on mice that were at least one month old. The current study was designed to evaluate the time-course of changes in Cx46 and Cx50 abundance at earlier post-natal ages in wild-type mice and in homozygotes from these two mutant mouse lines. We have also examined how the expression of a mutant connexin in the lens affects the post-translational modifications of the co-expressed wild-type connexin (as detected by changes in electrophoretic mobility patterns).

2. Materials and Methods

2.1. Mice

Wild-type and homozygous Cx50D47A mutant mice (also known as *No2* or ENU-326) [13] were maintained in the C3H mouse strain. Wild-type and homozygous Cx46fs380 mice were maintained on a mixed 129/C57BL6 background, as previously described [8]. All experiments were performed using animals that were wild-type or homozygous for the mutant connexin. All animal procedures were performed according to protocols approved by the University of Chicago Animal Care and Use Committee.

2.2. Immunoblotting

Lenses were harvested at 1, 4, 7, 14, and 21 days after birth in phosphate-buffered saline pH 7.4 (PBS). After dissection, lenses were homogenized in PBS containing 20 mM NaF, 10 mM Na_3VO_4, 2 mM phenylmethylsulfonyl fluoride (PMSF), 4 mM EDTA, and 1 tablet/7 mL cOmplete EDTA-free protease inhibitor cocktail (Roche Applied Science, Indianapolis, IN, USA), using a glass–glass homogenizer, followed by sonication. Homogenates were kept at −80 °C until use. The concentration of proteins in the homogenates was determined using the BioRad Protein Assay (BioRad, Hercules, CA, USA), a method based on the Bradford dye-binding procedure [14].

Immunoblots were performed as previously described [15–18]. Homogenate aliquots containing equal amounts of protein (100 μg for detection of Cx46 and 30 μg for detection of Cx50) were loaded in each lane. Proteins were resolved in sodium dodecyl sulfate-containing 8% polyacrylamide gels. After electrotransfer of the proteins onto Immobilon P membranes (Millipore, Bedford, MA, USA) using a wet transfer apparatus, membranes were stained with Ponceau S to confirm equivalence of loading and transfer, as previously performed [15]. Membranes were blocked with 5% non-fat dry milk in Tris buffered saline, pH 7.4, and then incubated with previously described affinity purified anti-Cx50 antibodies (directed against the carboxyl terminus of Cx50 (amino acids 231–433) [17] or previously described anti-Cx46 antibodies (directed against a synthetic peptide sequence from within the intracellular loop of mouse Cx46 (amino acids 109–129) [9] overnight at 4 °C. Membranes were rinsed and incubated with peroxidase-conjugated goat anti-rabbit IgG antibodies (catalog number: 111-035-144; lot number: 157038; Jackson ImmunoResearch Laboratories, Inc., West Grove, PA, USA) for 1 hour at room temperature. The binding

of secondary antibodies was detected using enhanced chemiluminescence GE Healthcare Amersham ECL Western Blotting Detection Reagents (ThermoFisher Scientific, Waltham, MA, USA).

The intensity of the bands was analyzed by densitometry using Adobe Photoshop (Adobe Systems, Inc., San Jose, CA, USA). Results are reported in arbitrary units that represent the density of the immunoreactive connexin bands. Comparisons are facilitated by loading a constant amount of lens protein in each lane. We have previously shown that this is more accurate for the assessment of changes in lens proteins than normalization to a "housekeeping" protein since there are substantial variations in the levels of those proteins with lens development, aging, and disease [15]. Three sets of independent experiments containing all ages were performed. Statistical significance was assessed using ANOVA; $p < 0.05$ was considered significant.

All studies were performed by comparing connexin levels in wild-type and mutant mice of the same line to avoid any confounding effects related to genetic differences. However, the levels of Cx46 and Cx50 were similar in homogenates of 1-month-old mice of the 129/C57BL6 and the C3H backgrounds (Supplementary Figure S1), suggesting that there are no intrinsic differences in the levels of Cx46 or Cx50 between the mouse lines used in this study.

2.3. Alkaline Phosphatase Treatment

Lenses from 7-day-old Cx50D47A and Cx46fs380 mice were dissected in PBS containing 1 tablet/7 mL cOmplete EDTA-free protease inhibitor cocktail (Roche Applied Science, Indianapolis, IN, USA) and 2 mM PMSF. Lenses were homogenized in the dissection solution followed by sonication. Homogenates were stored at −80 °C until use. Aliquots containing 80 μg of total proteins (to evaluate Cx46) or 20 μg total proteins (to evaluate Cx50) were incubated with or without calf intestinal alkaline phosphatase (M182A; Promega, Madison, WI, USA) overnight at 37 °C in 50 mM Tris-HCl (pH 9.3 at 25 °C), 1 mM $MgCl_2$, 0.1 mM $ZnCl_2$, and 1 mM spermidine. Then, alkaline phosphatase-treated and untreated samples were subjected to immunoblotting as described above.

2.4. Curve Fitting for The Decrease in Connexin Levels

The average densitometric values of the relative density of the immunoreactive bands obtained in three independent sets of experiments were fit to a single exponential of the form: $y = C^{*}e^{-k^{*}t}$, where "C" is the estimated initial densitometric value at day 0, "k" is the rate of decay, and "t" is time (in days) using GraphPad Prism version 8.0.1 for Windows (GraphPad Software, San Diego, CA, USA). To model the degradation of the co-expressed wild-type connexin by its "mixing" with the mutant connexin, we assumed that they could mix in different proportions (containing between 10 and 90% of each connexin). We calculated the values from these two equations for each of the time points, multiplied by different proportions (between 0.1:0.9 and 0.9:0.1), and generated curve fits after adding the values calculated in this manner.

3. Results

3.1. Levels and Electrophoretic Mobility Patterns of Lens Fiber Connexins Change with Age in Lenses of Wild-Type and Cx46fs380 Mice

We used immunoblotting to determine the electrophoretic migration and abundance of both Cx46 and Cx50 in homogenates prepared from the lenses of homozygous Cx46fs380 mice and their wild-type counterparts at different ages between 1 and 21 days after birth.

In the lenses of wild-type mice (mixed 129/C57BL6 background), Cx46 was detected throughout the time course as 2 prominent bands of 46 and 52 kDa (labeled Cx46-1 and Cx46-2, respectively, in Figure 1A). However, the relative proportion of Cx46 contained in the slower migrating band (Cx46-2) became more prominent in samples obtained from older mice. By 21 days, Cx46-2 accounted for 77% of the total Cx46 (Figure 1E).

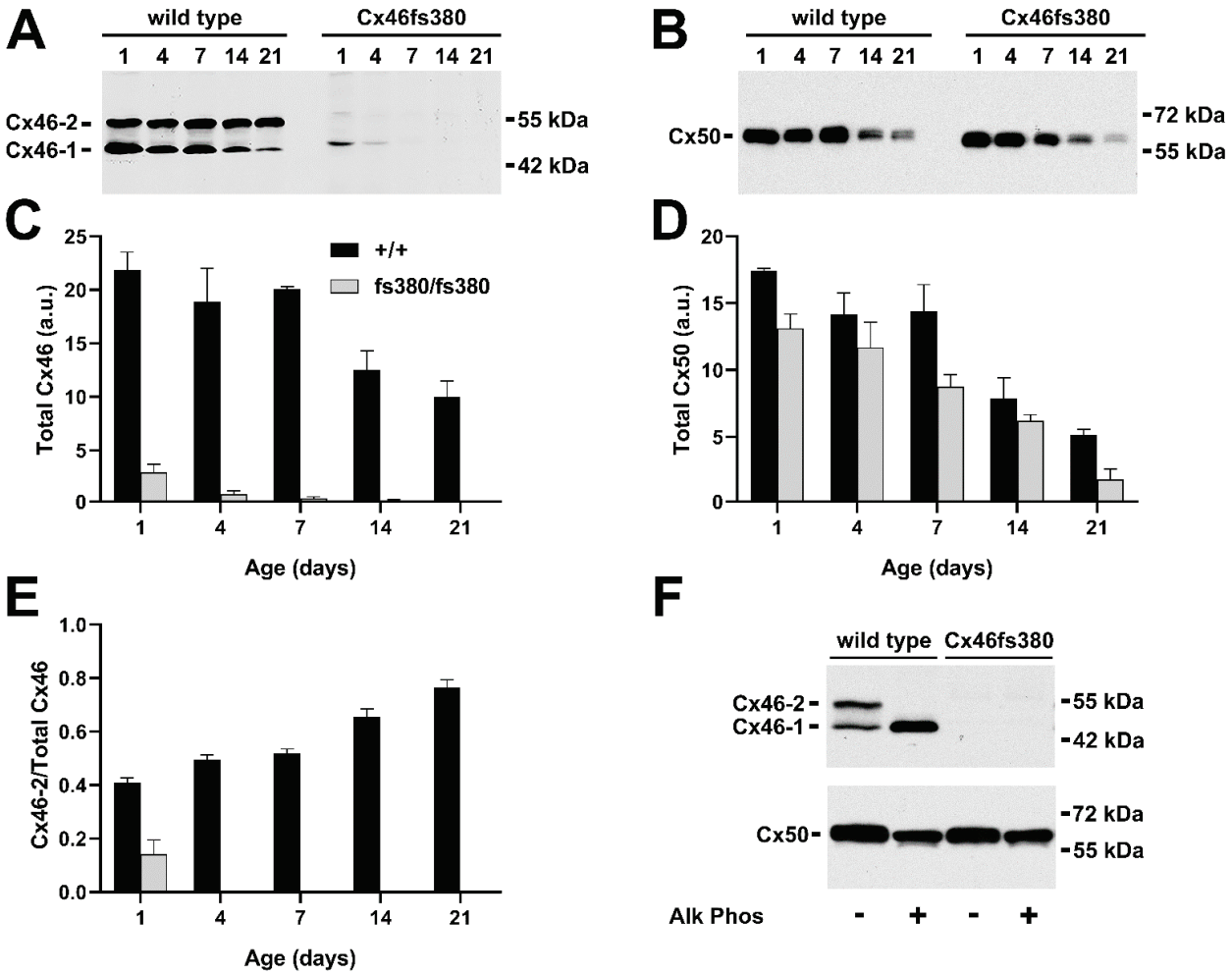

Figure 1. Immunoblot detection and quantification of Cx46 and Cx50 at various post-natal ages in wild-type and Cx46fs380 mice. (**A**,**B**) Immunoblots of Cx46 (**A**) and Cx50 (**B**) in lens homogenates from 1-, 4-, 7-, 14-, and 21-day-old wild-type and homozygous Cx46fs380 mice (129/C57BL6 background). The two major Cx46 bands are indicated as Cx46-1 and Cx46-2. The migration positions of the molecular mass markers are indicated on the right. (**C**,**D**) Graphs show the mean (bar) + SEM of the densitometric values of the immunoreactive Cx46 bands (**C**) and Cx50 bands (**D**) obtained from three independent experiments expressed in arbitrary units (a.u.). (**E**) Graph shows the mean (bar) + SEM of the ratio of Cx46-2 to total Cx46 from densitometric analysis of three independent experiments. (**F**) Immunoblot detection of Cx46 (upper panel) and Cx50 (lower panel) in homogenates from the lenses of 7-day-old wild-type or homozygous Cx46fs380 mice after incubation in the absence or presence of alkaline phosphatase (Alk Phos). The two major Cx46 bands are indicated as Cx46-1 and Cx46-2. The migration positions of the molecular mass markers are indicated on the right.

Cx50 was detected as a broad band of 60–65 kDa between post-natal days 1 and 7 (Figure 1B). At 14 and 21 days, Cx50 appeared as a doublet of bands that migrated similarly to the slowest electrophoretic mobility Cx50 bands detected at earlier ages. Compared to the abundance at post-natal day 1, the total abundance of Cx46 decreased by 54.3%, and the total abundance of Cx50 decreased by 70.1% over the first 21 days after birth (Figure 1C,D). Since the gels were normalized by equal protein loading, some of this decrease may represent the growth of the lens and an increase in the abundance of soluble proteins (crystallins) such that they represented a greater proportion of the lens proteins relative to the connexins.

In lenses from homozygous Cx46fs380 mice, the abundance of Cx46 was much less than that in wild-type mice, even at 1 day of age (13.5%), and the levels became almost

undetectable after post-natal day 4 (Figure 1A,C). At days 1 and 4, Cx46 was predominantly composed of a band with an estimated M_r of 48 kDa, which closely matches the predicted molecular mass of the Cx46fs380 mutant protein (49 kDa). A small proportion of Cx46 was detected as a slower migrating band (~55 kDa) at day 1 (14%), but it was not detectable at later ages (Figure 1A,E). In lenses from Cx46fs380 mice, the Cx50 immunoreactive bands appeared generally similar to those in the wild-type mice (Figure 1B); however, the total abundance of Cx50 decreased more severely with age in the mutant mice than in the wild-types (Figure 1D, $p < 0.05$ at day 21). No Cx46 or Cx50 bands were detected at lower M_r, implying that these samples did not contain cleaved products of Cx46 or Cx50.

3.2. Phosphorylation of Cx46 and Cx50 in Lenses of Wild-Type and Cx46fs380 Mice

Since both Cx46 and Cx50 are phosphoproteins, we tested whether the different electrophoretic forms of these proteins in wild-type and Cx46fs380 lenses represented posttranslational modification by phosphorylation. We treated homogenates prepared from 7-day-old lenses with alkaline phosphatase and then detected Cx46 and Cx50 by immunoblotting (Figure 1F). This treatment removed the slower mobility form (Cx46-2) detected in untreated wild-type samples and greatly increased the abundance of the faster electrophoretic form (Cx46-1). However, not all of the alkaline phosphatase treated Cx46 migrated identically to Cx46-1; some immunoreactive material migrated a little more slowly (Figure 1F). This observation suggested that Cx46-2 represented phosphorylated Cx46 forms that contained alkaline phosphatase sensitive phosphorylation sites, and that the progressive relative increase in this band in wild-type lenses represented an increasing proportion of phosphorylated Cx46 with age. No Cx46 bands were detected in homogenates of Cx46fs380 lenses in either untreated or alkaline phosphatase treated samples (Figure 1F). For Cx50, alkaline phosphatase treatment caused a small shift in the electrophoretic mobility of immunoreactive Cx50 material in homogenates of both wild-type and homozygous Cx46fs380 lenses, suggesting that both genotypes contained some alkaline phosphatase-sensitive phosphorylated Cx50.

3.3. Exponential Decay of Cx46 and Cx50 Levels in Lenses of Wild-Type and Cx46fs380 Mice

To further analyze the reductions in connexin levels in the wild-type and homozygous Cx46fs380 lenses, we quantified the data from three independent immunoblot experiments and normalized the densities to the value at post-natal day 1 for the corresponding experiment. Then, the data were fit to single exponential decay curves of the form $y = C^*e^{-k^*t}$ (Figure 2). This analysis showed that in the wild-type animals, the abundances of both Cx46 and Cx50 declined gradually with decay constants (k) of 0.0387 day^{-1} for Cx46 (Figure 2A) and 0.0574 day^{-1} for Cx50 (Figure 2C). As expected, the decay of Cx46 was much faster in the homozygous Cx46fs380 mutant lenses, with a k = 0.4807 day^{-1} (Figure 2B). The decay of Cx50 was also accelerated in the mutant lenses, with a k = 0.073 day^{-1} (Figure 2D).

We hypothesized that the increased disappearance of Cx50 (a wild-type connexin) in the lenses of homozygous Cx46fs380 mice might result from formation of mixed oligomers between Cx50 and the mutant Cx46 destined for degradation. To test this, we modeled the decay of Cx50 in the mutant lenses by adding different proportions of the decay curves for Cx50 in wild-type lenses (Figure 2C) and for Cx46 in the mutant lenses (Figure 2B). We obtained a rather close fit to the actual Cx50 data (presented in Figure 2D) when we used a mixing model containing 90% wild-type Cx50 and 10% mutant Cx46 with a k = 0.061 day^{-1} (Figure 2E). (Compare the red curve representing the values predicted by the model and the blue curve representing the experimental data in Figure 2E).

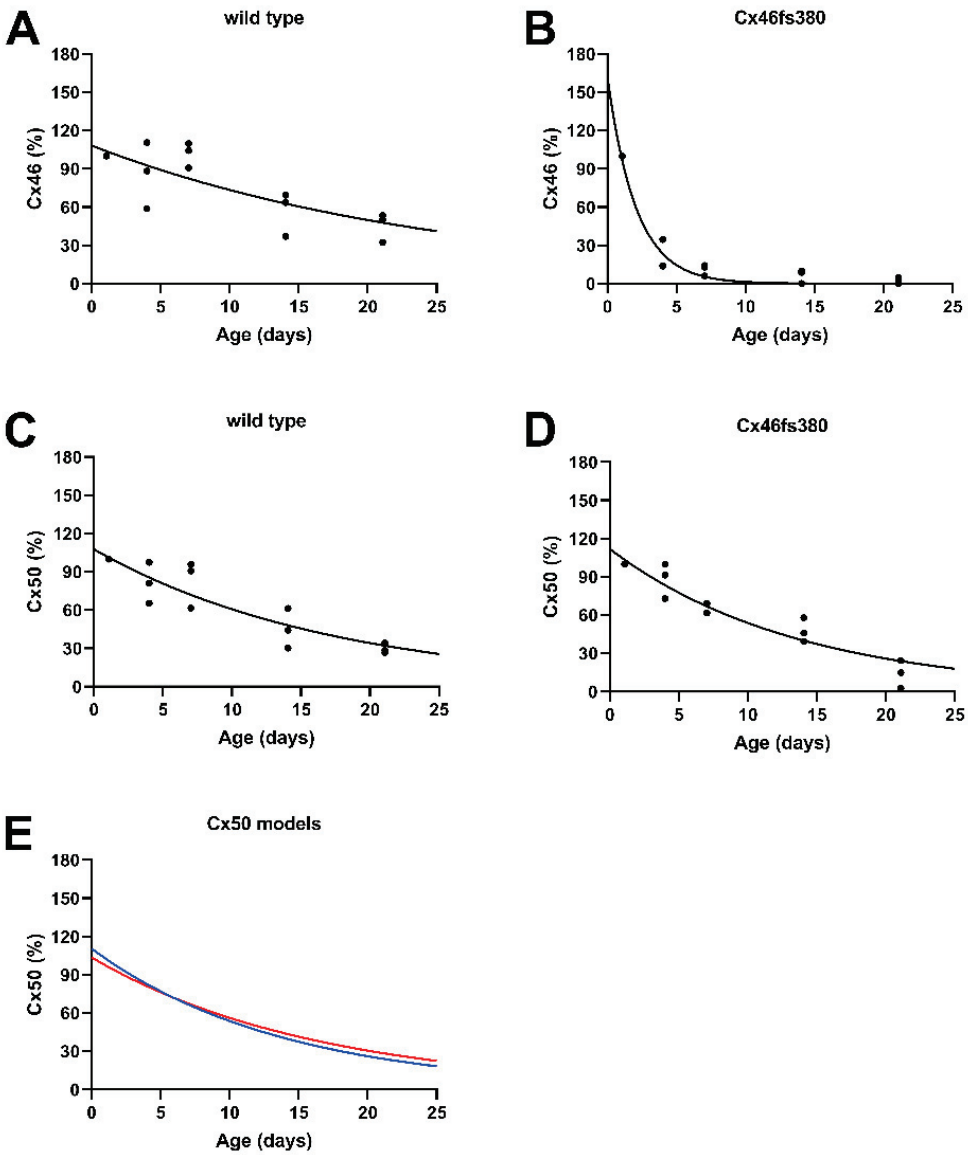

Figure 2. The age-dependent decreases in total levels of Cx46 and Cx50 in the lenses of wild-type and homozygous Cx46fs380 mice could be fit to single exponential curves. (**A**–**D**) The data from the three independent sets of immunoblots of connexin levels shown in Figure 1C,D were fit to single exponential decay curves of the form $y = C*e^{-k*t}$. (**A**,**B**) The data for Cx46 levels were best fit by $y = 108.216*e^{-0.0387*t}$ ($r^2 = 0.854$) in wild-type lenses (**A**), and by $y = 161.174*e^{-0.4807*t}$ ($r^2 = 0.997$) in Cx46fs380 lenses (**B**). (**C**,**D**) The data for Cx50 levels in wild-type lenses (**C**) were best fit by $y = 107.677*e^{-0.0574*t}$ ($r^2 = 0.9653$), and in homozygous Cx46fs380 lenses (**D**), they were best fit by $y = 111.807*e^{-0.073*t}$ ($r^2 = 0.9538$). (**E**) The impact of co-oligomerization of wild-type Cx50 with Cx46fs380 upon Cx50 decay in the homozygous Cx46fs380 lenses was modeled by adding different proportions of the curves from panels C and B. The best fit curve was generated using values corresponding to 90% wild-type Cx50 and 10% mutant Cx46, yielding the curve indicated by the red line ($y = 110.45*e^{-0.07*t}$). It is a rather close match to the curve fit to the actual Cx50 data shown in panel D (blue line).

3.4. Levels and Electrophoretic Mobility Patterns of Lens Fiber Connexins Change with Age in Lenses of Wild-Type and Cx50D47A Mice

We also used immunoblotting to determine the abundance and electrophoretic migration of Cx46 and Cx50 in lens homogenates from homozygous Cx50D47A mice and their wild-type counterparts at different ages between 1 and 21 days after birth.

In the lenses of wild-type mice (C3H background), the changes in abundances and in the different electrophoretic mobility forms of Cx46 and Cx50 were generally similar to our observations in the wild-type mouse lenses on the mixed 129/C57BL6 background. Cx46 was detected as two prominent bands of about 46 and 52 kDa (Cx46-1 and Cx46-2 in Figure 3A). The relative proportion of Cx46-2 increased in samples obtained from older mice; by 21 days, Cx46-2 accounted for 89% of the total Cx46 (Figure 3A,E). At post-natal day 1, Cx50 was detected as a broad band of 60-65 kDa. Over subsequent days, the electrophoretic mobility of immunoreactive Cx50 decreased and multiple separate bands were resolved in some samples (Figure 3B). Over the first 21 days of post-natal life, the total abundance of Cx46 decreased by 62%, and the total abundance of Cx50 decreased by 80% with respect to the levels detected at post-natal day 1 (Figure 3C,D).

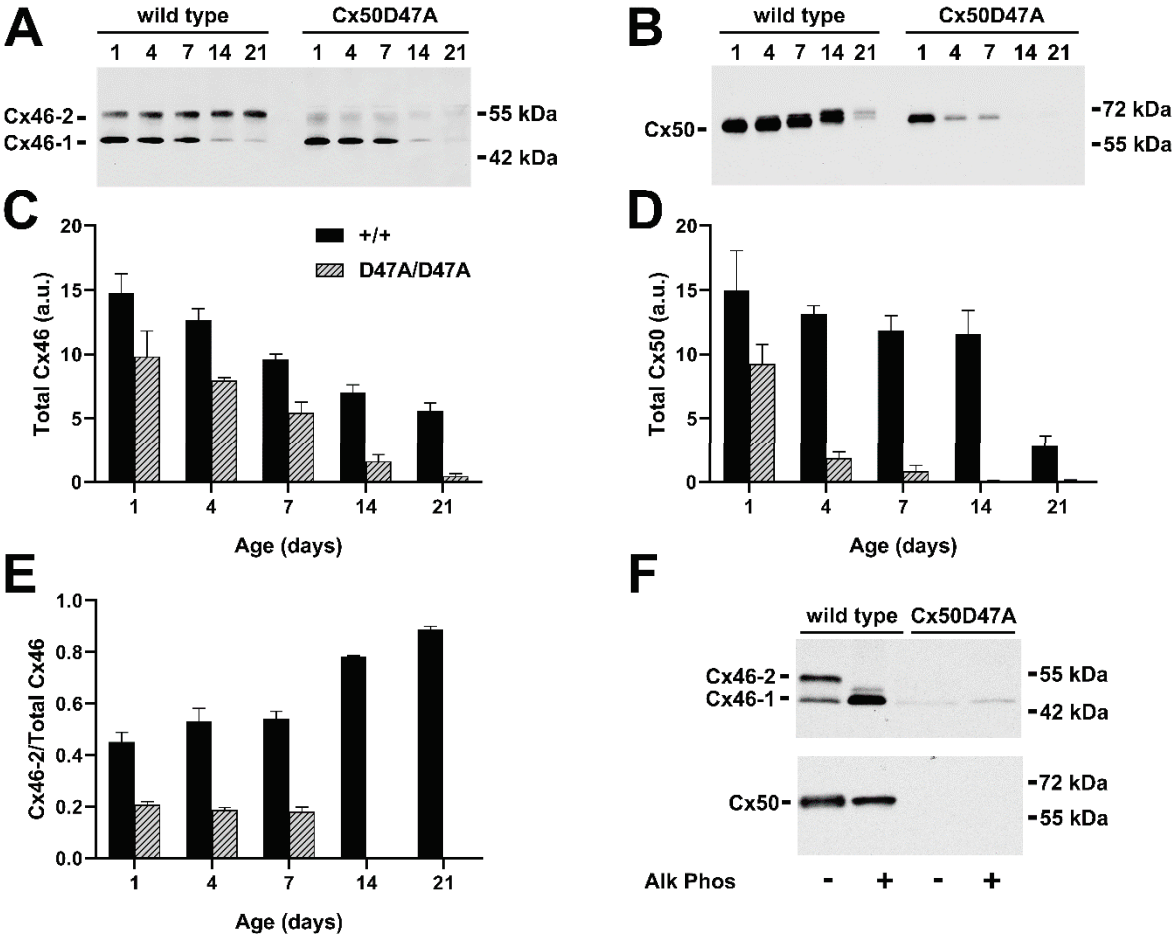

Figure 3. Immunoblot detection and quantification of Cx46 and Cx50 at various post-natal ages in wild-type and Cx50D47A mice. (**A**,**B**) Immunoblots of Cx46 (**A**) and Cx50 (**B**) in lens homogenates from 1-, 4-, 7-, 14-, and 21-day-old wild-type and homozygous Cx50D47A mice (C3H background). The two major Cx46 bands are indicated as Cx46-1 and Cx46-2. The migration positions of the molecular mass markers are indicated on the right. (**C**,**D**) Graphs show the mean (bar) + SEM of the densitometric values of the immunoreactive Cx46 bands (**C**) and Cx50 bands (**D**) obtained from three independent experiments expressed in arbitrary units (a.u.). (**E**) Graph shows the mean (bar) + SEM of the ratio of Cx46-2 to total Cx46 from densitometric analysis of three independent experiments. (**F**) Immunoblot detection of Cx46 (upper panel) and Cx50 (lower panel) in homogenates from the lenses of 7-day-old wild-type or homozygous Cx50D47A mice after incubation in the absence or presence of alkaline phosphatase (Alk Phos). The two major Cx46 bands are indicated as Cx46-1 and Cx46-2. The migration positions of the molecular mass markers are indicated on the right.

In lenses from homozygous Cx50D47A mice, Cx46 was predominantly detected at the electrophoretic mobility of Cx46-1, representing ~80% of total Cx46 at all ages where substantial amounts of Cx46 were detectable (Figure 3A,E). Additionally, the total abundance of Cx46 decreased much faster in the homozygous Cx50D47A mice than in the wild-type counterparts (Figure 3C). In contrast to the changes in electrophoretic mobility of Cx50 in wild-type lenses, the mobility of Cx50 bands did not appear different at any of the ages studied in the homozygous Cx50D47A lenses (Figure 3B). The total abundance of Cx50 decreased much more rapidly in the homozygous than in the wild-type animals; it was nearly undetectable at 14 and 21 post-natal days in the Cx50D47A mutant mice (Figure 3B,D). We did not detect Cx46 or Cx50 bands at lower M_r, suggesting the absence of cleaved forms of Cx46 or Cx50 in these samples.

3.5. Phosphorylation of Cx46 and Cx50 in Lenses of Wild-Type and Cx50D47A Mice

The alkaline phosphatase treatment of homogenates prepared from the lenses of wild-type mice of the C3H background produced results that were generally similar to those obtained in lenses of wild-type mice of the mixed 129/C57BL6 background (Figure 3F). The slower migrating band of Cx46 (Cx46-2) present in the untreated sample of wild-type lenses collapsed into the faster migrating band (Cx46-1), consistent with Cx46-2 representing phosphorylated forms (Figure 3F). In these experiments, we clearly detected a Cx46 band of intermediate mobility (just above Cx46-1) that may represent Cx46 with a different post-translational modification or modified by phosphate that was not removed by the alkaline phosphatase treatment (Figure 3F). The breadth of the Cx50 band was somewhat reduced by the treatment with alkaline phosphatase (Figure 3F). In lens samples from homozygous Cx50D47A mice, the major Cx46 band (Cx46-1) was weakly detected, but unaffected in mobility or intensity by alkaline phosphatase treatment. Comparable gel loading and exposure yielded no detectable Cx50 bands in the untreated or alkaline phosphatase-treated sample from a Cx50D47A lens homogenate.

Taken together with the images shown in Figure 3A,B, these results imply that phosphorylation of Cx46 (and likely Cx50) is greatly reduced in the lenses of Cx50D47A mutant mice as compared to wild-type animals.

3.6. Exponential Decay of Cx46 and Cx50 Levels in Lenses of Wild-Type and Cx50D47A Mice

To test whether the reductions in connexin levels in the lenses of wild-type and homozygous Cx50D47A mice presented in Figure 3 also followed a single exponential, we normalized the densities of the immunoreactive bands obtained from three independent experiments to the value obtained at post-natal day 1 for the corresponding experiment and fitted the values to a curve of the form $y = C^*e^{-k^*t}$. For the wild-type mice in the C3H background, this analysis revealed that the abundances of both Cx46 and Cx50 declined gradually with decay constants of 0.0477 day^{-1} for Cx50 (Figure 4A) and 0.0513 day^{-1} for Cx46 (Figure 4C). These decay constants were similar to those obtained for lenses of wild-type mice from the mixed 129/C57BL6 background. In comparison, in the homozygous Cx50D47A mutants, the decay of Cx50 was much faster with a k = 0.4665 day^{-1} (Figure 4B). The decay of Cx46 was also accelerated in the mutant lenses with a k = 0.1151 day^{-1} (Figure 4D).

We also assessed whether the degradation of wild-type Cx46 in the Cx50D47A mice could be explained by mixing of wild-type Cx46 with the mutant Cx50 by adding different proportions of the curves that had been fit to the wild-type Cx46 and the mutant Cx50 data. However, we were unable to identify a combination of the two curves that fit the data very closely. Figure 4E shows the curve obtained with the combination that approximated better to the data (60% Cx46 and 40% mutant Cx50, illustrated with a red line, k = 0.072), but it still has a poor correspondence to the curve fit to the actual Cx46 data (blue line). A better fit for the Cx46 data was obtained only if the proportion of mutant and wild-type connexins was varied at each time point; this required changing the proportion of mixing

from 86% wild-type Cx46 and 14% mutant Cx50D47A at post-natal day 1 to 30% wild-type Cx46 and 70% mutant Cx50 at post-natal day 21 (matching the blue line in Figure 4E).

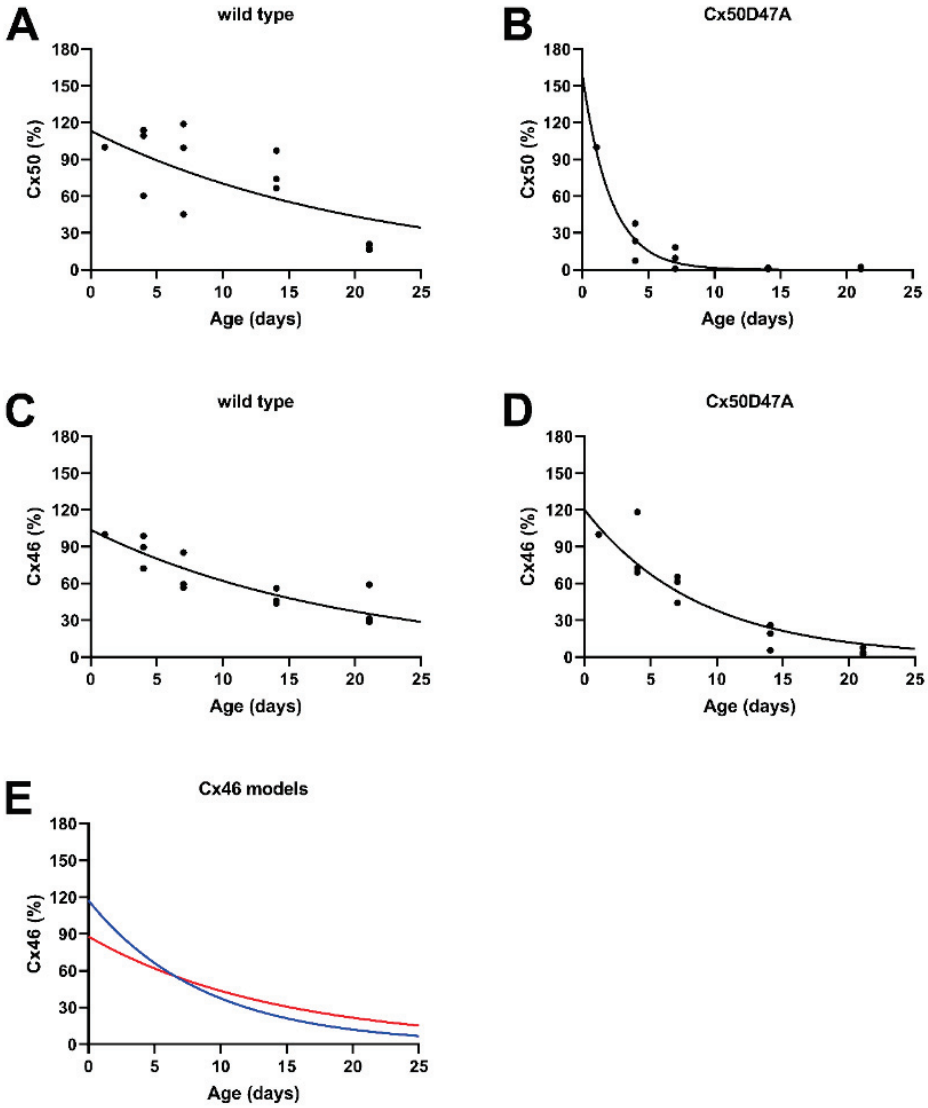

Figure 4. The data regarding the age-dependent decreases in total levels of Cx46 and Cx50 in the lenses of wild-type and homozygous Cx50D47A mice could be fit to single exponential curves. (**A**–**D**) The data from the three independent sets of immunoblots of connexin levels shown in Figure 3C,D were fit to single exponential decay curves of the form $y = C*e^{-k*t}$. (**A**) For Cx50 levels in wild-type (C3H background) mice, the data were best fit by $y = 113*e^{-0.0477*t}$ ($r^2 = 0.7333$). (**B**) For Cx50 levels in Cx50D47A mice, the data were best fit by $y = 159.095*e^{-0.4665*t}$ ($r^2 = 0.9944$). (**C**) For Cx46 levels in wild-type mice (C3H background), the data were best fit by $y = 103.7676*e^{-0.0513*t}$ ($r^2 = 0.9516$). (**D**) For Cx46 levels in Cx50D47A mice, the data were best fit by $y = 120.179*e^{-0.1151*t}$ ($r^2 = 0.99418$). (**E**) The impact of co-oligomerization between wild-type Cx46 and Cx50D47A upon Cx46 decay in the Cx50D47A mice was modeled by adding different proportions of the values from the curves shown in panels C and B. This approach did not yield a very satisfactory match. The example shown as a red line represents a curve generated using 60% wild-type Cx46 (**C**) and 40% mutant Cx50 (**B**). The curve fit to the actual Cx46 data (from panel **D**) is shown as a blue line (which could also be generated by progressively reducing the relative proportion of wild-type Cx46 from 86% at day 1 to 30% at day 21).

4. Discussion

In the current study, the total levels of both Cx46 and Cx50 decreased between 1 and 21 days after birth in wild-type animals. Because the gels were loaded with equal amounts of lens protein in each lane, these data show a decrease in the relative abundance of the connexins compared to total lens proteins (not necessarily a change in the absolute connexin abundance). This relative decrease likely results from the significant increase in abundance of other lens proteins (mainly crystalllins) at these ages, associated with the lens growth that occurs over this period. Although unlikely, we cannot discard the possibility that some of the connexins may have undergone full degradation as the lens continued to grow over the time frame of our studies.

The change in the electrophoretic banding pattern of the lens fiber cell connexins in wild-type lenses with increasing age likely represents post-translational "maturation" of the proteins. This interpretation is substantiated by the results of the alkaline phosphatase treatment experiments, which show that most of the immunoreactive connexin collapsed into the band with the fastest electrophoretic mobility. In addition, these experiments indicate that the change in the electrophoretic mobility primarily represents the phosphorylation of the proteins. Both Cx46 and Cx50 are known to be phosphoproteins [6,19–24]. Previous immunoblotting experiments using ovine, bovine, and rat samples have shown that alkaline phosphatase treatment modifies the electrophoretic mobility of immunoreactive Cx46 and Cx50 [6,19–22]. In rat lenses, Cx46 is mainly detected as two bands of 46 and 54 kDa; both forms are present at embryonic ages, but the slower (phosphorylated) form predominates in young adults [21]. Our alkaline phosphatase experiments also showed the presence of immunoreactive Cx46 with a modification that was not sensitive to alkaline phosphatase treatment. This may not be surprising since other modifications (including acetylation, nitrosylation, and carbamylation) have been detected in Cx46 (reviewed in Retamal and Altenberg [25]). In Cx43, some phosphates are removed by acid phosphatase [26].

Our previous studies in transfected cells have elucidated cell biological aspects of the defects conferred by these connexin mutations. The Cx50D47A mutant is largely retained in the biosynthetic pathway [27], and, therefore, it forms few (if any) gap junctions at the plasma membrane. Immunofluorescence performed using flatmounts of the lens epithelium from Cx50D47A mice confirms that most of the immunoreactive Cx50 localizes in the cytoplasm [9]. For Cx46fs380, the abnormal cytoplasmic tail created by the frameshift mutation generates a retrieval/retention signal in the mutant protein [28], limiting the formation of gap junctions. In the current study, we detected a small amount of Cx46fs380 protein by immunoblotting at post-natal day 1 (Figure 1A). Moreover, some Cx46fs380 was detected at a slower mobility (~55 kDa), consistent with it being phosphorylated like the wild-type protein. This observation is consistent with our previous observation of a near absence of Cx46 gap junctional plaques in 1-month-old mice that were homozygous for Cx46fs380 [8]. In the Cx50D47A lenses, Cx46 also seemed to be post-translationally modified as some of it migrated with an M_r of ~55 kDa.

The faster decrease in levels of the mutant connexin in homozygous Cx46fs380 and Cx50D47A lenses compared with the decrease in Cx46 and Cx50 in the corresponding wild-type lenses most likely represents the increased degradation of the mutant proteins. Since both of the mutants are retained in components of the biosynthetic pathway, it is likely that they are degraded as the cells differentiate and degrade their organelles to become mature lens fiber cells.

In both mutant mouse lines, the expression of a mutant lens fiber cell connexin affected the co-expressed wild-type connexin. However, some of the effects (and likely the mechanisms underlying them) were different.

In Cx46fs380 mice, the electrophoretic mobility of the different Cx50 forms appeared largely unaffected by the expression of the Cx46 mutant (Figure 1B). In contrast, in Cx50D47A lenses only a very small fraction of Cx46 was detected as the Cx46-2 form (Figure 3A), implying that expression of the mutant Cx50 in the lens had major effects on the post-translational modification of Cx46.

Cx46 and Cx50 can form mixed (heteromeric) channels, as shown by their co-immunoprecipitation from sheep lens membranes [5] and by their formation of channels with properties that differ from those of the homomeric Cx46 or Cx50 channels when co-expressed in *Xenopus* oocytes [29] or in transfected cells [30]. However, the true extent of mixing between wild-type Cx50 and wild-type Cx46 in the lens (as well as their true absolute amounts) are not known. The accelerated decay of wild-type Cx50 in homozygous Cx46fs380 lenses compared to wild-type lenses can be explained by a relatively small amount (10%) of mixing (co-oligomerization) between wild-type Cx50 and the mutant Cx46fs380 (Figure 2E). Since Cx46fs380 has a retention/retrieval signal, it is likely that some mixed oligomers (containing Cx46fs380 and wild-type Cx50) are retained in the biosynthetic pathway and subsequently degraded. The relatively estimated small amount of co-oligomerization between these proteins may reflect the differential abundances of the proteins in epithelial and fiber cells. Cx46 is almost exclusively expressed in fiber cells [8,31,32]. In contrast, there is substantial expression of Cx50 in lens epithelial cells [32], especially at early postnatal ages when Cx50-mediated coupling accounts for 63% of the coupling in epithelial cells [33]. Therefore, epithelial Cx50 must contribute significantly to the total Cx50 level at early ages.

In contrast, Cx50D47A has major effects on both the maturation/modification of the Cx46 protein and its stability. In these animals, Cx46 shows very little shift between Cx46-1 and Cx46-2 forms. The faster decay of wild-type Cx46 in Cx50D47A lenses as compared to wild-type lenses cannot be explained by the mixing of a constant amount of the wild-type Cx46 with the mutant Cx50. Although the data could be fit by assuming an age-dependent increase in the proportion of mutant Cx50 co-oligomerizing with wild-type Cx46, we consider this interpretation extremely unlikely because the levels of the mutant Cx50 approached zero at the later time points. While co-oligomerization between wild-type Cx46 and Cx50D47A may contribute to the decrease in the wild-type connexin, it is likely that the impaired differentiation [9] and induction of endoplasmic reticulum stress [15] in these lenses have more significant roles. Either of these processes might have affected levels of Cx46 and its post-translational modifications by altering protein synthesis and degradation pathways or kinase activities. In addition, the phosphorylation state of the connexins might have affected hetero-oligomerization.

These findings might have implications for other cell types because multiple connexins are co-expressed in many different kinds of cells. Cx40, Cx43, and Cx45 are co-expressed in cardiac myocytes [34,35]. Cx32 and Cx26 are both present in hepatocytes [36], and levels of Cx26 are reduced in Cx32 knock-out mice [37]. Many different connexins (including Cx26, Cx30, Cx30.3, Cx31.1, Cx31, and Cx43) are expressed in the epidermal cells of the skin (reviewed in Scott et al. [38]), and some Cx26 mutants have been shown to affect co-expressed Cx43 even though Cx26 and Cx43 do not normally co-oligomerize [39]. Our data suggest that a mutant of one of these connexins might affect the phosphorylation and stability of the other co-expressed connexins through different mechanisms, either directly (through co-oligomerization followed by degradation) or indirectly, by stimulating major cellular pathways. The consequent alterations in connexin abundance and its post-translational modifications (which often result in changes in channel abundance and/or function) might alter the extent of intercellular communication in these cells.

Supplementary Materials: The following supporting information can be downloaded at: https://www.mdpi.com/article/10.3390/cells11182786/s1, Figure S1: Wild-type lenses of two different genetic backgrounds have comparable levels of the lens fiber cell connexins.

Author Contributions: Conceptualization, V.M.B. and E.C.B.; investigation, O.J. and P.J.M.; formal analysis, O.J., P.J.M. and V.M.B.; writing—original draft preparation, O.J. and E.C.B.; writing—review and editing, O.J., P.J.M., V.M.B. and E.C.B.; visualization, O.J.; supervision and project administration, V.M.B. and E.C.B.; and funding acquisition, V.M.B. and E.C.B. All authors have read and agreed to the published version of the manuscript.

Funding: This work was supported by National Institutes of Health grant R01-EY030914 (to E.C.B. and V.M.B.). The content of this article is solely the responsibility of the authors and does not necessarily represent the official views of the National Institutes of Health.

Institutional Review Board Statement: The animal study protocol was approved by the Institutional Animal Care and Use Committee of The University of Chicago (ACUP# 71405, 9/24/2021).

Informed Consent Statement: Not applicable.

Data Availability Statement: Not applicable.

Conflicts of Interest: The authors declare no conflict of interest. The funders had no role in the design of the study; in the collection, analyses, or interpretation of data; in the writing of the manuscript; or in the decision to publish the results.

References

1. Sáez, J.C.; Berthoud, V.M.; Braňes, M.C.; Martínez, A.D.; Beyer, E.C. Plasma membrane channels formed by connexins: Their regulation and functions. *Physiol. Rev.* **2003**, *83*, 1359–1400. [CrossRef]
2. Beyer, E.C.; Berthoud, V.M. The family of connexin genes. In *Connexins*; Harris, A.L., Locke, D., Eds.; Humana Press: Totowa, NJ, USA, 2009; pp. 3–26.
3. Beyer, E.C.; Berthoud, V.M. Gap junction gene and protein families: Connexins, innexins, and pannexins. *Biochim. Biophys. Acta-Biomembr.* **2017**, *1860*, 5–8. [CrossRef]
4. Mathias, R.T.; Kistler, J.; Donaldson, P. The lens circulation. *J. Membr. Biol.* **2007**, *216*, 1–16. [CrossRef] [PubMed]
5. Jiang, J.X.; Goodenough, D.A. Heteromeric connexons in lens gap junction channels. *Proc. Natl. Acad. Sci. USA* **1996**, *93*, 1287–1291. [CrossRef] [PubMed]
6. Myers, J.B.; Haddad, B.G.; O'Neill, S.E.; Chorev, D.S.; Yoshioka, C.C.; Robinson, C.V.; Zuckerman, D.M.; Reichow, S.L. Structure of native lens connexin 46/50 intercellular channels by cryo-EM. *Nature* **2018**, *564*, 372–377. [CrossRef]
7. Berthoud, V.M.; Ngezahayo, A. Focus on lens connexins. *BMC Cell Biol.* **2017**, *18* (Suppl. 1), 6. [CrossRef] [PubMed]
8. Berthoud, V.M.; Minogue, P.J.; Yu, H.; Snabb, J.I.; Beyer, E.C. Connexin46fs380 causes progressive cataracts. *Invest. Opthalmol. Vis. Sci.* **2014**, *55*, 6639–6648. [CrossRef] [PubMed]
9. Berthoud, V.M.; Minogue, P.J.; Yu, H.; Schroeder, R.; Snabb, J.I.; Beyer, E.C. Connexin50D47A decreases levels of fiber cell connexins and impairs lens fiber cell differentiation. *Invest. Opthalmol. Vis. Sci.* **2013**, *54*, 7614–7622. [CrossRef] [PubMed]
10. Minogue, P.J.; Gao, J.; Zoltoski, R.K.; Novak, L.A.; Mathias, R.T.; Beyer, E.C.; Berthoud, V.M. Physiological and optical alterations precede the appearance of cataracts in Cx46fs380 mice. *Invest. Opthalmol. Vis. Sci.* **2017**, *58*, 4366–4374. [CrossRef] [PubMed]
11. Gao, J.; Minogue, P.J.; Beyer, E.C.; Mathias, R.T.; Berthoud, V.M. Disruption of the lens circulation causes calcium accumulation and precipitates in connexin mutant mice. *Am. J. Physiol. Cell Physiol.* **2018**, *314*, C492–C503. [CrossRef]
12. Berthoud, V.M.; Gao, J.; Minogue, P.J.; Jara, O.; Mathias, R.T.; Beyer, E.C. The connexin50D47A mutant causes cataracts by calcium precipitation. *Invest. Opthalmol. Vis. Sci.* **2019**, *60*, 2336–2346. [CrossRef] [PubMed]
13. Favor, J. A comparison of the dominant cataract and recessive specific-locus mutation rates induced by treatment of male mice with ethylnitrosourea. *Mutat. Res.* **1983**, *110*, 367–382. [CrossRef]
14. Bradford, M.M. A rapid and sensitive method for the quantitation of microgram quantities of protein utilizing the principle of protein-dye binding. *Anal. Biochem.* **1976**, *72*, 248–254. [CrossRef]
15. Berthoud, V.M.; Minogue, P.J.; Lambert, P.A.; Snabb, J.I.; Beyer, E.C. The cataract-linked mutant connexin50D47A causes endoplasmic reticulum stress in mouse lenses. *J. Biol. Chem.* **2016**, *291*, 17569–17578. [CrossRef]
16. Jara, O.; Mysliwiec, H.; Minogue, P.J.; Berthoud, V.M.; Beyer, E.C. p62/Sequestosome 1 levels increase and phosphorylation is altered in Cx50D47A lenses, but deletion of p62/sequestosome 1 does not improve transparency. *Mol. Vis.* **2020**, *26*, 204–215. [PubMed]
17. Berthoud, V.M.; Minogue, P.J.; Guo, J.; Williamson, E.K.; Xu, X.; Ebihara, L.; Beyer, E.C. Loss of function and impaired degradation of a cataract-associated mutant connexin50. *Eur. J. Cell Biol.* **2003**, *82*, 209–221. [CrossRef] [PubMed]
18. Minogue, P.J.; Beyer, E.C.; Berthoud, V.M. A connexin50 mutant, CX50fs, that causes cataracts is unstable, but is rescued by a proteasomal inhibitor. *J. Biol. Chem.* **2013**, *288*, 20427–20434. [CrossRef] [PubMed]
19. TenBroek, E.; Arneson, M.; Jarvis, L.; Louis, C. The distribution of the fiber cell intrinsic membrane proteins MP20 and connexin46 in the bovine lens. *J. Cell Sci.* **1992**, *103*, 245–257. [CrossRef]
20. TenBroek, E.M.; Johnson, R.; Louis, C.F. Cell-to-cell communication in a differentiating ovine lens culture system. *Invest. Ophthalmol. Vis. Sci.* **1994**, *35*, 215–228.
21. Jiang, J.X.; Paul, D.L.; Goodenough, D.A. Posttranslational phosphorylation of lens fiber connexin46: A slow occurrence. *Invest. Ophthalmol. Vis. Sci.* **1993**, *34*, 3558–3565.
22. Gupta, V.K.; Berthoud, V.M.; Atal, N.; Jarillo, J.A.; Barrio, L.C.; Beyer, E.C. Bovine connexin44, a lens gap junction protein: molecular cloning, immunologic characterization, and functional expression. *Invest. Ophthalmol. Vis. Sci.* **1994**, *35*, 3747–3758.

23. Shearer, D.; Ens, W.; Standing, K.; Valdimarsson, G. Posttranslational modifications in lens fiber connexins identified by off-line-HPLC MALDI-quadrupole time-of-flight mass spectrometry. *Invest. Opthalmol. Vis. Sci.* **2008**, *49*, 1553–1562. [CrossRef] [PubMed]
24. Wang, Z.; Schey, K.L. Phosphorylation and truncation sites of bovine lens connexin 46 and connexin 50. *Exp. Eye Res.* **2009**, *89*, 898–904. [CrossRef] [PubMed]
25. Retamal, M.A.; Altenberg, G.A. Role and posttranslational regulation of Cx46 hemichannels and gap junction channels in the eye lens. *Front. Physiol.* **2022**, *13*, 864948. [CrossRef] [PubMed]
26. Oh, S.Y.; Grupen, C.G.; Murray, A.W. Phorbol ester induces phosphorylation and down-regulation of connexin 43 in WB cells. *Biochim. Biophys. Acta* **1991**, *1094*, 243–245. [CrossRef]
27. Arora, A.; Minogue, P.J.; Liu, X.; Addison, P.K.; Russel-Eggitt, I.; Webster, A.R.; Hunt, D.M.; Ebihara, L.; Beyer, E.C.; Berthoud, V.M.; et al. A novel connexin50 mutation associated with congenital nuclear pulverulent cataracts. *J. Med Genet.* **2008**, *45*, 155–160. [CrossRef] [PubMed]
28. Minogue, P.J.; Liu, X.; Ebihara, L.; Beyer, E.C.; Berthoud, V.M. An aberrant sequence in a connexin46 mutant underlies congenital cataracts. *J. Biol. Chem.* **2005**, *280*, 40788–40795. [CrossRef]
29. Ebihara, L.; Xu, X.; Oberti, C.; Beyer, E.C.; Berthoud, V.M. Co-expression of lens fiber connexins modifies hemi-gap-junctional channel behavior. *Biophys. J.* **1999**, *76*, 198–206. [CrossRef]
30. Hopperstad, M.G.; Srinivas, M.; Spray, D.C. Properties of gap junction channels formed by Cx46 alone and in combination with Cx50. *Biophys. J.* **2000**, *79*, 1954–1966. [CrossRef]
31. Gong, X.; Li, E.; Klier, G.; Huang, Q.; Wu, Y.; Lei, H.; Kumar, N.M.; Horwitz, J.; Gilula, N.B. Disruption of α_3 connexin gene leads to proteolysis and cataractogenesis in mice. *Cell* **1997**, *91*, 833–843. [CrossRef]
32. Rong, P.; Wang, X.; Niesman, I.; Wu, Y.; Benedetti, L.E.; Dunia, I.; Levy, E.; Gong, X. Disruption of *Gja8* (α8 connexin) in mice leads to microphthalmia associated with retardation of lens growth and lens fiber maturation. *Development* **2002**, *129*, 167–174. [CrossRef]
33. White, T.W.; Gao, Y.; Li, L.; Sellitto, C.; Srinivas, M. Optimal lens epithelial cell proliferation is dependent on the connexin isoform providing gap junctional coupling. *Invest. Opthalmol. Vis. Sci.* **2007**, *48*, 5630–5637. [CrossRef]
34. Kanter, H.L.; Saffitz, J.E.; Beyer, E.C. Cardiac myocytes express multiple gap junction proteins. *Circ. Res.* **1992**, *70*, 438–444. [CrossRef]
35. Davis, L.M.; Kanter, H.L.; Beyer, E.C.; Saffitz, J.E. Distinct gap junction protein phenotypes in cardiac tissues with disparate conduction properties. *J. Am. Coll. Cardiol.* **1994**, *24*, 1124–1132. [CrossRef]
36. Nicholson, B.; Dermietzel, R.; Teplow, D.; Traub, O.; Willecke, K.; Revel, J.P. Two homologous protein components of hepatic gap junctions. *Nature* **1987**, *329*, 732–734. [CrossRef]
37. Nelles, E.; Bützler, C.; Jung, D.; Temme, A.; Gabriel, H.D.; Dahl, U.; Traub, O.; Stümpel, F.; Jungermann, K.; Zielasek, J.; et al. Defective propagation of signals generated by sympatheric nerve stimulation in the liver of connexin32-deficient mice. *Proc. Natl. Acad. Sci. USA* **1996**, *93*, 9565–9570. [CrossRef] [PubMed]
38. Scott, C.A.; Tattersall, D.; O'Toole, E.A.; Kelsell, D.P. Connexins in epidermal homeostasis and skin disease. *Biochim. Biophys. Acta-Biomembr.* **2012**, *1818*, 1952–1961. [CrossRef] [PubMed]
39. Rouan, F.; White, T.; Brown, N.; Taylor, A.M.; Lucke, T.W.; Paul, D.L.; Munro, C.S.; Uitto, J.; Hodgins, M.B.; Richard, G. trans-dominant inhibition of connexin-43 by mutant connexin-26: Implications for dominant connexin disorders affecting epidermal differentiation. *J. Cell Sci.* **2001**, *114*, 2105–2113. [CrossRef] [PubMed]

cells

MDPI

Article

Mapping the Universe of Eph Receptor and Ephrin Ligand Transcripts in Epithelial and Fiber Cells of the Eye Lens

Michael P. Vu and Catherine Cheng *

School of Optometry and Vision Science Program, Indiana University, Bloomington, IN 47405, USA
* Correspondence: ckcheng@iu.edu

Abstract: The eye lens is a transparent, ellipsoid organ in the anterior chamber of the eye that is required for fine focusing of light onto the retina to transmit a clear image. Cataracts, defined as any opacity in the lens, remains the leading cause of blindness in the world. Recent studies in humans and mice indicate that Eph–ephrin bidirectional signaling is important for maintaining lens transparency. Specifically, mutations and polymorphisms in the EphA2 receptor and the ephrin-A5 ligand have been linked to congenital and age-related cataracts. It is unclear what other variants of Ephs and ephrins are expressed in the lens or whether there is preferential expression in epithelial vs. fiber cells. We performed a detailed analysis of Eph receptor and ephrin ligand mRNA transcripts in whole mouse lenses, epithelial cell fractions, and fiber cell fractions using a new RNA isolation method. We compared control samples with EphA2 knockout (KO) and ephrin-A5 KO samples. Our results revealed the presence of transcripts for 12 out of 14 Eph receptors and 8 out of 8 ephrin ligands in various fractions of lens cells. Using specific primer sets, RT-PCR, and sequencing, we verified the variant of each gene that is expressed, and we found two epithelial-cell-specific genes. Surprisingly, we also identified one Eph receptor variant that is expressed in KO lens fibers but is absent from control lens fibers. We also identified one low expression ephrin variant that is only expressed in ephrin-A5 control samples. These results indicate that the lens expresses almost all Ephs and ephrins, and there may be many receptor–ligand pairs that play a role in lens homeostasis.

Keywords: RT-PCR; EphA2; ephrin-A5; knockout; variants; Eph-ephrin; bidirectional signaling

1. Introduction

In the anterior chamber of the eye, the lens, an ellipsoid and transparent tissue, is responsible for the fine focusing of light onto the retina to transmit a clear image. The function of the lens depends on its shape, biomechanical properties, clarity, and refractive index [1]. Despite decades of study, cataracts, defined as any opacity in the normally clear lens, remain the leading cause of blindness in the world [2]. The causes for congenital cataracts due to genetic mutations have been studied, but the cellular and molecular mechanisms that lead to age-related cataracts remain unclear.

Recent studies have shown that the dysfunction of Eph–ephrin bidirectional signaling leads to congenital and age-related cataracts in human patients [3–14]. Erythropoietin-producing hepatocellular carcinoma (Eph) receptors are the largest class of receptor tyrosine kinases (RTK). Eph receptors bind to a class of ligands, known as ephrins, and the binding of the receptor and ligand leads to a unique bidirectional signaling pathway with forward signaling in the Eph-bearing cell and reverse signaling in the ephrin-bearing cell [15–17]. Eph–ephrin bidirectional signaling is important for many cellular functions, including cell migration, proliferation, adhesion, and patterning [18–21]. Virtually all cells express a complement of Ephs and ephrins. There are 14 Eph receptors that are divided into EphAs (9 members, 1–8 and 10) and EphBs (5 members, 1–4 and 6), based on their sequence similarity and ligand affinity [17,22–26]. Ephrin ligands are categorized by structure into ephrin-As (5 members, 1–5), which are anchored via a glycosylphosphatidylinositol (GPI)

moiety to the membrane, and ephrin-Bs (3 members, 1–3), which have a transmembrane region and a short cytoplasmic tail [17,24,25,27]. In human patients, mutations of the *EPHA2* gene cause congenital [3–9] and age-related [10–13] cataracts, while polymorphisms of the *EFNA5* gene, which encodes the ephrin-A5 protein, are linked to age-related cataracts [11].

The lens is composed of two cell types, a monolayer of epithelial cells covering the anterior hemisphere and a bulk mass of elongated and differentiated fiber cells [1]. The lens capsule is a basement membrane that surrounds the entire tissue, and lens epithelial cells are strongly adhered to the lens capsule [1]. Anterior epithelial cells are quiescent and thought to nourish the fiber cell underneath, and epithelial cells at the lens equator proliferate, migrate, elongate, and differentiate into new layers of lens fiber cells [28–30]. The addition of fiber cell layers along the lens equator drives life-long lens growth. Studies in mouse models indicate that EphA2 is required for hexagonal packing, for the organization of equatorial lens epithelial cells [31–33], and for fiber cell maturation [33–35], while ephrin-A5 is needed for maintaining the quiescence of anterior epithelial cells [32,36]. Recent works reveal that EphA2 and ephrin-A5 affect lens fiber cell patterning [33,34,37], which alters tissue biomechanical properties [34]. Immunostaining studies indicate that ephrin-A5 is mainly in the anterior epithelial cells, anterior tips of fiber cells, and peripheral equatorial fibers in mouse lenses [32,33,36]. In contrast, EphA2 proteins are mainly found along the equatorial epithelial cell and fiber cell membranes and in anterior fiber cell tips [10,32,33,36]. From these studies, it is possible that EphA2 and ephrin-A5 are a receptor–ligand pair at the anterior tips of lens fiber cells [33,34]. However, the diverse roles of EphA2 and ephrin-A5 in different populations of lens epithelial cells and the unique subcellular localization of these proteins in the lens suggest that they are not a receptor–ligand pair in most cells of the lens [32]. Thus, it is likely that EphA2 and ephrin-A5 interact with other ephrin ligands and Eph receptors, respectively, to regulate the homeostasis of lens epithelial cells and fiber cells.

In this study, we conducted a comprehensive analysis to determine which Eph receptors and ligands are present in adult mouse lenses using RNA isolation, reverse transcription (RT), polymerase chain reaction (PCR), and Sanger sequencing. In addition to screening RNA samples from whole lenses, we separated lens epithelial cells and fiber cells for RNA isolation using our new protocol [38]. We compared 6-week-old samples from control, *EphA2*$^{-/-}$, and *ephrin-A5*$^{-/-}$ lenses. Of the 14 Eph receptors and 8 ephrin ligands, we verified that transcripts for 12 Ephs and 8 ephrins are present in the lens. Our data revealed 1 Eph receptor and 1 ephrin ligand that are only expressed in lens epithelial cells. In addition, there is 1 Eph receptor that is expressed in KO lens fiber cells, but not in the control samples. We compared our RT-PCR and sequencing data with microarray data. Overall, the adult mouse lens expresses most EphAs and all EphBs, ephrin-As, and ephrin-Bs; thus, much more work needs to be conducted to identify all cogent receptor–ligand pairs and understand their role in maintaining lens health and homeostasis.

2. Materials and Methods

2.1. Mice

Mice were maintained in accordance with an approved animal protocol (Indiana University Bloomington Institutional Animal Care and Use Committee, protocol #21-010) and the ARVO Statement for the Use of Animals in Ophthalmic and Vision Research. Generations of *ephrin-A5*$^{-/-}$ and *EphA2*$^{-/-}$ mice were previously described [31,36,39,40]. All mice were maintained in the C57BL/6J background with wild-type *Bfsp*2 (CP49) genes. Genotyping was completed using automated qPCR on toe and/or tail snips (Transnetyx, Cordova, TN, USA). Male and female littermates were used for experiments.

2.2. RNA Isolation from Epithelial Cells

RNA from epithelial cells were obtained by decapsulating freshly dissected lenses using a modified version of a published protocol [38]. Samples were collected from three control (*EphA2*$^{+/+}$ and *ephrin-A5*$^{+/+}$) and three knockout (*EphA2*$^{-/-}$ and *ephrin-A5*$^{-/-}$)

6-week-old mice. After dissected lenses were cleaned of unrelated tissues, tweezers were used to gently puncture the lens at the equator. Shallow punctures prevented the fiber cells from adhering to the lens capsule and lens epithelial cell layer. A pair of lens capsules with the lens epithelial cells from one mouse were then placed into 0.4 mL of cold TRIzol (Invitrogen, Waltham, MA, USA, Cat# 15596026). Samples were then incubated at room temperature for 30 min. For phase separation, 0.2 mL of chloroform was added to each sample before tubes were shaken vigorously for 15 s. Samples were incubated at room temperature for 10–15 min and centrifuged at 14,000× *g* for 15 min at 4 °C. The aqueous phase was transferred to new RNase-free microcentrifuge tubes. Two volumes of RNA binding buffer per 1 volume of aqueous phase was added to each sample. Then, an equal volume of 100% ethanol (Fisher Scientific, Waltham, MA, USA, Cat# BP2818500), relative to the volume within the tube, was added before the samples were inverted to gently mix. The rest of the RNA isolation was performed with the RNA clean and concentrator kit (Zymo Research, Tustin, CA, USA, Cat# R1013), according to manufacturer instructions and two additional steps. The first additional step was another centrifugation after the final RNA wash buffer centrifugation to remove excess wash buffer. The second additional step was a 2-min waiting step after the addition of DNase/Rnase-free water to the filter in the spin column. The addition of this step allowed for higher recovery of RNA. RNA samples were then incubated at 60 °C for 10 min before being stored at 4 °C overnight for concentration quantification the next day using the NanoDrop One (Thermo Fisher Scientific, Waltham, MA, USA, Version 2.6.0.6., Cat# ND-ONE-W). RNA was stored at −80 °C until use.

2.3. RNA Isolation from Fiber Cells, Whole Lens Samples, or Positive Control Samples

RNA isolation from fiber cells, whole lens, or positive control samples were processed using the same protocol [41]. Whole lens and fiber cell samples were collected from four control (*EphA2*$^{+/+}$ and *ephrin-A5*$^{+/+}$) and four knockout (*EphA2*$^{-/-}$ and *ephrin-A5*$^{-/-}$) 6-week-old mice. Fiber cell samples were collected from the same mice used for epithelial cell RNA isolation, while whole lens RNA sample was isolated from another mouse. A control brain sample was collected from a 9-week-old wild-type C57BL/6J mouse. Lenses from the same mouse were cleaned of other attached tissues, and pairs of lenses or fiber cell masses (after lens capsule and epithelial cell removal) from one mouse were pooled into one sample. For whole lenses and fiber cells masses, 0.4 mL TRIzol was used for homogenization. For the brain positive control sample, 1 mL of TRIzol per 50–100 mg of tissue was used for homogenization. Samples were homogenized with RNase Zap (Sigma-Aldrich, St. Louis, MO, USA, Cat# R2020)-treated polypropylene microcentrifuge pestles, until no large pieces of tissue remained. Homogenized samples were incubated at room temperature for 5 min before 0.4 mL chloroform (Fisher Scientific, Cat# AA22920K2), per 1 mL TRIzol, was added. Samples were then shaken vigorously for 15 s and incubated at room temperature for 3 min. After incubation, the samples were centrifuged at 12,000× *g* for 15 min at 4 °C. The aqueous phase was transferred to RNase-free microcentrifuge tubes. Then, half the sample's volume of 100% isopropanol (Fisher Scientific, Cat# AC327270010) was added before the samples were mixed by brief vortexing. The samples were incubated at room temperature for 10 min and then centrifuged at 12,000× *g* for 10 min at 4 °C. The supernatant was decanted, and the RNA pellet was washed with 75% ethanol (in diethyl pyrocarbonate (DEPC)-treated water), using a volume equal to the volume of TRIzol used. The samples were then vortexed briefly, so that the pellet floats in solution. Then, the samples were centrifuged at 7500× *g* for 5 min at 4 °C. After centrifugation, the ethanol wash was decanted, and the RNA pellet was allowed to air dry for 5–10 min, with the microcentrifuge tube being inverted. The RNA pellets were then dissolved in 20 μL of DNase/RNase-free water before incubating for 10 min at 60 °C. The samples were then kept at 4 °C overnight for quantification the next day using the NanoDrop One. RNA was stored at −80 °C until use.

2.4. Primer Design

Primer design was performed with the National Center for Biotechnology Information (NCBI) Primer-BLAST website [https://www.ncbi.nlm.nih.gov/tools/primer-blast/ (accessed on 2 September 2022)]. Primers were designed to span exon–exon junctions, when possible, and were specific to each gene. For validated variants, specific primer sets were designed for each variant, when possible, utilizing the differences in sizes of the resulting PCR products from one set of primers or sequencing when the difference is <15 nucleotides. PCR products were between 500–2200 bp (Table S1).

2.5. Reverse Transcription and Polymerase Chain Reaction (RT-PCR)

Reverse transcription was performed using SuperScript III (Thermo Fisher Scientific, Cat.# 18080-051) and Oligo$(dT)_{20}$ primer (50 μM), following the manufacturer's instructions. The cDNA was used immediately or stored at −20 °C until use.

Polymerase chain reaction was performed using Quick-Load *Taq* 2X master mix (New England Biolabs, Ipswich, MA, USA, Cat# M0271S), following the manufacturer instructions. The reactions were loaded into the MiniAmp Thermal Cycler (Thermo Fisher Scientific, Version 0.2.9, Cat# A37834). The thermocycling conditions are as follows. There was one cycle of 95 °C for 30 s, followed by 45 cycles of 95 °C for 30 s, 53.5–55 °C for 30 s (temperature varied, based on the primers, info provided in Table S1) and 68 °C for 1 min per 1 kb of expected PCR product length. A final cycle of 68 °C for 5 min finished the PCR reaction. PCR products were maintained at 4 °C before storage at −20 °C or gel electrophoresis.

2.6. Gel Electrophoresis and DNA Extraction from Gel Pieces

Gel electrophoresis was performed using 0.8% or 2% agarose (Fisher Scientific, Cat# S53) gels with GelGreen (Biotium, Fremont, CA, USA, Cat# 41005). The DNA ladder used was GeneRuler 100 bp (Thermo Fisher Scientific, Cat# SM0241) or GeneRuler 1 kb Plus (Thermo Fisher Scientific, Cat# SM1331). Samples with multiple variants and with product sizes under 1000 bp were run on 2% gels to better separate the bands for gel extraction and DNA sequencing. Gels were imaged using PrepOne Sapphire Blue LED illuminator (Embi Tec, San Diego, CA, USA, Cat# PI-1000). Gel extraction was performed by cutting out the individual bands from the gels using a clean razor and placing the gel piece into a microcentrifuge tube that was then processed with the QIAquick gel extraction kit (Qiagen, Hilden, Germany, Cat# 28704), following the manufacturer's instructions. The extracted DNA was then prepared for sequencing, according to Quintarabio's (Cambridge, MA, USA) sample submission and shipping instructions. The sequencing results were compared in NCBI nucleotide BLAST to confirm the identity of each PCR product.

2.7. Microarray Data Comparison

Microarray data were obtained from the iSyTE database [https://research.bioinformatics.udel.edu/iSyTE/ppi/expression.php (accessed on 13 September 2022)], searching for Ephs and ephrins. A standard lens gene expression search was performed for mouse mm10 species, with normalized expression comparison. The data that were used for Table 2 and Table S2 were from the developmental dataset for Affymetrix 430 2.0 epithelial P28 and P56, as well as Illumina WG-6 v2.0 P30, P42, and P52. For Table 2, we also listed other mouse tissues with high expression of Ephs and ephrins, according to each gene's expression level information in the NCBI gene database.

3. Results

3.1. EphA Transcripts in the Lens

We analyzed RNA transcripts with specific primer pairs for *Epha1–8* and *Epha10* in control, *EphA2*$^{-/-}$, and *ephrin-A5*$^{-/-}$ whole lens, epithelial cell, and fiber cell samples from 6-week-old mice. We found transcripts for *Epha1*, *Epha2*, *Epha3* variant 1, *Epha4*, *Epha5* variants 3, 9, 12, and 14, *Epha7* variant 2, and *Epha8* in all samples tested (Figure 1). As

expected, *Epha2* transcripts are absent from the *EphA2*$^{-/-}$ samples. Variants 1 and 2 of *Epha3* differ by one amino acid, and *Epha3* variant 1 has an additional amino acid, Q478. The presence of *Epha3* variant 1 in lens samples was confirmed by sequencing of the PCR product. *Epha5* has 14 different variants with different splicing patterns and lengths. We used sequencing to confirm the presence of four variants of *Epha5* in the lens. *Epha7* has three variants, 1, 2, and 3. *Epha7* variants 1 and 3 differ by four amino acids, and variant 1 is longer, with the addition of 601–604 KFPG amino acids. We detected *Epha7* variant 1 in whole lens and epithelial cells samples of the control and KO samples, as well as in KO fiber cell samples (Figure 1, magenta boxes). *Epha7* variant 2 is a shorter variant lacking multiple exons and has a different and shorter C-terminus than variants 1 and 3. Sequencing confirmed the presence of the *Epha7* variant 2 in all lens samples. We did not detect *Epha6* or *Epha10* in any samples. There are two variants, 1 and 2, for *Epha10*. Variant 2 of *Epha10* is much shorter than variant 1, due to loss of exons, and has a unique C-terminus, compared to variant 1. Positive control PCR products from brain RNA samples were used to confirm primer sets and PCR conditions for the *Epha*5 variants 1, 4, 5, 6, 8, and 10 and the *Epha6* and *Epha10* experiments.

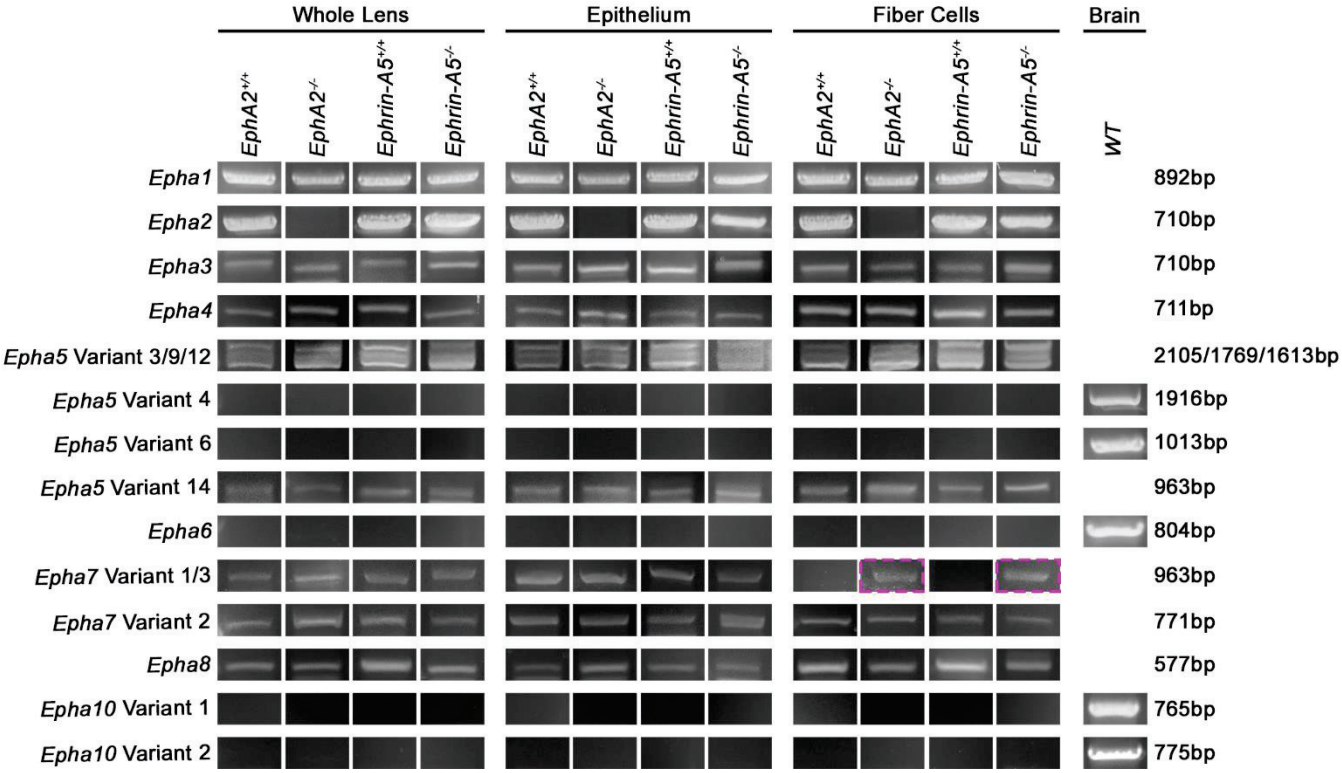

Figure 1. *Epha* transcripts in whole lens, lens epithelial cell, or lens fiber cell RNA samples from 6-week-old *EphA2*$^{+/+}$, *EphA2*$^{-/-}$, *ephrin-A5*$^{+/+}$, and *ephrin-A5*$^{-/-}$ mice. Positive control was brain RNA isolated from a wild-type (*WT*) control mouse. We detected *Epha1*, *Epha2*, *Epha3* variant 1, *Epha4*, *Epha5* variants 3, 9, 12, and 14, *Epha7* variants 1 and 2, and *Epha8* in the lens. As expected, *Epha2* was not detected in *EphA2*$^{-/-}$ lens samples. *Epha7* variant 1 was detected in all whole lens and epithelial cell samples and in the fiber cells of *EphA2*$^{-/-}$ and *ephrin-A5*$^{-/-}$ lenses (magenta boxes). We did not detect *Epha6* or *Epha10* in the lens.

3.2. EphB Transcripts in the Lens

Next, we tested for the presence of *Ephb1–4* and *Ephb6* transcripts in the control and KO samples. We detected *Ephb1* variant 1, *Ephb2* variant 2, *Ephb3*, *Ephb4* variants 1 and 2, and *Ephb6* transcripts in all lens samples (Figure 2). The *Ephb1* variant 1 is a longer isoform, and variant 2 lacks one of the coding exons. *Ephb1* variants 1 and 2 have the same N- and C-termini. Specific primers were designed to distinguish between *Ephb1* variants 1 and 2.

The lens only expresses *Ephb1* variant 1, and the primers for *Ephb1* variant 2 were verified by the positive control brain RNA sample. *Ephb2* variant 1 has one additional amino acid, Q477, compared to variant 2. Sequencing verified that the lens expresses *Ephb2* variant 2. *Ephb4* also has two variants, and due to an alternate in-frame splice site, variant 2 is a shorter transcript. Specific primers designed for each variant and sequencing confirm that both variants 1 and 2 of *Ephb4* are expressed in the lens. *Ephb6* also has two variants, but the two variants are identical in the coding region and differ by a four-nucleotide difference in the 5′ untranslated region (UTR).

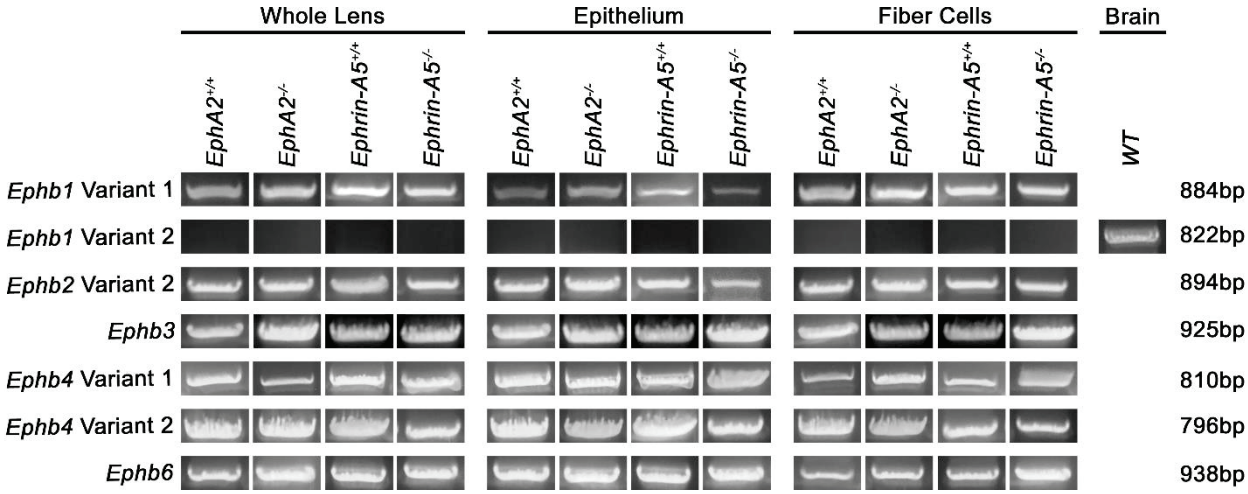

Figure 2. *Ephb* transcripts in whole lens, lens epithelial cell, or lens fiber cell RNA samples from 6-week-old *EphA2*$^{+/+}$, *EphA2*$^{-/-}$, *ephrin-A5*$^{+/+}$, and *ephrin-A5*$^{-/-}$ mice. Positive control was brain RNA isolated from a *WT* control mouse. We detected *Ephb1* variant 1, *Ephb2* variant 2, *Ephb3*, *Ephb4* variants 1 and 2, and *Ephb6* in the lens. We did not detect *Ephb1* variant 2 in the lens.

In total, the lens expresses 12 of the 14 *Eph* genes. Due to the variants in multiple genes, we found 14 *Eph* transcripts in our samples. Most notably, the *Epha7* variant 1 is normally only expressed in lens epithelial cells, but is present in the lens fiber cells of *EphA2*$^{-/-}$ and *ephrin-A5*$^{-/-}$ samples.

3.3. Ephrin-A Transcripts in the Lens

Ephrin-A proteins are encoded by the *Efna* genes. We performed experiments to determine whether *Efna1–5* are present in the lens. Our results show that *Efna1* variant 1, *Efna2*, *Efna3* variant 1, *Efna4*, and *Efna5* variants 1 and 2 transcripts are present in all lens samples (Figure 3). As expected, the *Efna5* transcripts are absent in the *ephrin-A5*$^{-/-}$ samples. *Efna1* variant 2 is missing a part of the 5′ UTR and coding region, resulting in a shorter transcript, compared to variant 1. Specific forward primers for *Efna1* variants 1 and 2 revealed that the lens expresses the longer *Efna1* variant 1 transcript in both epithelial cells and fiber cells, while *Efna1* variant 2 is only expressed in lens epithelial cells. *Efna3* has 7 variants. *Efna3* variants 1 and 2 differ by one exon in the 3′ coding region and can be distinguished by PCR product size. We found *Efna3* variant 1 transcripts in all lens samples. With sequencing verification, we could only detect very low levels of *Efna3* variant 2 transcripts in the *ephrin-A5*$^{+/+}$ control samples (Figure 3, magenta boxes). *Efna3* variants 3, 4, and 5 have identical coding regions and are shorter transcripts with a start codon in the middle of the variant 1 sequence. There are minor differences in the 5′ UTR of *Efna3* variants 3, 4, and 5 from the 5′ coding region of *Efna3* variant 1; thus, specific primers to test for *Efna3* variants 3, 4, and 5 could not be designed. *Efna3* variants 6 and 7 have identical coding regions and are shorter transcripts with a start codon in the middle of the variant 2 sequence. There are some differences in the 5′ UTR of variants 6 and 7 from the 5′ coding region of variant 2, but specific primers could not be designed to distinguish between variants 2, 6, and 7. Interestingly, the lens expresses both variants of *Efna5*. *Efna5*

variant 2 lacks one exon and is shorter than variant 1, but both transcripts have the same N- and C-termini sequence.

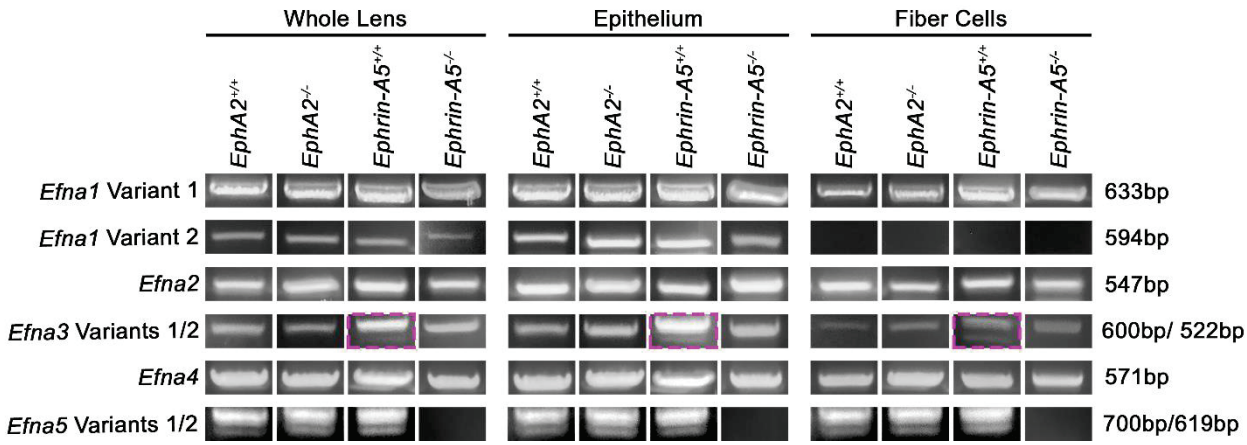

Figure 3. *Efna* transcripts, which encode for ephrin-A proteins, in whole lens, lens epithelial cell, or lens fiber cell RNA samples from 6-week-old *EphA2*$^{+/+}$, *EphA2*$^{-/-}$, *ephrin-A5*$^{+/+}$, and *ephrin-A5*$^{-/-}$ mice. We detected *Efna1* variant 1, *Efna2*, *Efna3* variant 1, *Efna4*, and *Efna5* variants 1 and 2 in the lens. *Efna1* variant 2 was detected in the whole lens and epithelial cells, but not detected in fiber cells. *Efna3* variant 2 was only detected in *ephrin-A5*$^{+/+}$ lens samples (magenta boxes).

3.4. Ephrin-Bs Transcripts in the Lens

The last group of genes tested were *Efnb1–3*, which encode for ephrin-B1–3. We detected *Efnb1* and *Efnb2* variant 1 in all lens samples (Figure 4). *Efnb2* has two variants, and variant 2 is shorter by 93 base pairs. *Efnb2* variants 1 and 2 have the same N- and C-termini sequence. We did not detect the smaller *Efnb2* variant 2 band in any of the lens samples. Interestingly, *Efnb3* transcripts are only found in lens epithelial cells. Overall, we found transcripts for all eight *Efn* genes in the lens. Notably, *Efna5* variants 1 and 2 were both expressed in the lens, and *Efnb3* was only found in lens epithelial cells. All PCR and sequencing results are summarized in Table 1.

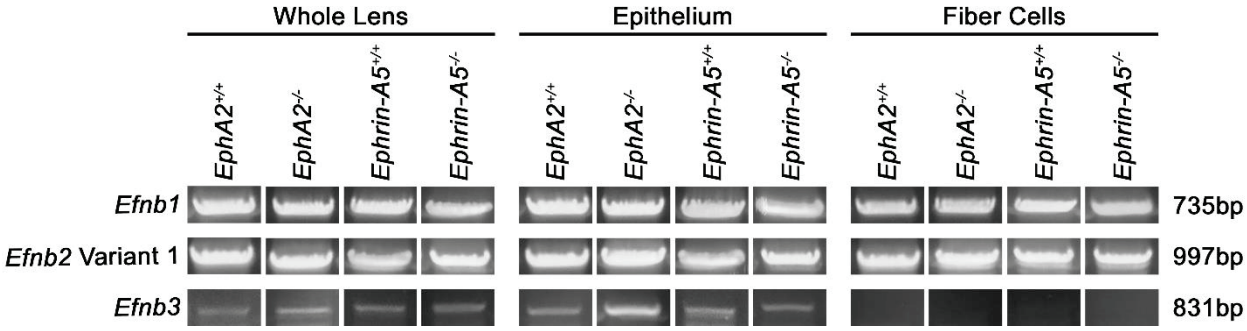

Figure 4. *Efnb* transcripts, which encode for ephrin-B proteins, in whole lens, lens epithelial cell, or lens fiber cell RNA samples from 6-week-old *EphA2*$^{+/+}$, *EphA2*$^{-/-}$, *ephrin-A5*$^{+/+}$, and *ephrin-A5*$^{-/-}$ mice. We detected *Efnb1* and *Efnb2* variant 1 in the lens. *Efnb3* was detected in the whole lens and epithelial cells, but not detected in fiber cells.

Table 1. *Eph* and *Efn* transcripts in the lens.

Gene	Whole Lens				Epithelium				Fiber Cells			
	EphA2		*Ephrin-A5*		*EphA2*		*Ephrin-A5*		*EphA2*		*Ephrin-A5*	
	+/+	-/-	+/+	-/-	+/+	-/-	+/+	-/-	+/+	-/-	+/+	-/-
Epha1	✓				✓				✓			
Epha2	✓	KO	✓	✓	✓	KO	✓	✓	✓	KO	✓	✓
Epha3 Variant 1	✓				✓				✓			
Epha3 Variant 2	n.d.				n.d.				n.d.			
Epha4	✓				✓				✓			
Epha5 Variant 1	n.d.				n.d.				n.d.			
Epha5 Variant 2	n.d.				n.d.				n.d.			
Epha5 Variant 3	✓				✓				✓			
Epha5 Variant 4	n.d.				n.d.				n.d.			
Epha5 Variant 5	n.d.				n.d.				n.d.			
Epha5 Variant 6	n.d.				n.d.				n.d.			
Epha5 Variant 7	n.d.				n.d.				n.d.			
Epha5 Variant 8	n.d.				n.d.				n.d.			
Epha5 Variant 9	✓				✓				✓			
Epha5 Variant 10	n.d.				n.d.				n.d.			
Epha5 Variant 11	n.d.				n.d.				n.d.			
Epha5 Variant 12	✓				✓				✓			
Epha5 Variant 13	n.d.				n.d.				n.d.			
Epha5 Variant 14	✓				✓				✓			
Epha6	n.d.				n.d.				n.d.			
Epha7 Variant 1	✓				✓				n.d.	✓	n.d.	✓
Epha7 Variant 2	✓				✓				✓			
Epha7 Variant 3	n.d.				n.d.				n.d.			
Epha8	✓				✓				✓			
Epha10 Variant 1	n.d.				n.d.				n.d.			
Epha10 Variant 2	n.d.				n.d.				n.d.			
Ephb1 Variant 1	✓				✓				✓			
Ephb1 Variant 2	n.d.				n.d.				n.d.			
Ephb2 Variant 1	n.d.				n.d.				n.d.			
Ephb2 Variant 2	✓				✓				✓			
Ephb3	✓				✓				✓			
Ephb4 Variant 1	✓				✓				✓			
Ephb4 Variant 2	✓				✓				✓			
*Ephb6*Variant 1	✓				✓				✓			
*Ephb6*Variant 2	✓				✓				✓			
Efna1 Variant 1	✓				✓				✓			
*Efna1*Variant 2	✓				✓				n.d.			
Efna2	✓				✓				✓			
Efna3 Variant 1 *	✓				✓				✓			
Efna3 Variant 2 *	n.d.	n.d.	✓	n.d.	n.d.	n.d.	✓	n.d.	n.d.	n.d.	✓	n.d.
Efna4	✓				✓				✓			
*Efna5*Variant 1	✓	✓	✓	KO	✓	✓	✓	KO	✓	✓	✓	KO
Efna5 Variant 2	✓	✓	✓	KO	✓	✓	✓	KO	✓	✓	✓	KO
Efnb1	✓				✓				✓			
Efnb2 Variant 1	✓				✓				✓			
Efnb2 Variant 2	n.d.				n.d.				n.d.			
Efnb3	✓				✓				n.d.			

+/+ = wild-type or control; −/− or KO = knockout; n.d. = not detected; blue = detected in all lens fractions; orange = detected in some lens fractions; yellow highlight = detected in lens epithelial fractions, but not in lens fiber cell fractions; * There are two shorter variants of *Efna3*, variants 3/4/5 and variants 6/7, that cannot be distinguished by RT-PCR.

3.5. Data Comparison with Adult Lens Microarray Data

We compared our RT-PCR results to the *Eph* and *Efn* microarray data available in iSyte 2.0 from the Affymetrix 430 2.0 and Illumina WG-6 v2.0 arrays [42]. We chose to compare our data from 6-week-old mice with data from wild-type lenses at postnatal day 28 (P28) from the epithelium and at P56 from the whole lens on the Affymetrix

platform and results from wild-type whole lenses from P30, P42, and P52 on the Illumina arrays with our data. It should be noted that the data from the two different microarray platforms should not be compared to each other, due to differences in technology for the two arrays. We designated detected (✓) or not detected (n.d.) for the microarray data (Table 2) and included the normalized lens expression numbers for each gene from iSyte 2.0 (Supplemental Table S2). The normalized lens expression values for the two different chip sets were in different ranges. Our data matches closely with the microarray data, except for a few of the genes. We detected the expression of *Epha8*, but the array data did not, and we did not detect *Epha6*, but the Affymetrix array did. Neither microarray tested for *Epha10*.

Table 2. *Eph* and *Efn* transcripts in lens microarray studies and other tissues.

Gene	iSyte 2.0					NCBI
	Affymetrix 430 2.0		Illumina WG-6 v2.0			
	P28 Epi	P56	P30	P42	P52	Other tissues with high expression
Epha1	✓	✓	✓	✓	✓	Duodenum, intestines, lung
Epha2	✓	✓	✓	✓	✓	Duodenum, intestines, lung
Epha3	✓	✓	✓	✓	✓	Embryonic/adult brain, embryonic limb
Epha4	✓	✓	✓	✓	✓	Embryonic/adult brain, embryonic limb, heart
Epha5	✓	✓	✓	✓	✓	Embryonic/adult brain
Epha6	✓	✓	n.d.	n.d.	n.d.	Adult brain
Epha7	✓	✓	✓	✓	✓	Embryonic/adult brain, embryonic limb
Epha8 [1]	n.d	n.d	n.d	n.d	n.d	Embryonic brain, adult cerebellum
Epha10 [2]	N/A	N/A	N/A	N/A	N/A	Embryonic/adult brain, testis
Ephb1	✓	✓	✓	✓	✓	Embryonic/adult brain
Ephb2	✓	✓	✓	✓	✓	Embryonic brain, adrenal, colon, intestines
Ephb3	✓	✓	n.d.	n.d.	n.d.	Embryonic limb, colon, lung, stomach
Ephb4	✓	✓	✓	✓	✓	Embryonic limb, colon, lung, ovary
Ephb6	✓	✓	✓	✓	✓	Thymus, adult cortex
Efna1	✓	✓	✓	✓	✓	Duodenum, lung, intestines
Efna2	✓	✓	n.d.	n.d.	n.d.	Embryonic brain, embryonic liver, ovary
Efna3	✓	✓	n.d.	n.d.	n.d.	Embryonic brain, embryonic limb, stomach
Efna4	✓	✓	✓	✓	✓	Embryonic limb, duodenum, ovary
Efna5	✓	✓	✓	✓	✓	Embryonic brain, embryonic limb, bladder
Efnb1	✓	✓	✓	✓	✓	Colon, duodenum, lung, ovary
Efnb2	✓	✓	✓	✓	✓	Colon, lung
Efnb3 [3]	✓	✓	✓	✓	✓	Embryonic brain, embryonic limb, heart

n.d. = not detected. Bolded genes were detected in our RT-PCR experiments; [1] *Epha8* was detected at low levels in E15.5 and P0 lenses on the Illumina WG-6 v1.1 microarray; [2] *Epha10* was not tested in any of the reported arrays on iStye 2.0; [3] *Efnb3 i*s only expressed in lens epithelial cells.

In Table 2, we also list other mouse tissues with high expression of each *Eph* or *Efn*. We wanted to determine whether there were other tissues with similar expression patterns of *Eph* or *Efn* as in the lens. The lens expresses many of the genes also detected in the brain, lung, and the gastrointestinal tract. However, no other tissues expressed as many *Eph* or *Efn*, compared to the lens.

4. Discussion

Our data shows that the adult mouse lens expresses 7 *Epha*, 5 *Ephb*, 5 *Efna*, and 3 *Efnb* transcripts. Counting all the different variants, we detected 18 *Ephs* and 11 *Efns* in the lens. Of these isoforms, three are only expressed in lens epithelial cells, *Epha7* variant 1, *Efna1* variant 2, and *Efnb3*. *Epha7* variant 1 is also aberrantly expressed in the *EphA2*$^{-/-}$ and *ephrin-A5*$^{-/-}$ lens fiber cells. Interestingly, we only found *Efna3* variant 2 in the control *ephrin-A5*$^{+/+}$ samples. This variant has very faint PCR bands, but was consistently present in the control *ephrin-A5*$^{+/+}$ whole lens, epithelial cell, and fiber cell samples. It is not clear why *EphA2*$^{+/+}$ samples do not also express *Efna3* variant 2. However, this does suggest that, even among control "wild-type" animals, there could be slight strain differences.

This notion is supported by our previous work, showing differences between our control animals vs. pure C57BL6/J wild-type mice [43].

Our data reveals that the loss of EphA2 or ephrin-A5 causes abnormal expression of *Epha7* variant 1 transcripts in KO lens fiber cells. This unexpected result was our first clue about compensatory upregulation or deregulation in KO animals. In addition to our data, a recent work described marked downregulation of *Epha5* transcripts in developing lenses with the disruption of the musculoaponeurotic fibrosarcoma (*MAF*) family of proteins [44]. The data from RNA-seq plates did not distinguish between the 14 variants of *Epha5*. MAFs encode basic leucine zipper transcription factors that are known to be important for lens development and to be involved cataractogenesis [44–50]. There may be other insights that can be gleaned from the microarray data between the control, *EphA2*$^{-/-}$, and *ephrin-A5*$^{-/-}$ lens samples. Comparison of our RT-PCR results and previous microarray data indicate a good match between the information from these data sets for most of the *Eph* and *Efn* isoforms. We may be able to use microarrays to quickly screen our KO lenses for highly upregulated or downregulated *Ephs* and *Efns* and examine large groups of other genes.

Our new method to isolate RNA from epithelial cells allows for ~20–30 PCR reactions, allowing for the efficient screening of transcripts. This protocol makes it possible to identify epithelial-cell specific isoforms. We had presumed that, in the whole lens samples, the fiber cell RNA content would dominate over the smaller amount of RNA from the lens epithelial cells. Different from our investigation of tropomyosin transcripts in whole lens [41] vs. epithelial cells [51], where several isoforms of tropomyosin were only detected in epithelial cell samples, we surprisingly found three epithelial cell-specific *Eph*/*Efn* transcripts (*Epha7* variant 1, *Efna1* variant 2, and *Efnb3*) that were also present in whole lens samples. Of note, *Efnb3* did not have other variants expressed in fiber cells, but it was detected on both microarray platforms in both the epithelial and whole lens samples. Our data suggests that RNA from epithelial cells can be detected in whole lens samples; however, very low expression epithelial-cell-exclusive genes may still be difficult to detect in whole lens samples.

The large number of isoforms and variants of *Ephs* and *Efns* found in adult mouse lenses greatly complicates our search for lens receptor–ligand pairs. EphA receptors mainly bind to ephrin-As, while EphB receptors usually interact with ephrin-Bs [52,53]. Less common are the cross-interactions between EphAs and ephrin-Bs or EphBs and ephrin-As [27,54]. Each receptor can interact with multiple ligands, and similarly, each ligand can bind to multiple receptors [54]. This leads to a complex and large matrix of possible receptor–ligand pairs. To tackle the next phase of this project, we will be designing specific TaqMan real-time PCR assays to uncover changes in *Eph* and *Efn* expression levels between our control and KO samples. This may help us narrow down the list of priority isoforms to study in our KO mouse lines. Following the identification of priority isoforms for study, we plan to perform Western blotting, co-immunoprecipitation, immunostaining, and/or proximity ligation assay to determine the protein localization and receptor–ligand pairs.

Supplementary Materials: The following supporting information can be downloaded at: https://www.mdpi.com/article/10.3390/cells11203291/s1, Table S1: Primers, PCR product size, and PCR temperature; Table S2: Normalized lens expression of Eph and Efn transcripts in lens microarray studies.

Author Contributions: Conceptualization, resources, supervision, project administration, funding acquisition, C.C.; methodology, validation, formal analysis, data curation, writing—original draft preparation, writing—review and editing, visualization, C.C. and M.P.V. All authors have read and agreed to the published version of the manuscript.

Funding: This research was funded by grant R01 EY032056 from the National Eye Institute (to C.C.).

Institutional Review Board Statement: Not applicable.

Informed Consent Statement: Not applicable.

Data Availability Statement: The authors will provide a detailed description of methods and original data upon request.

Acknowledgments: We thank Arya S. Musthyala and Jackson T. Clark for technical assistance and Roberta B. Nowak for helpful discussion and troubleshooting advice.

Conflicts of Interest: The authors declare no conflict of interest.

References

1. Lovicu, F.J.; Robinson, M.L. *Development of the Ocular Lens*; Cambridge University Press: Cambridge, UK, 2004; 398 p.
2. WHO, World Health Organization: World Report on Vision. 2019. Available online: https://www.who.int/publications/i/item/9789241516570 (accessed on 8 October 2019).
3. Berry, V.; Pontikos, N.; Albarca-Aguilera, M.; Plagnol, V.; Massouras, A.; Prescott, D.; Moore, A.T.; Arno, G.; Cheetham, M.E.; Michaelides, M. A recurrent splice-site mutation in *EPHA2* causing congenital posterior nuclear cataract. *Ophthalmic Genet.* **2017**, *39*, 236–241. [CrossRef] [PubMed]
4. Dave, A.; Laurie, K.; Staffieri, S.E.; Taranath, D.; Mackey, D.A.; Mitchell, P.; Wang, J.J.; Craig, J.; Burdon, K.P.; Sharma, S. Mutations in the EPHA2 Gene Are a Major Contributor to Inherited Cataracts in South-Eastern Australia. *PLoS ONE* **2013**, *8*, e72518. [CrossRef] [PubMed]
5. Kaul, H.; Riazuddin, S.A.; Shahid, M.; Kousar, S.; Butt, N.H.; Zafar, A.U.; Khan, S.N.; Husnain, T.; Akram, J.; Hejtmancik, J.F.; et al. Autosomal recessive congenital cataract linked to EPHA2 in a consanguineous Pakistani family. *Mol. Vis.* **2010**, *16*, 511–517. [PubMed]
6. Li, D.; Wang, S.; Ye, H.; Tang, Y.; Qiu, X.; Fan, Q.; Rong, X.; Liu, X.; Chen, Y.; Yang, J.; et al. Distribution of gene mutations in sporadic congenital cataract in a Han Chinese population. *Mol. Vis.* **2016**, *22*, 589–598.
7. Park, J.E.; Son, A.I.; Hua, R.; Wang, L.; Zhang, X.; Zhou, R. Human Cataract Mutations in EPHA2 SAM Domain Alter Receptor Stability and Function. *PLoS ONE* **2012**, *7*, e36564. [CrossRef]
8. Zhai, Y.; Zhu, S.; Li, J.; Yao, K. A Novel Human Congenital Cataract Mutation in EPHA2 Kinase Domain (p.G668D) Alters Receptor Stability and Function. *Investig. Opthalmol. Vis. Sci.* **2019**, *60*, 4717–4726. [CrossRef]
9. Zhang, T.; Hua, R.; Xiao, W.; Burdon, K.P.; Bhattacharya, S.S.; Craig, J.E.; Shang, D.; Zhao, X.; Mackey, D.A.; Moore, A.T.; et al. Mutations of the *EPHA2* receptor tyrosine kinase gene cause autosomal dominant congenital cataract. *Hum. Mutat.* **2009**, *30*, E603–E611. [CrossRef]
10. Jun, G.; Guo, H.; Klein, B.E.K.; Klein, R.; Wang, J.J.; Mitchell, P.; Miao, H.; Lee, K.E.; Joshi, T.; Buck, M.; et al. EPHA2 Is Associated with Age-Related Cortical Cataract in Mice and Humans. *PLoS Genet.* **2009**, *5*, e1000584. [CrossRef]
11. Lin, Q.; Zhou, N.; Zhang, N.; Qi, Y. Mutational Screening of EFNA5 in Chinese Age-Related Cataract Patients. *Ophthalmic Res.* **2014**, *52*, 124–129. [CrossRef]
12. Sundaresan, P.; Ravindran, R.D.; Vashist, P.; Shanker, A.; Nitsch, D.; Talwar, B.; Maraini, G.; Camparini, M.; Nonyane, B.A.S.; Smeeth, L.; et al. EPHA2 Polymorphisms and Age-Related Cataract in India. *PLoS ONE* **2012**, *7*, e33001. [CrossRef]
13. Tan, W.; Hou, S.; Jiang, Z.; Hu, Z.; Yang, P.; Ye, J. Association of EPHA2 polymorphisms and age-related cortical cataract in a Han Chinese population. *Mol. Vis.* **2011**, *17*, 1553–1558.
14. Murugan, S.; Cheng, C. Roles of Eph-Ephrin Signaling in the Eye Lens Cataractogenesis, Biomechanics, and Homeostasis. *Front. Cell Dev. Biol.* **2022**, *10*. [CrossRef]
15. Pitulescu, M.E.; Adams, R.H. Eph/ephrin molecules—a hub for signaling and endocytosis. *Genes Dev.* **2010**, *24*, 2480–2492. [CrossRef]
16. Pasquale, E.B. Eph receptors and ephrins in cancer: Bidirectional signalling and beyond. *Nat. Cancer* **2010**, *10*, 165–180. [CrossRef]
17. Darling, T.K.; Lamb, T.J. Emerging Roles for Eph Receptors and Ephrin Ligands in Immunity. *Front. Immunol.* **2019**, *10*, 1473. [CrossRef]
18. Zhang, X.-Q.; Takakura, N.; Oike, Y.; Inada, T.; Gale, N.W.; Yancopoulos, G.D.; Suda, T. Stromal cells expressing ephrin-B2 promote the growth and sprouting of ephrin-B2+ endothelial cells. *Blood* **2001**, *98*, 1028–1037. [CrossRef]
19. Davy, A.; Robbins, S.M. Ephrin-A5 modulates cell adhesion and morphology in an integrin-dependent manner. *EMBO J.* **2000**, *19*, 5396–5405. [CrossRef]
20. Davy, A.; Gale, N.W.; Murray, E.W.; Klinghoffer, R.A.; Soriano, P.; Feuerstein, C.; Robbins, S.M. Compartmentalized signaling by GPI-anchored ephrin-A5 requires the Fyn tyrosine kinase to regulate cellular adhesion. *Genes Dev.* **1999**, *13*, 3125–3135. [CrossRef]
21. Holmberg, J.; Clarke, D.L.; Frisén, J. Regulation of repulsion versus adhesion by different splice forms of an Eph receptor. *Nat.* **2000**, *408*, 203–206. [CrossRef]
22. Lisabeth, E.M.; Falivelli, G.; Pasquale, E.B. Eph Receptor Signaling and Ephrins. *Cold Spring Harb. Perspect. Biol.* **2013**, *5*, a009159. [CrossRef]
23. Noberini, R.; de la Torre, E.R.; Pasquale, E.B. Profiling Eph receptor expression in cells and tissues: A targeted mass spec-trometry approach. *Cell Adh. Migr.* **2012**, *6*, 102–112. [CrossRef]
24. Pasquale, E.B. Eph–ephrin promiscuity is now crystal clear. *Nat. Neurosci.* **2004**, *7*, 417–418. [CrossRef]
25. Pasquale, E.B. Eph–receptor signalling casts a wide net on cell behaviour. *Nat. Rev. Mol. Cell Biol.* **2005**, *6*, 462–475. [CrossRef]
26. Himanen, J.-P.; Saha, N.; Nikolov, D.B. Cell–cell signaling via Eph receptors and ephrins. *Curr. Opin. Cell Biol.* **2007**, *19*, 534–542. [CrossRef]

27. Kullander, K.; Klein, R. Mechanisms and functions of eph and ephrin signalling. *Nat. Rev. Mol. Cell Biol.* **2002**, *3*, 475–486. [CrossRef]
28. Piatigorsky, J. Lens differentiation in vertebrates. A review of cellular and molecular features. *Differentiation* **1981**, *19*, 134–153. [CrossRef]
29. Kuszak, J.R.; Mazurkiewicz, M.; Jison, L.; Madurski, A.; Ngando, A.; Zoltoski, R.K. Quantitative analysis of animal model lens anatomy: Accommodative range is related to fiber structure and organiza-tion. *Vet Ophthalmol* **2006**, *9*, 266–280. [CrossRef]
30. Kuszak, J.; Zoltoski, R.; Sivertson, C. Fibre cell organization in crystalline lenses. *Exp. Eye Res.* **2003**, *78*, 673–687. [CrossRef]
31. Cheng, C.; Ansari, M.M.; Cooper, J.A.; Gong, X. EphA2 and Src regulate equatorial cell morphogenesis during lens development. *Development* **2013**, *140*, 4237–4245. [CrossRef]
32. Cheng, C.; Fowler, V.M.; Gong, X. EphA2 and ephrin-A5 are not a receptor-ligand pair in the ocular lens. *Exp. Eye Res.* **2017**, *162*, 9–17. [CrossRef]
33. Zhou, Y.; Shiels, A. Epha2 and Efna5 participate in lens cell pattern-formation. *Differentiation* **2018**, *102*, 1–9. [CrossRef] [PubMed]
34. Cheng, C. EphA2 and Ephrin-A5 Guide Eye Lens Suture Alignment and Influence Whole Lens Resilience. *Investig. Opthalmol. Vis. Sci.* **2021**, *62*, 3. [CrossRef] [PubMed]
35. Cheng, C.; Wang, K.; Hoshino, M.; Uesugi, K.; Yagi, N.; Pierscionek, B. EphA2 Affects Development of the Eye Lens Nucleus and the Gradient of Refractive Index. *Investig. Opthalmol. Vis. Sci.* **2022**, *63*, 2. [CrossRef] [PubMed]
36. Cheng, C.; Gong, X. Diverse Roles of Eph/ephrin Signaling in the Mouse Lens. *PLoS ONE* **2011**, *6*, e28147. [CrossRef]
37. Shi, Y.; De Maria, A.; Bennett, T.; Shiels, A.; Bassnett, S. A Role for *Epha2* in Cell Migration and Refractive Organization of the Ocular Lens. *Investig. Opthalmol. Vis. Sci.* **2012**, *53*, 551–559. [CrossRef]
38. Parreno, J.; Emin, G.; Vu, M.P.; Clark, J.T.; Aryal, S.; Patel, S.D.; Cheng, C. Methodologies to unlock the molecular expression and cellular structure of ocular lens epithelial cells. *Front. Cell Dev. Biol.* **2022**, *10*, 1827. [CrossRef]
39. Frisén, J.; Yates, P.A.; McLaughlin, T.; Friedman, G.C.; O'Leary, D.D.; Barbacid, M. Ephrin-A5 (AL-1/RAGS) is essential for proper retinal axon guidance and topographic mapping in the mammalian vis-ual system. *Neuron* **1998**, *20*, 235–243. [CrossRef]
40. Brantley-Sieders, D.M.; Caughron, J.; Hicks, D.; Pozzi, A.; Ruiz, J.C.; Chen, J. EphA2 receptor tyrosine kinase regulates endothelial cell migration and vascular assembly through phosphoinositide 3-kinase-mediated Rac1 GTPase activation. *J. Cell Sci.* **2004**, *117*, 2037–2049. [CrossRef]
41. Cheng, C.; Nowak, R.B.; Amadeo, M.B.; Biswas, S.K.; Lo, W.K.; Fowler, V.M. Tropomyosin 3.5 protects the F-actin networks required for tissue biomechanical properties. *J. Cell Sci.* **2018**, *131*, jcs222042. [CrossRef]
42. Kakrana, A.; Yang, A.; Anand, D.; Djordjevic, D.; Ramachandruni, D.; Singh, A.; Huang, H.; Ho, J.W.K.; A Lachke, S. iSyTE 2.0: A database for expression-based gene discovery in the eye. *Nucleic Acids Res.* **2017**, *46*, D875–D885. [CrossRef]
43. Cheng, C.; Gao, J.; Sun, X.; Mathias, R.T. Eph-ephrin Signaling Affects Eye Lens Fiber Cell Intracellular Voltage and Membrane Conductance. *Front. Physiol.* **2021**, *12*, 2072. [CrossRef]
44. Patel, S.D.; Anand, D.; Motohashi, H.; Katsuoka, F.; Yamamoto, M.; Lachke, S.A. Deficiency of the bZIP transcription factors Mafg and Mafk causes misexpression of genes in distinct pathways and results in lens embryonic developmental defects. *Front. Cell Dev. Biol.* **2022**, *10*, 981893. [CrossRef]
45. Agrawal, S.A.; Anand, D.; Siddam, A.D.; Kakrana, A.; Dash, S.; Scheiblin, D.A.; Dang, C.A.; Terrell, A.M.; Waters, S.M.; Singh, A.; et al. Compound mouse mutants of bZIP transcription factors Mafg and Mafk reveal a regulatory network of non-crystallin genes associated with cataract. *Qual. Life Res.* **2015**, *134*, 717–735. [CrossRef]
46. Anand, D.; Agrawal, S.A.; Slavotinek, A.; Lachke, S.A. Mutation update of transcription factor genes FOXE3, HSF4, MAF, and PITX3 causing cataracts and other develop-mental ocular defects. *Hum. Mutat.* **2018**, *39*, 471–494.
47. Jamieson, R.V.; Perveen, R.; Kerr, B.; Carette, M.; Yardley, J.; Heon, E.; Wirth, M.G.; Van Heyningen, V.; Donnai, D.; Munier, F.; et al. Domain disruption and mutation of the bZIP transcription factor, MAF, associated with cataract, ocular anterior segment dysgenesis and coloboma. *Hum. Mol. Genet.* **2002**, *11*, 33–42. [CrossRef]
48. Kawauchi, S.; Takahashi, S.; Nakajima, O.; Ogino, H.; Morita, M.; Nishizawa, M.; Yasuda, K.; Yamamoto, M. Regulation of Lens Fiber Cell Differentiation by Transcription Factor c-Maf. *J. Biol. Chem.* **1999**, *274*, 19254–19260. [CrossRef]
49. Kim, J.I.; Li, T.; Ho, I.-C.; Grusby, M.J.; Glimcher, L.H. Requirement for the c-Maf transcription factor in crystallin gene regulation and lens development. *Proc. Natl. Acad. Sci.* **1999**, *96*, 3781–3785. [CrossRef]
50. Ring, B.Z.; Cordes, S.P.; A Overbeek, P.; Barsh, G.S. Regulation of mouse lens fiber cell development and differentiation by the Maf gene. *Development* **2000**, *127*. [CrossRef]
51. Parreno, J.; Amadeo, M.B.; Kwon, E.H.; Fowler, V.M. Tropomyosin 3.1 Association With Actin Stress Fibers is Required for Lens Epithelial to Mesenchymal Transition. *Investig. Opthalmol. Vis. Sci.* **2020**, *61*, 2. [CrossRef]
52. Himanen, J.-P.; Chumley, M.J.; Lackmann, M.; Li, C.; A Barton, W.; Jeffrey, P.D.; Vearing, C.; Geleick, D.; A Feldheim, D.; Boyd, A.W.; et al. Repelling class discrimination: Ephrin-A5 binds to and activates EphB2 receptor signaling. *Nat. Neurosci.* **2004**, *7*, 501–509. [CrossRef]
53. Takemoto, M.; Fukuda, T.; Sonoda, R.; Murakami, F.; Tanaka, H.; Yamamoto, N. Ephrin-B3-EphA4 interactions regulate the growth of specific thalamocortical axon populations in vitro. *Eur. J. Neurosci.* **2002**, *16*, 1168–1172. [CrossRef] [PubMed]
54. Gale, N.W.; Holland, S.J.; Valenzuela, D.M.; Flenniken, A.; Pan, L.; Ryan, T.E.; Henkemeyer, M.; Strebhardt, K.; Hirai, H.; Wilkinson, D.; et al. Eph Receptors and Ligands Comprise Two Major Specificity Subclasses and Are Reciprocally Compartmentalized during Embryogenesis. *Neuron* **1996**, *17*, 9–19. [CrossRef]

cells

MDPI

Article

The Immediate Early Response of Lens Epithelial Cells to Lens Injury

Samuel G. Novo, Adam P. Faranda, Mahbubul H. Shihan, Yan Wang, Ananya Garg and Melinda K. Duncan *

Department of Biological Sciences, University of Delaware, Newark, DE 19716, USA
* Correspondence: duncanm@udel.edu; Tel.: +1-302-831-0533; Fax: +1-302-831-2281

Abstract: Cataracts are treated by lens fiber cell removal followed by intraocular lens (IOL) implantation into the lens capsule. While effective, this procedure leaves behind numerous lens epithelial cells (LECs) which undergo a wound healing response that frequently leads to posterior capsular opacification (PCO). In order to elucidate the acute response of LECs to lens fiber cell removal which models cataract surgery (post cataract surgery, PCS), RNA-seq was conducted on LECs derived from wild type mice at 0 and 6 h PCS. This analysis found that LECs upregulate the expression of numerous proinflammatory cytokines and profibrotic regulators by 6 h PCS suggesting rapid priming of pathways leading to inflammation and fibrosis PCS. LECs also highly upregulate the expression of numerous immediate early transcription factors (IETFs) by 6 h PCS and immunolocalization found elevated levels of these proteins by 3 h PCS, and this was preceded by the phosphorylation of ERK1/2 in injured LECs. Egr1 and FosB were among the highest expressed of these factors and qRT-PCR revealed that they also upregulate in explanted mouse lens epithelia suggesting potential roles in the LEC injury response. Analysis of lenses lacking either Egr1 or FosB revealed that both genes may regulate a portion of the acute LEC injury response, although neither gene was essential for expression of either proinflammatory or fibrotic markers at later times PCS suggesting that IETFs may work in concert to mediate the LEC injury response following cataract surgery.

Keywords: lens; cataract surgery; wound healing; immediate early genes; inflammation

1. Introduction

The lens is a transparent tissue that refracts light onto the retina and is thus critical for high resolution vision [1]. Cataract, the clouding of the ocular lens due to age, metabolic dysfunction, genetic abnormalities, or ocular injury, was historically the predominate cause of human blindness [2]. However, over the past 50 years, the global burden of cataract has been greatly reduced due to the development of cost effective extracapsular/phacoemulsification cataract extraction methods coupled with the implantation of artificial intraocular lenses which restore vision [3].

While modern cataract surgery has revolutionized the practice of ophthalmology, like all surgeries, it results in elevated inflammation at the wound site [4–6] leading to post-surgical pain and discomfort. As ocular inflammation can also trigger retinal edema, retinal detachment, and exacerbate uveitis [6–10] as well as fibrotic conditions [11,12], it is typically aggressively treated with a combination of steroids and NSAIDs either via eye drops [13,14] or "drop-less" methods [15] which instill anti-inflammatories into the eye at the time of surgery. While these drugs are highly effective, post-surgical inflammation still does occur, and is clinically observed as "flare" [16] defined by increases in the protein concentration of the aqueous humor and the influx of inflammatory cells into the anterior segment of the eye by 20–24 h post cataract surgery (PCS) [17,18].

Concomitant with inflammation, lens epithelial cells (LECs) left behind after cataract surgery undergo a wound healing response characterized by their increased proliferation and migration which occurs simultaneously with their phenotypic conversion into

either myofibroblasts [19] or aberrant lens fiber cells [20,21]. Early in the development of extracapsular cataract surgery methods, these migratory lens–derived cells (LCs) would rapidly populate the posterior lens capsule, leading to the development of posterior capsular opacification (PCO) within weeks or months following cataract surgery. However, advanced IOL designs now physically sequester LCs to the capsular bag periphery, preventing their migration into the optical axis [11], which greatly reduced the incidence of PCO within a year following surgery. However, longer term, PCO is still of clinical concern as lens derived myofibroblasts persist years or even decades following cataract surgery [22], and can escape from the capsular bag periphery leading to PCO development at extended times PCS [23,24].

While the pathogenesis of ocular inflammation PCS has been attributed to mechanical disruption of the blood/aqueous barrier during surgery [25,26], the underlying molecular mechanisms driving this have not been well characterized. However, it has long been recognized that poor control of inflammation is associated with increased risks of retinal damage and aggressive PCO development PCS highlighting the importance of studying its etiology [7]. We recently discovered that the LECs remaining behind after lens fiber cell removal in both mouse [18,27,28] and human (manuscript in preparation) models of cataract surgery massively remodel their transcriptome by 24 h PCS to express high levels of both pro-inflammatory cytokines and fibrotic marker mRNAs. While our prior study found that LECs express elevated protein levels of some inflammatory cytokines by 3–6 h PCS [18], neither the extent of this initial pro-inflammatory response nor potential mechanisms regulating it were known.

Here, we used RNAseq to globally profile the transcriptional changes that mouse LECs undergo by six hours after fiber cell removal in a mouse model of cataract surgery in order to characterize the acute response of these cells to surgery and tested the function of two potential regulators of this initial response.

2. Methods

2.1. Animals

All procedures using mice comply with the Association for Research in Vision and Ophthalmology on the Use of Animals in Vision and Ophthalmologic Research and were approved by the University of Delaware Institutional Animal Care and Use Committee under protocol #1039-2021-1. Animals were bred and maintained in ventilated caging at the University of Delaware animal facility under a 14/10 h light-dark cycle and received food ad libitum.

Mice harboring a germline deletion of the Egr1 (Egr1KO) gene were obtained from the Jackson Laboratory ((JAX stock #012924; B6N; 129-*Egr1*^{tm1Jmi}/J) [29], where they were deposited by Dr. Jeffery Milbrandt, Washington University School of Medicine, St. Louis. These mice were genotyped for lack of an intact Egr1 gene via PCR analysis utilizing the following primers: Common forward: 5′-GGG-CAC-AGG-GGA-TGG-GAA-TG-3′, Wildtype reverse: 5′-AAC-CGG-CCC-AGC-AAG-ACA-CC-3′, Mutant reverse:5′-CTC-GTG-CTT-TAC-GGT-ATC-GC-3′.

Mice harboring a FosB allele where exon 2 and 3 are flanked by lox *p* sites (Fosb$^{tm1.1Nes}$) [30]. were obtained from Drs. Alfred Robinson (Michigan State University) and Eric Nestler (Icahn School of Medicine at Mount Sinai). MLR10 cre mice (Tg(Cryaa-cre)10Mlr) binding site modified alpha-A crystallin promoter [31] were obtained on an FVB/N background from Dr. Michael Robinson (Miami University, Oxford, OH, USA) and backcrossed to C57Bl/6 mice for over 10 generations at the University of Delaware. Mice lacking the FosB gene from the lens (FosBcKO mice) were generated by mating Fosb$^{tm1.1Nes}$ mice with Tg(Cryaa-cre)10Mlr mice. Mice were genotyped for the presence of the floxed FosB allele, and MLR10cre transgene via PCR utilizing the following primers: FosB flox forward: 5′-GCT-GAA-GGA-GAT-GGG-TAA-CAG-3′ and reverse: 5′-AAG-CCT-GGT-ATG-GTG-A-3′: MLR10cre forward: 5′-CCT-GTT-TTG-CAC-GTT-CAC-CG-3′ and reverse: 5′-ATG-CTT-CTG-TCC-GTT-TGC-CG-3′. Successful deletion of exon 2 and 3 of the FosB gene was confirmed by

PCR using genomic DNA isolated from adult mouse lenses utilizing the following primers: forward: 5′-TTC-CCT-TCC-TAT-TTG-TAG-AGC-GTA-G-3′ and reverse: 5′-TGC-TAC-TTG-TGC-CTC-GGT-TTC-C-3′.

2.2. Morphological Analysis

Histological analysis was conducted by isolating eyes from euthanized mice and immediately fixing them in Davidson's Fixative Solution (Electron Microscopy Sciences, Hatfield, PA, USA). The fixed eyes were sent to HistoWiz (Brooklyn, NY, USA), where they were sectioned and stained with hematoxylin and eosin (H&E). The H&E stained slides were then photographed on a Zeiss Axio Observer epifluorescent microscope (Carl Zeiss Inc., Gottingen, Germany).

Lens clarity was assessed by viewing isolated lenses using darkfield optics. Lens optical properties were assessed following previously described methods [32,33] by placing the lenses on a 200-mesh electron microscopy grid. Images were collected with a Zeiss Stemi SV microscope fitted with a darkfield base (Carl Zeiss Inc., Gottingen, Germany).

Lens measurements were conducted by taking images of the reflection of the lens through a 45° mirror (face = 5 mm × 5 mm) (Edmund Optics, Barrington, NJ, USA) as previously described [34] in a plastic box with 1XPBS. The mirror was positioned at a constant distance from the lens and an in-focus image of the mirror edge (length = 5 mm) was also collected for distance calibration. Image measurements were calculated by Fiji ImageJ v52 [35] based on the distance calibration.

2.3. Mouse Cataract Surgery Model

Lens fiber cells were surgically removed from living 3–5 months old mice of both sexes to simulate the extracapsular lens extraction surgery typically performed to treat human cataract [36,37]. Notably, this surgery differs from human cataract surgery in that an anterior capsulotomy is not performed and the lens fiber cell mass is removed as a single unit. Generally, no additional aspiration of lens cortical material is needed for complete fiber cell removal in this method. Samples were collected from euthanized animals at various times post fiber cell removal including 0, 1, 3, 6, 12, 24, 48, 72, and/or 120 h post surgery (post cataract surgery, PCS).

2.4. Next Generation RNA Sequencing and Bioinformatic Analysis

Lens capsular bags with the attached lens cells (LCs) were dissected at either 0 or 6 h PCS. Samples from five independent animals were pooled to create a single biological replicate, then flash frozen on dry ice as previously described [27,28].

Total RNA was extracted from each biological replicate using the RNeasy Mini Kit from Qiagen (Cat No./ID: 74104). RNA libraries were prepared using the SMARTer® Stranded Total RNA-Seq Kit-Pico Input Mammalian (Takara Bio USA, Inc., Mountain View, CA, USA) and sequenced by DNA Link, USA (1000 S Hope St. unit 521 Los Angeles, CA 90015, USA) on a Novaseq 6000 (Los Angeles, CA, USA). Read pairs (101 nucleotides long) were aligned to the Ensembl primary assembly of the mouse GRCm38 genome [38] using the default parameters of Hisat2 [39]. Using the HTseq-Count in union mode [40], read pairs aligned to the genomic features annotated in an Ensembl Mouse GTF file were quantified as gene level counts. The Ensembl version 100 GTF file was used for the initial analysis, and the Ensembl version 104 GTF File was used for later analyses. Following the merging of overlapping exons, length normalized abundance estimates, Fragments per Kilobase-Million (FPKM), were calculated from gene level counts using the total length of all known exons for a given gene.

Samples were partitioned for Trimmed Median of Means (TMM) scaling [41,42] and differential expression analyses were performed based on the objective of a particular contrast.

The edgeR statistical package (version 3.30.3) was used to estimate the magnitude and statistical significance of differential gene expression, with robust dispersion estimates [41,42].

For the initial analysis, edgeR's "Quasi-Likelihood F-Test (QLF-Test) was used for differential expression analysis. It was later determined that in certain cases, the QLF-Test may be overly conservative for data derived from this experiment, thus edgeR's "exact test" was used for the subsequent analysis. As significant effort had been applied to the interpretation of the initial study results, and DEG detected by the QLF-Test are usually also captured by the exact test, re-analysis of the initial study was considered unnecessary. Genes with at least 10 mapped reads in at least three samples were considered to have "detectable" levels of expression. Genes failing "detectable" criteria were removed using edgeR's "filterByExpr" function [43], prior to running statistical tests. Biologically significant differentially expressed genes (DEGs) were characterized as genes exhibiting a statistically significant difference in expression using edgeR's default method to adjust for False Discovery Rate (FDR ≤ 0.05); a difference in expression level greater than 2 FPKM between PCS conditions, Fold Change (FC) greater than 2 in either the positive or negative direction and expressed at a level greater than 2 FPKM as previously used [44].

2.5. Pathway Analyses

iPathwayGuide (Advaita Bioinformatics, Plymouth, MI, USA) pathway analysis was performed on all statistically significant DEGs defined as those exhibiting a fold change $\geq |2|$ and FDR ≤ 0.05. iPathwayGuide uses Impact Analysis, which considers the directed interactions of DEGs within a pathway (as defined by the Kyoto Encyclopedia of Genes and Genomes, KEGG [45], Release 96.0 + 11–21, Nov 20) and if more pathway participants are observed in the DEG list than would be estimated by chance [46–48]. Gene ontology comparisons were made against the 14 October 2020 release of the Gene Ontology Consortium database [49].

2.6. Lens Dissections, Culture and RNA Extractions

Mouse lenses were dissected from the eye after mouse sacrifice using sterile forceps. The lens capsule was removed from the lens then suspension cultured in Medium 199 (ThermoFisher Scientific, Waltham, MA, USA) with 1% penicillin-streptomycin for 6 h or immediately placed into 600 μL of Trizol (two lens capsules/biological replicate; ThermoFisher Scientific, Waltham, MA, USA) and stored at −20 °C. After 6 h of culture, the explants were also placed in Trizol (2 capsules per biological replicate) and stored at −20 °C. Crude RNA was isolated following manufacturer methods and was further purified using the RNA Clean & Concentrator™-5 kit (ZYMO Research, Irvine, CA, USA). Isolated RNA was stored in −80 °C until use.

2.7. cDNA Synthesis and Quantitative RT-PCR

cDNA was synthesized from lens cell RNA using the iScript cDNA Synthesis Kit (Bio-Rad, Hercules, CA and used for real-time quantitative PCR (qRT-PCR) conducted using the Power SYBR Green kit (Invitrogen Life Technology, Carlsbad, CA, USA) using the gene-specific primers shown in Supplementary Table S1. Three biological replicates were analyzed with 2 technical replicates each for each experimental condition and fold-change calculated using the ΔΔCT-method with GAPDH as the housekeeping gene. Statistical significance was determined using a Student's two sample *t*-test.

2.8. Immunofluorescence and Confocal Imaging

Quantitative immunofluorescence was conducted to determine protein level expression in ocular tissue as previously described [50,51]. Briefly, eyes were placed in Optimum Cutting Temperature (OCT) Media (Tissue Tek, Torrance, CA, USA) following harvest and stored at −80 °C. The frozen blocks were then sectioned at 16μm using the Leica CM3050 cryostat (Leica Microsystems, Buffalo Grove, IL, USA) and placed on Color Frost plus microscope slides (Fisher Scientific, Hampton, NH, USA). Slides were fixed under conditions chosen to best optimize staining for the antibody of interest (Supplementary Table S2). Following fixation, blocking buffer optimized for each antibody (100 μL) was applied to

each slide for 1 h at room temperature in a humid chamber (see Supplementary Table S2). Immediately afterwards, the primary antibody diluted in blocking buffer is applied and incubated for either 1 h at room temperature or overnight in 4 °C depending on the antibody (Supplementary Table S2). After primary antibody incubation, slides were washed three times in 1XPBS for 5 min, then the species appropriate Alexa Fluor 488/568 (ThermoFisher Scientific, Waltham, MA, USA) conjugated secondary antibody (if needed) is used at a 1:200 dilution in blocking solution which includes a 1:2000 dilution of Draq-5 (ThermoFisher Scientific, Waltham, MA, USA) to stain DNA and incubated for 1 h at room temperature. After washing, samples were wet mounted in a glycerol based antifade and cover slipped prior to imaging.

During confocal imaging, the negative control was used to measure minimum laser threshold levels to subtract from other experimental images [50,51], in order, to set a baseline, which removes low levels of non-specific binding caused by the secondary antibody. Each immunofluorescence staining experiment was performed with a minimum of three biological replicates. Imaging of the lens capsule and associated lens cells was performed on either a Zeiss LSM780 or Zeiss LSM880 confocal microscope (Carl Zeiss Inc., Gottingen, Germany). The confocal imaging of all slides in the same experiment were imaged the same day using the same imaging parameters to allow direct comparison of experimental conditions and reduce variability [51]. For some figures, brightness and contrast were adjusted post confocal acquisition for optimum viewing on various platforms, but in all cases identical adjustments were on images to be directly compared.

2.9. ImageJ Quantification and Statistical Analysis

Immunofluorescence intensities were quantified on a minimum of three independent biological replicates as previously described (Shihan et al., 2021a). All statistics were performed using either a Student's *t*-test (correct for multiple comparisons using the Holm-Šídák method) or one-way ANOVA with Tukey's post hoc test. Data are presented as mean ± standard error (SE) with statistical differences considered significant when $p \leq 0.05$.

3. Results

Lens epithelial cells of both mice and humans drastically upregulate the expression of numerous inflammatory mediators and fibrotic marker genes by 24 h post cataract surgery (PCS) [18,52]. However, the mechanisms by which lens fiber cell removal drives this transcriptomic shift were unknown. As the earliest change we have observed in lens-derived cells (LCs) post fiber cell removal is the initial upregulation of inflammatory mediators at 6 h PCS [18], we conducted an unbiased RNAseq analysis on wild type mice at 6 h PCS to elucidate potential mechanisms regulating this process. The raw and processed data for this analysis is deposited in the Gene expression omnibus database under accession number GSE206563.

3.1. Lens Epithelial Cells Upregulate the Expression of Numerous Pro-Inflammatory Cytokines by 6 h PCS, but Do Not Yet Upregulate the Expression of Fibrotic Markers

RNAseq revealed that the normal adult mouse epithelium expresses mRNAs encoded by 17,981 genes while 913 genes were differentially expressed at 6 h PCS by at least two fold at a false discovery rate (FDR) corrected p value ≤ 0.05. Filtering these differentially expressed genes (DEGs) for their likelihood to effect cellular biology ("biologically significant" genes exhibit a minimum expression level of 2 FPKM in either condition and at least a 2 Fragments per Kilobase-Million (FPKM) absolute change in expression level [44]), as previously described, revealed 615 DEGs with 547 DEGs being upregulated and 68 DEGs being downregulated (Figure 1A, see Supplementary Table S3).

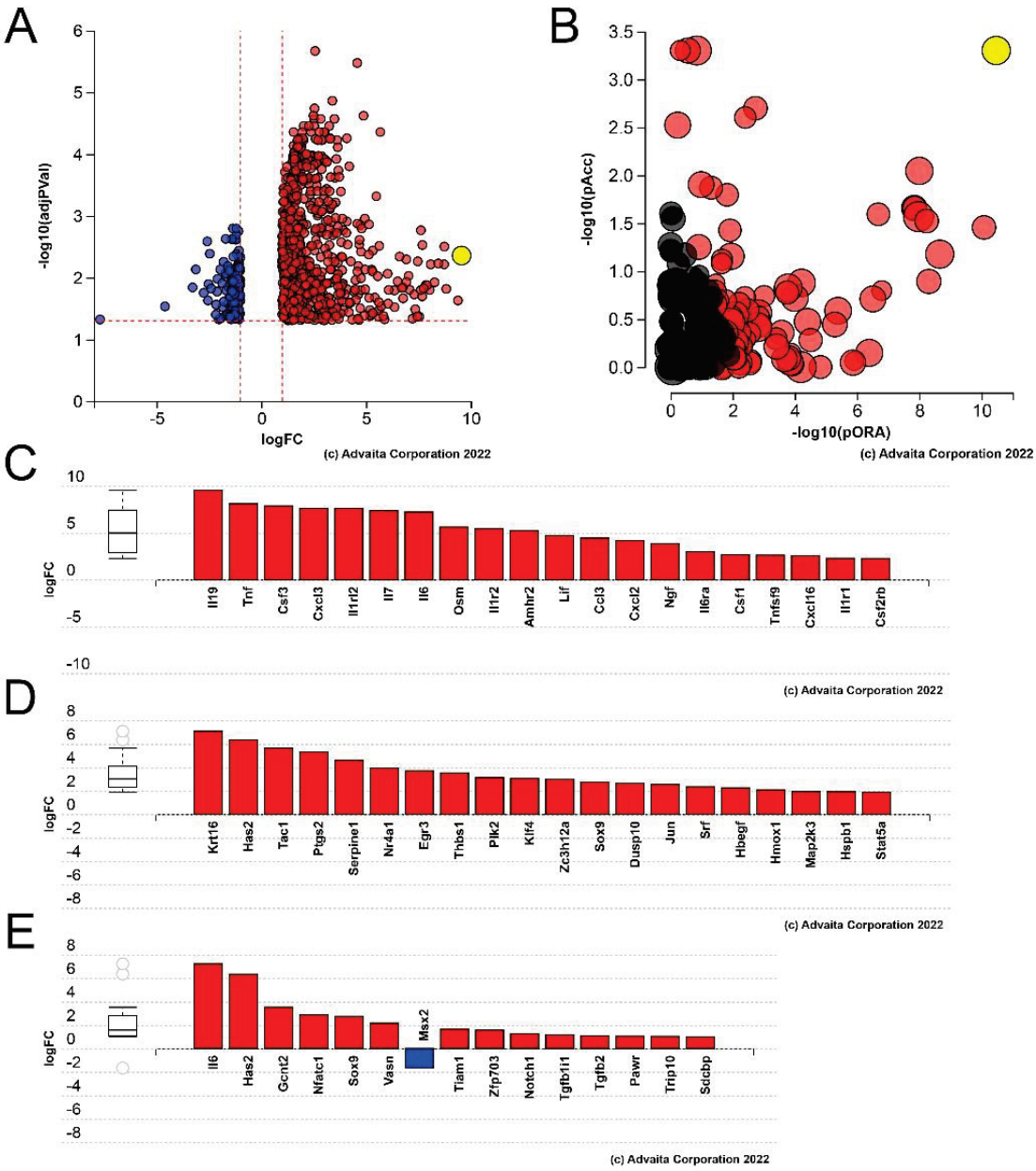

Figure 1. Advaita iPathway analysis of genes differentially expressed at 6 h PCS in LECs. (**A**) Volcano plot of genes (represented by either a blue dot for negative fold change or red dot for positive fold change) whose expression was statistically different in 6 h PCS LECs. Yellow dot represents Il19. (**B**) Impact analysis of the 6 h PCS DEGs predicting that the KEGG pathway "cytokine-cytokine receptor interaction" (p-value of 1.120×10^{-8}) (yellow dot) is the most significantly impacted pathway. While other impacted KEGG pathways are represented by the other dots with black dots being non-significant KEGG pathways and red dots being significant KEGG pathways. (**C**) Bar graph showing which cytokine-cytokine receptor interaction genes are differentially expressed in LECs at 6 h PCS. (**D**) Bar graph showing the "epithelial cell migration" (p-value = 9.600×10^{-5}) genes differentially expressed in 6 h PCS LECs. (**E**) Bar graph showing the DEGs implicated in the "epithelial to mesenchymal transition" (p-value = 0.003) pathway.

Advaita iPathway Guide analysis of the DEGs detected in lens epithelial cells (LECs) at 6 h PCS revealed that, like at 24 h PCS [18], the "cytokine-cytokine receptor interaction" pathway was the most impacted with a p-value of 1.120×10^{-8} (Figure 1B). Of the 615 biologically significant DEGs, the top most upregulated gene at 6 h PCS was Il19, which

is implicated in the inflammatory response [53] (Figure 1A, Table 1) while the mRNA for Ptgs2 which encodes the cyclooxygenase Cox2 was upregulated 37 fold and Csf3 was upregulated 233 fold (Table 1) consistent with our prior observation that both Cox2 and Csf3 were upregulated at the protein level in LECs by 6 h PCS [18].

Table 1. Top 20 most upregulated genes in mouse LECs at 6 h PCS.

Gene Symbol	Gene Name	Wild Type 0H FPKM	Wild Type 6H FPKM	Fold Change	FDR
Il19	Interleukin 19	0.00	3.38	753.97	4.39×10^{-3}
Krtap4-16	Keratin associated protein 4–16	0.00	2.14	427.68	3.14×10^{-3}
Csf3	Colony Stimulating Factor 3	0.11	21.34	232.91	1.31×10^{-2}
Il6	Interleukin 6	0.07	8.55	149.03	4.61×10^{-2}
Fosb	FBJ osteosarcoma oncogene B	1.89	198.30	130.49	9.36×10^{-3}
Ptx3	Pentraxin 3	1.08	105.47	120.93	5.05×10^{-3}
Esm1	Endothelial cell-specific molecule 1	0.16	12.52	96.90	4.56×10^{-3}
Iqcn	IQ motif containing N	0.16	8.66	67.98	1.58×10^{-2}
C2cd4b	C2 calcium-dependent domain containing 4B	0.15	8.17	65.46	8.63×10^{-3}
Emp1	Epithelial membrane protein 1	1.85	76.36	51.28	4.39×10^{-5}
Ifi202b	Interferon activated gene 202B	0.09	3.64	47.32	9.48×10^{-3}
Arc	Activity regulated cytoskeletal associated protein	5.64	183.82	39.94	3.64×10^{-3}
Ptgs2	Prostaglandin-endoperoxide synthase 2	0.65	20.96	39.62	7.93×10^{-3}
Plaur	Plasminogen activator, urokinase receptor	0.18	5.54	36.69	4.17×10^{-2}
Klf2	Kruppel-like factor 2	1.14	28.17	30.60	1.11×10^{-3}
Htr1d	5-hydroxytrptamine receptor 1D	0.54	13.06	29.37	2.39×10^{-5}
Rnf125	Ring finger protein 125	0.18	4.17	27.65	1.60×10^{-3}
F3	Coagulation factor III	1.97	43.91	27.01	3.80×10^{-3}
Lif	Leukemia inhibitory factor	1.50	33.10	26.40	1.41×10^{-3}
Fgl2	Fibrinogen-like protein 2	0.56	11.78	26.39	3.12×10^{-2}

In addition, the DEGs detected at 6 h PCS were significantly enriched in those mapping to pathways necessary for posterior capsular opacification (PCO) pathogenesis including those involved in "epithelial cell migration" (p-value = 9600×10^{-5}) and "epithelial to mesenchymal transition" (p-value = 0.003) (Figure 1D,E). Despite this, fibrotic marker mRNAs commonly associated with fibrotic PCO pathogenesis are not significantly upregulated in LECs by 6 h PCS (Table 2) which suggests that LECs induce inflammatory responses prior to fibrotic responses after lens injury.

Table 2. The expression of classic fibrotic markers does not significantly change in mouse LECs by 6 h PCS.

Gene Symbol	Gene Name	Wild Type 0 h FPKM	Wild Type 6 h FPKM	Fold Change	FDR
Col1a1	Collagen, type I, alpha 1	1.53	7.24	5.80	2.14×10^{-1}
Tnc	Tenascin C	0.65	1.10	2.10	3.43×10^{-1}
Acta2	α Smooth Muscle Actin	53.17	63.90	1.48	7.06×10^{-1}
Itgav	Integrin alpha V	27.55	31.57	1.42	7.71×10^{-2}
Vtn	Vitronectin	23.57	27.60	1.41	6.02×10^{-1}
Fn1	Fibronectin 1	2.79	2.16	−1.03	9.70×10^{-1}
Itgb1	Integrin beta 1	56.79	56.59	1.24	4.17×10^{-1}

While these data revealed that numerous genes were rapidly upregulated PCS, the mechanisms driving this upregulation were unclear. Notably, Advaita iPathway guide Impact analysis of the DEGs in LECs 6 h after lens fiber cell removal revealed that genes involved in Mitogen activated kinase (MAPK) pathways were enriched in this gene set (Figure 2A; p-value = 1.165×10^{-6}). Immunostaining of LECs for phosphorylated ERK1/2

(pERK1/2) revealed that nuclear pERK1/2 levels were sharply elevated at 1 h PCS, decrease by 3 h PCS, then begin to increase again to variable extents by 6 h PCS (Figure 2B–D).

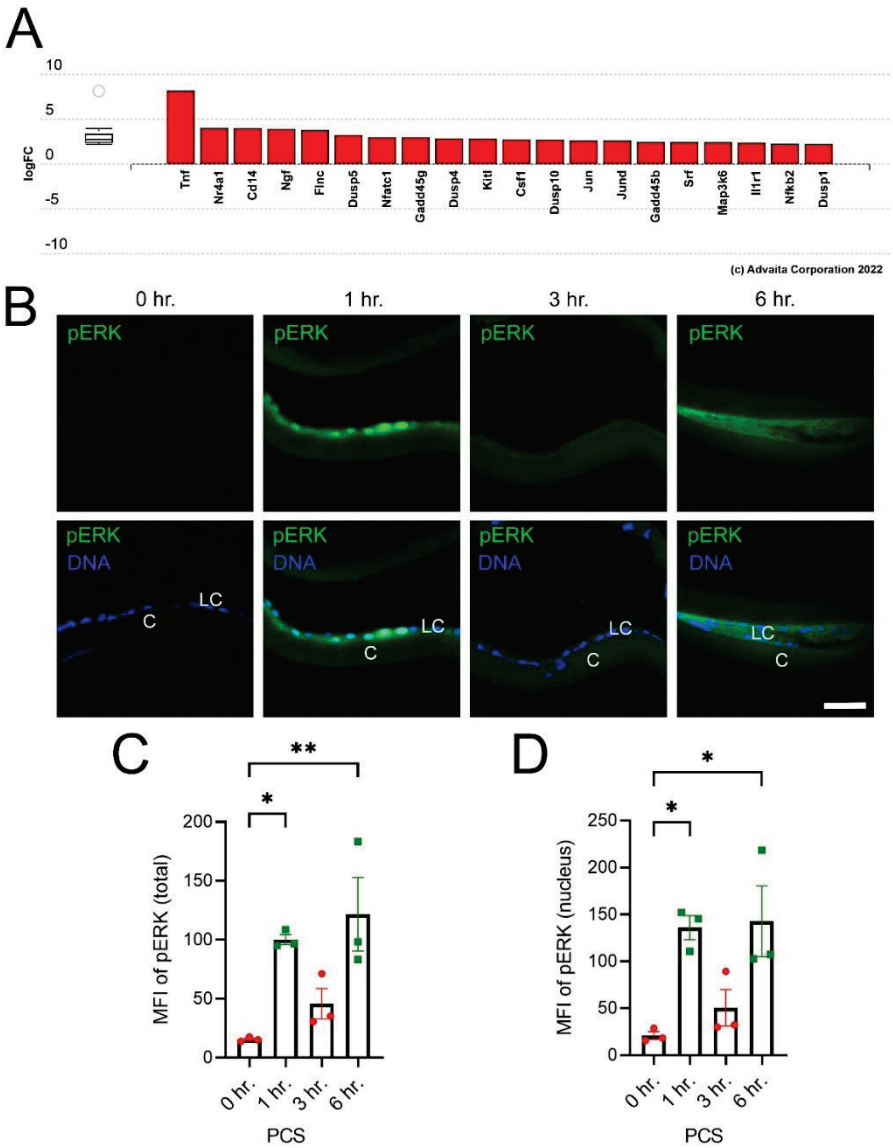

Figure 2. MAPK signaling is acutely activated in LECs after lens injury (**A**) Bar graph of Advaita iPathway analysis of genes differentially expressed in LECs at 6 h PCS associated with MAPK signaling. (**B**) Immunostaining of pERK1/2 (green) in LECs isolated either immediately after lens fiber cell removal (0 h) or 1, 3 or 6 h later. Blue represents DNA. Scale bar = 35 µm (**C**) Quantitiation of total pERK1/2 levels in LECs obtained from three independent biological replicates (**D**) Quantitation of nuclear pERK1/2 levels in LECs obtained from three biological replicates. * represents $p \leq 0.05$; ** represents $p \leq 0.01$. The red dots and green squares in C & D both represent the individual biological replicate values for their corresponding bar in the bar graph.

3.2. Many Immediate Early Transcription Factors Are Upregulated in LECs by 6 h PCS

The changes in the LEC transcriptome at 6 h PCS revealed that LECs rapidly induce the expression of many genes after lens fiber cell removal, however, it was less clear how these changes in RNA levels are regulated. Interestingly, FosB, a member of AP1 family of transcription factors, was one of the most induced and abundantly expressed upregulated genes (130 fold change; FPKM = 198) in LECs at 6 h PCS (Table 1). FosB is also recognized to be an immediate early transcription factor (IETF) as its expression is often rapidly induced

by cell signaling cascades such as MAPK [54,55]. Notably, comparison between the list of genes differentially expressed in LECs at 0 versus 6 h PCS with a list of IETFs identified in other studies [56,57], revealed that the expression of 27 different IETFs are induced by LECs at 6 h after lens fiber cell removal (Table 3).

Table 3. IETFs differentially expressed in wildtype mouse LECs at 6 h PCS.

Gene Symbol	Gene Name	Wild Type 0 h FPKM	Wild Type 6 h FPKM	Fold Change	FDR
Fosb	FBJ osteosarcoma oncogene B	1.89	198.30	130.49	9.36×10^{-3}
Klf2	Kruppel-like factor 2	1.14	28.17	30.60	1.11×10^{-3}
Nr4a1	Nuclear receptor subfamily 4, group A, member 1	8.67	105.28	15.14	3.35×10^{-2}
Zfp36	Zinc finger protein 36	13.93	163.10	14.56	7.59×10^{-3}
Ier2	Immediate early response 2	10.16	111.54	13.66	1.43×10^{-2}
Egr3	Early growth response 3	1.26	13.40	13.09	2.40×10^{-2}
Ier5	Immediate early response 5	5.55	55.82	12.30	5.95×10^{-5}
Egr1	Early growth response 1	33.41	328.89	12.10	3.09×10^{-2}
Atf3	Activating transcription factor 3	33.02	268.96	10.17	3.76×10^{-2}
Ier3	Immediate early response 3	3.45	28.17	9.94	2.35×10^{-4}
Junb	Jun B proto-oncogene	20.98	160.07	9.51	2.97×10^{-3}
Maff	V-maf musculoaponeurotic fibrosarcoma oncogene family, protein F	12.55	89.64	8.82	1.31×10^{-4}
Klf4	Kruppel-like factor 4	25.06	166.32	8.21	3.38×10^{-3}
Egr2	Early growth response 2	0.88	5.49	7.61	4.84×10^{-2}

3.3. IETF MRNA and Protein Levels Acutely Upregulate in LECs at 6 h PCS then Rapidly Fall

We have compiled a database of global gene expression changes occurring in LECs between 0–120 h PCS as measured by bulk RNAseq (lens injury response time series/LIRTS, unpublished) and used this to discover the dynamics of IETF expression in LECs from 0–120 h PCS. This revealed that the mRNA levels of these genes are typically highly induced at 6 h PCS, then sharply downregulate by 24 h PCS (Figure 3). As IETFs have the potential to be mediating the LEC wound healing response, we then validated whether a select set of the IETFs whose mRNA levels upregulate in injured mouse lenses in vivo are also upregulated at the protein level. This analysis revealed that the protein levels of FosB, Egr1, Fos (cFos), JunB and Jun (cJun) all upregulate robustly and significantly in LECs by 6 h PCS, and then begin to downregulate over the next 5 days (Figure 4). Next, we attempted to understand whether this rapid induction of IETF expression in LECs PCS was driven by a cell autonomous LEC response or was triggered by something in the ocular environment. Lenses were dissected, and the lens capsule with attached LECs was either immediately frozen or placed into culture in serum free media for six hours. qRT-PCR analysis of these samples revealed that both FosB and Egr1 mRNA levels upregulate in LECs after 6 h of culture (Figure 5) demonstrating that IETF induction by LECs following injury can occur in the absence of signals from other ocular structures.

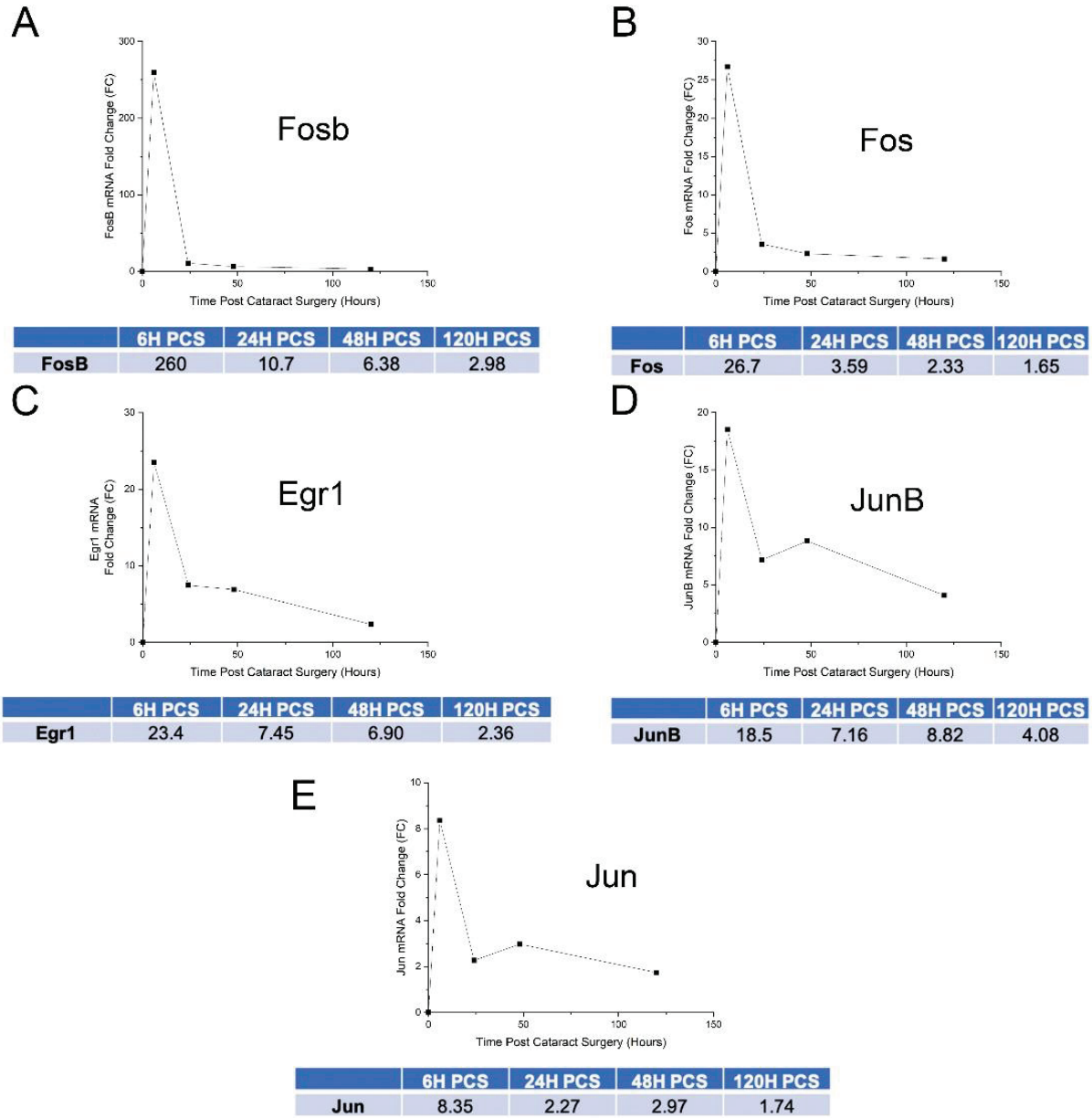

	6H PCS	24H PCS	48H PCS	120H PCS
FosB	260	10.7	6.38	2.98

	6H PCS	24H PCS	48H PCS	120H PCS
Fos	26.7	3.59	2.33	1.65

	6H PCS	24H PCS	48H PCS	120H PCS
Egr1	23.4	7.45	6.90	2.36

	6H PCS	24H PCS	48H PCS	120H PCS
JunB	18.5	7.16	8.82	4.08

	6H PCS	24H PCS	48H PCS	120H PCS
Jun	8.35	2.27	2.97	1.74

Figure 3. Expression dynamics of select IETFs as revealed by bulk RNAseq expression profiling performed between 0–120 h PCS. (**A**) mRNA expression time course for FosB. (**B**) mRNA expression time course for Fos (cFos). (**C**) mRNA expression time course for Egr1. (**D**) mRNA expression time course for JunB. (**E**) mRNA expression time course for Jun (cJun). The Y axis represents fold expression level in comparison to levels observed in naïve LECs.

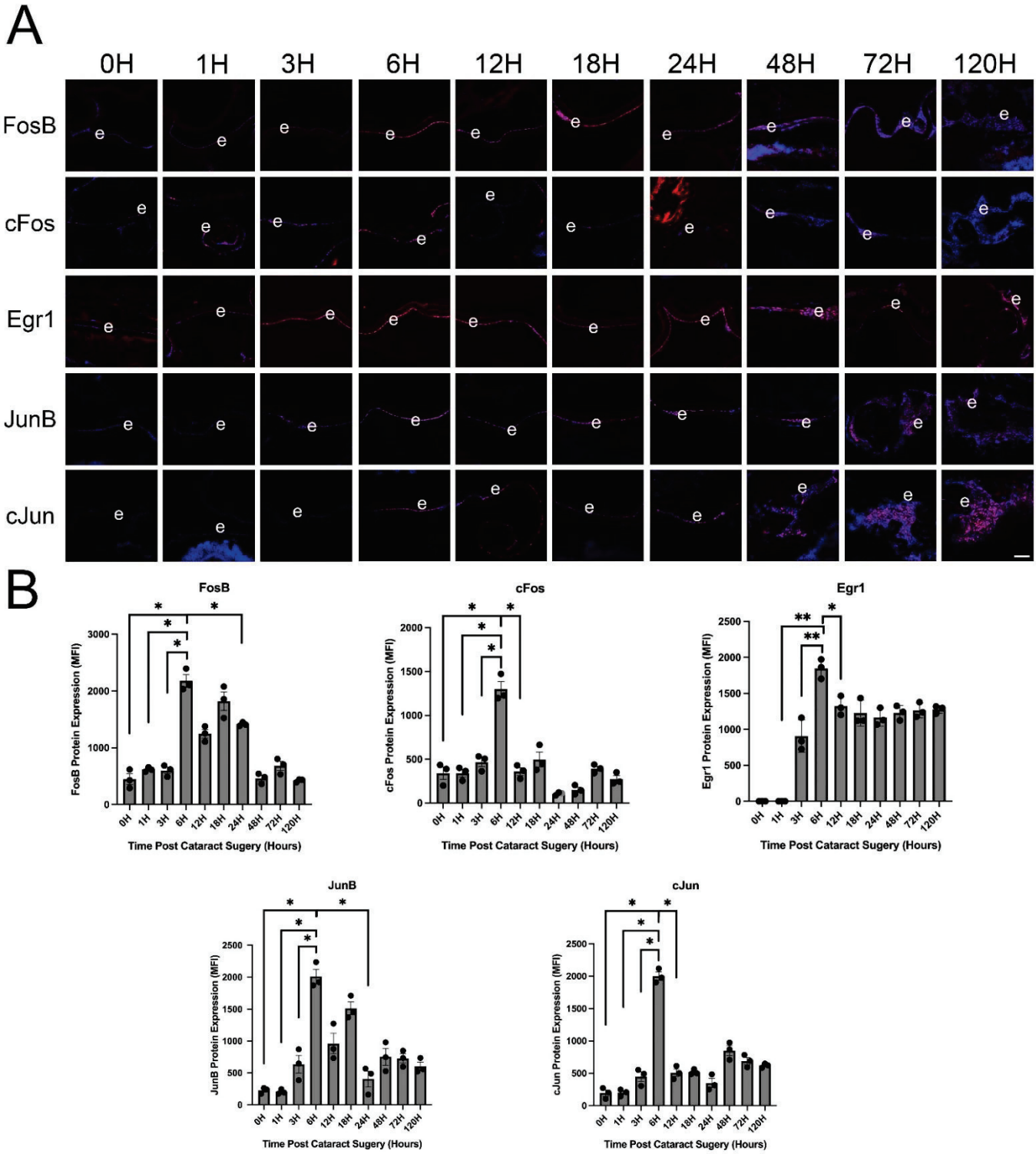

Figure 4. Protein expression of select IETFs in injured mouse lens epithelial cells at various times post lens fiber cell removal. (**A**) Immunolocalization of each studied IETF during the first 120 h (5 days) PCS. Red represents the IETF of interest, Blue represents DNA/cell nuclei. Scale bar = 70 µm. (**B**) Bar graphs representing quantification of the data shown in panel A. FosB * p-value $\leq$ 0.0001; cFos * p-value $\leq$ 0.0001; Egr1 * p-value $\leq$ 0.002 ** p-value $\leq$ 0.0001; JunB * p-value $\leq$ 0.0001; cJun * p-value $\leq$ 0.0001. The black dots in B represent the individual biological replicates for each bar in the bar graph.

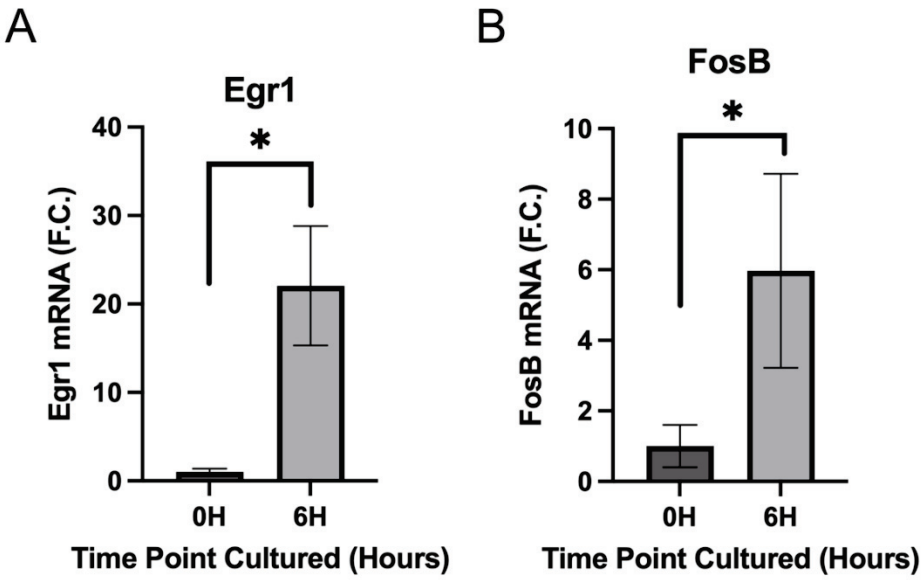

Figure 5. Investigation of the effect of 6 h ex vivo culture on Egr1 and FosB levels in LECs by qRT-PCR (**A**) Egr1 mRNA levels significantly upregulate in LECs after six hours of ex vivo culture (* p-value ≤ 0.01) (**B**) FosB mRNA levels signficantly upregulate in LECs after six hours of ex vivo culture (* p-value ≤ 0.025) FC-fold change from RNA levels obtained from LECs immediately after isolation.

3.4. Removal of the Gene Encoding the IETF Egr1 from the Lens Only Has a Minor Impact on Lens Phenotype

While IETF expression acutely upregulates in LECs at both the RNA and protein levels PCS, their role in the lens injury response was unknown. Notably, Egr1, the most abundantly expressed IETF at the mRNA level (Table 3) which also upregulates at the protein level at 6 h PCS (Figure 4), is a negative regulator of myopia [58] whose expression upregulates in the lens following selenite stress [59] as well as Hsf4 [60] and β1-integrin gene deletion [61]. While the functional importance of Egr1 in the wild type lens is unclear, removal of the Egr1 gene from β1-integrin conditional knockout lenses partially rescued their fibrotic/apoptotic phenotype [61]. Thus, we investigated the possible function of Egr1 in the LEC injury response using Egr1 knockout (Egr1KO) mice [29].

We first confirmed that Egr1KO mice did not express the Egr1 protein (and validated the Egr1 antibody used in this study) by quantitative immunofluorescence (Supplementary Figure S1). Morphologically, adult Egr1KO lenses were the same size as those from their wildtype littermates, but exhibited subtle refractive abnormalities and focal opacities. Hematoxylin and eosin (H&E) staining suggest that Egr1KO lenses are phenotypically similar to wildtype although they may have a slight disorganization of their transition zone (Supplementary Figure S1) suggesting that Egr1 may play a role in regulating adult lens structure.

3.5. Egr1 May Mediate a Portion of the Injury Response of LECs PCS

To investigate the role of Egr1 on the inflammatory and fibrotic response of LECs PCS, we first conducted a candidate gene approach. As previously described [18], we found that Cxcl1, Cox2 and S100a9 protein expression are all upregulated in wild type LECs at 24 h PCS while the upregulation of Cxcl1 and Cox2 was attenuated in Egr1KO mice. However, it appears that the inflammatory response is not globally attenuated as S100a9 expression upregulated normally in Egr1KO LECs at 24 h PCS (Figure 6A,C). Further protein levels for the fibrotic markers Gremlin1 and Tenascin C upregulate in wildtype LECs by 48 h PCS as previously reported [11,62] and this upregulation was not affected in Egr1KO LECs (Figure 6B,C) even though Egr1 has been reported to regulate the fibrotic response in other systems [63].

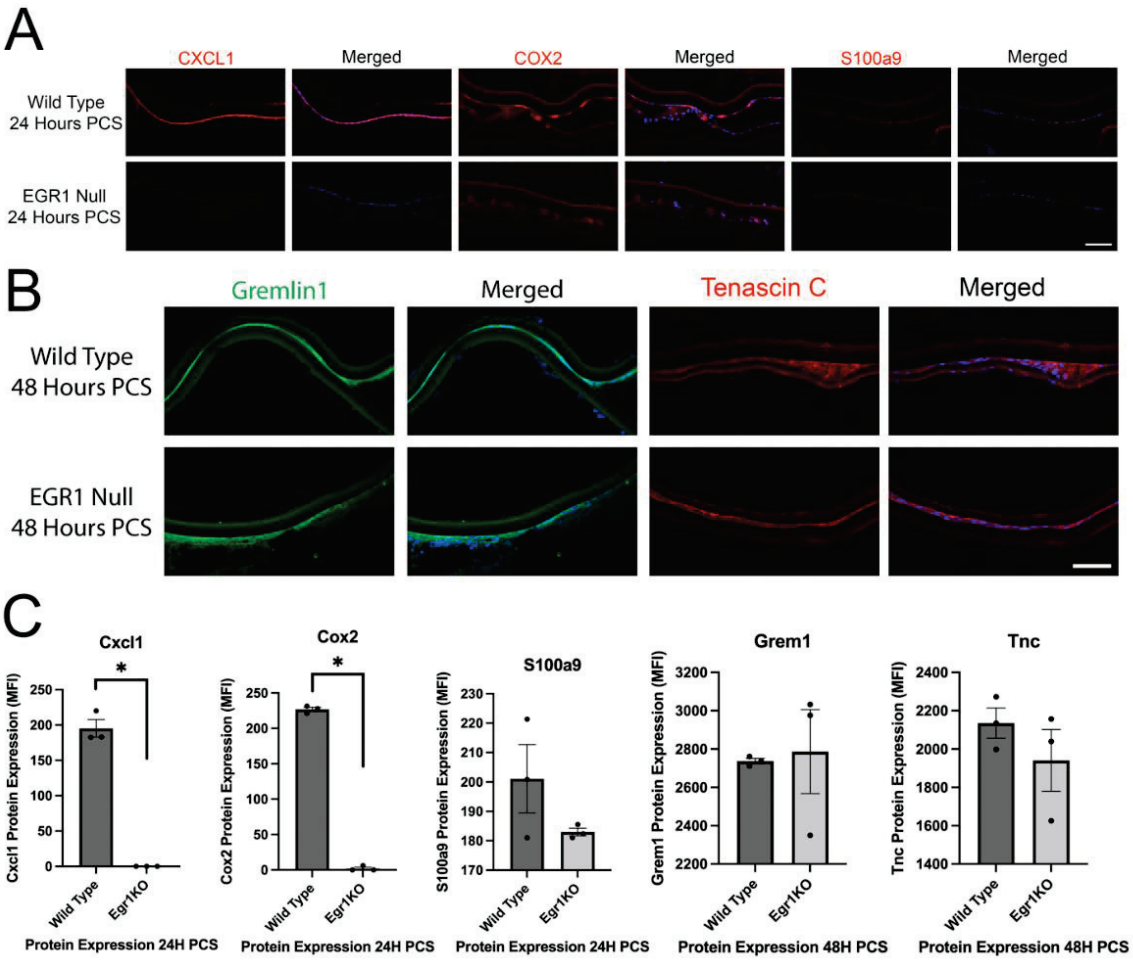

Figure 6. Egr1KO LECs attenuate a portion of their inflammatory response PCS but the fibrotic response was not affected. (**A**) Immunofluorescence analysis of the proinflammatory mediators Cxcl1, Cox2 and S100a9 (red) in LECs from wild type and Egr1KO mice at 24 h PCS. Blue = DNA, Scale bar = 70 μm. (**B**) Immunofluorescence analysis of the fibrotic markers Gremlin1 (green) and Tenascin C (red) in LECs from wild type and Egr1KO mice at 48 h PCS. Blue = DNA, Scale bar = 70 μm. (**C**) Quantitation of the data shown in panels A and B. Cxcl1 and Cox2, * represents $p \leq 0.01$; S100a9, $p = 0.26$; Gremlin 1, $p = 0.84$; Tenascin C, $p = 0.42$. The black dots in C represent the individual biological replicates for each bar in the bar graph.

3.6. Deletion of the IETF Egr1 Only Slightly Affects the Transcriptome of Uninjured LECs but Altered a Portion of the Acute LEC Injury Response

As the function of Egr1 in the adult lens was still obscure following phenotypic and candidate gene investigations, RNAseq was then performed on wildtype and Egr1KO LECs isolated either immediately after lens fiber cell removal surgery or 6 h PCS, a time when Egr1 levels are robustly elevated at both the mRNA and protein levels (Figures 3 and 4).

Comparison of wild type and Egr1KO LECs isolated immediately after lens fiber cell removal revealed that only 59 genes were differentially expressed by at least two-fold (FDR corrected p value ≤ 0.05), with 13 of these genes being upregulated and 46 being downregulated in Egr1KO LECs. Advaita iPathway guide analysis of the DEGs did not reveal any significantly impacted pathways common between the genes, although, 28 of the DEGs did map to the gene ontology term "cellular response to stimulus" (FDR corrected $p = 0.04$). These include the reduced expression of several genes encoding known regulators or targets of the MAPK pathway including Dusp5, Dusp10, Socs3, Arc, Ier5, Mt2 in naïve Egr1KO LECs (Supplementary Table S4; data deposited in the gene expression omnibus under #GSE206574).

Comparison between the transcriptomes of Egr1KO and wildtype LECs at 6 h PCS revealed 115 genes to be significantly differentially expressed by at least two fold (FDR corrected p value ≤ 0.05), with 72 of these genes being upregulated and 43 being downregulated DEGs. Filtering these DEGs for expression changes likely to be biologically significant [44], revealed 73 DEGs with 52 DEGs being upregulated and 21 DEGs downregulated in Egr1KO LECs at 6 h PCS compared to wild type (Supplementary Table S5/GEO#GSE206574). The most upregulated and downregulated genes in Egr1KO LECs at 6 h PCS can be found in Tables 4 and 5, respectively.

Table 4. Topmost upregulated DEGS in Egr1KO LECs at 6 h PCS.

Gene Symbol	Gene Name	Wild Type 6 h FPKM	Egr1KO 6 h FPKM	Fold Change	FDR
Pebp4	Phosphatidylethanolamine binding protein 4	0.14	2.18	14.58	3.33×10^{-3}
Dio3	Deiodinase, iodothyronine type III	0.38	3.29	8.56	9.90×10^{-4}
H2-Aa	Histocompatibility 2, class II antigen A, alpha	0.37	2.88	7.67	4.98×10^{-3}
H2-Eb1	Histocompatibility 2, class II antigen E beta	0.87	6.63	7.50	1.23×10^{-2}
Cd74	CD74 antigen	4.77	24.04	5.02	2.73×10^{-2}
Cxcl1	Chemokine (C-X-C motif) ligand 1	15.11	68.71	4.55	7.51×10^{-7}
Fbn2	Fibrillin 2	0.60	2.65	4.42	2.60×10^{-3}
Il3ra	Interleukin 3 receptor, alpha chain	0.71	3.17	4.41	2.79×10^{-2}
Bmp2	Bone morphogenetic protein 2	5.37	23.64	4.40	5.02×10^{-4}
Slc6a13	Solute carrier family 6, member 13	2.60	11.31	4.34	3.62×10^{-3}

Table 5. Topmost downregulated DEGs seen in Egr1KO LECs at 6 h PCS.

Gene Code	Gene Name	Wild Type 6 h FPKM	Egr1KO 6 h FPKM	Fold Change	FDR
Sst	Somatostatin	6.71	0.13	−39.55	4.98×10^{-3}
Krt5	Keratin 5	14.06	0.64	−21.81	2.89×10^{-2}
C1ql2	Complement component 1	4.94	0.68	−7.08	9.20×10^{-3}
Rit2	Ras-like without CAAX 2	3.51	0.52	−6.66	4.24×10^{-2}
Zfp804a	Zinc finger protein 804A	2.42	0.37	−6.32	2.22×10^{-2}
Col6a3	Collagen, type VI, alpha 3	36.99	5.97	−6.19	3.91×10^{-3}
Spc25	SPC25	14.50	2.88	−5.02	2.14×10^{-3}
Map2k3os	Mitogen-activated protein kinase kinase 3, opposite strand	4.04	0.77	−5.01	2.89×10^{-2}
Rab7b	RAB7B, member Ras oncogene family	4.88	1.01	−4.79	2.22×10^{-2}
Galnt13	Polypeptide N-acetylgalactosaminyltransferase13	2.76	0.64	−4.25	2.22×10^{-2}

3.7. Egr1KO LECs Upregulate Zonule Associated Genes upon Lens Injury

Inspection of the DEGs in Egr1KO LECs at 6 h PCS revealed that the mRNA levels of fibrillin 1 and fibrillin 2, two components of the ciliary zonule that maintains the position of the lens within the eye [64,65], were upregulated compared to wild type LECs at 6 h PCS. In order to evaluate Egr1's involvement in zonular homeostasis, we compared the set of genes differentially expressed between wildtype and Egr1KO LECs to a set of 91 human proteins that proteomic analysis indicates to be the primary constituents of zonular fibers [65]. We observed 5 mouse homologs of human zonular genes with biologically significant and elevated differential expression at six hours PCS in Egr1KO LECs compared to WT (Table 6). This suggests that acute elevation of Egr1 levels apparently represses injury-associated elevation of zonule gene expression in LECs.

Table 6. Egr1KO LECs express elevated levels of genes that encode zonule associated proteins at 6 h PCS.

Gene Code.	Gene Name	Wild Type 6 h FPKM	Egr1KO 6 h FPKM	Fold Change	FDR
Fbn2	Fibrillin 2	0.60	2.65	4.42	2.60×10^{-3}
Fbn1	Fibrillin 1	8.27	30.34	3.67	1.55×10^{-2}
Col18a1	Collagen, type XVIII, alpha 1	21.09	71.66	3.40	2.79×10^{-2}
Ltbp2	Latent transforming growth factor beta binding protein 2	6.54	21.56	3.30	2.70×10^{-2}
Ltbp1	Latent transforming growth factor beta binding protein 1	6.54	17.41	2.66	5.22×10^{-3}

Advaita iPathway analysis of the DEGs in Egr1KO LECs at 6H revealed that the "antigen processing and presentation" pathway (p-value = 4.147×10^{-6}) was the pathway most impacted by Egr1 gene deletion. In addition, genes mapping to the "cytokine-cytokine receptor interaction" (p-value = 0.003), "cell adhesion molecule" (p-value = 0.003) and ECM receptor interaction (p-value = 0.045) gene ontology terms were enriched in the Egr1KO 6H DEGs (Figure 7).

3.8. Generation, Validation and Morphological Analysis of FosB Conditional Knock Out Mice

After the investigation of the Egr1KO LEC injury phenotype, the role of IETFs in regulating the response of LECs to lens fiber cell removal was still obscure. Thus, we investigated the role of FosB in the acute response of LECs to lens injury as it was one of the most upregulated genes (Table 1) and most upregulated IETFs (Table 3) at 6 h PCS. As FosB null mice exhibit nurturing defects [66], we generated mice lacking a functional FosB gene just in the lens (FosBcKO) by breeding a mouse carrying a floxed FosB allele [30] to a mouse containing the MLR10 lens specific cre recombinase transgene [31] (Figure 8A). The complete deletion of the floxed region of the FosB gene was validated by PCR analysis of DNA from mouse lens (Figure 8B) and further confirmation was validated at the protein level via immunofluorescence (Figure 8C,D). FosBcKO lens were the same size as the WT lens (Figure 8F), but similar to the Egr1KO lens, exhibit focal opacities visible by both brightfield and darkfield imaging (Figure 8E). Hematoxylin and eosin (H&E) staining demonstrated that FosBcKO lenses and WT lenses are histologically similar but FosBcKO appear to have a slight disorganization of the transition zone (Figure 8E).

3.9. Acute FosB Elevation PCS May Regulate a Portion of Both the Inflammatory and Fibrotic Responses Post Cataract Surgery

To investigate the role of FosB on the inflammatory response PCS, we first conducted a candidate gene approach based upon the top upregulated and expressed inflammatory cytokines found in [18]. This analysis revealed that Cox2 expression was significantly downregulated in FosBcKO mice at 24 h PCS although Cxcl1 levels were not significantly affected (Figure 9). At 72 h PCS, a time point where fibrotic markers upregulate robustly in injured LECs, FosBcKO LECs exhibit much less Tenascin C upregulation than normal although levels of the fibrotic marker of Gremlin1 was similar between FosBcKO and wild type LECs (Figure 10).

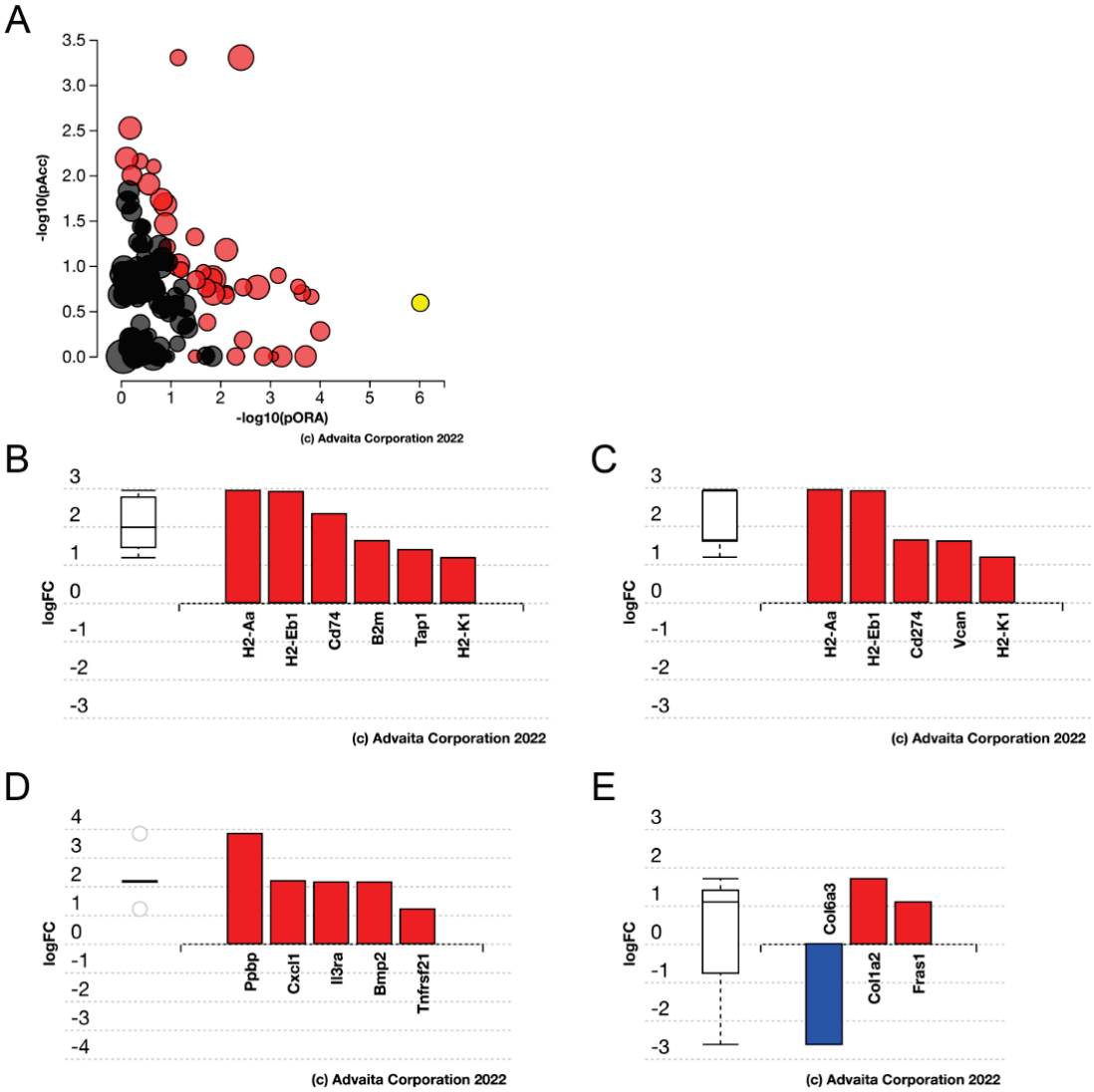

Figure 7. Advaita iPathway analysis of differentially expressed pathways/genes between 6 h Egr1KO and 6 h WT LECs. (**A**) Impact analysis of the DEGs suggest that the KEGG pathway map "antigen processing and presentation" (p-value = 4.147×10^{-6}) (yellow dot) is the most significantly impacted pathway in the 6 h LECs. Other impacted KEGG pathways are represented by the other dots with black dots being non-significant KEGG pathways and red dots being significant KEGG pathways. (**B**) Bar graph showing the antigen processing and presentation genes that are differentially expressed in the 6H Egr1KO LECs. (**C**) Bar graph showing the cell adhesion molecules (p-value = 0.003) pathway of genes differentially expressed in the 6H Egr1KO LECs. (**D**) Bar graph showing the cytokine-cytokine receptor interaction (p-value = 0.003) pathway of genes differentially expressed in the 6H Egr1KO LECs. (**E**) Bar graph showing the ECM receptor interaction (p-value = 0.045) pathway of genes differentially expressed in the 6H Egr1KO LECs.

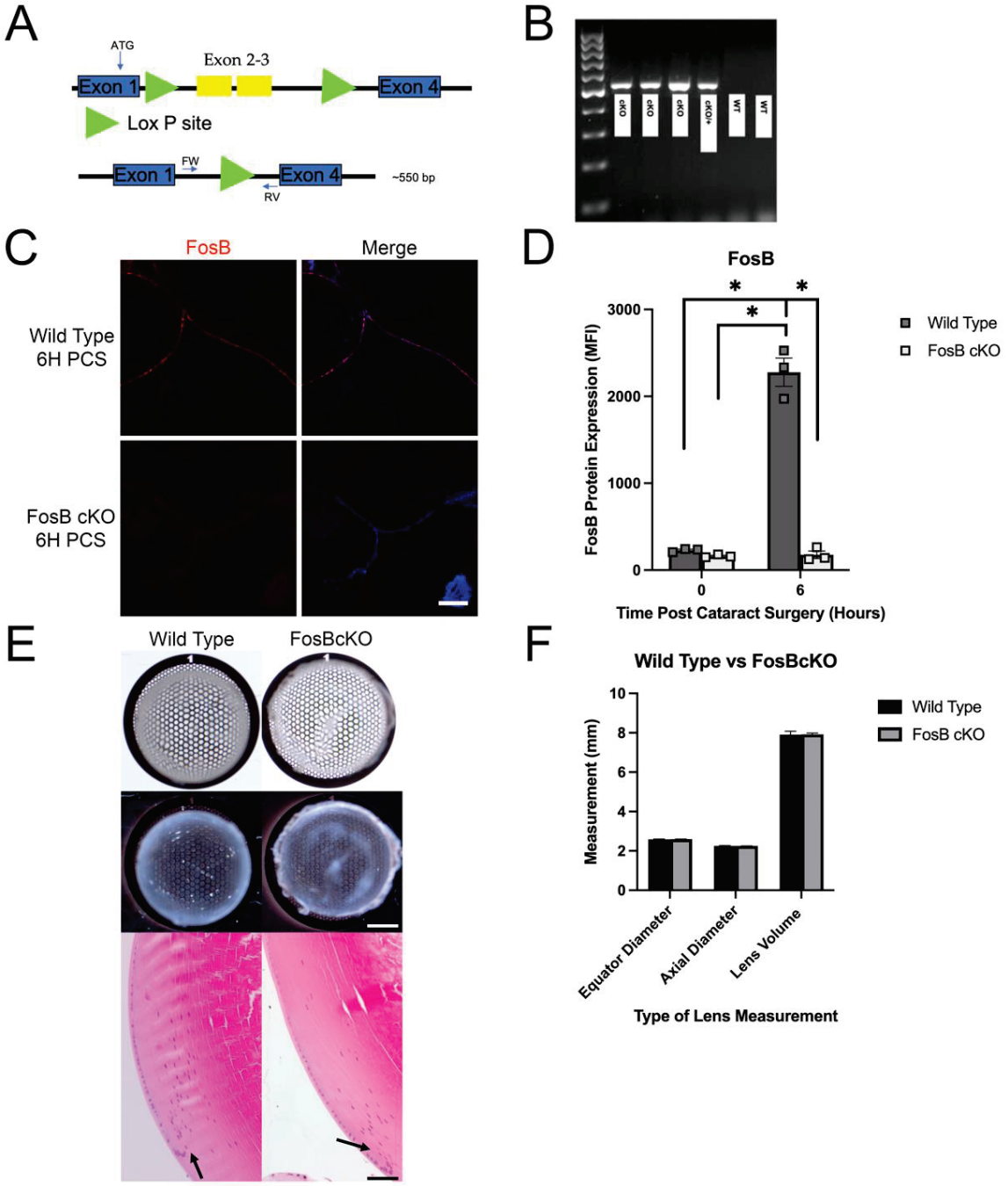

Figure 8. Creation of mice lacking the FosB gene from the lens (FosBcKO) and characterization of its lens phenotype. (**A**) Diagram of the floxed FosB allele before and after cre recombinase mediated deletion. The FosB allele used in this study is flanked by 2 Lox *p* sites (green triangles) around exons 2 and 3. After recombination, the FosB allele has exons 2 and 3 excised. Location of the genotyping primers used to confirm successful excision is indicated by FW and RV. (**B**) PCR analysis of lens DNA obtained from FosBcKO mice showing successful removal of exons 2 and 3. (**C**) Protein validation of the absence of the FosB protein (Red) in FosBcKO LECs via immunofluorescence at 6H PCS (Scale bar 70 μm) (Blue is DNA). (**D**) Quantification of the protein validation experiment in (**C**) * p-value < 0.0001. (**E**) Grid analysis, dark field imaging (Scale bar 50 μm) and H&E staining of the FosBcKO lens (right images) compared to the Wild type lens (left images) (Scale bar 100 μm). The black arrows are utilized to point out the disorganization in the transition zone of the lens. (**F**) Quantification of lens measurements obtained from the FosBcKO lens showing that they were of similar size to wildtype.

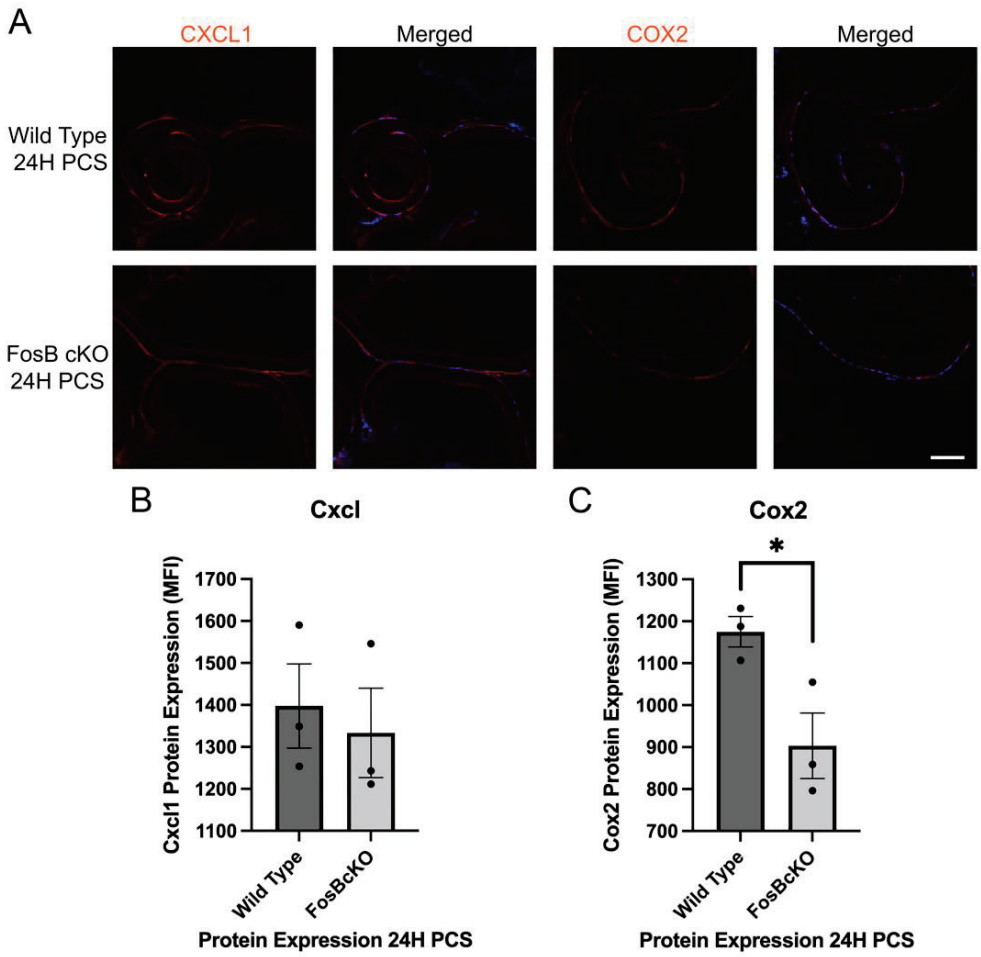

Figure 9. Inflammatory mediator protein expression in FosBcKO LECs compared to Wild Type at 24 h PCS. (**A**) Immunofluorescent staining for the proinflammatory mediators Cxcl1 and Cox2 (red) at 24 h PCS. Blue is DNA and Scale bar = 70 µm. (**B**) Quantification of Cxcl1 levels in LECs at 24 h PCS by immunofluorescence $p = 0.97$. (**C**) Quantification of Cox2 levels in LECs at 24 H PCS by immunofluorescence * represents p-value ≤ 0.01. The black dots in B & C represent the individual biological replicates for each bar in the bar graph.

3.10. Acute FosB Upregulation PCS Regulates Many Genes in Injured LECs

To further investigate the role of FosB in naïve LECs and the LEC injury response, RNAseq was conducted on LECs isolated from wild type and FosBcKO mice at 0 h and 6 h PCS. Notably, uninjured FosBcKO LECs only expressed 43 genes at levels statistically different from wild type, only 25 of which met the biological significant criteria of [44]) showing that the naïve lens transcriptome is only minimally impacted by the absence of FosB (Supplementary Table S6/GEO#GSE206574). However, comparison between FosBcKO and wildtype LECs at 6 h PCS revealed 874 genes to be differentially expressed, 589 meeting the biological significance criteria of [44], 485 DEGs being upregulated and 104 downregulated in FosBcKO LECs (Supplementary Table S7/GEO#GSE206574). The top most upregulated and downregulated genes in this comparison are presented in Tables 7 and 8.

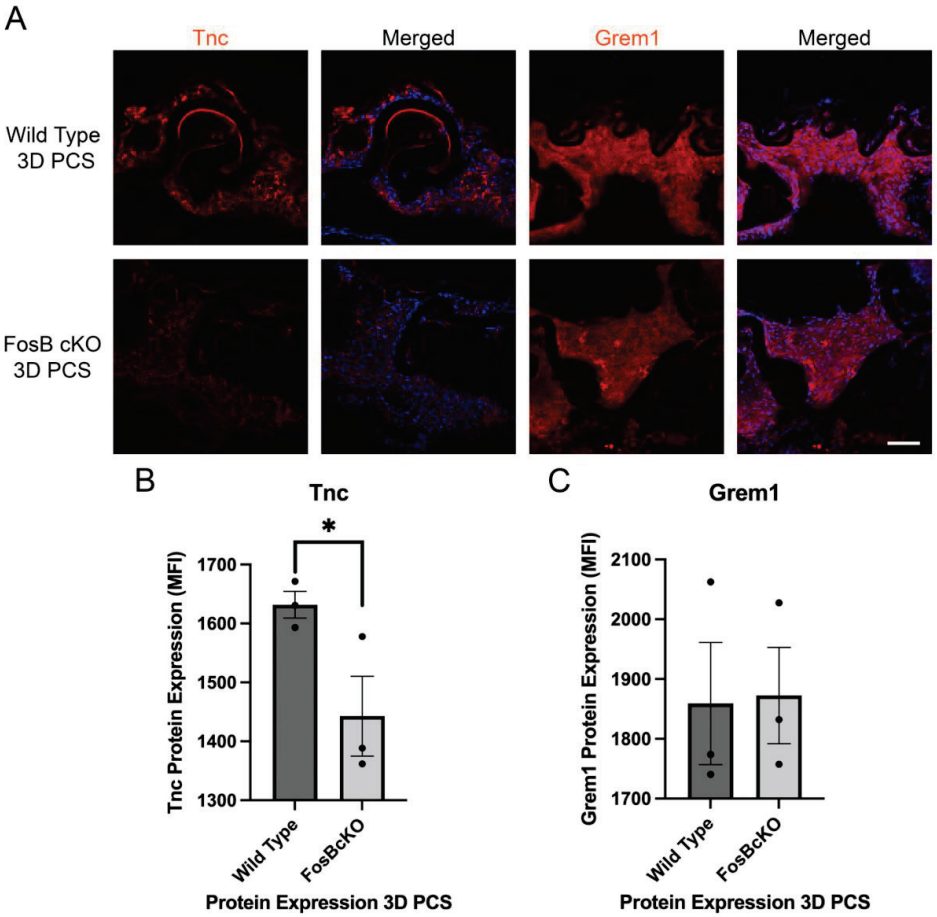

Figure 10. Fibrotic marker protein expression in FosBcKO LECs at 72 h PCS via immunofluorescence. (**A**) The fibrotic markers, Gremlin1 and Tenascin C (red) in wild type and and FosBcKO LECs at 72 h PCS. Blue = DNA, Scale bar = 70 µm. (**B**) Quantitation of Tenascin C protein levels in LECs at 72 h PCS analyzed by immunofluorescence * p-value ≤ 0.05. (**C**) Quantitation of Gremlin1 protein levels in LECs at 72 h PCS analyzed by immunofluorescence $p = 0.99$. The black dots in B & C represent the individual biological replicates for each bar in the bar graph.

Table 7. Top most upregulated DEGs in FosBcKO LECs at 6 h PCS.

Gene Code	Gene Name	Wild Type 6 h FPKM	FosBcKO 6 h FPKM	Fold Change	FDR
Dio3	Deiodinase, iodothyronine type III	0.39	10.75	27.00	4.19×10^{-24}
Pebp4	Phosphatidylethanolamine binding protein 4	0.14	4.11	26.88	4.75×10^{-12}
Clec14a	C-type lectin domain family 14, member a	0.09	2.48	24.75	2.60×10^{-8}
Edn3	Endothelin 3	0.22	3.76	17.00	1.78×10^{-8}
Foxi3	Forkhead box i3	0.83	12.46	14.80	1.39×10^{-10}
Kcnj13	Potassium inwardly rectifying channel, subfamily J, member 13	0.74	11.13	14.74	6.61×10^{-8}
Defb9	Defensin beta 9	0.80	12.02	14.46	2.14×10^{-7}
Fbn2	Fibrillin 2	0.61	8.81	14.27	3.60×10^{-14}
Dsg2	Desmoglein 2	0.36	5.07	13.78	6.46×10^{-24}
Gpx3	Glutathione peroxidase 3	55.77	735.90	13.19	1.38×10^{-14}

Table 8. Top most downregulated DEGs in FosBcKO LECs at 6 h PCS.

Gene Code	Gene Name	Wild Type 6 h FPKM	FosBcKO 6 h FPKM	Fold Change	FDR
Slc29a4	Solute carrier family 29	6.89	0.87	−7.86	2.95×10^{-4}
Sox30	SRY box 30	3.17	0.43	−7.24	1.17×10^{-3}
Gjb3	Gap junction protein, beta 3	4.37	0.62	−7.06	2.73×10^{-2}
Cdcp3	CUB domain containing protein 3	8.71	1.60	−5.43	1.54×10^{-8}
Gjb4	Gap junction protein, beta 4	8.02	1.52	−5.29	3.36×10^{-3}
H1f8	H1.8 linker histone	35.69	6.96	−5.13	1.18×10^{-3}
Cdsn	Corneodesmosin	3.16	0.75	−4.21	1.12×10^{-4}
Alpk2	Alpha-kinase 2	3.24	0.78	−4.16	5.48×10^{-3}
Asb5	Ankyrin repeat and SOCs box-containing 5	6.02	1.45	−4.16	5.48×10^{-3}
Cd109	CD109 antigen	4.25	1.06	−4.01	1.71×10^{-2}

Several DEGs at 6 h PCS with higher expression in FosBcKO LECs compared to wildtype appeared to be associated with zonule formation. As a result, a list of zonules genes from a previous study [65] were used as a filter and revealed that FosBcKO LECs upregulate the expression of zonule genes upon lens injury and at 6 h PCS, this resulted in their elevated expression compared to wildtype (Table 9).

Table 9. Genes encoding zonule components that are upregulated in FosBcKO LECs at 6 h PCS compared to wildtype.

Gene Code	Gene Name	Wild Type 6 h FPKM	FosBcKO 6 h FPKM	Fold Change	FDR
Fbn2	Fibrillin 2	0.61	8.81	14.27	3.60×10^{-14}
Fbn1	Fibrillin 1	8.52	105.46	12.38	6.38×10^{-11}
Col18a1	Collagen, type XVIII, alpha 1	21.68	233.53	10.77	1.43×10^{-9}
Ltbp2	Latent transforming growth factor beta binding protein 2	6.72	72.04	10.71	2.55×10^{-10}
Nid2	Nidogen 2	1.59	16.90	10.58	4.08×10^{-10}
Efemp1	Epidermal growth factor-containing fibulin-like extracellular matrix protein 1	18.34	135.34	7.37	4.46×10^{-12}
Prelp	Proline arginine-rich end leucine-rich repeat	14.44	83.96	5.81	3.11×10^{-11}
Col9a2	Collagen, type IX, alpha 2	6.41	34.69	5.41	1.78×10^{-8}
Hmcn1	Hemicentin 1	0.95	4.20	4.41	1.09×10^{-10}
Ltbp1	Latent transforming growth factor beta binding protein 1	6.75	24.79	3.67	1.32×10^{-10}
Megf	Multiple EGF-like domains 6	1.27	4.39	3.45	4.86×10^{-5}
Loxl1	Lysyl oxidase-like 1	26.12	64.47	2.47	6.21×10^{-4}
Ltbp3	Latent transforming growth factor beta binding protein 3	23.90	52.78	2.21	1.58×10^{-4}
Ctsd	Cathepsin D	31.84	70.16	2.20	4.60×10^{-5}
Timp3	Tissue inhibitor of metalloproteinase 3	94.83	198.21	2.09	1.40×10^{-2}
Tgfb3	Transforming growth factor, beta 3	2.83	5.74	2.03	1.21×10^{-2}
Agrn	Agrin	8.37	16.96	2.03	1.42×10^{-3}

Advaita iPathway analysis revealed that the lack of FosB in LECs compared to WT LECs causes the "cytokine-cytokine receptor interaction" pathway (p-value = 1.655×10^{-6}) to be the most upregulated signaling pathway (Figure 11). In addition, there is an upregulation of cell adhesion molecules (p-value = 7.754×10^{-6}), ECM-receptor interaction (p-value = $4.252 \times$

10^{-5}), and complement and coagulation cascades (p-value = 4.528×10^{-5}) when there is the absence of FosB in the LECs PCS compared to WT LECs PCS.

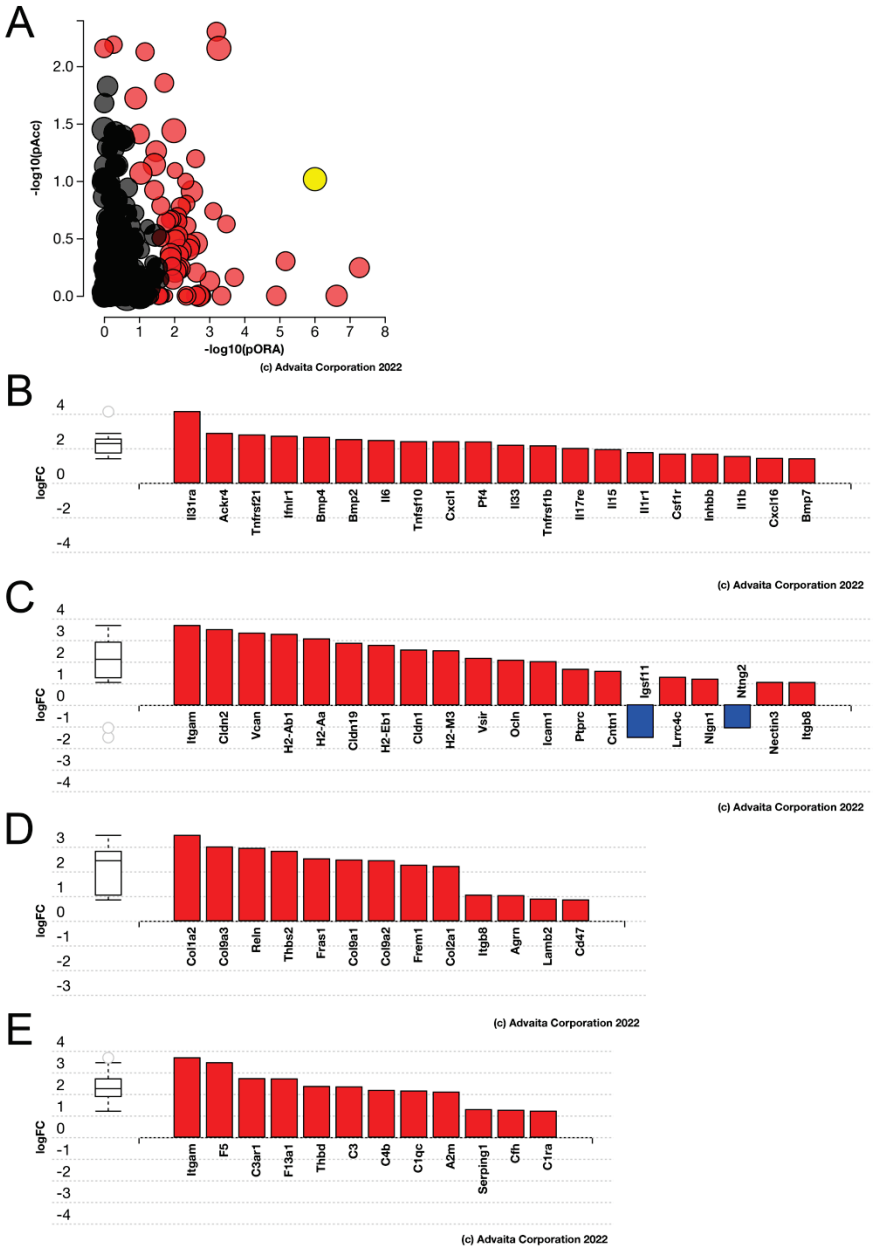

Figure 11. Advaita iPathway analysis of differentially expressed pathways/genes between 6 h FosBcKO and 6 h WT LECs. (**A**) Impact analysis of the DEGs suggest that the KEGG pathway map "cytokine-cytokine receptor interaction" (p-value = 1.655×10^{-6}) (yellow dot) is the most significantly impacted pathway in the 6 h LECs. Other impacted KEGG pathways are represented by the other dots with black dots being non-significant KEGG pathways and red dots being significant KEGG pathways. (**B**) Bar graph showing the cytokine-cytokine receptor interaction genes that are differentially expressed in the 6 h FosBcKO LECs. (**C**) Bar graph showing the cell adhesion molecules (p-value = 7.754×10^{-6}) pathway of genes differentially expressed in the 6 h FosBcKO LECs. (**D**) Bar graph showing the ECM-receptor interaction (p-value = 4.252×10^{-5}) pathway of genes differentially expressed in the 6 h FosBcKO LECs. (**E**) Bar graph showing the complement and coagulation cascades (p-value = 4.528×10^{-5}) pathway of genes differentially expressed in the 6 h FosBcKO LECs.

4. Discussion

Extracapsular cataract extraction followed by intraocular lens implantation [3] is a marvel of modern medicine that has greatly reduced the worldwide burden of cataract-associated visual disability. While great methodological advances have improved the outcomes of this procedure over the past 50 years, post-surgical ocular inflammation [6] can still be problematic in the short term. Longer term, patients still have a significant risk of developing posterior capsular opacification (PCO) during the first decade following surgery [24]. Inflammation following cataract surgery is usually attributed to surgically induced breaks in the blood-aqueous barrier [25,26], and PCO is attributed to elevated TGFβ signaling [12,67] in lens epithelium cells retained on the lens capsular bag following surgery. However, the mechanisms by which cataract surgery induces these negative sequelae are still obscure.

Our prior work found that inflammation markers upregulate in LECs following lens fiber cell removal as early as 6 h post cataract surgery (PCS) with maximal upregulation by 24 h PCS [18] while it takes 48–72 h after surgery for TGFβ signaling leading to lens epithelial cell (LEC) fibrotic responses to elevate [18,36,62]. Here, we used RNAseq to globally evaluate the changes in LEC biology at 6 h PCS and identified a group of transcription factors that might be regulating the LEC injury response which contributes to ocular inflammation and PCO.

4.1. LECs Rapidly Induce the Expression of Pro-Inflammatory Cytokines after Lens Fiber Cell Removal but Fibrotic Responses Are More Delayed

Here, RNAseq confirmed that LECs upregulate the expression of numerous genes encoding pro-inflammatory cytokines by 6 h PCS, including Il19 [68], Csf3 [69], Il6 [70], and Ptgs2 [71], consistent with our prior study showing that select proinflammatory cytokines upregulate at the protein level by 6 h PCS [18]. As signaling from such cytokines can both loosen endothelial tight junctions and chemoattract neutrophils and macrophages to sites of tissue injury [72–75], this suggests that the LECs left on the lens capsular bag following cataract surgery may contribute to the loosening of the blood-aqueous barrier that leads to ocular inflammation (flare plus cells) [16] that is apparent by 24 h PCS.

Further, while remnant LECs still express most lens epithelial cell markers at pre-injury levels at 6 h PCS and did not upregulate mRNAs encoding classic fibrotic markers by this time, they already appear to have elevated the expression of numerous genes needed to set the stage for PCO pathogenesis. Particularly, the upregulated DEGs in LECs at 6 h PCS are enriched in those known to participate in epithelial-mesenchymal transition (EMT) and cell migration pathways which are important for PCO pathogenesis [76]. Notably, these genes are induced in LECs 1–2 days prior to upregulation of the αVβ8-integrin [11] expression needed to activate latent TGFβ and subsequent Smad2/3 phosphorylation which drives the long-term fibrotic response of LECs PCS. These data suggest that LECs are rapidly reprogrammed in response to lens injury/cataract surgery and this sets the stage for later TGFβ pathway mediated loss of lens epithelial marker gene expression and induction of the myofibroblast phenotype.

4.2. Mitogen Activated Protein Kinase Signaling and Immediate Early Transcription Factor Expression Are Rapidly Induced in LECs Following Lens Fiber Cell Removal

Bioinformatic analysis of the DEGs detected in LECs at 6 h PCS found that many genes map to the gene ontology term, mitogen activated protein kinase (MAPK) signaling. Further, direct inspection of the DEGs found that the expression of numerous immediate early transcription factors (IETFs), which are known to be the first genes whose expression is elevated by MAPK signaling in other systems [77,78], were elevated by 6 h PCS. We subsequently experimentally confirmed that these observations which suggests that the lens wound healing response is triggered by an event occurring during cataract surgery that leads to acute MAPK pathway activation and subsequent IETF expression. As isolated

LEC/lens capsule complexes subjected to 6 h of ex vivo serum-free culture also induce the expression of IETFs, this response appears to be autonomous to LECs themselves.

While future work is needed to identify the trigger of MAPK signaling, there are several possibilities. Danger-associated molecular patterns (DAMPs) are intracellular proteins which are released upon cellular injury. They can bind to DAMP receptors (Toll-like receptors are the best characterized members of this class) which activates several downstream signaling pathways including MAPK [79]. While cataract surgery would be expected to release known DAMPs such as αA- and αB- crystallins [80] into the ocular environment, inspection of the LEC transcriptome for DAMP receptors suggested that this pathway may not be the acute trigger of the LEC injury response as their expression levels are low in naïve LECs. However, DAMP receptors may play a role in later LEC responses post-surgery as their expression elevates at later times PCS. Alternatively, the biomechanical stress placed on the remnant LECs during fiber cell removal could be the trigger. Biomechanical stress on the lens has been reported to acutely induce the expression of IETFs in LECs [81,82] and when the biomechanical stress is high or prolonged, anterior subcapsular cataract develops [83,84], which like PCO, often involves the EMT of LECs [85]. Notably, naïve LECs do express some known biomechanical sensors including β1-integrin [61] and Piezo1 [86] which, when activated, upregulate the ERK/MAPK signaling cascade and subsequent IETF expression in other systems [87,88].

4.3. The IETFs Egr1 and FosB Regulate Some Aspects of the Lens Wound Healing Response

IETFs are known to regulate wound healing responses in non-lens cell types [89–92], however their functions in the lens are obscure. Here, we found that numerous IETFs upregulate rapidly in injured LECs then downregulate their expression later, although the kinetics of this downregulation varies between IETFs. Here, we tested the function of two of the most upregulated IETFs in LECs, Egr1 and FosB in the lens wound healing response as both genes can be under the control of ERK/MAPK signaling [77,78] and are known to regulate both inflammation [93,94] and fibrosis [63,89] in other tissues.

The absence of Egr1 does not induce major changes to normal lens biology either at the level of structure/transparency nor the global LEC transcriptome. This is consistent with prior reports identifying a role for Egr1 in scleral growth during compensatory myopia in mice although no effects on lens transparency are noted. Prior work has found that Egr1 upregulates in LEC in response to cellular stresses ranging from a loss of calcium homoeostasis due to selenite stress [59] and the loss of β1-integrin [61] while this study found Egr1 expression to rapidly elevate after lens fiber cell removal. However, the function of Egr1 in lens biology is still obscure. While we previously found that deletion of Egr1 from lenses lacking the gene encoding β1-integrin rescued [61] a portion of the LEC phenotype, the genes that Egr1 regulates that lead to lens destruction are still unknown. Here, we found that deletion of Egr1 from lenses subjected to injury only affected the expression of 73 genes, and surprisingly the handful of inflammatory cytokines among this list exhibited elevated expression in Egr1 null LECs at 6 h PCS, including Cxcl1 (4.55 fold), a known Egr1 target gene [94]. However, by 24 h PCS, Egr1 null LECs did exhibit reduced levels of Cxcl1 compared to wild type controls. While the mechanisms that underlay these results are unclear, Egr1 is known to function as both a transcriptional activator and repressor depending on context. LECs do express appreciable levels of the mRNAs encoding the Egr1 co-repressors Nab1 and Nab2 which could explain why Cxcl1 mRNA levels are elevated in Egr1 nulls at 6 h PCS as Cxcl1 is a known Egr1 target gene. It is possible that Egr1 shifts function later in the injury response as Cxcl1 levels are reduced at the protein level in Egr1 null LECs at 24 h PCS which is more consistent with other studies that suggest that Egr1 can activate the inflammatory response in non-lens cells [93,94]. It is also possible that the small effect of Egr1 deletion on the acute injury transcriptome derives from the large number of IETFs (who have similar or identical DNA binding sites) with elevated expression at 6 h PCS creating a "bulk" effect to drive the injury response so that loss of any one component only has a minor effect on the global injury response [95–97].

Like Egr1KO lenses, FosBcKO lenses exhibit neither major structural defects nor large changes in the LEC transcriptome. While it has been reported that elevated expression of the delta FosB (ΔFosB) variant in the lens can result in posterior subcapsular cataract [98], the apparently normal phenotype of FosBcKO lenses is not surprising in light of the low level of FosB expression in healthy LECs. In contrast, LECs lacking FosB exhibit many changes to their acute transcriptomic response to lens fiber cell removal with 874 DEGs detected in FosBcKO LECs at 6 h PCS. However, in contrast to our initial predictions, FosBcKO LECs exhibit higher expression of inflammatory markers than wildtype LECs at 6 h PCS.

FosB is a member of the AP1 family of transcription factors that mediates its function as either a homodimer or a heterodimer with other members of this family. The complexity of FosB function is further expanded by its numerous splice forms including ΔFosB which is a stable transcriptional repressor [99,100]. As the vast majority of the injury related DEGs detected in FosBcKO LECs are upregulated, including other IETFs such as JunB and Ier3 as well as Itgb8 (2 fold) which is critical for TGFβ activation [11] by injured LECs, it is possible that FosB elevation upon lens injury buffers the acute injury response by repressing the action of other IETFs.

5. Conclusions

This study revealed that lens epithelial cells that remain attached to the lens capsule following lens fiber cell removal modeling cataract surgery greatly reprogram their transcriptome by 6 h post surgery which likely sets the stage for subsequent post surgical ocular inflammation and fibrosis/PCO pathogenesis. The rapid elevation of MAPK signaling as measured by ERK phosphorylation post cataract surgery and the subsequent induction of immediate early transcription factor expression suggests that injury induced cell signaling driving the immediate early response sets the stage for the conditions needed to induce the epithelial-mesenchymal transition of lens epithelial cells to myofibroblasts. Further work is necessary to identify the molecular mechanisms by which lens fiber cell removal triggers this response and which IETFs play the most critical roles in setting the stage for later epithelial mesenchymal transition of lens epithelial cells and subsequent fibrotic PCO.

Supplementary Materials: The following supporting information can be downloaded at: https://www.mdpi.com/article/10.3390/cells11213456/s1, Figure S1: Phenotype of the adult Egr1KO lens; Table S1: List of all qRT-PCR primers; Table S2: Primary antibodies used in this study; Table S3: Differential expression of genes between naïve WT LECs and those isolated 6 h PCS; Table S4: Genes differentially expressed in naïve adult mouse LECs due to deletion of the Egr1 gene; Table S5: Genes differentially expressed in between WT adult mouse LECs and those lacking the Egr1 gene at 6 hours PCS; Table S6: Genes differentially expressed in naïve adult mouse LECs due to deletion of the Fosb gene; Table S7: Genes differentially expressed in between WT adult mouse LECs and those lacking the Fosb gene at 6 hours PCS.

Author Contributions: Conceptualization, S.G.N. and M.K.D.; methodology, Y.W. and A.P.F.; investigation, S.G.N., A.P.F., M.H.S., Y.W. and A.G.; data curation, A.P.F.; writing—original draft preparation, S.G.N.; writing—review and editing, S.G.N., M.K.D. and M.H.S.; visualization, S.G.N., A.P.F. and M.K.D.; supervision, M.K.D.; project administration, M.K.D.; funding acquisition, S.G.N. and M.K.D. All authors have read and agreed to the published version of the manuscript.

Funding: This study was supported by National Institutes of Health Grant (EY028597) to MKD; SGN received a Sigma Xi Grant-in-Aid of Research; INBRE program grant P20 GM103446 and the State of Delaware supported the University of Delaware Core Bioimaging Facility; (NIH grant 1S10 RR027273-01) funded the acquisition of the confocal microscope used in this study.

Institutional Review Board Statement: The animal study protocol was approved by the Institutional Review Board of the University of Delaware (protocol code 1039, approved 12 January 2021).

Data Availability Statement: The RNAseq data presented in this manuscript can be obtained at the Gene Expression Omnibus under accession numbers GSE206563 and GSE206574.

Conflicts of Interest: The authors declare no conflict of interest.

References

1. Wormstone, M.; Wride, M.A. The ocular lens: A classic model for development, physiology and disease. *Philos. Trans. R. Soc. B Biol. Sci.* **2011**, *366*, 1190–1192. [CrossRef] [PubMed]
2. Liu, Y.C.; Wilkins, M.; Kim, T.; Malyugin, B.; Mehta, J.S. Cataracts. *Lancet* **2017**, *390*, 600–612. [CrossRef]
3. Ang, B. Cataract Surgery Steps: From Start to Finish. Victoria, Australia: Vision-and-Eye-Health.com. 2022. Available online: https://www.vision-and-eye-health.com/cataractsurgery-steps.html (accessed on 24 October 2022).
4. Khairallah, M.; Kahloun, R.; Bourne, R.; Limburg, H.; Flaxman, S.R.; Jonas, J.B.; Keeffe, J.; Leasher, J.; Naidoo, K.; Pesudovs, K.; et al. Number of People Blind or Visually Impaired by Cataract Worldwide and in World Regions, 1990 to 2010. *Investig. Opthalmol. Vis. Sci.* **2015**, *56*, 6762–6769. [CrossRef] [PubMed]
5. Diagourtas, A.; Petrou, P.; Georgalas, I.; Oikonomakis, K.; Giannakouras, P.; Vergados, A.; Papaconstantinou, D. Bleb failure and intraocular pressure rise following Nd: Yag laser capsulotomy. *BMC Ophthalmol.* **2017**, *17*, 18. [CrossRef]
6. Ascaso, F.J.; Huerva, V.; Grzybowski, A. The Role of Inflammation in the Pathogenesis of Macular Edema Secondary to Retinal Vascular Diseases. *Mediat. Inflamm.* **2014**, *2014*, 432685. [CrossRef] [PubMed]
7. Teh, B.L.; Megaw, R.; Borooah, S.; Dhillon, B. Optimizing cataract surgery in patients with age-related macular degeneration. *Surv. Ophthalmol.* **2017**, *62*, 346–356. [CrossRef] [PubMed]
8. Palestine, A.G.; Pecen, P.E.; Siringo, F.; Colo, A. Retinal Detachments in Patients with Uveitis. Newtown Square, PA, USA: Review of Ophthalmology. 2017. Available online: https://www.reviewofophthalmology.com/article/retinal-detachments-in-patients-with-uveitis (accessed on 10 July 2019).
9. Bhutto, I.; Lutty, G. Understanding age-related macular degeneration (AMD): Relationships between the photoreceptor/retinal pigment epithelium/Bruch's membrane/choriocapillaris complex. *Mol. Asp. Med.* **2012**, *33*, 295–317. [CrossRef]
10. Abbouda, A.; Tortorella, P.; Restivo, L.; Santoro, E.; De Marco, F.; La Cava, M. Follow-Up Study of Over Three Years of Patients with Uveitis after Cataract Phacoemulsification: Outcomes and Complications. *Semin. Ophthalmol.* **2015**, *31*, 532–541. [CrossRef]
11. Shihan, M.H.; Novo, S.G.; Wang, Y.; Sheppard, D.; Atakilit, A.; Arnold, T.D.; Rossi, N.M.; Faranda, A.P.; Duncan, M.K. αVβ8 integrin targeting to prevent posterior capsular opacification. *JCI Insight* **2021**, *6*, e145715. [CrossRef]
12. Wormstone, I.M. Posterior Capsule Opacification: A Cell Biological Perspective. *Exp. Eye Res.* **2002**, *74*, 337–347. [CrossRef]
13. Juthani, V.V.; Clearfield, E.; Chuck, R.S. Non-steroidal anti-inflammatory drugs versus corticosteroids for controlling inflammation after uncomplicated cataract surgery. *Cochrane Database Syst. Rev.* **2017**, *2017*, CD010516. [CrossRef]
14. Colin, J. The Role of NSAIDs in the Management of Postoperative Ophthalmic Inflammation. *Drugs* **2007**, *67*, 1291–1308. [CrossRef] [PubMed]
15. Liegner, J.; Grzybowski, A.; Galloway, M.; Lindstrom, R. Dropless Cataract Surgery: An Overview. *Curr. Pharm. Des.* **2017**, *23*, 558–564. [CrossRef] [PubMed]
16. Sawa, M. Laser flare-cell photometer: Principle and significance in clinical and basic ophthalmology. *Jpn. J. Ophthalmol.* **2016**, *61*, 21–42. [CrossRef] [PubMed]
17. Song, P.; Li, P.; Geng, W.; Qin, M.; Su, S.; Zhou, T.; Yuan, Y.; Zhang, G.; Wu, J.; Ji, M.; et al. Cytokines possibly involved in idiopathic epiretinal membrane progression after uncomplicated cataract surgery. *Exp. Eye Res.* **2022**, *217*, 108957. [CrossRef] [PubMed]
18. Jiang, J.; Shihan, M.H.; Wang, Y.; Duncan, M.K. Lens Epithelial Cells Initiate an Inflammatory Response Following Cataract Surgery. *Investig. Opthalmology Vis. Sci.* **2018**, *59*, 4986–4997. [CrossRef]
19. Eldred, J.A.; Zheng, J.; Chen, S.; Wormstone, I.M. An In Vitro Human Lens Capsular Bag Model Adopting a Graded Culture Regime to Assess Putative Impact of IOLs on PCO Formation. *Investig. Opthalmology Vis. Sci.* **2019**, *60*, 113–122. [CrossRef]
20. Raj, S.M.; Vasavada, A.R.; Johar, S.R.K.; Vasavada, V.A.; Vasavada, V.A. Post-operative capsular opacification: A review. *Int. J. Biomed. Sci.* **2007**, *3*, 237–250. Available online: https://www.ncbi.nlm.nih.gov/pmc/articles/PMC3614664/ (accessed on 12 October 2021).
21. Findl, O.; Neumayer, T.; Hirnschall, N.; Buehl, W. Natural Course of Elschnig Pearl Formation and Disappearance. *Investig. Opthalmology Vis. Sci.* **2010**, *51*, 1547–1553. [CrossRef]
22. Bisevac, J.; Anisimova, N.S.; Nagymihály, R.; Kristianslund, O.; Katta, K.; Noer, A.; Sharafetdinov, I.H.; Drolsum, L.; Moe, M.C.; Malyugin, B.E.; et al. Long-term myofibroblast persistence in the capsular bag contributes to the late spontaneous in-the-bag intraocular lens dislocation. *Sci. Rep.* **2020**, *10*, 20532. [CrossRef]
23. Donachie, P.H.J.; Barnes, B.L.; Olaitan, M.; Sparrow, J.M.; Buchan, J.C. The Royal College of Ophthalmologists' National Ophthalmology Database study of cataract surgery: Report 9, Risk factors for posterior capsule opacification. *Eye* **2022**, *29*, 552–560. [CrossRef] [PubMed]
24. Shihan, M.H.; Novo, S.G.; Duncan, M.K. Cataract surgeon viewpoints on the need for novel preventative anti-inflammatory and anti-posterior capsular opacification therapies. *Curr. Med Res. Opin.* **2019**, *35*, 1971–1981. [CrossRef] [PubMed]
25. Wormstone, I.M.; Eldred, J.A. Experimental models for posterior capsule opacification research. *Exp. Eye Res.* **2016**, *142*, 2–12. [CrossRef]
26. Pande, M.V.; Spalton, D.J.; Kerr-Muir, M.G.; Marshall, J. Postoperative inflammatory response to phacoemulsification and extracapsular cataract surgery: Aqueous flare and cells. *J. Cataract Refract. Surg.* **1996**, *22*, 770–774. [CrossRef]

27. Faranda, A.P.; Shihan, M.H.; Wang, Y.; Duncan, M.K. The effect of sex on the mouse lens transcriptome. *Exp. Eye Res.* **2021**, *209*, 108676. [CrossRef]
28. Faranda, A.P.; Shihan, M.H.; Wang, Y.; Duncan, M.K. The aging mouse lens transcriptome. *Exp. Eye Res.* **2021**, *209*, 108663. [CrossRef]
29. Lee, S.L.; Tourtellotte, L.C.; Wesselschmidt, R.L.; Milbrandt, J. Growth and Differentiation Proceeds Normally in Cells Deficient in the Immediate Early Gene NGFI-A. *J. Biol. Chem.* **1995**, *270*, 9971–9977. [CrossRef]
30. Ohnishi, Y.N.; Eagle, A.L.; Ohnishi, Y.H.; Cahill, M.E.; Wirtz, A.J.; Robinson, A.J.; Nestler, E.J. Generation and Validation of a Floxed Fosb Mouse Line. 2017. Available online: https://www.biorxiv.org/content/10.1101/179309v1 (accessed on 24 October 2022).
31. Zhao, H.; Yang, Y.; Rizo, C.M.; Overbeek, P.A.; Robinson, M.L. Insertion of a Pax6 Consensus Binding Site into the αA-Crystallin Promoter Acts as a Lens Epithelial Cell Enhancer in Transgenic Mice. *Investig. Opthalmology Vis. Sci.* **2004**, *45*, 1930–1939. [CrossRef]
32. Scheiblin, D.A.; Gao, J.; Caplan, J.L.; Simirskii, V.N.; Czymmek, K.J.; Mathias, R.T.; Duncan, M.K. Beta-1 integrin is important for the structural maintenance and homeostasis of differentiating fiber cells. *Int. J. Biochem. Cell Biol.* **2014**, *50*, 132–145. [CrossRef]
33. Shiels, A.; King, J.M.; Mackay, D.S.; Bassnett, S. Refractive Defects and Cataracts in Mice Lacking Lens Intrinsic Membrane Protein-2. *Investig. Opthalmology Vis. Sci.* **2007**, *48*, 500–508. [CrossRef]
34. Gokhin, D.S.; Nowak, R.B.; Kim, N.E.; Arnett, E.E.; Chen, A.C.; Sah, R.L.; Clark, J.I.; Fowler, V.M. Tmod1 and CP49 Synergize to Control the Fiber Cell Geometry, Transparency, and Mechanical Stiffness of the Mouse Lens. *PLoS ONE* **2012**, *7*, e48734. [CrossRef] [PubMed]
35. Schindelin, J.; Arganda-Carreras, I.; Frise, E.; Kaynig, V.; Longair, M.; Pietzsch, T.; Preibisch, S.; Rueden, C.; Saalfeld, S.; Schmid, B.; et al. Fiji: An open-source platform for biological-image analysis. *Nat. Methods* **2012**, *9*, 676–682. [CrossRef] [PubMed]
36. Mamuya, F.A.; Wang, Y.; Roop, V.H.; Scheiblin, D.A.; Zajac, J.C.; Duncan, M.K. The roles of $\alpha_V$integrins in lensEMTand posterior capsular opacification. *J. Cell. Mol. Med.* **2014**, *18*, 656–670. [CrossRef] [PubMed]
37. Desai, V.D.; Wang, Y.; Simirskii, V.; Duncan, M.K. CD44 expression is developmentally regulated in the mouse lens and increases in the lens epithelium after injury. *Differentiation* **2010**, *79*, 111–119. [CrossRef] [PubMed]
38. Yates, A.D.; Achuthan, P.; Akanni, W.; Allen, J.; Alvarez-Jarreta, J.; Amode, M.R.; Armean, I.M.; Azov, A.G.; Bennett, R.; Bhai, J.; et al. Ensembl 2020. *Nucleic Acids Res.* **2020**, *48*, D682–D688. [CrossRef]
39. Kim, D.; Paggi, J.M.; Park, C.; Bennett, C.; Salzberg, S.L. Graph-based genome alignment and genotyping with HISAT2 and HISAT-genotype. *Nat. Biotechnol.* **2019**, *37*, 907–915. [CrossRef]
40. Anders, S.; Pyl, P.T.; Huber, W. HTSeq—A Python framework to work with high-throughput sequencing data. *Bioinformatics* **2015**, *31*, 166–169. [CrossRef]
41. Robinson, M.D.; Oshlack, A. A scaling normalization method for differential expression analysis of RNA-seq data. *Genome Biol.* **2010**, *11*, R25. [CrossRef]
42. Phipson, B.; Lee, S.; Majewski, I.J.; Alexander, W.S.; Smyth, G.K. Robust hyperparameter estimation protects against hypervariable genes and improves power to detect differential expression. *Ann. Appl. Stat.* **2016**, *10*, 946–963. [CrossRef]
43. Chen, Y.; Lun, A.T.L.; Smyth, G.K. From reads to genes to pathways: Differential expression analysis of RNA-Seq experiments using Rsubread and the edgeR quasi-likelihood pipeline. *F1000Research* **2016**, *5*, 1438. [CrossRef]
44. Manthey, A.L.; Terrell, A.M.; Lachke, S.A.; Polson, S.W.; Duncan, M.K. Development of novel filtering criteria to analyze RNA-sequencing data obtained from the murine ocular lens during embryogenesis. *Genom. Data* **2014**, *2*, 369–374. [CrossRef] [PubMed]
45. Kanehisa, M.; Furumichi, M.; Tanabe, M.; Sato, Y.; Morishima, K. KEGG: New perspectives on genomes, pathways, diseases and drugs. *Nucleic Acids Res.* **2017**, *45*, D353–D361. [CrossRef] [PubMed]
46. Tarca, A.L.; Draghici, S.; Khatri, P.; Hassan, S.S.; Mittal, P.; Kim, J.-S.; Kim, C.J.; Kusanovic, J.P.; Romero, R. A novel signaling pathway impact analysis. *Bioinformatics* **2008**, *25*, 75–82. [CrossRef] [PubMed]
47. Draghici, S.; Khatri, P.; Tarca, A.L.; Amin, K.; Done, A.; Voichita, C.; Georgescu, C.; Romero, R. A systems biology approach for pathway level analysis. *Genome Res.* **2007**, *17*, 1537–1545. [CrossRef] [PubMed]
48. Ahsan, S.; Drăghici, S. Identifying Significantly Impacted Pathways and Putative Mechanisms with iPathwayGuide. *Curr. Protoc. Bioinform.* **2017**, *57*, 7.15.1–7.15.30. [CrossRef]
49. Ashburner, M.; Ball, C.A.; Blake, J.A.; Botstein, D.; Butler, H.; Cherry, J.M.; Davis, A.P.; Dolinski, K.; Dwight, S.S.; Eppig, J.T.; et al. Gene ontology: Tool for the unification of biology. *Nat. Genet.* **2000**, *25*, 25–29. [CrossRef]
50. A Reed, N.; Oh, D.-J.; Czymmek, K.J.; Duncan, M.K. An immunohistochemical method for the detection of proteins in the vertebrate lens. *J. Immunol. Methods* **2001**, *253*, 243–252. [CrossRef]
51. Shihan, M.H.; Novo, S.G.; Le Marchand, S.J.; Wang, Y.; Duncan, M.K. A simple method for quantitating confocal fluorescent images. *Biochem. Biophys. Rep.* **2021**, *25*, 100916. [CrossRef]
52. Novo, S.G. Injury Drives Inflammation, then Fibrosis: The Response of the Lens Epithelium to Cataract Surgery Dissertation in Partial Fulfillment of the Ph.D. In *Biological Sciences*; University of Delaware: Newark, DE, USA, 2022; in press; Available online: https://udspace.udel.edu/ (accessed on 24 October 2022).
53. Fujimoto, Y.; Kuramoto, N.; Yoneyama, M.; Azuma, Y.-T. Interleukin-19 as an Immunoregulatory Cytokine. *Curr. Mol. Pharmacol.* **2020**, *14*, 191–199. [CrossRef]

54. Kuroda, K.O.; Meaney, M.J.; Uetani, N.; Fortin, Y.; Ponton, A.; Kato, T. ERK-FosB signaling in dorsal MPOA neurons plays a major role in the initiation of parental behavior in mice. *Mol. Cell. Neurosci.* **2007**, *36*, 121–131. [CrossRef]
55. Granet, C.; Vico, A.G.L.; Alexandre, C.; Lafage-Proust, M.-H. MAP and src kinases control the induction of AP-1 members in response to changes in mechanical environment in osteoblastic cells. *Cell. Signal.* **2002**, *14*, 679–688. [CrossRef]
56. Tyssowski, K.; DeStefino, N.R.; Cho, J.-H.; Dunn, C.J.; Poston, R.G.; Carty, C.E.; Jones, R.D.; Chang, S.M.; Romeo, P.; Wurzelmann, M.K.; et al. Different Neuronal Activity Patterns Induce Different Gene Expression Programs. *Neuron* **2018**, *98*, 530–546.e11. [CrossRef] [PubMed]
57. Tullai, J.W.; Schaffer, M.E.; Mullenbrock, S.; Sholder, G.; Kasif, S.; Cooper, G.M. Immediate-Early and Delayed Primary Response Genes Are Distinct in Function and Genomic Architecture. *J. Biol. Chem.* **2007**, *282*, 23981–23995. [CrossRef]
58. Schippert, R.; Burkhardt, E.; Feldkaemper, M.; Schaeffel, F. Relative Axial Myopia in*Egr-1*(ZENK) Knockout Mice. *Investig. Opthalmology Vis. Sci.* **2007**, *48*, 11–17. [CrossRef] [PubMed]
59. Nakajima, T.; Belusko, P.; Walkup, R.D.; Azuma, M.; Shearer, T.R. Involvement of Egr-1 in lens epithelial cell death induced by selenite. *Exp. Eye Res.* **2006**, *82*, 874–878. [CrossRef] [PubMed]
60. Tian, R.; Xu, Y.; Dou, W.-W.; Zhang, H. Bioinformatics analysis of microarray data to explore the key genes involved in HSF4 mutation-induced cataract. *Int. J. Ophthalmol.* **2018**, *11*, 910–917. [CrossRef] [PubMed]
61. Wang, Y.; Terrell, A.M.; Riggio, B.A.; Anand, D.; Lachke, S.; Duncan, M.K. β1-Integrin Deletion From the Lens Activates Cellular Stress Responses Leading to Apoptosis and Fibrosis. *Investig. Opthalmology Vis. Sci.* **2017**, *58*, 3896–3922. [CrossRef]
62. Shihan, M.H.; Kanwar, M.; Wang, Y.; Jackson, E.E.; Faranda, A.P.; Duncan, M.K. Fibronectin has multifunctional roles in posterior capsular opacification (PCO). *Matrix Biol.* **2020**, *90*, 79–108. [CrossRef]
63. Bhattacharyya, S.; Wu, M.; Fang, F.; Tourtellotte, W.; Feghali-Bostwick, C.; Varga, J. Early growth response transcription factors: Key mediators of fibrosis and novel targets for anti-fibrotic therapy. *Matrix Biol.* **2011**, *30*, 235–242. [CrossRef]
64. Jones, W.; Rodriguez, J.; Bassnett, S. Targeted deletion of fibrillin-1 in the mouse eye results in ectopia lentis and other ocular phenotypes associated with Marfan syndrome. *Dis. Model. Mech.* **2019**, *12*, dmm037283. [CrossRef]
65. De Maria, A.; Wilmarth, P.A.; David, L.L.; Bassnett, S. Proteomic Analysis of the Bovine and Human Ciliary Zonule. *Investig. Opthalmology Vis. Sci.* **2017**, *58*, 573–585. [CrossRef] [PubMed]
66. Brown, J.R.; Ye, H.; Bronson, R.T.; Dikkes, P.; Greenberg, M.E. A Defect in Nurturing in Mice Lacking the Immediate Early Gene fosB. *Cell* **1996**, *86*, 297–309. [CrossRef]
67. de Iongh, R.; Wederell, E.; Lovicu, F.; McAvoy, J. Transforming Growth Factor-β-Induced Epithelial-Mesenchymal Transition in the Lens: A Model for Cataract Formation. *Cells Tissues Organs* **2005**, *179*, 43–55. [CrossRef]
68. Leigh, T.; Scalia, R.G.; Autieri, M.V. Resolution of inflammation in immune and nonimmune cells by interleukin-19. *Am. J. Physiol. Physiol.* **2020**, *319*, C457–C464. [CrossRef]
69. Presicce, P.; Park, C.-W.; Senthamaraikannan, P.; Bhattacharyya, S.; Jackson, C.; Kong, F.; Rueda, C.M.; DeFranco, E.; Miller, L.A.; Hildeman, D.A.; et al. IL-1 signaling mediates intrauterine inflammation and chorio-decidua neutrophil recruitment and activation. *JCI Insight* **2018**, *3*, e98306. [CrossRef] [PubMed]
70. Smith, S.; Wu, P.W.; Seo, J.J.; Fernando, T.; Jin, M.; Contreras, J.; Montano, E.N.; Gabhann, J.N.; Cunningham, K.; Widaa, A.; et al. IL-16/miR-125a axis controls neutrophil recruitment in pristane-induced lung inflammation. *JCI Insight* **2018**, *3*, e120798. [CrossRef] [PubMed]
71. Simon, L.S. Role and regulation of cyclooxygenase-2 during inflammation. *Am. J. Med.* **1999**, *106*, 37S–42S. [CrossRef]
72. Lucchini, A.C.; Gachanja, N.N.; Rossi, A.G.; Dorward, D.A.; Lucas, C.D. Epithelial Cells and Inflammation in Pulmonary Wound Repair. *Cells* **2021**, *10*, 339. [CrossRef]
73. Chi, Z.; Melendez, A.J. Role of Cell Adhesion Molecules and Immune-Cell Migration in the Initiation, Onset and Development of Atherosclerosis. *Cell Adhes. Migr.* **2007**, *1*, 171–175. [CrossRef]
74. Camilleri, M. Leaky gut: Mechanisms, measurement and clinical implications in humans. *Gut* **2019**, *68*, 1516–1526. [CrossRef]
75. Naik, S.; Larsen, S.; Gomez, N.C.; Alaverdyan, K.; Sendoel, A.; Yuan, S.; Polak, L.; Kulukian, A.; Chai, S.; Fuchs, E. Inflammatory memory sensitizes skin epithelial stem cells to tissue damage. *Nature* **2017**, *550*, 475–480. [CrossRef] [PubMed]
76. Eldred, J.A.; Dawes, L.J.; Wormstone, I.M. The lens as a model for fibrotic disease. *Philos. Trans. R. Soc. B Biol. Sci.* **2011**, *366*, 1301–1319. [CrossRef] [PubMed]
77. Gregg, J.; Fraizer, G. Transcriptional Regulation of EGR1 by EGF and the ERK Signaling Pathway in Prostate Cancer Cells. *Genes Cancer* **2011**, *2*, 900–909. [CrossRef] [PubMed]
78. Fujioka, S.; Niu, J.; Schmidt, C.; Sclabas, G.M.; Peng, B.; Uwagawa, T.; Li, Z.; Evans, D.B.; Abbruzzese, J.L.; Chiao, P.J. NF-κB and AP-1 Connection: Mechanism of NF-κB-Dependent Regulation of AP-1 Activity. *Mol. Cell. Biol.* **2004**, *24*, 7806–7819. [CrossRef] [PubMed]
79. Peroval, M.Y.; Boyd, A.C.; Young, J.R.; Smith, A.L. A Critical Role for MAPK Signalling Pathways in the Transcriptional Regulation of Toll Like Receptors. *PLoS ONE* **2013**, *8*, e51243. [CrossRef]
80. Dulle, J.E.; Fort, P.E. Crystallins and neuroinflammation: The glial side of the story. *Biochim. et Biophys. Acta (BBA)-Gen. Subj.* **2016**, *1860*, 278–286. [CrossRef]
81. Shirai, K.; Saika, S.; Okada, Y.; Miyamoto, T.; Ueyama, T.; Ohnishi, Y. Transcriptional activation in lens epithelial cells following an ocular blunt trauma. *J. Cataract Refract. Surg.* **2005**, *31*, 1226–1230. [CrossRef]

82. Shirai, K.; Okada, Y.; Saika, S.; Senba, E.; Ohnishi, Y. Expression of Transcription Factor AP-1 in Rat Lens Epithelial Cells during Wound Repair. *Exp. Eye Res.* **2001**, *73*, 461–468. [CrossRef]
83. Tang, J.; Salzman, I.J.; Sable, M.D. Traumatic cataract formation after vigorous ocular massage. *J. Cataract Refract. Surg.* **2003**, *29*, 1641–1642. [CrossRef]
84. Gremida, A.; Kassem, I.; Traish, A. Anterior capsular rupture following blunt ocular injury. *Digit. J. Ophthalmol.* **2011**, *17*, 66–68. [CrossRef]
85. Lovicu, F.J.; Schulz, M.W.; Hales, A.M.; Vincent, L.N.; Overbeek, P.A.; Chamberlain, C.G.; McAvoy, J.W. Tgfβ induces morphological and molecular changes similar to human anterior subcapsular cataract. *Br. J. Ophthalmol.* **2002**, *86*, 220–226. Available online: https://www.ncbi.nlm.nih.gov/pmc/articles/PMC1771017/ (accessed on 12 October 2021). [CrossRef] [PubMed]
86. Allen, A.; Maddala, R.; Eldawy, C.; Rao, P.V. Mechanical Load and Piezo1 Channel Regulated Myosin II Activity in Mouse Lenses. *Int. J. Mol. Sci.* **2022**, *23*, 4710. [CrossRef] [PubMed]
87. Shishido, S.; Bã¶nig, H.; Kim, Y.-M. Role of Integrin Alpha4 in Drug Resistance of Leukemia. *Front. Oncol.* **2014**, *4*, 99. [CrossRef]
88. Wu, X.; Hu, J.; Li, G.; Li, Y.; Zhang, J.; Wang, F.; Hu, L.; Fan, Z.; Lü, S.; Ding, G.; et al. Biomechanical stress regulates mammalian tooth replacement via the integrin β1-RUNX2-Wnt pathway. *EMBO J.* **2019**, *39*, e102374. [CrossRef]
89. Ramachandran, A.; Gong, E.M.; Pelton, K.; Ranpura, S.A.; Mulone, M.; Seth, A.; Gomez, P.; Adam, R.M. FosB Regulates Stretch-Induced Expression of Extracellular Matrix Proteins in Smooth Muscle. *Am. J. Pathol.* **2011**, *179*, 2977–2989. [CrossRef] [PubMed]
90. Baron, V.T.; Pio, R.; Jia, Z.; Mercola, D. Early Growth Response 3 regulates genes of inflammation and directly activates IL6 and IL8 expression in prostate cancer. *Br. J. Cancer* **2015**, *112*, 755–764. [CrossRef] [PubMed]
91. Bahrami, S.; Drabløs, F. Gene regulation in the immediate-early response process. *Adv. Biol. Regul.* **2016**, *62*, 37–49. [CrossRef] [PubMed]
92. Andreucci, J.J.; Grant, D.; Cox, D.M.; Tomc, L.K.; Prywes, R.; Goldhamer, D.J.; Rodrigues, N.; Bédard, P.-A.; McDermott, J.C. Composition and Function of AP-1 Transcription Complexes during Muscle Cell Differentiation. *J. Biol. Chem.* **2002**, *277*, 16426–16432. [CrossRef]
93. Cervantes-Madrid, D.L.; Nagi, S.; Gustafsson, A.A. FosB transcription factor regulates COX-2 expression in colorectal cancer cells without affecting PGE2 expression. *Oncol. Lett.* **2017**, *13*, 1411–1416. [CrossRef]
94. Shin, S.Y.; Lee, J.M.; Lim, Y.; Lee, Y.H. Transcriptional regulation of the growth-regulated oncogene α gene by early growth response protein-1 in response to tumor necrosis factor α stimulation. *Biochim. et Biophys. Acta* **2013**, *1829*, 1066–1074. [CrossRef]
95. Veremeyko, T.; Yung, A.W.Y.; Anthony, D.C.; Strekalova, T.; Ponomarev, E.D. Early Growth Response Gene-2 Is Essential for M1 and M2 Macrophage Activation and Plasticity by Modulation of the Transcription Factor CEBPβ. *Front. Immunol.* **2018**, *9*, 2515. [CrossRef] [PubMed]
96. Zhou, L.; Xue, C.; Chen, Z.; Jiang, W.; He, S.; Zhang, X. c-Fos is a mechanosensor that regulates inflammatory responses and lung barrier dysfunction during ventilator-induced acute lung injury. *BMC Pulm. Med.* **2022**, *22*, 9. [CrossRef] [PubMed]
97. Zenz, R.; Eferl, R.; Scheinecker, C.; Redlich, K.; Smolen, J.; Schonthaler, H.B.; Kenner, L.; Tschachler, E.; Wagner, E.F. Activator protein 1 (Fos/Jun) functions in inflammatory bone and skin disease. *Arthritis Res. Ther.* **2007**, *10*, 201. [CrossRef] [PubMed]
98. Kelz, M.B.; Kuszak, J.R.; Yang, Y.; Ma, W.; Steffen, C.; Al-Ghoul, K.; Zhang, Y.J.; Chen, J.; Nestler, E.J.; Spector, A. Deltafosb-induced cataract. *Invest. Ophthalmol. Vis. Sci.* **2000**, *41*, 3523–3538. Available online: https://www.ncbi.nlm.nih.gov/pubmed/11006248 (accessed on 16 September 2022). [PubMed]
99. McClung, C.A.; Nestler, E.J. Regulation of gene expression and cocaine reward by CREB and ΔFosB. *Nat. Neurosci.* **2003**, *6*, 1208–1215. [CrossRef]
100. Nestler, E.J. Transcriptional mechanisms of addiction: Role of ΔFosB. *Philos. Trans. R. Soc. B Biol. Sci.* **2008**, *363*, 3245–3255. [CrossRef]

cells

MDPI

Article

PI3K Isoform-Specific Regulation of Leader and Follower Cell Function for Collective Migration and Proliferation in Response to Injury

Morgan D. Basta [1], A. Sue Menko [1,2] and Janice L. Walker [1,2,*]

[1] Department of Pathology, Anatomy and Cell Biology, Sidney Kimmel Medical College, Thomas Jefferson University, Philadelphia, PA 19107, USA
[2] Department of Ophthalmology, Sidney Kimmel Medical College, Thomas Jefferson University, Philadelphia, PA 19107, USA
* Correspondence: janice.walker@jefferson.edu

Abstract: To ensure proper wound healing it is important to elucidate the signaling cues that coordinate leader and follower cell behavior to promote collective migration and proliferation for wound healing in response to injury. Using an ex vivo post-cataract surgery wound healing model we investigated the role of class I phosphatidylinositol-3-kinase (PI3K) isoforms in this process. Our findings revealed a specific role for p110α signaling independent of Akt for promoting the collective migration and proliferation of the epithelium for wound closure. In addition, we found an important role for p110α signaling in orchestrating proper polarized cytoskeletal organization within both leader and wounded epithelial follower cells to coordinate their function for wound healing. p110α was necessary to signal the formation and persistence of vimentin rich-lamellipodia extensions by leader cells and the reorganization of actomyosin into stress fibers along the basal domains of the wounded lens epithelial follower cells for movement. Together, our study reveals a critical role for p110α in the collective migration of an epithelium in response to wounding.

Keywords: collective migration; leader cell; follower cell; wound healing; PI3K; p110α

1. Introduction

Collective migration involves the coordinated movement of cells that maintain contact with one another as they migrate [1–3]. It is an essential aspect of morphogenesis during embryonic development, tissue regeneration, and wound healing, as well as cancer progression [1–3]. During collective migration, leader cells and follower cells must establish front-to rear polarity and synchronize their function to undergo directional movement [2,4,5]. To this end, leader and follower cells need to coordinate their cytoskeletal activity and mechanically couple to maintain contact with one another and produce traction forces to drive the group of cells forward. An important feature of leader cells is their ability to polarize and form protrusions to drive movement [1,2,5]. Less understood is how follower cells actively participate in collective migration. One way is through their formation of cryptic lamellipodia protrusions along their basal domains to help produce traction forces to promote migration [2,6–8]. Additionally, critical are cell–cell junctions, the fundamental way that biomechanical inputs are communicated to the group of moving cells [9]. A balance of myosin II generated forces are needed to maintain connectivity between cells and provide forces to propel the group of cells forward [7,10,11]. Together, leader and follower cells respond to cues such as chemokine signals for polarized directional movement. However, much remains to be discovered regarding which signaling cues coordinate leader and follower cell behavior and orchestrate cooperation of their cytoskeletal activities for collective migration in response to injury.

Candidate signaling cues for regulating leader and follower cell behavior in response to injury include the class I phosphatidylinositol-3-kinases (PI3Ks) due to their ability to impact cells at multiple levels including sensing chemotactic gradients, generating protrusion formation, regulating cell-matrix and cadherin mediated cell–cell junction formation and promoting proliferation [12–18]. Furthermore, class I PI3Ks can exist in multiple isoforms that can sense diverse signaling inputs, adding another level of regulation [19]. PI3K consists of a regulatory (i.e., p85) and 110 kDa (p110) catalytic subunit [19–21]. Its catalytic subunit can be subdivided into subclass IA isoforms consisting of p110α, p110β, p110δ and subclass IB that consists of the isoform p110γ [19–21]. While p110α, p110β are ubiquitously expressed p110γ and p110δ exhibit more restrictive expression patterns [19–21]. PI3K signaling occurs at the plasma membrane to generate the lipid product phosphatidylinositol-3,4,5 trisphosphate (PIP3) by the phosphorylation of the 3′ hydroxyl group on the inositol head group of phosphatidylinositol-4,5-bisphosphate (PIP2) [19]. PIP3 can then activate downstream substrates including Akt and Rac GEFs such as Vav and PREX [18,22]. Moreover, PI3Ks can crosstalk with Rho GTPase family members, which are connected to regulating the cytoskeleton and cadherin cell–cell junctions, essential aspects of collective migration [23]. Compared to single cell migration far fewer studies exist regarding the role of PI3K in collective migration. In a study using Madin-Darby canine kidney (MDCK) cells, PI3K signaling was restricted to leader cells and critical to leader cell survival and proper collective migration [24]. Even less is understood about the role of PI3K isoforms in coordinating leader-follower cell behavior for collective migration in response to injury.

We previously established an ex vivo post-cataract surgery model to investigate leader-follower cell behavior in response to injury. In this model it is possible to study leader cell directed collective movement of wounded lens epithelial cells across a native basement extracellular matrix (ECM) environment (the cell-denuded lens capsule) for wound healing [7,25]. Wound healing across the lens basement membrane is completed by day 3 post-injury [7,25,26]. Here, collective migration involves heterotypic cell interactions between CD44+ resident immune leader cells and the follower wounded lens epithelia cells [27]. In response to injury, resident immune cells become activated to migrate to the leading edge to serve as leader cells to direct the movement of the follower cells, the wounded lens epithelial cells [27]. CD44+ resident immune leader cells extend vimentin-rich protrusions at the wound edge and vimentin function is required for extension and wound healing [26,28]. The collectivity of the wounded lens epithelial cells is maintained by apical ZO-1 junctions as well as N-cadherin junctions that extend all along their apical-lateral cell–cell membranes [7]. Active myosin forces are found at apical cell–cell junctions to maintain interconnection of the wounded epithelial cells [7]. Basally, wounded lens epithelial follower cells reorganize actin from a cortical distribution into stress fibers that connect cryptic lamellipodia containing atypical cadherin junctions between cells along the basal substrate [7]. These cryptic lamellipodia are enriched for active myosin II at the front of the cell abutting the tailing edge of the cell behind it in the moving monolayer [7]. Apical and basal myosin function was critical to proper organization of the wounded epithelial monolayer and wound healing as treatment with blebbistatin resulted in loss of proper apical-basal polarity, changes in cell shape and an uncontrolled migration response leading to faster wound healing [7]. In the current study we used the ex vivo post-cataract surgery model to investigate PI3K class I specific isoform-specific function in orchestrating proliferation, leader and follower cell cytoskeletal organization, myosin II activity, and cell behavior in response to wounding. Our findings indicate that resident immune leader cell and wounded epithelial follower cell function are regulated in a PI3K isoform specific manner for wound healing.

2. Materials and Methods

2.1. Model and Treatments

Ex vivo post-cataract surgery cultures were prepared on isolated lenses from E15 chick embryos (Poultry Futures, Lititz, PA, USA) using methods previously described [7,26,29,

30]. Briefly, a method paralleling cataract surgery is performed on isolated lenses to remove the lens fiber cells leaving behind epithelial cells that are tightly adherent to the lens capsule. Star shaped explants are created in which wound healing can be followed across the fiber-cell denuded basement membrane lens capsule. Explants were cultured in Media 199 (Invitrogen, Calsbad, CA, USA) with 1% penicillin/streptomycin (Mediatech-Cellgro, Manassas, VA, USA), 1% L-glutamine (Mediatech-Cellgro), and 10% fetal calf serum (Invitrogen). For wound healing studies, ex vivo post-cataract surgery cultures were treated at either time 0 or Day 1 for 24hr or until Day 3. To inhibit PI3K p110 isoforms, 1 μM HS-173 (Selleckchem, Houston, TX, USA), 3 μM GSK2636771 (Selleckchem, Houston, TX, USA), and 3 μM Duvelisib (Selleckchem, Houston, TX, USA) were used. To inhibit AKT, 3 μM MK-2206 (Selleckchem, Houston, TX, USA) was used. Cultures were fixed in 4% formaldehyde or extracted in Triton X-100/Octyl glucoside (Triton/OG) extraction buffer (44.4 mM n-octyl β-d-glucopyranoside, 1% Triton X-100, 100 mM NaCl, 1 mM $MgCl_2$, 5 mM EDTA, 10 mM imidazole) with protease/phosphatase inhibitor cocktail (Cell Signaling Technology, Aldrich, Danvers, MA, USA).

2.2. Phase Microscopy and Wound Healing

Phase contrast images at the leading edge of the wound were taken of Day 1 or Day 2 ex vivo post-cataract surgery cultures with a Nikon Eclipse T*i* microscope. Images of wound healing were taken daily (Day 0, Day 1, Day 2, Day 3) using an AZ100 Nikon microscope and wound areas were measured using NIS elements image-analysis software.

2.3. Immunofluorescence, EdU-Labeling, and Confocal Microscopy

For immunofluorescence staining, fixed cultures were permeabilized with 0.25% Triton-X-100, blocked with 5% goat serum prior to incubation with primary antibodies. Primary antibodies for immunolabeling included: Vimentin (AMF-17b, DSHB, Iowa City, IA, USA) Phospho-Myosin Light Chain 2 (Thr18/Ser19, Cell Signaling 3674, Danvers, MA, USA). The AMF-17b monoclonal antibody to vimentin was deposited by Fulton, A.B. Cultures were counterstained with DAPI (Biolegend, San Diego, CA, USA) to identify nuclei and fluorescent-conjugated Phalloidin (Invitrogen, Waltham, MA, USA) to label filamentous actin. Following primary antibodies, cultures were incubated with fluorescent conjugated secondary antibodies (Jackson Immunoresearch, West Grove, PA, USA). To detect proliferating cells, cultures were EdU-labeled with 10 μM EdU for 30 min and the Click-iT EdU imaging kit (Invitrogen, Carlsbad, CA, USA) was used following manufacturer's instructions. Images were taken on a confocal Zeiss 800. Z-stacks were collected at 0.33 μm and 3D-structural images were created from Zeiss 800 confocal microscope using Imaris ×64 v9.5.1 software surface rendering tool.

2.4. Western Blot and Wes Protein Analysis

Ex vivo post-cataract surgery cultures were extracted on Time 0. For western blot analysis of PI3K p110 isoform expression, 10–20 μg of protein was loaded per lane and separated by 4–12% SDS-PAGE and transferred at 4° on PVDF membranes. Membranes were blocked using 5% milk for 1 h and incubated overnight at 4° with primary antibodies: PI3K p110α (4249, Cell Signaling, Danvers, MA, USA), p110β (sc-376641, Santa Cruz, Dallas, TX, USA), and p110γ (sc-7177, Santa Cruz, Dallas, TX, USA). Following primary antibody incubation, HRP-conjugated mouse, or rabbit secondary antibodies (Bio-Rad, Hercules, CA, USA) were incubated for 1hr, and membranes were exposed to ECL+ chemiluminescence-substrate-detection reagent using ProteinSimple machine. For Wes protein analysis ex vivo post-cataract surgery cultures were extracted on day 3 and 1 μg of protein was loaded per well. For analysis of pAKT and total AKT, phosphor-AKT (4060, Ser473, Cell Signaling, Danvers, MA, USA) and AKT antibody (9272, Cell Signaling, Danvers, MA, USA) were added and the protocol was followed per manufacturer's instructions using Simple Western Automated Western Blot Wes Instrument. (Biotechne, Minneapolis, MN, USA) as previously described [31].

2.5. Statistical Analysis

Statistical analyses for data quantification were performed using GraphPad Prism Software (GraphPad, San Diego, CA, USA). Data is presented at ±SEM from 2 or 3 independent experiments and appropriate statistical analyses were performed for all quantified experiments according to the figure legends.

3. Results

3.1. Collective Migration for Wound Healing in Response to Cataract Surgery Injury Occurs in a PI3K Isoform-Specific Manner Independent of Akt Signaling

Using our previously established ex vivo post-cataract surgery chicken wound healing explant cultures (Figure 1A) we investigated the role of class I PI3K isoforms in signaling collective migration in response to lens injury. To create these wounded explant cultures, a cataract surgery microsurgery is performed on isolated lenses, which removes the differentiated fiber cells that comprise the bulk of this tissue. This process leaves behind the lens epithelial cells that are tightly adherent to the basement membrane capsule along with the associated lens resident immune cells. Additional cuts are made to the lens capsule to flatten the explant on the culture dish, creating a star-shaped culture in which the lens epithelial and resident immune cells are located cell-side up in the points of the star. This region is termed the original attachment zone (OAZ) (Figure 1Ai). In response to injury, resident immune cell leader cells rapidly populate the wound edge and direct the wounded lens epithelial follower cells to migrate collectively across the cell denuded basement membrane to close the wound (Figure 1Aii, see model). This region is referred to as the central migration zone (CMZ). Wound closure is typically completed by D3 post-injury (Figure 1Aiii).

A previous study showed that class I PI3K isoforms p110α, p110β and p110γ are all expressed in the lens [32]. Consistent with these findings we observed the expression of p110α, p110β and p110γ class I PI3K p110 isoforms in the wounded explant cultures at time 0 (Supplemental Figure S1). To determine the potential function of these three class I PI3K p110 isoforms in wound closure, ex vivo post-cataract surgery cultures were treated with vehicle or PI3K p110 isoform specific inhibitors, HS-173 (HS) to p110α; GSK2636771 (GSK) to p110β, or Duvelisib (Duv) to p110δ/γ, from time 0 through day 3. In DMSO-treated cultures the wound was closed within three days (Figure 1C, DMSO, D3). Impact of each p110-specific inhibitor on activation of AKT (pser-473 AKT/total AKT), a principal PI3K downstream effector, was determined on day 3 post-treatment (Figure 1B). The greatest level of inhibition of AKT signaling was observed with the p110α inhibitor HS-173 in the wounded lens. Next most impactful inhibition of AKT activation occurred with the p110γ/δ inhibitor Duvelisib, with the p110β inhibitor GSK2636771 having the least impact (Figure 1B). These findings show that the link of these different p110 isoforms to AKT downstream signaling was isoform specific in the lens. Similarly, suppression of PI3K p110α signaling had the greatest impact on wound closure, with only approximately 67% closure on day 3 post-injury (Figure 1C). In contrast, treatment with GSK2636771 to block p110β had no effect on wound closure and showed a similar wound healing trend as vehicle control (Figure 1C). Treatment with Duvelisib to block p110γ/δ also slowed wound repair, but not as pronounced as inhibition of p110α, with 87% closure by D3 (Figure 1C). These studies suggest that both p110α and p110γ/δ function in promoting wound healing in response to lens injury.

There are many downstream signaling effectors of PI3K, most common among them AKT and Rac. We examined whether the impact of PI3K signaling on promoting lens wound repair involved signaling through AKT. For these studies, ex vivo wounded explants were treated with vehicle DMSO or the AKT specific inhibitor MK-2206 (MK) from time 0 through day 3 (Figure 1D,E). Treatment with MK effectively suppressed activation of AKT (pAKT/total AKT) expression (Figure 1D). However, blocking Akt had no effect on closure of the cataract surgery wound (Figure 1E). In the presence of both vehicle and MK treatment,

wound closure was complete by day 3 post-injury (Figure 1E). These findings show that PI3K isoform-dependent wound closure involves an alternative downstream effector(s).

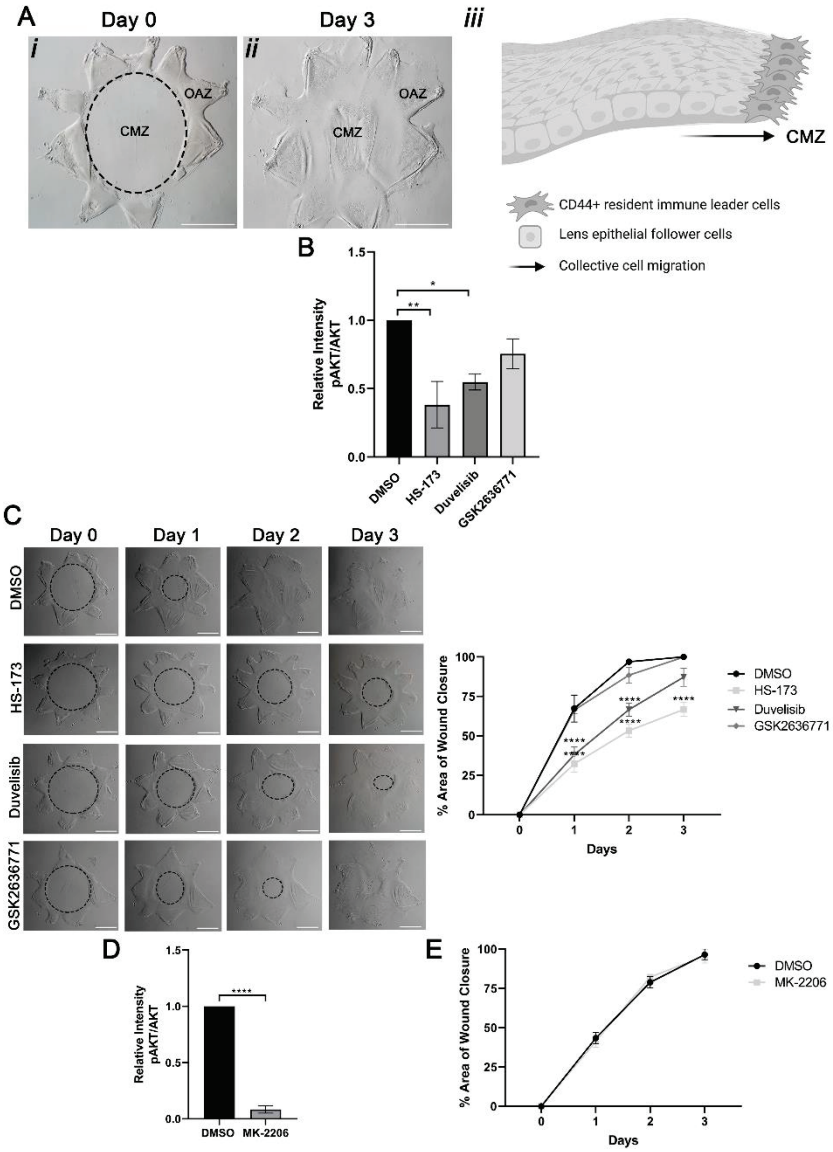

Figure 1. Wound healing in response to cataract surgery injury occurs in a PI3K isoform-specific manner. (**A**) Depiction of ex vivo post-cataract surgery culture to study mechanisms of wound repair across the cell-denuded endogenous basement membrane in the center of the lens capsule. Ex vivo post-cataract surgery explant on day 0 depicts the wounded lens epithelial cells within the original attachment zone (OAZ) and the cell-denuded central migration zone (CMZ) (i). In response to injury, collective migration across the endogenous basement membrane in the CMZ is driven by leader cells that direct the migration of the wounded epithelial follower cells (ii), arrow depicts the direction of wound healing. Collective migration across the CMZ for wound repair is completed by day 3 post-injury (iii). (**B**,**C**) Ex vivo post-cataract surgery explants were treated from Time 0 through Day 3 with individual PI3K isoform inhibitors, HS-173 for p110α; GSK2636771 for p110β; or Duvelisib for p110δ/γ. (**B**) Graph from Wes analysis depicts the efficacy of individual PI3K isoform inhibitors compared to vehicle control by examining the relative intensity of the PI3K effector, phosphorylated-AKT (pAKT) relative to total AKT expression compared to GAPDH (loading control). (**C**) Phase microscopy shows open wound area (dotted black circle) for vehicle vs. PI3K inhibitor treatment from Day 0 through Day 3. Graph depicts % area of wound closure. Results show that blocking p110α with HS-173 had the largest impact on inhibiting wound closure. (**D**,**E**) Ex vivo post-cataract

surgery explants were treated with vehicle (DMSO) or the AKT specific inhibitor, MK-2206 from Time 0 through Day 3. (**D**) MK-2206 suppressed pAKT relative to total AKT expression and GAPDH (loading control). (**E**) Graph of % wound closure shows that treatment with MK-2206 had no effect on wound closure. *p*-values were determined from one-way ANOVA (**B**), two-way ANOVA with multiple comparisons (**B**,**C**) or unpaired *t*-test (**D**,**E**). (**B**, * $p < 0.05$, ** $p < 0.01$; **C**, **** $p < 0.0001$ and **D** **** $p < 0.0001$). Data is expressed as ± SEM from 2 (**D**,**E**) or 3 (**B**,**C**) independent experiments. Magnification bars = 1000 μm (**A**,**C**).

3.2. p110α Is Required to Promote and Maintain Extension of Vimentin-Rich Lamellipodial Protrusions by Leader Cells

To examine the mechanism of how p110α promotes collective migration following wounding we determined the specific effects of blocking p110α on the function of resident immune cells at the leading edge of the cataract surgery wound. Our previous studies showed that the leader cells, a vimentin-rich cell population, play an essential role in mediating lens post-cataract surgery wound healing, and that vimentin function is required for their extension of lamellipodial processes along the basement membrane substrate [26]. Here, we investigated the impact of blocking p110α function on vimentin-rich lamellipodial extension by leader cells (modeled in Figure 2A). Ex vivo post-cataract surgery cultures were exposed to the HS-173 inhibitor to block p110α from day 0 through day 1 post-wounding and compared to vehicle DMSO treated controls. The extension of processes by leader cells was examined by both phase microscopy imaging (Figure 2B–E) and by confocal microscopy imaging after immunolabeling for vimentin (Figure 2F,G). Phase contrast images show that the HS-173 p110α inhibitor blocked extension of normal protrusions by leader cells at the wound edge on day 1 (Figure 2B–E). Immunolabeling for the cytoskeletal protein vimentin highlights this failure to extend lamellipodial processes along the substrate (Figure 2G, HS-173) that are normally rich in vimentin (Figure 2F, DMSO). In the presence of HS-173 the leader cells at the at the wound edge remained round (Figure 2G).

The extension of lamellipodial processes by leader cells at the wound edge is required for directional persistence. Our findings showed that p110α is necessary to initiate extension of these vimentin rich protrusions. Next, we asked whether p110α is also required to maintain lamellipodial processes that had been already extended by leader cells along the substrate. For these studies, the HS-173 p110α inhibitor was added to the cataract surgery explant cultures at day 1 post-injury, after the extension of the vimentin-rich lamellipodial protrusions by leader cells. Phase images were acquired at the wound edge both prior to exposure to the inhibitor (Figure 3A,B, D1 post-injury) and following 1 day exposure to HS-173 (Figure 3D, D2 post-injury) or DMSO vehicle control (Figure 3C, D2 post-injury). In vehicle controls, the leader cells continued to extend protrusions along the cell-denuded basement membrane substrate in D2 wounded explants (Figure 3C). Exposure to the HS-173 inhibitor resulted in failure of leader cells to maintain these cellular protrusions (Figure 3D). Labeling for vimentin further confirmed these findings showing that p110α is required to maintain the extension of vimentin-rich lamellipodial protrusions by leader cells (Figure 3F). Treatment with HS-173 caused the collapse of vimentin-rich extensions (Figure 3F) that are commonly observed in the control explants (Figure 3E). Similar to blocking p110α from time 0, exposure of the cataract surgery wounded cultures to the HS-173 inhibitor from D1 through D3 also impaired wound closure, with the wound still remaining 33% open at culture D3 (Figure 4). These studies show that p110α function is critical to regulate both the formation and maintenance of vimentin rich lamellipodial extension by leader cells and suggest p110α function is required throughout the wound healing process for wound closure.

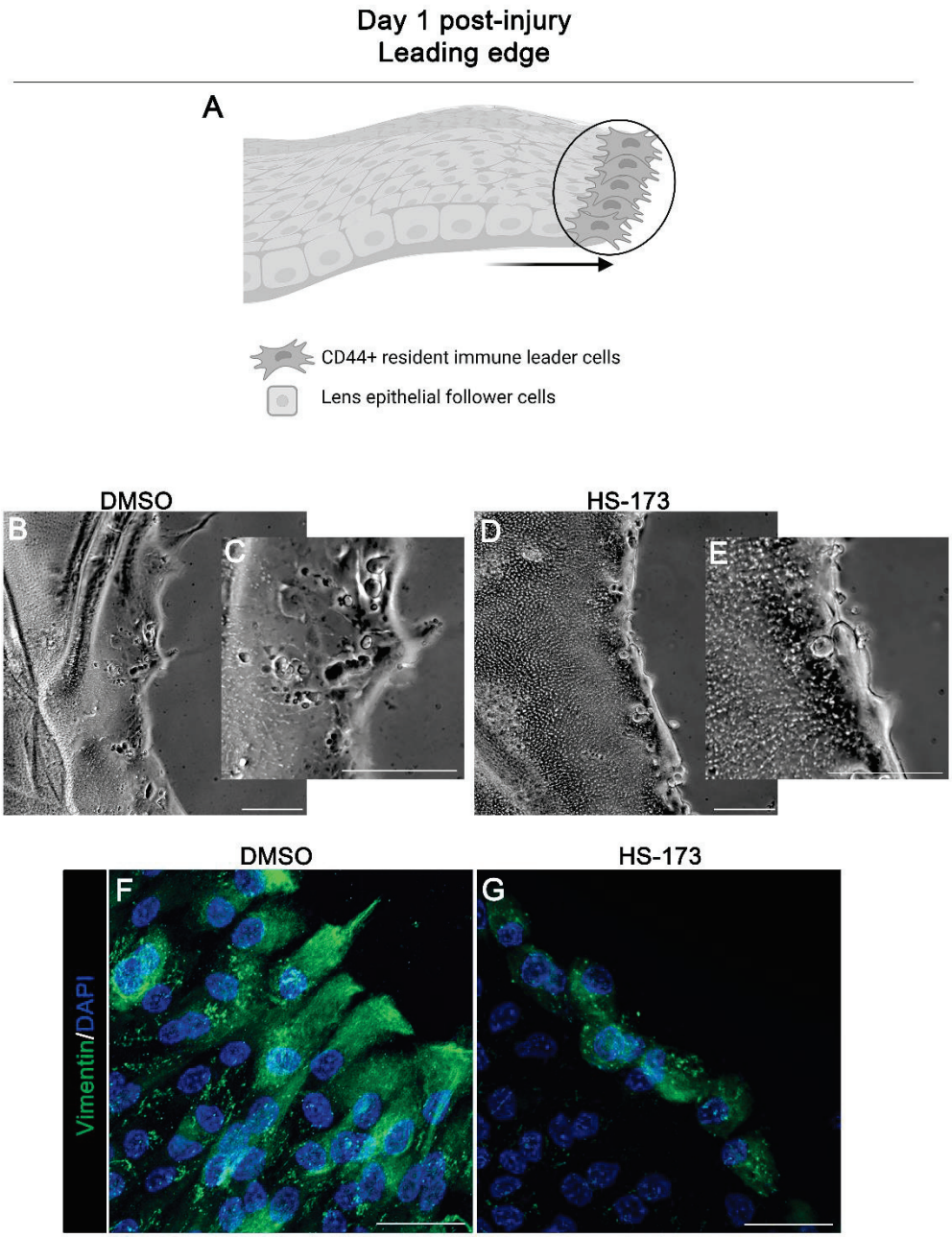

Figure 2. p110α is required to initiate extension of vimentin rich lamellipodial of leader cells. (**A**) Model of CMZ highlighting our region of interest (leader cells, black circle) for these studies. (**B**–**G**) Ex vivo post-cataract surgery explants were treated with HS-173 to inhibit p110α from Time 0 for 24 h (Day 1 post-injury). (**B**) Phase contrast imaging shows that in the presence of DMSO leader cells extend protrusions at the wound edge. (**D**) In contrast, HS-173 blocked leader cell protrusion at the wound edge. Regions in (**B**,**D**) are shown at higher magnification (**C**,**E**). (**F**,**G**) Cataract surgery explants day 1 post-treatment were immunolabeled for vimentin (green) and counterstained for DAPI (blue). Confocal images revealed vimentin-rich lamellipodia extensions at the leading edge were blocked by HS-173 treatment (**G**) compared to vehicle control (**F**). Magnification bars = 50 μm (**B**–**E**) and 20 μm (**F**,**G**).

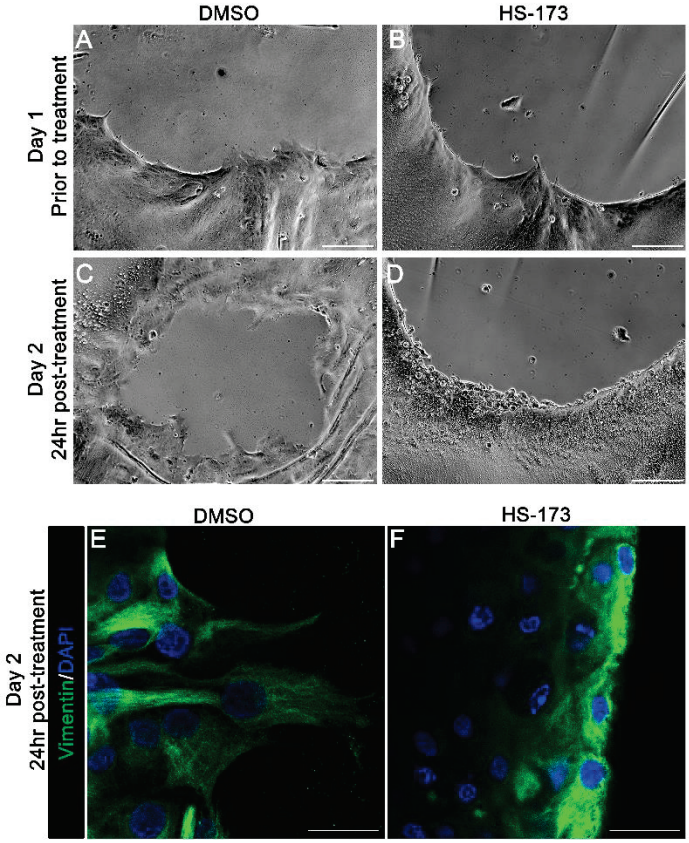

Figure 3. p110α is required to maintain the extension of vimentin-rich lamellipodia of leader cells. (**A**–**F**) Ex vivo post-cataract surgery explants were treated with vehicle (DMSO) or HS-173 to inhibit p110α from Day 1 for 24 h (Day 2 post-injury). (**A**,**B**) Phase contrast imaging on Day 1 shows the extension of protrusions by leader cells at the wound edge prior to treatment. (**C**,**D**) In contrast, phase contrast imaging on Day 2 (24 h post-treatment) revealed that HS-173-treated leader cells failed to maintain protrusions compared to vehicle controls. (**E**,**F**) Day 2 explants following 24 h of treatment were immunolabeled for vimentin (green) and counterstained for DAPI (blue). Confocal images revealed that maintenance of vimentin-rich lamellipodia extensions was blocked by HS-173 treatment (**F**) compared to vehicle controls (**E**). Magnification bars = 50 μm (**A**–**D**) and 20 μm (**E**,**F**).

3.3. p110α Regulates the Reorganization of F-Actin along the Basal Surface of the Wounded Epithelial Cells

To examine the mechanism of how p110α promotes collective migration following wounding, we determined the specific effects of blocking p110α on the wounded lens epithelium, the follower cells in our culture model. Our previous studies show that actomyosin mechanical cues are critical for the organization of the wounded lens epithelial cells within the collectively migrating monolayer [7]. Active (phospho) myosin was found to localize to apical junctional complex that maintains cell–cell contact between wounded epithelial cells [7]. At the same time, the organization of actin stress fibers is induced along the basal cell compartment of the migrating epithelium where it is linked to cadherin junctions that are located in cryptic lamellipodia. This mechanical coupling is driven by active myosin to promote movement of the epithelium along the substrate [7]. Here, we investigated whether p110α signaling has a role in the regulation of apical and/or basal actomyosin organization in the wounded lens epithelial cells (modeled in Figure 5A). For these studies, ex vivo wounded cultures were treated with vehicle (DMSO) or the p110α inhibitor, HS-173 on day 0 through day 1 (Figure 5). The wounded explant cultures were immunolabeled for active myosin using an antibody that recognizes dually phosphorylated (Thr18/ser19) regulator light chain (RLC) of myosin II (Figure 5C,D,F,G; Figure 6B,C,E,F,H,I) and co-labeled for F-actin with fluorescent-conjugated phalloidin (Figure 5B,D,E,G,H–M;

Figure 6A,C,D,F,G,I). Confocal z-stacks were acquired to determine changes in actomyosin organization and/or myosin activity along the apical (Figure 5B–G,J–M) and basal (Figure 6) domains of the wounded lens epithelial follower cells.

Confocal microscopy images focused along the apical surfaces of the migrating wounded epithelial cells revealed that exposure to the HS-173 inhibitor treatment decreased active (phospho)myosin at the apical vertices of the wounded lens epithelial cells (Figure 5C,F, arrowhead). Importantly, labeling of F-actin demonstrated that blocking p110α activation maintained the normal tightly packed columnar morphology of the lens epithelium (Figure 5E,K,M). Vehicle controls show the flattened migratory phenotype of the lens epithelium (Figure 5B,J,L) that was previously shown to characterize the collective migration of lens epithelial cells post-wounding [7]. The morphology of the lens epithelium in the presence of the HS-173 inhibitor also resembles the wounded epithelial cells at time 0 post-injury (Supplemental Figure S2A). 3D surface structures created from confocal z-stacks of cultures labeled for F-actin and nuclei highlight the compact organization of wounded epithelial follower cells with HS-173 treatment compared to vehicle alone (Figure 5H,I).

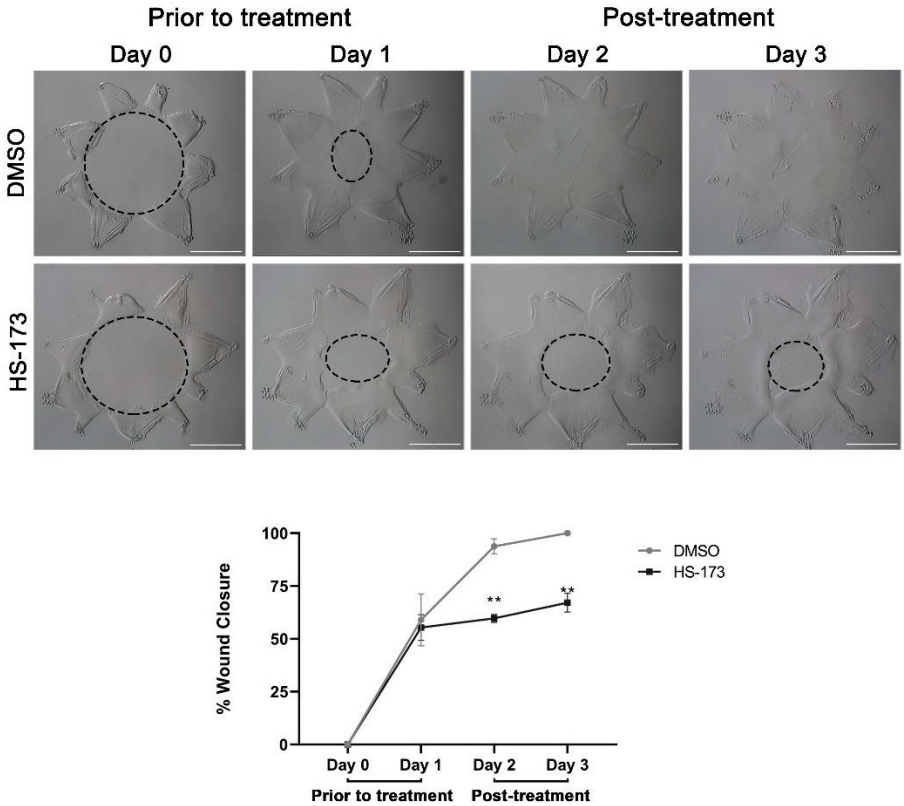

Figure 4. p110α is required throughout the wound healing process to sustain wound closure. Ex vivo post-cataract surgery explants were treated with HS-173 to inhibit p110α from Day 1 to Day 3 post-injury. Phase microscopy and wound area measurements show the wound area prior to treatment on Day 0 and Day 1 and post-treatment with vehicle or HS-173 on Day 2 and Day 3 (dotted black circle). Graph depicts % wound closure and revealed that HS-173 is required throughout the wound healing process to drive wound closure. *p*-values were determined from two-way ANOVA with multiple comparisons (** $p < 0.01$). Data is expressed as ±SEM from 3 independent experiments. Magnification bars = 1000 μm.

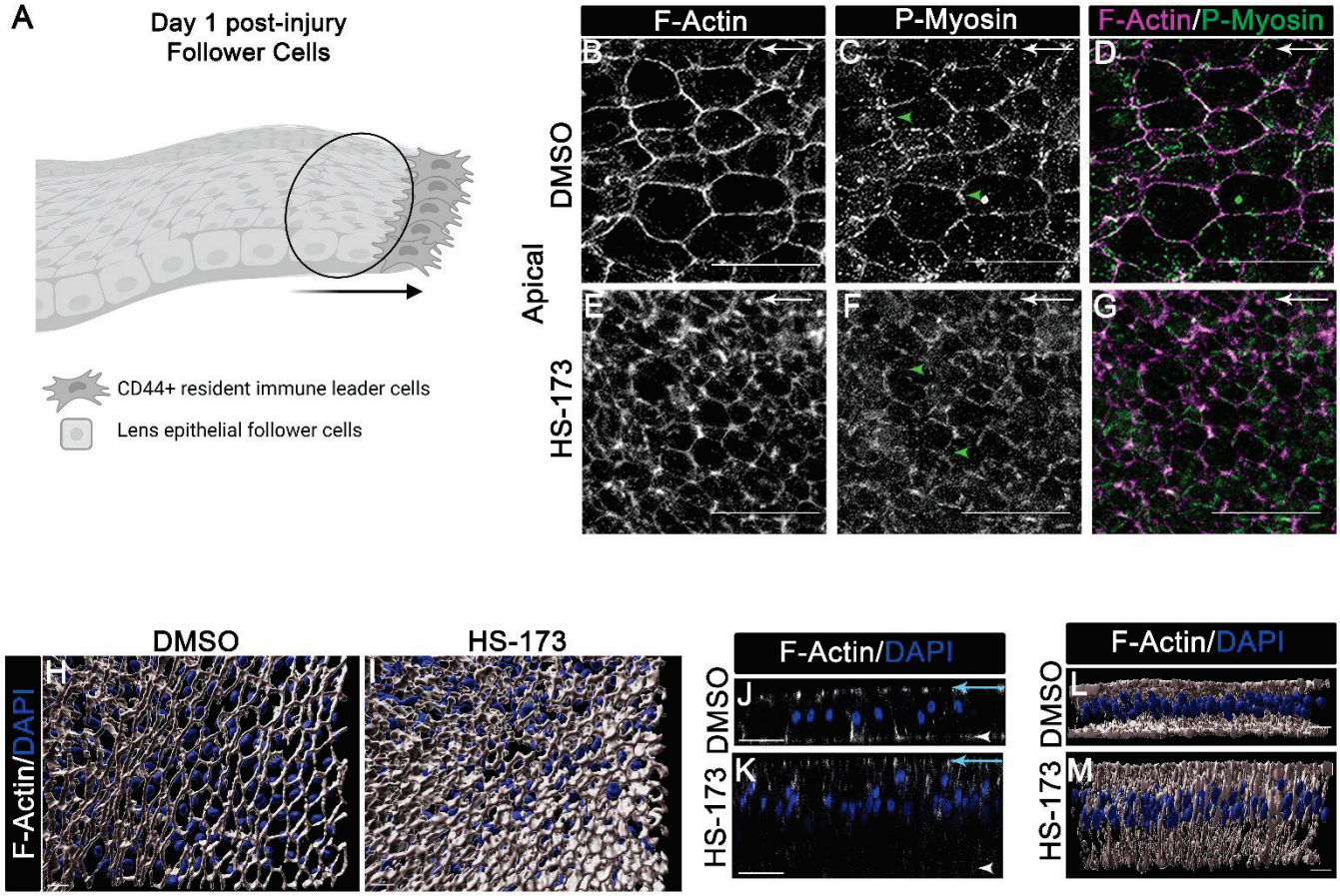

Figure 5. Impact of blocking p110α on the apical organization of the wounded lens epithelial follower cells post-injury. (**A**) Model of CMZ highlighting our region of interest (follower cells, black circle) for these studies. (**B**–**M**) Ex vivo post-cataract surgery explants were treated with vehicle control or HS-173 to inhibit p110α from Time 0 for 24 h (Day 1 post-injury). Cultures were labeled with phalloidin to identify filamentous actin (F-actin, white (**B**,**E**), purple (**D**,**G**)) and immunolabeled for active myosin (p-myosin, white (**C**,**F**), green (**D**,**G**)). (**B**–**G**) Confocal images of follower cells focused apically revealed a cortical distribution of actomyosin at cell–cell border with vehicle and HS-173 treatment. However, HS-173 treatment revealed differences in active myosin distribution at apical vertices (see arrowheads) and a more compact organization of the monolayer compared to vehicle control (**E**,**G**). 3D structures from confocal z-stacks, which were labeled for F-actin (white) and nuclei (DAPI, blue) were created to allow the better visualization of the compact organization of wounded epithelial follower cells with HS-173 and vehicle treatment (**H**,**I**). (**J**,**K**) Orthogonal views from confocal z-stacks of cultures labeled for F-actin (white) and nuclei (DAPI, blue) were created to reveal height differences in the wounded epithelial cells of HS-173 vs. DMSO-treated cultures. (**L**,**M**) 3D structures of orthogonal views were created from the same region in (**J**,**K**) to further highlight shape differences. Magnification bars = 20 μm (**B**–**G**,**J**,**K**) or 5 μm (**H**,**I**). (**B**–**G**) arrows show direction of cell migration.

While inhibiting p110α signaling did not affect the distribution of apical F-actin, the wound-induced organization of basal actin structures was blocked (Figure 6A compared to Figure 6D). In vehicle controls, F-actin stress fibers were induced to form that co-localized with active (phospho) myosin (Figure 6A–C). These actomyosin filaments are expected to be linked to N-cadherin that localization to cryptic lamellipodia [7], and propel the wounded epithelial follower cells along the basal substrate. In the HS-173 treated wounded explants F-actin maintained a cortical distribution and at these cell–cell contacts F-actin was co-localized with active myosin (Figure 6D–F). Interestingly, the cortical distribution of actin along the basal surfaces of the wounded epithelial cells with HS-173 treatment

parallels that of wounded epithelial cells located in the OAZ at time 0 post-injury ([7], Supplemental Figure S2B). Additionally, for comparison, confocal images of wounded epithelial cells from the OAZ of vehicle control were imaged along their basal surfaces at day 1 post-injury following labeling for F-actin and active myosin (Figure 6G–I). In contrast to wounded lens epithelial cells migrating across the cell-denuded basement membrane of the CMZ, F-actin and active myosin were distributed cortically in the wounded lens epithelial cells that remain associated with the OAZ (Figure 6G–I). These results show that lens epithelial follower cells treated with HS-173 share a similar cortical organization of actomyosin along their basal surfaces as the nonmotile, wounded lens epithelial cells in the OAZ of vehicle controls. These findings suggest that p110α signaling is needed to induce reorganization of actomyosin along the basal domains of the wounded epithelial cells for collective migration during wound healing.

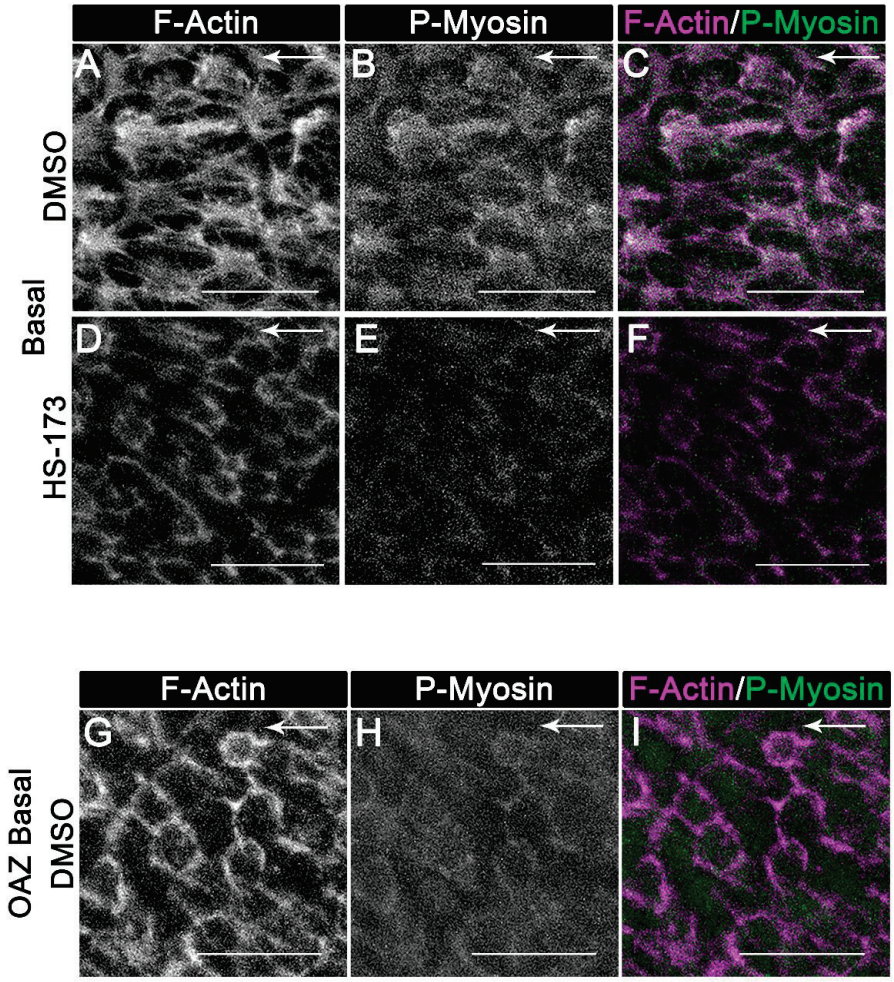

Figure 6. Role for p110α in regulating reorganization of actomyosin along the basal surface of the lens epithelial follower cells for wound healing. (**A**–**F**) Ex vivo post-cataract surgery explants were treated with vehicle control or HS-173 to inhibit p110α from Time 0 for 24 h (Day 1 post-injury). Cultures were labeled with phalloidin to identify filamentous actin (F-actin, white (**A**,**D**,**G**), purple (**C**,**F**,**I**)) and immunolabeled for active myosin II (P-myosin, white (**B**,**E**,**H**), green (**C**,**F**,**I**)). Confocal images along the basal surface of the wounded lens epithelium revealed that (**A**–**C**) normal basal actomyosin reorganization into stress fibers within wounded epithelial cells is blocked with (**D**–**F**) HS-173 treatment. (**G**–**I**) Confocal images along the basal surface of the wounded epithelial cell located in the OAZ are shown for comparison to HS-173 treated cells (**D**–**F**) revealing a similarity in basal actomyosin organization of HS-173 basal follower cells to nonmoving wounded epithelial cells in the OAZ. Magnification bars = 20 μm and arrows show direction of cell migration (**A**–**I**).

3.4. p110α Is Required for Epithelial Cell Proliferation in Response to Wounding

In the lens, p110α function has previously been linked to regulating lens epithelial cell proliferation during lens development [33]. Since wound healing typically requires both collective migration and proliferation for wound closure, we next determined whether p110α may also regulate proliferation in response to wounding. Ex vivo post-cataract surgery cultures were treated with vehicle or HS-173 on day 0 and EdU labeled for 30 min on day 1 post-treatment. Cultures were counterstained with DAPI to identify nuclei and imaged at the wound edge of the CMZ. Treatment with HS-173 resulted in a major block in proliferation compared to vehicle control (Figure 7A–E). These findings show that p110α is critical to signal proliferation for re-epithelialization associated with wound closure in response to cataract surgery wounding.

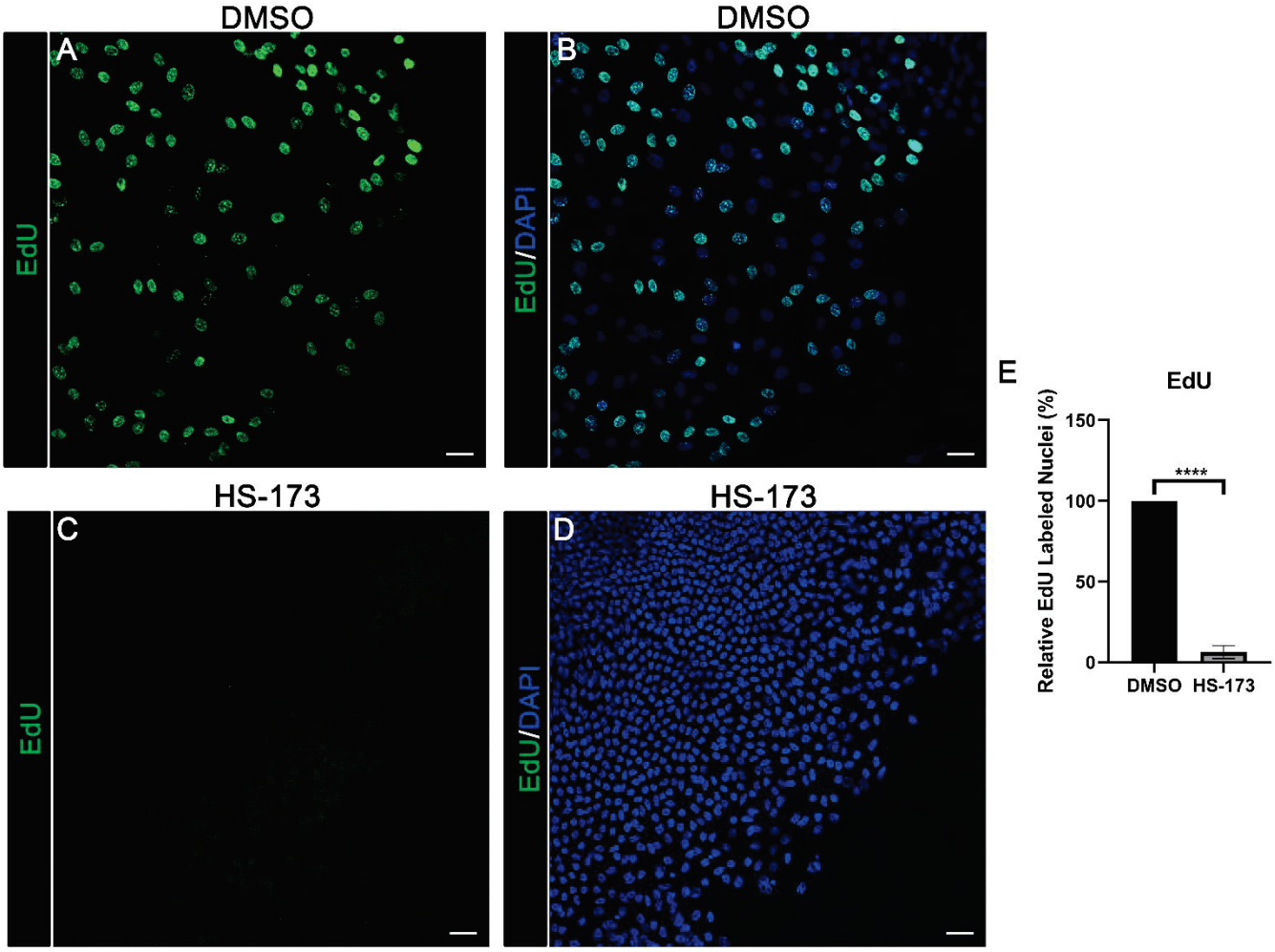

Figure 7. p110α is required for promoting cell proliferation in the central migratory zone during wound healing. (**A**–**E**) Time 0 ex vivo post-cataract surgery explants were treated with vehicle (DMSO) or HS-173 to inhibit p110α for 24 h (Day 1 post-injury) and labeled for 30min with EdU (green) (**A**,**C**) and counterstained with DAPI (blue) (**B**,**D**). (**E**) Graph depicts the change in the relative % of EdU positive cells within the CMZ region in vehicle compared to HS-173 treated cultures. Cell proliferation was blocked with HS-173 treatment. Vehicle was normalized to 100%. *p*-values were determined from unpaired *t*-test (**E**, **** $p < 0.0001$). Data is expressed as ± SEM from 3 independent experiments (**E**). Magnification bars = 20 μm (**A**–**D**).

4. Discussion

The PI3K p110α catalytic subunit has been linked to the development of fibrosis associated with hepatic stellate cells in liver fibrosis [34]. In a previous study from our lab

of a post-cataract surgery model we showed that signaling through this PI3K isoform was associated with the emergence and expansion of myofibroblasts, the cellular culprits of lens fibrotic disease [31]. Here, we have focused on the mechanisms of collective migration of the epithelium to close the cataract surgery-induced wound. Using a wound healing model, our studies revealed that collective migration and proliferation for wound healing occur in a PI3K isoform-specific manner in response to cataract surgery injury. We found that PI3K p110α is an essential signaling cue to orchestrate proliferation and the distinct reorganization of polarized cytoskeletal activities of both resident immune leader cells and wounded lens epithelial cells for their collective movement in response to injury. Furthermore, we found that the PI3K/Akt signaling axis alone was insufficient to promote p110α induced collective migration, suggesting the involvement of other downstream effectors of PI3Kp110α signaling such as Rac, similar to the role of p110α in fibrosis [31]. For efficient movement it is necessary for polarized cells to extend protrusions persistently toward the direction of a chemotactic signal [15,35–37]. Our studies uncovered a key role for p110α in regulating the ability of leader cells to polarize, initiate, and maintain extended lamellipodia protrusions at the wound edge, critical to propel the directional migration of the connected group of epithelial cells forward toward the center of the wound. At this same time, p110α was required in wounded lens epithelial cells to signal reorganization of the actomyosin cytoskeleton into stress fibers along their basal domains. Here, actomyosin-rich stress fibers interconnect cryptic lamellipodia of each follower cell to mechanically couple the wounded epithelial cells to help drive the monolayer forward behind the leading edge for wound closure. Overall, our studies reveal p110α as a central coordinator of the wound healing response to cataract surgery injury.

Prior studies link PI3K, and PI3K p110α subunit to regulating cellular protrusion formation through impacting actin dynamics [13,38–41]. The results of the present investigation uncover a role for PI3K p110α in both initiating the formation of these protrusive processes as well as in the maintenance of these vimentin-rich lamellipodia extensions by resident immune cells that is critical for their persistent movement. In the cataract surgery wound healing model, leader cells extend vimentin-rich lamellipodia that are actin poor [26] and we previously showed that vimentin function is required for lamellipodial extension by leader cells at the wound edge and for proper wound closure [26]. Our new findings link the PI3K p110α isoform as an upstream regulator of vimentin intermediate filament dynamics of leader cells. How PI3K p110α regulates vimentin organization in leader cells is an intriguing question for future investigations. Prior studies indicate a role for PI3K in the regulation of vimentin organization. In a study with endothelial cells, PDGF was shown to induce reorganization of vimentin in a PI3K dependent manner [42]. In that study, inhibiting PI3K prevented the PDGF induced retraction of vimentin from the endothelial cell membrane [42]. In another study, PI3Kγ was shown to regulate leukocyte transendothelial cell migration through its ability to phosphorylate vimentin to induce vimentin disassembly [43]. In both these studies, PI3K has a role in signaling the disassembly of vimentin filaments. In contrast, our studies suggest that PI3K is necessary for organizing vimentin into polarized lamellipodial structures extended on the substrate by leader cells. The discrepancy in these findings suggests that PI3K regulates vimentin dynamics in a cell and context-dependent manner. Another possibility is that PI3K is necessary to create the polarizing signal at the membrane for vimentin filaments to be organized and extended at the leading edge in the direction of wound repair. In dictostyelium an amplified gradient of PIP3 is created at the leading edge to polarize the cell, creating a "cellular compass" for the cell to move in the direction of a chemoattractant gradient [13,16]. The chemokine SDF-1 is a possible upstream regulator of PI3K for chemokine-directed migration of the leader cells. SDF-1 can activate PI3K to induce accumulation of PIP3 within cells, such as T-cells [44,45] and we previously found that gene expression of SDF-1 and its receptor CXCR4 are upregulated 1hr post-cataract surgery injury [46]. Future studies are needed to better understand the molecular mechanism(s) by which PI3K p110α regulates polar-

ized vimentin organization within leader cells for lamellipodial formation and directional movement during wound healing.

Coincident with the requirement for PI3K p110α induced changes in leader cells to promote lamellipodia protrusions we found that p110α is also critical for inducing changes in cell shape and cytoskeletal organization of the wounded epithelial cells that is linked with their transition from a stable epithelium to a migrating cell monolayer. There are several scenarios by which PI3K p110α injury induced signaling may regulate the wounded epithelial cells to undergo changes to a migratory phenotype. One involves the ability of PI3K p110α to signal spatiotemporal control over actomyosin stress fiber formation along the basal domains of the wounded epithelial cells through the activation of RhoGTPases that are linked to regulating actin cytoskeleton dynamics [22,47]. It is also possible that loss of polarized cytoskeletal function in leader cells to form persistent protrusions for directional migration by inhibition of PI3K p110α impacts signaling cues to the wounded follower cells necessary to establish front-to-rear polarity for collective migration. Our previous study showed that ablation of leader cell function slowed wound healing [30]. Whether leader cell function is critical to communicate changes to the wounded lens epithelial cells to coordinate their distinct polarized cytoskeletal activities for collective movement is not yet clear. Furthermore, we did not observe alterations in the cortical distribution of actin or myosin at apical cell–cell junctions when PI3K p110α function was inhibited. This does not preclude the possibility that dynamics of cadherin cell–cell junctions are altered which would contribute to the inability of the epithelial cells to undergo dynamic changes to undergo movement. In support of this possibility, PI3K p110α was shown to regulate endothelial cell–cell adherens junctions, which became strengthened when p110α was inhibited through a mechanism that involving cadherin tyrosine phosphorylation [48]. It is also possible that p110α induced proliferation is necessary for collective migration in response to cataract surgery wounding. An interesting study in Zebrafish kidney development showed a link between migration and proliferation [49]. In this study, collective migration induces cell stretch signals to promote PI3K dependent proliferation and blocking proliferation led to an inhibition of collective migration for kidney morphogenesis [49].

Overall, our studies reveal PI3K p110α as a critical coordinator of proliferation and polarized cytoskeletal dynamics within leader and follower cells to promote collective migration for proper wound healing in response to injury. While beyond the goals of the current study, it will be of future interest to elucidate whether PI3K p110α signals these processes through the same or distinct downstream effector(s). Lastly, our studies show that the post-cataract surgery model is a useful tool to exploit to better understand heterotypic leader and follower cell interactions for collective movement, which may provide insight into how this process leads to pathological outcomes such as cancer progression.

Supplementary Materials: The following supporting information can be downloaded at: https://www.mdpi.com/article/10.3390/cells11213515/s1, Figure S1: PI3K class I isoform expression in response to cataract surgery wounding; Figure S2: F-Actin organization within wounded lens epithelial cells at T0 post-injury.

Author Contributions: Conceptualization, J.L.W. and A.S.M.; methodology, M.D.B.; formal analysis, M.D.B.; investigation, M.D.B.; writing—original draft preparation, M.D.B., J.L.W.; writing—review and editing, M.D.B., J.L.W., A.S.M.; visualization, M.D.B., J.L.W., A.S.M.; supervision, J.L.W., A.S.M.; Funding acquisition, J.L.W., A.S.M., M.D.B. All authors have read and agreed to the published version of the manuscript.

Funding: This research was funded by Grants to J.L.W. and A.S.M., and National Institute of Health grant EY026159 to J.L.W. National Institute of Health grant EY021784 to ASM. M.D.B. was supported by the National Institute of Arthritis and Musculoskeletal and Skin Disease of the National Institute of Health T32 AR 52273-15.

Institutional Review Board Statement: The study was conducted in accordance with the Declaration of Helsinki and approved by the Institutional Review Board of Thomas Jefferson University Institutional Animal Care and Use Committee (IACUC, Approval code: 01651-1). This study was also

in compliance with the Association for Research in Vision and Ophthalmology (ARVO) Statement of the Use of Animals in Ophthalmic and Vision Research.

Informed Consent Statement: Not Applicable.

Data Availability Statement: Not Applicable.

Acknowledgments: We would like to thank Heather Paulson for excellent technical assistance.

Conflicts of Interest: The authors declare no conflict of interest.

References

1. Jain, S.; Ladoux, B.; Mege, R.M. Mechanical plasticity in collective cell migration. *Curr. Opin. Cell Biol.* **2021**, *72*, 54–62. [CrossRef] [PubMed]
2. Qin, L.; Yang, D.; Yi, W.; Cao, H.; Xiao, G. Roles of leader and follower cells in collective cell migration. *Mol. Biol. Cell* **2021**, *32*, 1267–1272. [CrossRef] [PubMed]
3. Rorth, P. Collective cell migration. *Annu. Rev. Cell Dev. Biol.* **2009**, *25*, 407–429. [CrossRef] [PubMed]
4. Capuana, L.; Bostrom, A.; Etienne-Manneville, S. Multicellular scale front-to-rear polarity in collective migration. *Curr. Opin. Cell Biol.* **2020**, *62*, 114–122. [CrossRef]
5. Mayor, R.; Etienne-Manneville, S. The front and rear of collective cell migration. *Nat. Rev. Mol. Cell Biol.* **2016**, *17*, 97–109. [CrossRef]
6. Farooqui, R.; Fenteany, G. Multiple rows of cells behind an epithelial wound edge extend cryptic lamellipodia to collectively drive cell-sheet movement. *J. Cell Sci.* **2005**, *118*, 51–63. [CrossRef]
7. Menko, A.S.; Bleaken, B.M.; Walker, J.L. Regional-specific alterations in cell-cell junctions, cytoskeletal networks and myosin-mediated mechanical cues coordinate collectivity of movement of epithelial cells in response to injury. *Exp. Cell Res.* **2014**, *322*, 133–148. [CrossRef]
8. Ozawa, M.; Hiver, S.; Yamamoto, T.; Shibata, T.; Upadhyayula, S.; Mimori-Kiyosue, Y.; Takeichi, M. Adherens junction regulates cryptic lamellipodia formation for epithelial cell migration. *J. Cell Biol.* **2020**, *219*, e202006196. [CrossRef]
9. Khalil, A.A.; de Rooij, J. Cadherin mechanotransduction in leader-follower cell specification during collective migration. *Exp. Cell Res.* **2019**, *376*, 86–91. [CrossRef]
10. Lange, J.R.; Fabry, B. Cell and tissue mechanics in cell migration. *Exp. Cell Res.* **2013**, *319*, 2418–2423. [CrossRef]
11. Aranjuez, G.; Burtscher, A.; Sawant, K.; Majumder, P.; McDonald, J.A. Dynamic myosin activation promotes collective morphology and migration by locally balancing oppositional forces from surrounding tissue. *Mol. Biol. Cell* **2016**, *27*, 1898–1910. [CrossRef] [PubMed]
12. Di-Luoffo, M.; Ben-Meriem, Z.; Lefebvre, P.; Delarue, M.; Guillermet-Guibert, J. PI3K functions as a hub in mechanotransduction. *Trends Biochem. Sci.* **2021**, *46*, 878–888. [CrossRef] [PubMed]
13. Cain, R.J.; Ridley, A.J. Phosphoinositide 3-kinases in cell migration. *Biol. Cell* **2009**, *101*, 13–29. [CrossRef] [PubMed]
14. Yu, J.S.; Cui, W. Proliferation, survival and metabolism: The role of PI3K/AKT/mTOR signalling in pluripotency and cell fate determination. *Development* **2016**, *143*, 3050–3060. [CrossRef] [PubMed]
15. Sarris, M.; Sixt, M. Navigating in tissue mazes: Chemoattractant interpretation in complex environments. *Curr. Opin. Cell Biol.* **2015**, *36*, 93–102. [CrossRef] [PubMed]
16. Bourne, H.R.; Weiner, O. A chemical compass. *Nature* **2002**, *419*, 21. [CrossRef]
17. Gambardella, L.; Vermeren, S. Molecular players in neutrophil chemotaxis–focus on PI3K and small GTPases. *J. Leukoc Biol.* **2013**, *94*, 603–612. [CrossRef]
18. Lien, E.C.; Dibble, C.C.; Toker, A. PI3K signaling in cancer: Beyond AKT. *Curr. Opin Cell Biol.* **2017**, *45*, 62–71. [CrossRef]
19. Thorpe, L.M.; Yuzugullu, H.; Zhao, J.J. PI3K in cancer: Divergent roles of isoforms, modes of activation and therapeutic targeting. *Nat. Rev. Cancer* **2015**, *15*, 7–24. [CrossRef]
20. Vanhaesebroeck, B.; Whitehead, M.A.; Pineiro, R. Molecules in medicine mini-review: Isoforms of PI3K in biology and disease. *J. Mol. Med.* **2016**, *94*, 5–11. [CrossRef]
21. Vanhaesebroeck, B.; Guillermet-Guibert, J.; Graupera, M.; Bilanges, B. The emerging mechanisms of isoform-specific PI3K signalling. *Nat. Rev. Mol. Cell Biol.* **2010**, *11*, 329–341. [CrossRef] [PubMed]
22. Campa, C.C.; Ciraolo, E.; Ghigo, A.; Germena, G.; Hirsch, E. Crossroads of PI3K and Rac pathways. *Small GTPases* **2015**, *6*, 71–80. [CrossRef] [PubMed]
23. Fukata, M.; Kaibuchi, K. Rho-family GTPases in cadherin-mediated cell-cell adhesion. *Nat. Rev. Mol. Cell Biol.* **2001**, *2*, 887–897. [CrossRef] [PubMed]
24. Yamaguchi, N.; Mizutani, T.; Kawabata, K.; Haga, H. Leader cells regulate collective cell migration via Rac activation in the downstream signaling of integrin beta1 and PI3K. *Sci. Rep.* **2015**, *5*, 7656. [CrossRef] [PubMed]
25. Walker, J.L.; Bleaken, B.M.; Wolff, I.M.; Menko, A.S. Establishment of a Clinically Relevant Ex Vivo Mock Cataract Surgery Model for Investigating Epithelial Wound Repair in a Native Microenvironment. *J. Vis. Exp.* **2015**, e52886. [CrossRef] [PubMed]
26. Menko, A.S.; Bleaken, B.M.; Libowitz, A.A.; Zhang, L.; Stepp, M.A.; Walker, J.L. A central role for vimentin in regulating repair function during healing of the lens epithelium. *Mol. Biol. Cell* **2014**, *25*, 776–790. [CrossRef] [PubMed]

27. Menko, A.S.; DeDreu, J.; Logan, C.M.; Paulson, H.; Levin, A.V.; Walker, J.L. Resident immune cells of the avascular lens: Mediators of the injury and fibrotic response of the lens. *FASEB J.* **2021**, *35*, e21341. [CrossRef] [PubMed]
28. Walker, J.L.; Bleaken, B.M.; Romisher, A.R.; Alnwibit, A.A.; Menko, A.S. In wound repair vimentin mediates the transition of mesenchymal leader cells to a myofibroblast phenotype. *Mol. Biol. Cell* **2018**, *29*, 1555–1570. [CrossRef]
29. Walker, J.L.; Wolff, I.M.; Zhang, L.; Menko, A.S. Activation of SRC kinases signals induction of posterior capsule opacification. *Invest. Ophthalmol. Vis. Sci.* **2007**, *48*, 2214–2223. [CrossRef]
30. Walker, J.L.; Zhai, N.; Zhang, L.; Bleaken, B.M.; Wolff, I.; Gerhart, J.; George-Weinstein, M.; Menko, A.S. Unique precursors for the mesenchymal cells involved in injury response and fibrosis. *Proc. Natl. Acad. Sci. USA* **2010**, *107*, 13730–13735. [CrossRef]
31. Menko, A.S.; Walker, J.L. The Pro-Fibrotic Response to Lens Injury Is Signaled in a PI3K Isoform-Specific Manner. *Biomolecules* **2022**, *12*, 1181. [CrossRef] [PubMed]
32. Gheyas, R.; Ortega-Alvarez, R.; Chauss, D.; Kantorow, M.; Menko, A.S. Suppression of PI3K signaling is linked to autophagy activation and the spatiotemporal induction of the lens organelle free zone. *Exp. Cell Res.* **2022**, *412*, 113043. [CrossRef] [PubMed]
33. Sellitto, C.; Li, L.; Vaghefi, E.; Donaldson, P.J.; Lin, R.Z.; White, T.W. The Phosphoinosotide 3-Kinase Catalytic Subunit p110alpha is Required for Normal Lens Growth. *Invest. Ophthalmol. Vis. Sci.* **2016**, *57*, 3145–3151. [CrossRef] [PubMed]
34. Son, M.K.; Ryu, Y.L.; Jung, K.H.; Lee, H.; Lee, H.S.; Yan, H.H.; Park, H.J.; Ryu, J.K.; Suh, J.K.; Hong, S.; et al. HS-173, a novel PI3K inhibitor, attenuates the activation of hepatic stellate cells in liver fibrosis. *Sci. Rep.* **2013**, *3*, 3470. [CrossRef]
35. Petrie, R.J.; Doyle, A.D.; Yamada, K.M. Random versus directionally persistent cell migration. *Nat. Rev. Mol. Cell Biol.* **2009**, *10*, 538–549. [CrossRef]
36. Pankov, R.; Endo, Y.; Even-Ram, S.; Araki, M.; Clark, K.; Cukierman, E.; Matsumoto, K.; Yamada, K.M. A Rac switch regulates random versus directionally persistent cell migration. *J. Cell Biol.* **2005**, *170*, 793–802. [CrossRef]
37. Laufer, J.M.; Hauser, M.A.; Kindinger, I.; Purvanov, V.; Pauli, A.; Legler, D.F. Chemokine Receptor CCR7 Triggers an Endomembrane Signaling Complex for Spatial Rac Activation. *Cell Rep.* **2019**, *29*, 995–1009.e6. [CrossRef]
38. Zhang, L.J.; Tao, B.B.; Wang, M.J.; Jin, H.M.; Zhu, Y.C. PI3K p110alpha isoform-dependent Rho GTPase Rac1 activation mediates H2S-promoted endothelial cell migration via actin cytoskeleton reorganization. *PLoS ONE* **2012**, *7*, e44590. [CrossRef]
39. Zeller, K.S.; Idevall-Hagren, O.; Stefansson, A.; Velling, T.; Jackson, S.P.; Downward, J.; Tengholm, A.; Johansson, S. PI3-kinase p110alpha mediates beta1 integrin-induced Akt activation and membrane protrusion during cell attachment and initial spreading. *Cell Signal.* **2010**, *22*, 1838–1848. [CrossRef]
40. Wan, G.; Pehlke, C.; Pepermans, R.; Cannon, J.L.; Lidke, D.; Rajput, A. The H1047R point mutation in p110 alpha changes the morphology of human colon HCT116 cancer cells. *Cell Death Discov.* **2015**, *1*, 15044. [CrossRef]
41. Yip, S.C.; El-Sibai, M.; Coniglio, S.J.; Mouneimne, G.; Eddy, R.J.; Drees, B.E.; Neilsen, P.O.; Goswami, S.; Symons, M.; Condeelis, J.S.; et al. The distinct roles of Ras and Rac in PI 3-kinase-dependent protrusion during EGF-stimulated cell migration. *J. Cell Sci.* **2007**, *120*, 3138–3146. [CrossRef] [PubMed]
42. Valgeirsdottir, S.; Claesson-Welsh, L.; Bongcam-Rudloff, E.; Hellman, U.; Westermark, B.; Heldin, C.H. PDGF induces reorganization of vimentin filaments. *J. Cell Sci.* **1998**, *111 Pt 14*, 1973–1980. [CrossRef]
43. Barberis, L.; Pasquali, C.; Bertschy-Meier, D.; Cuccurullo, A.; Costa, C.; Ambrogio, C.; Vilbois, F.; Chiarle, R.; Wymann, M.; Altruda, F.; et al. Leukocyte transmigration is modulated by chemokine-mediated PI3Kgamma-dependent phosphorylation of vimentin. *Eur. J. Immunol.* **2009**, *39*, 1136–1146. [CrossRef] [PubMed]
44. Sotsios, Y.; Whittaker, G.C.; Westwick, J.; Ward, S.G. The CXC chemokine stromal cell-derived factor activates a Gi-coupled phosphoinositide 3-kinase in T lymphocytes. *J. Immunol.* **1999**, *163*, 5954–5963. [PubMed]
45. Curnock, A.P.; Logan, M.K.; Ward, S.G. Chemokine signalling: Pivoting around multiple phosphoinositide 3-kinases. *Immunology* **2002**, *105*, 125–136. [CrossRef]
46. Walker, J.L.; Menko, A.S. Immune cells in lens injury repair and fibrosis. *Exp. Eye Res.* **2021**, *209*, 108664. [CrossRef]
47. Sit, S.T.; Manser, E. Rho GTPases and their role in organizing the actin cytoskeleton. *J. Cell Sci.* **2011**, *124*, 679–683. [CrossRef]
48. Cain, R.J.; Vanhaesebroeck, B.; Ridley, A.J. The PI3K p110alpha isoform regulates endothelial adherens junctions via Pyk2 and Rac1. *J. Cell Biol.* **2010**, *188*, 863–876. [CrossRef]
49. Vasilyev, A.; Liu, Y.; Hellman, N.; Pathak, N.; Drummond, I.A. Mechanical stretch and PI3K signaling link cell migration and proliferation to coordinate epithelial tubule morphogenesis in the zebrafish pronephros. *PLoS ONE* **2012**, *7*, e39992. [CrossRef]

cells

MDPI

Article

Imaging Cataract-Specific Peptides in Human Lenses

Kevin L. Schey *, Zhen Wang, Kristie L. Rose and David M. G. Anderson

Department of Biochemistry and Mass Spectrometry Research Center, Vanderbilt University School of Medicine, Nashville, TN 37232, USA
* Correspondence: k.schey@vanderbilt.edu

Abstract: Age-related protein truncation is a common process in long-lived proteins such as proteins found in the ocular lens. Major truncation products have been reported for soluble and membrane proteins of the lens, including small peptides that can accelerate protein aggregation. However, the spatial localization of age-related protein fragments in the lens has received only limited study. Imaging mass spectrometry (IMS) is an ideal tool for examining the spatial localization of protein products in tissues. In this study we used IMS to determine the spatial localization of small crystallin fragments in aged and cataractous lenses. Consistent with previous reports, the pro-aggregatory αA-crystallin 66–80 peptide as well as αA-crystallin 67–80 and γS-crystallin 167–178 were detected in normal lenses, but found to be increased in nuclear cataract regions. In addition, a series of γS-crystallin C-terminal peptides were observed to be mainly localized to cataractous regions and barely detected in transparent lenses. Other peptides, including abundant αA3-crystallin peptides were present in both normal and cataract lenses. The functional properties of these crystallin peptides remain unstudied; however, their cataract-specific localization suggests further studies are warranted.

Keywords: imaging mass spectrometry; ocular lens; protein degradation; cataract

1. Introduction

Age-related nuclear cataract (ARNC) is the most common form of age-related lens opacification and is a leading cause of visual impairment [1]. Lens protein aggregation and the resulting scattering of light causes the opacification and multiple mechanisms have been proposed to lead to protein modification. Importantly, lens proteins are long-lived proteins (LLPs) and they can undergo many post-translational modifications over a lifetime that spans many decades [2–5]. Thus, the ocular lens is an ideal tissue to examine such changes given that the proteins localized in the central lens nucleus are as old as the donor. Modifications that have been characterized in aged human lenses include: deamidation, truncation, isomerization, racemization, and crosslinking [4–8]. An important aspect of lens protein modification is the specific location where such modifications occur as this information helps to decipher if modifications are age-related. Furthermore, identification of cataract-specific modifications may suggest potential cataractogenic mechanisms. Thus, spatially resolved studies are necessary to link lens age-related protein modifications to the lens nucleus and nuclear cataract.

Imaging mass spectrometry (IMS) is an imaging technology that can provide spatial localization for proteins, peptides, lipids, and metabolites with high spatial resolution [9,10]. IMS has been applied to lens tissue to define the location of lens proteins and their modified forms in human lenses as a function of age [4,11,12]. Based on these studies, lens protein truncation begins early in life and leads to highly truncated protein forms in older nuclear fiber cells. Indeed, a large number of crystallin peptides have been discovered in aged human lenses [13,14]. One peptide, αA-crystallin 66–80, has been shown to induce protein aggregation [15], suggesting that age-related truncation products can have deleterious effects in the lens. Furthermore, IMS analysis of a guinea pig model of ARNC showed that protein truncation in the lens nucleus was accelerated with hyperbaric oxygen (HBO)

treatment [16]. Thus, knowledge of cataract-specific protein truncation products would inform on potentially cataractogenic properties of such peptides.

In this study, we employed IMS to image crystallin peptides in aged and cataractous human lenses. Specific peptides were reproducibly observed in nuclear cataract regions while not observed in age-matched transparent lenses. Other peptides were excluded from cataractous regions.

2. Materials and Methods

2.1. Tissue Preparation for Imaging Mass Spectrometry (IMS)

Human lenses were acquired from National Disease Research Interchange (NDRI) (Philadelphia, PA, USA), the South Carolina Lions Eye Bank (Charleston, SC, USA) or as a gift from Dr. Donita Garland (Ocular Genomics Institute at Massachusetts Eye and Ear, Harvard University, Cambridge, MA, USA). All lenses were stored at −80 °C until use. Information related to lenses used in this study can be found in the Supplemental Section S1. Each lens was sectioned equatorially to 10 μm thickness using a CM 3050 cryostat (Leica CM 3050S, Leica Microsystems Inc., Bannockburn, IL, USA). Tissue sections were thaw-mounted on conductive Indium-Tin-Oxide (ITO) coated slides (Delta Technologies, Loveland, CO, USA) and vacuum desiccated for 30 min. To remove lipids, the sections were washed twice with 70% ethanol for 1 min followed by washing with 100% ethanol for 1 min. The sections were then dried in a vacuum desiccator. To enable matrix-assisted laser desorption ionization (MALDI), tissue sections were spray-coated with 2,5-dihydroxybenzoic acid (DHB) matrix (20 mg/mL in 70% ACN containing 0.1% TFA) using a TM sprayer (HTX Technologies, LLC, Carrboro, NC, USA). The TM Sprayer was operated using the following settings: flow rate 0.1 mL/min, nozzle velocity of 700 mm/min, nozzle temperature at 85 °C, track spacing at 3 mm, number of passes of 8 and nitrogen pressure 9.5 psi. After matrix application, tissue sections were rehydrated at 85 °C for 3 min in a sealed chamber containing 50 μL of 50 mM acetic acid.

2.2. MALDI Data Acquisition

MALDI imaging mass spectrometry experiments were performed using a Bruker Rapiflex Tissuetyper (Bruker Daltonics, Billerica, MA, USA) equipped with a Smartbeam 3D 10 kHz 355 nm Nd:YAG laser™ 3D laser. m/z calibration was accomplished via a linear external calibration using a mix of bovine insulin, equine cytochrome c, bovine ubiquitin I, and equine myoglobin (Bruker Daltonik, Billerica, MA, USA). Mass spectrometric analyses were performed in the linear, positive ionization mode over a mass-to-charge (m/z) range of m/z 1200 to m/z 20,000. The ionization laser was scanned across the tissue surface with a raster step size of 60 μm and spectra from 2000 laser shots per pixel (tissue position) were averaged to produce a spectrum. Low molecular weight crystallin fragments were also analyzed in a positive ion reflector MS mode, to improve mass resolution, over an m/z range of m/z 950 to m/z 5000 and with a laser raster step size of 150 μm. Spectra from 500 laser shots were used to produce an average spectrum. The mass spectrometer was calibrated with a peptide mixture (Leu-enkephalin, Angiotensin II, Fibrinopeptide B, ACTH fragment (1–24), and insulin chain B). Ion images were generated using FlexImaging software (Version 4.1, Bruker Daltonics, Billerica, MA, USA) using RMS normalization.

To measure the accurate masses of the signals observed in IMS data in the cortex and nucleus regions, tissue from the cortex (within 400 μm from the capsule) and inner nucleus region (within 500 μm from the center) of a 55 Y.O. (C_5_1) cataract lens and the cortex region of 54 Y.O. (N_5_1) normal transparent lens was captured by laser capture microdissection (LCM). The LCM procedure was conducted using a PALM UV Laser MicroBeam laser capture microdissection system (Carl-Zeiss, Oberkochen, Germany) on tissue sections of 12 μm thickness on glass slides. The capture was done using a laser pressure catapulting (LPC) method and 37% laser energy. An area of roughly 1 mm^2 was collected for each sample. The samples were collected in 20 μL of water and mixed with acetonitrile containing 2%TFA to final acetonitrile concentration of 5% and loaded on C18

SpinTips (Thermo Scientific, Rockford, IL, USA). The samples were washed with 0.1%TFA and eluted in 2.5 μL of 70% acetonitrile containing 0.1%TFA. The samples were mixed with 2.5 μL of saturated α-cyano-4-hydroxycinnamic acid (CHCA) matrix (Sigma-Aldrich, St Louis, MO, USA) in 70% acetonitrile (0.1%TFA) and masses were measured with high accuracy (<5 ppm) in a Bruker SolariX 15T FT-ICR mass spectrometer (Bruker Daltonics, Billerica, MA, USA) equipped with a Smartbeam II 2 kHz Nd:YAG (355 nm) laser. The mass spectrometer was externally calibrated prior to analysis using a peptide mixture (Leu-enkephalin, Angiotensin II, Fibrinopeptide B, ACTH fragment (1–24), and insulin chain B). The mass spectrometer was operated in positive ion mode and data were collected from m/z 700 to 4500 at a mass resolution of ~155,000 at m/z = 2360.2393.

2.3. Peptide Identification and LC-MS/MS Analysis

To identify the peptides that correspond to the low molecular weight signals in MALDI imaging results, peptides were extracted from the nucleus region of two cataract lenses using 20% acetonitrile, 80% water as described previously [17]. The samples were diluted using 0.1% formic acid to reduce the acetonitrile concentration to 3% and loaded onto a C18 trap column (50 mm × 150 μm) packed with Phenomenex Jupiter resin (5 μm mean particle size, 300 Å pore size). The trap column was connected with a fused silica capillary analytical column (150 mm × 100 μm) packed with Phenomenex Jupiter resin (3 μm mean particle size, 300 Å pore size). Peptides were analyzed by LC-MS/MS on a LTQ Orbitrap Velos (Thermo Scientific, San Jose, CA, USA) mass spectrometer coupled to an Eksigent NanoLC system. Mobile phase solvents consisted of 0.1% formic acid in water (solvent A) and 0.1% formic acid in acetonitrile (solvent B). Peptides were gradient eluted at a flow rate of 500 nL/min using the following gradient: 2–45%B in 40 min; 45–90%B in 15 min; 90%B for 2 min; 90–2%B in 1 min; and 2%B for 15 min (column equilibration). Peptides were introduced into the LTQ Orbitrap Velos using a nanoelectrospray source. The instrument was operated using a combined method consisting of both data-dependent electron transfer dissociation (ETD) and targeted ETD scan events. MS1 acquisition was performed in the Orbitrap (R = 60,000) with an AGC target value of 1e6. The MSn AGC target value of 9e5 was used in the Orbitrap and 2e4 in the ion trap. Dynamic exclusion (repeat count 1, exclusion list size 500, and exclusion duration 15 s) was enabled. For ETD, an isolation width of 3 m/z and reaction time of 80 ms were used. The ETD reagent ion AGC target was 3e6. ETD MS/MS spectra were interpreted manually.

3. Results

3.1. Detection of Low Molecular Signals in Cataract Nucleus

In this study, an untargeted approach using imaging mass spectrometry (IMS) was used to examine protein degradation in different regions of normal and cataract human lenses. In addition to intact crystallins and longer truncated crystallin fragments reported previously [9], IMS analysis also revealed lower molecular weight (LMW) signals and some of these signals were only detected in the nucleus region of nuclear cataract lenses. A typical IMS result is shown in Figure 1, which shows the presence of signals at m/z 2933 and 4098 in the nucleus of the two cataract lenses (55 Y.O. (C_5_1) and 56 Y.O. (C_5_2)). These two signals were not present in the nucleus of a 54 Y.O. (N_5_1) normal transparent lens.

Note that Figure 1 also showed the presence of a signal at m/z 2933 in the cortex of both normal and cataract lenses. Due to absence of this signal in the inner cortex and outer nucleus region, we hypothesized that the signal in the cortex could represent a different peptide with similar molecular weight to the one in the nucleus. Due to the low mass resolving power of the linear MALDI-TOF instrument used in this experiment, two molecules with close molecular weights, i.e., nominal isobars, could not be mass resolved. To test this hypothesis, tissues from the cortex and nucleus regions were collected by LCM and the samples were analyzed using a high mass resolution FT-ICR mass spectrometer. The results shown in Figure 2 confirmed our hypothesis. The protonated ion in the 54 Y.O.(N_5_1) cortex region has measured m/z value of 2930.4939 and the measured m/z

value in 55 Y.O. (C_5_1) cataract lens cortex was 2930.4999, but the signal in the nucleus region has measured m/z value of 2931.6001. This result confirmed the 2933 signal in the cortex region shown Figure 1 corresponds to a different peptide from the signal in the cataract nucleus. The signal at m/z 2930.4939 in the lens cortex has not been identified in subsequent LC-MS/MS experiments of nuclear extracts; however, the mass matches a βB2-crystallin 182–205 peptide with a mass error 4.2 ppm and this βB2-crystallin peptide was previously reported to be present in human lenses [13].

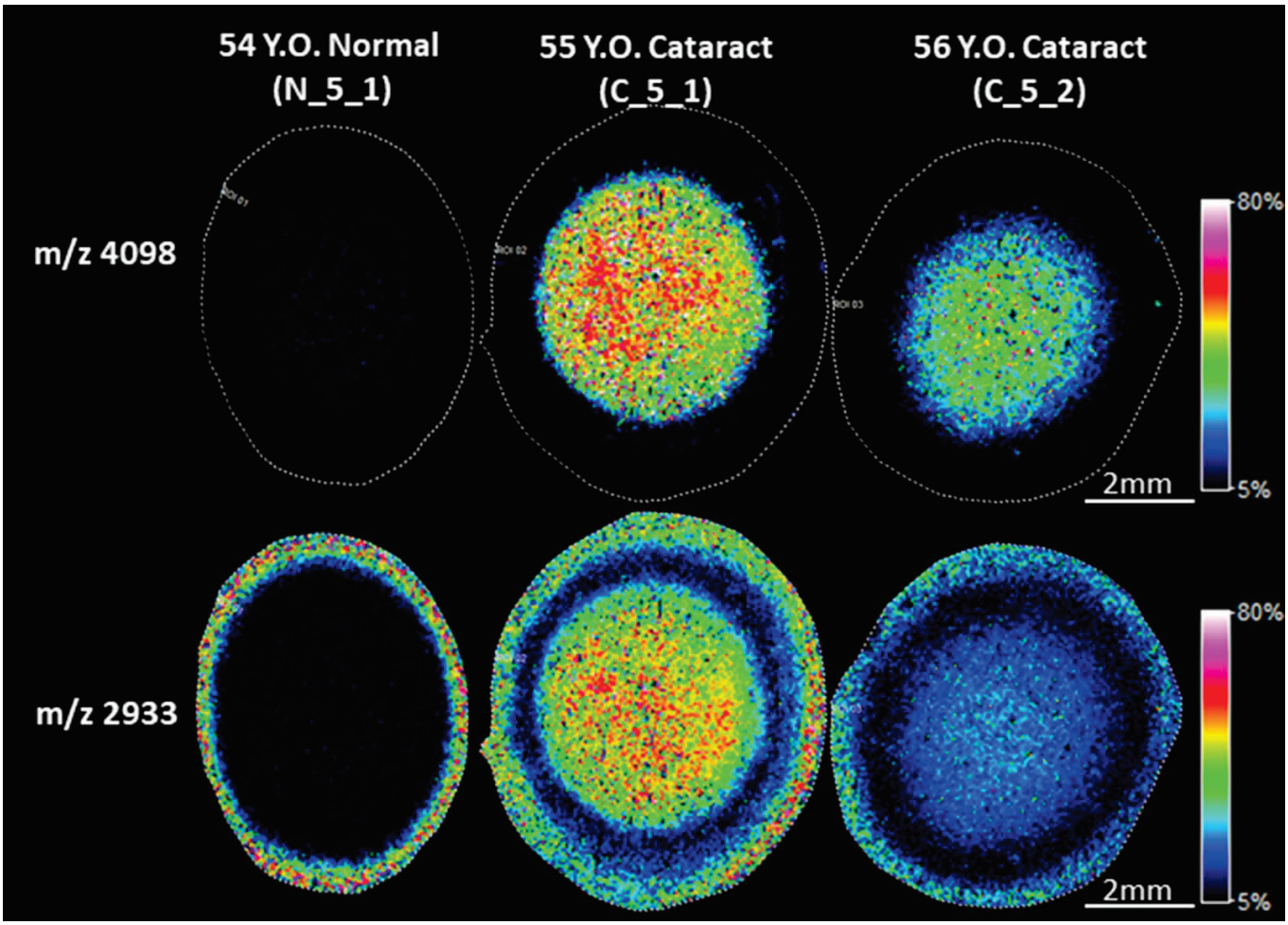

Figure 1. Cataract-specific signals in the nucleus of cataract lenses. Imaging mass spectrometry (IMS) analysis of human lens sections was performed on Bruker Rapiflex Tissuetyper using a 60 μm raster step size. IMS analysis identified two signals with m/z values of 4098 and 2933 that were only detected in the nucleus of cataract lenses, but not in normal lens nucleus. Accurate mass measurement confirmed m/z 2933 signal in the cortex region represent a different peptide than that represented by the signal in the cataract nucleus. Signal represents peak m/z value ± 0.1% m/z unit.

3.2. Identification of Signals Detected by IMS and Further Confirmation of Cataract Specificity

Identification of the peptides at m/z 2933 and 4098 was performed based on their accurate masses and their tandem mass spectra in LC-MS/MS experiments. To identify these signals, a 20% acetonitrile extract from the nucleus region of a 70 Y.O. (C_7_1) cataract lens was analyzed by LC-MS/MS. The base peak chromatogram from the LC-MS/MS analysis is shown in Figure 3 which further confirms the presence of two abundant signals with the measured mass of a protonated ion ([MH]+) of 2931.5942 and 4096.1988. These measured masses match γS-crystallin peptide sequences 154–178 and 145–178, respectively, within 1 ppm mass accuracy. Their identifications were further confirmed by their tandem mass spectra. The ETD tandem mass spectrum of γS-crystallin peptide 154–178 (+4 ion)

is shown in Figure 4A displaying excellent matches to the peptide sequence with a series of c and z ions. The tandem mass spectrum for γS-crystallin peptide 145–178 (+6 ion) can be found in Figure 4B. In addition to these two γS peptide signals, manual analysis of the major LC-MS/MS signals confirmed the presence of multiple γS-crystallin, βA3-crystallin and γD-crystallin C-terminal peptides in the cataract lens nucleus sample. These signals are labeled in the base peak chromatogram (Figure 3). A list of these peptides with their measured and predicted masses is shown in Table 1.

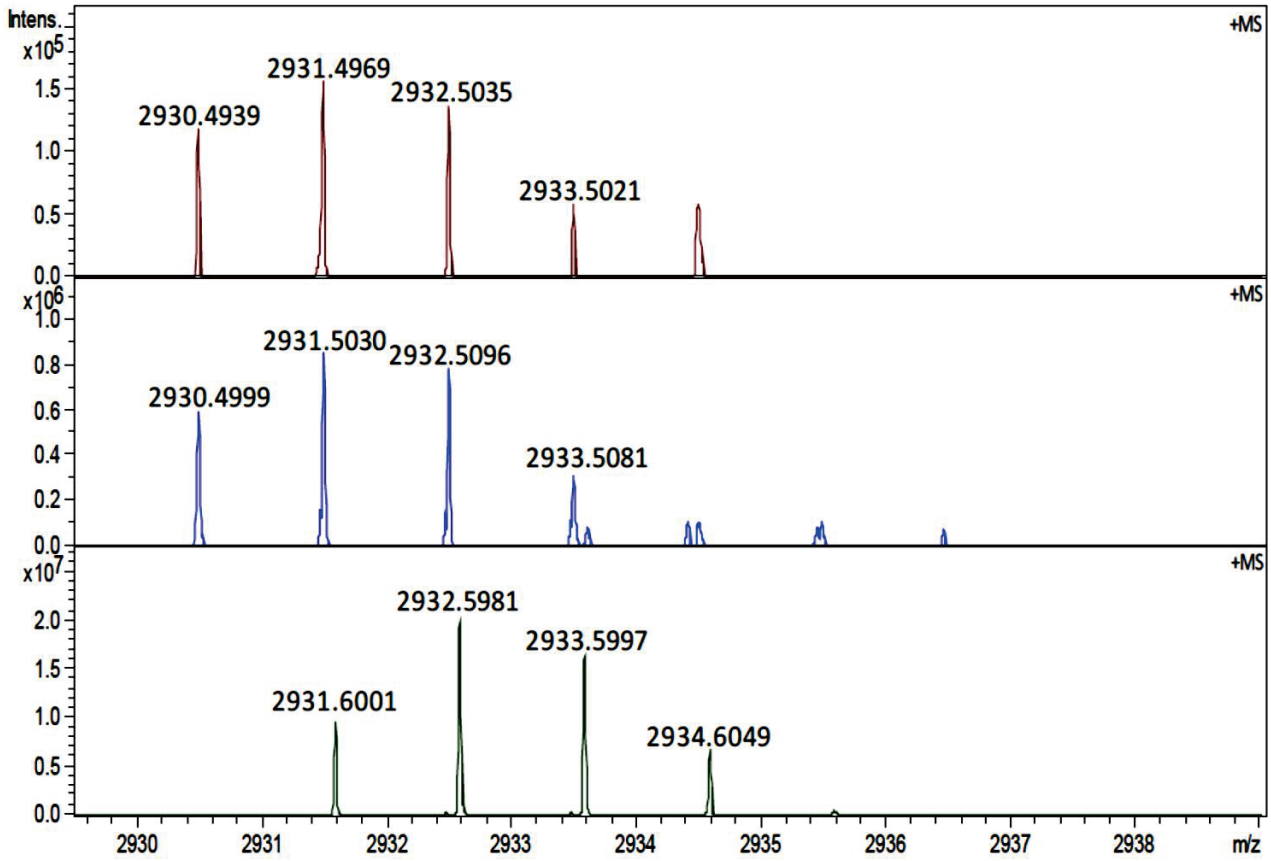

Figure 2. Accurate mass measurement of the signal at m/z 2933 in cortex and nucleus regions using an FT-ICR mass spectrometer. The positive mode mass spectra from LCM captured cortex and nucleus samples were zoomed in to show the isotopic distribution of signals at m/z 2933. The protonated ion in a 54 Y.O. (N_5_1) normal lens cortex region (**top row**) has a measured monoisotopic mass of 2930.4939 Da and 2930.4999 Da in 55 Y.O. (C_5_1) cataract lens cortex (**middle row**), but has a measured monoisotopic mass of 2931.6001 Da in 55 Y.O. cataract lens nucleus (**bottom row**).

To further confirm whether γS-crystallin peptides 154–178 and 145–178 are indeed cataract-specific, several IMS datasets were acquired from multiple human lenses. The data are shown in Figure S1. The results from multiple datasets, acquired on different instruments and using different experimental conditions, consistently confirmed the presence of γS-crystallin 154–178 and γS-crystallin 145–178 in cataract lens nuclei, but not in normal lenses. A weak signal of γS-crystallin 145–178 can sometimes be detected in aged normal lens (70 Y.O. (N_7_1) and 78 Y.O. (N_7_2)), but the signal intensity of this peptide was significantly stronger in age-matched cataract lens nuclei. Moreover, a mild nuclear cataract could have been missed in the evaluation of these aged lenses.

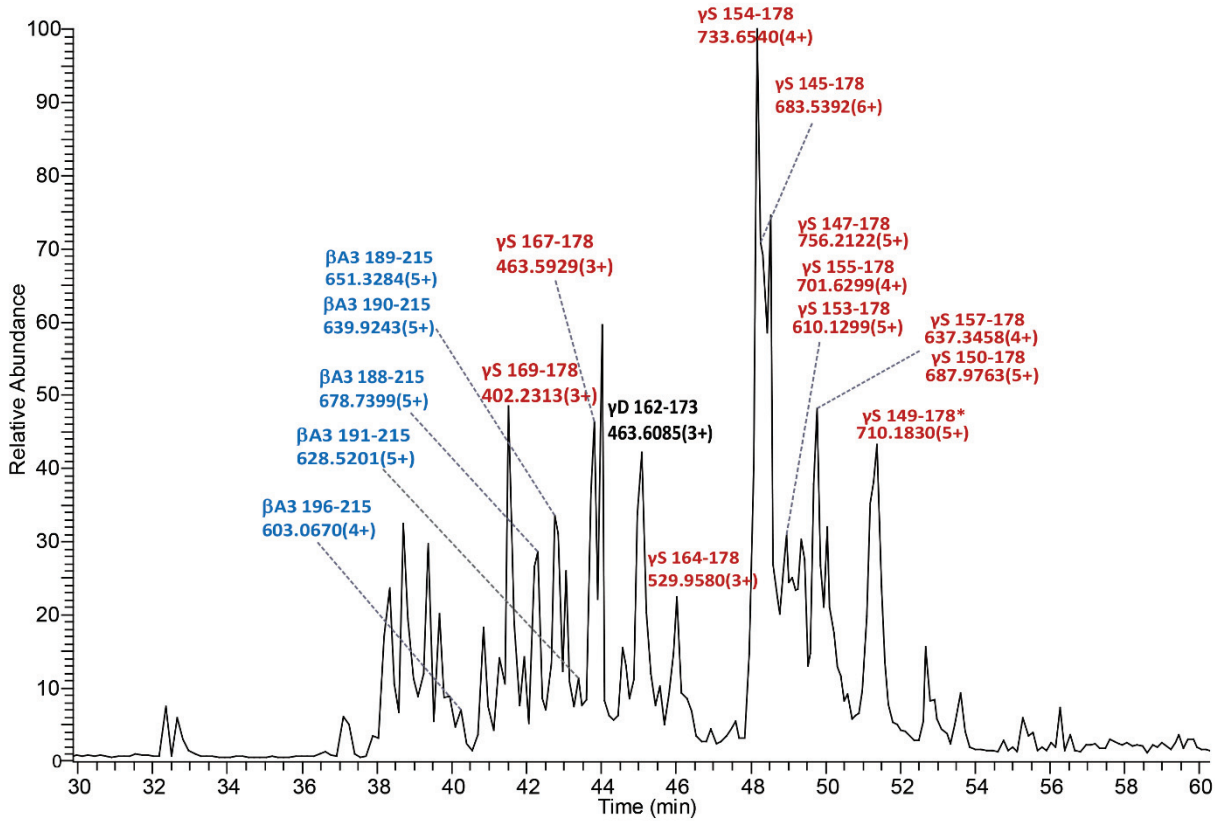

Figure 3. The base peak chromatogram of LC-MS/MS analysis of the extract from a 70 Y.O. (C_7_1) nucleus of a cataract lens. The base peak chromatogram is dominated by strong signals of γS- and βA3-crystallin fragments. Two strongest signals are identified as γS154–178 and γS145–178. Other base peak signals were identified as γS-crystallin C-terminal peptides (red), βA3-crystallin C-terminal peptides (blue) and a γD-crystallin C-terminal peptide (black). * indicates pyroGlu at the N-terminus.

IMS data were also acquired in a low mass range using a higher mass resolution reflector MALDI-TOF instrument. The results can be found in Figure 5. Consistent with aforementioned results, γS-crystallin 154–178 and γS-crystallin 145–178 were detected in cataract nuclei, but not in cataract cortex and normal lenses. Other than γS-crystallin 145–178 and γS-crystallin 154–178, other signals that were highly abundant in the cataract nucleus compared to cortex tissue in cataract and normal lenses were also detected (Figure 5). The signal at m/z 1204 was identified as γS-crystallin 169–178. Other signals at m/z 1849 and m/z 1779 correspond to αA-crystallin 66–80 and αA-crystallin 67–80, respectively. Consistent with previous reports [13,14,18], a weak signal of αA 66–80 and 67–80 was detected in the normal lens, but intensities of these peptides were significantly higher in the cataract lenses. The accurate mass measurement again showed the signal at nominal m/z 1389 corresponds to two peptides γS-crystallin 167–178 and γD-crystallin 162–173. As shown in Figure S2, the signal in the cortex was mainly from γS-crystallin 167–178 (calculated m/z 1388.7645), but in the nucleus, intensities of both γS-crystallin 167–178 and γD-crystallin 162–173 (calculated m/z 1388.8121) were similar. Therefore, both peptides contribute roughly equally to the signal at m/z 1389 in the nucleus. The weak signal of γS-crystallin 167–178 in normal lens and cataract lens cortex was also consistent with previous reports [13,14,19].

3.3. Low Molecular Weight Signals in Normal Lenses

As shown in Figure 3, some strong LMW signals are identified as βA3-crystallin peptides. Unlike γS-crystallin peptides, IMS analysis showed βA3-crystallin peptides were detected in both normal and cataract lenses. IMS results from three middle-aged lenses

are shown in Figure 6. These results suggest that βA3-crystallin undergoes degradation and this process starts earlier than γS-crystallin degradation since strong signals from βA3-crystallin 188–215 and βA3-crystallin 189–215 can be detected in the cortical fiber cells of the middle-aged lenses. Signals from βA3-crystallin fragments did not show a difference between normal lens cortex and cataract lens cortex, however, signals from the longer peptides, especially βA3-crystallin 188–215, dramatically decreased and the signal from the shorter fragments (βA3-crystallin 191–215 and 192–215) significantly increased in the nucleus of the cataract lenses. The longest βA3-crystallin C-terminal peptide detected was 187–215 and shorter peptides were detected corresponding to removal of residues from the new N-terminus. These results suggest that initial cleavage occurs at the Asp186-His187 peptide bond, that further degradation of peptide products continues with age, and that this process is elevated in the cataract nucleus.

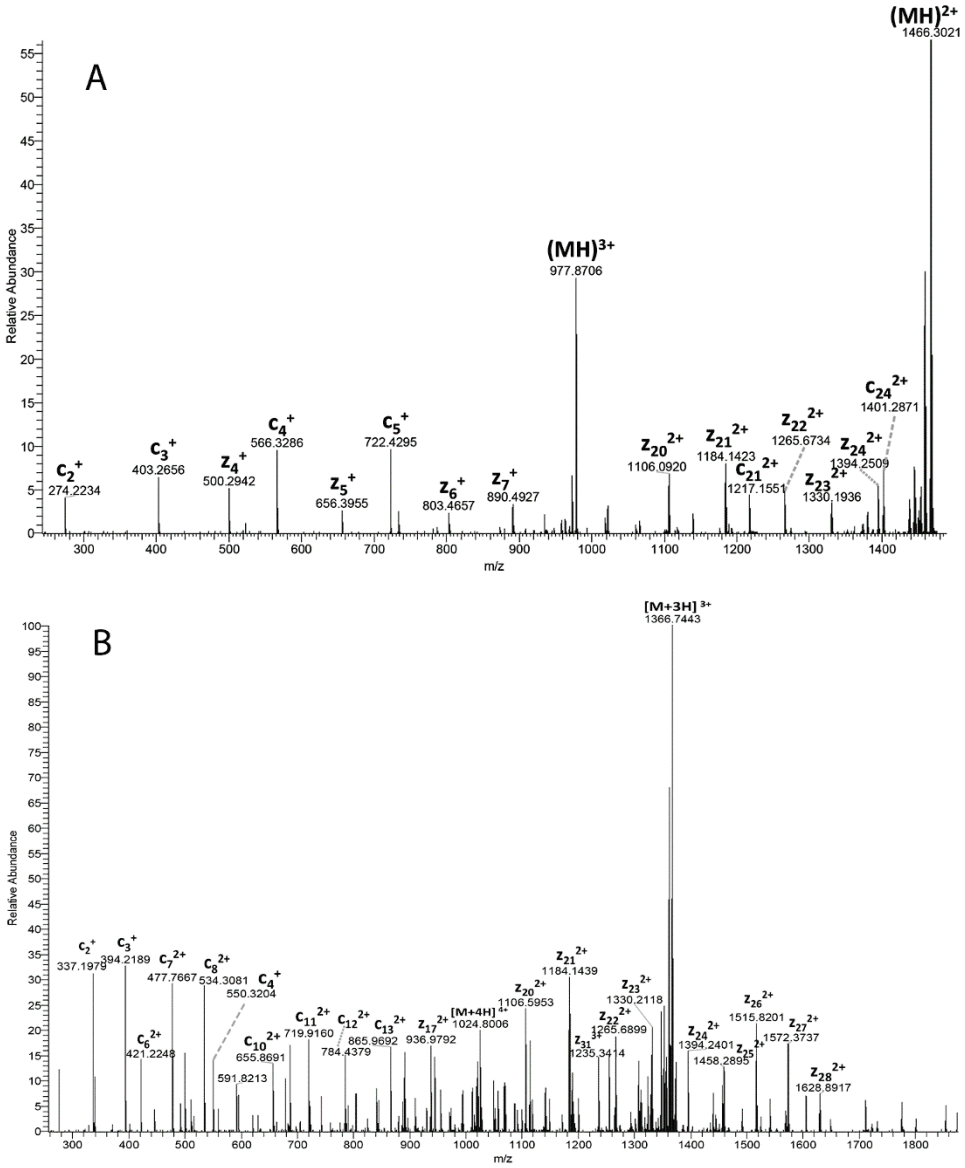

Figure 4. ETD tandem mass spectra of: (**A**) γS-crystallin 154–178 (+4 charged ion) and (**B**) γS-crystallin 145–178 (+6 charged ion). All masses labeled represent the monoisotopic masses.

Table 1. Identified major γS-, γD- and βA3-crystallin peptides in the nucleus of a 70 Y.O. (C_7_1) cataract lens.

Protein	Predicted *m/z* [a]	Observed *m/z*	Error (ppm)
Gamma S 145–178	4096.1992	4096.1988	0.1
Gamma S 147–178	3777.0347	3777.0319	0.74
Gamma S 149–178 (pyroGlu)	3546.8856	3546.8859	0.1
Gamma S 150–178	3435.8536	3435.8524	0.35
Gamma S 153-178	3046.6221	3046.6204	0.56
Gamma S 154–178	2931.5952	2931.5942	0.35
Gamma S 155–178	2803.5002	2803.4978	0.87
Gamma S 157–178	2546.3627	2546.3614	0.52
Gamma S 164–178	1587.8602	1587.8594	0.47
Gamma S 167–178	1388.7645	1388.7641	0.25
Gamma S 169–178	1204.6797	1204.6793	0.29
Beta A3 188–215	3389.6747	3389.6704	1.3
Beta A3 189–215	3252.6158	3252.6129	0.89
Beta A3 190–215	3195.5943	3195.5924	0.6
Beta A3 191–215	3138.5729	3138.5714	0.5
Beta A3 196–215	2409.2494	2409.2462	1.3
Gamma D 162–173	1388.8121	1388.8109	0.83

[a] monoisotopic *m/z*.

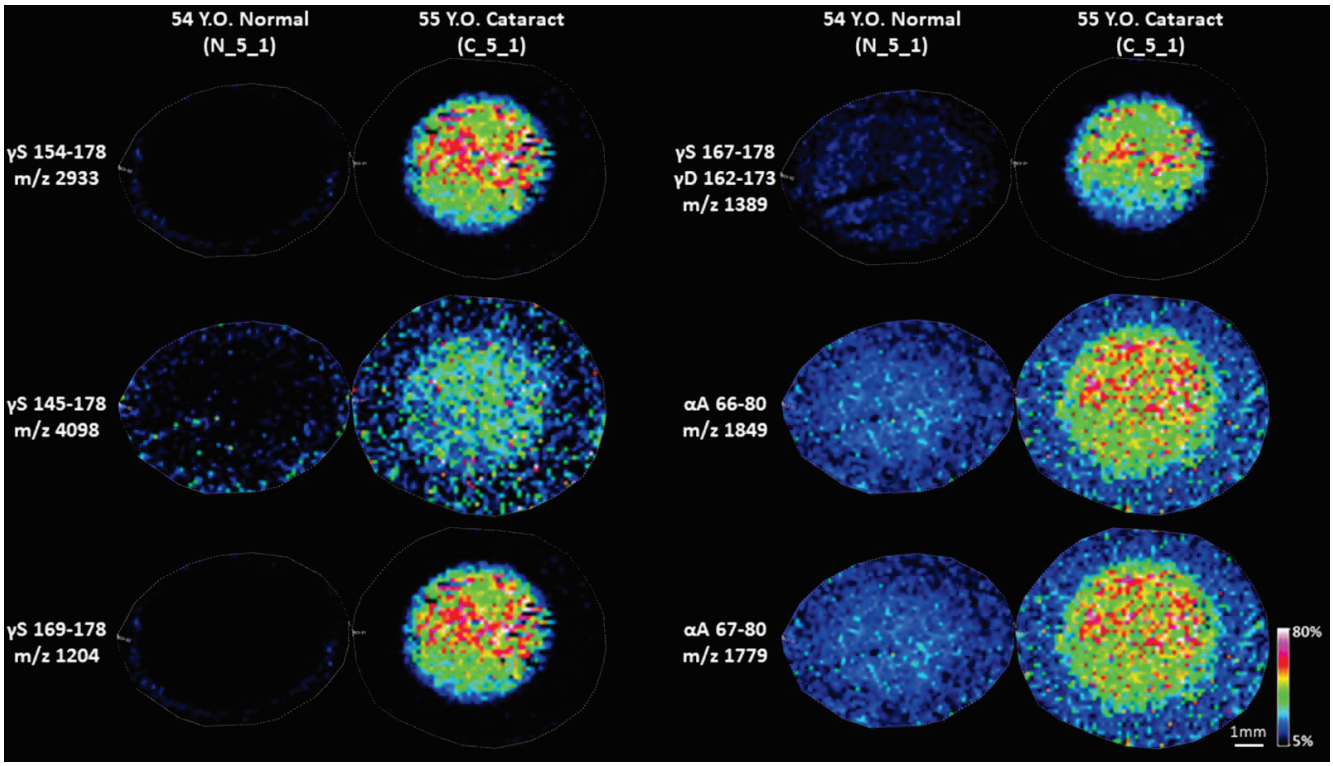

Figure 5. IMS images of LMW fragments specific or highly enriched in cataract lenses. Images were acquired on Bruker Rapiflex Tissuetyper using a 150 μm raster step size. Signal represents peak *m/z* value ± 0.01% *m/z* unit.

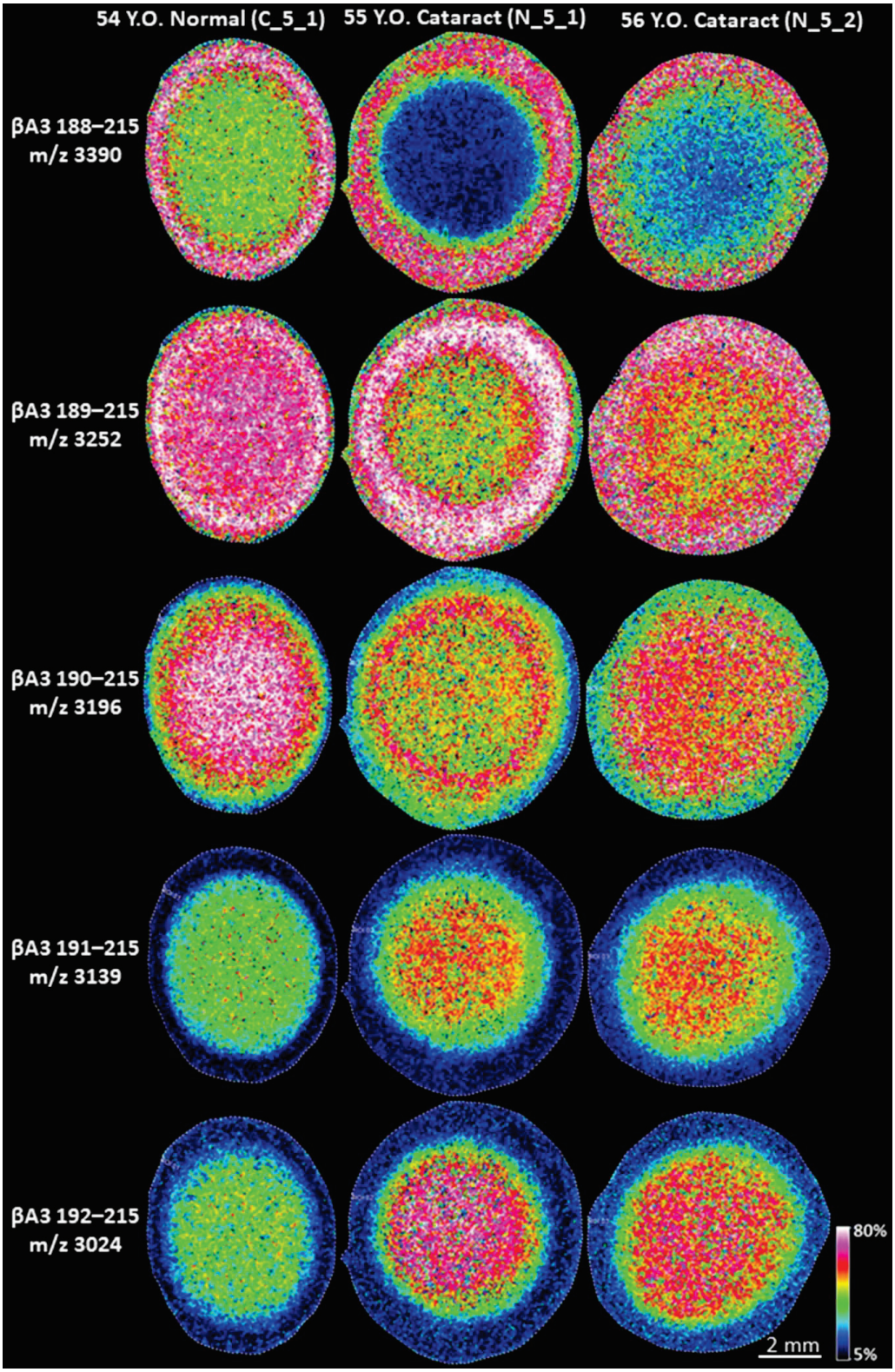

Figure 6. IMS analysis of βA3 peptides in normal and cataract lenses. IMS analysis of human lens sections was performed on Bruker Rapiflex Tissuetyper using a 60 μm raster step size. Multiple βA3-crystallin fragments were detected in normal and cataract lenses. The protein cleavage started in lens cortex and βA3 fragments were further degraded and their formation was accelerated in cataract lens nuclei. Signal represents peak m/z value ± 0.1% m/z unit.

4. Discussion

Accumulation of low molecular weight (LMW) crystallin fragments in aged and cataract lenses has been characterized by multiple investigators [12–14,17,18] and some major crystallin fragments, including peptides from αA-, αB- and βA3-crystallins [13–15,18], have been repeatedly reported. However, with the exception of γS-crystallin 167–178 and 2–22 peptides, other γS-crystallin LMW peptides have not been reported. In this study, we identify LMW peptides from the γS-crystallin C-terminus as the dominating signals in the nucleus region of nuclear cataract lenses. Most noteworthy, these LMW fragments are cataract-specific since they were either not detected or were of very low abundance in normal lenses by IMS. One might ask why these abundant γS-crystallin peptides in cataract lens nucleus were not detected previously [13,14]. We speculate that the reason is due to the strong membrane binding and hydrophobic properties of these peptides. As previously suggested, γS-crystallin 167–178 can only be extracted from the membrane with NaOH or ethanol [18]. Thus, the peptides reported in this study are likely to be strongly bound to fiber cell membranes. In fact, the γS-crystallin 167–178 peptide has been reported to strongly bind to the cell membrane and may also affect water permeability [18]. Thus, the hydrophobic properties of C-terminal γS-crystallin peptides could induce protein aggregation and/or plasma membrane binding.

γS-crystallin, formerly known as βS-crystallin, belongs to the βγ-crystallin superfamily of lens crystallins. Based on sequence homology and predicted tertiary structure, γS-crystallin was found to be more closely related to the monomeric γ-crystallins than to the oligomeric β-crystallins and its name was changed to γS-crystallin [20]. γS-Crystallin is synthesized postnatally and is highly abundant in the ocular lens [21], whereas other γ-crystallins are primarily synthesized before birth and are mainly present in the lens nucleus [21]. Multiple single-residue mutations in γS-crystallin were reported to be associated with formation of different types of cataract [22]. Deamidation of Asn76 in γS-crystallin was found in greater abundance in cataract lenses compared to normal lenses [7]. The finding of the LMW γS-crystallin peptides to be specifically present in the nucleus of nuclear cataract lenses further supports the importance of γS-crystallin during cataractogenesis. Consistent with our results, it was reported that the monomeric full length of γS-crystallin was diminished in nuclear cataract lenses [23]. Clearly, extensive degradation of γS-crystallin occurs in nuclear cataract. How the properties of the observed C-terminal fragments contribute to opacification remains to be elucidated.

Our finding of cataract-specific LMW fragments in nuclear cataracts support the hypothesis that the development of cataract is due, at least in part, to the aggregation of crystallin fragments generated by the breakdown of crystallin proteins [15,24]. The discovery of a LMW αA-crystallin peptide, residues 66–80, that induced protein aggregation and light scattering as well as caused loss of α-crystallin chaperone activity [15] also supports this hypothesis [13,15]. We observed this specific αA-crystallin peptide in cataractous lens nuclei along with αA-crystallin 67–80. In addition to LMW peptides, truncated crystallins have been found to be more prone to aggregation [18].

Considering the potential protein aggregation properties of the LMW fragments, it is important to understand the mechanisms that mediate the cleavage of crystallins. No protease has been linked with previously reported LMW peptides [13,14]. Human βA3-crystallin was reported to possess autodegradative serine protease activity that could be responsible for degradation of the βA3-crystallin N-terminus (Gln4-Ala5 and Lys17-Met18) [25], however, this would not explain the formation of the βA3-crystallin C-terminal fragments. The longest βA3-crystallin C-terminal fragment is βA3-crystallin 187–215 corresponding to cleavage at Asp186. We believe the peptide 187–215 is formed first followed by further removal of residues from the N-terminus resulting in multiple peptides with different lengths. Our IMS results also confirm that the formation of βA3-crystallin peptides starts in young cortical fiber cells and the peptides formed were further degraded in the nucleus. Similarly, the formation of γD-crystallin 162–173 corresponds to cleavage at Asn 161. Spontaneous cleavage at Asp and Asn through a succinimide intermediate [26] or

Glu or Gln through a glutarimide [27] is a well-known mechanism for protein cleavage and this process is also coupled with deamidation, isomerization, and racemization of Asn or Gln residues [26]. These mechanisms explain truncation, deamidation and isomerization at many different Asn, Asp, Gln and Glu residues throughout the lens proteome, especially the ones that are followed by small, flexible residues such as glycine [26,28,29]. Another spontaneous cleavage mechanism, i.e., cleavage on the N-terminal side of Ser that may involve an intein-like mechanism [19,30] could be responsible for the formation of γS-crystallin 167–178. Both proposed mechanisms are expected to occur in both normal and cataract lenses and, correspondingly, predicted LMW peptides can be detected in both normal and cataract lenses.

The two major cataract-specific γS-crystallin peptides detected in this study are produced by cleavage after Asn144 and Asp153. Therefore, similar to other lens peptides, spontaneous cleavage through a succinimide intermediate could also contribute to the formation of these peptides. Additional removal of N-terminus residues generates other shorter γS-crystallin peptides detected in nucleus of cataract lenses. However, the succinimide mechanism is a common mechanism that is responsible for the most prevalent modifications such as deamidation and isomerization in aged normal lenses [4,8,31]. It is questionable why these γS-crystallin peptides were only detected in cataract lens nuclei if a common aging mechanism is responsible for the formation of these peptides. In addition, succinimide mediated deamidation and truncation is characterized by formation of multiple isomers after deamidation and truncation. From our LC-MS/MS analysis of trypsin digested human lens samples, multiple isomers can be detected for the βA3-crystallin 178–193 (containing Asp186) and γD-crystallin 154–163 (containing Asn161); however, the γS-crystallin peptide 132–146 (plus deamidation) and 149–154 were present as single peaks indicating lack of isomerization (data not shown). Even though cleavage at Asn144 and Asp153 in γS-crystallin occurs at Asp and Asn residues, this cleavage may be through a different mechanism other than through a succinimide intermediate. Another possible explanation is that LMW peptides formed in normal lenses can be effectively degraded, but this degradation process is lost in cataract lenses resulting in accumulation of these peptides. Further study is needed to understand the mechanism for formation and accumulation of LMW γS-crystallin fragments in cataract lenses.

Supplementary Materials: The following supporting information can be downloaded at: https://www.mdpi.com/article/10.3390/cells11244042/s1, Figure S1: IMS analysis of γS 145–178 and γS 154–178 in normal and cataract lenses; Figure S2: The accurate mass measurement of the signal at m/z 1389; Section S1.

Author Contributions: K.L.S. & Z.W. wrote the manuscript. K.L.S., Z.W., D.M.G.A. & K.L.R. were involved in the planning of experiments, acquiring data, and editing the manuscript. All authors have read and agreed to the published version of the manuscript.

Funding: This research was funded by National Institutes of Health grant number R01 EY013462 and P30 EY008126.

Data Availability Statement: The raw data is available on request that should be send to k.schey@vanderbilt.edu.

Acknowledgments: The authors acknowledge Donita Garland of the Ocular Genomics Institute at Massachusetts Eye and Ear, Harvard Medical School for providing some nuclear cataract lenses. The authors also acknowledge the funding support by National Institutes of Health by grants R01 EY013462 and P30 EY008126 and the use of Proteomics and Tissue Imaging Core Facility of the Vanderbilt University Mass Spectrometry Research Center.

Conflicts of Interest: The authors have no potential conflict of interest to declare.

References

1. Congdon, N.; Vingerling, J.R.; Klein, B.E.K.; West, S.; Friedman, D.; Kempen, J.; O'Colmain, B.; Wu, S.-Y.; Taylor, H.R. Eye Diseases Prevalence Research Group Prevalence of Cataract and Pseudophakia/Aphakia Among Adults in the United States. *Arch. Ophthalmol.* **2004**, *122*, 487–494. [CrossRef] [PubMed]
2. Truscott, R.J.; Schey, K.L.; Friedrich, M.G. Old Proteins in Man: A Field in its Infancy. *Trends Biochem. Sci.* **2016**, *41*, 654–664. [CrossRef] [PubMed]
3. Takemoto, L. Quantitation of C-terminal modification of alpha-A crystallin during aging of the human lens. *Exp. Eye Res.* **1995**, *60*, 721–724. [PubMed]
4. Wilmarth, P.A.; Tanner, S.; Dasari, S.; Nagalla, S.R.; Riviere, A.; Bafna, V.; Pevzner, P.A.; David, L.L. Age-related changes in human crystallins determined from comparative analysis of post-translational modifications in young and aged lens: Does deamidation contribute to crystallin insolubility? *J. Proteome Res.* **2006**, *5*, 2554–2566. [CrossRef] [PubMed]
5. Grey, A.C.; Schey, K.L. Age-Related Changes in the Spatial Distribution of Human Lens α-Crystallin Products by MALDI Imaging Mass Spectrometry. *Investig. Opthalmology Vis. Sci.* **2009**, *50*, 4319–4329. [CrossRef] [PubMed]
6. Takemoto, L.; Boyle, D. Increased deamidation of asparagine during human senile cataractogenesis. *Mol. Vis.* **2000**, *6*, 164–168.
7. Hooi, M.Y.; Raftery, M.J.; Truscott, R.J. Racemization of two proteins over our lifespan: Deamidation of asparagine 76 in gammaS crystallin is greater in cataract than in normal lenses across the age range. *Investig. Ophthalmol. Vis. Sci.* **2012**, *53*, 3554–3561. [CrossRef]
8. Lyon, Y.A.; Sabbah, G.M.; Julian, R.R. Differences in α-crystallin isomerization reveal the activity of protein isoaspartyl methyltransferase (PIMT) in the nucleus and cortex of human lenses. *Exp. Eye Res.* **2018**, *171*, 131–141. [CrossRef]
9. Seeley, E.H.; Caprioli, R.M. Molecular imaging of proteins in tissues by mass spectrometry. *Proc. Natl. Acad. Sci. USA* **2008**, *105*, 18126–18131. [CrossRef]
10. Buchberger, A.R.; Delaney, K.; Johnson, J.; Jillian, J. Mass Spectrometry Imaging: A Review of Emerging Advancements and Future Insights. *Anal. Chem.* **2017**, *90*, 240–265. [CrossRef]
11. Wenke, J.L.; Rose, K.L.; Spraggins, J.M.; Schey, K.L. MALDI Imaging Mass Specrometry Spatially Maps Age-Related Deami-dation and Truncation of Human Lens Aquaporin-0. *Investig. Ophthalmol. Vis. Sci.* **2015**, *56*, 7398–7405. [CrossRef] [PubMed]
12. Anderson, D.M.; Nye-Wood, M.G.; Rose, K.L.; Donaldson, P.J.; Grey, A.C.; Schey, K.L. MALDI imaging mass spectrometry of β- and γ-crystallins in the ocular lens. *J. Mass Spectrom.* **2020**, *55*, e4473. [CrossRef] [PubMed]
13. Santhoshkumar, P.; Udupa, P.; Murugesan, R.; Sharma, K.K. Significance of Interactions of Low Molecular Weight Crystallin Fragments in Lens Aging and Cataract Formation. *J. Biol. Chem.* **2008**, *283*, 8477–8485. [CrossRef]
14. Su, S.-P.; McArthur, J.D.; Aquilina, J.A. Localization of low molecular weight crystallin peptides in the aging human lens using a MALDI mass spectrometry imaging approach. *Exp. Eye Res.* **2010**, *91*, 97–103. [CrossRef] [PubMed]
15. Santhoshkumar, P.; Raju, M.; Sharma, K.K. αA-crystallin peptide SDRDKFVIFLDVKHF accumulating in aging lens impairs the function of α-crystallin and induces lens protein aggregation. *PLoS ONE.* **2011**, *6*, e19291. [CrossRef]
16. Giblin, F.J.; Anderson, D.M.; Han, J.; Rose, K.L.; Wang, Z.; Schey, K.L. Acceleration of age-induced proteolysis in the guinea pig lens nucleus by in vivo exposure to hyperbaric oxygen: A mass spectrometry analysis. *Exp. Eye Res.* **2021**, *210*, 108697. [CrossRef]
17. Schey, K.L.; Anderson, D.M.; Rose, K.L. Spatially-Directed Protein Identification from Tissue Sections by Top-Down LC-MS/MS with Electron Transfer Dissociation. *Anal. Chem.* **2013**, *85*, 6767–6774. [CrossRef]
18. Srivastava, O.; Srivastava, K.; Chaves, J.; Gill, A. Post-translationally modified human lens crystallin fragments show aggregation in vitro. *Biochem. Biophys. Rep.* **2017**, *10*, 94–131. [CrossRef]
19. Friedrich, M.G.; Lam, J.; Truscott, R.J. Degradation of an old human protein: Age-dependent cleavage of gammaS-crystallin generates a peptide that binds to cell membranes. *J. Biol. Chem.* **2012**, *287*, 39012–39020. [CrossRef]
20. Quax-Jeuken, Y.; Driessen, H.; Leunissen, J.; Quax, W.; de Jong, W.; Bloemendal, H. beta s-Crystallin: Structure and evolution of a distinct member of the beta gamma-superfamily. *EMBO J.* **1985**, *4*, 2597–2602. [CrossRef]
21. Thomson, J.A.; Augusteyn, R.C. Ontogeny of human lens crystallins. *Exp. Eye Res.* **1985**, *40*, 393–410. [CrossRef] [PubMed]
22. Vendra, V.P.R.; Khan, I.; Chandani, S.; Muniyandi, A.; Balasubramanian, D. Gamma crystallins of the human eye lens. *Biochim. Biophys. Acta (BBA)-Gen. Subj.* **2016**, *1860*, 333–343. [CrossRef] [PubMed]
23. Schey, K.L.; Wang, Z.; Friedrich, M.G.; Garland, D.L.; Truscott, R.J. Spatiotemporal changes in the human lens proteome: Critical insights into long-lived proteins. *Prog. Retin. Eye Res.* **2019**, *76*, 100802. [CrossRef] [PubMed]
24. David, L.L.; Shearer, T.R. Role of proteolysis in lenses: A review. *Lens. Eye Toxic. Res.* **1989**, *6*, 725–747. [PubMed]
25. Gupta, R.; Chen, J.; Srivastava, O.P. A serine-type protease activity of human lens betaA3-crystallin is responsible for its auto-degradation. *Mol. Vis.* **2010**, *16*, 2242–2252. [PubMed]
26. Voorter, C.E.; de Haard-Hoekman, W.A.; Oetelaar, P.J.V.D.; Bloemendal, H.; De Jong, W.W. Spontaneous peptide bond cleavage in aging alpha-crystallin through a succinimide intermediate. *J. Biol. Chem.* **1988**, *263*, 19020–19023. [CrossRef]
27. Friedrich, M.G.; Wang, Z.; Schey, K.L.; Truscott, R.J.W. Spontaneous Cleavage at Glu and Gln Residues in Long-Lived Proteins. *ACS Chem. Biol.* **2021**, *16*, 2244–2254. [CrossRef]
28. Ball, L.E.; Garland, D.L.; Crouch, R.K.; Schey, K.L. Post-translational Modifications of Aquaporin 0 (AQP0) in the Normal Human Lens: Spatial and Temporal Occurrence. *Biochemistry* **2004**, *43*, 9856–9865. [CrossRef]
29. Geiger, T.; Clarke, S. Deamidation, isomerization, and racemization at asparaginyl and aspartyl residues in peptides. Succinimide-linked reactions that contribute to protein degradation. *J. Biol. Chem.* **1987**, *262*, 785–794.

30. Clarke, N.D. A proposed mechanism for the self-splicing of proteins. *Proc. Natl. Acad. Sci. USA* **1994**, *91*, 11084–11088. [CrossRef]
31. Hains, P.G.; Truscott, R.J.W. Post-Translational Modifications in the Nuclear Region of Young, Aged, and Cataract Human Lenses. *J. Proteome Res.* **2007**, *6*, 3935–3943. [CrossRef] [PubMed]

cells

MDPI

Review

Autophagy Requirements for Eye Lens Differentiation and Transparency

Lisa Brennan [1], M. Joseph Costello [2], J. Fielding Hejtmancik [3], A. Sue Menko [4,5], S. Amer Riazuddin [6], Alan Shiels [7] and Marc Kantorow [1,*]

1 Department of Biomedical Science, Schmidt College of Medicine, Florida Atlantic University, Boca Raton, FL 33460, USA
2 Department of Cell Biology and Physiology, University of North Carolina, Chapel Hill, NC 27599, USA
3 Ophthalmic Genetics and Visual Function Branch, National Eye Institute, National Institutes of Health, Bethesda, MD 20892, USA
4 Department of Pathology, Anatomy and Cell Biology, Sidney Kimmel Medical College, Thomas Jefferson University, Philadelphia, PA 19107, USA
5 Department of Ophthalmology, Sidney Kimmel Medical College, Thomas Jefferson University, Philadelphia, PA 19107, USA
6 The Wilmer Eye Institute, Johns Hopkins University School of Medicine, Baltimore, MD 21287, USA
7 Department of Ophthalmology and Visual Sciences, Washington University School of Medicine, St. Louis, MO 63110, USA
* Correspondence: mkantoro@health.fau.edu

Abstract: Recent evidence points to autophagy as an essential cellular requirement for achieving the mature structure, homeostasis, and transparency of the lens. Collective evidence from multiple laboratories using chick, mouse, primate, and human model systems provides evidence that classic autophagy structures, ranging from double-membrane autophagosomes to single-membrane autolysosomes, are found throughout the lens in both undifferentiated lens epithelial cells and maturing lens fiber cells. Recently, key autophagy signaling pathways have been identified to initiate critical steps in the lens differentiation program, including the elimination of organelles to form the core lens organelle-free zone. Other recent studies using ex vivo lens culture demonstrate that the low oxygen environment of the lens drives HIF1a-induced autophagy via upregulation of essential mitophagy components to direct the specific elimination of the mitochondria, endoplasmic reticulum, and Golgi apparatus during lens fiber cell differentiation. Pioneering studies on the structural requirements for the elimination of nuclei during lens differentiation reveal the presence of an entirely novel structure associated with degrading lens nuclei termed the nuclear excisosome. Considerable evidence also indicates that autophagy is a requirement for lens homeostasis, differentiation, and transparency, since the mutation of key autophagy proteins results in human cataract formation.

Keywords: autophagy; lens; differentiation; cataract

1. Introduction

The lens is a unique encapsulated tissue comprised of an anterior layer of cuboidal epithelial cells overlying a core of elongated and transparent fiber cells [1–3]. The precise coordination of multiple signaling, transcriptional, and translational pathways is essential for the differentiation of immature lens epithelial cells into elongated, organelle-free, and transparent lens fiber cells. The differentiation of lens epithelial cells into lens fiber cells is continuous throughout life. Consistent with this, disruption of the lens differentiation program during development or later in life results in the formation of cataract, which, despite advances in cataract surgery, remains a leading cause of visual disability worldwide [4,5].

The lens differentiation program is initiated in epithelial cells located at the lens equator (Figure 1). Upon activation by FGF [6–8], IGF [9,10], and possibly other inductive signals, these cells exit the cell cycle and detach from the capsule in the lens transition

zone [2,11] (Figure 1). The resulting nascent lens fiber cells subsequently initiate a maturation program characterized by cellular elongation [2], loss of organelles to form the lens organelle-free zone (OFZ) [1,12], and the abundant expression of crystallin proteins that reach concentrations as high as 450 mg/mL [13]. Key to the process of lens differentiation are a wide range of cellular remodeling events, including the elimination of organelles during OFZ formation. Although a number of proteolytic and other enzymatic processes have been demonstrated to be essential for lens fiber cell formation and the formation of the lens OFZ, the full range of pathways and components required for lens fiber cell remodeling and maturation remain to be identified. Recent data have provided evidence that autophagy is a critical requirement for lens fiber cell remodeling, organelle degradation, and transparency. This review summarizes our current knowledge of the role of autophagy in lens fiber cell differentiation, organelle elimination, and transparency.

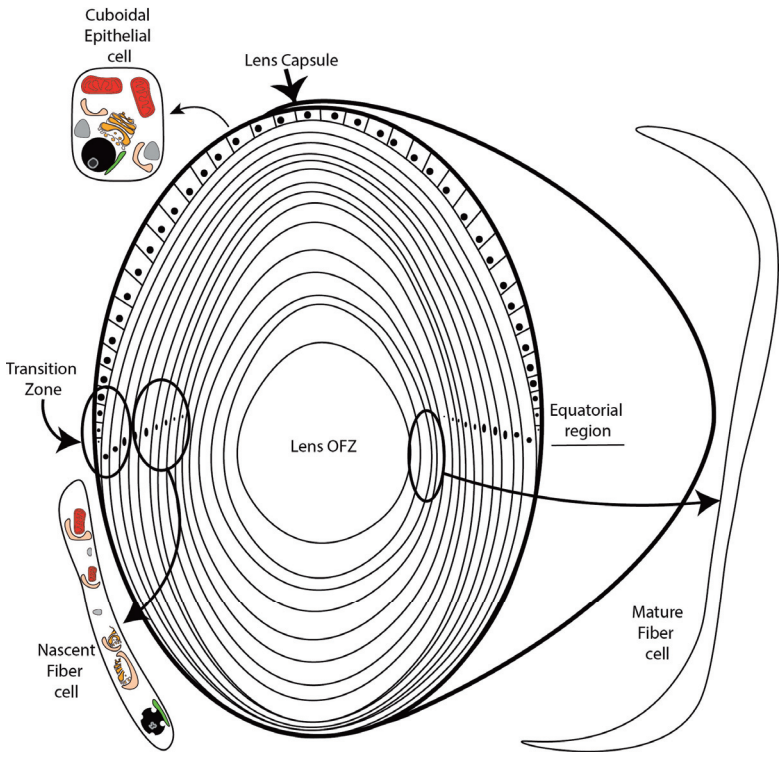

Figure 1. Anterior to posterior (sagittal) schematic of the eye lens. The lens is bound by a collagenous capsule. An anterior layer of largely quiescent cuboidal epithelial cells overlies a core of elongated protein-packed organelle-free fiber cells. Epithelial cells at the lens equator/transition zone exit the cell cycle, detach from the capsule, turn, and begin to elongate. This process of continuous differentiation adds layer after concentric layer onto the lens. Nascent fiber cells begin to elongate and show the first signs of autophagy-driven organelle degradation. Fully mature fiber cells, which are devoid of organelles, comprise the core of the lens in the region known as the organelle-free zone (OFZ).

2. Autophagy Overview

Autophagy is a cellular process that degrades and/or recycles damaged or excess cellular components. This process is particularly important for the development and homeostasis of tissues requiring high turnover or removal of cellular components, such as lens cells that undergo remodeling and organelle degradation during their differentiation program. Autophagy can be divided into three main types: macroautophagy, microautophagy, and chaperone-mediated autophagy [14,15]. During macroautophagy (hereafter termed autophagy), the target component is sequestered into a newly formed double-membrane structure called an isolation membrane or phagophore, which matures into

an autophagosome. Autophagosomes ultimately fuse with lysosomes to form autolysosomes, wherein cellular components are degraded by resident acid hydrolases, creating molecular building blocks for recycling [16]. By contrast, in microautophagy, cytosolic material is directly engulfed by lysosomes [17]. Finally, in chaperone-mediated autophagy, specific proteins containing key recognition motifs are unfolded by cytosolic chaperones and translocated across the lysosomal membrane by the lysosomal-associated membrane protein 2A (LAMP2A) [18]. Autophagy can be further divided into the selective and non-selective forms. In the non-selective form, cellular components are randomly engulfed by autophagosomes, usually in response to stress or starvation conditions [19]. In selective forms of autophagy, specific organelles or molecules are targeted by autophagy receptors. The selective forms of autophagy include mitophagy (mitochondria), ER-phagy (endoplasmic reticulum), aggrephagy (protein aggregates), ribophagy (ribosomes), and xenophagy (foreign pathogens) [20].

While autophagy occurs at a basal level in all cells, it can be upregulated in response to cellular stress, such as nutrient or energy deprivation [21,22]. However, autophagy can also be upregulated if cells are required to carry out large-scale remodeling during development or differentiation, such as that required for lens fiber cell formation [23]. Impaired or deficient autophagy has been linked with multiple diseases, including cancer and neurodegenerative disease as well as metabolic disease and aging [24]. Broadly, the classic autophagy pathway can be divided into the following steps: initiation and nucleation of the phagophore, elongation and closure of the autophagosome, fusion with lysosomes, and finally, degradation of the cargo. These steps will be described briefly here, although they are discussed in detail in a number of excellent reviews [14,15,22,25–28]. The induction of autophagy is controlled by the activity of the mechanistic target of rapamycin (MTOR). Active mTOR inhibits the phosphorylation of UNC51-like kinase (ULK1) in the initiation complex consisting of ULK1 and its substrates ATG13 and RB1CC1/FIP200. When autophagy is induced, the ULK1 serine/threonine kinase is activated via autophosphorylation, binding ATG13, which bridges it to the scaffolding protein RB1CC1/FIP200, recruiting this induction complex to the forming phagophore [25]. The source of the membrane for the forming phagophore has been proposed to be plasma membrane or mitochondria, depending on the cell type and/or stress studied. However, several studies suggest that structures called omegasomes, which arise from the ER through the transfer of lipid membranes by WD-repeat proteins interacting with phosphoinositides (WIPIs) and ATG2, are the main source of phagophore in mammals [29,30]. Induction is followed by nucleation, which involves the recruitment of the ATG14-containing class III phosphatidylinositol 3-kinase (PtdIns3K) complex. This complex consists of PIK3C3/VPS34, PIK3R4/p150, and BECN1 (Vps30). Regulation of this complex occurs through proteins that interact with Beclin1 (BECN1), such as BCL2, which binds BECN1 and prevents its interaction with PIK3C3 or positive regulators such as AMBRA1 [25–27]. The elongation and closure of the phagophore involve conjugation systems consisting of ubiquitin-like proteins, namely the ATG12–ATG5-ATG16L1 complex and the well-studied ATG8/LC3 proteins. The ATG8 family proteins are divided into two subgroups: the LC3 (light chain 3) subfamily, which includes LC3A, LC3B, LC3B2, and LC3C, and the g-aminobutyric acid receptor-associated protein (GABARAP) subfamily, which includes GABARAP, GABARAPL1, and GABARAPL2 [25,26,31,32]. LC3B is commonly studied, and it is accepted as a marker of autophagosome formation in the classic autophagy pathway [33]. The ATG12–ATG5-ATG16L1 complex associates with the phagophore and dissociates once the autophagosome has been formed. LC3 is cleaved at its c-terminus by ATG4, yielding a cytosolic form. LC3-I. LC3-I is then conjugated with phosphatidylethanolamine (PE), producing LC3-II, which is embedded into the autophagosomal membrane [25,26,28]. Lipids are supplied to the expanding autophagosomal membrane via a combination of ATG2 and ATG9, two intermembrane and interleaflet lipid transporters [34–37]. Recent structural data show that ATG2 is a rod-like molecule with a hydrophobic tunnel that transports lipids, while ATG9 is a scramblase that redistributes those lipids in the autophagosome membrane [34]. In addition to ubiquitination systems,

PI3P-binding ATG proteins (ATG18 and ATG21) and members of the WD-repeat protein that interact with the phosphoinositides (WIPI) family are required for the closure of the autophagosome [38]. Completely mature autophagosomes fuse with lysosomes in a process that involves the tether and SNARE proteins [26,28]. Here, the cargo is degraded and its components are recycled. In 2009, an ATG5/ATG7-independent autophagy pathway was discovered by Nishidia et al. [39], demonstrating an alternative to the classic autophagy pathway described above. In the alternative pathway, autophagosomes are generated in a Rab9-dependent manner through the fusion of isolation membranes with vesicles derived from the trans-Golgi and late endosomes [39]. Studies in the lens, as detailed in this review, have identified the involvement of selective and non-selective autophagy in both lens homeostasis and key elements of the differentiation process. These studies suggest that both the classic and alternative autophagy pathways are operating contemporaneously in the lens, indicating a redundancy between the pathways and highlighting the critical need for autophagy in lens homeostasis and differentiation.

3. Signaling Regulators Control the Induction of Autophagy to Form the OFZ

The process of eliminating lens organelles begins with the differentiating fiber cells in the center of the lens and expands outwards toward the lens equator [40], with a distinct border maintained between the developing lens organelle-free zone (OFZ) and the surrounding nascent fiber cells that still retain their organelles (Figure 1). Studies of the developing chick embryo lens provided some of the earliest evidence that the removal of lens organelles to form the OFZ involved an autophagic mechanism [41,42]. This was followed by studies showing that the removal of fiber cell organelles, including their mitochondria, ER, and Golgi, is achieved through the induction of autophagy-promoting signaling pathways [41,43,44]. It was also found that the signaling events that induce the removal of the lens fiber cell nuclei involve autophagic pathways. Nuclear elimination is a more complex process than the removal of non-nuclear organelles. It requires the regulation of multiple signaling pathways [43], ensuring that the end stage of the OFZ formation is accomplished without inducing fiber cell death [44]. In the mature lens, after the organelles are eliminated, homeostasis is maintained by factors supplied through cell–cell junctions [45,46] and the lens microcirculation system [47,48].

As the lens develops, suppression of the signaling effectors in the center of the lens that induce autophagy occurs coordinately with the removal of the lens organelles [41,43]. These include both the MAPK JNK [41] and PI3K [43] pathways and their downstream effectors Jun [41], Akt [43], mTOR, raptor, and p70S6K [41,43]. Their suppression induces molecules essential to the autophagy process, such as LC3B-II and BECN1, which localize to the autophagic vesicles in the central region of the lens where the lens organelles are removed [41,43]. BECN1 functions to promote the assembly of the phagophore membrane and participates in the initiating events in the autophagy pathway, while LCB3-II has key functions in the expansion of phagophore membranes, directing cargo to the phagophore, and the fusion of phagophores to form autophagosomes [33]. Importantly, both of these autophagy proteins localize specifically to the autophagic vesicles within which the lens organelles are being eliminated [41]. Together with electron microscopy analyses, these immunolocalization studies provided strong evidence that the non-nuclear organelles of the lens are removed in the autophagic vesicles to form the OFZ, as induced by the autophagy-signaling pathways [41]. In contrast to the requirement for the inhibition of Class I PI3K signaling for the induction of lens organelle elimination, it was reported that the Class III PI3K Pik3c3 does not have a role in mediating lens organelle loss [49].

The best studied autophagy signaling pathway is the "self-eating" process associated with the cellular response to stress, such as occurs in nutrient starvation and hypoxia and involves the suppression of the PI3K/Akt/mTOR/p70S6K signaling axis [50]. This pathway leads to the formation of autophagosomes that digest organelles to supply cells in a stress environment with the nutrients required to maintain/restore their homeostasis. It is the Class 1 family PI3Ks that are directly involved in the pathways that regulate autophagy [51].

They consist of both catalytic (p110α-δ) and regulatory (p85, p101) subunits, with Akt and Rac serving as their major downstream effectors [52]. The earliest evidence that the suppression of PI3K signaling is linked to lens OFZ formation is found in studies with a primary differentiating lens epithelial cell culture system that forms organoid structures called lentoids [53]. While inhibiting PI3K signaling has no impact on primary undifferentiated lens epithelial cells, blocking PI3K signaling after lentoid formation induces the elimination of the nuclei in these organoid structures, the hallmark of lens OFZ formation [54]. Years later, suppression of the canonical autophagy-inducing PI3K/Akt/p70S6K signaling axis was definitively linked to OFZ formation in the developing lens [43]. Both this PI3K/Akt signaling axis and the MAP kinase JNK signaling pathway were found to play essential roles in regulating the temporal removal of the mitochondria, ER, and Golgi from the central lens fiber cells to form the OFZ during development. These signaling pathways function through their impact on the mTORC1 complex proteins and the activation state (phosphorylation) of p70S6K [41,43]. The role of JNK in regulating the phosphorylation state of the mTORC1 complex proteins mTOR and raptor to induce autophagy was first discovered in these studies of lens development [41].

Functional studies performed ex vivo with isolated lenses placed in organ culture prior to OFZ formation provided direct evidence that the inhibition of both the JNK- and PI3K-dependent signaling pathways provides the mechanism for the induction of autophagy to removal lens organelles [41,43]. The inhibition of JNK signaling blocked the phosphorylation of the mTORC1 complex proteins mTOR and raptor and their downstream target p70S6K in lens fiber cells, initiating autophagy through the induction of the autophagy molecules ULK1 and Beclin and the conversion of LC3B-I into LC3B-II [41]. This resulted in the premature removal of the mitochondria, ER, and Golgi in the LCB3+ autophagic vesicles from the fiber cells in the center of the lens and the condensation and elimination of the central fiber cell nuclei [41]. Similar results were achieved by exposing organ cultured lenses to rapamycin [41], a drug that blocks the activation of mTOR to induce autophagy [55].

Inhibiting PI3K activity in lens organ cultures blocks the activation of Akt and the PI3K/Akt/mTORC1 complex effector p70S6K in lens fiber cells, signaling the conversion of LC3B-I into LC3B-II [43], which are all elements of the classical autophagy-induction pathway [33]. The exposure of lenses to pan-PI3K inhibitors that suppress the activation of all PI3K p100 catalytic subunits and their downstream effectors induces autophagy and the premature elimination of organelles, including the nuclei, from central lens fiber cells [43]. However, while the specific inhibition of the PI3K downstream effector Akt induces autophagy and the autophagy-dependent elimination of the lens mitochondria and ER, alone it is insufficient for the removal of lens nuclei [43]. These findings revealed that the suppression of another major PI3K target, such as Rac, is also required for nuclear elimination during the formation of the OFZ.

As lens fiber cells are the only cell type in which the nuclei are removed and long-term survival maintained, it is not surprising that the removal of their nuclei is a complex, multistep, and highly regulated process that protects them as their nuclear material is eliminated. It is expected that autophagy is required during lens nuclear elimination for the removal of nuclear breakdown products. Autophagic mechanisms involve the fusion of autophagic vesicles with lysosomes that contain the acid hydrolases that digest proteins, lipids, carbohydrates, and nucleic acids [56]. Similar to autophagosomes, LAMP+ lysosomes form in the lens fiber cells in a differentiation-state-specific manner [43]. Consistent with their function in the premature elimination of lens organelles, the LAMP protein and the formation of LAMP+ lysosomal vesicles are induced by the exposure of lenses to PI3K pathway inhibitors [43]. Another related finding is the link between phospholipase A/acyltransferases (PLAATs) [57] and the elimination of lens organelles [58]. The translocation of PLATT enzymes to the phospholipid membranes of mitochondria causes the deformation of the mitochondrial surface and the subsequent loss of mitochondrial membrane potential [59]. While depolarization of the mitochondria is not induced when PI3K

activity is suppressed [43], the mitochondria become depolarized during lens development just prior to the time that they are delivered to the autophagosomes for elimination [60]. These findings suggest that PLAATs are likely to promote mitochondrial membrane depolarization during lens fiber cell differentiation, which drives the damaged mitochondria to the autophagic vesicles for their elimination.

Phosphoinositide-3-kinase-interacting protein 1 (PIK3IP1) is a membrane-linked p85-like subunit that binds to the p110 catalytic subunits of PI3K, blocking their interaction with the p85 regulatory subunit and preventing activation of the p110 catalytic subunit [61]. RNAseq studies revealed that this novel and little-studied negative regulator of PI3K signaling is highly upregulated in lens fiber cells, where it could function as the endogenous inhibitor of PI3K signaling to induce the autophagy-dependent formation of the OFZ [43]. In the developing lens, PIK3IP1 associates with the p110α, p110β, and p110γ catalytic subunits of PI3K specifically in the lens fiber cells at developmental times when autophagy is induced to remove the lens organelles [43]. This discovery provides the first evidence that PIK3IP1 is an endogenous regulator of PI3K signaling in the developing lens likely responsible for inducing the autophagy-dependent spatiotemporal removal of organelles to form the OFZ.

4. Autophagy Mechanisms in Non-Nuclear Organelle Degradation

A long-unanswered question in lens biology concerns how lens fiber cells eliminate their organelles to form the lens OFZ. Only three cell types remove all of their organelles in the absence of a specific stress and as part of their differentiation process: reticulocytes, keratinocytes, and lens fiber cells. In contrast to lens fiber cells that live as long as the lens itself, reticulocytes mature to become short-lived erythrocytes with a life span of 120 days, while keratinocytes terminally differentiate into corneocytes at the upper layer of the epidermis and are ultimately shed.

The mechanism of mitochondrial removal in reticulocytes has provided clues as to how this might be achieved during lens differentiation. A number of studies demonstrated that the selective autophagy pathway, namely mitophagy, was responsible for mitochondrial elimination in reticulocytes [62–65]. When Costello et al. [42] discovered mitochondria in autophagic vesicles throughout the differentiating fiber cells of the chick lens, this suggested a similar role for mitophagy in the elimination of mitochondria in the lens [42]. Mitophagy is the process whereby damaged or excess mitochondria are removed and their contents recycled for quality and quantity control [19]. Mitophagy is mediated by a number of receptors, some of which are targeted to the outer mitochondrial membrane, such as PARKIN, BNIP3, BNIP3L(Nix), FUNDC1, BCL2L13, FKBP8, and ATG32 [19,66]. Briefly, these receptors target mitochondria so that they are recognized by the forming autophagosomes, and the engulfed mitochondria are subsequently delivered to the lysosomes for degradation. Of particular relevance to the lens is the mitophagy protein BCL2 interacting protein 3-like BNIP3L(Nix), which has previously been shown to be essential for the removal of mitochondria in reticulocytes [62–64,67,68]. BNIP3L contains an Atg8-family protein-interacting region/LC3-interacting region (AIM/LIR) domain in its cytosolic n-terminus that binds Atg8/LC3 proteins to target the mitochondria to the autophagy machinery [68]. It forms a stable homodimer via its C-terminal transmembrane domain that inserts into the mitochondrial outer mitochondrial membrane. Recent studies have shown that dimerization is regulated by phosphorylation, and it is critical for the interaction with the Atg8 proteins and the recruitment of autophagy vesicles for mitochondrial elimination [69].

Examination of the spatial distribution of the BNIP3L transcript and protein in both chick [70] and mouse lenses [71] showed that both were higher in lens fiber cells in which mitochondrial elimination was taking place. The lenses of a global BNIP3L knockout mouse retained mitochondria at the center of the P1 and P14 lenses, demonstrating a requirement for BNIP3L in their elimination [71]. Interestingly, examination of BNIP3L knockout mouse lenses for levels of both the endoplasmic reticulum and Golgi apparatus

showed that these two organelles were also retained in the center of the lens [71]. Although previous work had localized BNIP3L to the ER in non-lens cells [72], a role in ER quality or quantity control had not been established in these studies, and no other study had localized BNIP3L to the Golgi apparatus, demonstrating a novel role for BNIP3L. The findings in the BNIP3L knockout mice suggested that BNIP3L was responsible for the elimination of three non-nuclear organelles to form the OFZ of the lens.

Previous work in a number of cell types demonstrated that the master regulator of the hypoxic response, hypoxia-inducible transcription factor a (HIF1a), regulated hypoxia-induced autophagy by upregulating the expression of BNIP3L [73]. Under normoxic conditions (21% O_2), the HIF1a protein is targeted for degradation by members of the 2-oxoglutarate-dependent dioxygenase superfamily of prolyl hydroxylases (PHD1, PHD2, and PHD3) through the hydroxylation of the proline resides in its oxygen-dependent domain [74,75]. Hydroxylated HIF1a associates with the von Hippel–Lindau tumor suppressor protein that targets HIF1a for rapid proteasomal degradation [74,75]. A further method of regulation involves the hydroxylation of an asparaginyl moiety in the c-terminus domain by factor-inhibiting HIF (FIH). This hydroxylation reduces the HIF1a transcriptional activity by disrupting its association with the important co-factors p300 and CREB-binding protein (CBP) [74–76]. Both PHDs and FIH are oxygen-dependent enzymes; therefore, in reduced oxygen conditions, the HIF1a protein is no longer targeted for degradation. Instead, it translocates to the nucleus, where it dimerizes with constitutively expressed HIF1b (ARNT) and other co-factors to regulate the expression of the genes required for the hypoxic response [74–76].

Consistent with a role for HIF1a in BNIP3L expression in the lens, the lens is one of very few tissues to reside in a hypoxic environment. During development, the fetal vasculature made up of the tunica vasculosa lentis and the anterior pupillary membrane feeds the lens [77]; however, shortly before birth, the vasculature regresses, leaving the lens without a direct oxygen supply [78]. The lens, therefore, relies on the diffusion of oxygen across the cornea and through the aqueous humor. In addition, the high number of active mitochondria in the anterior epithelial layer consume much of the surface oxygen [79–82]. Measurements of oxygen levels in both human and bovine lenses confirm that the oxygen level at the surface of the lens is around 2% O_2 and that the lens contains an oxygen gradient with an almost 20% drop in oxygen levels from the surface to the core [80,81]. This gradient creates a hypoxic microenvironment in the region of the lens, the transition zone, where organelle elimination is being initiated (Figure 1). Consistent with this, incubation of embryonic chick lenses in hypoxic or low oxygen conditions (1% O_2) accelerated the degradation of non-nuclear organelles relative to lenses in normoxic conditions (21% O_2) [83]. In addition, exposure of embryonic chick lenses to an antagonist of the PHD cofactor α-ketoglutarate, dimethyloxalylglycine (DMOG), under normoxic conditions stabilized the HIF1a protein, increased the BNIP3L transcript and protein levels, and enhanced the degradation of non-nuclear organelles [83]. By contrast, inhibition of HIF1a transcriptional activity under hypoxic conditions (1% O_2) in the same chick lens model using the chemical inhibitor Chetomin decreased the transcript and protein levels of BNIP3L and reduced the elimination of non-nuclear organelles relative to degradation in lenses incubated in hypoxia alone [83]. ChIP-qPCR confirmed that HIF1a binds to the 5′ untranslated region of the BNIP3L gene following the treatment of embryonic chick lenses with the HIF1a activator DMOG [83]. Collectively, the evidence suggests that the low oxygen environment of the lens promotes HIF1a-induced autophagy via the induction of BNIP3L expression. Combined with the presence of large numbers of autophagosomes containing remnants of mitochondria, the most easily identifiable organelle during degradation, these data suggest that hypoxia-induced autophagy is key to organelle elimination in the lens forming the lens OFZ and to continued organelle degradation during lens differentiation.

5. Lens Autophagy Structures

Autophagy is a conserved catabolic process in which a double-membrane phagophore encloses cellular material that is destined for degradation via fusion with a lysosome containing hydrolytic enzymes. In the original description of autophagy in liver by Dr. C. de Duve in 1965 [84,85], autophagic vesicles with heterogenous contents were observed with their double-membrane covering using the thin section electron microscopy technique, which has become the gold standard for identifying autophagic vesicles and contributed to the characterization of numerous other cellular organelles and processes, leading to the Nobel Prize for de Duve, Claude, and Palade in 1974. The primary contribution to this 1974 Nobel Prize by Dr. de Duve was the discovery of the lysosome and peroxisome, and about four decades later in 2016, Dr. Y. Ohsumi was awarded the Nobel Prize for the molecular description of the autophagic process. The discoveries of the 1974 laureates formed the basis for modern cell biology, and their approaches highlighting the value of morphology are still important today, allowing us to describe a new organelle, the nuclear excisosome, in chick embryo lenses that degrades the nuclear envelope toward forming the organelle-free zone (OFZ) [86]. More recently, we described the nuclear excisosome in the prosimian Galago (bush baby) monkey lens, where the cellular structures are distinct from those in the chick embryo lens but carry out essentially the same function [87]. Presented here are several examples of autophagic vesicles in lenses from different species and recent observations on autophagy and the nuclear excisosome in the Galago (bush baby) monkey model.

Discounting some uncertainty in the literature about the presence of autophagy in the lens, we have been able to identify numerous autophagic vesicles in the epithelium and developing fiber cells from several species, initially in adult human lenses and chick embryo lenses [42]. In this first morphological study of lens autophagy, we emphasized the heterogeneous contents of the autophagic vesicles, some of which was consistent with the mitochondria or multilamellar lipid. Such lipid arrays with 5 nm spacing (indicating a minimal protein content) were proposed to be conserved and recycled, and their appearance is a common feature of the autophagy processes in the lenses examined [42]. The vesicle coverings were mainly single membranes, indicating that the degradation had proceeded to the autolysosome stage, although there was no doubt about their identification as autophagic vesicles. Around the same time, a study of modified mouse lenses was published that clearly showed the double-membrane profile of the autophagic vesicles [88], which was subsequently confirmed in chick embryo lenses a year later [41]. To emphasize the typical appearance of the autophagic vesicles in the vertebrate lens, the results concerning macaque monkey lenses illustrate the appearance and distribution of the autophagic vesicles (Figure 2). Note the micron-sized autophagic vesicles at low magnification in the epithelium and young fiber cells. Nearly circular and low density due to degradation, they are numerous up to the OFZ, supporting the proposal that they are involved in OFZ formation. At high magnification in the insets, the heterogenous contents and double-membrane profiles are pronounced in these examples of autophagosomes. Similar preservations of autophagosomes in a variety of species are presented (Figure 3) and show features of the original objects being degraded. Although whole mitochondria are easily recognizable, fragments still maintain the unique features of the envelope or cristae (Figure 3A). The high density and circular profile shown in Figure 3B can indicate the source being condensed protein, as found in multilamellar bodies [89]. A 25 nm diameter tubular object, consistent with a microtubule commonly found free in the cytoplasm, when occasionally captured in segments in an autophagic vesicle (Figure 3C) is representative of the degradative and recycling processes.

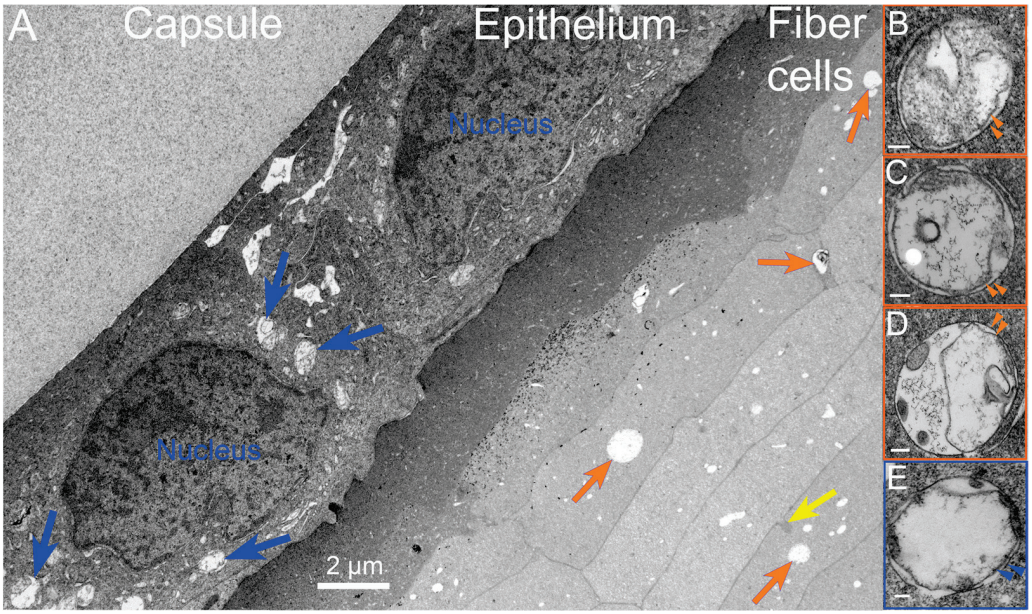

Figure 2. Low-magnification transmission electron microscopy (TEM) overview of the outer cortex of an adult macaque monkey lens. (**A**) This image, taken near the equatorial plane, displays the capsule, which is nearly homogeneous (about 10 µm thick), and the epithelium (about 7 µm thick), which has a very smooth interface with the capsule. The epithelium contains two prominent nuclei and numerous organelles, including autophagic vesicles (blue arrows) showing the classic double-membrane profile and heterogeneous contents. A narrow band of elongating fiber cells is generally more darkly stained, with the cells having irregular cross-sections that blend into classical fiber cells, which form radial cell columns and have flattened hexagonal shapes (about 2 × 10 µm). Several autophagic vesicles are labeled (orange arrows), and one ball-and-socket interdigitation (yellow arrow) typical of this region is about 0.5 µm long. (**B**–**E**) Insets are examples of autophagosomes from different regions in the same sample to illustrate the double-membrane structures (double arrowheads) at high magnification. The scale bars in the insets are 100 nm. (**B**) Autophagic vesicle shows degradation of cytoplasmic material in the space between two large irregular vesicles. A small segment of ER appears just outside the autophagic vesicle (upper left). (**C**) Extensive protein degradation in the center leaves a typical reticulated network. A vesicular structure with three thin lipid bilayers is darkly stained and next to a low-density vesicle-like circular profile, probably representing material lost during processing, which illustrates that the uniform background staining in all the examples is preserved fluid after degradation by hydrolytic enzymes. A segment of ER is preserved (upper right). (**D**) A variety of vesicular structures are being degraded along with protein, leaving reticulated patterns. A segment of ER is preserved (lower right). (**E**) Degradation has proceeded in this epithelial autophagic vesicle interior, leaving a few fragments extending into the preserved fluid.

The epithelium near the equator of Galago (bush baby) monkey lenses is specialized for the production of nuclear excisosomes and for the extensive autophagy supporting the synthetic activity. The large autophagic vesicles are clearly of two distinct variations (Figure 4). The autophagic vesicle close to a nucleus (on the right) is classic in that it appears to originate from the outer nuclear envelope, which is also the beginning of the ER. It contains a variety of degrading proteins, membrane vesicles, and multilamellar lipid arrays. The outer membrane is modified from the initial phagophore double membrane. The paired closely associated membranes appear to partially fuse into tubules, which, when cut longitudinally, appear as double membranes (Figure 4, long red arrows) and, when cut cross-sectionally, appear as small circular profiles (Figure 4, red arrowheads), giving the overall appearance of a scalloped perimeter. This arrangement may provide a porous meshwork covering for the autophagic vesicle, allowing hydrolytic enzymes to enter and degraded products to exit. An autophagic vesicle of nearly the same size (Figure 4, left)

shows the expected degradation of circular vesicles and protein but is formed by the membranes of adjacent epithelial cells by enlarging the extracellular space between the cells and sealing the ends (Figure 3, white arrows). The material within the extracellular space is most likely generated locally based on the lack of material entering from the capsule into the outer layers of the epithelium and the large size of the extracellular space compartments. The area in sections devoted to these and classic autophagy vesicles is nearly equal to the area of the nucleus, indicating enhanced autophagic activity. The morphological data, therefore, support the hypothesis that the material in the cytoplasm enters the extracellular space via exocytosis along with hydrolytic enzymes to degrade the contents.

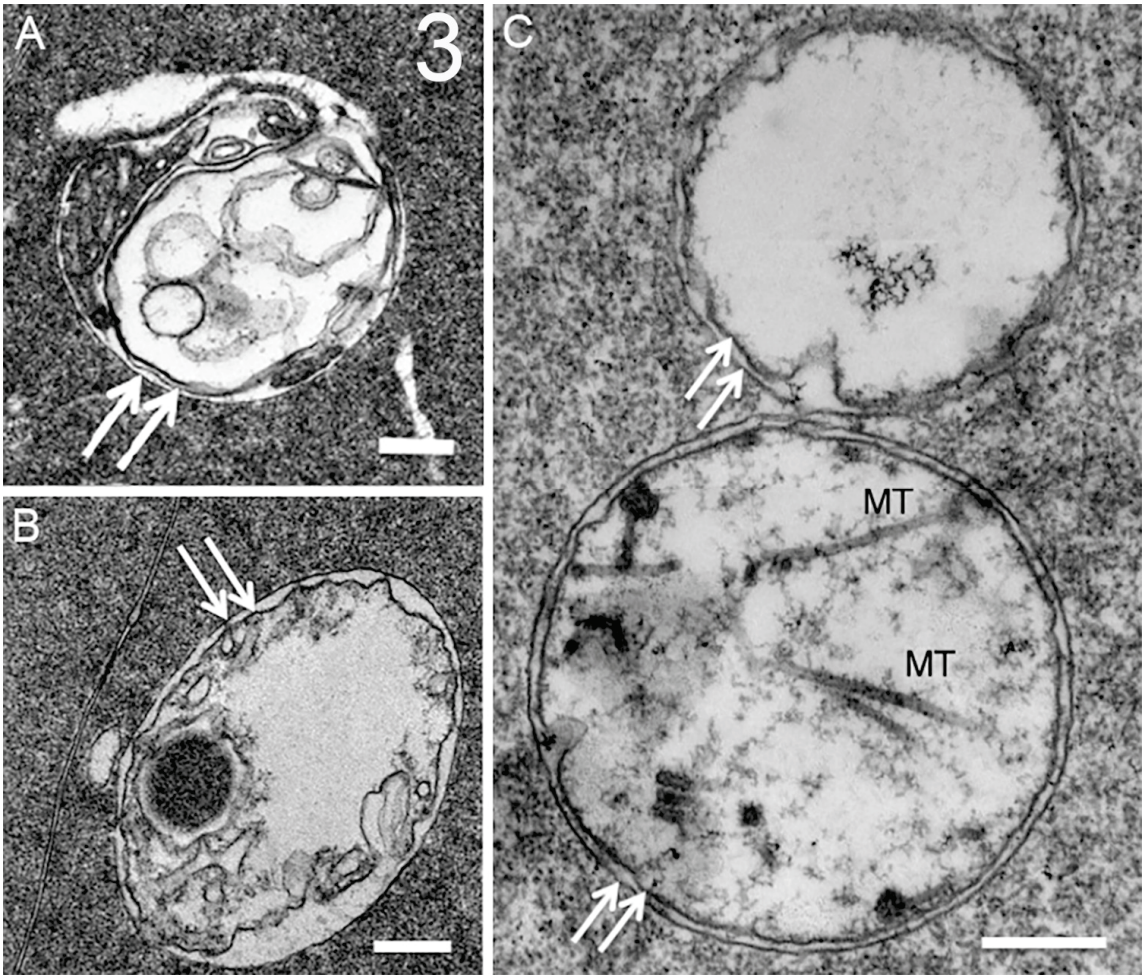

Figure 3. Similar double-membrane autophagosomes are found in lens fiber cells from a variety of diverse species. (**A**) Heterogeneous contents include an elongated structure (upper left), which has internal membranes that are probably partially degraded mitochondrial cristae. Adult human donor lens. (**B**) Heterogeneous contents include a dark, circular, and uniformly stained object that is similar to the core of MLBs (multilamellar bodies). Chick embryo D15 lens. (**C**) Lower double-membrane vesicle displays several structures that are most likely microtubule segments (MT, linear 25 nm diameter tubules), which could only occur within an autophagic vesicle. Adult rabbit lens. Scale bars are 250 nm. Double-membrane cover is indicated by arrows in all four examples.

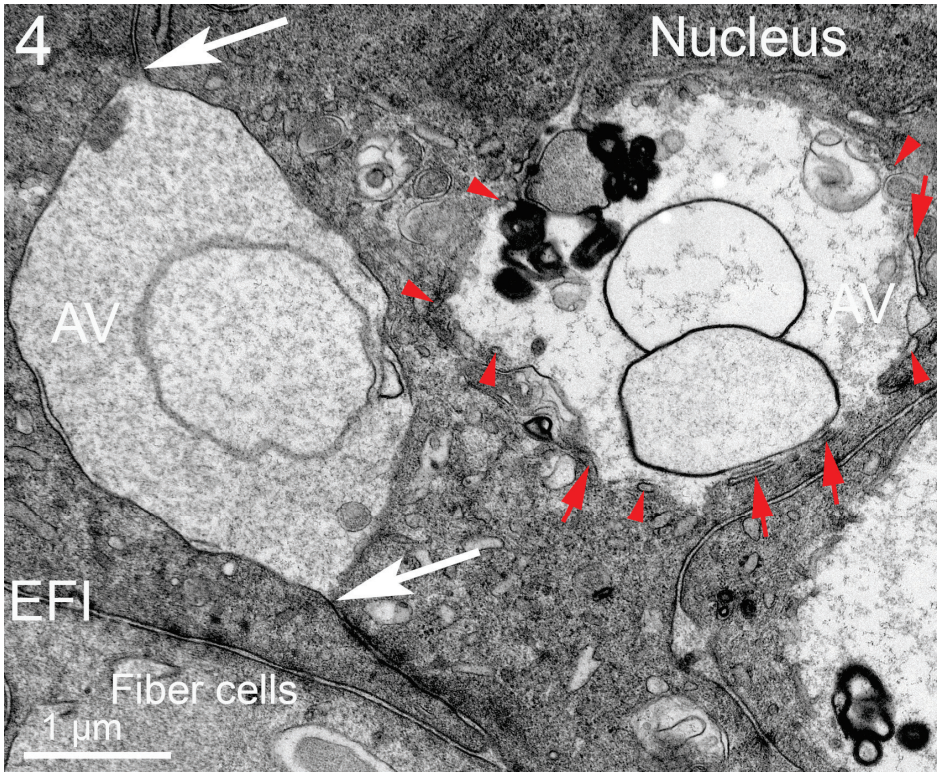

Figure 4. Extensive autophagic activity in the equatorial epithelium of prosimian Galago (bush baby) monkey lenses. A large autophagosome (AV) is observed in contact with a nucleus (upper right), which probably signals the supply of new ER membrane for expansion. The double-membrane surface is modified to present interconnected tubules with two membranes visible (red arrows) and cross-sections that are round or oval (red arrowheads). These membrane processes form an open meshwork that surrounds the autophagic vesicle, allowing hydrolytic enzymes to enter and degradation products to exit, including here from the degradation of proteins, large vesicles, and pure lipid aggregates (densely stained clusters with 5 nm spacing visible at higher magnification). This is an example of a classic autophagic vesicle. By contrast, the large autophagic vesicle on the left (AV) has a different structure and origin. Note that the large internal space is surrounded by a single membrane that pinches off at the borders (white arrows), suggesting that the space is equivalent to the extracellular space between the adjacent cells and that the membrane covering is derived from plasma membranes, not the ER or another internal organelle. In this initial form, the extracellular space structure should more appropriately be called a vacuole rather than a vesicle. The heterogeneous contents are in the process of degradation but, in this case, most likely arrive through cellular secretion, as do the hydrolytic enzymes causing the degradation. This is an example of a new type of autophagic vesicle that significantly increases autophagy in this epithelium near the lens equator. The unique origin can be confirmed by following the double membrane from the lower sealed point (lower white arrow) to the interface with the fiber cells at the epithelial–fiber cell interface (EFI), where the punctate adherens junctions along the EFI extend into the epithelium.

Recent literature suggests that the membranes contributing to autophagic vesicles may be diverse, including organelles other than the ER as well as the plasma membrane [90]. This is the first example of the space between the epithelial cells being converted into an autophagic vesicle in the lens or any tissue. The production of the nuclear excisosome in the Galago (bush baby) lenses is extensive based on the number of bead-on-a-string structures visible in the confocal images (Figure 5A) [87]. The active unit is the unique four-membrane structure mainly contained in the narrow string or rod-like structure to the right of the contact region with the nucleus (Figure 5A, arrow) [87]. The cross-section of the rod gives the four-membrane profile with the dark core (Figure 5B), which has a pronounced mitochondrial tail from the mitochondrion responsible for its formation in

the epithelium. This complex then moves around the fulcrum and enters the cytoplasm of a young fiber cell, where it will eventually migrate to a nucleus to be degraded, such as shown for a different four-membrane complex (Figure 5C). At high magnification, the core is surrounded by a single membrane (membrane 1), and it is adjacent to a pair of cristae membranes (membranes 2 and 3). On the left is an attached mitochondrion (M) that appears to be contributing its cristae and is covered by a membrane (membrane 4) that has fused with the outer nuclear envelope membrane to initiate degradation, as evidenced by the dense cluster of pure lipid multilayers (with 5 nm spacing, inset). The images support the hypothesis that the nuclear excisosome releases enzymes from the modified cristae (membranes 2 and 3) to break down the nuclear envelope membranes and release lipids analogous to the nuclear excisosomes described previously that do not display the attached mitochondria [87]. It is common to observe the four-membrane structure with an attached mitochondrion and rare to see a free mitochondrion in the fiber cell cytoplasm (although many are seen in the epithelium), suggesting that the energy for the autophagic and nuclear excisosome-controlled degradation processes is provided by the attached mitochondria.

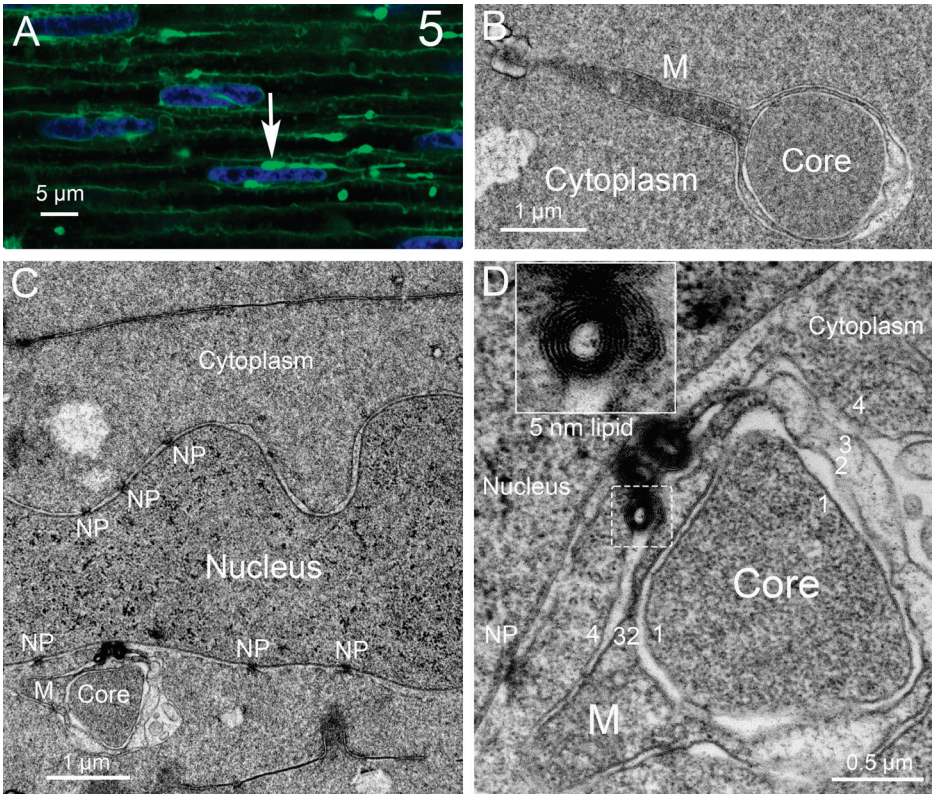

Figure 5. Nuclear excisosomes in a Galago (bush baby) monkey lens. (**A**) Confocal imaging (Zeiss 880 Airyscan super-resolution) shows the nuclei near the OFZ being degraded by nuclear excisosomes (NE). Lipid-rich globular structures (arrow) and thin linear strands are labeled with the membrane dye, DiI. (**B**) TEM of an NE strand cut in a cross-section with a core surrounded by four membranes and a large tail of the mitochondrion, which gave rise to the structure in the equatorial epithelium. The NE is free in the cytoplasm and remains so until it contacts a nucleus. (**C**) Binding of an NE with an attached mitochondrion (M) to a nuclear envelope to initiate degradation. Six nuclear pores are indicated (NP). (**D**) Degradation has begun based on the release of 5 nm multilayer aggregates of lipids (boxed region and inset). The core is surrounded by a single membrane (numbered 1), and outside the core is the pair of cristae membranes (numbered 2, 3) connected to the mitochondrion (M) and most likely releasing the enzymes needed for the degradation of the nuclear envelope. The outer membrane (numbered 4) is visible in several locations, including connecting to the covering of the mitochondrion.

6. Evidence against Autophagy in Organelle Elimination

Despite the numerous studies detailed in Sections 3–5 demonstrating the roles of autophagy and mitophagy in lens organelle degradation to form the OFZ, evidence to the contrary does exist. The recent analysis of the OFZ formation of in vivo lenses from zebrafish and mice report that the PLAAT1 and PLAAT3 enzymes, respectively, cause membrane damage and loss of membranous organelles without involving autophagy [58]. Alterations in the membrane structure documented in electron micrographs included rupture of the outer mitochondrial membrane, leaving exposed edges, and internal swelling and disruption of cristae [58]. These observations were supported by a study using HeLa cells in a culture treated with PLAAT3, which showed similar damage to the mitochondria, endoplasmic reticulum, and other organelles [59]. Such distinctive changes to the membranes were not observed in chick embryo or adult Galago (bush baby) lenses where high-resolution electron micrographs were available from the epithelium through the OFZ [86,87]. For example, Figure 5B in this review displays a nuclear excisosome with an attached mitochondrion that has an intact and smooth membrane around the mitochondria and the four-membrane structure. Similarly, the nuclear excisosome attached to the degrading nucleus in Figure 5C and D shows a smooth uniform membrane around the mitochondria up to the point of contact with the outer nuclear envelope membrane. Previous studies in the embryonic chick lens show mitochondria in various states of degradation in the autolysosomes [42], suggesting membrane rupture is not part of the organelle degradation process, at least not in chick lens. The PLAAT studies support the hypothesis that the specific actions of PLAATs in the lens contribute to lens OFZ formation and that these functions may differ among species. However, studies on PLAATs alone do not rule out the possibility that a multitude of overlapping mechanisms are likely involved in coordinating the degradation of lens organelles.

One of the first studies to examine the role of autophagy in lens OFZ formation utilized an ATG5 knockout mouse [91]. The lenses of the ATG5$^{-/-}$ mouse showed degradation of both the nuclei and endoplasmic reticulum 0.5 days post-birth. The authors also concluded in this study that autophagy is not required for organelle degradation in erythrocytes [91]; however, many studies have since shown that BNIP3L-mediated mitophagy is the key pathway for mitochondrial elimination in reticulocytes [62–64,67,68]. This data suggests that while an ATG5 pathway is not required, autophagy/mitophagy could still play a role in organelle elimination in the lens in the same way as it does for erythrocytes. In a further study, the conditional knockout of ATG5 or PIK3C3 in mouse lenses also failed to prevent organelle degradation for OFZ formation [49]. This confirms the initial data showing that ATG5 is not alone required for OFZ formation. The lens-specific deletion of PIK3C3, which is involved in ATG/7-independent autophagy, also failed to prevent OFZ formation [49]. This raises the question of whether a single mediator such as BNIP3L could recruit autophagosomes to organelles targeted for degradation regardless of the pathway of initiation. As detailed in Section 4, BNIP3L knockout mouse lenses retain organelles [71], while BNIP3L contains an AIM/LIR domain that can recruit LC3B-labelled autophagosomes, although it has not been shown that BNIP3L interacts with the Rab9a-generated autophagosomes formed in the alternative pathway. It is also possible that there is some redundancy between the pathways and that the large-scale degradation of organelles uniquely required for lens OFZ formation may result in both pathways being highly active and called upon at the same time in the region of the lens where the organelles are actively being eliminated. A double knockout of both pathways could provide some evidence of this, although the complex mix of multifunctional proteins that are involved in autophagy means it is difficult to completely ablate the process through genetic modifications. Although non-classical autophagy pathways have not been identified in the lens, the lens indeed expresses all of the components required for alternative autophagy [70]. Further evidence comes from data from ATG5 KO mice, which suggests that an alternative pathway does function in the lens, since organelles are still degraded in the absence of ATG5 [49]. Mutations in the scaffolding protein FYCO1, which functions in the transport of autophagic vesicles along microtubules,

result in autosomal recessive congenital cataracts [92]. The knockout of FYCO1 in mice was shown to result in decreased autophagosomes and retention of organelles in the lens [93]. In contrast, a separate FYCO1 knockout mouse showed normal degradation of the nuclei, mitochondria, and ER [94]. Additional evidence of autophagy involvement in organelle elimination for OFZ formation is provided by gold standard electron micrographs showing mitochondria contained within autolysosomes throughout the region of the lens where organelle degradation takes place [42]. To date, only mitochondria have been identified in autolysosomes, since other organelles have less distinguishable morphology in EM analysis. Curiously, a study by McWilliams et al. using a MitoQ reporter mouse found widespread autophagy but little mitophagy in mouse lenses [95]. This stands in contrast to studies by Basu et al., who showed the co-localization of the autophagosome marker LC3B and mitochondrial marker TOMM20 throughout embryonic chick lenses [41]. Although much of the evidence of autophagy-mediated organelle elimination discussed in Sections 3–5 is derived from ex vivo cultured lenses, EMs of lenses with no chemical manipulation suggest that it is an ongoing process during lens development and differentiation [42]. It is clear that the myriad proteins and pathways involved in autophagy/mitophagy make it a complex process to study; however, robust evidence suggests that it plays a role in organelle elimination.

7. Role of Autophagy in Cataractogenesis

Mutations in a number of autophagy-associated genes have been implicated in inherited cataracts (Figure 6). Early speculation that autophagy was linked to cataract arose when progressive posterior polar/subcapsular cataracts were associated with mutations in *CHMP4B* (charged multivesicular body protein 4b), a core subunit of the endosomal sorting complex required for transport-III (ESCRT-III) machinery, which is important for cellular membrane remodeling and scission processes, including, but not limited to, autophagy [96–98]. Germline knockout of the mouse *Chmp4b* gene (also known as *mSnf7-2*) was found to be embryonically lethal and the loss of *Chmp4b* expression caused autophagosome accumulation in cultured cortical neurons and fly eyes [99,100]. Heterologous overexpression studies suggested that a mutant form of *CHMP4B* (p.D129V), which is associated with human cataract, impaired the endosomal pathway [96] and also inhibited binding to chromatin, thereby implicating CHMP4B in the autophago-lysosomal degradation of micronuclei and other extra-nuclear chromatin [101]. In addition to early-onset forms of autosomal dominant cataract [96,102–104], *CHMP4B* variants have recently been associated with age-related nuclear cataract [105] (https://cat-map.wustl.edu, accessed on 29 November 2022). Whereas germline knock-in of the CHMP4B-(p.D129V) mutant did not elicit cataract in heterozygous mice, homozygous mice were embryonically lethal, and the conditional knockdown of CHMP4B in the lens resulted in severe inhibition of lens growth and fiber cell differentiation, rendering cataract modeling studies challenging [106]. While CHMP4B has been shown to participate in endolysosome membrane repair [107,108], endoplasmic reticulum (ER)-phagy [109], and phagophore closure during mitophagy [110], the exact pathogenic mechanism(s) underlying CHMP4B-related cataract remains unclear. Beyond autophagy defects, impaired cytokinetic abscission, which is associated with reduced CHMP4B accumulation at the intercellular bridges between PI3K-C2a deficient lens epithelial cells, has been shown to result in early lens senescence and cataract formation in fish, mice, and humans [111], suggesting that multiple pathogenic pathways may contribute to CHMP4B-related cataract formation.

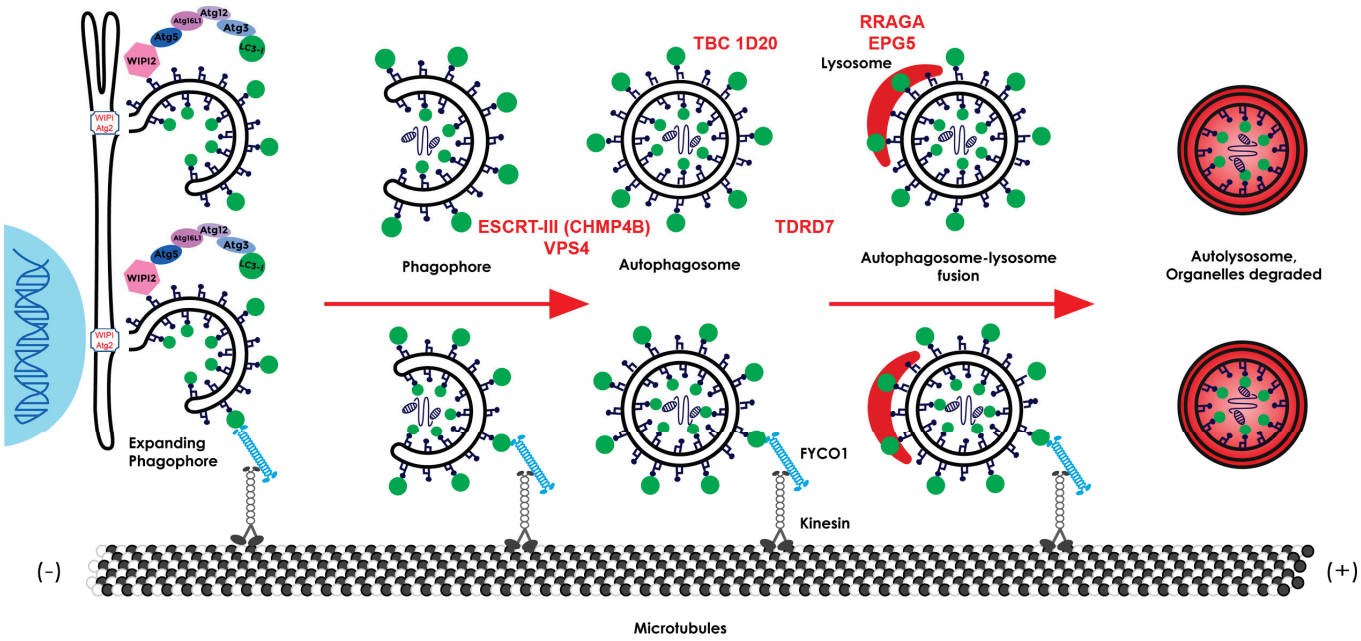

Figure 6. Overview of autophagy, with the components implicated in human cataractogenesis shown in red above the steps in which they are active (shown as red arrows). FYCO1 is shown below, binding to LC3 and PtdIns(3)P, which are active through the formation of the autolysosome.

Autosomal recessive congenital cataracts are also linked to mutations in the scaffolding protein FYCO1, which is important in the transport of autophagic vesicles by microtubules [92]. Since then, *FYCO1* mutations have been shown to be a relatively common cause of cataract, causing about 2.2% of reported independently ascertained families, although this can increase dramatically in some isolated populations, accounting for almost 14% of autosomal recessive cataracts in the Pakistani population [112] and 86% of inherited cataracts in the Yakut population of Eastern Siberia [113]. FYCO1 forms a complex with RAB7 and LC3 that mediates microtubule plus end-directed transport for selective autophagy [114,115]. The binding of FYCO1 and RAB7 is facilitated by NINL (NLP), which accelerates the formation of autophagosomes [116], and the phosphorylation of LC3B by STK4 decreases the FYCO1 binding and transport of autophagosomes [117]. LC3-FYCO1 binding occurs through the LIR sequence on FYCO1, and when the complex occurs, FYCO1 undergoes a conformational change that allows binding to PtdIns(3)P. The LIR in the FYCO1 extends over nine amino acids and is an F-type motif that appears to be specific to LCA [118,119]. FYCO1 also appears to be required for mTORC1 activation in concert with ZFYVE27 (protrudin) by relocating lysosomes containing mTOR to the plasma membrane [120]. The role of FYCO1 in inherited cataracts has been confirmed in mouse models [93,94]. Lenses from FYCO1 knockout mice show extensive vacuoles and large irregularly shaped fiber cells, while lens cells show increased expression of autophagy genes at the mRNA and protein levels but decreased autophagosomes and autophagic flux accompanied by the accumulation of p62 and retention of organelles, including the ER, Golgi apparatus, and mitochondria, in differentiating fiber cells [93]. While previous studies showed FYCO1 to be required for efficient basal autophagy [118], in the lens it appears to have a major impact on the elevated levels of autophagy required to eliminate organelles during lens fiber cell differentiation [93].

Mutations in RRAGA, a GTPase regulator of the mTORC1 pathway, have been associated with autosomal dominant congenital nuclear cataracts [121]. Mutations in RRAGA upregulated mTORC1 phosphorylation and thereby decreased autophagy. Mutations in *TDRD7*, a component of the RNA granules active in RNA processing and expressed in many tissues, have been shown to cause isolated hereditary cataracts as well as cataracts associated with glaucoma or azoospermia [122,123], and this gene has also been associated

with age-related cataract [115,124]. The depletion of TDRD7 in mice and humans causes the failure of autophagosome fusion with lysosomes, resulting in autophagosome accumulation and disruption of autophagic flux [125]. In addition, several multisystem genetic syndromes featuring cataracts have been associated with other autophagy-related genes. Loss of function mutations in the gene responsible for TBC1D20 (TBC1 domain family, member 20) have been shown to cause autosomal recessive Warburg micro syndrome 4, which involves eye, brain, and endocrine abnormalities in humans, and male infertility with nuclear cataracts in blind-sterile mice [126,127]. TBC1D20 is a GTPase-activating protein that functions as a regulator of autophagosome maturation, which is consistent with an important role for autophagy in maintaining lens transparency. Homozygous or compound heterozygous mutations in the gene responsible for EPG5 (ectopic P-granules autophagy protein 5) have been found to underlie Vici syndrome, a rare autosomal recessive disorder involving agenesis of the corpus callosum, cataracts in about 76% of patients, cardiomyopathy, psychomotor delay, hypopigmentation, and combined immunodeficiency [128–130]. EPG5 has been implicated in autolysosome formation, and muscle biopsies and fibroblasts from Vici syndrome patients reveal a severe defect in autophagosomal clearance, resulting in the failed delivery of autophagic cargo to lysosomes. Recently, mutations in the ESCRT-III-associated protein VPS4A (vacuole protein sorting 4a) have been shown to cause an autosomal dominant syndrome characterized by severe neurodevelopmental delay, growth impairment, congenital dyserythropoietic anemia, and cataracts [131,132]. VPS4A is an ATPase that regulates the dynamics of ESCRT-III subunits, including CHMP4B, and expression studies of several human VPS4A mutants were consistent with dominant negative effects resulting in enlarged endosomes.

The deletion of Atg5 in mice has been associated with age-related cataracts and the deletion of Pik3C3 with congenital cataracts in mice [49], although neither deletion alone appeared to affect organelle degradation, and neither molecule has been associated with cataracts in humans. Unexpectedly, the ablation of Gja8b in zebrafish was found to decrease macroautophagy and cause cataracts, which could be relieved by the autophagy stimulator rapamycin [133]. Finally, autophagy-independent mechanisms for lens organelle degradation involving DNASE2B and the phospholipases in the phospholipase A/acyltransferase (PLAAT) family have been discovered [58]. However, it remains to be determined if DNASE2B and/or PLAAT gene variants are associated with cataracts.

8. Summary

The collective findings from multiple laboratories using chick and mouse model systems, non-human primates, and clinical studies in humans provide evidence that autophagy is essential for achieving mature lens structure, homeostasis, and transparency. The key autophagy structures, ranging from double-membrane autophagosomes to single-membrane autolysosomes, are found throughout the lens in both epithelia and fiber cells, which are involved in multiple tissue-remodeling and protein recycling events important for both lens epithelial cell homeostasis and lens fiber cell differentiation. Autophagy in the lens is coordinated by the precise regulation of the key signaling pathways that initiate autophagy to drive the critical steps in the lens differentiation program, such as the elimination of organelles to form the core lens organelle-free zone. The low oxygen environment of the lens drives HIF1a-induced autophagy via the upregulation of BNIP3L expression, resulting in the specific elimination of the mitochondria, endoplasmic reticulum, and Golgi apparatus during lens fiber cell differentiation. Finally, pioneering studies on the structural requirements for the elimination of nuclei during lens differentiation reveal the presence of an entirely novel structure associated with degrading lens nuclei, which is termed the nuclear excisosome. Thus, cataract resulting from the mutation of key autophagy proteins in both humans and animal models strongly suggests that autophagy is a requirement for lens differentiation and transparency, and both structural and mechanistic studies delineating the role of autophagy in the lens provide a theoretical basis for this.

Funding: This work was supported by the National Institutes of Health, USA, National Eye Institute, USA, Grant Number EY029708 (M.K.), NIH/NEI grants R01 EY008148 (M.J.C.) and P30 EY05722 (Duke Eye Center Core Grant) (M.J.C.), NEI/NIH R01 EY026478 (S.M.), NEI/NIH R01 EY028899 (A.S.), and NEI project ZIA EY000281-30 (J.F.H.).

Institutional Review Board Statement: Not applicable.

Informed Consent Statement: Not applicable.

Conflicts of Interest: The authors declare no conflict of interest.

References

1. Bassnett, S. On the mechanism of organelle degradation in the vertebrate lens. *Exp. Eye Res.* **2009**, *88*, 133–139. [CrossRef] [PubMed]
2. Menko, A.S. Lens epithelial cell differentiation. *Exp. Eye Res.* **2002**, *75*, 485–490. [CrossRef] [PubMed]
3. Wride, M.A. Lens fibre cell differentiation and organelle loss: Many paths lead to clarity. *Philos. Trans. R. Soc. Lond. B Biol. Sci.* **2011**, *366*, 1219–1233. [CrossRef] [PubMed]
4. Kupfer, C. The National Eye Institute's low vision education program: Improving quality of life. *Ophthalmology* **2000**, *107*, 229–230. [CrossRef] [PubMed]
5. Khairallah, M.; Kahloun, R.; Bourne, R.; Limburg, H.; Flaxman, S.R.; Jonas, J.B.; Keeffe, J.; Leasher, J.; Naidoo, K.; Pesudovs, K.; et al. Number of People Blind or Visually Impaired by Cataract Worldwide and in World Regions, 1990 to 2010. *Investig. Ophthalmol. Vis. Sci.* **2015**, *56*, 6762–6769. [CrossRef]
6. Li, H.; Mao, Y.; Bouaziz, M.; Yu, H.; Qu, X.; Wang, F.; Feng, G.-S.; Shawber, C.; Zhang, X. Lens differentiation is controlled by the balance between PDGF and FGF signaling. *PLoS Biol.* **2019**, *17*, e3000133. [CrossRef]
7. Lovicu, F.J.; McAvoy, J.W. FGF-induced lens cell proliferation and differentiation is dependent on MAPK (ERK1/2) signalling. *Development* **2001**, *128*, 5075–5084. [CrossRef]
8. Chamberlain, C.G.; McAvoy, J.W. Induction of lens fibre differentiation by acidic and basic fibroblast growth factor (FGF). *Growth Factors* **1989**, *1*, 125–134. [CrossRef]
9. Klok, E.j.; Lubsen, N.H.; Chamberlain, C.G.; McAvoy, J.W. Induction and Maintenance of Differentiation of Rat Lens Epithelium by FGF-2, Insulin and IGF-1. *Exp. Eye Res.* **1998**, *67*, 425–431. [CrossRef]
10. Basu, S.; Rajakaruna, S.; De Arcangelis, A.; Zhang, L.; Georges-Labouesse, E.; Menko, A.S. α6 integrin transactivates insulin-like growth factor receptor-1 (IGF-1R) to regulate caspase-3-mediated lens epithelial cell differentiation initiation. *J. Biol. Chem.* **2014**, *289*, 3842–3855. [CrossRef]
11. Mochizuki, T.; Masai, I. The lens equator: A platform for molecular machinery that regulates the switch from cell proliferation to differentiation in the vertebrate lens. *Dev. Growth Differ.* **2014**, *56*, 387–401. [CrossRef]
12. Brennan, L.; Disatham, J.; Kantorow, M. Mechanisms of organelle elimination for lens development and differentiation. *Exp. Eye Res.* **2021**, *209*, 108682. [CrossRef]
13. Hejtmancik, J.F.; Riazuddin, S.A.; McGreal, R.; Liu, W.; Cvekl, A.; Shiels, A. Lens Biology and Biochemistry. *Prog. Mol. Biol. Transl. Sci.* **2015**, *134*, 169–201.
14. Yu, G.; Klionsky, D.J. Life and Death Decisions—The Many Faces of Autophagy in Cell Survival and Cell Death. *Biomolecules* **2022**, *12*, 866. [CrossRef]
15. Gómez-Virgilio, L.; Silva-Lucero, M.-D.; Flores-Morelos, D.-S.; Gallardo-Nieto, J.; Lopez-Toledo, G.; Abarca-Fernandez, A.-M.; Zacapala-Gómez, A.-E.; Luna-Muñoz, J.; Montiel-Sosa, F.; Soto-Rojas, L.O.; et al. Autophagy: A Key Regulator of Homeostasis and Disease: An Overview of Molecular Mechanisms and Modulators. *Cells* **2022**, *11*, 2262. [CrossRef]
16. Xie, Z.; Klionsky, D.J. Autophagosome formation: Core machinery and adaptations. *Nat. Cell Biol.* **2007**, *9*, 1102–1109. [CrossRef]
17. Hubbard, V.M.; Valdor, R.; Macian, F.; Cuervo, A.M. Selective autophagy in the maintenance of cellular homeostasis in aging organisms. *Biogerontology* **2012**, *13*, 21–35. [CrossRef]
18. Kaushik, S.; Cuervo, A.M. The coming of age of chaperone-mediated autophagy. *Nat. Rev. Mol. Cell Biol.* **2018**, *19*, 365–381. [CrossRef]
19. Vargas, J.N.S.; Hamasaki, M.; Kawabata, T.; Youle, R.J.; Yoshimori, T. The mechanisms and roles of selective autophagy in mammals. *Nat. Rev. Mol. Cell Biol.* **2022**, 1–19. [CrossRef]
20. Wang, L.; Daniel, D.J.; Klionsky, J.; Han-Ming Shen, H.M. The emerging mechanisms and functions of microautophagy. *Nat. Rev. Mol. Cell Biol.* **2022**, 1–18. [CrossRef]
21. Kroemer, G.; Marino, G.; Levine, B. Autophagy and the integrated stress response. *Mol. Cell* **2010**, *40*, 280–293. [CrossRef] [PubMed]
22. Levine, B.; Yuan, J. Autophagy Cell Death: Innocent Convict? *J. Clin. Investig.* **2005**, *115*, 2679–2688. [CrossRef] [PubMed]
23. Mizushima, N.; Komatsu, M. Autophagy: Renovation of cells and tissues. *Cell* **2011**, *147*, 728–741. [CrossRef] [PubMed]
24. Lu, G.; Wang, Y.; Shi, Y.; Zhang, Z.; Huang, C.; He, W.; Wang, C.; Shen, H. Autophagy in health and disease: From molecular mechanisms to therapeutic target. *MedComm* **2022**, *3*, e150. [CrossRef] [PubMed]
25. Shibutani, S.T.; Yoshimori, T. A current perspective of autophagosome biogenesis. *Cell Res.* **2014**, *24*, 58–68. [CrossRef]

26. Majeed, S.T.; Majeed, R.; Andrabi, K.I. Expanding the view of the molecular mechanisms of autophagy pathway. *J. Cell. Physiol.* **2022**, *237*, 3257–3277. [CrossRef]
27. Parzych, K.R.; Klionsky, D.J. An overview of autophagy: Morphology, mechanism, and regulation. *Antioxid. Redox Signal.* **2014**, *20*, 460–473. [CrossRef]
28. Yang, Z.; Klionsky, D.J. An overview of the molecular mechanism of autophagy. In *Autophagy in Infection and Immunity. Current Topics in Microbiology and Immunology*; Springer: Berlin/Heidelberg, Germany, 2009; Volume 335, pp. 1–32.
29. Hayashi-Nishino, M.; Fujita, N.; Noda, T.; Yamaguchi, A.; Yoshimori, T.; Yamamoto, A. A subdomain of the endoplasmic reticulum forms a cradle for autophagosome formation. *Nat. Cell Biol.* **2009**, *11*, 1433–1437. [CrossRef]
30. Ylä-Anttila, P.; Vihinen, H.; Jokitalo, E.; Eskelinen, E.-L. 3D tomography reveals connections between the phagophore and endoplasmic reticulum. *Autophagy* **2009**, *5*, 1180–1185. [CrossRef]
31. Kabeya, Y.; Mizushima, N.; Yamamoto, A.; Oshitani-Okamoto, S.; Ohsumi, Y.; Yoshimori, T. LC3, GABARAP and GATE16 localize to autophagosomal membrane depending on form-II formation. *J. Cell. Sci.* **2004**, *117*, 2805–2812. [CrossRef]
32. Shpilka, T.; Weidberg, H.; Pietrokovski, S.; Elazar, Z. Atg8: An autophagy-related ubiquitin-like protein family. *Genome Biol.* **2011**, *12*, 226. [CrossRef]
33. Klionsky, D.J.; Abdel-Aziz, A.K.; Abdelfatah, S.; Abdellatif, M.; Abdoli, A.; Abel, S.; Abeliovich, H.; Abildgaard, M.H.; Abudu, Y.P.; Acevedo-Arozena, A.; et al. Guidelines for the use and interpretation of assays for monitoring autophagy. In *Autophag*, 4th ed.; Taylor & Francis: Abingdon, UK, 2021; Volume 17, pp. 1–382.
34. Noda, N.N. Atg2 and Atg9: Intermembrane and interleaflet lipid transporters driving autophagy. *Biochim. Biophys. Acta Mol. Cell Biol. Lipids* **2021**, *1866*, 158956. [CrossRef]
35. Kakuta, S.; Yamamoto, H.; Negishi, L.; Kondo-Kakuta, C.; Hayashi, N.; Ohsumi, Y. Atg9 vesicles recruit vesicle-tethering proteins Trs85 and Ypt1 to the autophagosome formation site. *J. Biol. Chem.* **2012**, *287*, 44261–44269. [CrossRef]
36. Matoba, K.; Kotani, T.; Tsutsumi, A.; Tsuji, T.; Mori, T.; Noshiro, D.; Sugita, Y.; Nomura, N.; Iwata, S.; Ohsumi, Y.; et al. Atg9 is a lipid scramblase that mediates autophagosomal membrane expansion. *Nat. Struct. Mol. Biol.* **2020**, *27*, 1185–1193. [CrossRef]
37. Orii, M.; Tsuji, T.; Ogasawara, Y.; Fujimoto, T. Transmembrane phospholipid translocation mediated by Atg9 is involved in autophagosome formation. *J. Cell Biol.* **2021**, *220*, e202009194. [CrossRef]
38. Nakamura, S.; Yoshimori, T. New insights into autophagosome-lysosome fusion. *J. Cell Sci.* **2017**, *130*, 1209–1216. [CrossRef]
39. Nishida, Y.; Arakawa, S.; Fujitani, K.; Yamaguchi, H.; Mizuta, T.; Kanaseki, T.; Komatsu, M.; Otsu, K.; Tsujimoto, Y.; Shimizu, S. Discovery of Atg5/Atg7-independent alternative macroautophagy. *Nature* **2009**, *461*, 654–658. [CrossRef]
40. Bassnett, S.; Mataic, D. Chromatin Degradation in Differentiating Fiber Cells of the Eye Lens. *J. Cell Biol.* **1997**, *137*, 37–49. [CrossRef]
41. Basu, S.; Rajakaruna, S.; Reyes, B.; Van Bockstaele, E.; Menko, A.S. Suppression of MAPK/JNK-MTORC1 signaling leads to premature loss of organelles and nuclei by autophagy during terminal differentiation of lens fiber cells. *Autophagy* **2014**, *10*, 1193–1211. [CrossRef]
42. Costello, M.J.; Brennan, L.A.; Basu, S.; Chauss, D.; Mohamed, A.; Gilliland, K.O.; Johnsen, S.; Menko, A.S.; Kantorow, M. Autophagy and mitophagy participate in ocular lens organelle degradation. *Exp. Eye Res.* **2013**, *116*, 141–150. [CrossRef]
43. Gheyas, R.; Ortega-Alvarez, R.; Chauss, D.; Kantorow, M.; Menko, A.S. Suppression of PI3K signaling is linked to autophagy activation and the spatiotemporal induction of the lens organelle free zone. *Exp. Cell Res.* **2022**, *412*, 113043. [CrossRef] [PubMed]
44. Menko, A.S. The link between inhibition of PI3K signaling, induction of autophagy, and elimination of organelles to form the lens organelle-free zone. *Autophagy Rep.* **2022**, *1*, 238–241. [CrossRef]
45. Quan, Y.; Du, Y.; Tong, Y.; Gu, S.; Jiang, J.X. Connexin Gap Junctions and Hemichannels in Modulating Lens Redox Homeostasis and Oxidative Stress in Cataractogenesis. *Antioxidants* **2021**, *10*, 1374. [CrossRef] [PubMed]
46. Cheng, C.; Nowak, R.B.; Gao, J.; Sun, X.; Biswas, S.K.; Lo, W.-K.; Mathias, R.T.; Fowler, V.M. Lens ion homeostasis relies on the assembly and/or stability of large connexin 46 gap junction plaques on the broad sides of differentiating fiber cells. *Am. J. Physiol. Cell Physiol.* **2015**, *308*, C835–C847. [CrossRef]
47. Mathias, R.T.; Kistler, J.; Donaldson, P. The lens circulation. *J. Membr. Biol.* **2007**, *216*, 1–16. [CrossRef]
48. Donaldson, P.; Kistler, J.; Mathias, R. Molecular solutions to mammalian lens transparency. *Physiology* **2001**, *16*, 118–123. [CrossRef]
49. Morishita, H.; Eguchi, S.; Kimura, H.; Sasaki, J.; Sakamaki, Y.; Robinson, M.L.; Sasaki, T.; Mizushima, N. Deletion of autophagy-related 5 (Atg5) and Pik3c3 genes in the lens causes cataract independent of programmed organelle degradation. *J. Biol. Chem.* **2013**, *288*, 11436–11447. [CrossRef]
50. Levine, B.; Klionsky, D.J. Development by Self-Digestion: Molecular Mechanisms and Biological Functions of Autophagy. *Dev. Cell* **2004**, *6*, 463–477. [CrossRef]
51. Yu, X.; Long, Y.C.; Shen, H.M. Differential regulatory functions of three classes of phosphatidylinositol and phosphoinositide 3-kinases in autophagy. *Autophagy* **2015**, *11*, 1711–1728. [CrossRef]
52. Vanhaesebroeck, B.; Stephens, L.; Hawkins, P. PI3K signalling: The path to discovery and understanding. *Nat. Rev. Mol. Cell Biol.* **2012**, *13*, 195–203. [CrossRef]
53. Menko, A.S.; Klukas, K.A.; Johnson, R.G. Chicken embryo lens cultures mimic differentiation in the lens. *Dev. Biol.* **1984**, *103*, 129–141. [CrossRef]
54. Weber, G.F.; Menko, A.S. Phosphatidylinositol 3-kinase is necessary for lens fiber cell differentiation and survival. *Investig. Ophthalmol. Vis. Sci.* **2006**, *47*, 4490–4499. [CrossRef]

55. Kim, Y.C.; Guan, K.L. mTOR: A pharmacologic target for autophagy regulation. *J. Clin. Investig.* **2015**, *125*, 25–32. [CrossRef]
56. Yang, C.; Wang, X. Lysosome biogenesis: Regulation and functions. *J. Cell Biol.* **2021**, *220*, e202102001. [CrossRef]
57. Uyama, T.; Tsuboi, K.; Ueda, N. An involvement of phospholipase A/acyltransferase family proteins in peroxisome regulation and plasmalogen metabolism. *FEBS Lett.* **2017**, *591*, 2745–2760. [CrossRef]
58. Morishita, H.; Eguchi, T.; Tsukamoto, S.; Sakamaki, Y.; Takahashi, S.; Saito, C.; Koyama-Honda, I.; Mizushima, N. Organelle degradation in the lens by PLAAT phospholipases. *Nature* **2021**, *592*, 634–638. [CrossRef]
59. Watanabe, S.; Nihongaki, Y.; Itoh, K.; Uyama, T.; Toda, S.; Watanabe, S.; Inoue, T. Defunctionalizing intracellular organelles such as mitochondria and peroxisomes with engineered phospholipase A/acyltransferases. *Nat. Commun.* **2022**, *13*, 4413. [CrossRef]
60. Weber, G.F.; Menko, A.S. The canonical intrinsic mitochondrial death pathway has a non-apoptotic role in signaling lens cell differentiation. *J. Biol. Chem.* **2005**, *280*, 22135–22145. [CrossRef]
61. Zhu, Z.; He, X.; Johnson, C.; Stoops, J.; Eaker, A.E.; Stoffer, D.S.; Bell, A.; Zarnegar, R.; DeFrances, M.C. PI3K is negatively regulated by PIK3IP1, a novel p110 interacting protein. *Biochem. Biophys. Res. Commun.* **2007**, *358*, 66–72. [CrossRef]
62. Novak, I.; Kirkin, V.; McEwan, D.G.; Zhang, J.; Wild, P.; Rozenknop, A.; Rogov, V.; Löhr, F.; Popovic, D.; Occhipinti, A.; et al. Nix is a selective autophagy receptor for mitochondrial clearance. *EMBO Rep.* **2010**, *11*, 45–51. [CrossRef]
63. Sandoval, H.; Thiagarajan, P.; Dasgupta, S.K.; Schumacher, A.; Prchal, J.T.; Chen, M.; Wang, J. Essential role for Nix in autophagic maturation of erythroid cells. *Nature* **2008**, *454*, 232–235. [CrossRef] [PubMed]
64. Schweers, R.L.; Zhang, J.; Randall, M.S.; Loyd, M.R.; Li, W.; Dorsey, F.C.; Kundu, M.; Opferman, J.T.; Cleveland, J.L.; Miller, J.L.; et al. NIX is required for programmed mitochondrial clearance during reticulocyte maturation. *Proc. Natl. Acad. Sci. USA* **2007**, *104*, 19500–19505. [CrossRef] [PubMed]
65. Zhang, J.; Ney, P.A. Mechanisms and biology of B-cell leukemia/lymphoma 2/adenovirus E1B interacting protein 3 and Nip-like protein X. *Antioxid. Redox Signal.* **2011**, *14*, 1959–1969. [CrossRef] [PubMed]
66. Onishi, M.; Yamano, K.; Sato, M.; Matsuda, N.; Okamoto, K. Molecular mechanisms and physiological functions of mitophagy. *EMBO J.* **2021**, *40*, e104705. [CrossRef] [PubMed]
67. Zhang, J.; Ney, P.A. Role of BNIP3 and NIX in cell death, autophagy, and mitophagy. *Cell Death Differ.* **2009**, *16*, 939–946. [CrossRef]
68. Diwan, A.; Koesters, A.G.; Odley, A.M.; Pushkaran, S.; Baines, C.P.; Spike, B.T.; Daria, D.; Jegga, A.G.; Geiger, H.; Aronow, B.J.; et al. Unrestrained erythroblast development in Nix−/− mice reveals a mechanism for apoptotic modulation of erythropoiesis. *Proc. Natl. Acad. Sci. USA* **2007**, *104*, 6794–6799. [CrossRef]
69. Marinkovic, M.; Sprung, M.; Novak, I. Dimerization of mitophagy receptor BNIP3L/NIX is essential for recruitment of autophagic machinery. *Autophagy* **2021**, *17*, 1232–1243. [CrossRef]
70. Chauss, D.; Basu, S.; Rajakaruna, S.; Ma, Z.; Gau, V.; Anastas, S.; Brennan, L.A.; Hejtmancik, J.F.; Menko, A.S.; Kantorow, M. Differentiation state-specific mitochondrial dynamic regulatory networks are revealed by global transcriptional analysis of the developing chicken lens. *G3 Genes Genomes Genet.* **2014**, *4*, 1515–1527. [CrossRef]
71. Brennan, L.A.; McGreal-Estrada, R.; Logan, C.M.; Cvekl, A.; Menko, A.S.; Kantorow, M. BNIP3L/NIX is required for elimination of mitochondria, endoplasmic reticulum and Golgi apparatus during eye lens organelle-free zone formation. *Exp. Eye Res.* **2018**, *174*, 173–184. [CrossRef]
72. Diwan, A.; Matkovich, S.J.; Yuan, Q.; Zhao, W.; Yatani, A.; Brown, J.H.; Molkentin, J.D.; Kranias, E.G.; Dorn, G.W. Endoplasmic reticulum-mitochondria crosstalk in NIX-mediated murine cell death. *J. Clin. Investig.* **2009**, *119*, 203–212. [CrossRef]
73. Bellot, G.; Garcia-Medina, R.; Gounon, P.; Chiche, J.; Roux, D.; Pouysségur, J.; Mazure, N.M. Hypoxia-induced autophagy is mediated through hypoxia-inducible factor induction of BNIP3 and BNIP3L via their BH3 domains. *Mol. Cell. Biol.* **2009**, *29*, 2570–2581. [CrossRef]
74. Cummins, E.P.; Taylor, C.T. Hypoxia-responsive transcription factors. *Pflügers Arch.* **2005**, *450*, 363–371. [CrossRef]
75. Kenneth, N.S.; Rocha, S. Regulation of gene expression by hypoxia. *Biochem. J.* **2008**, *414*, 19–29. [CrossRef]
76. Brahimi-Horn, M.C.; Pouysségur, J. HIF1 at a glance. *J. Cell Sci.* **2009**, *122*, 1055–1057. [CrossRef]
77. Lutty, G.A.; McLeod, D.S. Development of the hyaloid, choroidal and retinal vasculatures in the fetal human eye. *Prog. Retin. Eye Res.* **2018**, *62*, 58–76. [CrossRef]
78. Goldberg, M.F. Persistent Fetal Vasculature (PFV): An Integrated Interpretation of Signs and Symptoms Associated with Persistent Hyperplastic Primary Vitreous (PHPV) LIV Edward Jackson Memorial Lecture. *Am. J. Ophthalmol.* **1997**, *124*, 587–626. [CrossRef]
79. Bassnett, S.; McNulty, R. The effect of elevated intraocular oxygen on organelle degradation in the embryonic chicken lens. *J. Exp. Biol.* **2003**, *206*, 4353–4361. [CrossRef]
80. Beebe, D.C.; Shui, Y.-B.; Siegfried, C.J.; Holekamp, N.M.; Bai, F. Preserve the (intraocular) environment: The importance of maintaining normal oxygen gradients in the eye. *Jpn. J. Ophthalmol.* **2014**, *58*, 225–231. [CrossRef]
81. McNulty, R.; Wang, H.; Mathias, R.T.; Ortwerth, B.J.; Truscott, R.J.W.; Bassnett, S. Regulation of tissue oxygen levels in the mammalian lens. *J. Physiol.* **2004**, *559*, 883–898. [CrossRef]
82. Shestopalov, V.I.; Bassnett, S. Expression of autofluorescent proteins reveals a novel protein permeable pathway between cells in the lens core. *J. Cell Sci.* **2000**, *113*, 1913–1921. [CrossRef]
83. Brennan, L.; Disatham, J.; Kantorow, M. Hypoxia regulates the degradation of non-nuclear organelles during lens differentiation through activation of HIF1a. *Exp. Eye Res.* **2020**, *198*, 108129. [CrossRef] [PubMed]
84. Baudhuin, P.; Beaufay, H.; de Duve, C. Combined biochemical and morphological study of particulate fractions from rat liver. *J. Cell Biol.* **1965**, *26*, 219–243. [CrossRef] [PubMed]

85. De Duve, C.; Wattiaux, R. Functions of Lysosomes. *Ann. Rev. Physiol.* **1966**, *28*, 435–492. [CrossRef] [PubMed]
86. Costello, M.J.; Brennan, L.A.; Mohamed, A.; Gilliland, K.O.; Johnsen, S.; Kantorow, M. Identification and Ultrastructural Characterization of a Novel Nuclear Degradation Complex in Differentiating Lens Fiber Cells. *PLoS ONE* **2016**, *11*, e0160785. [CrossRef]
87. Costello, M.J.; Gilliland, K.O.; Mohamed, A.; Schey, K.L.; Johnsen, S.; Brennan, L.A.; Kantorow, M. Novel mitochondrial derived Nuclear Excisosome degrades nuclei during differentiation of prosimian Galago (bush baby) monkey lenses. *PLoS ONE* **2020**, *15*, e0241631. [CrossRef]
88. Wignes, J.A.; Goldman, J.W.; Weihl, C.C.; Bartley, M.G.; Andley, U.P. p62 expression and autophagy in alphaB-crystallin R120G mutant knock-in mouse model of hereditary cataract. *Exp. Eye Res.* **2013**, *115*, 263–273. [CrossRef]
89. Costello, M.J.; Johnsen, S.; Metlapally, S.; Gilliland, K.O.; Frame, L.; Balasubramanian, D. Multilamellar spherical particles as potential sources of excessive light scattering in human age-related nuclear cataracts. *Exp. Eye Res.* **2010**, *91*, 881–889. [CrossRef]
90. Pavel, M.; Rubinsztein, D.C. Mammalian autophagy and the plasma membrane. *FEBS J.* **2017**, *284*, 672–679. [CrossRef]
91. Matsui, M.; Yamamoto, A.; Kuma, A.; Ohsumi, Y.; Mizushima, N. Organelle degradation during the lens and erythroid differentiation is independent of autophagy. *Biochem. Biophys. Res. Commun.* **2006**, *339*, 485–489. [CrossRef]
92. Chen, J.; Ma, Z.; Jiao, X.; Fariss, R.; Kantorow, W.L.; Kantorow, M.; Pras, E.; Frydman, M.; Pras, E.; Riazuddin, S.; et al. Mutations in FYCO1 cause autosomal-recessive congenital cataracts. *Am. J. Hum. Genet.* **2011**, *88*, 827–838. [CrossRef]
93. Khan, S.Y.; Ali, M.; Kabir, F.; Na, C.H.; Delannoy, M.; Ma, Y.; Qiu, C.; Costello, M.J.; Hejtmancik, J.F.; Riazuddin, S.A. The role of FYCO1-dependent autophagy in lens fiber cell differentiation. *Autophagy* **2022**, *18*, 2198–2215. [CrossRef]
94. Satoh, K.; Takemura, Y.; Satoh, M.; Ozaki, K.; Kubota, S. Loss of FYCO1 leads to cataract formation. *Sci. Rep.* **2021**, *11*, 13771. [CrossRef]
95. McWilliams, T.G.; Prescott, A.R.; Villarejo-Zori, B.; Ball, G.; Boya, P.; Ganley, I.G. A comparative map of macroautophagy and mitophagy in the vertebrate eye. *Autophagy* **2019**, *15*, 1296–1308. [CrossRef]
96. Shiels, A.; Bennett, T.M.; Knopf, H.L.; Yamada, K.; Yoshiura, K.-I.; Niikawa, N.; Shim, S.; Hanson, P.I. CHMP4B, a novel gene for autosomal dominant cataracts linked to chromosome 20q. *Am. J. Hum. Genet.* **2007**, *81*, 596–606. [CrossRef]
97. Lefebvre, C.; Legouis, R.; Culetto, E. ESCRT and autophagies: Endosomal functions and beyond. *Semin. Cell Dev. Biol.* **2018**, *74*, 21–28. [CrossRef]
98. Olmos, Y. The ESCRT Machinery: Remodeling, Repairing, and Sealing Membranes. *Membranes* **2022**, *12*, 633. [CrossRef]
99. Lee, J.-A.; Beigneux, A.; Ahmad, S.T.; Young, S.G.; Gao, F.-B. ESCRT-III dysfunction causes autophagosome accumulation and neurodegeneration. *Curr. Biol.* **2007**, *17*, 1561–1567. [CrossRef]
100. Lee, J.A.; Gao, F.B. Roles of ESCRT in autophagy-associated neurodegeneration. *Autophagy* **2008**, *4*, 230–232. [CrossRef]
101. Sagona, A.P.; Nezis, I.P.; Stenmark, H. Association of CHMP4B and autophagy with micronuclei: Implications for cataract formation. *BioMed Res. Int.* **2014**, *2014*, 974393. [CrossRef]
102. Zhang, X.H.; Da Wang, J.; Jia, H.Y.; Zhang, J.S.; Li, Y.; Xiong, Y.; Li, J.; Li, X.X.; Huang, Y.; Zhu, G.Y.; et al. Mutation profiles of congenital cataract genes in 21 northern Chinese families. *Mol. Vis.* **2018**, *24*, 471–477.
103. Jackson, D.; Malka, S.; Harding, P.; Palma, J.; Dunbar, H.; Moosajee, M. Molecular diagnostic challenges for non-retinal developmental eye disorders in the United Kingdom. *Am. J. Med. Genet. C Semin. Med. Genet.* **2020**, *184*, 578–589. [CrossRef] [PubMed]
104. Wang, X.; Wang, D.; Wang, Q.; Huang, W.; Dongye, M.; Zhang, X.; Lin, D.; Lin, Z.; Li, J.; Hu, W.; et al. Broadening the Mutation Spectrum in GJA8 and CHMP4B: Novel Missense Variants and the Associated Phenotypes in Six Chinese Han Congenital Cataracts Families. *Front. Med.* **2021**, *8*, 713284. [CrossRef] [PubMed]
105. Yonova-Doing, E.; Zhao, W.; Igo, R.P.; Wang, C.; Sundaresan, P.; Lee, K.E.; Jun, G.R.; Alves, A.C.; Chai, X.; Chan, A.S.Y.; et al. Common variants in SOX-2 and congenital cataract genes contribute to age-related nuclear cataract. *Commun. Biol.* **2020**, *3*, 755. [CrossRef] [PubMed]
106. Zhou, Y.; Bennett, T.M.; Shiels, A. A charged multivesicular body protein (CHMP4B) is required for lens growth and differentiation. *Differentiation* **2019**, *109*, 16–27. [CrossRef]
107. Skowyra, M.L.; Schlesinger, P.H.; Naismith, T.V.; Hanson, P.I. Triggered recruitment of ESCRT machinery promotes endolysosomal repair. *Science* **2018**, *360*, eaar5078. [CrossRef]
108. Radulovic, M.; O Schink, K.; Wenzel, E.M.; Nähse, V.; Bongiovanni, A.; Lafont, F.; Stenmark, H. ESCRT-mediated lysosome repair precedes lysophagy and promotes cell survival. *EMBO J.* **2018**, *37*, e99753. [CrossRef]
109. Loi, M.; Raimondi, A.; Morone, D.; Molinari, M. ESCRT-III-driven piecemeal micro-ER-phagy remodels the ER during recovery from ER stress. *Nat. Commun.* **2019**, *10*, 5058. [CrossRef]
110. Zhen, Y.; Spangenberg, H.; Munson, M.J.; Brech, A.; Schink, K.O.; Tan, K.-W.; Sørensen, V.; Wenzel, E.M.; Radulovic, M.; Engedal, N.; et al. ESCRT-mediated phagophore sealing during mitophagy. *Autophagy* **2020**, *16*, 826–841. [CrossRef]
111. Gulluni, F.; Prever, L.; Li, H.; Krafcikova, P.; Corrado, I.; Lo, W.-T.; Margaria, J.P.; Chen, A.; De Santis, M.C.; Cnudde, S.J.; et al. PI(3,4)P2-mediated cytokinetic abscission prevents early senescence and cataract formation. *Science* **2021**, *374*, eabk0410. [CrossRef]
112. Chen, J.; Wang, Q.; Cabrera, P.E.; Zhong, Z.; Sun, W.; Jiao, X.; Chen, Y.; Govindarajan, G.; Naeem, M.A.; Khan, S.N.; et al. Molecular Genetic Analysis of Pakistani Families with Autosomal Recessive Congenital Cataracts by Homozygosity Screening. *Invest. Ophthalmol. Vis. Sci.* **2017**, *58*, 2207–2217. [CrossRef]

113. Barashkov, N.A.; Konovalov, F.A.; Borisova, T.V.; Teryutin, F.M.; Solovyev, A.V.; Pshennikova, V.G.; Sapojnikova, N.V.; Vychuzhina, L.S.; Romanov, G.P.; Gotovtsev, N.N.; et al. Autosomal recessive cataract (CTRCT18) in the Yakut population isolate of Eastern Siberia: A novel founder variant in the FYCO1 gene. *Eur. J. Hum. Genet.* **2021**, *29*, 965–976. [CrossRef]
114. Pankiv, S.; Alemu, E.A.; Brech, A.; Bruun, J.-A.; Lamark, T.; Øvervatn, A.; Bjørkøy, G.; Johansen, T. FYCO1 is a Rab7 effector that binds to LC3 and PI3P to mediate microtubule plus end-directed vesicle transport. *J. Cell Biol.* **2010**, *188*, 253–269. [CrossRef]
115. Choquet, H.; Melles, R.B.; Anand, D.; Yin, J.; Cuellar-Partida, G.; Wang, W.; Hoffmann, T.J.; Nair, K.S.; Hysi, P.G.; Lachke, S.A.; et al. A large multiethnic GWAS meta-analysis of cataract identifies new risk loci and sex-specific effects. *Nat. Commun.* **2021**, *12*, 3595. [CrossRef]
116. Xiao, W.; Yeerken, D.; Li, J.; Li, Z.; Jiang, L.; Li, D.; Fu, M.; Ma, L.; Song, Y.; Zhang, W.; et al. Nlp promotes autophagy through facilitating the interaction of Rab7 and FYCO1. *Signal Transduct. Target. Ther.* **2021**, *6*, 152. [CrossRef]
117. Nieto-Torres, J.L.; Shanahan, S.-L.; Chassefeyre, R.; Chaiamarit, T.; Zaretski, S.; Landeras-Bueno, S.; Verhelle, A.; Encalada, S.E.; Hansen, M. LC3B phosphorylation regulates FYCO1 binding and directional transport of autophagosomes. *Curr. Biol.* **2021**, *31*, 3440–3449.e7. [CrossRef]
118. Olsvik, H.L.; Lamark, T.; Takagi, K.; Larsen, K.B.; Evjen, G.; Øvervatn, A.; Mizushima, T.; Johansen, T. FYCO1 Contains a C-terminally Extended, LC3A/B-preferring LC3-interacting Region (LIR) Motif Required for Efficient Maturation of Autophagosomes during Basal Autophagy. *J. Biol. Chem.* **2015**, *290*, 29361–29374. [CrossRef]
119. Cheng, X.; Wang, Y.; Gong, Y.; Li, F.; Guo, Y.; Hu, S.; Liu, J.; Pan, L. Structural basis of FYCO1 and MAP1LC3A interaction reveals a novel binding mode for Atg8-family proteins. *Autophagy* **2016**, *12*, 1330–1339. [CrossRef]
120. Hong, Z.; Pedersen, N.M.; Wang, L.; Torgersen, M.L.; Stenmark, H.; Raiborg, C. PtdIns3P controls mTORC1 signaling through lysosomal positioning. *J. Cell Biol.* **2017**, *216*, 4217–4233. [CrossRef]
121. Chen, J.H.; Huang, C.; Zhang, B.; Yin, S.; Liang, J.; Xu, C.; Huang, Y.; Cen, L.P.; Ng, T.K.; Zheng, C.; et al. Mutations of RagA GTPase in mTORC1 Pathway Are Associated with Autosomal Dominant Cataracts. *PLoS Genet.* **2016**, *12*, e1006090. [CrossRef]
122. Lachke, S.A.; Alkuraya, F.S.; Kneeland, S.C.; Ohn, T.; Aboukhalil, A.; Howell, G.R.; Saadi, I.; Cavallesco, R.; Yue, Y.; Tsai, A.C.; et al. Mutations in the RNAGranule Component TDRD7 Cause Cataract and Glaucoma. *Science* **2011**, *331*, 1571–1576. [CrossRef]
123. Tan, Y.-Q.; Tu, C.; Meng, L.; Yuan, S.; Sjaarda, C.; Luo, A.; Du, J.; Li, W.; Gong, F.; Zhong, C.; et al. Loss-of-function mutations in TDRD7 lead to a rare novel syndrome combining congenital cataract and nonobstructive azoospermia in humans. *Genet. Med.* **2019**, *21*, 1209–1217. [CrossRef] [PubMed]
124. Zheng, C.; Wu, M.; He, C.-Y.; An, X.-J.; Sun, M.; Chen, C.-L.; Ye, J. RNA granule component TDRD7 gene polymorphisms in a Han Chinese population with age-related cataract. *J. Int. Med. Res.* **2014**, *42*, 153–163. [CrossRef] [PubMed]
125. Tu, C.; Li, H.; Liu, X.; Wang, Y.; Li, W.; Meng, L.; Wang, W.; Li, Y.; Li, D.; Du, J.; et al. TDRD7 participates in lens development and spermiogenesis by mediating autophagosome maturation. *Autophagy* **2021**, *17*, 3848–3864. [CrossRef] [PubMed]
126. Liegel, R.P.; Handley, M.T.; Ronchetti, A.; Brown, S.; Langemeyer, L.; Linford, A.; Chang, B.; Morris-Rosendahl, D.J.; Carpanini, S.; Posmyk, R.; et al. Loss-of-function mutations in TBC1D20 cause cataracts and male infertility in blind sterile mice and Warburg micro syndrome in humans. *Am. J. Hum. Genet.* **2013**, *93*, 1001–1014. [CrossRef] [PubMed]
127. Sidjanin, D.J.; Park, A.K.; Ronchetti, A.; Martins, J.; Jackson, W.T. TBC1D20 mediates autophagy as a key regulator of autophagosome maturation. *Autophagy* **2016**, *12*, 1759–1775. [CrossRef]
128. Cullup, T.; Kho, A.L.; Dionisi-Vici, C.; Brandmeier, B.; Smith, F.; Urry, Z.; A Simpson, M.; Yau, S.; Bertini, E.; McClelland, V.; et al. Recessive mutations in EPG5 cause Vici syndrome, a multisystem disorder with defective autophagy. *Nat. Genet.* **2013**, *45*, 83–87. [CrossRef]
129. Byrne, S.; Jansen, L.; U-King-Im, J.M.; Siddiqui, A.; Lidov, H.G.; Bodi, I.; Smith, L.; Mein, R.; Cullup, T.; Dionisi-Vici, C.; et al. EPG5-related Vici syndrome: A paradigm of neurodevelopmental disorders with defective autophagy. *Brain* **2016**, *139*, 765–781. [CrossRef]
130. Ehmke, N.; Parvaneh, N.; Krawitz, P.; Ashrafi, M.-R.; Karimi, P.; Mehdizadeh, M.; Krüger, U.; Hecht, J.; Mundlos, S.; Robinson, P.N. First description of a patient with Vici syndrome due to a mutation affecting the penultimate exon of EPG5 and review of the literature. *Am. J. Med. Genet. Part A* **2014**, *164*, 3170–3175. [CrossRef]
131. Rodger, C.; Flex, E.; Allison, R.J.; Sanchis-Juan, A.; Hasenahuer, M.A.; Cecchetti, S.; French, C.E.; Edgar, J.R.; Carpentieri, G.; Ciolfi, A.; et al. De Novo VPS4A Mutations Cause Multisystem Disease with Abnormal Neurodevelopment. *Am. J. Hum. Genet.* **2020**, *107*, 1129–1148. [CrossRef]
132. Seu, K.G.; Trump, L.R.; Emberesh, S.; Lorsbach, R.B.; Johnson, C.; Meznarich, J.; Underhill, H.R.; Chou, S.T.; Sakthivel, H.; Nassar, N.N.; et al. VPS4A Mutations in Humans Cause Syndromic Congenital Dyserythropoietic Anemia due to Cytokinesis and Trafficking Defects. *Am. J. Hum. Genet.* **2020**, *107*, 1149–1156. [CrossRef]
133. Ping, X.; Liang, J.; Shi, K.; Bao, J.; Wu, J.; Yu, X.; Tang, X.; Zou, J.; Shentu, X. Rapamycin relieves the cataract caused by ablation of Gja8b through stimulating autophagy in zebrafish. *Autophagy* **2021**, *17*, 3323–3337. [CrossRef]

Disclaimer/Publisher's Note: The statements, opinions and data contained in all publications are solely those of the individual author(s) and contributor(s) and not of MDPI and/or the editor(s). MDPI and/or the editor(s) disclaim responsibility for any injury to people or property resulting from any ideas, methods, instructions or products referred to in the content.

cells

MDPI

Review

Myo/Nog Cells: The Jekylls and Hydes of the Lens

Jacquelyn Gerhart † and Mindy George-Weinstein *,†

Division of Research, Philadelphia College of Osteopathic Medicine, Philadelphia, PA 19131, USA; jacquelynge@pcom.edu
* Correspondence: mindygw@pcom.edu
† These authors contributed equally to this work.

Abstract: Herein, we review a unique and versatile lineage composed of Myo/Nog cells that may be beneficial or detrimental depending on their environment and nature of the pathological stimuli they are exposed to. While we will focus on the lens, related Myo/Nog cell behaviors and functions in other tissues are integrated into the narrative of our research that spans over three decades, examines multiple species and progresses from early stages of embryonic development to aging adults. Myo/Nog cells were discovered in the embryonic epiblast by their co-expression of the skeletal muscle-specific transcription factor MyoD, the bone morphogenetic protein inhibitor Noggin and brain-specific angiogenesis inhibitor 1. They were tracked from the epiblast into the developing lens, revealing heterogeneity of cell types within this structure. Depletion of Myo/Nog cells in the epiblast results in eye malformations arising from the absence of Noggin. In the adult lens, Myo/Nog cells are the source of myofibroblasts whose contractions produce wrinkles in the capsule. Eliminating this population within the rabbit lens during cataract surgery reduces posterior capsule opacification to below clinically significant levels. Parallels are drawn between the therapeutic potential of targeting Myo/Nog cells to prevent fibrotic disease in the lens and other ocular tissues.

Keywords: Myo/Nog; MyoD; Noggin; BAI1; myofibroblasts; fibrosis; lens; retina; PCO; PVR

1. Discovery of Myo/Nog Cells in the Embryo

Myo/Nog cells were discovered during our search for the origin of the skeletal muscle lineage, which, at the time, was reported to occur in the embryonic somites under the influence of factors released by surrounding tissues [1–4]. A few outliers to this well documented induction of cell fate demonstrated that the tissues which give rise to the somites, including epiblast, contain cells that differentiate into skeletal muscle in culture, even when grown in serum-free medium [5–8]. In vivo, we detected approximately 14 cells in the epiblast of the *chick* embryo blastocyst and 70 cells by the onset of gastrulation that expressed mRNA for the skeletal muscle-specific transcription factor MyoD (Figure 1B) [9] that, along with other members of its family, regulate the specification of cells to the skeletal muscle lineage [10–12].

Fortuitously, a monoclonal antibody (mAb) we generated against mesoderm cells, named G8, specifically bound to cells with MyoD mRNA in the epiblast (Figure 1B) and fetal organs lacking skeletal muscle [13–15]. The antigen recognized by the G8 mAb was later identified as brain-specific angiogenesis inhibitor 1 (BAI1) [16], a member of the adhesion G protein-coupled receptor family [17,18]. Functions of BAI1 include, among others, inhibition of angiogenesis and mediation of myocyte fusion to form multinucleated myofibers and phagocytosis [17–24]. The G8 epitope lies within the third thrombospondin repeat of BAI1′s extracellular domain [16], thereby enabling us to use the G8 mAb to isolate, track and target MyoD-positive (+) cells.

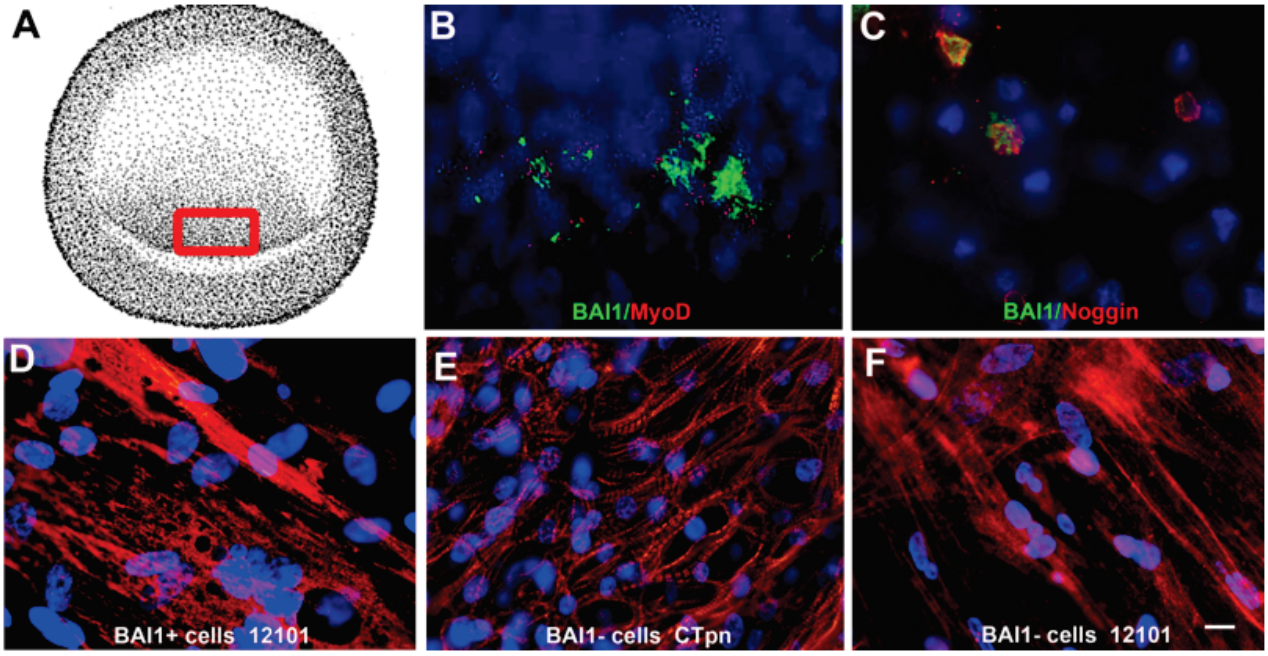

Figure 1. Cells that co-express MyoD, Noggin and BAI1 in the embryonic epiblast differentiate into skeletal muscle in vitro. In situ hybridization and immunofluorescence localization revealed a small population of cells that co-expressed BAI1 (green) and MyoD mRNA (red) (**B**) and Noggin protein (red) (**C**) in the posterior/medial epiblast of *chick* embryos before the onset of gastrulation (red box in **A**). Nuclei are stained with Hoechst dye (blue). Labeling with the skeletal muscle-specific 12,101 mAb demonstrated that BAI1-positive Myo/Nog cells isolated from the epiblast differentiated into skeletal myofibers when cultured in serum-free medium (**D**). BAI1-negative epiblast cells were labeled with a mAb to cardiac muscle-specific troponin T (**E**). Addition of Noggin to the medium resulted in the synthesis of the 12,101 antigen in BAI1-negative cells (**F**). Bar = 13 μM.

BAI1+/MyoD+ cells isolated from the *chick* embryo epiblast with the G8 mAb differentiated into skeletal muscle and fused to form multinucleated myofibers with sarcomeres when cultured in serum-free medium [14] (Figure 1D). BAI1-negative (−) cells differentiated predominantly into cardiac muscle (Figure 1E) unless they were cultured in medium conditioned by BAI1+ cells in which they underwent skeletal myogenesis [14]. We speculated that the factor(s) released by the BAI1+ cells in vitro was related to the mechanism regulating myogenesis in the somites involving inhibition of bone morphogenetic protein (BMP) signaling via Noggin [25–28]. This hypothesis was validated when skeletal myogenesis was induced in BAI1- cultures by substituting BAI1+ cell-conditioned medium with Noggin [14] (Figure 1F). Noggin mRNA and protein were then localized exclusively in epiblast cells that expressed MyoD and BAI1 in vivo (Figure 1C). The triple-positive cells were named Myo/Nog to reflect their capacity to differentiate into skeletal muscle and release Noggin.

The anti-BAI1 G8 mAb was also used to track Myo/Nog cells from the chick embryo epiblast into all three germ layers and their derivatives [29–31]. Only a subpopulation of cells in the somites expressed BAI1+/Noggin+ [29], suggesting that Myo/Nog cells are a separate lineage from myogenic cells induced within the mesoderm. BAI1+ epiblast cells were also tracked into the pre-lens placode and lens vesicle, and later were localized in the equatorial and germinative zones, anterior epithelium and between the primary fiber cells [31] (Figure 2A–D). BAI1+ cells continue to express MyoD and Noggin in the lens (Figure 2E,F) and other non-skeletal muscle tissues in the embryo and fetus. Myo/Nog cells were tracked into the heart and brain, and those present in the fetal intestine differentiated into skeletal muscle in culture [13,30]. These studies demonstrated Myo/Nog cells' stable commitment to the skeletal muscle lineage and capacity for regulating BMP signaling

regardless of their environment. Our cell-tracking experiments revealed for the first time that the developing lens consists of two populations, the lens epithelial cell (LEC) lineage and Myo/Nog cells.

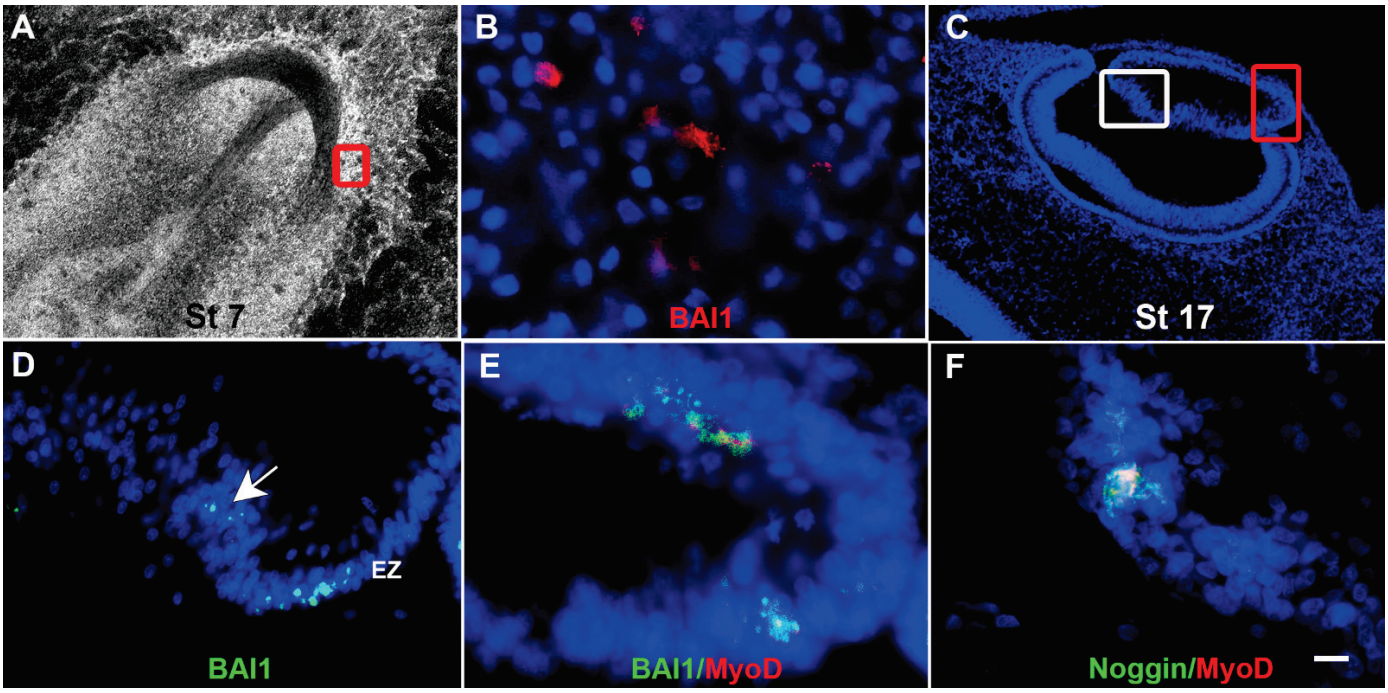

Figure 2. Epiblast-derived Myo/Nog cells are integrated into the developing lens. Myo/Nog cells were fluorescently labeled with the BAI1 mAb in the epiblast and the embryos were incubated for 1–3 days. Sections were stained with Hoechst dye to label nuclei (blue). In the stage 7 embryo, Myo/Nog cells were found in the pre-lens placode (boxed area in (**A**) shown at high magnification in (**B**)). A stage 17 eye is shown in (**C**). The area within the red box is shown at higher magnification in (**D**,**E**). The white box delineates the enlargement in (**F**). Prelabeled Myo/Nog cells were found in the equatorial zone (EZ) of the lens (**D**) and among the differentiating primary lens fiber cells (arrow in (**D**)). BAI1+ and Noggin+ cells (green) co-expressed MyoD mRNA (red) throughout the lens (**E**,**F**). Overlap of green and red appears yellow in merged images. Bar = 135 μM in (**A**), 13 μM in (**B**) and (**D**–**F**) and 56 μM in (**C**).

2. Roles of Myo/Nog Cells in the Developing Embryo

The functions of Myo/Nog cells during development were revealed in a series of experiments in which they were eliminated in the *chick* embryo epiblast by lysing them with the anti-BAI1 G8 mAb and complement [29,31,32]. Once depleted, Myo/Nog cells did not reappear in the embryo and Noggin was not detected in other cell types. The absence of Myo/Nog cells resulted in an expansion of BMP signaling and severe malformations of the ventral body wall, central nervous system and eyes (Figure 3C,D), an absence of skeletal muscle and expansion of cardiac muscle [29,31,32]. These defects phenocopied to a large extent in Noggin null mice [33–38]. Eye malformations ranged from anophthalmia to lens dysgenesis and overgrowth of the retina [29,31] (Figure 3C,D). Treatment with the G8 mAb or complement alone did not impair eye development (not shown). Replacing Myo/Nog cells with beads soaked in Noggin prevented ocular defects and other malformations (Figure 3E,F) and restored skeletal muscle differentiation in the somites [29,31]. Thus, Myo/Nog cells' release of Noggin is indispensable for normal development, including eye morphogenesis.

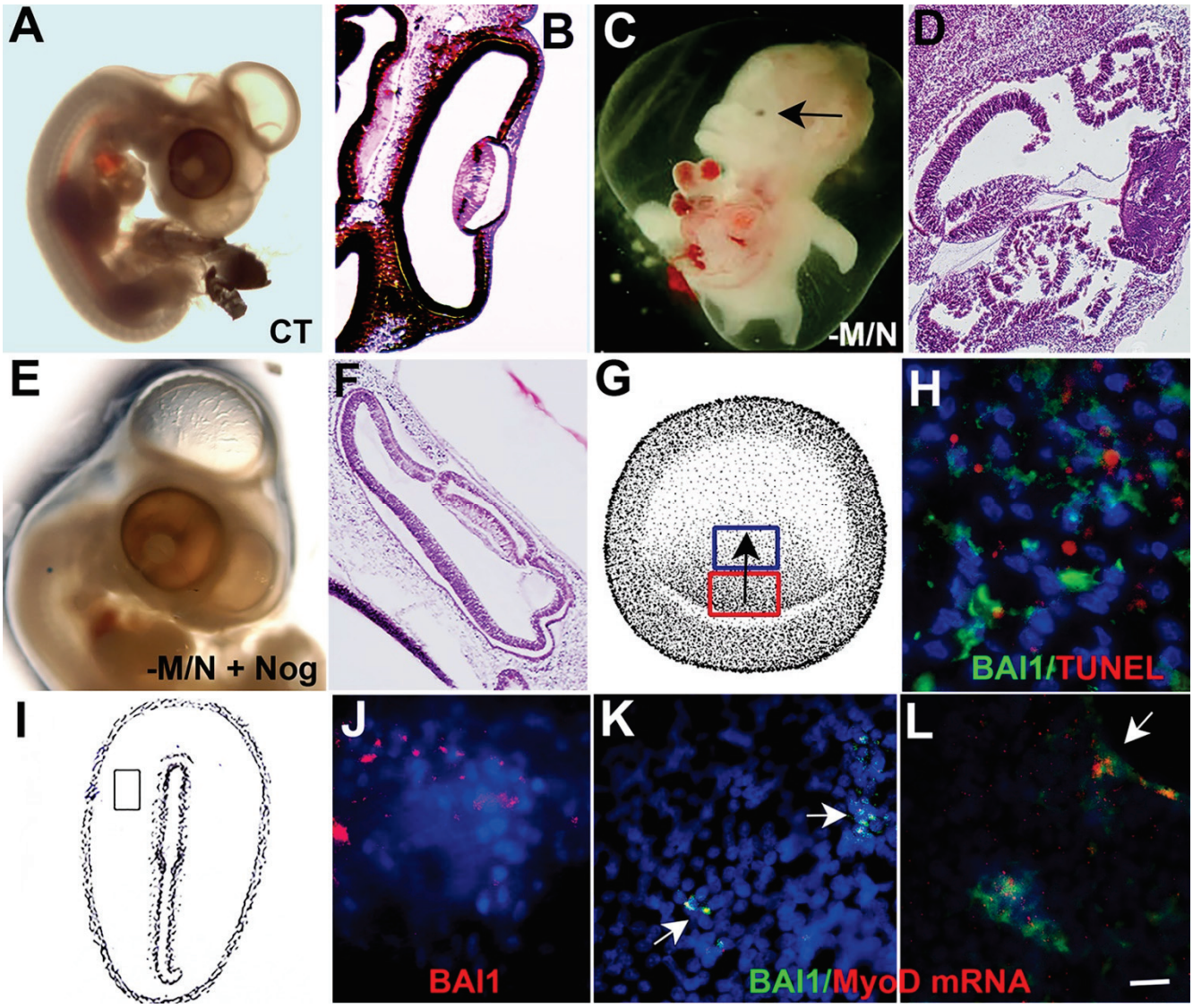

Figure 3. Myo/Nog cells are required for normal eye development and migrate to wounds in the embryo. Myo/Nog cells were eliminated in the *chick* embryo epiblast by incubating the embryo in the BAI1 mAb and complement. Embryos were incubated for approximately 5 days. Some embryos received beads soaked in Noggin (Nog) a day after treatment. A normal PBS control embryo (CT) and an H&E-stained section of the eye are shown in (**A**,**B**). Depletion of Myo/Nog cells resulted in malformations of the body wall and eyes, including microphthalmia (arrow in (**C**)) and dysgenesis of the lens and retina (**D**). Addition of Noggin-soaked beads prevented malformations caused by Myo/Nog cell depletion (**E**,**F**). Embryos treated with the D4 mAb and complement to eliminate a separate population of cells in the central epiblast (blue box in (**G**)) stimulated the migration of BAI1-labeled Myo/Nog cells (green) from the posterior/medial epiblast (red box in (**G**)) to TUNEL+ cells (red) (**H**). The direction of migration is indicated by the arrow in H. A puncture wound was produced in the day-1 chick embryo lateral to the primitive streak (boxed area in (**I**)). BAI1+ cells (red) surrounded the wound (**J**). BAI1+ (green) cells containing MyoD mRNA (red) were present in niches in explants of fetal chick lens tissue (arrows in (**K**)). Within two days after plating, BAI1+/MyoD mRNA+ cells had migrated to the cut edge of the tissue (arrow in (**L**)). Bar = 5 mM in (**A**,**C**), 56 μM in (**B**,**D**), 2.5 mM in (**E**), 41 μM in (**F**) and 13 μM in (**H**–**L**).

Noggin binds to BMPs -2, -4 and -7 and prevents receptor binding [39,40]. Knockout of BMPs and exogenous or overexpressed Noggin have been used as tools to define the roles of BMPs during lens development [41]. BMPs -2, -4 and -7 are important for the specification of the ectoderm to the lens epithelial cell lineage, formation and invagination of the lens placode and lens fiber cell differentiation [42–52]. Although BMPs are required for eye development, the intensity of their signaling must be regulated [53–55]. Our studies illustrate that Myo/Nog cells' release of Noggin is a physiological mechanism that titrates the effects of BMPs in the lens and this is accomplished with a small number of cells [31].

Another role for Myo/Nog cells was revealed in a control experiment in which a separate subpopulation of cells in the central epiblast was depleted using the D4 mAb and complement [32]. Elimination of D4+ cells reduced the size of the embryo but the eyes appeared normal. Lysis of D4+ cells stimulated a rapid increase in the number of Myo/Nog cells and their migration from the posterior/medial epiblast to dying cells in the central epiblast [32] (Figure 3G,H).

Myo/Nog cells also rapidly accumulate around puncture wounds in the embryo (Figure 3J) and incisions made in the fetal lens to produce capsular bag cultures [56–58] (Figure 3L). BAI1+/MyoD mRNA+ cells were initially present in niches in the lens explants [59] (Figure 3K). Tracking the cells with the anti-BAI1 G8 mAb demonstrated their rapid migration to the cut edges of the tissue (Figure 3L) and synthesis of MyoD protein and alpha-smooth muscle actin (α-SMA) [59], a marker of vascular smooth muscle cells and myofibroblasts [60]. Lysis of Myo/Nog cells with the G8 mAb and complement prevented the emergence of α-SMA+ cells [59]. These studies of embryonic and fetal chick tissues revealed that Myo/Nog cells home to dying cells and wounds. Myo/Nog cells' response to injury in an adult mammalian lens and retina will be described below.

3. Myo/Nog Cells in the Adult Eye

The next phase of our exploration of Myo/Nog cells involved characterizing their behaviors in normal and diseased tissues of adult mammals. Similar to the *chick* embryo, Myo/Nog cells are present in low numbers in all adult tissues and organs analyzed thus far, from *mice* to *humans* [16,61–70]. Within the eye, Myo/Nog cells are residents of the lens, cornea, ciliary body, retina and choroid [16,62,63,66–68,70–72] (Figure 4). They also are present on the zonules of Zinn migrating towards the lens from the ciliary body [64] (Figure 4F). In the adult lens, Myo/Nog cells are associated with LECs in the equatorial, bow and anterior regions and are present but rare among the fiber cells [62,64,66,68] (Figure 4B,C).

Behavior of Myo/Nog Cells in Explant Cultures of Anterior Human Lens Tissue

The behaviors of Myo/Nog cells in the adult lens were initially studied in serum-free explant cultures of anterior tissue removed from patients undergoing cataract surgery. MyoD+, Noggin+ and BAI1+ cells were associated with the apical surface of LECs [62,71]. They were also found at the cut edge of the tissue and surrounding wounds within the epithelium where they extended processes towards wrinkles in the capsule (Figure 5A–C). Myo/Nog cells synthesized α-SMA, sarcomeric myosin and skeletal muscle-specific troponin T and the T-tubule-associated 12,101 protein [62] (Figure 5A–C). Only Noggin+/BAI1+ cells were co-labeled with antibodies to striated muscle proteins [62]. The appearance of MyoD, α-SMA and multiple striated muscle proteins defines the differentiated progeny of Myo/Nog cells as myofibroblasts that were shown decades ago to resemble single-nucleated skeletal myocytes [60,73–76].

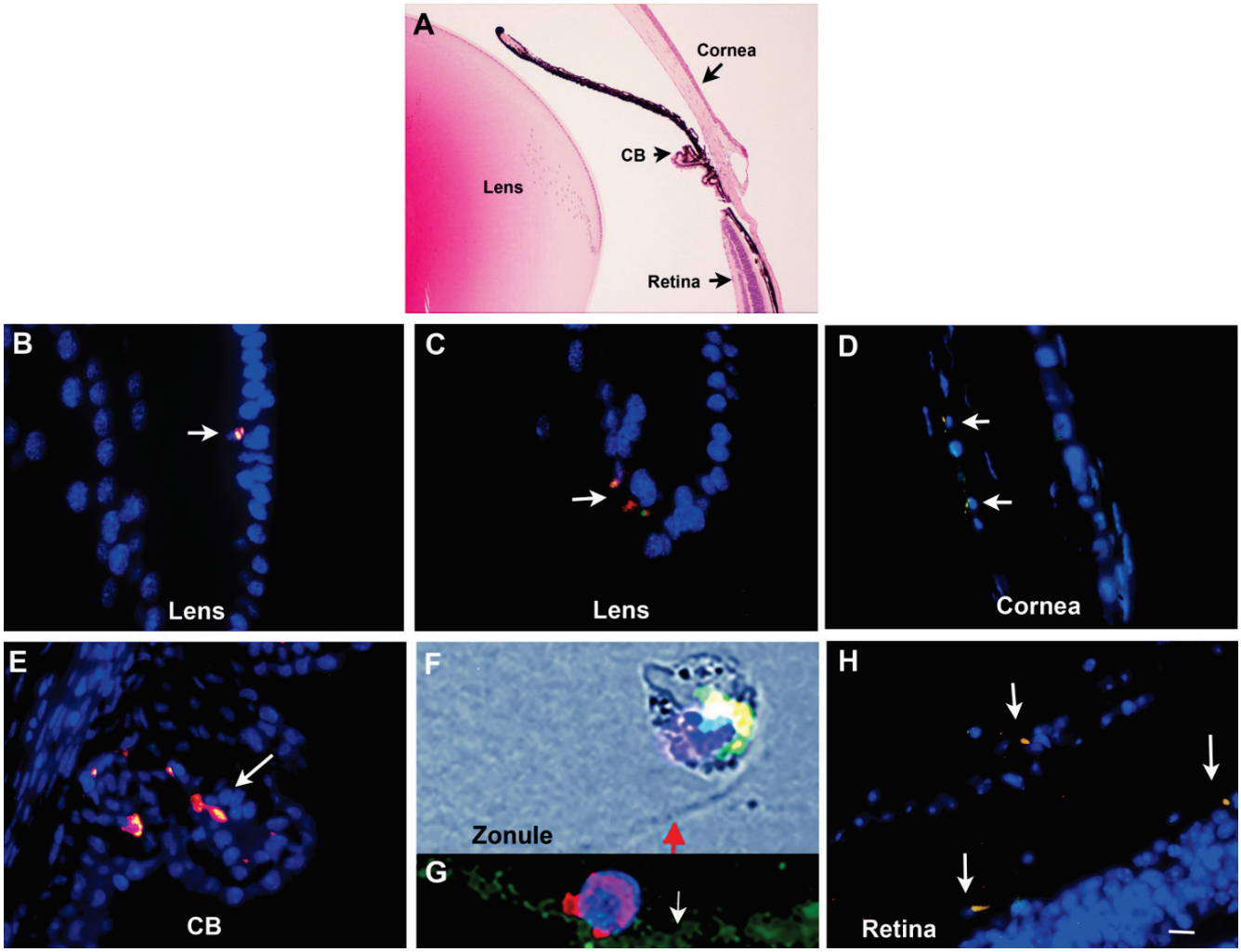

Figure 4. Myo/Nog cells are present throughout the adult *mouse* eye. Sections of the adult *mouse* eye were stained with H&E (**A**) or double-labeled with antibodies to BAI1 (red) and Noggin (**B**–**F**,**H**) or fibrillin (green) (**G**). The overlap of red and green appears yellow in merged images. Nuclei were stained with Hoechst dye (blue). Arrows point to Myo/Nog cells in the equatorial (**B**) and bow regions (**C**) of the lens, the endothelial layer of the cornea (**D**), ciliary body (CB) (**E**) and on the zonules of Zinn (arrows in (**F**,**G**)). Each layer of the retina contained a small number of Myo/Nog cells (**H**). Bar = 55 μM in (**A**), 9 μM in (**B**–**E**,**G**,**H**) and 6.5 μM in (**F**).

Differentiating Myo/Nog cells rapidly filled in a wound produced by scratching the epithelium (Figure 5E,F). Depletion of Myo/Nog cells in *human* lens explants with the anti-BAI1 G8 mAb and complement reduced the number of cells populating the scratch wound (Figure 5G) and eliminated cells with MyoD and striated myosin throughout the explant in 5-day cultures [62]. Expression of α-SMA was detected in LECs lacking BAI1 in explants depleted of Myo/Nog cells and treated with transforming growth factor beta 1 (TGF-β1) [62] (Figure 5). TGF-β2, a known inducer of epithelial to mesenchymal transition and expression of α-SMA in the lens [58,77–88], was added to explant cultures in an effort to stimulate the migration and transdifferentiation of LECS to myofibroblasts in the absence of Myo/Nog cells. TGF-β2, but not TGF-β1, resulted in the loss of the majority of LECs within 48 h [62] (Figure 5H). Co-addition of Noggin prevented LEC loss, and although the cells filled the wound, they did not synthesize MyoD or sarcomeric myosin [62] (Figure 5I,J). These results suggest that the combination of TGF-β2 and hyperactive BMP signaling is toxic to LECs, and Myo/Nog cells may modulate interactions between the two pathways. Combinatorial effects of these signaling pathways was also revealed in explant cultures of

rat lens epithelial cells in which the addition of BMP-7 suppressed TGF-β2′s induction of an epithelial to mesenchymal transition [89].

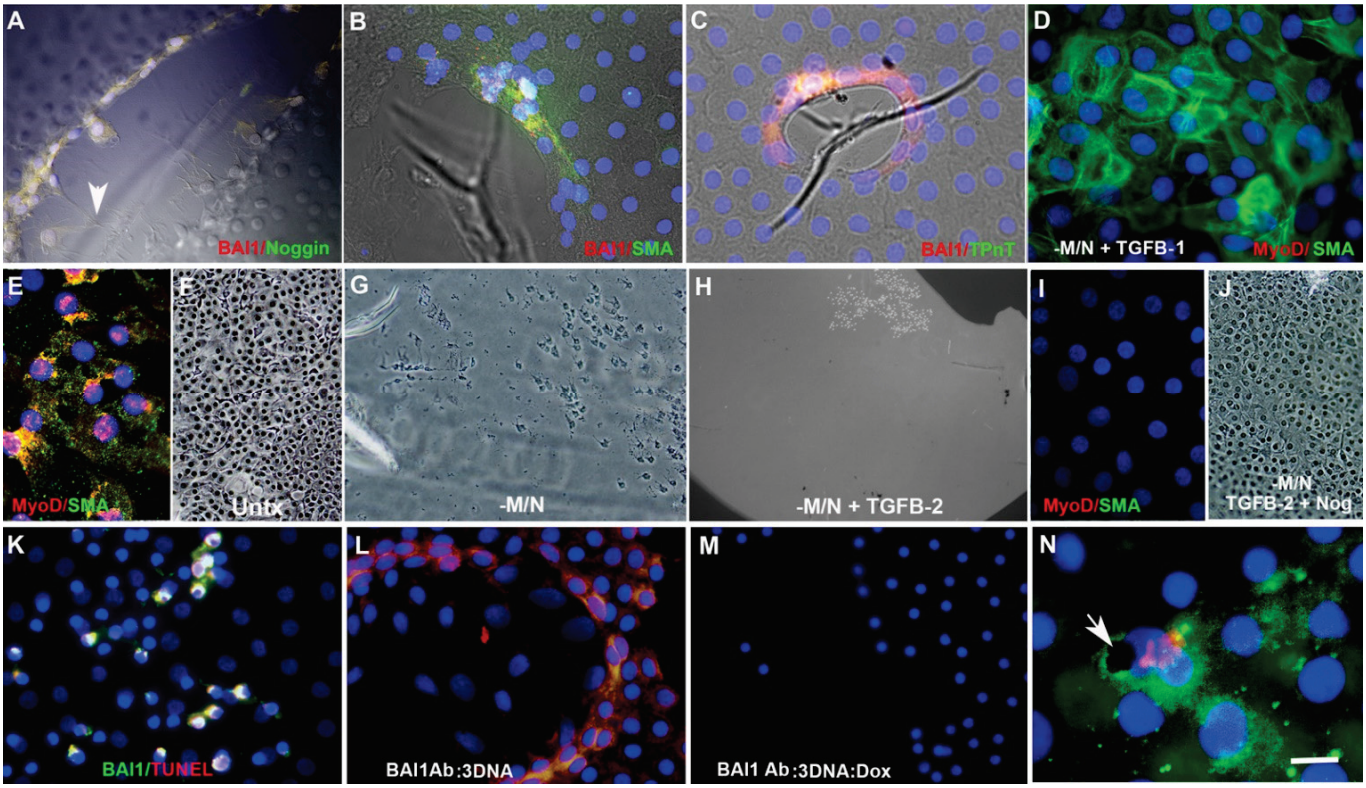

Figure 5. Myo/Nog cells are the source of myofibroblasts and phagocytose dead cells in human anterior lens explant cultures. Anterior lens tissue was obtained from patients undergoing cataract surgery and cultured in serum-free medium. Myo/Nog cells double-labeled with antibodies to BAI1 (red) and Noggin, α-SMA and skeletal muscle-specific troponin T (green) surrounded wounds in the epithelium (**A**–**C**) and extended processes towards wrinkles in the capsule (arrow in (**A**)). They also migrated onto the capsule and synthesized α-SMA after producing a scratch wound in 2-day cultures (**E**). Cells filling the scratch wound in the presence of Myo/Nog cells are shown in the phase contrast photomigraph (**F**). Myo/Nog cells were depleted with the anti-BAI1 mAb and complement (-M/N) (**G**–**J**). Treatment of explants with TGF-β1 after Myo/Nog cell depletion contained α-SMA+/BAI1-cells (**D**). Scratch wounds contained fewer cells on the capsule after Myo/Nog cell depletion (**G**). Incubation with TGF-β2 in the absence of Myo/Nog cells resulted in detachment of most cells from the capsule (**H**). Addition of Noggin (Nog) to TGF-β2 treated cultures prevented detachment and promoted migration into the wound, but the cells did not express MyoD or α-SMA (**I**,**J**). Explants were treated on days 2 and 13 with the BAI1 mAb conjugated to 3DNA nanocarriers intercalated with doxorubicin (BAI1 Ab:3DNA:Dox) (**K**,**M**). TUNEL staining revealed apoptotic BAI1+ cells (**K**). BAI1+/α-SMA+ cells migrated into the scratch wound in 30-day control cultures treated with BAI1 Ab:3DNA lacking doxorubicin (**L**). BAI1+/Noggin+ were not present in explants treated with BAI1 Ab:3DNA:Dox (**M**). Anterior lens explants were labeled with lysosensor red dye and then treated with doxorubicin to induce apoptosis. Treated cells were added to untreated explant cultures. BAI1+ cells (green) phagocytosed cells prelabeled with lysosenser dye (red) and killed with doxorubicin (black) (arrow in **N**). Bar = 9 μM in (**A**–**E**,**I**,**K**–**N**), 27 μM in (**F**–**I**).

The long-term effects of Myo/Nog cell depletion in human lens tissue were explored in 30-day serum-free explant cultures [71]. In these experiments, Myo/Nog cells were depleted with the BAI1 mAb conjugated to 3DNA nanocarriers intercalated with doxorubicin (BAI1 Ab:3DNA:Dox) (Figure 5K). The drug was not toxic to surrounding LECs (Figure 5K). Treatment with BAI1 Ab:3DNA:Dox, but not the conjugate without doxorubicin, on the 1st and 13th days in culture eliminated Myo/Nog cells and myofibroblasts throughout the tissue and within a scratch wound one month after plating (Figure 5L,M). These studies illustrate that Myo/Nog cells are the progenitors of lens myofibroblasts in explants of human anterior lens tissue.

We also utilized the *human* anterior lens explant model to examine the response of Myo/Nog cells to dying cells [68]. Explants were labeled with a dye that remains within the plasma membrane and only fluoresces when phagocytosed into acidic compartments of other cells. The tissue was incubated with a high dose of free doxorubicin, dissociated and the cells were added to untreated explants. BAI1+ Myo/Nog cells engulfed prelabeled dead cells containing doxorubicin [68] (Figure 5N).

Myo/Nog cells also phagocytose beads injected into the anterior chamber to induce glaucoma in *mice*, tattoo ink in human skin and dead cells in the retina [68,70]. Antibodies to markers of the monocyte lineage, ionized calcium binding adaptor molecule 1 (Iba1) and F4/80, did not bind to Myo/Nog cells in the skin, eyes or brain [16,61,68,72]. However, CD68, which is expressed in microglia, macrophages, other leukocytes, fibroblasts and endothelial cells [90,91], was found in a small subpopulation of BAI1+/Noggin+ cells in a *mouse* model of proliferative vitreoretinopathy (PVR) in a study described below [70]. This was not surprising because both CD68 and BAI1 are receptors for phosphatidylserine (PS) present in the outer leaflet of the plasma membrane of apoptotic cells [19,20,92,93]. We are unaware of reports showing that monocytes, macrophages or microglia express MyoD and Noggin, and expression of BAI1 in macrophages is controversial [94]. Therefore, we conclude that the Myo/Nog and monocyte lineages are distinct but have overlapping functions in clearance.

4. Role of Myo/Nog Cells in Posterior Capsule Opacification

A fibrotic wound healing response, called posterior capsule opacification (PCO), occurs in approximately 20% of adults and most children within two years of cataract surgery [95–100]. PCO is characterized by the migration of cells and their differentiation to myofibroblasts whose contractions produce vision-impairing wrinkles in the posterior capsule [87,99,101,102]. We injected BAI1 Ab:3DNA:Dox into the *rabbit* lens during cataract surgery to test whether Myo/Nog cells are progenitors of myofibroblasts that cause PCO in vivo. In this aggressive model of PCO, a minimum of 80% of *rabbits* developed PCO within one month of surgery [66,103]. The drug dramatically reduced the number of myofibroblasts and wrinkles in the capsule without off-target effects [66] (Figure 6A–D). PCO, peripheral and anterior capsule opacification were reduced to below clinically significant levels [66]. This study established that Myo/Nog cells are the progenitors of myofibroblasts in the lens in vivo and revealed a potential therapeutic approach to preventing PCO.

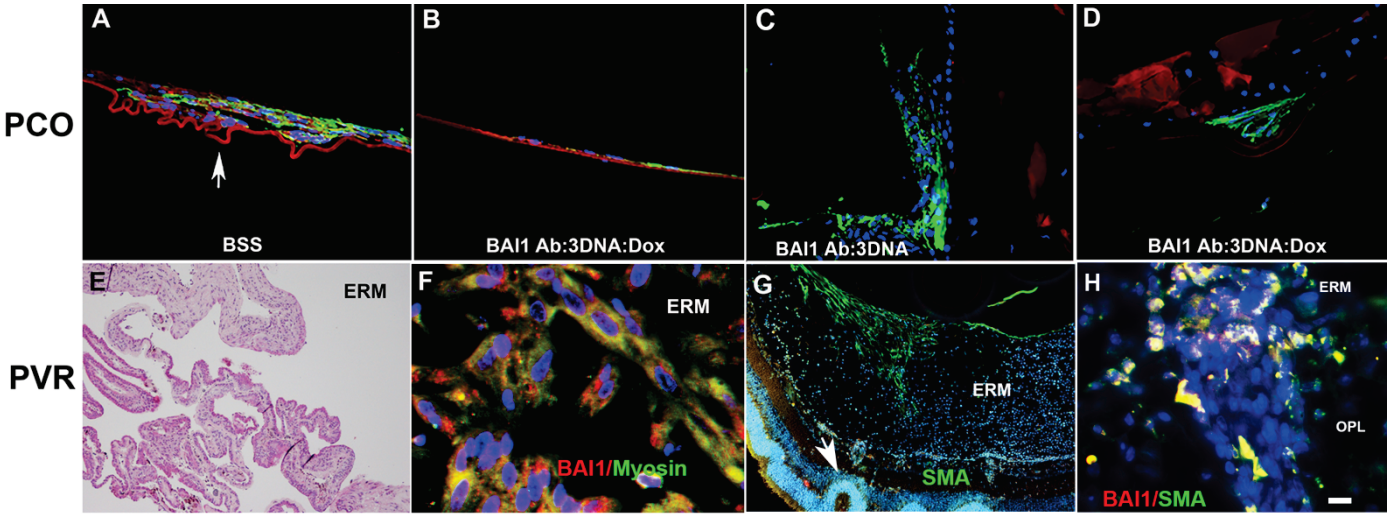

Figure 6. Myo/Nog cells differentiate into myofibroblasts in posterior capsule opacification (PCO) and proliferative vitreoretinopathy (PVR). Rabbit lenses were injected with balanced saline solution (BSS) (**A**,**C**) or BAI1 Ab:3DNA:Dox (**B**,**D**) during cataract surgery. Lenses were harvested 30 days later and sections were labeled with an antibody to SMA (green) (**A**–**D**). SMA and wrinkles (arrow) were abundant in lenses injected with BSS) (**A**). Depletion of Myo/Nog cells significantly reduced α-SMA+ myofibroblasts and wrinkles in the capsule (**B**,**D**). Human epiretinal membranes (ERM) removed from patients with PVR were sectioned and stained with H&E (**E**) or antibodies to BAI1 (red) and striated muscle myosin (green) (**F**). Overlap of red and green in merged images appears yellow. Nuclei were labeled with Hoechst dye (blue). Myosin+ myofibroblasts express BAI1 in human epiretinal membranes (**F**). PVR was induced in the mouse retina by injecting SF6 gas and human ARPE-19 cells into the vitreous. Sections were double labeled with antibodies to BAI1 (red) and α-SMA (green) (**G**,**H**). BAI1+ myofibroblasts were present in epiretinal membranes and throughout the retina (**G**,**H**) and overlaid areas of detachment (arrow in **G**). OPL = outer plexiform layer. Bar = 27 μM in (**A**–**D**), 9 μM in (**E**–**H**) and 135 μM in (**G**).

5. Additional Behaviors of Myo/Nog Cells in the Lens and Related Phenomena in Other Tissues

Having identified Myo/Nog cells as the progenitors of myofibroblasts in the lens, we turned our attention to PVR, a fibrotic disease that most often occurs in response to the repair of rhegmatogenous retinal detachment [104–109]. PVR is characterized by the formation of membranes on the inner surface of the retina (epiretinal), and/or behind or within the retina [104–106]. Myofibroblasts accumulate within the membranes and their contractions apply traction on the retina that may cause re-detachment [104–106,110]. In *human* epiretinal membranes, greater than 99% of cells with α-SMA, MyoD and striated muscle myosin II heavy chain co-expressed BAI1 and Noggin [67] (Figure 6F).

To examine the behavior of Myo/Nog cells during ERM formation, we utilized a *mouse* model in which PVR is induced by injecting SF_6 gas and human retinal pigmented epithelial cells (ARPE-19) into the vitreous [111]. This model recapitulates disease progression seen in *humans* and other species. Myo/Nog cells were present on the inner surface of the retina early in the process of PVR induction and were the predominant cell type in ERMs [70]. They were the only cells that synthesized α-SMA apart from vascular smooth muscle and striated muscle myosin II [70]. Differentiated Myo/Nog cells overlaid retinal folds and areas of detachment (Figure 6G) and were present throughout the retina with disease progression (Figure 6H). Few leukocytes were present in the eye at all stages of PVR, indicating that inflammation did not appear to be a significant factor in Myo/Nog cell activation in this model. However, subpopulations of Myo/Nog cells expressed CD18 and CD45, markers for all leukocytes, and CD68 that is present in cells of the monocyte lineage [70]. We concluded that the death of *human* RPE cells was the likely stimulus for

proliferation and migration of Myo/Nog cells and their engulfment of cell corpses [70], as occurs in other tissues, including the lens [68].

Although Myo/Nog cells are a distinct lineage in the lens, subpopulations of BAI1+ cells in *human* anterior lens explant cultures synthesized the beaded filament proteins filensin and CP49 that were considered specific markers of differentiated lens fibers [112–115]. Less than six percent of the total cells in the tissue fixed within 10 min of capsulorhexis were labeled with BAI1 or beaded filament antibodies [65]. Approximately 52% of filensin+ and 8% of CP49+ subpopulations contained BAI1 [65].

In parallel experiments, we were examining sarcomas with features of skeletal muscle for Myo/Nog cell markers. With the information in hand from lens tissue, we added filensin and CP49 to our screens for BAI1 and Noggin expression. Most cells expressing BAI1 and Noggin in cultures of *human* cell lines derived from alveolar and embryonal rhabdomyosarcoma (RMS) tumors contained beaded filaments [65] (Figure 7A–D). BAI1+/filensin+/CP49+ cells also were found in tissue sections from four subtypes of *human* RMS (Figure 7D–G) and Wilms tumors [65]. Leiomyosarcoma smooth muscle tumors, skin carcinomas, melanomas and normal skeletal muscle contained BAI1+/Noggin+ cells but they lacked detectable levels of filensin and CP49 [65]. These analyses revealed that beaded filament expression occurs outside of the lens and their localization in Myo/Nog-like cells appears to be diagnostic of tumors with features of skeletal muscle.

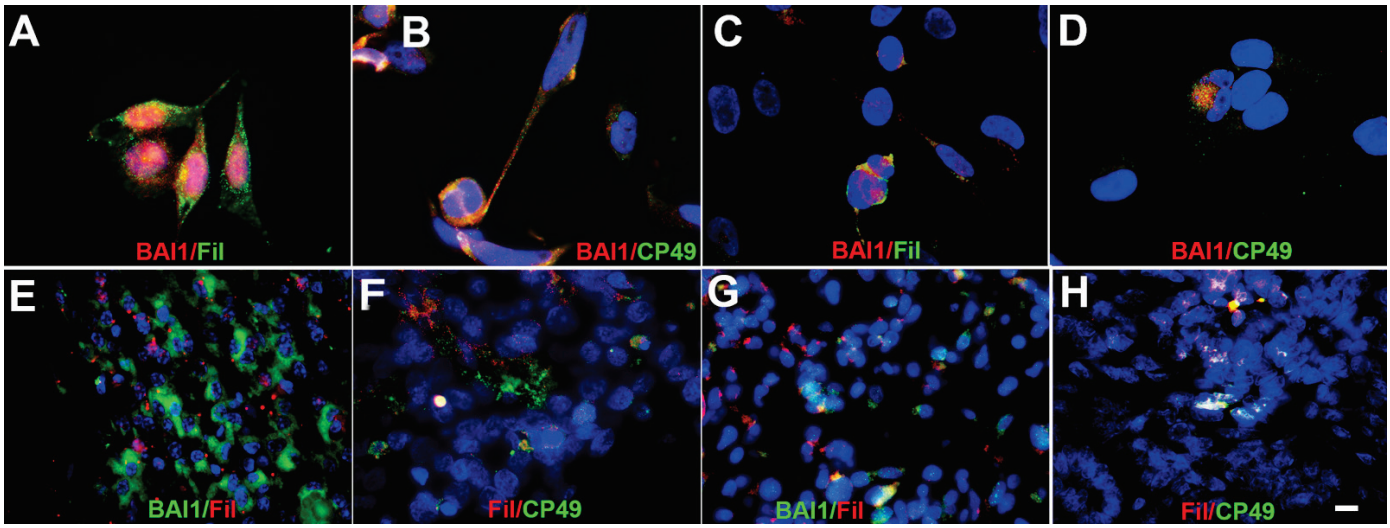

Figure 7. BAI1+ cells in *human* rhabdomyosarcoma cell lines and tumors express beaded filament proteins. Cultures of RC13 (**A**,**B**) and RD RMS cell lines (**C**,**D**) derived from alveolar and embryonal RMS tumors, respectively, were double labeled with antibodies to BAI1 (red) and filensin (Fil) or CP49 (green). Nuclei were stained with Hoechst dye (blue). Both cell lines contained cells that co-expressed BAI1 and beaded filaments (**A**–**D**). Tissue sections of alveolar (**D**,**E**) and embryonal RMS tumors (**F**,**G**) were double-labeled with the BAI1 mAb (green) and an anti-sense probe for filensin mRNA (red) (**D**) or an antibody to filensin (green) (**D**,**F**). Double labels also were performed with antibodies to filensin (red) and CP49 (green) (**E**,**G**). BAI1+ cells expressed filensin and filensin co-localized with CP49 (**D**–**H**). Bar = 9 μM.

6. The Road Ahead

During the past decade, we have focused primarily on testing potential therapeutic applications of depleting or adding Myo/Nog cells in the eye. However, basic questions related to the Myo/Nog lineage during the early stages of development remain unanswered. Although all three markers of Myo/Nog cells are identifiable in a small subpopulation in the blastocyst, it is unknown whether one or all of these molecules are present in the fertilized oocyte and sequestered with cell division or if their expression is induced regionally within the epiblast. Given the stability of expression of MyoD, Noggin and

BAI1, even in the highly inductive environment of the developing embryo, it is reasonable to hypothesize that Myo/Nog cells of the adult are derived from founders in the early epiblast.

Thus far we have not observed evidence for Myo/Nog cell multipotency, and therefore, these cells appear to be progenitors and not stem cells. Are they subject to mutations that promote tumorigenesis with aging, and if so, are they progenitors of RMS and Wilms sarcomas? In this regard, co-expression of Myo/Nog markers with filensin and CP49 within cultured explants of human lens tissue and tumors with features of skeletal muscle, but not other tumors or normal muscle, may provide insight into the regulation of beaded filament expression in Myo/Nog and differentiating LECs and possibly during transformation.

Myo/Nog cell functions during lens development need to be further characterized. Exogenous or overexpressed Noggin delays lens fiber differentiation and expands the undifferentiated anterior lens epithelium [46,47,51,52]. A hypothesis worth testing is that the small population of Myo/Nog cells releases enough Noggin to balance LEC proliferation with differentiation and to maintain a population of lens fiber progenitor cells. Myo/Nog cells may also be involved in early stages of LEC induction, as suggested by studies in which *human* embryonic and induced pluripotent stem cells were treated with Noggin in the first stage of a three-step process to promote the development of lens progenitor cells and lentoid bodies [116–120].

Under homeostatic conditions, Myo/Nog cells are either slowly or non-dividing and synthesize Noggin without detectable translation of MyoD mRNA or expression of skeletal muscle proteins [9,13,15,29,30]. Several stimuli, including cell death, hypoxia, the presence of foreign material and wounding that occurs from surgical excision, abrasion, puncture and light damage, promote the expansion and migration of Myo/Nog cells [32,59,61,62,64,67,69–72]. The rapidity of their activation in adults was demonstrated in the lens in response to cataract surgery [66], the brain after focal injury [69] and in the skin where Myo/Nog cells emerge from their niche associated with hair follicles and populate the wound within 24 h of epidermal abrasion [61]. Paracrine factors that direct the migration of Myo/Nog cells are largely unknown but are predicted to be released from dying cells [121] and alter their adhesive properties as they become mobile and stationary again. The importance of Myo/Nog cell adhesion for differentiation was demonstrated in vitro by optimizing the composition of the extracellular matrix substrate to promote attachment, survival and formation of multinucleated skeletal myofibers [8,14,15].

Myo/Nog cell-derived myofibroblasts in PCO and PVR are, for the most part, single-nucleated cells that appear to lack sarcomeres. Skeletal myoblast fusion was shown to involve BAI1's binding to PS on apoptotic cells in vitro and in vivo [20]. It is possible that BAI1+ myofibroblasts do not fuse due to a paucity of apoptotic cells in the aggregate. The absence of visible striations at the light microscopy level may indicate an absence of integrin beta-1 interactions with other membrane complexes and cytoskeletal elements that mediate sarcomere formation [122].

Contractions produced by Myo/Nog cell-derived myofibroblasts may be beneficial for wound closure in some tissues, but in the lens and retina, force generation perturbs architecture and impairs vision. Targeting Myo/Nog cells to prevent fibrotic disease in the lens is the most straightforward therapeutic application of our basic and translational research. The optimal anti-BAI1:3DNA:Dox concentration for depleting Myo/Nog cells and preventing PCO did not exhibit off-target effects when injected into the rabbit lens [66]. Reduction of Myo/Nog cells following cataract surgery is not expected to adversely affect LECs that remain after polishing and assist with securing the intraocular lens [123].

Myo/Nog cells are also a potential target for preventing PVR and retinal detachment [67,70]. Killing Myo/Nog cells in the normal retina did not appear to affect the tissue; however, in a model of oxygen-induced retinopathy, their depletion resulted in an increase in neuronal cell death [72]. Addition of Myo/Nog cells to the vitreous following severe light damage or into the brain following focal injury decreased cell death [63,69]. Therefore, the outcome of killing Myo/Nog cells to prevent PVR is expected to depend

on the extent to which the retina is compromised at the time of intervention and whether enough of these cells remain or repopulate the tissue to mediate neuroprotection. The mechanism whereby Myo/Nog cells support neuronal viability is under investigation, and once identified, may lead to an approach that combines their depletion with the addition of a neuroprotective factor.

In PCO and PVR, Myo/Nog cell-derived myofibroblasts continue to express BAI1 [66,67,70]. Targeting BAI1 to deliver a cytotoxin could conceivably be used as a non-surgical form of treatment, as well as preventing disease onset. Not all BAI1+/Noggin+ cells express muscle proteins in the fibrotic lens and retina, suggesting that a subpopulation undergoes self-renewal to maintain a pool of progenitor cells during active disease.

Myofibroblasts also appear in other ocular diseases [87]. Myo/Nog cells are present throughout the eye, and therefore, may be a source of myofibroblasts in the cornea, as well as the lens and retina. Behaviors of Myo/Nog cells in glaucoma are also worthy of exploration. Related questions are whether they become activated in response to increased intraocular pressure and if their differentiation and contraction narrow the outflow passages. The phagocytic function of Myo/Nog cells highlights the importance of examining their role in maintaining the patency of the trabecular meshwork and Schlemm's canal for outflow of the aqueous humor. In the lens, Myo/Nog cells' appearance among lens fiber cells raises the possibility that they engage in phagocytosis that may be important for maintaining transparency. The relative contributions of Myo/Nog cells, macrophages and microglia to clearance in the eye are likely to vary between tissues and the extent of inflammation.

Myo/Nog cells' behaviors of populating wounds and phagocytosis are shared with cells that mediate innate immunity. We characterized Myo/Nog cells as non-professional phagocytes to distinguish them from macrophages, microglia, neutrophils and epithelial cells (specialized phagocytes) that also engage in clearance [68]. Additional functions of Myo/Nog cells distinguish them from hematopoietic cell lineages, i.e., regulation of BMP signaling, skeletal myofiber formation and myofibroblast differentiation. Myo/Nog cells fit more broadly into the category of mediators of acquired resilience, defined as a stress-induced regulation of self-protective and self-repair mechanisms [124]. Phagocytosis, homing to wounds, differentiation to contractile myofibroblasts and mediation of neuroprotection are examples of Myo/Nog cells' self-protective and repair behaviors. Our ongoing studies of the role of Myo/Nog cells' production of BAI1 in regulating angiogenesis in the eye may identify another important self-protective mechanism to slow the progression of pathological vascularization.

Our research has identified Myo/Nog cells as sole expressors of BAI1, MyoD and Noggin in the eye, mediators of phagocytosis and the source of myofibroblasts in the lens and retina. Myo/Nog cells are expected to be progenitors of myofibroblasts in other ocular tissues, as well as the heart, lung, kidney and liver whose functions are also compromised by fibrosis. Defining the molecular stimuli that activate Myo/Nog cells and trigger their proliferation, migration and differentiation may lead to additional therapeutic strategies to prevent and treat fibrotic disease. Their roles in regulating BMP signaling, neuroprotection and possibly angiogenesis could also be leveraged for therapeutic purposes.

Author Contributions: J.G. and M.G.-W. conceptualized and administrated the research projects and analyzed and curated the data. J.G. was responsible for development of methodologies, formal analyses, validation of the data and reviewing and editing the manuscript. M.G.-W. wrote the original draft of the manuscript and acquiring funding. All authors have read and agreed to the published version of the manuscript.

Funding: Funding for the studies was obtained from the National Institutes of Health HD33086, HD36650, HD40185, HD043157 and AR052326 to M. George-Weinstein, GM061702 and AR052326 to K. Knudsen, EY08747 and EY024549 to P. FitzGerald, P30EY001319 to A. Kuriyan, HD to J. Lash, CA070739 to S. Gilmour; EY014258 to A. S. Menko, and EY019571 to J. Walker; the March of Dimes Foundation 6-FY409-299, BioStrategies Partners and the Sharpe-Strumia Research Foundation SSRFs 2010–2015 to M. George-Weinstein, W. W. Smith Charitable Trust to M. George-Weinstein and S. Gilmour, an anonymous program project award to M. George-Weinstein, A. Bravo-Nuevo; Research to Prevent Blindness to A. Kuriya, L. Werner and N. Mamalis, Alcon Research Institute and Macula Society to A. Kuryian; the Howard Hughes Medical Institute to H. Weintraub; Genisphere LLC; and the Australian National Health and Medical Research Council Dementia Research Development Fellowship to S. Purushothuman.

Institutional Review Board Statement: Studies involving human tissue were approved by the Institutional Review Board of the Philadelphia College of Osteopathic Medicine. The investigations were carried out following the rules of the Declaration of Helsinki of 1975 (https://www.wma.net/what-we-do/medical-ethics/declaration-of-helsinki/), revised in 2013. URL last accessed on 23 June 2023. Informed consent was obtained from all subjects involved in the studies.

Informed Consent Statement: All research involving animals was approved by Institutional Animal Care and Use Committees.

Data Availability Statement: The RC13 and RD rhabdomyosarcoma cell lines were obtained from the American Type Culture Collection.

Acknowledgments: The authors acknowledge the invaluable contributions of our collaborators, students and colleagues from PolyProbe, Inc., Genisphere LLC and CodeBio Therapeutics. This manuscript is dedicated to the memories of these outstanding scientists and our esteemed colleagues, Karen Knudsen, Jay Lash and Harold Weintraub.

Conflicts of Interest: The authors are co-inventors of a patent describing the use of the G8 mAb to target and isolate BAI1-expressing cells. The authors have no financial relationship surrounding this technology.

References

1. Pownall, M.E.; Gustafsson, M.K.; Emerson, C.P., Jr. Myogenic regulatory factors and the specification of muscle progenitors in vertebrate embryos. *Annu. Rev. Cell Dev. Biol.* **2002**, *18*, 747–783. [CrossRef] [PubMed]
2. Buckingham, M.; Vincent, S.D. Distinct and dynamic myogenic populations in the vertebrate embryo. *Curr. Opin. Genet. Dev.* **2009**, *19*, 444–453. [CrossRef] [PubMed]
3. Chal, J.; Pourquie, O. Making muscle: Skeletal myogenesis in vivo and in vitro. *Development* **2017**, *144*, 2104–2122. [CrossRef]
4. Scaal, M.; Marcelle, C. Chick muscle development. *Int. J. Dev. Biol.* **2018**, *62*, 127–136. [CrossRef]
5. Choi, J.; Schultheiss, T.; Lu, M.; Wachtler, F.; Kuruc, N.; Franke, W.W.; Bader, D.; Fischman, D.A.; Holtzer, H. Founder cells for the cardiac and skeletal myogenic lineages. In precursors are critical components of cell fate analyses. In *Cellular and Molecular Biology of Muscle Development*; Stockdale, L.H.K.a.F.E., Ed.; A. R. Liss: New York, NY, USA, 1989; pp. 27–36.
6. Chen, Y.; Solursh, M. The determination of myogenic and cartilage cells in the early chick embryo and the modifying effect of retinoic acid. *Rouxs Arch. Dev. Biol.* **1991**, *200*, 162–171. [CrossRef]
7. George-Weinstein, M.; Gerhart, J.V.; Foti, G.J.; Lash, J.W. Maturation of myogenic and chondrogenic cells in the presomitic mesoderm of the chick embryo. *Exp. Cell Res.* **1994**, *211*, 263–274. [CrossRef]
8. George-Weinstein, M.; Gerhart, J.; Reed, R.; Flynn, J.; Callihan, B.; Mattiacci, M.; Miehle, C.; Foti, G.; Lash, J.W.; Weintraub, H. Skeletal myogenesis: The preferred pathway of chick embryo epiblast cells in vitro. *Dev. Biol.* **1996**, *173*, 279–291. [CrossRef]
9. Gerhart, J.; Baytion, M.; DeLuca, S.; Getts, R.; Lopez, C.; Niewenhuis, R.; Nilsen, T.; Olex, S.; Weintraub, H.; George-Weinstein, M. DNA dendrimers localize MyoD mRNA in presomitic tissues of the chick embryo. *J. Cell Biol.* **2000**, *149*, 825–834. [CrossRef]
10. Buckingham, M.; Rigby, P.W. Gene regulatory networks and transcriptional mechanisms that control myogenesis. *Dev. Cell* **2014**, *28*, 225–238. [CrossRef]
11. Hernandez-Hernandez, J.M.; Garcia-Gonzalez, E.G.; Brun, C.E.; Rudnicki, M.A. The myogenic regulatory factors, determinants of muscle development, cell identity and regeneration. *Semin. Cell Dev. Biol.* **2017**, *72*, 10–18. [CrossRef] [PubMed]
12. Lassar, A.B. Finding MyoD and lessons learned along the way. *Semin. Cell Dev. Biol.* **2017**, *72*, 3–9. [CrossRef] [PubMed]
13. Gerhart, J.; Bast, B.; Neely, C.; Iem, S.; Amegbe, P.; Niewenhuis, R.; Miklasz, S.; Cheng, P.F.; George-Weinstein, M. MyoD-positive myoblasts are present in mature fetal organs lacking skeletal muscle. *J. Cell Biol.* **2001**, *155*, 381–392. [CrossRef]
14. Gerhart, J.; Neely, C.; Stewart, B.; Perlman, J.; Beckmann, D.; Wallon, M.; Knudsen, K.; George-Weinstein, M. Epiblast cells that express MyoD recruit pluripotent cells to the skeletal muscle lineage. *J. Cell Biol.* **2004**, *164*, 739–746. [CrossRef]

15. Strony, R.; Gerhart, J.; Tornambe, D.; Perlman, J.; Neely, C.; Dare, J.; Stewart, B.; George-Weinstein, M. NeuroM and MyoD are expressed in separate subpopulations of cells in the pregastrulating epiblast. *Gene Expr. Patterns* **2005**, *5*, 387–395. [CrossRef]
16. Gerhart, J.; Bowers, J.; Gugerty, L.; Gerhart, C.; Martin, M.; Abdalla, F.; Bravo-Nuevo, A.; Sullivan, J.T.; Rimkunas, R.; Albertus, A.J.; et al. Brain-specific angiogenesis inhibitor 1 is expressed in the Myo/Nog cell lineage. *PLoS ONE* **2020**, *15*, e0234792. [CrossRef]
17. Stephenson, J.R.; Purcell, R.H.; Hall, R.A. The BAI subfamily of adhesion GPCRs: Synaptic regulation and beyond. *Trends Pharmacol. Sci.* **2014**, *35*, 208–215. [CrossRef] [PubMed]
18. Nishimori, H.; Shiratsuchi, T.; Urano, T.; Kimura, Y.; Kiyono, K.; Tatsumi, K.; Yoshida, S.; Ono, M.; Kuwano, M.; Nakamura, Y.; et al. A novel brain-specific p53-target gene, BAI1, containing thrombospondin type 1 repeats inhibits experimental angiogenesis. *Oncogene* **1997**, *15*, 2145–2150. [CrossRef]
19. Park, D.; Tosello-Trampont, A.C.; Elliott, M.R.; Lu, M.; Haney, L.B.; Ma, Z.; Klibanov, A.L.; Mandell, J.W.; Ravichandran, K.S. BAI1 is an engulfment receptor for apoptotic cells upstream of the ELMO/Dock180/Rac module. *Nature* **2007**, *450*, 430–434. [CrossRef] [PubMed]
20. Hochreiter-Hufford, A.E.; Lee, C.S.; Kinchen, J.M.; Sokolowski, J.D.; Arandjelovic, S.; Call, J.A.; Klibanov, A.L.; Yan, Z.; Mandell, J.W.; Ravichandran, K.S. Phosphatidylserine receptor BAI1 and apoptotic cells as new promoters of myoblast fusion. *Nature* **2013**, *497*, 263–267. [CrossRef]
21. Kaur, B.; Brat, D.J.; Devi, N.S.; Van Meir, E.G. Vasculostatin, a proteolytic fragment of brain angiogenesis inhibitor 1, is an antiangiogenic and antitumorigenic factor. *Oncogene* **2005**, *24*, 3632–3642. [CrossRef]
22. Zhu, D.; Li, C.; Swanson, A.M.; Villalba, R.M.; Guo, J.; Zhang, Z.; Matheny, S.; Murakami, T.; Stephenson, J.R.; Daniel, S.; et al. BAI1 regulates spatial learning and synaptic plasticity in the hippocampus. *J. Clin. Investig.* **2015**, *125*, 1497–1508. [CrossRef]
23. Billings, E.A.; Lee, C.S.; Owen, K.A.; D'Souza, R.S.; Ravichandran, K.S.; Casanova, J.E. The adhesion GPCR BAI1 mediates macrophage ROS production and microbicidal activity against Gram-negative bacteria. *Sci. Signal.* **2016**, *9*, ra14. [CrossRef] [PubMed]
24. Elliott, M.R.; Zheng, S.; Park, D.; Woodson, R.I.; Reardon, M.A.; Juncadella, I.J.; Kinchen, J.M.; Zhang, J.; Lysiak, J.J.; Ravichandran, K.S. Unexpected requirement for ELMO1 in clearance of apoptotic germ cells in vivo. *Nature* **2010**, *467*, 333–337. [CrossRef]
25. Hirsinger, E.; Duprez, D.; Jouve, C.; Malapert, P.; Cooke, J.; Pourquie, O. Noggin acts downstream of Wnt and Sonic Hedgehog to antagonize BMP4 in avian somite patterning. *Development* **1997**, *124*, 4605–4614. [CrossRef]
26. Dietrich, S.; Schubert, F.R.; Healy, C.; Sharpe, P.T.; Lumsden, A. Specification of the hypaxial musculature. *Development* **1998**, *125*, 2235–2249. [CrossRef]
27. Reshef, R.; Maroto, M.; Lassar, A.B. Regulation of dorsal somitic cell fates: BMPs and Noggin control the timing and pattern of myogenic regulator expression. *Genes Dev.* **1998**, *12*, 290–303. [CrossRef] [PubMed]
28. Tonegawa, A.; Takahashi, Y. Somitogenesis controlled by Noggin. *Dev. Biol.* **1998**, *202*, 172–182. [CrossRef]
29. Gerhart, J.; Elder, J.; Neely, C.; Schure, J.; Kvist, T.; Knudsen, K.; George-Weinstein, M. MyoD-positive epiblast cells regulate skeletal muscle differentiation in the embryo. *J. Cell Biol.* **2006**, *175*, 283–292. [CrossRef]
30. Gerhart, J.; Neely, C.; Elder, J.; Pfautz, J.; Perlman, J.; Narciso, L.; Linask, K.K.; Knudsen, K.; George-Weinstein, M. Cells that express MyoD mRNA in the epiblast are stably committed to the skeletal muscle lineage. *J. Cell Biol.* **2007**, *178*, 649–660. [CrossRef]
31. Gerhart, J.; Pfautz, J.; Neely, C.; Elder, J.; DuPrey, K.; Menko, A.S.; Knudsen, K.; George-Weinstein, M. Noggin producing, MyoD-positive cells are crucial for eye development. *Dev. Biol.* **2009**, *336*, 30–41. [CrossRef] [PubMed]
32. Gerhart, J.; Scheinfeld, V.L.; Milito, T.; Pfautz, J.; Neely, C.; Fisher-Vance, D.; Sutter, K.; Crawford, M.; Knudsen, K.; George-Weinstein, M. Myo/Nog cell regulation of bone morphogenetic protein signaling in the blastocyst is essential for normal morphogenesis and striated muscle lineage specification. *Dev. Biol.* **2011**, *359*, 12–25. [CrossRef]
33. Anderson, R.M.; Lawrence, A.R.; Stottmann, R.W.; Bachiller, D.; Klingensmith, J. Chordin and noggin promote organizing centers of forebrain development in the mouse. *Development* **2002**, *129*, 4975–4987. [CrossRef]
34. Bachiller, D.; Klingensmith, J.; Kemp, C.; Belo, J.A.; Anderson, R.M.; May, S.R.; McMahon, J.A.; McMahon, A.P.; Harland, R.M.; Rossant, J.; et al. The organizer factors Chordin and Noggin are required for mouse forebrain development. *Nature* **2000**, *403*, 658–661. [CrossRef]
35. Brunet, L.J.; McMahon, J.A.; McMahon, A.P.; Harland, R.M. Noggin, cartilage morphogenesis, and joint formation in the mammalian skeleton. *Science* **1998**, *280*, 1455–1457. [CrossRef]
36. Choi, M.; Stottmann, R.W.; Yang, Y.P.; Meyers, E.N.; Klingensmith, J. The bone morphogenetic protein antagonist noggin regulates mammalian cardiac morphogenesis. *Circ. Res.* **2007**, *100*, 220–228. [CrossRef] [PubMed]
37. McMahon, J.A.; Takada, S.; Zimmerman, L.B.; Fan, C.M.; Harland, R.M.; McMahon, A.P. Noggin-mediated antagonism of BMP signaling is required for growth and patterning of the neural tube and somite. *Genes Dev.* **1998**, *12*, 1438–1452. [CrossRef]
38. Stottmann, R.W.; Berrong, M.; Matta, K.; Choi, M.; Klingensmith, J. The BMP antagonist Noggin promotes cranial and spinal neurulation by distinct mechanisms. *Dev. Biol.* **2006**, *295*, 647–663. [CrossRef]
39. Gazzerro, E.; Canalis, E. Bone morphogenetic proteins and their antagonists. *Rev. Endocr. Metab. Disord.* **2006**, *7*, 51–65. [CrossRef] [PubMed]
40. Zimmerman, L.B.; De Jesus-Escobar, J.M.; Harland, R.M. The Spemann organizer signal noggin binds and inactivates bone morphogenetic protein 4. *Cell* **1996**, *86*, 599–606. [CrossRef] [PubMed]

41. Shu, D.Y.; Lovicu, F.J. Insights into Bone Morphogenetic Protein-(BMP-) Signaling in Ocular Lens Biology and Pathology. *Cells* **2021**, *10*, 2604. [CrossRef]
42. Furuta, Y.; Hogan, B.L. BMP4 is essential for lens induction in the mouse embryo. *Genes Dev.* **1998**, *12*, 3764–3775. [CrossRef] [PubMed]
43. Dudley, A.T.; Lyons, K.M.; Robertson, E.J. A requirement for bone morphogenetic protein-7 during development of the mammalian kidney and eye. *Genes Dev.* **1995**, *9*, 2795–2807. [CrossRef]
44. Jena, N.; Martin-Seisdedos, C.; McCue, P.; Croce, C.M. BMP7 null mutation in mice: Developmental defects in skeleton, kidney, and eye. *Exp. Cell Res.* **1997**, *230*, 28–37. [CrossRef] [PubMed]
45. Wawersik, S.; Purcell, P.; Rauchman, M.; Dudley, A.T.; Robertson, E.J.; Maas, R. BMP7 acts in murine lens placode development. *Dev. Biol.* **1999**, *207*, 176–188. [CrossRef]
46. Faber, S.C.; Robinson, M.L.; Makarenkova, H.P.; Lang, R.A. Bmp signaling is required for development of primary lens fiber cells. *Development* **2002**, *129*, 3727–3737. [CrossRef]
47. Beebe, D.; Garcia, C.; Wang, X.; Rajagopal, R.; Feldmeier, M.; Kim, J.Y.; Chytil, A.; Moses, H.; Ashery-Padan, R.; Rauchman, M. Contributions by members of the TGFbeta superfamily to lens development. *Int. J. Dev. Biol.* **2004**, *48*, 845–856. [CrossRef]
48. Chang, B.; Smith, R.S.; Peters, M.; Savinova, O.V.; Hawes, N.L.; Zabaleta, A.; Nusinowitz, S.; Martin, J.E.; Davisson, M.L.; Cepko, C.L.; et al. Haploinsufficient Bmp4 ocular phenotypes include anterior segment dysgenesis with elevated intraocular pressure. *BMC Genet.* **2001**, *2*, 18. [CrossRef]
49. Solursh, M.; Langille, R.M.; Wood, J.; Sampath, T.K. Osteogenic protein-1 is required for mammalian eye development. *Biochem. Biophys. Res. Commun.* **1996**, *218*, 438–443. [CrossRef]
50. de Iongh, R.U.; Lovicu, F.J.; Overbeek, P.A.; Schneider, M.D.; Joya, J.; Hardeman, E.D.; McAvoy, J.W. Requirement for TGFbeta receptor signaling during terminal lens fiber differentiation. *Development* **2001**, *128*, 3995–4010. [CrossRef]
51. Belecky-Adams, T.L.; Adler, R.; Beebe, D.C. Bone morphogenetic protein signaling and the initiation of lens fiber cell differentiation. *Development* **2002**, *129*, 3795–3802. [CrossRef] [PubMed]
52. Boswell, B.A.; Overbeek, P.A.; Musil, L.S. Essential role of BMPs in FGF-induced secondary lens fiber differentiation. *Dev. Biol.* **2008**, *324*, 202–212. [CrossRef] [PubMed]
53. Sjodal, M.; Edlund, T.; Gunhaga, L. Time of exposure to BMP signals plays a key role in the specification of the olfactory and lens placodes ex vivo. *Dev. Cell* **2007**, *13*, 141–149. [CrossRef] [PubMed]
54. Hung, F.C.; Zhao, S.; Chen, Q.; Overbeek, P.A. Retinal ablation and altered lens differentiation induced by ocular overexpression of BMP7. *Vis. Res.* **2002**, *42*, 427–438. [CrossRef] [PubMed]
55. Huang, J.; Liu, Y.; Filas, B.; Gunhaga, L.; Beebe, D.C. Negative and positive auto-regulation of BMP expression in early eye development. *Dev. Biol.* **2015**, *407*, 256–264. [CrossRef]
56. Liu, C.S.; Wormstone, I.M.; Duncan, G.; Marcantonio, J.M.; Webb, S.F.; Davies, P.D. A study of human lens cell growth in vitro. A model for posterior capsule opacification. *Investig. Ophthalmol. Vis. Sci.* **1996**, *37*, 906–914.
57. Wormstone, I.M.; Liu, C.S.; Rakic, J.M.; Marcantonio, J.M.; Vrensen, G.F.; Duncan, G. Human lens epithelial cell proliferation in a protein-free medium. *Investig. Ophthalmol. Vis. Sci.* **1997**, *38*, 396–404.
58. Saxby, L.; Rosen, E.; Boulton, M. Lens epithelial cell proliferation, migration, and metaplasia following capsulorhexis. *Br. J. Ophthalmol.* **1998**, *82*, 945–952. [CrossRef]
59. Walker, J.L.; Zhai, N.; Zhang, L.; Bleaken, B.M.; Wolff, I.; Gerhart, J.; George-Weinstein, M.; Menko, A.S. Unique precursors for the mesenchymal cells involved in injury response and fibrosis. *Proc. Natl. Acad. Sci. USA* **2010**, *107*, 13730–13735. [CrossRef]
60. Gabbiani, G. The myofibroblast in wound healing and fibrocontractive diseases. *J. Pathol.* **2003**, *200*, 500–503. [CrossRef]
61. Gerhart, J.; Hayes, C.; Scheinfeld, V.; Chernick, M.; Gilmour, S.; George-Weinstein, M. Myo/Nog cells in normal, wounded and tumor-bearing skin. *Exp. Dermatol.* **2012**, *21*, 466–468. [CrossRef]
62. Gerhart, J.; Greenbaum, M.; Scheinfeld, V.; Fitzgerald, P.; Crawford, M.; Bravo-Nuevo, A.; Pitts, M.; George-Weinstein, M. Myo/Nog cells: Targets for preventing the accumulation of skeletal muscle-like cells in the human lens. *PLoS ONE* **2014**, *9*, e95262. [CrossRef] [PubMed]
63. Brandli, A.; Gerhart, J.; Sutera, C.K.; Purushothuman, S.; George-Weinstein, M.; Stone, J.; Bravo-Nuevo, A. Role of Myo/Nog Cells in Neuroprotection: Evidence from the Light Damaged Retina. *PLoS ONE* **2017**, *12*, e0169744. [CrossRef] [PubMed]
64. Gerhart, J.; Withers, C.; Gerhart, C.; Werner, L.; Mamalis, N.; Bravo-Nuevo, A.; Scheinfeld, V.; FitzGerald, P.; Getts, R.; George-Weinstein, M. Myo/Nog cells are present in the ciliary processes, on the zonule of Zinn and posterior capsule of the lens following cataract surgery. *Exp. Eye Res.* **2018**, *171*, 101–105. [CrossRef]
65. Gerhart, J.; Behling, K.; Paessler, M.; Milton, L.; Bramblett, G.; Garcia, D.; Pitts, M.; Hurtt, R.; Crawford, M.; Lackman, R.; et al. Rhabdomyosarcoma and Wilms tumors contain a subpopulation of noggin producing, myogenic cells immunoreactive for lens beaded filament proteins. *PLoS ONE* **2019**, *14*, e0214758. [CrossRef] [PubMed]
66. Gerhart, J.; Werner, L.; Mamalis, N.; Infanti, J.; Withers, C.; Abdalla, F.; Gerhart, C.; Bravo-Nuevo, A.; Gerhart, O.; Getts, L.; et al. Depletion of Myo/Nog Cells in the Lens Mitigates Posterior Capsule Opacification in Rabbits. *Investig. Ophthalmol. Vis. Sci.* **2019**, *60*, 1813–1823. [CrossRef]
67. Gerhart, J.; Morrison, N.; Gugerty, L.; Telander, D.; Bravo-Nuevo, A.; George-Weinstein, M. Myo/Nog cells expressing muscle proteins are present in preretinal membranes from patients with proliferative vitreoretinopathy. *Exp. Eye Res.* **2020**, *197*, 108080. [CrossRef]

68. Gerhart, J.; Gugerty, L.; Lecker, P.; Abdalla, F.; Martin, M.; Gerhart, O.; Gerhart, C.; Johal, K.; Bernstein, J.; Spikes, J.; et al. Myo/Nog cells are nonprofessional phagocytes. *PLoS ONE* **2020**, *15*, e0235898. [CrossRef]
69. Joseph-Pauline, S.; Morrison, N.; Braccia, M.; Payne, A.; Gugerty, L.; Mostoller, J.; Lecker, P.; Tsai, E.J.; Kim, J.; Martin, M.; et al. Acute Response and Neuroprotective Role of Myo/Nog Cells Assessed in a Rat Model of Focal Brain Injury. *Front. Neurosci.* **2021**, *15*, 780707. [CrossRef]
70. Crispin, M.; Gerhart, J.; Heffer, A.; Martin, M.; Abdalla, F.; Bravo-Nuevo, A.; Philp, N.J.; Kuriyan, A.E.; George-Weinstein, M. Myo/Nog Cells Give Rise to Myofibroblasts during Epiretinal Membrane Formation in a Mouse Model of Proliferative Vitreoretinopathy. *Investig. Ophthalmol. Vis. Sci.* **2023**, *64*, 1. [CrossRef]
71. Gerhart, J.; Greenbaum, M.; Casta, L.; Clemente, A.; Mathers, K.; Getts, R.; George-Weinstein, M. Antibody-Conjugated, DNA-Based Nanocarriers Intercalated with Doxorubicin Eliminate Myofibroblasts in Explants of Human Lens Tissue. *J. Pharmacol. Exp. Ther.* **2017**, *361*, 60–67. [CrossRef]
72. Bravo-Nuevo, A.; Brandli, A.A.; Gerhart, J.; Nichols, J.; Pitts, M.; Sutera, C.K.; Assali, S.; Scheinfeld, V.; Prendergast, G.C.; Stone, J.; et al. Neuroprotective effect of Myo/Nog cells in the stressed retina. *Exp. Eye Res.* **2016**, *146*, 22–25. [CrossRef] [PubMed]
73. Sappino, A.P.; Schurch, W.; Gabbiani, G. Differentiation repertoire of fibroblastic cells: Expression of cytoskeletal proteins as marker of phenotypic modulations. *Lab. Investig.* **1990**, *63*, 144–161. [PubMed]
74. Schaart, G.; Pieper, F.R.; Kuijpers, H.J.; Bloemendal, H.; Ramaekers, F.C. Baby hamster kidney (BHK-21/C13) cells can express striated muscle type proteins. *Differentiation* **1991**, *46*, 105–115. [CrossRef]
75. Ogata, I.; Saez, C.G.; Greenwel, P.; Ponce, M.d.L.; Geerts, A.; Leinwand, L.A.; Rojkind, M. Rat liver fat-storing cell lines express sarcomeric myosin heavy chain mRNA and protein. *Cell Motil. Cytoskelet.* **1993**, *26*, 125–132. [CrossRef]
76. Mayer, D.C.; Leinwand, L.A. Sarcomeric gene expression and contractility in myofibroblasts. *J. Cell Biol.* **1997**, *139*, 1477–1484. [CrossRef]
77. Wormstone, I.M.; Tamiya, S.; Anderson, I.; Duncan, G. TGF-beta2-induced matrix modification and cell transdifferentiation in the human lens capsular bag. *Investig. Ophthalmol. Vis. Sci.* **2002**, *43*, 2301–2308.
78. Liu, J.; Hales, A.M.; Chamberlain, C.G.; McAvoy, J.W. Induction of cataract-like changes in rat lens epithelial explants by transforming growth factor beta. *Investig. Ophthalmol. Vis. Sci.* **1994**, *35*, 388–401.
79. Kurosaka, D.; Muraki, Y.; Inoue, M.; Katsura, H. TGF-beta 2 increases alpha-smooth muscle actin expression in bovine retinal pigment epithelial cells. *Curr. Eye Res.* **1996**, *15*, 1144–1147. [CrossRef]
80. Gordon-Thomson, C.; de Iongh, R.U.; Hales, A.M.; Chamberlain, C.G.; McAvoy, J.W. Differential cataractogenic potency of TGF-beta1, -beta2, and -beta3 and their expression in the postnatal rat eye. *Investig. Ophthalmol. Vis. Sci.* **1998**, *39*, 1399–1409.
81. Richiert, D.M.; Ireland, M.E. TGF-beta elicits fibronectin secretion and proliferation in cultured chick lens epithelial cells. *Curr. Eye Res.* **1999**, *18*, 62–71. [CrossRef] [PubMed]
82. Lee, E.H.; Joo, C.K. Role of transforming growth factor-beta in transdifferentiation and fibrosis of lens epithelial cells. *Investig. Ophthalmol. Vis. Sci.* **1999**, *40*, 2025–2032.
83. Marcantonio, J.M.; Rakic, J.M.; Vrensen, G.F.; Duncan, G. Lens cell populations studied in human donor capsular bags with implanted intraocular lenses. *Investig. Ophthalmol. Vis. Sci.* **2000**, *41*, 1130–1141.
84. Saika, S.; Okada, Y.; Miyamoto, T.; Ohnishi, Y.; Ooshima, A.; McAvoy, J.W. Smad translocation and growth suppression in lens epithelial cells by endogenous TGFbeta2 during wound repair. *Exp. Eye Res.* **2001**, *72*, 679–686. [CrossRef]
85. Wormstone, I.M.; Tamiya, S.; Eldred, J.A.; Lazaridis, K.; Chantry, A.; Reddan, J.R.; Anderson, I.; Duncan, G. Characterisation of TGF-beta2 signalling and function in a human lens cell line. *Exp. Eye Res.* **2004**, *78*, 705–714. [CrossRef]
86. Dawes, L.J.; Eldred, J.A.; Anderson, I.K.; Sleeman, M.; Reddan, J.R.; Duncan, G.; Wormstone, I.M. TGF beta-induced contraction is not promoted by fibronectin-fibronectin receptor interaction, or alpha SMA expression. *Investig. Ophthalmol. Vis. Sci.* **2008**, *49*, 650–661. [CrossRef] [PubMed]
87. Shu, D.Y.; Lovicu, F.J. Myofibroblast transdifferentiation: The dark force in ocular wound healing and fibrosis. *Prog. Retin. Eye Resarch* **2017**, *60*, 44–65. [CrossRef]
88. Flokis, M.; Lovicu, F.J. FGF-2 Differentially Regulates Lens Epithelial Cell Behaviour during TGF-beta-Induced EMT. *Cells* **2023**, *12*, 827. [CrossRef]
89. Shu, D.Y.; Wojciechowski, M.C.; Lovicu, F.J. Bone Morphogenetic Protein-7 Suppresses TGFbeta2-Induced Epithelial-Mesenchymal Transition in the Lens: Implications for Cataract Prevention. *Investig. Ophthalmol. Vis. Sci.* **2017**, *58*, 781–796. [CrossRef]
90. Ramprasad, M.P.; Terpstra, V.; Kondratenko, N.; Quehenberger, O.; Steinberg, D. Cell surface expression of mouse macrosialin and human CD68 and their role as macrophage receptors for oxidized low density lipoprotein. *Proc. Natl. Acad. Sci. USA* **1996**, *93*, 14833–14838. [CrossRef]
91. Gottfried, E.; Kunz-Schughart, L.A.; Weber, A.; Rehli, M.; Peuker, A.; Muller, A.; Kastenberger, M.; Brockhoff, G.; Andreesen, R.; Kreutz, M. Expression of CD68 in non-myeloid cell types. *Scand. J. Immunol.* **2008**, *67*, 453–463. [CrossRef]
92. Sokolowski, J.D.; Nobles, S.L.; Heffron, D.S.; Park, D.; Ravichandran, K.S.; Mandell, J.W. Brain-specific angiogenesis inhibitor-1 expression in astrocytes and neurons: Implications for its dual function as an apoptotic engulfment receptor. *Brain Behav. Immun.* **2011**, *25*, 915–921. [CrossRef] [PubMed]

93. Sambrano, G.R.; Steinberg, D. Recognition of oxidatively damaged and apoptotic cells by an oxidized low density lipoprotein receptor on mouse peritoneal macrophages: Role of membrane phosphatidylserine. *Proc. Natl. Acad. Sci. USA* **1995**, *92*, 1396–1400. [CrossRef] [PubMed]
94. Hsiao, C.C.; van der Poel, M.; van Ham, T.J.; Hamann, J. Macrophages Do Not Express the Phagocytic Receptor BAI1/ADGRB1. *Front. Immunol.* **2019**, *10*, 962. [CrossRef]
95. Sharma, N.; Pushker, N.; Dada, T.; Vajpayee, R.B.; Dada, V.K. Complications of pediatric cataract surgery and intraocular lens implantation. *J. Cataract Refract. Surg.* **1999**, *25*, 1585–1588. [CrossRef]
96. Baratz, K.H.; Cook, B.E.; Hodge, D.O. Probability of Nd:YAG laser capsulotomy after cataract surgery in Olmsted County, Minnesota. *Am. J. Ophthalmol.* **2001**, *131*, 161–166. [CrossRef]
97. Boureau, C.; Lafuma, A.; Jeanbat, V.; Smith, A.F.; Berdeaux, G. Cost of cataract surgery after implantation of three intraocular lenses. *Clin. Ophthalmol.* **2009**, *3*, 277–285. [PubMed]
98. Apple, D.J.; Solomon, K.D.; Tetz, M.R.; Assia, E.I.; Holland, E.Y.; Legler, U.F.; Tsai, J.C.; Castaneda, V.E.; Hoggatt, J.P.; Kostick, A.M. Posterior capsule opacification. *Surv. Ophthalmol.* **1992**, *37*, 73–116. [CrossRef]
99. Awasthi, N.; Guo, S.; Wagner, B.J. Posterior capsular opacification: A problem reduced but not yet eradicated. *Arch. Ophthalmol.* **2009**, *127*, 555–562. [CrossRef]
100. Moisseiev, J.; Bartov, E.; Schochat, A.; Blumenthal, M. Long-term study of the prevalence of capsular opacification following extracapsular cataract extraction. *J. Cataract Refract. Surg.* **1989**, *15*, 531–533. [CrossRef]
101. Wormstone, I.M.; Wang, L.; Liu, C.S. Posterior capsule opacification. *Exp. Eye Res.* **2009**, *88*, 257–269. [CrossRef]
102. McDonnell, P.J.; Zarbin, M.A.; Green, W.R. Posterior capsule opacification in pseudophakic eyes. *Ophthalmology* **1983**, *90*, 1548–1553. [CrossRef] [PubMed]
103. Gwon, A. The Rabbit in Cataract/IOL Surgery. In *Animal Models in Eye Research*; Academic Press: Cambridge, MA, USA, 2008; pp. 184–203.
104. Pastor, J.C. Proliferative vitreoretinopathy: An overview. *Surv. Ophthalmol.* **1998**, *43*, 3–18. [CrossRef] [PubMed]
105. Idrees, S.; Sridhar, J.; Kuriyan, A.E. Proliferative Vitreoretinopathy: A Review. *Int. Ophthalmol. Clin.* **2019**, *59*, 221–240. [CrossRef] [PubMed]
106. Shahlaee, A.; Woeller, C.F.; Philp, N.J.; Kuriyan, A.E. Translational and clinical advancements in management of proliferative vitreoretinopathy. *Curr. Opin. Ophthalmol.* **2022**, *33*, 219–227. [CrossRef]
107. Pastor, J.C.; de la Rua, E.R.; Martin, F. Proliferative vitreoretinopathy: Risk factors and pathobiology. *Prog. Retin. Eye Res.* **2002**, *21*, 127–144. [CrossRef]
108. Morescalchi, F.; Duse, S.; Gambicorti, E.; Romano, M.R.; Costagliola, C.; Semeraro, F. Proliferative vitreoretinopathy after eye injuries: An overexpression of growth factors and cytokines leading to a retinal keloid. *Mediat. Inflamm.* **2013**, *2013*, 269787. [CrossRef]
109. Nagasaki, H.; Shinagawa, K.; Mochizuki, M. Risk factors for proliferative vitreoretinopathy. *Prog. Retin. Eye Res.* **1998**, *17*, 77–98. [CrossRef]
110. Glaser, B.M.; Cardin, A.; Biscoe, B. Proliferative vitreoretinopathy. The mechanism of development of vitreoretinal traction. *Ophthalmology* **1987**, *94*, 327–332. [CrossRef]
111. Heffer, A.; Wang, V.; Sridhar, J.; Feldon, S.E.; Libby, R.T.; Woeller, C.F.; Kuriyan, A.E. A Mouse Model of Proliferative Vitreoretinopathy Induced by Intravitreal Injection of Gas and RPE Cells. *Transl. Vis. Sci. Technol.* **2020**, *9*, 9. [CrossRef]
112. Ireland, M.E.; Wallace, P.; Sandilands, A.; Poosch, M.; Kasper, M.; Graw, J.; Liu, A.; Maisel, H.; Prescott, A.R.; Hutcheson, A.M.; et al. Up-regulation of novel intermediate filament proteins in primary fiber cells: An indicator of all vertebrate lens fiber differentiation? *Anat. Rec.* **2000**, *258*, 25–33. [CrossRef]
113. Sandilands, A.; Prescott, A.R.; Carter, J.M.; Hutcheson, A.M.; Quinlan, R.A.; Richards, J.; FitzGerald, P.G. Vimentin and CP49/filensin form distinct networks in the lens which are independently modulated during lens fibre cell differentiation. *J. Cell Sci.* **1995**, *108 Pt 4*, 1397–1406. [CrossRef]
114. FitzGerald, P.G.; Casselman, J. Discrimination between the lens fiber cell 115 kd cytoskeletal protein and alpha-actinin. *Curr. Eye Res.* **1990**, *9*, 873–882. [CrossRef] [PubMed]
115. Ireland, M.; Maisel, H. Identification of native actin filaments in chick lens fiber cells. *Exp. Eye Res.* **1983**, *36*, 531–536. [CrossRef]
116. Cvekl, A.; Camerino, M.J. Generation of Lens Progenitor Cells and Lentoid Bodies from Pluripotent Stem Cells: Novel Tools for Human Lens Development and Ocular Disease Etiology. *Cells* **2022**, *11*, 3516. [CrossRef] [PubMed]
117. Yang, C.; Yang, Y.; Brennan, L.; Bouhassira, E.E.; Kantorow, M.; Cvekl, A. Efficient generation of lens progenitor cells and lentoid bodies from human embryonic stem cells in chemically defined conditions. *FASEB J.* **2010**, *24*, 3274–3283. [CrossRef] [PubMed]
118. Qiu, X.; Yang, J.; Liu, T.; Jiang, Y.; Le, Q.; Lu, Y. Efficient generation of lens progenitor cells from cataract patient-specific induced pluripotent stem cells. *PLoS ONE* **2012**, *7*, e32612. [CrossRef]
119. Li, D.; Qiu, X.; Yang, J.; Liu, T.; Luo, Y.; Lu, Y. Generation of Human Lens Epithelial-Like Cells From Patient-Specific Induced Pluripotent Stem Cells. *J. Cell Physiol.* **2016**, *231*, 2555–2562. [CrossRef] [PubMed]
120. Fu, Q.; Qin, Z.; Jin, X.; Zhang, L.; Chen, Z.; He, J.; Ji, J.; Yao, K. Generation of Functional Lentoid Bodies From Human Induced Pluripotent Stem Cells Derived From Urinary Cells. *Investig. Ophthalmol. Vis. Sci.* **2017**, *58*, 517–527. [CrossRef]
121. Medina, C.B.; Ravichandran, K.S. Do not let death do us part: 'find-me' signals in communication between dying cells and the phagocytes. *Cell Death Differ.* **2016**, *23*, 979–989. [CrossRef]

122. Schwander, M.; Leu, M.; Stumm, M.; Dorchies, O.M.; Ruegg, U.T.; Schittny, J.; Muller, U. Beta1 integrins regulate myoblast fusion and sarcomere assembly. *Dev. Cell* **2003**, *4*, 673–685. [CrossRef]
123. Spalton, D.J.; Russell, S.L.; Evans-Gowing, R.; Eldred, J.A.; Wormstone, I.M. Effect of total lens epithelial cell destruction on intraocular lens fixation in the human capsular bag. *J. Cataract Refract. Surg.* **2014**, *40*, 306–312. [CrossRef] [PubMed]
124. Stone, J.; Mitrofanis, J.; Johnstone, D.M.; Falsini, B.; Bisti, S.; Adam, P.; Nuevo, A.B.; George-Weinstein, M.; Mason, R.; Eells, J. Acquired Resilience: An Evolved System of Tissue Protection in Mammals. *Dose Response* **2018**, *16*, 1559325818803428. [CrossRef] [PubMed]

Disclaimer/Publisher's Note: The statements, opinions and data contained in all publications are solely those of the individual author(s) and contributor(s) and not of MDPI and/or the editor(s). MDPI and/or the editor(s) disclaim responsibility for any injury to people or property resulting from any ideas, methods, instructions or products referred to in the content.

cells

MDPI

Article

Lens Epithelial Explants Treated with Vitreous Humor Undergo Alterations in Chromatin Landscape with Concurrent Activation of Genes Associated with Fiber Cell Differentiation and Innate Immune Response

Anil Upreti [1,2], Stephanie L. Padula [1,2], Jared A. Tangeman [1,2], Brad D. Wagner [2], Michael J. O'Connell [3], Tycho J. Jaquish [1,2], Raye K. Palko [2], Courtney J. Mantz [2], Deepti Anand [4], Frank J. Lovicu [5], Salil A. Lachke [4,6] and Michael L. Robinson [1,2,*]

1 Cell, Molecular and Structural Biology Program, Miami University, Oxford, OH 45056, USA
2 Department of Biology and Center for Visual Sciences, Miami University, Oxford, OH 45056, USA
3 Department of Statistics, Miami University, Oxford, OH 45056, USA
4 Department of Biological Sciences, University of Delaware, Newark, DE 19716, USA
5 Molecular and Cellular Biomedicine, School of Medical Sciences, and Save Sight Institute, The University of Sydney, Sydney, NSW 2006, Australia
6 Center for Bioinformatics and Computational Biology, University of Delaware, Newark, DE 19716, USA
* Correspondence: robinsm5@miamioh.edu

Abstract: Lens epithelial explants are comprised of lens epithelial cells cultured in vitro on their native basement membrane, the lens capsule. Biologists have used lens epithelial explants to study many different cellular processes including lens fiber cell differentiation. In these studies, fiber differentiation is typically measured by cellular elongation and the expression of a few proteins characteristically expressed by lens fiber cells in situ. Chromatin and RNA was collected from lens epithelial explants cultured in either un-supplemented media or media containing 50% bovine vitreous humor for one or five days. Chromatin for ATAC-sequencing and RNA for RNA-sequencing was prepared from explants to assess regions of accessible chromatin and to quantitatively measure gene expression, respectively. Vitreous humor increased chromatin accessibility in promoter regions of genes associated with fiber differentiation and, surprisingly, an immune response, and this was associated with increased transcript levels for these genes. In contrast, vitreous had little effect on the accessibility of the genes highly expressed in the lens epithelium despite dramatic reductions in their mRNA transcripts. An unbiased analysis of differentially accessible regions revealed an enrichment of cis-regulatory motifs for RUNX, SOX and TEAD transcription factors that may drive differential gene expression in response to vitreous.

Keywords: ATAC-seq; RNA-seq; lens; development; differentiation; explants; immune; motif; chromatin

1. Introduction

The exquisite and relatively simple design of the transparent ocular lens has made this unique tissue a source of experimental interest for well over a century. Surrounded by a collagen IV-rich capsule, the lens remains isolated from other cell types and is not innervated or vascularized. Within the confines of the lens capsule, the anterior hemisphere of the lens is lined by a subcapsular layer of cuboidal epithelial cells. Above the equator, a band of epithelial cells provides the proliferative force that fuels the life-long growth of the lens. At the lens equator, epithelial cells begin the morphological transition into elongated secondary fiber cells that make up the bulk of the lens structure. Although the central epithelial cells in the adult lens normally remain quiescent, the entire epithelium retains the capacity for proliferation and subsequent fiber cell differentiation. Lens epithelia undergo enormous physical and biochemical changes during their differentiation into

fibers, including apical-basal elongation, elaborate lateral interdigitation, the accumulation of high concentrations of specific crystallin proteins and the loss of all membrane-bound organelles [1–3]. In its native state, maintenance of lens polarity depends on the influence of the ocular media; the aqueous humor on its anterior (epithelial) surface and the vitreous humor on its posterior (fiber mass) surface [4,5].

Many different biomedical disciplines have benefited from studies conducted on the lens. Spemann, in 1901, exploited the lens as the first model of embryonic induction when he showed in the frog, *Rana fusca*, that the early formation of the lens from the head surface ectoderm required the underlying optic vesicle [6]. The external accessibility and stereotypical, continuous pattern of epithelial proliferation and fiber cell formation has made the lens a particularly useful tissue for studying cellular differentiation. The ability of some salamanders to regenerate fully functional lenses from pigmented cells of the dorsal iris has contributed much to our understanding of cellular reprogramming [7,8]. A small upstream (~400 bp) region of the mouse αA-crystallin gene can drive lens-specific gene expression [9] and this made the lens a popular tissue for some of the earliest transgenic studies in mammals. The first demonstration of the use of Cre recombinase for tissue-specific gene deletion in mammals also utilized the lens [10]. Though naturally resistant to cancer, the lens can form tumors when both tumor suppressors Rb and p53 are inactivated [11,12]. This observation spurred numerous investigations of cell cycle regulation using the lens as an experimental platform [13]. From a medical perspective, cataract represents the most common lens disease and results from any condition that causes the loss of lens transparency. Despite highly successful surgical treatment for cataracts, the epithelial to mesenchymal transition (EMT) of lens epithelial cells that remain following cataract surgery frequently lead to posterior capsular opacification (PCO), the most common complication of this procedure [14,15]. The fibrotic EMT response of lens epithelial cells following cataract surgery has many similarities to the pathogenic pathways leading to numerous human diseases [16,17].

The lens epithelial explant system, initially established using embryonic chick epithelia, provided a way to observe fiber cell differentiation in vitro [18]. The creation of lens epithelial explants requires the removal of the lens fiber cells mass prior to pinning the lens capsule, with adherent epithelial cells, flat onto a culture dish. In contrast to primary dissociated lens epithelial cells or cultured lens epithelial cell lines, explanted lens epithelial cells retain their lateral attachments to neighboring cells as well as to their native basement membrane [19]. The ability to easily manipulate culture conditions made the lens epithelial explant system an extremely useful model to uncover the factors that promote lens fiber cell differentiation or those that lead to lens EMT and fibrosis [20–26]. The lens epithelial explant system was first applied to mammals by the McAvoy laboratory who showed that retina-conditioned media induced elongation and the accumulation of fiber-specific β- and γ-crystallins in explanted rat lens epithelium [27]. Later, this same group demonstrated that vitreous humor could effectively induce these changes as well [28]. Abundant evidence suggests that fibroblast growth factors (FGFs) are the most potent source of fiber differentiating activity of retina-conditioned media [29] and vitreous humor [30] in explanted lens epithelial cells; however, vitreous clearly contains other fiber cell-promoting activity beyond that of FGF alone [30–32].

The vitreous humor occupies the space between the lens and retina in the eye. While the vitreous humor is mostly water, it also contains abundant collagen fibrils, hyaluronic acid, and a host of other proteins and peptides [33]. Given the close proximity to both the lens and retina, it is not surprising that the vitreous humor would contain substances secreted by both tissues. In addition to FGFs, the vitreous humor contains other ligands for receptor tyrosine kinases including IGF1 [34], PDGF [35], EGF [36], HGF [37], VEGF [38,39] and EphrinA1 [33]. The vitreous also contains precursors of active TGFβ, CTGF and GDF [33] as well as BMP [40], all ligands of the TGFβ receptor superfamily. The levels of these signaling molecules within the vitreous varies with the physiological state of the eye

and all have the potential to impact fiber cell differentiation, largely due to their ability to modulate ERK or SMAD activity [30,41–44].

Cell elongation and the appearance of β- and γ-crystallins in lens epithelial cells once defined the fiber cell differentiation process; however, modern transcriptomic technologies have now made it possible to distinguish lens epithelial cells from lens fiber cells in a much more thorough way. RNA-seq studies have comprehensively cataloged genes that are differentially expressed between lens epithelial and fiber cells in the developing mouse [45,46] and chick [47]. More recently, a genome-wide analysis of chromatin accessibility by ATAC-seq revealed differential regions of opened and closed chromatin that define these two cell types during mid-gestation and neonatal mouse lens development [48]. Similarly, RNA-seq and ATAC-seq studies have compared lens epithelial cells and fiber cells in the developing chick embryo [49]. Analysis of single cell RNA-seq in zebrafish [50] and single nuclei RNA-seq in humans [51] suggests a continuum of lens cell states, rather than discrete gene expression differences along a differentiation pathway from anterior lens epithelium to mature fibers.

Given the ability to extensively analyze both gene expression and chromatin accessibility, rather than select defined differentiation markers, we sought to analyze lens fiber cell differentiation in the mouse lens epithelial explant system induced by vitreous humor. To do so, we conducted both RNA-seq and ATAC-seq analyses of cultured lens epithelia cultured with or without vitreous humor, an established inducer of fiber cell differentiation in lens epithelial explants [28,30,32]. This global analysis of gene expression modulation—going beyond a select few markers—stands to comprehensively inform on the genome-wide changes that are associated with in vitro fiber cell differentiation.

We have leveraged ATAC and RNA sequencing of cultured lens epithelia to characterize the genome-wide regulatory landscape of this historically valuable model of fiber cell differentiation. As expected, vitreous treatment induced a sharp repression of epithelial-identity genes, such as *Foxe3*, *Gja1*, and *Cdh1*. Conversely, the expression of fiber cell-identity genes such as *Cryba4*, *Hsf4*, and *Crybb1* were upregulated throughout time in culture. However, many fiber cell genes were only modestly increased in vitreous-treated explants relative to media-treated controls, suggesting that vitreous may exert its early pro-differentiation effects primarily through the suppression of epithelial identity, rather than the activation of fiber identity. Our findings expound promoter regions which undergo substantial expansions in accessibility in response to vitreous, many of which are known fiber cell-related genes, such as *Tmod1*, *Gja8*, and *Lgsn*. Paradoxically, we identify a broad set of gene promoters associated with epithelial identity that remain in a highly accessible state following vitreous treatment, despite dramatic reductions in their expression. Examples of such genes include *Dll1*, *Fzd1*, and *Kdr*. This suggests that there could be lingering vestiges of epithelial identity found within the chromatin organization of lens explants, even after 5 days of vitreous exposure. This should be closely considered by others in this field as they make use of this model system. Vitreous treatment induced broad activation of inflammatory and EMT gene sets within 5 days, as well as accessibility footprints indicative of AP1 binding activity, pointing toward widespread activation of stress-responsive factors. Finally, we identify broad signatures of RUNX1 binding activity in explants treated with 'differentiation' media and verify the enhanced expression of *RUNX1* in human lens fiber cells, suggesting a novel role for this factor in the establishment and maintenance of fiber cell identity. Collectively, our results provide an unprecedented portrait of the dynamic chromatin architecture within vitreous-treated lens epithelia and serve as a valuable resource to researchers seeking to wield this insightful model.

2. Materials and Methods

2.1. Animals

All procedures were approved by the Miami University Institutional Animal Care and Use Committee and complied with the ARVO Statement for the Use of Animals in Research, consistent with those published by the Institute for Laboratory Animal Research

(Guide for the Care and Use of Laboratory Animals). *FVB/N* mice were euthanized at postnatal day 8 (P8) by CO_2 asphyxiation followed by cervical dislocation.

2.2. Lens Epithelial Explant Generation and Culture

Mouse lens epithelial explants were prepared from postnatal day 8 (P8) mice as previously described [19,32]. Lenses were removed and placed into a 35 mm culture dish with pre-calibrated (37 °C and 5% CO_2) M-199 media supplemented with 1% antibiotic-antimycotic solution (ThermoFisher Scientific cat. 15240062) and 0.1% bovine serum albumin (Sigma-Aldrich cat. A7906) henceforth referred to as "culture medium (CM)". The lens capsule was torn at the posterior pole prior to removing the fiber cell mass. The remaining lens capsule with adherent epithelium was pinned flat to the base of the culture dish. Fresh bovine vitreous was collected as previously described [28] (courtesy of Kaiser Meat Market, Cedar Grove, IN, USA) prior to storage at −20 °C. For all treatment groups other than the Immediate Collection group, explants were cultured in culture media for 24 h after generation. Following this, some treatment groups were cultured in vitreous, diluted 50% (v/v) with culture media, henceforth referred to as "differentiation medium (DM)", for 1 day or 5 days.

2.3. RNA-Seq Library Preparation and Sequencing

RNA-seq analyses were carried out for each condition with three biological repilcates. Each replicate consisted of 12 explants. Explants were collected in 1.5 mL Eppendorf tubes. Total RNA was extracted using the RNEasy Mini Kit (Qiagen cat. 74104) following the manufacturer's instructions. The RNA Integrity Number (RIN) was determined using an Agilent 2100 Bioanalyzer and samples with RIN > 7 were used for sequencing. Samples ranged from 400 ng to 1 µg of total RNA. RNA libraries were constructed by DNA Link (Los Angeles, CA, USA) using a TruSeq (Illumina) library prep kit. The library was sequenced on the Illumina NovaSeq 6000 sequencer platform. Sequences consisted of 100 base paired-end reads to a minimum depth of 26 million reads per sample.

2.4. RNA Seq Data Analysis

Raw reads were quality-analyzed using FastQC (Babraham Bioinformatics- FastQC A Quality Control tool for High Throughput Sequence Data) [52,53] and MultiQC [54]. Low-quality bases and adapters were trimmed using Cutadapt 3.4 [55] and Trim Galore 0.6.5-1 with the parameters -q 20 –phred33 –length 20 [56]. Mouse genome GRCm39 version: M27 was indexed using Hisat2 (2.1.0-4) [57], incorporating splice junctions from Gencode GTF gencode.vM27.annotation.gtf file [58]. Gene counts were generated using Stringtie2.1.5 [59] and gencode GTF annotation gencode.vM27.annotation.gtf. Differential expression testing was performed with DESeq2 [60]. Differentially expressed genes (DEGs) are defined throughout by an adj. p-value ≤ 0.05, and $\log_2$ fold change (LFC) ≥ 1.5 criteria were applied. In these cases, the p-value was adjusted using the Benjamin-Hochberg correction individually for each pairwise comparison made.

Clustering of DEGs was performed with K-means clustering using normalized RNA-seq counts [61]. Specifically, the kmeans function (part of the "stats" package in R) was used with the Hartigan-Wong algorithm [62,63]. Pathway enrichment analysis was performed with gProfiler (R package) [64]. All individual clusters obtained from K-means clustering were used for GO term analysis in groups to reduce biases. This analysis resulted in p-values associated with each cluster for each identified GO term, facilitating consideration of biological functions associated with each cluster. The obtained p-values were $-\log_{10}$ normalized prior to visualization as a bar chart. All figures were generated in the R environment.

Gene set enrichment analysis (GSEA) was performed on the normalized count matrix obtained from DESeq2, and murine genes were converted to human orthologs [65,66]. GSEA was performed using 1000 permutations and gene set permutations with gene set size filters; min = 15 and max = 500. Hallmark gene set was used for analysis. The newborn

FVB/N mouse lens epithelium and fiber data were downloaded from the GEO database with the SRA accessor: SRP040480 [45].

2.5. RT-qPCR Validation of RNA-Seq Data

Select genes identified by RNA-Seq were validated using RT-qPCR. RNA was extracted as described above, and samples were reverse transcribed into cDNA using oligo (dT) primers and random primers using ImProm-II™ Reverse Transcription System (A3800), according to manufacturer's instructions. The RT-qPCR assays were performed in triplicate biological replicates and triplicate technical replicates using GoTaq qPCR Master Mix (A6001) and the Bio-Rad CFX Connect. Pre-designed primers from primerbank (https://pga.mgh.harvard.edu/primerbank/, accessed on 18 January 2023) were ordered and obtained from IDT technologies (Table S1). The comparative ΔΔCt method was used to determine relative gene expression levels compared to housekeeping genes (*Eef1a1*) and relative mRNA was normalized to immediately collected explants (IMD). Prior to statistical analysis, fold change values were log-transformed in order to promote conformity to modeling assumptions. One-way ANOVA was performed in R using the stats package [63], and Levene's test was applied using the car package [67] to assess homogeneity of variances. Following ANOVA, means and standard error were computed using the R package emmeans [68]. For samples with 3 groups, Tukey's Honest Significant Difference test was used post-hoc to calculate adjusted p values [63]. One gene, *Runx3*, was expressed below the threshold of detection of the assay in a single condition. For *Runx3*, a two-sample equal variances t-test [63] was used to calculate p value.

2.6. ATAC-Seq Library Preparation and Sequencing

ATAC-seq library preparation was performed using the ATAC-Seq Kit (Active Motif cat.53150) per the manufacturer's instructions. Briefly, four lens epithelial explants per sample (biological replicate) were collected in ice-cold PBS. Two biological replicates were conducted for each ATAC-seq condition. The samples were centrifuged at 8000× g for 5 min at 4 °C. 100 μL of ATAC lysis buffer was added to the samples after aspirating the PBS. The explant samples were pipetted vigorously until visibly broken. The total number and quality (round shape without blebbing) of isolated nuclei was accessed by trypan blue staining that ranged between 80,000–120,000 per sample. Following nuclei validation, the samples were centrifuged, tagmented and PCR amplified. The amplified DNA was purified and indexed (Dual indexing following manufacturer protocol) to create sequence-ready libraries. The libraries were quantified using a Qubit 4 Fluorometer with the dsDNA Quantitation, high sensitivity kit (ThermoFisher Scientific, cat. Q32851). Final libraries were quality validated using the Bioanalyzer HS DNA Kit (Agilent, cat. 5067-4626). Validated libraries passing in-house quality control were sent to Novogene (Sacramento, CA, USA) for sequencing with a HiSeq platform using 150 base paired-end reads to a depth of greater than 30 million reads.

2.7. ATAC-Seq Data Analysis

Raw reads were trimmed using Cutadapt 3.4 and Trim Galore 0.6.5-1 with the trimming parameters -q 20 –phred33 –length 20. Alignment of raw reads to the *Mus musculus* genome GRCm39 was performed with Bowtie2 [69] using the parameters -X 2000 –very-sensitive-local –no-mixed –no-discordant –no-dovetail. Peaks were called for samples individually with MACS2 [70] using parameters -f BAMPE -g mm -q 0.05. Peaks aligning to the mitochondrial chromosome were discarded. Differential accessibility testing of peak regions and peak summits was performed with DESeq2. Differentially accessible regions (DARs) identifed by DESeq2 were those with a Log_2 fold change of $\geq$1.5 and adjusted p-value (p-adjust) of $\leq$0.05. ATAC coverage tracks were visualized using the Integrative Genomics Viewer (IGV) [71]. Prior to visualization, BAM files were converted to BIGWIG format and normalized using the bamCoverage –binSize 1 and –scaleFactor parameter

using the inverse of DESeq2 size factors. Accessibility heatmaps were generated using deepTools computeMatrix reference-point and plotHeatmap functions [72].

2.8. Genomic Annotation and Motif Prediction

Peak annotations to the nearest TSS were performed using ChIPseeker [73]. Binned motif analysis was executed using the monaLisa R package [74] and the JASPAR 2022 vertebrate motif database [75]. For monaLisa analysis, all differentially accessible peak summits ($|\text{LFC}| \geq 1.5$ and adj. p-value ≤ 0.05) between conditions were identified. This was further partitioned into differentially accessible regions (DARs) regulated by DM and CM from 1 or 5 days. Finally, the subset regions (promoter vs. remaining accessible regions) were subjected to motif prediction using the monaLisa R package. Occurrences of motifs of interest were annotated back to the moue genome using the monaLisa function findMotifhits. Furthermore, the difference in the distribution of the genomic annotation of promoters and remaining regions were analyzed using ChiPseeker. The identified motif annotated regions were manually verified using IGV. Venn diagrams were made using Venny [76].

2.9. Single Cell Data Analysis

The single cell data on human ocular anterior segment [51] was accessed and visualized in the Broad Institute's Single cell portal (https://singlecell.broadinstitute.org/single_cell/study/SCP1841/, accessed on 19 September 2022). The dot blot and TSNE plots were downloaded from the same portal.

2.10. Relationship between ATAC-Seq and RNA Seq

To compute the overall correlation between the ATAC-seq and RNA-seq data, the normalized counts were computed for both data sets using DEseq2 in R. Then the ATAC-seq peaks were matched to genes based on the gene with the nearest promoter. For genes with multiple nearby ATAC-seq peaks, the ATAC-seq counts were averaged. Then the Pearson correlation coefficient was computed for average normalized counts across all samples for all genes.

To compare the results from the clustering analysis of the differential gene expression and differentially accessible regions, the ATAC-seq peaks were once again matched to the genes with the nearest promoters. Then, a cross-table was generated to indicate the number of genes in each pair of RNA-seq and ATAC-seq clusters. A Chi-squared test of independence was run to determine whether the cluster sets were independent. A permutation-based analysis of this table indicated which cluster pairs were associated with each other. Using fixed cluster sizes, the RNAseq and ATACseq clusters were randomly permuted 100,000 times. For each permutation, a new cross-table was generated, and the permuted cell counts were compared to the observed cell counts. Clusters were considered to be associated if less than 5 percent of the permuted counts for that cell were greater than or equal to the observed count.

To determine a potential relationship between basal accessibility and transcriptional output, all annotated mouse transcripts were ordered by average expression across biological replicates within each condition. Ordered loci were used as input for the deepTools2 command line suite [72]. The functions computeMatrix and plotHeatmap were used to plot heatmaps of normalized ATAC signal for transcripts within each quintile of expression bin.

3. Results

3.1. Chromatin Accessibility and Gene Expression Changes in Lens Epithelial Explants Resulting from Explanting, the Addition of Vitreous, and Time in Culture

To analyze how the process of in vitro culture with and without the addition of bovine vitreous changes chromatin accessibility and gene expression in lens epithelial explants, we harvested lens epithelia from postnatal day 8 (P8) mice and explanted the epithelium in a culture dish supplemented with either culture media (CM) or differentiation media

(DM). Following lens explant culture, samples were harvested at five specific time points for the collection of chromatin and RNA. These were (A) immediately after collection of the epithelium (IMD), (B) after 24 h in CM (Day 0), (C) after an additional day in CM (D1_CM) or DM (D1_DM), (D) after an additional (relative to Day 0) 5 days in CM (D5_CM) or DM (D5_ DM) (Figure 1A). Our experimental design consists of many variables that can affect both chromatin organization and gene expression. These include: (i) the trauma induced by the physical removal of the epithelium and the establishment of in vitro culture, best represented by the D0 treatment; (ii) the time in culture, represented by the D1 and D5 samples and (iii) differential effects of unsupplemented culture medium and the addition of vitreous, represented by the differences between the CM and DM treated samples. We reasoned that day 0 (D0) would best reflect immediate changes resulting from in vitro culture, while D1 would reflect immediate differences resulting from the addition of vitreous in the DM condition. In previous experiments in neonatal rat lens epithelial explants, immunologically detectable β-crystallin expression was evident after five days of 50% vitreous treatment [30].

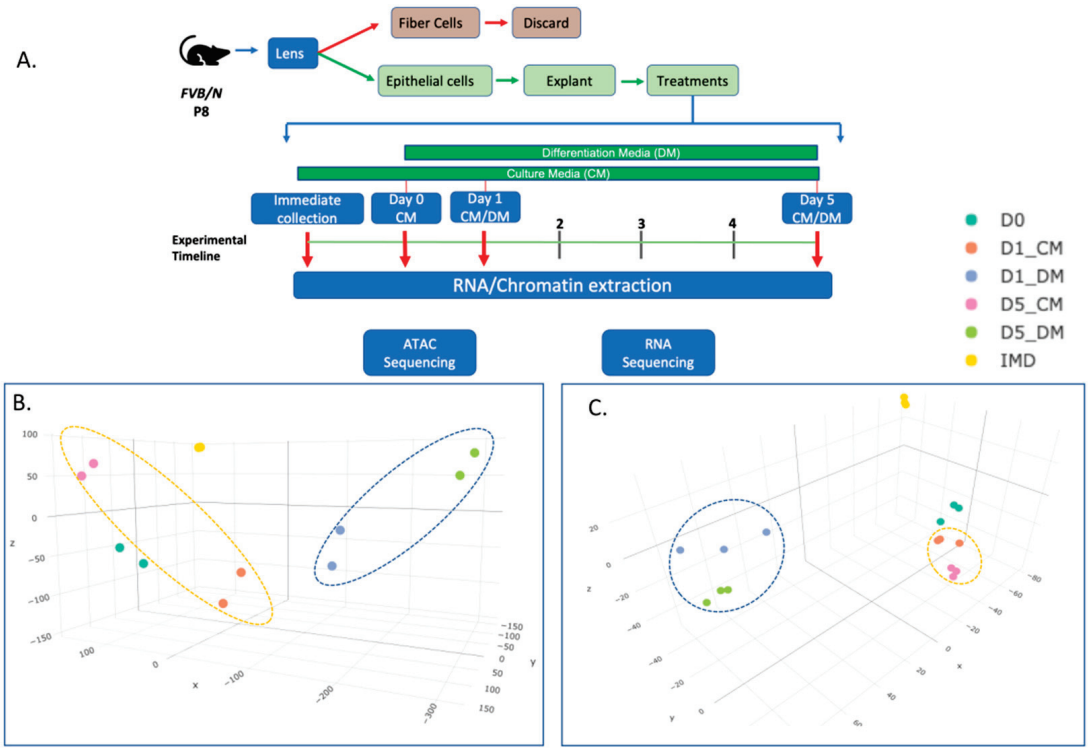

Figure 1. Profiling chromatin accessibility and gene expression in lens epithelial explants. (**A**) Overall experimental procedure. (**B**,**C**) 3-dimensional principal component analysis of ATAC- seq (**B**), and RNA-seq (**C**) summarizes the variation present in normalized chromatin accessibility and gene expression values across six conditions. The yellow dashed oval encompasses the variation for culture media as a function of time, whereas the blue dashed oval encompasses the variation for differentiation media as a function of time.

We performed three-dimensional principal component analysis (3D-PCA) on both the ATAC-seq (Figure 1B) and the RNA-seq (Figure 1C) datasets obtained. The first three components PC1, PC2 and PC3 were plotted as X, Y and Z axes to observe the major components shaping each dataset. For both the ATAC-seq and the RNA-seq PCA plots, the X axis represents the primary dimension of variation (PC1) and clearly separates the DM-treated samples from the other samples. With respect to the ATAC-seq data, with two replicates per treatment, and the RNA-seq data, with three replicates per treatment, the IMD replicates occupy nearly the same space on each of the plots. Moreover, the replicates within each treatment are consistently clustered together on both the ATAC-seq and RNA-

seq PCA plots, underscoring a high concordance between our biological replicates. The overall similarity of the biological replicates and the effect of treatments can be alternatively visualized by a distance matrix heatmap for the ATAC-seq data (Figure S1A) and the RNA-seq data (Figure S1B).

3.2. Clustering of ATAC-Seq and RNA-Seq Data to Evaluate Effects of In Vitro Culture, Time in Culture, and the Addition of Vitreous Humor on Chromatin Organization and Gene Expression

We sought to generate an overview of meaningful changes in gene expression in response to our tested treatments. To this end, we employed a series of pairwise comparisons that stand to capture changes in expression that are relevant to our questions of interest. To examine the effect of explanting only, we analyzed IMD vs. D0. In addition, we compared both the IMD and D0 treatments to the CM and DM treated groups at both time points, which revealed genes responsive to the effects of culture and vitreous relative to our baseline conditions. Finally, we tested all possible pairwise combinations of our CM and DM treated explants at both times in culture, which revealed genes that were undergoing changes in response to vitreous, time in culture, or both. From these comparisons, we then generated a non-redundant list of differentially expressed genes and performed K-means clustering to organize them into clusters representing archetypal expression patterns within our dataset. These comparisons identified differentially accessible regions (DARs) and differentially expressed genes (DEGs) from the ATAC-seq and RNA-seq datasets, respectively.

The K-means clustering of DARs from the pairwise comparisons of the treatments revealed six clusters of genomic coordinates encompassing a total of 129,635 distinct genomic fragments that changed in specific ways (Figure 2A and Table S2). After defining these clusters, we used Chipseeker to assign genes to each DAR based on the nearest promoter region(s). This information made it possible to search for gene ontology (GO) terms associated with each cluster to assess the biological significance of the changes in chromatin accessibility (Table S3). This analysis made it easier to identify how the genomic landscape changed in lens explants with both time in culture and with differential media (representative GO terms are shown in Figure 2B). Cluster A (22,965 sites) represents regions that become more accessible immediately after explanting (D0) and after long term culture in unsupplemented media (D5_CM) but generally becomes less accessible with DM. Cluster A was enriched with GO terms for inflammatory process, and MAPK cascade. Cluster B (19,103 sites) exhibited the opposite accessibility profile of cluster A and was enriched for actin filament-based process, and actin cytoskeletal organization. Cluster C (20,723 sites) exhibited the highest accessibility in the D5_DM.

Samples were enriched for GO terms such as regulation of cell migration, and transcription repressor complex. Cluster D (30,694 sites) exhibited the highest accessibility in the IMD samples and lowest accessibility in the D5_DM samples treatments and was enriched for GO terms including cell morphogenesis involved in differentiation, and the calcium signaling pathway. Cluster E (21,240 sites) represented regions that are inaccessible in the IMD samples with increased accessibility in both D0 and in DM treated samples. Cluster E was enriched for GO terms like positive regulation of cell differentiation, and cell-substrate adhesion. Cluster F (14,910 sites) exhibited the highest accessibility in D1_CM samples and this cluster was enriched for terms including extracellular matrix, and cell morphogenesis involved in differentiation. These observations suggest that each treatment results in a dynamic shift in epigenetic landscape, with the potential to impart functional significance by impacting nearby transcription.

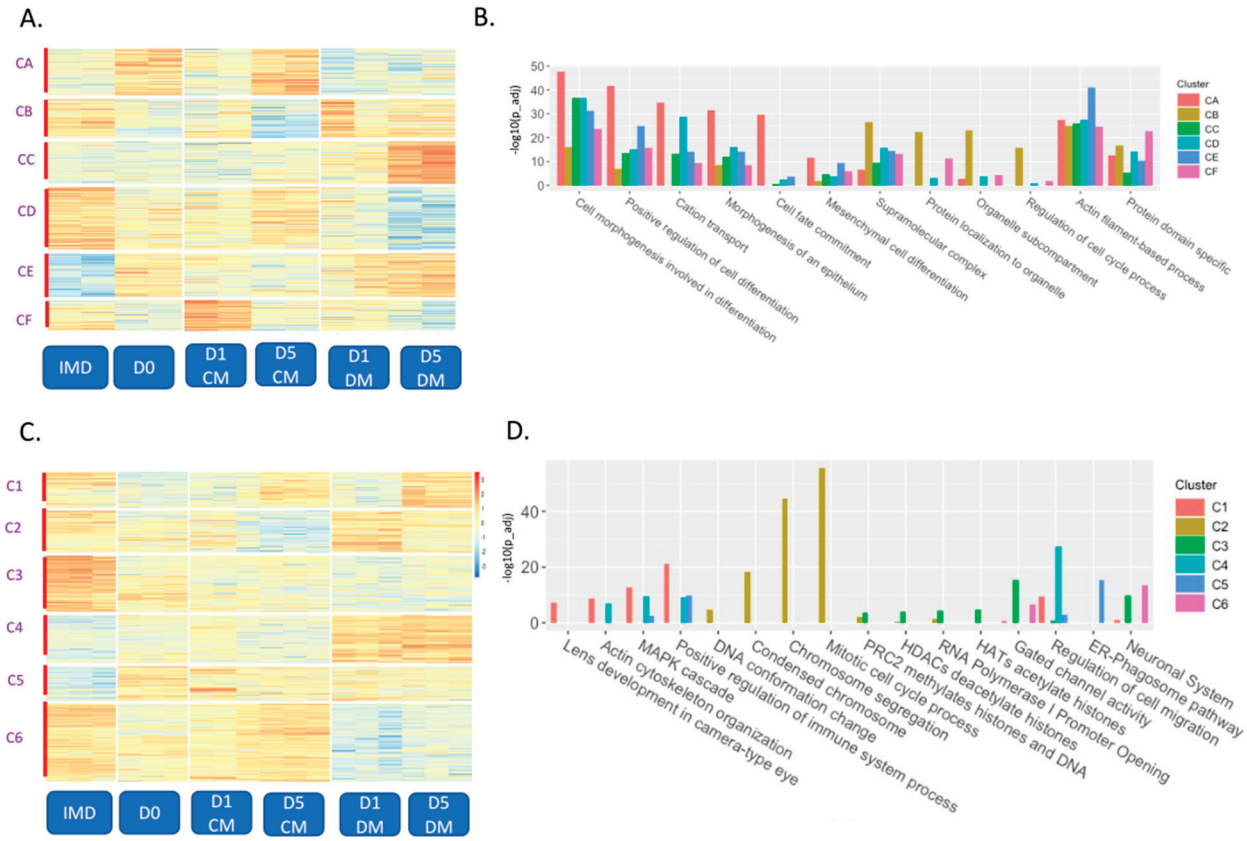

Figure 2. Clustering of differentially accessible regions and differentially expressed genes reveals a distinct signature of chromatin landscape and transcriptome as a function of time and culture conditions. (**A**) K-mean clustering was performed on all DARs across all fifteen pairwise comparisons (IMD vs D0, IMD_vs_D1_CM, IMD_vs_D5_CM, IMD vs D1_DM, IMD vs D5_DM, D0 vs D1_CM, D0 vs D5_CM, D0 vs D1_DM, D0 vs D5_DM, D1_CM vs D5_CM, D1_CM vs _D1_DM, D1_DM vs D5_DM, D1_CM_vs_D5_DM, D1_DM_vs_D5_CM, D5_DM vs D5_CM) by the criteria $\log_2$ fold change ≥ 1.5 and adjusted *p*-value (*p*-adjust) of ≤ 0.05 (n = 129,635 DARs), resulting in six clusters. (**B**) The bar chart displays select gene ontology terms associated with each cluster for ATAC-seq. The negative $\log_{10}$ of the *p*-value for each selected GO term is plotted on the y-axis, with each cluster represented by a different color. (**C**) K-mean clustering was performed on all DEGs across all fifteen pairwise comparisons by the criteria $\log_2$ fold change ≥ 1.5 and adjusted *p*-value (*p*-adjust) of ≤ 0.05 (n = 9044 DEGs), resulting in six clusters. (**D**) Bar chart displaying the significance ($-\log_{10}$ *p*-value was plotted) of DEGs for selected GO terms associated with each cluster represented by different colors.

The effects of explanting and differential media appeared to have more impact on chromatin accessibility than did time in culture. DAR clusters B, C and E generally gain chromatin accessibility in response to vitreous addition, and of these, cluster E represents the most dramatically different from the accessibility profile of the native lens epithelium represented by the IMD sample. In contrast, DAR cluster D exhibited largely accessible chromatin in the IMD samples that become distinctly less accessible in the DM media, particularly at day 5. DAR clusters A and F exhibited the highest accessibility in the D5_CM and D1_CM conditions, respectively. DAR clusters A and E represented regions that gained accessibility within 24 h of explanting while clusters B, D and F lost accessibility at this time point. All clusters exhibited nearly opposite accessibility profiles in the CM versus DM conditions. DAR clusters B, C and E exhibited higher accessibility in the DM condition while clusters A, D and F were less accessible in the DM than the CM condition. In no case did a cluster exhibit a similar trend in accessibility with time in the DM and CM conditions.

As we did for the ATAC-seq data, we used K-means clustering to independently analyze the RNA-seq data from each of the fifteen pairwise comparisons described above

and performed GO analysis to the genes assigned to each cluster. The K-means clustering of DEGs also revealed six distinct clusters from a total of 9044 DEGs (Figure 2C, Table S4). Selected GO terms for each cluster are shown on a bar plot (Figure 2D) with the full list of GO terms associated with each cluster shown in Table S5. Cluster 1 (1098 genes) represented genes with high expression in the IMD and D5_DM samples and low expression in the D0 samples. Cluster 1 is enriched with genes associated with lens development (*Bfsp1*, *Mip*, *Lim2*, *Hsf4*), actin cytoskeleton organization (*Myo5c*, *Myo7a*, *Rhoh*, *Rac2*) and regulation of the immune system (*Tnf*, *Ccr1*, *Csf1r*, *Tlr7*). Cluster 2 (1291 genes) represented genes with low expression in the D5_CM samples, high expression in the D1_DM samples, and moderate expression in the IMD and D5_DM samples. Cluster 2 was enriched for genes associated with chromosome segregation (*Cenpn, Spag5, Aurkb, Bub1b*), the cell cycle (*Cdc6*, *Cdk1*, *Ccne1*, *Pcna*) and mitosis (*Birc5*, *Ube2c*, *Cdc14a*). Cluster 3 (1731 genes) represented genes with high expression in the IMD samples and was associated with several terms suggestive of chromatin reorganization, including those associated with the polycomb repressive complex 2 (*H2ac6*, *H4C9*, *H2bc11*, *H2bc12*) and histone acetylation/deacetylation (*H2bc3*, *H2bc15*, *H3c14*, *H4f16*) and gated channel activity (*Gabra2*, *Kcnq1*, *Scna4*, *Clcn2*). Cluster 4 (1477 genes) represented genes with high expression in the D1_DM and D5_DM samples and was highly enriched for cell migration and epithelial to mesenchymal transition (EMT) genes (*Mmp7*, *Fn1*, *Col1a1*, *Snal1*). Cluster 5 (1062 genes) represented genes with low expression in the IMD samples and moderate expression in all the explanted samples including several genes associated with phagocytosis (*Rab7b*, *Slc11a1*, *Tap1*, *Clec4e*). Cluster 6 (2385 genes) represented genes with high expression in the IMD samples and samples treated with CM but low in DM treated samples. This cluster contained several genes associated with neuronal development (*Mapt*, *Map2*, *L1cam*, *Trpm1*).

Similarly, clustering of DEGs revealed that the addition of vitreous to cultured lens epithelia upregulated many genes associated with fiber cell differentiation and immune system processes and downregulated many genes highly expressed in the lens epithelium. DEG clusters 1, 2 and 4 exhibited specific upregulation upon the addition of vitreous (D1_DM and D5_DM). Of these, the DEGs in cluster 2 exhibited specific upregulation at D1_DM and were enriched with genes associated with proliferation and the upregulation of MAPK signaling (*Cdk1*, *Myc*, *Spry4*, *Etv1*, *Etv4*, *Etv5*), suggesting an immediate response to the addition of growth factors present in the vitreous humor. In contrast, DEG cluster 1 exhibited specific upregulation in the D5_DM condition. This cluster contained most of the crystallin genes associated with fiber cell differentiation (*Crybb1*, *Crybb3*, *Cryba4*, *Crygb*, *Crygc*, *Crygd*, *Cryge*, *Crygs*) as well as other genes highly expressed in fiber cells such as *Nav3*, *Mip*, *Lim2*, *Hsf4* and *Dnase2b*. Cluster 4 also contained genes highly expressed in fiber cells (*Pla2g7*, *Slc2a3*, *Jag1* and *Lgsn*) but this cluster also contained a large number of genes associated with extracellular matrix, fibrosis and immune response (for example: *Tgbi*, *Fn1*, *Mmp7*, *Mmp9*, *Col5a3*, *Ccl6*, *Ereg*, *Axl*, *Csf3*, *C3*, *Krt16*, *Cd44*). Clusters 3 and 6 exhibited high expression in the IMD, lens epithelium samples, but lower expression in all other conditions. Cluster 6, in particular, exhibited significant downregulation upon the addition of vitreous (D1_DM and D5_DM). In agreement with this, both clusters contained genes highly expressed in the lens epithelium. These included notch ligands (*Dll4* and *Dll3*) and *Rgs6* in cluster 3 and epithelial genes including *Foxe3*, *Kdr*, *Sulf1*, *Pdgfra*, *Cdh1*, *Gja1*, *Npnt* and *Podn* in cluster 6.

An overall correlation between the number of differentially expressed genes and differentially accessible regions was analyzed for each of the cluster for RNA-seq and ATAC-seq (Table 1). The strongest association was observed for ATAC cluster CD and RNA-seq cluster C6.

Table 1. The six clusters of ATAC-seq and six clusters of RNA-seq were compared to determine if specific clusters of DARs corresponded to specific DEG clusters. The highlighted boxes represent clusters that are associated with each other based on the permutation method described in Section 2.9. CA–CF represent ATAC-seq clusters and C1–C6 represent RNA seq clusters.

	CA	CB	CC	CD	CE	CF
C1	267	157	153	227	67	37
C2	300	163	129	198	107	66
C3	433	198	152	417	78	91
C4	395	141	236	166	269	46
C5	296	96	106	124	152	36
C6	487	434	217	514	119	119

Furthermore, concordance of the ATAC seq signal with gene expression was analyzed for the D1 and D5 data (Table 2) to further dissect the relation between the datasets (Table 2). The highest concordance was observed between the accessible regions and the corresponding gene expression for D5_DM samples.

Table 2. All the accessible regions were annotated to the nearest promoter and analyzed for the common changes in the chromatin accessibility with changes in gene expression. ATAC-seq CM up represents the accessible regions for culture media treated samples with increased accessibility. Similarly, ATAC-seq DM up represents increased accessibility for differentiation media. RNA-seq CM up represents genes that are upregulated in culture media and RNA seq DM up genes that are upregulated in differentiation media.

	ATAC-Seq CM_D1 Up	**ATAC-Seq No Difference**	**ATAC-Seq DM_D1_Up**
RNA seq CM_1_up	12	3382	193
RNA seq no difference	61	9180	405
RNA seq DM_1_up	26	4221	145
	ATAC-Seq CM_D5_Up	**ATAC-Seq no Difference**	**ATAC-Seq DM_D5_Up**
RNA seq CM_D5_up	636	2434	915
RNA seq no difference	1848	5881	2580
RNA seq DM_D5_up	593	2544	1131

We analyzed the relationship of chromatin accessibility at transcription start sites (TSS) with gene expression throughout the genome in all experimental conditions. We uniformly observed a high agreement between basal gene expression and TSS accessibility (Figure 3). The normalized count matrix for the entirety of the ATAC-seq accessible regions and RNA-seq gene expression datasets were used to calculate the correlation between ATAC-seq and RNA-seq. This analysis led to an r value of 0.404 (Figure S2).

We next sought to determine whether genes that exhibit expression patterns that are linked to promoter region accessibility could be associated with specific biological processes that explain the response to vitreous. To do this, we categorized DEGs observed after 5 days of DM treatment into categories based on the degree of correlation between gene expression and promoter region accessibility (Table S6, Figure S3). Interestingly, genes which exhibited a strong positive correlation (n = 115) were associated with apelin signaling. A large number of genes exhibited a moderate positive correlation between expression and promoter accessibility (n = 2062), and were strongly enriched for genes associated with mitosis, epithelial proliferation, mesenchymal cell differentiation, and fibroblast proliferation. In contrast, the genes without any detectable correlation were related to diverse functions, including organelle structure, endosomes, microtubule organization, rRNA metabolism, actin filaments, and supramolecular fiber organization. This set of genes could collectively represent a broad set of processes regulated by vitreous for which

promoter accessibility is not a primary driver of gene expression changes. We observed a relatively smaller number of genes which exhibited moderate negative (n = 1152) or strong negative (n = 27) correlation with gene expression, which may reflect the paradoxical nature of an opposing relationship between promoter accessibility and expression. Genes with moderate negative correlation tended to overlap many of the processes observed for genes with no correlation, suggesting a functional similarity between genes of these categories.

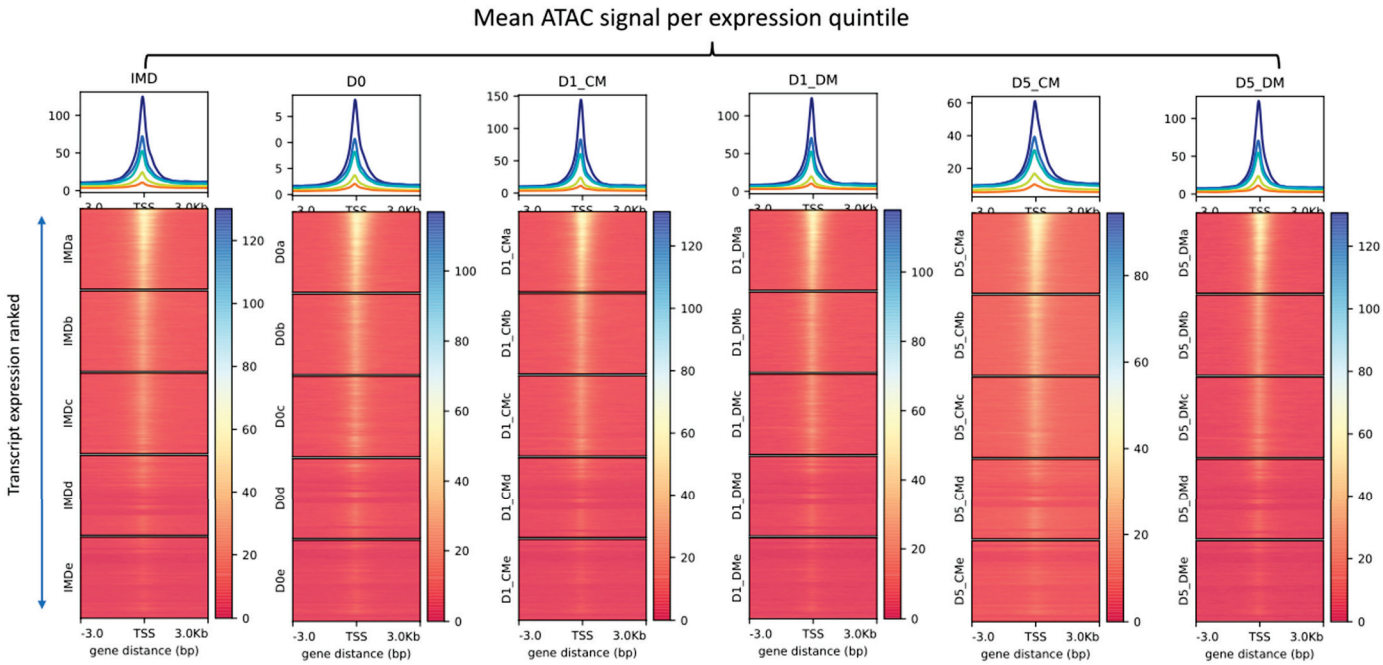

Figure 3. Relationship between transcriptional output and TSS chromatin accessibility across all conditions. The replicates for both RNAseq and ATACseq samples were collapsed for analysis. The highly expressed transcripts were ordered and divided into quintiles based on gene expression levels. The mean change in accessibility signal for each quintile is represented with different colored lines in the line graphs. Top panels: dark blue = 1st quintile, light blue = 2nd quintile, green = 3rd quintile, yellow = 4th quintile, orange = 5th quintile.

We selected a list of 90 genes in different categories to look at more closely in order to discern more about the biology and developmental state of our explants upon culture and vitreous addition. These genes were based on those differentially expressed between lens epithelial cells and lens fiber cells [33] or on genes associated with particular GO terms. These genes were divided into five classes: (a) twenty-four immune response-related (Immune) genes, (b) twenty-four lens fiber cell-related (Fib) genes, (c) twenty lens epithelial cell-related (Epi) genes, (d) seven mitogen activated protein kinase-related (MAPK) genes and (e) fifteen extracellular matrix-related (ECM) genes. Both ATAC-seq and RNA-seq clusters associated with each of these genes were identified to see if there was any obvious correlation between the two cluster sets (Table S7). With the exception of RNA cluster 6, the majority of the selected genes in all RNA clusters were in ATAC cluster A. For cluster 6, 27.8% of the genes were in ATAC cluster A and 61.1% of the genes were in ATAC cluster B. Although some genes in every RNA-seq cluster were assigned to ATAC cluster A, the largest proportion of the ATAC cluster A genes (47.1%) were in RNA cluster 4. RNA clusters 1 and 6 made up 35.3% and 64.7% of the genes in ATAC cluster B, respectively. Of the genes in ATAC cluster C, 78.6% came from RNA cluster 4. Few of the 90 selected genes were found in ATAC clusters D (1), E (2) and F (4) and none of these genes were found in RNA clusters 1 or 3.

3.3. Assessment of Genome-Wide Dynamic Changes in Chromatin Accessibility with the Addition of Vitreous Humor

To discern where changes in the chromatin landscape occur relative to genes, the accessible regions identified by ATACseq were annotated using CHIPseeker. CHIPseeker categorizes the accessible regions as associated with promoters, introns, exons, untranslated regions (UTRs), or intergenic. These regions are further broken down as proximal promoters (within 1 kb of the TSS), intermediate promoters (within 1–2 kb of the TSS) and distal promoters (within 2–3 kb of the TSS), first exon, other exon, first intron, other intron, 5′ untranslated region (5′ UTR), 3′ untranslated region (3′ UTR), downstream intergenic (within 300 kb of the 3′UTR), and distal intergenic (>300 kb of the 3′UTR) regions. We observed that the proportion of accessible chromatin regions corresponding to promoters decreased with time in DM-treated samples, while the proportion of distal intergenic accessible regions increased with time, relative to the IMD samples (Figure 4). In contrast, the CM-treated samples exhibited the opposite accessibility profile, with increased proximal promoter accessibility and decreased distal intergenic region accessibility with time relative to the IMD samples (Figure 4). We observe the same phenomenon if we focus only on the DARs between the CM- and DM-treated samples for each day (Figure S4). Again, the number of accessible promoters for CM media increased from 615 on D1 to 5973 on D5 (9.7 fold) whereas those in the DM explants increased from 1260 on D1 to 4054 on D5 (3.2 fold). However, the non-promoter accessible regions for CM-treated explants increased from 2442 on D1 to 16,954 on D5 (6.9 fold) and in the DM-treated explants the number of accessible non-promoter regions increased from 6950 on D1 to 20,493 on D5 (2.9 fold). Overall, DM treatment of lens epithelia leads to a less substantial increase in both promoter and non-promoter accessibility with time relative to the lens epithelial explants cultured in CM.

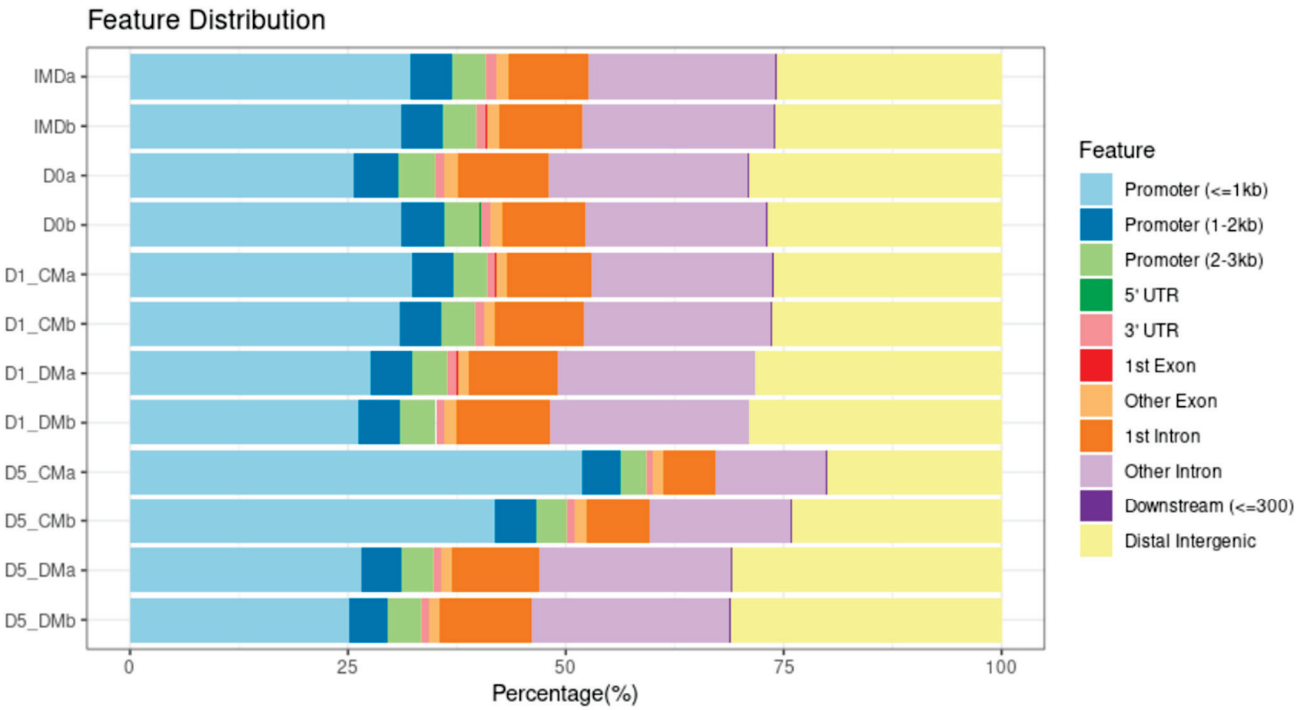

Figure 4. Gene annotation of all accessible regions for ATAC-seq using Chipseeker across six conditions. The total accessible regions are represented as a percentage to compare the proportion of changes in genomic features. The accessible regions are divided into eleven categories 1. proximal promoters (within 1 kb of the TSS), 2. intermediate promoters (within 1–2 kb of the TSS), 3. distal promoters (within 2–3 kb of the TSS), 4. first exon, 5. other exons, 6. first intron, 7. other introns, 8. 5′ untranslated region (5′ UTR), 9. 3′ untranslated region (3′ UTR), 10. downstream intergenic (within 300 kb of the 3′UTR), and 11. distal intergenic (>300 kb of the 3′UTR) regions.

3.4. Specific Changes in Chromatin Accessibility and Gene Expression in Vitreous-Treated Lens Epithelial Explants with Respect to Fiber Cell Differentiation

Given the extensive use of lens epithelial explants to model lens fiber cell differentiation, we investigated how the chromatin landscape and transcription of genes associated with lens fiber cells changed in the different treatment groups. Analyzing the genomic regions associated with genes highly expressed in lens fiber cells, we observed genomic accessibility patterns near the promoter regions (Figures 5A and S5). The promoters of some genes (for example: *Gja3, Bnip3, Hsf4, Grygn, Maf, Mip* and *Arid3b*) exhibited a constitutive accessibility pattern (no evidence of changes in accessibility in the IMD samples and in all treatments). A second pattern (exemplified by: *Gja8*, *Carhsp1*, *Grygs*, *Slc2a3*, *Elf3*, *Jga1*, *Dach2*, *Sox1*, *Crybb3*, *Cryba4/Crybb1*, *Lctl* and *Lim2*) exhibited a relative increase of accessibility in the IMD and DM treated conditions, but a loss of accessibility in the CM treatments. Several of the promoters in this group also exhibited a transient accessibility increase in the D1 CM that was lost by D5 (Figure S5). A third set of gene promoters (e.g.,: *Caprin2*, *Crygd*, *Fabp5*, *Cd24a* and *Mitf*) were accessible in the IMD samples, but exhibited increased accessibility with DM treatment. A fourth group of genes (e.g.,: *Tmod1* and *Bache*) had promoters that were relatively inaccessible in the IMD samples with increased accessibility in D0 and/or CM but exhibited peak accessibility in the DM treatments. Finally, a fifth group of promoters (e.g.,: *Lgsn*, *Dnase2b* and *Nav3*) did not show discernable/relative enrichment of ATAC signal in any treatments except the DM samples.

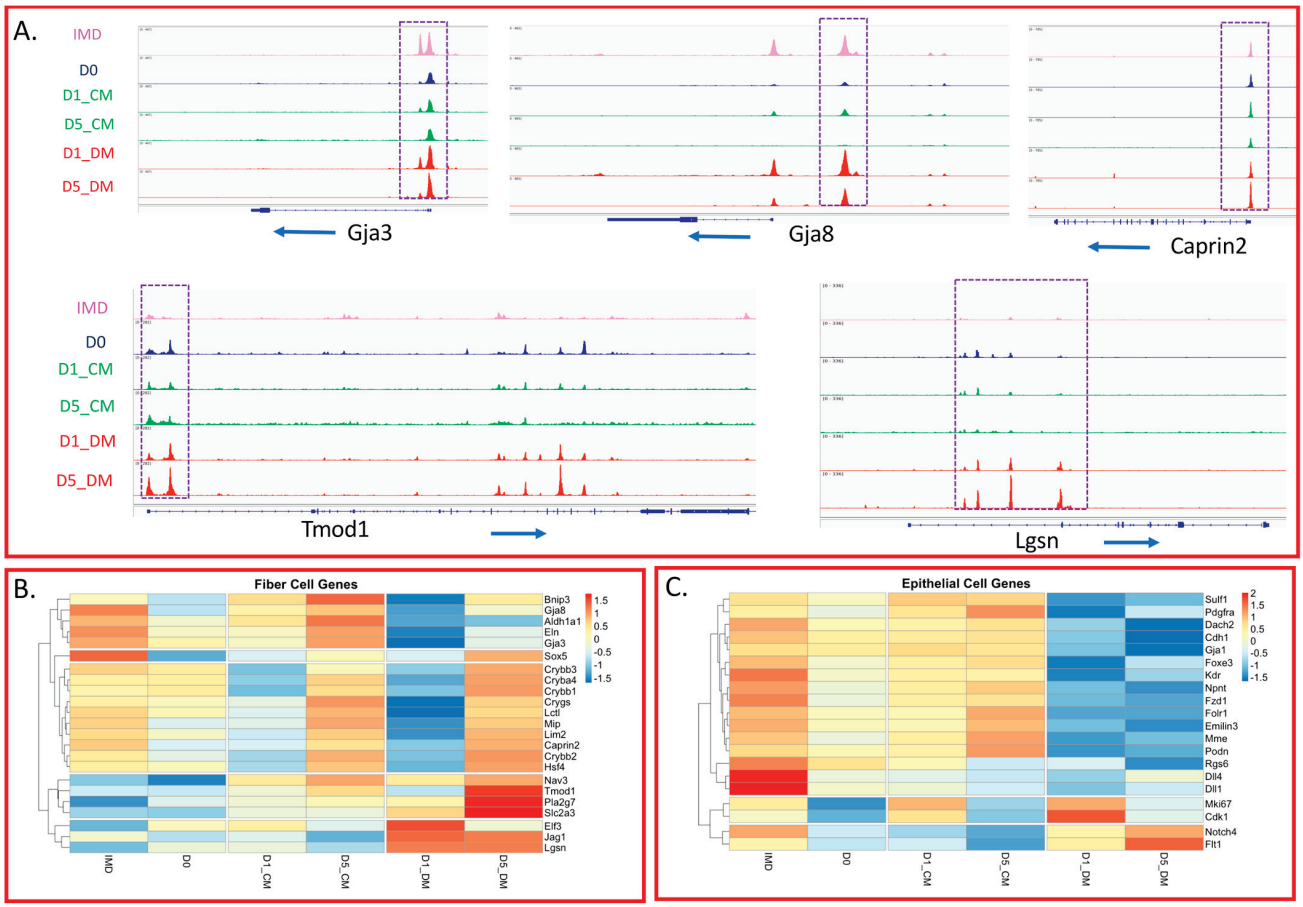

Figure 5. Fiber cell genes are active in D5 samples whereas epithelial cell genes are downregulated in DM samples. (**A**) Genomic browser view display of *Gja3*, *Gja8*, *Caprin2*, *Tmod1*, and *Lgsn* with normalized counts for ATAC-seq in the coverage tracks above. The dotted line represents the area of accessibility in promoter regions. (**B**) The z-score heatmap displays RNA-seq expression values for fiber cell-specific genes. (**C**) The z-score heatmap displays RNA-seq expression values for epithelial cell-specific genes.

We observed interesting patterns in gene expression with respect to genes associated with fiber cell differentiation (Figure 5B). One group of genes that included *Tmod1*, *Pa2g7*, and *Slc2a3* exhibited very low expression in the P8 lens epithelium (IMD) and only reached high expression levels after 5 days of vitreous exposure. Therefore, high expression of these genes requires more than short term exposure to factors present in the vitreous humor. A second group of genes including *Elf3*, *Jag1*, and *Lgsn*, exhibited low expression in the IMD condition and high expression when exposed to vitreous starting at D1. This was the only group of fiber-cell genes that failed to exhibit a dramatic relative decline in expression after one day of vitreous exposure (D1_DM). The third gene expression pattern (characterized by *Gja8*, *Aldh1a1*, and *Eln*) exhibited high expression in IMD and D5_CM conditions and very low expression after one day of vitreous exposure that only increased slightly at 5 days. High expression of these genes appeared independent of vitreous during the culture period. Yet another class of fiber-cell genes, including *Crybb3*, *Cryba4*, *Crygs*, *Mip*, and *Hsf4*, underwent an unexpected, transient decrease in expression at D1 for both CM- and DM-treated samples. However, expression of these genes was increased to similar levels in both CM- and DM-treated samples, revealing that expression of these genes is enhanced independently of vitreous treatment within 5 days of culture.

The observed initial decline in fiber cell gene expression upon the addition of vitreous contrasts with the increased chromatin accessibility seen for most of these genes in the D1_DM samples. This observation mirrors the initial drop in crystallin transcript expression following the addition of FGF2 in rat lens epithelial explants [77]. Unsurprisingly, genes associated with MAPK signaling (*Etv1*, *Etv4*, *Etv5*, *Spry1*, and *Spry4*), upstream of fiber cell differentiation, exhibit an increase in expression following the addition of vitreous that is significantly higher in D5_DM than in D1_DM (Figure S6). This would be consistent with a requirement of sustained MAPK for the expression of several genes associated with fiber cell differentiation [78].

Fiber cell differentiation, while often characterized by the increased expression of genes and proteins preferentially found in lens fiber cells, also involves the loss of transcripts and proteins preferentially found in lens epithelial cells. We examined the chromatin accessibility of promoter regions of genes preferentially expressed in the epithelium to compare the accessibility in the native lens epithelium (IMD) with that in the DM-treated explants (Figure S7). For the majority of the genes we examined (14 of 22, including *Pax6*, *Pdgfra*, *Cdh1*, *Gja1*, *Fzd1*, *Emilin3*, *Dll1* and *Cdk1*) the accessibility near the transcription start site remained the same or declined slightly in the DM relative to the IMD samples. In a few cases (*Kdr, Mme*, *Tulp3*, *Npnt*, and *Igsf3*) the accessibility increased in DM, and in other cases (*Foxe3*, *Islr* and *Podn*) the accessibility significantly declined in DM relative to the IMD samples.

To explore how the lens transcriptome changes with our treatments with respect to genes that typify the lens epithelium, we selected 20 genes that are preferentially expressed in lens epithelial cells over lens fiber cells in newborn lenses [45]. The expression of most of these genes declined upon treatment with DM (Figure 5C). The typical pattern (exhibited by *Foxe3*, *Cdh1* and *Fzd1*) is moderate to high expression in the IMD samples, followed by a drop upon explanting (D0) with some recovery in CM and drastically reduced expression in DM. Some exceptions include the proliferation-related genes (*Cdk1* and *Mki67*) where long term culture in CM or DM resulted in expression declines, but the initial addition of vitreous (D1-DM) results in a dramatically increased expression. Likewise, some genes (for example, *Notch4* and *Flt1*) exhibited a reduced expression in D0 and CM but an increased expression in DM.

We also performed a statistical analysis of the top 30 most significant differentially expressed protein-coding genes between epithelial and fiber cells ranked by adjusted *p* value from a previous RNA-seq study on newborn mouse lens [45] by comparing the expression of these genes between the IMD and D5_DM condition. In the D5_DM samples, 20 of the top 30 "lens epithelial genes" were downregulated, while only 2 of these genes were upregulated. In contrast, only 5 of the 30 "fiber cell genes" were differentially

regulated between the IMD and D5_DM condition but all of these were upregulated in DM. A Fisher's exact test indicated a significant association between the gene sets ($p = 0.0003$).

3.5. Increases in Both Promoter Accessibility and Gene Expression for Epithelial to Mesenchymal Transition and Inflammatory Response Genes Induced by Vitreous Humor

We observed a very consistent pattern of increased accessibility in the promoters of genes associated with immune activation, inflammation, and fibrosis with the addition of DM (Figure S8). In many cases, these genes were inaccessible (for example, *Krt16*), or barely accessible (for example, *Tnfrs11b*) in the IMD condition (Figure 6A). Likewise, when examining a representative list of immune-response-related genes (Figure 6B) or genes associated with ECM organization (Figure S9A), we typically found very low expression in the IMD samples with significant upregulation in DM media. We used gene set enrichment analysis (GSEA) to conduct a comprehensive pairwise comparison of the IMD versus D5_DM gene expression. This analysis utilized hallmark gene sets to identify differential sample enrichment for well-defined biological states. Among the most enriched states identified in the D5_DM sample were epithelial to mesenchymal transition and inflammatory response (Figure 6C). These findings provide compelling evidence that the addition of vitreous humor to lens epithelial explants leads to a pronounced EMT/inflammatory response.

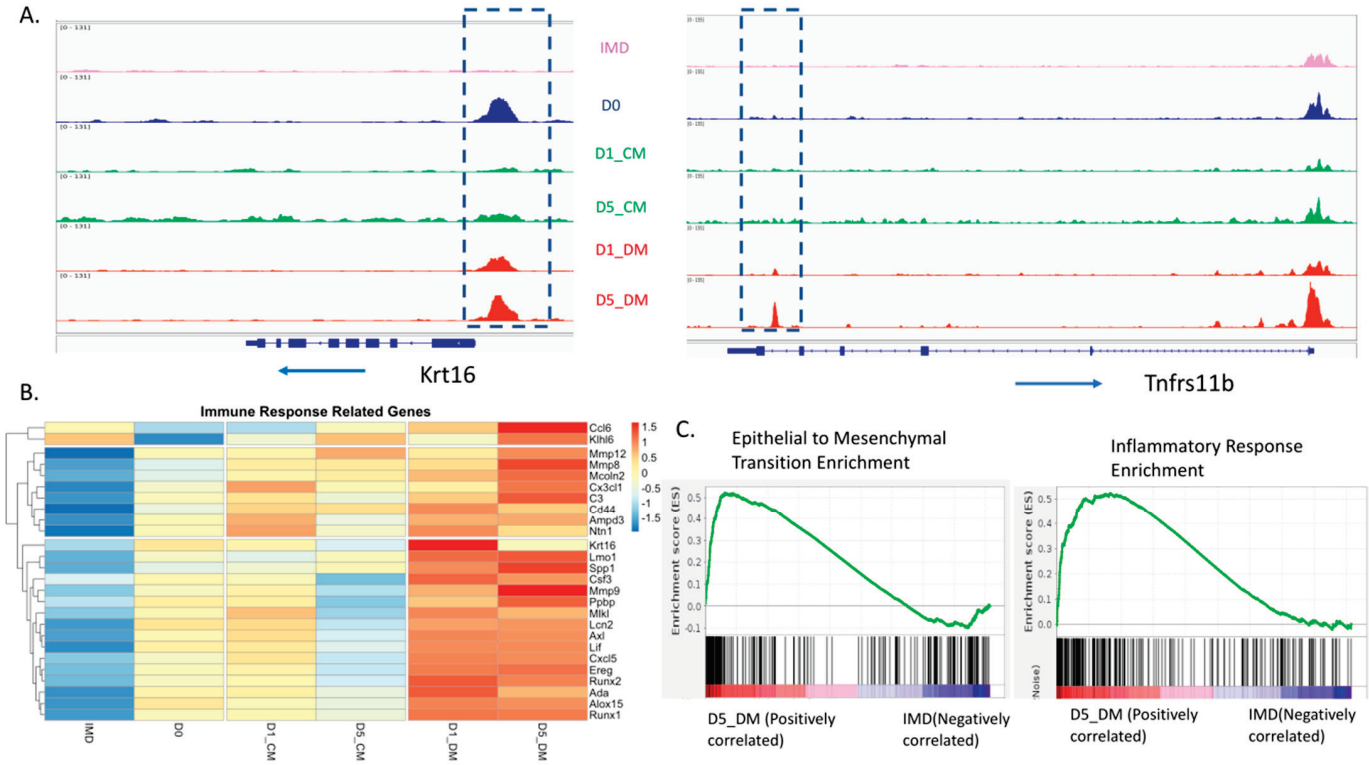

Figure 6. Immune response and epithelial to mesenchymal transition were observed in D5_DM samples compared to any other condition. (**A**) Genomic browser view display of *Krt16* and *Tnfrs11b* with normalized counts for ATAC-seq in the coverage tracks above. The dotted line represents the area of accessibility in promoter regions. (**B**) The z-score heatmap displays RNA-seq expression values for immune response-related genes. (**C**) Gene set enrichment analysis (GSEA) was performed on normalized RNA-seq expression values from IMD and D5_DM samples. The vertical black lines represent the gene in the query list, whereas the green line represents the enrichment score for each gene (vertical black line). D5_DM dataset (represented with a red scale with red being D5_DM and blue being IMD) is enriched for epithelial to mesenchymal transition and inflammatory response. The normalized enrichment score for Epithelial to Mesenchymal Transition and Inflammatory Response is 1.29 and 1.25 respectively.

3.6. Evaluation of Transcription Factor Binding Motifs in DARs Induced in Lens Epithelial Explants by the Addition of Vitreous Humor

Transcription factor binding within regions of open chromatin can drive specific changes in gene expression. With this in mind, we broadly divided the differentially accessible regions found between CM- and DM-treated explants into either promoter or non-promoter regions. We then searched these regions for transcription factor motifs using the monaLisa R package software.

We identified a total of 148 transcription factor motifs, using a significance cutoff of ($p < 0.00005$), within DARs of the DM-treated explants. Of these, a total of 24 and 57 motifs were enriched in the D1_DM and D5_DM non-promoter regions, respectively and 22 and 45 motifs enriched in the D1_DM and D5_DM promoter regions, respectively (Figures S10 and S11). A total of 18 of the 148 motifs were enriched in all the conditions (Figure S12). To prioritize the biological significance of these predicted transcription factor binding sites, we compared the list of 148 motifs with the transcription factors that exhibited differential expression in the DM-treated samples. This narrowed down the transcription factor transcripts to a list of 6 that were down-regulated and 11 that were up-regulated in DM (Figure 7A). Among the 6 down-regulated transcription factor genes, three were members of the Sox gene family (*Sox6*, *Sox17* and *Sox18*). The other three were *Fos, Aft3* and *Tead4.* Members of the Sox gene family were also prominent in the up-regulated transcription factors (*Sox3, Sox 4, Sox5, Sox9, Sox10* and *Sox11*), as were all three members of the Runx family (*Runx1*, *Runx2* and *Runx3*). The remaining two up-regulated transcription factor genes were *Tfap2c* and *Batf*. Of the transcription factor genes up-regulated in DM, only *Sox4* and *Sox5* exhibited high expression in the IMD (native lens epithelium).

We also examined our RNA-seq data set to identify transcription factor genes that were expressed, but not differentially regulated in any of our experimental conditions. Relying on a list of all transcription factor-encoding genes in the mouse genome [79], we identified 825 genes that met these criteria (Table S8). Presumably, these genes represent a list of factors which are present in lens explants and may exert differential chromatin-binding activity but are not regulated at the transcript level. Interestingly, at the top of this list is *Pax6*, reflecting its high expression in lens cells. Moreover, near the top of the list are *Smad3*, *Smarcc1*, *Six3*, and *Tead2*. Motifs for these transcription factors that were over-represented in accessible chromatin in the D1_DM and D5_DM explants are annotated with an asterisk in Figures S10 and S11, respectively.

We independently repeated our explant experiments to validate our RNA-seq results on selected genes using RT-qPCR. As expected, we observed evidence for increased transcript abundance of fiber cell genes *Slc2a3* and *Caprin2* after 5 days of vitreous treatment, relative to the CM control. This experiment confirmed that *Runx1, Runx2, Runx3* and *Sox10* exhibited a significantly increased expression in the D5_DM condition relative to the native lens epithelium (IMD). All of these transcription factors, with the exception of *Runx2*, also exhibited a significantly increased expression in the D5_DM condition versus the D5_CM condition (Figure S13). Similarly, RT-qPCR provided evidence of a reduced *Tead4* abundance in D5_DM samples relative to D5_CM. Interestingly, RT-qPCR analysis of *Sox9* abundance failed to produce evidence of an elevated expression in response to vitreous treatment. Thus, the interpretation of our RNAseq results should be balanced with this observation, which could potentially be ascribed to differences between the assays, such as detection sensitivity, alternate cDNA generation approaches, or the reliance of RT-qPCR on a calibrator gene.

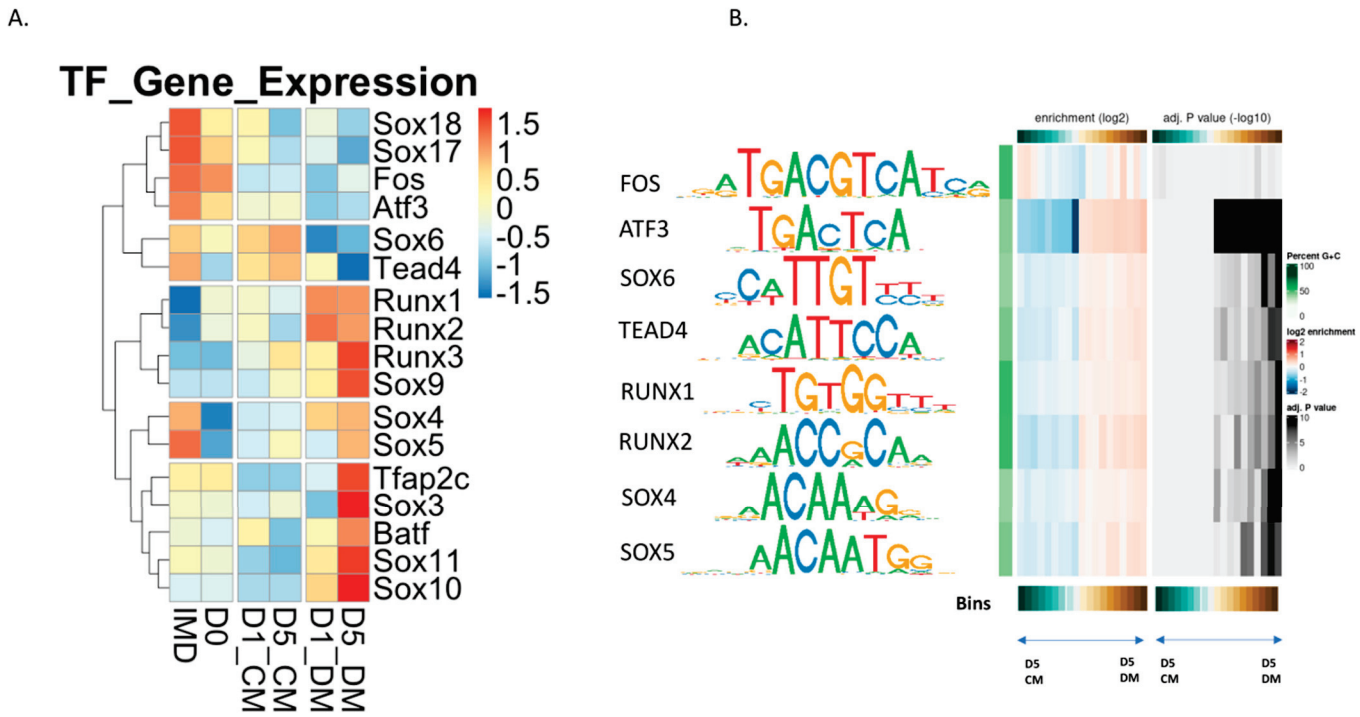

Figure 7. Overrepresented motifs in accessible regions (both promoter and non-promoter regions) at day 5. The monaLisa software was used to bin differentially accessible summits by accessibility across D5_DM and D5_CM conditions. Each bin was analyzed for the overrepresentation of the transcription factors motif using JASPAR 2022 database. Enriched motifs identified at −log10(0.00005) in bins were recorded. The associated transcription factor's gene expression of the identified motifs is represented as a z-score heatmap (**A**). (**B**) The selected motifs enriched in D5_DM with increased transcript expression in endogenous human single-cell lens data (see Figure S12) are represented and plotted. The green heatmap indicates GC content. The blue and red heatmap represents the motif enrichment whereas white and black heatmap represents the adj. *p*-value. The center bin represents the zero enrichment and non-significant, whereas the left and right bins represent the progressively increased log fold change values, with the end value being the highest log-fold change.

To compare the expression of these transcription factors in DM-treated explants with endogenous lens cells, we examined the expression of these 18 transcription factor genes from a recently published human snRNA-seq dataset from an adult anterior segment [51]. Nine of the eighteen transcription factor genes were expressed in at least 5% of the 13,900 lens cells in the human snRNA-seq dataset. In adult human lenses, *RUNX1* and *RUNX2* are more prominently expressed in fiber cells than in epithelial cells. In contrast, *TEAD4* and *FOS* are more prominently expressed in epithelial cells. *ATF3* expression appeared highest in cells of the transitional zone and early fiber differentiation. Of the Sox genes, only *SOX4*, *SOX5* and *SOX6* were prominently expressed in the adult lens data set (Figure S14). We examined the presence of the motifs for each of these nine transcription factor genes in the DARs from CM- and DM-treated samples (Figure 7B). We examined each motif in terms of increasing $\log_2$ fold change (LFC) value (left heat map) and adjusted *p*-value (right heat map). In each case, the D5_CM versus D5_DM DAR data are represented by different bins with the center bin of each heat map representing no LFC or the least significance, with LFC and significance increasing in each direction from the center for the left and right heat maps, respectively. Binding motifs for RUNX1, RUNX2, TEAD4, SOX6 and SOX4 were highly overrepresented amongst regions with increased accessibility in DM-treated samples at D5. In contrast, ATF3 motifs are more uniformly enriched in D5_DM DARs without respect to LFC.

We again utilized monaLisa to annotate the positions of the motifs for the nine transcription factors that were differentially expressed in the DM treatments, and significantly

expressed in the adult human lens, in the DARs between the CM- and DM-treated samples. We then searched to determine if these annotated motifs were present in the promoter regions of genes characteristically expressed in lens fiber cells or lens epithelial cells (Figure 8, Table S9). We found several TEAD motifs in gene promoter regions, including those for *Foxe3*, *Gja1* and *Dll1* (Figure 8A) genes that are primarily expressed in lens epithelial cells. We also found SOX and RUNX motifs in the promoters of several genes including *Tmod1*, *Dnase2b* and *Crybb3* (Figure 8B), and *Slc2a3*, *Nav3* and *Jag1* (Figure 8C), respectively; all genes expressed predominantly in lens fiber cells.

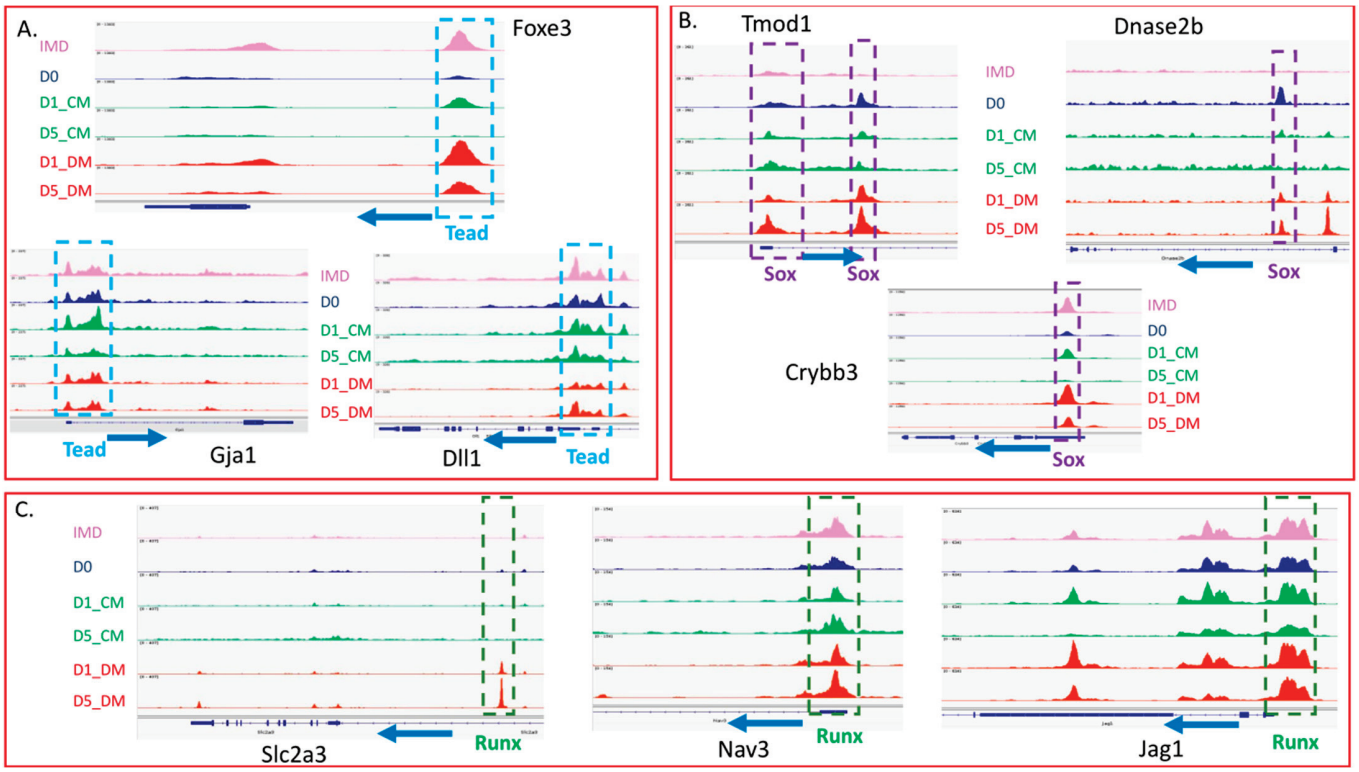

Figure 8. The genomic browser displays ATAC-signal proximal to DARs containing associated motifs. The dotted line represents the regions in the promoter of the representative genes with the motif sequence. (**A**) TEAD binding motifs for epithelial cell-specific genes *Foxe3*, *Gja1*, *Dll1*. (**B**) SOX binding motifs for fiber-specific genes *Tmod1*, *Dnase2b*, *Crybb3*. (**C**) RUNX binding motifs for fiber-specific genes *Slc2a3*, *Nav3*, *Jag1*.

4. Discussion

The lens epithelial explant system has served as an in vitro model of lens fiber cell differentiation for nearly sixty years. While other methods of lens epithelial cell culture, notably dissociated primary cultures of embryonic chick lens epithelial cells, have proven useful for gaining insights into mechanisms of fiber cell differentiation [42,80,81], only the lens epithelial explant system maintains normal contact between the epithelial cells, as well as epithelial cell contact to their native basement membrane, the lens capsule. Studies in lens epithelial explants provided the fundamental framework for the theory that lens polarity relied on a gradient of FGF activity within the eye [28,82,83], a theory that later found support from studies in vivo [84–87]. While purified FGF reliably induces morphological changes and the expression of a set of proteins characteristic of fiber cell differentiation, other factors present in the ocular media (vitreous humor) undoubtedly support lens fiber cell differentiation [30–32,88]. Clearly, endogenous fiber cell differentiation follows stereotypical changes in chromatin organization that impact the lens transcriptome [48,49]. Here, we provide a comprehensive evaluation of how the addition of vitreous humor

changes both the chromatin landscape and transcriptional profile in lens epithelial explants with respect to fiber cell differentiation.

While several genes associated with fiber cell differentiation were already accessible in lens epithelial cells, we observed a consistent trend of increased accessibility in the promoter regions of many such genes following the addition of vitreous humor. This increased accessibility was not observed in explants treated with unsupplemented culture media. Only rarely did we observe the addition of vitreous reducing promoter accessibility in genes associated with fiber differentiation. In contrast, the addition of vitreous had a less consistent effect on genes highly expressed in the lens epithelium. Often the accessibility of these genes remained the same or slightly decreased following the addition of vitreous. Overall, the majority of genes characteristic of both lens epithelial cells and lens fiber cells are accessible in the lens epithelium and either become more accessible (in the case of fiber genes) or change little (in the case of epithelial genes) upon the addition of vitreous. However, after one day of vitreous exposure (D1_DM), there was a characteristic drop in the level of transcripts for many fiber cell-associated genes (Figure 5B). This initial drop in differentiation-associated mRNA transcripts upon the addition of vitreous is reminiscent of the drop in crystallin transcripts seen in P3 rat lens epithelial explants 20 h after the addition of FGF2 [77]. This reduction was explained by increased mRNA turnover following FGF addition. A similar phenomenon may be responsible for the reduction in differentiation-related transcripts in lens explants 24 h after vitreous addition. At day 5, the increase in fiber differentiation-related transcripts was modest and often only slightly increased over that seen in the un-supplemented culture medium. This observation does not match the increased accessibility seen in many of these same genes in the D5_DM condition. We suggest that the explants treated with vitreous for only five days may not have had time to upregulate many of the differentiation-associated transcripts to the extent that we would see with longer culture. Previously, we found that vitreous exposure for 10 days led to a stronger expression of gamma crystallins and MIP protein than exposure for 5 days in P8 mouse lens epithelial explants [32]. It also is probable that the expression of many genes associated with fiber cell differentiation would follow a sustained increase in Erk signaling [30,41], and many of these genes increased from day 1 to day 5 (Figure S5). In contrast, the drop in the expression of genes associated with lens epithelium was dramatic at one day and maintained at five days of vitreous exposure (Figure 5C).

Based on many previous studies, we expected that the addition of vitreous humor would induce the expression of transcripts related to fiber cell differentiation. However, we did not anticipate the dramatic and widespread upregulation of immune system- and EMT-related transcripts upon the addition of vitreous. These upregulated transcripts were accompanied by significant increases in promoter accessibility in the presence of vitreous humor. In previous studies using lens epithelial explants to model fibrotic changes seen in posterior capsule opacification, TGFβ was often added to the culture medium as an inducing agent for EMT [89–92]. However, our observations suggest that the addition of vitreous is sufficient to induce many gene expression changes associated with EMT and fibrosis (Figures 5 and S8). Interestingly, these genes are not typically expressed in the native lens epithelium and are not upregulated during endogenous fiber cell differentiation. This suggests that the in vitro culture conditions, combined with the addition of vitreous humor, ectopically upregulate the expression of these immune-/ECM-related genes. While the vitreous humor is in contact with the posterior lens fiber cells, the anterior lens epithelial cells do not normally come into direct contact with vitreous. It is possible that the combination of in vitro culture and the potential activation (via post-mortem surgical collection) of inflammatory mediators, including TGFβ, could amplify an immune response in the explants exposed to vitreous. Alternatively, the expression of these inflammation-related genes in response to vitreous may be suppressed within the intact eye.

Others have used the lens epithelial explant system to model pathogenic changes which occur in cataract [33,34] and posterior capsular opacification (PCO) [35–43]. Since the creation of lens epithelial explants involves traumatic removal of the fiber cell mass and

in vitro culture, it is likely that explanting alone causes gene expression changes consistent with inflammation or trauma. A transcriptomic analysis of mouse lens epithelial cells in a cataract surgery model demonstrated many gene expression changes consistent with inflammation and fibrosis 24 h after the removal of the fiber cell mass [44]. However, our results demonstrate that the addition of vitreous humor enhances the expression of EMT/inflammatory markers over that of just explanting alone. In fact, the addition of vitreous humor to explanted lens epithelium may mimic the conditions that surviving lens epithelial cells encounter following cataract surgery, that leads to pathologic PCO.

To our knowledge, this work is the first to describe both genome-wide changes in gene expression and chromatin accessibility in lens epithelial explants induced to differentiate in vitro. One of the advantages of this approach is to make predictions about the transcription factors that may drive the observed changes in gene expression. We undertook an analysis of DARs to search for transcription factor binding motifs that are present in promoter regions of genes associated with either fiber cell differentiation or lens epithelial cells. After filtering the motifs identified in the promoter regions for transcription factors that displayed differential expression in the DM-treated samples, we identified six downregulated and twelve upregulated transcription factors. We then searched for these eighteen motifs in genes of interest. This analysis identified TEAD (a downregulated transcription factor) motifs in several lens epithelial genes (*Foxe3*, *Gja1* and *Dll1*) that decrease their level of expression with DM exposure. Likewise, we discovered SOX motifs in promoters of genes, including *Tmod1*, *Dnase2b* and *Crybb3* and RUNX motifs in the promoters of genes including *Slc2a3*, *Nav3* and *Jag1*, all of which are upregulated in fiber cells. Although the transcription factors PAX6, FOXE3 and PROX1 clearly play unique and important roles in lens development, we found no evidence that the DM treatment induced accessibility changes in binding motifs for these sites relative to the CM treatment using our stringent p-value criterion ($p < 0.00005$). We should note that the JASPAR 2022 vertebrate database of transcription factor binding profiles that we used [75] does not contain a FOX3 binding motif, but none of the FOX-family binding motifs present in the database showed evidence for DM-induced accessibility changes.

SOX transcription factors clearly play an important role in lens development. Distinct Sox genes are required both for lens induction (e.g., *Sox2*) [93,94] and for fiber cell differentiation (e.g., *Sox1*) [95]. SOX1 directly interacts with a promoter element in the gamma crystallin gene cluster and in its absence fiber cells fail to elongate and gamma crystallin expression is abolished [96]. While neither *Sox1* nor *Sox2* appear to be upregulated within five days of vitreous exposure, other Sox transcription factor genes (*Sox9*, *Sox10* and *Sox11*) are, and may be recruited to cis-regulatory sites to drive fiber cell differentiation in the explants. SOX transcription factors can also interact with other transcription factors such as PAX6 [95] or POU2f1 [97] to regulate lens gene expression. The *Dnase2b* promoter may provide an example of this type of cis-regulatory grammar as the accessible regions that we identified contain HSF4 and PAX6 consensus motifs, both of which have been previously suggested to regulate transcription at this locus [98], as well as motifs for SOX transcription factors (Figure S15).

In contrast to SOX transcription factors, there exists little information to suggest that RUNX transcription factors play an essential role in lens development. Mice lacking *Runx1* die as embryos from hematopoietic failure [99,100] and mice lacking *Runx2* exhibit neonatal lethality from respiratory failure [101,102]. *Runx3* knockout mice have a variety of phenotypes involving the nervous, digestive, immune, skeletal and respiratory systems [103–107]. Although *Runx1* and *Runx3* play a role in lacrimal gland morphogenesis and regeneration [108], functions for these transcription factors in lens development remain unknown, despite the expression of *RUNX1* in maturing fiber cells of adult human lenses [51]. RUNX motifs were also previously identified as uniquely enriched in the open chromatin peaks from mouse E14.5 lens fibers relative to lens epithelium [48]. RUNX transcription factors are involved in hematopoiesis and immune responses. Given the extensive upregulation of immune-related genes upon the addition of vitreous, it is possible that increased expression

of RUNX transcription factors may facilitate lens fiber cell differentiation in vitro in a way that would not normally occur in vivo. The specific role of RUNX transcription factors in lens development remains to be experimentally verified.

The motifs for ATF3, and AP1 transcription factor family members in general, are dramatically enriched in chromatin that becomes accessible upon the addition of vitreous humor (Figures 7, S9 and S10). These basic region leucine zipper transcription factors exhibit considerable ability to form heterodimers that bind similar cAMP-responsive (CRE), TPA-responsive (TRE) or MAF-recognition (MARE) elements [109,110]. ATF4 is essential for lens fiber formation [111] and is upregulated in several different rodent cataract models where it plays a role in ER stress/unfolded protein response [112–116]. Although the ATF3 motif was specifically highlighted in Figure 7, our experimental approach does not delineate which specific ATF family members are driving the chromatin accessibility changes induced by vitreous exposure.

Large changes in chromatin accessibility, and subsequent responses in gene expression, are likely driven by nucleosome repositioning or other epigenetic changes driven by chromatin remodeling enzymes. Unsurprisingly, some of these chromatin remodeling enzymes exhibit differential expression in response to vitreous. For example, *Prdm13, Tet1, Hdac11, Prdm9,* and *Tet3* are differentially upregulated in DEG clusters 3 or 6, characteristic of the native lens epithelium. However, other epigenetic remodeling enzymes exhibited increased expression in response to vitreous. Some of these include *Hdac9, Dnmt1,* and *Dntm3l* which are upregulated in DEG clusters 1, 2, and 4, respectively.

Lens epithelial explants have provided a way to model lens fiber cell differentiation in vitro for decades [19]. Within this system both FGF [29,83,117–123] and vitreous humor [30,117] have been shown to induce proliferation, elongation and the expression of several proteins characteristic of lens fiber cells. These changes in lens epithelial cell behavior are thought to result from the activation of both ERK and AKT [124]. In fact, other signaling pathways that can promote ERK and AKT activation can induce fiber cell differentiation independently of FGFR signaling [32,125]. Here, for the first time, we have provided a genome-wide comprehensive evaluation of vitreous-induced lens fiber differentiation in lens epithelial explants that includes both changes in chromatin architecture and changes in gene expression. We conclude that vitreous induces increased accessibility in the promoters of many genes associated with fiber cell differentiation and with the activation of immune responses and epithelial to mesenchymal transition. Vitreous also induces the suppression of transcripts characteristic of lens epithelial cells and increases in transcripts associated with fiber cell differentiation and fibrotic responses. The increased promoter accessibility in immune- and ECM-related genes appears to be a feature of the lens epithelial explant system that is not shared by endogenous lens fiber cell differentiation.

Supplementary Materials: The following are available online at https://www.mdpi.com/article/10.3390/cells12030501/s1, Figure S1. Heatmap displays blind hierarchical clustering of normalized ATAC-seq peak signal (A) for each sample and normalized RNA-seq signal (B). Figure S2. Scatterplot showing the normalized counts for all genes, averaged across all samples. The ATAC-seq peaks were matched to genes based on the nearest promoter. When more than one ATAC-seq peak was matched to a gene, the normalized ATAC-seq counts for that gene were averaged. Figure S3. Dot plot displays biological pathways associated with genes that are differentially regulated in the presence of vitreous. Genes are categorized by whether promoter accessibility shows strong positive correlation ($r > 0.9$), moderate positive correlation ($0.9 > r > 0.3$), no correlation ($0.3 > r > -0.3$), moderate negative correlation ($-0.3 > r > -0.9$), or strong negative correlation ($r < -0.9$) with gene expression. Points only shown for terms with adjusted $p < 0.05$. Figure S4. Genomic annotation of DARs using Chipseeker across D1 and D5 samples. represented in terms of percentage. The DARs are represented as percentages to compare the proportion of changes in genomic features. Figure S5. Genomic browser view display for fiber cell-specific genes *Pla2g7*, *Cryba4/Crybb1*, *Crygc*, *Crybb2/Crybb3*, *Lim2* and *Lctl*. The dotted line represents the regions of our interest. Figure S6. MAPK signaling genes are active in DM samples. (A) Genomic browser view display for MAPK signaling genes increased accessibility for D5_DM samples. (B) The z-score heatmap displays RNA-seq expression values for MAPK signaling

genes. Figure S7. Genomic browser view display for epithelial cell-specific genes *Dll1*, *Emilin3*, *Fzd1*, *Podn*, *Islr*, *Foxe3*, *Npnt*, *Tulp3 and Igsf3.* The dotted line represents the regions of our interest. Figure S8. Genomic browser view display for immune response genes and ECM organization genes *Ampd3*, *Rnf141*, *Ereg*, *Lmo1*, *Spp1*, *Mmp12* and *Mmp9.* The dotted line represents the regions of our interest. Figure S9. The z-score heatmap displays RNA-seq expression values for ECM organization genes. Figure S10. Overrepresented motifs in open regions of D5_DM non-promoter regions (A) and D5_DM promoter regions (B). Enriched motifs identified at −log10(0.05) in bins were recorded. The green heatmap indicates GC content. The blue and red heatmap represents the enrichment whereas white and black heatmap represents the adj. *p*-value. An asterisk (*) indicates transcription factors that are expressed at a constant level in all conditions. Figure S11. Overrepresented motifs in open regions of D1_DM non-promoter regions (A) and D1_DM promoter regions (B). Enriched motifs identified at −log10(0.05) in bins were recorded. The green heatmap indicates GC content. The blue and red heatmap represents the enrichment whereas white and black heatmap represents the adj. *p*-value. An asterisk (*) indicates transcription factors that are expressed at a constant level in all conditions. Figure S12. Venn diagram representing the identified motifs across D1 and D5 for differentiation media treated samples. All the identified motifs were classified to find common motifs and unique motifs associated with each condition. Figure S13. The relative expression of key genes was assessed via RT-qPCR. The expression of *Runx3* was below the threshold of detection in the immediate collection samples (IMD) and was excluded from analysis. *p*-values are displayed for conditions that did not reach statistical significance ($p > 0.05$). Significant *p*-values are indicated: *$p < 0.05$, ** $p < 0.005$, *** $p < 0.0005$, **** $p < 0.00005$. Adjusted *p*-values shown for samples with >2 conditions. Error bars represent standard error of mean estimates. Figure S14. The genes expressed for the selected transcription factors in human lens cells. This analysis was done using broad Institute's Single cell portal (50). (A) The dot blot represents the percentage of the cell expressing the transcript in each stage. The row means value represents the expression (high red vs. low blue). (B) UMAP for some of the representative transcription factors Runx1 and Tead4 representing the expression pattern. Figure S15. PAX6, SOX10, and HSF4 motifs are present within accessible regions across the *Dnase2b* gene body and promoter. ATAC peaks were annotated using JASPAR consensus motifs for PAX6 (MA0069.1), SOX10 (MA0442.2), and HSF4 (MA0771.1) and plotted on a genome browser. Accessible regions containing the motifs are highlighted in pink. Table S1. Primers use for RT-qPCR. Table S2. Chromosome coordinates for all differentially accessible regions with their cluster name. Table S3. Gene Ontology (GO) for all DARs with the associated GO ID and significance represented as VA, VB, VC, VD, VE and VF for six clusters listed in Table S1. Table S4. All differentially expressed genes (DEGs) with their cluster number. Table S5. Gene Ontology (GO) for all DEGs with the associated GO ID and significance represented as V1, V2, V3, V4, V5 and V6 for six cluster listed in Table S3. Table S6. Pearson correlation analysis for all DEGs with their promoter region accessibility. Table S7. Correlation between DARs and DEGs for selected genes in five classes (Extra Cellular Matrix (ECM), Lens Fiber Cell gene (Fiber), Lens Epithelial Cell genes (Epithelial), Mitogen activated Protein Kinase genes (MAPK), Immune related genes (Immune)). Table S8. Transcription factor-encoding genes that are expressed but not differentially regulated in any experimental condition. Table S9. Predicted motif annotation for selected transcription factors using monaLisa.

Author Contributions: Conceptualization, A.U. and M.L.R.; methodology, A.U, M.L.R., B.D.W., S.L.P. and T.J.J.; software, A.U., J.A.T. and M.J.O.; validation, A.U., J.A.T., S.A.L., D.A. and F.J.L.; formal analysis, A.U., J.A.T. and M.J.O.; investigation, A.U. and M.L.R.; resources, A.U., B.D.W., S.L.P., R.K.P. and M.L.R.; data curation, A.U. and M.L.R.; writing—original draft preparation, A.U. and M.L.R.; writing—review and editing, A.U., M.L.R., J.A.T., S.L.P., T.J.J., M.J.O., R.K.P., C.J.M., D.A., S.L.P. and F.J.L.; visualization, A.U.; supervision, M.L.R.; project administration, M.L.R. and B.D.W.; funding acquisition, M.L.R., A.U. and R.K.P. All authors have read and agreed to the published version of the manuscript.

Funding: This work was supported by National Eye Institute grants R01 EY012995 and R21 EY031092 to M.L.R and R01 EY021505 to S.A.L., and the *James & Beth Lewis* endowed Professorship to M.L.R. D.A. was supported by the Knights Templar Pediatric Ophthalmology Career Starter Grant Award. J.A.T. was supported by the National Institute of Neurological Disorders and Stroke grant F99NS129167. In addition, the Miami University Graduate School, Department of Biology, as well as the Miami University Doctoral-Undergraduate Opportunity Scholarship to R.K.P. and A.U., supported this work.

Institutional Review Board Statement: The animal study protocol was approved by the Institutional Review Board of Miami University (protocol code: 997_2024_Jun and approval date: 4 June 2021).

Informed Consent Statement: Not applicable.

Data Availability Statement: The data discussed in this publication have been deposited in NCBIs Gene Expression Omnibus (Edgar et al., 2002: https://doi.org/10.1093/nar/30.1.207) and are accessible through GEO Series accession number GSE215953 (https://www.ncbi.nlm.nih.gov/geo/query/acc.cgi?acc=GSE215953). All code will be made available upon reasonable request to the authors.

Acknowledgments: We acknowledge and thank the staff (Andor Kiss and Xiaoyun Deng) of the Center for Bioinformatics and Functional Genomics (CBFG) at Miami University for instrumentation and computational support. Jacob Weaver for providing his valuable feedback to the manuscript.

Conflicts of Interest: The authors declare no conflict of interest. The funders had no role in the design of the study; in the collection, analyses, or interpretation of data; in the writing of the manuscript, or in the decision to publish the results.

References

1. Audette, D.S.; Scheiblin, D.A.; Duncan, M.K. The Molecular Mechanisms Underlying Lens Fiber Elongation. *Exp. Eye Res.* **2017**, *156*, 41–49. [CrossRef]
2. Brennan, L.; Disatham, J.; Kantorow, M. Mechanisms of Organelle Elimination for Lens Development and Differentiation. *Exp. Eye Res.* **2021**, *209*, 108682. [CrossRef] [PubMed]
3. Cvekl, A.; Eliscovich, C. Crystallin Gene Expression: Insights from Studies of Transcriptional Bursting. *Exp. Eye Res.* **2021**, *207*, 108564. [CrossRef] [PubMed]
4. Coulombre, J.L.; Coulombre, A.J. Lens development: Fiber elongation and lens orientation. *Science* **1963**, *142*, 1489–1490. [CrossRef]
5. Yamamoto, Y. Growth of Lens and Ocular Environment: Role of Neural Retina in the Growth of Mouse Lens as Revealed by an Implantation Experiment. *Dev. Growth Differ.* **1976**, *18*, 273–278. [CrossRef]
6. Spemann, H. Uber Korrelationen in Der Entwicklung Des Auges. *Verh. Anat. Ges.* **1901**, *15*, 61–79.
7. Henry, J.J.; Tsonis, P.A. Molecular and Cellular Aspects of Amphibian Lens Regeneration. *Prog. Retin. Eye Res.* **2010**, *29*, 543–555. [CrossRef]
8. Maki, N.; Tsonis, P.A.; Agata, K. Changes in Global Histone Modifications during Dedifferentiation in Newt Lens Regeneration. *Mol. Vis.* **2010**, *16*, 1893–1897.
9. Overbeek, P.A.; Chepelinsky, A.B.; Khillan, J.S.; Piatigorsky, J.; Westphal, H. Lens-Specific Expression and Developmental Regulation of the Bacterial Chloramphenicol Acetyltransferase Gene Driven by the Murine Alpha A-Crystallin Promoter in Transgenic Mice. *Proc. Natl. Acad. Sci. USA* **1985**, *82*, 7815–7819. [CrossRef] [PubMed]
10. Lakso, M.; Sauer, B.; Mosinger, B., Jr.; Lee, E.J.; Manning, R.W.; Yu, S.H.; Mulder, K.L.; Westphal, H. Targeted Oncogene Activation by Site-Specific Recombination in Transgenic Mice. *Proc. Natl. Acad. Sci. USA* **1992**, *89*, 6232–6236. [CrossRef]
11. Pan, H.; Griep, A.E. Altered Cell Cycle Regulation in the Lens of HPV-16 E6 or E7 Transgenic Mice: Implications for Tumor Suppressor Gene Function in Development. *Genes Dev.* **1994**, *8*, 1285–1299. [CrossRef]
12. Fromm, L.; Shawlot, W.; Gunning, K.; Butel, J.S.; Overbeek, P.A. The Retinoblastoma Protein-Binding Region of Simian Virus 40 Large T Antigen Alters Cell Cycle Regulation in Lenses of Transgenic Mice. *Mol. Cell. Biol.* **1994**, *14*, 6743–6754. [CrossRef] [PubMed]
13. Griep, A.E. Cell Cycle Regulation in the Developing Lens. *Semin. Cell Dev. Biol.* **2006**, *17*, 686–697. [CrossRef]
14. Taiyab, A.; West-Mays, J. Lens Fibrosis: Understanding the Dynamics of Cell Adhesion Signaling in Lens Epithelial-Mesenchymal Transition. *Front. Cell Dev. Biol.* **2022**, *10*, 886053. [CrossRef]
15. Wormstone, I.M.; Wormstone, Y.M.; Smith, A.J.O.; Eldred, J.A. Posterior Capsule Opacification: What's in the Bag? *Prog. Retin. Eye Res.* **2021**, *82*, 100905. [CrossRef]
16. Li, M.; Luan, F.; Zhao, Y.; Hao, H.; Zhou, Y.; Han, W.; Fu, X. Epithelial-Mesenchymal Transition: An Emerging Target in Tissue Fibrosis. *Exp. Biol. Med.* **2016**, *241*, 1–13. [CrossRef]
17. Shirai, K.; Tanaka, S.-I.; Lovicu, F.J.; Saika, S. The Murine Lens: A Model to Investigate in Vivo Epithelial-Mesenchymal Transition. *Dev. Dyn.* **2018**, *247*, 340–345. [CrossRef] [PubMed]
18. Philpott, G.W.; Coulombre, A.J. Lens development. II. The Differentiation of Embryonic Chick Lens Epithelial Cells In Vitro and In Vivo. *Exp. Cell Res.* **1965**, *38*, 635–644. [CrossRef] [PubMed]
19. West-Mays, J.A.; Pino, G.; Lovicu, F.J. Development and Use of the Lens Epithelial Explant System to Study Lens Differentiation and Cataractogenesis. *Prog. Retin. Eye Res.* **2010**, *29*, 135–143. [CrossRef]
20. Liu, J.; Hales, A.M.; Chamberlain, C.G.; McAvoy, J.W. Induction of Cataract-like Changes in Rat Lens Epithelial Explants by Transforming Growth Factor Beta. *Investig. Ophthalmol. Vis. Sci.* **1994**, *35*, 388–401.
21. Hales, A.M.; Schulz, M.W.; Chamberlain, C.G.; McAvoy, J.W. TGF-Beta 1 Induces Lens Cells to Accumulate Alpha-Smooth Muscle Actin, a Marker for Subcapsular Cataracts. *Curr. Eye Res.* **1994**, *13*, 885–890. [CrossRef]

22. Davidson, M.G.; Wormstone, M.; Morgan, D.; Malakof, R.; Allen, J.; McGahan, M.C. Ex Vivo Canine Lens Capsular Sac Explants. *Arbeitsphysiologie* **2000**, *238*, 708–714. [CrossRef] [PubMed]
23. Choi, J.; Park, S.Y.; Joo, C.-K. Hepatocyte Growth Factor Induces Proliferation of Lens Epithelial Cells through Activation of ERK1/2 and JNK/SAPK. *Investig. Ophthalmol. Vis. Sci.* **2004**, *45*, 2696–2704. [CrossRef]
24. Taliana, L.; Evans, M.D.M.; Ang, S.; McAvoy, J.W. Vitronectin Is Present in Epithelial Cells of the Intact Lens and Promotes Epithelial Mesenchymal Transition in Lens Epithelial Explants. *Mol. Vis.* **2006**, *12*, 1233–1242.
25. Jun, J.H.; Sohn, W.-J.; Lee, Y.; Chang, S.D.; Kim, J.-Y. Experimental Lens Capsular Bag Model for Posterior Capsule Opacification. *Cell Tissue Res.* **2014**, *357*, 101–108. [CrossRef] [PubMed]
26. Xie, L.; Santhoshkumar, P.; Reneker, L.W.; Sharma, K.K. Histone Deacetylase Inhibitors Trichostatin A and Vorinostat Inhibit TGFβ2-Induced Lens Epithelial-to-Mesenchymal Cell Transition. *Investig. Ophthalmol. Vis. Sci.* **2014**, *55*, 4731–4740. [CrossRef] [PubMed]
27. Campbell, M.T.; McAvoy, J.W. Onset of Fibre Differentiation in Cultured Rat Lens Epithelium under the Influence of Neural Retina-Conditioned Medium. *Exp. Eye Res.* **1984**, *39*, 83–94. [CrossRef]
28. Schulz, M.W.; Chamberlain, C.G.; de Iongh, R.U.; McAvoy, J.W. Acidic and Basic FGF in Ocular Media and Lens: Implications for Lens Polarity and Growth Patterns. *Development* **1993**, *118*, 117–126. [CrossRef]
29. Chamberlain, C.G.; McAvoy, J.W. Induction of Lens Fibre Differentiation by Acidic and Basic Fibroblast Growth Factor (FGF). *Growth Factors* **1989**, *1*, 125–134. [CrossRef]
30. Wang, Q.; McAvoy, J.W.; Lovicu, F.J. Growth Factor Signaling in Vitreous Humor-Induced Lens Fiber Differentiation. *Invest. Ophthalmol. Vis. Sci.* **2010**, *51*, 3599–3610. [CrossRef]
31. Huang, J.-X.; Feldmeier, M.; Shui, Y.-B.; Beebe, D.C. Evaluation of Fibroblast Growth Factor Signaling during Lens Fiber Cell Differentiation. *Investig. Ophthalmol. Vis. Sci.* **2003**, *44*, 680–690. [CrossRef]
32. Padula, S.L.; Sidler, E.P.; Wagner, B.D.; Manz, C.J.; Lovicu, F.J.; Robinson, M.L. Lens Fiber Cell Differentiation Occurs Independently of Fibroblast Growth Factor Receptor Signaling in the Absence of Pten. *Dev. Biol.* **2020**, *467*, 1–13. [CrossRef]
33. Murthy, K.R.; Goel, R.; Subbannayya, Y.; Jacob, H.K.; Murthy, P.R.; Manda, S.S.; Patil, A.H.; Sharma, R.; Sahasrabuddhe, N.A.; Parashar, A.; et al. Proteomic Analysis of Human Vitreous Humor. *Clin. Proteom.* **2014**, *11*, 29. [CrossRef]
34. Beebe, D.C.; Silver, M.H.; Belcher, K.S.; Van Wyk, J.J.; Svoboda, M.E.; Zelenka, P.S. Lentropin, a Protein That Controls Lens Fiber Formation, Is Related Functionally and Immunologically to the Insulin-like Growth Factors. *Proc. Natl. Acad. Sci. USA* **1987**, *84*, 2327–2330. [CrossRef]
35. Cassidy, L.; Barry, P.; Shaw, C.; Duffy, J.; Kennedy, S. Platelet Derived Growth Factor and Fibroblast Growth Factor Basic Levels in the Vitreous of Patients with Vitreoretinal Disorders. *Br. J. Ophthalmol.* **1998**, *82*, 181–185. [CrossRef] [PubMed]
36. Majima, K. Presence of Growth Factor in Human Vitreous. *Ophthalmologica* **1997**, *211*, 226–228. [CrossRef] [PubMed]
37. Katsura, Y.; Okano, T.; Noritake, M.; Kosano, H.; Nishigori, H.; Kado, S.; Matsuoka, T. Hepatocyte Growth Factor in Vitreous Fluid of Patients with Proliferative Diabetic Retinopathy and Other Retinal Disorders. *Diabetes Care* **1998**, *21*, 1759–1763. [CrossRef]
38. Shui, Y.-B.; Wang, X.; Hu, J.S.; Wang, S.-P.; Garcia, C.M.; Potts, J.D.; Sharma, Y.; Beebe, D.C. Vascular Endothelial Growth Factor Expression and Signaling in the Lens. *Investig. Ophthalmol. Vis. Sci.* **2003**, *44*, 3911–3919. [CrossRef] [PubMed]
39. Brooks, H.L., Jr.; Caballero, S., Jr.; Newell, C.K.; Steinmetz, R.L.; Watson, D.; Segal, M.S.; Harrison, J.K.; Scott, E.W.; Grant, M.B. Vitreous Levels of Vascular Endothelial Growth Factor and Stromal-Derived Factor 1 in Patients with Diabetic Retinopathy and Cystoid Macular Edema before and after Intraocular Injection of Triamcinolone. *Arch. Ophthalmol.* **2004**, *122*, 1801–1807. [CrossRef]
40. Boswell, B.A.; Lein, P.J.; Musil, L.S. Cross-Talk between Fibroblast Growth Factor and Bone Morphogenetic Proteins Regulates Gap Junction-Mediated Intercellular Communication in Lens Cells. *Mol. Biol. Cell* **2008**, *19*, 2631–2641. [CrossRef]
41. Lovicu, F.J.; McAvoy, J.W. FGF-Induced Lens Cell Proliferation and Differentiation Is Dependent on MAPK (ERK1/2) Signalling. *Development* **2001**, *128*, 5075–5084. [CrossRef] [PubMed]
42. Boswell, B.A.; Musil, L.S. Synergistic Interaction between the Fibroblast Growth Factor and Bone Morphogenetic Protein Signaling Pathways in Lens Cells. *Mol. Biol. Cell* **2015**, *26*, 2561–2572. [CrossRef] [PubMed]
43. Shu, D.Y.; Lovicu, F.J. Insights into Bone Morphogenetic Protein-(BMP-) Signaling in Ocular Lens Biology and Pathology. *Cells* **2021**, *10*, 2604. [CrossRef]
44. Boswell, B.A.; Korol, A.; West-Mays, J.A.; Musil, L.S. Dual Function of TGFβ in Lens Epithelial Cell Fate: Implications for Secondary Cataract. *Mol. Biol. Cell* **2017**, *28*, 907–921. [CrossRef] [PubMed]
45. Hoang, T.V.; Kumar, P.K.R.; Sutharzan, S.; Tsonis, P.A.; Liang, C.; Robinson, M.L. Comparative Transcriptome Analysis of Epithelial and Fiber Cells in Newborn Mouse Lenses with RNA Sequencing. *Mol. Vis.* **2014**, *20*, 1491–1517.
46. Zhao, Y.; Zheng, D.; Cvekl, A. A Comprehensive Spatial-Temporal Transcriptomic Analysis of Differentiating Nascent Mouse Lens Epithelial and Fiber Cells. *Exp. Eye Res.* **2018**, *175*, 56–72. [CrossRef]
47. Chauss, D.; Basu, S.; Rajakaruna, S.; Ma, Z.; Gau, V.; Anastas, S.; Brennan, L.A.; Hejtmancik, J.F.; Menko, A.S.; Kantorow, M. Differentiation State-Specific Mitochondrial Dynamic Regulatory Networks Are Revealed by Global Transcriptional Analysis of the Developing Chicken Lens. *G3* **2014**, *4*, 1515–1527. [CrossRef]
48. Zhao, Y.; Zheng, D.; Cvekl, A. Profiling of Chromatin Accessibility and Identification of General Cis-Regulatory Mechanisms That Control Two Ocular Lens Differentiation Pathways. *Epigenetics Chromatin* **2019**, *12*, 27. [CrossRef]

49. Disatham, J.; Chauss, D.; Gheyas, R.; Brennan, L.; Blanco, D.; Daley, L.; Menko, A.S.; Kantorow, M. Lens Differentiation Is Characterized by Stage-Specific Changes in Chromatin Accessibility Correlating with Differentiation State-Specific Gene Expression. *Dev. Biol.* **2019**, *453*, 86–104. [CrossRef]
50. Farnsworth, D.R.; Posner, M.; Miller, A.C. Single Cell Transcriptomics of the Developing Zebrafish Lens and Identification of Putative Controllers of Lens Development. *Exp. Eye Res.* **2021**, *206*, 108535. [CrossRef]
51. van Zyl, T.; Yan, W.; McAdams, A.M.; Monavarfeshani, A.; Hageman, G.S.; Sanes, J.R. Cell Atlas of the Human Ocular Anterior Segment: Tissue-Specific and Shared Cell Types. *Proc. Natl. Acad. Sci. USA* **2022**, *119*, e2200914119. [CrossRef] [PubMed]
52. FastQC. A Quality Control Tool for High Throughput Sequence Data; Babraham Bioinformatics Web Site. Available online: http://www.bioinformatics.babraham.ac.uk/projects/fastqc/ (accessed on 1 November 2021).
53. Babraham Bioinformatics-FastQC A Quality Control Tool for High Throughput Sequence Data. Available online: https://www.bioinformatics.babraham.ac.uk/projects/fastqc/ (accessed on 7 July 2022).
54. Ewels, P.; Magnusson, M.; Lundin, S.; Käller, M. MultiQC: Summarize Analysis Results for Multiple Tools and Samples in a Single Report. *Bioinformatics* **2016**, *32*, 3047–3048. [CrossRef]
55. Martin, M. Cutadapt Removes Adapter Sequences from High-Throughput Sequencing Reads. *EMBnet.journal* **2011**, *17*, 10. [CrossRef]
56. Babraham Bioinformatics-Trim Galore! Available online: https://www.bioinformatics.babraham.ac.uk/projects/trim_galore/ (accessed on 7 July 2022).
57. Kim, D.; Paggi, J.M.; Park, C.; Bennett, C.; Salzberg, S.L. Graph-Based Genome Alignment and Genotyping with HISAT2 and HISAT-Genotype. *Nat. Biotechnol.* **2019**, *37*, 907–915. [CrossRef] [PubMed]
58. Frankish, A.; Diekhans, M.; Jungreis, I.; Lagarde, J.; Loveland, J.E.; Mudge, J.M.; Sisu, C.; Wright, J.C.; Armstrong, J.; Barnes, I.; et al. GENCODE 2021. *Nucleic Acids Res.* **2021**, *49*, D916–D923. [CrossRef] [PubMed]
59. Skovaka/Stringtie2. Available online: https://github.com/skovaka/stringtie2 (accessed on 7 July 2022).
60. Love, M.I.; Huber, W.; Anders, S. Moderated Estimation of Fold Change and Dispersion for RNA-Seq Data with DESeq2. *Genome Biol.* **2014**, *15*, 550. [CrossRef] [PubMed]
61. Jin, X.; Han, J. K-Means clustering. In *Encyclopedia of Machine Learning and Data Mining*; Springer: Boston, MA, USA, 2017; pp. 695–697. ISBN 9781489976857.
62. Hartigan, J.A.; Wong, M.A. Algorithm AS 136: A K-Means Clustering Algorithm. *J. R. Stat. Soc. Ser. C. Appl. Stat.* **1979**, *28*, 100. [CrossRef]
63. R Core Team R: A Language and Envirronment for Statistical Computing. Available online: https//www.R-project.org/ (accessed on 1 October 2021).
64. Raudvere, U.; Kolberg, L.; Kuzmin, I.; Arak, T.; Adler, P.; Peterson, H.; Vilo, J. G:Profiler: A Web Server for Functional Enrichment Analysis and Conversions of Gene Lists (2019 Update). *Nucleic Acids Res.* **2019**, *47*, W191–W198. [CrossRef] [PubMed]
65. Mootha, V.K.; Lindgren, C.M.; Eriksson, K.-F.; Subramanian, A.; Sihag, S.; Lehar, J.; Puigserver, P.; Carlsson, E.; Ridderstråle, M.; Laurila, E.; et al. PGC-1α-Responsive Genes Involved in Oxidative Phosphorylation Are Coordinately Downregulated in Human Diabetes. *Nat. Genet.* **2003**, *34*, 267–273. [CrossRef]
66. Subramanian, A.; Tamayo, P.; Mootha, V.K.; Mukherjee, S.; Ebert, B.L.; Gillette, M.A.; Paulovich, A.; Pomeroy, S.L.; Golub, T.R.; Lander, E.S.; et al. Gene Set Enrichment Analysis: A Knowledge-Based Approach for Interpreting Genome-Wide Expression Profiles. *Proc. Natl. Acad. Sci. USA* **2005**, *102*, 15545–15550. [CrossRef]
67. Fox, J.; Weisberg, S. *An R Companion to Applied Regression*, 3rd ed.; SAGE Publications: Thousand Oaks, CA, USA, 2018; ISBN 9781544336473.
68. Lenth, R.V. Emmeans: Estimated Marginal Means, Aka Least-Squares Means. Available online: https://CRAN.R-project.org/package=emmeans (accessed on 27 January 2023).
69. Langmead, B.; Salzberg, S.L. Fast Gapped-Read Alignment with Bowtie 2. *Nat. Methods* **2012**, *9*, 357–359. [CrossRef]
70. Zhang, Y.; Liu, T.; Meyer, C.A.; Eeckhoute, J.; Johnson, D.S.; Bernstein, B.E.; Nusbaum, C.; Myers, R.M.; Brown, M.; Li, W.; et al. Model-Based Analysis of ChIP-Seq (MACS). *Genome Biol.* **2008**, *9*, R137. [CrossRef]
71. Thorvaldsdóttir, H.; Robinson, J.T.; Mesirov, J.P. Integrative Genomics Viewer (IGV): High-Performance Genomics Data Visualization and Exploration. *Brief. Bioinform.* **2013**, *14*, 178–192. [CrossRef] [PubMed]
72. Ramírez, F.; Ryan, D.P.; Grüning, B.; Bhardwaj, V.; Kilpert, F.; Richter, A.S.; Heyne, S.; Dündar, F.; Manke, T. DeepTools2: A next Generation Web Server for Deep-Sequencing Data Analysis. *Nucleic Acids Res.* **2016**, *44*, W160-5. [CrossRef] [PubMed]
73. Yu, G.; Wang, L.-G.; He, Q.-Y. ChIPseeker: An R/Bioconductor Package for ChIP Peak Annotation, Comparison and Visualization. *Bioinformatics* **2015**, *31*, 2382–2383. [CrossRef] [PubMed]
74. Machlab, D.; Burger, L.; Soneson, C.; Rijli, F.M.; Schübeler, D.; Stadler, M.B. MonaLisa: An R/Bioconductor Package for Identifying Regulatory Motifs. *Bioinformatics* **2022**, *38*, 2624–2625. [CrossRef]
75. Castro-Mondragon, J.A.; Riudavets-Puig, R.; Rauluseviciute, I.; Lemma, R.B.; Turchi, L.; Blanc-Mathieu, R.; Lucas, J.; Boddie, P.; Khan, A.; Manosalva Pérez, N.; et al. JASPAR 2022: The 9th Release of the Open-Access Database of Transcription Factor Binding Profiles. *Nucleic Acids Res.* **2022**, *50*, D165–D173. [CrossRef] [PubMed]
76. Oliveros, J.C. Venny; An Interactive Tool for Comparing Lists with Venn's Diagrams. Available online: https://bioinfogp.cnb.csic.es/tools/venny/index.html (accessed on 10 November 2022).

77. Wang, X.; Garcia, C.M.; Shui, Y.-B.; Beebe, D.C. Expression and Regulation of Alpha-, Beta-, and Gamma-Crystallins in Mammalian Lens Epithelial Cells. *Investig. Ophthalmol. Vis. Sci.* **2004**, *45*, 3608–3619. [CrossRef]
78. Iyengar, L.; Wang, Q.; Rasko, J.E.J.; McAvoy, J.W.; Lovicu, F.J. Duration of ERK1/2 Phosphorylation Induced by FGF or Ocular Media Determines Lens Cell Fate. *Differentiation* **2007**, *75*, 662–668. [CrossRef]
79. Hu, H.; Miao, Y.-R.; Jia, L.-H.; Yu, Q.-Y.; Zhang, Q.; Guo, A.-Y. AnimalTFDB 3.0: A Comprehensive Resource for Annotation and Prediction of Animal Transcription Factors. *Nucleic Acids Res.* **2019**, *47*, D33–D38. [CrossRef]
80. Menko, A.S.; Klukas, K.A.; Johnson, R.G. Chicken Embryo Lens Cultures Mimic Differentiation in the Lens. *Dev. Biol.* **1984**, *103*, 129–141. [CrossRef] [PubMed]
81. Musil, L.S. Primary Cultures of Embryonic Chick Lens Cells as a Model System to Study Lens Gap Junctions and Fiber Cell Differentiation. *J. Membr. Biol.* **2012**, *245*, 357–368. [CrossRef]
82. Chamberlain, C.G.; McAvoy, J.W. Evidence That Fibroblast Growth Factor Promotes Lens Fibre Differentiation. *Curr. Eye Res.* **1987**, *6*, 1165–1169. [CrossRef]
83. McAvoy, J.W.; Chamberlain, C.G. Fibroblast Growth Factor (FGF) Induces Different Responses in Lens Epithelial Cells Depending on Its Concentration. *Development* **1989**, *107*, 221–228. [CrossRef] [PubMed]
84. Garcia, C.M.; Yu, K.; Zhao, H.; Ashery-Padan, R.; Ornitz, D.M.; Robinson, M.L.; Beebe, D.C. Signaling through FGF Receptor-2 Is Required for Lens Cell Survival and for Withdrawal from the Cell Cycle during Lens Fiber Cell Differentiation. *Dev. Dyn.* **2005**, *233*, 516–527. [CrossRef] [PubMed]
85. Zhao, H.; Yang, T.; Madakashira, B.P.; Thiels, C.A.; Bechtle, C.A.; Garcia, C.M.; Zhang, H.; Yu, K.; Ornitz, D.M.; Beebe, D.C.; et al. Fibroblast Growth Factor Receptor Signaling Is Essential for Lens Fiber Cell Differentiation. *Dev. Biol.* **2008**, *318*, 276–288. [CrossRef]
86. Garcia, C.M.; Huang, J.; Madakashira, B.P.; Liu, Y.; Rajagopal, R.; Dattilo, L.; Robinson, M.L.; Beebe, D.C. The Function of FGF Signaling in the Lens Placode. *Dev. Biol.* **2011**, *351*, 176–185. [CrossRef]
87. Boswell, B.A.; Overbeek, P.A.; Musil, L.S. Essential Role of BMPs in FGF-Induced Secondary Lens Fiber Differentiation. *Dev. Biol.* **2008**, *324*, 202–212. [CrossRef]
88. Belecky-Adams, T.L.; Adler, R.; Beebe, D.C. Bone Morphogenetic Protein Signaling and the Initiation of Lens Fiber Cell Differentiation. *Development* **2002**, *129*, 3795–3802. [CrossRef] [PubMed]
89. Liu, Z.Z.G.; Taiyab, A.; West-Mays, J.A. MMP9 Differentially Regulates Proteins Involved in Actin Polymerization and Cell Migration during TGF-β-Induced EMT in the Lens. *Int. J. Mol. Sci.* **2021**, *22*, 11988. [CrossRef]
90. Symonds, J.G.; Lovicu, F.J.; Chamberlain, C.G. Posterior Capsule Opacification-like Changes in Rat Lens Explants Cultured with TGFbeta and FGF: Effects of Cell Coverage and Regional Differences. *Exp. Eye Res.* **2006**, *82*, 693–699. [CrossRef]
91. Taiyab, A.; Holms, J.; West-Mays, J.A. β-Catenin/Smad3 Interaction Regulates Transforming Growth Factor-β-Induced Epithelial to Mesenchymal Transition in the Lens. *Int. J. Mol. Sci.* **2019**, *20*, 2078. [CrossRef]
92. Nahomi, R.B.; Pantcheva, M.B.; Nagaraj, R.H. AB-Crystallin Is Essential for the TGF-B2-Mediated Epithelial to Mesenchymal Transition of Lens Epithelial Cells. *Biochem. J.* **2016**, *473*, 1455–1469. [CrossRef] [PubMed]
93. Kamachi, Y.; Uchikawa, M.; Collignon, J.; Lovell-Badge, R.; Kondoh, H. Involvement of Sox1, 2 and 3 in the Early and Subsequent Molecular Events of Lens Induction. *Development* **1998**, *125*, 2521–2532. [CrossRef] [PubMed]
94. Dvorakova, M.; Macova, I.; Bohuslavova, R.; Anderova, M.; Fritzsch, B.; Pavlinkova, G. Early Ear Neuronal Development, but Not Olfactory or Lens Development, Can Proceed without SOX2. *Dev. Biol.* **2020**, *457*, 43–56. [CrossRef] [PubMed]
95. Kondoh, H.; Uchikawa, M.; Kamachi, Y. Interplay of Pax6 and SOX2 in Lens Development as a Paradigm of Genetic Switch Mechanisms for Cell Differentiation. *Int. J. Dev. Biol.* **2004**, *48*, 819–827. [CrossRef] [PubMed]
96. Nishiguchi, S.; Wood, H.; Kondoh, H.; Lovell-Badge, R.; Episkopou, V. Sox1 Directly Regulates the Gamma-Crystallin Genes and Is Essential for Lens Development in Mice. *Genes Dev.* **1998**, *12*, 776–781. [CrossRef] [PubMed]
97. Donner, A.L.; Episkopou, V.; Maas, R.L. Sox2 and Pou2f1 Interact to Control Lens and Olfactory Placode Development. *Dev. Biol.* **2007**, *303*, 784–799. [CrossRef] [PubMed]
98. He, S.; Pirity, M.K.; Wang, W.-L.; Wolf, L.; Chauhan, B.K.; Cveklova, K.; Tamm, E.R.; Ashery-Padan, R.; Metzger, D.; Nakai, A.; et al. Chromatin Remodeling Enzyme Brg1 Is Required for Mouse Lens Fiber Cell Terminal Differentiation and Its Denucleation. *Epigenetics Chromatin* **2010**, *3*, 21. [CrossRef] [PubMed]
99. Okuda, T.; van Deursen, J.; Hiebert, S.W.; Grosveld, G.; Downing, J.R. AML1, the Target of Multiple Chromosomal Translocations in Human Leukemia, Is Essential for Normal Fetal Liver Hematopoiesis. *Cell* **1996**, *84*, 321–330. [CrossRef]
100. Wang, Q.; Stacy, T.; Binder, M.; Marin-Padilla, M.; Sharpe, A.H.; Speck, N.A. Disruption of the Cbfa2 Gene Causes Necrosis and Hemorrhaging in the Central Nervous System and Blocks Definitive Hematopoiesis. *Proc. Natl. Acad. Sci. USA* **1996**, *93*, 3444–3449. [CrossRef] [PubMed]
101. Komori, T.; Yagi, H.; Nomura, S.; Yamaguchi, A.; Sasaki, K.; Deguchi, K.; Shimizu, Y.; Bronson, R.T.; Gao, Y.H.; Inada, M.; et al. Targeted Disruption of Cbfa1 Results in a Complete Lack of Bone Formation Owing to Maturational Arrest of Osteoblasts. *Cell* **1997**, *89*, 755–764. [CrossRef] [PubMed]
102. Otto, F.; Thornell, A.P.; Crompton, T.; Denzel, A.; Gilmour, K.C.; Rosewell, I.R.; Stamp, G.W.; Beddington, R.S.; Mundlos, S.; Olsen, B.R.; et al. Cbfa1, a Candidate Gene for Cleidocranial Dysplasia Syndrome, Is Essential for Osteoblast Differentiation and Bone Development. *Cell* **1997**, *89*, 765–771. [CrossRef] [PubMed]

103. Inoue, K.-I.; Ozaki, S.; Shiga, T.; Ito, K.; Masuda, T.; Okado, N.; Iseda, T.; Kawaguchi, S.; Ogawa, M.; Bae, S.-C.; et al. Runx3 Controls the Axonal Projection of Proprioceptive Dorsal Root Ganglion Neurons. *Nat. Neurosci.* **2002**, *5*, 946–954. [CrossRef]
104. Levanon, D.; Bettoun, D.; Harris-Cerruti, C.; Woolf, E.; Negreanu, V.; Eilam, R.; Bernstein, Y.; Goldenberg, D.; Xiao, C.; Fliegauf, M.; et al. The Runx3 Transcription Factor Regulates Development and Survival of TrkC Dorsal Root Ganglia Neurons. *EMBO J.* **2002**, *21*, 3454–3463. [CrossRef]
105. Li, Q.L.; Ito, K.; Sakakura, C.; Fukamachi, H.; Inoue, K.I.; Chi, X.Z.; Lee, K.Y.; Nomura, S.; Lee, C.W.; Han, S.B.; et al. Causal Relationship between the Loss of RUNX3 Expression and Gastric Cancer. *Cell* **2002**, *109*, 113–124. [CrossRef] [PubMed]
106. Taniuchi, I.; Osato, M.; Egawa, T.; Sunshine, M.J.; Bae, S.C.; Komori, T.; Ito, Y.; Littman, D.R. Differential Requirements for Runx Proteins in CD4 Repression and Epigenetic Silencing during T Lymphocyte Development. *Cell* **2002**, *111*, 621–633. [CrossRef] [PubMed]
107. Fainaru, O.; Shseyov, D.; Hantisteanu, S.; Groner, Y. Accelerated Chemokine Receptor 7-Mediated Dendritic Cell Migration in Runx3 Knockout Mice and the Spontaneous Development of Asthma-like Disease. *Proc. Natl. Acad. Sci. USA* **2005**, *102*, 10598–10603. [CrossRef] [PubMed]
108. Voronov, D.; Gromova, A.; Liu, D.; Zoukhri, D.; Medvinsky, A.; Meech, R.; Makarenkova, H.P. Transcription Factors Runx1 to 3 Are Expressed in the Lacrimal Gland Epithelium and Are Involved in Regulation of Gland Morphogenesis and Regeneration. *Investig. Ophthalmol. Vis. Sci.* **2013**, *54*, 3115–3125. [CrossRef] [PubMed]
109. Gazon, H.; Barbeau, B.; Mesnard, J.-M.; Peloponese, J.-M., Jr. Hijacking of the AP-1 Signaling Pathway during Development of ATL. *Front. Microbiol.* **2017**, *8*, 2686. [CrossRef]
110. Chen, M.; Liu, Y.; Yang, Y.; Qiu, Y.; Wang, Z.; Li, X.; Zhang, W. Emerging Roles of Activating Transcription Factor (ATF) Family Members in Tumourigenesis and Immunity: Implications in Cancer Immunotherapy. *Genes Dis.* **2022**, *9*, 981–999. [CrossRef] [PubMed]
111. Tanaka, T.; Tsujimura, T.; Takeda, K.; Sugihara, A.; Maekawa, A.; Terada, N.; Yoshida, N.; Akira, S. Targeted Disruption of ATF4 Discloses Its Essential Role in the Formation of Eye Lens Fibres. *Genes Cells* **1998**, *3*, 801–810. [CrossRef] [PubMed]
112. Fatma, N.; Singh, P.; Chhunchha, B.; Kubo, E.; Shinohara, T.; Bhargavan, B.; Singh, D.P. Deficiency of Prdx6 in Lens Epithelial Cells Induces ER Stress Response-Mediated Impaired Homeostasis and Apoptosis. *Am. J. Physiol. Cell Physiol.* **2011**, *301*, C954–C967. [CrossRef] [PubMed]
113. Mulhern, M.L.; Madson, C.J.; Danford, A.; Ikesugi, K.; Kador, P.F.; Shinohara, T. The Unfolded Protein Response in Lens Epithelial Cells from Galactosemic Rat Lenses. *Investig. Ophthalmol. Vis. Sci.* **2006**, *47*, 3951–3959. [CrossRef]
114. Zhou, Y.; Bennett, T.M.; Shiels, A. Lens ER-Stress Response during Cataract Development in Mip-Mutant Mice. *Biochim. Biophys. Acta* **2016**, *1862*, 1433–1442. [CrossRef]
115. Yang, J.; Zhou, S.; Gu, J.; Wang, Y.; Guo, M.; Liu, Y. Differences in Unfolded Protein Response Pathway Activation in the Lenses of Three Types of Cataracts. *PLoS ONE* **2015**, *10*, e0130705. [CrossRef]
116. Berthoud, V.M.; Minogue, P.J.; Lambert, P.A.; Snabb, J.I.; Beyer, E.C. The Cataract-Linked Mutant Connexin50D47A Causes Endoplasmic Reticulum Stress in Mouse Lenses. *J. Biol. Chem.* **2016**, *291*, 17569–17578. [CrossRef]
117. Lovicu, F.J.; Chamberlain, C.G.; McAvoy, J.W. Differential Effects of Aqueous and Vitreous on Fiber Differentiation and Extracellular Matrix Accumulation in Lens Epithelial Explants. *Investig. Ophthalmol. Vis. Sci.* **1995**, *36*, 1459–1469.
118. Klok, E.j.; Lubsen, N.H.; Chamberlain, C.G.; McAvoy, J.W. Induction and Maintenance of Differentiation of Rat Lens Epithelium by FGF-2, Insulin and IGF-1. *Exp. Eye Res.* **1998**, *67*, 425–431. [CrossRef]
119. McAvoy, J.W.; Chamberlain, C.G.; de Iongh, R.U.; Richardson, N.A.; Lovicu, F.J. The Role of Fibroblast Growth Factor in Eye Lens Development. *Ann. N. Y. Acad. Sci.* **1991**, *638*, 256–274. [CrossRef]
120. Dawes, L.J.; Sugiyama, Y.; Tanedo, A.S.; Lovicu, F.J.; McAvoy, J.W. Wnt-Frizzled Signaling Is Part of an FGF-Induced Cascade That Promotes Lens Fiber Differentiation. *Investig. Ophthalmol. Vis. Sci.* **2013**, *54*, 1582–1590. [CrossRef] [PubMed]
121. Golestaneh, N.; Fan, J.; Fariss, R.N.; Lo, W.-K.; Zelenka, P.S.; Chepelinsky, A.B. Lens Major Intrinsic Protein (MIP)/Aquaporin 0 Expression in Rat Lens Epithelia Explants Requires Fibroblast Growth Factor-Induced ERK and JNK Signaling. *J. Biol. Chem.* **2004**, *279*, 31813–31822. [CrossRef] [PubMed]
122. Saravanamuthu, S.S.; Gao, C.Y.; Zelenka, P.S. Notch Signaling Is Required for Lateral Induction of Jagged1 during FGF-Induced Lens Fiber Differentiation. *Dev. Biol.* **2009**, *332*, 166–176. [CrossRef] [PubMed]
123. Lovicu, F.J.; McAvoy, J.W. Structural Analysis of Lens Epithelial Explants Induced to Differentiate into Fibres by Fibroblast Growth Factor (FGF). *Exp. Eye Res.* **1989**, *49*, 479–494. [CrossRef]
124. Wang, Q.; Stump, R.; McAvoy, J.W.; Lovicu, F.J. MAPK/ERK1/2 and PI3-Kinase Signalling Pathways Are Required for Vitreous-Induced Lens Fibre Cell Differentiation. *Exp. Eye Res.* **2009**, *88*, 293–306. [CrossRef] [PubMed]
125. Madakashira, B.P.; Kobrinski, D.A.; Hancher, A.D.; Arneman, E.C.; Wagner, B.D.; Wang, F.; Shin, H.; Lovicu, F.J.; Reneker, L.W.; Robinson, M.L. Frs2α Enhances Fibroblast Growth Factor-Mediated Survival and Differentiation in Lens Development. *Development* **2012**, *139*, 4601–4612. [CrossRef]

Disclaimer/Publisher's Note: The statements, opinions and data contained in all publications are solely those of the individual author(s) and contributor(s) and not of MDPI and/or the editor(s). MDPI and/or the editor(s) disclaim responsibility for any injury to people or property resulting from any ideas, methods, instructions or products referred to in the content.

cells

MDPI

Article

FGF-2 Differentially Regulates Lens Epithelial Cell Behaviour during TGF-β-Induced EMT

Mary Flokis [1] and Frank J. Lovicu [1,2,*]

[1] Molecular and Cellular Biomedicine, School of Medical Sciences, Faculty of Medicine and Health, The University of Sydney, Sydney, NSW 2006, Australia
[2] Save Sight Institute, The University of Sydney, Sydney, NSW 2006, Australia
* Correspondence: frank.lovicu@sydney.edu.au

Abstract: Fibroblast growth factor (FGF) and transforming growth factor-beta (TGF-β) can regulate and/or dysregulate lens epithelial cell (LEC) behaviour, including proliferation, fibre differentiation, and epithelial–mesenchymal transition (EMT). Earlier studies have investigated the crosstalk between FGF and TGF-β in dictating lens cell fate, that appears to be dose dependent. Here, we tested the hypothesis that a fibre-differentiating dose of FGF differentially regulates the behaviour of lens epithelial cells undergoing TGF-β-induced EMT. Postnatal 21-day-old rat lens epithelial explants were treated with a fibre-differentiating dose of FGF-2 (200 ng/mL) and/or TGF-β2 (50 pg/mL) over a 7-day culture period. We compared central LECs (CLECs) and peripheral LECs (PLECs) using immunolabelling for changes in markers for EMT (α-SMA), lens fibre differentiation (β-crystallin), epithelial cell adhesion (β-catenin), and the cytoskeleton (alpha-tropomyosin), as well as Smad2/3- and MAPK/ERK1/2-signalling. Lens epithelial explants cotreated with FGF-2 and TGF-β2 exhibited a differential response, with CLECs undergoing EMT while PLECs favoured more of a lens fibre differentiation response, compared to the TGF-β-only-treated explants where all cells in the explants underwent EMT. The CLECs cotreated with FGF and TGF-β immunolabelled for α-SMA, with minimal β-crystallin, whereas the PLECs demonstrated strong β-crystallin reactivity and little α-SMA. Interestingly, compared to the TGF-β-only-treated explants, α-SMA was significantly decreased in the CLECs cotreated with FGF/TGF-β. Smad-dependent and independent signalling was increased in the FGF-2/TGF-β2 co-treated CLECs, that had a heightened number of cells with nuclear localisation of Smad2/3 compared to the PLECs, that in contrast had more pronounced ERK1/2-signalling over Smad2/3 activation. The current study has confirmed that FGF-2 is influential in differentially regulating the behaviour of LECs during TGF-β-induced EMT, leading to a heterogenous cell population, typical of that observed in the development of post-surgical, posterior capsular opacification (PCO). This highlights the cooperative relationship between FGF and TGF-β leading to lens pathology, providing a different perspective when considering preventative measures for controlling PCO.

Keywords: transforming growth factor-beta (TGF-β); fibroblast growth factor (FGF); epithelial-mesenchymal transition (EMT); fibrosis; cataract; lens

1. Introduction

The ocular lens is a transparent, avascular tissue responsible for transmitting light onto the retina. It contains two cell types: cuboidal epithelial cells and adjacent elongate fibre cells, both comprised of specialized molecular (e.g., crystallins) and cytoskeletal (e.g., intermediate filaments) properties to facilitate vision [1]. Ocular growth factors, such as fibroblast growth factor (FGF) and transforming growth factor-beta (TGF-β), are key regulators of different cellular processes in the lens, including epithelial cell proliferation [2–4], fibre differentiation [1,5–10], and epithelial–mesenchymal transition (EMT) that lead to lens pathology [11–17]. In situ, FGF is thought to be required for regulating normal lens cell processes in a spatially dependent manner, as previously reviewed [1].

TGF-β can regulate and/or concurrently dysregulate normal lens homeostasis, cell growth, and survival, by altering lens epithelial cell (LEC) morphology [17–19]. The dysregulation of lens epithelial cell architecture induced by TGF-β is characterized by EMT, a phenomenon that has been widely reviewed [20–22], with normal cuboidal LECs transitioning to become aberrant migratory, contractile myofibroblastic cells. These myofibroblastic cells can aggregate to form a fibrotic plaque leading to cataracts [23–25]. To date, cataracts, that have been extensively reviewed and studied, are still considered the most common form of blindness worldwide [26–28], with the only form of treatment being surgical intervention. Despite the effectiveness of surgery, posterior capsular opacification (PCO), known also as a secondary cataract, may result post surgery, requiring further intervention [29–31]. PCO results from the aberrant behaviour of LECs left after surgery, with these cells either undergoing EMT to form a posterior subcapsular plaque (fibrotic PCO) [11,24,25,32], or differentiating into aberrant fibre cells leading to Elschnig's pearls and Soemmerring's ring (regenerative, pearl PCO) [33], as previously reviewed [34,35]. While these two different spatially distinct epithelial PCO pathologies are well characterised [36,37], the underlying molecular mechanisms regarding their formation are poorly understood.

Numerous models have established TGF-β-induced lens EMT responses in humans [14], embryonic chicks [13,38], and murine cell lines and explant models [13,15,25,32,39]. In dissociated embryonic chick lens epithelial cells treated with TGF-β, we see a heterogenous response, with some cells undergoing fibre differentiation, while others undergo EMT [13,40]. In in vitro studies using mammalian lens epithelia, exogenous treatment of LECs with TGF-β results in a homogenous EMT response [17,41–43]. In situ, however, anterior subcapsular cataracts (ASCs) develop in transgenic mice in response to elevated activity of ocular TGF-β [44]; the subcapsular plaques are comprised a heterogenous population of aberrant lens fibre cells and myofibroblastic cells, similar to those seen in human cataracts [24]. The in situ transgenic mouse model ideally replicates the human clinical pathology of fibrotic cataracts, that is attributed to the endogenous ocular milieu of different growth factors and cytokines, that do not act in isolation, unlike what we have in vitro. Since two disparate lens epithelial phenotypes contribute to ASC and PCO, it is important to better understand how they are derived, and the putative interplay of the different ocular factors involved.

While FGF is well established in regulating lens epithelial cell proliferation and fibre differentiation, it has also previously been shown to influence TGF-β-induced EMT and aberrant cell behaviour, promoting wound healing, repair, and fibrogenesis [5,16,41,45]. For example, different relatively low doses of FGF-2 (2.5–20 ng/mL) can exacerbate TGF-β2 (0.5–3 ng/mL)-induced lens opacification in intact rat lenses, with the higher dose combinations exhibiting the most pronounced response, resulting in dense cellular plaques and elevated deposition of ECM [16]. In contrast, other studies have shown that FGF can counteract and antagonise EMT in rodent LECs [14,15]. Rat lens epithelial cell explants cotreated with a relatively low dose of TGF-β2 (50 pg/mL) and a lower dose of FGF-2 (10 ng/mL) still formed spindle-like cells typical of EMT; however, with minimal cell loss compared to explants treated with TGF-β2 alone [15]. This increased cell survival was unique to FGF as other regulatory ocular growth factors (e.g., EGF, IGF, HGF, or PDGF) could not block the hallmark features of TGF-β-induced EMT, including lens capsular wrinkling, apoptosis, and cell loss [15,46].

The influence of FGF regulating TGF-β-induced EMT may be attributed to the putative crosstalk between various downstream intracellular signalling pathways; the TGF-β-canonical Smad2/3-dependent proteins, and non-canonical mitogen-activated protein kinases (MAPK), such as extracellular signal-regulated kinase (ERK1/2) [14,38,47–49]. Studies using mouse LEC lines (MLECs) showed that cotreatment of cells with FGF-2 (10 ng/mL) and TGF-β2 (10 ng/mL) resulted in elongated fibroblastic-like cells and enhanced cell migratory mechanisms, with elevated ERK1/2-signalling [14]. Interestingly, in human lens epithelial cells (HLECs) from this same study, cotreated with the same doses of FGF-2/TGF-β2, they report on the antagonistic behaviour of FGF-2 with a reduction in cy-

toskeletal markers involved in stress fibre formation [14]. It is clear from these studies that there is no consistency in cell responsiveness to both FGF/TGF-β across different species.

In the current study, we characterized the influence that FGF has on TGF-β-induced cell behaviour in rat lens explants to best model the conditions needed to promote a heterogenous cell population typical of fibrotic cataracts as seen in situ. We demonstrate that a high fibre-differentiating dose of FGF is protective of TGF-β-induced EMT in peripheral lens epithelia; however, this is not evident in central lens epithelia induced by TGF-β. This emulates the spatial phenotypic response of lens cells seen in human PCO and may serve as a model to better understand the mechanisms leading to this post-surgical pathology.

2. Materials and Methods

2.1. Animals and Tissue Culture

All procedures conducted abided by the Australian Code for animal care and usage for scientific purposes and the Association for Research in Vision and Ophthalmology (ARVO) Statement for the Use of Animals for Ophthalmic and Vision biomedical research (USA). The experiments were approved by the Animal Ethics Committee of The University of Sydney, NSW, Australia (AEC# 2021/1913). Wistar rats (*rattus norvegicus*) at 21-days of age (P21 $\pm$ 1 day) were humanely euthanized with CO_2 followed by cervical dislocation.

2.2. Lens Epithelial Explants

All collected primary rat ocular tissues were kept in medium 199 with Earle's Salts (M199) (11825015, Gibco™, Thermo Fisher Scientific, Sydney, NSW, Australia) in 35 mm Nunc™ culture dishes (NUN150460, Thermo Fisher Scientific). The media was supplemented with 2.5 μg/mL Amphotericin B (15290-018, Gibco™, Thermo Fisher Scientific), 0.1% bovine serum albumin (BSA) (9048-46-8, Sigma-Aldrich Corp., St. Louis, MO, USA), 0.1 μg/mL L-glutamine (200 mM) (25030081, Gibco™, Life Technologies, Carlsbad, CA, USA), and penicillin (100 IU/mL)/streptomycin (100 μg/mL) (15140-122, Gibco™, Life Technologies). The collected eyes were placed under a dissecting microscope to remove the lenses. The posterior capsule of the lens was torn using fine forceps and the remaining intact anterior capsule containing a sheet of lens epithelial cells (LECs) was pinned to the base of the culture dish using the gentle pressure of the forceps, as previously described [5]. Explants were maintained in a humidified incubator (37 °C, 5% CO_2).

Different doses of recombinant human TGF-β2 (302-B2-002, R&D systems, Minneapolis, MN, USA) were used to induce EMT in the lens explants, as previously described [39]. A lower dose of TGF-β2 (50 pg/mL) gave a more regulated EMT response over 7 days, while a higher dose (200 pg/mL) was used to induce a more rapid EMT response in the lens explants over this same time period. To determine the impact of FGF-2 on TGF-β2-induced lens EMT, we cotreated TGF-β2-treated LECs with either a low proliferating dose of recombinant human FGF-2 (5 ng/mL: 233-FB, R&D systems) or a high fibre-differentiating dose of FGF-2 (200 ng/mL) [10,50]. Control explants had no growth factors added to the media.

2.3. Assessment of Cell Morphology and Immunofluorescence

Cultured LEC explants were monitored and photographed daily over 7 days using phase contrast microscopy (Leica FireCam imaging, Leica Microsystems, Version 1.5, 2007). To examine the extent of how transdifferentiated cells modulated the underlying lens capsule, some treated explants were rinsed with filtered Milli-Q H_2O to debride all cells from the explant to completely expose the underlying lens capsule. Phase contrast images were captured before and after rinsing.

Following the different growth factor treatments, at set time points, the explants were fixed in 10% neutral buffered formalin (NBF; HT501320-9.5L, Sigma-Aldrich Corp) for 10 min, followed by 3 $\times$ 5 min rinses in phosphate-buffered saline (PBS) supplemented with BSA (0.1%, *v*/*w*; PBS/BSA). The cells were permeabilized using PBS/BSA supplemented with Tween-20 (0.05%, *v*/*v*; 3 $\times$ 5 min), followed by subsequent rinses in PBS/BSA (2 $\times$ 5 min). The explants were then incubated at room temperature for 30 min with 3%

normal goat serum (NGS diluted in PBS/BSA, *w*/*v*), before adding the primary antibodies; anti-mouse α-SMA (A2547, Sigma-Aldrich Corp.), anti-alpha tropomyosin (Tpm; α/9d; provided by Prof. Gunning, University of New South Wales, Sydney, NSW, Australia), anti-rabbit β-catenin (ab6302, Abcam, Fremont, CA, USA), anti-β-crystallin, and anti-total-Smad2/3 (t-Smad2/3: 8685, Cell Signaling Tech., Danvers, MA, USA), all diluted 1:100 in NGS/PBS/BSA. The explants were incubated overnight at 4 °C, followed by rinsing in PBS/BSA (3 × 5 min). The respective secondary antibodies were then applied for a 2 h incubation at room temperature: goat anti-rabbit IgG Alexa-Fluor® 488 (ab150077, Abcam), and goat anti-mouse Alexa-Fluor® 594 (ab150116, Abcam), all diluted 1:1000 in PBS/BSA. Three 5 min rinses in PBS/BSA were followed before a 5 min application of 3 µg/mL bis-benzimide (H33342 trihydrochloride, Hoechst counterstain, B2261, Sigma-Aldrich) diluted in PBS/BSA. The explants were rinsed again before mounting with 10% glycerol in PBS and imaged using epifluorescence microscopy (Leica DMLB 100S with DFC-450C camera, Leica Application Suite, Version 4.8, 2021).

2.4. SDS-Page and Western Blotting

Cultured lens epithelial explants at set time points were rinsed in cold PBS. The central and peripheral regions of the explants were isolated using a scalpel blade to delineate each region. A central square of tissue, no more than a third of the explant diameter (central LECs, CLECs), and the remaining surrounding peripheral LECs (PLECs) were isolated separately. CLEC and PLEC protein was harvested, pooled into allocated Eppendorf tubes, and lysed with cold radioimmunoprecipitation assay (RIPA) lysis buffer containing 150 mM NaCl, 0.5% sodium deoxycholate, 0.1% Sodium dodecyl sulphate (SDS), 1 mM sodium orthovanadate, 1 mM NaF, 50 mM Tris-HCl (pH 7.5), 0.1% Triton X-100, phosphatase (PhosSTOP™), and protease (cOmplete™) EASYpacks inhibitor tablets (04906837001 and 05892970001; Roche Applied Science, Basel, Switzerland). LECs were homogenized and centrifuged for 10 min at 4 °C (14,400× *g*) for lysate/supernatant separation. Quantification of the total lens protein of each supernatant sample was conducted using a Pierce™ Micro bicinchoninic acid (BCA) protein assay reagent kit (23235; Thermo Fisher Scientific).

LEC protein sample lysates were prepared using 5% 2-mercaptoethanol (M6250, Sigma-Aldrich) combined with 2× Laemmli sample buffer at a 1:1 (*v*/*v*) ratio (1610737, Bio-Rad Laboratories, NSW, Australia). For electrophoresis, 10 µg of protein lysates were loaded onto 12% SDS-PAGE gels for 20 min at 70 V followed by 2 h at 120 V. LEC protein was then transferred onto an immobilon®-PSQ polyvinylidene fluoride (PVDF) membrane (ISEQ00010, Merck Millipore, Rahway, NJ, USA) for 1 h at 100 V. PVDF membranes were incubated in 2.5% BSA blocking buffer diluted in tris-buffered saline with 0.1% Tween-20 (TBST) and incubated for 1 h with agitation at room temperature. Primary antibodies were added to the membranes and left overnight to incubate (at 4 °C): anti-mouse α-SMA, anti-GAPDH (G8795, Sigma-Aldrich Corp.), anti-tropomyosin alpha, and anti-β-crystallin, t-Smad2/3, phospho-Smad2/3 (p-Smad2/3, 8828, Cell Signalling Tech., Danvers, MA, USA), phospho-ERK1/2 (p-ERK1/2, 9101, Cell Signalling Tech.), and total-ERK1/2 (t-ERK1/2, 9102, Cell Signalling Tech.), all diluted in blocking buffer/TBST at 1:1000, apart from α-SMA and GAPDH (1:2000). Following overnight incubation, the membranes were rinsed in TBST (3 × 5 min) and incubated with the appropriate horseradish peroxidase (HRP)-conjugated secondary antibodies for 2 h at room temperature: HRP-conjugated goat anti-rabbit IgG (7074, Cell Signalling Tech.) and horse anti-mouse IgG (7076, Cell Signalling Tech.), diluted in TBST at 1:5000. The membranes were rinsed in TBST (3 × 10 min) followed by the application of an immobilon chemiluminescent HRP substrate for 3–5 min (WBKLS0500, Merck Millipore). Protein chemiluminescent signals were imaged using Bio-Rad ChemiDoc™ MP imaging.

Following immunolabeling, PVDF membranes were stripped for 10 min in stripping buffer (10% SDS, 0.5 M Tris HCl pH 6.8, Milli-Q H_2O, and 0.8% 2-mercaptoethanol) with gentle agitation. The membranes were then washed in TBST (3 × 5 min) and re-blocked in blocking buffer/TBST for 1 h. Following blocking, the membranes were probed for

loading control GAPDH (1:2000, 1 h) and incubated with an HRP-conjugated horse anti-mouse secondary antibody for 1 h prior to chemiluminescent signalling analysis. Protein densitometry was carried out using Bio-Rad ImageLab software (Version 6.1.0, 2019).

2.5. Statistical Analysis

For each experimental analysis, three independent experiments were carried out. For every experiment, a minimum of three individual replicates (n = 3) per treatment group (different treatment of explants) were used. For Western blotting, each group contained up to eight explants to isolate central and peripheral lens cells that were randomly obtained from different P21 rats. For measuring changes in protein expression, we used densitometry to calculate the selected protein intensity relative to the loading control (GAPDH).

For Western blot experiments examining differences in Smad-dependent (Smad2/3) and Smad-independent (MAPK/ERK1/2) activity, phosphorylated protein expression was calculated using the following ratio: relative phosphorylated density per total protein.

Prior to the use of one-way analysis of variance (ANOVA), several assumptions were tested and confirmed; we assumed equal standard deviation (SD) and residuals appeared normally distributed. Based on these confirmed assumptions, we compared the differences among the means of all treatment groups using one-way ANOVA, followed by Tukey's multiple comparisons post-hoc test. All data acquired were plotted appropriately using GraphPad Prism software version 9.0 (GraphPad Software Inc., San Diego, CA, USA).

To quantify the spatial differences in t-Smad2/3 immunoreactivity, six separate images of central and peripheral regions were captured per explant across three randomized explants per treatment group, over three individual experiments. Nuclear and cytoplasmic localisation of t-Smad2/3 was manually counted using ImageJ's Cell Counter plugin. The mean percentage of t-Smad2/3 nuclear and cytoplasmic fluorescence was calculated and statistically analysed using GraphPad Prism.

Tabled data were represented as the standard error of the mean (±SEM) and probability values, where $p < 0.05$ was considered statistically significant.

3. Results

3.1. FGF-2 Promotes a Spatially Dependent TGF-β2-Induced EMT Response in Lens Epithelial Explants

We examined the efficacy of different doses of FGF-2 in modulating the effect of TGF-β2 on lens epithelial cells induced to undergo EMT. Using phase contrast microscopy, control LECs without FGF-2 or TGF-β2 treatment (Figure 1A,E), as well as explants treated with only a low dose of FGF-2, demonstrated no significant morphological changes and retained their epithelial phenotype over the culture period. When the lens epithelial explants were treated with a low dose of TGF-β2 (50 pg/mL), this promoted an EMT response across the entire explant, similar to a higher dose (200 pg/mL) of TGF-β2, albeit at a slower rate, consistent with previous studies [42].

With different dose combinations of FGF-2 and TGF-β2, most cells in the explants underwent a uniform EMT response over 5 days, with the exception of cells in the explants cotreated with a relatively high dose of FGF-2 (200 ng/mL) and the lower dose of TGF-β2 (Figure 1), where we observed a differential response between CLECs and PLECs (Table 1, Supplementary Figure S1).

The cells in the lens epithelial explants treated with the high a fibre-differentiating dose of FGF-2 elongated over 5 days (Figure 1B,F), compared to the control LEC explants (no growth factor treatment; Figure 1A,E). This FGF-induced fibre differentiation response was more pronounced in PLECs compared to CLECs (Figure 1B,F). LECs in explants treated with a low dose of TGF-β2 (Figure 1C,G) displayed prominent EMT by day 5, with the LECs losing their uniform packing and adhesion as they transdifferentiated into myofibroblastic cells. TGF-β2 treatment also led to increased cellular blebbing (refractile bodies) and apoptotic cell loss, evident by areas of bare lens capsule that displayed prominent signs of capsular modification in the form of wrinkling throughout the explant. When the explants

were cotreated with TGF-β2 and FGF-2, CLECs underwent similar morphological transformations by day 5 (Figure 1D) to that seen with TGF-β2-treatment alone (Figure 1C,G). In contrast, PLECs in the explants cotreated with FGF-2/TGF-β2 showed no evidence of EMT (Figure 1H), instead demonstrating morphological changes more consistent with that observed in the explants treated with FGF-2 alone (Figure 1B,F).

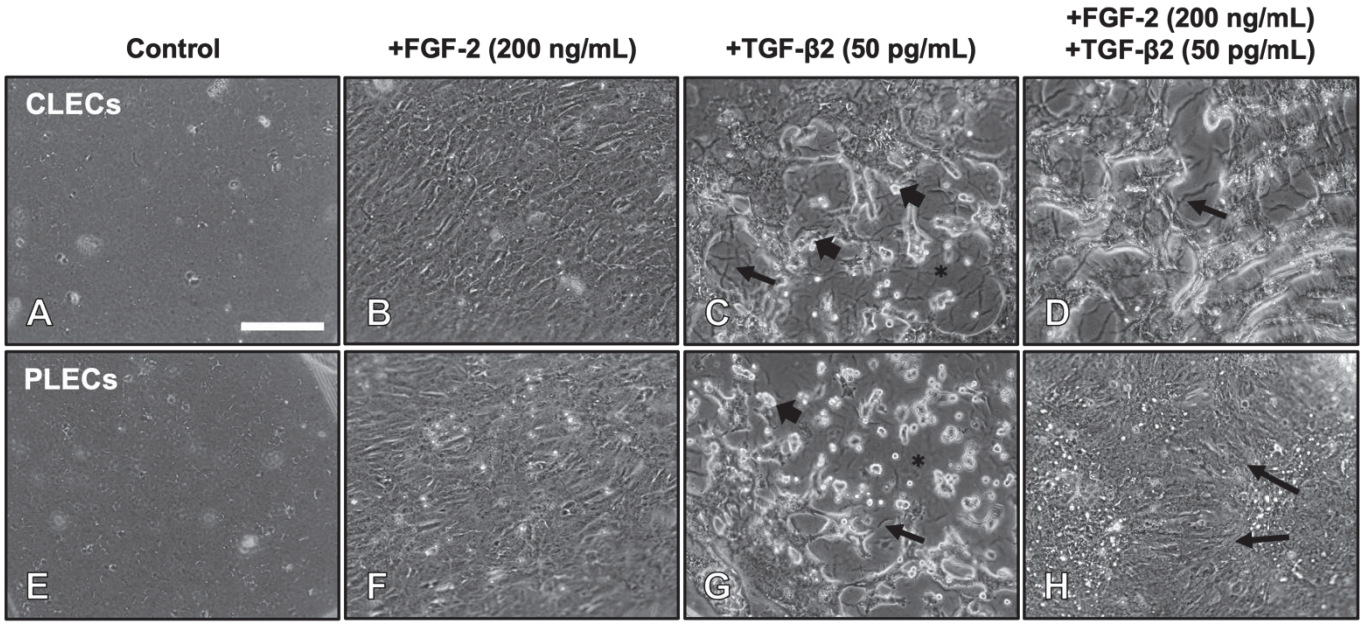

Figure 1. FGF-2 promotes a spatially dependent TGF-β2-induced EMT response in lens epithelial explants. Control LECs maintained a cobblestone-like epithelial phenotype after 5 days (**A**,**E**). FGF-2-induced cell elongation typical of lens fibre differentiation (**B**,**F**). TGF-β2 induced EMT, highlighted by elongated myofibroblastic cells, with prominent cell blebbing/refractile bodies ((**C**,**G**), arrowheads) and loss of cells exposing the lens capsule (asterisk) with capsular wrinkling (arrows). FGF-2 and TGF-β2 cotreated explants led to EMT of CLECs (**D**) but a fibre differentiation response in PLECs ((**H**), arrows). Scale bar: 200 μm.

Table 1. Regional, dose-dependent effects of FGF-2 and TGF-β2 on LEC explants.

Treatment	Concentration		Regional Cell Response in Explant	
	FGF-2 (ng/mL)	TGF-β2 (pg/mL)	FGF-2 (ng/mL)	TGF-β2 (pg/mL)
f/t	5	50	EMT	EMT
f/T	5	200	EMT	EMT
F/t	200	50	EMT	*Fibre Differentiation*
F/T	200	200	EMT	EMT

Low dose FGF-2 (f); low dose TGF-β2 (t); high dose FGF-2 (F); high dose TGF-β2 (T).

PLECs in cotreated explants exhibited changes in the LEC phenotype as early as day 3 (Supplementary Figure S2H). Debridement of all cells at this time revealed the underlying lens capsule with no apparent capsular modulation (no folds or wrinkles) in either control (Supplementary Figure S3A,D) or FGF-2 treated (Supplementary Figure S3B,E) explants. In the TGF-β2-treated explants, increased capsular modulation was apparent with wrinkling and folds in the central explant regions (Supplementary Figure S3C) and in the peripheral regions (Supplementary Figure S3F). Consistent with the differential cell response in the central and peripheral regions of the F/t-cotreated explants (Figure 2A,A1,A3), the explants exhibited capsular modulation only in the central explant region (Figure 2A2), with no capsular wrinkling observed in the peripheral region (Figure 2A4).

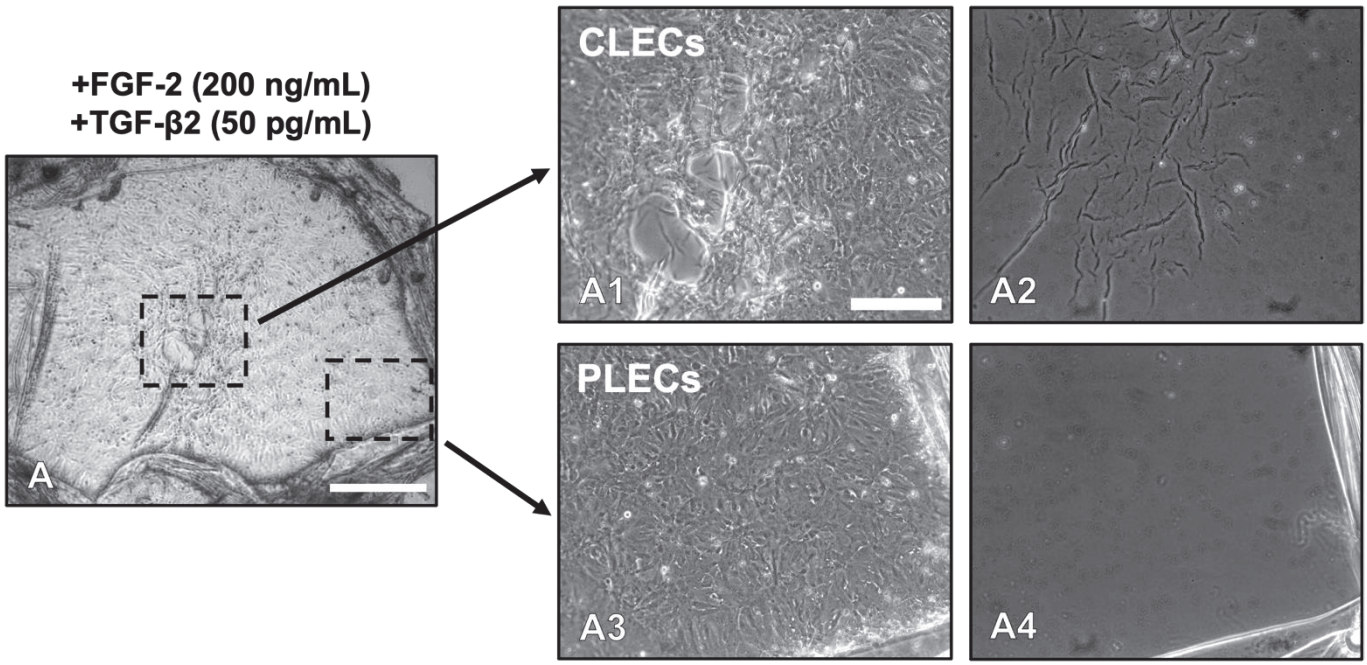

Figure 2. Lens capsule modulation during TGF-β2-induced EMT. Seventy-two h post treatment, the explants were rinsed consecutively in filtered Milli-Q H_2O to remove all lens epithelial cells and view the underlying lens capsule. In the F/t cotreated explants (**A**,**A1**,**A3**), after cell removal (**A2**,**A4**), capsular wrinkling was only apparent in regions that were previously populated with CLECs (**A2**), with no wrinkling visible in regions that were previously populated with PLECs (**A4**). Scale bar: 400 μm (**A**), 200 μm (**A1**–**A4**).

We observed that with ongoing culture (up to 7 days), regardless of the explant region or treatment, all of the cells exposed to TGF-β2 (200 pg/mL) are lost by 7 days (Supplementary Figure S4A); however, in the cotreated explants (F/t), with continual supplementation of the media with FGF-2 (200 ng/mL) after day 3 of culture, this promoted cell survival, whereby we continue to observe many myofibroblastic cells in the central region of the explants (Supplementary Figure S4B) and, similarly, relatively normal lens cells at the periphery of the explants are also maintained (Supplementary Figure S4C).

3.2. FGF-2 Promotes Spatial Differences in Labelling for EMT and Fibre Differentiation Markers in TGF-β2-Treated LECs

3.2.1. Immunofluorescent Labelling

We used immunofluorescence to characterise the different cell types in explants treated with TGF-β2 and/or FGF-2 over 3 days, labeling for lens fibre differentiation markers, β-crystallin, and alpha-tropomyosin (α/9d), as well as the EMT marker, α-SMA (Figure 3). Isotype controls for all of the antibodies show little to no specific labelling. Control LECs throughout the explant exhibited no reactivity for β-crystallin and/or α-SMA after 3 days of culture (Figure 3A), labelling only for α/9d (Figure 3B). FGF-2-treated LECs exhibited strong reactivity for β-crystallin throughout the explant (Figure 3C,I), with stronger labelling in PLECs (Figure 3I). Treatment with FGF-2 did not promote α-SMA reactivity in any cultured lens epithelia. FGF-2-treated CLECs presented diffuse α/9d-reactivity (Figure 3F), while PLECs had a more defined reactivity for α/9d, highlighting actin filaments in the elongating, differentiating fibre cells (Figure 3L). LECs treated with only TGF-β2 displayed clear evidence of an EMT response, with strong reactivity for α-SMA, with no β-crystallin observed throughout the explant (Figure 3D,J).

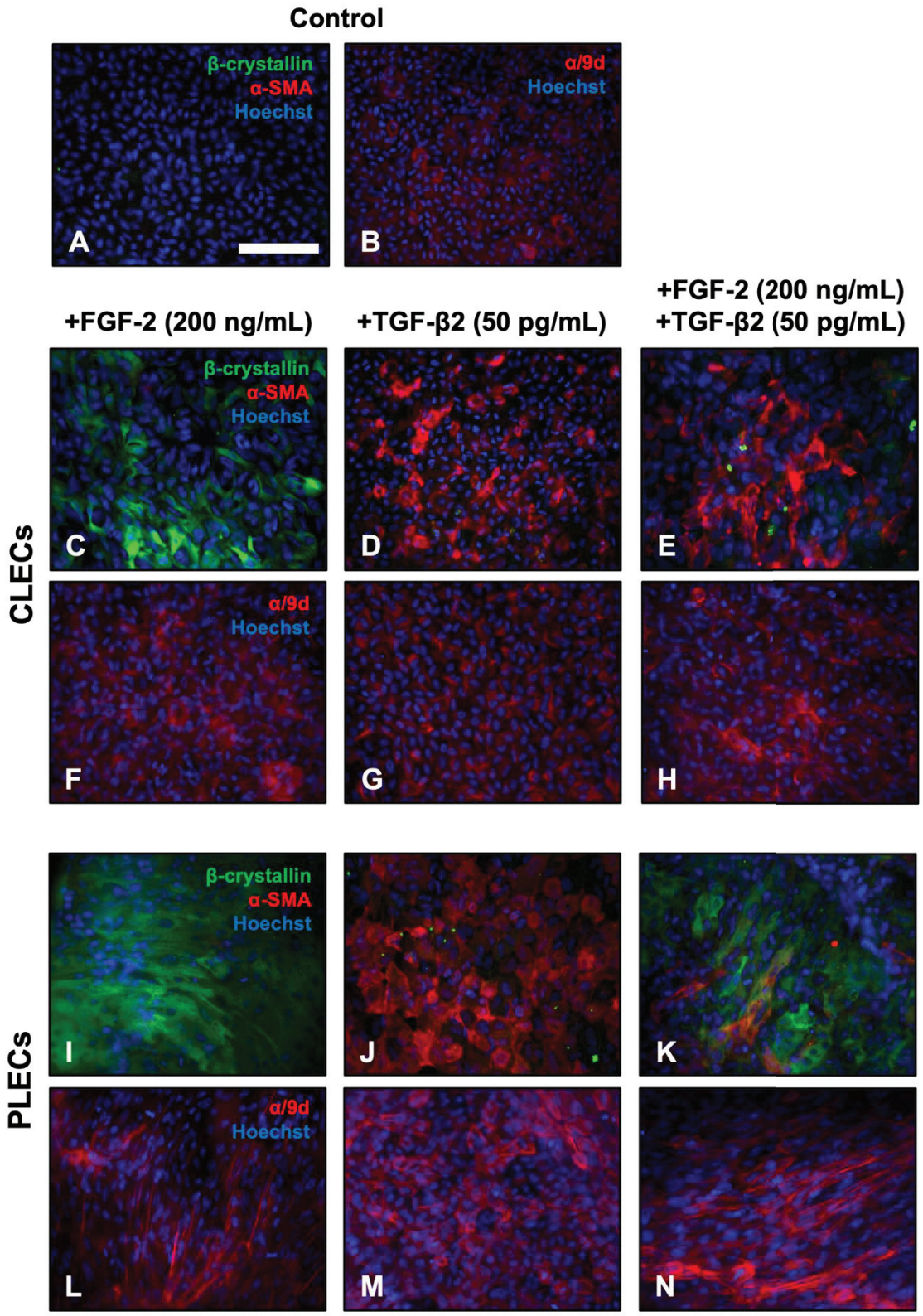

Figure 3. FGF-2 modulates EMT and fibre differentiation markers in TGF-b2-treated LECs. Immunolabeling of β-crystallin (green), α-SMA (red), and alpha-tropomyosin (α/9d; red), counterstained with Hoechst nuclear stain (blue), in CLECs (**C**–**H**) and PLECs (**I**–**N**) following 3 days of culture with no growth factors (Control, (**A**,**B**)), FGF-2 (200 ng/mL; (**C**,**F**,**I**,**L**)), and TGF-β2 (50 pg/mL; (**D**,**G**,**J**,**M**)), or cotreated with FGF-2 and TGF-β2 (**E**,**H**,**K**,**N**). Images are representative of three independent experiments. Scale bar: 100 μm.

TGF-β2-treated CLECs had a highly specific localisation of α/9d to actin stress fibres (Figure 3G), which were also very prominent in PLECs (Figure 3M). Unlike cells treated with only FGF-2 or only TGF-β2, that had a relatively uniform label for the different markers across the entire explant, in the FGF-2/TGF-β2 cotreated explants, we observed distinct spatial differences in the labelling of the markers, consistent with our earlier morphological observations. The CLECs in the TGF-β2/FGF-2-treated explants predominantly labelled for α-SMA with little to no β-crystallin reactivity at day 3 (Figure 3E), similar to the explants treated with only TGF-β2 (Figure 3D,J). In contrast, the PLECs in these same cotreated explants displayed the inverse label, with strong reactivity primarily for β-crystallin in elongated cells, with few neighboring smaller cells immunolabelling for α-SMA (Figure 3K). This differential β-crystallin and α-SMA reactivity in the cotreated explants was sustained up to 5 days of culture (Supplementary Figure S5). Stronger labelling for α/9d was also observed throughout the cotreated explants (Figure 3H,N), highlighting the marked elongation of peripheral fibre-like cells (Figure 3K,N), as well as central myofibroblastic cells (Figure 3E,H).

3.2.2. Western Blotting

Alpha-Smooth Muscle Actin. We quantified protein changes in the treated explants using Western blotting. CLECs had a significant increase in α-SMA when treated with TGF-β2, compared to the relatively lower levels in the control (NT) and FGF-2-treated explants ($p < 0.0001$) (Figure 4A,C). FGF-2 treatment did not impact α-SMA levels in the CLECs compared to the control cells ($p = 0.3429$). In the FGF-2/TGF-β2 cotreated explants, there was a significant reduction in α-SMA levels in the CLECs relative to the TGF-β2 alone CLECs ($p < 0.0001$). In fact, these CLECs in the cotreated explants displayed no significant difference in levels of α-SMA compared to the CLECs of the control ($p > 0.9999$) or FGF-2 alone ($p = 0.3249$) explants. In the PLECs of the FGF-2/TGF-β2 cotreated explants, consistent with the reduced EMT response, there were reduced α-SMA levels when compared to the CLECs, comparable to the lower α-SMA levels seen in the PLECs of the control ($p = 0.7371$), FGF-2 ($p > 0.9999$)-, and TGF-β2-treated explants ($p = 0.0053$) (Figure 4B,D). The PLECs in the explants treated with FGF-2 alone did not have increased α-SMA levels when compared to the control cells ($p = 7366$); however, the PLECs in the explants treated with TGF-β2 alone had significantly increased α-SMA levels, compared to the control ($p = 0.0203$) and the FGF-2-treated ($p = 0.0053$) explants.

β-crystallin. When compared to the control cells, there was no significant difference in the levels of β-crystallin in the CLECs of the explants treated with FGF-2 ($p = 0.8742$) (Figure 4A,C). Treatment with TGF-β2 did not significantly increase levels of β-crystallin in the CLECs compared to the control ($p = 0.5844$), FGF-2 ($p = 0.2260$) or the cotreated explants ($p = 0.1459$). We did observe a significant decrease in β-crystallin in the CLECs of the cotreated explants, relative to the control ($p = 0.0160$) and FGF-2 ($p = 0.0044$)-treated explants (Figure 4A,C). Treatment of the explants with FGF-2 significantly increased β-crystallin levels in the PLECs when compared to the PLECs of the control ($p = 0.0374$) and the TGF-β2-treated explants ($p = 0.0003$) (Figure 4B,D). The PLECs in the explants treated with TGF-β2 alone had reduced β-crystallin levels when compared to the control PLECs ($p = 0.0222$). The PLECs of the explants cotreated with FGF-2/TGF-β2 had slightly elevated β-crystallin levels in comparison to the PLECs of the control ($p = 0.6396$) or the TGF-β2-treated ($p = 0.0056$) explants (Figure 4B,D).

Alpha-Tropomyosin. α/9d levels were significantly elevated only in the CLECs and PLECs of the TGF-β2-treated explants, when compared to the corresponding cells of all other treatment groups (Figure 4A–D). For the CLECs, levels of α/9d in the control explants were reduced in both the FGF-2 ($p = 0.0924$)- and FGF-2/TGF-β2-treated explants ($p = 0.0959$) and were significantly reduced when compared to the elevated α/9d levels found in the CLECs of the TGF-β2-treated explants (control vs. TGF-β2, $p = 0.0034$; FGF-2 vs. TGF-β2, $p = 0.0002$) (Figure 4C). In the PLECs, there was no obvious difference in the levels of α/9d across all of the treatment groups (Figure 4B), except for elevated levels in

the PLECs of the TGF-β2-treated explants as mentioned (control vs. TGF-β2, $p = 0.0103$; FGF-2 vs. TGF-β2, $p = 0.0039$; TGF-β2 vs. FGF-2/TGF-β2, $p = 0.0249$) (Figure 4D).

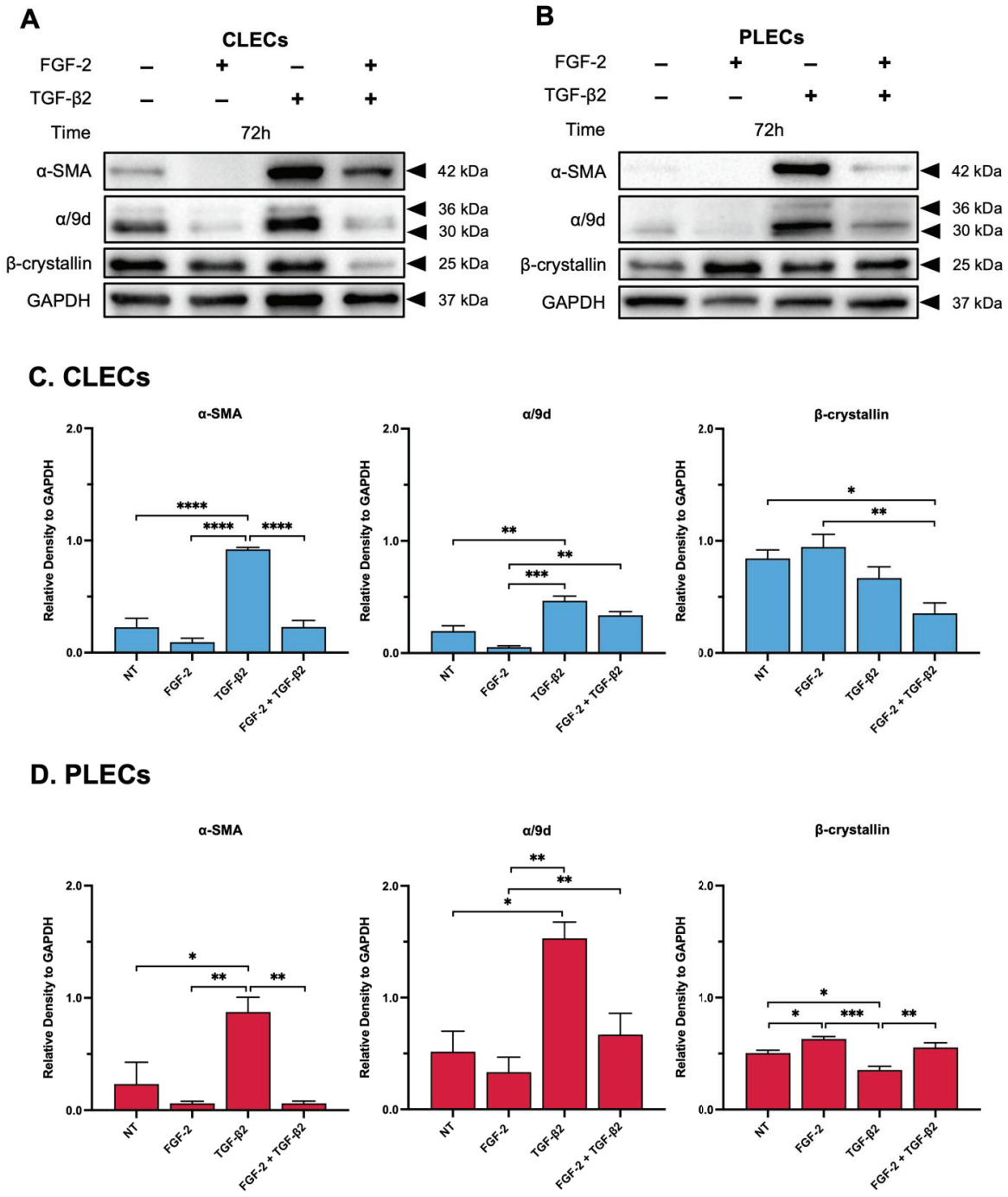

Figure 4. FGF-2 modulates levels of different protein markers in TGF-β2-treated LECs. Representative Western blot for alpha-tropomyosin (α/9d), α-SMA, and β-crystallin in the control (non-treated, NT), FGF-2, TGF-β2, and FGF-2/TGF-β2 cotreated CLECs (**A**,**C**) and PLECs (**B**,**D**). Protein levels were normalized relative to GAPDH levels (**C**,**D**). One-way ANOVA with the mean ± SEM and post-hoc Tukey's multiple comparisons test (* $p < 0.0332$, ** $p < 0.0021$, *** $p < 0.002$, **** $p < 0.001$).

3.3. Impact of FGF-2 on TGF-β2-Mediated Intracellular Signalling

3.3.1. Nuclear Translocation of Smad2/3

Given that FGF-2 can differentially regulate TGF-β2-mediated LEC behaviour, we tested its impact on TGF-β2 mediated Smad2/3-signalling. Active TGF-β2-signalling is evident with the nuclear translocation of phosphorylated Smad2/3 (Figure 5).

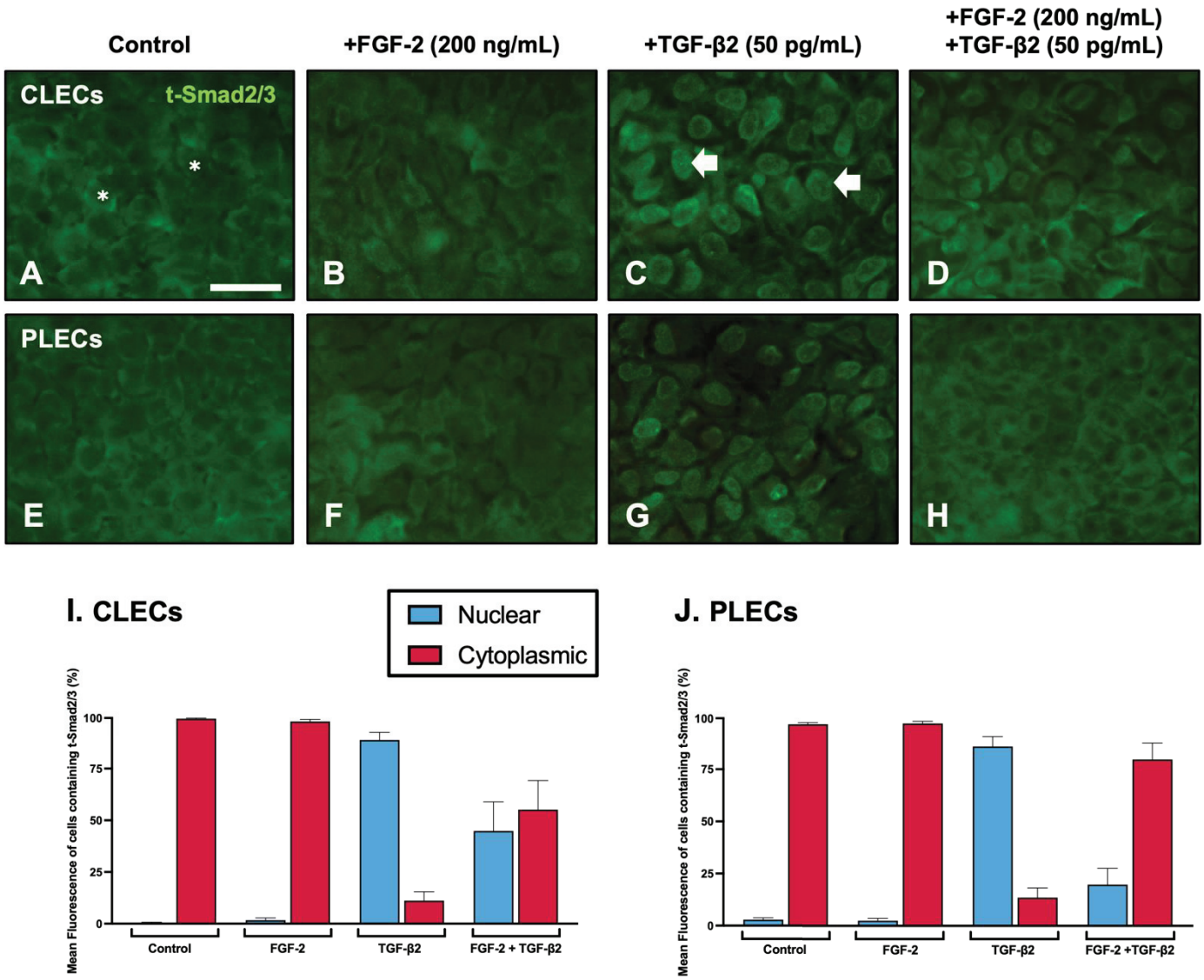

Figure 5. FGF-2 modulates TGFβ-2-induced Smad2/3 nuclear translocation. Immunolabelling of total Smad2/3 (t-Smad2/3, green) in LEC explants following two hours of culture (**A**–**H**). CLECs (**A**–**D**) and PLECs (**E**–**H**) in explants treated with no growth factors (control; (**A**,**E**)), FGF-2 (200 ng/mL; (**B**,**F**)), TGF-β2 (50 pg/mL; (**C**,**G**)), or cotreated with FGF-2/TGF-β2 (**D**,**H**). Examples of cytosolic (asterisks) and nuclear (arrowheads) localisation. Mean percentage (±SEM) fluorescence of cells with nuclear (blue) and cytoplasmic (red) t-Smad2/3 localisation in CLECs (**I**) and PLECs (**J**). Scale bar: 50 μm.

After 2 h of culture, in both the control (Figure 5A,E) and the FGF-2 (Figure 5B,F)-treated explants, we do not see any Smad2/3 nuclear localisation: 0.45–2.81% nuclear labelling (Table 2, Figure 5I,J). In contrast, distinct nuclear localisation of Smad2/3 was evident throughout the TGF-β2-treated explants (Figure 5C,G): 86.44–88.8% nuclear labelling. In the lens epithelial explants cotreated with FGF-2/TGF-β2, we observed prominent nuclear translocation of Smad2/3 in the CLECs (Figure 5D,I): 44.87% nuclear labelling;

however, in the PLECs the Smad2/3-labelling was primarily cytosolic with significantly reduced nuclear labelling: 19.85% (Table 2, Figure 5H,J).

Table 2. Nuclear vs. cytoplasmic localisation of t-Smad2/3 in CLECs and PLECs.

Localisation of t-Smad2/3 (Total Mean % of Fluorescence)				
Treatment	**CLECs**		**PLECs**	
	Nuclear	**Cytoplasmic**	**Nuclear**	**Cytoplasmic**
Control	0.35 ± 0.351	99.65 ± 0.351	2.91 ± 0.833	97.09 ± 0.833
FGF-2 (200 ng/mL)	1.70 ± 0.988	98.30 ± 0.988	2.55 ± 1.047	97.45 ± 1.047
TGF-β2 (50 pg/mL)	88.80 ± 4.217	11.20 ± 4.217	86.40 ± 5.444	13.60 ± 5.444
FGF-2 (200 ng/mL) + TGF-β2 (50 pg/mL)	44.87 ± 14.058	55.13 ± 14.058	19.85 ± 9.090	80.15 ± 9.090

The values are the mean percentage of fluorescence of t-Smad2/3 reactivity (%) ± SEM. *Abbreviations*: Central lens epithelial cells (CLECs); control (non-treated explants); peripheral lens epithelial cells (PLECs). Refer to Figure 5.

3.3.2. Smad2/3-Signalling

Treatment of the explants with FGF-2 did not impact p-Smad2/3 levels in CLECs when compared to similar levels in the control CLECs (p = 0.9768, Figure 6A,B) or the PLECs (p = 0.9310, Figure 6D,E) after 6 h of culture. Consistent with our immunofluorescent nuclear localisation of Smad2/3 (Figure 5), TGF-β2 significantly elevated p-Smad2/3 levels in the CLECs compared to the CLECs of the control explants (p = 0.0061) and the FGF-2-treated explants (p = 0.0101) (Figure 6A,B). In the CLECs of the explants cotreated with FGF/TGF-β2, there was no significant difference in p-Smad2/3 levels when compared to the CLECs of the TGF-β2 (p = 0.5944)- and the FGF-2-treated explants (p = 0.0585); however, p-Smad2/3 levels significantly increased in the cotreated CLECs compared to the control explants (p = 0.0334) (Figure 6A,B). In the PLECs, the TGF-β2 treated explants exhibited elevated p-Smad2/3 levels in comparison to the control (p = 0.0178), FGF-2 alone (p = 0.0403), and cotreated PLEC explants (p = 0.6496, Figure 5D,E) (Figure 6D,E). Compared to the control- and FGF-2-treated PLEC explants, cotreatment with FGF-2/TGF-β2 increased p-Smad2/3 levels (p = 0.0933 for the control, p = 0.2122 for FGF-2) (Figure 6D,E).

3.3.3. MAPK/ERK1/2-Signalling

Levels of phosphorylated ERK1/2 (p-ERK1/2) remained constant in the CLECs of the control and FGF-2-treated (p = 0.7703, Figure 6A,C) explants after 6 h but were elevated in the PLECs of the FGF-2-treated explants, compared to the control PLECs (p = 0.0140, Figure 6D,F). TGF-β2 treatment of the explants slightly increased p-ERK1/2 activity in the CLECs compared to the levels in the CLECs of the control (p = 0.0227) and FGF-2 treated explants (p = 0.0880) (Figure 6A,C). In contrast, the PLECs of the TGF-β2-treated explants had decreased p-ERK1/2 levels compared to the PLECs of the control (p = 0.6711) and FGF-2-treated explants (p = 0.0033) (Figure 6D,F). The CLECs in the explants cotreated with FGF-2/TGF-β2 had reduced p-ERK1/2 levels in comparison to the CLECs in the TGF-β2-treated (p = 0.0174), FGF-2-treated (p = 0.6641), and control explants (p = 0.9972) (Figure 6A,C). Interestingly, the PLECs of the cotreated explants demonstrated a significant increase in their p-ERK1/2 levels in contrast to the low levels in the PLECs of the control (p = 0.0195) and TGF- β2 treated explants (p = 0.0242) (Figure 6D,F).

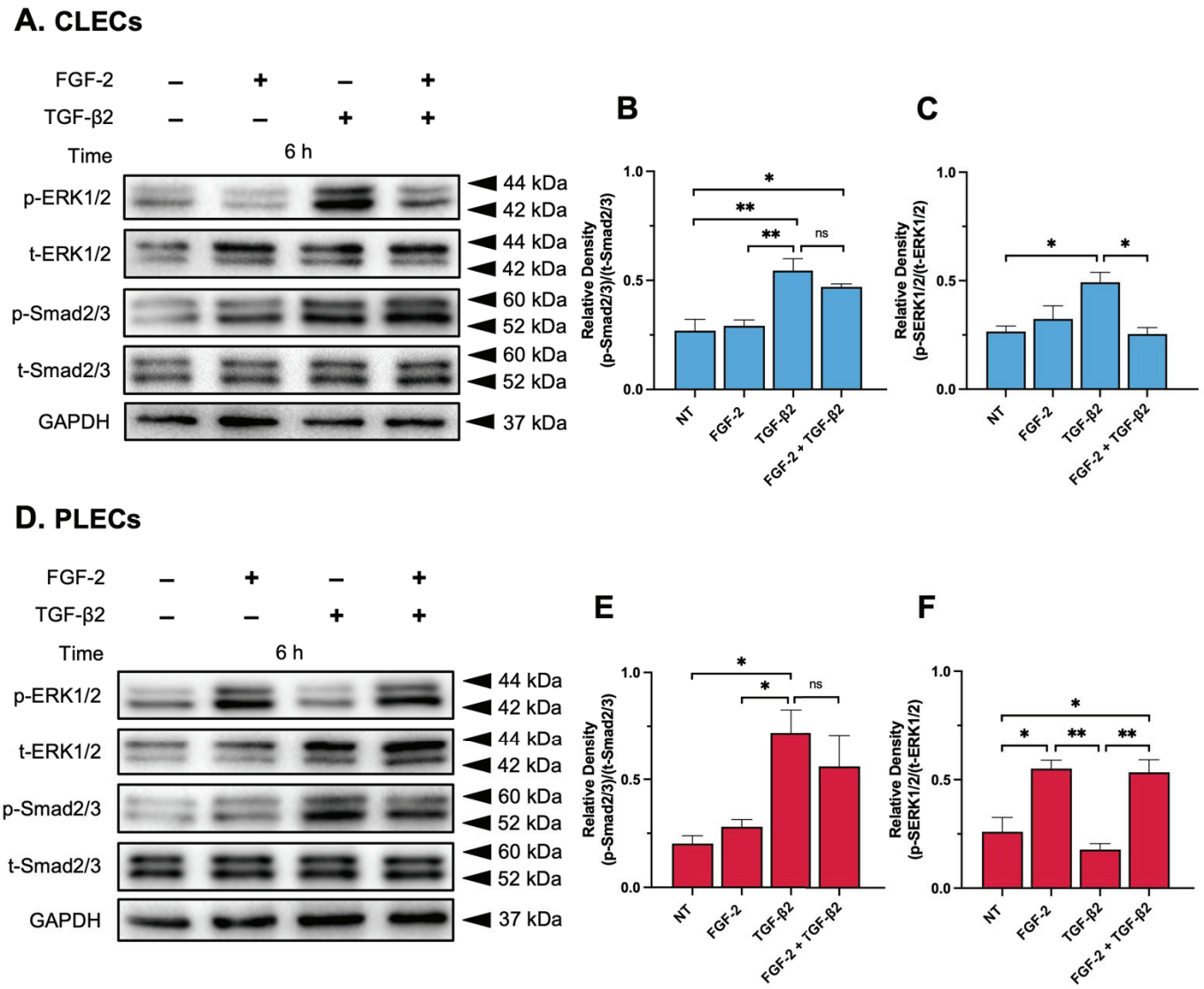

Figure 6. FGF-2 modulates TGF-β2-signalling. Representative Western blots demonstrating protein levels of phosphorylated and total Smads (p-Smad2/3 and t-Smad2/3) and MAPK/ERK1/2 (p-ERK1/2 and t-ERK1/2) in the control (non-treated, NT), FGF-2, TGF-β2, and FGF-2/TGF-β2 cotreated CLECs (**A**–**C**) and PLECs (**D**–**F**). The protein densitometry analysis shows changes in the levels of relative phosphorylation of Smad2/3 (**B**,**E**) and ERK1/2 (**C**,**F**). One-way ANOVA with the mean ± SEM and post-hoc Tukey's multiple comparisons test (ns = not significant, * $p < 0.0332$, ** $p < 0.0021$).

4. Discussion

The present study has demonstrated the impact of FGF-2 on the behaviour of lens epithelial cells induced to undergo EMT in response to TGF-β. A lens-fibre-differentiating dose of FGF-2 was able to block TGF-β2-induced lens EMT in only the peripheral LECs in explants (equivalent to the germinative region of the intact lens) and not in the central (more anterior) lens epithelia. As seen in previous wholemount rat lens epithelial cell explant models, we have demonstrated that CLECs and PLECs exposed to TGF-β2 alone undergo an EMT response, with no evidence of lens fibre differentiation [24,41,51]; however, in combination with FGF-2, FGF-2 potentiates this TGF-β2-induced activity, with elevation of canonical Smad2/3 signalling activity, as well as EMT-associated markers, more so in the CLECs.

For our lens epithelial explant model, we used relatively low doses of TGF-β2 (50 and 200 pg/mL) to induce an EMT response across a short culture period [48,52]. This dose is physiologically representative of concentrations of TGF-β2 in its mature (approx. 100 pg/mL) and total (>3000 pg/mL) forms observed in situ [53]. In addition, it is comparable to active forms of TGF-β2 (approx. 100–400 pg/mL) found in cataractous patients [53–57]. Our use of a lower TGF-β2 dose contrasts to other studies that have used much higher doses (0.5–1.5 ng/mL) to elicit an EMT response in rodent lens cells [13,14,16], which could potentially lead to off-target growth factor signalling activity. Exogenous addition of FGF-2 at a high dose encourages all lens epithelial cells (both CLECs and PLECs) to undergo a change in cell morphology typical of fibre differentiation [3,4,58,59]. In explants cotreated with TGF-β2 and FGF-2, FGF-2 appeared to protect PLECs from TGF-β-induced EMT by promoting a fibre differentiation response. We showed that the PLECs in these FGF-2/TGF-β2 cotreated explants had prominent elongated fibres, reminiscent of many earlier studies from our laboratory [59]. An elevated dose of TGF-β2, was able to prevent any fibre differentiation in the PLECs, leading to an enhanced EMT response in both central and peripheral cells. In addition, we demonstrated that the PLECs in the cotreated explants did not exhibit contractile properties as evidenced by the lack of capsular wrinkling in this region, unlike the region of the CLECs undergoing EMT. The inhibition of lens epithelial cell contraction by FGF despite the presence of TGF-β has been shown in other fibrotic models to be dose dependent, such as in bovine LECs cultured in collagen I gel [60] and valvular interstitial cells (VICs) modelling valvular fibrosis [61], which is also correlated with reduced α-SMA expression.

We not only report how TGF-β can impact FGF-induced lens cell responsiveness but how FGF in turn influences TGF-β-induced responses in LECs, the main focus of our study. When we examined for changes in cytoskeletal and stress-fibre associated proteins, the CLECs in TGF-β/FGF-cotreated lens explants exhibited predominant α-SMA localisation and little to no β-crystallin, suggesting that these cells cannot resist the EMT process, despite the presence of a high differentiating dose of FGF-2. The co-influence of FGF-2 and TGF-β on fibre differentiation, epithelial, and EMT-associated marker expression has previously been reported in other models, including human lung epithelial cells and rat alveolar epithelial-like cells [62], as well as E10 chick lens epithelial cells [13], and the lenses of postnatal mice [10]. Despite the CLECs in the TGF-β/FGF-cotreated explants undergoing a prominent EMT response, we noted reduced α-SMA and α/9d levels, compared to the TGF-β-alone-treated explants, suggesting that FGF-2 may be potentially compromising Tpm activity (a recruiter for actin assembly) and attenuating α-SMA stress fibre association. It has been previously shown that FGF may influence Tpm activity and expression, as well as cell biomechanics, in the presence of TGF-β [14]. For example, when murine LECs (MLECs) are cotreated with FGF-2/TGF-β2, the loss of Tpm1 corresponded with decreased α-SMA reactivity [14]. This same study also confirmed FGF-2 modulation of Tpm in HLECs, when cotreated with TGF-β2, with a significant reduction in both Tpm1 and Tpm2 levels [14]. We localized Tpm (α/9d) in LECs undergoing different phenotypic changes in fibre differentiation, but more compellingly in cells undergoing EMT, where it was associated with the α-SMA-reactive stress fibres of myofibroblasts. This may be attributed to the fact that the α/9d antibody we used specifically targets several isoform splice variant products of the αTm gene (TPM1), including Tpm1.4, Tpm1.6–1.9, and Tpm2.1, with some cross-reactivity also for Tpm3.1 [63]. Tpm1.6, Tpm2.1, and Tpm3.1 have all previously been characterized as being stress-fibre associated and are suggested to play a role in TGF-β induced EMT [64–66]. FGF has shown a role in propagating stress-induced EMT in conjunction with TGF-β in other pathologies, such as wound healing in mice skin keratinocytes [45] and in the tumor stromal cell microenvironment of prostate fibroblasts [47]. Consistent with our findings, Koike et al. (2020) [45] found that FGF-2 could not solely induce EMT in mice keratinocytes; however, in keratinocytes cotreated with FGF-2 and TGF-β1, there was a significant upregulation of cell migratory/motility and EMT-associated genes (e.g., *VIM* and *SNAI2*), similar to keratinocytes with only TGF-β1

stimulation. In a non-transformed mouse mammary gland epithelial cell line (NMuMG), TGF-β modulated FGF receptor activation, increased FGF-2 cell sensitivity, and promoted an EMT response through activation of ERK1/2 signalling [49], highlighting the synergistic signalling role of these two growth factors.

To determine how FGF-2 was modulating and antagonizing TGF-β2-induced EMT in PLECs of cotreated LEC explants, we explored changes in their signalling activity, namely changes to Smad2/3 and ERK1/2. In cotreated lens epithelial explants, we saw stronger signalling for the respective pathways in different regions; CLECs undergoing EMT had more pronounced p-Smad2/3 activity, while PLECs undergoing fiber differentiation had more pronounced p-ERK1/2-signalling. FGF is a well-known regulator of ERK1/2 within the lens, with its marked phosphorylation evident in lens cells within minutes post treatment [3,4,67,68]. While ERK1/2 has been shown to be required for lens epithelial cell proliferation, it is also very important for lens fiber differentiation [4,67–70]. This differs from TGF-β2-induced EMT, where we found that while ERK is also involved in this EMT process, blocking ERK1/2 does not completely block TGF-β2-mediated EMT progression in lens epithelia [39,48,52]. In fact, canonical Smad2/3-signalling is most evident in EMT, as shown here in our cotreated CLECs, and in many earlier studies examining TGF-β2-induced lens EMT [11,13,38,52,71,72].

While we and others have shown FGF-2 is not able to promote Smad2/3-signalling in LECs [10], FGF-2 was shown to impede nuclear localisation of Smad2/3 in PLECs in explants cotreated with TGF-β2; however, in CLECs of these same explants, FGF-2 appeared to have less of an impact on TGF-β2-induced Smad2/3-activity. How FGF-2 directly blocks Smad2/3 activity in PLECs is not clear but given the strong ERK1/2 activation in these cells, this may favour lens fibre differentiation and cell survival, as we see here and has been shown by others [2,3,67,73]. Conversely, FGF-mediated ERK1/2 signalling can correlate with the upregulation of TGF-β activity, as seen in other fibrosis models [14,49,74–76], as well as the current study where TGF-β-induced CLECs are associated with elevated ERK1/2-signalling. Similar to the current study, in valvular interstitial cells (VICs) modelling valvular fibrosis, it was shown that inhibition of this fibrosis was dependent on FGF-2-mediated MAPK signalling when cotreated with TGF-β1 [61]. This study demonstrated that FGF (10 ng/mL) prevented Smad3 nuclear localisation in VICs cotreated with TGF-β1 (5 ng/mL), and at higher doses (100 ng/mL), it was able to perturb TGF-β1-mediated α-SMA expression [61], highlighting the ability of FGF to modulate canonical TGF-β signalling activity and downstream gene expression.

Although not completely understood, crosstalk between FGF and TGF-β signalling has proven influential in mediating various fibrotic disorders and carcinoma progression. For example, a study implementing mouse tumor-associated endothelial cells (TECs) demonstrated how FGF can promote a differential cell response by reducing TGF-β-induced contractile and myofibroblastic properties, while concurrently promoting cell proliferation and motility [75]. A similar finding was observed in primary human dermal fibroblasts (HDFs), whereby FGF-2 with TGF-β1 cotreatment, both positively and negatively regulated fibroblast transition into cancer-associated fibroblasts (CAFs) [77]. This same study also showed how this FGF-2/TGF-β1 treatment of HDFs can downregulate common CAF-activated and EMT-associated markers (e.g., *ACTA2*, *ITGA11*, and *COL1A1*) as well as upregulating cell motility and morphogenetic genes (e.g., *HGF* and *BMP2*) [77].

Research into the mechanisms surrounding differential types of PCO involving lens fibre cell types is ongoing and it is believed to be due to FGF/TGF-β interactions during EMT induction [13,15,16,38,74,78]. As FGF is a major factor influencing normal lens fibre differentiation, it is important to understand what promotes aberrant fibre differentiation during pearl PCO development at the lens equator [13,24,35,79]. In situ, for ASC and for post-operative PCO, more anterior lens epithelial cells are likely exposed to a high insult of TGF-β, and relatively low levels of FGF are normally found in the aqueous humour. At the lens equator, however, epithelial cells in the posterior chamber are regularly exposed to elevated levels of FGF, and regardless of any increased TGF-β levels, the cells here likely

undergo aberrant fibre differentiation, leading to pearl PCO. This may result from the heightened sensitivity to FGF of these peripheral LECs, namely due to their elevated levels of high-affinity FGF receptor tyrosine kinase (RTK) receptors, compared to the central lens epithelia [6,58,80,81]. In situ, during lens fibrosis, we do not see EMT resulting in cell death, likely due to survival growth factors present within the ocular media. Given the findings from the current study, we propose that FGF is a putative survival factor in situ, maintaining fiber cells at the lens equator and the myofibroblastic phenotype leading to fibrotic PCO. Further studies investigating differences/changes in levels of FGF and TGF-β receptors, between central and peripheral lens cells in cotreated explants, may be a key factor in determining lens cell fates in situ. We also cannot rule out that changes in the expression of RTK antagonists, such as Sprouty and Spreds [69,70,82], including those more specific for FGF, such as Sef [83], in these active regions of the lens may be protective of peripheral LECs from any aberrant TGF-β insult of which they have previously been reported to block [69].

5. Conclusions

A fine balance between levels of FGF-2 and TGF-β2 can promote differential responses in lens epithelial cells. More specifically, this responsiveness is spatially regulated, with the anterior central lens epithelia more sensitive to EMT induction, whilst peripheral cells primarily undergo fibre differentiation in the presence of high levels of FGF, avoiding apoptotic cell death associated with EMT. This induced heterogeneous population of cells in lens epithelial explants may provide an alternative model better suited to the study of the cellular processes at play in situ, leading to the formation of ASC, and more importantly both fibrotic and pearl forms of PCO.

Supplementary Materials: The following supporting information can be downloaded at: https://www.mdpi.com/article/10.3390/cells12060827/s1, Figure S1: FGF dose-dependent modulation of TGF-β2-induced EMT; Figure S2: FGF-2 modulates LEC behaviour during TGF-β2-induced EMT; Figure S3: Lens capsule modulation; Figure S4: Re-supplementation of FGF-2 promotes cell survival; Figure S5: FGF-2 modulates EMT and fibre differentiation markers in TGF-β2-treated LECs.

Author Contributions: Conceptualization, F.J.L. and M.F.; methodology, M.F.; software, M.F.; validation, M.F. and F.J.L.; formal analysis, M.F.; investigation, M.F.; resources, M.F. and F.J.L.; data curation, M.F.; writing—original draft preparation, M.F.; writing—review and editing, F.J.L.; visualization, M.F. and F.J.L.; supervision, F.J.L.; project administration, F.J.L.; funding acquisition, F.J.L. All authors have read and agreed to the published version of the manuscript.

Funding: This research received no external funding.

Institutional Review Board Statement: All animal experimentation was approved by the Animal Ethics Committee of The University of Sydney, NSW, Australia (AEC# 2021/1913).

Informed Consent Statement: Not applicable.

Data Availability Statement: Not applicable.

Acknowledgments: We would like to thank Professor Peter Gunning from the University of New South Wales, Australia, for providing the anti-tropomyosin alpha-1 antibody (α/9d).

Conflicts of Interest: M.F. and F.J.L. declare no conflict of interest.

Abbreviations

ASC	Anterior subcapsular cataract
α-SMA	Alpha-smooth muscle actin
α/9d	Alpha tropomyosin 9d antibody
CLECs	Central lens epithelial cells
EMT	Epithelial–mesenchymal transition
ERK	Extracellular signal-regulated kinase
FGF	Fibroblast growth factor
LECs	Lens epithelial cells
MAPK	Mitogen-activated protein kinase
PLECs	Peripheral lens epithelial cells
PCO	Posterior capsular opacification
TGF-β	Transforming growth factor-beta
Tpm	Tropomyosin

References

1. Lovicu, F.J.; McAvoy, J.W. Growth factor regulation of lens development. *Dev. Biol.* **2005**, *280*, 1–14. [CrossRef]
2. Iyengar, L.; Patkunanathan, B.; Mcavoy, J.W.; Lovicu, F.J. Growth factors involved in aqueous humour-induced lens cell proliferation. *Growth Factors* **2009**, *27*, 50–62. [CrossRef]
3. Iyengar, L.; Wang, Q.; Rasko, J.E.J.; McAvoy, J.W.; Lovicu, F.J. Duration of ERK1/2 phosphorylation induced by FGF or ocular media determines lens cell fate. *Differentiation* **2007**, *75*, 662–668. [CrossRef]
4. Lovicu, F.J.; McAvoy, J.W. FGF-induced lens cell proliferation and differentiation is dependent on MAPK (ERK1/2) signalling. *Development* **2001**, *128*, 5075–5084. [CrossRef]
5. West-Mays, J.A.; Pino, G.; Lovicu, F.J. Development and use of the lens epithelial explant system to study lens differentiation and cataractogenesis. *Prog. Retin. Eye Res.* **2009**, *29*, 135–143. [CrossRef] [PubMed]
6. De Iongh, R.U.; Lovicu, F.J.; Hanneken, A.; Baird, A.; McAvoy, J.W. FGF receptor-1 (flg) expression is correlated with fibre differentiation during rat lens morphogenesis and growth. *Dev. Dyn.* **1996**, *206*, 412–426. [CrossRef]
7. Chamberlain, C.G.; McAvoy, J.W. Fibre differentiation and polarity in the mammalian lens: A key role for FGF. *Prog. Retin. Eye Res.* **1997**, *16*, 443–478. [CrossRef]
8. Zhao, H.; Yang, T.; Madakashira, B.P.; Thiels, C.A.; Bechtle, C.A.; Garcia, C.M.; Zhang, H.; Yu, K.; Ornitz, D.M.; Beebe, D.C.; et al. Fibroblast growth factor receptor signaling is essential for lens fiber cell differentiation. *Dev. Biol.* **2008**, *318*, 276–288. [CrossRef] [PubMed]
9. Chamberlain, C.G.; McAvoy, J.W. Induction of Lens Fibre Differentiation by Acidic and Basic Fibroblast Growth Factor (FGF). *Growth Factors* **1989**, *1*, 125–134. [CrossRef]
10. Wang, D.; Wang, E.; Liu, K.; Xia, C.-H.; Li, S.; Gong, X. Roles of TGFβ and FGF signals during growth and differentiation of mouse lens epithelial cell in vitro. *Sci. Rep.* **2017**, *7*, 7274. [CrossRef] [PubMed]
11. Wormstone, I.M.; Anderson, I.K.; Eldred, J.A.; Dawes, L.J.; Duncan, G. Short-term exposure to transforming growth factor β induces long-term fibrotic responses. *Exp. Eye Res.* **2006**, *83*, 1238–1245. [CrossRef]
12. Wormstone, I.M.; Tamiya, S.; Anderson, I.; Duncan, G. TGF-beta2-induced matrix modification and cell transdif-ferentiation in the human lens capsular bag. *Investig. Ophth. Vis. Sci.* **2002**, *43*, 2301–2308.
13. Boswell, B.A.; Korol, A.; West-Mays, J.A.; Musil, L.S. Dual function of TGFβ in lens epithelial cell fate: Implications for secondary cataract. *Mol. Biol. Cell* **2017**, *28*, 907–921. [CrossRef]
14. Kubo, E.; Shibata, S.; Shibata, T.; Kiyokawa, E.; Sasaki, H.; Singh, D.P. FGF2 antagonizes aberrant TGFβ regulation of tropomyosin: Role for posterior capsule opacity. *J. Cell. Mol. Med.* **2017**, *21*, 916–928. [CrossRef] [PubMed]
15. Mansfield, K.J.; Cerra, A.; Chamberlain, C.G. FGF-2 counteracts loss of TGFbeta affected cells from rat lens explants: Implications for PCO (after cataract). *Mol. Vis.* **2004**, *10*, 521–532.
16. Cerra, A.; Mansfield, K.J.; Chamberlain, C.G. Exacerbation of TGF-beta-induced cataract by FGF-2 in cultured rat lenses. *Mol. Vis.* **2003**, *9*, 689–700. [PubMed]
17. de Iongh, R.U.; Wederell, E.; Lovicu, F.J.; McAvoy, J.W. Transforming Growth Factor-β-Induced Epithelial-Mesenchymal Transition in the Lens: A Model for Cataract Formation. *Cells Tissues Organs* **2005**, *179*, 43–55. [CrossRef] [PubMed]
18. Lovicu, F.J.; Flokis, M.; Wojciechowski, M.; Mao, B.; Shu, D. Understanding Fibrotic Cataract: Regulation of TGFβ-Mediated Pathways Leading to Lens Epithelial to Mesenchymal Transition (EMT). *J. Jpn. Soc. Cataract. Res.* **2020**, *32*, 23–32.
19. Xu, J.; Lamouille, S.; Derynck, R. TGF-beta-induced epithelial to mesenchymal transition. *Cell Res.* **2009**, *19*, 156–172. [CrossRef]
20. Nieto, M.A.; Huang, R.Y.-J.; Jackson, R.A.; Thiery, J.P. EMT: 2016. *Cell* **2016**, *166*, 21–45. [CrossRef]
21. Kalluri, R.; Neilson, E.G. Epithelial-mesenchymal transition and its implications for fibrosis. *J. Clin. Investig.* **2003**, *112*, 1776–1784. [CrossRef] [PubMed]
22. Martinez, G.; de Iongh, R.U. The lens epithelium in ocular health and disease. *Int. J. Biochem. Cell Biol.* **2010**, *42*, 1945–1963. [CrossRef] [PubMed]

23. Marcantonio, J.M.; Syam, P.P.; Liu, C.S.C.; Duncan, G. Epithelial transdifferentiation and cataract in the human lens. *Exp. Eye Res.* **2003**, *77*, 339–346. [CrossRef] [PubMed]
24. Lovicu, F.J.; Steven, P.; Saika, S.; McAvoy, J.W. Aberrant Lens Fiber Differentiation in Anterior Subcapsular Cataract Formation: A Process Dependent on Reduced Levels of Pax6. *Investig. Ophthalmol. Vis. Sci.* **2004**, *45*, 1946–1953. [CrossRef]
25. Jiang, J.; Shihan, M.H.; Wang, Y.; Duncan, M.K. Lens Epithelial Cells Initiate an Inflammatory Response Following Cataract Surgery. *Investig. Ophthalmol. Vis. Sci.* **2018**, *59*, 4986–4997. [CrossRef]
26. Liu, Y.C.; Wilkins, M.; Kim, T.; Malyugin, B.; Mehta, J.S. Cataracts. *Lancet* **2017**, *390*, 600–612. [CrossRef]
27. Abdulhussein, D.; Hussein, M.A. WHO Vision 2020: Have We Done It? *Ophthalmic Epidemiol.* **2022**, 1–9. [CrossRef]
28. GBD Blindness and Vision Impairment Collaborators; Vision Loss Expert Group of the Global Burden of Disease Study. Trends in prevalence of blindness and distance and near vision impairment over 30 years: An analysis for the Global Burden of Disease Study. *Lancet Glob. Health* **2021**, *9*, e130–e143. [CrossRef]
29. Vasavada, A.R.; Praveen, M.R. Posterior Capsule Opacification After Phacoemulsification: Annual Review. *Asia-Pacific J. Ophthalmol.* **2014**, *3*, 235–240. [CrossRef]
30. Karahan, E.; Er, D.; Kaynak, S. An Overview of Nd:YAG Laser Capsulotomy. *Med. Hypothesis Discov. Innov. Ophthalmol.* **2014**, *3*, 45–50.
31. Pandey, S.K.; Apple, D.J.; Werner, L.; Maloof, A.J.; Milverton, E.J. Posterior capsule opacification: A review of the aetiopathogenesis, experimental and clinical studies and factors for prevention. *Indian J. Ophthalmol.* **2004**, *52*, 99–112.
32. Lovicu, F.J.; Shin, E.H.; McAvoy, J.W. Fibrosis in the lens. Sprouty regulation of TGFβ-signaling prevents lens EMT leading to cataract. *Exp. Eye Res.* **2015**, *142*, 92–101. [CrossRef]
33. D'Antin, J.C.; Tresserra, F.; Barraquer, R.I.; Michael, R. Soemmerring's Rings Developed around IOLs, in Human Donor Eyes, Can Present Internal Transparent Areas. *Int. J. Mol. Sci.* **2022**, *23*, 13294. [CrossRef]
34. Wormstone, I.M.; Wormstone, Y.M.; Smith, A.J.O.; Eldred, J.A. Posterior capsule opacification: What's in the bag? *Prog. Retin. Eye Res.* **2020**, *82*, 100905. [CrossRef]
35. Wormstone, I.M.; Eldred, J.A. Experimental models for posterior capsule opacification research. *Exp. Eye Res.* **2016**, *142*, 2–12. [CrossRef] [PubMed]
36. Lu, C.; Yu, S.; Song, H.; Zhao, Y.; Xie, S.; Tang, X.; Yuan, X. Posterior capsular opacification comparison between morphology and objective visual function. *BMC Ophthalmol.* **2019**, *19*, 40. [CrossRef] [PubMed]
37. Aslam, T.M.; Aspinall, P.; Dhillon, B. Posterior capsule morphology determinants of visual function. *Graefe's Arch. Clin. Exp. Ophthalmol.* **2003**, *241*, 208–212. [CrossRef]
38. Boswell, B.A.; VanSlyke, J.K.; Musil, L.S. Regulation of Lens Gap Junctions by Transforming Growth Factor Beta. *Mol. Biol. Cell* **2010**, *21*, 1686–1697. [CrossRef] [PubMed]
39. Shu, D.Y.; Wojciechowski, M.; Lovicu, F.J. ERK1/2-mediated EGFR-signaling is required for TGFβ-induced lens epithelial-mesenchymal transition. *Exp. Eye Res.* **2019**, *178*, 108–121. [CrossRef] [PubMed]
40. Musil, L.S. Primary Cultures of Embryonic Chick Lens Cells as a Model System to Study Lens Gap Junctions and Fiber Cell Differentiation. *J. Membr. Biol.* **2012**, *245*, 357–368. [CrossRef]
41. Liu, J.; Hales, A.M.; Chamberlain, C.G.; McAvoy, J.W. Induction of cataract-like changes in rat lens epithelial explants by transforming growth factor beta. *Investig. Ophthalmol. Vis. Sci.* **1994**, *35*, 388–401.
42. Shu, D.Y.; Wojciechowski, M.C.; Lovicu, F.J. Bone Morphogenetic Protein-7 Suppresses TGFβ2-Induced Epithelial-Mesenchymal Transition in the Lens: Implications for Cataract Prevention. *Investig. Ophthalmol. Vis. Sci.* **2017**, *58*, 781–796. [CrossRef]
43. Lovicu, F.J.; Schulz, M.W.; Hales, A.M.; Vincent, L.N.; Overbeek, P.A.; Chamberlain, C.G.; McAvoy, J.W. TGFβ induces morphological and molecular changes similar to human anterior subcapsular cataract. *Br. J. Ophthalmol.* **2002**, *86*, 220. [CrossRef] [PubMed]
44. Srinivasan, Y.; Lovicu, F.J.; A Overbeek, P. Lens-specific expression of transforming growth factor beta1 in transgenic mice causes anterior subcapsular cataracts. *J. Clin. Investig.* **1998**, *101*, 625–634. [CrossRef]
45. Koike, Y.; Yozaki, M.; Utani, A.; Murota, H. Fibroblast growth factor 2 accelerates the epithelial–mesenchymal transition in keratinocytes during wound healing process. *Sci. Rep.* **2020**, *10*, 1–13. [CrossRef] [PubMed]
46. Maruno, K.A.; Lovicu, F.J.; Chamberlain, C.G.; WMcAvoy, J. Apoptosis is a feature of TGFß-induced cataract. *Clin. Exp. Optom.* **2002**, *85*, 76–82. [CrossRef] [PubMed]
47. Strand, D.W.; Liang, Y.-Y.; Yang, F.; Barron, D.A.; Ressler, S.J.; Schauer, I.G.; Feng, X.-H.; Rowley, D.R. TGF-β in-duction of FGF-2 expression in stromal cells requires integrated smad3 and MAPK pathways. *Am. J. Clin. Exp. Urol.* **2014**, *2*, 239–248.
48. Wojciechowski, M.C.; Mahmutovic, L.; Shu, D.Y.; Lovicu, F.J. ERK1/2 signaling is required for the initiation but not progression of TGFβ-induced lens epithelial to mesenchymal transition (EMT). *Exp. Eye Res.* **2017**, *159*, 98–113. [CrossRef]
49. Shirakihara, T.; Horiguchi, K.; Miyazawa, K.; Ehata, S.; Shibata, T.; Morita, I.; Miyazono, K.; Saitoh, M. TGF-β regulates isoform switching of FGF receptors and epithelial-mesenchymal transition. *EMBO J.* **2011**, *30*, 783–795. [CrossRef] [PubMed]
50. Wang, Q.; McAvoy, J.W.; Lovicu, F.J. Growth Factor Signaling in Vitreous Humor–Induced Lens Fiber Differentiation. *Investig. Ophthalmol. Vis. Sci.* **2010**, *51*, 3599–3610. [CrossRef]
51. de Iongh, R.U.; Lovicu, F.J.; Overbeek, P.A.; Schneider, M.D.; Joya, J.; Hardeman, E.D.; McAvoy, J.W. Requirement for TGFbeta receptor signaling during terminal lens fiber differentiation. *Development* **2001**, *128*, 3995–4010. [CrossRef]

52. Shu, D.Y.; Lovicu, F.J. Enhanced EGF receptor-signaling potentiates TGFβ-induced lens epithelial-mesenchymal transition. *Exp. Eye Res.* **2019**, *185*, 107693. [CrossRef] [PubMed]
53. Kokawa, N.; Sotozono, C.; Nishida, K.; Kinoshita, S. High total TGF-β2 levels in normal human tears. *Curr. Eye Res.* **1996**, *15*, 341–343. [CrossRef] [PubMed]
54. Yamamoto, N.; Itonaga, K.; Marunouchi, T.; Majima, K. Concentration of Transforming Growth Factor β2 in Aqueous Humor. *Ophthalmic Res.* **2005**, *37*, 29–33. [CrossRef] [PubMed]
55. Ochiai, Y.; Ochiai, H. Higher Concentration of Transforming Growth Factor-β in Aqueous Humor of Glaucomatous Eyes and Diabetic Eyes. *Jpn. J. Ophthalmol.* **2002**, *46*, 249–253. [CrossRef] [PubMed]
56. Agarwal, P.; Daher, A.M.; Agarwal, R. Aqueous humor TGF-β2 levels in patients with open-angle glaucoma: A meta-analysis. *Mol. Vis.* **2015**, *21*, 612–620. [PubMed]
57. Cousins, S.W.; McCabe, M.M.; Danielpour, D.; Streilein, J.W. Identification of transforming growth factor-beta as an immunosuppressive factor in aqueous humor. *Investig. Ophthalmol. Vis. Sci.* **1991**, *32*, 2201–2211.
58. de Iongh, R.U.; Lovicu, F.J.; Chamberlain, C.G.; McAvoy, J.W. Differential expression of fibroblast growth factor receptors during rat lens morphogenesis and growth. *Investig. Ophthalmol. Vis. Sci.* **1997**, *38*, 1688–1699.
59. Dawes, L.J.; Sugiyama, Y.; Lovicu, F.J.; Harris, C.G.; Shelley, E.J.; McAvoy, J.W. Interactions between lens epithelial and fiber cells reveal an intrinsic self-assembly mechanism. *Dev. Biol.* **2014**, *385*, 291–303. [CrossRef]
60. Kurosaka, D.; Kato, K.; Nagamoto, T.; Negishi, K. Growth factors influence contractility and alpha-smooth muscle actin expression in bovine lens epithelial cells. *Investig. Ophthalmol. Vis. Sci.* **1995**, *36*, 1701–1708.
61. Cushing, M.C.; Mariner, P.D.; Liao, J.; Sims, E.A.; Anseth, K.S. Fibroblast growth factor represses Smad-mediated myofibroblast activation in aortic valvular interstitial cells. *FASEB J.* **2008**, *22*, 1769–1777. [CrossRef]
62. Ramos, C.; Becerril, C.; Montaño, M.; García-De-Alba, C.; Ramírez, R.; Checa, M.; Pardo, A.; Selman, M. FGF-1 reverts epithelial-mesenchymal transition induced by TGF-β1 through MAPK/ERK kinase pathway. *Am. J. Physiol. Cell. Mol. Physiol.* **2010**, *299*, L222–L231. [CrossRef] [PubMed]
63. Schevzov, G.; Whittaker, S.P.; Fath, T.; Lin, J.J.-C.; Gunning, P.W. Tropomyosin isoforms and reagents. *Bioarchitecture* **2011**, *1*, 135–164. [CrossRef] [PubMed]
64. Cheng, C.; Nowak, R.B.; Amadeo, M.B.; Biswas, S.K.; Lo, W.-K.; Fowler, V.M. Tropomyosin 3.5 protects the F-actin networks required for tissue biomechanical properties. *J. Cell Sci.* **2018**, *131*, jcs222042. [CrossRef] [PubMed]
65. Parreno, J.; Amadeo, M.B.; Kwon, E.H.; Fowler, V.M. Tropomyosin 3.1 association with actin stress fibers is required for lens epithelial to mesenchymal transition. *Investig. Ophthalmol. Vis. Sci.* **2020**, *61*, 2. [CrossRef] [PubMed]
66. Gateva, G.; Kremneva, E.; Reindl, T.; Kotila, T.; Kogan, K.; Gressin, L.; Gunning, P.W.; Manstein, D.J.; Michelot, A.; Lappalainen, P. Tropomyosin Isoforms Specify Functionally Distinct Actin Filament Populations In Vitro. *Curr. Biol.* **2017**, *27*, 705–713. [CrossRef]
67. Wang, Q.; Stump, R.; McAvoy, J.W.; Lovicu, F.J. MAPK/ERK1/2 and PI3-kinase signalling pathways are required for vitreous-induced lens fibre cell differentiation. *Exp. Eye Res.* **2008**, *88*, 293–306. [CrossRef] [PubMed]
68. Le, A.-C.N.; Musil, L.S. FGF Signaling in Chick Lens Development. *Dev. Biol.* **2001**, *233*, 394–411. [CrossRef]
69. Shin, E.H.; Zhao, G.; Wang, Q.; Lovicu, F.J. Sprouty gain of function disrupts lens cellular processes and growth by restricting RTK signaling. *Dev. Biol.* **2015**, *406*, 129–146. [CrossRef]
70. Susanto, A.; Zhao, G.; Wazin, F.; Feng, Y.; Rasko, J.E.; Bailey, C.G.; Lovicu, F.J. Spred negatively regulates lens growth by modulating epithelial cell proliferation and fiber differentiation. *Exp. Eye Res.* **2019**, *178*, 160–175. [CrossRef]
71. Saika, S.; Kono-Saika, S.; Ohnishi, Y.; Sato, M.; Muragaki, Y.; Ooshima, A.; Flanders, K.C.; Yoo, J.; Anzano, M.; Liu, C.-Y.; et al. Smad3 Signaling Is Required for Epithelial-Mesenchymal Transition of Lens Epithelium after Injury. *Am. J. Pathol.* **2004**, *164*, 651–663. [CrossRef]
72. Saika, S.; Miyamoto, T.; Ishida, I.; Shirai, K.; Ohnishi, Y.; Ooshima, A.; McAvoy, J.W. TGFbeta-Smad signalling in postoperative human lens epithelial cells. *Br. J. Ophthalmol.* **2002**, *86*, 1428–1433. [CrossRef] [PubMed]
73. Stolen, C.M.; Jackson, M.W.; Griep, A.E. Overexpression of FGF-2 modulates fiber cell differentiation and survival in the mouse lens. *Development* **1997**, *124*, 4009–4017. [CrossRef]
74. Kubo, E.; Shibata, T.; Singh, D.P.; Sasaki, H. Roles of TGF β and FGF Signals in the Lens: Tropomyosin Regulation for Posterior Capsule Opacity. *Int. J. Mol. Sci.* **2018**, *19*, 3093. [CrossRef] [PubMed]
75. Akatsu, Y.; Takahashi, N.; Yoshimatsu, Y.; Kimuro, S.; Muramatsu, T.; Katsura, A.; Maishi, N.; Suzuki, H.; Inazawa, J.; Hida, K.; et al. Fibroblast growth factor signals regulate transforming growth factor-β-induced endothelial-to-myofibroblast transition of tumor endothelial cells via Elk1. *Mol. Oncol.* **2019**, *13*, 1706–1724. [CrossRef] [PubMed]
76. Strutz, F.; Zeisberg, M.; Renziehausen, A.; Raschke, B.; Becker, V.; Kooten, C.V.; Müller, G.A. TGF-β1 induces proliferation in human renal fibroblasts via induction of basic fibroblast growth factor (FGF-2). *Kidney Int.* **2001**, *59*, 579–592. [CrossRef]
77. Bordignon, P.; Bottoni, G.; Xu, X.; Popescu, A.S.; Truan, Z.; Guenova, E.; Kofler, L.; Jafari, P.; Ostano, P.; Röcken, M.; et al. Dualism of FGF and TGF-β Signaling in Heterogeneous Cancer-Associated Fibroblast Activation with ETV1 as a Critical Determinant. *Cell Rep.* **2019**, *28*, 2358–2372.e6. [CrossRef]
78. Symonds, J.G.; Lovicu, F.J.; Chamberlain, C.G. Posterior capsule opacification-like changes in rat lens explants cultured with TGFβ and FGF: Effects of cell coverage and regional differences. *Exp. Eye Res.* **2006**, *82*, 693–699. [CrossRef]
79. Lovicu, F.J.; Chamberlain, C.G.; McAvoy, J.W. Differential effects of aqueous and vitreous on fiber differentiation and extracellular matrix accumulation in lens epithelial explants. *Investig. Ophthalmol. Vis. Sci.* **1995**, *36*, 1459–1469.

80. Kondo, T.; Ishiga-Hashimoto, N.; Nagai, H.; Takeshita, A.; Mino, M.; Morioka, H.; Kusakabe, K.T.; Okada, T. Expression of transforming growth factor β and fibroblast growth factor 2 in the lens epithelium of Morioka cataract mice. *Congenit. Anom.* **2014**, *54*, 104–109. [CrossRef]
81. Lovicu, F.J.; McAvoy, J.W. The age of rats affects the response of lens epithelial explants to fibroblast growth factor. An ultrastructural analysis. *Investig. Ophthalmol. Vis. Sci.* **1992**, *33*, 2269–2278.
82. Zhao, G.; Bailey, C.G.; Feng, Y.; Rasko, J.; Lovicu, F.J. Negative regulation of lens fiber cell differentiation by RTK antagonists Spry and Spred. *Exp. Eye Res.* **2018**, *170*, 148–159. [CrossRef] [PubMed]
83. Newitt, P.; Boros, J.; Madakashira, B.P.; Robinson, M.L.; Reneker, L.W.; McAvoy, J.W.; Lovicu, F.J. Sef is a negative regulator of fiber cell differentiation in the ocular lens. *Differentiation* **2010**, *80*, 53–67. [CrossRef] [PubMed]

Disclaimer/Publisher's Note: The statements, opinions and data contained in all publications are solely those of the individual author(s) and contributor(s) and not of MDPI and/or the editor(s). MDPI and/or the editor(s) disclaim responsibility for any injury to people or property resulting from any ideas, methods, instructions or products referred to in the content.

cells

MDPI

Article

High-Throughput Transcriptomics of *Celf1* Conditional Knockout Lens Identifies Downstream Networks Linked to Cataract Pathology

Archana D. Siddam [1,†], Matthieu Duot [1,2,†], Sarah Y. Coomson [1,†], Deepti Anand [1], Sandeep Aryal [1], Bailey A. T. Weatherbee [1], Yann Audic [2], Luc Paillard [2,*] and Salil A. Lachke [1,3,*]

[1] Department of Biological Sciences, University of Delaware, Newark, DE 19716, USA
[2] CNRS, IGDR (Institut de Génétique et Développement de Rennes), Univ. Rennes, UMR 6290, Rennes, F-35000 Rennes, France
[3] Center for Bioinformatics and Computational Biology, University of Delaware, Newark, DE 19716, USA
* Correspondence: luc.paillard@univ-rennes1.fr (L.P.); salil@udel.edu (S.A.L.)
† These authors contributed equally to this work.

Abstract: Defects in the development of the ocular lens can cause congenital cataracts. To understand the various etiologies of congenital cataracts, it is important to characterize the genes linked to this developmental defect and to define their downstream pathways that are relevant to lens biology and pathology. Deficiency or alteration of several RNA-binding proteins, including the conserved RBP Celf1 (CUGBP Elav-like family member 1), has been described to cause lens defects and early onset cataracts in animal models and/or humans. Celf1 is involved in various aspects of post-transcriptional gene expression control, including regulation of mRNA stability/decay, alternative splicing and translation. *Celf1* germline knockout mice and lens conditional knockout (*Celf1*^{cKO}) mice develop fully penetrant cataracts in early postnatal stages. To define the genome-level changes in RNA transcripts that result from *Celf1* deficiency, we performed high-throughput RNA-sequencing of *Celf1*^{cKO} mouse lenses at postnatal day (P) 0. *Celf1*^{cKO} lenses exhibit 987 differentially expressed genes (DEGs) at cut-offs of >1.0 log2 counts per million (CPM), $\geq\pm0.58$ log2 fold-change and <0.05 false discovery rate (FDR). Of these, 327 RNAs were reduced while 660 were elevated in *Celf1*^{cKO} lenses. The DEGs were subjected to various downstream analyses including iSyTE lens enriched-expression, presence in Cat-map, and gene ontology (GO) and representation of regulatory pathways. Further, a comparative analysis was done with previously generated microarray datasets on *Celf1*^{cKO} lenses P0 and P6. Together, these analyses validated and prioritized several key genes mis-expressed in *Celf1*^{cKO} lenses that are relevant to lens biology, including known cataract-linked genes (e.g., *Cryab*, *Cryba2*, *Cryba4*, *Crybb1*, *Crybb2*, *Cryga*, *Crygb*, *Crygc*, *Crygd*, *Cryge*, *Crygf*, *Dnase2b*, *Bfsp1*, *Gja3*, *Pxdn*, *Sparc*, *Tdrd7*, etc.) as well as novel candidates (e.g., *Ell2* and *Prdm16*). Together, these data have defined the alterations in lens transcriptome caused by Celf1 deficiency, in turn uncovering downstream genes and pathways (e.g., structural constituents of eye lenses, lens fiber cell differentiation, etc.) associated with lens development and early-onset cataracts.

Keywords: lens; eye; cataracts; RNA-binding protein; Cugbp1; development; post-transcriptional control; transcriptome; RNA-sequencing; microarrays

1. Introduction

Morphogenesis of the vertebrate ocular lens has been studied for over 100 years [1]. In addition to uncovering key principles in developmental biology, understanding the process of lens formation has helped identify genetic causes underlying human lens defects, such as congenital cataracts [2,3]. Indeed, thus far, several regulatory pathways involved in lens development have been identified [4]. While the majority of these studies were focused on signaling and transcriptional regulation [4,5], research over the past ~10 years

has shown that RNA-binding protein (RBP)-based post-transcriptional control of gene expression plays key roles in lens development [6,7]. These findings have shown that the expressions of several RBPs, namely, Caprin2, Celf1 (Cugbp1), Rbm24 and Tdrd7, are conserved in lens development across multiple vertebrate species [8–16]. Deficiency or mutation in these RBPs in animal models or humans are associated with eye and/or lens defects/cataracts [17–23]. Functional studies have indicated that these RBPs have a distinct role in spatiotemporal control over key factors in lens development. However, compared to our understanding of signaling and transcription, our knowledge on lens regulatory networks impacted by perturbation of these RBPs is limited.

Celf1 has three RNA-recognition motifs (RRMs) that allow it to bind to its target RNAs and is known to mediate RNA localization, decay/stability, alternative splicing and translation [24–27]. It has been shown that in the majority of the cases, binding of Celf1 protein to its target mRNA results in the destabilization of the latter [28]. Previously, we demonstrated that *Celf1* germline knockout (KO) or conditional KO (cKO) in the lens results in fully penetrant congenital cataracts in mice. Celf1-knockdown in fish and frogs also results in lens defects, suggesting that Celf1 plays an important role in vertebrate lens development [9]. We previously characterized specific aspects of Celf1 deficiency-based lens defects in mice, demonstrating that Celf1-mediated negative control at the translational level over the cyclin-D kinase inhibitor $p27^{Kip1}$ was important for achieving optimal phosphorylation of nuclear lamin proteins, which in turn is critical for fiber cell nuclear envelope breakdown in normal lens development. This, in addition to Celf1′s positive control of mRNA expression levels of the nuclease Dnase2b, was found to be necessary for nuclear degradation in fiber cells [9]. Subsequently, we showed that Celf1 also played a role in achieving proper protein levels and spatiotemporal distribution of key transcription factors (TFs) in the lens. Indeed, Celf1 was found to be necessary for restriction of the expression of Prox1 protein to fiber cells and that of Pax6 to the anterior epithelium of the lens (AEL), as well as early fiber differentiating cells in normal lens development [10].

While these studies have uncovered specific aspects of Celf1 function in the lens, high-throughput RNA-sequencing (RNA-seq)-based transcriptome analyses of Celf1-deficient mouse lenses has not been described. Such an analysis will identify, on the genome-level, different mRNAs that are altered upon Celf1 deficiency, shedding further light on Celf1′s role in lens development and offering new explanations regarding how alterations in its downstream pathways may contribute to lens pathology in *Celf1*^{cKO} mice. In the present study, we address this critical knowledge gap by performing RNA-seq analysis on newborn lenses from *Celf1*^{cKO} mice and identifying cohorts of differentially expressed genes (e.g., *Cryab*, *Cryba2*, *Cryba4*, *Crybb1*, *Crybb2*, *Cryga*, *Crygb*, *Crygc*, *Crygd*, *Cryge*, *Crygf*, *Dnase2b*, *Bfsp1*, *Gja3*, *Pxdn*, *Sparc*, *Tdrd7*, etc.) and pathways (e.g., structural constituents of eye lens, lens development in camera-type eye, lens fiber cell differentiation, etc.) associated with lens development and cataracts.

2. Materials and Methods

2.1. Animals

The University of Delaware Institutional Animal Care and Use Committee (IACUC) reviewed and approved the animal protocols described in this study. The Association for Research in Vision and Ophthalmology (ARVO) statement for the use of animals in ophthalmic and vision research was followed for animal experiments. The strategy for generating *Celf1* lens-specific conditional knockout mice is previously described [9]. Briefly, breeding was set up to generate mice (referred to as *Celf1*^{cKO}) carrying one *Celf1* germline knockout allele, (referred to as *Celf1*^{lacZKI}), one *Celf1* conditional knockout allele (exon five flanked by *loxP* sites, referred to as *Celf1*^{flox}) and the lens Cre deleter mouse line P0-3.9GFPCre (The Jackson Laboratory: 024578; henceforth referred to as *Pax6GFPCre*) that initiates Cre expression in the lens placode at embryonic day E9.5 [8,9,29]. GFPCre protein is detected to be highly and predominantly expressed in cells of the lens and pancreatic

lineage in this deleter line [29,30], which has been used for generating lens-conditional knockout [8–10,29,31]. In the past, mice heterozygous for the *Pax6GFPCre* allele were not found to exhibit any lens defects and were used as a control [9]. *Celf1*^{flox} mice without the *Cre* allele were used as a control unless otherwise noted. Briefly, the breeding scheme was as follows. Mice containing *Celf1*^{lacZKI} allele were crossed with *Pax6GFPCre* transgenic mouse line to generate *Pax6GFPCre*:*Celf1*^{lacZKI}. These were in turn crossed with mice homozygous for the *Celf1* allele in *loxP* sites flank exon 5 (*Celf1*$^{flox/flox}$) to generate mice that carried one allele of Pax6GFPCre, one allele of *Celf1*^{lacZKI} and one allele of *Celf1*^{flox}. These mice were of mixed backgrounds with contributions from C57BL/6 and FVB strains. Plugs were checked and the day of birth was designated as postnatal day 0 (P0).

2.2. Lens RNA Isolation

Lens tissue was micro-dissected from the control and *Celf1*^{cKO} mice, flash-frozen on dry ice and stored at −80 °C until further use. Two P0 lenses were pooled per biological replicate, and three biological replicates each were used for the control and *Celf1*^{cKO} mice for RNA isolation using the RNeasy mini kit (Qiagen, Germantown, TN, USA) for RNA-sequencing. For microarray analysis, total RNA was isolated using RNeasy mini kit (Qiagen) from P6 lenses (1 lens per biological replicate) from *Celf1*^{cKO} and control (*Celf1*$^{lacZKI/+}$) mice. RNA quality was evaluated by Bioanalyzer at the University of Delaware and RNA samples with an RNA quality number (RQN) above 8 were considered for microarrays or library preparation and RNA-sequencing.

2.3. RNA-Sequencing and Analysis

Total RNA from the control and *Celf1*^{cKO} P0 mouse lens tissue was used for RNA-sequencing (strand-specific, paired-end 150 bp-libraries) using the Illumina HiSeq 2500 sequencer at the University of Kansas Medical Center Genomics Core. FastQC was used to evaluate the quality of raw paired-end reads. The RNA-sequencing data reported here is submitted to the NCBI Gene Expression Omnibus (GEO) database under series GSE227293. Raw sequences were trimmed to remove the adaptor sequence. Trimmed sequences were aligned on to the mouse genome (GRCm38.p6) with the STAR software (STAR(2.7.8a)) [32], and only uniquely mapped reads were retained for downstream analysis. Reads were associated to genes by featureCount (v2.0.0) [33], and only genes with >0.2 CPM (counts per million) were considered for differential gene expression analysis. The R package edgeR [34] was used to identify differentially expressed genes (DEGs), Fold Change (FC) > 1.5 (|logFC| > 0.58), False Discovery Rate (FDR) < 0.05 and an average expression in log2 CPM > 1.0.

2.4. Microarray Analysis

Total RNA from *Celf1*^{cKO} and control (*Celf1*$^{lacZKI/+}$) mouse lenses at stage P6 were isolated as stated above and microarray analysis was performed using the MouseWG-6 v2.0 BeadChip platform (Illumina, San Diego, CA, USA) following previously described protocols [9]. The previously unreported microarray data on stage P6 is submitted to NCBI Gene Expression Omnibus (GEO) database under series GSE225303. Previously generated microarray data on *Celf1*^{cKO} and control (wild-type) mouse lenses at stage P0 (deposited in GEO, GSE101393) was also used for comparative analysis in the present study. For these datasets, gene expression was estimated based on the fluorescence signal intensity of probes associated to specific genes. In cases where multiple probes were associated to the same gene, the expression of the gene was calculated as the logarithmic average of the signals from all probes assigned to the gene. Only the probes that had a fluorescence signal intensity significantly higher than background in at least two samples were retained for downstream differential gene expression analysis. The R package edgeR [34] was used to identify DEGs, with FC > 1.5 (|logFC| > 0.58), FDR <0.05 and an average expression signal > 2 5 (LogSignal > 4.6) cut-offs.

2.5. Prioritization of DEGs by Cat-Map, iSyTE, Expression in Fiber vs. Epi, and Pathway Analysis

Celf1^{cKO} lens DEGs were examined in the context of Cat-Map, iSyTE, preferential expression in lens fiber cells vs. epithelial cells, and pathway analysis as follows.

2.5.1. Cat-Map: Cataract Associated Genes

Celf1^{cKO} lens DEGs known to be associated with cataracts were identified by comparing individual gene names (mouse gene name) for DEGs to the 454 genes (human gene name) listed in the database CatMap (vOct 21) [35]. This identified a subset of genes that were differentially expressed in *Celf1*^{cKO} lenses and whose deficiency or alterations were also associated with human cataracts.

2.5.2. iSyTE: Gene Expression Enrichment in the Lens

To determine the expression enrichment score of the *Celf1*^{cKO} lens DEGs in the normal lens—compared to the whole embryonic body (WB)—in different development stages, we used the database iSyTE [36]. iSyTE contains microarray data from normal mouse lenses at different development stages and the WB reference dataset. The lens-enriched expression scores of the *Celf1*^{cKO} lens DEGs were calculated as the maximum expression of the genes at either E10.5, E12.5, E14.5, E16.5, E17.5, E19.5 or P0, normalized by their expression WB. *Celf1*^{cKO} lens DEGs with an expression enrichment score >1.5 ($|\log FC| > 0.58$) were considered to have enriched expression in normal lens development.

2.5.3. *Celf1*^{cKO} DEGs Preferentially Expressed in Normal Lens Fiber Cells or Epithelial Cells

To identify *Celf1*^{cKO} DEGs preferentially expressed in either normal lens fiber cells (FCs) or the anterior epithelial lens (AEL; also referred to as lens epithelial cells) previously generated data on these lens cell types was used [37]. This data is based on RNA-seq analysis on wild-type (WT) mice at stage P0, which identified 3516 and 3975 genes to be preferentially expressed in FCs and AEL, respectively, based on cut-offs of padj < 0.05 and FC > 1.5.

2.5.4. *Celf1*^{cKO} DEGs Independently Identified as RNA Targets of CELF1 Protein by CLIP-Seq in a Human Cell Line

To identify the subset of *Celf1*^{cKO} DEGs directly regulated by CELF1 protein, we examined previously generated crosslinked immunoprecipitation coupled with RNA-sequencing (CLIP-seq) data using CELF1 antibody on the human cell line Hela [38]. In this study, RNAs encoded by 3025 human genes that are bound in cellulo by the CELF1 protein have been identified by CLIP-seq in human Hela cells. We found 2825 (93.4%) mouse orthologs corresponding to these identified targets. Comparative analysis was done between these orthologs and the *Celf1*^{cKO} lens DEGs to identify genes that are recognized as RNA targets of CELF1 proteins.

2.5.5. Gene Ontology (GO) Term and Pathways Analysis

The R package ClusterProfiler (v3.18.0) [39] was used to identify Gene Ontology (GO) terms enriched in *Celf1*^{cKO} DEGs by GO enrichment analysis as well as gene set enrichment analysis (GSEA), GO biological process (BP), GO cellular component (CC), and molecular functions (MF). GO analysis in turn led to insights into specific pathways that are altered due to Celf1 deficiency in the lens.

2.5.6. Immunostaining Analysis

Immunostaining was performed as previously described [11,40]. Briefly, mouse embryonic head tissue from stage E16.5 was fixed in 4% paraformaldehyde (PFA) (prepared in 1× phosphate buffer saline, PBS) for 30 min on ice, followed by transfer to 30% sucrose overnight at 4 °C. Once the tissue settled at the bottom, indicating that it was equilibrated, it was mounted in OCT (Tissue Tek, Torrance, CA, USA), frozen and stored at −80 °C until cryosectioning. Cryostat was used to obtain sections of 16 μm thickness. For im-

munostaining, sections were blocked in a solution of 5% chicken serum, 1% BSA, 0.1% Tween (prepared in 1× PBS) for 1 h at room temperature (RT). The section was subjected to primary antibody (Cryg antibody, Santa Cruz Biotechnology #sc-22415, at 1:100 dil. in 5% chicken serum; E-cad antibody, Cell Signaling #4065, at 1:100 dil. in 5% chicken serum) by overnight incubation at 4 °C. On the following day, slides were washed three times with 1× PBS and incubated for 1 h at RT with the secondary antibody, chicken anti-goat IgG conjugated to Alexa Fluor 488 (1:200 dil.) or anti-rabbit IgG conjugated to Alexa Fluor 594 (1:200 dil.) (Life Technologies, Carlsbad, CA, USA) with the nuclear stain DRAQ5 (1:2000 dil.) (Biostatus Limited, Leicestershire, UK). Slides were washed three times in 1× PBS, mounted and imaged using Zeiss LSM 780 confocal configured with Argon/Krypton laser (488 nm and 561 nm excitation lines) and Helium Neon laser (633 nm excitation line) (Carl Zeiss Inc., White Plains, NY, USA). Adobe Photoshop CS6 (Version: 13.0.0) was used for adjustment of brightness/contrast applied consistently for all images.

3. Results

3.1. Generation of RNA-Seq Datasets from Celf1^{cKO} and Control Lenses

Lenses were micro-dissected, and RNA was isolated from stage P0 *Celf1*^{cKO} and control mice as described in detail in the Methods section. An experimental and computational pipeline was developed for RNA-seq analyses (Figure 1). Paired-end, 150 bp-long libraries were prepared, sequenced and analyzed using this strategy. For control and *Celf1*^{cKO} samples, an average of 55.1 million reads per replicate were obtained and aligned using STAR software (STAR(2.7.8a)) [32] (Table S1). On average, 77.3% of the reads were uniquely mapped to the *Mus musculus* reference genome (GRCm38.p6) (Table S1).

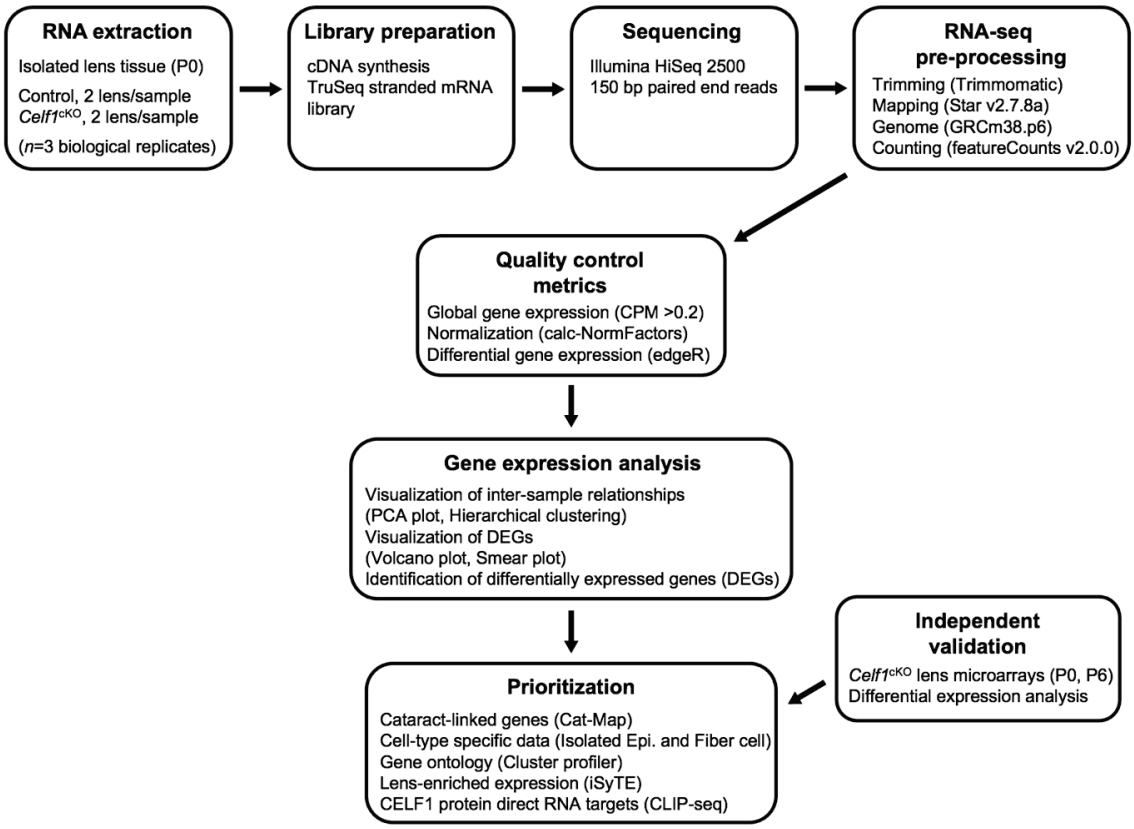

Figure 1. RNA-sequencing (RNA-seq) analysis flowchart. A flowchart outlining the experimental design and bioinformatics pipeline to determine differentially expressed genes between control and *Celf1*^{cKO} lenses and their downstream analysis.

3.2. Quality Control of RNA-Seq Datasets

We first examined the Celf1 transcript profiles in *Celf1*^{cKO} and control lenses by visualization of the RNA-seq mapped reads using the software IGV (2.8.10) (mm10) [41] and found Celf1 mRNA to be reduced in *Celf1*^{cKO} lenses (Figure 2A, Table S2). Since the conditional knockout strategy involves removal of exon 5 (Figure 2B), we quantified the inclusion of exon 5 in Celf1 mRNA in *Celf1*^{cKO} and control lenses. It is expected that exon 5 will be deleted by Cre recombinase driven by the *Pax6GFPCre* allele only in *Celf1*^{cKO} lenses, which in turn will result in a premature stop codon. This analysis shows that while control lenses had normal inclusion of exon 5, on average, *Celf1*^{cKO} lenses had 48.3% reduced *Celf1* transcripts that contained exon 5 (Figure 2C,D). Together, these data validate Cre-mediated deletion of *Celf1* in *Celf1*^{cKO} lenses. To assess the quality of the datasets on the global level, principal component analysis (PCA) was performed, which showed that control replicate samples clustered together and separately from *Celf1*^{cKO} replicate samples (Figure 3A). Additionally, hierarchical clustering between samples clearly separated control replicates from *Celf1*^{cKO} replicates (Figure 3B). Together, these analyses validate that Cre-mediated recombination of the *Celf1* conditional knockout allele driven by the *Pax6GFP* Cre-deleter line resulted in global transcriptome changes in the *Celf1*^{cKO} lens. This further confirmed that although Cre-deletion did not result in all *Celf1* transcripts being devoid of exon 5 in *Celf1*^{cKO} lenses, it was sufficient to generate transcriptome changes that result in lens defects.

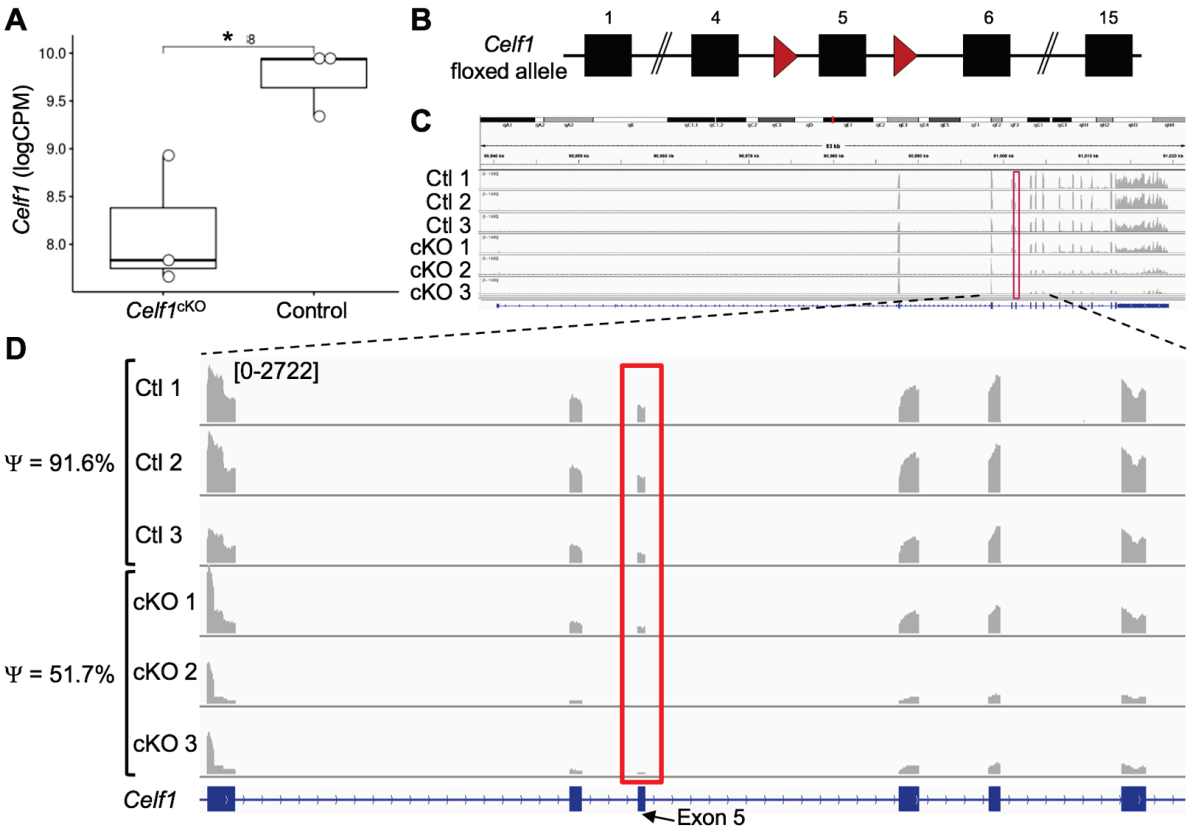

Figure 2. RNA-seq confirms reduction of *Celf1* mRNA in *Celf1*^{cKO} mouse lenses. (**A**) Celf1 mRNA levels in logCPM (counts per million) are significantly reduced in *Celf1*^{cKO} lenses compared to control ($n = 3$) as estimated by Student's *t*-test (asterisk indicates $p < 0.05$). (**B**) Schematic of *Celf1* floxed allele showing exon 5 flanked by loxP sites (red arrowheads). (**C**) Visualization of the mapped reads on mouse *Celf1* locus, which at high magnification (**D**) shows that, compared to control lens samples 1–3 that exhibit inclusion of *Celf1* exon 5 in an average of 91.6% of transcripts (represented by Ψ), *Celf1*^{cKO} lens samples 1–3 show an average of only 51.7% of transcripts include *Celf1* exon 5 (represented by Ψ). The proportion of transcripts containing exon 5 is estimated by exon junction analysis.

3.3. Identification of Differentially Expressed Genes (DEGs) in Celf1^{cKO} Lens

Based on cut-off criteria of normalized expression counts >1 log2 counts per million (CPM) averaged across all replicates, >0.58 log2 fold-change and false discovery rate (FDR) < 0.05, a total of 987 differentially expressed genes (DEGs) were identified in *Celf1*^{cKO} lenses, which is visualized by a volcano plot and a smear plot (Figure 4A,B). Of the 987 DEGs, 660 are found to be elevated while 327 are found to be reduced in *Celf1*^{cKO} lenses (Table S2). Further, RNA-seq analysis confirmed the reduction in *Dnase2b* mRNA and elevation of *p21* (*Cdkn1a*) mRNA in *Celf1*^{cKO} lenses (Table S2), as was expected based on our previous findings [9].

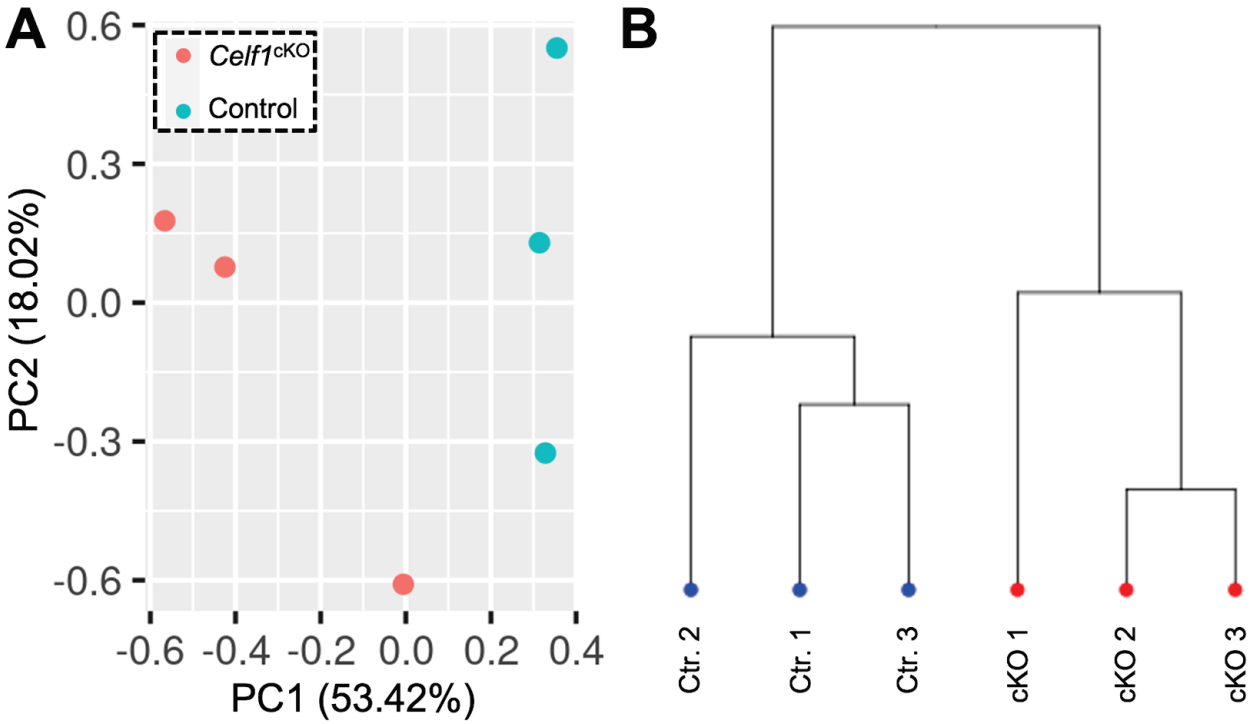

Figure 3. Validation of replicates for control and *Celf1*^{cKO} lens RNA-seq datasets. (**A**) Principal component analysis (PCA) of RNA-seq samples shows principal component 1 (PC1) segregates the control replicates from *Celf1*^{cKO} replicates. PC1 is responsible for 53.42% of the variance. (**B**) The control and *Celf1*^{cKO} replicates can be segregated as per hierarchical clustering analysis based on expression of all genes.

3.4. Relevance of Celf1^{cKO} Lens DEGs to Lens Development and Cataracts

Next, we sought to prioritize *Celf1*^{cKO} lens DEG candidates that are relevant to lens development and are involved in cataract pathology. Toward this goal, we performed comparative analyses with publicly available datasets relevant to lens biology and pathology. For identifying DEGs linked to cataracts, we used the Cat-Map database [35]. For identifying DEGs exhibiting enriched expression in embryonic lens development, we used the iSyTE database [36]. For identifying DEGs that are preferentially expressed either in the epithelium or fiber cells, we used transcriptome datasets on isolated epithelial and fiber cells [37].

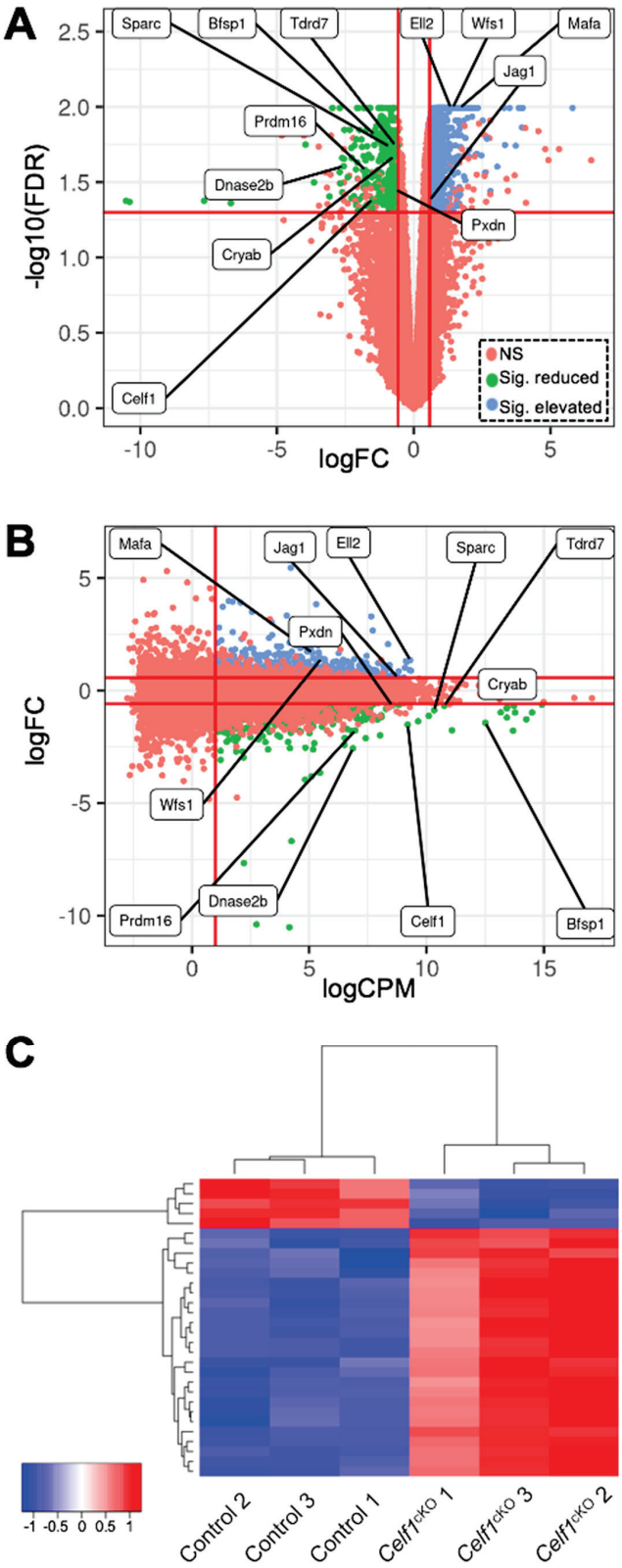

Figure 4. Identification of differentially expressed genes (DEGs) in *Celf1*^{cKO} lens. (**A**) Volcano plot and (**B**) smear plot show the different cut-offs used to identify DEGs between *Celf1*^{cKO} and control lens RNA-seq samples. With cut-off FDR < 0.05, |logFC| > 0.58, logCPM > 1.0, 660 genes and 327 genes were found to be significantly elevated and reduced, respectively, between *Celf1*^{cKO} and control lens samples. NS, not significant. Key cataract/lens-relevant DEGs are labelled in (**A**,**B**). (**C**) Heat map of all significant DEGs in *Celf1*^{cKO} lenses compared to control.

3.4.1. Prioritization of *Celf1*^{cKO} Lens DEGs Using the Cat-Map Database

Comparison of the 987 DEGs with Cat-Map identified 43 genes (including *Celf1*) that are linked to cataracts in humans and/or animal models (Table 1). These genes include several crystallins (e.g., *Cryab*, *Crybb2*, *Cryga*, *etc.*), membrane proteins (e.g., *Gja3*), signaling pathway proteins (e.g., *Jag1*) and other RBPs (e.g., *Tdrd7*). Altered expression of these genes may together contribute to the lens defects observed in *Celf1*^{cKO} mice.

Table 1. *Celf1*^{cKO} lens DEGs linked to cataracts in the Cat-Map database.

Symbol	logFC	logCPM	FDR	Symbol	logFC	logCPM	FDR
Lgsn	−3.957	4.826	0.02	*Tdrd7*	−0.673	10.755	0.02
Gjb6	−3.08	1.224	0.04	*Cryba4*	−0.671	13.735	0.02
Dnase2b	−2.565	6.866	0.03	*Pxdn*	−0.667	8.535	0.04
Lctl	−1.985	8.025	0.01	*Flnb*	−0.664	5.836	0.02
Crybb2	−1.763	11.087	0.03	*Crybb1*	−0.623	14.92	0.02
Celf1	−1.511	9.204	0.04	*Jag1*	0.582	8.78	0.04
Bfsp1	−1.428	12.513	0.02	*Psmc3*	0.587	7.955	0.03
Adgrl2	−1.326	5.119	0.03	*Ube2a*	0.597	4.673	0.03
Crygb	−1.275	14.257	0.02	*Nploc4*	0.6	6.468	0.02
Cryba2	−1.195	13.429	0.02	*Sec23a*	0.681	7.201	0.01
Gja3	−1.12	10.1	0.02	*Klc1*	0.724	8.255	0.02
Dnmbp	−1.109	8.04	0.01	*Ercc6*	0.803	4.453	0.02
Ulk4	−1.07	2.037	0.02	*Atm*	0.811	4.526	0.05
Crygd	−0.973	14.5	0.01	*Rnf149*	0.857	3.842	0.02
Cryga	−0.968	13.166	0.01	*Agps*	0.907	5.422	0.02
Sparc	−0.874	10.326	0.02	*Ptn*	1.047	5.652	0.01
Sord	−0.815	4.669	0.02	*Polr3b*	1.08	4.807	0.02
Loxl1	−0.793	6.509	0.02	*Pqbp1*	1.247	5.673	0.01
Crygc	−0.788	13.425	0.01	*Pgrmc1*	1.258	6.345	0.02
Ace	−0.785	5.561	0.046	*Wfs1*	1.421	5.521	0.01
Fkrp	−0.745	4.324	0.022	*Mafa*	1.684	5.134	0.01
Cryab	−0.73	13.439	0.021				

3.4.2. Prioritization of *Celf1*^{cKO} Lens DEGs Using the iSyTE Database

The 987 DEGs were examined for their potential lens-enriched expression in iSyTE at stages E10.5, E12.5, E14.5, E16.5, E17.5, E19.5 and P0. Out of 282 reduced genes in the *Celf1*^{cKO} lens, 71.7% (n = 203) were found to have lens-enriched expression in at least one of the stages examined (Figure 5A,B; Table S3). In contrast, out of 607 elevated genes in the *Celf1*^{cKO} lens, the majority of the genes 65.9% (n = 400) did not exhibit lens-enriched expression (Figure 5A,B; Table S3). Furthermore, when only the DEGs that do not exhibit lens-enriched expression are considered, a vast majority (83.5%) are found to be elevated in iSyTE (Figure 5C). In this analysis, 98 DEGs were not found in iSyTE lens microarray datasets. This may be due to differences between the two transcriptomics approaches (see Discussion). This analysis suggests that Celf1 may contribute to maintaining normal lens developmental transcriptome by negatively regulating genes not normally enriched in the lens as well as positively regulating genes, likely indirectly, which are normally enriched in the lens. This analysis also identified new potential regulators in lens development (e.g., *Ell2*) (Table S3).

3.4.3. Prioritization of *Celf1*^{cKO} Lens DEGs Using Isolated Epithelial and Fiber Cell Transcriptome Data

At early stages of embryonic development, Celf1 exhibits high expression in fiber cells and in later stages is also expressed in epithelial cells [9]. This suggests that it may play a role in transcriptome regulation of both cell types. To examine the impact of Celf1 deficiency in genes preferentially expressed in either epithelial or fiber cells, we compared the 987 DEGs with previously described transcriptome data from isolated epithelial and

fiber cells from mouse P0 lenses. First, of the 327 genes reduced in *Celf1*^{cKO} lenses, the majority of the genes (72.5%, n = 237) were found to be preferentially expressed in either fiber or epithelial cells (Table 2; Table S4). Of these, the majority of the genes (55.6%, n = 182) were preferentially expressed in fiber cells (Table 2; Table S4). In contrast, 16.8% of reduced genes (n = 55) were preferentially expressed in epithelial cells. Next, of the 660 genes elevated in *Celf1*^{cKO} lenses, the majority of the genes (52.7%, n = 348) did not show preferential expression in either fiber cells or epithelial cells. Of these, the majority of the genes (32.0%, n = 211) were preferentially expressed in fiber cells compared to epithelial cells (15.3%, n = 101). These data indicate that a deficiency of Celf1 has a substantial impact on transcripts expressed in both fiber cells and epithelial cells. However, the extent of Celf1′s impact is greater on fiber cells compared to epithelial cells. Indeed, independent validation by immunostaining shows that the fiber cell-enriched gamma crystallins are reduced in *Celf1*^{cKO} lenses, in agreement with RNA-seq analysis (Figure S1). Finally, similar to iSyTE data analysis, the upregulated genes in *Celf1*^{cKO} lenses appear to not be enriched in either epithelial or fiber cells in normal lens development. Further, the majority of the elevated genes that are not enriched in epithelial or fiber cells (52.7%, n = 348) are also not enriched in iSyTE, suggesting that in normal lens development, Celf1 is necessary, either directly or indirectly, to repress the expression of these genes.

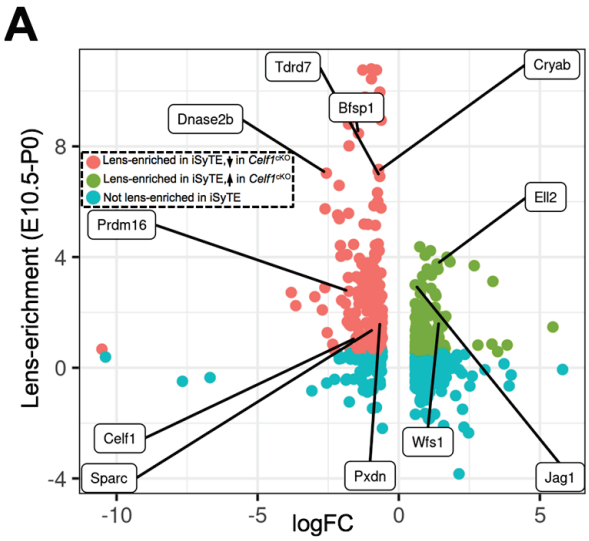

B

889* DEGs	Reduced in *Celf1*^{cKO} (n=282)	Elevated in *Celf1*^{cKO} (n=607)
Lens-enriched in iSyTE between E10.5-P0	203 (71.7%)	207 (34.1%)
Not Lens-enriched in iSyTE	79 (28.3%)	400 (65.9%)

*98 DEGs not found in iSyTE

C

889* DEGs	Reduced in *Celf1*^{cKO}	Elevated in *Celf1*^{cKO}
Lens-enriched in iSyTE between E10.5-P0 (n=410)	203 (49.5%)	207 (50.5%)
Not Lens-enriched in iSyTE (n=479)	79 (16.5%)	400 (83.5%)

Figure 5. Examination of iSyTE-based lens-enriched expression of *Celf1*^{cKO} lens DEGs. (**A**) Quadrant plot of *Celf1*^{cKO} lens DEGs (logFC on x-axis) and their respective lens-enrichment score between stages E10.5 and P0 as per iSyTE (y-axis). The threshold of lens-enrichment is >1.5 fold-change in the lens as per in silico subtraction-based comparison to WB reference dataset. (**B**) Quantification table of reduced and elevated *Celf1*^{cKO} lens DEGs with respect to their lens-enrichment score in normal lens development. (**C**) Quantification table, in which percent of lens-enriched DEGs or lens non-enriched DEGs are either reduced or elevated in *Celf1*^{cKO} lens DEGs.

Table 2. *Celf1*^{cKO} lens DEGs preferentially expressed in normal lens fiber cells (FCs) or anterior epithelium of the lens (AEL).

Total DEGs (n = 987)	**Reduced in *Celf1*^{cKO} Lens (n = 327)**	**Elevated in *Celf1*^{cKO} Lens (n = 660)**
Preferentially exp. in FCs	182	211
Preferentially exp. in AEL	55	101
Not preferentially exp. in FCs or AEL	90	348

3.4.4. Prioritization of *Celf1*^{cKO} Lens DEGs Using CLIP-Seq Data Identifying Direct RNA Targets of CELF1 Protein in a Human Cell Line

Celf1 encodes a protein containing three RRMs that enable it to bind to its target RNAs and mediate post-transcriptional regulation of gene expression. Previously, CLIP-seq analysis with a CELF1 antibody has been applied to identify the direct-bound RNA targets of CELF1 protein in the human cell line, Hela [38]. Comparative analysis showed that 32.2% (n = 318) of the 987 *Celf1*^{cKO} lens DEGs are also identified in this CLIP-seq dataset. Further, within these 318 DEGs that are directly bound by CELF1 protein, the majority (83.0%; n = 264) are found to be significantly elevated in *Celf1*^{cKO} lenses. While 21 of these 318 *Celf1*^{cKO} lens DEGs were not found in iSyTE, 32.4% (n = 103) of these DEGs are found to exhibit enriched expressed in normal lenses in iSyTE, while 61.0% (n = 194) are not lens-enriched (Table 3). Of the 318 DEGs, the majority are not preferentially expressed in either FCs or AEL and are elevated in *Celf1*^{cKO} lenses (n = 149) (Table 4). Among the DEGs preferentially expressed in either cell type, the majority are preferentially expressed in FCs (n = 104).

Table 3. *Celf1*^{cKO} lens DEGs selected by cross-linked immunoprecipitation (CLIP) that exhibit enriched expression in normal lenses as per iSyTE.

DEGs Selected by CLIP (n = 297 [1])	Reduced in *Celf1*^{cKO} Lens (n = 50)	Elevated in *Celf1*^{cKO} Lens (n = 247)
Lens enriched-exp. in iSyTE	26	77
Not lens enriched-exp. in iSyTE	24	170

[1] 21 of the DEGs selected by CLIP were not found in iSyTE.

Table 4. *Celf1*^{cKO} lens DEGs selected by cross-linked immunoprecipitation (CLIP) that are preferentially expressed in normal lens fiber cells (FCs) or anterior epithelium of the lens (AEL).

DEGs Selected by CLIP (n = 318)	Reduced in *Celf1*^{cKO} Lens (n = 54)	Elevated in *Celf1*^{cKO} Lens (n = 264)
Preferentially exp. in FCs	30	74
Preferentially exp. in AEL	9	41
Not preferentially exp. in FCs or AEL	15	149

3.5. Gene Ontology and Pathway Analysis of Celf1^{cKO} *Lens DEGs*

Next, we examined the different pathways that were represented in *Celf1*^{cKO} lens DEGs. Toward this goal, we performed pathway enrichment analysis by examining gene ontology (GO) enrichment separately on all DEGs, elevated DEGs and reduced DEGs, compared to all the genes expressed in the RNA-seq data. In parallel, GSEA (gene set enrichment analyses) were performed on all the genes in the RNA-seq data that had an expression of at least 1 logCPM and based on their logFC rank. Further, we performed the GI enrichment analysis on a subset of these DEGs that are found to have enriched expression in the lens by iSyTE described in Section 3.4.2. We also performed this analysis on a subset of these DEGs that are preferentially expressed in epithelial or fiber cells described in Section 3.4.3. GSEA analysis was not performed on this subset of DEGs because a large number of genes are required for optimal analysis. This analysis identified "structural constituent of eye lens" (GO:0005212), "lens development in camera-type eye" (GO:0002088), and "visual perception" (GO:0007601) among the top enriched GO terms in 327 reduced DEGs in *Celf1*^{cKO} lenses (Figure 6; Table S5). The same GO terms were identified among reduced DEGs that exhibit enriched expression in normal lens development as per iSyTE (Figure 7) as well as reduced DEGs that are preferentially expressed in normal fiber cells (Figure 8), and these GO terms were also identified by the GSEA analysis as reduced (Table S5). Further, among the reduced DEGs that are preferentially expressed in fiber cells, the GO term "lens fiber cell differentiation" (GO:0070306) was

also found to be significantly enriched. These GO categories identified candidate genes with known functions in the lens and/or those associated with cataracts. Among these are several crystallins, *Bfsp1*, *Gja3*, *Tdrd7*, etc. (Table S5). Only two GO terms were found to be enriched among reduced DEGs that are preferentially expressed in epithelial cells. These are "extracellular matrix" (GO:0031012) and "cell projection membrane" (GO:0031253). GSEA analysis and GO enrichment analysis of all the 660 elevated DEGs, or 207 elevated DEGs with enriched expression in normal lens development as per iSyTE, or 211 elevated DEGs preferentially expressed in normal fiber cells, commonly identified, among others, the GO terms, "proton transporting ATPase activity, rotational mechanism" (GO:0046961) and "cytoplasmic vesicle membrane" (GO:0030659) to be enriched. Additionally, in all the 660 elevated DEGs, the GO terms "calcium-dependent protein binding" (GO:0048306), "clathrin coat of coated pit" (GO:0030132), "organelle subcompartment" (GO:0031984) and "protein kinase inhibitor activity" (GO:0004860) were also found to be enriched (Table S5). The majority of the GO terms described above were also identified when all the DEGs or the DEGs with lens-enriched expression, or the DEGs preferentially expressed in fiber cells were considered. Further, of the 453 elevated DEGs that do not have an enriched expression in normal lenses, the GO terms "cytoplasmic vesicle membrane" (GO:0030659), "proton-transporting V-type ATPase complex" (GO:0016471) and "proteasome complex" (GO:0000502) were found to be enriched. Finally, GO term analysis of reduced DEGs that were also identified in CLIP showed enrichment of the terms related to "positive-regulation of brown fat cell differentiation" (GO:0090335) (Figure 9). Among elevated DEGs also identified in CLIP, the GO terms, "translational initiation" (GO:0045948), "clathrin-coated vesicle" (GO:0030136), "ribonucleoprotein complex binding" (GO:0043021) and "calcium-dependent protein binding" (GO:0048306) were identified (Table S5). A subset of these GO terms was also found to be enriched when all DEGs that are identified by CLIP were considered. Thus, GO term analysis identifies pathways whose perturbations contribute to the cataract pathology observed in *Celf1*^{cKO} lenses, which are further highlighted in the Discussion below.

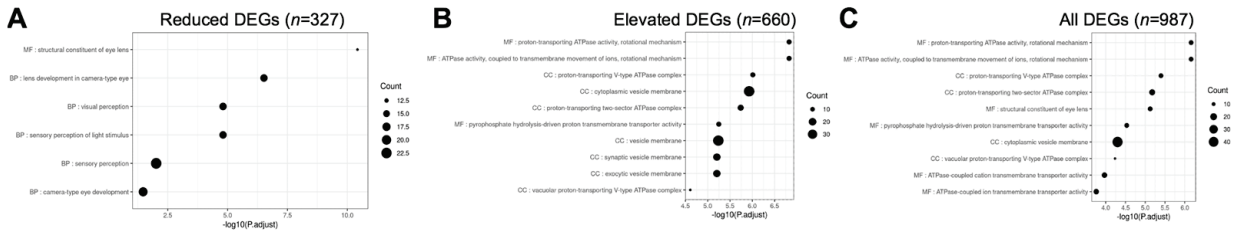

Figure 6. Gene ontology (GO) and pathway analysis on *Celf1*^{cKO} lens DEGs obtained from RNA-seq. The top significant GO terms enriched in (**A**) reduced DEGs, (**B**) elevated DEGs, and (**C**) all DEGs in *Celf1*^{cKO} lenses.

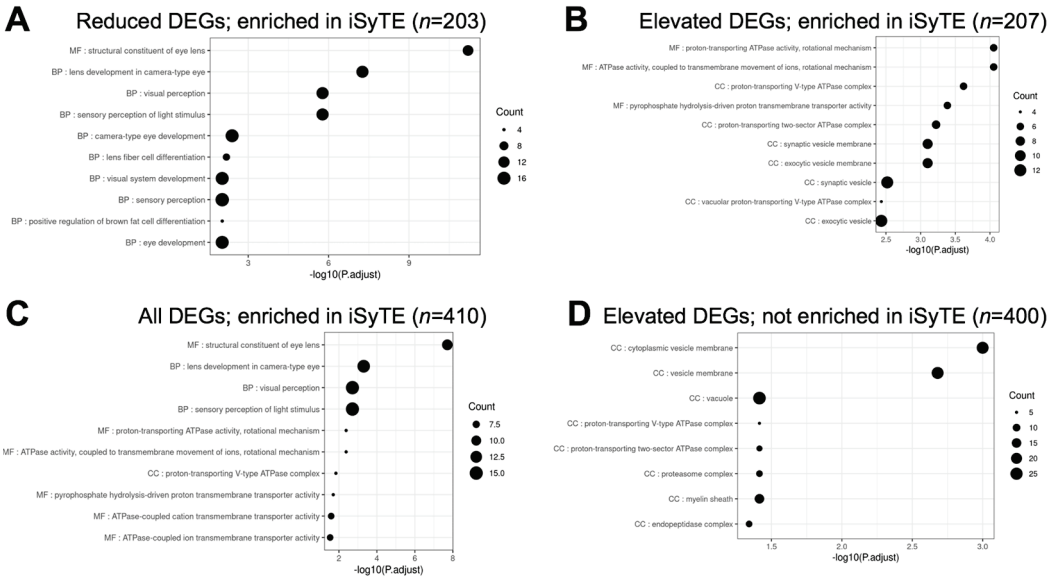

Figure 7. Gene ontology (GO) and pathway analysis on *Celf1*^{cKO} DEGs analyzed by iSyTE. The top significant GO terms enriched in (**A**) reduced DEGs, (**B**) elevated DEGs, and (**C**) all DEGs that exhibit enriched expression in normal lenses as per iSyTE. (**D**) The top significant GO terms enriched in *Celf1*^{cKO} lens elevated DEGs that do not exhibit enriched expression in normal lenses.

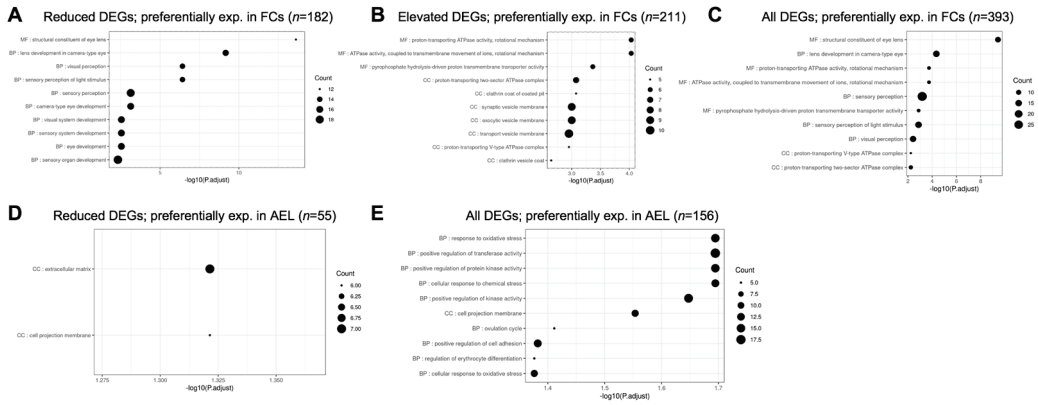

Figure 8. Gene ontology (GO) and pathway analysis on *Celf1*^{cKO} lens DEGs preferentially expressed in the anterior epithelium of the lens (AEL) and fiber cells (FCs). The top significant GO terms enriched in (**A**) reduced DEGs, (**B**) elevated DEGs, and (**C**) all DEGs that are preferentially expressed in normal FCs. The top significant GO terms enriched in (**D**) reduced DEGs and (**E**) all DEGs that are preferentially expressed in normal AEL. No significant GO terms were identified in *Celf1*^{cKO} elevated DEGs expressed in normal AEL.

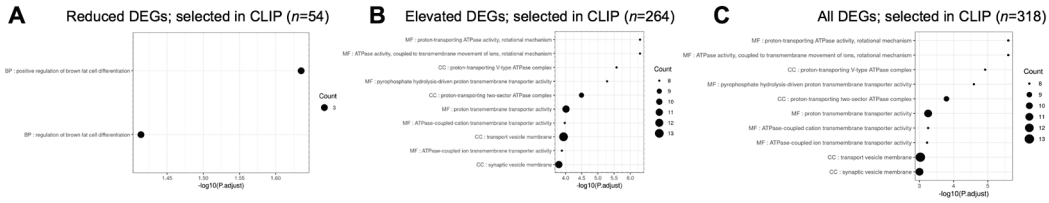

Figure 9. Gene ontology (GO) and pathway analysis on *Celf1*^{cKO} lens DEGs that are also identified in CLIP-seq dataset. The top significant GO terms enriched in (**A**) reduced DEGs, (**B**) elevated DEGs, and (**C**) all DEGs that are also identified in CELF1 cross-linked immunoprecipitation followed by RNA-sequencing (CLIP-seq) data on the human cell line (Hela cells).

3.6. Comparative Analysis of Celf1^{cKO} Lens DEGs Identified by RNA-Seq and Microarrays

Next, we sought to compare *Celf1*^{cKO} lens DEGs identified by RNA-seq with DEGs that are identified by expression microarrays so as to provide independent validation of the DEGs that can be used for prioritization of candidates. For *Celf1*^{cKO} lenses, published expression microarray data is available for stage P0. There is also unpublished expression microarray data on *Celf1*^{cKO} lenses for stage P6. We first performed differential expression analysis on *Celf1*^{cKO} lens microarray data for stage P0 and P6. This analysis identified 549 DEGs at P0 and 665 DEGs at P6 (Figures 10 and S2; Table S6). Of these, 322 were elevated and 227 were reduced at P0, while 304 were elevated and 361 were reduced at P6. Comparative analysis identified 174 DEGs to be commonly elevated and 78 DEGs to be commonly reduced between RNA-seq and microarrays at P0. Comparative analysis identified 158 DEGs to be commonly elevated and 90 DEGs to be commonly reduced between RNA-seq and microarrays at P6. There is a higher number of DEGs found to be elevated or reduced by the RNA-seq approach at P0. This may be due to technical differences in the two approaches. While microarrays are limited by a predetermined number of genes represented on the array, RNA-seq has no such limitation. Further, while RNA-seq provides individual sequence reads, microarrays depend on probe binding kinetics which may impact their sensitivities. Further, there is a higher number of DEGs found to be mis-expressed by microarrays at P6 compared to P0, which is expected because of the progression of the lens defects. Together, this analysis provides independent validation of numerous DEGs that are mis-expressed upon Celf1 deficiency in the lens (Table S6). Furthermore, among the *Celf1*^{cKO} lens DEGs commonly identified by RNA-seq and microarrays, 84 found at the RNA-seq (P0)–microarray (P0) comparison and 54 found at the RNA-seq (P0)–microarray (P6) comparison were also found to be directly bound by Celf1 protein as per CLIP data (Table S7).

A

	RNA-seq (P0) (*n*=987)	Microarrays (P0) (*n*=549)	Microarrays (P6) (*n*=665)
Elevated *Celf1*^{cKO} DEGs	660 (66.9%)	322 (58.7%)	304 (45.7%)
Reduced *Celf1*^{cKO} DEGs	327 (33.1%)	227 (41.3%)	361 (54.3%)

B

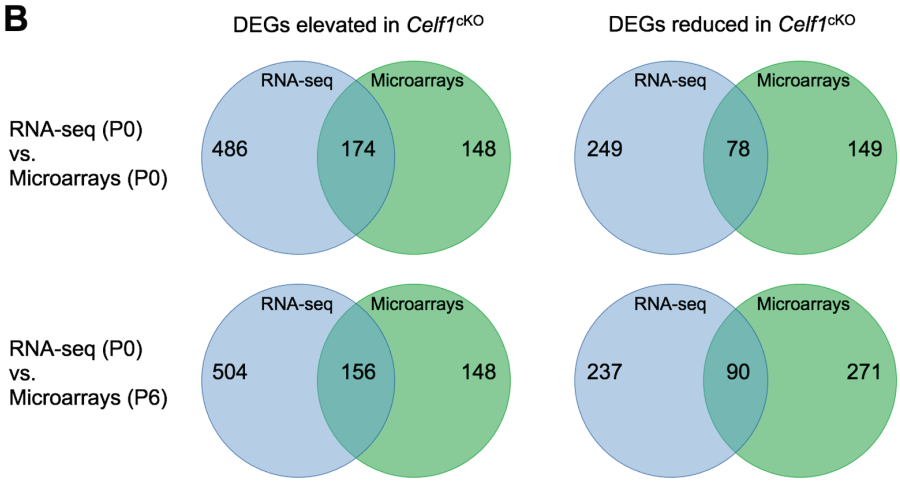

Figure 10. Comparative analysis of *Celf1*^{cKO} lens DEGs obtained from RNA-seq and microarrays. (**A**) List of elevated and reduced differentially expressed genes (DEGs) in *Celf1*^{cKO} lenses as identified by RNA-seq at stage P0 and microarrays at stage P0 and P6. (**B**) Venn diagrams indicating elevated or reduced *Celf1*^{cKO} lens DEGs commonly—or exclusively—identified by RNA-seq and microarray analysis at P0 and P6.

4. Discussion

Celf1 encodes an RNA-binding protein that has been associated with various tissue development/cell differentiation and developmental defects/diseases. Celf1 has a role in cells as different as sperm, muscle, and lens cells, among others, and its alterations are associated with various types of cancer and developmental defects including heart defects, myotonic dystrophy and cataracts [6,25,27,42–49]. As an RBP, Celf1 can mediate gene expression control by directly binding to target RNAs and impact their intracellular localization, splicing, stability/decay or translation [38].

Mouse models of *Celf1* deficiency exhibit cataracts and other pathologies [9,10,43]. In the past, different proteins/pathways that are altered due to Celf1-decificiency have been characterized (e.g., $p27^{Kip1}$, Dnase2b, Pax6 and Prox1). For example, previous work described how Celf1 post-transcriptionally controls the dosage of $p27^{Kip1}$ protein by reducing it in fiber cell differentiation, while also being necessary for optimal levels of the nuclease Dnase2b in the lens. Further, Celf1 also functions to negatively control $p21^{Cip1}$ in the lens. Together, these actions of Celf1 result in proper degradation of fiber cell nuclei thereby contributing to optimal refraction of light and lens transparency [9]. Celf1 is also necessary for proper spatiotemporal expression of Prox1 and Pax6 transcription factors in lens development; the disruption of which further contributes to the lens defects [10]. Additionally, an absence of Celf1 is expected to lead to changes to the lens transcriptome that result in lens defects and cataracts. To gain insights into such global perturbations, we performed high-throughput RNA-seq and examined the differentially expressed genes in the *Celf1*^{cKO} lens. While there have been reports on RNA-seq on Celf1 perturbations, in the context of the lens, these are limited to cell lines and not the lens tissue [50,51]. The only transcriptome data available on *Celf1*-deficient lens tissue is on a microarray platform. While microarrays are informative, they have limitations as they depend on probe binding kinetics and can only report on a predefined set of genes. On the other hand, RNA-seq does not present such limitations and offers greater depth of global changes in transcripts.

While the *Celf1*^{cKO} lens exhibits 987 DEGs, interestingly the majority of genes were found to be elevated, suggesting that Celf1 protein—either directly or indirectly—has negative control over these transcripts in normal lenses. However, because 327 were found to be reduced in *Celf1*^{cKO} lenses, this suggests that Celf1 is also necessary for positive control over these genes that may be important for proper lens development. We aimed to identify both, "established" cataract-linked genes as well as potentially novel candidates that are differentially expressed upon Celf1 deficiency. To address the former, we performed analysis of *Celf1*^{cKO} RNA-seq data with respect to the known cataract-linked genes contained in the Cat-Map database. This helped identify the established cataract-linked genes that are significantly impacted because of Celf1 deficiency. On the other hand, the iSyTE database informs on both established cataract-linked genes as well as novel genes that are relevant to lens biology. Therefore, we also performed comparative analysis of *Celf1*^{cKO} RNA-seq data with respect to the genes recognized as lens-enriched in the iSyTE database. Indeed, in addition to identifying known cataract-linked genes, this analysis also identified novel genes with potential functions in the lens. We elaborate below on these findings.

Among the DEGs, 43 genes, including *Celf1*, have previously been linked to cataracts in humans or animal models as per Cat-Map. The majority of these (>60%) were found to be reduced in *Celf1*^{cKO} lenses. This includes *Dnase2b* which is significantly reduced in *Celf1*^{cKO} lenses. Because Dnase2b is necessary for proper nuclear degradation in lens fiber cell differentiation [52] and was also previously found to be a direct RNA target of Celf1 protein in the lens [9], this finding renders confidence in the RNA-seq data. Additionally, several other genes linked to human cataracts were found to be significantly reduced in *Celf1*^{cKO} lenses. These include the crystallins *Cryab*, *Cryba2*, *Cryba4*, *Crybb1*, *Crybb2*, *Cryga*, *Crygb*, *Crygc* and *Crygd*, the connexins *Gjb6* and *Gja3*, the membrane protein *Bfsp1*, the extracellular matrix associated peroxidase *Pxdn*, as well as other post-transcriptional regulatory proteins such as *Tdrd7* [35]. Interestingly, *Celf1*^{cKO} lenses also exhibit significant reduction of *Sparc*, whose deficiency is known to cause cataracts in mice [53]. Because

the majority of these key cataract-linked genes are preferentially expressed in fiber cells, this suggests that Celf1 has a major function in controlling fiber cell transcriptome. This finding also suggests that significant reduction of these cohorts of cataract-linked genes may contribute to the cataract pathology in *Celf1*^{cKO} lenses. Furthermore, 16 DEGs that are associated with cataracts were found to be elevated in *Celf1*^{cKO} lenses. This suggests that Celf1 is necessary for optimal transcript levels of genes (neither too high, nor too low) that are critical for lens transparency.

While Cat-Map allows identification of a subset of DEGs that are known to be associated with cataracts, to gain further insights into the impact of *Celf1* deficiency on transcripts relevant to lens biology, comparative analysis was performed using iSyTE. This allowed identification of DEGs that exhibit enriched expression in normal lenses, which has previously been found to be predictive of functions in the lens [30,36,54–56]. Thus, mis-regulation of such candidates can potentially contribute to lens pathology. The majority of the genes that are reduced upon *Celf1*-deficiency are found to exhibit enriched expression in normal lens development. Thus, it can be hypothesized that the sub-optimal expression levels of these lens-enriched transcripts could contribute to the cataract pathology. Interestingly, the majority of the DEGs that are elevated in *Celf1*^{cKO} lenses are not found to have enriched expression in normal lens development. Thus, this suggests that elevated expression of these transcripts upon *Celf1*-deficiency may contribute to alterations in lens development.

While iSyTE lens-enrichment is helpful, iSyTE data is primarily based on whole lenses. Celf1 is known to be highly expressed in fiber cells, but later in development it is also known to be expressed in epithelial cells, suggesting that it may have a function in both cell types in the lens [9,10]. Therefore, *Celf1*^{cKO} lens DEGs were examined for their preferential expression in normal isolated lens epithelial or fiber cells. The majority of the DEGs were found to be not preferentially expressed in either cell type and were also found to be elevated in *Celf1*^{cKO} lenses. Thus, similar to the iSyTE lens-enrichment analysis, the cell-type (gene expression in either epithelial or fiber cells) specific analysis reinforces the hypothesis that this subset of non-enriched, elevated *Celf1*^{cKO} DEGs should not be expressed at such high transcript levels for proper lens development. Apart from the DEGs that do not exhibit cell type-preferred expression, the majority of the remaining DEGs are preferentially expressed in fiber cells. This suggests that Celf1′s impact on the lens is primarily through its function in fiber cells. However, it should be noted that *Celf1*^{cKO} DEGs were identified from whole lens samples, which are expected to have higher levels of transcripts from fiber cells compared to epithelial cells. Thus, the sensitivity toward examination of epithelial DEGs is comparatively low. In future, this can be addressed by performing spatial transcriptomics, for example, by conducting RNA-seq on isolated epithelial and fiber cells from *Celf1*^{cKO} lenses. Alternately, this can also be addressed by performing single cell RNA-seq analysis on *Celf1*^{cKO} lenses.

The above analyses inform on the overall impact of Celf1 on normal lens development. To gain insights into the subset of DEGs that are potential direct RNA targets of Celf1 protein, comparative analysis was performed with CLIP-seq data on CELF1 protein in a human cell line. Although this data is from humans, and not mice, and from a non-lens cell line, this analysis identified 32% of *Celf1*^{cKO} lens DEG transcripts to be directly bound by the CELF1 protein in cellulo. The majority of these direct RNA targets of Celf1 protein are found to be elevated in the *Celf1*^{cKO} lens. This supports the hypothesis that Celf1 protein is necessary to directly bind and repress the expression of hundreds of RNAs that are not highly enriched in the normal lens. Among the cell-type preferentially expressed DEGs that are also identified in CLIP-seq, the majority are preferentially expressed in fiber cells, suggesting that the direct impact of Celf1 is higher in the lens fiber cells compared to lens epithelial cells.

Of the *Celf1*^{cKO} lens total DEGs, 32% represent a high number of Celf1-direct RNA targets identified, especially considering that this cell line is not lens-derived and thus may not optimally represent lens gene expression, in addition to other caveats such as

the suboptimal expression of Celf1 accessory protein/RNA. Thus, it can be hypothesized that the number of direct DEG RNA targets of the Celf1 protein in the lens may be even higher. This can be addressed in the future by performing CLIP-seq on lens cell lines or whole lens tissue. Further, among the direct RNA targets of Celf1 identified by CLIP-seq, is the transcription elongation factor for RNA polymerase II 2 (Ell2), which exhibits highly enriched expression in normal lens development as per iSyTE. Interestingly, Ell2 expression is significantly elevated in *Celf1*^{cKO} lenses, suggesting that Celf1 protein may function to achieve optimal transcript levels of this key regulatory protein, which is involved in transcription control. Thus, this analysis gives new insights into the specific Celf1 targets that are common regardless of the difference in these cell types (lens vs. Hela) and furthermore are also indicative of the similarities in Celf1 function across different species, namely, mouse and human.

To identify pathways that are altered upon Celf1-deficiency, GSEA analysis and GO term analysis was performed on *Celf1*^{cKO} lens total DEGs, as well as the subset of DEGs prioritized by different approaches. Broadly, DEGs reduced in *Celf1*^{cKO} lenses were found to be enriched in pathways that are relevant to lens development (e.g., "structural constituent of eye lens" (GO:0005212) and "lens development in camera-type eye" (GO:0002088)), while the elevated DEGs represented pathways not enriched in normal lenses (e.g., "proton transporting ATPase activity, rotational mechanism" (GO:0046961), "cytoplasmic vesicle membrane" (GO:0030659) and "calcium-dependent protein binding" (GO:0048306)). Additionally, the GO term "lens fiber cell differentiation" (GO:0070306) was enriched for DEGs that are reduced upon Celf1-deficiency and are also preferentially expressed in normal fiber cells, suggesting that key fiber cell expressed genes are under positive control of Celf1. Interestingly, the GO terms "extracellular matrix" (GO:0031012) and "cell projection membrane" (GO:0031253) were enriched for DEGs preferentially expressed in normal epithelial cells, suggesting that Celf1 may have a distinct role in positive regulation of these processes in epithelial cells. Finally, the GO term "positive-regulation of brown fat cell differentiation" (GO:0090335) was enriched in the subset of reduced DEGs that are direct RNA targets of Celf1 protein. This GO term contained the transcription factor Prdm16, which is independently found to exhibit high lens-enriched expression in iSyTE, especially at/beyond secondary fiber cell differentiation at E16.5. Thus, alteration of *Prdm16* expression in *Celf1*^{cKO} lenses, its identification as a direct RNA target of Celf1 protein, and its enriched expression in normal lenses together make Prdm16 a high-priority candidate whose role in lens development and pathology can be examined in the future.

Together, these various analyses provide insights into lens pathology in *Celf1*^{cKO} mice and identified numerous promising candidates that may be critical for proper lens development. To further prioritize direct RNA targets of Celf1 protein that play a key role in the lens, we used previously reported as well as new microarray transcriptomic analysis on *Celf1*^{cKO} lenses at different postnatal stages (P0 and P6). This allows independent validation of hundreds of DEGs identified by RNA-seq in the *Celf1*^{cKO} lens. Along with the various prioritization approaches described in this report, especially the CLIP-seq analysis that identified direct targets of Celf1 (in addition to other parameters such as, lens-enriched expression in iSyTE, preferential expression in epithelial or fiber cells, etc.), the microarray data identifies high-confidence candidates in the lens for future studies. These analyses show that upon Celf1 deficiency, a cohort of cataract-linked genes are misexpressed (e.g., the crystallins *Cryab*, *Cryba2*, *Cryba4*, *Crybb1*, *Crybb2*, *Cryga*, *Crygb*, *Crygc* and *Crygd*, the connexins *Gjb6* and *Gja3*, the membrane protein *Bfsp1*, the extracellular matrix associated peroxidase *Pxdn*, and the post-transcriptional regulator *Tdrd7*), in addition to alterations in distinct pathways, thus indicating that multiple factors likely contribute to the manifestation of the cataract defect. Importantly, the present analyses identify as yet unappreciated and novel high-priority candidates in the lens for defining new pathways involved in lens biology (e.g., Ell2 and Prdm16) that likely also contribute to the cataracts resulting from Celf1 deficiency. In particular, the following targets are promising. Ell2, a transcription elongation factor, that functions in a fundamental regulatory process—

considered ubiquitously important—in transcription. This is because Ell2 facilitates the release of the RNA Polymerase II from its "pause" in early stages of transcription, which in turn allows the enzyme to proceed with transcription of its target genes. The present study shows that Celf1 functions in controlling the proper dosage of Ell2 in the lens, and thus opens up a new direction in lens research by encouraging the question: are factors like Ell2—that play a critical role in a ubiquitously important regulatory process—specifically recruited for controlling expression of key genes in the lens, a tissue that is known to produce extremely high levels of transcripts that in turn get translated into abundant levels of proteins (e.g., crystallins, which reach concentrations of 450 mg/mL in the lens). Further, this study, by prioritizing Prdm16 which is significantly reduced in Celf1-deficient lenses, has led to the identification of a new transcription factor in the lens, further investigation of which will advance the understanding of gene expression control in this tissue.

5. Conclusions

This study reports on the impact of Celf1-deficiency on the early postnatal lens transcriptome. Application of various analyses such as identification in Cat-Map, lens-enriched expression in iSyTE, preferential expression in epithelial or fiber cells, identification as direct RNA target in CLIP-seq data, and GO term enrichment provides insights into key transcriptomic events that are under the control of Celf1 in normal lens development and whose alterations contribute to lens pathology, which includes several established cataract-linked genes such as crystallins, connexins, membrane proteins, etc. Finally, along with independent validation by microarrays, this study provides a new cohort of high-confidence genes (e.g., *Ell2*, *Prdm16*, etc.) for future investigations in lens development.

Supplementary Materials: The following are available online at https://www.mdpi.com/article/10.3390/cells12071070/s1, Figure S1: *Celf1*^{cKO} lens exhibits reduced gamma crystallin expression, Figure S2: Volcano plot and smear plot of *Celf1*^{cKO} lens microarray datasets at P0 and P6, Table S1: Summary of RNA-seq reads and mapping, Table S2: Differential gene expression analysis of *Celf1*^{cKO} lens by RNA-seq, Table S3: iSyTE lens-enriched expression of *Celf1*^{cKO} lens DEGs identified by RNA-seq, Table S4: Epithelial- and fiber cell-preferred expression of *Celf1*^{cKO} lens DEGs identified by RNA-seq, Table S5: GSEA analysis of *Celf1*^{cKO} lens RNA-seq data, Table S6: Gene ontology analysis of *Celf1*^{cKO} lens DEGs, Table S7: Differential gene expression analysis of *Celf1*^{cKO} lens by microarrays at P0 and P6, Table S8: *Celf1*^{cKO} lens DEGs commonly identified by RNA-seq and microarrays.

Author Contributions: Conceptualization, A.D.S. and S.A.L.; methodology, A.D.S., M.D., S.Y.C. and Y.A.; validation, A.D.S., S.Y.C., S.A. and B.A.T.W.; formal analysis, M.D., S.Y.C. and D.A.; writing—original draft preparation, A.D.S., M.D., S.Y.C. and S.A.L.; writing—review and editing, A.D.S., M.D., S.Y.C., D.A., S.A., B.A.T.W., Y.A., L.P. and S.A.L.; supervision, L.P. and S.A.L.; project administration, S.A.L.; funding acquisition, S.A.L. All authors have read and agreed to the published version of the manuscript.

Funding: This research was funded by the National Institutes of Health (NIH), grant number R01 EY021505 to S.A.L., D.A. was supported by the Knights Templar Pediatric Ophthalmology Career Starter Grant Award. A.D.S. and S.A. were supported by a Fight For Sight Summer Fellowship. S.A. also received support from Sigma Xi through a fellowship.

Institutional Review Board Statement: The study was conducted according to the guidelines of the Association for Research in Vision and Ophthalmology (ARVO) Statement for the use of animals in ophthalmic and vision research and approved by the Institutional Review Board (Institutional Animal Care and Use Committee (IACUC)) of the University of Delaware (protocol number 1226 approved 1 October 2022).

Informed Consent Statement: Not applicable.

Data Availability Statement: The RNA-sequencing data and the microarray data described here will be submitted to the Gene Expression Omnibus.

Conflicts of Interest: The authors declare no conflict of interest.

References

1. Harland, R.M.; Grainger, R.M. Xenopus Research: Metamorphosed by Genetics and Genomics. *Trends Genet.* **2011**, *27*, 507–515. [CrossRef] [PubMed]
2. Graw, J. Mouse Models of Cataract. *J. Genet.* **2009**, *88*, 469–486. [CrossRef]
3. Shiels, A.; Hejtmancik, J.F. Inherited Cataracts: Genetic Mechanisms and Pathways New and Old. *Exp. Eye Res.* **2021**, *209*, 108662. [CrossRef]
4. Cvekl, A.; Zhang, X. Signaling and Gene Regulatory Networks in Mammalian Lens Development. *Trends Genet.* **2017**, *33*, 677–702. [CrossRef]
5. Lachke, S.A.; Maas, R.L. Building the Developmental Oculome: Systems Biology in Vertebrate Eye Development and Disease. *Wiley Interdiscip. Rev. Syst. Biol. Med.* **2010**, *2*, 305–323. [CrossRef]
6. Lachke, S.A. RNA-Binding Proteins and Post-Transcriptional Regulation in Lens Biology and Cataract: Mediating Spatiotemporal Expression of Key Factors That Control the Cell Cycle, Transcription, Cytoskeleton and Transparency. *Exp. Eye Res.* **2022**, *214*, 108889. [CrossRef]
7. Dash, S.; Siddam, A.D.; Barnum, C.E.; Janga, S.C.; Lachke, S.A. RNA-Binding Proteins in Eye Development and Disease: Implication of Conserved RNA Granule Components. *Wiley Interdiscip. Rev. RNA* **2016**, *7*, 527–557. [CrossRef] [PubMed]
8. Dash, S.; Dang, C.A.; Beebe, D.C.; Lachke, S.A. Deficiency of the RNA Binding Protein Caprin2 Causes Lens Defects and Features of Peters Anomaly. *Dev. Dyn.* **2015**, *244*, 1313–1327. [CrossRef]
9. Siddam, A.D.; Gautier-Courteille, C.; Perez-Campos, L.; Anand, D.; Kakrana, A.; Dang, C.A.; Legagneux, V.; Méreau, A.; Viet, J.; Gross, J.M.; et al. The RNA-Binding Protein Celf1 Post-Transcriptionally Regulates P27Kip1 and Dnase2b to Control Fiber Cell Nuclear Degradation in Lens Development. *PLoS Genet.* **2018**, *14*, e1007278. [CrossRef] [PubMed]
10. Aryal, S.; Viet, J.; Weatherbee, B.A.T.; Siddam, A.D.; Hernandez, F.G.; Gautier-Courteille, C.; Paillard, L.; Lachke, S.A. The Cataract-Linked RNA-Binding Protein Celf1 Post-Transcriptionally Controls the Spatiotemporal Expression of the Key Homeodomain Transcription Factors Pax6 and Prox1 in Lens Development. *Hum. Genet.* **2020**, *139*, 1541–1554. [CrossRef]
11. Dash, S.; Brastrom, L.K.; Patel, S.D.; Scott, C.A.; Slusarski, D.C.; Lachke, S.A. The Master Transcription Factor SOX2, Mutated in Anophthalmia/Microphthalmia, Is Post-Transcriptionally Regulated by the Conserved RNA-Binding Protein RBM24 in Vertebrate Eye Development. *Hum. Mol. Genet.* **2020**, *29*, 591–604. [CrossRef]
12. Lachke, S.A.; Alkuraya, F.S.; Kneeland, S.C.; Ohn, T.; Aboukhalil, A.; Howell, G.R.; Saadi, I.; Cavallesco, R.; Yue, Y.; Tsai, A.C.-H.; et al. Mutations in the RNA Granule Component TDRD7 Cause Cataract and Glaucoma. *Science* **2011**, *331*, 1571–1576. [CrossRef]
13. Barnum, C.E.; Al Saai, S.; Patel, S.D.; Cheng, C.; Anand, D.; Xu, X.; Dash, S.; Siddam, A.D.; Glazewski, L.; Paglione, E.; et al. The Tudor-Domain Protein TDRD7, Mutated in Congenital Cataract, Controls the Heat Shock Protein HSPB1 (HSP27) and Lens Fiber Cell Morphology. *Hum. Mol. Genet.* **2020**, *29*, 2076–2097. [CrossRef] [PubMed]
14. Lorén, C.E.; Schrader, J.W.; Ahlgren, U.; Gunhaga, L. FGF Signals Induce Caprin2 Expression in the Vertebrate Lens. *Differentiation* **2009**, *77*, 386–394. [CrossRef] [PubMed]
15. Nakazawa, K.; Shichino, Y.; Iwasaki, S.; Shiina, N. Implications of RNG140 (Caprin2)-Mediated Translational Regulation in Eye Lens Differentiation. *J. Biol. Chem.* **2020**, *295*, 15029–15044. [CrossRef]
16. Shao, M.; Lu, T.; Zhang, C.; Zhang, Y.-Z.; Kong, S.-H.; Shi, D.-L. Rbm24 Controls Poly(A) Tail Length and Translation Efficiency of Crystallin MRNAs in the Lens via Cytoplasmic Polyadenylation. *Proc. Natl. Acad. Sci. USA* **2020**, *117*, 7245–7254. [CrossRef] [PubMed]
17. Chen, J.; Wang, Q.; Cabrera, P.E.; Zhong, Z.; Sun, W.; Jiao, X.; Chen, Y.; Govindarajan, G.; Naeem, M.A.; Khan, S.N.; et al. Molecular Genetic Analysis of Pakistani Families with Autosomal Recessive Congenital Cataracts by Homozygosity Screening. *Investig. Ophthalmol. Vis. Sci.* **2017**, *58*, 2207–2217. [CrossRef]
18. Fernández-Alcalde, C.; Nieves-Moreno, M.; Noval, S.; Peralta, J.M.; Montaño, V.E.F.; Del Pozo, Á.; Santos-Simarro, F.; Vallespín, E. Molecular and Genetic Mechanism of Non-Syndromic Congenital Cataracts. Mutation Screening in Spanish Families. *Genes* **2021**, *12*, 580. [CrossRef]
19. Kandaswamy, D.K.; Prakash, M.V.S.; Graw, J.; Koller, S.; Magyar, I.; Tiwari, A.; Berger, W.; Santhiya, S.T. Application of WES Towards Molecular Investigation of Congenital Cataracts: Identification of Novel Alleles and Genes in a Hospital-Based Cohort of South India. *Int. J. Mol. Sci.* **2020**, *21*, 9569. [CrossRef]
20. Tan, Y.-Q.; Tu, C.; Meng, L.; Yuan, S.; Sjaarda, C.; Luo, A.; Du, J.; Li, W.; Gong, F.; Zhong, C.; et al. Loss-of-Function Mutations in TDRD7 Lead to a Rare Novel Syndrome Combining Congenital Cataract and Nonobstructive Azoospermia in Humans. *Genet. Med.* **2019**, *21*, 1209–1217. [CrossRef]
21. Tanaka, T.; Hosokawa, M.; Vagin, V.V.; Reuter, M.; Hayashi, E.; Mochizuki, A.L.; Kitamura, K.; Yamanaka, H.; Kondoh, G.; Okawa, K.; et al. Tudor Domain Containing 7 (Tdrd7) Is Essential for Dynamic Ribonucleoprotein (RNP) Remodeling of Chromatoid Bodies during Spermatogenesis. *Proc. Natl. Acad. Sci. USA* **2011**, *108*, 10579–10584. [CrossRef]
22. Zheng, C.; Wu, M.; He, C.-Y.; An, X.-J.; Sun, M.; Chen, C.-L.; Ye, J. RNA Granule Component TDRD7 Gene Polymorphisms in a Han Chinese Population with Age-Related Cataract. *J. Int. Med. Res.* **2014**, *42*, 153–163. [CrossRef] [PubMed]
23. Choquet, H.; Melles, R.B.; Anand, D.; Yin, J.; Cuellar-Partida, G.; Wang, W.; 23andMe Research Team; Hoffmann, T.J.; Nair, K.S.; Hysi, P.G.; et al. A Large Multiethnic GWAS Meta-Analysis of Cataract Identifies New Risk Loci and Sex-Specific Effects. *Nat. Commun.* **2021**, *12*, 3595. [CrossRef] [PubMed]

24. Bauermeister, D.; Claußen, M.; Pieler, T. A Novel Role for Celf1 in Vegetal RNA Localization during Xenopus Oogenesis. *Dev. Biol.* **2015**, *405*, 214–224. [CrossRef] [PubMed]
25. Vlasova-St Louis, I.; Dickson, A.M.; Bohjanen, P.R.; Wilusz, C.J. CELFish Ways to Modulate MRNA Decay. *Biochim. Biophys. Acta* **2013**, *1829*, 695–707. [CrossRef]
26. Zheng, Y.; Miskimins, W.K. CUG-Binding Protein Represses Translation of P27Kip1 MRNA through Its Internal Ribosomal Entry Site. *RNA Biol.* **2011**, *8*, 365–371. [CrossRef]
27. Ladd, A.N.; Charlet, N.; Cooper, T.A. The CELF Family of RNA Binding Proteins Is Implicated in Cell-Specific and Developmentally Regulated Alternative Splicing. *Mol. Cell. Biol.* **2001**, *21*, 1285–1296. [CrossRef]
28. Vlasova, I.A.; Tahoe, N.M.; Fan, D.; Larsson, O.; Rattenbacher, B.; Sternjohn, J.R.; Vasdewani, J.; Karypis, G.; Reilly, C.S.; Bitterman, P.B.; et al. Conserved GU-Rich Elements Mediate MRNA Decay by Binding to CUG-Binding Protein 1. *Mol. Cell.* **2008**, *29*, 263–270. [CrossRef]
29. Rowan, S.; Conley, K.W.; Le, T.T.; Donner, A.L.; Maas, R.L.; Brown, N.L. Notch Signaling Regulates Growth and Differentiation in the Mammalian Lens. *Dev. Biol.* **2008**, *321*, 111–122. [CrossRef]
30. Lachke, S.A.; Ho, J.W.K.; Kryukov, G.V.; O'Connell, D.J.; Aboukhalil, A.; Bulyk, M.L.; Park, P.J.; Maas, R.L. ISyTE: Integrated Systems Tool for Eye Gene Discovery. *Investig. Ophthalmol. Vis. Sci.* **2012**, *53*, 1617–1627. [CrossRef]
31. Rowan, S.; Siggers, T.; Lachke, S.A.; Yue, Y.; Bulyk, M.L.; Maas, R.L. Precise Temporal Control of the Eye Regulatory Gene Pax6 via Enhancer-Binding Site Affinity. *Genes. Dev.* **2010**, *24*, 980–985. [CrossRef] [PubMed]
32. Dobin, A.; Davis, C.A.; Schlesinger, F.; Drenkow, J.; Zaleski, C.; Jha, S.; Batut, P.; Chaisson, M.; Gingeras, T.R. STAR: Ultrafast Universal RNA-Seq Aligner. *Bioinformatics* **2013**, *29*, 15–21. [CrossRef] [PubMed]
33. Liao, Y.; Smyth, G.K.; Shi, W. FeatureCounts: An Efficient General Purpose Program for Assigning Sequence Reads to Genomic Features. *Bioinformatics* **2014**, *30*, 923–930. [CrossRef] [PubMed]
34. Chen, Y.; Lun, A.T.L.; Smyth, G.K. From Reads to Genes to Pathways: Differential Expression Analysis of RNA-Seq Experiments Using Rsubread and the EdgeR Quasi-Likelihood Pipeline. *F1000Research* **2016**, *5*, 1438. [CrossRef]
35. Shiels, A.; Bennett, T.M.; Hejtmancik, J.F. Cat-Map: Putting Cataract on the Map. *Mol. Vis.* **2010**, *16*, 2007–2015.
36. Kakrana, A.; Yang, A.; Anand, D.; Djordjevic, D.; Ramachandruni, D.; Singh, A.; Huang, H.; Ho, J.W.K.; Lachke, S.A. ISyTE 2.0: A Database for Expression-Based Gene Discovery in the Eye. *Nucleic Acids Res.* **2018**, *46*, D875–D885. [CrossRef]
37. Zhao, Y.; Zheng, D.; Cvekl, A. A Comprehensive Spatial-Temporal Transcriptomic Analysis of Differentiating Nascent Mouse Lens Epithelial and Fiber Cells. *Exp. Eye Res.* **2018**, *175*, 56–72. [CrossRef]
38. Le Tonquèze, O.; Gschloessl, B.; Legagneux, V.; Paillard, L.; Audic, Y. Identification of CELF1 RNA Targets by CLIP-Seq in Human HeLa Cells. *Genom. Data* **2016**, *8*, 97–103. [CrossRef]
39. Yu, G.; Wang, L.-G.; Han, Y.; He, Q.-Y. ClusterProfiler: An R Package for Comparing Biological Themes among Gene Clusters. *OMICS* **2012**, *16*, 284–287. [CrossRef]
40. Agrawal, S.A.; Anand, D.; Siddam, A.D.; Kakrana, A.; Dash, S.; Scheiblin, D.A.; Dang, C.A.; Terrell, A.M.; Waters, S.M.; Singh, A.; et al. Compound Mouse Mutants of BZIP Transcription Factors Mafg and Mafk Reveal a Regulatory Network of Non-Crystallin Genes Associated with Cataract. *Hum. Genet.* **2015**, *134*, 717–735. [CrossRef]
41. Thorvaldsdóttir, H.; Robinson, J.T.; Mesirov, J.P. Integrative Genomics Viewer (IGV): High-Performance Genomics Data Visualization and Exploration. *Brief. Bioinform.* **2013**, *14*, 178–192. [CrossRef]
42. Beisang, D.; Bohjanen, P.R.; Vlasova-St. Louis, I.A. CELF1, a Multifunctional Regulator of Posttranscriptional Networks. In *Binding Protein*; Abdelmohsen, K., Ed.; InTech: London, UK, 2012; ISBN 978-953-51-0758-3.
43. Kress, C.; Gautier-Courteille, C.; Osborne, H.B.; Babinet, C.; Paillard, L. Inactivation of CUG-BP1/CELF1 Causes Growth, Viability, and Spermatogenesis Defects in Mice. *Mol. Cell. Biol.* **2007**, *27*, 1146–1157. [CrossRef] [PubMed]
44. Cifdaloz, M.; Osterloh, L.; Graña, O.; Riveiro-Falkenbach, E.; Ximénez-Embún, P.; Muñoz, J.; Tejedo, C.; Calvo, T.G.; Karras, P.; Olmeda, D.; et al. Systems Analysis Identifies Melanoma-Enriched pro-Oncogenic Networks Controlled by the RNA Binding Protein CELF1. *Nat. Commun.* **2017**, *8*, 2249. [CrossRef]
45. Chaudhury, A.; Cheema, S.; Fachini, J.M.; Kongchan, N.; Lu, G.; Simon, L.M.; Wang, T.; Mao, S.; Rosen, D.G.; Ittmann, M.M.; et al. CELF1 Is a Central Node in Post-Transcriptional Regulatory Programmes Underlying EMT. *Nat. Commun.* **2016**, *7*, 13362. [CrossRef] [PubMed]
46. House, R.P.; Talwar, S.; Hazard, E.S.; Hill, E.G.; Palanisamy, V. RNA-Binding Protein CELF1 Promotes Tumor Growth and Alters Gene Expression in Oral Squamous Cell Carcinoma. *Oncotarget* **2015**, *6*, 43620–43634. [CrossRef] [PubMed]
47. Matsui, T.; Sasaki, A.; Akazawa, N.; Otani, H.; Bessho, Y. Celf1 Regulation of Dmrt2a Is Required for Somite Symmetry and Left-Right Patterning during Zebrafish Development. *Development* **2012**, *139*, 3553–3560. [CrossRef]
48. Timchenko, N.A.; Cai, Z.J.; Welm, A.L.; Reddy, S.; Ashizawa, T.; Timchenko, L.T. RNA CUG Repeats Sequester CUGBP1 and Alter Protein Levels and Activity of CUGBP1. *J. Biol. Chem.* **2001**, *276*, 7820–7826. [CrossRef]
49. Philips, A.V.; Timchenko, L.T.; Cooper, T.A. Disruption of Splicing Regulated by a CUG-Binding Protein in Myotonic Dystrophy. *Science* **1998**, *280*, 737–741. [CrossRef]
50. Xiao, J.; Jin, S.; Wang, X.; Huang, J.; Zou, H. CELF1 Selectively Regulates Alternative Splicing of DNA Repair Genes Associated With Cataract in Human Lens Cell Line. *Biochem. Genet.* **2022**. [CrossRef]
51. Xiao, J.; Tian, X.; Jin, S.; He, Y.; Song, M.; Zou, H. CELF1 Promotes Matrix Metalloproteinases Gene Expression at Transcriptional Level in Lens Epithelial Cells. *BMC Ophthalmol.* **2022**, *22*, 122. [CrossRef]

52. Nishimoto, S.; Kawane, K.; Watanabe-Fukunaga, R.; Fukuyama, H.; Ohsawa, Y.; Uchiyama, Y.; Hashida, N.; Ohguro, N.; Tano, Y.; Morimoto, T.; et al. Nuclear Cataract Caused by a Lack of DNA Degradation in the Mouse Eye Lens. *Nature* **2003**, *424*, 1071–1074. [CrossRef] [PubMed]
53. Gilmour, D.T.; Lyon, G.J.; Carlton, M.B.; Sanes, J.R.; Cunningham, J.M.; Anderson, J.R.; Hogan, B.L.; Evans, M.J.; Colledge, W.H. Mice Deficient for the Secreted Glycoprotein SPARC/Osteonectin/BM40 Develop Normally but Show Severe Age-Onset Cataract Formation and Disruption of the Lens. *EMBO J.* **1998**, *17*, 1860–1870. [CrossRef] [PubMed]
54. Anand, D.; Lachke, S.A. Systems Biology of Lens Development: A Paradigm for Disease Gene Discovery in the Eye. *Exp. Eye Res.* **2017**, *156*, 22–33. [CrossRef]
55. Anand, D.; Kakrana, A.; Siddam, A.D.; Huang, H.; Saadi, I.; Lachke, S.A. RNA Sequencing-Based Transcriptomic Profiles of Embryonic Lens Development for Cataract Gene Discovery. *Hum. Genet.* **2018**, *137*, 941–954. [CrossRef] [PubMed]
56. Aryal, S.; Anand, D.; Hernandez, F.G.; Weatherbee, B.A.T.; Huang, H.; Reddy, A.P.; Wilmarth, P.A.; David, L.L.; Lachke, S.A. MS/MS in Silico Subtraction-Based Proteomic Profiling as an Approach to Facilitate Disease Gene Discovery: Application to Lens Development and Cataract. *Hum. Genet.* **2020**, *139*, 151–184. [CrossRef] [PubMed]

Disclaimer/Publisher's Note: The statements, opinions and data contained in all publications are solely those of the individual author(s) and contributor(s) and not of MDPI and/or the editor(s). MDPI and/or the editor(s) disclaim responsibility for any injury to people or property resulting from any ideas, methods, instructions or products referred to in the content.

cells

MDPI

Article

Spatiotemporal Localisation of Heparan Sulphate Proteoglycans throughout Mouse Lens Morphogenesis

Tayler F. L. Wishart [1,*] and Frank J. Lovicu [1,2,*]

[1] Molecular and Cellular Biomedicine, School of Medical Sciences, The University of Sydney, Sydney, NSW 2006, Australia
[2] Save Sight Institute, The University of Sydney, Sydney, NSW 2006, Australia
* Correspondence: tayler.wishart@sydney.edu.au (T.F.L.W.); frank.lovicu@sydney.edu.au (F.J.L.)

Abstract: Heparan sulphate proteoglycans (HSPGs) consist of a core protein decorated with sulphated HS-glycosaminoglycan (GAG) chains. These negatively charged HS-GAG chains rely on the activity of PAPSS synthesising enzymes for their sulfation, which allows them to bind to and regulate the activity of many positively charged HS-binding proteins. HSPGs are found on the surfaces of cells and in the pericellular matrix, where they interact with various components of the cell microenvironment, including growth factors. By binding to and regulating ocular morphogens and growth factors, HSPGs are positioned to orchestrate growth factor-mediated signalling events that are essential for lens epithelial cell proliferation, migration, and lens fibre differentiation. Previous studies have shown that HS sulfation is essential for lens development. Moreover, each of the full-time HSPGs, differentiated by thirteen different core proteins, are differentially localised in a cell-type specific manner with regional differences in the postnatal rat lens. Here, the same thirteen HSPG-associated GAGs and core proteins as well as PAPSS2, are shown to be differentially regulated throughout murine lens development in a spatiotemporal manner. These findings suggest that HS-GAG sulfation is essential for growth factor-induced cellular processes during embryogenesis, and the unique and divergent localisation of different lens HSPG core proteins indicates that different HSPGs likely play specialized roles during lens induction and morphogenesis.

Keywords: lens development; heparan sulphate proteoglycan (HSPG); PAPSS; syndecan; glypican

1. Introduction

During early embryogenesis, the morphogenesis of the eye lens begins with the proximal interaction between the surface head ectodermal cells with the evaginating optic vesicle, resulting in a thickening of this apposing ectoderm to become the lens placode. The apical constriction of these cells leads to placode invagination to form the lens pit, which will separate from the neighbouring head ectoderm to form the hollow lens vesicle. The cells at the anterior aspect of the lens vesicle will differentiate to form the lens epithelium, while the posterior lens vesicle cells elongate to form the primary lens fibre cells. The elongation of these primary fibres that extend to reach the overlying epithelium rids the vesicle of its lumen to form the basic structure of the lens [1,2]. From this point onwards, the lens continues to grow, as proliferating epithelia at the lens equator exit the cell cycle and elongate and differentiate to form secondary fibre cells, displacing the older fibre cells towards the centre of the lens [1,2]. As fibre cells mature, there is autophagy of their nuclear material and organelles, and the formation of specialized membrane interdigitations, as they acquire their distinctive transparency, a characteristic that allows the lens to perform its primary function to transmit and focus light onto the retina [3].

Lens development and maintenance are governed by the interplay of a complex network of signalling molecules within the ocular microenvironment [4]. Extensive research conducted over several decades has led to the identification of these crucial molecules

and elucidation of their distinct and complementary functions in regulating specific morphogenic events and cellular behaviour [5,6]. Secreted primarily from the different ocular tissues, including the lens, retina and ciliary body, these diffusible growth factors, including members of the fibroblast growth factor (FGF) [7–9], Wnt [10–12], bone morphogenetic protein (BMP) [13,14] and Hedgehog (Hh) [15,16] families, that are found in the ocular milieu, influence lens cell behaviour (i.e., proliferation, migration, differentiation, and cell death) [4]. For the defined stages of lens morphogenesis, these factors need to be tightly controlled in a spatial and temporal manner to regulate the induction, and anteroposterior, left–right, and dorsoventral patterning of the lens [5,6]. While the various effects of growth factors on lens cell behaviour are well known, and often overlapping, the mechanisms governing the movement of these factors through the extracellular space, their precise arrival and signal transmission within target cells, remains unknown. Recent studies in mice and other animal models have highlighted the significance of heparan sulphate proteoglycans (HSPGs) localised to the cell membrane and extracellular matrix (ECM) of tissues, in facilitating the signalling and distribution of growth factors, respectively [17].

HSPGs are composed of a specific core protein structure, covalently linked to a small number of heparan sulphate (HS) glycosaminoglycan (GAG) chains. Of the thirteen full-time HSPGs, they are divided into three major families depending on this core protein structure: the transmembrane family (i.e., syndecans), glycerophosphatidylinositide (GPI)-anchored family (i.e., glypicans) and the secreted family (e.g., perlecan, agrin, and collagen XVIII) [17,18]. The syndecans and glypicans are generally localised to the cell surface, whereas perlecan, agrin, and collagen XVIII are more commonly found in the ECM and basement membranes [17].

In the synthesis of HS-GAG chains, HS sulfotransferases facilitate the transfer of sulphate ions (SO4-) from the sulphate-donor molecule, 3′-phosphoadenosine 5′-phosphosulfate (PAPS), to HS-GAGs. PAPS is a crucial and rate-limiting sulphate donor molecule that regulates all post-translational sulfation reactions in the golgi apparatus and is produced by cellular PAPS synthetases (PAPSS1/2) [19,20]. The negatively charged sulphate groups of the HS-GAG chains interact with the positively charged lysine/arginine-rich regions of many proteins [17], allowing HSPGs to interact with and modulate the activity of various growth factors including FGFs [21,22], BMPs [23,24], Wnts [25,26], Hh [27,28], and ECM molecules, such as integrins [29,30], laminin [31], and fibronectin [32].

The downstream effects of HSPG–protein interactions include the activation of high-affinity receptor signalling complexes, and the mediation of intracellular signalling cascades leading to the activation of key effector genes and changes in the cell behaviour and phenotype [17,33]. The pleiotropic modulation of growth factor receptor signalling by HSPGs (altering ligand density and activity) can locally stabilise mitogen and morphogen gradients at the tissue level [33]. These gradients are critical for organogenesis and for the maintenance of normal tissue homeostasis [34]. As the activity of HSPGs primarily depends on its fine structure (i.e., sulphation) and location (i.e., the cell surface or ECM) of their HS-GAG glycosaminoglycan chains, the specific activity of HSPGs in a given cell-type or tissue, at a given time can be determined by its HSPG profile: the localisation of HSPG core proteins and its complement of HS-GAG sulfation enzymes [17,33]. Previously, we have shown all HSPG core proteins are present in the postnatal rat lens, localised to its epithelia, fibres and basement membrane, the lens capsule, in unique and distinct expression patterns that align with key functional regions [35]. The distinct spatial and temporal expression of HSPGs implies that differentiating lens cells may acquire a unique set of HSPGs, leading to specific patterns of HS–protein interactions and function during lens morphogenesis. Here, we report for the first time the comprehensive spatial and temporal localisation of all HSPGs in the developing murine lens. Taken together with the current literature, we highlight putative roles for specific HSPGs during key stages of lens development, as well as provide support for the requirement of HS sulphation in growth factor-induced lens cellular processes.

2. Materials and Methods

2.1. Animals

Animal experimentation protocols were authorized by The University of Sydney Animal Ethics Committee and were conducted in accordance with the guidelines established by the National Health and Medical Research Council (Australia) as well as the Association for Research in Vision and Ophthalmology's declaration for the Use of Animals in Ophthalmic and Vision Research. Mouse conception was recorded as midnight on the day of mating and embryos were routinely collected post conception at embryonic (E) day 9.5 (E9.5), E10.5, E11.5, E14.5, and E16.5, representing key stages of lens development (see Figure 1). Pregnant FvB/N mice were sacrificed by asphyxiation with carbon dioxide, and embryos were extracted and sacrificed by decapitation. Embryonic heads were collected for histological processing. Ten-day-old (P10) albino Wistar rats (*Rattus norvegicus*) were sacrificed by asphyxiation with carbon dioxide followed by cervical dislocation.

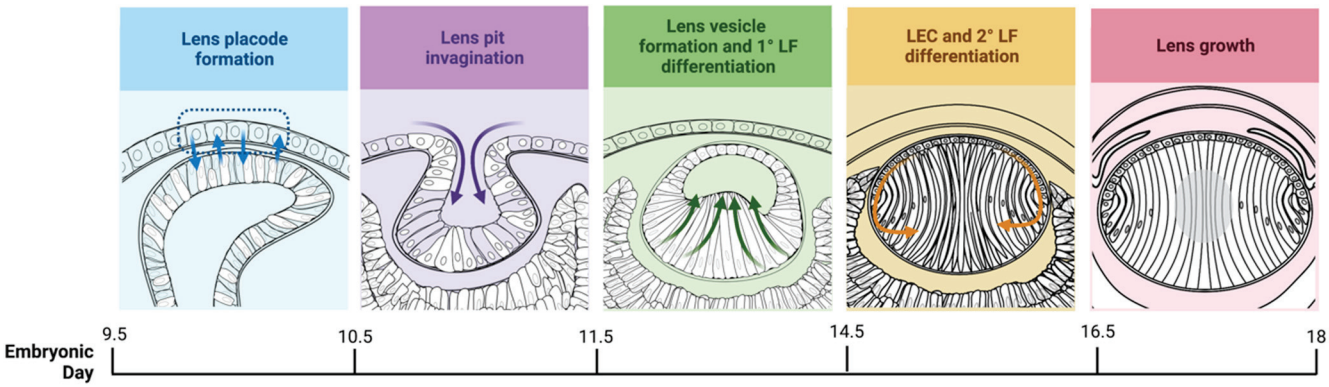

Figure 1. Representative stages of murine lens development. Arrows in lens placode formation indicate inductive interactions. Other arrows indicate cell movements/growth.

2.2. Immunolabelling of Heparan Sulphate Proteoglycans

Intact embryonic heads were collected and fixed for 24 h in 10% neutral buffered formalin (NBF; Sigma, Castle Hill, NSW, Australia) before processing for routine paraffin embedding. Paraffin-embedded tissues were serially sectioned at 5–6 µm. Mid-sagittal sections of embryonic heads from at least three independent animals were used for immunolabelling and for periodic acid–Schiff's (PAS) staining to highlight lens morphology. Monoclonal antibodies were used to detect all highly sulphated HSPGs as previously described [35]. Embryonic head sections were first labelled for highly sulphated forms of HS-GAG (HS-GAG F58-10E4, 370255; Amsbio LLC, Abingdon, UK). We also labelled for sulphated chondroitin sulphate (CS)-GAGs (CS-56, C8035; Sigma), as some HSPGs (syndecans -1/-3, agrin and collagen XVIII) carry CS-GAG chains alongside their predominant HS-GAG chains. To characterize the spatial localisation of the different HSPGs in the developing murine lens, we immunolabelled mid-sagittal sections using commercially available antibodies (see Supplementary Table S1). For all immunofluorescent labelling studies, cell nuclei were counter-labelled with bisbenzimide (Hoechst 33258; Sigma). Images in figures are oriented with the ventral side positioned to the right and the dorsal side to the left. Controls were included to account for any effects of autofluorescence (unlabelled tissue controls), secondary antibodies (chain-specific isotype and secondary antibody alone controls), co-labelling effects (single label controls), and nuclear staining (no Hoechst controls). Tissue samples from at least three individual animals (up to 6 eyes) at different stages of development were used for each label/antibody investigated.

A light microscope equipped with epifluorescence (Leica DMLB 100S, DFC-450C camera and LAS software v4.8.0, Leica Microsystems, Wetzlar, Germany) was used for PAS-staining (brightfield). For immunolabelling (immunofluorescence) studies, images were captured using a ZEISS LSM-800 microscope with an AxioCam 506 camera and ZEN

Blue Edition v2.3 software (Carl Zeiss, Jena, Germany), or a ZEISS AxioScan.Z1 microscope with a Hamamatsu ORCA-flash 4.0 v2 camera and ZEN SlideScan 2012 software (Carl Zeiss). All images were saved as uncompressed tagged information field format (TIFF) files at 16-bit depth. Image processing was performed using Photoshop v21.1.1 (Adobe, Inc., San Jose, CA, USA) and ImageJ (FIJI) v2.0 (Wayne Rasband, NIH, Bethesda, MD, USA) on the Mac OS X 10.15.6 (Apple Inc., Cupertino, CA, USA) and Windows 10 (Microsoft Inc., Seattle, WA, USA) operating systems.

3. Results

A summary of the labelling for HS-GAG, CS-GAG, PAPSS2, and all thirteen HSPG core proteins during murine lens development is outlined in Table 1.

3.1. PAPS Synthetase-2 Is Localised to the Developing Mouse Lens

We first immunolabelled the PAPSS2 (HSPG sulfation) in the developing mouse lens (Figure 2). PAPSS2 reactivity was absent from all early eye structures, including cells comprising the lens placode (E9.5, Figure 2(A1)), and lens pit (E10.5, Figure 2(A2)). It was not until E11.5, in the lens vesicle that PAPSS2 immunolabelling appeared, strongly localised to the elongating primary lens fibre cells (Figure 2(A3)). This fibre-specific label persisted and was also observed in the early secondary lens fibre cells at E14.5 (Figure 2(A4–A7)) and E16.5 (Figure 2(A8–A10)). At E16.5, PAPSS2 reactivity was also evident in the anterior lens epithelium but was not present in the lens capsule (Figure 2(A9)).

3.2. Heparan Sulphate Is the Predominant Sulphated Glycosaminoglycan Expressed throughout Murine Lens Development

HSPG core proteins can carry HS-GAG GAG chains or a combination of both HS-GAG and CS-GAG chains. To determine which of these two GAG species represents the major "active" sulphated fraction of HSPGs in the developing lens, the distribution of HS-GAG and CS-GAG was compared during key stages of lens development (Figure 3(A1–A8,B1–B8)) using antibodies specific for the sulphated domains on HS-GAG (HS-10E4, Figure 3(C1–C8)) or CS-GAG (CS-56, Figure 3(D1–D8)) chains. HS-GAG chain labelling was first observed at very low levels in the cells of the lens placode (E9.5, Figure 3(C1)) with stronger labelling in the lens pit (E10.5, Figure 3(C2)). At E11.5 (Figure 3(C3)), HS-GAG labelling was prominent in the developing lens capsule, anterior lens epithelium and ubiquitously in elongating primary lens fibre cells. HS-GAG reactivity was maintained in the lens capsule and cytoplasm of anterior epithelial cells at E14.5 (Figure 3(C4)) and E16.5 (Figure 3(C5–C8)). The HS-GAG chain labelling was the strongest throughout the cytoplasm of secondary lens fibre cells (Figure 3(C4)), with decreased reactivity at the germinative and transitional zones (Figure 3(C4,C8)). The concentrated immunolabelling of HS-GAG was also observed at the posterior tips (E14.5, Figure 3(C4)) and in the nuclei (Figure 3(C4,C7)) of elongating secondary fibre cells. Although absent from the extracellular matrix of the early developing eye (E9.5 and E10.5; Figure 3(B1,B2)), HS-GAG was strongly associated with the matrix connecting the posterior lens vesicle and early retina (Figure 3(C3)), and the developing vitreous humour from E14.5 (Figure 3(C4)). In contrast to the localisation of active HS-GAG chains in early lens development, CS-GAG chain labelling was primarily observed in the pericellular matrix (Figure 3(D1–D3)). CS-GAG immunolabelling was completely absent from the lens placode (Figure 3(D1)), lens pit (Figure 3(D2)), and lens vesicle (E11.5, Figure 3(D3)). Similarly, CS-GAG reactivity was first observed at low levels in the E14.5 lens capsule, anterior lens epithelium, and anterior pole of the secondary lens fibre cells (Figure 3(D4)). CS-GAG immunostaining was strongly correlated with the extracellular matrix at all early stages of eye development, particularly in the preplacode matrix (E9.5; Figure 3(D1)), and the interstitial matrix connecting the invaginating lens pit and optic cup (E10.5; Figure 3(D2)) and surrounding the lens vesicle (E11.5; Figure 3(D3)). CS-GAG was weakly evident in the ocular humours in the later stages of eye development (E14.5 and E16.5; Figure 3(D4–D6)). CS-GAG immunolabelling was absent from

the lens capsule at E16.5 (Figure 3(D5,D6,D8)), and decreased in the fibre cells relative to E14.5 (Figure 3(D7,D8)). The CS-GAG labelling remained in the anterior lens epithelium (Figure 3(D5)) and decreased in the germinative and transitional zones (Figure 3(D8)).

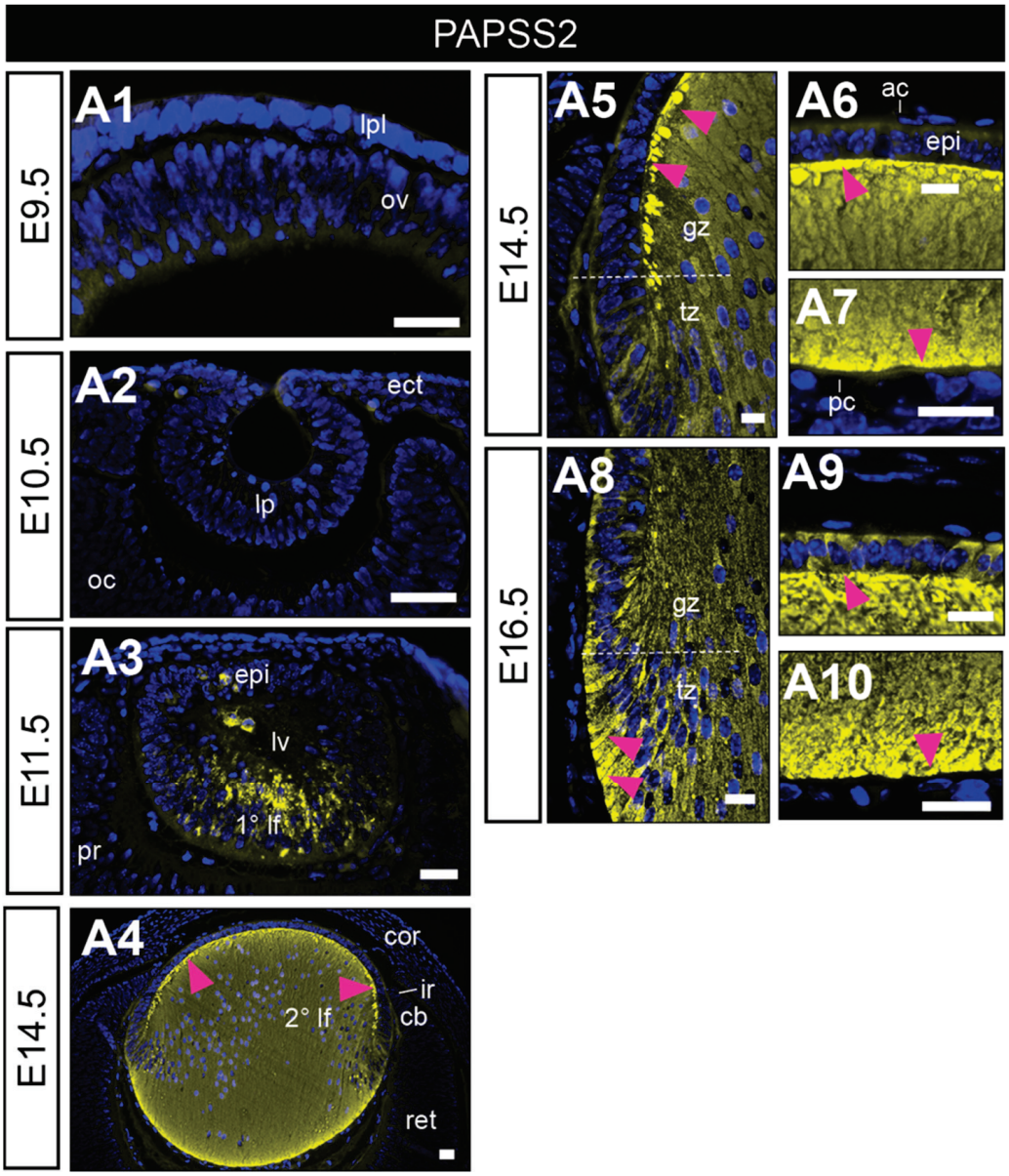

Figure 2. Immunolocalisation of PAPS synthetase-2 in the developing murine eye. Mid-sagittal mouse (FvB/N) eye sections from embryonic day-9.5 (E9.5; (**A1**), E10.5 (**A2**), E11.5 (**A3**), E14.5 (**A4**–**A7**) and E16.5 (**A8**–**A10**)) labelled for 3′-Phosphoadenosine 5′-Phosphosulphate Synthase 2 (PAPSS2; yellow). Nuclei counterstained with Hoechst (blue). Dotted white lines indicate lens equator (**A5**,**A8**). Magenta arrowheads indicate localisation at lens fibre tips (**A5**–**A10**). Lens placode (lpl), optic vesicle (ov), head ectoderm (ect), lens pit (lp), optic cup (oc), lens vesicle (lv), anterior lens epithelium (epi), primary lens fibre cells (1° lf), secondary lens fibre cells (2° lf), cornea (cor), retina (ret), ciliary body (cb), iris (ir), germinative zone (gz), transitional zone (tz), anterior lens capsule (ac), and posterior lens capsule (pc). Scale bars = 25 µm. Images in figures are oriented with ventral side positioned to the right and the dorsal side to the left.

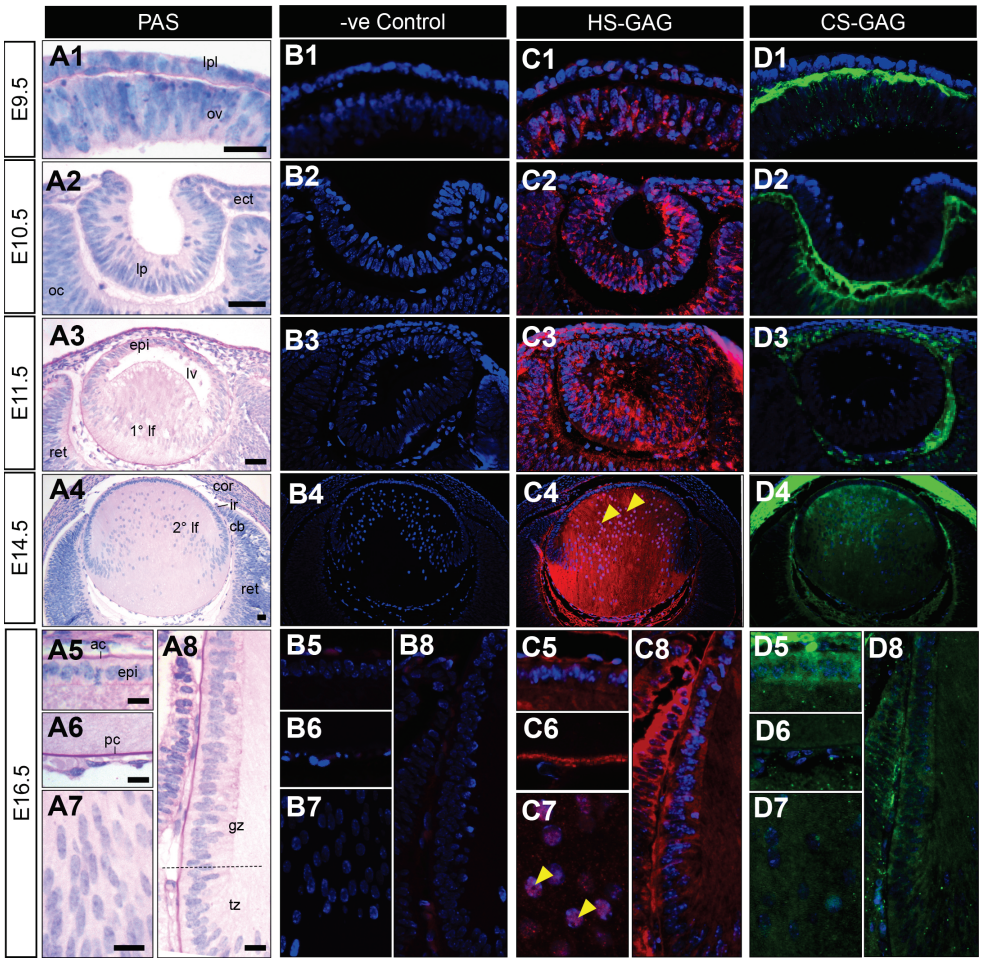

Figure 3. Distribution of sulphated GAGs in mouse eye development. Eye sections from embryonic day 9.5 (E9.5; (**A1**,**B1**,**C1**,**D1**), E10.5 (**A2**,**B2**,**C2**,**D2**), E11.5 (**A3**,**B3**,**C3**,**D3**), E14.5 (**A4**,**B4**,**C4**,**D4**), and E16.5 (**A5**–**A8**,**B5**–**B8**,**C5**–**C8**,**D5**–**D8**)) FvB/N mice. Mid-sagittal eye sections stained with periodic acid–Schiff's (PAS, (**A1**–**A8**)) show cell morphology. Sections stained with a secondary antibody only show representative negative controls (negative control; (**B1**–**B8**)). Sections labelled the highly sulphated "active" forms of heparan sulphate (HS-GAG, red, (**C1**–**C8**)) or chondroitin sulphate (CS-GAG, green, (**D1**–**D8**)) glycosaminoglycan chains. Nuclei counterstained with Hoechst (blue). Yellow arrowheads indicate nuclear localisation (**C4**,**C7**). Dotted lines indicate the lens equator (**A8**). The lens placode (lpl), head ectoderm (ect), preplacodal matrix (ppm); optic vesicle (ov), lens pit (lp), optic cup (oc), lens vesicle (lv), anterior lens epithelium (epi), primary lens fibre cells (1° lf), secondary lens fibre cells (2° lf), cornea (cor), retina (ret), ciliary body (cb), iris (ir), germinative zone (gz), transitional zone (tz), anterior lens capsule (ac), posterior lens capsule (pc). Scale bars = 25 μm. Images in the figures are oriented with a ventral side positioned to the right and the dorsal side to the left.

3.3. Syndecan HSPGs Are Differentially Spatially Localised in the Lens throughout Development

The different syndecan HSPGs differ in their expression, both temporally and spatially, at all major stages of eye development. Syndecan-1 remains absent from the developing lens until E16.5, where it is strongly localised to the lens capsule and posterior vessels of the tunica vasculosa lentis (tvl). Weak syndecan-1 staining is also observed in a subset of anterior lens epithelial cells and anterior secondary fibre cell tips (Figure 4(A5)). Syndecan-2 (Figure 4(B1)), -3 (Figure 4(C1)) and -4 (Figure 4(D1)) are found at E9.5 in both the optic vesicle and the lens placode. The expressions of these syndecans persist at embryonic day 10.5, with strong labelling in the lens pit and optic cup (Figure 4(B2,C2,D2)). Syndecan-2 strongly stained throughout the invaginating lens pit, while syndecan-3 and -4 labelled particularly strong in the posterior cells of the lens pit (Figure 4(C2,D2)). At E11.5, the prospective

lens epithelial cells and elongating primary lens fibre cells showed strong labelling of syndecan-2 (Figure 4(B3)) and -3 (Figure 4(C3)). For syndecan-2, this label was restricted to the primary lens fibres and absent from the anterior aspect of the lens (Figure 4(D3)). Syndecan-1 was absent from the lens up to E11.5, where it first appears to localise to the inner aspect of the retina (Figure 4(A3)). At E14.5, the localisation of each of the syndecans was distinct from each other. Syndecan-1 was primarily localised to the differentiating retinal ganglion cells, and the lens capsule and blood vessels (Figure 4(A4)). Syndecan-2 was strongly localised to the lens capsule, tvl, lens epithelial cells, and nuclei of fibre cells. It also showed strong localisation in the cornea and developing iris (Figure 4(B4)). Syndecan-3 (Figure 4(D3)) and -4 (Figure 4(D4)) were both present in the lens epithelium and fibres in different patterns. Syndecan-3 staining was primarily observed in the secondary lens fibres, concentrated on the anterior fibre tips. It was absent from newer secondary lens fibre cells (Figure 4(C4)). On the other hand, syndecan-4 staining was primarily observed in early secondary fibre cells, with distinct staining at the anterior and posterior fibre cell tips (Figure 4(D4)). These expression patterns were maintained at E16.5 for syndecan-2 (Figure 4(B5–B8)), -3 (Figure 4(C5–C8)), and -4 (Figure 4(D5–D8)). At E16.5, syndecan-1 was still absent from the lens cells, but strongly localised to the lens capsule (Figure 4(A5–A8)).

3.4. Glypican HSPGs Differ in Temporal Expression at Key Stages of Lens/Eye Development

At E9.5, glypican-4 is exclusively localised to the pre-placodal matrix (Figure 5(D1)), while glypican-2, -5, and -6 are present in both the lens placode cells and optic vesicle (Figure 5(B1,C1,E1,F1)). Glypican-1 was absent at this early stage (Figure 5(A1)). By E10.5, all glypicans were present in the lens pit and optic cup, apart from glypican-4, that was localised to the extracellular matrix between the lens pit and optic cup (Figure 5(D2)). The label for glypican-3 and -5 was concentrated upon the basal aspect of the lens pit in the presumptive primary lens fibre cells (Figure 5(C2,E2)). Glypican-1, -2, -5, and -6 were also present in the surface head ectoderm (Figure 5(A2,B2,E2,F2)). All glypicans were present in the lens vesicle (Figure 5(A2,B2,C2,E2,F2)), except for glypican-4, that was primarily localised to the lens capsule, differentiating retinal ganglion cells, and posterior lens blood vessels (Figure 5(D3)). At E11.5, glypican-3 stained all lens vesicle cells diffusely, with more intense staining in the presumptive lens epithelial cells (Figure 5(C3)). Glypican-1, -2, -5, and -6 were predominantly localised to the posterior elongating primary lens fibre cells (Figure 5(A3,B3,E3,F3)). These glypicans were mostly localised in a concentrated region at the posterior tips of the primary lens fibres, apart from glypican-6, that strongly labelled all fibre cells (Figure 5(F3)). From E14.5, the expression of glypicans was generally consistent. Glypican-1 (Figure 5(A4–A8)), -2 (Figure 5(B4–B8)), -3 (Figure 5(C4–C8)), and -5 (Figure 5(E4–E8)) were predominantly localised to the lens epithelium and newly differentiating secondary lens fibre cells, where perinuclear staining was observed for all four glypicans (Figure 5(A7,B7,C7,E7)). Glypican-4 was absent from lens cells, with some punctate staining in the anterior lens epithelium, and strong localisation to the lens capsule (Figure 5(D4–D8)). Glypican-6 was absent from the epithelium and transitional zone, but strongly labelled the cytoplasm of the fibre cells (Figure 5(F4–F8)).

Postnatally, in the 10-day-old rat lens, labelling for glypican-5 was localised to both epithelial and fibre cells, with stronger labelling at the germinative and transitional zones (Supplementary Figure S1(B1–B4)). Glypican-5 was also found in the corneal epithelium and endothelium (Supplementary Figure S1(B5,B7)), ciliary non-pigmented epithelium (Supplementary Figure S1(B8)), and in remnant blood vessels of the tunica vasculosa lentis (Supplementary Figure S1(B4)). Glypican-5 was absent from the lens capsule (Supplementary Figure S1(B1,B2,B4)).

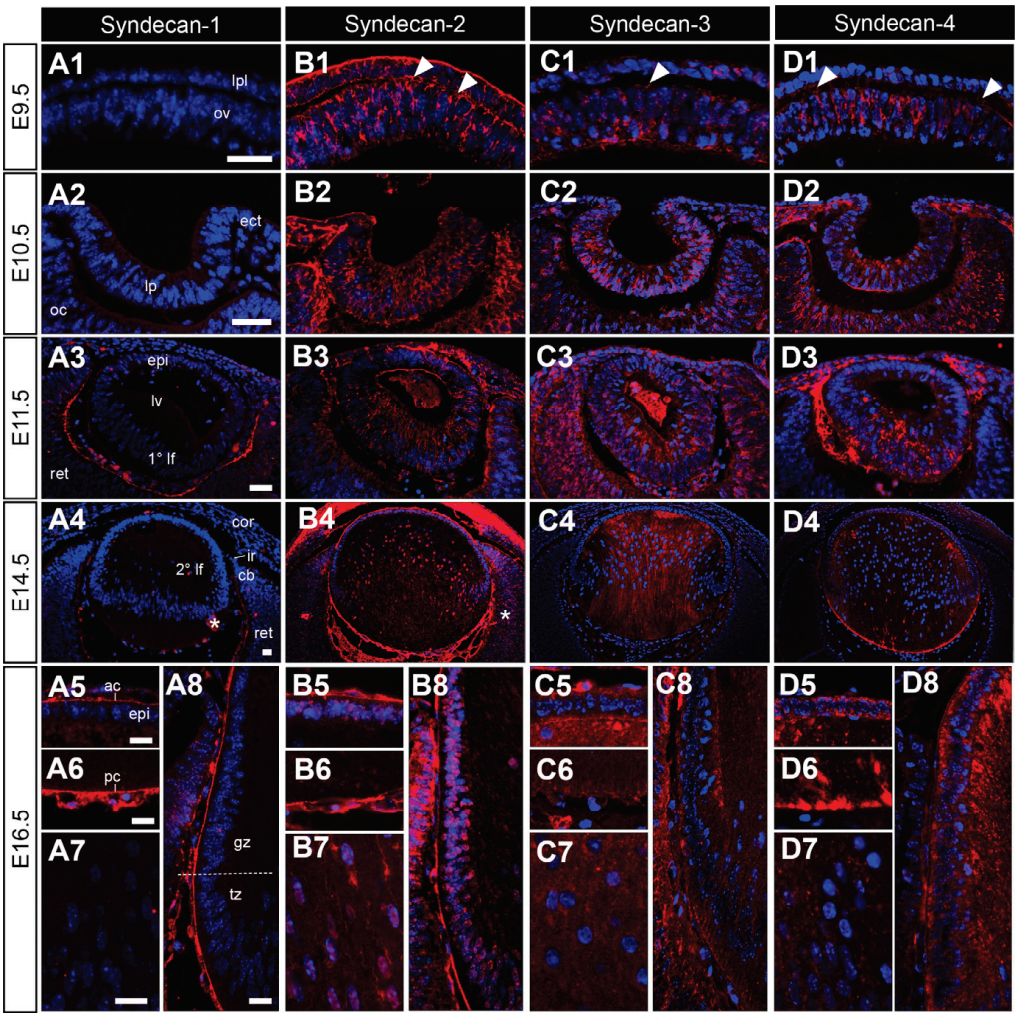

Figure 4. Distribution of syndecan core proteins in the developing mouse eye. Mid-sagittal sections from embryonic day-9.5 (E9.5; (**A1**,**B1**,**C1**,**D1**)), E10.5 (**A2**,**B2**,**C2**,**D2**), i5cat (**A3**,**B3**,**C3**,**D3**), E14.5 (**A4**,**B4**,**C4**,**D4**) and E16.5 (**A5**–**A8**,**B5**–**B8**,**C5**–**C8**,**D5**–**D8**)) FvB/N mice. Sections labelled for syndecan-1 (**A1**–**A8**), syndecan-2 (**B1**–**B8**), syndecan-3 (**C1**–**C8**), or syndecan-4 (**D1**–**D8**) HSPG core proteins (red). Nuclei counterstained with Hoechst (blue). Labelling of cell nuclei indicated in (**B7**,**B8**). White arrowheads indicate the staining of lens fibre cell tips (**C4**–**C6**,**C8**,**D3**, **D4**,**D6**–**D8**). The dotted line indicates the lens equator (**A8**). Lens placode (lpl), head ectoderm (ect), preplacodal matrix (ppm), optic vesicle (ov), lens pit (lp), optic cup (oc), lens vesicle (lv), anterior lens epithelium (epi), primary lens fibre cells (1° lf), secondary lens fibre cells (2° lf), cornea (cor), retina (ret), ciliary body (cb), iris (ir), germinative zone (gz), transitional zone (tz), anterior lens capsule (ac), and posterior lens capsule (pc). Scale bars = 25 µm. * denotes artefact. Images in the figures are oriented with the ventral side positioned to the right and the dorsal side to the left.

3.5. Localisation of High-Molecular-Weight HSPGs Extends beyond the Lens Capsule

Immunoreactivity for perlecan is weak in early lens structures (Figure 6(A1,A2)) but labelling appears to be stronger in the matrix and basement membranes of the E11.5 eye (Figure 6(A3)). At this stage, perlecan is observed in the anterior cells of the lens vesicle (Figure 6(A3)). This pattern of staining is maintained in the fully formed lens at E14.5 and E16.5, with perlecan mostly restricted to the lens capsule and anterior lens epithelium (Figure 6(A4–A8)). Diffuse perlecan staining was observed in the nuclei of some differentiating lens fibre cells (Figure 6(A7)). Both collagen XVIII/endostatin (Figure 6(B1,B2)) and agrin (Figure 6(C1,C2)) were observed in the cells of the lens placode and lens pit. Collagen XVIII/endostatin reactivity was restricted to a punctate label in the primary lens fibres

of the lens vesicle (Figure 6(B3)). This label persisted in the E14.5 lens (Figure 6(B4)). At E16.5, collagen XVIII/endostatin labelled in condensed patches throughout the cytoplasm of both lens epithelial and fibre cells (Figure 6(B5–B8)). On the other hand, agrin stained strongly throughout the cells of the lens vesicle, concentrated apically in the presumptive anterior lens epithelial cells, and basally in the new elongating primary lens fibre cells (Figure 6(C3)). From E14.5, agrin immunoreactivity was strongly visible throughput the cytoplasm of the central lens fibre cells (Figure 6(C4)), and this label persisted in the E16.5 lens (Figure 6(C5–C8)). Agrin was clearly associated with a subset of fibre cell nuclei (Figure 6(C4,C7)). Agrin staining was almost completely absent from the anterior lens epithelium and transitional zone (Figure 6(C4,C5,C8) and Table 1).

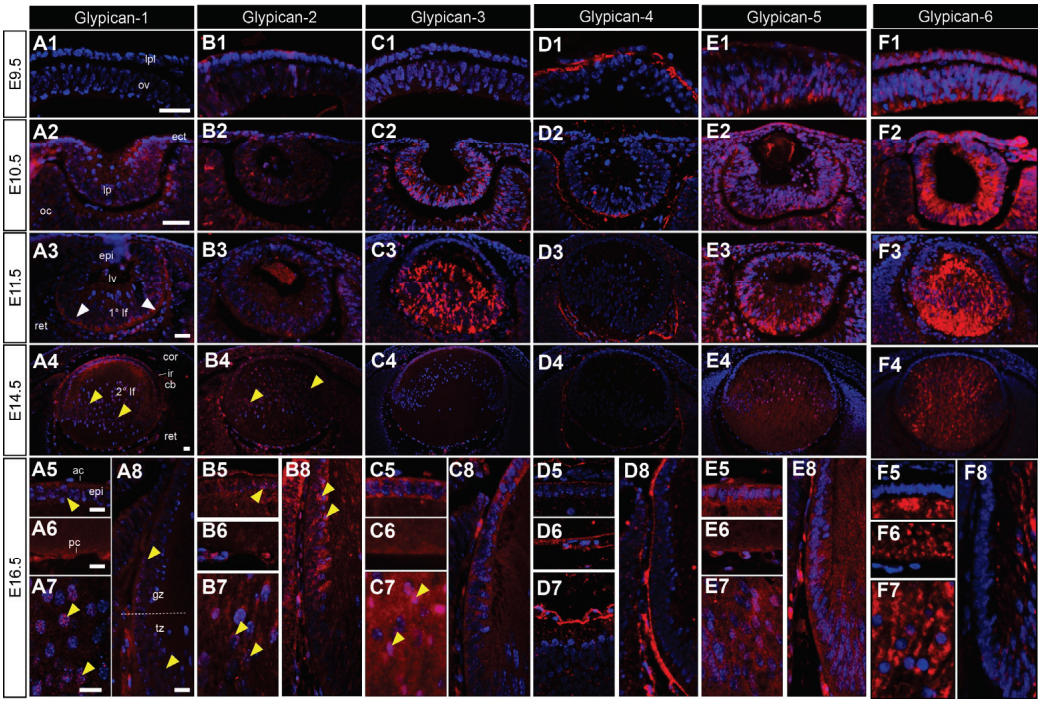

Figure 5. Distribution of glypican core proteins in the developing mouse eye. Mid-sagittal sections from embryonic day-9.5 (E9.5; (**A1–F1**)), E10.5 (**A2–F2**), E11.5 (**A3–F3**), E14.5 (**A4–F4**), and E16.5 (**A5–A8**,**B5–B8**,**C5–C8**,**D5–D8**,**E5–E8**,**F5–F8**) FvB/N mice. Sections labelled for glypican-1 (**A1–A8**), glypican-2 (**B1–B8**); glypican-3 (**C1–C8**), glypican-4 (**D1–D8**), glypican-5 (**E1–E8**), or glypican-6 (**F1–F8**) HSPG core proteins (red). Nuclei counterstained with Hoechst dye (blue). Yellow arrowheads indicate nuclear localisation (**A4**,**A5**,**A7**,**A8**,**B4**,**B5**,**B7**,**B8**,**C7**). White arrowheads indicate the staining of lens fibre cell tips (**A3**). Dotted lines indicate lens equator (**A8**). Lens placode (lpl), head ectoderm (ect), preplacodal matrix (ppm), optic vesicle (ov), lens pit (lp), optic cup (oc), lens vesicle (lv), anterior lens epithelium (epi), primary lens fibre cells (1° lf), secondary lens fibre cells (2° lf), cornea (cor), retina (ret), ciliary body (cb), iris (ir), germinative zone (gz), transitional zone (tz), anterior lens capsule (ac), and posterior lens capsule (pc). Scale bars = 25 µm. Images in figures are oriented with ventral side positioned to the right and the dorsal side to the left.

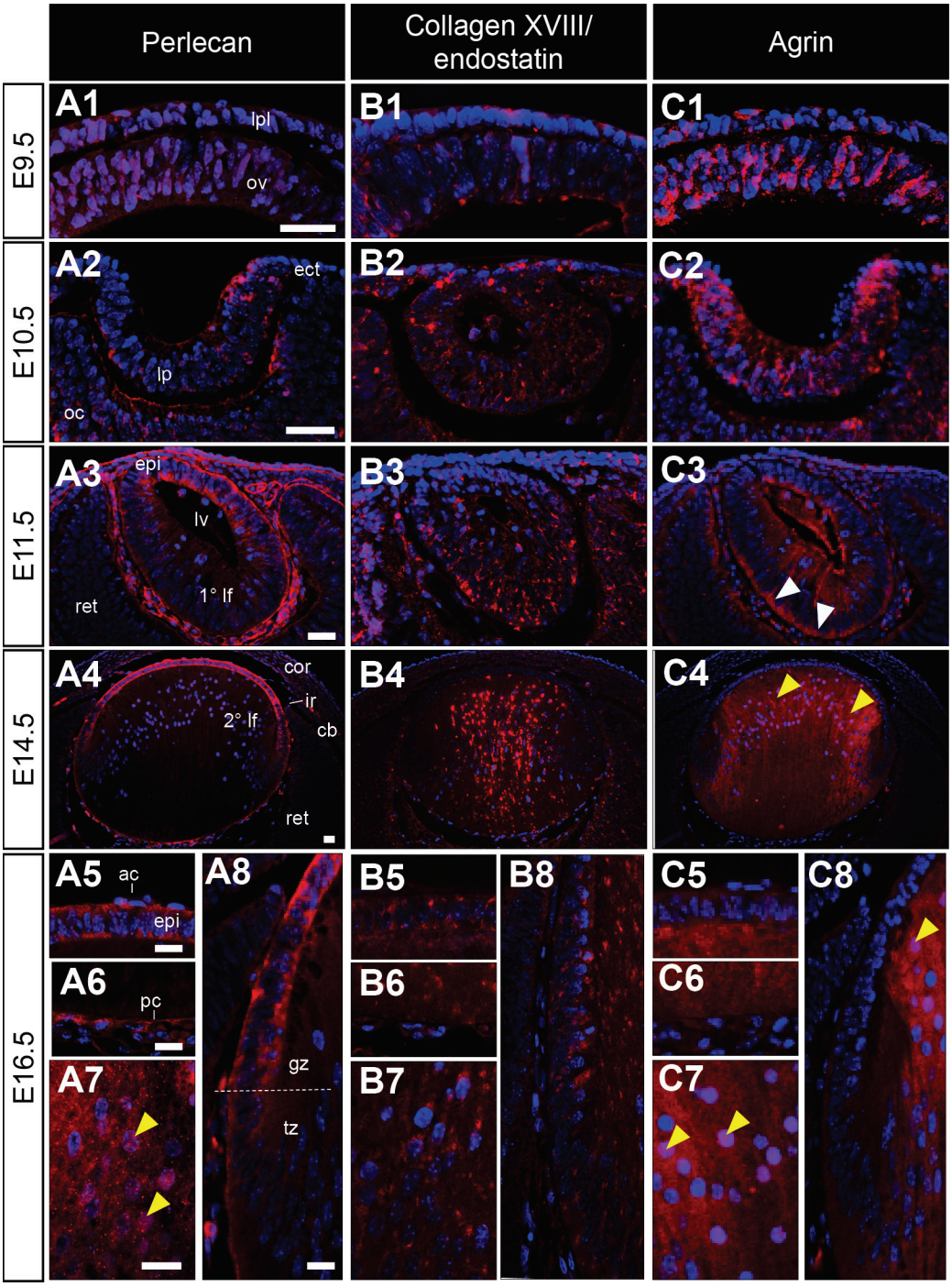

Figure 6. Distribution of high-molecular-weight HSPG core proteins in the developing mouse eye. Mid-sagittal sections from embryonic day-9.5 (E9.5; (**A1**–**C1**)), E10.5 (**A2**–**C2**), E11.5 (**A3**–**C3**), E14.5 (**A4**–**C4**), and E16.5 (**A5**–**A8**,**B5**–**B8**,**C5**–**C8**) FvB/N mice. Sections labelled for perlecan (**A1**–**A8**), collagen-XVIII/endostatin (**B1**–**B8**), or agrin (**C1**–**C8**) HSPG core proteins (red). Nuclei counterstained with Hoechst dye (blue). Yellow arrowheads indicate nuclear localisation (**A7**,**C4**,**C7**,**C8**). White arrowheads indicate the staining of the lens fibre cell tips (**C3**). Dotted lines indicate the lens equator (**A8**). The lens placode (lpl), head ectoderm (ect), optic vesicle (ov), lens pit (lp), optic cup (oc), lens vesicle (lv), anterior lens epithelium (epi), primary lens fibre cells (1° lf), secondary lens fibre cells (2° lf), cornea (cor), retina (ret), ciliary body (cb), iris (ir), germinative zone (gz), transitional zone (tz), anterior lens capsule (ac), and posterior lens capsule (pc). Scale bars = 25 µm. Images in figures are oriented with ventral side positioned to the right and the dorsal side to the left.

Table 1. Summary of HSPG immunolocalisation in mouse eye lens development.

Embryonic Day		GAG	Other	Core Proteins
E9.5	Lens placode	HS		Sdc2, Sdc3, Sdc4, Gpc2, Gpc4, Gpc5, Gpc6, perlecan, collagen XVIII, agrin
	Optic vesicle	HS, CS		Sdc2, Sdc3, Sdc4, Gpc2, Gpc5, Gpc6, perlecan, collagen XVIII, agrin
	Preplacodal matrix	CS		Sdc2, Sdc4, Gpc4, Agrin
E10.5	Lens pit	HS		Sdc2, Sdc3, Sdc4, Gpc1, Gpc2, Gpc3, Gpc5, Gpc6, perlecan, collagen XVIII, agrin
	Head ectoderm	HS		Sdc2, Sdc3, Sdc4, Gpc1, Gpc2, Gpc3, Gpc4, Gpc5, Gpc6, perlecan, agrin
	Optic cup	HS, CS		Sdc2, Sdc3, Sdc4, Gpc1, Gpc2, Gpc3, Gpc4, Gpc5, Gpc6, perlecan, collagen XVIII, agrin
	Extracellular matrix (lens pit-optic cup)	CS		Sdc2, Gpc4, perlecan?
E11.5	Anterior lens epithelium	HS	PAPSS2	Sdc2, Sdc3, Sdc4, Gpc1, Gpc2, Gpc3, perlecan, collagen XVIII, agrin
	1° lens fibre cells	HS	PAPSS2	Sdc2, Sdc3, Sdc4, Gpc1, Gpc2, Gpc3, Gpc5, Gpc6, perlecan, collagen XVIII, agrin
	Lens capsule	HS		Sdc1, Sdc2, Gpc4, perlecan
E14.5	Anterior lens epithelium	HS *, CS		Sdc2 *, Sdc3, Sdc4, Gpc1, Gpc2, Gpc3, Gpc4, perlecan, collagen XVIII
	2° lens fibre cells	HS *, CS	PAPSS2	Sdc2 *, Sdc3, Sdc4, Gpc1, Gpc2, Gpc3, Gpc5, Gpc6, collagen XVIII, agrin
	Lens capsule	HS, CS		Sdc1, Sdc2, Gpc2, Gpc4, perlecan
	Tunica vasculosa lentis	HS, CS		Sdc1, Sdc2, Gpc1, Gpc2, Gpc4, Gpc5, perlecan
E16.5	Anterior lens epithelium	HS *, CS		Sdc2 *, Sdc3, Sdc4, Gpc1 *, Gpc2 *, Gpc3 *, Gpc5, perlecan, collagen XVIII, agrin
	2° lens fibre cells	HS *, CS	PAPSS2	Sdc2 *, Sdc3, Sdc4, Gpc1 *, Gpc2 *, Gpc3 *, Gpc5, Gpc6, perlecan *, collagen XVIII, agrin *
	Lens capsule	HS		Sdc1, Sdc2, Gpc4, perlecan
	Tunica vasculosa lentis	HS, CS		Sdc1, Sdc2, Gpc1, Gpc2, Gpc4, Gpc5, perlecan

* Nuclear localisation in cells.

4. Discussion

While there are many reports to date studying vertebrate lens morphogenesis and the growth factors involved, less is understood about how these different growth factors are positioned to drive this development. Given the important role of HSPGs in regulating many growth factors, together with recent studies implicating HSPGs as essential for the induction and development of the eye, here we present the most comprehensive spatiotemporal labelling of all the different HSPG core proteins and their associated GAGs throughout murine lens development. This study complements and extends from our earlier report on the localisation of HSPGs in the postnatal rat lens [35], wherein we described how the defined patterns of all HSPGs associate with lens cellular activity. Of note is that our earlier study reported the absence of glypican 5 in the postnatal lens, of which we now have corrected and clearly show that it is indeed also present in the lens when using a more selective and effective commercial antibody. Given that all HSPGs are expressed in the lens, by linking the defined localisation of their respective HSPG core proteins, along with their reported mode of activity, it can provide valuable insights into their functional roles [36,37].

The activity of HSPGs is largely dependent on the distinct sulfotransferases of their HS chains, which source sulphate from PAPS produced by PAPSS1/2 synthetases [38,39]. Transcriptome data identify both *papss1* and *papss2* in the lens [40], with strong PAPSS2 protein labelling in the developing murine and postnatal rat eye, specifically in the lens [38]. Here, we found that PAPSS2 was absent in very early lens induction (i.e., lens placode, lens pit), with strong reactivity first appearing in the lens vesicle, distinctly labelling the elongating primary lens fibre cells. This fibre-specific label persisted and was later observed in secondary lens fibres at E14.5 and E16.5 when the differentiating lens epithelium also began to label strongly for PAPSS2. The weak to no immunolabelling for PAPSS2 in the lens placode and pit is of interest as we see the strong labelling of not only HS-GAG but many HSPGs that require PAPSS for their sulfation. The absence of PAPPS2 suggests that the activity of HSPGs in early lens induction may be largely mediated by HSPG core protein–protein interactions, and is independent of GAG–protein interactions, implying an expected low sulfation and binding potential of these HSPGs with ocular growth factors. An example of this is glypican-4, that only carries HS chains but does not overlap in expression with HS-GAG. Alternatively, it is also plausible that the other PAPSS isoform, PAPSS1 (encoded by the *papss1* gene), is the predominant sulphate donor at this early stage of lens development, consistent with transcript expression profiles from published embryonic mouse lens datasets [41–44].

The selectivity of interactions between HSPGs and proteins is not solely determined by the type of core protein (such as syndecan or glypican) or its location (for example, on the cell surface or in the extracellular matrix), but also by the precise structure (i.e., sulphation) of the HS-GAG chains. Although HSPGs are primarily composed of HS-GAGs, certain species such as syndecan-1/-3 [45,46], agrin [47], and collagen XVIII [48] may also carry CS-GAGs. Lens cells produce some proteoglycans carrying both HS-GAG and CS-GAG, although HS-GAG is the most common [35,49,50]. Consistent with this, here we report that HS-GAG, and not CS-GAG, is the predominant GAG associated with HSPGs throughout murine lens development. Unlike HS-GAG, CS-GAG was absent from the lens until E14.5, indicating that HS-GAGs are likely the major species regulating the early events of lens induction, invagination, and cell fate specification. The presence of CS-GAG in the pre-placodal and peri-lenticular matrix throughout development may suggest a role in cell–matrix interactions or morphogen gradient formation. In contrast, HS-GAG was absent from the ocular matrix throughout the early stages of lens development, instead appearing and localising predominantly to the presumptive and differentiating lens cells. These patterns were often associated with regions of lens cell activity (i.e., lens placode, posterior aspect of lens pit/vesicle and lens transitional zone). The expression patterns of HS-GAG and CS-GAG in the developing lens suggest that both GAG types may have overlapping and distinct roles in regulating functional cellular processes. For instance, fibre differentiation may be regulated by both GAG types, while morphogen gradient formation in the lens capsule may be predominantly regulated by HS-GAG. In other tissues, such as the developing brain, HS-GAG and CS-GAG have been shown to serve distinct functional roles, with CS-GAG stabilizing existing synaptic connections and HS-GAG stimulating the formation of new synapses [51]. These functional differences are likely due to the selective interaction of each GAG type with different proteins in a structure-dependent manner [52]. The reported differential localisation of HS-GAG and CS-GAG [51,53,54] is consistent with their distinct functional roles [55].

Most of the HSPG core proteins that we examined localised to the cells of the surface head ectoderm and optic vesicle; however, syndecan-1 and glypican-1 were both absent at this stage. Despite being a traditionally cell-associated HSPG, glypican-4 was absent from the head ectoderm and optic vesicle but was strongly localised to the pre-placodal matrix. Similarly, syndecan-2, which is traditionally a cell-associated HSPG, was also observed in the pre-placodal matrix, along with the surface head ectoderm and optic vesicle, consistent with previous reports of syndecan-2 being a matrix-associated HSPG in ocular tissues [35,56]. The pre-placodal matrix is thought to prevent this defined region

of proliferative head ectodermal cells from spreading, so that their continued proliferation and progressive cell crowding thickens this region of the ectoderm to form the lens placode [57]. The regulated signalling activities of several mitogens and morphogens, such as BMPs, Hh, FGFs, and Wnts, orchestrate the inductive events associated with the optic vesicle-presumptive lens interaction [58,59], and all these growth factors have been shown to be regulated by the HSPGs that we localise to the lens placode [60–64]. FGF, Hh, BMP, and Wnt-signalling are each essential regulators in eye development, with their on/off switching essential for different stages of lens development [6], and defects in their signalling activity shown to compromise lens development. While the sustained inductive signalling of BMP and FGF are essential for lens placode development and the early stages of lens specification [65], these early stages also require the inhibition of Hh- [16] and Wnt- [66] signalling, with heightened Hh-signalling activity shown to suppress lens formation in zebrafish [67]. Later in lens morphogenesis, Wnt-signalling is activated to promote epithelial cell adhesion, integrity, and polarity, as well as fibre differentiation [11,66,68,69]. Constitutively active Hh-signalling through its receptor, patched, promotes epithelial maintenance at the expense of fibre differentiation [70]. Thus, the inhibition of Hh-signalling, once again with fibre cell differentiation, is essential for normal lens development. BMP-signalling promotes apical constriction and pro-survival signals during lens placode invagination and drives proliferation of lens epithelial cells and cell cycle exit at the transitional zone, that is bolstered by FGF-signalling driving lens epithelial cell proliferation and fibre differentiation [13,14,71].

The spatiotemporal regulation of the ocular morphogens, together with other extracellular signalling proteins, forms the basis of lens patterning, polarity, growth, and cell fate specification [1,6,72], that are regulated by the many HSPGs we report to be expressed herein. Many of these same HSPGs regulate other matrix-related proteins, including β1-integrins and fibronectin [73–75], that are also co-localised to the early lens placode cells, and play an essential role in this inductive process [76–79].

Glypicans are predominantly expressed during embryonic development, and increasing evidence suggests that they are major regulators of morphogenic signalling and gradient events in development, controlling left/right and dorsal/ventral patterning, as well as controlling tissue size and growth cues [80]. Genetic and biochemical studies have shown that glypicans can stimulate or inhibit the signalling pathways triggered by Wnts, Hh, BMPs, and FGFs, that have been mentioned to be responsible for patterning and tissue formation during embryogenesis, depending on the context of the tissue to drive growth patterning events [80]. Not surprisingly, mutations in genes encoding glypicans often result in developmental abnormalities or overgrowth [80]. For instance, Glypican-3 has been shown to inhibit hedgehog signalling during development by competitively binding to the ligand, preventing it from binding to patched, through a HS-GAG independent process [61]. Similarly, Glypicans-1, -3, and -4 negatively regulate BMP-signalling by competing with BMP receptors for ligand binding in a similar fashion [81,82]. On the other hand, glypicans seem to both positively and negatively regulate Wnt-signalling in different developmental systems. Glypican-4 promotes cardiac specification and differentiation by attenuating canonical Wnt- and BMP-signalling [81], while glypican-1 can act as a Wnt-coreceptor to activate Wnt-signalling [82]. For different morphogens, glypicans seem to mainly activate or enhance signalling. Glypicans can interact with FGFs and their receptors to stabilize their assembly and enhance downstream ERK1/2 or PI3K/Akt, as well as bind to TGF-β and its receptors to promote SMAD-signalling [82].

As the mouse lens placode and optic vesicle invaginate at E10.5, we find that most of the HSPG core proteins localise to the cells of the lens pit, with syndecan-1 and glypican-4 yet to appear. Glypican-4 was predominantly localised to the surrounding matrix together with syndecan-2 and perlecan. Here, we begin to observe subtle changes between some of the core proteins, such as syndecan-4, that appears to distinctly label the posterior tips of lens pit cells, with the majority of the other core proteins localising diffusely throughout all the lens pit cells. BMP-4/-7 activity [83] and the downstream activation of GTPases

(RhoA, Rac1, ROCK) drive changes in cytoskeletal architecture essential for cell elongation, apical constriction, and epithelial invagination during lens pit formation [84]. Glypican-3 is well established as a primary regulator of cellular responses of BMP-4/-7 in developing tissues [85], although emerging evidence suggests that other HSPGs, such as agrin [86] and syndecan-3 [87], may also play tissue-specific roles in BMP regulation. On the other hand, the syndecans are major regulators of RhoA/Rac1/ROCK GTPase-signalling and cytoskeletal modifications, through interactions with the intracellular domains of their core proteins [88–90].

As the mouse lens acquires more of an antero-posterior polarity with the formation of the lens vesicle at E11.5, we see that the acute change in posterior lens vesicle cell elongation to form the first primary fibres is associated with much HSPG activity. In the first instance, we not only have PAPPS2 appearing in these cells, but also co-localising with HS-GAG and the core proteins of most HSPGs, suggesting their putative roles in the differentiation, attachment, and elongation of primary lens fibre cells. Syndecan-1 continues to remain absent not only from lens cells but from all developing eye structures. Given that PAPSS2 appears distinctly at this developmental stage, overlapping with many HSPGs and HS-GAGs, this suggests a marked rise in HS sulfotransferase activity that may be essential to drive primary lens fibre differentiation. With the differentiation of the primary fibres, we also have the concomitant differentiation of the anterior lens vesicle cells to form the epithelium. Lens epithelial cell differentiation is known to be regulated by Wnt/beta-catenin signalling [68] which in turn is regulated by glypican-3 [91], that is perfectly positioned for this, given the strong reactivity we observe in the anterior lens cells.

While we show that glypicans appear to generally localise in similar patterns to syndecans, the glypicans display temporal differences in their onset. This may be indicative of different core proteins regulating different developmental/cell fate specification/patterning events. It may be the case that the variable spatiotemporal localisation of the different HSPGs, particularly glypicans, throughout lens development is representative at least in part by their differential regulation of the morphogenetic switches in signalling events [80]. Although no lens-specific phenotypes have been reported for animals deficient in glypicans, compensatory regulation between closely related HSPGs (i.e., glypicans-2/-4 and -3/-5) is likely. Our understanding of this family of HSPGs and how they function in different tissues is still very limited.

The larger secreted HSPGs, perlecan [35,92–94], collagen XVIII [35,92], and agrin [35,95] are recognized as the predominant HSPGs in the postnatal lens capsule; however, we have previously reported different patterns of other HSPG core proteins (syndecans-1/-2/-4 and glypicans-2/-4) in the postnatal rat lens capsule: syndecan-2 and perlecan are abundant throughout the lens capsule, while syndecan-4, glypican-2, glypican-4, collagen XVIII/endostatin, and agrin are restricted to the outer reticular lamina of the lens capsule [35]. In contrast, syndecan-1-labelling appeared to be uniquely limited to the basal lamina. In the developing mouse eye, we only observed a subset of these HSPGs in the lens capsule (syndecans-1/-2/-4, glypican-4 and perlecan), suggesting that some HSPGs (i.e., glypican-2, collagen XVIII, and agrin) are deposited in the capsule at later stages. Of the minor HSPG core proteins we observed in the developing lens, three are syndecans, that bind to several structural and matrix regulatory proteins found in the lens capsule (e.g., collagen IV, laminin, fibronectin and integrins), and have previously been implicated as key regulators of ECM assembly, cell–matrix interactions, and cell adhesion [38].

Perlecan exists in an antero-posterior gradient in the lens capsule, consistent with complimentary antero-posterior gradients of FGF bioavailability and signalling activity [96,97]. Perlecan HSPGs are also required for the structural integrity of the lens capsule [36], as it is shown here to be progressively deposited to the capsule over the course of lens development, consistent with its label in the embryonic chick lens [98]. While the other large secreted high-molecular-weight HSPGs, collagen XVIII, and agrin are often reported to be associated with ECM and basement membranes, here we report that both these core proteins are present from the earliest stages of lens development, primarily within the cells

of the presumptive and developing lens, and are not observed in the lens capsule, as we previously reported in the postnatal rat lens [38]. Rather, they are primarily associated with the lens epithelium, and show particularly strong staining in lens fibre cells. Mice deficient for *col18a1*, encoding the collagen XVII core protein, have a widespread malformation of ocular tissues [99,100], with the overexpression of the endostatin domain of Collagen XVIII leading to cataract and structurally compromised basement membranes [101,102]. The overexpression of agrin also produces a dysgenic phenotype that is specific to the eye [95]. Similarly, the knock-down of agrin in zebrafish embryos results in a small eye and lens phenotype, leading to decreased HS-GAG staining in the lens, but not retina, suggesting that other HSPGs may be upregulated in response to this loss of agrin [103]. The knockdown of agrin in zebrafish also leads to selectively decreased FGF-signalling and the downstream activity of MAPK/ERK in the lens, providing strong evidence that agrin is likely regulating FGF-ERK signalling activity in the developing lens [103]. Interestingly, the strong pattern of HSPG-labelling in the posterior lens vesicle cells mirrors that of phospho-ERK1/2 staining [104]. Since FGF/ERK-signalling is required for lens fibre cell elongation [105], and agrin is strongly localised to both the rapidly elongating primary and secondary lens fibres, it may be playing an important role in FGF-induced lens fibre differentiation. Notably, agrin is absent from the transitional zone of the lens, where cells exit the cell cycle and begin to differentiate into fibres, instead of selectively staining the elongated/ing lens fibres.

Here, we report on the immunolabelling of HS-GAG and specific core proteins in the nuclei of lens epithelial cells (syndecan-2) and fibre cells (syndecan-2, glypican-1, glypican-5, perlecan, and agrin). Some of these HSPGs have previously been reported in the cell nuclei of other tissues, such as glypican-1 (neurons, glial cells); [106] and agrin (developing rat brain cells) [107], while other HSPGs (i.e., glypican-5), to the best of our knowledge, are reported herein for the first time in the nuclei of lens cells. HS-GAG and HSPG core proteins in select cell types have been proposed to play roles in the transport of cargo or growth factor/receptor complexes to the cell nucleus (e.g., FGF/FGFR) to regulate gene expression [35,108]. The presence or absence of HSPGs correlates with cellular function, phenotype, and changes in cell cycle phases, suggesting that their placement in the nucleus may control cellular function [35,108]. Here, we report that most HSPGs associated with lens cell nuclei are present in the transitional zone or in new fibre cells, where the lens epithelial cells exit the cell cycle and undergo major morphological changes to differentiate into fibre cells, suggesting that these specific HSPGs may play a regulatory role in these processes. Further investigations are necessary to elucidate the specific functional roles of HSPGs in lens cells. The current study is the first to comprehensively map all HSPG localisation in a developing tissue during organogenesis. The unique patterns of expression observed here for HSPG core proteins in the developing lens imply that, during differentiation, lens cells acquire a distinct set of HSPGs that may interact selectively with proteins, resulting in distinct patterns of HS-protein binding and signalling regulation. Moreover, our findings suggest that different HSPGs may play distinct and overlapping roles at different stages of lens induction and morphogenesis. In conjunction with earlier research, our findings also suggest that HS-GAG sulfation is necessary for growth factor-induced cellular processes in the lens, and that PAPSS2 plays a distinct temporal role as a sulphate donor. By further characterizing and specifically modulating the different sulphated HSPGs expressed in the lens, we hope to better understand how HSPGs regulate different growth factor-mediated signalling, and its respective lens cell behaviour. With this, the specific roles of HSPGs in modulating growth factor activity could facilitate the development of innovative approaches for manipulating cellular behaviour. Such strategies could have broader implications beyond the context of lens biology and diseases, extending to other growth factor-mediated pathologies.

Supplementary Materials: The following supporting information can be downloaded at: https://www.mdpi.com/article/10.3390/cells12101364/s1, Figure S1: Distribution of glypican-5 core protein in the 10-day-old rat eye; Table S1: Primary antibodies used for GAG and core protein immunolocalisation.

Author Contributions: Conceptualization, T.F.L.W. and F.J.L.; methodology, T.F.L.W.; software, T.F.L.W.; validation, T.F.L.W.; formal analysis, T.F.L.W.; investigation, T.F.L.W.; resources, F.J.L.; data curation, T.F.L.W.; writing—original draft preparation, T.F.L.W.; writing—review and editing, T.F.L.W. and F.J.L.; visualization, T.F.L.W.; supervision, F.J.L.; project administration, T.F.L.W. and F.J.L.; funding acquisition, T.F.L.W. and F.J.L. All authors have read and agreed to the published version of the manuscript.

Funding: This research was supported by internal funding by the Save Sight Institute, The University of Sydney, NSW, Australia.

Institutional Review Board Statement: The animal study protocol was approved by The University of Sydney Animal Ethics Committee (AEC #2021/1913) and conducted in accordance with the guidelines set by the National Health and Medical Research Council (Australia).

Acknowledgments: We would like to acknowledge the gift of the perlecan antibody from Marie Dziadek, The University of NSW, NSW, Australia.

Conflicts of Interest: The authors declare no conflict of interest.

References

1. McAvoy, J.W.; Chamberlain, C.G.; de Longh, R.U.; Hales, A.M.; Lovicu, F.J. Lens development. *Eye* **1999**, *13*, 425–437. [CrossRef]
2. Lovicu, F.J.; Ang, S.; Chorazyczewska, M.; McAvoy, J.W. Deregulation of lens epithelial cell proliferation and differentiation during the development of TGFβ-induced anterior subcapsular cataract. *Dev. Neurosci.* **2004**, *26*, 446–455. [CrossRef]
3. Wormstone, M.I.; Wride, M.A. The ocular lens: A classic model for development, physiology and disease. *Philos. Trans. R. Soc. B Biol. Sci.* **2011**, *366*, 1190–1192. [CrossRef]
4. Lovicu, F.J.; McAvoy, J.W. Growth factor regulation of lens development. *Dev. Biology* **2005**, *280*, 1–14. [CrossRef]
5. Cvekl, A.; Ashery-Padan, R. The cellular and molecular mechanisms of vertebrate lens development. *Development* **2014**, *141*, 4432–4447. [CrossRef]
6. Cvekl, A.; Zhang, X. Signaling and Gene Regulatory Networks in Mammalian Lens Development. *Trends Genet.* **2017**, *33*, 677–702. [CrossRef]
7. McAvoy, J.W.; Chamberlain, C.G.; de Iongh, R.U.; Richardson, N.A.; Lovicu, F.J. The role of fibroblast growth factor in eye lens development. *Ann. N.Y. Acad. Sci.* **1991**, *638*, 256–274. [CrossRef]
8. Faber, S.C.; Dimanlig, P.; Makarenkova, H.P.; Shirke, S.; Ko, K.; Lang, R.A. Fgf receptor signaling plays a role in lens induction. *Development* **2001**, *128*, 4425–4438. [CrossRef]
9. Robinson, M.L. An essential role for FGF receptor signaling in lens development. *Semin. Cell Dev. Biol.* **2006**, *17*, 726–740. [CrossRef]
10. De Iongh, R.U.; Abud, H.E.; Hime, G.R. WNT/Frizzled signaling in eye development and disease. *Front. Bioscience* **2006**, *11*, 2442–2464. [CrossRef]
11. Chen, Y.; Stump, R.J.W.; Lovicu, F.J.; Shimono, A.; McAvoy, J.W. Wnt signaling is required for organization of the lens fiber cell cytoskeleton and development of lens three-dimensional architecture. *Dev. Biol.* **2008**, *324*, 161–176. [CrossRef]
12. Sugiyama, Y.; Lovicu, F.J.; McAvoy, J.W. Planar cell polarity in the mammalian eye lens. *Organogenesis* **2011**, *7*, 191–201. [CrossRef] [PubMed]
13. Faber, S.C.; Robinson, M.L.; Makarenkova, H.P.; Lang, R.A. Bmp signaling is required for development of primary lens fiber cells. *Development* **2002**, *129*, 3727–3737. [CrossRef]
14. Shu, D.Y.; Lovicu, F.J. Insights into Bone Morphogenetic Protein—(BMP-) Signaling in Ocular Lens Biology and Pathology. *Cells* **2021**, *10*, 2604. [CrossRef]
15. Tsonis, P.A.; Vergara, M.N.; Spence, J.R.; Madhavan, M.; Kramer, E.L.; Call, M.K.; Santiago, W.G.; Vallance, J.E.; Robbins, D.J.; Del Rio-Tsonis, K. A novel role of the hedgehog pathway in lens regeneration. *Dev. Biol.* **2004**, *267*, 450–461. [CrossRef] [PubMed]
16. Pillai-Kastoori, L.; Wen, W.; Wilson, S.G.; Strachan, E.; Lo-Castro, A.; Fichera, M.; Musumeci, S.A.; Lehmann, O.J.; Morris, A.C. Sox11 Is Required to Maintain Proper Levels of Hedgehog Signaling during Vertebrate Ocular Morphogenesis. *PLoS Genet.* **2014**, *10*, e1004491. [CrossRef]
17. Sarrazin, S.; Lamanna, W.C.; Esko, J.D. Heparan sulfate proteoglycans. *Cold Spring Harb. Perspect. Biol.* **2011**, *3*, a004952. [CrossRef] [PubMed]
18. Dreyfuss, J.L.; Regatieri, C.V.; Jarrouge, T.R.; Cavalheiro, R.P.; Sampaio, L.O.; Nader, H.B. Heparan sulfate proteoglycans: Structure, protein interactions and cell signaling. *An. Acad. Bras. Cienc.* **2009**, *81*, 409–429. [CrossRef]
19. Wong, K.O.; Wong, K.P. Direct measurement and regulation of 3"-phosphoadenosine 5-"phosphosulfate (PAPS) generation in vitro. *Biochem. Pharmacol.* **1996**, *52*, 1187–1194. [CrossRef]
20. Schröder, E.; Gebel, L.; Eremeev, A.A.; Morgner, J.; Grum, D.; Knauer, S.K.; Bayer, P.; Mueller, J.W. Human PAPS Synthase Isoforms Are Dynamically Regulated Enzymes with Access to Nucleus and Cytoplasm. *PLoS ONE* **2012**, *7*, e29559. [CrossRef]
21. Quarto, N.; Amalric, F. Heparan sulfate proteoglycans as transducers of FGF-2 signalling. *J. Cell Sci.* **1994**, *107 Pt 11*, 3201–3212. [CrossRef] [PubMed]

22. Ornitz, D.M. FGFs, heparan sulfate and FGFRs: Complex interactions essential for development. *BioEssays* **2000**, *22*, 108–112. [CrossRef]
23. Ashikari-Hada, S.; Habuchi, H.; Kariya, Y.; Itoh, N.; Reddi, A.H.; Kimata, K. Characterization of Growth Factor-binding Structures in Heparin/Heparan Sulfate Using an Octasaccharide Library. *J. Biol. Chem.* **2004**, *279*, 12346–12354. [CrossRef]
24. Pegge, J.; Tatsinkam, A.J.; Rider, C.C.; Bell, E. Heparan sulfate proteoglycans regulate BMP signalling during neural crest induction. *Dev. Biol.* **2020**, *460*, 108–114. [CrossRef] [PubMed]
25. Fuerer, C.; Habib, S.J.; Nusse, R. A study on the interactions between heparan sulfate proteoglycans and Wnt proteins. *Dev. Dyn.* **2010**, *239*, 184–190. [CrossRef] [PubMed]
26. Mii, Y.; Takada, S. Heparan Sulfate Proteoglycan Clustering in Wnt Signaling and Dispersal. *Front. Cell Dev. Biol.* **2020**, *8*, 631. [CrossRef] [PubMed]
27. Carrasco, H.; Olivares, G.H.; Faunes, F.; Oliva, C.; Larraín, J. Heparan sulfate proteoglycans exert positive and negative effects in Shh activity. *J. Cell. Biochem.* **2005**, *96*, 831–838. [CrossRef]
28. Palma, V.; Carrasco, H.; Reinchisi, G.; Olivares, G.; Faunes, F.; Larraín, J. SHh activity and localization is regulated by perlecan. *Biol. Res.* **2011**, *44*, 63–67. [CrossRef]
29. Couchman, J.R.; Woods, A. Syndecan-4 and integrins: Combinatorial signaling in cell adhesion. *J. Cell Sci.* **1999**, *112*, 3415–3420. [CrossRef]
30. Yang, N. Syndecan-1-induced ECM fiber alignment requires integrin αvβ3 and syndecan-1 ectodomain and heparan sulfate chains. *PLoS ONE* **2016**, *11*, e0150132. [CrossRef]
31. Carulli, S.; Beck, K.; Dayan, G.; Boulesteix, S.; Lortat-Jacob, H.; Rousselle, P. Cell surface proteoglycans syndecan-1 and -4 bind overlapping but distinct sites in laminin α3 LG45 protein domain. *J. Biol. Chem.* **2012**, *287*, 12204–12216. [CrossRef] [PubMed]
32. Tumova, S.; Woods, A.; Couchman, J.R. Heparan sulfate chains from glypican and syndecans bind the Hep II domain of fibronectin similarly despite minor structural differences. *J. Biol. Chem.* **2000**, *275*, 9410–9417. [CrossRef] [PubMed]
33. Bishop, J.R.; Schuksz, M.; Esko, J.D. Heparan sulphate proteoglycans fine-tune mammalian physiology. *Nature* **2007**, *446*, 1030–1037. [CrossRef] [PubMed]
34. Hufnagel, L.; Kreuger, J.; Cohen, S.M.; Shraiman, B.I. On the role of glypicans in the process of morphogen gradient formation. *Dev. Biol.* **2006**, *300*, 512–522. [CrossRef]
35. Wishart, T.F.L.; Lovicu, F.J. An atlas of heparan sulfate proteoglycans in the postnatal rat lens. *Investig. Ophthalmol. Vis. Sci.* **2021**, *62*, 5. [CrossRef]
36. Rossi, M. Heparan sulfate chains of perlecan are indispensable in the lens capsule but not in the kidney. *EMBO J.* **2003**, *22*, 236–245. [CrossRef]
37. Pan, Y.; Woodbury, A.; Esko, J.D.; Grobe, K.; Zhang, X. Heparan sulfate biosynthetic gene Ndst1 is required for FGF signaling in early lens development. *Development* **2006**, *133*, 4933–4944. [CrossRef]
38. Wishart, T.F.L.; Lovicu, F.J. Heparan sulfate proteoglycans (HSPGs) of the ocular lens. *Prog. Retin. Eye Res.* **2023**, *93*, 101118. [CrossRef]
39. Qu, X.; Carbe, C.; Tao, C.; Powers, A.; Lawrence, R.; van Kuppevelt, T.H.; Cardoso, W.V.; Grobe, K.; Esko, J.D.; Zhang, X. Lacrimal gland development and Fgf10-Fgfr2b signaling are controlled by 2-O- and 6-O-sulfated heparan sulfate. *J. Biol. Chem.* **2011**, *286*, 14435–14444. [CrossRef]
40. Kakrana, A.; Yang, A.; Anand, D.; Djordjevic, D.; Ramachandruni, D.; Singh, A.; Huang, H.; Ho, J.W.K.; Lachke, S.A. ISyTE 2.0: A database for expression-based gene discovery in the eye. *Nucleic Acids Res.* **2018**, *46*, D875–D885. [CrossRef]
41. Khan, S.Y.; Hackett, S.F.; Lee, M.-C.W.; Pourmand, N.; Talbot, C.C.; Riazuddin, S.A. Transcriptome Profiling of Developing Murine Lens Through RNA Sequencing. *Investig. Opthalmol. Vis. Sci.* **2015**, *56*, 4919–4926. [CrossRef] [PubMed]
42. Hoang, T.V.; Kumar, P.K.R.; Sutharzan, S.; Tsonis, P.A.; Liang, C.; Robinson, M.L. Comparative transcriptome analysis of epithelial and fiber cells in newborn mouse lenses with RNA sequencing. *Mol. Vis.* **2014**, *20*, 1491–1517. [PubMed]
43. Cavalheiro, G.R.; Matos-Rodrigues, G.E.; Zhao, Y.; Gomes, A.L.; Anand, D.; Predes, D.; de Lima, S.; Abreu, J.G.; Zheng, D.; Lachke, S.A.; et al. N-myc regulates growth and fiber cell differentiation in lens development. *Dev. Biol.* **2017**, *429*, 105–117. [CrossRef]
44. Audette, D.S.; Anand, D.; So, T.; Rubenstein, T.B.; Lachke, S.A.; Lovicu, F.J.; Duncan, M.K. Prox1 and fibroblast growth factor receptors form a novel regulatory loop controlling lens fiber differentiation and gene expression. *Development* **2016**, *143*, 318–328. [CrossRef] [PubMed]
45. Kokenyesi, R.; Bernfield, M. Core protein structure and sequence determine the site and presence of heparan sulfate and chondroitin sulfate on syndecan-1. *J. Biol. Chem.* **1994**, *269*, 12304–12309. [CrossRef] [PubMed]
46. Gould, S.E.; Upholt, W.B.; Kosher, R.A. Characterization of Chicken Syndecan-3 as a Heparan Sulfate Proteoglycan and Its Expression during Embryogenesis. *Dev. Biol.* **1995**, *168*, 438–451. [CrossRef] [PubMed]
47. Winzen, U.; Cole, G.J.; Halfter, W. Agrin is a chimeric proteoglycan with the attachment sites for heparan sulfate/chondroitin sulfate located in two multiple serine-glycine clusters. *J. Biol. Chem.* **2003**, *278*, 30106–30114. [CrossRef]
48. Dong, S.; Cole, G.J.; Halfter, W. Expression of collagen XVIII and localization of its glycosaminoglycan attachment sites. *J. Biol. Chem.* **2003**, *278*, 1700–1707. [CrossRef]
49. Heathcote, J.G.; Orkin, R.W. Biosynthesis of Sulphated Macromolecules by Rabbit Lens Epithelium. I. Identification of the Major Macromolecules Synthesized by Lens Epithelial Cells in vitro. *J. Cell. Biol.* **1984**, *99*, 852–860. [CrossRef]

50. Mohan, P.S.; Spiro, R.G. Characterization of heparan sulfate proteoglycan from calf lens capsule and proteoglycans synthesized by cultured lens epithelial cells. Comparison with other basement membrane proteoglycans. *J. Biol. Chem.* **1991**, *266*, 8567–8575. [CrossRef]
51. Maeda, N.; Ishii, M.; Nishimura, K.; Kamimura, K. Functions of chondroitin sulfate and heparan sulfate in the developing brain. *Neurochem. Res.* **2011**, *36*, 1228–1240. [CrossRef] [PubMed]
52. Vallet, S.D.; Clerc, O.; Ricard-Blum, S. Glycosaminoglycan-Protein Interactions: The First Draft of the Glycosaminoglycan Interactome. *J. Histochem. Cytochem.* **2020**, *69*, 93–104. [CrossRef] [PubMed]
53. Clark, S.J.; Keenan, T.D.L.; Fielder, H.L.; Collinson, L.J.; Holley, R.J.; Merry, C.L.R.; van Kuppevelt, T.H.; Day, A.J.; Bishop, P.N. Mapping the differential distribution of glycosaminoglycans in the adult human retina, choroid, and sclera. *Investig. Opthalmol. Vis. Sci.* **2011**, *52*, 6511–6521. [CrossRef] [PubMed]
54. Smetsers, T.F.C.M.; van de Westerlo, E.M.A.; ten Dam, G.B.; Clarijs, R.; Versteeg, E.M.M.; van Geloof, W.L.; Veerkamp, J.H.; van Muijen, G.N.P.; van Kuppevelt, T.H. Localization and characterization of melanoma-associated glycosaminoglycans: Differential expression of chondroitin and heparan sulfate epitopes in melanoma. *Cancer Res.* **2003**, *63*, 2965–2970. [PubMed]
55. Karamanos, N.K.; Piperigkou, Z.; Theocharis, A.D.; Watanabe, H.; Franchi, M.; Baud, S.; Brézillon, S.; Götte, M.; Passi, A.; Vigetti, D.; et al. Proteoglycan chemical diversity drives multifunctional cell regulation and therapeutics. *Chem. Rev.* **2018**, *118*, 9152–9232. [CrossRef] [PubMed]
56. Filla, M.S.; David, G.; Weinreb, R.N.; Kaufman, P.L.; Peters, D.M. Distribution of syndecans 1-4 within the anterior segment of the human eye: Expression of a variant syndecan-3 and matrix-associated syndecan-2. *Exp. Eye Res.* **2004**, *79*, 61–74. [CrossRef]
57. Huang, J.; Rajagopal, R.; Liu, Y.; Dattilo, L.K.; Shaham, O.; Ashery-Padan, R.; Beebe, D.C. The mechanism of lens placode formation: A case of matrix-mediated morphogenesis. *Dev. Biol.* **2011**, *355*, 32–42. [CrossRef]
58. Lang, R.A. Pathways regulating lens induction in the mouse. *Int. J. Dev. Biol.* **2004**, *48*, 783–791. [CrossRef]
59. Gunhaga, L. The lens: A classical model of embryonic induction providing new insights into cell determination in early development. *Philos. Trans. Biol. Sci.* **2011**, *366*, 1193–1203. [CrossRef]
60. Rapraeger, A.C. Syndecan-Regulated Receptor Signaling. *J. Cell. Biol.* **2000**, *149*, 995–997. [CrossRef]
61. Capurro, M.I.; Xu, P.; Shi, W.; Li, F.; Jia, A.; Filmus, J. Glypican-3 inhibits Hedgehog signaling during development by competing with patched for Hedgehog binding. *Dev. Cell* **2008**, *14*, 700–711. [CrossRef] [PubMed]
62. Bányai, L.; Sonderegger, P.; Patthy, L. Agrin binds BMP2, BMP4 and TGFβ1. *PLoS ONE* **2010**, *5*, e10758. [CrossRef]
63. Seppinen, L.; Pihlajaniemi, T. The multiple functions of collagen XVIII in development and disease. *Matrix Biol.* **2011**, *30*, 83–92. [CrossRef]
64. Kerever, A.; Mercier, F.; Nonaka, R.; de Vega, S.; Oda, Y.; Zalc, B.; Okada, Y.; Hattori, N.; Yamada, Y.; Arikawa Hirasawa, E. Perlecan is required for FGF-2 signaling in the neural stem cell niche. *Stem Cell Res.* **2014**, *12*, 492–505. [CrossRef]
65. Jin, H.; Fisher, M.; Grainger, R.M. Defining progressive stages in the commitment process leading to embryonic lens formation. *Genesis* **2012**, *50*, 728–740. [CrossRef]
66. Fujimura, N. WNT/β-Catenin Signaling in Vertebrate Eye Development. *Front. Cell. Dev. Biol.* **2016**, *4*, 138. [CrossRef]
67. Barth, K.A.; Wilson, S.W. Expression of zebrafish nk2. 2 is influenced by sonic hedgehog/vertebrate hedgehog-1 and demarcates a zone of neuronal differentiation in the embryonic forebrain. *Development* **1995**, *121*, 1755–1768. [CrossRef] [PubMed]
68. Stump, R.; Ang, S.; Chen, Y.J.; von Bahr, T.; Lovicu, F.J.; Pinson, K.; de Iongh, R.U.; Yamaguchi, T.P.; Sassoon, D.A.; McAvoy, J.W. A role for Wnt/beta-catenin signaling in lens epithelial differentiation. *Dev. Biol.* **2003**, *259*, 48–61. [CrossRef] [PubMed]
69. Dawes, L.J.; Sugiyama, Y.; Tanedo, A.S.; Lovicu, F.J.; McAvoy, J.W. Wnt-frizzled signaling is part of an FGF-induced cascade that promotes lens fiber differentiation. *Investig. Opthalmol. Vis. Sci.* **2013**, *54*, 1582–1590. [CrossRef]
70. Kerr, C.L.; Huang, J.; Williams, T.; West-Mays, J.A. Activation of the hedgehog signaling pathway in the developing lens stimulates ectopic FoxE3 expression and disruption in fiber cell differentiation. *Investig. Ophthalmol. Vis. Sci.* **2012**, *53*, 3316–3330. [CrossRef]
71. Boswell, B.A.; Overbeek, P.A.; Musil, L.S. Essential role of BMPs in FGF-induced secondary lens fiber differentiation. *Dev. Biol.* **2008**, *324*, 202–212. [CrossRef] [PubMed]
72. Wederell, E.D.; De Iongh, R.U. Extracellular matrix and integrin signaling in lens development and cataract. *Semin. Cell. Dev. Biol.* **2006**, *17*, 759–776. [CrossRef] [PubMed]
73. Morgan, M.R.; Humphries, M.J.; Bass, M.D. Synergistic control of cell adhesion by integrins and syndecans. *Nat. Rev. Mol. Cell. Biol.* **2007**, *8*, 957–969. [CrossRef]
74. Kim, M.-S.; Saunders, A.M.; Hamaoka, B.Y.; Beachy, P.A.; Leahy, D.J. Structure of the protein core of the glypican Dally-like and localization of a region important for hedgehog signaling. *Proc. Natl. Acad. Sci. USA* **2011**, *108*, 13112–13117. [CrossRef] [PubMed]
75. Roper, J.A.; Williamson, R.C.; Bass, M.D. Syndecan and integrin interactomes: Large complexes in small spaces. *Curr. Opin. Struct. Biol.* **2012**, *22*, 583–590. [CrossRef] [PubMed]
76. Parmigiani, C.; McAvoy, J. Localisation of laminin and fibronectin during rat lens morphogenesis. *Differentiation* **1984**, *28*, 53–61. [CrossRef] [PubMed]
77. Zelenka, P.S. Regulation of cell adhesion and migration in lens development. *Int. J. Dev. Biol.* **2004**, *48*, 857–865. [CrossRef]
78. Simirskii, V.N.; Wang, Y.; Duncan, M.K. Conditional deletion of β1-integrin from the developing lens leads to loss of the lens epithelial phenotype. *Dev. Biol.* **2007**, *306*, 658–668. [CrossRef] [PubMed]
79. Pathania, M.; Wang, Y.; Simirskii, V.N.; Duncan, M.K. β1-integrin controls cell fate specification in early lens development. *Differentiation* **2016**, *92*, 133–147. [CrossRef]

80. Filmus, J. The function of Glypicans in the mammalian embryo. *Am. J. Physiol. Cell. Physiol.* **2022**, *322*, C694–C698. [CrossRef]
81. Strate, I.; Tessadori, F.; Bakkers, J. Glypican4 promotes cardiac specification and differentiation by attenuating canonical Wnt and Bmp signaling. *Development* **2015**, *142*, 1767–1776. [CrossRef] [PubMed]
82. Pan, J.; Ho, M. Role of glypican-1 in regulating multiple cellular signaling pathways. *Am. J. Physiol. Cell. Physiol.* **2021**, *321*, C846–C858. [CrossRef] [PubMed]
83. Jidigam, V.K.; Srinivasan, R.C.; Patthey, C.; Gunhaga, L. Apical constriction and epithelial invagination are regulated by BMP activity. *Biol. Open* **2015**, *4*, 1782–1791. [CrossRef]
84. Chauhan, B.K.; Lou, M.; Zheng, Y.; Lang, R.A. Balanced Rac1 and RhoA activities regulate cell shape and drive invagination morphogenesis in epithelia. *Proc. Natl. Acad. Sci. USA* **2011**, *108*, 18289–18294. [CrossRef]
85. Grisaru, S. Glypican-3 modulates BMP- and FGF-mediated effects during renal branching morphogenesis. *Dev. Biol.* **2001**, *231*, 31–46. [CrossRef] [PubMed]
86. Souza, A.T.P.; Lopes, H.B.; Oliveira, F.S.; Weffort, D.; Freitas, G.P.; Adolpho, L.F.; Fernandes, R.R.; Rosa, A.L.; Beloti, M.M. The extracellular matrix protein Agrin is expressed by osteoblasts and contributes to their differentiation. *Cell Tissue Res.* **2021**, *386*, 335–347. [CrossRef]
87. Fisher, M.C.; Li, Y.; Seghatoleslami, M.R.; Dealy, C.N.; Kosher, R.A. Heparan sulfate proteoglycans including syndecan-3 modulate BMP activity during limb cartilage differentiation. *Matrix Biol.* **2006**, *25*, 27–39. [CrossRef]
88. Bass, M.D.; Morgan, M.R.; Humphries, M.J. Integrins and syndecan-4 make distinct, but critical, contributions to adhesion contact formation. *Soft Matter* **2007**, *3*, 372–376. [CrossRef]
89. Okina, E.; Manon-Jensen, T.; Whiteford, J.R.; Couchman, J.R. Syndecan proteoglycan contributions to cytoskeletal organization and contractility. *Scand. J. Med. Sci. Sports* **2009**, *19*, 479–489. [CrossRef]
90. Tsoyi, K.; Chu, S.G.; Patino-Jaramillo, N.G.; Wilder, J.; Villalba, J.; Doyle-Eisele, M.; McDonald, J.; Liu, X.; El-Chemaly, S.; Perrella, M.A.; et al. Syndecan-2 attenuates radiation-induced pulmonary fibrosis and inhibits fibroblast activation by regulating PI3K/Akt/ROCK pathway via CD148. *Am. J. Cell. Mol. Biol.* **2018**, *58*, 208–215. [CrossRef]
91. Kolluri, A.; Ho, M. The Role of Glypican-3 in Regulating Wnt, YAP, and Hedgehog in Liver Cancer. *Front. Oncol.* **2019**, *9*, 708. [CrossRef]
92. Uechi, G.; Sun, Z.; Schreiber, E.M.; Halfter, W.; Balasubramani, M. Proteomic View of Basement Membranes from Human Retinal Blood Vessels, Inner Limiting Membranes, and Lens Capsules. *J. Proteome Res.* **2014**, *13*, 3693–3705. [CrossRef] [PubMed]
93. Wu, W.; Tholozan, F.M.; Goldberg, M.W.; Bowen, L.; Wu, J.; Quinlan, R.A. A gradient of matrix-bound FGF-2 and perlecan is available to lens epithelial cells. *Exp. Eye Res.* **2014**, *120*, 10–14. [CrossRef] [PubMed]
94. DeDreu, J.; Walker, J.L.; Menko, A.S. Dynamics of the lens basement membrane capsule and its interaction with connective tissue-like extracapsular matrix proteins. *Matrix Biol.* **2021**, *96*, 18–46. [CrossRef]
95. Fuerst, P.G.; Rauch, S.M.; Burgess, R.W. Defects in eye development in transgenic mice overexpressing the heparan sulfate proteoglycan agrin. *Dev. Biol.* **2007**, *303*, 165–180. [CrossRef] [PubMed]
96. Chamberlain, C.G.; McAvoy, J.W. Fibre differentiation and polarity in the mammalian lens: A key role for FGF. *Prog. Retin. Eye Res.* **1997**, *16*, 443–478. [CrossRef]
97. Hubka, K.M.; Carson, D.D.; Harrington, D.A.; Farach-Carson, M.C. Perlecan domain I gradients establish stable biomimetic heparin binding growth factor gradients for cell migration in hydrogels. *Acta Biomater.* **2019**, *97*, 385–398. [CrossRef]
98. Soulintzi, N.; Zagris, N. Spatial and temporal expression of perlecan in the early chick embryo. *Cells Tissues Organs* **2007**, *186*, 243–256. [CrossRef]
99. Fukai, N.; Eklund, L.; Marneros, A.G.; Oh, S.P.; Keene, D.R.; Tamarkin, L.; Niemelä, M.; Ilves, M.; Li, E.; Pihlajaniemi, T.; et al. Lack of collagen XVIII/endostatin results in eye abnormalities. *EMBO J.* **2002**, *21*, 1535–1544. [CrossRef]
100. Marneros, A.G.; Keene, D.R.; Hansen, U.; Fukai, N.; Moulton, K.; Goletz, P.L.; Moiseyev, G.; Pawlyk, B.S.; Halfter, W.; Dong, S.; et al. Collagen XVIII/endostatin is essential for vision and retinal pigment epithelial function. *EMBO J.* **2004**, *23*, 89–99. [CrossRef]
101. Elamaa, H.; Sormunen, R.; Rehn, M.; Soininen, R.; Pihlajaniemi, T. Endostatin Overexpression Specifically in the Lens and Skin Leads to Cataract and Ultrastructural Alterations in Basement Membranes. *Am. J. Pathol.* **2005**, *166*, 221–229. [CrossRef]
102. Aikio, M.; Hurskainen, M.; Brideau, G.; Hägg, P.; Sormunen, R.; Heljasvaara, R.; Gould, D.B.; Pihlajaniemi, T. Collagen XVIII short isoform is critical for retinal vascularization, and overexpression of the Tsp-1 domain affects eye growth and cataract formation. *Investig. Ophthalmol. Vis. Sci.* **2013**, *54*, 7450–7462. [CrossRef]
103. Liu, I.H.; Zhang, C.; Min, J.K.; Cole, G.J. Retina development in zebraf ish requires the heparan sulfate proteoglycan agrin. *Dev. Neurobiol.* **2008**, *68*, 877–898. [CrossRef] [PubMed]
104. Zhao, H.; Yang, T.; Madakashira, B.P.; Thiels, C.A.; Bechtle, C.A.; Garcia, C.M.; Zhang, H.; Yu, K.; Ornitz, D.M.; Beebe, D.C.; et al. Fibroblast growth factor receptor signaling is essential for lens fiber cell differentiation. *Dev. Biol.* **2008**, *318*, 276–288. [CrossRef] [PubMed]
105. Lovicu, F.J.; McAvoy, J.W. FGF-induced lens cell proliferation and differentiation is dependent on MAPK (ERK1/2) signalling. *Development* **2001**, *128*, 5075–5084. [CrossRef]
106. Liang, Y.; Häring, M.; Roughley, P.J.; Margolis, R.K.; Margolis, R.U. Glypican and biglycan in the nuclei of neurons and glioma cells: Presence of functional nuclear localization signals and dynamic changes in glypican during the cell cycle. *J. Cell. Biol.* **1997**, *139*, 851–864. [CrossRef] [PubMed]

107. Expression of agrin in the developing and adult rat brain. *Neuroscience* **1997**, *76*, 581–596. [CrossRef]
108. Stewart, M.D.; Sanderson, R.D. Heparan sulfate in the nucleus and its control of cellular functions. *Matrix Biol.* **2014**, *35*, 56–59. [CrossRef]

Disclaimer/Publisher's Note: The statements, opinions and data contained in all publications are solely those of the individual author(s) and contributor(s) and not of MDPI and/or the editor(s). MDPI and/or the editor(s) disclaim responsibility for any injury to people or property resulting from any ideas, methods, instructions or products referred to in the content.

cells

MDPI

Article

Independent Membrane Binding Properties of the Caspase Generated Fragments of the Beaded Filament Structural Protein 1 (BFSP1) Involves an Amphipathic Helix

Miguel Jarrin [1,2], Alexia A. Kalligeraki [1,2], Alice Uwineza [1,2], Chris S. Cawood [1,2], Adrian P. Brown [1], Edward N. Ward [1,2], Khoa Le [2,3], Stefanie Freitag-Pohl [4], Ehmke Pohl [2,4], Bence Kiss [5], Antal Tapodi [1,2,5,*] and Roy A. Quinlan [1,2,3]

1 Department of Biosciences, Upper Mountjoy Science Site, The University of Durham, South Road, Durham DH1 3LE, UK; r.a.quinlan@durham.ac.uk (R.A.Q.)
2 Biophysical Sciences Institute, Durham University, Upper Mountjoy, South Road, Durham DH1 3LE, UK
3 Department of Biological Structure, University of Washington, Seattle, WA 98195, USA
4 Department of Chemistry, Durham University, Lower Mountjoy, South Road, Durham DH1 3LE, UK
5 Department of Biochemistry and Medical Chemistry, Medical School, University of Pécs, 7624 Pécs, Hungary
* Correspondence: antal.tapodi@aok.pte.hu

Abstract: Background: BFSP1 (beaded filament structural protein 1) is a plasma membrane, Aquaporin 0 (AQP0/MIP)-associated intermediate filament protein expressed in the eye lens. BFSP1 is myristoylated, a post-translation modification that requires caspase cleavage at D433. Bioinformatic analyses suggested that the sequences 434–452 were α-helical and amphipathic. Methods and Results: By CD spectroscopy, we show that the addition of trifluoroethanol induced a switch from an intrinsically disordered to a more α-helical conformation for the residues 434–467. Recombinantly produced BFSP1 fragments containing this amphipathic helix bind to lens lipid bilayers as determined by surface plasmon resonance (SPR). Lastly, we demonstrate by transient transfection of non-lens MCF7 cells that these same BFSP1 C-terminal sequences localise to plasma membranes and to cytoplasmic vesicles. These can be co-labelled with the vital dye, lysotracker, but other cell compartments, such as the nuclear and mitochondrial membranes, were negative. The N-terminal myristoylation of the amphipathic helix appeared not to change either the lipid affinity or membrane localisation of the BFSP1 polypeptides or fragments we assessed by SPR and transient transfection, but it did appear to enhance its helical content. Conclusions: These data support the conclusion that C-terminal sequences of human BFSP1 distal to the caspase site at G433 have independent membrane binding properties via an adjacent amphipathic helix.

Keywords: lens; cataract; intermediate filaments; amphipathic helix; oligomerisation; intrinsically disordered domain; lipid binding; post-translational myristoylation; membrane scaffold

1. Introduction

The transparency and optical function of the eye lens depends upon a functional intermediate filament network [1,2]. In addition to vimentin, there is a pair of intermediate filament proteins that are highly expressed in the lens and form an iconic cytoskeletal structure of the eye lens called the beaded filament [3,4]. For this reason, they are identified as Bead Filament Structural Proteins 1 and 2 [5]. Mutations in both proteins cause cataracts ((https://cat-map.wustl.edu/, accessed on 5 May 2023); [6]), and the targeted removal from the mouse genome not only affects the biomechanical properties of the lens [7], but also affects the transparency and optical properties of the lens ([8–12]; reviewed in [1,2,13,14]) and their loss can also prevent emmetropia developing [15]. BFSP1 (beaded filament structural protein 1; filensin; CP95) and its orthologues are found from cephalopods to mammals [16]. Similar to other intermediate filament proteins, BFSP1 has a central α-helical

rod domain flanked by N- and C-terminal domains, although the C-terminal domain is striking because it exhibits lower sequence conservation between species ([2,17]; Figure S1), which is not seen for other intermediate filament proteins such as vimentin. There are, however, some sequences that are highly conserved across species [18,19] and these include the site of a caspase cleavage site (DVPD; human BFSP1 430–433) and adjacent myristoylation signal ([19,20]; (GGQISK; human BFSP1 434–439)). Post-translational myristoylation following caspase cleavage is a recognised mechanism for adding this fatty acid to an exposed N-terminal glycine [21,22] so much so that it is incorporated into computational tools to predict myristoylation sites in the human reference proteome with BFSP1 (Q06002) identified as a probable hit [23]. Imaging mass spectrometry has confirmed BFSP1 myristoylation occurs at G434 following caspase cleavage in BFSP1 [18,24]. This post-translational myristoylation event occurs in a distinct region of the lens as the transition from vimentin to beaded filaments completes [25,26]. This represents an important transition point for the lens, but also because it is the first myristoylation event to be identified in the spectrum of intermediate filament post-translational modifications [27–30].

The cleavage, release and myristoylation of BFSP1 at G434 then contribute to the regulation of the major water channel protein, AQP0, in the lens [18]. AQP0 and BFSP1 interact directly [31], as shown by chemical cross-linking studies that identified the interaction to occur between BFSP1 450–465 and AQP0 239–259 [31]. The site was identified after tryptic digestion of the cross-linked sample. This demonstrates that BFSP1 binds the C-terminal region of AQP0, a domain that is crucial to its water channel regulation [32,33]. This observation implies that AQP0 could facilitate the binding of BFSP1 [20,24,26,34,35] and its myristoylated fragments [18] to the lens fibre cell plasma membranes. These BFSP1 fragments derived from the C-terminus are tightly associated with the lens plasma membranes and resist extraction with both urea and sodium hydroxide [18], a biochemical property of integral membrane proteins [36]. Myristoylation is an important regulatory post-translation modification that helps target proteins to specific membranes and subcellular compartments [21,37,38]. In the case of some membrane-targeted proteins, such as Adenosine diphosphate Ribosylation Factors (ARF), myristoylation can, however, affect the conformation of the adjacent peptide and change its affinity for the membrane [39,40] and can determine its membrane association [41]. It is important, therefore, to determine whether the caspase released and myristoylated fragments of BFSP1 do or do not require AQP0 for their avid association with lens membranes or whether this property is attributable to sequences/motifs in the C-terminal sequences of BFSP1 itself.

Although there is no crystallographic data for BFSP1, an AlphaFold2 prediction is available (https://alphafold.ebi.ac.uk/entry/Q12934, accessed on 5 May 2023). AlphaFold2 predicts that the BFSP1 tail domain is mostly intrinsically disordered, but it does predict a short α-helix at the cryptic myristoylation site, G434. Structural data are available for ARF proteins [40,41], and in their case, an amphipathic helix is preceded by N-terminal glycine that is myristoylated. An amphipathic helix behaves similarly to an integral membrane protein in terms of its urea/alkali resistance to extraction from membranes [42], suggesting a possible mechanism to explain how the BFSP1 C-terminal domain fragments associate with the lens membranes. It remains to be determined whether the AlphaFold2 prediction for a short α-helix and whether an amphipathic helix could be formed by the residues immediately distal to the myristoylation site G434 in human BFSP1.

Here we investigate the membrane binding properties of BFSP1 and C-terminal domain fragments generated by caspase cleavage. Using chemically synthesised polypeptides, we show that the BFSP1 region 434–467 adopts an α-helical secondary structure in the presence of trifluoroethanol (TFE) that is enhanced by the presence of a myristoyl group. Using recombinantly expressed and purified fragments from the C-terminal domain of BFSP1, we use surface plasmon resonance (SPR) to measure a sub-micromolar K_D for the BFSP1 fragment 434–548. Transient transfection of tissue culture cells with eGFP-tagged constructs demonstrates that providing the 434–460 sequence was present, the transfected C-terminal BFSP1 fragment from the C-terminal domain would localise to the plasma

membranes and some intracellular membrane compartments. Our data support the conclusion that myristoylation occurs at the N-terminus of an amphipathic helix, and any BFSP1 C-terminal domain fragments containing this region have the capacity to associate with cell membranes independent of the lens water channel protein AQP0.

2. Materials and Methods

2.1. Bioinformatic Analyses

Potential lipid binding regions in the C-terminal region of BFSP1 were identified using HELIQUEST ([43]; https://heliquest.ipmc.cnrs.fr, accessed on 10 March 2023; version 2.0, Nice, France). The analysis assumed an α-helix and analysed the sequence using an 18-residue window. The "Discrimination factor" was calculated as described [44] using the formula D = 0.944 (<μH>) + 0.33 (*z*), where μH is the calculated hydrophobic moment and *z* is the calculated net charge. The combined use of the HELIQUEST discrimination factor and the Eisenberg plot methodology is a robust bioinformatics approach to identifying lipid-binding regions [45]. The fIDPnn webserver (http://biomine.cs.vcu.edu/servers/flDPnn/, accessed on 17 February 2023; version 1, Richmond, VA, USA) was used to assess the intrinsic disorder of the same region [46]. The MemBrain 3.0 webserver was used to assess the amphipathic helix-forming propensity of the C-terminal domain of BFSP1 (http://www.csbio.sjtu.edu.cn/bioinf/MemBrain/, accessed on 17 February 2023; version 1; Shanghai, China [47]). Sequence alignment of human (Q12934 BFSP1_Human), bovine (Q06002 BFSP1_BOVIN) and rat (Q02435 BFSP1_Rat) downloaded from UniProt [48] was produced using COBALT [49]. AlphaFold2, a protein structure predicting algorithm, was used to predict secondary sequence features of the BFSP1 C-terminal sequence 434–665 [50,51]. The predicted structure was viewed, and images of this region were produced using iCn3D [52].

2.2. Cloning, Expression and Purification of Human BFSP1, Its Fragments and CRYAB

These experimental details have been given in detail previously [18]. Briefly, full-length human BFSP1 was originally obtained from Source Bioscience (http://www.lifesciences.sourcebioscience.com/IMAGE, accessed on 17 February 2023, clones 6154051 and 5406467; Nottingham, UK). Constructs encompassing and within the domain 434–665 of BFSP1 were generated by PCR and, after sequencing, were sub-cloned into pET23b vectors to include a C-terminal hexa-histidine tag and the residues LE encoded by the XhoI site where the amplified fragments were cloned in frame with the His-tag of the vector. Recombinant His-tagged BFSP1 fragments were purified by affinity chromatography on nickel columns according to the manufacturer's instructions (His-Select Nickel Affinity Gel; Sigma-Aldrich, Poole, UK) and with a final purification step using a size exclusion column (Sephadex G10; Sigma-Aldrich, Poole, UK). In some instances, a Superose 6 10/300 column (Cytiva Lifesciences, Cardiff, UK) was used as a final purification step. Fractions containing the protein of interest were pooled and concentrated in an Amicon Stirred Cell and ultracell regenerated cellulose membranes with 10 and 3 kDa cut-off as appropriate. Recombinant human CRYAB was also produced recombinantly in *E.coli* as described previously [53]. Native bovine BFSP1 was purified from eye lenses as described previously [54]. The identity of the protein products was confirmed by SDS-PAGE, followed by mass spectrometry.

For expression in mammalian tissue culture cells, BFSP1 constructs were subcloned into pEGFP-N3 (http://www.clontech.com/UK/Support/Applications/Using_Fluorescent_Proteins/EGFP_Vectors, accessed on 14 May 2023; Mountain View, CA, USA) with the eGFP added to the C-terminal end of the expressed BFSP1 construct as detailed previously [18].

2.3. Extraction of Lipids from Bovine Lens Cell Membranes

Bovine lens membranes were prepared as described [55]. The aqua-dissection method allowed membrane fractions to be prepared from the cortex and nucleus of the bovine lens resulting in four fractions corresponding to 18–11 mm, 11–8 mm, 8–6 mm and lastly 6–0 mm. Lens lipids were then extracted from 40 to 50 mg wet weight of each of these

isolated bovine lens cell membranes using a Bligh and Dyer method [56]. Bovine lens cell membranes (10 mg/mL) per sample were centrifuged, and pellets were resuspended in 1 mL of 10 mM $NaPO_4$, 100 mM NaCl, 5 mM EDTA, and pH 7.4 buffer. Samples were incubated for 30 min with 2 mL of dichloromethane: methanol (vol ratio 1:2). After incubation, 0.67 mL dichloromethane was added and 1.2 mL of 0.9% (*w*/*v*) KCl. Samples were centrifuged at 1000× *g* for 1 min. The lower phase was transferred to a new centrifuge tube and evaporated under nitrogen. Samples were stored at −20 °C.

2.4. Purification of Lens Membrane Lipids for SPR

Samples of the extracted bovine lens membrane lipids were warmed for 5 min at room temperature prior to incubating for a further 5 min at 37 °C. They were then resuspended in 10 mM $NaPO_4$, 150 mM NaCl, pH 7.8, to a final concentration of 6.8 mg/mL. The resuspended lipid samples were resuspended mechanically both by alternating vortex and pipet for 5 min and then incubated for a further 10 min at 37 °C. The lipid samples were then heated to 90 °C and then allowed to cool on the bench to room temperature prior to 20 min sonication in a water bath and a final 5 min incubation at 37 °C. Immediately prior to use and the lipid preparation was mechanically agitated for 5 min. A 1:1 mixture of the lipids extracted from the lens membranes corresponding to the 11–8 mm and 8–6 mm regions of the lens was used to coat the L1 chip as per the manufacturer's instructions (GE Healthcare).

2.5. Surface Plasmon Resonance to Measure Lipid-Binding of BFSP1 Constructs

Surface Plasmon Resonance (SPR) was used to assess the membrane binding properties of BFSP1 and its various domains. SPR experiments were conducted on a Biacore X100 (GE Healthcare, Uppsala, Sweden) using an L1 chip (GE Healthcare). Biacore X100 Control Software (Version: 2.0.1) with the Plus upgrade software, using the Kinetics/Affinity analysis workflow strategy according to the manufacturer's instructions with 4 analysis cycles. The molecular weights used for the different BFSP1 constructs were 434–665 (44 kDa); 434–548 (26 kDa) and 494–550 (5.9 kDa). Molecular weights for human BFSP1 (74.5 kDa), bovine BFSP1 (83.1 kDa) and human CRYAB (20.2 kDa) were calculated using the online Expasy web resource (https://web.expasy.org/compute_pi/, accessed on 11 May 2023). All except the bovine BFSP1 were recombinantly produced proteins. CRYAB is a lens protein with membrane binding potential [57,58] and was used as a positive control. The L1 chip surface was cleaned by injecting 60 mM NaOH: Isopropanol (vol 3:2) and washed thoroughly with 10 mM $NaPO_4$, 150 mM NaCl, pH 7.8. Liposomes (0.5 mg/mL) prepared from extracted lens membrane lipids were deposited on sensor chips at a low flow rate (10 μL/min) until a stable resonance unit (RU) level was obtained. Five different concentrations of full-length BFSP1 (human and bovine) and human BFSP1 fragments derived from the C-terminal domain (434–665, 434–548 and 494–550) in 10 mM $NaPO_4$, 150 mM NaCl, pH 7.8 buffer were injected. The lipid surface was regenerated with 60 mM NaOH: isopropanol (vol ratio 3:2), providing a consistent baseline that was subsequently observed. All analyses were performed at 25 °C. Experiments determining the dissociation constant (K_D) values were performed in triplicate.

2.6. Circular Dichroism Measurements

CD spectra were recorded from 280 to 180 nm with a Jasco-1500 spectropolarimeter (JASCO International Co. Ltd., Tokyo, Japan). Spectra were acquired at 20 °C using a 0.1 cm path length quartz cell, averaged over three scans at a scan speed of 20 nm/min, a bandwidth of 3.0 nm, 8 s digital integration time, and 0.5 nm resolution. Following baseline correction, the observed ellipticity, θ (mdeg), was converted to molar ellipticity, [Θ] (deg cm^2/dmol), using the relationship [Θ] = θM/10(*lc*) where '*l*' is the path length in centimetres, '*c*' is concentration in g/L, and M is the average molecular weight (g/mol). All spectra were corrected with the appropriate blank. The peptides corresponding to residues 434–467 of BFSP1 were chemically synthesized ±N-terminal myristoyl group, then

purified and characterised by Mass Spectrometry by the company Intavis Bioanalytical Instruments Aktiengesellshaft (Köln, Germany). Purified peptides were dissolved in water and trifluoroethanol (TFE; 30% (v/v)) to induce secondary structure formation [59], as previously suggested, to study the amphipathic helix in bee venom [60]. The α-helical content in 30% (v/v) TFE was determined using the online analysis resource (DiChroWeb: http://dichroweb.cryst.bbk.ac.uk/html/home.shtml, accessed on 4 May 2023; Version 1; London, UK [61]) using the algorithm CDSSTR [62] and reference set 7 of proteins [63].

2.7. Proteomic Analyses of Bovine Lens Membrane Preparations

Trypsin was added in a 1:50 weight/weight ratio to a bovine lens membrane sample. Typically, 50 µg of lens membrane protein was digested by overnight incubation at 37 °C. The digestion was terminated by adding trifluoroacetic acid (TFA). The final clean-up and fractionation of each digest were made using StageTips contained two SCX filter pieces as described [64]. Peptide analysis by LC-MS was performed on a SCIEX TripleTOF 6600 mass spectrometer linked to an Eksigent nanoLC 425 chromatography system via a 50-µm ESI electrode in a DuoSpray source (SCIEX). Sample injection and peptide separation used a trap and eluted method flowing at 5 µL/min. Peptides were loaded and washed on a YMC TriArt C18 guard column (1/32, 5 µm, 5 × 0.5 mm) followed by online chromatographic separation performed over 33 min on a YMC TriArt C18 column (1/32″, 12 nm, S-3 µm, 150 × 0.3 mm). A linear gradient of 5–35% (v/v) acetonitrile, 0.1% (v/v) formic acid over 20 min was then shifted to 80% (v/v) acetonitrile, 0.1% (v/v) formic acid over 2 min. The column was washed for 3 min before returning to 5% (v/v) acetonitrile, 0.1% (v/v) formic acid over to 2 min and re-equilibration for 6 min. Data-dependent LC-MS-MS acquisition was programmed for the time period 0.1–24 min. Once completed, the source voltage was lowered from 5500 to 0 V. Each MS cycle comprised a 250 ms precursor-ion scan from 350 to 1500 m/z followed by fragmentation of up to 10 selected ions for 100 ms each. This generated MS/MS spectra of 100 to 1500 m/z (cycle time 1.3 s). The switch criteria applied were +2 to +5 ions of intensity > 400 cps, with a rolling exclusion time of 12 s.

LC-MS/MS peak lists in (.mgf) format were generated from (.wiff) format data files using MSConvert in the ProteoWizard suite of proteomic software tools and peptide/protein identification used PEAKS X+ software (Bioinformatics Solutions Inc., Waterloo, ON, Canada). Default precursor and product ion tolerances for a TripleTOF spectrometer were specified, along with the following modifications: fixed—carbamidomethyl [C], variable—oxidation [M], acetylation [N-term], deamidation [NQ], oxidation [HW]. Search databases were a UniProt bovine reference proteome (March 2019, 22,285 entries) plus 194 known proteomic experiment contaminants, or a human reference proteome (February 2017, 20,106 entries) plus 161 contaminants. Peptide FDR was set at 1%, and a filter of 2 unique peptides was applied to identified proteins.

2.8. SDS PAGE and Immunoblotting

Protein samples were resuspended in SDS sample buffer (1 mM EDTA pH 7.8, 50 mM Tris-HCl pH 6.8 and 1% (w/v) SDS) and then mixed with 4× Laemmli sample buffer (containing 2.854 M β-mercaptoethanol) ([65] as modified in [18]). Protein samples were separated on either 10, 12 or 15% (w/v) polyacrylamide gels at 100 V depending on the relative electrophoretic mobility of the sample under investigation. Protein standards (PageRuler Plus, 10–250 kDa; ThermoFisher Scientific, Warrington, UK) were included. Coomassie blue staining (0.25% (w/v) Coomassie Brilliant Blue R250, Merckmillipore, Watford, UK) was used for protein detection, and once de-stained gels were imaged using either an Azure 300 or Thermofisher Scientific iBRIGHT imaging systems.

For immunoblotting, proteins separated by SDS-PAGE were transferred to nitrocellulose membrane for blotting using the semi-dry method, as detailed previously [18]. Briefly, after Ponceau dye staining to check the transfer, the membrane was blocked with 10% (w/v) milk powder and 6% (w/v) bovine serum albumin (Fraction V, Merck) in Tris-HCl Buffered Saline (TBS) at room temperature, for 2 h. Next, membranes were probed

with a commercially available BFSP1 rabbit polyclonal antibody, the Atlas Antibody S38 (HPA042038-100UL, Sigma–Aldrich). Primary antibody binding was detected using EIA Grande Anti-Rabbit IgG Horseradish Peroxidase Conjugate (Cat. No. 172-1019) diluted in 3% (*w*/*v*) BSA in TBS. A signal was detected using the Azure 300 imaging system by the chemiluminescent method.

2.9. Eukaryotic Cell Culture, Incubation with Recombinant BFSP1 Fragments, Transient Transfections of BFSP1 Constructs and Live Cell Imaging

The mammary carcinoma cell line, MCF7, was grown in DMEM supplemented with glutamine, penicillin, streptomycin and 10% (*v*/*v*) foetal bovine serum. MCF7 cells were seeded on glass coverslips in six-well plates prior to transient transfection of the peGFP-N3 vectors containing various BFSP1 constructs, including the G434A mutation, to prevent myristoylation of the BFSP1 434–548 fragments. Purified plasmids were mixed with the GeneJuice™ transfection reagent (Novagen; http://www.emdmillipore.com/life-science-research/novagen/, accessed on 14 May 2023, Watford, UK) according to the manufacturer's guidelines. Cells were left overnight before live cell imaging by light microscopy using Zeiss LSM 710 confocal microscope in a chamber maintained with 5% (*v*/*v*) CO_2 and at 37 °C.

To identify which intracellular membrane compartments of MCF7 cells could be labelled with eGFP tagged BFSP1 434–548, 434–460 and 494–550, cells were transiently transfected using Lipofectamine 2000 according to the manufacturer's instructions (Thermofisher Scientific, UK). After overnight incubation, an hour before starting live cell imaging, the following vital dyes were added; Bodipy 493/505 (2 μL/mL), Hoescht 33342 (H33342) 2 μL/mL and Mitotracker 1/3000 either alone or in combination with each other according to manufacturer's instructions (Thermofisher Scientific, UK). In addition, in some cases, transiently transfected cells were treated with 10 μM tamoxifen (MP Biochemicals) to induce plasma membrane blebbing [66].

3. Results

3.1. The C-Terminal Sequences of BFSP1 Contain an Amphipathic Helix That Spans the Myristoylation Motif and Predicted α-Helix

Human BFSP1 is a 665-residue protein. The N-terminal sequences contain an α-helical-rich region and C-terminal sequences in which there is a highly conserved caspase site (430–433) and myristoylation signal (434–439, Figures 1A and S1).

Both the myristoylation and, therefore, by inference so too the caspase cleavage site, have been confirmed by mass spectrometry [20]. This is an example of post-translational myristoylation and was predicted by a recently developed search engine SVMyr for such events [23]. Using two different caspase prediction programmes (GrabCas [67] and CasCleave 2 [68]), three caspase sites were identified within residues 430–665 for human BFSP1 by the two programmes (Figure S2A), but only two in the equivalent region of Bovine BFSP1 (Figure S2B). We confirmed the presence of the D433 site but also identified a second caspase cleavage site with the recognition sequence SFVD (Bovine BFSP1 477–480; Figure S2C). These data suggest that the other caspase sites identified within the C-terminal sequences of BFSP1 are potentially bone-fide cleavage sites in addition to the one adjacent to the myristoylation sequence. These need to be confirmed experimentally, as we have done here for the D480 site in bovine BFSP1, but collectively these data and the bioinformatic predictions suggest that both the caspase cleavage and myristoylation of the C-terminal fragments released from BFSP1 are important to its function and the regulation of AQP0 [57,69].

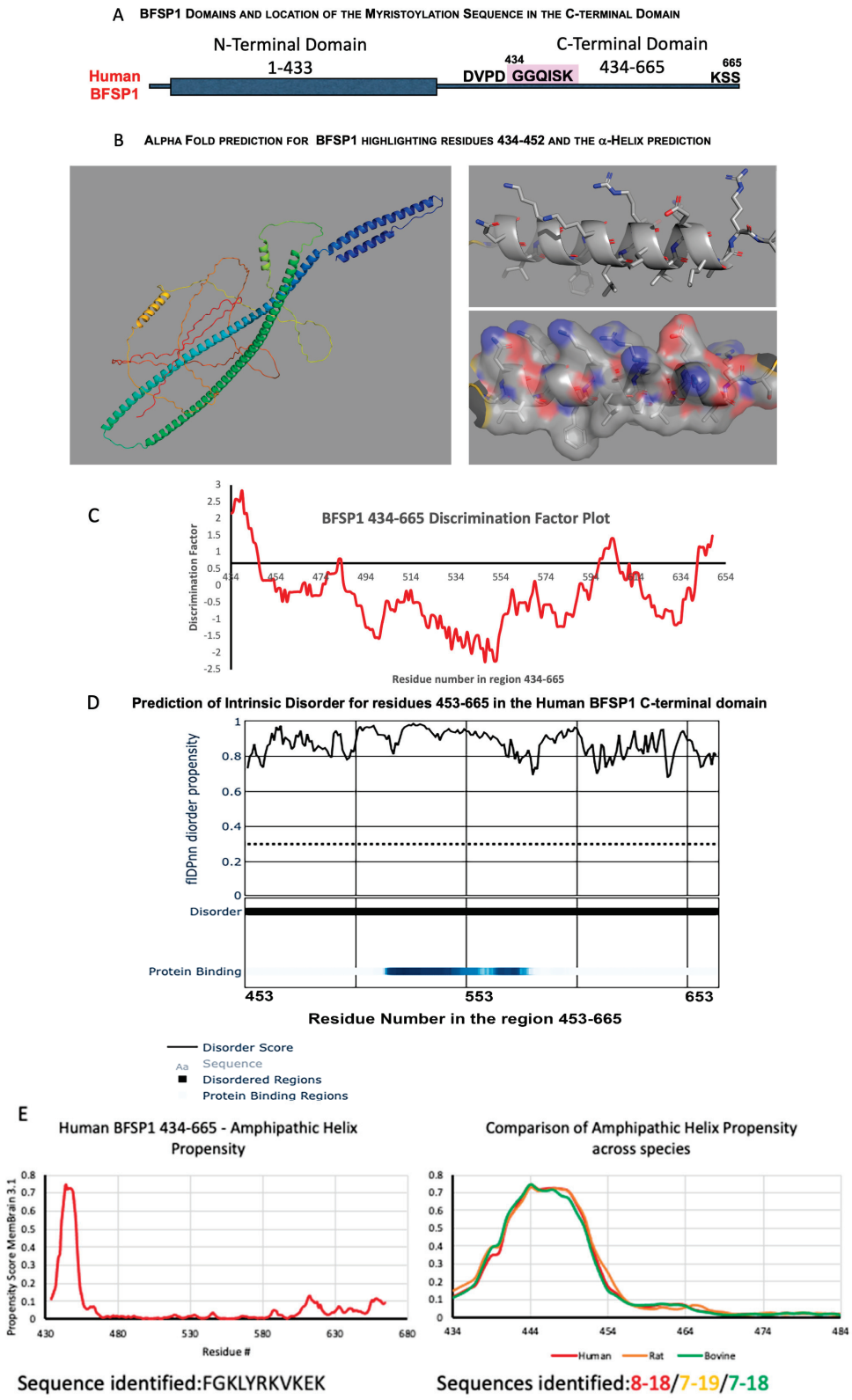

Figure 1. Bioinformatic analyses of BFSP1 and its C-terminal sequences 434–665. Human BFSP1 is a 665-residue protein, with a large α-helical rod domain (grey rectangle) and a C-terminal domain containing a cryptic myristoylation site (GGQISK) that is released by caspase cleavage at site 433

(**A**). AlphaFold2 predicted with high confidence an α-helix for residues 434–452, whilst the remaining C-terminal sequences had low/very low secondary structure prediction (**B**). HELIQUEST was used to calculate the discrimination factor (DF) over the region 434–665, with the X-axis intersect set to a DF of 0.68 as the threshold for identifying LBDs. The strongest score was received for the sequence 434–453 (**C**), but others were identified starting at residues 597 and 641 in the absence of predicted α-helix. The C-terminal BFSP1 sequences (454–665) were predicted to have a considerable intrinsic disorder as predicted using the algorithm fIDPnn (**D**). A minimum threshold score of 0.3 is indicated (---), but most of the BFSP1 453–665 sequences scored $\geq$ 0.8, indicative of significant disorder potential (**D**). A region potentially involved in protein-protein interactions was identified between 520 and 550 (dark blue bar; **D**). The 434–665 sequences were assessed for their propensity to form amphipathic helices, and one region was identified within the BFSP1 region 434–455 (**E**). The same region was identified in rat and bovine sequences (**E**), in line with the observation that the caspase recognition site and the myristoylation sequences are highly conserved across species [18].

Interestingly, AlphaFold2 predicted an α-helix overlapping the myristoylation signal and spanning the region 434–452 (Figure 1B). The remaining C-terminal sequences lacked other secondary structures according to that prediction. The algorithm HELIQUEST is used to identify potential lipid-binding domains (LBDs) by combining a Discrimination Factor with the presence of α-helices (Figure 1C). That bioinformatic analysis strongly suggested the presence of an amphipathic helix spanning residues 434–452 (See Figure S3 for full HELIQUEST analysis of sequences 434–665). Using the fIDPnn algorithm (Figure 1D), the 434–452 region, similar to the rest of the C-terminal sequences, is predicted to be intrinsically disordered, which does not entirely support the AlphaFold2 prediction for the 434–452 sequences. The high probability that a predicted α-helix would combine to produce an amphipathic helix was, however, reinforced by the MemBrain3 algorithm designed to identify such motifs (Figure 1E). The amphipathic helix prediction was consistent between human, rat and cow BFSP1, with a major peak between 434 and 454 and a shoulder extending to residues 466–468 between the three mammals (Figure 1E), which corresponds to the Heliquest discrimination factor remaining above the 0.68 threshold [45] until residue 464 (Figure 1A).

To confirm the presence of an α-helix and to monitor the influence of the myristoyl group on their structure, peptides covering residues 434–467 were chemically synthesised. CD spectroscopy revealed a disordered peptide with no α-helical content when dissolved in water (Figure 2A), but in the presence of 30% (v/v) TFE, the spectra for both the myristoylated and unmyristoylated peptides changed to include distinct minima (Figure 2B).

It was noticeable that the presence of the myristoyl group enhanced the spectra for the 434–467 peptide with the minima shifting from 204.5 to 206 and a distinct minimum now at 221 nm suggests α-helical structure (Figure 2B,C) as observed for other amphipathic helices [42,60] including ARF1 [39] and BAR-domain peptides [70]. However, such a secondary structure only becomes apparent when the CD spectra are measured in the presence of TFE and other reagents, such as SDS, that promote the formation of amphipathic helices [60].

3.2. The BFSP1 C-Terminal Sequences Distal to 434 Bind Lipid Membranes Independently of AQP0

For these studies, human BFSP1 and various fragments were produced recombinantly in *E.coli* (Figure 3). These included full-length BFSP1, 1–433, 434–665, 434–548 and finally, 494–550.

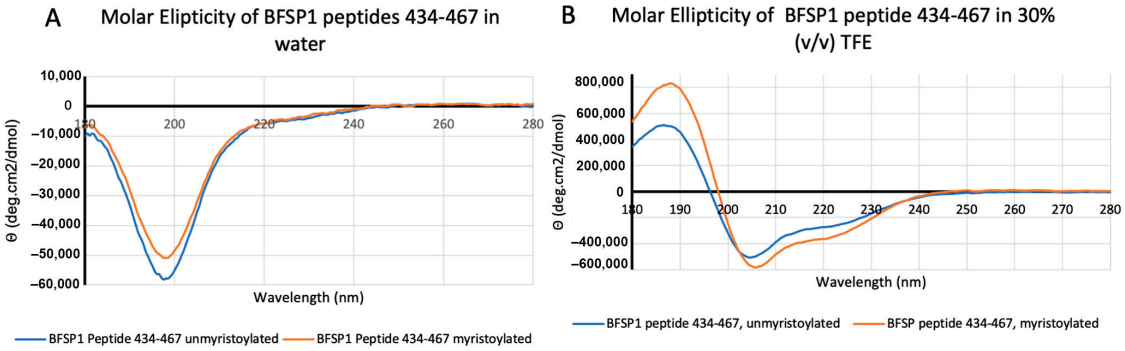

C Solutions from the CDSSTR method on DiChroWeb using reference set 7

Helix 1	Helix 2	Strand 1	Strand 2	Turns	Unordered	Total
Unmyristoylated peptide BFSP1 434-467 (NRMSD:0.016)						
0.14	**0.11**	0.08	0.06	0.15	**0.47**	1.01
Myristoylated peptide BFSP1 434-467 (NRMSD: 0.08)						
0.23	**0.16**	0.07	0.06	0.16	**0.32**	1

Figure 2. CD spectrum for myristoylated and unmyristoylated peptides spanning residues 434–467 in BFSP1. The CD spectra for chemically synthesized peptides spanning the residues 434–467 of human BFSP1 ± a myristoyl group were measured in water (**A**) and in (**B**) 30% (v/v) TFE. Peptides (0.05 mg/mL) were measured in a Jasco Quartz cell (0556) with a 0.1cm pathlength. Spectra shown are buffer blanked. Note the shift in the minima (206/220 nm) for the myristoylated peptide, which is reflected in the increased α-helical content as indicated from the CDSSTR outputs (**C**).

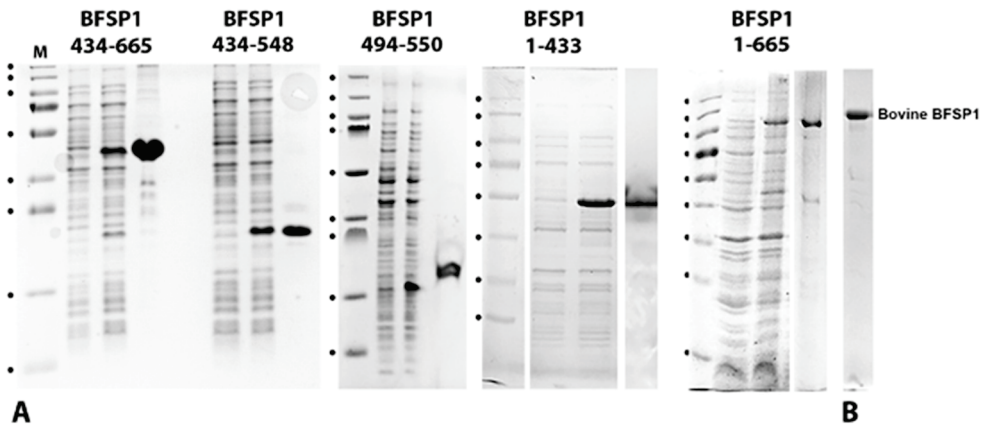

Figure 3. Recombinant expression and purification of the BFSP1 protein domains used in these studies. (**A**). BFSP1 and the domains 434–665, 434–548 and 494–550 were cloned into pET vectors, and their expression was induced by the addition of IPTG. In each of the panels, a sample of the uninduced, followed by a sample after a 3 h induction with IPTG and the subsequent affinity purified proteins are shown. The same markers (M) were used, although the acrylamide concentration changed; 10% (w/v) for BFSP1 1–665; 12% (w/v) for BFSP1 434–665 and 434–548; and lastly, 15% (w/v) for BFSP1 494–550. Markers correspond to 250, 130, 100, 70, 55, 35, 25, 15, and 10 kDa, respectively. (**B**). Bovine BFSP1 purified from bovine lenses.

It is noticeable that the fragments from the BFSP1 C-terminal domain all migrated with slower-than-expected relative mobility according to their calculated molecular weights. We interpreted this as the most likely dimerization of the 434–665, 434–548 and 494–550 fragments, given the expected effects of SDS on the amphipathic helix that spans residues 434–447 (Figure 1C,E) and the predicted protein-protein interactions in the region 519–551

(Figure 1D; protein binding indicator). The fragment 434–548 was selected because of an additional predicted caspase site at residues 546–549 in Human BFSP1 (Figure S2) and the 494–550 as a control where no amphipathic helices or LBDs were predicted by the HELIQUEST algorithm (Figure 1C). These fragments (Figure 4A–C), as well as full-length bovine and human BFSP1, were then used to measure by SPR their relative affinities for a lipid bilayer derived from lens membranes formed on the L1 chip. Examples of the sensorgram plots and corresponding equilibrium dissociation constant, K_D calculations are provided for the recombinant BFSP1 fragments 434–665 (Figure 4A), 434–548 (Figure 4B) and 494–550 (Figure 4C).

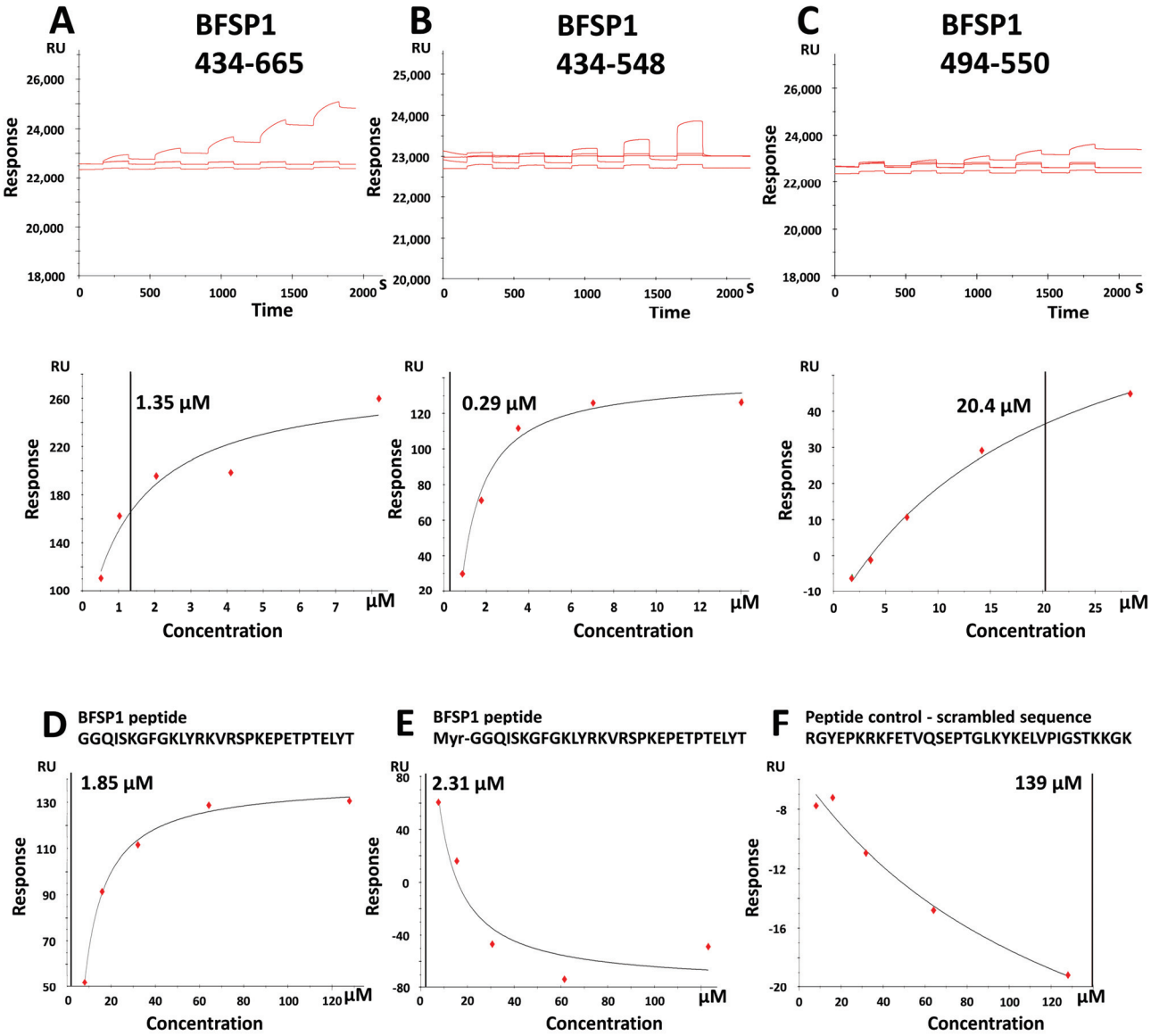

Figure 4. SPR measurement of the KD for BFSP1 C-terminal domain sequences. The sensorgram and calculated affinity (Equilibrium dissociation constant; K_D) of the BFSP1 fragments 434–548 (**A**), 434–548 (**B**) and 494–550 (**C**) for L1 biosensor chip loaded with bovine lens membrane lipids over a five-point concentration range. The plots of RU against concentration for BFSP1 434–665 (**A**), 434–548 (**B**) and 494–550 (**C**). The fragments were produced recombinantly in *E.coli*, and the final protein preparations after SEC purification used for the SPR experiments are shown in the insets of each panel. The chemically synthesized peptides of BFSP1 434–467 ± myristate (**D**,**E**) were compared to a scrambled peptide control (**F**). In all the plots (**A**–**F**), the K_D value is included in the plot and can be cross-referenced to Tables 1 and 2.

Table 1. SPR Measurement of KD for BFSP1 protein and C-terminal domain regions binding to Bovine Lens Fibre Cell Membrane Lipids.

Bovine BFSP1 (Native)	Human BFSP1 (Recomb.)	Human BFSP1 434–665	Human BFSP1 434–548	Human BFSP1 494–550	
6.02×10^{-6}	1.32×10^{-6}	3.06×10^{-6}	1.60×10^{-7}	1.05×10^{-5}	
6.75×10^{-6}	3.43×10^{-6}	1.34×10^{-6}	2.88×10^{-7}	2.04×10^{-5}	
7.52×10^{-6}	3.94×10^{-6}	2.19×10^{-6}	2.24×10^{-7}	1.53×10^{-5}	
6.76×10^{-6}	2.90×10^{-6}	2.20×10^{-6}	2.24×10^{-7}	1.54×10^{-5}	Mean
4.34×10^{-7}	8.02×10^{-7}	4.94×10^{-7}	3.70×10^{-8}	2.86×10^{-6}	SEM

Table 2. Effect of myristoylation on the lipid-binding of a polypeptide BFSP1 434–467.

Unmyristoylated BFSP1 434–467	Myristoylated BFSP1 434–467	Scrambled Polypeptide Control	
1.85×10^{-6}	2.19×10^{-6}	1.39×10^{-4}	
2.42×10^{-6}	2.31×10^{-6}	1.67×10^{-4}	
2.13×10^{-6}	$\mathbf{2.25 \times 10^{-6}}$	$\mathbf{1.53 \times 10^{-4}}$	Mean
2.83×10^{-7}	5.85×10^{-8}	1.37×10^{-5}	SEM

Table 1 summarises the calculated K_D for these fragments and for full-length bovine BFSP1 purified from bovine lenses and recombinant human BFSP1. From these data, the BFSP1 434–548 fragment had the greatest affinity as compared to both full-length and other C-terminal sequences of human BFSP1. In addition, removing the sequences 549–665 increased the affinity of the 434–548 fragment for the eye lens lipids compared to 434–665 (Figure 4A,B, respectively; Table 1).

The sequences 494–550 (Figure 4C, Table 1) were similar in affinity to that of recombinant human CRYAB (Figure S4), a lens protein also identified with membrane binding properties [57,58]. Interestingly, full-length human BFSP1 and native bovine BFSP1 had similar affinities to the 434–665 fragment (Table 1), suggesting that sequences within the 434–665 region could be responsible for the binding of both full-length BFSP1 to lens membrane lipids (Figure 4A,B; Table 1). In addition, their affinity was similar to that observed for both the myristoylated and unmyristoylated polypeptides spanning residues 434–467 in human BFSP1 (Figure 4D,E respectively compared to Figure 4F; Table 2).

These data suggest that myristoylation had little effect on the affinity for lens lipids (Table 2). However, it is noticeable that the recombinant fragment spanning residues 434–548 had the greatest affinity for bovine lens membrane lipids (Table 1) compared to the polypeptides spanning 434–467 (Table 2), suggesting that there could also be a contribution from the sequences 467–548 to membrane binding.

3.3. Transient Transfections of eGFP Labelled BFSP1 Constructs Confirms Membrane Association for Fragments Containing the Amphipathic Helix

The transient transfection of a human epithelial cell line MCF7 with eGFP-tagged BFSP1 C-terminal sequences was undertaken to evidence that these constructs (Figure 5A) could associate with membranes in living cells (Figure 5B).

Only those C-terminal sequences that contained the amphipathic helix and adjacent C-terminal sequences localised to the plasma membrane and internal membranes of transfected cells (Figure 5B). These were the fragments 434–548, 434–665 and 434–460. It is worth noting that for all three constructs, it was not only the plasma membranes, but also large cytoplasmic vesicular structures that were eGFP positive. The nuclear membranes, however, remained negative (Figure 5B), suggesting there was selectivity in the observed membrane binding. The BFSP1 C-terminal fragments 461–548 and 550–665 did not localise to any membrane compartments, but their eGFP signal remained in the cytoplasmic com-

partment (Figure 5B). Preventing myristoylation by transfecting the mutant G434A-548 did not prevent its membrane localisation.

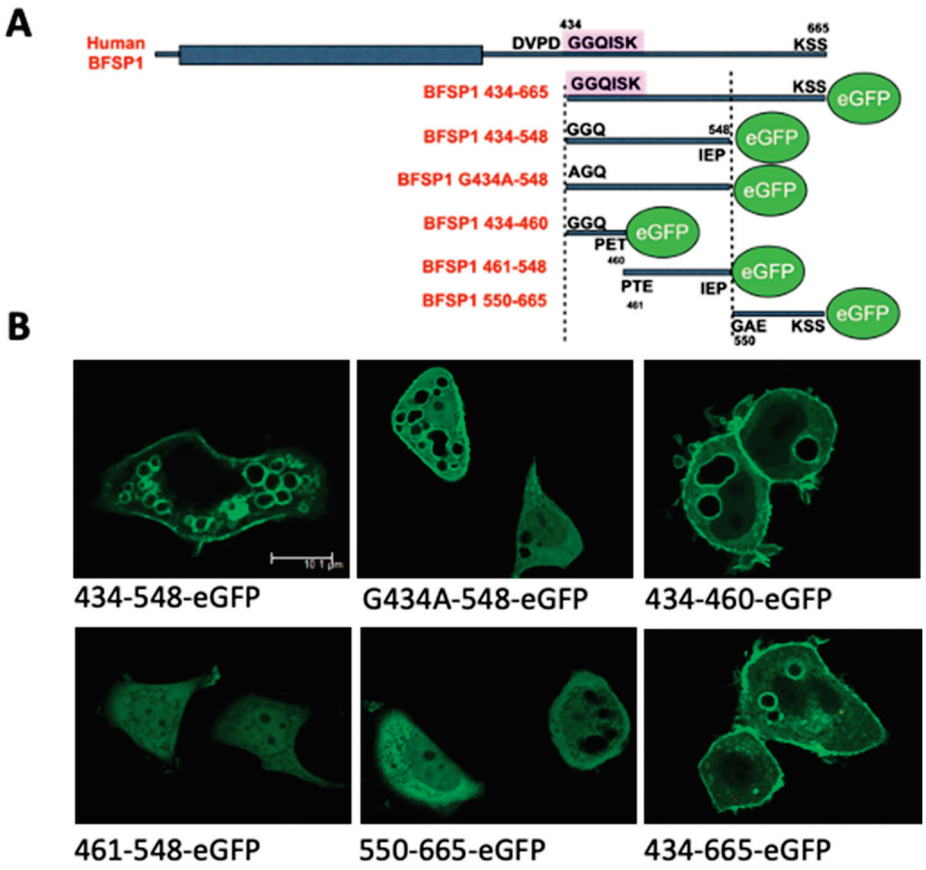

Figure 5. Transient transfection of C-terminal domain fragments from BFSP1 confirms 434–460 as a bone fide LBD. A series of eGFP-tagged BFSP1 constructs derived from the C-terminal domain designed to confirm the membrane binding of the amphipathic helix associated with the region 434–452 were subcloned into the peGFP-N3 vector (**A**). Transient transfection of these different constructs into MCF7 cells produced prominent plasma membrane staining for some (**B**; 434–665; G434–P548; A434–P548), but not all constructs (**B**; 461–548, 550–548). Furthermore, preventing myristoylation by replacing the N-terminal glycine residue with alanine (G434A) did not prevent the plasma membrane localization of BFSP1 434–548, suggesting that myristoylation was not necessary for its plasma membrane, or internal membrane localisation. Scale bar = 10 μm (**B**).

To identify which intracellular compartments were targets for labelling with the BFSP1 sequence 434–548, the vital dyes, Bodipy, Mitotracker and Lysotracker were used to counter label MCF7 cells and then followed by live cell imaging (Figure 6, red channel). Hoechst 33342 was used to label the nucleus (Figure 6, blue channel).

Intracellular vesicles were Bodipy positive (Figure 6 control, red channel), and these were also eGFP positive when transiently transfected with 434–548, but not 494–550. Mitochondrial membranes were negative but lysosomal membranes were positive (Figure 6; green channel) when transfected with 434–548 (Figure 6; arrows, green channel). In some cases, tamoxifen treatment was used to induce plasma membrane blebbing [66], and those vesicular structures that appeared to be extruding from the plasma membrane were also positive for eGFP BFSP1 434–665 and eGFP BFSP1 434–548, but not eGFP BFSP1 494–550 (Figure 6; green channel). These transfection data support the conclusion that the BFSP1 434–548 sequences can direct the association of BFSP1 to membrane compartments in living cells.

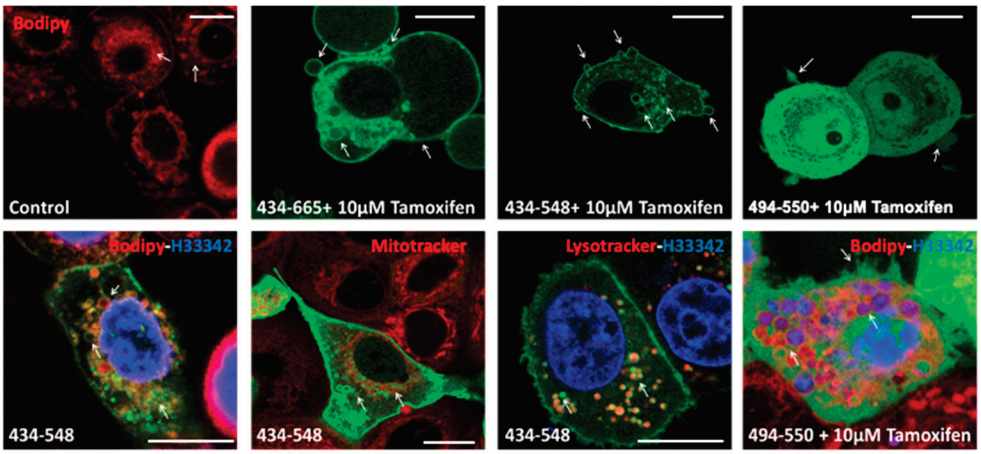

Figure 6. Localisation of BFSP1 434–548 with the lysosomal compartment. MCF7 cells were transiently transfected with BFSP1 434–548 and 434–665 tagged with eGFP and monitored by lice cell imaging. Transfected cells were labelled with the vital dyes, Lysotracker, Mitotracker, Bodipy 494/503 (Bodipy) and Hoechst 33324 *H33324) to follow the distribution of the fragments 434–548, 494–550 and 434–665 in transiently transfected MCF7 cells. Bodipy labelled internal membranes (arrows; Control), and in BFSP1 434–548 transfected cells, these were also co-labelled with eGFP (434–548; arrows). Note the absence (arrows; 434–548) of co-staining of mitochondria (Mitotracker; green channel) and BFSP1 434–548 (green channel), but that the lysosomal marker, Lysotracker (red channel), overlapped (arrows; 434–548) with BFSP1 434–548 signal (green channel). Tamoxifen (10 μM) induced membrane blebbing resulted in 434–548 and 434–665 labelled blebs, but this was not seen in cells transfected with BFSP1 494–554. Scale bars = 10 μm.

4. Discussion

4.1. BFSP1 Contains an Amphipathic Helix at Residues 434–452

The aim of this study was to determine whether the BFSP1 C-terminal domain of BFSP1 had the capacity to bind lens membrane lipids independently of AQP0, an integral membrane protein shown to interact with BFSP1 by chemical cross-linking [31]. We generated data from CD spectroscopy (Figure 2), SPR (Figure 4, Tables 1 and 2) and transient transfections of eGFP-tagged BFSP1 constructs (Figures 5 and 6) that support this conclusion. The bioinformatic analyses (Figure 1) suggested that a reason for the independent association of the C-terminal sequences of BFSP1 with lens fibre cell membranes [16,20,24,26,34,35] is the presence of an amphipathic helix spanning residues 434–451. Furthermore, the CD spectroscopy data show that a chemically synthesized polypeptide spanning residues 434–467 adopted an intrinsically disordered structure in water (Figure 2) in line with the fIDPnn prediction (Figure 1D) and that the inclusion of TFE [59] induced an α-helical transition (Figure 2) supporting the Heliquest amphipathic helix prediction (Figures 1C and S3). SDS can also provide the hydrophobic environment needed to induce the transition from unstructured to an α-helical domain for amphipathic helices, and we suggest this contributes to the unexpectedly slower relative mobility observed by SDS PAGE of the recombinantly expressed fragments (Figure 3). This important detail was not considered in earlier studies concerning the proteolytic processing of BFSP1 [24,34] and points to the oligomerisation and membrane-directed scaffolding potential for these BFSP1 C-terminal fragments containing the amphipathic helix and the adjacent intrinsically disordered sequences.

The presence of an amphipathic helix is essential for membrane association and membrane remodelling activities. For example, the small GTPases, Atg proteins, ENTH/ANTH-containing proteins and the BAR-domain all require amphipathic helices for their function [71]. Rhodopsin recovery depends upon recoverin binding to an amphipathic helix in its N-terminus [72]. In a broader neurological context, synapse evolution and function owe much to the protein complexin and its amphipathic helix [73]. The amphipathic helix is

key to the membrane association and targeting of such proteins as ARF1 [40,42] and other ARF family members [41]. In the case of Arfrp1 and Arl14, their amphipathic helices are sufficient to target these proteins to their appropriate membrane compartment [41]. Interestingly, naturally occurring mutations have been reported in amphipathic helix-containing membrane fission-inducing proteins and are the basis of human diseases [71] such as centronuclear myopathy (amphiphysin 2), Charcot-Marie-Tooth disease (GDAP1), Parkinson's disease (α-synuclein). It is perhaps no coincidence that when the C-terminal domain of BFSP1 is deleted, cataract develops [74], and there are many sequence variants listed for BFSP1 434–548 (https://www.uniprot.org/uniprotkb/Q12934/entry#disease_variants, accessed on 10 May 2023) some such as E468Q listed as likely to be disease-causing, as well as 14 other variants within the amphipathic helix itself that deserve further investigation. For example, Q436R, Y445C and R446S all change the hydrophobic moment of the amphipathic helix in BFSP1, changing the Discrimination Factor scores (Table 3), indicating such sequence variants could have both structural and functional consequences worthy of further investigation.

Table 3. Change in the Heliquest Discrimination Factor as a result of reported sequence variants in the 434–464 sequence of BFSP1, which includes the amphipathic helix (grey highlight). In this table, three sequence variants (Q436R, Y445C and R446S) reported for human BFSP1 (https://www.uniprot.org/uniprotkb/Q12934/entry#disease_variants, accessed on 10 May 2023) are analysed using the Heliquest algorithm (https://heliquest.ipmc.cnrs.fr, accessed on 10 May 2023). The values for the Hydrophic moment (HM) for z (net charge) and then used to calculate the Discrimination Factor (DF) for the wild type and three variants as indicated. Those sequences where a hydrophobic face is predicted are indicated (grey highlight), and DFs that are either higher or lower than the wild type of sequence are indicated (bold).

BFSP1 434–454 (Wild Type)	**Wild Type**			**Q436R**			**Y445C**			**R446S**		
Peptide Sequence Scan	**HM**	**z**	**DF**	**HM**	**z**	**DF**	**HM**	**z**	**DF**	**DM**	**z**	**DF**
GGQISKGFGKLYRKVKEK	0.53932	5	2.15911808	0.56706	6	**2.51530464**	0.55949	5	**2.17815856**	0.49211	4	**1.78455184**
GQISKGFGKLYRKVKEKV	0.59755	5	2.2140872	0.62717	6	**2.57204848**	0.61913	5	**2.23445872**	0.55201	4	**1.84109744**
RISKGFGKLYRKVKEKVR	0.63442	6	2.57889248	0.66175	7	**2.934692**	0.65431	6	**2.59766864**	0.58691	5	**2.20404304**
ISKGFGKLYRKVKEKVRS	0.62845	6	2.5732568	0.62845	6	2.5732568	0.64803	6	**2.59174032**	0.58061	5	**2.19809584**
SKGFGKLYRKVKEKVRSP	0.57526	6	2.52304544	0.57526	6	2.52304544	0.59602	6	**2.54264288**	0.52872	5	**2.14911168**
KGFGKLYRKVKEKVRSPK	0.56039	7	2.83900816	0.56039	7	2.83900816	0.57893	7	**2.85650992**	0.51154	6	**2.46289376**
GFGKLYRKVKEKVRSPKE	0.54099	5	2.16069456	0.54099	5	2.16069456	0.55961	5	**2.17827184**	0.49222	4	**1.78465568**
FGKLYRKVKEKVRSPKEP	0.54667	5	2.16605648	0.54667	5	2.16605648	0.56336	5	**2.18181184**	0.49629	4	**1.78849776**
GKLYRKVKEKVRSPKEPE	0.4226	4	1.7189344	0.4226	4	1.7189344	0.43641	4	**1.73197104**	0.37039	3	**1.33964816**
KLYRKVKEKVRSPKEPET	0.41416	4	1.71096704	0.41416	4	1.71096704	0.42877	4	**1.72475888**	0.36327	3	**1.33292688**
LYRKVKEKVRSPKEPETP	0.35341	3	1.32361904	0.35341	3	1.32361904	0.36259	3	**1.33228496**	0.29968	2	**0.94289792**
YRKVKEKVRSPKEPETPT	0.28225	3	1.256444	0.28225	3	1.256444	0.29517	3	**1.26864048**	0.22951	2	**0.87665744**
RKVKEKVRSPKEPETPTE	0.26427	2	0.90947088	0.26427	2	0.90947088	0.26427	2	0.90947088	0.21098	1	**0.52916512**

4.2. Potential Contribution of the Amphipathic Helix and Myristoylation to BFSP1 Structure and Function in the Lens

On binding to a membrane, the amphipathic helix will usually orient itself parallel to the membrane plane. Its hydrophobic side will insert into the bilayer, while the hydrophilic face will interact with the headgroups of the lipids in the membrane [71]. The lipid composition of the lens plasma membranes depends upon the differentiation status of the fibre cells, which is related to whether they are present in the lens nucleus or the lens cortex and the age of the lens [75]. Our studies used lipids extracted from the nucleus of bovine lenses and, therefore, will be enriched in cholesterol and sphingolipid. Clearly, it will be important to investigate how the lipid composition affects BFSP1 binding, but our transient transfection studies evidence that the amphipathic helix in BFSP1 is sufficient to direct membrane association of eGFP in MCF7 cells (Figures 5 and 6). Our data also suggest that other sequences within the 434–548 region likely influence the infinity (cf.

Tables 1 and 2). Our data show that there is membrane selectivity as neither the nuclear nor the mitochondrial membranes were labelled (Figure 6). Intracellular vesicles and the lysosomal membranes were, however, labelled (Figure 6). Both are critical to lens differentiation in organelle removal [76,77] and for aquaporin trafficking by a lysosomal-associated unconventional protein secretion mechanism [78]. Then the process of lens fibre cell compaction [79] and the fenestration of lens fibre cells leading to the formation of a stratified syncytium [80] will require an amphipathic helix containing proteins to be involved. Epitope mapping of bovine BFSP1 showed that the very C-terminal region becomes concentrated on the cell membranes in the bovine lens nucleus [24], which in the context of the data presented here, provides a different perspective on how beaded filaments and aquaporins affect the optical properties of the lens [18,33,81].

BFSP1 is the first intermediate filament protein identified to possess an amphipathic helix and the first to be identified that undergoes post-translational myristoylation. Our data are consistent with the view that myristoylation is not necessary for the membrane association of the 434–548 fragment (Figure 5B), but our previous study has demonstrated that myristoylation of this BFSP1 fragment is important to its regulation of AQP0 [18]. The presence of an amphipathic helix provides yet another mechanism to mediate the membrane association of an intermediate filament protein. Periplakin links vimentin, and the BFSP1 assembly partner BFSP2 to lens membranes [82] and is part of the EPPD complex [83], as well as plakoglobin [84] that links partners to the plasma membrane via the cadherins [83]. Whilst it is recognised that intermediate filaments impart physical properties to the membranes they support [85], there is also a growing appreciation that non-filamentous forms of cytoplasmic intermediate filament proteins, such as vimentin, have functions in the extracellular space [86,87]. The release of a C-terminal fragment of BFSP1 that contains an amphipathic helix capable of association with intracellular vesicles and with secreted membrane vesicles evidences a new cellular role for BFSP1.

5. Patents

The work described here forms the basis for the following patents that are pending (PCT/HU2021/050057 WO 2022/090752).

Supplementary Materials: The following supporting information can be downloaded at: https://www.mdpi.com/article/10.3390/cells12121580/s1, Figure S1: Alignment of BFSP1 protein sequences. Human (Q12934 BFSP1_Human), bovine (Q06002 BFSP1_BOVIN) and rat (Q02435 BFSP1_Rat) BFSP1 sequences were downloaded from UniProt [48] and aligned using COBALT [49]. The structural features were derived from the AlphaFold2 prediction [51], with the rod domain (red bar; residues 40–320). This rod domain comprises several α-helical regions, namely Coil 1A (residues 421–75), Coil 1B (residues 85–184) and Coil 2 (residues 202–320). Members of the intermediate filament protein family contain conserved motifs at either end of the rod domain, and these are indicated in Coil 1A and Coil 2. The rod domain is conserved between humans, cows and rats (identical residues in red; non-identical in blue; species-specific insertions or deletions in grey lowercase). The rod domain is flanked by unstructured regions, and these are striking in their lack of sequence homology. Of those sequences that are conserved within these unstructured regions, the post-translational myristoylation site (caspase and myristoylation sites indicated) and associated amphipathic helix (purple bar; residues 434–460 as predicted by heliQuest (https://heliquest.ipmc.cnrs.fr, accessed on 10 May 2023); see below) are indicated. Figure S2: Identification of a second Caspase Cleavage Site (SVFD) in bovine BFSP1. A. Identification and conservation of potential caspase recognition sites in the C-terminal sequences distal to the myristoylation sequence in human and bovine BFSP1 using GrabCas [67] and CasCleave 2 [68]. B. Schematic comparing the predicted human and bovine caspase cleavage sites and the proteomic strategy to identify the bovine BFSP1 434 and 480 sites. C. Identification of a second caspase cleavage site in the C-terminal sequences of bovine BFSP1 at residue 480. Bovine lens membranes from the lens cortex were subjected to trypsin cleavage, removal of SDS, and then MS-MS identification of the peptides eluted in ReX-Buffer 4 [64]. The search focused on tryptic peptides lacking a C-terminal arginine or lysine. The analysis identified a new caspase site at residues 477–480 (SFVD) in bovine BFSP1. Figure S3: Output from the HeliQuest analysis for

the human BFSP1 sequence 434–665. Figure S4: Affinity of recombinant human CRYAB for bovine lens lipids as measured by SPR. Recombinant human CRYAB was assessed for its affinity to the same L1 chip coated with lipids prepared from bovine lens membranes. An affinity of 22.83 μM was measured.

Author Contributions: R.A.Q. conceived the experimental approach and wrote the first draft of the manuscript. M.J. and A.T. provided experimental data with the help of A.A.K., A.U., A.P.B., C.S.C., S.F.-P., E.P., K.L., E.N.W. and B.K., M.J. and A.T. also contributed to the refinement of the experimental analyses and the editing of the first draft. All authors have read and agreed to the published version of the manuscript.

Funding: This work was supported by funding from Fight for Sight (M.J., A.T., R.A.Q.; Fight for Sight UK grant #1584/85) and from the National Eye Research Charity (A.K.K.; SAC014) are gratefully acknowledged. AW was funded via the LDLensRad project that received funding from the Euratom research and training programme 2014–2018 in the framework of the CONCERT (grant agreement No. 662287). E.N.W. and K.L. were funded by a vacation scholarship from the Biophysical Sciences Institute. This publication reflects only the author's view. Responsibility for the information and views expressed therein lies entirely with the authors. The European Commission is not responsible for any use that may be made of the information it contains.

Institutional Review Board Statement: Not applicable.

Informed Consent Statement: Not applicable.

Data Availability Statement: The data presented in this study are available on request from the corresponding author. The data are not publicly available due to privacy reasons.

Acknowledgments: We thank Ian Cummins for his support and encouragement as we started the proteomic analyses before his passing on 4 June 2019. We thank Beth Bromley for access and advice to the CD instrument and Ian Edwards for helping maintain the SPR facilities.

Conflicts of Interest: The authors declare no conflict of interest. The funders had no role in the design of this study; in the collection, analyses, or interpretation of data; in the writing of the manuscript; or in the decision to publish the results.

References

1. Quinlan, R.A.; Clark, J.I. Insights into the Biochemical and Biophysical Mechanisms Mediating The Longevity of the Transparent Optics of the Eye Lens. *J. Biol. Chem.* **2022**, *298*, 102537. [CrossRef] [PubMed]
2. Perng, M.D.; Quinlan, R.A. Seeing is believing! The optical properties of the eye lens are dependent upon a functional intermediate filament cytoskeleton. *Exp. Cell. Res.* **2005**, *305*, 1–9. [CrossRef] [PubMed]
3. Carter, J.M.; Hutcheson, A.M.; Quinlan, R.A. In vitro studies on the assembly properties of the lens beaded filament proteins: Co-assembly with a-crystallin but not with vimentin. *Exp. Eye Res.* **1995**, *60*, 181–192. [CrossRef] [PubMed]
4. Maisel, H.; Perry, M.M. Electron microscope observations on some structural proteins of the chick lens. *Exp. Eye Res.* **1972**, *14*, 7–12. [CrossRef]
5. Song, S.; Landsbury, A.; Dahm, R.; Liu, Y.; Zhang, Q.; Quinlan, R.A. Functions of the intermediate filament cytoskeleton in the eye lens. *J. Clin. Investig.* **2009**, *119*, 1837–1848. [CrossRef]
6. Shiels, A.; Hejtmancik, J.F. Inherited cataracts: Genetic mechanisms and pathways new and old. *Exp. Eye Res.* **2021**, *209*, 108662. [CrossRef]
7. Fudge, D.S.; McCuaig, J.V.; Van Stralen, S.; Hess, J.F.; Wang, H.; Mathias, R.T.; FitzGerald, P.G. Intermediate filaments regulate tissue size and stiffness in the murine lens. *Investig. Ophthalmol. Vis. Sci.* **2011**, *52*, 3860–3867. [CrossRef]
8. Sandilands, A.; Prescott, A.R.; Wegener, A.; Zoltoski, R.K.; Hutcheson, A.M.; Masaki, S.; Kuszak, J.R.; Quinlan, R.A. Knockout of the intermediate filament protein CP49 destabilises the lens fibre cell cytoskeleton and decreases lens optical quality, but does not induce cataract. *Exp. Eye Res.* **2003**, *76*, 385–391. [CrossRef]
9. Sandilands, A.; Wang, X.; Hutcheson, A.M.; James, J.; Prescott, A.R.; Wegener, A.; Pekny, M.; Gong, X.; Quinlan, R.A. Bfsp2 mutation found in mouse 129 strains causes the loss of CP49 and induces vimentin-dependent changes in the lens fibre cell cytoskeleton. *Exp. Eye Res.* **2004**, *78*, 109–123. [CrossRef]
10. Alizadeh, A.; Clark, J.; Seeberger, T.; Hess, J.; Blankenship, T.; FitzGerald, P.G. Targeted deletion of the lens fiber cell-specific intermediate filament protein filensin. *Investig. Ophthalmol. Vis. Sci.* **2003**, *44*, 5252–5258. [CrossRef]
11. Alizadeh, A.; Clark, J.I.; Seeberger, T.; Hess, J.; Blankenship, T.; Spicer, A.; FitzGerald, P.G. Targeted genomic deletion of the lens-specific intermediate filament protein CP49. *Investig. Ophthalmol. Vis. Sci.* **2002**, *43*, 3722–3727.
12. Kwon, H.J.; Shikinaka, K.; Kakugo, A.; Furukawa, H.; Osada, Y.; Gong, J.P. Motility and structural polymorphism of polymer-actin complex gel. *J. Nanosci. Nanotechnol.* **2007**, *7*, 844–847. [CrossRef] [PubMed]

13. FitzGerald, P.G. Lens intermediate filaments. *Exp. Eye Res.* **2009**, *88*, 165–172. [CrossRef] [PubMed]
14. Landsbury, A.; Perng, M.D.; Pohl, E.; Quinlan, R.A. Functional symbiosis between the intermediate filament cytoskeleton and small heat shock proteins. In *Small Stress Proteins and Human Diseases*; Nova Science Publishers Inc.: Hauppauge, NY, USA, 2010; pp. 55–87.
15. Kalligeraki, A.A.; Isted, A.; Jarrin, M.; Uwineza, A.; Pal, R.; Saunter, C.D.; Girkin, J.M.; Obara, B.; Quinlan, R.A. Three-dimensional data capture and analysis of intact eye lenses evidences emmetropia-associated changes in epithelial cell organization. *Sci. Rep.* **2020**, *10*, 16898. [CrossRef] [PubMed]
16. FitzGerald, P.G.; Casselman, J. Immunologic conservation of the fiber cell beaded filament. *Curr. Eye Res.* **1991**, *10*, 471–478. [CrossRef]
17. Der Perng, M.; Zhang, Q.; Quinlan, R.A. Insights into the beaded filament of the eye lens. *Exp. Cell. Res.* **2007**, *313*, 2180–2188. [CrossRef]
18. Tapodi, A.; Clemens, D.M.; Uwineza, A.; Jarrin, M.; Goldberg, M.W.; Thinon, E.; Heal, W.P.; Tate, E.W.; Nemeth-Cahalan, K.; Vorontsova, I.; et al. BFSP1 C-terminal domains released by post-translational processing events can alter significantly the calcium regulation of AQP0 water permeability. *Exp. Eye Res.* **2019**, *185*, 107585. [CrossRef]
19. Masaki, S.; Quinlan, R.A. Gene structure and sequence comparisons of the eye lens specific protein, filensin, from rat and mouse: Implications for protein classification and assembly. *Gene* **1997**, *201*, 11–20. [CrossRef]
20. Wang, Z.; Obidike, J.E.; Schey, K.L. Posttranslational modifications of the bovine lens beaded filament proteins filensin and CP49. *Investig. Ophthalmol. Vis. Sci.* **2010**, *51*, 1565–1574. [CrossRef]
21. Martin, D.D.; Beauchamp, E.; Berthiaume, L.G. Post-translational myristoylation: Fat matters in cellular life and death. *Biochimie* **2011**, *93*, 18–31. [CrossRef]
22. Lemarié, F.L.; Sanders, S.S.; Nguyen, Y.; Martin, D.D.O.; Hayden, M.R. Full-length huntingtin is palmitoylated at multiple sites and post-translationally myristoylated following caspase-cleavage. *Front. Physiol.* **2023**, *14*, 1086112. [CrossRef] [PubMed]
23. Madeo, G.; Savojardo, C.; Martelli, P.L.; Casadio, R. SVMyr: A Web Server Detecting Co- and Post-translational Myristoylation in Proteins. *J. Mol. Biol.* **2022**, *434*, 167605. [CrossRef] [PubMed]
24. Sandilands, A.; Prescott, A.R.; Hutcheson, A.M.; Quinlan, R.A.; Casselman, J.T.; FitzGerald, P.G. Filensin is proteolytically processed during lens fiber cell differentiation by multiple independant pathways. *Eur. J. Cell. Biol.* **1995**, *67*, 238–253. [PubMed]
25. Wang, Z.; Ryan, D.J.; Schey, K.L. Localization of the lens intermediate filament switch by imaging mass spectrometry. *Exp. Eye Res.* **2020**, *198*, 108134. [CrossRef] [PubMed]
26. Sandilands, A.; Prescott, A.R.; Carter, J.M.; Hutcheson, A.M.; Quinlan, R.A.; Richards, J.; FitzGerald, P.G. Vimentin and CP49/Filensin form distinct networks in the lens which are independantly modulated during lens fibre cell differentiation. *J. Cell. Sci.* **1995**, *108*, 1397–1406. [CrossRef]
27. Griesser, E.; Vemula, V.; Mónico, A.; Pérez-Sala, D.; Fedorova, M. Dynamic posttranslational modifications of cytoskeletal proteins unveil hot spots under nitroxidative stress. *Redox Biol.* **2021**, *44*, 102014. [CrossRef]
28. Kaus-Drobek, M.; Mücke, N.; Szczepanowski, R.H.; Wedig, T.; Czarnocki-Cieciura, M.; Polakowska, M.; Herrmann, H.; Wysłouch-Cieszyńska, A.; Dadlez, M. Vimentin S-glutathionylation at Cys328 inhibits filament elongation and induces severing of mature filaments in vitro. *Febs J.* **2020**, *287*, 5304–5322. [CrossRef]
29. MacTaggart, B.; Kashina, A. Posttranslational modifications of the cytoskeleton. *Cytoskeleton* **2021**, *78*, 142–173. [CrossRef]
30. Snider, N.T.; Ku, N.O.; Omary, M.B. The sweet side of vimentin. *Elife* **2018**, *7*, e35336. [CrossRef]
31. Wang, Z.; Schey, K.L. Identification of a direct Aquaporin-0 binding site in the lens-specific cytoskeletal protein filensin. *Exp. Eye Res.* **2017**, *159*, 23–29. [CrossRef]
32. Schey, K.L.; Petrova, R.S.; Gletten, R.B.; Donaldson, P.J. The Role of Aquaporins in Ocular Lens Homeostasis. *Int. J. Mol. Sci.* **2017**, *18*, 2693. [CrossRef] [PubMed]
33. Varadaraj, K.; FitzGerald, P.G.; Kumari, S.S. Deletion of beaded filament proteins or the C-terminal end of Aquaporin 0 causes analogous abnormal distortion aberrations in mouse lens. *Exp. Eye Res.* **2021**, *209*, 108645. [CrossRef] [PubMed]
34. Brunkener, M.; Georgatos, S.D. Membrane-binding properties of filensin, a cytoskeletal protein of the lens fibre cells. *J. Cell. Sci.* **1992**, *103*, 709–718. [CrossRef] [PubMed]
35. Wang, Z.; Schey, K.L. Proteomic Analysis of Lipid Raft-Like Detergent-Resistant Membranes of Lens Fiber Cells. *Investig. Ophthalmol. Vis. Sci.* **2015**, *56*, 8349–8360. [CrossRef]
36. Milks, L.C.; Kumar, N.M.; Houghten, R.; Unwin, N.; Gilula, N.B. Topology of the 32-kd liver gap junction protein determined by site-directed antibody localizations. *EMBO J.* **1988**, *7*, 2967–2975. [CrossRef] [PubMed]
37. Giglione, C.; Meinnel, T. Mapping the myristoylome through a complete understanding of protein myristoylation biochemistry. *Progress. Lipid Res.* **2022**, *85*, 101139. [CrossRef]
38. Wright, M.H.; Heal, W.P.; Mann, D.J.; Tate, E.W. Protein myristoylation in health and disease. *J. Chem. Biol.* **2010**, *3*, 19–35. [CrossRef]
39. Harroun, T.A.; Bradshaw, J.P.; Balali-Mood, K.; Katsaras, J. A structural study of the myristoylated N-terminus of ARF1. *Biochim. Biophys. Acta* **2005**, *1668*, 138–144. [CrossRef]
40. Liu, Y.; Kahn, R.A.; Prestegard, J.H. Structure and membrane interaction of myristoylated ARF1. *Structure* **2009**, *17*, 79–87. [CrossRef]

41. Yang, F.; Li, T.; Peng, Z.; Liu, Y.; Guo, Y. The amphipathic helices of Arfrp1 and Arl14 are sufficient to determine subcellular localizations. *J. Biol. Chem.* **2020**, *295*, 16643–16654. [CrossRef]
42. Brass, V.; Bieck, E.; Montserret, R.; Wölk, B.; Hellings, J.A.; Blum, H.E.; Penin, F.; Moradpour, D. An amino-terminal amphipathic alpha-helix mediates membrane association of the hepatitis C virus nonstructural protein 5A. *J. Biol. Chem.* **2002**, *277*, 8130–8139. [CrossRef] [PubMed]
43. Gautier, R.; Douguet, D.; Antonny, B.; Drin, G. HELIQUEST: A web server to screen sequences with specific alpha-helical properties. *Bioinformatics* **2008**, *24*, 2101–2102. [CrossRef] [PubMed]
44. Keller, R.C. New user-friendly approach to obtain an eisenberg plot and its use as a practical tool in protein sequence analysis. *Int. J. Mol. Sci.* **2011**, *12*, 5577–5591. [CrossRef] [PubMed]
45. Keller, R.C. Prediction of lipid-binding regions in cytoplasmic and extracellular loops of membrane proteins as exemplified by protein translocation membrane proteins. *J. Membr. Biol.* **2013**, *246*, 21–29. [CrossRef] [PubMed]
46. Hu, G.; Katuwawala, A.; Wang, K.; Wu, Z.; Ghadermarzi, S.; Gao, J.; Kurgan, L. flDPnn: Accurate intrinsic disorder prediction with putative propensities of disorder functions. *Nat. Commun.* **2021**, *12*, 4438. [CrossRef]
47. Feng, S.H.; Xia, C.Q.; Zhang, P.D.; Shen, H.B. Ab-Initio Membrane Protein Amphipathic Helix Structure Prediction Using Deep Neural Networks. *IEEE/ACM Trans. Comput. Biol. Bioinform./IEEE ACM* **2022**, *19*, 795–805. [CrossRef]
48. UniProt: The Universal Protein Knowledgebase in 2023. *Nucleic Acids Res.* **2023**, *51*, D523–D531. [CrossRef]
49. Papadopoulos, J.S.; Agarwala, R. COBALT: Constraint-based alignment tool for multiple protein sequences. *Bioinformatics* **2007**, *23*, 1073–1079. [CrossRef]
50. Jumper, J.; Evans, R.; Pritzel, A.; Green, T.; Figurnov, M.; Ronneberger, O.; Tunyasuvunakool, K.; Bates, R.; Žídek, A.; Potapenko, A.; et al. Highly accurate protein structure prediction with AlphaFold. *Nature* **2021**, *596*, 583–589. [CrossRef]
51. Varadi, M.; Anyango, S.; Deshpande, M.; Nair, S.; Natassia, C.; Yordanova, G.; Yuan, D.; Stroe, O.; Wood, G.; Laydon, A.; et al. AlphaFold Protein Structure Database: Massively expanding the structural coverage of protein-sequence space with high-accuracy models. *Nucleic Acids Res.* **2022**, *50*, D439–D444. [CrossRef]
52. Wang, J.; Youkharibache, P.; Marchler-Bauer, A.; Lanczycki, C.; Zhang, D.; Lu, S.; Madej, T.; Marchler, G.H.; Cheng, T.; Chong, L.C.; et al. iCn3D: From Web-Based 3D Viewer to Structural Analysis Tool in Batch Mode. *Front. Mol. Biosci.* **2022**, *9*, 831740. [CrossRef] [PubMed]
53. Sharma, S.; Conover, G.; Elliott, J.L.; Perng, M.D.; Herrmann, H.; Quinlan, R.A. αB-crystallin is a sensor for assembly intermediates and for the subunit topology of desmin intermediate filaments. *Cell. Stress. Chaperones* **2017**, *22*, 613–626. [CrossRef] [PubMed]
54. Perng, M.D.; Sandilands, A.; Kuszak, J.; Dahm, R.; Wegener, A.; Prescott, A.R.; Quinlan, R.A. The intermediate filament systems in the eye lens. *Intermed. Filam. Cytoskelet.* **2004**, *78*, 597–624.
55. Uwineza, A.; Cummins, I.; Jarrin, M.; Kalligeraki, A.A.; Barnard, S.; Mol, M.; Degani, G.; Altomare, A.A.; Aldini, G.; Schreurs, A.; et al. Identification and quantification of ionising radiation-induced oxysterol formation in membranes of lens fibre cells. *Adv. Redox Res.* **2023**, *7*, 100057. [CrossRef]
56. Bligh, E.G.; Dyer, W.J. A rapid method of total lipid extraction and purification. *Can. J. Biochem. Physiol.* **1959**, *37*, 911–917. [CrossRef]
57. Cobb, B.A.; Petrash, J.M. alpha-Crystallin Chaperone-like Activity and Membrane Binding in Age-Related Cataracts. *Biochemistry* **2002**, *41*, 483–490. [CrossRef]
58. Borchman, D.; Tang, D. Binding capacity of alpha-crystallin to bovine lens lipids. *Exp. Eye Res.* **1996**, *63*, 407–410. [CrossRef]
59. Roccatano, D.; Colombo, G.; Fioroni, M.; Mark, A.E. Mechanism by which 2,2,2-trifluoroethanol/water mixtures stabilize secondary-structure formation in peptides: A molecular dynamics study. *Proc. Natl. Acad. Sci. USA* **2002**, *99*, 12179–12184. [CrossRef]
60. Konno, K.; Hisada, M.; Fontana, R.; Lorenzi, C.C.; Naoki, H.; Itagaki, Y.; Miwa, A.; Kawai, N.; Nakata, Y.; Yasuhara, T.; et al. Anoplin, a novel antimicrobial peptide from the venom of the solitary wasp Anoplius samariensis. *Biochim. Biophys. Acta* **2001**, *1550*, 70–80. [CrossRef]
61. Miles, A.J.; Ramalli, S.G.; Wallace, B.A. DichroWeb, a website for calculating protein secondary structure from circular dichroism spectroscopic data. *Protein Sci.* **2022**, *31*, 37–46. [CrossRef]
62. Sreerama, N.; Woody, R.W. Estimation of protein secondary structure from circular dichroism spectra: Comparison of CONTIN, SELCON, and CDSSTR methods with an expanded reference set. *Anal. Biochem.* **2000**, *287*, 252–260. [CrossRef] [PubMed]
63. Sreerama, N.; Venyaminov, S.Y.; Woody, R.W. Estimation of protein secondary structure from circular dichroism spectra: Inclusion of denatured proteins with native proteins in the analysis. *Anal. Biochem.* **2000**, *287*, 243–251. [CrossRef] [PubMed]
64. Rappsilber, J.; Mann, M.; Ishihama, Y. Protocol for micro-purification, enrichment, pre-fractionation and storage of peptides for proteomics using StageTips. *Nat. Protoc.* **2007**, *2*, 1896–1906. [CrossRef] [PubMed]
65. Laemmli, U. Cleavage of structural proteins during the assembly of the head of bacteriophage T4. *Nature* **1970**, *277*, 680–685. [CrossRef]
66. Cui, Q.; Tashiro, S.; Onodera, S.; Minami, M.; Ikejima, T. Autophagy preceded apoptosis in oridonin-treated human breast cancer MCF-7 cells. *Biol. Pharm. Bull.* **2007**, *30*, 859–864. [CrossRef] [PubMed]
67. Backes, C.; Kuentzer, J.; Lenhof, H.P.; Comtesse, N.; Meese, E. GraBCas: A bioinformatics tool for score-based prediction of Caspase- and Granzyme B-cleavage sites in protein sequences. *Nucleic Acids Res.* **2005**, *33*, W208–W213. [CrossRef] [PubMed]

68. Wang, M.; Zhao, X.M.; Tan, H.; Akutsu, T.; Whisstock, J.C.; Song, J. Cascleave 2.0, a new approach for predicting caspase and granzyme cleavage targets. *Bioinformatics* **2014**, *30*, 71–80. [CrossRef] [PubMed]
69. Nakazawa, Y.; Oka, M.; Furuki, K.; Mitsuishi, A.; Nakashima, E.; Takehana, M. The effect of the interaction between aquaporin 0 (AQP0) and the filensin tail region on AQP0 water permeability. *Mol. Vis.* **2011**, *17*, 3191–3199. [PubMed]
70. Robustelli, J.; Baumgart, T. Membrane partitioning and lipid selectivity of the N-terminal amphipathic H0 helices of endophilin isoforms. *Biochim. Biophys. Acta Biomembr.* **2021**, *1863*, 183660. [CrossRef]
71. Zhukovsky, M.A.; Filograna, A.; Luini, A.; Corda, D.; Valente, C. Protein Amphipathic Helix Insertion: A Mechanism to Induce Membrane Fission. *Front. Cell. Dev. Biol.* **2019**, *7*, 291. [CrossRef]
72. Higgins, M.K.; Oprian, D.D.; Schertler, G.F. Recoverin binds exclusively to an amphipathic peptide at the N terminus of rhodopsin kinase, inhibiting rhodopsin phosphorylation without affecting catalytic activity of the kinase. *J. Biol. Chem.* **2006**, *281*, 19426–19432. [CrossRef] [PubMed]
73. Lottermoser, J.A.; Dittman, J.S. Complexin Membrane Interactions: Implications for Synapse Evolution and Function. *J. Mol. Biol.* **2023**, *435*, 167774. [CrossRef] [PubMed]
74. Ramachandran, R.D.; Perumalsamy, V.; Hejtmancik, J.F. Autosomal recessive juvenile onset cataract associated with mutation in BFSP1. *Hum. Genet.* **2007**, *121*, 475–482. [CrossRef] [PubMed]
75. Borchman, D.; Yappert, M.C. Lipids and the ocular lens. *J. Lipid Res.* **2010**, *51*, 2473–2488. [CrossRef] [PubMed]
76. Costello, M.J.; Brennan, L.A.; Mohamed, A.; Gilliland, K.O.; Johnsen, S.; Kantorow, M. Identification and Ultrastructural Characterization of a Novel Nuclear Degradation Complex in Differentiating Lens Fiber Cells. *PLoS ONE* **2016**, *11*, e0160785. [CrossRef]
77. Bassnett, S. Lens organelle degradation. *Exp. Eye Res.* **2002**, *74*, 1–6. [CrossRef]
78. Gletten, R.B.; Cantrell, L.S.; Bhattacharya, S.; Schey, K.L. Lens Aquaporin-5 Inserts into Bovine Fiber Cell Plasma Membranes via Unconventional Protein Secretion. *Investig. Ophthalmol. Vis. Sci.* **2022**, *63*, 5. [CrossRef]
79. Bassnett, S.; Costello, M.J. The cause and consequence of fiber cell compaction in the vertebrate lens. *Exp. Eye Res.* **2017**, *156*, 50–57. [CrossRef]
80. Shi, Y.; Barton, K.; De Maria, A.; Petrash, J.M.; Shiels, A.; Bassnett, S. The stratified syncytium of the vertebrate lens. *J. Cell. Sci.* **2009**, *122*, 1607–1615. [CrossRef]
81. FitzGerald, P.; Sun, N.; Shibata, B.; Hess, J.F. Expression of the type VI intermediate filament proteins CP49 and filensin in the mouse lens epithelium. *Mol. Vis.* **2016**, *22*, 970–989.
82. Yoon, K.H.; Fitzgerald, P.G. Periplakin Serves as a Linker for Both Vimentin and the Highly Divergent Beaded Filament Proteins in the Ocular Lens. *Investig. Ophthalmol. Vis. Sci.* **2008**, *50*, 1283–1289. [CrossRef] [PubMed]
83. Straub, B.K.; Boda, J.; Kuhn, C.; Schnoelzer, M.; Korf, U.; Kempf, T.; Spring, H.; Hatzfeld, M.; Franke, W.W. A novel cell-cell junction system: The cortex adhaerens mosaic of lens fiber cells. *J. Cell. Sci.* **2003**, *116*, 4985–4995. [CrossRef]
84. Franke, W.W.; Kapprell, H.P.; Cowin, P. Plakoglobin is a component of the filamentous subplasmalemmal coat of lens cells. *Eur. J. Cell. Biol.* **1987**, *43*, 301–315. [PubMed]
85. Quinlan, R.A.; Schwarz, N.; Windoffer, R.; Richardson, C.; Hawkins, T.; Broussard, J.A.; Green, K.J.; Leube, R.E. A rim-and-spoke hypothesis to explain the biomechanical roles for cytoplasmic intermediate filament networks. *J. Cell. Sci.* **2017**, *130*, 3437–3445. [CrossRef] [PubMed]
86. Patteson, A.E.; Vahabikashi, A.; Goldman, R.D.; Janmey, P.A. Mechanical and Non-Mechanical Functions of Filamentous and Non-Filamentous Vimentin. *Bioessays* **2020**, *42*, e2000078. [CrossRef]
87. Suprewicz, Ł.; Swoger, M.; Gupta, S.; Piktel, E.; Byfield, F.J.; Iwamoto, D.V.; Germann, D.; Reszeć, J.; Marcińczyk, N.; Carroll, R.J.; et al. Extracellular Vimentin as a Target against SARS-CoV-2 Host Cell Invasion. *Small* **2022**, *18*, e2105640. [CrossRef]

Disclaimer/Publisher's Note: The statements, opinions and data contained in all publications are solely those of the individual author(s) and contributor(s) and not of MDPI and/or the editor(s). MDPI and/or the editor(s) disclaim responsibility for any injury to people or property resulting from any ideas, methods, instructions or products referred to in the content.

cells

MDPI

Article

Eye Lens Organoids Made Simple: Characterization of a New Three-Dimensional Organoid Model for Lens Development and Pathology

Matthieu Duot [1,2,†], Roselyne Viel [3,†], Justine Viet [1], Catherine Le Goff-Gaillard [1], Luc Paillard [1], Salil A. Lachke [2,4,‡], Carole Gautier-Courteille [1,*,‡] and David Reboutier [1,*,‡]

1 CNRS, UMR 6290, Institut de Génétique et Développement de Rennes (IGDR), Université de Rennes, 35000 Rennes, France
2 Department of Biological Sciences, University of Delaware, Newark, DE 19716, USA
3 CNRS, Inserm UMS Biosit, H2P2 Core Facility, Université de Rennes, 35000 Rennes, France
4 Center for Bioinformatics and Computational Biology, University of Delaware, Newark, DE 19716, USA
* Correspondence: carole.gautier-courteille@univ-rennes1.fr (C.G.-C.); david.reboutier@univ-rennes1.fr (D.R.); Tel.: +33-2-23-23-47-81 (C.G.-C.); +33-2-23-23-46-10 (D.R.)
† These authors contributed equally to this work.
‡ These authors contributed equally to this work.

Abstract: Cataract, the opacification of the lens, is the leading cause of blindness worldwide. Although effective, cataract surgery is costly and can lead to complications. Toward identifying alternate treatments, it is imperative to develop organoid models relevant for lens studies and drug screening. Here, we demonstrate that by culturing mouse lens epithelial cells under defined three-dimensional (3D) culture conditions, it is possible to generate organoids that display optical properties and recapitulate many aspects of lens organization and biology. These organoids can be rapidly produced in large amounts. High-throughput RNA sequencing (RNA-seq) on specific organoid regions isolated via laser capture microdissection (LCM) and immunofluorescence assays demonstrate that these lens organoids display a spatiotemporal expression of key lens genes, e.g., *Jag1*, *Pax6*, *Prox1*, *Hsf4* and *Cryab*. Further, these lens organoids are amenable to the induction of opacities. Finally, the knockdown of a cataract-linked RNA-binding protein encoding gene, *Celf1*, induces opacities in these organoids, indicating their use in rapidly screening for genes that are functionally relevant to lens biology and cataract. In sum, this lens organoid model represents a compelling new tool to advance the understanding of lens biology and pathology and can find future use in the rapid screening of compounds aimed at preventing and/or treating cataracts.

Keywords: cataract; eye lens; organoid; pathophysiology; *Celf1*

1. Introduction

The lens, in conjunction with the cornea, is responsible for the focusing of light onto the retina, thus creating a clear image [1]. It is a fully transparent biological tissue that involves extreme cell differentiation processes. At the histological level, the lens is composed of an anterior monolayered epithelium containing proliferating cells in the equatorial region that later exit the cell cycle and progressively differentiate into fiber cells [2]. These latter cells form the lens cortex once the differentiation process is complete. To achieve lens transparency, fiber cells lengthen extensively (~1000X), produce large amounts of refractive proteins called crystallins, and eliminate their organelles, including their nuclei [3,4]. Lens clouding or cataract is the leading cause of blindness worldwide. While the primary reason for the development of cataracts is aging, they can also be induced by environmental factors or have a congenital origin, often triggered by genetic predispositions or abnormalities [5,6]. To date, the only treatment for cataracts is surgery, which consists of replacing the clouded lens with an artificial implant. Although it is effective, surgery is costly and can have

side effects that are far from harmless [7]. Therefore, efforts to develop drugs to treat cataracts have been initiated [8–10]. Animal models such as zebrafish [11], Xenopus [12], chicken or mammals, namely, rodents, dogs or macaques [13], are used for the study of lens pathophysiology. However, a major bottleneck toward developing anti-cataract drugs remains the lack of an adequate biological model for intensive drug screening.

In recent years, biology and medicine have undergone a revolution with the advent of particular three-dimensional (3D) cultures called organoids [14]. These are in vitro cellular models that mimic several aspects of the structure and function of the corresponding organ. Lens epithelium explants were a first generation of 3D lens cultures [15]. Later on, lentoid bodies, which are 3D cellular structures emerging from various types of 2D stem cell cultures [16–18], or individual micro-lenses grown from lens epithelial cells or pluripotent stem cells [19,20] were described. Although these models have very interesting molecular and/or optical characteristics, they do not exhibit any particular organization reminiscent of the histology of the lens [21]. Moreover, they often require sequential treatments via individual or combined growth factors and remain tricky and time-consuming to implement. Consequently, they generally (except for the paper from Murphy and colleagues [19]) do not allow for high-throughput studies.

The goal of the present study was to develop a mammalian organoid lens model that could be generated rapidly and is more convenient to use. As a starting point, we considered a previous paper, which shows that lens epithelium can regenerate a functional lens after its ablation in several vertebrate models [22]. This capacity relies on the presence of lens stem or progenitor cells that sustain self-renewal. A characterization of these cells demonstrated that they express *Pax6* and *Bmi1* and that they are able to spontaneously generate lentoid bodies. The 21EM15 mouse lens epithelial cell (LEC) line expresses *Pax6* and *Bmi1* and can spontaneously form lentoid bodies in vitro [23,24]. However, these lentoid bodies have not been characterized, and the culture conditions needed to controllably induce 21EM15 cells to become such 3D structures have not been defined.

Therefore, in the present study, we sought to derive the culture conditions that could generate lens organoids from 21EM15 cells *en masse*. Further, we sought to undertake their detailed characterization to evaluate their utility in studying genes and pathways relevant to lens biology and pathology. Our work indicates that by using simple 3D culture conditions, we can generate numerous lens organoids in a short period of time. These organoids show very interesting optical properties and recapitulate lens physiology at the molecular, histological and cellular levels. In addition, our results demonstrate the possibility to induce various types of opacities, thus mimicking cataract, in these organoids. As a whole, the 21EM15 organoids should therefore provide the lens community with a compelling new model to advance the understanding of lens biology and pathology. From a clinical point of view, although derived from mice, these organoids can potentially be used to screen compounds that could have effects on the prevention and/or treatment of cataracts.

2. Materials and Methods

2.1. Cell Culture

21EM15 (obtained from Dr. John Reddan, Oakland University, Rochester, MI, USA) and HaCat cells (ATCC) were cultured in DMEM with 4.5 g/L glucose, L-glutamine and sodium pyruvate (Life Technologies, Carlsbad, CA, USA) including 10% Fetal Bovine Serum (Eurobio, Les Ulis, France) and 1% penicillin-streptomycin (Life Technologies, Carlsbad, CA, USA). A253 cells (ATCC) were cultured in McCoy 5A with 4.5 g/L glucose, L-glutamine and sodium pyruvate (Life Technologies, Carlsbad, CA, USA) including 10% Fetal Bovine Serum (Eurobio, Les Ulis, France) and 1% penicillin-streptomycin (Life Technologies, Carlsbad, CA, USA). All three cell lines were cultured in 100 mm cell culture-treated Petri dishes (Corning) with 10 mL of culture medium. The cells were grown at 37 °C in a water-saturated atmosphere with 5% CO_2. These cells grow well in these conditions and are usually 80% confluent after three days in culture (after 10% seeding). Cells were passaged three times per week.

2.2. Organoid Culture

Round-bottom 96-well plates were coated with poly(2-hydroxyethylmethacrylate) (Polyhema) (Sigma, Saint-Louis, MO, USA) 1 week before cell culture. Polyhema was first dissolved at 50 mg/mL in 95% EtOH. This stock solution was then diluted to 30 mg/mL with absolute ethanol. For coating, each well, except for the outermost ones, was filled with 50 μL of a 30 mg/mL solution of Polyhema before the plate was allowed to dry overnight. For culture, the outermost wells were filled with 200 μL PBS to avoid evaporation. The remaining wells were seeded with 10,000 cells and filled with 200 μL culture medium for 10 days prior to experiments.

2.3. Histology and Image Acquisition

For histological analyses, organoids were washed with 1X PBS, and then fixed for 24 h in 4% pH 7 buffered formalin and processed for paraffin wax embedding in an Excelsior ES automaton (Thermo Scientific, Waltham, MA, USA). Paraffin-embedded tissue was sectioned at 4 μm, mounted on positively charged slides and dried at 58 °C for 60 min. Immunohistochemical staining was performed on the Discovery ULTRA Automated IHC stainer (Roche Diagnostics, Rotkreuz, Switzerland) using the Ventana detection kit (Ventana Medical Systems, Tucson, AZ, USA). For fluorescent labeling, following deparaffination with Discovery wash solution (Ventana Medical Systems, Tucson, AZ, USA) at 75 °C for 8 min, antigen retrieval was performed using Ventana Tris-based buffer solution, pH 8, at 95 °C to 100 °C for 40 min. Endogen peroxidase was blocked with 3% H2O2 for 12 min. After rinsing, slides were incubated at 37 °C for 60 min with primary antibodies. Signal enhancement was performed using a secondary HRP-conjugated antibody at 37 °C for 16 min and DISCOVERY Rhodamine Kit (Roche Diagnostics, Rotkreuz, Switzerland) for 8 min. For fluorescence multiplex labeling, slides were prepared as follows: For the first sequence, following deparaffination with Discovery wash solution (Ventana Medical Systems, Tucson, AZ, USA) at 75 °C for 8 min, antigen retrieval was performed using Ventana proprietary, Tris-based buffer solution, pH 8, at 95 °C to 100 °C for 40 min. Endogen peroxidase was blocked with 3% H_2O_2 for 12 min. After rinsing, slides were incubated at 37 °C for 60 min with primary antibody, rabbit anti-PROX1. Signal enhancement was performed using a goat anti-rabbit HRP at 37 °C for 16 min and DISCOVERY Rhodamine Kit (542–568 nm) for 8 min. For the second sequence, slides were neutralized with Discovery inhibitor (Ventana Medical Systems, Tucson, AZ, USA) for 8 min. After rinsing, slides were incubated at 37 °C for 60 min with primary antibody mouse anti-JAG1. Signal enhancement was performed using a goat anti-mouse HRP at 37 °C for 16 min and DISCOVERY cy5 Kit for 8 min. For the third sequence, slides were neutralized with Discovery inhibitor (Ventana Medical Systems, Tucson, AZ, USA) for 8 min. After rinsing, slides were incubated at 37 °C for 60 min with primary antibody, rabbit anti-PAX6. Signal enhancement was performed using a goat anti-rabbit HRP at 37 °C for 16 min and DISCOVERY Fam Kit for 8 min. DAPI staining was used to visualize DNA/nucleus. For chromogenic labeling, following deparaffination with EZ Prep (Roche Diagnostics, Rotkreuz, Switzerland) at 75 °C for 8 min, antigen retrieval was performed using CC1 buffer (Roche Diagnostics, Rotkreuz, Switzerland), pH 8.0, at 95 °C to 100 °C for 40 min. Endogen peroxidase was blocked with 3% H_2O_2 for 12 min. After rinsing, slides were incubated at 37 °C for 60 min with primary antibodies. Signal enhancement was performed using a secondary HRP-conjugated antibody at 37 °C for 16 min and revealed using the OmniMap DAB kit (Roche Diagnostics, Rotkreuz, Switzerland). The slides were counterstained with the Mayer's hematoxylin. Antibodies were as follows: Ki67, ab16667 dilution 1/200 (Abcam, Cambridge, UK); Cleaved Caspase 3, #9661 dilution 1/250 (Cell Signaling Technology, Danvers, MA, USA); Lamin B1, A16909 dilution 1/200 (Abclonal, Woburn, MA, USA); Laminin Z0097 dilution 1/200 (Dako, Glostrup, Denmark); PAX6 AB2237 dilution 1/200 (Sigma, Saint-Louis, MO, USA); JAG1 sc390177 dilution 1/200 (Santa Cruz, Dallas, TX, USA); PROX1 925202 dilution 1/200 (BioLegend, San Diego, CA, USA); CRYAB ADI-SPA-223 dilution 1/200 (Enzo Life Science, Farminfdale, NY, USA); HSF4 HPA048584, dilution 1/200 (Atlas Antibodies, Voltavägen, Sweden); TOMM20 ab186735 dilution 1/5000 (Abcam, Cambridge, UK); Fibrillarin 32639 dilution 1/100 H2P2 (Cell Signaling Technology,

Danvers, MA, USA). HES staining was realized on an ST 5020 automaton (Leica, Wetzlar, Germany). Bright field images were acquired using a digital slide scanner Nanozoomer (Hamamatsu, Shizuoka, Japan), while fluorescence microscopy images were acquired using a DeltaVision Elite setup equipped with a Nikon IX71 microscope and a CoolSnap HQ camera (Imsol, Preston, UK).

2.4. Transparency and Light Focalization

Transparency was assessed by placing the organoids on an electron microscopy copper grid (mesh 300) for 30 s and imaging them with an AZ100 macroscope (Nikon, Tokyo, Japan). Light focalization was quantified using an Axio Observer inverted microscope (Zeiss, Iena Germany). Briefly, a stack of images starting from the focus and progressively lowering the objective under the sample was acquired. For each image of the z-stack, the maximum light intensity at the center of the spheroid and the mean intensity in the field around the spheroid were quantified. The ratio of the maximum light intensity to the mean intensity was then calculated and plotted to produce a graph.

2.5. 21EM15 2D and 3D RNA Isolation

RNAs were isolated using the Nucleospin kit (Macherey-Nagel, Düren, Germany) from a 100 mm Petri dish of 21EM15 cell culture at 80% confluence (2D) or 60 organoids (3D) for each replicate.

2.6. Laser Capture Microdissection

For each replicate, 120 organoids were washed with 1X PBS and pelleted before being included in OCT and then snap-frozen using a SnapFrost 80 deep freezer (Excilone, Elancourt, France). The frozen OCT block was then mounted onto a cryostat (Leica, Wetzlar, Germany) and cut to obtain 10 µm sections. The sections were then deposited on polyethylene naphthalate (PEN) membrane frame slides. OCT was removed via multiple washes: 2 washes in 70° ethanol (−20 °C; 5 min), 1 wash in 90% ethanol (RT; 20 min), 1 wash in 100% ethanol (RT; 20 min) and 3 washes in 100% Xylene (RT; 1 min). The internal or external regions of the spheroids were microdissected using an Arcturus XT laser capture microdissection setup (Excilone, Elancourt, France). The RNA was isolated from these samples using the Arcturus PicoPure kit (Excilone, Elancourt, France).

2.7. 3′ End RNA Sequencing (RNA-Seq) and Analysis

Libraries were prepared from the extracted RNAs using the QuantSeq 3′ mRNA-Seq library Kit (Lexogen, Vienna, Austria). The 3′ end seq library was sequenced (strand-specific, 150 bp) using Illumina NovaSeq 6000. Quality of the sequence was validated using FastaQC, and only sense reads were used for the analysis. The RNA-seq data are available on the NCBI Gene Expression Omnibus (GEO) database under GSE228547 series. The adaptor sequence and the poly(A) tail were trimmed from the raw sequences, and only read lengths greater than 20 nucleotides were retained. Trimmed sequences were aligned using the STAR software (STAR (v2.7.8a)) [25] onto the mouse genome (GRCm38.p6). Only uniquely mapped reads were conserved for the analysis. Reads were associated with genes using FeatureCounts (v1.6.0) [26]. For differential gene expression analysis, only genes with an expression of >0.2 cpm (counts per million) were considered. The R package, edgeR (v3.32.1) [27], was used to identify significantly differentially expressed genes (DEGs), with the following as as cut-offs: |Fold Change| (FC) > 2 (|logFC| > 1) and a False Discovery Rate (FDR) < 0.05.

2.8. Gene Expression Data Analysis

To determine the pattern of expression of the 2D or 3D DEGs in the mice embryonic lens, we used microarray data from the iSyTE 2.0 database [28] to identify genes that exhibited lens-enriched expression in normal lens development across stages E14.5 to P0. As described previously, a comparison of global gene expression data between lens and

whole embryonic body tissue (WB) allows for the estimation of lens-enriched expression. To compare the regional transcriptomic profile between organoid and lens, we used previously generated RNA-seq data to identify DEGs with an expression profile specific to isolated FC or LEC [29]. These data correspond to WT mice at the E14.5, E16.5, E18.5 and P0.5 stages. The identification of genes with an expression profile specific to FC or LEC was based on cut-offs of *p*-value adjusted to <0.05 and $|FC| > 2$.

3. Results

3.1. 21EM15 Spheroids Are Transparent and Have the Ability to Focus Light

To test their ability to grow under 3D culture conditions, we seeded 21EM15 cells in 96-well culture plate wells coated with polyhema. Twenty-four hours after seeding, the vast majority of the cells were assembled into round spheroids, with no isolated cell being observed. Upon subsequent culture, these spheroids grew in size (Supplemental Figure S1A), acquiring an ovoid asymmetric shape between days 3 and 7. Thereafter, culturing the spheroids beyond day 10 only resulted in limited changes in their overall appearances (Supplemental Figure S1A). At day 10, the 21EM15 spheroids were transparent, contrary to the spheroids generated with two other epithelial cell lines grown in the same conditions, namely, human epithelial keratinocytes (HaCaT cells) or head and neck squamous cell carcinoma A253 cells (Figure 1A). We then tested the capacity of the 21EM15 spheroids to focus light following a previously described approach [19]. Briefly, we imaged the spheroids at different z-positions starting from the focus (Figure 1B). A very bright light spot was observed at the center of the 21EM15 spheroids at a specific z-position (Figure 1C), suggesting that they had acquired properties to focus light. We quantified the light-focusing ability as the ratio of the maximum light intensity at the center of the spheroid to the mean intensity around the spheroid (Figure 1C,D). This ratio reached values well above 1 at z-positions below the focus in the 21EM15 spheroids, confirming their capacity to focus light (Figure 1D); this was not observed in the HaCaT spheroids (Supplemental Figure S1B).

3.2. Transcriptome Analysis of 21EM15 Spheroids Reveals Strong Similarities with Lens Development

During their growth, the 21EM15 spheroids acquire an asymmetric shape and optical properties to focus light. To gain insights into the molecular modifications associated with these morphological changes and assess whether they may be relevant to lens development, we compared the transcriptome landscapes of 21EM15 spheroids with those of mouse lenses at several stages of development. We profiled the gene expression in the 21EM15 spheroids via 3′ end RNA sequencing (Supplemental Table S1) and we retrieved the gene expression levels of mouse lenses from the iSyTE 2.0 database [28]. In iSyTE 2.0, "lens-enrichment" is estimated as the log-ratio of gene expression in the lens to gene expression in the whole embryonic body (WB). Using a WB comparative analysis, we similarly estimated gene enrichment in 3D 21EM15 cultures. We compared the 10% most enriched genes in 3D cultures (n = 1032; 10,320 genes in total) with the 10% most enriched genes in the E14.5 lenses (n = 1032). We found that 198 genes were present at the overlap of the two datasets, which was far above what was expected by chance ($p = 8.7 \times 10^{-22}$; hypergeometric test). Irrespective of the threshold set to classify the genes as top-enriched (between 0 and 10%), the number of genes observed in the overlap of top-enriched genes in the 3D cultures and top-enriched genes in the E14.5 lenses largely exceeded what was expected (Figure 2A). Nine genes were present in the overlap of the top 1% most enriched genes in the E14.5 lenses and the top 1% most enriched genes in the 3D cultures, whereas only one gene was expected by chance. Among these genes were *Cryab*, *Six3*, *Adamtsl4*, *Cp* (encoding ceruloplasmin), *Crim1*, *Dkk3* and *Nupr1*, all of which are known to be directly linked to lens pathophysiology (Figure 2A). We obtained similar results for all lens development stages present in iSyTE 2.0 (E10.5, E12.5, E14.5, E16.5, E17.5 and E19.5; data not shown). Together, these results reveal an overlap in the expression of key genes between 21EM15 spheroids and normal lenses.

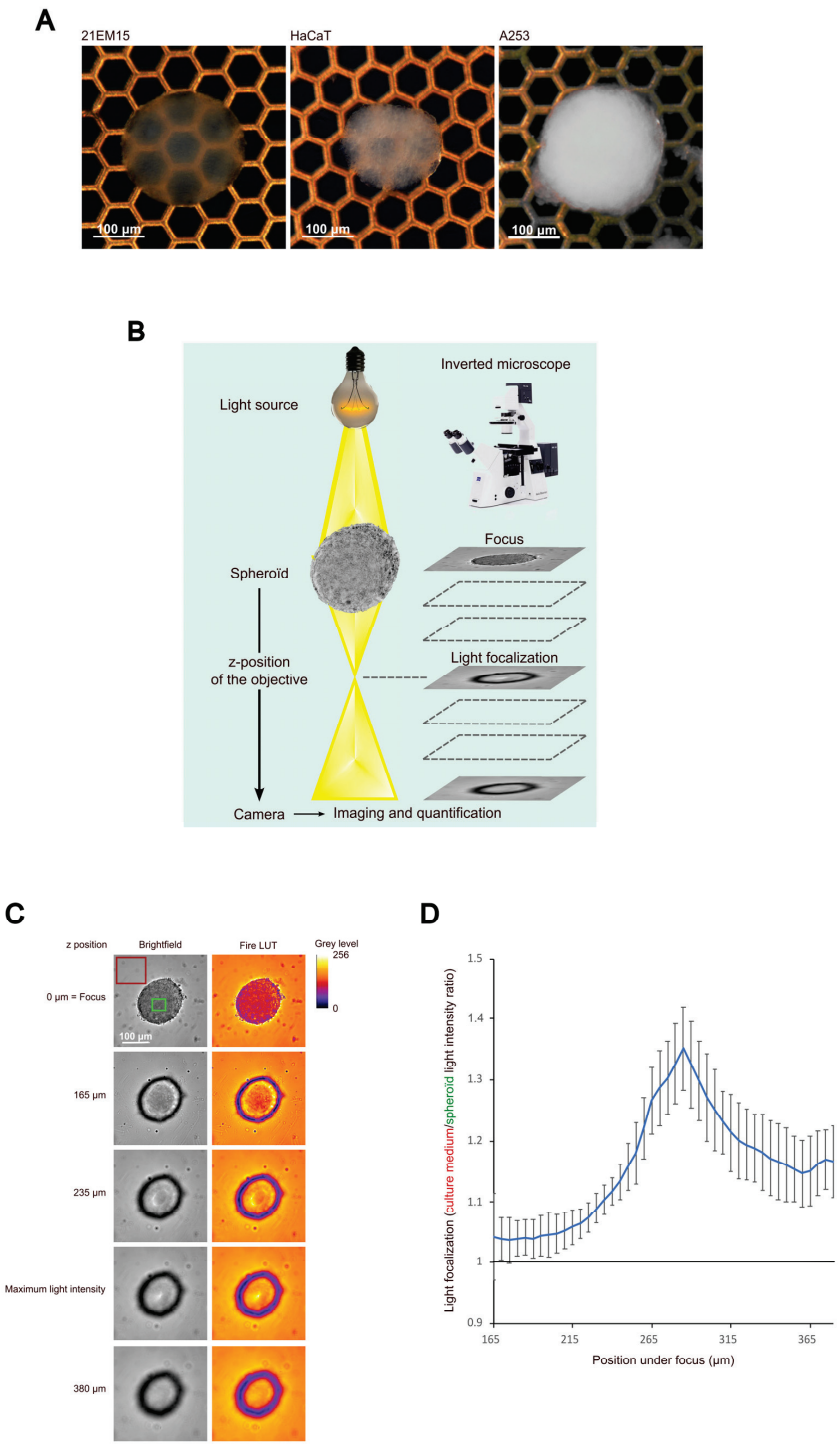

Figure 1. 21EM15 spheroids are transparent and can focus light. (**A**) Macroscopic views of 10-day old 21EM15, HaCaT or A253 spheroids formed with 10,000 cells. The electron microscopy grid allows for the evaluation of transparency. (**B**) Schematic of the imaging setup for quantifying the light-focusing ability of spheroids. (**C**) Microscopic images of a 21EM15 spheroid showing its ability to transmit and focus light. The mean intensity of light transmitted by the medium, and the maximum intensity of light transmitted by the spheroid used for quantification are, respectively, indicated by the red and the green squares. (**D**) Graph showing the light-focusing ability of the 21EM15 spheroids calculated as the ratio between the mean intensity measured in the red square and the maximum intensity measured in the green square. This graph is representative of 5 independent experiments with $n = 12$ spheroids for each experiment. Error bars represent standard deviations. All spheroids were generated from 10,000 cells.

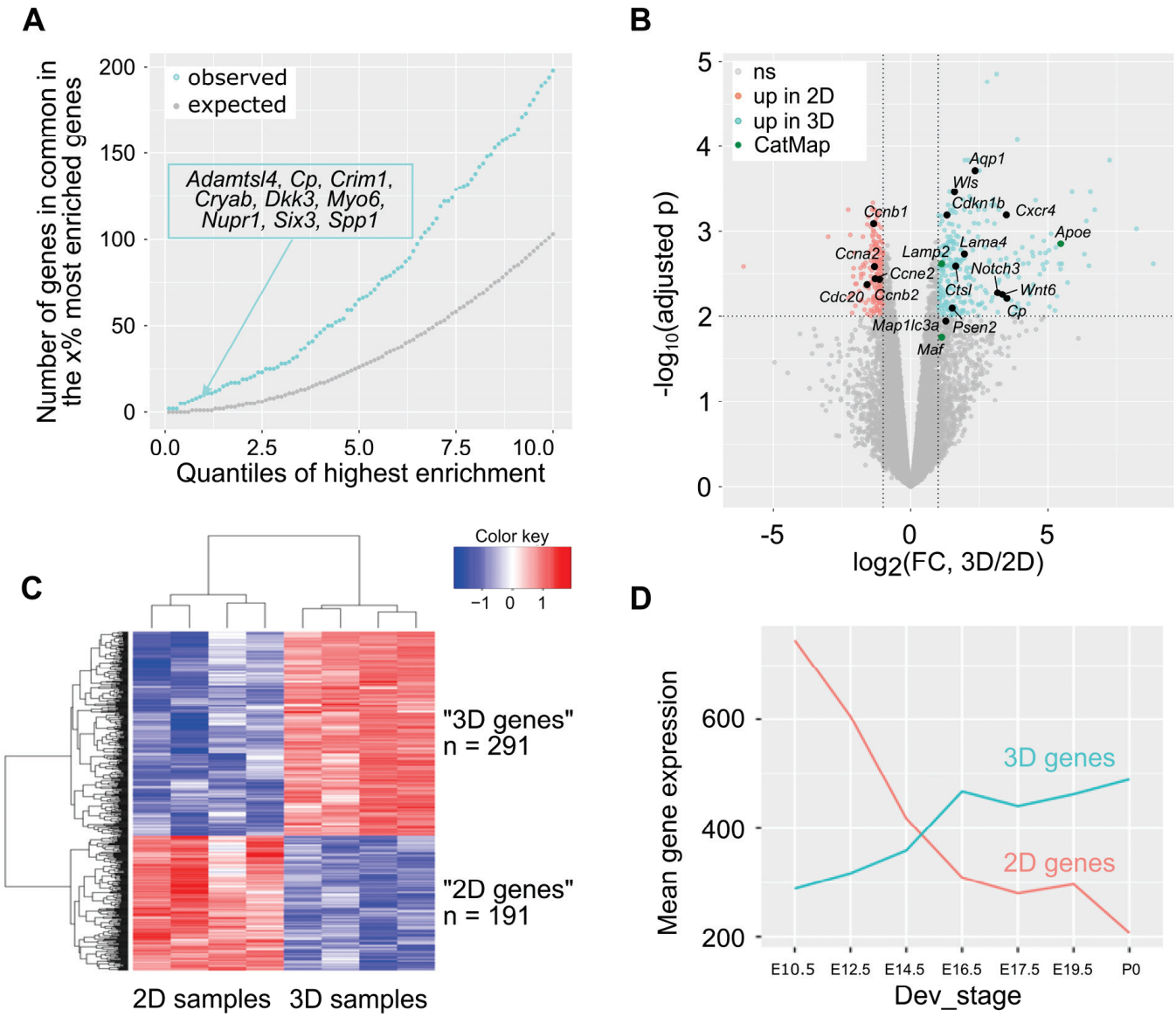

Figure 2. Growing 21EM15 cells in 3D culture conditions captures aspects of gene expression in lens development. (**A**) We ranked all the genes expressed in mouse E14.5 lens and in 21EM15 3D cultures (n = 10,320) based on lens enrichment (expression in the lens compared to whole body) as described in [28]. We separately listed the percentages (x%) of the most enriched genes in the lens and in 3D cultures for several x values ranging from 0 to 10 (X-axis). For each x value, we retrieved the genes in common between the x% of most enriched genes in lens and the x% of most enriched genes in 3D cultures. The Y-axis shows the number of shared genes for each x value. Blue represents the observed number. Grey represents the number expected if enrichment in 3D 21EM15 cultures is independent from enrichment in E14.5 lenses. The inset is the list of genes that are in both the 1% most enriched genes in 3D 21EM15 cultures and in the 1% most enriched genes in E14.5 lenses. (**B**) Volcano plot showing the statistical significance (Benjamini–Hochberg-adjusted p-value; −log10 scale) against the fold change (log2 scale) of the expression in 2D and 3D samples. This analysis identifies 482 differentially expressed genes (FDR < 0.01 and log2(FC) > 1 in absolute value), among which 291 are upregulated in 3D samples and 191 are upregulated in 2D samples. Genes that are found to be linked to cataract in the Cat-Map database are indicated. (**C**) Heat map of differentially expressed genes in 21EM15 spheroids (3D samples) and 21EM15 2D cultures. (**D**) Mean expression of the 191 "2D genes" and the 291 "3D genes" throughout lens development. (**A**,**D**) data for gene expression in lens are from iSyTE 2.0 [28].

Next, we wanted to assess the contributions of the culture conditions (3D vs. 2D) to gene expression, especially as it relates to the lens. To carry this out, we profiled gene expression in the 21EM15 2D cultures via 3′ end RNA sequencing in the same conditions as the 3D spheroids (Supplemental Table S1). A principal component analysis and a hierarchical clustering analysis showed that the 2D and 3D samples cluster separately from each other (Supplemental Figure S2A,B). We therefore used these datasets to identify differentially expressed genes (DEGs). At FDR = 0.01 and log2 (Fold Change) > 1 in absolute value, this analysis uncovered 291 genes that were elevated and 191 genes that were reduced in the 3D spheroids (Figure 2B). The elevated 291 genes are referred to as "3D genes", and the reduced 191 genes are referred to as "2D genes". As expected, the heat map of these 482 DEGs showed a clear separation between these two sets of genes (Figure 2C). Several genes elevated under 2D conditions of growth relate to the cell cycle, such as *Ccnb1*, *Ccnb2*, *Ccnb1*, *Ccne2* and *Cdc20* (Figure 2B). This indicates that culturing 21EM15 in 3D conditions reduces the expression of cell cycle genes comparted to growth under 2D conditions. Conversely, several genes elevated under 3D growth conditions are relevant to lens development (Figure 2B). These include *Apoe*, *Aqp1*, *Cdkn1b*, *Cp*, *Ctsl*, *Cxcr4*, *Lama4*, *Maf*, *Map1lc3a*, *Notch3*, *Psen2*, *Wnt6* and *Wls.*

Finally, we used iSyTE 2.0 to examine the expression of these DEGs in normal lens development [28]. On average, 2D genes are more expressed than 3D genes in early lens developmental stages (e.g., E10.5, when the lens placode has invaginated into a "lens pit"), and their expression decreases as the lens progresses in development (Figure 2D). Conversely, the mean expression of 3D genes increases progressively in normal lens development (Figure 2D). Hence, switching the culture conditions of 21EM15 cells from 2D to 3D spheroids partly recapitulates gene expression changes in normal lens development. Together, these data show that culturing 21EM15 in 3D conditions reinforces their similarity with normal mouse lenses, particularly at later stages of development.

3.3. 21EM15 3D Cultured Cells form Multilayered Lens Organoids

The lens is surrounded by a basal lamina called the capsule. Under the capsule and starting from the anterior pole of the lens, there is a quiescent epithelium, containing cells that proliferate in the "germinal zone" and exit the cell cycle at the "transition zone" to initiate differentiation into fiber cells that contribute to the bulk of the lens. Differentiation into fibers cells is characterized by the remodeling of the cytoskeleton, leading to the elongation of the cells, accompanied by high levels of expression of key lens proteins (e.g., crystallins, membrane proteins, etc.) and the progressive loss of cellular organelles [3,4]. As 21EM15 cells that are cultured as 3D spheroids express genes associated with lens differentiation, we wanted to characterize their structures to identify whether different cell types emerge through a process of differentiation. A histological analysis showed that twelve hours after seeding under 3D conditions, the 21EM15 cells clustered to form a non-organized flattened structure (Figure 3A). Twenty-four hours after seeding, the structure was spherical with a rather homogenous cellular content. Ten days after seeding, the spheroids showed a different appearance with distinct zones: an external zone with round nuclei, an intermediate zone with elongated nuclei, and an internal zone with cells characterized by an intense pink cytoplasm and small compacted nuclei (Figure 3A). Importantly, the internal zone was off-centered, revealing that the initial central symmetry of the spheroid was broken during the 10-day culture (Figure 3A). This is in line with previous observations that the spheroid acquires an ovoid shape after a few days of culture (Supplemental Figure S1A).

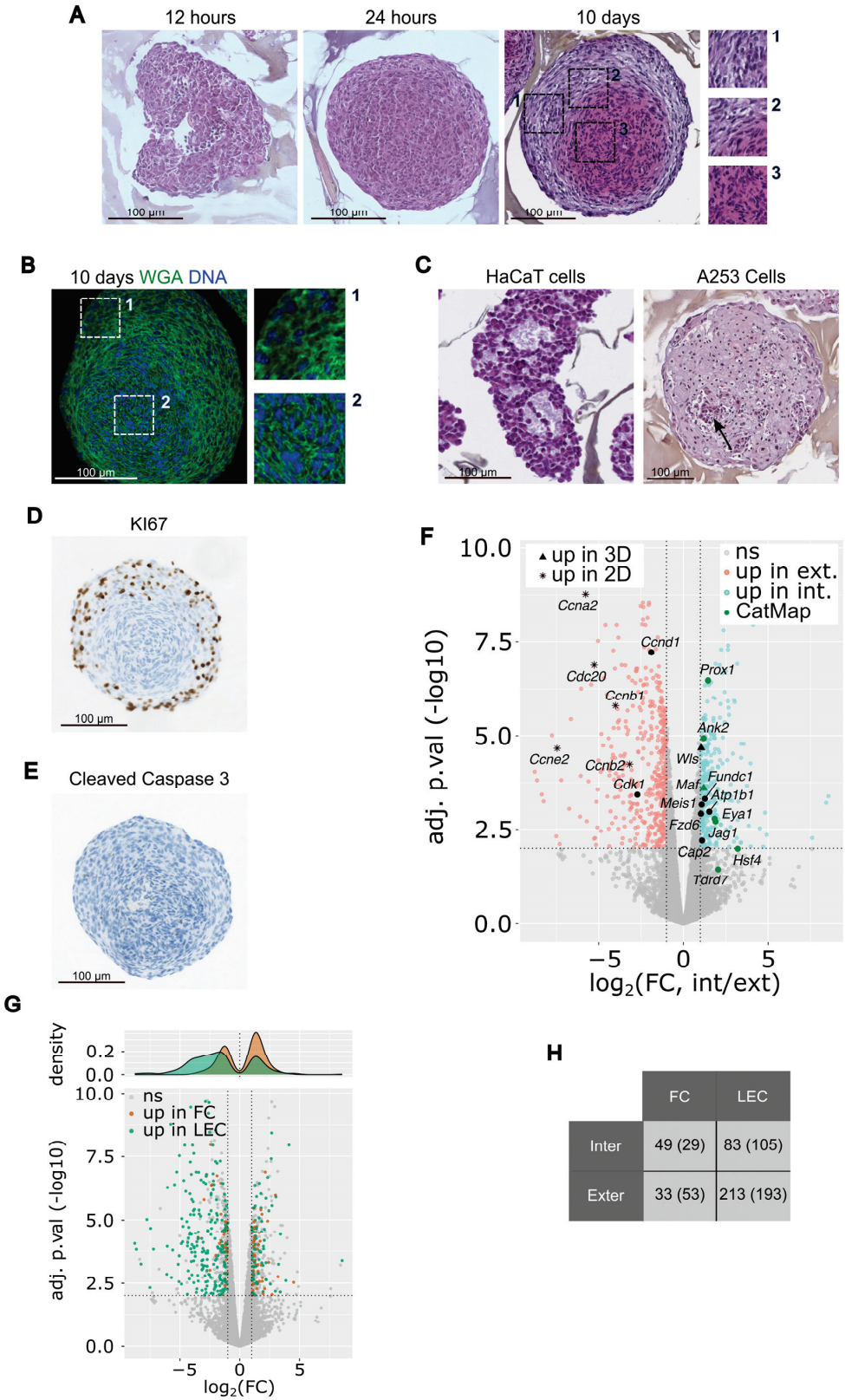

	FC	LEC
Inter	49 (29)	83 (105)
Exter	33 (53)	213 (193)

Figure 3. 21EM15 LECs 3D cultures differentiate to form multilayered lens organoids. (**A**) Histological analysis of 21EM15 spheroids grown for 12 h, 24 h or 10 days, stained with Hematoxylin, Eosin and Safran (HES). The insets show the three different histological regions. (**B**) Microscopic image of a 21EM15 spheroid stained with Wheat Germ Agglutinin (WGA) to show distinct cellular boundaries. Insets show details of the outer (1) or inner regions (2). (**C**) Histological analysis of HaCaT or A253

spheroids grown for 10 days (HES staining). The arrow shows a necrotic region. (**D**) Histological analysis showing the localization of KI67 in a 10-day-old 21EM15 spheroid. (**E**) Cleaved Caspase 3 staining of 10-day-old 21EM15 spheroid, revealing an absence of cells undergoing apoptosis. For (**A**–**E**), data are representative of at least 3 independent experiments; $n = 30$ organoids. (**F**) Volcano plot showing the statistical significance (Benjamini–Hochberg-adjusted p-value; −log10 scale) against the fold change (FC; log2 scale) of the expression in internal and external regions microdissected from 21EM15 spheroids. This analysis identifies 793 differentially expressed genes (FDR < 0.01 and log2(FC) > 1 in absolute values), among which 328 are upregulated in internal regions and 465 are upregulated in external regions. "Up in 2D" and "Up in 3D" correspond to genes, respectively, upregulated in 2D culture or upregulated in 3D culture in Figure 2B. Black solid symbols correspond to genes that are of particular significance regarding the lens. (**G**) Lower panel, same volcano plot as in F, with genes that are overexpressed in microdissected lens epithelial cells (LEC) and fiber cells (FC) [30] colored in green and orange, respectively. Higher panel, density plot showing the distribution of fold changes (log2 scale) for FC and LEC genes. (**H**) Contingency table showing the number of genes that are enriched in FC or LEC compared to internal and external regions. The numbers in the brackets represent the value that is expected in the event that the enrichment in FC or LEC is unrelated to the enrichment in internal or external regions, respectively. The difference between the expected and the observed value indicates that a higher number of genes than expected are found to be enriched both in FC and internal regions, as well as in LEC and external regions.

To evaluate cell compartmentalization in the core of the spheroid, we visualized the cells' boundaries using WGA (wheat germ agglutinin), a membrane marker. The core of the spheroid is composed of highly compacted cells when compared to the cortex (Figure 3B). This indicates that the cells located at the central region of the spheroid undergo a phenomenon of packing. As controls, histological sections of the HaCaT and A253 spheroids were generated (Figure 3C). After 10 days of culture, the specific organization of cells was not observed in these controls. HaCaT spheroids are made of cells roughly aggregated and cavities likely filled with an extracellular matrix, while A253 spheroids are made of homogenously distributed cells with a clear pink cytoplasm and some spots of necrotic cells (Figure 3C). As 21EM15 spheroids constantly grow over a period of more than 10 days (see Supplemental Figure S1B), we wanted to determine which cells were responsible for their growth. Staining with the KI67 antigen, an established marker of proliferation, shows that proliferating cells are essentially localized in the external region of the spheroid and that cells stop proliferating once their nuclei are elongated (Figure 3D). The observation that only a few cells are able to proliferate is consistent with the finding that many cell cycle-related genes are down-regulated in 3D cultures (Figure 2B). Cells undergoing apoptosis were not observed after 10 days of culture (Figure 3E).

The above data indicate that 21EM15 spheroids are made up of at least three distinct regions. We next sought to determine the gene expression landscape within the different layers of the spheroids. Toward this goal, the most internal and external regions were isolated by laser capture microdissection (LCM) and subjected to 3′ end RNA sequencing (Supplemental Table S2). Due to technical limitations, we were unable to microdissect the intermediate region. We retained $n = 3$ external region samples and $n = 4$ internal region samples based on PCA (Supplemental Figure S3A). We identified 793 DEGs (FDR = 0.01, and log2 (Fold Change) > 1 in absolute value). Of these, 465 exhibited enriched expression in the external region and 328 exhibited enriched expression in the internal region (Figure 3F). The heat map of these 793 DEGs separates "external genes" from "internal genes" (Supplemental Figure S3B). Among the genes that are overexpressed in the internal region, we found genes known to be expressed in fiber cells like *Ank2*, *Atp1b1*, *Cap2*, *Eya1*, *Fundc1*, *Fzd6*, *Hsf4*, *Jag1*, *Maf*, *Meis1*, *Prox1*, *Tdrd7* and *Wls*. Among the genes that are overexpressed in the external region, we found genes known to be expressed in lens epithelial cells like *Ccna2*, *Ccnb1*, *Ccnb2*, *Ccnd1*, *Ccne2*, *Cdc20* and *Cdk1*.

To globally assess the resemblance of the internal and external regions of 21EM15 spheroids with lens fiber and epithelial cells, respectively, we retrieved the transcriptomic

data from microdissected E14.5 epithelial cells and lens fiber cells [30]. Of the 793 DEGs, 378 are also enriched either in E14.5 lens epithelium or fiber cells. The "external genes" (negative $\log_2$(FC) in Figure 3G) are enriched in lens epithelial genes (green spots), whereas "internal genes" (positive $\log_2$(FC) in Figure 3G) are enriched in lens fiber cells (orange spots). The contingency table shown in Figure 3H confirms this bias ($p = 2.1 * 10^{-6}$; chi-squared test). These data confirm that the transcriptome of the internal region resembles that of lens fiber cells and the transcriptome of the external region resembles that of lens epithelial cells. Further, while 2D cultures of 21EM15 cells have overlapping expressions with lens epithelial cells, growing the cells in 3D culture conditions commits the internal cells toward a differentiation program overlapping with lens fiber cells. Taken together, our results show that the 3D 21EM15 cultures self-organize and establish different cell types expressing specific gene sets, thus mimicking certain aspects of lens development. Moreover, these structures are able to break their original central symmetry to establish axial symmetry, which is characteristic of organoid development [31–33]. Thus, henceforth, the 3D 21EM15 cultures will be referred to as 21EM15 "organoids".

3.4. Morphological Organization of 21EM15 Organoids Partially Recapitulates Lens Patterning

Different regions or cell types within the lens can be characterized by the expression of specific markers. From the transcriptomic studies described above, we identified a subset of key genes involved in lens development to be differentially expressed between the inner and outer regions (see Supplemental Table S2). Our next objective was to confirm that key lens genes have specific expression patterns that are relevant to the organization of a whole lens. For this purpose, we examined the expression and the localization of structural components such as Laminin, a major component of basal lamina including the lens capsule, and αB-Crystallin (CRYAB), a major component of lens fiber cells in later developmental stages [34,35]. We also examined transcription factors such as PAX6, PROX1 (elevated in fiber cells) and signaling molecules such as JAG1 [1,36,37]. Laminin was found to be present in two or three layers of the outermost cells (Figure 4A). It was also present in the most peripheral part of the lens, but only in the form of a single outer basal lamina [35]. Immunostaining showed that nuclear PAX6 is present in an internal region surrounding the central core of the organoid, composed of highly compacted cells (Figure 4B). Consistent with symmetry breaking, it then extends toward the central axis. JAG1 is also found in an asymmetric distribution, as it is enriched in the membranes of cells localized in two lateral areas surrounding the central axis of the organoid (Figure 4B). PROX1 is present in two regions: in the cytoplasm of cells that most strongly express *Jag1*, and in the nuclei of cells that more weakly express *Jag1* and are localized along the central axis (Figure 4B,C). Finally, αB-Crystallin is low/absent in the external cell layers but high in the cortex and the core of the organoid with both cytoplasmic and nuclear localization (Figure 4D).

One of the most striking characteristics of fiber cell differentiation is the progressive degradation of cellular organelles such as nuclei and mitochondria [38]. In the lens, these various events can be highlighted by the observation of components of the nuclear envelope and of the mitochondria or by the expression of specific transcription factors [39–42]. We sought to examine whether similar cellular changes occurred in 21EM15 organoids. We found that Lamin-B1 (LMNB1), a component of the nuclear envelope, progressively disappears from the exterior to the interior of the organoid (Figure 5A). While Lamin-B1 labeling surrounds the nucleus in a continuous manner in the outermost cells, this labeling becomes more and more discontinuous toward the inner region of the organoid until it completely disappears. Concomitantly, we observed a gradual change in the nuclei shape accompanied by chromatin compaction evoking pyknosis (Figure 5B). These nuclei are not transcriptionally active in cells located in the center of the organoids (Figure 5C), as indicated by the progressive loss of nuclear Fibrillarin (FBL), which is considered as a marker of the transcriptional status of fiber cell nuclei [43]. Mitochondria are also in a process of degradation, as indicated by the decrease in TOMM20 labeling, which is a constituent of the mitochondria external membrane, toward the center of the organoid

(Figure 5D). Conversely, the expression of *Hsf4*, a gene encoding transcription factor whose downstream targets are considered to be involved in organelle degradation [40,44], increases in the core region relative to the outer region (Figure 5E,F).

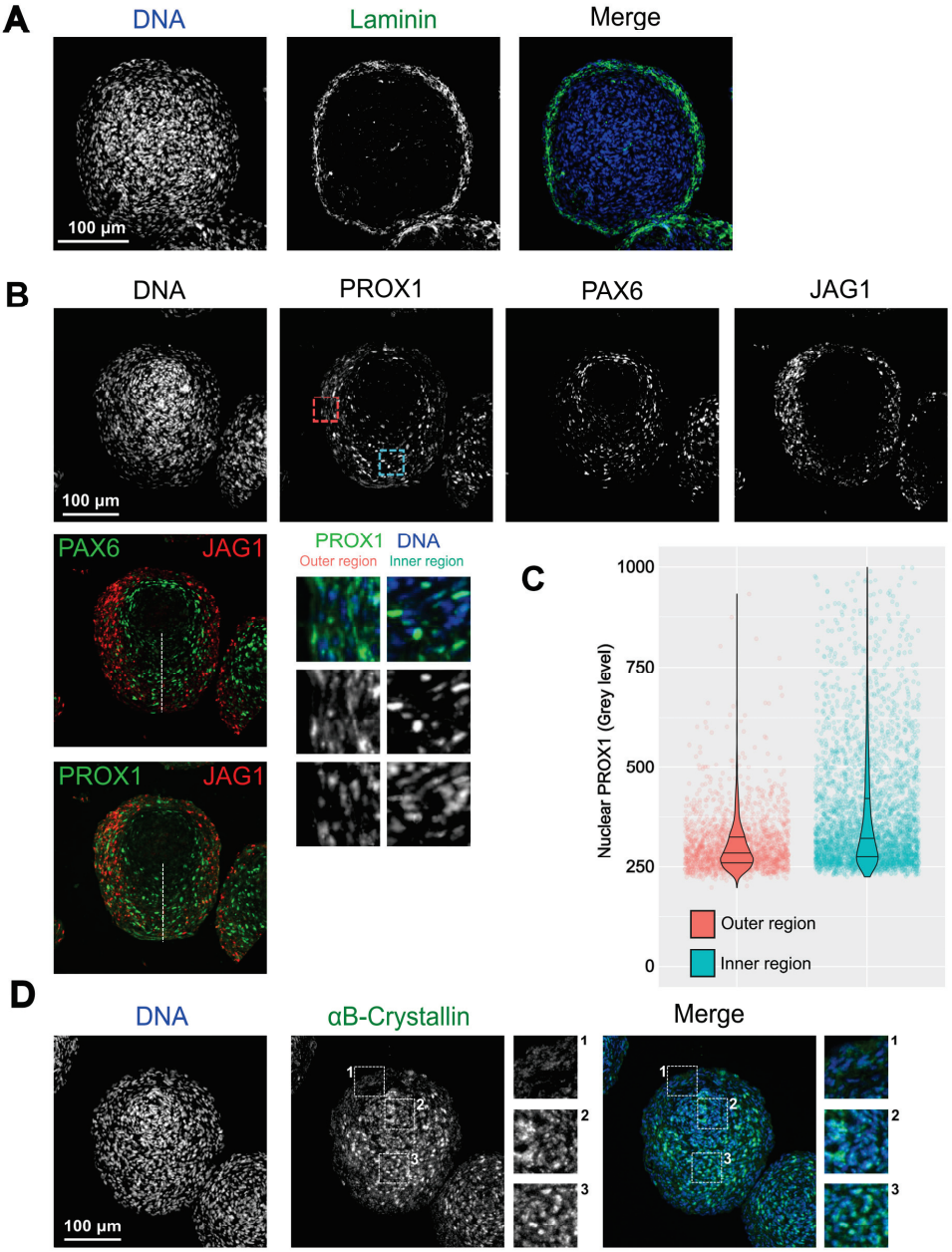

Figure 4. Morphological organization of 21EM15 organoids partially recapitulates eye lens patterning. (**A**) Immunofluorescence (IF) microscopy reveals the localization of Laminin on the outer region of the organoid. (**B**) Multiplex microscopic images indicate the localization of the expressed proteins, PAX6, PROX1 and JAG1. The red and blue squares correspond to the typical areas (respectively, the outer and inner regions) used to display the magnification insets presented below the grey level image of PROX1 and to quantify the PROX1 nuclear labeling shown in (**C**). The white dashed line symbolizes the central axis of the organoid. (**C**) Violin plots combined with jittered scattered plots showing that PROX1 is enriched in the nuclei of cells located in the inner region. This graph is representative of three independent experiments; $n = 30$ organoids. $p < 2.2 \times 10^{-16}$; Wilcoxon rank sum test with continuity correction. (**D**) IF images showing the localization of αB-Crystallin. Insets show the enlargement of the outer region, the central axis and the core of the organoid. Data are representative of at least three independent experiments; $n = 30$ organoids.

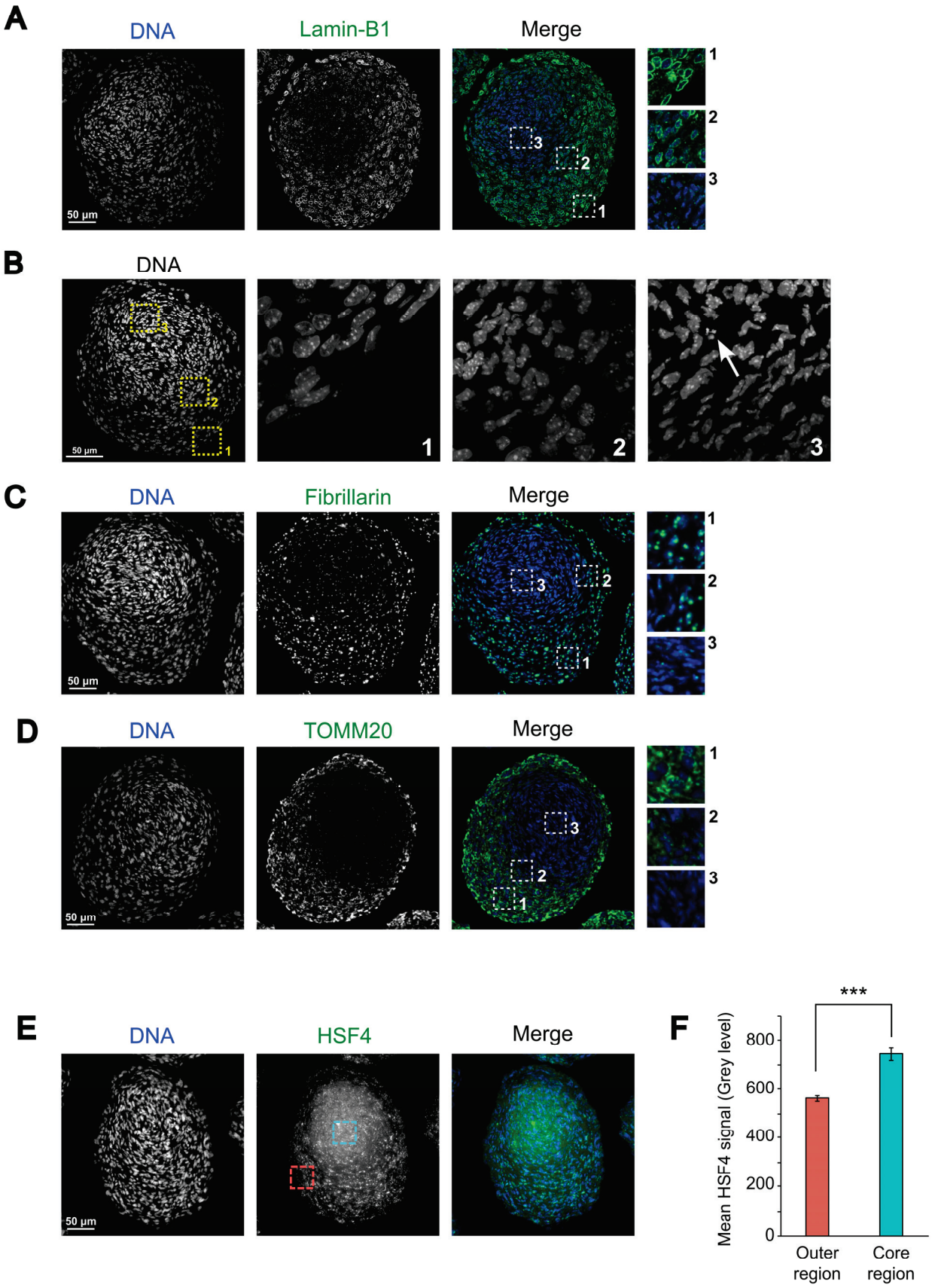

Figure 5. Cells located in the core of lens organoid are engaged in a process of organelle degradation. (**A**) IF microscopy images of 10-day-old lens organoid showing the localization of Lamin-B1.

(**B**) Microscopy images showing the appearance of nuclei in three different areas of an organoid. The arrow points out a nucleus with pyknotic features. (**C**) Nuclei located in the core of the organoid show reduced transcriptional activity, as evidenced by decreased levels of Fibrillarin, which has previously been used as a marker of the transcriptional state of lens fiber cells. (**D**) The decrease in TOMM20 labeling indicates that the organoid core cells are engaged in mitochondrial degradation. (**E**) IF microscopy images showing the localization of HSF4. The red and blue squares correspond to the typical areas (respectively, the outer and inner regions) used to quantify the HSF4 mean signal quantified in (**F**). (**F**) Histogram presenting the quantification of the mean HSF4 signal in the outer and core regions of the organoids. This graph is representative of three independent experiments; $n = 30$ organoids. Asterisks indicate a p-value of <0.001. Error bars represent standard deviations.

Taken together, these results suggest that, similar to the cellular and morphological changes accompanying lens development, the 21EM15 organoids are organized into specific expression domains for key lens proteins like αB-Crystallin, PAX6, PROX1 and JAG1. Moreover, the cells lying in the internal-most region commit to a process of organelle degradation reminiscent of what is observed in the whole lens. Our results thus show that 21EM15 organoids recapitulate specific molecular aspects and the morphological organization of the lens.

3.5. 21EM15 Organoids Model Lens Cataract

As the organoids described above present interesting optical, morphological, histological, molecular and functional characteristics, we explored if they could be utilized as a model to uncover the pathophysiology of the lens. Cataract can be induced by H_2O_2 or hypertonic NaCl treatments in dissected lens [45]. Therefore, we incubated 8-day-old 21EM15 organoids for 48 h with these compounds (at previously used concentrations) and evaluated their transparency and light-focusing ability. We found that H_2O_2 does not trigger changes in transparency or light-focusing ability for concentrations ranging from 0 to 350 μM, but organoids become opaque and cease to transmit light at concentrations above 500 μM (Figure 6A,B). Increasing concentrations of NaCl (from 1.25% to 1.7%) gradually reduce organoid transparency (Figure 6A), but only the highest concentration has a significant impact on light-focusing ability (Figure 6C). We next sought to examine whether the 21EM15 organoid model could be applied to test the functions of genes associated with cataract. We previously showed that *Celf1* deletion in a germline or lens conditional manner causes early-onset cataract in mice [46]. We therefore tested the transparency and light-focusing ability of organoids made from 21EM15 cells stably expressing an shRNA targeting the *Celf1* gene [46,47]. Interestingly, *Celf1* knockdown reduces organoids' transparency, as observed in mice deficient in *Celf1* (Figure 6D). It also reduces the light-focusing property of 21EM15 organoids (Figure 6E). All together, these results demonstrate that 21EM15 organoids are new models that can be used to study cataract.

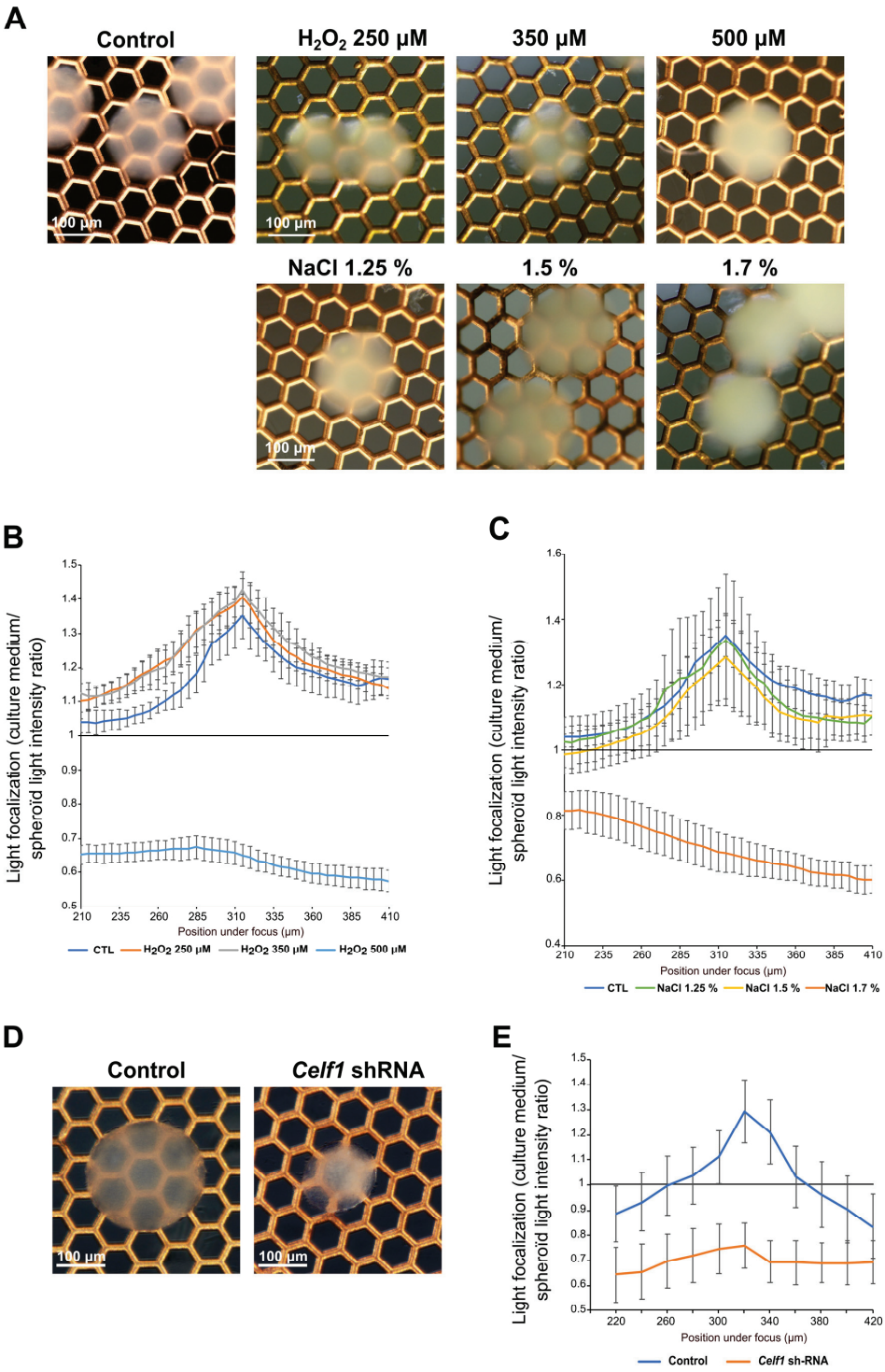

Figure 6. 21EM15 lens organoids can be induced to develop opacity. (**A**) Macroscopic views of 10-day-old lens organoids treated with the indicated concentrations of H_2O_2 or NaCl. The electron microscopy grid allows for the evaluation of transparency. (**B**) Graph showing the light-focusing ability of the 21EM15 lens organoids treated with increasing concentrations of H_2O_2. (**C**) Graph showing the light-focusing ability of the 21EM15 lens organoids treated with increasing concentrations of NaCl. (**D**) Macroscopic views of lens organoids expressing control or *Celf1*-targeting shRNA. The electron microscopy grid allows for the evaluation of transparency. (**E**) Graph showing the light-focusing ability of the 21EM15 lens organoids expressing control or *Celf1*-targeting shRNA. Graphs B, C and E are representative of three independent experiments with n = 12 organoids that are 10 days old for each experiment. Error bars represent standard deviations.

4. Discussion

In the present study, we developed a mouse 3D lens model that can be rapidly generated and can be applied to study processes relevant to lens biology. It has specific optical properties, including transparency and light-focusing ability (Figure 1). We characterized this model using a combination of histological, transcriptomic and immunohistochemical/immunofluorescence approaches. This analysis revealed that, similarly to the lens, 21EM15 lens organoids comprise three main regions, including a peripheral layer, an intermediate part and a core region. Transparency and light-focusing ability indicate that even though the histological organization of the 21EM15 organoids is simplified compared to a true lens, it is sufficient to bring relevant optical properties. In addition to transparency and light-focusing ability, a refractive index measurement, as described by Young and colleagues [48], could also be very useful in the future to assess the influence of cellular organization on organoid optics.

When grown in 2D culture conditions, 21EM15 cells express typical LEC genes [23]. In the present study, we used 3′ end RNA-seq to profile the transcriptomes of 21EM15 2D and 3D cultures, and of laser-microdissected internal and external regions of the organoids. These analyses show that, regardless of how they are grown (2D or 3D), 21EM15 cells express various crystallin genes, such as *Cryab*, *Cryba4*, *Crybg1*, *Crybg3*, *Cryz*, *Cryzl2* and *Cryl1* (see supplemental Table S1). Terrell and colleagues [23] showed that various α and βγ crystallin transcripts (*Cryaa*, *Cryab*, *Cryba4* and *Crygs*) are expressed in 21EM15 cells. Using 3′ end RNAseq, we could confirm the expressions of *Cryab* and *Cryba4* but were unable to confirm the presence of *Cryaa* and *Crygs* in 2D or 3D 21EM15 cells. This may be related to the different methods used (Microarray vs. 3′ end RNA-seq) [23]. Nevertheless, both studies show that *Cryba4* is expressed in these cells. These findings, along with the property of CRYBA4 protein to form homodimers, suggest that it likely makes a key contribution toward the refractive properties observed in the organoids. This is further likely because transcripts encoding gamma crystallins (*Cryga*, *Crygb*, *Crygc*, *Crygd* and *Cryge*)—which are the other major contributors for transparency in the developing lens—are not significantly expressed in these cells. Interestingly, this suggests that the lens organoids exhibit a gene expression strategy for transparency (i.e., high *Cryba4*) that is observed in later stages in the lens. Further, while they are expressed, other crystallin encoding genes such as *Crybg1* and *Crybg3* are less likely to contribute to the refractive properties of the organoids based on previous findings [49,50]. Thus, our transcriptome expression analysis of 2D and 3D cultures, in addition to previous expression microarray data on the 21EM15 cell line [23] as well as the established knowledge on the function of several crystallins [51–59] offer an explanation toward the basis of refractive properties in these organoids. More importantly, these results also indicate that a subset of genes associated with lens development and fiber cell differentiation are induced under 3D culture conditions (Figure 2D). Among this set of genes, we found *Six3*, a well-characterized lens development gene [60]; *Cp*, which is typically expressed in lens epithelium [61]; *Cryab*, *Crim1* and *Nupr1*, which are expressed in lens fiber cells [26,32,61,62] and *Dkk3*, which is a component of the Wnt signaling pathway involved in lens development [62] (Figure 2B). An RNA-seq analysis also shows that the genes elevated in the external region of the lens organoids are enriched for candidates that are related to the cell cycle function (*Ccna2*, *Ccnb1*, *Ccnb2*, *Ccnd1*, *Ccne2*, *Cdc20* and *Cdk1*), whereas those elevated in the internal region are enriched for candidates involved in the Pax6 regulatory pathway (*Cap2* and *Meis1*), Notch and Wnt signaling (*Jag1*, *Wls* and *Fzd6*), Maf pathway (*Maf* and *Eya1*), lens fiber cell morphology and physiology (*Ank2*, *Atp1b1*, *Prox1* and *Tdrd7*) and organelle degradation (*Hsf4* and *Fundc1*) (Figure 3F and Supplemental Table S2). These results are relevant to lens organization, as the anterior epithelium is involved in lens growth and the cortex is the place where fiber cells progressively differentiate [3,4].

Accordingly, KI67 staining shows that only the external cells are proliferative (Figure 3D). We also found the outermost region to be positive for Laminin staining (Figure 4A). Laminin is a glycoprotein specific of basal lamina. It is present in the capsule, a cell-free structure

around the lens [35]. In 21EM15 organoids, Laminin appears to be secreted by cells in the first two or three layers that are encompassed into this extracellular matrix. We were unable to detect E-cadherin or FOXE3 labeling in these external-most cell layers, suggesting that organoid epithelial cells do not fully recapitulate properties of lens anterior epithelium, which express E-cadherin or FOXE3 [63,64] (data not shown). This suggests that while 21EM15 cells are able to proliferate or enter the early stages of fiber cell differentiation, they cannot become true epithelial cells in the culture conditions that we used. One possible explanation relates to the fact that 21EM15 cells were likely selected based on their ability to proliferate rapidly [23]. Although it is now established that the anterior epithelium contains stem cells [2,22], the 21EM15 cells probably originate from the germinative zone and are therefore engaged in the early stages of the fiber cell differentiation process, preventing them from committing to the epithelial fate. Interestingly, they express *Pax6* and *Bmi1*, which are required for lens epithelial cells to regenerate a functional lens [22], but also typical stem cell marker genes like *Nes*, *Chrd*, *Sox4, Sox9, Sox12* and *Klf4* [23]. They are also able to spontaneously form lentoid bodies [23,24]. Finally, we show here, based on a histological analysis, that symmetry is broken in 3D 21EM15 cell cultures (Figures 3A, 4 and 5). Symmetry breaking is a general hallmark of organoid development [31–33]. Taken together, these observations suggest that 21EM15 cells possess stem cell-like properties accounting for their ability to form lens organoids.

A key property of lens fiber cells is the elimination of organelles, as they are potential sources of light scattering. We tested if this also applies to the core region of 21EM15 organoids. Several gene regulatory networks involved in autophagy or nuclear degradation in the lens have been identified [38,65]. One of them involves the transcription factor HSF4, a major regulator of membrane organelle degradation in the lens [39,43,66,67]. Accordingly, we found in immunostaining experiments that HSF4 is more abundant in the core than in the peripheral region of the organoid (Figure 5E). At the RNA level, *Bnip3l*, *Lamp1*, *Fundc1* and *Smurf1*, which are also involved in organelle degradation [38,65], also exhibit elevated expression in the core region compared to the outer region of organoids (Supplemental Table S2). The high expression of these genes is accompanied by an apparently complete degradation of the mitochondria, as inferred from the loss of TOMM20 staining, which is a mitochondrial marker that is commonly used to assess mitophagy in various cell types including lens fiber cells [38,41,68] (Figure 5D). The shape of the nuclei is also strongly affected in the organoid core, with some nuclei clearly showing a pyknosis-like appearance (Figure 5B). Pyknotic nuclei are characteristic of various types of terminal cell differentiation processes requiring nucleus degradation, as in red cells or lens fiber cells [69]. In addition to organelle degradation, fiber cell differentiation is also featured by a strong expression of crystallins, which involves PAX6 and, to some extent, HSF4 [34]. αB-Crystallin (*Cryab*) is poorly expressed in the outer region, whereas it is enriched in the central region where *Pax6* is expressed, as revealed by both 3′ end RNAseq on laser-microdissected regions (Supplemental Table S2; FDR = 0.03) and IF (Figure 4D). This is similar to the expression pattern of αb-Crystallin in wild-type lenses, wherein it is high in fiber cells compared to epithelial cells in later stages of development [30]. Together, these data show that, while the outermost layers of 21EM15 organoids resemble lens epithelial cells, their core regions resemble fiber cells.

In the lens, the transition zone is the area where cells of the anterior epithelium exit the cell cycle and begin differentiation into fiber cells that contribute to the bulk of the lens tissue. Beyond the transition zone, the cells sequentially elongate and degrade their organelles while expressing key lens development master genes. We were unable to profile the transcriptome of the intermediate region of 21EM15 organoids due to technical limitations in laser microdissection. However, we gained significant insights into this zone via the immunostaining of PAX6, JAG1 and PROX1 (Figure 4). These key genes function to orchestrate the development of these different regions of the lens [1,70]. The function of JAG1 is to keep epithelial cells from the germinative zone undifferentiated and to make sure they keep proliferating by activating Notch signaling [66,67,70]. PAX6

and PROX1, respectively, trigger cell cycle exit and are associated with the expression of crystallins and cell elongation during secondary fiber cell differentiation [68,71–74]. PROX1 exhibits dynamic expression and localization in lens cells. PROX1 is first located in the cytoplasm in the anterior epithelium, and then becomes nuclear in the transition zone, where it is involved in orchestrating fiber cell elongation and differentiation [36,73]. 21EM15 organoids show an interesting distribution of these three key genes. JAG1 is consistently localized in the lateral regions and severely reduced near the central axis, in contrast to PAX6, which is highly expressed in a ring-like manner surrounding the organoid core and in the central axis. The changes in PROX1 localization seem to recapitulate its endogenous lens expression. While there is diffused cytoplasmic labeling of PROX1 in the *Jag1*-expressing region, PROX1 becomes nuclear along the central axis, a region where *Pax6* is quite highly expressed. It is interesting to note that the cells that exhibit nuclear PROX1 are located in the area where the cells are the most elongated, indicating that the organoids recapitulate this functional aspect of PROX1, similar to endogenous lens development (Figure 3A right and Figure 4B).

From a developmental point of view, 21EM15 organoids do not form the lens vesicle that is typical of mammals, and their development is more reminiscent of what happens in the fish eye [75]. This is probably due to the fact that the environment of the organoid is very simplified compared with what happens in the whole eye. Nevertheless, the fact that differentiation events occur, and that the expression of key lens genes is spatially regulated, accompanied by significant cellular changes (nuclei and mitochondria), makes this system a valuable tool for more in-depth studies. In particular, it could be used to understand the signaling pathways responsible for the cell polarity of the lens, its morphological asymmetry and the acquisition of its optical properties.

Overall, these results show that 21EM15 organoids recapitulate several aspects of lens organization, gene expression profiles, biological processes or optical properties. We therefore summarized these data in a model (Figure 7). In this model, we were unable to formally identify a canonical epithelium. We termed the outermost zone comprising the first layers of cells that are proliferative and are embedded in Laminin as the "capsuloid". The capsuloid likely corresponds to the fusion of the capsule and the germinative zone of the lens epithelium. The lateral region expressing *Jag1* and *Ki67* is probably a mix of more or less proliferating cells (as indicated by their expression of *Ki67*) and early differentiating cells (expressing *Jag1*). Although cells from the germinative zone do not express *Jag1*, it is tempting to compare this region of the organoid to the germinative zone in the lens, where cells that express *Jag1* would prevent cell cycle exit and the fiber cell differentiation of proliferating cells. In a more internal region, between the germinative zone and the central axis of the organoid, cells begin to express *Pax6* and *Cryab*, and PROX1 becomes nuclear. This region is characteristic of the transition zone in endogenous lens development, where the cells progressively engage in the process of fiber cell differentiation. Interestingly, along the central axis and around the organoid nucleus, the cells no longer express *Jag1*. However, these cells still express *Pax6*, PROX1 is nuclear, and most importantly, exhibits elongation (Figure 4B). Cells in the central-most region exhibit a very intensely stained "pink" cytoplasm in histological analysis, reminiscent of the lens, with pyknotic nuclei and strong expressions of *Hsf4* and *Cryab*. They also show features that are consistent with the degradation of their organelles (loss of Lamin B, TOMM20 and Fibrillarin markers). All of these data suggest ongoing cellular and molecular processes in the lens organoids that contribute to transparency.

Finally, we addressed the suitability of 21EM15 organoids as a tool for studying lens opacity or cataracts (Figure 6). We observed that two previously established treatments to induce cataract, namely, the exposure to H_2O_2 and NaCl, are also able to induce opacity in 21EM15 organoids. This is significant, as previously, H_2O_2 was shown to model the events leading to age-related cataract [76–78]. Further, treatment with hyperosmotic NaCl was shown to trigger osmotic stress and disrupt the fluid balance of lens, which is frequently associated with dry eye disease and diabetic cataracts [79–81]. Thus, 21EM15 organoids

could be applied to further understand how these processes induce cataract. Finally, we also observed that the knockdown of the cataract-linked RNA-binding protein encoding gene, *Celf1*, reduces 21EM15 organoids' transparency and light-focusing properties. CELF1 is involved in the regulation of mRNA splicing, stability or translation [82], and its inactivation in mice leads to the misregulation of post-transcriptional gene expression control in the lens and cataract [46,47,83]. These results indicate that 21EM15 organoids respond to cataractogenic conditions that are representative of a wide range of lens-related etiologies (e.g., age-related cataract, diabetic cataract and genetic cataract) and thus can be used to further advance knowledge on lens pathology.

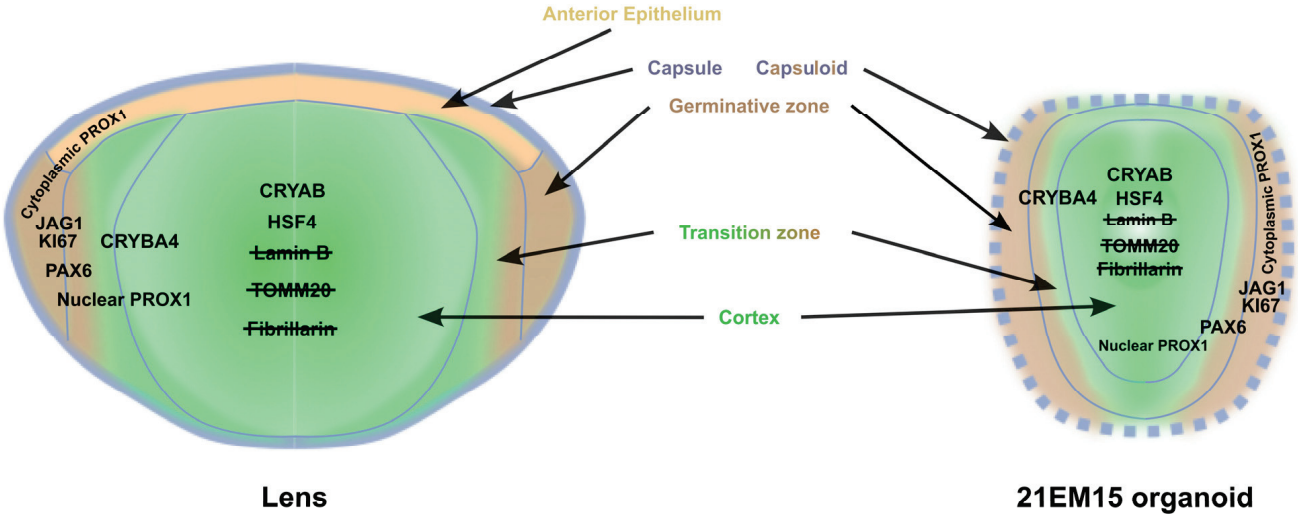

Figure 7. Model for 21EM15 lens organoid organization. This model shows that, unlike the lens, 21EM15 organoids lack the typical lens capsule and anterior epithelium. Instead, there is a zone that we term "capsuloid", comprising the outer layers of proliferative cells embedded in a Laminin layer. Further inwards and from the outside in, 21EM15 organoids recapitulate several aspects of the organization of the lens, with a region corresponding to the germinal zone, where *Ki67* and *Jag1* are expressed, followed by a transition zone that expresses *Pax6* and where PROX1 progressively becomes nuclear. Along the central axis of the organoid, PROX1 is predominantly nuclear, and cells progressively degrade their organelles, such as nuclei (loss of Lamin B and Fibrillarin) and mitochondria (loss of TOMM20 signal), and begin to express *Hsf4* and *Cryab*. These events correspond closely to those described in the normal lens cortex.

5. Conclusions

In conclusion, our work presents a new mouse organoid model that is effective and easy to set up and does not require the development of technical skills in stem cell culture. For a limited investment, both in terms of technique and time, this allows us to relatively rapidly obtain lens organoids that recapitulate specific aspects of lens biology, with the added possibility of performing a functional genetic analysis in a cost-effective manner. The 21EM15 organoids therefore provide the lens community with a compelling new model to improve the understanding of lens biology. Cataract remains a major public health problem that is currently only treated with surgery. It would therefore be interesting to develop drug treatments, particularly in order to offer alternatives to populations in countries that do not have ready access to surgery, or to prevent cataract formation in populations exposed to cataractogenic conditions. From a clinical point of view, these lens organoids should make it possible to develop screens to identify compounds that impact the prevention and/or treatment of cataracts.

Supplementary Materials: The following supporting information can be downloaded at https://www.mdpi.com/article/10.3390/cells12202478/s1, Figure S1: Growth pattern and light-focusing properties of 21EM15 spheroid. (A) Wide field microscopy images and histogram showing the qualitative and quantitative analysis of the growth of 21EM15 spheroids over time. Graph is representative of three independent experiments with n = 12 spheroids for each experiment. Error bars represent standard deviations. (B) Microscopic images of 21EM15 and HaCat spheroids. Organoids derived from HaCaT cells are not able to focus light compared to organoids derived from 21EM15 cells. The graph on the right is representative of three independent experiments with n = 12 spheroids for each experiment. Error bars represent standard deviations; Figure S2: Quality control of RNA-seq of 21EM15 3D and 2D cultures. (A) Principal Component Analysis (PCA) of RNA-sequencing (RNA-seq) datasets from lens culture. In the first dimension, the four samples from 3D cultures (blue) are grouped and separated from the four samples from 2D cultures (red). (B) Dendrogram based on RNA-seq data. The four 3D samples (spheroids, red) and the 2D samples (blue) segregate into distinct clusters; Figure S3: Quality control of RNA-seq of laser-captured microdissected 21EM15 spheroids. (A) Principal Component Analysis of gene expression. The four samples microdissected from internal regions cluster together. Three out of four samples microdissected from external regions cluster together, and are clearly separated from the samples microdissected from internal regions in the first dimension. The fourth external region sample differs from the three other ones and we removed it for subsequent analyses. (B) Heat map of the 793 DEGs, which separates "internal genes" from "external genes"; Table S1: Gene expression in 2D and 3D cultures, measured by 3′ end RNAseq. Columns B–D, gene identification (Ensembl ID, Entrez ID, and gene symbol). Columns E, logFC, log2(expression in 2D cultures/expression in 3D cultures). logCPM, log 2 counts per million. Column G, F, F-test. Column H, PValue, p-value for the expression in 2D and 3D culture, Student's t test. Column I, FDR, adjusted p-value, Benjamini-Hochberg adjustment. Column J, CatMap, a boolean for the gene being present in the CatMap database. Columns K–N, WT_2D_1 to WT_2D_4, gene expression values in 4 2D samples. Columns O–R, WT_3D_1 to WT_3D_4, gene expression values in 4 3D samples. WT_3D_1 to WT_3D_4, gene expression values in 4 3D samples. Columns S–T, logCPM_WT_2D and logCPM_WT_3D, log 2 counts per million in 2D and 3D samples. Column U, gene description; Table S2: Gene expression in laser-microdissected external and internal regions. Columns B–D, gene identification (Ensembl ID, Entrez ID, and gene symbol). Columns E, logFC, log2(expression in internal region/expression in external region). logCPM, log 2 counts per million. Column G, F, F-test. Column H, PValue, p-value for the expression in internal and external regions, Student's t test. Column I, FDR, adjusted p-value, Benjamini-Hochberg adjustment. Column J, CatMap, a boolean for the gene being present in the CatMap database. Columns K-N, μdiss_WT_Inter_1 to μdiss_WT_Inter_4, gene expression values in 4 internal regions. Columns O-Q, μdiss_WT_Exter_1 to μdiss_WT_Exter_3, gene expression values in 3 external regions. Columns R-S, logCPM_μdiss_WT_Inter and logCPM_μdiss_WT_Exter, log 2 counts per million in internal and external regions. Column T, gene description.

Author Contributions: Conceptualization, C.G.-C. and D.R.; data curation, M.D. and L.P.; formal analysis, M.D. and L.P.; methodology, M.D., C.G.-C. and D.R.; resources, S.A.L.; investigation, M.D., C.G.-C., D.R., R.V., J.V. and C.L.G.-G.; writing—original draft preparation, D.R.; writing—review and editing, C.G.-C., C.L.G.-G., S.A.L., L.P. and D.R.; visualization, C.G.-C. and D.R.; supervision, C.G.-C., S.A.L., L.P. and D.R.; project administration, C.G.-C. and L.P.; funding acquisition, L.P. and S.A.L. All authors have read and agreed to the published version of the manuscript.

Funding: L.P. was supported by a grant from Retina France. S.A.L. was supported by the National Institutes of Health/National Eye Institute (R01 EY021505 and R01 EY029770).

Institutional Review Board Statement: Not applicable.

Informed Consent Statement: Not applicable.

Data Availability Statement: The RNA-seq data are available on the NCBI Gene Expression Omnibus (GEO) database under GSE228547 series.

Acknowledgments: We thank the Biosit platforms (Rennes, France) for giving us access to their facilities, and notably MRic (microscopy) and H2P2 (histology). We particularly thank Alain Fautrel and Nicolas Mouchet (H2P2 facility) for providing fruitful discussions.

Conflicts of Interest: The authors declare no conflict of interest.

References

1. Cvekl, A.; Zhang, X. Signaling and Gene Regulatory Networks in Mammalian Lens Development. *Trends Genet.* **2017**, *33*, 677–702. [CrossRef]
2. Bassnett, S.; Šikić, H. The Lens Growth Process. *Prog. Retin. Eye Res.* **2017**, *60*, 181–200. [CrossRef]
3. Bassnett, S.; Shi, Y.; Vrensen, G.F.J.M. Biological Glass: Structural Determinants of Eye Lens Transparency. *Philos. Trans. R. Soc. Lond. B Biol. Sci.* **2011**, *366*, 1250–1264. [CrossRef] [PubMed]
4. Liu, Z.; Huang, S.; Zheng, Y.; Zhou, T.; Hu, L.; Xiong, L.; Li, D.W.-C.; Liu, Y. The Lens Epithelium as a Major Determinant in the Development, Maintenance, and Regeneration of the Crystalline Lens. *Prog. Retin. Eye Res.* **2022**, *92*, 101112. [CrossRef] [PubMed]
5. Shiels, A.; Hejtmancik, J.F. Inherited Cataracts: Genetic Mechanisms and Pathways New and Old. *Exp. Eye Res.* **2021**, *209*, 108662. [CrossRef] [PubMed]
6. Shiels, A.; Hejtmancik, J.F. Biology of Inherited Cataracts and Opportunities for Treatment. *Annu. Rev. Vis. Sci.* **2019**, *5*, 123–149. [CrossRef] [PubMed]
7. Liu, Y.-C.; Wilkins, M.; Kim, T.; Malyugin, B.; Mehta, J.S. Cataracts. *Lancet* **2017**, *390*, 600–612. [CrossRef] [PubMed]
8. Daszynski, D.M.; Santhoshkumar, P.; Phadte, A.S.; Sharma, K.K.; Zhong, H.A.; Lou, M.F.; Kador, P.F. Failure of Oxysterols Such as Lanosterol to Restore Lens Clarity from Cataracts. *Sci. Rep.* **2019**, *9*, 8459. [CrossRef] [PubMed]
9. Makley, L.N.; McMenimen, K.A.; DeVree, B.T.; Goldman, J.W.; McGlasson, B.N.; Rajagopal, P.; Dunyak, B.M.; McQuade, T.J.; Thompson, A.D.; Sunahara, R.; et al. Pharmacological Chaperone for Alpha-Crystallin Partially Restores Transparency in Cataract Models. *Science* **2015**, *350*, 674–677. [CrossRef]
10. Zhao, L.; Chen, X.J.; Zhu, J.; Xi, Y.B.; Yang, X.; Hu, L.D.; Ouyang, H.; Patel, S.H.; Jin, X.; Lin, D.; et al. Lanosterol Reverses Protein Aggregation in Cataracts. *Nature* **2015**, *523*, 607–611. [CrossRef]
11. Goishi, K.; Shimizu, A.; Najarro, G.; Watanabe, S.; Rogers, R.; Zon, L.I.; Klagsbrun, M. AlphaA-Crystallin Expression Prevents Gamma-Crystallin Insolubility and Cataract Formation in the Zebrafish Cloche Mutant Lens. *Development* **2006**, *133*, 2585–2593. [CrossRef] [PubMed]
12. Viet, J.; Reboutier, D.; Hardy, S.; Lachke, S.A.; Paillard, L.; Gautier-Courteille, C. Modeling Ocular Lens Disease in Xenopus. *Dev. Dyn.* **2019**, *249*, 610–621. [CrossRef] [PubMed]
13. Chang, C.-C. *Animal Models of Ophthalmic Diseases*; Springer International Publishing: Cham, Switzerland, 2016.
14. Zhao, Z.; Chen, X.; Dowbaj, A.M.; Sljukic, A.; Bratlie, K.; Lin, L.; Fong, E.L.S.; Balachander, G.M.; Chen, Z.; Soragni, A.; et al. Organoids. *Nat. Rev. Methods Primers* **2022**, *2*, 1–21. [CrossRef] [PubMed]
15. O'Connor, M.D.; McAvoy, J.W. In Vitro Generation of Functional Lens-like Structures with Relevance to Age-Related Nuclear Cataract. *Investig. Ophthalmol. Vis. Sci.* **2007**, *48*, 1245–1252. [CrossRef] [PubMed]
16. Anchan, R.M.; Lachke, S.A.; Gerami-Naini, B.; Lindsey, J.; Ng, N.; Naber, C.; Nickerson, M.; Cavallesco, R.; Rowan, S.; Eaton, J.L.; et al. Pax6- and Six3-Mediated Induction of Lens Cell Fate in Mouse and Human ES Cells. *PLoS ONE* **2014**, *9*, e115106. [CrossRef] [PubMed]
17. Fu, Q.; Qin, Z.; Jin, X.; Zhang, L.; Chen, Z.; He, J.; Ji, J.; Yao, K. Generation of Functional Lentoid Bodies From Human Induced Pluripotent Stem Cells Derived From Urinary Cells. *Investig. Ophthalmol. Vis. Sci.* **2017**, *58*, 517–527. [CrossRef]
18. Yang, C.; Yang, Y.; Brennan, L.; Bouhassira, E.E.; Kantorow, M.; Cvekl, A. Efficient Generation of Lens Progenitor Cells and Lentoid Bodies from Human Embryonic Stem Cells in Chemically Defined Conditions. *FASEB J.* **2010**, *24*, 3274–3283. [CrossRef] [PubMed]
19. Murphy, P.; Kabir, M.H.; Srivastava, T.; Mason, M.E.; Dewi, C.U.; Lim, S.; Yang, A.; Djordjevic, D.; Killingsworth, M.C.; Ho, J.W.K.; et al. Light-Focusing Human Micro-Lenses Generated from Pluripotent Stem Cells Model Lens Development and Drug-Induced Cataract in Vitro. *Development* **2018**, *145*, dev155838. [CrossRef]
20. Plüss, C.J.; Kustermann, S. A Human Three-Dimensional In Vitro Model of Lens Epithelial Cells as a Model to Study Mechanisms of Drug-Induced Posterior Subcapsular Cataracts. *J. Ocul. Pharmacol. Ther.* **2019**, *36*, 56–64. [CrossRef]
21. Cvekl, A.; Camerino, M.J. Generation of Lens Progenitor Cells and Lentoid Bodies from Pluripotent Stem Cells: Novel Tools for Human Lens Development and Ocular Disease Etiology. *Cells* **2022**, *11*, 3516. [CrossRef]
22. Lin, H.; Ouyang, H.; Zhu, J.; Huang, S.; Liu, Z.; Chen, S.; Cao, G.; Li, G.; Signer, R.A.J.; Xu, Y.; et al. Lens Regeneration Using Endogenous Stem Cells with Gain of Visual Function. *Nature* **2016**, *531*, 323–328. [CrossRef] [PubMed]
23. Terrell, A.M.; Anand, D.; Smith, S.F.; Dang, C.A.; Waters, S.M.; Pathania, M.; Beebe, D.C.; Lachke, S.A. Molecular Characterization of Mouse Lens Epithelial Cell Lines and Their Suitability to Study RNA Granules and Cataract Associated Genes. *Exp. Eye Res.* **2015**, *131*, 42–55. [CrossRef] [PubMed]
24. Weatherbee, B.A.T.; Barton, J.R.; Siddam, A.D.; Anand, D.; Lachke, S.A. Molecular Characterization of the Human Lens Epithelium-Derived Cell Line SRA01/04. *Exp. Eye Res.* **2019**, *188*, 107787. [CrossRef] [PubMed]
25. Dobin, A.; Davis, C.A.; Schlesinger, F.; Drenkow, J.; Zaleski, C.; Jha, S.; Batut, P.; Chaisson, M.; Gingeras, T.R. STAR: Ultrafast Universal RNA-Seq Aligner. *Bioinformatics* **2013**, *29*, 15–21. [CrossRef] [PubMed]
26. Liao, Y.; Smyth, G.K.; Shi, W. featureCounts: An Efficient General Purpose Program for Assigning Sequence Reads to Genomic Features. *Bioinformatics* **2014**, *30*, 923–930. [CrossRef] [PubMed]
27. Chen, Y.; Lun, A.T.L.; Smyth, G.K. From Reads to Genes to Pathways: Differential Expression Analysis of RNA-Seq Experiments Using Rsubread and the edgeR Quasi-Likelihood Pipeline. *F1000Research* **2016**, *5*, 1438. [CrossRef] [PubMed]

28. Kakrana, A.; Yang, A.; Anand, D.; Djordjevic, D.; Ramachandruni, D.; Singh, A.; Huang, H.; Ho, J.W.K.; Lachke, S.A. iSyTE 2.0: A Database for Expression-Based Gene Discovery in the Eye. *Nucleic Acids Res.* **2018**, *46*, D875–D885. [CrossRef] [PubMed]
29. Zhao, Y.; Wilmarth, P.A.; Cheng, C.; Limi, S.; Fowler, V.M.; Zheng, D.; David, L.L.; Cvekl, A. Proteome-Transcriptome Analysis and Proteome Remodeling in Mouse Lens Epithelium and Fibers. *Exp. Eye Res.* **2019**, *179*, 32–46. [CrossRef]
30. Zhao, Y.; Zheng, D.; Cvekl, A. A Comprehensive Spatial-Temporal Transcriptomic Analysis of Differentiating Nascent Mouse Lens Epithelial and Fiber Cells. *Exp. Eye Res.* **2018**, *175*, 56–72. [CrossRef]
31. Anand, G.M.; Megale, H.C.; Murphy, S.H.; Weis, T.; Lin, Z.; He, Y.; Wang, X.; Liu, J.; Ramanathan, S. Controlling Organoid Symmetry Breaking Uncovers an Excitable System Underlying Human Axial Elongation. *Cell* **2023**, *186*, 497–512.e23. [CrossRef]
32. Brassard, J.A.; Lutolf, M.P. Engineering Stem Cell Self-Organization to Build Better Organoids. *Cell Stem Cell* **2019**, *24*, 860–876. [CrossRef] [PubMed]
33. Serra, D.; Mayr, U.; Boni, A.; Lukonin, I.; Rempfler, M.; Challet Meylan, L.; Stadler, M.B.; Strnad, P.; Papasaikas, P.; Vischi, D.; et al. Self-Organization and Symmetry Breaking in Intestinal Organoid Development. *Nature* **2019**, *569*, 66–72. [CrossRef] [PubMed]
34. Cvekl, A.; McGreal, R.; Liu, W. Lens Development and Crystallin Gene Expression. *Prog. Mol. Biol. Transl. Sci.* **2015**, *134*, 129–167. [CrossRef]
35. DeDreu, J.; Walker, J.L.; Menko, A.S. Dynamics of the Lens Basement Membrane Capsule and Its Interaction with Connective Tissue-like Extracapsular Matrix Proteins. *Matrix Biol.* **2021**, *96*, 18–46. [CrossRef] [PubMed]
36. Duncan, M.K.; Cui, W.; Oh, D.-J.; Tomarev, S.I. Prox1 Is Differentially Localized during Lens Development. *Mech. Dev.* **2002**, *112*, 195–198. [CrossRef] [PubMed]
37. Garg, A.; Hannan, A.; Wang, Q.; Makrides, N.; Zhong, J.; Li, H.; Yoon, S.; Mao, Y.; Zhang, X. Etv Transcription Factors Functionally Diverge from Their Upstream FGF Signaling in Lens Development. *Elife* **2020**, *9*, e51915. [CrossRef] [PubMed]
38. Brennan, L.; Disatham, J.; Kantorow, M. Mechanisms of Organelle Elimination for Lens Development and Differentiation. *Exp. Eye Res.* **2021**, *209*, 108682. [CrossRef] [PubMed]
39. Costello, M.J.; Brennan, L.A.; Basu, S.; Chauss, D.; Mohamed, A.; Gilliland, K.O.; Johnsen, S.; Menko, S.; Kantorow, M. Autophagy and Mitophagy Participate in Ocular Lens Organelle Degradation. *Exp. Eye Res.* **2013**, *116*, 141–150. [CrossRef]
40. Cui, X.; Liu, H.; Li, J.; Guo, K.; Han, W.; Dong, Y.; Wan, S.; Wang, X.; Jia, P.; Li, S.; et al. Heat Shock Factor 4 Regulates Lens Epithelial Cell Homeostasis by Working with Lysosome and Anti-Apoptosis Pathways. *Int. J. Biochem. Cell Biol.* **2016**, *79*, 118–127. [CrossRef]
41. Imai, F.; Yoshizawa, A.; Fujimori-Tonou, N.; Kawakami, K.; Masai, I. The Ubiquitin Proteasome System Is Required for Cell Proliferation of the Lens Epithelium and for Differentiation of Lens Fiber Cells in Zebrafish. *Development* **2010**, *137*, 3257–3268. [CrossRef]
42. Morishita, H.; Eguchi, S.; Kimura, H.; Sasaki, J.; Sakamaki, Y.; Robinson, M.L.; Sasaki, T.; Mizushima, N. Deletion of Autophagy-Related 5 (Atg5) and Pik3c3 Genes in the Lens Causes Cataract Independent of Programmed Organelle Degradation. *J. Biol. Chem.* **2013**, *288*, 11436–11447. [CrossRef] [PubMed]
43. Sandilands, A.; Hutcheson, A.M.; Long, H.A.; Prescott, A.R.; Vrensen, G.; Löster, J.; Klopp, N.; Lutz, R.B.; Graw, J.; Masaki, S.; et al. Altered Aggregation Properties of Mutant Gamma-Crystallins Cause Inherited Cataract. *EMBO J.* **2002**, *21*, 6005–6014. [CrossRef] [PubMed]
44. Cui, X.; Wang, L.; Zhang, J.; Du, R.; Liao, S.; Li, D.; Li, C.; Ke, T.; Li, D.W.-C.; Huang, H.; et al. HSF4 Regulates DLAD Expression and Promotes Lens De-Nucleation. *Biochim. Biophys. Acta (BBA)-Mol. Basis Dis.* **2013**, *1832*, 1167–1172. [CrossRef] [PubMed]
45. Ruiss, M.; Kronschläger, M.; Schlatter, A.; Dechat, T.; Findl, O. Comparison of Methods to Experimentally Induce Opacification and Elasticity Change in Ex Vivo Porcine Lenses. *Sci. Rep.* **2021**, *11*, 23406. [CrossRef] [PubMed]
46. Siddam, A.D.; Gautier-Courteille, C.; Perez-Campos, L.; Anand, D.; Kakrana, A.; Dang, C.A.; Legagneux, V.; Méreau, A.; Viet, J.; Gross, J.M.; et al. The RNA-Binding Protein Celf1 Post-Transcriptionally Regulates p27Kip1 and Dnase2b to Control Fiber Cell Nuclear Degradation in Lens Development. *PLoS Genet.* **2018**, *14*, e1007278. [CrossRef] [PubMed]
47. Aryal, S.; Viet, J.; Weatherbee, B.A.T.; Siddam, A.D.; Hernandez, F.G.; Gautier-Courteille, C.; Paillard, L.; Lachke, S.A. The Cataract-Linked RNA-Binding Protein Celf1 Post-Transcriptionally Controls the Spatiotemporal Expression of the Key Homeodomain Transcription Factors Pax6 and Prox1 in Lens Development. *Hum. Genet.* **2020**, *139*, 1541–1554. [CrossRef]
48. Young, L.K.; Jarrin, M.; Saunter, C.D.; Quinlan, R.A.; Girkin, J.M. Non-Invasive in Vivo Quantification of the Developing Optical Properties and Graded Index of the Embryonic Eye Lens Using SPIM. *Biomed. Opt. Express* **2018**, *9*, 2176–2188. [CrossRef]
49. Khago, D.; Bierma, J.C.; Roskamp, K.W.; Kozlyuk, N.; Martin, R.W. Protein Refractive Index Increment Is Determined by Conformation as Well as Composition. *J. Phys. Condens. Matter* **2018**, *30*, 435101. [CrossRef]
50. Mahendiran, K.; Elie, C.; Nebel, J.-C.; Ryan, A.; Pierscionek, B.K. Primary Sequence Contribution to the Optical Function of the Eye Lens. *Sci. Rep.* **2014**, *4*, 5195. [CrossRef]
51. Wistow, G. The Human Crystallin Gene Families. *Hum. Genom.* **2012**, *6*, 26. [CrossRef]
52. Clark, A.R.; Lubsen, N.H.; Slingsby, C. sHSP in the Eye Lens: Crystallin Mutations, Cataract and Proteostasis. *Int. J. Biochem. Cell Biol.* **2012**, *44*, 1687–1697. [CrossRef] [PubMed]
53. Clark, J.I. Functional Sequences in Human alphaB Crystallin. *Biochim. Biophys. Acta* **2016**, *1860*, 240–245. [CrossRef] [PubMed]

54. Nourazaran, M.; Yousefi, R.; Moosavi-Movahedi, F.; Panahi, F.; Hong, J.; Moosavi-Movahedi, A.A. The Structural and Functional Consequences of Melatonin and Serotonin on Human αB-Crystallin and Their Dual Role in the Eye Lens Transparency. *Biochim. Biophys. Acta (BBA)-Proteins Proteom.* **2023**, *1871*, 140928. [CrossRef] [PubMed]
55. Boelens, W.C. Cell Biological Roles of αB-Crystallin. *Prog. Biophys. Mol. Biol.* **2014**, *115*, 3–10. [CrossRef] [PubMed]
56. Sprague-Piercy, M.A.; Rocha, M.A.; Kwok, A.O.; Martin, R.W. α-Crystallins in the Vertebrate Eye Lens: Complex Oligomers and Molecular Chaperones. *Annu. Rev. Phys. Chem.* **2021**, *72*, 143–163. [CrossRef] [PubMed]
57. Hejtmancik, J.F.; Riazuddin, S.A.; McGreal, R.; Liu, W.; Cvekl, A.; Shiels, A. Lens Biology and Biochemistry. *Prog. Mol. Biol. Transl. Sci.* **2015**, *134*, 169–201. [CrossRef]
58. Quinlan, R. Cytoskeletal Competence Requires Protein Chaperones. *Prog. Mol. Subcell. Biol.* **2002**, *28*, 219–233. [CrossRef]
59. Ho, D.W.H.; Yap, M.K.H.; Ng, P.W.; Fung, W.Y.; Yip, S.P. Association of High Myopia with Crystallin Beta A4 (CRYBA4) Gene Polymorphisms in the Linkage-Identified MYP6 Locus. *PLoS ONE* **2012**, *7*, e40238. [CrossRef]
60. Oliver, G.; Loosli, F.; Köster, R.; Wittbrodt, J.; Gruss, P. Ectopic Lens Induction in Fish in Response to the Murine Homeobox Gene Six3. *Mech. Dev.* **1996**, *60*, 233–239. [CrossRef]
61. Wang, Y.; Mahesh, P.; Wang, Y.; Novo, S.G.; Shihan, M.H.; Hayward-Piatkovskyi, B.; Duncan, M.K. Spatiotemporal Dynamics of Canonical Wnt Signaling during Embryonic Eye Development and Posterior Capsular Opacification (PCO). *Exp. Eye Res.* **2018**, *175*, 148–158. [CrossRef]
62. Harned, J.; Fleisher, L.N.; McGahan, M.C. Lens Epithelial Cells Synthesize and Secrete Ceruloplasmin: Effects of Ceruloplasmin and Transferrin on Iron Efflux and Intracellular Iron Dynamics. *Exp. Eye Res.* **2006**, *83*, 721–727. [CrossRef] [PubMed]
63. Pontoriero, G.F.; Smith, A.N.; Miller, L.-A.D.; Radice, G.L.; West-Mays, J.A.; Lang, R.A. Co-Operative Roles for E-Cadherin and N-Cadherin during Lens Vesicle Separation and Lens Epithelial Cell Survival. *Dev. Biol.* **2009**, *326*, 403–417. [CrossRef] [PubMed]
64. Landgren, H.; Blixt, A.; Carlsson, P. Persistent FoxE3 Expression Blocks Cytoskeletal Remodeling and Organelle Degradation during Lens Fiber Differentiation. *Investig. Ophthalmol. Vis. Sci.* **2008**, *49*, 4269–4277. [CrossRef] [PubMed]
65. Bassnett, S. On the Mechanism of Organelle Degradation in the Vertebrate Lens. *Exp. Eye Res.* **2009**, *88*, 133–139. [CrossRef] [PubMed]
66. Rowan, S.; Conley, K.W.; Le, T.T.; Donner, A.L.; Maas, R.L.; Brown, N.L. Notch Signaling Regulates Growth and Differentiation in the Mammalian Lens. *Dev. Biol.* **2008**, *321*, 111–122. [CrossRef] [PubMed]
67. Saravanamuthu, S.S.; Gao, C.Y.; Zelenka, P.S. Notch Signaling Is Required for Lateral Induction of Jagged1 during FGF-Induced Lens Fiber Differentiation. *Dev. Biol.* **2009**, *332*, 166–176. [CrossRef] [PubMed]
68. Shaham, O.; Smith, A.N.; Robinson, M.L.; Taketo, M.M.; Lang, R.A.; Ashery-Padan, R. Pax6 Is Essential for Lens Fiber Cell Differentiation. *Development* **2009**, *136*, 2567–2578. [CrossRef]
69. McAvoy, J.W.; Richardson, N.A. Nuclear Pyknosis during Lens Fibre Differentiation in Epithelial Explants. *Curr. Eye Res.* **1986**, *5*, 711–715. [CrossRef]
70. Mochizuki, T.; Masai, I. The Lens Equator: A Platform for Molecular Machinery That Regulates the Switch from Cell Proliferation to Differentiation in the Vertebrate Lens. *Dev. Growth Differ.* **2014**, *56*, 387–401. [CrossRef]
71. Shaham, O.; Menuchin, Y.; Farhy, C.; Ashery-Padan, R. Pax6: A Multi-Level Regulator of Ocular Development. *Prog. Retin. Eye Res.* **2012**, *31*, 351–376. [CrossRef]
72. Cvekl, A.; Ashery-Padan, R. The Cellular and Molecular Mechanisms of Vertebrate Lens Development. *Development* **2014**, *141*, 4432–4447. [CrossRef] [PubMed]
73. Wigle, J.T.; Chowdhury, K.; Gruss, P.; Oliver, G. Prox1 Function Is Crucial for Mouse Lens-Fibre Elongation. *Nat. Genet.* **1999**, *21*, 318–322. [CrossRef] [PubMed]
74. Audette, D.S.; Anand, D.; So, T.; Rubenstein, T.B.; Lachke, S.A.; Lovicu, F.J.; Duncan, M.K. Prox1 and Fibroblast Growth Factor Receptors Form a Novel Regulatory Loop Controlling Lens Fiber Differentiation and Gene Expression. *Development* **2016**, *143*, 318–328. [CrossRef] [PubMed]
75. Richardson, R.; Tracey-White, D.; Webster, A.; Moosajee, M. The Zebrafish Eye-a Paradigm for Investigating Human Ocular Genetics. *Eye* **2017**, *31*, 68–86. [CrossRef] [PubMed]
76. Spector, A.; Wang, G.M.; Wang, R.R.; Garner, W.H.; Moll, H. The Prevention of Cataract Caused by Oxidative Stress in Cultured Rat Lenses. I. H2O2 and Photochemically Induced Cataract. *Curr. Eye Res.* **1993**, *12*, 163–179. [CrossRef] [PubMed]
77. Spector, A. Oxidative Stress-Induced Cataract: Mechanism of Action. *FASEB J.* **1995**, *9*, 1173–1182. [CrossRef]
78. Hernebring, M.; Adelöf, J.; Wiseman, J.; Petersen, A.; Zetterberg, M. H2O2-Induced Cataract as a Model of Age-Related Cataract: Lessons Learned from Overexpressing the Proteasome Activator PA28αβ in Mouse Eye Lens. *Exp. Eye Res.* **2021**, *203*, 108395. [CrossRef]
79. Gu, Y.; Xu, B.; Feng, C.; Ni, Y.; Hong, N.; Wang, J.; Jiang, B. Topical Use of NaCl Solution with Different Concentration Affects Lens Transparency in Anesthetized Mice. *Curr. Eye Res.* **2016**, *41*, 943–950. [CrossRef]
80. Butler, P.A. Reversible Cataracts in Diabetes Mellitus. *J. Am. Optom. Assoc.* **1994**, *65*, 559–563.
81. Obrosova, I.G.; Chung, S.S.M.; Kador, P.F. Diabetic Cataracts: Mechanisms and Management. *Diabetes Metab. Res. Rev.* **2010**, *26*, 172–180. [CrossRef]

82. Dasgupta, T.; Ladd, A.N. The Importance of CELF Control: Molecular and Biological Roles of the CUG-BP, Elav-like Family of RNA-Binding Proteins. *Wiley Interdiscip. Rev. RNA* **2012**, *3*, 104–121. [CrossRef]
83. Siddam, A.D.; Duot, M.; Coomson, S.Y.; Anand, D.; Aryal, S.; Weatherbee, B.A.T.; Audic, Y.; Paillard, L.; Lachke, S.A. High-Throughput Transcriptomics of Celf1 Conditional Knockout Lens Identifies Downstream Networks Linked to Cataract Pathology. *Cells* **2023**, *12*, 1070. [CrossRef]

Disclaimer/Publisher's Note: The statements, opinions and data contained in all publications are solely those of the individual author(s) and contributor(s) and not of MDPI and/or the editor(s). MDPI and/or the editor(s) disclaim responsibility for any injury to people or property resulting from any ideas, methods, instructions or products referred to in the content.

cells

MDPI

Article

Identification of Small Molecules for Prevention of Lens Epithelium-Derived Cataract Using Zebrafish

Kineret Taler, Nour Zatari, Mohammad Iqbal Lone, Shahar Rotem-Bamberger and Adi Inbal *

Department of Medical Neurobiology, Institute for Medical Research—Israel-Canada, The Hebrew University-Hadassah Medical School, Jerusalem 9112002, Israel; kineret.taler@mail.huji.ac.il (K.T.); nour.zatari@mail.huji.ac.il (N.Z.); iqbalzoo84@gmail.com (M.I.L.); shahar.rotem@mail.huji.ac.il (S.R.-B.)
* Correspondence: adi.inbal@mail.huji.ac.il

Abstract: Cataract is the leading cause of blindness worldwide. It can be treated by surgery, whereby the damaged crystalline lens is replaced by a synthetic lens. Although cataract surgery is highly effective, a relatively common complication named posterior capsular opacification (PCO) leads to secondary loss of vision. PCO is caused by abnormal proliferation and migration of residual lens epithelial cells (LECs) that were not removed during the surgery, which results in interruption to the passage of light. Despite technical improvements to the surgery, this complication has not been eradicated. Efforts are being made to identify drugs that can be applied post-surgery, to inhibit PCO development. Towards the goal of identifying such drugs, we used zebrafish embryos homozygous for a mutation in *plod3* that develop a lens phenotype with characteristics of PCO. Using both biased and unbiased approaches, we identified small molecules that can block the lens phenotype of the mutants. Our findings confirm the relevance of zebrafish *plod3* mutants' lens phenotype as a model for lens epithelium-derived cataract and add to our understanding of the molecular mechanisms that contribute to the development of this pathology. This understanding should help in the development of strategies for PCO prevention.

Keywords: zebrafish; *plod3*; Lysyl hydroxylase 3; cataract; posterior capsular opacification; small molecule screen; Erlotinib; 4-PBA

1. Introduction

Transparency of the ocular lens is critical for normal vision, and when compromised, results in cataract, one of the leading causes of blindness for many millions of people worldwide [1]. The only treatment for cataract is surgical removal of the impaired lens from its capsule, a thick basement membrane that surrounds the lens, followed by insertion of a synthetic lens into the remaining capsular bag [2]. The most common complication of this widely used procedure is posterior capsular opacification (PCO) that leads to secondary visual impairment [3]. PCO occurs when residual lens epithelial cells (LECs) that remain firmly attached to the capsule migrate to the posterior capsule where they can form two types of pathologies, fibrotic PCO and pearl PCO. In fibrotic PCO, LECs undergo an epithelial–mesenchymal transition (EMT), forming plaques of fibroblastic/myofibroblastic cells that cause lens capsule wrinkling, eventually distorting the passage of light along the visual axis [3,4]. Pearl PCO, also referred to as regenerative or regeneratory PCO, is very common and causes most vision loss post cataract surgery [5,6]. In pearl PCO, residual LECs generate globular structures named Elschnig pearls, thought to be the result of aberrant differentiation towards a lens fiber cell fate. These structures can significantly interfere with vision if they accumulate on the visual axis [7]. Both types of lens epithelial pathologies are also observed in another primary form of cataract, anterior subcapsular cataract (ASC) [3,4]. To date, the main PCO preventative strategy has been to try to eliminate all epithelial cells from the capsular bag; however, this has not proven effective with most methods, inducing other serious ocular problems [4,8,9]. An alternative approach is to

devise molecular strategies to stabilize the lens epithelial cells in order to maintain the normal epithelial phenotype and prevent cataractous changes.

Most studies addressing molecular aspects of PCO development and prevention are conducted using in vitro systems, including cell culture and tissue explants [10,11]. In vivo models for PCO include transgenic (Tg) mice, genetically engineered to overexpress transforming growth factor β (TGFβ), specifically in the lens [12]. Recently, we have shown that zebrafish embryos homozygous for loss of function mutations in *plod3*, which encodes for the collagen-modifying enzyme lysyl-hydroxylase 3 (Lh3), fail to generate a normal lens capsule. This failure is likely due to the inability to properly modify Collagen IV, a major and critical component of basement membranes. Homozygous mutant larvae develop round cellular masses of partially differentiated lens fiber cells from the lens epithelium. The development of these masses resembles that of pearl PCO and ASC, and can therefore serve as an in vivo model for spontaneous development of lens epithelium-derived cataracts [13]. Importantly, human patients with reduced Lh3 function present with childhood cataracts; however, these have not been characterized [14].

In all models described above, aberrant TGFβ signaling was shown to drive the development of the lens epithelial pathologies [13,15–17]; however, because of its normal role in the eye, inhibition of TGFβ signaling cannot readily be used for prevention of PCO and therefore other therapeutic strategies must be identified.

In this study, we continued to use zebrafish *plod3* mutant embryos in search of molecular strategies to prevent the development of cell masses in mutant lenses, given their similarities to pearl PCO. We took two approaches to look for compounds that can inhibit development of cell masses from LECs: (1) a biased, knowledge-based approach based on the cellular abnormalities we expect from the loss of Lh3 activity and from a group of cells that exhibit increased growth; (2) an unbiased, discovery-based approach based on screening small molecule libraries. We found two small molecules that efficiently inhibit the lens phenotype, namely 4-Phenylbutyric acid (4-PBA), an ER stress and HDAC inhibitor, and Erlotinib, an epidermal growth factor receptor (EGFR) inhibitor. We further showed that the mTOR inhibitor rapamycin is not an efficient inhibitor of the pearl PCO-like phenotype. Our findings strengthen the link between the zebrafish lens phenotype and PCO in humans and contribute knowledge regarding the molecular and cellular abnormalities that promote the development of this lens epithelium-derived pathology. Hence, zebrafish *plod3* mutants can serve as an additional in vivo model in research and development of treatments for prevention of PCO.

2. Materials and Methods

2.1. Fish Lines

plod3^{vu222} and *plod3*^{tv205} have been described [13,18]. *plod3*^{vu222} mutation is hypomorphic and was used for most experiments, as it better represents the situation in humans with reduced Lh3 function, given that complete loss of Lh3 function is lethal. *plod3*^{tv205} embryos that are homozygous for a null mutation were used in the small molecule screen as their more severe phenotype helped in scoring rescue during the screening process. Fish were maintained under standard conditions as described in "The Zebrafish Book" [19].

2.2. Small Molecule Screen and Treatments

For the chemical screen, we used aliquots of two small molecule libraries that were purchased from Karlsruhe Institute of Technology (KIT), Germany. The first, Enzo Screen-Well FDA approved drug library V2 (BML-2843), contained almost 800 FDA-approved drugs, and the second, Enzo Screen-Well ICCB Known Bioactives library (BML-2840), contained 472 biologically active compounds.

One compound was added into each well after 1:300 dilution in a total of 300 μL egg water ("Instant Ocean" salt, 0.3 g/L reverse-osmosis-treated H_2O) containing 0.003% N-phenylthiourea (PTU #P7629, Sigma-Aldrich, St. Louis, MO, USA). Four wells in each plate were treated with DMSO at a 1:300 dilution to serve as negative controls. Since

the concentration of almost all compounds in the libraries we used was 10 mM, the final concentration of the compounds was typically 33.3 μM (except in very few cases where the original concentration was 1 mM or 5 mM). Embryos were raised at 28.5 °C and the solution of the compound was replaced with a fresh one after 24 and after 48 h. Larvae were assessed for rescue of the lens phenotype at 3 and 4 days post-fertilization (dpf). The researchers performing the screen were not informed about the identity of the compounds at the time of the screen.

The following small molecules were also used: SB-431542 (sc-204265, Santa Cruz, Dallas, TX, USA) at a final concentration of 100 μM in egg water with 0.003% PTU and 0.1% DMSO; 4-PBA (P21005, Sigma) at a final concentration of 50 μM in egg water with 0.003% PTU; Erlotinib (SML2156, Sigma) at a final concentration of 9.2 μM in egg water with 0.003% PTU and 0.2% DMSO; rapamycin (sc-3504, Santa Cruz) at a final concentration of 25 μM in egg water with 0.003% PTU and 0.1% DMSO.

In experiments for determining the time window in which a specific compound is needed, each "time frame experiment" was conducted at least twice with a total of 50 or more lenses evaluated in each experimental group.

2.3. Histology and Immunohistochemistry

Histology using plastic sections was performed by fixing larvae with 4% paraformaldehyde (PFA) overnight at 4 °C, subsequent washing with PBT, dehydration in EtOH series and embedding in JB4 resin (Polysciences, Inc., Warrington, PA, USA) according to the manufacturer's instructions. We used LKB8800 Ultratome III microtome to cut 4 μm sections, which were stained with methylene blue-azure II [20].

We performed immunohistochemistry on cryosections. Following larvae fixation with 4% PFA overnight at 4 °C, larvae were washed with PBT, gradually transferred to 100% MeOH and kept at −20 °C. Subsequently, larvae were rehydrated with PBT and gradually transferred to 20% sucrose in 0.1 M phosphate buffer pH 7.4, incubated overnight at 4 °C and then embedded in 1.2% agarose + 5% sucrose in H_2O. Agarose blocks were kept in 30% sucrose overnight at 4 °C and then frozen using 2-methylbutane on liquid nitrogen. We cut 16 μm sections, which were placed on Superfrost™ Plus microscope slides (Thermo Scientific, Waltham, MA, USA) and dried overnight at room temperature. Slides were washed with PBS, fixed with 4% PFA at 4 °C for 20 min, washed again with PBS, followed by 1 h blocking in 20% PHT (20% goat serum, 0.5% Triton X-100 in PBS) or 10% goat serum +2% BSA in PBT. Subsequently, sections were incubated with primary antibody overnight at 4 °C in 1% PHT (1% serum, 0.5% Triton X-100 in PBS) or 10% goat serum +2% BSA in PBT, then washed with 1% PHT or PBT for 30 min at room temperature. Incubation with secondary antibody followed, for 0.5–1.5 h at room temperature or 37 °C, and then washing with 1% PHT or PBT for 30 min and mounting in 50% glycerol or Fluoroshield Mounting Medium with DAPI (ab104139, Abcam, Cambridge, UK).

All antibodies used in this study had been previously published and validated in zebrafish. Primary antibodies used were: rabbit anti-phospho-Smad3 (1:200) (ab52903, Abcam), rabbit anti-Phospho-p44/42 MAPK (Erk1/2) (Thr202/Tyr204) (1:200) (#9101, Cell Signaling, Danvers, MA, USA), rabbit anti-Phospho-S6 Ribosomal Protein (Ser240/244) (1:300) (Cell Signaling #2215), and monoclonal antibody 5E11 (1:200) (a kind gift from Prof. Jim Fadool, Florida State University, USA). Secondary antibodies were from Jackson ImmunoResearch: Alexa Fluor 647 AffiniPure donkey anti-rabbit IgG (H + L) (1:400), Cy3 AffiniPure donkey anti-rabbit IgG (H + L) (1:250), or Alexa Fluor 647 AffiniPure donkey anti-mouse IgG (H + L) (1:250).

2.4. Imaging

Imaging was performed using a Zeiss LSM 700 confocal system and Axio Imager M2 compound microscope, or with a Discovery.V8 stereoscope and AxioCam MRc digital camera (Zeiss, Oberkochen, Germany). To avoid interference by pigmentation, embryos were raised in the presence of PTU from approximately 22 hpf. For live imaging, we

mounted embryos in 0.5% low-melting-point agarose (#50101, Lonza, Basel, Switzerland) in 30% Danieau's solution (1740 mM NaCl, 21 mM KCl, 12 mM $MgSO_4 \cdot 7H_2O$, 18 mM $Ca(NO_3)_2$, 150 mM HEPES buffer) and 0.01% tricaine.

2.5. Data Quantification and Statistical Analyses

To quantify changes in rough endoplasmic reticulum width, we used ImageJ 1.43u software [21] and measured at least 25 sites in 3–4 different cells from two different embryos for each cell type and genotype. Statistical analysis was performed using 1-tailed Student's *t*-test.

For quantification of the effect of small molecule treatments, we classified lens position in experimental groups, relative to the position of the lens in age-matched normal larvae, as either normal, outside or inside (closer to the retina) (Figure S1). We used χ^2 statistics to test for goodness of fit.

3. Results

3.1. Evidence for Rough Endoplasmic Reticulum Abnormalities in Lens Epithelium and Presumptive Cornea of plod3 Mutants

Our model of lens epithelium-derived cataract in zebrafish larvae was based on a mutation that causes loss of function in the collagen-modifying enzyme Lh3. Interference with the activity of Lh3 was expected to result in accumulation of misfolded proteins, potentially leading to abnormalities in the rough endoplasmic reticulum (RER) and resulting in endoplasmic reticulum (ER) stress. Indeed, it has been suggested that mutant *Plod3* mouse embryos develop ER stress [22]. ER stress could lead to many cellular responses, including enhancing the effects of TGFβ signaling [23], the latter being a critical driver of cellular mass formation in lenses of Lh3-deficient zebrafish embryos [13]. We therefore looked for evidence of ER abnormalities in lenses of *plod3* mutant zebrafish embryos. First, we injected embryos at the one-cell stage with synthetic mRNA encoding for the ER-eGFP fusion protein that localizes to RER [24], and examined the appearance of the fluorescent signal at 2 dpf in cryosections from lenses. This time point was chosen as it is when lens capsule formation has already begun and abnormalities in the anterior lens epithelium become apparent [13,25]. The results showed a clear difference between normal and mutant embryos, whereby in normal siblings EGFP fluorescence was more abundant and mostly diffuse throughout the cytoplasm, whereas in mutants the signal was reduced and localized to puncta within the cytoplasm of lens epithelial cells and presumptive corneal cells. These puncta were particularly large in the superficial-most layer of the developing corneal epithelium (Figure 1A,B; $n = 9$ and 8 eyes, respectively). Hence, already at a relatively low resolution, the appearance of the ER was markedly different between normal and *plod3* mutant lenses and presumptive cornea cells.

To better understand the change in RER appearance, we used transmission electron microscopy (TEM) and closely examined the anterior lens epithelium (ALE) and adjacent cells at 2 dpf. RER was much more abundant in presumptive corneal epithelial cells compared to ALE cells, in both normal siblings and in mutants. Although not abundant, some of the RER in the ALE of mutants appeared to have enlarged lumens compared to the ALE of normal siblings (Figure 1C,D; $n = 3$ eyes from each genotype). In the adjacent cells of the developing basal corneal epithelium where RER was very abundant, the lumens of RER in mutants were often mildly enlarged (Figure 1F,G). To quantify potential differences, we measured and compared the width of RER lumens in sections from normal and mutant lenses. Consistent with their appearance, lumen widths in ALE cells were on average slightly increased in mutants, although the difference was not significant (Figure 1E). In contrast, lumen widths in the basal epithelium layer of the developing cornea were significantly wider (Figure 1H). Enlarged RER lumens were likely due to accumulation of misfolded proteins and suggested the presence or development of ER stress in *plod3* mutant lens epithelium and neighboring tissues.

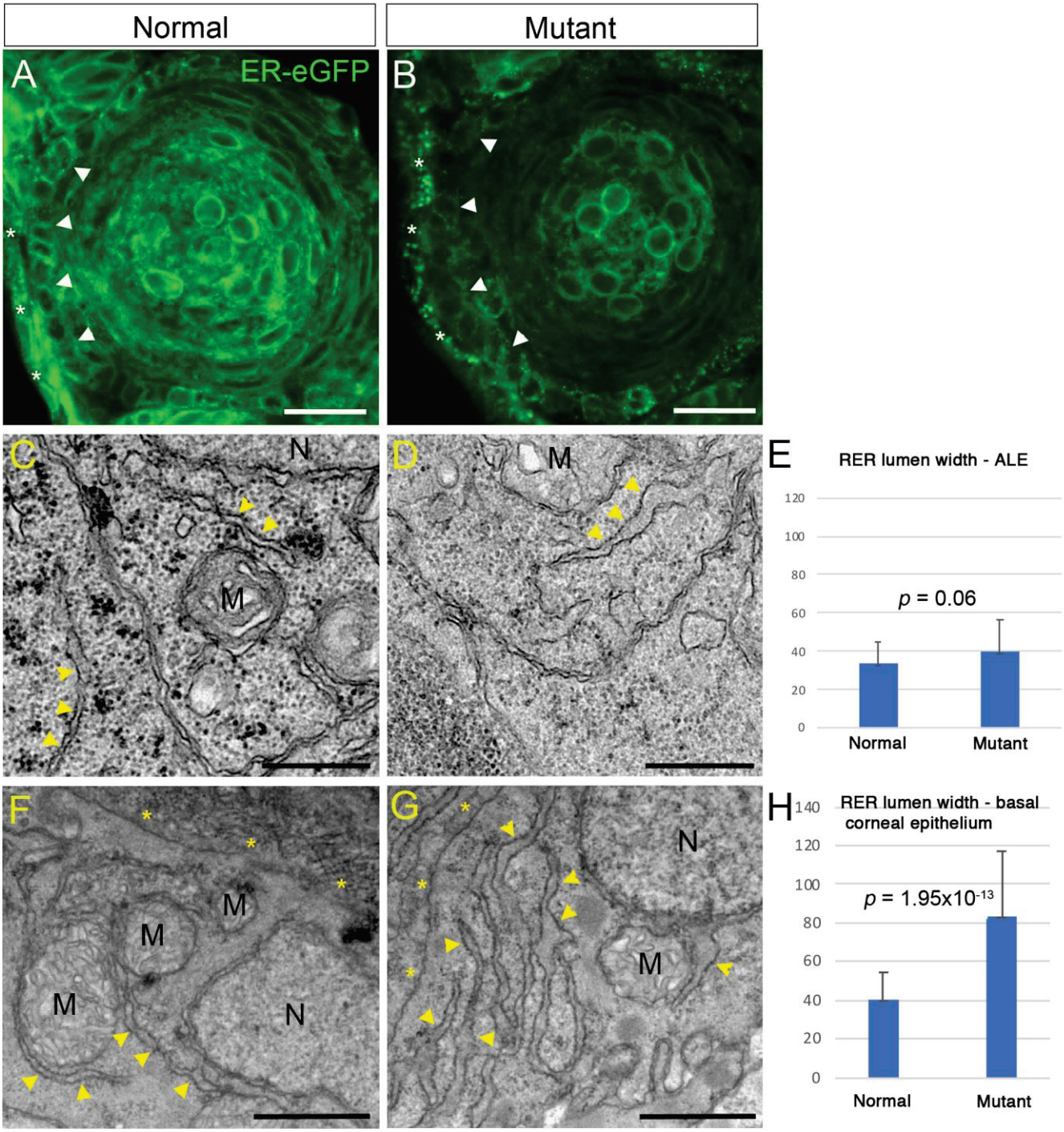

Figure 1. Abnormal rough endoplasmic reticulum (RER) in *plod3* mutants. (**A**,**B**) Single confocal sections from eyes of 2 dpf normal (**A**) and mutant (**B**) embryos expressing ER-eGFP. Arrowheads point at the ALE. Asterisks mark the presumptive cornea. Scale bars are 20 µm. (**C**,**D**,**F**,**G**) Transmission electron microscope images of ALE cells (**C**,**D**) and basal corneal epithelial cells (**F**,**G**) from 2 dpf normal (**C**,**F**) and mutant (**D**,**G**) embryos. Arrowheads point at RER. Asterisks in (**F**,**G**) are located by the basal cell membrane, next to the developing corneal stroma in (**F**), which is missing in (**G**). M, mitochondrion; N, nucleus. Scale bars are 500 nm (**C**,**D**) or 1 µm (**F**,**G**). (**E**,**H**) Graphs depicting measurements of RER width from mutant and normal cells in the ALE (**E**) or basal corneal epithelial cells (**H**). Numbers on the Y axis are width in µm. Error bars are standard deviation. *p* values are depicted.

3.2. 4-PBA Rescues the Lens Phenotype of plod3^{vu222} Mutants

The evidence for the presence of RER abnormalities that are consistent with ER stress prompted us to check whether inhibition of ER stress could block the formation of cellular masses in lenses of *plod3* mutants. Therefore, we treated zebrafish embryos from a cross between heterozygous *plod3^{vu222}* parents with 4-Phenylbutyric acid (4-PBA), an FDA-approved drug used to treat urea cycle disorders. 4-PBA is a chemical chaperon known to alleviate ER stress [26] and also has a histone deacetylase (HDAC) inhibitor activity [27]. We treated embryos from 26 hpf until 4 dpf and assessed their lens phenotype. This treatment resulted in a significant rescue of the lens phenotype, as evidenced by localization of the lenses in live larvae (Figure 2A,C,E). Histological sections confirmed that in correctly localized lenses, the ALE remained a monolayer, without overt evidence of abnormalities (Figure 2D). The shape of the lens was abnormal, with lateral bulges, suggesting that the lens capsule was still defective (Figure 2D) (compare to a wild-type lens, Figure S2).

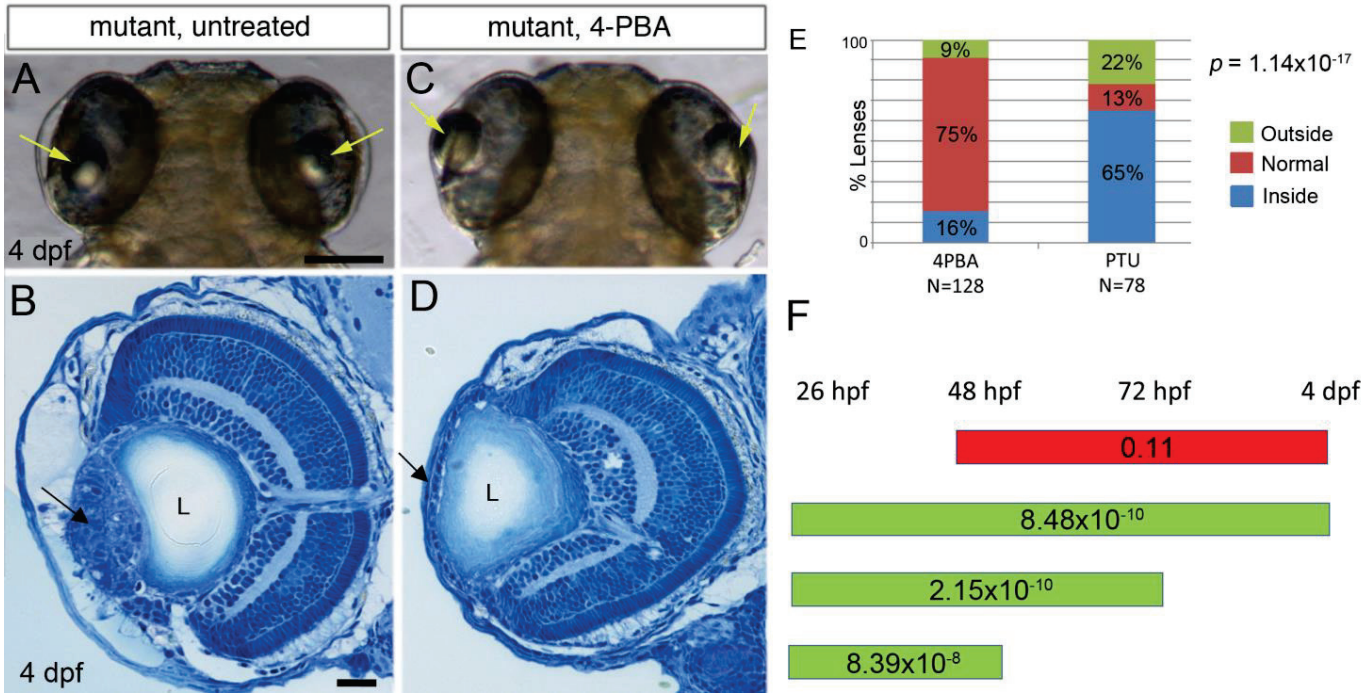

Figure 2. 4-PBA inhibits development of lens cell masses in *plod3* mutants: (**A**,**C**) Live 4 dpf *plod3^{vu222}* mutant larvae, untreated (**A**) or treated with 4-PBA from 26 hpf (**C**). Arrows point at lenses. (**B**,**D**) Histological sections of eyes from 4 dpf *plod3* mutant larvae, untreated (**B**) or treated with 4-PBA from 26 hpf (**D**). Arrow in (**B**) points at the abnormal cell mass and in (**D**) at the ALE that remains a monolayer. (**E**) Statistical analysis of the rescue with 4-PBA. Outside, normal and inside categories refer to the location of the lens relative to the normal location. N depicts the number of eyes analyzed. (**F**) Time windows of treatment with 4-PBA are represented by bars. Green bars show time windows with statistically significant rescue and red bar represents a time window in which no statistically significant rescue was observed. Numbers on bars are *p*-values. L, lens. Scale bars are 100 μm (**A**) or 20 μm (**B**).

To better define the timing during which 4-PBA was required for inhibiting the development of lens cell masses, we repeated the treatment over several time windows: 26–48 hpf, 26–72 hpf, 26–96 hpf and 48–96 hpf. In all treatments, larvae were evaluated at 4 dpf (~96 hpf) by gross morphology. We found that when treatment was initiated at 26 hpf and continued until 48 hpf, or 72 hpf, or 96 hpf, there was a significant rescue of lens localization (Figure 2F). In contrast, when treatment was initiated from 48 hpf until 96 hpf, there was no significant difference in lens localization between treated and untreated mutants (Figure 2F). These results show that the critical time window for 4-PBA treatment

is between 26 and 48 hpf, well before the formation of cell masses that begins only at 3 dpf. Hence, 4-PBA likely affects cell mass formation indirectly.

3.3. A Small Molecule Screen for Compounds That Can Rescue the Lens Phenotype of Lh3 Deficiency

The ability of small molecules, such as SB-431542 (an inhibitor of TGFβ type I receptor Alk5, [28]) and 4-PBA, to prevent the formation of cell masses in *plod3* mutant lenses prompted us to search for additional small molecules that can provide such rescue as potential drugs for prevention of PCO. Towards this goal, we performed a chemical screen using two small molecule libraries comprising over 1200 compounds (see Section 2).

plod3 homozygous mutant embryos were identified at approximately 24 hpf based on a transient mild phenotype of abnormal ventral body curvature, and placed in 48-well plates, 5 embryos per well, without chorions (Figure 3). At 26–28 hpf, one compound was added into each well, except for four wells in each plate that received DMSO at the same dilution and served as negative controls. Compound solution was replaced with a fresh one daily, and larvae were assessed for rescue of the lens phenotype by gross morphology at 3 and 4 dpf.

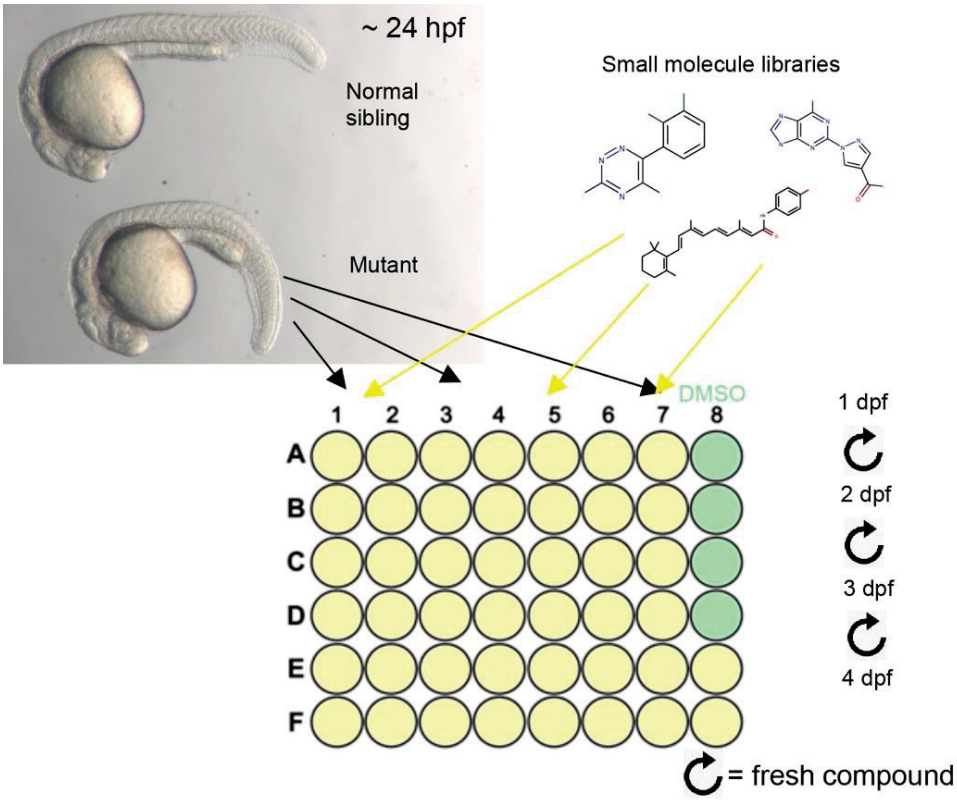

Figure 3. Design of the small molecule screen: Top left panel shows normal (top) and *plod3* mutant embryos at approximately 24 hpf. Mutants can be identified by their transient ventral curvature which is evident at this stage. Mutants were placed in 48-well plates, 5 per well, and compounds from the small molecule libraries were added and replaced daily until 4 dpf. Several wells in each plate were treated with DMSO as control.

The criteria for a potentially successful "hit" were clear improvement of the localization and shape of lenses by gross morphology, and no apparent deterioration in the general health and appearance of treated embryos. For compounds that were identified as potential "hits", we repeated the treatment twice to confirm the result. The screen yielded two compounds that provided a convincing rescue. The first was SB-431542, which we had previously shown could inhibit formation of the lens cellular masses [13]. The second compound was Erlotinib, an inhibitor of epidermal growth factor receptor (EGFR) signaling.

3.4. Suppression of plod3 Mutant Lens Phenotype by Erlotinib

Erlotinib binds the intracellular catalytic domain of EGFR tyrosine kinase and inhibits EGFR phosphorylation. It is used in treatment of several types of cancer as it blocks cell cycle progression by causing G1 arrest [29]. Following treatment with Erlotinib from 26 hpf until 4 dpf, development of cell masses in lenses of *plod3* mutant larvae was efficiently inhibited and lens localization was rescued (Figure 4A–E).

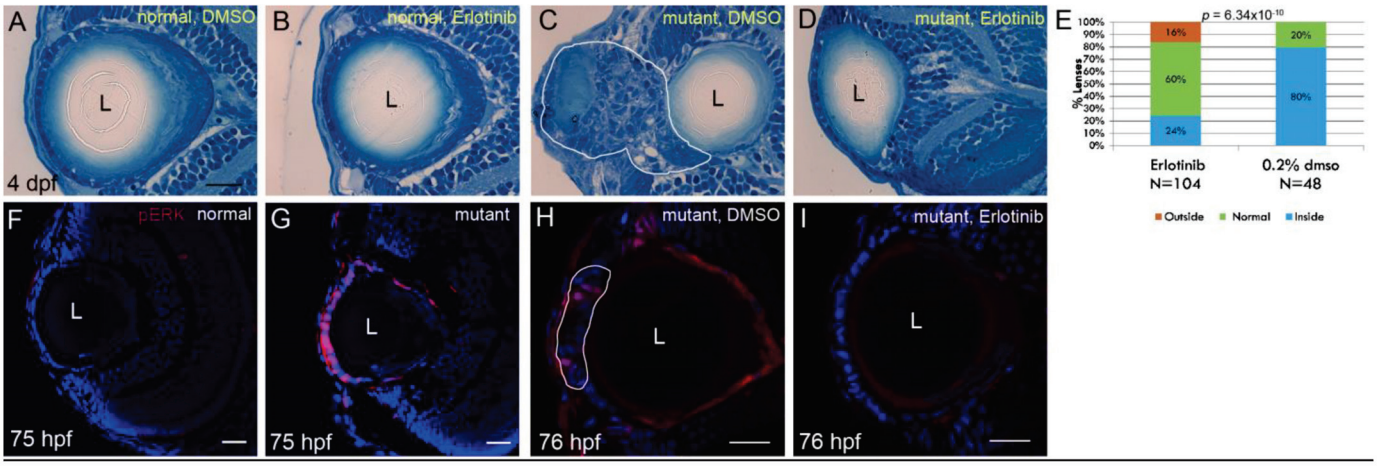

Figure 4. Erlotinib inhibits cell mass formation and phosphorylation of ERK1/2 in the ALE of *plod3* mutants: (**A**–**D**) Histological sections from eyes of 4 dpf normal (**A**,**B**) or *plod3* mutant (**C**,**D**) larvae. Larvae in (**A**,**C**) were treated from 1 to 4 dpf with vehicle (DMSO), whereas larvae in (**B**,**D**) were treated with Erlotinib. Scale bar is 20 µm. (**E**) Statistical analysis of the rescue of *plod3* lens phenotype by Erlotinib as determined by localization of the lens. Outside, normal and inside represent localization of the lens relative to the retina as compared to the localization in normal larvae. (**F**–**I**) Single confocal sections from eyes of 75–76 hpf normal (**F**) or *plod3* (**G**–**I**) mutant larvae, labeled with an antibody against pERK1/2 (red). Embryo in (**H**) was treated with DMSO and in (**I**) with Erlotinib. Nuclei (Dapi) are blue. L, lens. Scale bars are 20 µm.

To better characterize EGFR activity in lenses of normal and mutant larvae, we used antibodies against phosphorylated ERK1/2 (MAPK3 and MAPK1) to label eye tissue sections. ERK1/2 are two of the main downstream proteins that are activated by phosphorylation in response to EGFR signaling [30], and hence their phosphorylation serves as an indication of EGFR activation. At 75 hpf, lens epithelium of normal larvae showed no staining for phosphorylated ERK1/2 (pERK1/2) by immunohistochemistry (Figure 4F, n = 10). In contrast, *plod3*^{vu222} mutant lenses showed intense staining in the ALE, even though cell masses were not apparent yet (Figure 4G, n = 13). To confirm that Erlotinib acted by inhibiting EGFR signaling in the lens epithelium, we examined whether ERK1/2 phosphorylation was affected by the treatment. Consistent with this notion, in mutants that were treated with Erlotinib from 1 dpf, no pERK staining was present in the ALE (Figure 4I, n = 13), whereas in the vehicle-treated mutants, pERK-positive cells were present in developing masses (Figure 4H, n = 12). These results confirmed that the phosphorylation of ERK1/2 in lenses of *plod3*-deficient larvae was dependent on EGFR signaling.

3.5. TGFβ Signaling Functions Upstream of EGFR Signaling in Cell Mass Formation

Inhibition of TGFβ- or EGFR-signaling prevented formation of cell masses and maintained the ALE as a monolayer, raising the possibility that these pathways interact in this pathogenic process. To test this possibility, we first defined the time windows during which the activity of these pathways was required.

We had previously shown that to achieve rescue by inhibiting TGFβ signaling, the inhibition needs to be initiated by ~30 hpf [13]. To better define when TGFβ signaling promotes cell mass formation, we inhibited this pathway using SB-431542 during several

time windows and assessed the phenotype by observing lens localization at 4 dpf. The time windows of the treatments were 26 hpf–48 hpf, 26 hpf–72 hpf and 26 hpf–4 dpf. When treatment was ended before 4 dpf, the solution in which embryos were raised was replaced several times to wash out the inhibitor and the embryos were kept in egg water until 4 dpf. Treatment during all these time windows resulted in statistically significant rescue, with significance increasing in the more prolonged treatments (Figure 5A). These results suggest that the critical timing for TGFβ signaling is between 30 hpf to 48 hpf, since beginning treatment at 48 hpf failed to produce rescue of the lens phenotype [13]. Interestingly, we could not detect ectopic pSmad3 signal at 48 hpf in the ALE suggesting that another arm of the TGFβ pathway was activated at this developmental stage, i.e., the non-canonical TGFβ pathway.

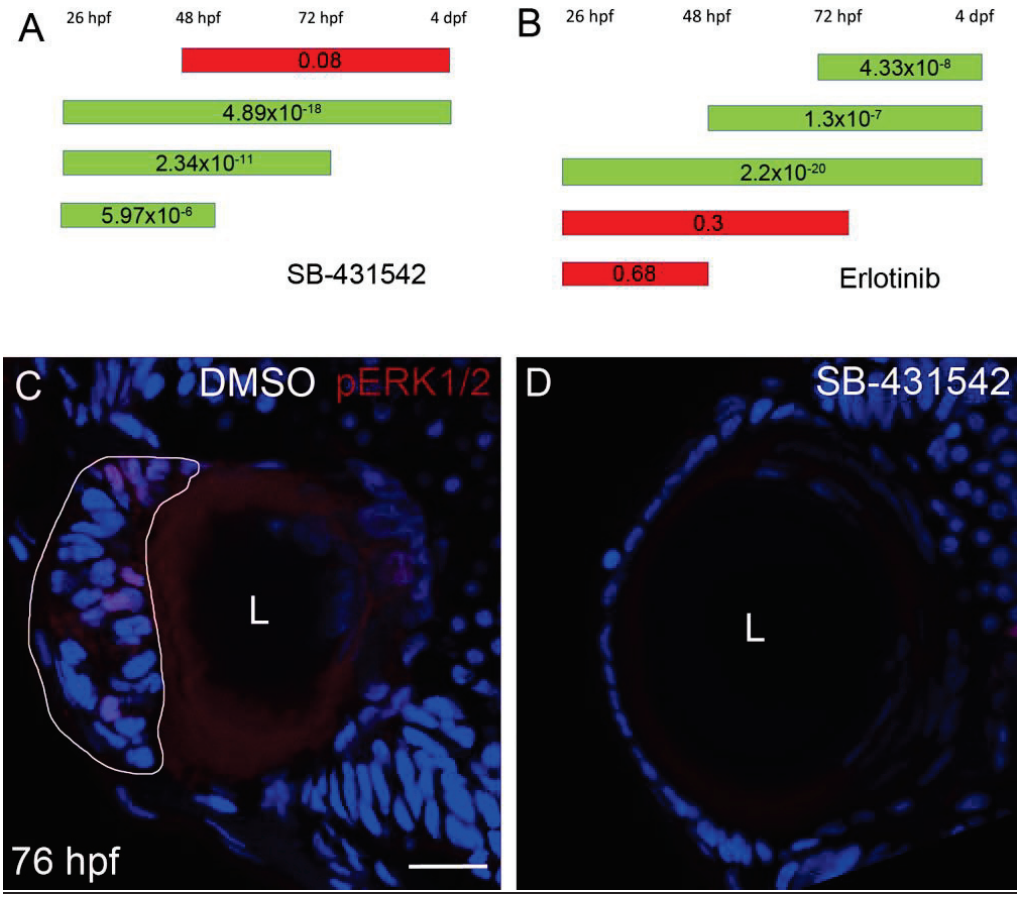

Figure 5. TGFβ signaling is upstream of EGFR signaling in *plod3* mutant lenses. (**A**,**B**) Timing experiments of rescue by TGFβ- and EGFR-signaling inhibition, respectively. Green bars show time windows with statistically significant rescue and red bars represent time windows in which no statistically significant rescue was observed. Numbers on bars are *p*-values. (**C**,**D**) Confocal single-plane sections from eyes of 76 hpf *plod3*^{vu222} mutants treated with vehicle (**C**) or with SB-431542 (**D**) from ~26 hpf to 76 hpf and labeled for pERK1/2 (red) and nuclei (Dapi, blue). L, lens. Scale bar is 20 μm.

Next, we similarly determined the time window during which EGFR signaling is required. The initial time windows of the treatments were 26 hpf–48 hpf, 26 hpf–72 hpf and 26 hpf–4 dpf. We found that when Erlotinib was added from 26 hpf to 48 hpf or 72 hpf, no significant rescue of lens localization was achieved. To further refine the time windows in which Erlotinib acts, we added treatments from 48 or 72 hpf. Indeed, when Erlotinib was added from 26 hpf, 48 hpf or 72 hpf to 96 hpf, a significant rescue of lens localization was evident (Figure 5B). These results show that inhibition of EGFR signaling is required from 3 dpf, just prior to cell mass formation. Consistent with this conclusion, at 48 hpf, no pERK labeling was evident in the ALE of mutant or normal embryos.

Given that TGFβ signaling was required at an earlier time window, we hypothesized that it functioned upstream of EGFR signaling. To further test this hypothesis, we treated *plod3*^{vu222} mutants with SB-431542 from ~30 hpf and examined pERK expression at 76 hpf. Larvae that were treated with the TGFβ receptor inhibitor showed no staining for pERK in the ALE (Figure 5C,D, n = 13 and 12, respectively), supporting the notion that TGFβ signaling acts upstream of, and is needed for, EGFR pathway activation.

3.6. 4-PBA Inhibits Only Late TGFβ Signaling and Does Not Inhibit EGFR Signaling

Having defined the time windows during which TGFβ and EGFR signaling promoted lens cell mass formation, we wished to find whether and how the activity of these pathways was influenced by 4-PBA treatment. Therefore, we treated mutant embryos with 4-PBA and examined the effect on TGFβ and EGFR signaling pathways by examining pSmad3 and pERK1/2 labeling, respectively.

First, we treated mutant embryos from 26 hpf to 4 dpf and labeled eye tissue sections for pSmad3. We chose 4 dpf to assess the effect on TGFβ signaling since at this time point pSmad3 was consistently and clearly upregulated. We found that 4-PBA treatment blocked cell mass formation and no pSmad3-positive cells were present in the ALE (Figure 6A,B; n = 8 and 15, respectively). Some pSmad3-positive cells were present in adjacent cells, such as in the ciliary marginal zone (CMZ), as often observed in normal larvae (Figure 6B).

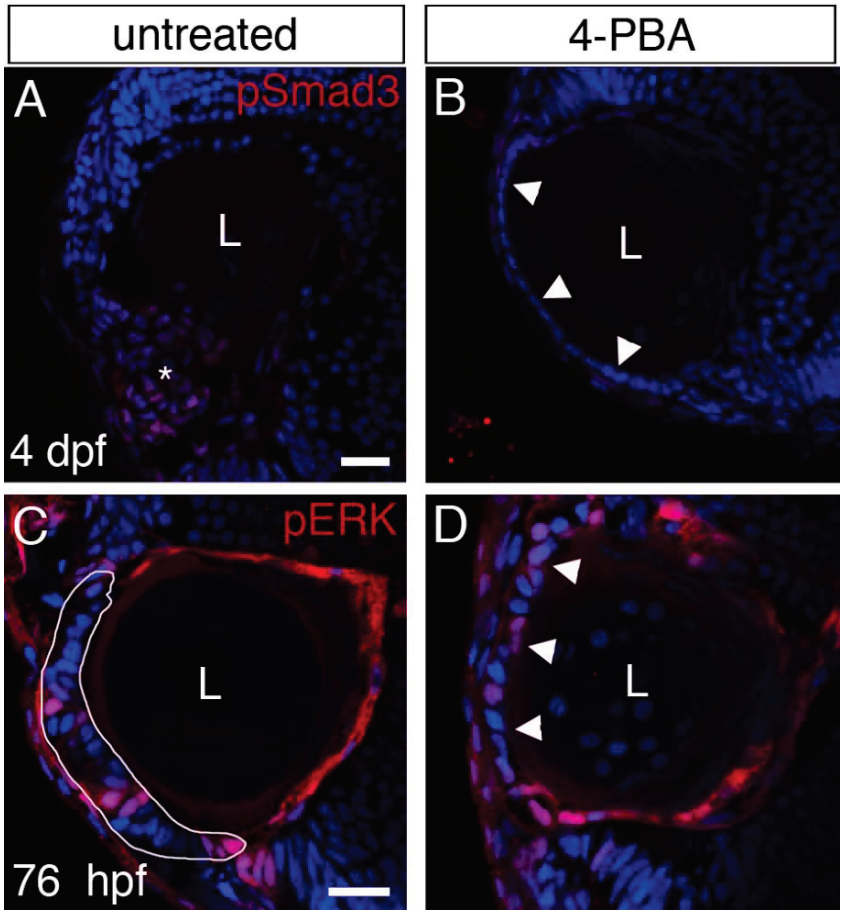

Figure 6. Effects of 4-PBA treatment on TGFβ and EGFR signaling. (**A**–**D**) Confocal single-plane sections from eyes of *plod3*^{vu222} mutants untreated (**A**,**C**) or treated with 4-PBA (**B**,**D**) from ~26 hpf. In (**A**,**B**), treatment was until ~96 hpf and sections were labeled for pSmad3 (red) and nuclei (Dapi, blue). In (**C**,**D**), treatment was until 76 hpf and sections were labeled for pERK1/2 (red) and nuclei (Dapi, blue). Asterisk in (**A**) marks the area of the cell mass where pSmad3 labeling is evident. Arrowheads in (**B**,**D**) point at the ALE. White line in (**C**) marks the periphery of the cell mass. L, lens. Scale bars are 20 μm.

Next, we treated embryos with 4-PBA from 26 hpf to 3 dpf and assayed for pERK1/2 labeling. Surprisingly, we found that pERK1/2 labeling was present even in treated larvae in which cell mass formation was blocked (Figure 6D; $n = 14$, n in C = 11).

These results indicate that EGFR activity in the ALE is not sufficient for driving cell mass formation and are consistent with a similar conclusion from previous work [31]. The results also suggest that 4-PBA does not inhibit TGFβ signaling at 1 dpf, since that would be expected to abolish EGFR activity as well.

3.7. Inhibition of mTOR Signaling Only Partially Limits Cell Mass Formation

Inhibition of EGFR signaling is aimed, at least in part, at blocking proliferation of LECs. Another pathway that is known to promote cell proliferation and growth is the mechanistic (formerly mammalian) target of rapamycin (mTOR) pathway. mTOR signaling can be activated by multiple factors, including TGFβ and EGFR signaling [32]. We therefore asked whether this pathway was upregulated in the ALE of *plod3* mutants as cell masses were forming. To test this possibility, we labeled tissue sections from eyes of 3 dpf normal and *plod3*^{vu222} mutant larvae for the phosphorylated form of ribosomal protein S6 kinase (pS6K), which is a commonly used readout for activation of mTOR signaling [33,34]. We found that, whereas pS6K signal was missing from the ALE of normal larvae, it was strongly upregulated in forming cell masses in the mutants (Figure 7B; $n = 8$, n in A = 8).

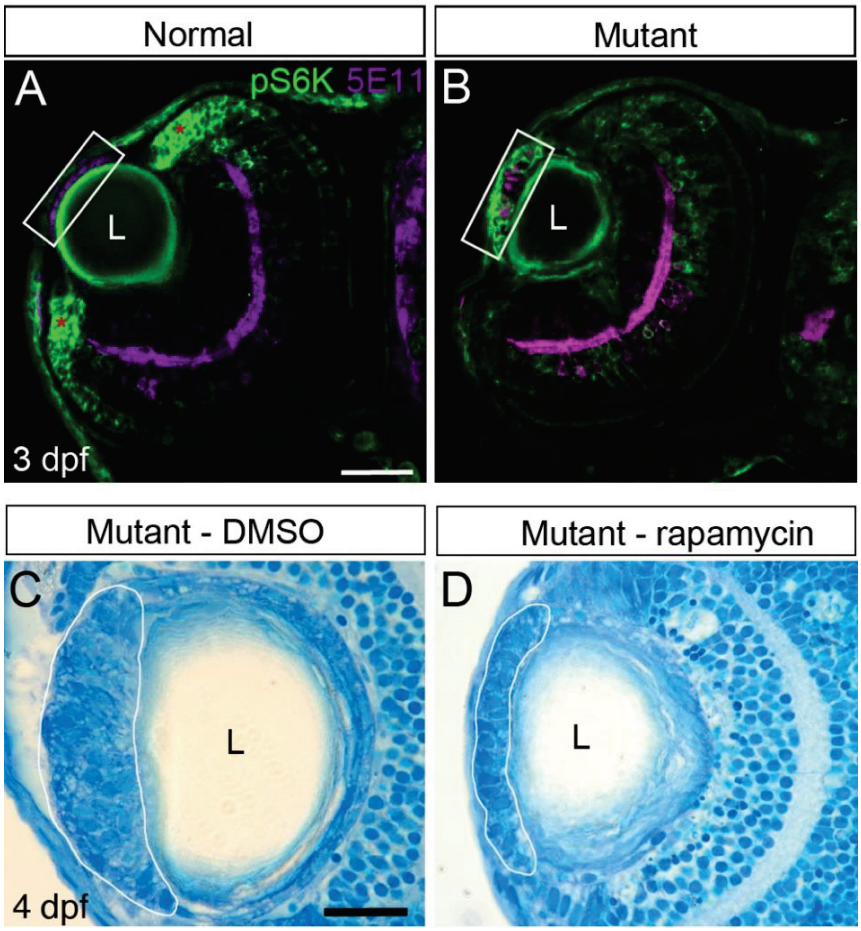

Figure 7. mTOR signaling contributes to cell mass growth. (**A**,**B**) Confocal single-plane sections from eyes of 3 dpf *plod3*^{vu222} larvae labeled for pS6K (green) and with 5E11 antibody that marks nuclei of ALE cells as well as a subset of amacrine cells (purple). pS6K staining in the mutant is increased in the developing mass and reduced in the ciliary marginal zones (marked by asterisks in (**A**)). White rectangles mark the ALE region. Scale bar is 50 μm. (**C**,**D**) Histological sections from eyes of 4 dpf *plod3*^{vu222} larvae treated from 26 hpf until ~96 hpf with vehicle (**C**) or rapamycin (**D**). White lines mark the periphery of cellular masses. Scale bar is 20 μm. L, lens.

mTOR signaling can be inhibited by rapamycin, which inhibits mTOR complex1 (mTORC1) activity [35], suggesting that treatment with rapamycin could block formation of lens cell masses in *plod3* mutants. We therefore treated embryos from 1 dpf until 4 dpf with different doses of rapamycin and evaluated the effect by gross morphology and by histological sections. From the different doses that were tested (2.5, 25 and 50 μM), treatment with 25 μM rapamycin led to partial inhibition of the lens phenotype, with treated larvae developing smaller masses than untreated ones (Figure 7C,D; $n > 15$ for each condition). However, the rescue achieved using this treatment was not as consistent as with inhibition of TGFβ or EGFR signaling or by treatment with 4-PBA. Therefore, while mTOR signaling likely contributes to the formation of cell masses, it is not essential for this pathology to develop.

4. Discussion

In this work, we describe the identification of small molecules that can prevent formation of cellular masses from the ALE of *plod3* mutant zebrafish larvae. Together with our previous work [13], the findings further our knowledge of the mechanisms that underlie the development of the cell masses and show additional similarities to the pathogenesis of cataracts derived from lens epithelium in humans. A summary of the findings is shown in Figure 8.

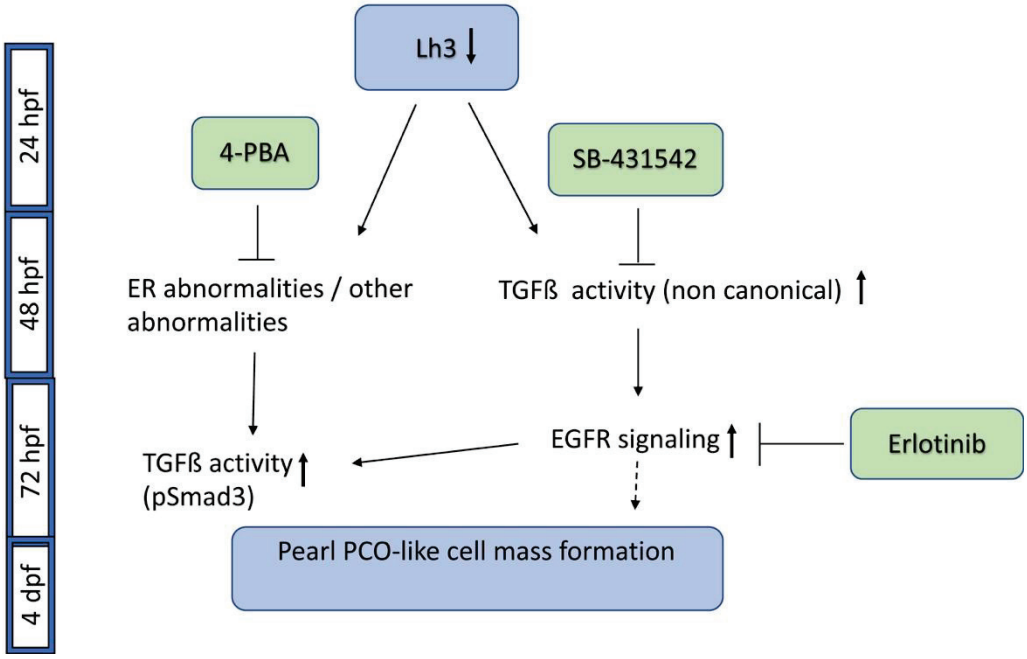

Figure 8. A schematic of pathways involved in plod3 mutant lens phenotype and small molecules that block phenotype development. Reduced function of Lh3 leads to ER abnormalities and possibly additional abnormalities by 2 dpf. Application of 4-PBA by ~28 hpf blocks phenotype development, likely by affecting these abnormalities. The TGFβ type I receptor inhibitor SB-431542 also blocks phenotype development if applied by ~28 hpf, suggesting early upregulation of non-canonical TGFβ signaling, as pSmad3 is not present before 3 dpf. Later on, around 72 hpf, increased EGFR signaling contributes to phenotype development downstream of TGFβ signaling, and blocking it by Erlotinib prevents phenotype development. Also around this time, as the cell mass develops, pSmad3-positive cells become apparent but the upregulation of this canonical TGFβ signaling occurs at a time point when blocking the pathway no longer prevents phenotype development. pSmad3 upregulation is dependent on the earlier phase of TGFβ signaling, on EGFR signaling and is also inhibited by 4-PBA. Timing of pathway and inhibitor activity as deduced from our experiments is depicted. The dashed line after EGFR signaling represents the finding that EGFR activation alone does not appear to drive cell mass formation.

4.1. Inhibition of Cell Mass Formation by 4-PBA

In our previous study, we showed that the lens cellular masses in *plod3*-deficient zebrafish larvae are derived from the ALE and proposed that their formation was driven in a non-cell-autonomous fashion by the abnormal lens capsule [13]. Nevertheless, the reduced function of Lh3 is expected to have cell-autonomous effects; Lh3 is a multifunctional enzyme with lysyl hydroxylase (LH), hydroxylysyl galactosyltransferase (GT) and galactosylhydroxylysyl glucosyltransferase (GGT) activities that functions in post-translational modifications of its substrates [36]. Hence, loss of Lh3 activity is expected to result in abnormalities in its substrate proteins leading to their misfolding and subsequent accumulation in the ER, thereby causing ER stress. Indeed, in Lh3 knockout mouse embryos, there was dilation of the ER with retention of Collagen IV, as well as enlargement of Golgi complexes and lysosomes [22,37]. Consistent with these reports, we also found altered appearance of the ER in the ALE and the adjacent developing corneal epithelium, which included mildly dilated ER. The expansion of the ER lumen in *plod3* mutants likely results from accumulation of misfolded proteins that were not properly modified by Lh3. This finding provided the basis for testing 4-PBA's ability to rescue the lens phenotype. Interestingly, even though 4-PBA efficiently inhibited formation of lens cellular masses, our preliminary transcriptome analyses did not detect changes that are typical of ER stress in *plod3* mutants at 2 dpf, e.g., upregulation of *chop, bip* and splicing of *xbp1*. Nevertheless, we did detect increased transcription of chaperons and genes implicated in endoplasmic reticulum-associated protein degradation (ERAD) (Taler, Zatari and Inbal, unpublished). Both an increase in ER size and ERAD are known mechanisms through which cells cope with accumulation of misfolded proteins [38,39]. Hence, it is possible that 4-PBA indeed rescues the phenotype through its chaperon function by relieving potential stress caused by protein accumulation. Alternatively, it is also possible that the rescue is mediated via its function as an HDAC inhibitor. The exact mechanism needs further investigation.

Our timing experiments show that 4-PBA activity is required to inhibit cell mass formation well before the phenotype becomes apparent. This result suggests that 4-PBA does not directly influence the mechanisms that drive the growth of LECs. Moreover, since the time window of 4-PBA activity parallels that of TGFβ, it raised the possibility that inhibiting TGFβ activity was the mechanism by which 4-PBA treatment yielded the rescue. However, this does not seem to be the case, as EGFR signaling, which is dependent on TGFβ activity, was not inhibited by 4-PBA treatment. Therefore, it appears that another mechanism promotes formation of cell masses in parallel to TGFβ and EGFR signaling.

The logic for testing 4-PBA as a candidate for prevention of LEC-derived cataract in *plod3*-mutant lenses is clear. However, an involvement of the ER in the pathogenesis of lens epithelium abnormalities could be unique to these mutants. It will be interesting to test whether 4-PBA can inhibit formation of PCO in models that are not related to Lh3 function.

4.2. Inhibition of Cell Mass Formation by Blocking TGFβ and EGFR Signaling

We identified Erlotinib as an efficient inhibitor of lens cell mass formation in an unbiased small molecule screen. This identification is in strong agreement with previous studies that implicated EGFR signaling in PCO and identified EGFR-inhibiting drugs, including Erlotinib, Gefitinib and Lapatinib as candidates for use in prevention of PCO after cataract surgery [40–46]. Interestingly, a recent study suggested that only fibrotic PCO is prevented by EGFR inhibitors [46]. We, however, found that the lens phenotype of *plod3* mutants, which is more similar to pearl PCO, is efficiently prevented by Erlotinib. The reason for the different findings is unclear but might be because different experimental systems were used in the two studies.

Our analysis of pERK1/2 labeling suggested that EGFR activity was elevated just before the formation of lens cell masses. The relevance of this finding to the development of cell masses was confirmed by using Erlotinib during different time windows. Thus, EGFR signaling likely plays a more direct role in formation of lens cell masses. TGFβ signaling, on the other hand, is required for cell mass formation in *plod3* mutants much

earlier, between 1 and 2 dpf [13], suggesting that it acts indirectly in promoting ALE cell masses. Furthermore, we showed that TGFβ signaling was required for the activation of EGFR signaling. These findings are consistent with data from a recent study which found that phosphorylation of EGFR occurred only 18 h after treatment of rat lens epithelial explants with TGFβ, suggesting that activation of EGFR by TGFβ is a downstream indirect signaling event [31].

TGFβ activity which drives cell mass formation appears to be from a non-canonical arm of the pathway, as pSmad3 is not upregulated by 2 dpf. Interestingly, in addition to its early role before 2 dpf, canonical TGFβ signaling is also upregulated in cellular masses at 3 dpf and onwards, as evidenced by positive pSmad3 labeling [13]. Whereas studies have shown that both canonical and non-canonical TGFβ signaling drive PCO formation (e.g., reviewed in [11,47]), in this study we found that the canonical activation of TGFβ signaling in the developing cell masses is not required for their development, as blocking it fails to rescue the phenotype. Rather, at 3 dpf, EGFR activity is required for cell mass formation and is dependent on earlier TGFβ signaling. Interestingly, the canonical TGFβ signaling at 3 dpf is dependent both on the earlier non-canonical signaling and on EGFR signaling [13], but its function is currently unclear.

EGFR activity appears to be permissive and not instructive, as evidenced by 4-PBA treatments that do not abolish pERK1/2 upregulation in the ALE but do inhibit cell mass formation. These observations are consistent with work showing that upregulation of EGFR signaling alone does not promote PCO [31].

Another point of interest is the apparent side effects of the different treatments. Whereas inhibition of TGFβ signaling often resulted in abnormal-looking ALECs [13], the histology of Erlotinib- and 4-PBA-treated larvae suggested that the ALECs of treated larvae were much more similar to normal ones. These data further support the notion that Erlotinib is a good candidate for the preventive treatment of PCO.

5. Conclusions

In conclusion, cell masses that develop in the lenses of zebrafish embryos and larvae with *plod3* loss of function show great similarity to pearl PCO. This similarity is demonstrated both by histology and by the underlying molecular mechanisms that drive the pathology formation, most prominently TGFβ and EGFR signaling. The non-canonical TGFβ signaling pathway plays a critical early and indirect role in the development of the pathology, whereas EGFR signaling plays a later, permissive role. Hence, in addition to providing information specifically relevant to the loss of Lh3 function, this work supports the notion that *plod3* zebrafish mutants can serve as an in vivo model for testing pharmacological strategies for prevention of PCO, the common complication of cataract surgeries.

Supplementary Materials: The following supporting information can be downloaded at: https://www.mdpi.com/article/10.3390/cells12212540/s1, Figure S1: Lens phenotypes in live *plod3* mutant 4 dpf larvae; Figure S2: Section of a normal lens.

Author Contributions: Conceptualization, K.T., N.Z. and A.I.; investigation, K.T., N.Z., M.I.L. and S.R.-B.; formal analysis, K.T. and N.Z.; supervision, A.I.; writing—original draft, K.T. and A.I.; writing—review and editing, N.Z., M.I.L. and A.I.; funding acquisition, A.I. All authors have read and agreed to the published version of the manuscript.

Funding: This research was funded by the Israel Science Foundation (ISF 801/17 to A.I.).

Institutional Review Board Statement: The animal study protocol was approved by the Hebrew University Authority for Biological and Biomedical Models. Ethics approval no. MD-17-15279-2.

Informed Consent Statement: Not applicable.

Data Availability Statement: Not applicable.

Acknowledgments: We thank Farouq Nather for excellent fish care, Yael Friedman for transmission electron microscopy and Jim Fadool for the 5E11 antibody. Special thanks to Esther and Barry Naiberg for generously supporting K.T.

Conflicts of Interest: The authors declare no conflict of interest.

References

1. GBD 2019 Blindness and Vision Impairment Collaborators. Causes of Blindness and Vision Impairment in 2020 and Trends over 30 Years, and Prevalence of Avoidable Blindness in Relation to VISION 2020: The Right to Sight: An Analysis for the Global Burden of Disease Study. *Lancet Glob. Health* **2021**, *9*, e144–e160. [CrossRef]
2. Liu, Y.C.; Wilkins, M.; Kim, T.; Malyugin, B.; Mehta, J.S. Cataracts. *Lancet* **2017**, *390*, 600–612. [CrossRef] [PubMed]
3. Wormstone, I.M.; Wang, L.; Liu, C.S. Posterior Capsule Opacification. *Exp. Eye Res.* **2009**, *88*, 257–269. [CrossRef] [PubMed]
4. Saika, S. Relationship between Posterior Capsule Opacification and Intraocular Lens Biocompatibility. *Prog. Retin. Eye Res.* **2004**, *23*, 283–305. [CrossRef] [PubMed]
5. Findl, O.; Buehl, W.; Bauer, P.; Sycha, T. Interventions for Preventing Posterior Capsule Opacification. *Cochrane Database Syst. Rev.* **2010**, CD003738. [CrossRef]
6. Cheng, C.-Y.; Yen, M.-Y.; Chen, S.-J.; Kao, S.-C.; Hsu, W.-M.; Liu, J.-H. Visual Acuity and Contrast Sensitivity in Different Types of Posterior Capsule Opacification. *J. Cataract. Refract. Surg.* **2001**, *27*, 1055–1060. [CrossRef]
7. Van Bree, M.C.J.; Van Der Meulen, I.J.E.; Franssen, L.; Coppens, J.E.; Reus, N.J.; Zijlmans, B.L.M.; Van Den Berg, T.J.T.P. Imaging of Forward Light-Scatter by Opacified Posterior Capsules Isolated from Pseudophakic Donor Eyes. *Investig. Opthalmol. Vis. Sci.* **2011**, *52*, 5587. [CrossRef]
8. Javitt, J.C.; Tielsch, J.M.; Canner, J.K.; Kolb, M.M.; Sommer, A.; Steinberg, E.P. National Outcomes of Cataract Extraction. Increased Risk of Retinal Complications Associated with Nd:YAG Laser Capsulotomy. The Cataract Patient Outcomes Research Team. *Ophthalmology* **1992**, *99*, 1487–1497. [CrossRef]
9. Pandey, S.K.; Apple, D.J.; Werner, L.; Maloof, A.J.; Milverton, E.J. Posterior Capsule Opacification: A Review of the Aetiopathogenesis, Experimental and Clinical Studies and Factors for Prevention. *Indian J. Ophthalmol.* **2004**, *52*, 99–112.
10. West-Mays, J.A.; Pino, G.; Lovicu, F.J. Development and Use of the Lens Epithelial Explant System to Study Lens Differentiation and Cataractogenesis. *Prog. Retin. Eye Res.* **2010**, *29*, 135–143. [CrossRef]
11. Wormstone, I.M.; Wormstone, Y.M.; Smith, A.J.O.; Eldred, J.A. Posterior Capsule Opacification: What's in the Bag? *Prog. Retin. Eye Res.* **2021**, *82*, 100905. [CrossRef]
12. Srinivasan, Y.; Lovicu, F.J.; Overbeek, P.A. Lens-Specific Expression of Transforming Growth Factor Beta1 in Transgenic Mice Causes Anterior Subcapsular Cataracts. *J. Clin. Invest.* **1998**, *101*, 625–634. [CrossRef]
13. Taler, K.; Weiss, O.; Rotem-Bamberger, S.; Rubinstein, A.M.; Seritrakul, P.; Gross, J.M.; Inbal, A. Lysyl Hydroxylase 3 Is Required for Normal Lens Capsule Formation and Maintenance of Lens Epithelium Integrity and Fate. *Dev. Biol.* **2020**, *458*, 177–188. [CrossRef] [PubMed]
14. Salo, A.M.; Cox, H.; Farndon, P.; Moss, C.; Grindulis, H.; Risteli, M.; Robins, S.P.; Myllyla, R. A Connective Tissue Disorder Caused by Mutations of the Lysyl Hydroxylase 3 Gene. *Am. J. Hum. Genet.* **2008**, *83*, 495–503. [CrossRef] [PubMed]
15. Liu, J.; Hales, A.M.; Chamberlain, C.G.; McAvoy, J.W. Induction of Cataract-like Changes in Rat Lens Epithelial Explants by Transforming Growth Factor Beta. *Invest. Ophthalmol. Vis. Sci.* **1994**, *35*, 388–401. [PubMed]
16. Hales, A.M.; Chamberlain, C.G.; McAvoy, J.W. Cataract Induction in Lenses Cultured with Transforming Growth Factor-Beta. *Invest. Ophthalmol. Vis. Sci.* **1995**, *36*, 1709–1713.
17. Lovicu, F.J.; Steven, P.; Saika, S.; McAvoy, J.W. Aberrant Lens Fiber Differentiation in Anterior Subcapsular Cataract Formation: A Process Dependent on Reduced Levels of Pax6. *Invest. Ophthalmol. Vis. Sci.* **2004**, *45*, 1946–1953. [CrossRef]
18. Schneider, V.A.; Granato, M. The Myotomal Diwanka (Lh3) Glycosyltransferase and Type XVIII Collagen Are Critical for Motor Growth Cone Migration. *Neuron* **2006**, *50*, 683–695. [CrossRef]
19. Westerfield, M. *The Zebrafish Book. A Guide for the Laboratory Use of Zebrafish (Danio Rerio)*, 4th ed.; University of Oregon Press: Eugene, OR, USA, 2000.
20. Humphrey, C.D.; Pittman, F.E. A Simple Methylene Blue-Azure II-Basic Fuchsin Stain for Epoxy-Embedded Tissue Sections. *Stain. Technol.* **1974**, *49*, 9–14. [CrossRef]
21. Schneider, C.A.; Rasband, W.S.; Eliceiri, K.W. NIH Image to ImageJ: 25 Years of Image Analysis. *Nat. Methods* **2012**, *9*, 671–675. [CrossRef]
22. Rautavuoma, K.; Takaluoma, K.; Sormunen, R.; Myllyharju, J.; Kivirikko, K.I.; Soininen, R. Premature Aggregation of Type IV Collagen and Early Lethality in Lysyl Hydroxylase 3 Null Mice. *Proc. Natl. Acad. Sci. USA* **2004**, *101*, 14120–14125. [CrossRef] [PubMed]
23. Kropski, J.A.; Blackwell, T.S. Endoplasmic Reticulum Stress in the Pathogenesis of Fibrotic Disease. *J. Clin. Invest.* **2018**, *128*, 64–73. [CrossRef] [PubMed]
24. Morishita, H.; Eguchi, T.; Tsukamoto, S.; Sakamaki, Y.; Takahashi, S.; Saito, C.; Koyama-Honda, I.; Mizushima, N. Organelle Degradation in the Lens by PLAAT Phospholipases. *Nature* **2021**, *592*, 634–638. [CrossRef]

25. Greiling, T.M.; Clark, J.I. Early Lens Development in the Zebrafish: A Three-Dimensional Time-Lapse Analysis. *Dev. Dyn.* **2009**, *238*, 2254–2265. [CrossRef] [PubMed]
26. Özcan, U.; Yilmaz, E.; Özcan, L.; Furuhashi, M.; Vaillancourt, E.; Smith, R.O.; Görgün, C.Z.; Hotamisligil, G.S. Chemical Chaperones Reduce ER Stress and Restore Glucose Homeostasis in a Mouse Model of Type 2 Diabetes. *Science* **2006**, *313*, 1137–1140. [CrossRef]
27. Iannitti, T.; Palmieri, B. Clinical and Experimental Applications of Sodium Phenylbutyrate. *Drugs RD* **2011**, *11*, 227–249. [CrossRef] [PubMed]
28. Inman, G.J.; Nicolás, F.J.; Callahan, J.F.; Harling, J.D.; Gaster, L.M.; Reith, A.D.; Laping, N.J.; Hill, C.S. SB-431542 Is a Potent and Specific Inhibitor of Transforming Growth Factor-Beta Superfamily Type I Activin Receptor-like Kinase (ALK) Receptors ALK4, ALK5, and ALK7. *Mol. Pharmacol.* **2002**, *62*, 65–74. [CrossRef]
29. Moyer, J.D.; Barbacci, E.G.; Iwata, K.K.; Arnold, L.; Boman, B.; Cunningham, A.; DiOrio, C.; Doty, J.; Morin, M.J.; Moyer, M.P.; et al. Induction of Apoptosis and Cell Cycle Arrest by CP-358,774, an Inhibitor of Epidermal Growth Factor Receptor Tyrosine Kinase. *Cancer Res.* **1997**, *57*, 4838–4848.
30. Wee, P.; Wang, Z. Epidermal Growth Factor Receptor Cell Proliferation Signaling Pathways. *Cancers* **2017**, *9*, 52. [CrossRef]
31. Shu, D.Y.; Lovicu, F.J. Enhanced EGF Receptor-Signaling Potentiates TGFbeta-Induced Lens Epithelial-Mesenchymal Transition. *Exp. Eye Res.* **2019**, *185*, 107693. [CrossRef]
32. Saxton, R.A.; Sabatini, D.M. MTOR Signaling in Growth, Metabolism, and Disease. *Cell* **2017**, *168*, 960–976. [CrossRef] [PubMed]
33. Brown, E.J.; Beal, P.A.; Keith, C.T.; Chen, J.; Bum Shin, T.; Schreiber, S.L. Control of P70 S6 Kinase by Kinase Activity of FRAP in Vivo. *Nature* **1995**, *377*, 441–446. [CrossRef] [PubMed]
34. Hay, N.; Sonenberg, N. Upstream and Downstream of MTOR. *Genes. Dev.* **2004**, *18*, 1926–1945. [CrossRef]
35. Li, J.; Kim, S.G.; Blenis, J. Rapamycin: One Drug, Many Effects. *Cell Metab.* **2014**, *19*, 373–379. [CrossRef] [PubMed]
36. Heikkinen, J.; Risteli, M.; Wang, C.; Latvala, J.; Rossi, M.; Valtavaara, M.; Myllyla, R. Lysyl Hydroxylase 3 Is a Multifunctional Protein Possessing Collagen Glucosyltransferase Activity. *J. Biol. Chem.* **2000**, *275*, 36158–36163. [CrossRef]
37. Ruotsalainen, H.; Sipila, L.; Vapola, M.; Sormunen, R.; Salo, A.M.; Uitto, L.; Mercer, D.K.; Robins, S.P.; Risteli, M.; Aszodi, A.; et al. Glycosylation Catalyzed by Lysyl Hydroxylase 3 Is Essential for Basement Membranes. *J. Cell Sci.* **2006**, *119*, 625–635. [CrossRef]
38. Bonifacino, J.S.; Weissman, A.M. Ubiquitin and the Control of Protein Fate in the Secretory and Endocytic Pathways. *Annu. Rev. Cell Dev. Biol.* **1998**, *14*, 19–57. [CrossRef] [PubMed]
39. Schuck, S.; Prinz, W.A.; Thorn, K.S.; Voss, C.; Walter, P. Membrane Expansion Alleviates Endoplasmic Reticulum Stress Independently of the Unfolded Protein Response. *J. Cell Biol.* **2009**, *187*, 525–536. [CrossRef]
40. Maidment, J.M. Regional Differences in Tyrosine Kinase Receptor Signaling Components Determine Differential Growth Patterns in the Human Lens. *Invest. Ophthalmol. Vis. Sci.* **2004**, *45*, 1427–1435. [CrossRef]
41. Huang, W.-R.; Fan, X.-X.; Tang, X. SiRNA Targeting EGFR Effectively Prevents Posterior Capsular Opacification after Cataract Surgery. *Mol. Vis.* **2011**, *17*, 2349–2355.
42. Wertheimer, C.; Liegl, R.; Kernt, M.; Mayer, W.; Docheva, D.; Kampik, A.; Eibl-Lindner, K.H. EGF Receptor Inhibitor Erlotinib as a Potential Pharmacological Prophylaxis for Posterior Capsule Opacification. *Graefes Arch. Clin. Exp. Ophthalmol.* **2013**, *251*, 1529–1540. [CrossRef]
43. Wertheimer, C.; Liegl, R.; Kernt, M.; Docheva, D.; Kampik, A.; Eibl-Lindner, K.H. EGFR-Blockade with Erlotinib Reduces EGF and TGF-B2 Expression and the Actin-Cytoskeleton Which Influences Different Aspects of Cellular Migration in Lens Epithelial Cells. *Curr. Eye Res.* **2014**, *39*, 1000–1012. [CrossRef]
44. Wertheimer, C.; Siedlecki, J.; Kook, D.; Mayer, W.J.; Wolf, A.; Klingenstein, A.; Kampik, A.; Eibl-Lindner, K. EGFR Inhibitor Gefitinib Attenuates Posterior Capsule Opacification in Vitro and in the Ex Vivo Human Capsular Bag Model. *Graefes Arch. Clin. Exp. Ophthalmol.* **2015**, *253*, 409–417. [CrossRef] [PubMed]
45. Shu, D.Y.; Wojciechowski, M.; Lovicu, F.J. ERK1/2-Mediated EGFR-Signaling Is Required for TGFβ-Induced Lens Epithelial-Mesenchymal Transition. *Exp. Eye Res.* **2019**, *178*, 108–121. [CrossRef] [PubMed]
46. VanSlyke, J.K.; Boswell, B.A.; Musil, L.S. ErbBs in Lens Cell Fibrosis and Secondary Cataract. *Investig. Opthalmol. Vis. Sci.* **2023**, *64*, 6. [CrossRef] [PubMed]
47. Wormstone, I.M.; Eldred, J.A.; Dawes, L.J. Fibrotic Modifications of the Lens Epithelium. In *Lens Epithelium and Posterior Capsular Opacification*; Saika, S., Werner, L., Lovicu, F.J., Eds.; Springer Japan: Tokyo, Japan, 2014; pp. 143–158. ISBN 978-4-431-54299-5.

Disclaimer/Publisher's Note: The statements, opinions and data contained in all publications are solely those of the individual author(s) and contributor(s) and not of MDPI and/or the editor(s). MDPI and/or the editor(s) disclaim responsibility for any injury to people or property resulting from any ideas, methods, instructions or products referred to in the content.

cells

MDPI

Article

ATF4 May Be Essential for Adaption of the Ocular Lens to Its Avascular Environment

Jiawen Xiang [1,2], Anthony J. Pompetti [1], Adam P. Faranda [1], Yan Wang [1], Samuel G. Novo [1], David Wan-Cheng Li [2] and Melinda K. Duncan [1,*]

[1] Department of Biological Sciences, University of Delaware, Newark, DE 19716, USA
[2] The State Key Laboratory of Ophthalmology, Zhongshan Ophthalmic Center, Sun Yat-sen University, Guangzhou 510230, China
* Correspondence: duncanm@udel.edu

Simple Summary: ATF4 is a transcription factor essential for the survival of the avascular lens due to its ability to regulate the expression of genes important for nutrient homeostasis.

Abstract: The late embryonic mouse lens requires the transcription factor ATF4 for its survival although the underlying mechanisms were unknown. Here, RNAseq analysis revealed that E16.5 *Atf4* null mouse lenses downregulate the mRNA levels of lens epithelial markers as well as known markers of late lens fiber cell differentiation. However, a comparison of this list of differentially expressed genes (DEGs) with other known transcriptional regulators of lens development indicated that ATF4 expression is not directly controlled by the previously described lens gene regulatory network. Pathway analysis revealed that the *Atf4* DEG list was enriched in numerous genes involved in nutrient transport, amino acid biosynthesis, and tRNA charging. These changes in gene expression likely result in the observed reductions in lens free amino acid and glutathione levels, which would result in the observed low levels of extractable lens protein, finally leading to perinatal lens disintegration. These data demonstrate that ATF4, via its function in the integrated stress response, is likely to play a crucial role in mediating the adaption of the lens to the avascularity needed to maintain lens transparency.

Keywords: ATF4; CREB-2; lens development; glutathione; amino acids; transporter

1. Introduction

The mammalian lens is a transparent avascular tissue with a high refractive index that is required for high-resolution vision [1]. This tissue arises from mutually inductive interactions between the head ectoderm and optic vesicle that lead to lens placode induction followed by its invagination to form the lens pit, then the lens vesicle. Cells in the posterior lens vesicle then elongate to produce primary fiber cells, while the anterior cells remain proliferative and generate secondary lens fiber cells through the remainder of the organism's life span [2]. The ability of the lens to refract light relies on numerous structural and biochemical adaptations including the precise ordering and packing of lens fiber cells [3], the accumulation of high concentrations of crystallin proteins in the lens fiber cell cytoplasm [4,5], the dismantling of light-scattering cell nuclei and organelles as lens fibers complete their differentiation [6,7], and the ability of the lens to survive and grow in the hypoxic and nutrient-poor environment arising from its avascularity [8].

The regulation of early lens development has been intensely studied for decades and key roles for numerous transcription factors including PAX6 [9–11], PROX1 [12,13], cMAF [14,15], and FOXE3 [16,17] have been elucidated and placed into a gene regulatory network that controls the development of the early lens from the head ectoderm [2,18]. However, much less is known about the transcriptional regulation of later steps in lens development, including the shifts in the lens fiber cell transcriptome that occur as these

cells terminally differentiate [19], and the differences in gene expression profiles seen in lens fibers born at different times during development [20–22].

Activating transcription factor 4 (ATF4/Creb2) was first identified by its ability to specifically bind to ATF, CRE, and Tax-responsive enhancer elements in lambda-based genetic screens [23] and was later found to play important roles in mediating diverse cellular stress responses [24–27]. Mice lacking the *Atf4* gene exhibit reduced perinatal survival due to severe fetal anemia, which arises from reduced fetal liver hematopoiesis [28] while surviving mice exhibit normal adult erythropoiesis although they are infertile with delayed/improper hair growth. Notably though, adult homozygous *Atf4* null mice invariably exhibit severe microphthalmia that arises late in embryonic development due to the degeneration of the lens via P53-mediated apoptosis [29,30]. While this phenotype was first described nearly 25 years ago, the mechanisms by which ATF4 regulates lens cell survival remained a mystery. Here we re-evaluate the phenotype of the *Atf4* null lens and utilize RNA-sequencing and bioinformatics to reveal the molecular mechanisms by which ATF4 regulates the latter stages of fetal lens development.

2. Materials and Methods

2.1. Animals

All mice were maintained under pathogen-free conditions at the University of Delaware animal facility under a 14 h light/10 h dark cycle. Animals of both sexes were used in these experiments, and no sex-dependent effects were noted, consistent with our prior report [31].

Mice heterozygous for a null mutation in the *Atf4* gene [28] were obtained from Timothy Townes Lab (B6;129-*Atf4*^{tm1Tow}) at the University of Alabama at Birmingham on a mixed C57Bl/6/129 genetic background. Note that the colony was not explicitly genotyped for the *Bfsp2* deletion mutation found in the 129 mouse strain [32], so it is possible that the *Atf4* null phenotype reported here is influenced by this naturally occurring mutation although RNAseq analysis suggests that *Bfsp2* mRNA is present in the lenses of these mice. *Atf4* null (ATF4$^{-/-}$) and wildtype littermate embryos were generated by the mating of mice heterozygous for this allele, with the date that the copulatory plug was identified defined as embryonic day(E) 0.5. All genotyping was performed by Transnetyx (Cordova, TN, USA) using probes *Atf4* wt-1 and neomycin.

2.2. Lens Diameter Measurement

Lenses were dissected from the eye and immersed in 1× PBS. Bright-field images were taken with a Zeiss Stemi SV 11 Apo Microscope, and lens diameters were determined using ImageJ (1.53k, Wayne Rasband and contributors, National Institutes of Health, USA, http://imagej.nih.gov/ij, Java 1.8.0_172 (64-bit). Average lens diameters were calculated and differences were assessed using the F test and two-tailed Student *t*-test. Data are presented as mean ± SEM, with differences considered significant at $p \leq 0.05$.

2.3. Histological Evaluation

Embryos were dissected and heads fixed in Modified Davidson's Fixative (Electron Microscopy Sciences, Hatfield, PA, USA, 64133-50) at room temperature overnight, then transferred into 70% ethanol. Fixed samples were paraffin-embedded at the University of Delaware Comparative Anatomy Laboratory and 5 μm sections were stained with hematoxylin and eosin using standard methods.

2.4. Immunostaining

Fresh tissue from embryonic mice was embedded in OCT (Tissue-Tek Sakura, Torrance, CA, USA, 4583) and 14 μm cryosections were prepared as previously described [33]. Sections were fixed under conditions specific to each antibody (Supplemental Table S6) and washed 3 times in PBS for 10 min each. Sections were blocked using a solution of 5% normal goat serum (NGS, Jackson ImmunoResearch, West Grove, PA, USA, 005-000-

121), 2% bovine serum albumin (BSA, Sigma-Aldrich, St Louis, MO, USA, A2153), and 0.2% Triton X-100 (Sigma-Aldrich, St Louis, MO, USA, T8787) in 1× PBS for 1 h, followed by three 10 min 1× PBS washes. The primary antibody was diluted in blocking buffer as described in Supplemental Table S6, overlaid on the sections, and incubated at 4 °C overnight. Following three 10 min washes with 1× PBS, slides were incubated in secondary antibody solution (5%NGS, 2% BSA, Draq5 (1:2000), 1:200 dilution of appropriate Alexa Fluor-labeled secondary antibody (Thermofisher, Waltham, MA, USA) in 1× PBS with or without the addition of fluorescein-labeled alpha-smooth muscle actin antibody) at room temperature for 1 h. Following three 10 min washes with PBS, slides were coverslipped and imaged on an LSM 780 Zeiss confocal microscope. Immunofluorescence was quantified by measuring mean fluorescence intensity (MFI) in the region of interest using Image J as previously described [34]. The number of animals analyzed in each experiment (biological replicates) is noted in the figure legends (i.e., "*n*"). Data were assessed using an F test and two-tailed Student *t*-test on data generated from a minimum of three biological replicates. Data are presented as mean ± SEM, and differences were considered significant at $p \leq 0.05$. The confocal imaging of all slides in the same experiment was imaged the same day using the same imaging parameters to allow direct comparison of experimental conditions and reduce variability. While quantification was performed on native images to ensure that signals were in the linear range, in some cases, brightness and contrast were adjusted post-confocal acquisition to create the figures presented here for optimum viewing, but in all cases, identical adjustments were made to images that are intended to be directly compared.

2.5. RNA Sequencing and Data Analysis

Lenses were dissected from E16.5 embryos generated from *Atf4*$^{+/-}$ intercross matings, and frozen on dry ice, while the embryos were genotyped as above. RNA was harvested from single pairs of wildtype and *Atf4* null lenses using the RNeasy Mini Kit from Qiagen (Germantown, MD, USA, catalog 74104) and shipped to DNAlink USA (Los Angeles, CA, USA) for library preparation and RNAseq analysis. RNA libraries were prepared using the SMARTer Stranded Total RNA-Seq Kit-Pico Input Mammalian (Takara Bio, Inc., Tokyo, Japan) and sequenced on a NovaSeq 6000 (Illumina, San Diego, CA, USA). The raw fastq files were run through Trim Galore [35] to remove library adapters and low-quality/short reads. Trimmed reads were then aligned to the RN45S rRNA sequence that encodes 28S, 18S, and 5S ribosomal RNAs with HISAT2, and any aligned reads were removed, then the resulting file was processed to create trimmed fastq files suitable for downstream analyses.

The *Mus musculus* GRCm39 Ensembl Release 104 primary assembly gene transfer format (GTF) file was obtained from https://ftp.ensembl.org/pub/release-104/fasta/mus_musculus/dna/ (accessed on 11 June 2021) and splice sites/exons were extracted. A comprehensive annotation table was then constructed by combining a table containing these features [36] with GRCm39 genome annotations obtained from Biomart [37,38]. Trimmed fastq files were aligned to the GRCm39 annotation file and each read assigned to a gene by HTSeq [39], and count files for each aligned gene generated. These primary count files were fed into EdgeR [40–42], where TMM normalization was performed and dispersion was estimated using a weighted likelihood empirical Bayes approach. The log2 fold change for each gene was calculated with the exactTest function in edgeR that uses gene-wise exact tests and data were expressed so that positive fold changes represent elevated expression in the Atf4 null lens compared to wildtype littermate controls. The normalized abundance of each transcript in each sample was calculated as fragments per kilobase million (FPKM).

Differentially expressed genes (DEGs) are those whose expression differences between wildtype and control exhibited false discovery rate (FDR)-corrected *p* values of less than 0.05. This DEG list was then further filtered using criteria previously proposed to identify genes whose expression differences were considered likely to be "biologically significant" [43] to the lens (absolute log fold change greater than 1, an absolute change in FPKM between the two conditions tested greater than 2, and at least one condition

with an FPKM greater than 2). Gene enrichment and pathway analysis were performed on the entire list of present genes considering all statistically significant DEGs between the wildtype and Atf4 null lens using Adviata's iPathway guide package (Ann Arbor, MI, USA).

Cross-experiment comparisons (Table 1) were used to predict whether ATF4 is involved in known biological processes by comparing the overlap between the DEGs detected in the *Atf4* null lens and those detected in other experiments of interest. First, a matrix is created that compares the proportions of non-differentially expressed genes to differentially expressed genes between the two experiments, and a one-sided Fisher's Exact test would compare the proportions and test for enrichment. The second was to look at the proportion of differentially expressed genes between the experiments that were up-regulated and down-regulated. The top-left quadrant would indicate concordant up-regulation and the bottom-right quadrant would indicate concordant down-regulation. The top-right and bottom-left quadrants would indicate discordant regulation. A two-sided Fisher's Exact test would compare these proportions and look at whether genes are observed going in a direction more than expected at random.

Table 1. Accession numbers used for cross-experiment comparisons in this study.

Name of Experiment	GEO Accession	Experiment Type	Library Source
Lens Superficial Cortex vs. Lens Epithelial Cells	GSE205379	Microarray	Transcriptomic
Lens Deep Cortex vs. Lens Superficial Cortex	GSE205379	Microarray	Transcriptomic
Prox1 Knockout vs. Wildtype	GSE69940	RNA-Seq	Transcriptomic
HSF4 Knockout vs. Wildtype	GSE22362	Microarray	Transcriptomic
Whole Lens E15.5 vs. Whole Lens E13.5	E15.5 (GSE49949) E13.5 (GSE69940)	RNA-Seq	Transcriptomic
ATF4 Knockout vs. Wildtype	GSE35681	ChIP-Seq	Genomic

2.6. Lens Protein Determination

Lenses were collected from E16.5 embryos generated from *Atf4*$^{+/-}$ intercross matings, frozen on dry ice, and genotyped as described above. Each pair of lenses from wildtype and Atf4 null embryos was homogenized in 70 µL of RIPA buffer (protease inhibitor 1:100 added) and the supernatant was collected following centrifugation (14,000× *g*, 4 °C, 15 min). Protein concentration was determined by the Pierce BCA assay (Thermo-Fisher Scientific, Waltham, MA, USA) using kit instructions from a standard curve created from 125–2000 µg/mL bovine serum albumen. Protein per lens (µg) was calculated by the protein concentration and lens average volume derived from the average diameter. Data are presented as mean ± SEM and were statistically analyzed by F test and two-tailed Student *t*-test, with differences considered significant at $p \leq 0.05$.

2.7. Glutathione Assays

E16.5 WT and *Atf4* null lenses were collected, and each pair of lenses was homogenized in 120 µL of 2 mM EDTA (in 1× PBS) buffer on ice, and the supernatant collected after centrifuging at 14,000× *g* at 4 °C for 10 min. Glutathione levels were determined following the protocol given in the Promega GSH-Glo Glutathione assay kit (Madison, WI, USA, v6911) and the luminescence signal was measured using a Promega GlowMax plate reader set on the default luminescence protocol. Standard curves were created by diluting a

5 mM standard GSH stock into 0.3125, 0.625, 1.25, 2.5, and 5 μM concentrations to calculate and sample GSH concentrations. The difference between data from WT and *Atf4* nulls was assessed via the F test and two-tailed Student *t*-test. Data are presented as mean ± SEM, and differences were considered significant at $p \leq 0.05$.

2.8. Reactive Oxygen Species Assays

E16.5 lenses were collected and each pair of lenses was immersed in room temperature Medium 199 (Corning, Corning, NY, USA). Each pair of lenses was then transferred into one well of 96-well plates, with 200 μL 7.5 μM dehydrorhodamine 123 (Invitrogen, Carlsbad, CA, USA, D23806) in Media 199. Plates were placed on ice for 30 min, then washed 3 times with cold 1× PBS, and fluorescence detection was performed on a Promega GlowMax plate reader. Data from wildtype and Atf4 null lenses were statistically analyzed using F and two-tailed Student's *t*-test. Data are presented as mean ± SEM, and differences were considered significant at $p \leq 0.05$.

2.9. Free Amino Acid Detection

E16.5 WT and ATF4$^{-/-}$ lenses were collected, and each pair of lenses was homogenized in 40 μL of 100 mM ammonium acetate, with 200 μM Ala isotope (L-Ala-1-^{13}C, Sigma-Aldrich, 489867) added as an internal standard, then centrifuged at 14,000× *g* at 4 °C for 15 min. The supernatant was collected, and then 120 μL of 0.2% formic acid in acetonitrile was added to each tube. The solution was placed on ice for 1 min, vortexed for 1 min, then centrifuged at 14,000× *g* at 4 °C for 15 min, and the supernatant was used for amino acid determination. LC-MS/MS analysis was performed by the University of Delaware Mass Spectrometry Core Facility using a Q-Exactive Orbitrap interfaced with Ultimate 3000 LC system (Thermo Fisher Scientific). Chromatographic separation was achieved using an Intrada amino acid column (3 μm, 3 × 50 mm column), with mobile phase A consisting of 100 mM ammonium formate and mobile phase B consisting of acetonitrile containing 0.1% formic acid. Sample elution was performed using a gradient starting at 8% mobile phase A/92% mobile phase B for 3 min, then increasing to 70% mobile phase A/30% mobile phase B for 12 min, with a column temperature of 35 °C and a flow rate of 0.6 mL/min. Acquisition of MS data scans (50–750 m/z) was performed using a data-dependent top 5 method, dynamically selecting the most abundant precursor ions from the survey scan for high-energy collision-induced dissociation (HCD) fragmentation using a stepped normalized collision energy of 25, 30, and 35 eV. Raw LC-MS data were analyzed by Xcalibur software (Thermofisher version 4.5), and amino acid concentrations were determined by comparisons with a standard amino acid mix diluted into 0.1, 1, 2, 5, and 10 μM concentrations to create a standard curve. The amino acid amount per lens was then calculated for each sample and statistically assessed using the F test and two-tailed Student's *t*-test. Data are presented as mean ± SEM, and differences were considered significant at $p \leq 0.05$.

3. Results

The first studies on ATF4 function in lens development reported that *Atf4* deletion led to morphological abnormalities in the lens starting in late embryonic development, with total disintegration of the lens seen by birth due to epithelial and/or fiber cell apoptosis [29,30]. While these investigations revealed that ATF4 is important for lens development and/or its homeostasis, the mechanisms by which ATF4 regulates these processes were unknown. In order to re-evaluate these phenotypes, we obtained a different *Atf4* null allele (*Atf4*^{tm1Tow}) established by replacing exon 3 and 4 of the *Atf4* gene, with a neomycin phosphotransferase cassette [28] (Figure 1A).

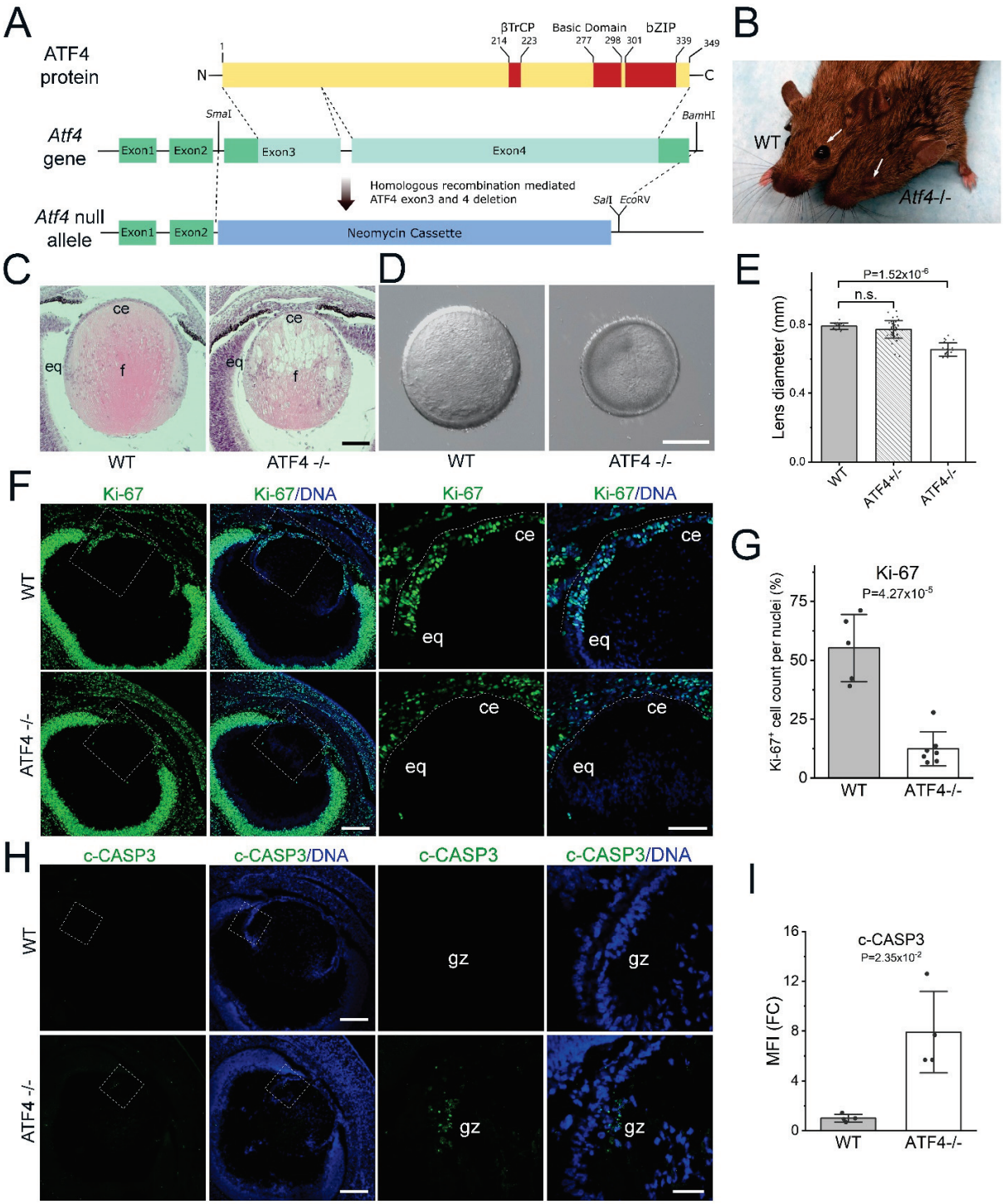

Figure 1. *Atf4* is required for lens epithelial cell proliferation and lens fiber cell survival during late embryonic development. (**A**) Mouse ATF4 protein primary structure (N, N terminus; C, C terminus; βTrCP, βTrCP-binding domain) and wildtype mouse *Atf4* gene structure (green represents non-coding portions of exons; aqua represents coding sequence). Note that alternate splicing can result in a three-exon transcript where exons 1,2 and the intervening intron encompass "exon 1" as described in the original paper describing this *Atf4* allele [28] with both of these splice variants producing the same protein [44]. The final structure of the *Atf4* null allele where the coding sequence located in exons 3 and 4 (exons 2 and 3 in [28]) was removed by homologous recombination (Sma1, BamH1, SalI, and EcoRV are restriction enzyme sites used in construct production) and replaced with

a neomycin resistance cassette (blue). (**B**) A two-month-old wildtype mouse (left) and its *Atf4* null (−/−) littermate (right). (**C**) Hematoxylin and eosin staining of paraffin sections generated from E16.5 wildtype eye (left) and E16.5 *Atf4* null eye (right, scale bar = 100 μm). (**D**) Bright-field image of representative E16.5 lenses microdissected from wildtype (WT, left) and *Atf4* null ($ATF4^{-/-}$; right) mice (scale bar = 300 μm). (**E**) Quantification of the diameters of lenses microdissected from E16.5 wildtype (WT, n = 18), heterozygote ($ATF4^{+/-}$, n = 48), and homozygote ($ATF4^{-/-}$, n = 23) mice. (**F**) Representative image obtained from sections of E16.5 wildtype and *Atf4* null eyes immunostained for the proliferation marker Ki-67 (green) and labeled with the DNA dye Draq5 (blue). Images on the left were generated from a 3 × 3 tile scan with a 20× objective (scale bar = 200 μm), and the boxed region is shown in a zoomed-in view on the right (scale bar = 100 μm). (**G**) Quantification of the percentage of lens epithelial cell nuclei positive for Ki-67 (WT, n = 5; $ATF4^{-/-}$, n = 5). (**H**) Immunostaining of E16.5 wildtype and *Atf4* null lenses for the apoptotic marker cleaved caspase 3 (green) and labeled with the DNA dye Draq5 (blue). Images on the left were collected via a 3 × 3 tile scan using a 20× objective (scale bar = 200 μm) with the boxed region representing the zoomed-in view shown on the right (scale bar = 40 μm). (**I**) Quantification of the fold change (FC) in mean fluorescence intensity (MFI) of cleaved-Caspase3 staining between WT and *Atf4* null lenses (WT, n = 4; $ATF4^{-/-}$, n = 4). *Abbreviations*: ce, central epithelium; eq, equator; gz, germinative zone; WT, wildtype.

3.1. ATF4 Is Required for Lens Epithelial Cell Proliferation and Survival during Late Embryonic Development

As previously described, mice homozygous for the $Atf4^{tm1Tow}$ allele exhibit high perinatal lethality [28], and consistent with the prior reports on other *Atf4* null alleles, surviving adult homozygotes lack externally visible eyes [28] (Figure 1B, arrows) while the remaining eye remnant lacks lens material [29]. Hematoxylin and eosin staining revealed that $Atf4^{tm1Tow}$ null lenses were typically grossly normal at E14.5 (Supplemental Figure S1), but by E16.5, $Atf4^{tm1Tow}$ null lenses are significantly smaller than normal (Figure 1C–E) with vacuoles apparent in central lens fibers (Figure 1C).

Staining of $Atf4^{tm1Tow}$ null lenses for KI-67, a marker of cell proliferation [45], revealed that over 50% of wildtype E16.5 LECs were active in the cell cycle, while fewer than 20% of mutant LECs were proliferating (Figure 1F,G). As apoptosis was previously reported to drive lens loss in *Atf4* null mice, we stained E16.5 wildtype and $Atf4^{tm1Tow}$ null lenses for cleaved-Caspase3 (c-CASP3), an apoptosis marker in the lens [46]. While, as expected, wildtype lenses had no apparent c-CASP3 staining, the germinative zone lens epithelium of $Atf4^{tm1Tow}$ null lenses exhibited patchy regions of c-CASP3 positivity (Figure 1H,I). Overall, the terminal lens phenotype of $Atf4^{tm1Tow}$ null lenses (loss of lens material after birth) was similar to the lens phenotype of the two previously described alleles [29,30]. However, the loss of lens material from $Atf4^{tm1Tow}$ homozygotes appears slightly delayed compared to that reported by Hettmann et al. [29]. These data suggest that ATF4 is required for LEC proliferation and survival in the late embryonic mouse lens.

3.2. Unfolded Protein Response Markers Are Only Modestly Affected in the Atf4 Null Lens

The unfolded protein response (UPR) allows cells to calibrate the folding capacity of the endoplasmic reticulum to the flux of newly produced secreted/membrane proteins, while its chronic activation leads to cell dysfunction leading to apoptosis [47]. Notably, numerous components of the UPR pathway are modestly activated in the developing lens [48] while chronic UPR can lead to cataract [49–51]. As ATF4 is a known UPR regulator [52], we investigated whether E16.5 $Atf4^{tm1Tow}$ null lenses have a defect in UPR during lens development. BIP/*grp78* is an endoplasmic reticulum chaperone whose expression typically upregulates during UPR [53]. As previously shown, BIP levels are highest in the lens epithelium and newly elongating fiber cells in wildtype lenses [48], while they are modestly attenuated in E16.5 $Atf4^{tm1Tow}$ null lenses (Supplemental Figure S2A,B). Similarly, the protein levels of neither CHOP/*Ddit3*, an ATF4 target, [54] nor XBP1 whose protein is selectively produced when the IRE1 UPR signaling pathway is activated [55]

were significantly altered in E16.5 *Atf4*^{tm1Tow} null lenses (Supplemental Figure S2A,C,D). However, the protein levels of eIF2α, a translational regulator that selectively synthesizes UPR pathway proteins, were modestly elevated in E16.5 *Atf4*^{tm1Tow} null equatorial lens epithelium (Figure 2B,D).

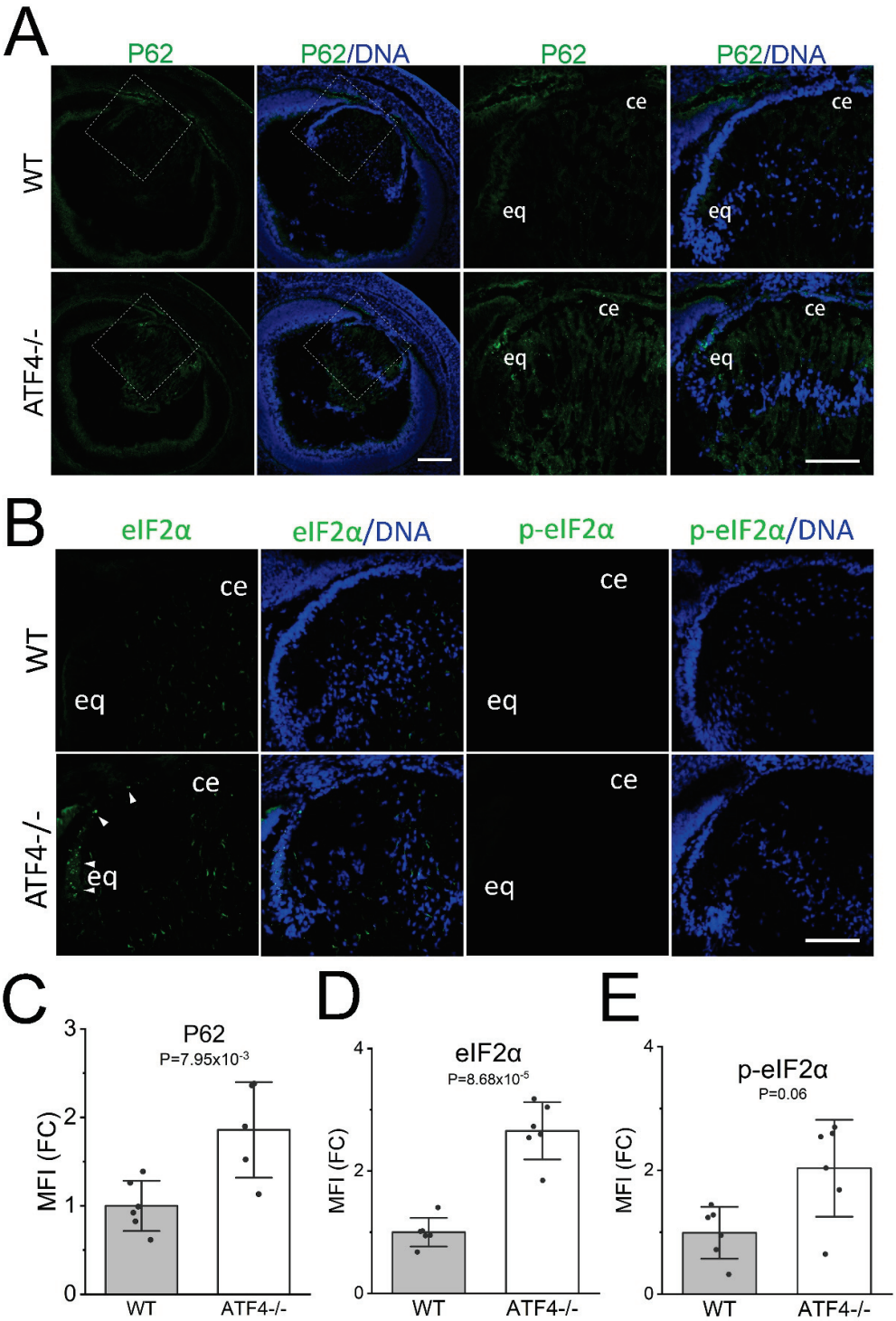

Figure 2. Only portions of the autophagy pathway are induced in the *Atf4* null lens. (**A**) Immunostaining of E16.5 wildtype and *Atf4* null (Atf4$^{-/-}$) lens for P62 (green) that is encoded by the *Sqtm1* (Sequestosome-1, Sqtm1) gene counterstained with Draq5 to detect DNA (blue). Images on the left

were generated from a 3 × 3 tile scan with a 20× objective (scale bar = 200 μm), and the boxed region is shown in a zoomed-in view on the right (scale bar = 100 μm). (**B**) Immunostaining of E16.5 wildtype and *Atf4* null lens for the eIF2α (left panels, green) and p-eIF2α (right panels, green) counterstained with Draq5 to detect DNA (blue) (scale bar = 100 μm). *Abbreviations*: ce, central epithelium; eq, equator. (**C**) Quantification of the mean fluorescent staining intensity of P62 immunostaining in the E16.5 wildtype (n = 6) and *Atf4* null (n = 5) lens. (**D**) Quantification of the mean fluorescent staining intensity of eIF2α immunostaining in the E16.5 wildtype (n = 6) and *Atf4* null (n = 6) lens. (**E**) Quantification of the mean fluorescent staining intensity of p-eIF2α immunostaining in the E16.5 wildtype (n = 6) and *Atf4* null (n = 6) lens.

3.3. RNAseq Revealed That ATF4 Regulates a Subset of the Lens Transcriptome

Although *Atf4*^{tm1Tow} null lenses exhibit modest changes in UPR response pathways, the genes that ATF4 regulates in the lens were still obscure. Thus, we performed RNAseq on lenses isolated from E16.5 *Atf4*^{tm1Tow} null embryos and their wildtype littermates to gain an unbiased insight into the potential function of ATF4 in the lens. Consistent with other studies [12,56], both wildtype and *Atf4*^{tm1Tow} null lenses express approximately 15,000 genes at sufficient abundance to pass the "filter by expression" threshold set in EdgeR [40–42]. Of these, 983 genes were differentially expressed based on FDR-corrected p value, with 368 genes upregulated and 615 genes downregulated (Supplemental Figure S3A, Supplemental Table S1). Filtering this list further using criteria that we previously proposed to robustly identify genes whose differential expression was likely to have biological significance (absolute fold change > 2, expression in at least one condition greater than 2 FPKM) [43] resulted in a list of 418 genes of potential interest representing 125 upregulated and 293 downregulated genes, including *Atf4* itself (Supplemental Table S1). While some *Atf4* mRNA was still detected in *Atf4*^{tm1Tow} null lenses, mapping of these transcripts to the mouse genome revealed that these reads solely represented residual transcription of the non-coding exons 1 and 2 and the intervening intron that is included in some *Atf4* splice variants (Supplemental Figure S3B). The deletion of the *Atf4* coding sequences in this mutant did not affect the expression of its upstream gene, *Mief1*, although the gene immediately downstream of the *Atf4* locus, *rps19bp1* that encodes AROS, a suppressor of P53 activity [57], was 2-fold downregulated, which may drive part of the P53-mediated apoptosis seen in the lens of *Atf4* null mice [29]. These data have been deposited in the Gene Expression Omnibus under accession number GSE206760.

3.4. Atf4 Null Lens Epithelial Cells Downregulate Known Lens Epithelial Markers While Upregulating α-SMA Expression

Inspection of the DEG list revealed that the mRNA levels of *FoxE3* [16] and E-cadherin/*Cdh1* [58], which are known regulators of the lens epithelial phenotype, were downregulated in the *Atf4* null lens (see Table 2, Supplemental Table S1). Immunostaining for FOXE3 (Figure 3A,D) and E-cadherin (Figure 3B,E) protein revealed that these reduced mRNA levels resulted in significant reductions in their protein expression in the E16.5 *Atf4* null lens. Meanwhile, α-smooth muscle actin (α-SMA) expression, which is often considered as a diagnostic marker of lens EMT [59,60], increased in E16.5 *Atf4* null lenses at both the mRNA (Supplemental Table S1) and protein (Figure 3C,F) levels. However, the upregulation of αSMA expression in the *Atf4* null lens appears to not indicate bona fide fibrotic transformation of the lens epithelium as the mRNA levels of other classic markers of LEC fibrosis such as tenascin C, fibronectin, and collagen I [61] are not significantly differentially expressed in *Atf4* null lenses (not shown, Supplemental Table S1).

Table 2. Genes with known lens expression/function differentially expressed in the E16.5 *Atf4* null lens.

Symbol	Description	Citation	Fold Change	FDR	Wildtype FPKM	*Atf4* KO FPKM
Foxe3	Forkhead box E3	[16]	−4.7	1.56×10^{-4}	140	30
Dnase2b	Deoxyribonuclease II beta	[62]	−3.7	2.72×10^{-8}	31	8.6
Birc7	Baculoviral IAP repeat-containing 7	[19]	−3.5	6.20×10^{-5}	18	5.3
Bfsp1	Beaded filament structural protein 1	[63]	−2.7	6.06×10^{-5}	2924	1094
Crybb2	Crystallin, beta B2	[64]	−2.7	9.45×10^{-3}	23	8.8
Crygb	Crystallin, gamma B	[65]	−2.7	6.84×10^{-5}	5582	2103
Crygf	Crystallin, gamma F	[65]	−2.5	8.17×10^{-4}	7129	2869
Cryba4	Crystallin, beta A4	[65]	−2.3	2.72×10^{-4}	4983	2138
Crygs	Crystallin, gamma S	[65]	−2.3	1.71×10^{-3}	280	125
Hopx	HOP homeobox	[66]	−2.1	3.59×10^{-2}	12	5.8
Crygd	Crystallin, gamma D	[65]	−2.0	9.70×10^{-3}	5561	2783
Caprin2	Caprin family member 2	[67]	−2.0	6.24×10^{-3}	100	51
Crygc	Crystallin, gamma C	[65]	−1.9	1.35×10^{-2}	2881	1496
Cryba2	Crystallin, beta A2	[65]	−1.9	1.74×10^{-2}	3397	1831
Hmgn3	High mobility group nucleosomal binding domain 3	[68]	−1.8	1.12×10^{-2}	137	78.50

3.5. ATF4 Likely Regulates a Portion of the Lens-Preferred Transcriptome Including Markers of Late Fiber Cell Differentiation

Inspection of the differentially expressed genes (DEGs) in the *Atf4* null lens revealed a number of genes with known functions in the ocular lens (Table 2) and comparison of the *Atf4* null DEGs with the iSyTE database, which evaluates genes for their enriched expression in the lens [69,70], revealed that 148 of the *Atf4* null DEGs exhibit lens-enriched expression in the E16.5 mouse lens ($p \leq 1.8 \times 10^{-65}$, Figure 4A, Supplemental Table S2). Notably, 140 of these lens-enriched genes were downregulated in the *Atf4* null lens, and iPathway guide analysis [71] revealed that the *Atf4* null DEGs were significantly over-represented in lens structural constituents (Figure 4B, $p \leq 5.8 \times 10^{-4}$). Comparison of the E16.5 *Atf4* null DEGs with DEGs detected in lenses lacking the transcription factor Prox1, which is a key regulator of lens fiber cell differentiation [12], revealed that over 250 genes were downregulated in both mutants (Figure 4C, Table 1, Supplemental Table S3; $p \leq 3.6 \times 10^{-8}$) suggesting that ATF4, like Prox1, may regulate the expression of genes important for lens function. As the *Atf4* null lenses form normally, then disintegrate in late embryonic lens development, we then compared the *Atf4* null DEGs with a list of genes that change expression in the mouse lens between E13.5 (right after primary lens fiber cell elongation is complete [12]) and E15.5 (near the onset of fiber cell denucleation and directly before the *Atf4* null phenotype is morphologically apparent [56]). This comparison revealed that over 380 genes that normally upregulate in mid-late lens development fail to do so in the *Atf4* null lens, suggesting that *Atf4* may play a key role in the later stages of lens fiber cell terminal differentiation (Figure 4D, Table 1, Supplemental Table S4). Consistent with this, known late lens fiber cell markers such as *DnaseIIb* (DNase II beta) [72] and *Birc7* [19] were downregulated in *Atf4* null lenses (Figure 4E). Next, we compared the DEGs found in the *Atf4* null lens with those observed in lenses null for *Hsf4*, which encodes a transcription factor important for late lens function [73] (Table 1). Interestingly, while 86 genes were differentially regulated in both *Atf4* and *Hsf4* null lenses ($p \leq 1 \times 10^{-23}$), there was not a significant correlation between the direction of their differential regulation ($p = 0.31$, not shown). Overall, these data show that ATF4 is an important player in the gene regulatory network (GRN) controlling the latter stages of embryonic lens development even though it appears to not be directly regulated by other known lens GRN components.

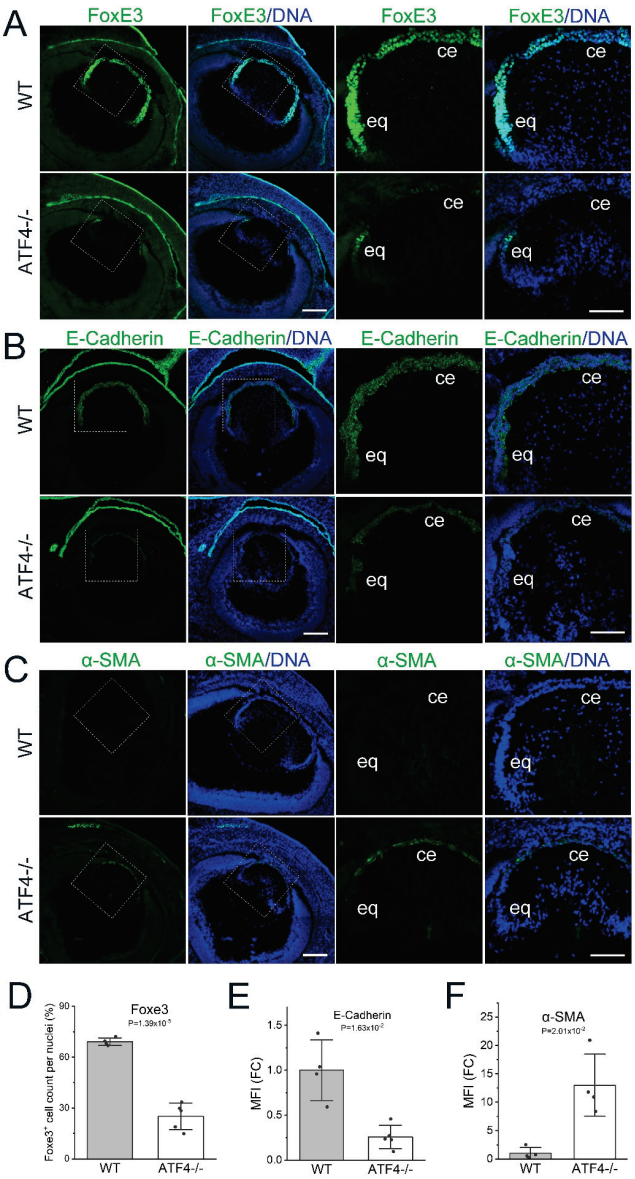

Figure 3. *Atf4* null lens epithelial cells downregulate known lens epithelial markers while upregulating α-SMA expression. (**A**) Immunostaining of E16.5 wildtype and *Atf4* null lens for FoxE3 (green) counterstained with Draq5 to detect DNA (blue). Images on the left were generated from a 3 × 3 tile scan with a 20× objective (scale bar = 200 μm), and the boxed region is shown in a zoomed-in view on the right (scale bar = 100 μm). (**B**) Immunostaining of E16.5 wildtype and *Atf4* null lens for E-cadherin (green) counterstained with Draq5 to detect DNA (blue). Images on the left were generated from a 3 × 3 tile scan with a 20× objective (scale bar = 200 μm), and the boxed region is shown in a zoomed-in view on the right (scale bar = 100 μm). (**C**) Immunostaining of E16.5 wildtype and *Atf4* null lens for α-SMA (green) counterstained with Draq5 to detect DNA (blue). Images on the left were generated from a 3 × 3 tile scan with a 20× objective (scale bar = 200 μm), and the boxed region is shown in a zoomed-in view on the right (scale bar = 100 μm). Abbreviations; ce, central epithelium; eq, equator. (**D**) Quantification of the percentage of lens epithelial cell nuclei positive for FoxE3 (WT, n = 5; ATF4$^{-/-}$, n = 5). (**E**) Quantification of the fold change (FC) in mean fluorescence intensity (MFI) of E-cadherin staining between WT (n = 4) and Atf4 null (n = 5) lenses. (**F**) Quantification of the fold change (FC) in mean fluorescence intensity (MFI) of α-SMA staining between WT (n = 4) and *Atf4* null (n = 4) lenses.

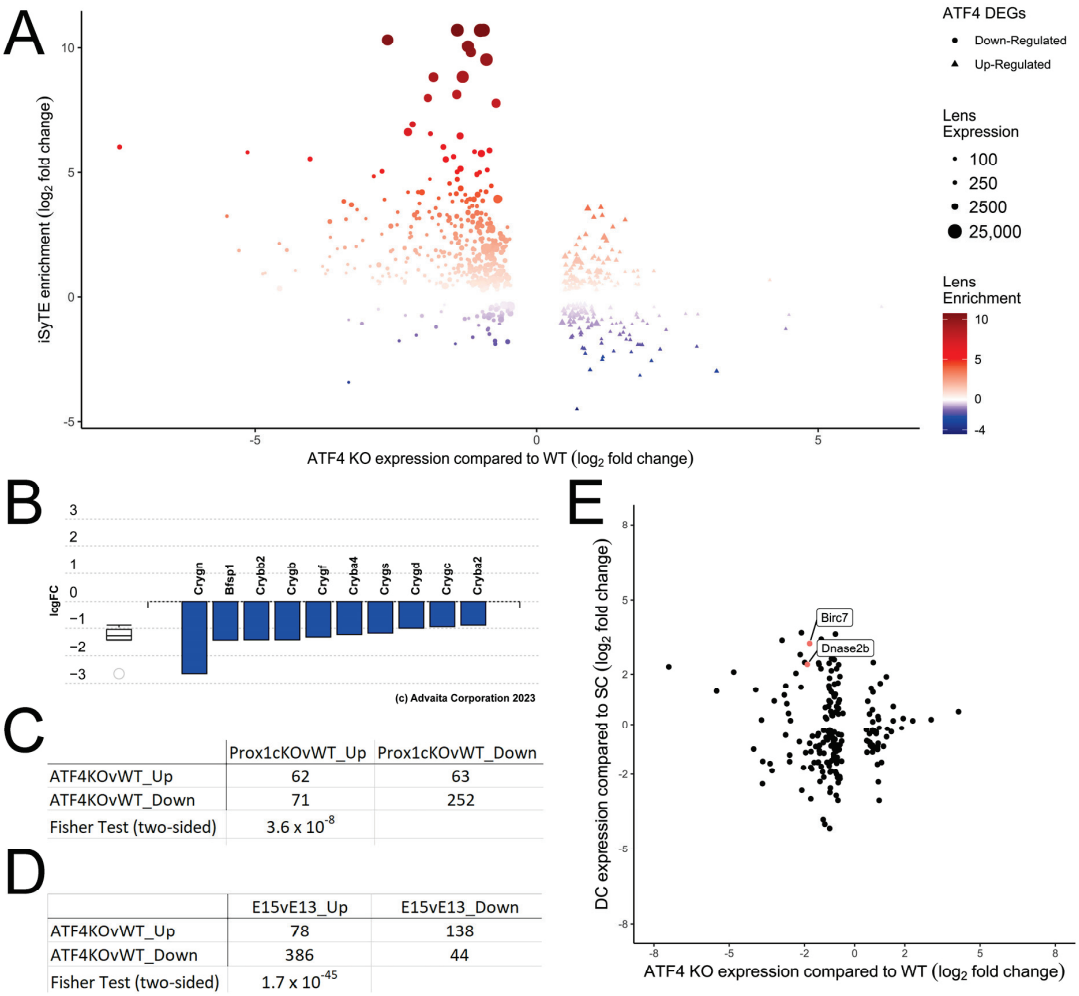

C

	Prox1cKOvWT_Up	Prox1cKOvWT_Down
ATF4KOvWT_Up	62	63
ATF4KOvWT_Down	71	252
Fisher Test (two-sided)	3.6×10^{-8}	

D

	E15vE13_Up	E15vE13_Down
ATF4KOvWT_Up	78	138
ATF4KOvWT_Down	386	44
Fisher Test (two-sided)	1.7×10^{-45}	

Figure 4. ATF4 likely regulates a portion of the lens-preferred transcriptome including markers of late fiber cell differentiation. (**A**) iSyTE enrichment analysis of *Atf4* null DEGs demonstrating that genes that are downregulated in the *Atf4* null lens are disproportionately over-represented in those exhibiting lens-preferred expression (**B**). Advaita iPathway guide analysis shows that genes differentially expressed in the *Atf4* null lens are over-represented in lens structural proteins. (**C**) Comparison between the DEGs observed in the *Atf4* null lenses with DEGs found in the *Prox1* null lens revealed a significant set of genes whose expression is downregulated in both mutants. (**D**) Comparison between the DEGs detected in the E16.5 *Atf4* null lens with those that change expression between E13.5 and E15.5 in the wildtype lens found that many genes that normally upregulate as embryonic lens development proceeds fail to do so in *Atf4* mutants. (**E**) Comparison between the Atf4 null DEG list with genes whose expression changes as superficial cortical fibers (SC) differentiate into deep cortical fibers (DC) revealed that some known markers of lens fiber cell terminal differentiation such as *Birc7* and *Dnase2b* are downregulated in the E16.5 *Atf4* null lens.

3.6. The Atf4 Null Lens Has Reduced mRNA Levels of Many Genes Regulating Amino Acid Metabolism and Reduced Free Amino Acid Pools

iPathway guide impact analysis [71] of the *Atf4* null gene list revealed that the DEGs are enriched in genes regulating amino acid biosynthesis ($p \leq 7.8 \times 10^{-6}$; Figure 5A). There is also an enrichment in genes mapping to the KEGG pathway amino acid metabolism ($p \leq 0.02$, not shown), and these included genes known to be involved in amino acid transport by cells (Figure 5B) and tRNA charging (Figure 5C). Notably, ATF4 binding to genes encoding nutrient transporters and amino-acyl tRNA synthases has been described previously in the literature [74,75], while mining of Chip atlas [76] for the ATF4-binding sites found in the mouse genome revealed that 148 of the differentially expressed genes in

the *Atf4* null lens, including nutrient transporters and amino-acyl t-RNA synthases, bind ATF4 within 1 kB of their transcriptional start site in mouse cells (see Supplemental Table S5). This suggests that ATF4 is a direct regulator of genes important for nutrient transport in the avascular lens.

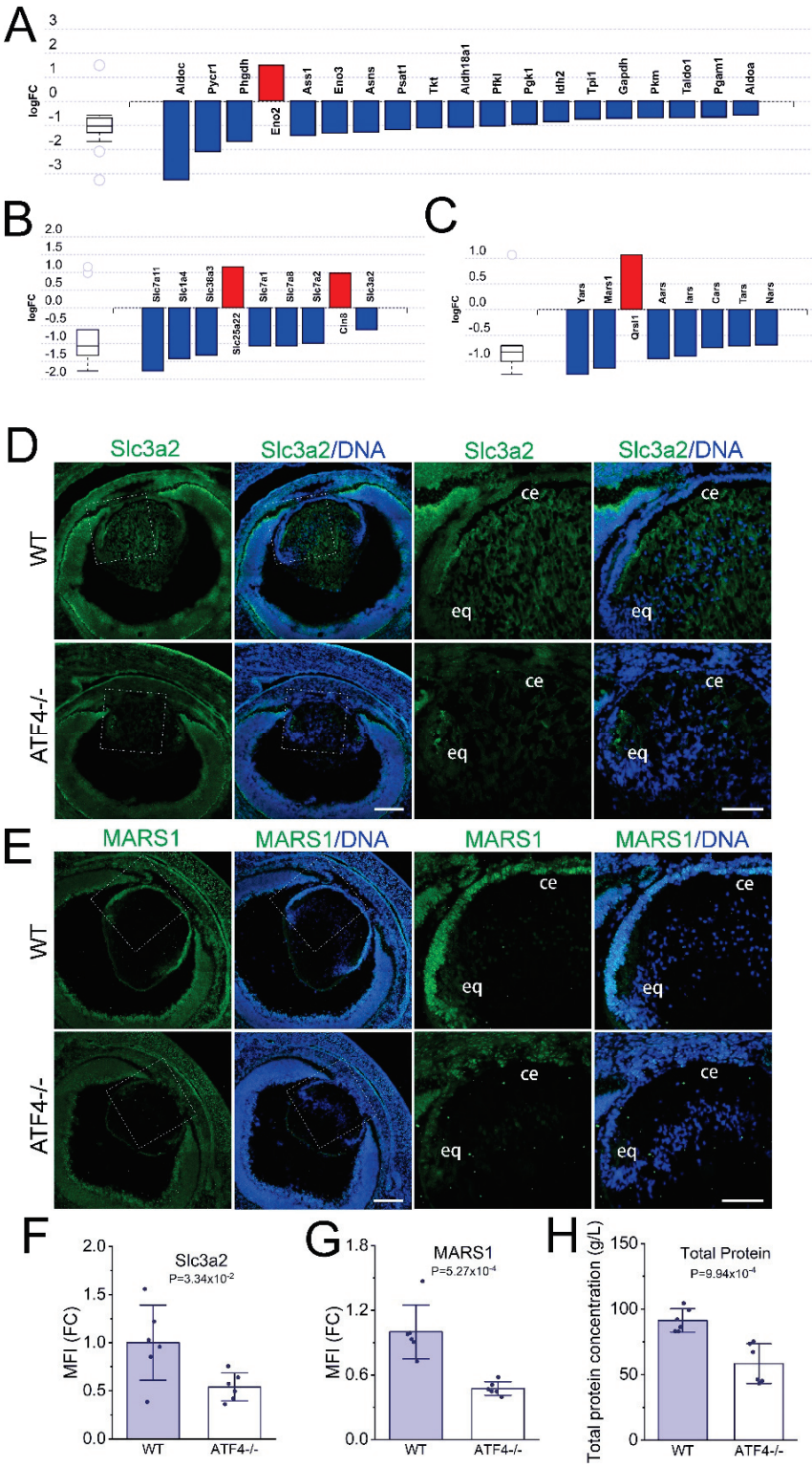

Figure 5. The mRNA levels for many genes encoding regulators of amino acid transport, synthesis, and t-RNA charging are reduced in the *Atf4* null lens. (**A**) Advaita iPathway guide analysis shows that *Atf4* null DEGs are over-represented in mRNAs encoding regulators of amino acid synthesis.

(**B**) Several mRNAs encoding amino acids transporters are differentially expressed in the *Atf4* null lens. (**C**) The levels of several mRNAs encoding enzymes responsible for t-RNA charging are reduced in *Atf4* null lenses. (**D**) Immunostaining of E16.5 wildtype and *Atf4* null lens for the amino acid transporter encoded by the *Slc3a2* gene (green) counterstained with Draq5 to detect DNA (blue). Images on the left were generated from a 3 × 3 tile scan with a 20× objective (scale bar = 200 μm), and the boxed region is shown in a zoomed-in view on the right (scale bar = 100 μm). (**E**) Immunostaining of E16.5 wildtype and *Atf4* null lens for the t-RNA charging enzyme Mars1 (green) counterstained with Draq5 to detect DNA (blue). Images on the left were generated from a 3 × 3 tile scan with a 20× objective (scale bar = 200 μm), and the boxed region is shown in a zoomed-in view on the right (scale bar = 100 μm). *Abbreviations:* ce, central epithelium; eq, equator. (**F**) Quantification of the mean fluorescent staining intensity of SLC3A2 immunostaining in the E16.5 wildtype (n = 6) and *Atf4* null (n = 6) lens. (**G**) Quantification of the mean fluorescent staining intensity of MARS1 immunostaining in the E16.5 wildtype (n = 6) and *Atf4* null (n = 6) lens. (**H**) Quantification of total soluble protein extractable from the E16.5 wildtype (n = 6) and *Atf4* null (n = 6) lens expressed as the concentration of protein per lens volume in order to normalize these values to account for the smaller size of the *Atf4* null lens.

Immunostaining for SLC3A2, an amino acid transporter whose mRNA is abundant in the wildtype lens (74 FPKM) but 1.5-fold downregulated in the *Atf4* null lens, revealed that it is broadly distributed in both lens epithelial and fiber cells of the wildtype lens while both expression domains are downregulated in the E16.5 *Atf4* null lens (Figure 5D,F). Consistent with the reduced expression of genes that regulate cellular amino acid concentration, LC-MS analysis of 16 different amino acids found that *Atf4* null lenses have significantly decreased levels of free Ala, Arg, Glu, Gly, Ile/Leu, Lys, Met, Phe, Pro, Thr, Tyr, and Val (Figure 6). Immunostaining for MARS1, which regulates methionine charging to its cognate tRNA [77], revealed that its expression is epithelial-preferred in the wildtype lens, while its levels were decreased in E16.5 *Atf4* null lenses (Figure 5E,G) consistent with the observed 2-fold decrease in its mRNA levels. As expected from these changes in gene expression, *Atf4* null lenses exhibited a 60% reduction in extractable protein compared to wildtype controls (Figure 5H). These data further support the idea that *Atf4* is important for regulating amino acid and protein metabolism in the lens.

3.7. Aft4 Null Lenses Have Reduced Levels of Several Glutathione Pathway Genes and Free Glutathione

Lenses not only require abundant pools of free amino acids to produce the high concentrations of protein needed for their high refractive index but also require high concentrations of the tripeptide glutathione as it is critical to protect long-lived lens proteins from oxidative damage [78]. Notably, iPathway guide analysis revealed that the mRNA encoding several proteins important for glutathione metabolism (Figure 7A; $p \leq 0.003$) were downregulated in the *Atf4* null lenses. Of these, glutathione peroxidase 1 (*Gpx1*), an enzyme important for long-term lens transparency that utilizes glutathione to detoxify hydrogen peroxide [79], is abundantly expressed at the mRNA level (175FPKM) in the wildtype embryonic lens, and this decreases 46% in the E16.5 *Atf4* null lens (94 FPKM). Immunolocalization of Gpx1 revealed that this protein is predominately found in the lens core that is predominately comprised of late differentiating fiber cells at this time point, while these levels were significantly reduced in the *Atf4* null lens (Figure 7B,C). We then investigated total glutathione (GSH) levels in E16.5 lenses and found that the *Atf4* null lens has significantly lower levels of GSH than wildtype (Figure 7D). As GSH is a major scavenger of reactive oxygen in the lens [78], we then assayed both wild type and *Atf4* null lenses for ROS (Figure 7E). While some individual *Atf4* null lenses were found to have elevated levels of ROS, as a population, these differences were not statistically significant.

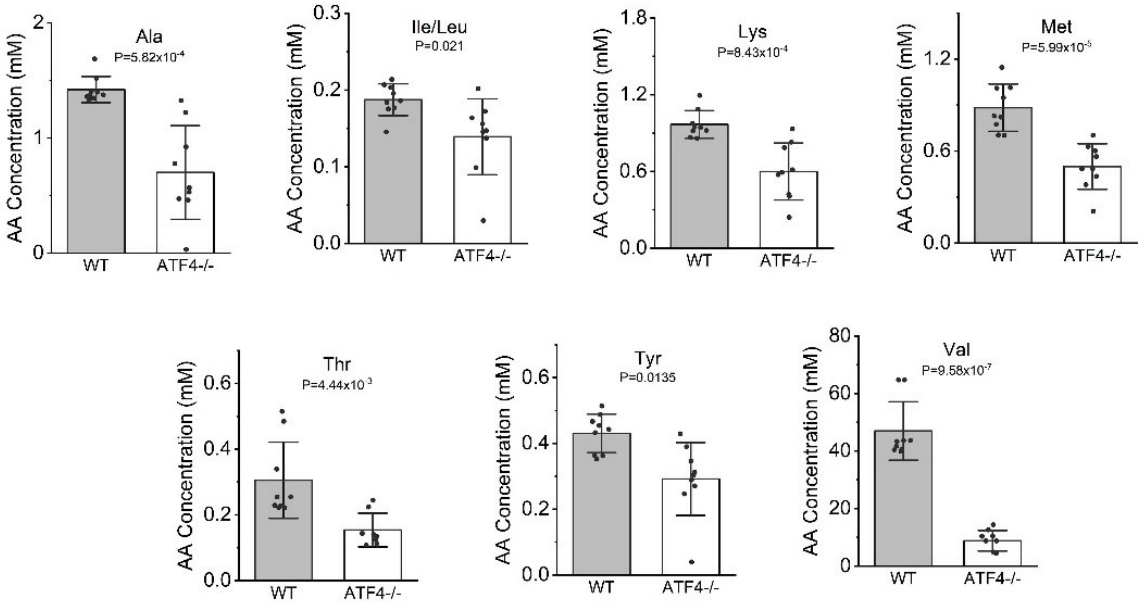

Figure 6. The *Atf4* null lenses have reduced free amino acid pools. Mass spectrometry analysis of free amino acid levels in E16.5 wildtype (n = 9) and *Atf4* null (n = 9) lenses revealed significant reductions in 7 different amino acids when considered either on the basis of concentration in the lens (normalized to lens volume), while 12 amino acids were found to have significantly lower absolute amounts per lens (Supplemental Figure S3).

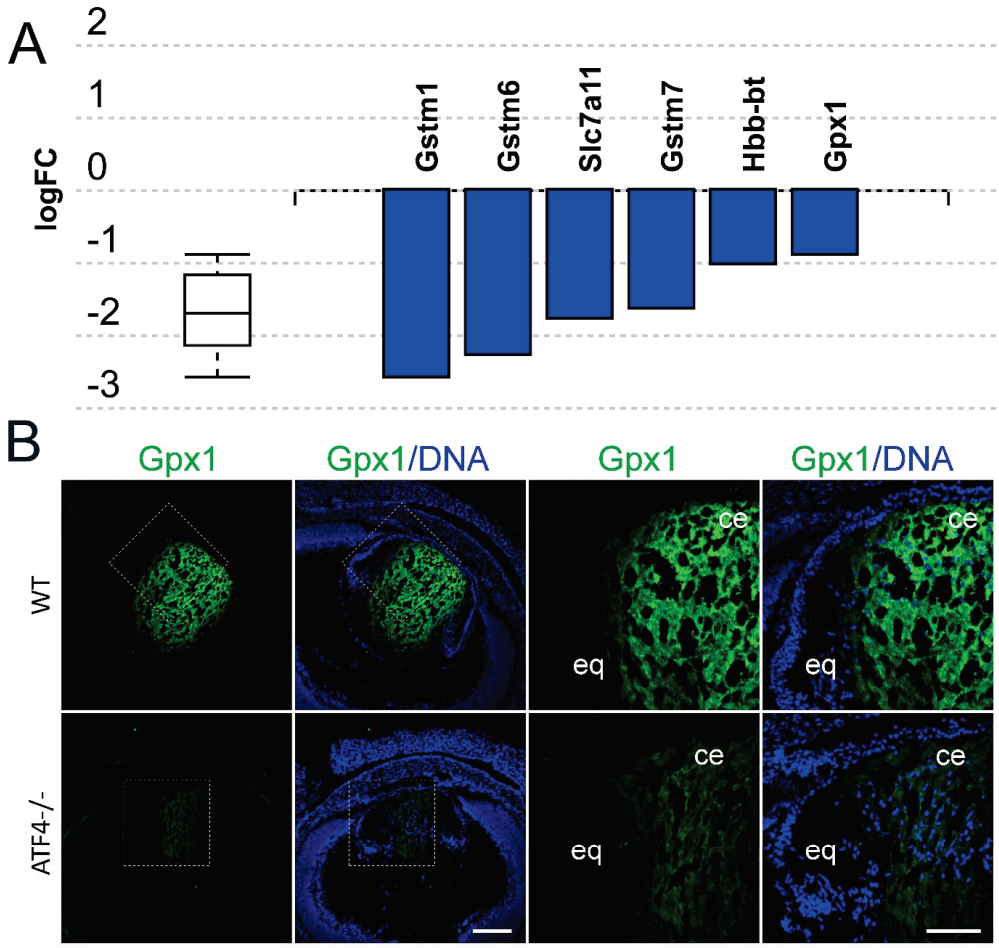

Figure 7. *Cont.*

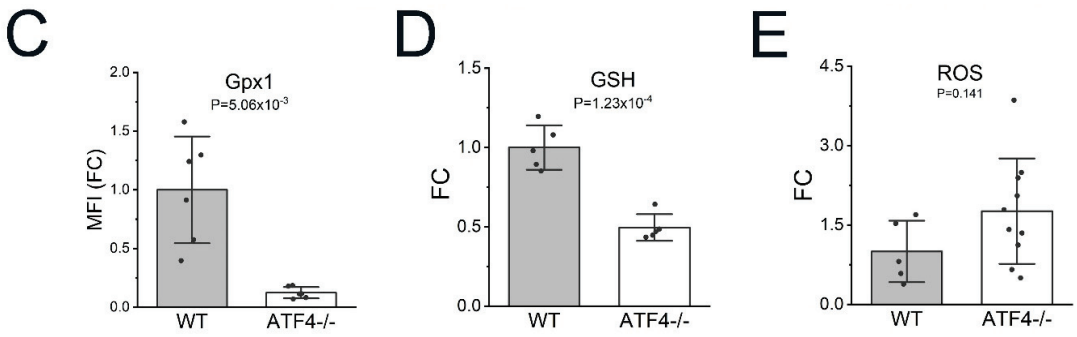

Figure 7. *Aft4* null lenses exhibit reduced mRNA levels of several genes encoding regulators of the glutathione pathway as well as free glutathione. (**A**) Advaita iPathway guide analysis of the DEGs found in the *Atf4* null lens revealed that multiple genes known to regulate glutathione metabolism are downregulated following *Atf4* deletion. (**B**) Immunostaining of E16.5 wildtype and *Atf4* null lens for glutathione peroxidase 1 (Gpx1, green) counterstained with Draq5 to detect DNA (blue). Images on the left were generated from a 3 × 3 tile scan with a 20× objective (scale bar = 200 μm), and the boxed region is shown in a zoomed-in view on the right (scale bar = 100 μm). *Abbreviations:* ce, central epithelium; eq, equator. (**C**) Quantification of the mean fluorescent staining intensity of Gpx1 immunostaining in the E16.5 wildtype (n = 6) and *Atf4* null (n = 6) lens based on fold change (FC) from mean levels found in the wildtype (WT) lens. (**D**) Quantification of free glutathione (GSH) levels in the E16.5 wildtype (n = 5) and *Atf4* null (n = 5) lens using the GSH Glo glutathione assay expressed as the fold change (FC) from mean levels found in the wildtype (WT) lens. (**E**) Quantification of reactive oxygen species (ROS) levels in living E16.5 lenses by incubating E16.5 wildtype (n = 5) and *Atf4* null (n = 10) lenses with non-fluorescent dehydrorhodamine 123 following measurement of ROS-driven production of fluorescent dehydrorhodamine 123 with a plate reader. These data are expressed as fold change (FC) from the mean levels found in the wildtype (WT) lens.

3.8. Atf4 Null Lenses May Have Alterations in Sugar Metabolism Compared to Wildtype

iPathway guide analysis also predicted that glycolysis/gluconeogenesis pathways as the second most significantly impacted in the *Atf4* null lens ($p = 2.2 \times 10^{-5}$; Figure 8A) with many of these involved in carbohydrate catabolism (p = 0.007; Figure 8B), while numerous genes mapping to the glucagon signaling pathway that includes *Atf4* itself (p = 0.003) were downregulated as well (Figure 8C). Consistent with its 16-fold downregulation in mRNA level, immunolocalization of glucagon (Gcg), a peptide hormone that regulates cellular glucose levels [80], revealed that its expression is predominately found in the lens epithelium of the E16.5 wildtype lens, while its levels were reduced in the *Atf4* null lens (Figure 8D,E). Immunostaining of PYGM/Myophosphorylase, an enzyme involved in glycogenolysis [81], revealed that it is expressed in all lens cells at E16.5 although it was more abundant in the lens epithelium, while its expression was significantly decreased in the *Atf4* null lens (Figure 8D,F) consistent with the observed 2.8-fold downregulation of its mRNA levels in the mutant lens.

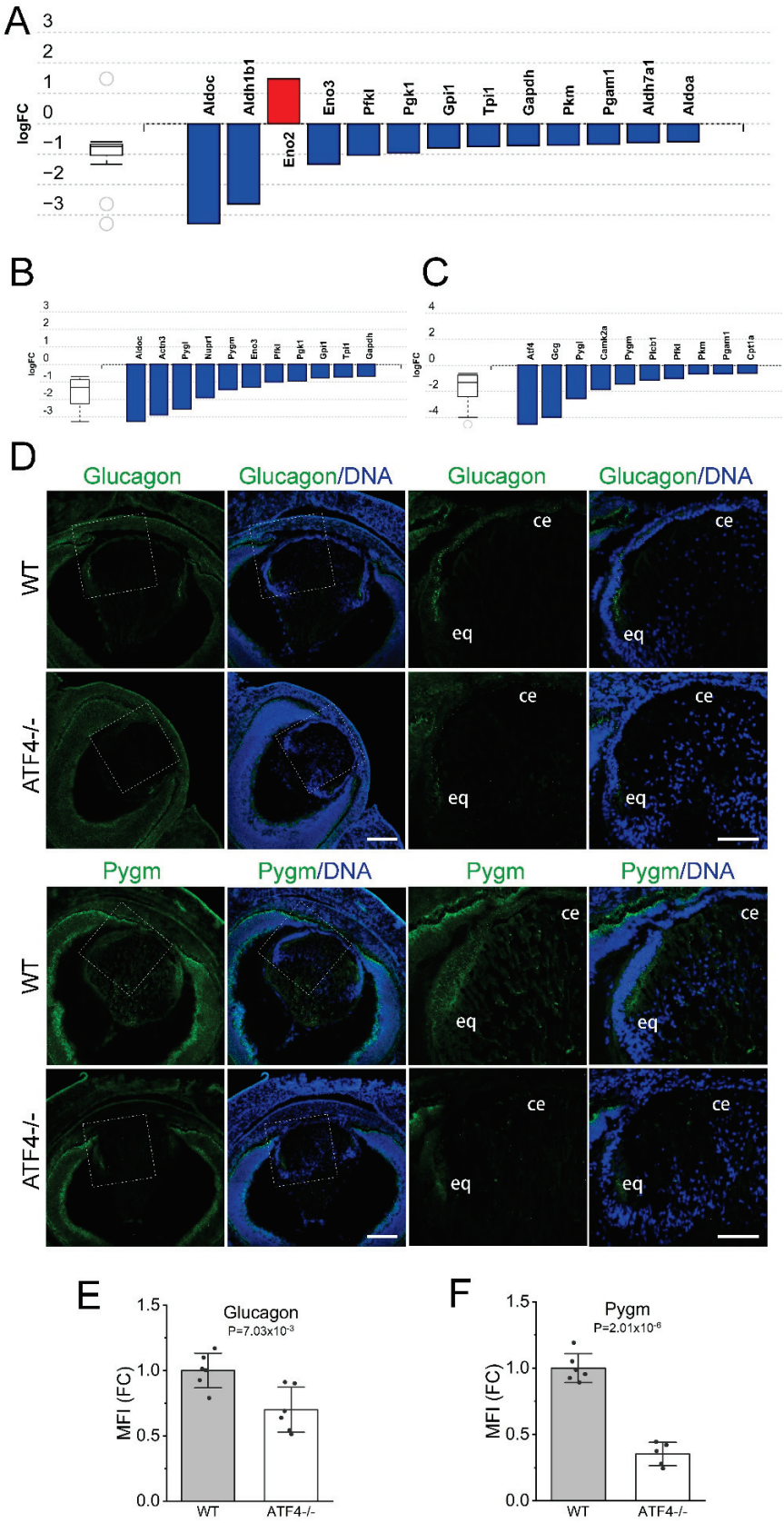

Figure 8. *Atf4* null lenses may have altered sugar metabolism compared to wild type. (**A**) Advaita iPathway guide analysis shows that *Atf4* null DEGs are over-represented in mRNAs encoding regulators of glycolysis/gluconeogenesis. (**B**) Several mRNAs encoding enzymes that function in

carbohydrate catabolism are differentially expressed in the *Atf4* null lens. (**C**) The levels of several mRNAs encoding proteins participating in the glucagon pathway are reduced in *Atf4* null lenses. (**D**) Immunostaining of E16.5 wildtype and *Atf4* null lens for glucagon (green) that is encoded by the *Gcg* gene and glycogen phosphorylase (muscle form, green) encoded by *Pygm* counterstained with Draq5 to detect DNA (blue). Images on the left were generated from a 3 × 3 tile scan with a 20× objective (scale bar = 200 μm), and the boxed region is shown in a zoomed-in view on the right (scale bar = 100 μm). *Abbreviations:* ce, central epithelium; eq, equator. (**E**) Quantification of the mean fluorescent staining intensity of glucagon immunostaining in the E16.5 wildtype (n = 6) and *Atf4* null (n = 6) lens. (**F**) Quantification of the mean fluorescent staining intensity of PYGM immunostaining in the E16.5 wildtype (n = 6) and *Atf4* null (n = 6) lens.

3.9. Only Portions of the Autophagy Pathway Are Induced in the Atf4 Null Lens

The reduced expression of genes involved in nutrient transport and utilization with concomitant reductions in free amino acid levels suggest that the E16.5 *Atf4* null lens is experiencing nutrient deprivation, a situation that would be expected to trigger autophagy via the eIF2α/ATF4 pathway [25]. Since ATF4 is not available in the *Atf4* null lens to drive that function, it is not unexpected that iPathway guide analysis of pathways impacted by *Atf4* deletion only found that 8/132 genes of the pathway "animal autophagy" were affected, and this relationship was not statistically significant (p = 0.66). However, P62 (encoded by the *Sqstm1* gene), a common marker of autophagy, was 2.9-fold upregulated in the *Atf4* null lens. This may reflect the 9-fold upregulation of *Ddit3* mRNA in the *Atf4* lens as this gene encodes CHOP, a transcription factor that is a direct transcriptional regulator of *Sqstm1* (p62) gene expression [25]. As expected, immunolocalization revealed little to no detectable P62 staining in the wildtype lens; however, we found that P62 protein levels were also significantly upregulated in the E16.5 *Atf4* null lens, particularly in the transition zone (Figure 2A,C). As the impairment of autophagy results in elevated steady-state P62 protein levels as the protein is degraded during the autophagy process [82], it is possible that this reflects either inefficient autophagy due to the lack of ATF4-mediated induction of autophagy genes or perhaps induction of P62 levels due to other cellular stress responses [83]. As autophagy also requires cap-independent translation via eIF2α phosphorylation, we also evaluated eIF2α levels and activation in the *Atf4* null lens. RNAseq analysis of EIF2S1 expression (the gene that encodes eIF2α) revealed that the wildtype and *Atf4* null lens express similar levels of its mRNA (27 vs. 29 FPKM; Supplemental Table S1). In contrast, immunolocalization of eIF2α protein found that the epithelial cells of the transition zone had modest, but significantly upregulated, levels in the *Atf4* null lens (Figure 2B,D). However, the levels of eIF2α phosphorylation on Ser51, which regulates its function in translational initiation, were not significantly changed in *Atf4* null lenses (Figure 2B,E).

4. Discussion

The lens is a unique cellular structure that has numerous structural and biochemical specializations that mediate its transparency and the high refractive index necessary for its function [1]. While our understanding of the key cell signaling cascades and transcription factors that regulate the cell fate decisions driving its early development from the head ectoderm is derived from intensive study over the past 30 years, much less is known about the regulation of key events driving the maturation of the lens into its final functional form. Notably, while the transcription factor ATF4 was first reported to play a critical role in late embryonic lens cell survival over 25 years ago [30], neither its position in the gene regulatory network driving lens development nor its function in the lens had been previously explored. This report seeks to close those knowledge gaps.

4.1. ATF4 as a Component of the Gene Regulatory Network (GRN) Regulating Lens Development

Atf4 mRNA expression has been reported to be epithelial-preferred in E14.5 mouse lenses via in situ hybridization [29]; however, bulk RNAseq profiling indicates that *Atf4*

mRNA is approximately 2-fold more abundant in mouse lens fibers than LECs [22,84]. ATF4 protein is detectable in all embryonic lens cells at E11.5, then decreases in lens fibers after E13.5 while remaining high in LECs [48]. Interrogation of previously reported gene expression profiles performed on lenses lacking key lens transcription factors revealed that *Atf4* mRNA was only downregulated 1.5-fold in *Prox1* null lenses [12], while *Atf4* expression was unaltered in lenses homozygous for *Hsf4* [73], homozygous for *Sip1* [56], or heterozygous for *Pax6* mutations [85]. In contrast, *Atf4* mRNA levels are induced 2.5-fold in 56-day-old *Klf4* null lenses, although they are unchanged in E16.5 *Klf4* nulls [86], the timepoint where the *Atf4* null phenotype manifests. Inspection of the DEG list from E16.5 *Atf4* null lenses revealed that the expression levels of genes encoding the vast majority of transcription factors known to regulate lens development including *Pax6*, *Prox1*, *Pitx3*, *cMaf*, *Ap2α*, *Sox2*, *Meis1/2*, and *Hsf4* were unaffected demonstrating that ATF4 is likely not upstream of these genes in the lens GRN. A notable exception to this observation was that the mRNA encoding the transcription factor *FoxE3*, a regulator of both early lens development and later lens epithelial phenotype [16,17], was 4.7-fold downregulated in the *Atf4* null lens. While this could indicate that ATF4 regulates the *FoxE3* gene directly, the late onset of the *Atf4* null lens phenotype compared to that of *FoxE3* mutants suggests that the loss of *FoxE3* expression is secondary to the apoptotic loss of the lens epithelium/induction of alpha-smooth muscle actin expression in *Atf4* nulls. Overall, these observations and the grossly normal initial morphogenesis of the *Atf4* null lens suggest that this gene is regulated independently of the GRN controlling early lens development.

4.2. ATF4 Appears to Not Regulate Developmental UPR in the Lens

ATF4 is a known regulator of the unfolded protein response (UPR), a molecular mechanism that fine-tunes the folding capacity of the endoplasmic reticulum (ER) to the flux of proteins transiting the secretory pathway in normal cells [87]. In cells unable to achieve this balance due to the presence of "unfoldable" mutant proteins or other failures of ER quality control, ATF4 participates with the other arms of the UPR pathway to trigger apoptotic pathways [26]. In the lens, modest UPR pathway activation was detected during normal lens development [48], while the presence of high levels of chronically unfoldable protein leads to activation of all three UPR arms, including elevated levels of ATF4 protein, elevation of UPR markers such a BIP, and low levels of apoptosis [49]. In contrast, we show here that while lenses lacking ATF4 undergo apoptosis, bioinformatic predictions did not reveal UPR as an enriched pathway in *Atf4* null lenses, and BIP (*HspA5*) mRNA levels are not altered even though its protein levels are modestly attenuated. Unexpectedly, *Atf4* null lenses exhibit a 9-fold elevation in *Ddit3/Chop* mRNA levels even though ATF4 is a known activator of *Ddit3* transcription during the UPR [52]. While elevations in *Ddit3* expression may explain why *Atf4* null lenses undergo apoptosis as it is considered a pro-apoptotic transcription factor [88], CHOP protein levels appear unaltered.

4.3. ATF4 Likely Regulates Genes Involved in Amino Acid Transport and Glutathione Pathways in Lens

ATF4 is selectively translated in cancer cells in response to amino acid starvation during the integrated stress response (ISR) via the action of the protein kinase GCN2 (encoded by the *Eif2ak4* gene) that senses low cellular amino acid levels. The newly produced ATF4 then transcriptionally activates numerous genes involved in amino acid homeostasis including those involved in amino acid synthesis and transport [27,89]. ATF4 production can also be induced by the activation of the mTORC1 complex that promotes both protein and glutathione synthesis in conditions conducive to cell growth although mTORC1-induced ATF4 only regulates a subset of the genes compared to ISR-induced ATF4 expression, predominately those involved in amino acid metabolism and aminoacyl tRNA synthesis [90].

Here we found that at least one major ATF4 function during lens development is the regulation of cellular amino acid levels and protein synthesis as *Atf4* null lenses exhibit

reduced levels of mRNAs encoding numerous proteins involved in amino acid synthesis and transport as well as critical regulators of t-RNA charging and glutathione metabolism. Notably, a comparison of the *Atf4* null lens DEGs with the Chip-Atlas database [76,91] revealed that many of the DEGs in the *Atf4* null lens are direct ATF4 target genes in other cellular contexts. These defects in gene expression likely explain the observation that *Atf4* null lenses have significant reductions in free amino acid, glutathione, and total protein content.

4.4. ATF4 Likely Functions to Metabolically Adapt the Lens to Its Avascular Environment

The ocular lens must remain avascular throughout life as the presence of blood/blood vessels in the optical axis would prevent light transmission to the retina although the lenses of most species are much larger than the maximum diameter that most cellular organoids/tissues/cancers can reach without a blood supply [92]. Notably, E16.5, the stage where the *Atf4* null mouse lens becomes phenotypically abnormal, is approximately 800 microns in diameter, while the center of avascular tumor organoids that have reached this size is typically apoptotic/necrotic due to nutrient deprivation and tissue hypoxia [93] (Figure 9A). The lens can function without a vasculature because it has evolved an intrinsic circulatory system in which sodium/potassium ATPase activity in the lens epithelium provides a motive force to move water and small nutrients/metabolites through the pericellular space while high levels of gap junctional coupling between lens fiber cells allow movement of small molecules within the fiber cells themselves [8].

However, even with an active lens circulation, it would be expected that the increasing diameter of the lens during embryonic development, along with the regression of the lens-associated tunica vasculosa lentis (which has begun by birth in mice) [94], would result in a drop in free amino acid levels and an increase in uncharged tRNAs within lens cells, potentially leading to the activation of GCN2 and subsequent translation of ATF4. This would result in the elevated expression of numerous nutrient transporters and amino acid biosynthesis enzymes while increasing the efficiency of tRNA charging by increasing the synthesis of tRNA synthetases that would collaborate to allow the lens to synthesize the high concentrations of protein needed for its refractive function (Figure 9B). As *Atf4* null lenses show reduced amino acid and protein levels, an increase in the autophagy marker P62, and finally disintegrate by birth via apoptosis, it is likely that ATF4 is critical for lenses to effectively adapt to their low-nutrient environment. Future studies are needed to determine whether *Atf4* is regulated by GCN2, mTORC1, or a combination of these pathways to increase the efficiency of nutrient transport in the lens as it outgrows the ability to bring in nutrients via diffusion.

Most ATP production in the adult lens is produced by glycolysis, likely due to the intrinsic hypoxia of the lens environment [95]. While genes mapping to the gene ontology terms related to "hypoxia" are not over-represented among the *Atf4* null DEGs, numerous genes encoding proteins important for glycolysis are expressed at lower levels in *Atf4* null lenses than littermate controls, a result consistent with prior reports that ATF4 mediates stress-induced shifts towards glycolytic metabolism in other cell types [96,97]. Notably, HIF1a, the canonical transcription factor mediating survival of hypoxic cells, is also abundant in the lens and necessary for postnatal lens survival and growth in mice [98,99] and lens fiber cell denucleation in chickens [100]. Both ATF4 and HIF1a pathways are often activated during cellular stress responses [101], and like HIF1a, ATF4 levels are oxygen-sensitive due to interactions with the PHD3 oxygen sensor [102]. However, the regulatory relationship between ATF4 and HIF1a is likely complex and may be cell-type-dependent. For instance, HIF1a blocks ATF4 expression in early cardiomyocytes even in the presence of cellular stress by binding to the *Atf4* promoter [103], while ATF4 and HIF1a proteins may physically interact in adult cardiomyocytes potentially enhancing hypoxia-induced cell death [104].

Notably, *Hif1a* mRNA levels are not altered in *Atf4* null lenses and treatment of chicken lens epithelial cells with an activator of HIF1α pathways induced the expression of numer-

ous genes associated with glycolysis without altering *Atf4* mRNA levels [105]. This suggests that HIF1α and ATF4 may function independently to establish glycolytic metabolism in the lens to sustain cellular ATP levels as the growing lens becomes increasingly hypoxic. Additional investigations will be required to determine whether ATF4 function in the lens is primarily related to establishing the needed amounts of nutrient transporter and glycolytic enzyme expression in the avascular lens or also helps the lens adapt to a low-oxygen environment in collaboration with Hif1α.

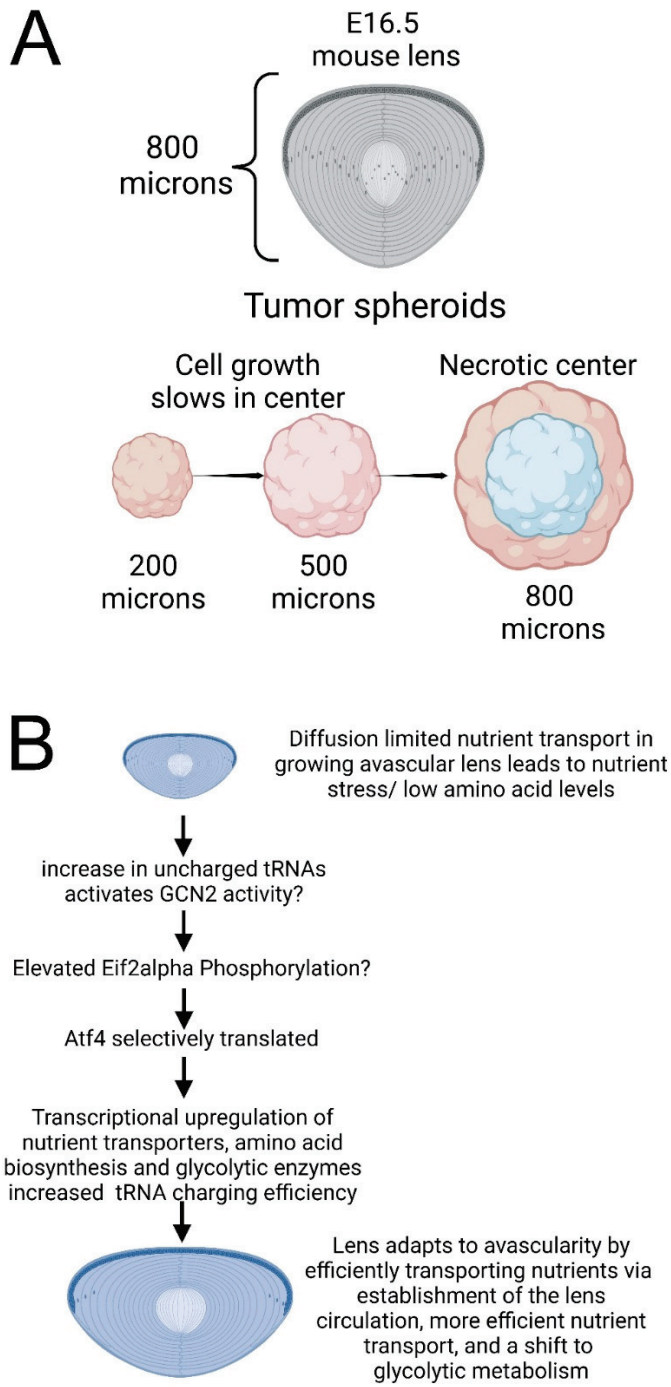

Figure 9. *Atf4* likely functions to metabolically adapt the lens to its avascular environment. (**A**) The normal embryonic mouse lens can grow to 800 microns in diameter by E16.5 without an invasive vasculature, while the center of avascular tumor organoids that have reached this size is typically

apoptotic/necrotic due to nutrient deprivation [106,107]. (**B**) Increasing the diameter of the embryonic lens along with the regression of the lens-associated tunica vasculosa lentis leads to nutrient stress/low amino acid levels, likely resulting in increases in uncharged tRNAs triggering the activation of GCN2 that results in selective translation of ATF4, so it can mediate transcriptional upregulation of nutrient transporters as well as amino acid biosynthesis and glycolytic enzymes, eventually increasing nutrient supply and tRNA charging efficiency. In conclusion, the lens adapts to avascularity by efficiently transporting nutrients via the establishment of the lens circulation, more efficient nutrient transport, and an ability to make ATP in a low-oxygen environment. Figure produced with Biorender.

5. Conclusions and Outstanding Questions

ATF4 is a transcription factor important for lens biology that likely acts independently of the classic lens development GRN to mediate the adaption of the lens to the nutrient deprivation resulting from its avascularity. It is currently unknown how *Atf4* transcript levels are regulated in the developing lens, the precise time point in lens development when ATF4 function becomes necessary, the key mechanisms that fine-tune its function to drive appropriate lens amino acid levels, or whether/how it interfaces with HIF1a during adaption of the lens to chronic tissue hypoxia. Notably, *Atf4* mRNA levels also upregulate sharply in lens epithelial cells by 6 h after lens injury and remain elevated for several days, while *Hif1a* mRNA levels decrease in injured LECs over this same time frame [22,61,108,109]. As ATF4 is best known as a mediator of cellular responses to acute stress in other tissues [26], the lens may be an ideal system to investigate how the diverse functions of Atf4 are differentially regulated during both normal tissue development and as a consequence of injury responses.

Supplementary Materials: The following supporting information can be downloaded at https://www.mdpi.com/article/10.3390/cells12222636/s1, Figure S1: Hematoxylin and eosin staining of the E14.5 wildtype and *Atf4* null lens. Figure S2: Expression of BiP, CHOP, and XBP1 protein in the E16.5 *Atf4* null lens. Figure S3: *Atf4* null lenses differentially regulate many genes and lack *Atf4* expression. Figure S4: The *Atf4* null lenses have reduced free amino acid pools when measured on a per lens basis; Table S1: Genes that are differentially expressed in the E16.5 *Atf4* null lens. Table S2: Genes that are differentially expressed in the E16.5 *Atf4* null lens which are predicted to be lens-enriched by iSyTE. Table S3: Genes that are differentially expressed in the E16.5 *Atf4* null lens that are also differentially expressed in the E13.5 *Prox1* null lens. Table S4: Genes that are differentially expressed in the E16.5 *Atf4* null lens that normally change expression in the lens between E13.5 and E15.5. Table S5: Genes that are differentially expressed in the E16.5 *Atf4* null lens that have experimentally determined ATF4 binding sites in their 5′ flanking sequence. Table S6: Detailed immunostaining conditions for the antibodies used in this study.

Author Contributions: Conceptualization, J.X., D.W.-C.L. and M.K.D.; Methodology, J.X., A.P.F., Y.W., S.G.N. and M.K.D.; Software, A.J.P. and A.P.F.; Validation, J.X.; Formal analysis, J.X., A.J.P. and A.P.F.; Investigation, J.X., A.J.P., Y.W. and S.G.N.; Data curation, A.J.P. and A.P.F.; Writing—original draft, J.X. and M.K.D.; Writing—review & editing, J.X., A.J.P., D.W.-C.L. and M.K.D.; Visualization, J.X., A.J.P. and M.K.D.; Supervision, M.K.D.; Project administration, M.K.D.; Funding acquisition, D.W.-C.L. and M.K.D. All authors have read and agreed to the published version of the manuscript.

Funding: The experiments described were supported by National Eye Institute grants EY028597-01 and EY015279-18 to M.K.D. J.X. was partially supported by a joint PhD student scholarship provided by the China Scholarship Council grant number 201806720017. The LSM 780 confocal microscope used in these studies was acquired with an S10 equipment grant S10RR027273-01 administered via the Delaware Bioimaging Center that is supported by the Delaware INBRE program (P20 GM103446). Bioinformatic analysis was performed on the BioMix compute cluster housed in the Delaware Biotechnology Institute that is supported by the State of Delaware and the Delaware INBRE program grant P20 GM103446. Amino acid analysis was performed by the University of Delaware Mass spectrometry core administered by the Center for Biomedical Research Excellence in Discovery of Molecular Probes and Therapeutic Leads that is supported by NIGMS grant P20GM104316. Histology presented in Supplemental Figure S1 was performed by the Histology Core of the Center

for Biomedical Research Excellence-Delaware Center for Musculoskeletal Research that is supported by NIGMS grant P20GM139760.

Institutional Review Board Statement: The animal protocol was approved by the Institutional Animal Care and Use Committee (IACUC) of The University of Delaware (protocol 1039 approved 12/1/2021).

Informed Consent Statement: Not applicable, not human subjects research.

Data Availability Statement: RNAseq data produced in this study have been deposited in the Gene Expression Omnibus under accession number GSE206760.

Acknowledgments: We are grateful to Timothy Townes (University of Alabama, Birmingham) for providing the *Atf4* null allele used in this study. Salil A. Lachke and Shaili Patel (Biological Sciences Department, University of Delaware) provided helpful advice on analysis methods for the embryonic lens, while PapaNii Asare-Okai and Yanbao Yu (Center for Biomedical Research Excellence in Therapeutic Leads, Mass Spectrometry Core, Department of Chemistry and Biochemistry, University of Delaware) provided advice on methods to analyze free amino acids in tissue and ran the LC-MS analyses and Charles Reilly (Delaware Center for Musculoskeletal Research, University of Delaware) performed histological analyses.

Conflicts of Interest: The authors declare no conflict of interest.

References

1. Bassnett, S.; Shi, Y.; Vrensen, G.F. Biological glass: Structural determinants of eye lens transparency. *Philos. Trans. R. Soc. Lond. B Biol. Sci.* **2011**, *366*, 1250–1264. [CrossRef]
2. Cvekl, A.; Zhang, X. Signaling and Gene Regulatory Networks in Mammalian Lens Development. *Trends Genet.* **2017**, *33*, 677–702. [CrossRef]
3. Kuszak, J.R. The ultrastructure of epithelial and fiber cells in the crystalline lens. *Int. Rev. Cytol.* **1995**, *163*, 305–350.
4. Duncan, M.K.; Cvekl, A.; Kantorow, M.; Piatigorsky, J. Lens crystallins. In *Development of the Ocular Lens*; Lovicu, F.J., Robinson, M.L., Eds.; Cambridge University Press: Cambridge, UK, 2004; 416p.
5. Cvekl, A.; McGreal, R.; Liu, W. Lens Development and Crystallin Gene Expression. *Prog. Mol. Biol. Transl. Sci.* **2015**, *134*, 129–167. [CrossRef]
6. Brennan, L.; Costello, M.J.; Hejtmancik, J.F.; Menko, A.S.; Riazuddin, S.A.; Shiels, A.; Kantorow, M. Autophagy Requirements for Eye Lens Differentiation and Transparency. *Cells* **2023**, *12*, 475. [CrossRef] [PubMed]
7. Bassnett, S. Lens organelle degradation. *Exp. Eye Res.* **2002**, *74*, 1–6. [CrossRef] [PubMed]
8. Mathias, R.T.; Kistler, J.; Donaldson, P. The lens circulation. *J. Membr. Biol.* **2007**, *216*, 1–16. [CrossRef]
9. Cvekl, A.; Zhao, Y.; Mcgreal, R.; Xie, Q.; Gu, X.; Zheng, D. Evolutionary Origins of Pax6 Control of Crystallin Genes. *Genome Biol. Evol.* **2017**, *9*, 2075–2092. [CrossRef]
10. Ashery-Padan, R.; Marquardt, T.; Zhou, X.; Gruss, P. Pax6 activity in the lens primordium is required for lens formation and for correct placement of a single retina in the eye. *Genes Dev.* **2000**, *14*, 2701–2711. [CrossRef]
11. Kamachi, Y.; Uchikawa, M.; Tanouchi, A.; Sekido, R.; Kondoh, H. Pax6 and SOX2 form a co-DNA-binding partner complex that regulates initiation of lens development. *Genes Dev.* **2001**, *15*, 1272–1286. [CrossRef] [PubMed]
12. Audette, D.S.; Anand, D.; So, T.; Rubenstein, T.B.; Lachke, S.A.; Lovicu, F.J.; Duncan, M.K. Prox1 and fibroblast growth factor receptors form a novel regulatory loop controlling lens fiber differentiation and gene expression. *Development* **2016**, *143*, 318–328. [CrossRef] [PubMed]
13. Wigle, J.T.; Chowdhury, K.; Gruss, P.; Oliver, G. Prox1 function is crucial for mouse lens-fibre elongation. *Nat. Genet.* **1999**, *21*, 318–322. [CrossRef]
14. Kim, J.I.; Li, T.; Ho, I.C.; Grusby, M.J.; Glimcher, L.H. Requirement for the c-Maf transcription factor in crystallin gene regulation and lens development. *Proc. Natl. Acad. Sci. USA* **1999**, *96*, 3781–3785. [CrossRef]
15. Kawauchi, S.; Takahashi, S.; Nakajima, O.; Ogino, H.; Morita, M.; Nishizawa, M.; Yasuda, K.; Yamamoto, M. Regulation of Lens Fiber Cell Differentiation by Transcription Factor c-Maf. *J. Biol. Chem.* **1999**, *274*, 19254–19260. [CrossRef] [PubMed]
16. Blixt, A.; Mahlapuu, M.; Aitola, M.; Pelto-Huikko, M.; Enerbäck, S.; Carlsson, P. A forkhead gene, FoxE3, is essential for lens epithelial proliferation and closure of the lens vesicle. *Genes Dev.* **2000**, *14*, 245–254. [CrossRef]
17. Brownell, I.; Dirksen, M.; Jamrich, M. Forkhead Foxe3 maps to the dysgenetic lens locus and is critical in lens development and differentiation. *Genesis* **2000**, *27*, 81–93. [CrossRef] [PubMed]
18. Anand, D.; Lachke, S.A. Systems biology of lens development: A paradigm for disease gene discovery in the eye. *Exp. Eye Res.* **2017**, *156*, 22–33. [CrossRef]
19. De Maria, A.; Bassnett, S. Birc7: A Late Fiber Gene of the Crystalline Lens. *Investig. Ophthalmol. Vis. Sci.* **2015**, *56*, 4823–4834. [CrossRef]

20. Cvekl, A.; Ashery-Padan, R. The cellular and molecular mechanisms of vertebrate lens development. *Development* **2014**, *141*, 4432–4447. [CrossRef]
21. Hejtmancik, J.F.; Beebe, D.C.; Ostrer, H.; Piatigorsky, J. d- and b-crystallin mRNA levels in the embryonic and posthatched chicken lens: Temporal and spatial changes during development. *Dev. Biol.* **1985**, *109*, 72–81. [CrossRef] [PubMed]
22. Faranda, A.P.; Shihan, M.H.; Wang, Y.; Duncan, M.K. The aging mouse lens transcriptome. *Exp. Eye Res.* **2021**, *209*, 108663. [CrossRef]
23. Reddy, T.R.; Tang, H.; Li, X.; Wong-Staal, F. Functional interaction of the HTLV-1 transactivator Tax with activating transcription factor-4 (ATF4). *Oncogene* **1997**, *14*, 2785–2792. [CrossRef] [PubMed]
24. Mahor, D.; Pandey, R.; Bulusu, V. TCA cycle off, ATF4 on for metabolic homeostasis. *Trends Biochem. Sci.* **2022**, *47*, 558–560. [CrossRef] [PubMed]
25. B'chir, W.; Maurin, A.C.; Carraro, V.; Averous, J.; Jousse, C.; Muranishi, Y.; Parry, L.; Stepien, G.; Fafournoux, P.; Bruhat, A. The eIF2α/ATF4 pathway is essential for stress-induced autophagy gene expression. *Nucleic Acids Res.* **2013**, *41*, 7683–7699. [CrossRef] [PubMed]
26. Wortel, I.M.N.; Van Der Meer, L.T.; Kilberg, M.S.; Van Leeuwen, F.N. Surviving Stress: Modulation of ATF4-Mediated Stress Responses in Normal and Malignant Cells. *Trends Endocrinol. Metab.* **2017**, *28*, 794–806. [CrossRef]
27. Rasmussen, B.B.; Adams, C.M. ATF4 Is a Fundamental Regulator of Nutrient Sensing and Protein Turnover. *J. Nutr.* **2020**, *150*, 979–980. [CrossRef]
28. Masuoka, H.C.; Townes, T.M. Targeted disruption of the activating transcription factor 4 gene results in severe fetal anemia in mice. *Blood* **2002**, *99*, 736–745. [CrossRef]
29. Hettmann, T.; Barton, K.; Leiden, J.M. Microphthalmia due to p53-mediated apoptosis of anterior lens epithelial cells in mice lacking the CREB-2 transcription factor. *Dev. Biol.* **2000**, *222*, 110–123. [CrossRef]
30. Tanaka, T.; Tsujimura, T.; Takeda, K.; Sugihara, A.; Maekawa, A.; Terada, N.; Yoshida, N.; Akira, S. Targeted disruption of ATF4 discloses its essential role in the formation of eye lens fibres. *Genes Cells* **1998**, *3*, 801–810. [CrossRef]
31. Faranda, A.P.; Shihan, M.H.; Wang, Y.; Duncan, M.K. The effect of sex on the mouse lens transcriptome. *Exp Eye Res.* **2021**, *209*, 108676. [CrossRef]
32. Alizadeh, A.; Clark, J.; Seeberger, T.; Hess, J.; Blankenship, T.; FitzGerald, P.G. Characterization of a mutation in the lens-specific CP49 in the 129 strain of mouse. *Investig. Ophthalmol. Vis. Sci.* **2004**, *45*, 884–891. [CrossRef] [PubMed]
33. Reed, N.A.; Oh, D.-J.; Czymmek, K.J.; Duncan, M.K. An immunohistochemical method for the detection of proteins in the vertebrate lens. *J. Immunol. Methods* **2001**, *253*, 243–252. [CrossRef]
34. Shihan, M.H.; Novo, S.G.; Le Marchand, S.J.; Wang, Y.; Duncan, M.K. A simple method for quantitating confocal fluorescent images. *Biochem. Biophys. Rep.* **2021**, *25*, 100916. [CrossRef]
35. Krueger, F.; James, F.; Ewels, P.; Afyounian, E.; Schuster-Boeckler, B. *FelixKrueger/TrimGalore: v0.6.7*, Zenodo; CERN: Geneva, Switzerland, 2021. [CrossRef]
36. Bullard, J.H.; Purdom, E.; Hansen, K.D.; Dudoit, S. Evaluation of statistical methods for normalization and differential expression in mRNA-Seq experiments. *BMC Bioinform.* **2010**, *11*, 94. [CrossRef]
37. Durinck, S.; Moreau, Y.; Kasprzyk, A.; Davis, S.; De Moor, B.; Brazma, A.; Huber, W. BioMart and Bioconductor: A powerful link between biological databases and microarray data analysis. *Bioinformatics* **2005**, *21*, 3439–3440. [CrossRef]
38. Durinck, S.; Spellman, P.T.; Birney, E.; Huber, W. Mapping identifiers for the integration of genomic datasets with the R/Bioconductor package biomaRt. *Nat. Protoc.* **2009**, *4*, 1184–1191. [CrossRef] [PubMed]
39. Anders, S.; Pyl, P.T.; Huber, W. HTSeq—A Python framework to work with high-throughput sequencing data. *Bioinformatics* **2015**, *31*, 166–169. [CrossRef]
40. Chen, Y.; Lun, A.T.; Smyth, G.K. From reads to genes to pathways: Differential expression analysis of RNA-Seq experiments using Rsubread and the edgeR quasi-likelihood pipeline. *F1000Research* **2016**, *5*, 1438. [CrossRef]
41. McCarthy, D.J.; Chen, Y.; Smyth, G.K. Differential expression analysis of multifactor RNA-Seq experiments with respect to biological variation. *Nucleic Acids Res.* **2012**, *40*, 4288–4297. [CrossRef] [PubMed]
42. Robinson, M.D.; McCarthy, D.J.; Smyth, G.K. edgeR: A Bioconductor package for differential expression analysis of digital gene expression data. *Bioinformatics* **2010**, *26*, 139–140. [CrossRef]
43. Manthey, A.L.; Terrell, A.M.; Lachke, S.A.; Polson, S.W.; Duncan, M.K. Development of novel filtering criteria to analyze RNA-sequencing data obtained from the murine ocular lens during embryogenesis. *Genom. Data* **2014**, *2*, 369–374. [CrossRef]
44. Chan, C.P.; Kok, K.H.; Tang, H.M.; Wong, C.M.; Jin, D.Y. Internal ribosome entry site-mediated translational regulation of ATF4 splice variant in mammalian unfolded protein response. *Biochim. Biophys. Acta* **2013**, *1833*, 2165–2175. [CrossRef]
45. Kreitz, S.; Fackelmayer, F.O.; Gerdes, J.; Knippers, R. The proliferation-specific human Ki-67 protein is a constituent of compact chromatin. *Exp. Cell Res.* **2000**, *261*, 284–292. [CrossRef]
46. Wang, Y.; Terrell, A.M.; Riggio, B.A.; Anand, D.; Lachke, S.A.; Duncan, M.K. beta1-Integrin Deletion From the Lens Activates Cellular Stress Responses Leading to Apoptosis and Fibrosis. *Investig. Ophthalmol. Vis. Sci.* **2017**, *58*, 3896–3922. [CrossRef]
47. Hetz, C. The unfolded protein response: Controlling cell fate decisions under ER stress and beyond. *Nat. Rev. Mol. Cell Biol.* **2012**, *13*, 89–102. [CrossRef] [PubMed]
48. Firtina, Z.; Duncan, M.K. Unfolded Protein Response (UPR) is activated during normal lens development. *Gene Expr. Patterns* **2011**, *11*, 135–143. [CrossRef]

49. Firtina, Z.; Danysh, B.P.; Bai, X.; Gould, D.B.; Kobayashi, T.; Duncan, M.K. Abnormal expression of collagen IV in lens activates unfolded protein response resulting in cataract. *J. Biol. Chem.* **2009**, *284*, 35872–35884. [CrossRef] [PubMed]
50. Ikesugi, K.; Yamamoto, R.; Mulhern, M.L.; Shinohara, T. Role of the unfolded protein response (UPR) in cataract formation. *Exp. Eye Res.* **2006**, *83*, 508–516. [CrossRef] [PubMed]
51. Alapure, B.V.; Stull, J.K.; Firtina, Z.; Duncan, M.K. The unfolded protein response is activated in connexin 50 mutant mouse lenses. *Exp. Eye Res.* **2012**, *102*, 28–37. [CrossRef]
52. Marton, M.; Banhegyi, G.; Gyongyosi, N.; Kalman, E.E.; Pettko-Szandtner, A.; Kaldi, K.; Kapuy, O. A systems biological analysis of the ATF4-GADD34-CHOP regulatory triangle upon endoplasmic reticulum stress. *FEBS Open Bio* **2022**, *12*, 2065–2082. [CrossRef]
53. Lee, A.S. The ER chaperone and signaling regulator GRP78/BiP as a monitor of endoplasmic reticulum stress. *Methods* **2005**, *35*, 373–381. [CrossRef]
54. Averous, J.; Bruhat, A.; Jousse, C.; Carraro, V.; Thiel, G.; Fafournoux, P. Induction of CHOP Expression by Amino Acid Limitation Requires Both ATF4 Expression and ATF2 Phosphorylation. *J. Biol. Chem.* **2004**, *279*, 5288–5297. [CrossRef]
55. Piperi, C.; Adamopoulos, C.; Papavassiliou, A.G. XBP1: A Pivotal Transcriptional Regulator of Glucose and Lipid Metabolism. *Trends Endocrinol. Metab.* **2016**, *27*, 119–122. [CrossRef]
56. Manthey, A.L.; Lachke, S.A.; FitzGerald, P.G.; Mason, R.W.; Scheiblin, D.A.; McDonald, J.H.; Duncan, M.K. Loss of Sip1 leads to migration defects and retention of ectodermal markers during lens development. *Mech. Dev.* **2014**, *131*, 86–110. [CrossRef]
57. Kim, E.J.; Kho, J.H.; Kang, M.R.; Um, S.J. Active regulator of SIRT1 cooperates with SIRT1 and facilitates suppression of p53 activity. *Mol. Cell* **2007**, *28*, 277–290. [CrossRef] [PubMed]
58. Pontoriero, G.F.; Smith, A.N.; Miller, L.A.; Radice, G.L.; West-Mays, J.A.; Lang, R.A. Co-operative roles for E-cadherin and N-cadherin during lens vesicle separation and lens epithelial cell survival. *Dev. Biol.* **2009**, *326*, 403–417. [CrossRef]
59. Marcantonio, J.M.; Vrensen, G.F. Cell biology of posterior capsular opacification. *Eye* **1999**, *13*, 484–488. [CrossRef] [PubMed]
60. Simirskii, V.N.; Wang, Y.; Duncan, M.K. Conditional deletion of beta1-integrin from the developing lens leads to loss of the lens epithelial phenotype. *Dev. Biol.* **2007**, *306*, 658–668. [CrossRef] [PubMed]
61. Shihan, M.H.; Kanwar, M.; Wang, Y.; Jackson, E.E.; Faranda, A.P.; Duncan, M.K. Fibronectin has multifunctional roles in posterior capsular opacification (PCO). *Matrix Biol.* **2020**, *90*, 79–108. [CrossRef]
62. Nakahara, M.; Nagasaka, A.; Koike, M.; Uchida, K.; Kawane, K.; Uchiyama, Y.; Nagata, S. Degradation of nuclear DNA by DNase II-like acid DNase in cortical fiber cells of mouse eye lens. *FEBS J.* **2007**, *274*, 3055–3064. [CrossRef] [PubMed]
63. Song, S.; Landsbury, A.; Dahm, R.; Liu, Y.; Zhang, Q.; Quinlan, R.A. Functions of the intermediate filament cytoskeleton in the eye lens. *J. Clin. Investig.* **2009**, *119*, 1837–1848. [CrossRef]
64. Zhang, J.; Li, J.; Huang, C.; Xue, L.; Peng, Y.; Fu, Q.; Gao, L.; Li, W. Targeted knockout of the mouse betaB2-crystallin gene (Crybb2) induces age-related cataract. *Investig. Ophthalmol. Vis. Sci.* **2008**, *49*, 5476–5483. [CrossRef] [PubMed]
65. Duncan, M.K.; Xie, L.; David, L.L.; Robinson, M.L.; Taube, J.R.; Cui, W.; Reneker, L.W. Ectopic Pax6 expression disturbs lens fiber cell differentiation. *Investig. Ophthalmol. Vis. Sci.* **2004**, *45*, 3589–3598. [CrossRef] [PubMed]
66. Vasiliev, O.; Rhodes, S.J.; Beebe, D.C. Identification and expression of Hop, an atypical homeobox gene expressed late in lens fiber cell terminal differentiation. *Mol. Vis.* **2007**, *13*, 114–124.
67. Dash, S.; Dang, C.A.; Beebe, D.C.; Lachke, S.A. Deficiency of the RNA binding protein caprin2 causes lens defects and features of Peters anomaly. *Dev. Dyn.* **2015**, *244*, 1313–1327. [CrossRef]
68. Lucey, M.M.; Wang, Y.; Bustin, M.; Duncan, M.K. Differential expression of the HMGN family of chromatin proteins during ocular development. *Gene Expr. Patterns* **2008**, *8*, 433–437. [CrossRef]
69. Kakrana, A.; Yang, A.; Anand, D.; Djordjevic, D.; Ramachandruni, D.; Singh, A.; Huang, H.; Ho, J.W.K.; Lachke, S.A. iSyTE 2.0: A database for expression-based gene discovery in the eye. *Nucleic Acids Res.* **2018**, *46*, D875–D885. [CrossRef] [PubMed]
70. Lachke, S.A.; Ho, J.W.; Kryukov, G.V.; O'Connell, D.J.; Aboukhalil, A.; Bulyk, M.L.; Park, P.J.; Maas, R.L. iSyTE: Integrated Systems Tool for Eye gene discovery. *Investig. Ophthalmol. Vis. Sci.* **2012**, *53*, 1617–1627. [CrossRef]
71. Ahsan, S.; Draghici, S. Identifying Significantly Impacted Pathways and Putative Mechanisms with iPathwayGuide. *Curr. Protoc. Bioinform.* **2017**, *57*, 7.15.1–7.15.30. [CrossRef]
72. Nishimoto, S.; Kawane, K.; Watanabe-Fukunaga, R.; Fukuyama, H.; Ohsawa, Y.; Uchiyama, Y.; Hashida, N.; Ohguro, N.; Tano, Y.; Morimoto, T.; et al. Nuclear cataract caused by a lack of DNA degradation in the mouse eye lens. *Nature* **2003**, *424*, 1071–1074. [CrossRef] [PubMed]
73. He, S.; Pirity, M.K.; Wang, W.L.; Wolf, L.; Chauhan, B.K.; Cveklova, K.; Tamm, E.R.; Ashery-Padan, R.; Metzger, D.; Nakai, A.; et al. Chromatin remodeling enzyme Brg1 is required for mouse lens fiber cell terminal differentiation and its denucleation. *Epigenetics Chromatin* **2010**, *3*, 21. [CrossRef]
74. Shan, J.; Zhang, F.; Sharkey, J.; Tang, T.A.; Örd, T.; Kilberg, M.S. The C/ebp-Atf response element (CARE) location reveals two distinct Atf4-dependent, elongation-mediated mechanisms for transcriptional induction of aminoacyl-tRNA synthetase genes in response to amino acid limitation. *Nucleic Acids Res.* **2016**, *44*, 9719–9732. [CrossRef]
75. Krokowski, D.; Han, J.; Saikia, M.; Majumder, M.; Yuan, C.L.; Guan, B.J.; Bevilacqua, E.; Bussolati, O.; Broer, S.; Arvan, P.; et al. A self-defeating anabolic program leads to beta-cell apoptosis in endoplasmic reticulum stress-induced diabetes via regulation of amino acid flux. *J. Biol. Chem.* **2013**, *288*, 17202–17213. [CrossRef] [PubMed]
76. Zou, Z.; Ohta, T.; Miura, F.; Oki, S. ChIP-Atlas 2021 update: A data-mining suite for exploring epigenomic landscapes by fully integrating ChIP-seq, ATAC-seq and Bisulfite-seq data. *Nucleic Acids Res.* **2022**, *50*, W175–W182. [CrossRef] [PubMed]

77. Ghosh, A.; Vishveshwara, S. A study of communication pathways in methionyl-tRNA synthetase by molecular dynamics simulations and structure network analysis. *Proc. Natl. Acad. Sci. USA* **2007**, *104*, 15711–15716. [CrossRef] [PubMed]
78. Fan, X.; Monnier, V.M.; Whitson, J. Lens glutathione homeostasis: Discrepancies and gaps in knowledge standing in the way of novel therapeutic approaches. *Exp. Eye Res.* **2017**, *156*, 103–111. [CrossRef]
79. Varadaraj, K.; Gao, J.; Mathias, R.T.; Kumari, S.S. GPX1 knockout, not catalase knockout, causes accelerated abnormal optical aberrations and cataract in the aging lens. *Mol. Vis.* **2022**, *28*, 11–20. [PubMed]
80. Jiang, G.; Zhang, B.B. Glucagon and regulation of glucose metabolism. *Am. J. Physiol. Endocrinol. Metab.* **2003**, *284*, E671–E678. [CrossRef]
81. Tarnopolsky, M.A. Myopathies Related to Glycogen Metabolism Disorders. *Neurotherapeutics* **2018**, *15*, 915–927. [CrossRef]
82. Klionsky, D.J.; Abdelmohsen, K.; Abe, A.; Abedin, M.J.; Abeliovich, H.; Acevedo Arozena, A.; Adachi, H.; Adams, C.M.; Adams, P.D.; Adeli, K.; et al. Guidelines for the use and interpretation of assays for monitoring autophagy (3rd edition). *Autophagy* **2016**, *12*, 1–222. [CrossRef]
83. Sabbieti, M.G.; Marchegiani, A.; Sufianov, A.A.; Gabai, V.L.; Shneider, A.; Agas, D. P62/SQSTM1 beyond Autophagy: Physiological Role and Therapeutic Applications in Laboratory and Domestic Animals. *Life* **2022**, *12*, 539. [CrossRef]
84. Zhao, Y.; Zheng, D.; Cvekl, A. A comprehensive spatial-temporal transcriptomic analysis of differentiating nascent mouse lens epithelial and fiber cells. *Exp. Eye Res.* **2018**, *175*, 56–72. [CrossRef] [PubMed]
85. Xie, Q.; Yang, Y.; Huang, J.; Ninkovic, J.; Walcher, T.; Wolf, L.; Vitenzon, A.; Zheng, D.; Gotz, M.; Beebe, D.C.; et al. Pax6 interactions with chromatin and identification of its novel direct target genes in lens and forebrain. *PLoS ONE* **2013**, *8*, e54507. [CrossRef] [PubMed]
86. Gupta, D.; Harvey, S.A.; Kenchegowda, D.; Swamynathan, S.; Swamynathan, S.K. Regulation of mouse lens maturation and gene expression by Kruppel-like factor 4. *Exp. Eye Res.* **2013**, *116*, 205–218. [CrossRef]
87. Mitra, S.; Ryoo, H.D. The unfolded protein response in metazoan development. *J. Cell Sci.* **2019**, *132*, jcs217216. [CrossRef]
88. Hu, H.; Tian, M.; Ding, C.; Yu, S. The C/EBP Homologous Protein (CHOP) Transcription Factor Functions in Endoplasmic Reticulum Stress-Induced Apoptosis and Microbial Infection. *Front. Immunol.* **2018**, *9*, 3083. [CrossRef]
89. Masson, G.R. Towards a model of GCN2 activation. *Biochem. Soc. Trans.* **2019**, *47*, 1481–1488. [CrossRef] [PubMed]
90. Torrence, M.E.; MacArthur, M.R.; Hosios, A.M.; Valvezan, A.J.; Asara, J.M.; Mitchell, J.R.; Manning, B.D. The mTORC1-mediated activation of ATF4 promotes protein and glutathione synthesis downstream of growth signals. *eLife* **2021**, *10*, e63326. [CrossRef] [PubMed]
91. Oki, S.; Ohta, T.; Shioi, G.; Hatanaka, H.; Ogasawara, O.; Okuda, Y.; Kawaji, H.; Nakaki, R.; Sese, J.; Meno, C. ChIP-Atlas: A data-mining suite powered by full integration of public ChIP-seq data. *EMBO Rep.* **2018**, *19*, e46255. [CrossRef]
92. Daster, S.; Amatruda, N.; Calabrese, D.; Ivanek, R.; Turrini, E.; Droeser, R.A.; Zajac, P.; Fimognari, C.; Spagnoli, G.C.; Iezzi, G.; et al. Induction of hypoxia and necrosis in multicellular tumor spheroids is associated with resistance to chemotherapy treatment. *Oncotarget* **2017**, *8*, 1725–1736. [CrossRef] [PubMed]
93. Mueller-Klieser, W.; Freyer, J.P.; Sutherland, R.M. Influence of glucose and oxygen supply conditions on the oxygenation of multicellular spheroids. *Br. J. Cancer* **1986**, *53*, 345–353. [CrossRef]
94. Mitchell, C.A.; Risau, W.; Drexler, H.C. Regression of vessels in the tunica vasculosa lentis is initiated by coordinated endothelial apoptosis: A role for vascular endothelial growth factor as a survival factor for endothelium. *Dev. Dyn.* **1998**, *213*, 322–333. [CrossRef]
95. Hejtmancik, J.F.; Riazuddin, S.A.; McGreal, R.; Liu, W.; Cvekl, A.; Shiels, A. Lens Biology and Biochemistry. *Prog. Mol. Biol. Transl. Sci.* **2015**, *134*, 169–201. [CrossRef]
96. Luo, S.; Zhang, C.; Gao, Z.; Jiang, L.; Li, Q.; Shi, X.; Kong, Y.; Cao, J. ER stress-enhanced HMGA2 plays an important role in Cr (VI)-induced glycolysis and inhibited oxidative phosphorylation by targeting the transcription of ATF4. *Chem. Biol. Interact.* **2023**, *369*, 110293. [CrossRef] [PubMed]
97. Yang, X.; Xia, R.; Yue, C.; Zhai, W.; Du, W.; Yang, Q.; Cao, H.; Chen, X.; Obando, D.; Zhu, Y.; et al. ATF4 Regulates CD4(+) T Cell Immune Responses through Metabolic Reprogramming. *Cell. Rep.* **2018**, *23*, 1754–1766. [CrossRef]
98. Chen, Y.; Doughman, Y.Q.; Gu, S.; Jarrell, A.; Aota, S.; Cvekl, A.; Watanabe, M.; Dunwoodie, S.L.; Johnson, R.S.; van Heyningen, V.; et al. Cited2 is required for the proper formation of the hyaloid vasculature and for lens morphogenesis. *Development* **2008**, *135*, 2939–2948. [CrossRef] [PubMed]
99. Shui, Y.B.; Arbeit, J.M.; Johnson, R.S.; Beebe, D.C. HIF-1: An age-dependent regulator of lens cell proliferation. *Investig. Ophthalmol. Vis. Sci.* **2008**, *49*, 4961–4970. [CrossRef]
100. Brennan, L.; Disatham, J.; Kantorow, M. Hypoxia regulates the degradation of non-nuclear organelles during lens differentiation through activation of HIF1a. *Exp. Eye Res.* **2020**, *198*, 108129. [CrossRef] [PubMed]
101. Chen, S.; Sang, N. Hypoxia-Inducible Factor-1: A Critical Player in the Survival Strategy of Stressed Cells. *J. Cell. Biochem.* **2016**, *117*, 267–278. [CrossRef]
102. Koditz, J.; Nesper, J.; Wottawa, M.; Stiehl, D.P.; Camenisch, G.; Franke, C.; Myllyharju, J.; Wenger, R.H.; Katschinski, D.M. Oxygen-dependent ATF-4 stability is mediated by the PHD3 oxygen sensor. *Blood* **2007**, *110*, 3610–3617. [CrossRef]
103. Guimaraes-Camboa, N.; Stowe, J.; Aneas, I.; Sakabe, N.; Cattaneo, P.; Henderson, L.; Kilberg, M.S.; Johnson, R.S.; Chen, J.; McCulloch, A.D.; et al. HIF1alpha Represses Cell Stress Pathways to Allow Proliferation of Hypoxic Fetal Cardiomyocytes. *Dev. Cell* **2015**, *33*, 507–521. [CrossRef]

104. Moulin, S.; Thomas, A.; Arnaud, C.; Arzt, M.; Wagner, S.; Maier, L.S.; Pepin, J.L.; Godin-Ribuot, D.; Gaucher, J.; Belaidi, E. Cooperation Between Hypoxia-Inducible Factor 1alpha and Activating Transcription Factor 4 in Sleep Apnea-Mediated Myocardial Injury. *Can. J. Cardiol.* **2020**, *36*, 936–940. [CrossRef] [PubMed]
105. Disatham, J.; Brennan, L.; Chauss, D.; Kantorow, J.; Afzali, B.; Kantorow, M. A functional map of genomic HIF1alpha-DNA complexes in the eye lens revealed through multiomics analysis. *BMC Genom.* **2021**, *22*, 497. [CrossRef] [PubMed]
106. Kasinskas, R.W.; Venkatasubramanian, R.; Forbes, N.S. Rapid uptake of glucose and lactate, and not hypoxia, induces apoptosis in three-dimensional tumor tissue culture. *Integr. Biol.* **2014**, *6*, 399–410. [CrossRef]
107. Luk, C.K.; Sutherland, R.M. Nutrient modification of proliferation and radiation response in EMT6/Ro spheroids. *Int. J. Radiat. Oncol. Biol. Phys.* **1987**, *13*, 885–895. [CrossRef]
108. Novo, S.G.; Faranda, A.P.; Shihan, M.H.; Wang, Y.; Garg, A.; Duncan, M.K. The Immediate Early Response of Lens Epithelial Cells to Lens Injury. *Cells* **2022**, *11*, 3456. [CrossRef]
109. Shihan, M.H.; Novo, S.G.; Wang, Y.; Sheppard, D.; Atakilit, A.; Arnold, T.D.; Rossi, N.M.; Faranda, A.P.; Duncan, M.K. alphaVbeta8 integrin targeting to prevent posterior capsular opacification. *JCI Insight* **2021**, *6*, e145715. [CrossRef] [PubMed]

Disclaimer/Publisher's Note: The statements, opinions and data contained in all publications are solely those of the individual author(s) and contributor(s) and not of MDPI and/or the editor(s). MDPI and/or the editor(s) disclaim responsibility for any injury to people or property resulting from any ideas, methods, instructions or products referred to in the content.

cells

MDPI

Article

Towards the Identification and Characterization of Putative Adult Human Lens Epithelial Stem Cells

Pandi Saranya [1,2], Madhu Shekhar [3], Aravind Haripriya [4], Veerappan Muthukkaruppan [1] and Chidambaranathan Gowri Priya [1,2,*]

[1] Department of Immunology and Stem Cell Biology, Aravind Medical Research Foundation, Madurai 625020, India; saranyapandi4995@gmail.com (P.S.); muthu@aravind.org (V.M.)
[2] Department of Biotechnology, Aravind Medical Research Foundation—Affiliated to Alagappa University, Karaikudi 630003, India
[3] Cataract and IOL Services, Aravind Eye Hospital and Post Graduate Institute of Ophthalmology, Madurai 625020, India; madhushekhardr@aravind.org
[4] Intraocular Lens and Cataract Services, Aravind Eye Hospital, Chennai 600077, India; haripriya@aravind.org
* Correspondence: gowri@aravind.org

Abstract: The anterior lens epithelium has the ability to differentiate into lens fibres throughout its life. The present study aims to identify and functionally characterize the adult stem cells in the human lens epithelium. Whole mounts of lens epithelium from donor eyes (normal/cataract) were immunostained for SOX2, gap junction protein alpha 1 (GJA1), PAX6, α, β and γ-crystallins, followed by a confocal analysis. The functional property of adult stem cells was analysed by their sphere forming ability using cultured lens epithelial cells from different zones. Based on marker expression, the lens epithelium was divided into four zones: the central zone, characterized by a small population of PAX6$^+$, GJA1$^-$, β-crystallin$^-$ and γ-crystallin$^-$ cells; the germinative zone, characterized by PAX6$^+$, GJA1$^+$, β-crystallin$^-$ and γ-crystallin$^-$; the transitional zone, characterized by PAX6$^+$, GJA1$^+$, β-crystallin$^+$ and γ-crystallin$^-$; and the equatorial zone, characterized by PAX6$^{+/-}$, GJA1$^+$, β-crystallin$^+$, and γ-crystallin$^+$ cells. The putative lens epithelial stem cells identified as SOX2$^+$ and GJA1 membrane expression negative cells were located only in the central zone (1.89 ± 0.84%). Compared to the other zones, a significant percentage of spheres were identified in the central zone (1.68 ± 1.04%), consistent with the location of the putative adult lens epithelial stem cells. In the cataractous lens, an absence of SOX2 expression and a significant reduction in sphere forming ability (0.33 ± 0.11%) were observed in the central zone. The above findings confirmed the presence of putative stem cells in the central zone of the adult human lens epithelium and indicated their probable association with cataract development.

Keywords: human lens epithelial stem cells; adult tissue-resident stem cells; central zone; sphere forming ability; cataract lens

1. Introduction

The crystalline lens is an avascular, transparent biconvex structure in the eye, composed of a capsule, anterior lens epithelium, cortex and nucleus. It is entirely derived from a head epidermal ectoderm. The lens epithelium has the ability to divide and differentiate into lens fibres throughout its life and can develop into a complete lens with oriented lens fibres in vitro through neural retinal inductive tissue interactions in mice [1]. The anterior lens epithelium in animals (rat, mouse and bovine) has been divided into different zones—the central, germinative, transitional and/or equatorial zones—based on the morphology of cells [2], proliferative potential [3], expression of markers [2] and label retaining cell property (LRCs) [4]. At the equatorial zone, the meridional rows mark the boundary of the epithelium and the onset of fibre cell differentiation [5]. By tracing

pulse labelled cells, it was identified that proliferating lens epithelial cells differentiate and migrate to the meridional row [3].

Lens regeneration has been reported after a lentectomy through the transdifferentiation of dorsal iris pigment epithelial cells or the cornea [6] and through spontaneous regeneration from residual lens epithelial cells following the removal of lens contents in several mammals [7]. In human lenses, epithelial cells in the central region were identified to have regenerative potential [8]. However, very little information is available on the various zones in the adult human anterior lens epithelium.

Adult tissue-specific stem cells have been found in almost all tissues of the human body and are responsible for maintaining homeostasis throughout life. These stem cells remain quiescent and divide if needed. Functionally, adult stem cells are characterized based on their slow cycling, LRC property [4], clonal analysis [9] and sphere forming ability [10].

Stem cells have been reported in the anterior lens epithelium, but their location remains controversial. Previous studies suggest that stem cells in the lens epithelium are located in the central zone based on (i) the localization of LRCs exclusively in the central zone of the mouse anterior lens epithelium [4], (ii) the development of a complete lens from the mouse anterior lens epithelium, excluding the equatorial region [1], (iii) the in vivo regeneration of a lens-like structure in congenital cataract patients, when the integrity of the central region (the lens capsule and lens epithelium) is maintained during a minimally invasive cataract surgery [8] and (iv) the expression of ABCG2/SOX2 in the central zone of the anterior lens epithelium using capsulotomy samples from cataract patients [11]. Contradicting the above observations, Yamamoto et al. (2008) [12] proposed the presence of stem cells expressing p75NTR and proliferating cell markers (PCNA, Cyclin D1, Cyclin B1 and Cyclin A1) in the region immediately anterior to the germinative zone of the mouse anterior lens epithelium. Further, the side-population cells with low Hoechst fluorescence (both blue and red) were located around the germinative zone in the mouse anterior lens epithelium [13]. A recent review of adult ocular stem cells indicated the presence of dividing lens epithelium stem/progenitor cells only in the equatorial zone, with the ability to differentiate into lens fibres [14].

Therefore, the present study focused on identifying and functionally characterizing the stem cells for lens epithelial cells in normal as well as cataractous human lens. The adult human anterior lens epithelium was divided into four zones based on the expression of the differentiated cell marker—a gap junction protein alpha 1 (GJA1) and crystallins. Since there are no exclusive markers for adult stem cells, putative lens epithelial stem cells were identified by combining two markers: (i) the transcription factor SOX2 and (ii) a differentiated cell marker GJA1. The expression of SOX2 has been reported to activate the development of the lens vesicle from the lens pit, and the weak expression of SOX2 along with high SOX1 expression have been found to be essential for the growth of the lens epithelium and fibre differentiation [15]. SOX2-expressing adult stem cells in mice have been traced to originate from foetal SOX2-positive epithelial progenitors [16]. SOX2, when co-expressed with Oct 4, Klf4 and c-Myc, was reported to de-differentiate somatic cells to a pluripotent state [17]. Hence, SOX2 was used as a positive marker to identify lens epithelial stem cells. Since reports on human epidermal stem cells and limbal epithelial stem cells indicated that these adult stem cells do not communicate through GJA1 and the expression of GJA1 was associated with differentiation, GJA1 was included as a negative marker [9,18,19].

$SOX2^+$ cells negative for membrane GJA1 expression were defined as putative lens epithelial stem cells and were identified to be located only in the central zone of the human anterior lens epithelium. The significantly higher percentage of sphere formation (including $SOX2^+$, $GJA1^-$ and $PAX6^+$ cells) from this zone confirmed the location. In the cataractous lens epithelium, the absence of SOX2 expression in the central zone as well as a significant reduction in their sphere forming ability indicated the loss of these putative stem cells.

2. Materials and Methods

2.1. Sample Collection

The whole and excised globes (after the removal of the cornea for transplantation) from donors having phakic lenses were obtained from Rotary Aravind International Eye Bank, Aravind Eye Hospital, Madurai. The eyes were procured by the eye bank after obtaining consent from the donor's family. The inclusion criteria for the selection of tissues were (i) eyes enucleated within 6 h of death and received at the research laboratory within 24 h, (ii) donor globes with normal and cataract lenses (opacification was observed during slit lamp examination at the eye bank) and (iii) donors with no history of ocular infection or systemic disease. Eyes from donors whose cause of death was due to either poison or a snake bite were excluded from the study. The human lenses from normal—31 donors, aged 40.65 ± 14.68 (mean ± SD) years (range: 20 to 71 years) and cataract—6 donors, aged 61.3 ± 13 (mean ± SD) years (range: 50 to 82 years) were included in the study. This study adhered to the tenets of the Declaration of Helsinki and was approved by the Institutional Review Board of the Aravind Medical Research Foundation and the Institutional Committee for Stem Cell Research (IRB2018015BAS).

2.2. Human Tissue Preparation

Whole Mount of the Human Anterior Lens Epithelium

The lens was positioned with the posterior side facing up under a stereo zoom microscope (Nikon SMZ645, Tokyo, Japan), and the posterior capsule was peeled [20]. The lens fibres were then gently removed. The whole mount of lens epithelium along with the lens capsule was used for immunostaining (Figure 1).

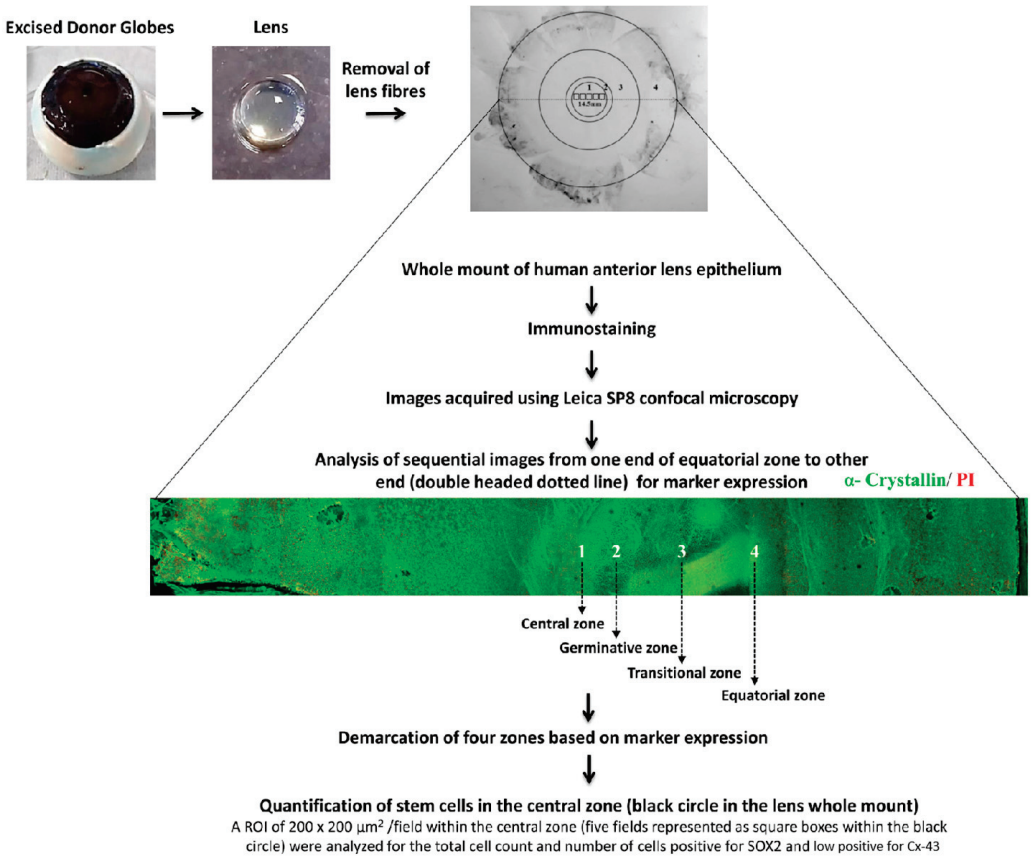

Figure 1. Characterization of human anterior lens epithelium: The human lens was dissected from the excised donor globe. After removal of the lens fibres, the whole mount of the human anterior lens

epithelium was immunostained for various markers, and images were acquired sequentially from one end of the whole mount to the other end using Leica SP8 confocal microscopy. A representative montaged confocal image of the human anterior lens epithelial whole mount immunostained for α–crystallin (FITC-green) and counterstained with propidium iodide (PI-red) is given. The four zones of the anterior lens epithelium (1-central zone; 2-germinative zone; 3-transitional zone; 4-equatorial zone) were identified based on the marker expression (Table 1). Quantification of the stem cells in the central zone (black circle) was carried out in five consecutive confocal images (represented as small black squares) using Leica software LAS AF 3.3.0.10134 (n = 3 donors). Within an ROI of 200 × 200 μm^2/image, the total number of lens epithelial cells (based on nuclear stain) and the number of $SOX2^+$ $GJA1^-$ cells were counted.

Table 1. Markers to demarcate the different zones in the human anterior lens epithelium. On the basis of the literature and the present study, the human anterior lens epithelium was identified and demarcated into four zones based on marker expression. The symbols "+", "−", and "+/−" stand for the presence of cells expressing a marker, the absence of marker expression, and both respectively.

Zones	Marker Expression									
	Based on the Literature					Present Study				
	SOX2 [16]	GJA1 [21]	β-cry [2]	γ-cry [2]	α-cry [22]	SOX2	GJA1	β-cry	γ-cry	α-cry
Central zone	−	+	−	−	+	+/−	−/+	−	−	+
Germinative zone	−	+	−	−	+	−	+	−	−	+
Transitional zone	−	+	+	−	+	−	+	+	−	+
Equatorial zone	+	+	+	+	+	−	+	+	+	+

2.3. Immunostaining

The entire anterior lens epithelium was spread on a glass slide, fixed either in 4% paraformaldehyde (PFA) (P6148, Sigma-Aldrich Corp., St. Louis, MO, USA) or methanol for 15 min and blocked with the avidin biotin blocking system. After overnight incubation at 22 °C with the primary antibody, the corresponding biotinylated secondary antibody was added and incubated for 1 h at 22 °C. Streptavidin fluorescein isothiocyanate (FITC, BD Pharmingen—San Diego, CA, USA) was added at a dilution of 1:1000 (in 1X PBS) and incubated for 1 h at 22 °C in the dark to visualize the marker. For double immunostaining, the anterior lens epithelium was incubated overnight at 22 °C with anti-connexin 43 (GJA1) antibody (the second primary antibody), followed by the corresponding biotinylated secondary antibody and streptavidin-Alexa 633 (Thermofisher Scientific—Waltham, MA, USA) at a dilution of 1:1000 in 1X PBS or with phalloidin—TRITC (1:400). Between steps, the slides were washed three times in 1X PBS, and the stained whole mounts were mounted with Vectashield mounting medium containing 4,6-diamidino-2-phenylindole (DAPI)/propidium iodide (PI) (H-1200-10/H-1300-10, Burlingame, CA, USA). During the immunostaining, the whole mount without the addition of primary antibody was used as a negative control. Primary and secondary antibodies used are listed in Table 2.

2.4. Confocal Microscopy Imaging

Acquisition of the immunostained whole mounts was carried out using a laser scanning microscope (Leica SP8 confocal microscope, Wetzlar, Germany), as previously described (Sunderasan et al., 2019) [23]. Briefly, fluorescent z-stack images were acquired using the following settings: the emission band width for DAPI ranged from 358 to 441 nm and FITC from 496 to 535 nm using laser blue 488; for PI/TRITC, from 555 to 600 nm using laser green 552, and for Alexa Fluor 633 from 640 to 725 nm using laser red 633. Using the

above-mentioned parameters, the images were acquired horizontally from one end to the other end of the whole mount of the anterior lens epithelium (Figure 1) using 10× as well as 63× objective.

Table 2. Primary and secondary antibodies used in this study.

Antibody	Species and Type	Manufacturer, City/State, Country	Catalogue Number	Dilution Factor
SOX2	Rabbit monoclonal	Abcam, Waltham, MA, USA	ab92494	1:100
Connexin-43 (GJA1)	Mouse monoclonal	BD Biosciences, Franklin Lakes, NJ, USA	610062	1:200
PAX6	Rabbit polyclonal	Proteintech, Manchester, UK	12323-1-AP	1:250
α-crystallin	Mouse monoclonal	SantaCruz Biotechnology, Dallas, TX, USA	sc-28306	1:50
β-crystallin	Mouse monoclonal	SantaCruz Biotechnology, Dallas, TX, USA	sc-374496	1:50
γ-crystallin	Mouse monoclonal	SantaCruz Biotechnology, Dallas, TX, USA	sc-365256	1:50
Phalloidin-TRITC	Synthetic: Peptide Sequence	Sigma, Saint Louis, MO, USA	P1951	1:400
anti-mouse	Goat polyclonal	Agilent, Santa Clara, CA, USA	E0433	1:200
anti-rabbit	Mouse monoclonal	SantaCruz Biotechnology, Dallas, TX, USA	sc-2491	1:200

2.5. Image Analysis

Sequential images were analysed from one end to the other end and montaged to represent the whole mount of the anterior lens epithelium (Figure 1). The total diameter of the whole anterior lens epithelium was measured horizontally using Leica Software (LAS AF 3.3.0.10134). The demarcation of four zones was carried out based on the measurement of regions positive/negative for GJA1, β-crystallin and γ-crystallin. The plasma membrane expression of GJA1 was defined by analysing the z-stack images of the positive cells (Figure S1). The putative lens epithelial stem cells were identified as cells expressing the stem cell marker/transcription factor SOX2 but negative for the membrane expression of the differentiated cell marker GJA1. For each donor tissue (n = 3 donors), five fields from the central zone were analysed for putative stem cell content. The percentage of putative lens epithelial stem cells was calculated by counting the total number of epithelial cells and the total number of putative stem cells in an ROI of 200 × 200 μm^2/field. The results were represented as the mean percentage ± standard error mean (SEM).

2.6. Lens Explant Cultures

The human anterior lens epithelial explant cultures were established from normal (n = 5) and cataractous (n = 3) human anterior lens epithelium as described by Lin et al., (2016) [8]. The whole mount of lens epithelium was prepared, and the explants were cut into 1 × 1 mm pieces from the central, germinative + transitional (since the germinative zone was too small (0.2 mm) to be separated, it was dissected with transitional zone) and

equatorial zone. Each explant was allowed to attach to a 35 mm dish (153066, Thermo Fisher Scientific, Waltham, MA, USA) coated with Matrigel (1:100) (354230, Corning, Tewksbury, MA, USA). The explants were then incubated at 37 °C for 4–6 min, and 1 mL of lens epithelial cell (LEC) medium (MEM (11095080, Gibco^{TM}, Life Technologies, Grand Island, NY, USA), 20% foetal bovine serum (10270106, Gibco^{TM}, Life Technologies, Paisley, UK), non-essential amino acid (M7145, Sigma-Aldrich, Gillingham, UK), penstrep (15140122, GibcoTM, Life Technologies, NY, USA), gentamicin (15710064, Gibco^{TM}, Life Technologies, NY, USA), SB431542 (04001010, Stemgent-REPROCELL, Beltsville, MD, USA)) was added. The growth was monitored under an inverted phase contrast microscope (Nikon Eclipse TS100, Tokyo, Japan), and the medium was changed on alternate days for two weeks.

2.7. Establishment of Lens Sphere Cultures

As described by Sundaresan et al. (2021) [24], the cultured cells were trypsinized, and 1×10^3 viable cells were seeded on ultra low attachment dishes (3471, Corning, Kennebunk, ME, USA). Further, the cells were maintained in sphere medium containing DMEM/F12 (1:1) + Glutamax^{TM} (10565018, Gibco^{TM}, Life Technologies, NY, USA), 2% B27 (17504044, Gibco^{TM}, Life Technologies, NY, USA), 20 ng/mL epidermal growth factor (PHG0311, Thermo Fisher Scientific, MA, USA), 20 ng/mL fibroblast growth factor (13256029, Gibco^{TM}, Thermo Fisher Scientific, MA, USA), 5 μg/mL heparin (375095, EMD Millipore Corp., Danvers, MA, USA), 0.1 mg/mL bovine serum albumin (B8894, Sigma), 2.5 mM L-glutamine (35050061, Gibco^{TM}, Life Technologies, NY, USA), and 250 μg/mL penicillin-streptomycin (15140122, GibcoTM, Life Technologies, NY, USA), and cultured. After 7 days of culture, spheres were imaged using an inverted phase contrast microscope (Nikon Eclipse TS-100, Tokyo, Japan) fitted with a camera, and ImageJ (https://imagej.nih.gov/ij/) (accessed on 21 November 2023) was used to determine the diameter of the spheres. For quantification, the total number of spheres $\geq$ 60 μm in diameter was counted in each dish, the percentage of spheres formed per 10^3 cells seeded was calculated, and the data were represented as mean $\pm$ SD. The statistical significance of the sphere forming ability of cultured cells from different zones was analysed by the Kruskal–Wallis test and between normal and cataract lens epithelial cells by the Wilcoxon rank sum test. Further, the lens spheres were centrifuged at 400 rpm for 3 min using a cytospin system (Thermo Shandon—Pittsburgh, PA, USA). The lens sphere cytosmears were fixed with 4% PFA, followed by immunostaining for SOX2, GJA1, and PAX6 as described under Section 2.3.

3. Results

3.1. Identification of Four Zones in Human Anterior Lens Epithelium

The demarcation of each zone was based on the expression of specific markers (Table 1). Analysis of the sequential confocal images of the immunostained lens epithelial whole mounts from one end of the equatorial zone to the other (n = 3 donor eyes/marker) identified that the gap junction protein GJA1 was expressed by all epithelial cells in the germinative, transition, and equatorial zones and only in 90.83 $\pm$ 5.9% of cells in the central zone (Figure 2B). The early elongation marker β-crystallin was positive in all cells of the transition and equatorial zones but was totally negative in the central and germinative zones (Figure 2C). The expression of the late elongation cell marker γ-crystallin was observed in all cells of the equatorial zone, while cells in the other zones were negative (Figure 2D). The neuroectodermal marker PAX6 was strongly expressed by almost all epithelial cells in the central, germinative and transitional zones and by 10.09 $\pm$ 0.12% of cells in the equatorial zone (Figure 2E). The lens epithelial marker α-crystallin was expressed by all of the epithelial cells in the four zones (Figure 2F).

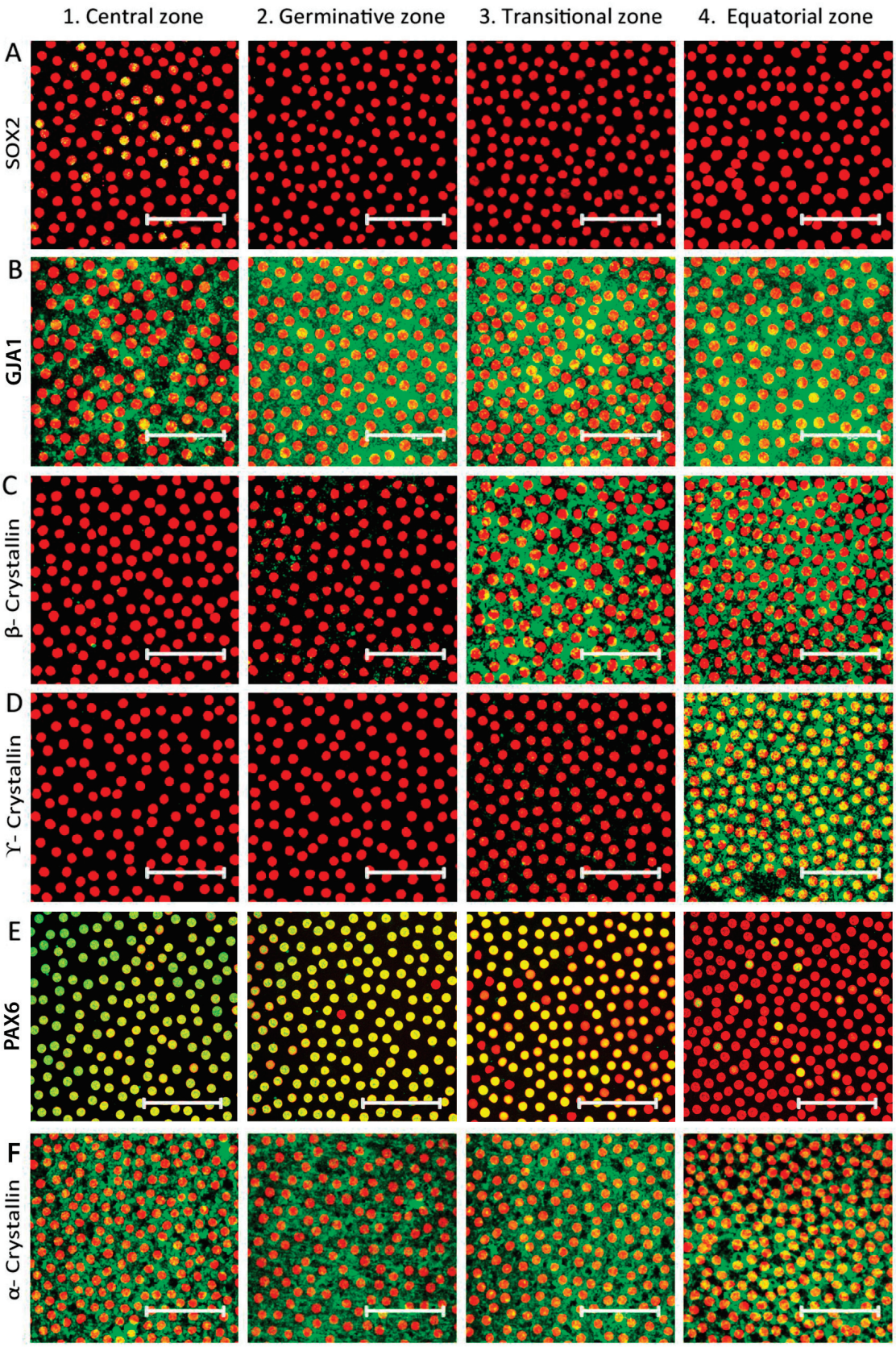

Figure 2. Identification of four zones based on specific markers in the human anterior lens epithelium. Representative confocal images of human anterior lens epithelial whole mounts immunostained for the markers (FITC-green) (**A**) SOX2, a stem cell marker, (**B**) GJA1, a differentiated cell marker, (**C**) β-crystallin, an early cell elongation marker, (**D**) γ-crystallin, late elongation marker, (**E**) PAX6,

a neuroectodermal marker and (**F**) α-crystallin, counterstained with propidium iodide (PI-red). Expression of SOX2 was observed in a few cells (green + red = yellow) in the central zone, while cells in the three other zones were negative (**A**); the presence of a small proportion of cells negative for GJA1 membrane expression, β-crystallin and γ-crystallin defined the central zone, while GJA1^{+} β-crystallin^{-} γ-crystallin^{-} cells confirmed the germinative zone (**B**); the GJA1^{+} β-crystallin^{+} γ-crystallin^{-} cells defined the transitional zone (**C**); and the equatorial zone was characterized by late elongation marker γ-crystallin (**D**). The nuclear expression of neuroectodermal marker PAX6 was observed in almost all cells from central to transition zone and only in a small population in the equatorial zone (**E**).The lens epithelial cell marker α-crystallin was expressed throughout the epithelium (**F**). Scale bar represents 50 μm.

The montaged images of the anterior lens epithelial whole mounts showed that the total length of the epithelium was 14.5 ± 0.7 mm (Figure 3). The central zone, measuring 1.66 ± 0.1 mm, included a population of GJA1^{-}, β-crystallin^{-}, γ-crystallin^{-}, and α-crystallin^{+} cells. The germinative zone, consisting of GJA1^{+}, β-crystallin^{-} and γ-crystallin^{-} cells, encompassed a region 0.2 mm peripheral to the central zone. The transitional zone with GJA1^{+}, β-crystallin^{+}, and γ-crystallin^{-} cells was identified to be 2.17 mm peripheral to the germinative zone. The equatorial zone, measuring 4.05 mm from the transitional zone, was characterized by GJA1^{+}, β-crystallin^{+} and γ-crystallin^{+} cells.

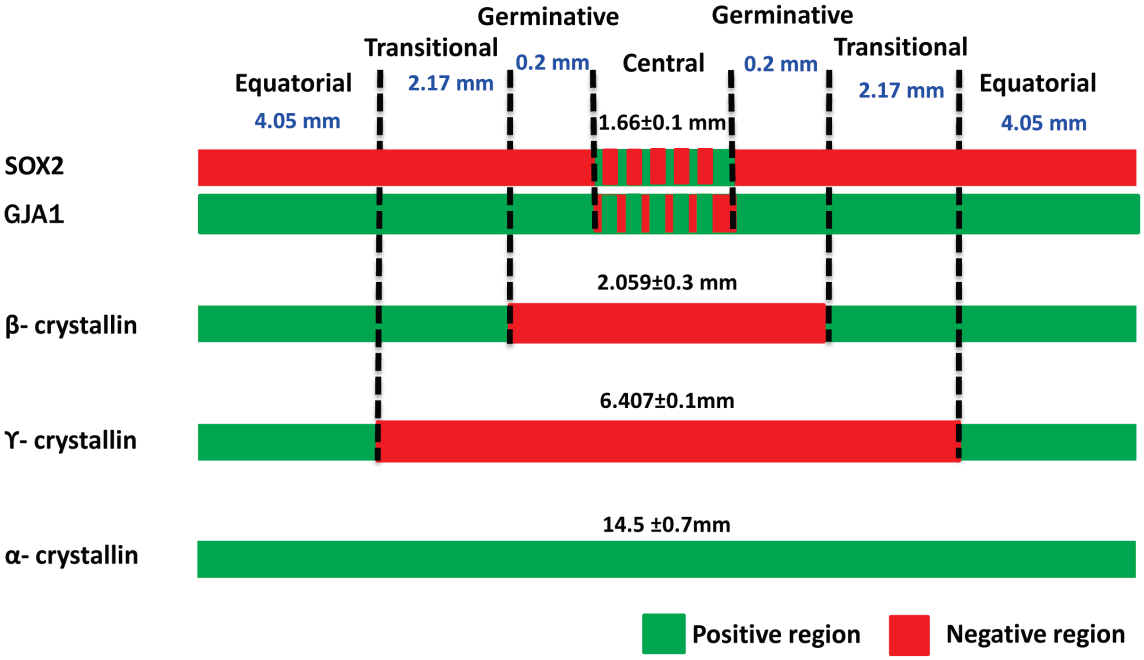

Figure 3. Characterization of four zones in the human anterior lens epithelium. Based on the expression of markers GJA1 and β-, γ- and α-crystallins in the lens epithelium, the length of the four zones was identified.

3.2. Identification and Location of Putative Adult Stem Cells in the Human Anterior Lens Epithelium

The putative adult stem cells in human lens epithelium were identified by the expression of the transcription factor SOX2. For confirmation, double immunostaining with the differentiated epithelial cell marker GJA1 was carried out (Figure 4A). The cells that expressed SOX2 and were negative for GJA1 membrane expression were defined as putative lens epithelial stem cells (Figure 4B). The sequential z-stack images of Figure 4B are given in Figure S1. Immunostaining for SOX2 and phalloidin highlighted the outline and structure of the lens epithelial cells (Figure 4C). Further, the sequential confocal images identified SOX2 expression in 9.16 ± 10.2% of cells in the central zone, while cells in the germinative,

transition and equatorial zones were all negative for this marker (Figure 2A). The presence of SOX2$^+$ GJA1$^-$ cells only in the central zone indicated that the putative stem cells for the human anterior lens epithelium are located in this region and not in other zones of the human anterior lens epithelium (Figure 4A).

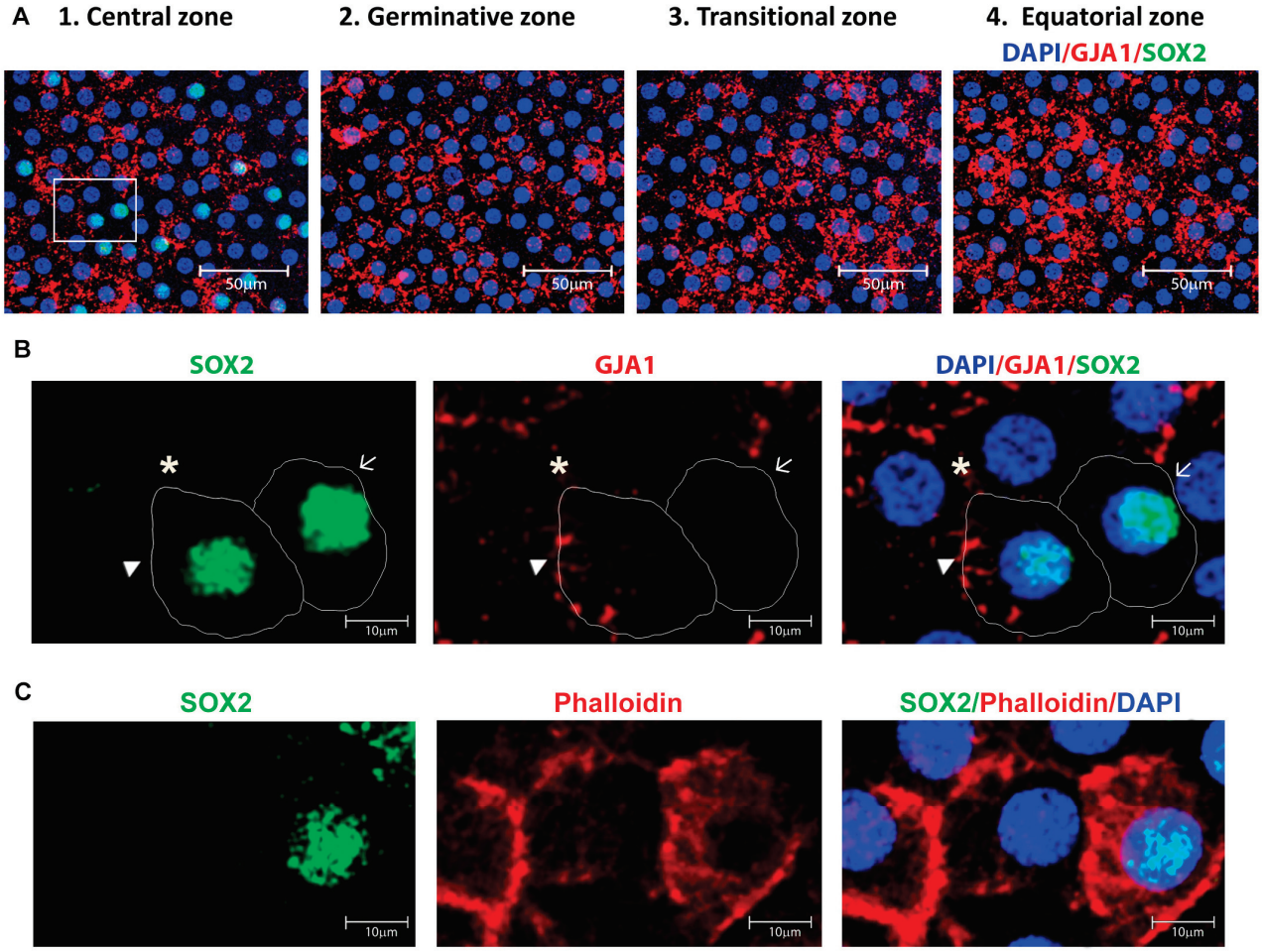

Figure 4. (**A**) Characterization of cells in the central zone of the human anterior lens epithelium. Representative confocal images of the whole mount of the human anterior lens epithelium immunostained for SOX2 (FITC-green) and GJA1 (Alexa 633-red), counterstained with 4,6-diamidino-2-phenylindole (DAPI-blue). The cells positive for SOX2 (green + blue = cyan) were present in the central zone. All of the epithelial cells in the germinative, transitional and equatorial zones were negative for SOX2 but positive for GJA1. (**B**) Higher magnification of the highlighted region (box in 4A) in the central zone indicated the presence of three populations of cells: SOX2$^+$ GJA1$^-$ cell (arrow); SOX2$^+$ GJA1$^+$ cell (arrow head) and SOX2$^-$ GJA1$^+$ cell (asterisk). The cells expressing SOX2 but negative for GJA1 were defined as putative stem cells, and such cells were restricted to the central zone. (**C**) Representative confocal imaging of the whole mount of the human anterior lens epithelium immunostained for SOX2 (FITC-green) and phalloidin (TRITC-red) highlighted the outline and structure of the lens epithelial cells.

Double immunostaining for SOX2 and GJA1 identified three populations of cells in the central zone (Figure 4B): (i) SOX2$^+$ GJA1$^-$ putative stem cells, (ii) SOX2$^+$ GJA1$^+$ cells, and (iii) SOX2$^-$ GJA1$^+$ cells. Further quantification of cells in an ROI of 200 $\times$ 200 µm^2 from five fields in the central zone per whole mount (n = 3) using ImageJ identified 1.89 $\pm$ 0.84% cells to be SOX2$^+$ GJA1$^-$ cells, 7.27 $\pm$ 5.07% to be SOX2$^+$ GJA1$^+$ cells, and the remaining 90.83 $\pm$ 5.9% to be SOX2$^-$ GJA1$^+$ cells (Table 3). All of the epithelial cells in the germinative, transition, and equatorial zones were SOX2$^-$ GJA1$^+$. Thus, the putative lens epithelial stem

cells identified as SOX2$^+$ GJA1$^-$ cells were confined to the central zone of the human lens epithelium.

Table 3. Distribution of cells expressing the stem cell marker SOX2 and differentiated epithelial cell marker GJA1 in the four zones of the whole mount of the human anterior lens epithelium. The putative stem cells, defined as SOX2$^+$ GJA1$^-$ cells, were present only in the central zone.

S. No	Zone	Percentage of Cells (Mean ± SEM) (n = 3 Donor Eyes)		
		SOX2$^+$ GJA1$^-$	SOX2$^+$ GJA1$^+$	SOX2$^-$ GJA1$^+$
1	Central zone	1.89 ± 0.84	7.27 ± 5.07	90.83 ± 5.9
2	Germinative zone	0	0	100
3	Transitional zone	0	0	100
4	Equatorial zone	0	0	100

The nuclear expression of SOX2 was absent in all of the cataract lens epithelium analysed (Figure 5A). Further, the presence of autofluorescing vacuoles (UV to far red range) was identified in a subset of cells only in the central zone of these cataractous donor lenses (Figure 5B).

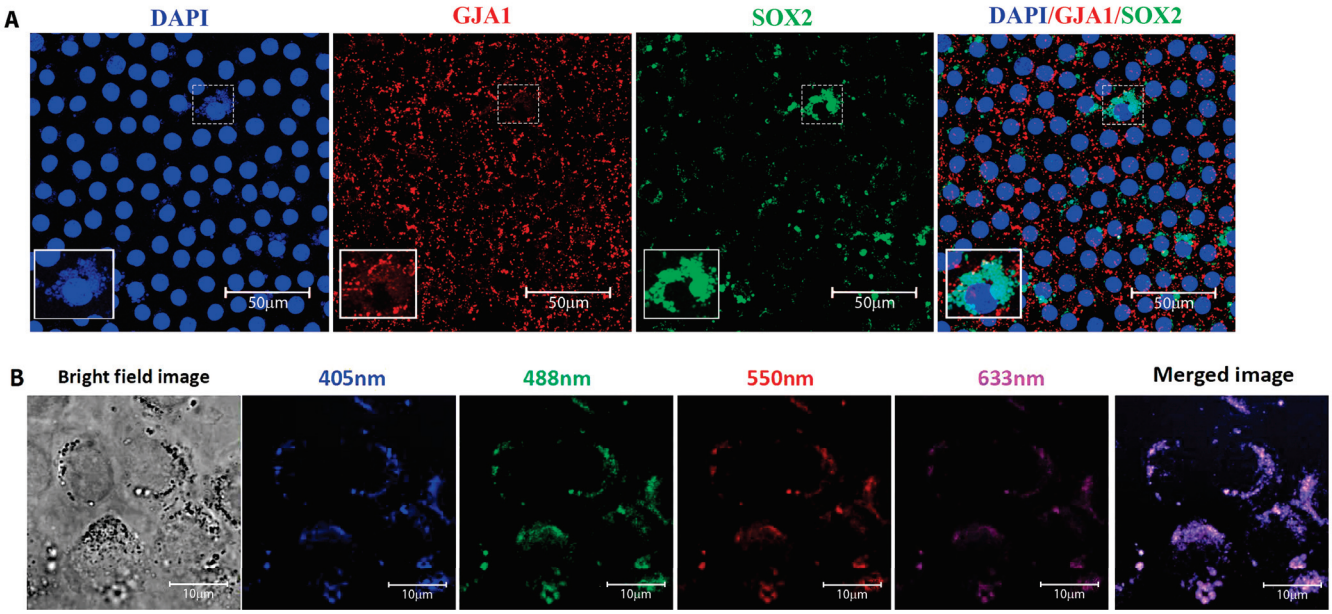

Figure 5. (**A**) Characterization of the cells in the central zone of cataractous human anterior lens epithelium. Representative confocal microscopic images of the whole mount of human cataractous lens epithelium immunostained for SOX2 (green) and GJA1 (red) counterstained with DAPI (blue). All of the epithelial cells were negative for SOX2 but positive for GJA1 (as evident from the red punctate expression in the inset of the overlay image). (**B**) The unstained cataractous donor lens whole mount revealed the presence of cytoplasmic vacuoles only in the central zone (bright field image). These vacuoles emitted autofluorescence (entire spectrum: UV to far red).

3.3. Functional Characterization of Lens Epithelial Cells—Sphere Forming Ability

The sphere forming ability of anterior lens epithelial cells was evaluated using explant cultures established from the central, germinative + transitional and equatorial zones. In a normal lens, cells in the outgrowth from the central zone consisted of cuboidal epithelial cells, while germinative and transitional zones showed a mixed population of epithelial and fibre-like cells, and the equatorial zone revealed the migrating cells from the explant to be fibre-like cells. In the cataractous lens, the outgrowth from the central zone as well as

germinative+transitional zones were a mixed population of epithelial and fibre-like cells, while those from the equatorial zone were fibre-like cells (Figure 6).

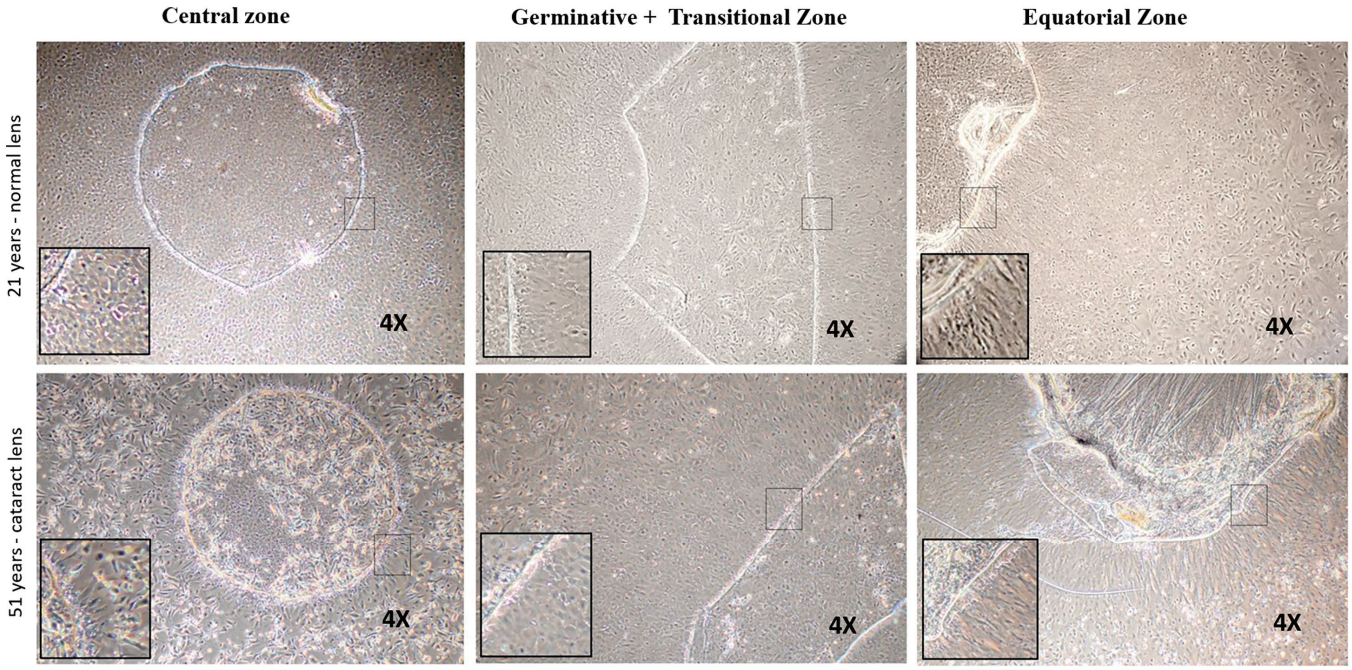

Figure 6. Representative phase contrast microscopic images of the explant cultured human lens epithelial cells from three zones of normal and cataract lens. In normal lens (**upper panel**): cells proliferated from the central zone were observed to be cuboidal; germinative and transitional zone showed a mixed population, and the equatorial zone revealed that the cells migrated from the explant were fibre-like cells. In cataract lens (**lower panel**): cells from central and germinative+transitional zones showed a mixed population while those from equatorial zone were fibre-like cells.

After 7 days of culture, the cells from the central zone were identified to have a significantly higher percentage of spheres-1.68 ± 1.0% (p = 0.007) compared to other zones (germinative + transitional zones-0.20 ± 0.28%and equatorial zone-0.04 ± 0.08%, Figure 7A). A significant reduction in the percentage of sphere forming ability (0.33 ± 0.11%) (p = 0.025) was observed in the cultured central zone cells from the cataractous lens epithelium, and no spheres were observed with the cells from other zones (Table 4).

Characterization of lens spheres (a minimum of three spheres from each culture) for the expression of the stem cell marker SOX2 revealed that the normal lens epithelium-derived spheres had SOX2 expression in almost all cells, whereas cataract lens epithelium-derived spheres had one or two cells with low expression (Figure 7B). Double immunostaining of spheres derived from normal central zone lens epithelial cells revealed the presence of SOX2 positive but GJA1 negative cells, confirming that the putative adult lens epithelial stem cells were localised in the central zone (Figure 7C). Further, the expression of PAX6 by all cells in the sphere confirmed the neuroectodermal origin of these lens epithelial cells (Figure 7B).

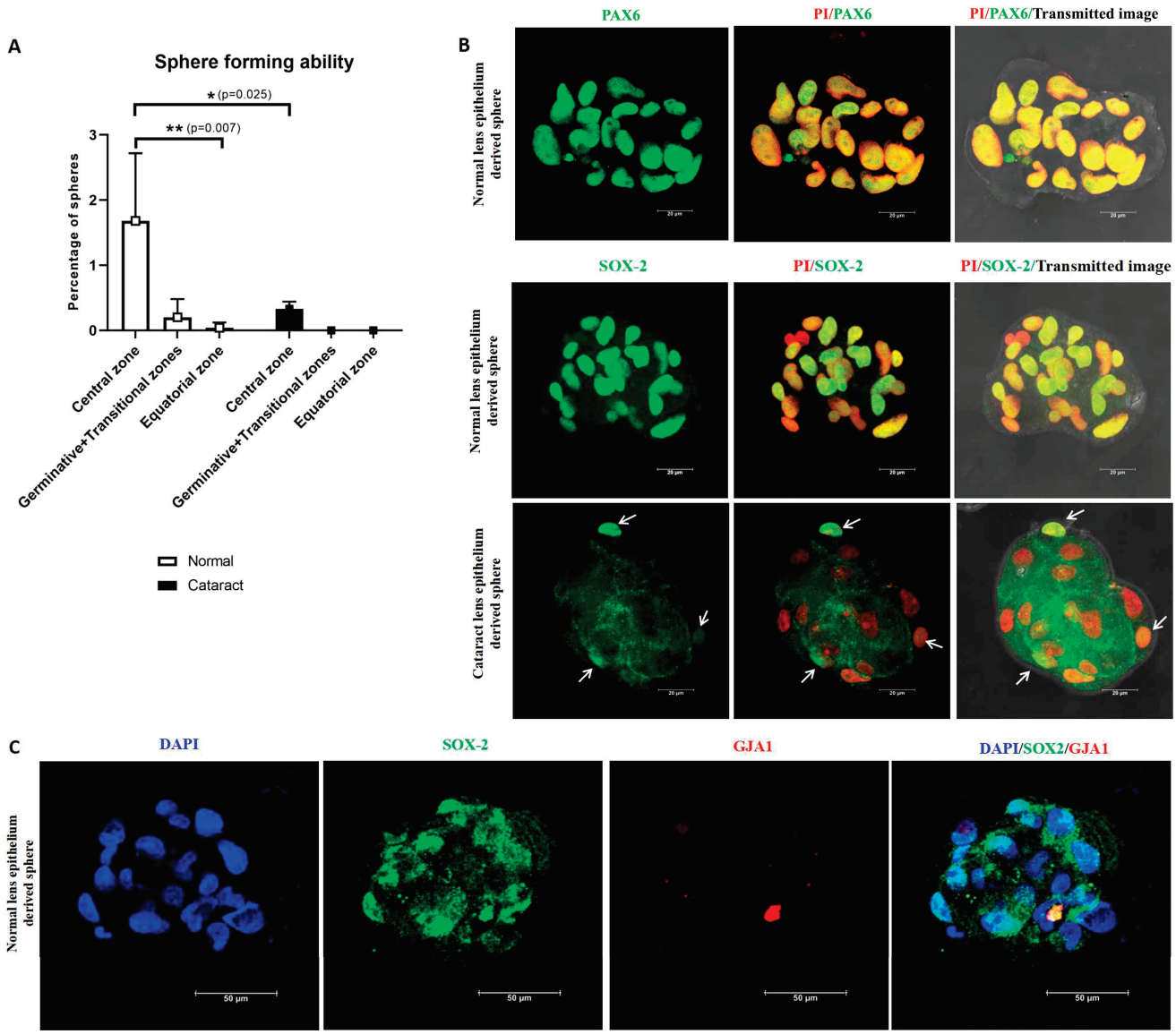

Figure 7. (**A**) The sphere forming ability of the cultured lens epithelial cells was analysed in both normal and cataract lens epithelium. The central zone alone had high sphere forming ability in normal lens epithelium, and a significant reduction was evident in cataract lens. * $p = 0.025$; ** $p = 0.007$. (**B**) Characterization of the human lens spheres derived from cultured central zone epithelial cells. Representative confocal microscopic images of lens spheres immunostained for PAX6/SOX2 (green) counterstained with propidium iodide (PI—red). The expression of PAX6 was evident in all cells in the sphere, and SOX2 was observed in most of the cells in the normal lens epithelium-derived spheres, while only a few cells in the spheres derived from the cataractous lens expressed SOX2 (arrows). Scale bar 20 µm. (**C**) Representative confocal microscopic images of a sphere derived from central zone double immunostained for SOX2 (green), GJA1 (red), counterstained with DAPI (blue). The SOX2 positive cells in the sphere were negative for GJA1.

Table 4. Percentage of spheres (≥60 μm) was analysed in normal (n = 5) and cataractous (n = 3) lens epithelial explant cultured cells. Central zone had higher percentage of sphere forming ability in normal lens, and that was significantly reduced in cataractous lens.

Spheres Formed/10^3 Cells (Spheres ≥ 60 μm)			
Age (Years)	**Central Zone (% of Spheres)**	**Germinative + Transitional Zone (% of Spheres)**	**Equatorial Zone (% of Spheres)**
Spheres established from normal lens epithelium			
18	1.3	0.6	0.2
20	1.1	0	0
21	3.1	0.4	0
41	2.4	0	0
54	0.5	0	0
Mean ± SD	1.68 ± 1.04	0.2 ± 0.28	0.04 ± 0.08
Spheres established from cataractous lens epithelium			
51	0.4	0	0
53	0.4	0	0
60	0.2	0	0
Mean ± SD	0.33 ± 0.11	0	0

4. Discussion

Adult tissue-resident stem cells are quiescent but have the ability to self-renew and to differentiate in response to the need, to maintain the tissue homeostasis throughout life [25]. These stem cells constitute 0.1–10% of cells in each tissue. They are mostly unipotent, lineage-specific and maintained in a unique microenvironment or niche. Adult tissue-resident stem cells are defined based on their phenotypic and functional characteristics. While there are no exclusive markers for adult stem cells, a combination of two or more markers/parameters is essential to identify stem cells [23,26–28]. Functionally, adult stem cells are defined based on their label-retaining cell property [2,24,29], clonal ability [9,30,31], sphere forming ability [10,24,32], side population property [33–35], ability to regenerate lineage-specific cells [8,36,37] and lineage tracing experiments [16,38,39]. With ageing, the adult stem cells decrease in number, as shown in human trabecular meshwork and dental pulp [23,40]. At the same time, ageing is also associated with a decrease in their function in some tissues, such as hematopoietic stem cells and hair follicle stem cells [41,42]. Therefore, understanding the basic biology of these adult tissue-resident stem cells is still evolving, as is their role in homeostasis, during ageing as well as in age-related diseases. In this study, the putative adult stem cells in the human anterior lens epithelium were characterized based on the immunostaining for stem cell marker SOX2 along with differentiated cell marker GJA1 (plasma membrane expression) and by sphere forming assay in normal and cataractous lens.

Characterization of the anterior lens epithelium has been carried out mostly in animals at early stages of development [3,22,43,44] based on their proliferative potential: the central zone with a low proliferative index, the germinative zone with a high proliferative index, and no proliferation in the transitional zone [45]. Ong et al. (2003) demonstrated different zones based on the cellular morphology (central, germinative and transitional zone) and indicated that the expression of β-crystallin, an early elongation marker (medial transition zone), preceded γ-crystallin, a late elongation marker (superficial cortical fibre region), in the bovine lens [2]. Based on this, in the present study, the β-crystallin$^+$ γ-crystallin$^-$ cells identified the transitional zone, and β-crystallin$^+$ γ- crystallin$^+$ cells the equatorial zone. While α-crystallin was expressed by all of the lens epithelial cells as reported earlier [22], a

small population of cells in the central zone were negative for the membrane expression of GJA1, the differentiated epithelial cell marker. All cells in the germinative zone were GJA1$^+$, β-crystallin$^-$ and γ-crystallin$^-$, distinguishing them from the central zone. The expression of PAX6 in the central to transitional zones of the human lens epithelium highlighted the neuroectodermal origin. Absence of PAX6 expression in γ-crystallin positive cells in the equatorial zone confirmed the previous report that the expression of PAX6 mRNA was lower in lens fibres compared to lens epithelium [46]. Since there are no previous studies on adult human lens epithelium, additional studies on the proliferative status of the cells are essential to confirm this demarcation of zones as reported in animal studies.

The putative adult tissue-resident stem cells were identified by immunophenotyping using the transcription factor SOX2 as a marker. SOX2 has been reported as a stem cell marker in several tissues, including human limbal epithelial [47], Muller glial [48], and neural stem cells [49], cultured human foetal lens epithelial cells [8], and several epithelial tissues of adult mice [16]. Kamatchi et al. (1998) demonstrated, in chick embryo, the sequential expression of SOX genes: strong expression of SOX2 at the stage of lens pit, lens vesicle, and lens epithelial formation [15] and replacement of SOX2 by SOX1 at the stage of lens fibre development [50]. The expression of SOX1 was significant for γ crystallin gene expression and elongation of lens fibre cells. Thus, the SOX genes—SOX2 and SOX1—are expressed during lens epithelium and fibre differentiation, respectively. Lineage tracing experiments in mice confirmed that the SOX2$^+$ adult stem cells, including the lens, originate from foetal SOX2$^+$ epithelial progenitors during development. The SOX2$^+$ cells were defined as stem cells, and SOX2$^-$ cells as differentiated cells [16]. The expression of SOX2 in human lens epithelium has been reported earlier by Fu et al. (2016), wherein they identified the expression of stem cell markers SOX2, ABCG2 and Ki67 in the central zone of younger people aged 0–10 years. Lin et al. (2016) demonstrated the presence of SOX2$^+$, PAX6$^+$, and BMI1$^+$ stem cells in cultured human lens epithelial cells. In this study, sequential analysis of the native human anterior lens epithelium (horizontally from one end of the equatorial zone towards the other end) from donors <60 years of age identified the presence of cells expressing the stem cell marker SOX2 only in the central zone, accounting for 9.16 ± 5.89% of central zone cells, similarly to the observations of Fu et al. (2016) in young donors.

In addition to using the positive expression of SOX2, we also used a negative marker to identify the adult lens epithelial stem cells. The significance of combining two parameters to identify stem cells was established in our previous studies on limbal epithelial stem cells [24], buccal mucosal epithelial stem cells [51], and trabecular meshwork stem cells [23], as well as by other groups [52,53]. In our study, the expression of SOX2 was analysed along with the membrane expression of the differentiated epithelial cell marker GJA1, which is one among the 10 connexins reported to be expressed in the differentiated cells in the human eye. Reports are available on the application of GJA1 as a negative marker in human limbal epithelial stem cells [19,26,54] and adult epidermal stem cells [18]. Absence of intercellular communication through the gap junction, specifically GJA1, might reflect the ability of the stem cells to retain the stemness in their microenvironment [19]. The plasma membrane expression of GJA1 was analysed in the present study using sequential confocal z-stack images. Double immunostaining with a plasma membrane marker is essential to confirm the membrane expression of GJA1 in the human lens epithelium.

Among the SOX2$^+$ cells identified in this study in the central zone, a fraction (1.89 ± 0.84%) was negative for the differentiated cell marker GJA1 (plasma membrane expression). Based on previous studies on GJA1 expression in adult ocular stem cells [19,26,54] and other stem cells [18,51], we hypothesize that the SOX2$^+$ GJA1$^+$ cells are derived from SOX2$^+$ GJA1$^-$ stem cells. Hence, we define cells positive for SOX2, PAX6, and α-crystallin and negative for GJA1 membrane expression, β and γ crystallins as putative lens epithelial stem cells. Further molecular studies are essential to elucidate the difference between SOX2$^+$ GJA1$^-$ and SOX2$^+$ GJA1$^+$ cells and to confirm that the SOX2$^+$ GJA1$^-$ cells represent

stem cells as well as to identify additional markers for the adult stem cells in the human lens epithelium.

For confirming the location of stem cells, the most widely used functional assay, the sphere forming assay, was carried out using cultured human lens epithelial cells from different zones. The formation of spheres under low adherence culture conditions has been reported in other tissues of the human eye, such as trabecular meshwork stem cells [24] and retinal pigment epithelial stem cells [55]. In the present study, the formation of a higher percentage of spheres by the cultured cells from the central zone (with cobblestone morphology) was demonstrated. In addition, most of the cells in these spheres were positive for SOX2 but negative for plasma membrane GJA1 expression and PAX6 positive, indicating the presence of a subpopulation of $SOX2^+$ cells that represent stem cells.

In this study, we defined the putative stem cells based on the presence of a small population of $SOX2^+$ cells that were negative for membrane expression of GJA1 in the central zone of native human lens epithelium and the presence of such cells ($SOX2^+$, $GJA1^-$, $PAX6^+$) in the spheres derived from cultured central zone cells. Further, the phenotypic ($SOX2^+$, $PAX6^+$, $GJA1^-$, β crystallin$^-$, γ crystallin$^-$ cells) and functional characterization (sphere formation) confirmed the putative stem cells to be located in the central zone of the human anterior lens epithelium. Having identified the location of putative stem cells in normal human anterior lens epithelium, the loss of $SOX2^+$ cells in the central zone of cataractous lens epithelium was confirmed. Similar observations were made in the anterior capsule obtained during cataract surgery by Fu et al. (2016) [11] and Turan and Turan (2020) [56]. In addition, a significant reduction in the percentage of spheres from the central zone of the cataractous lens epithelium was identified in the present study. Functional loss of adult stem cells in diseased conditions, e.g., exhaustion of myogenic stem cells in dystrophic muscle, indicate the significance of adult tissue-resident stem cells in maintaining tissue homeostasis [57]. The absence of $SOX2^+$ cells and the presence of autofluorescing vacuoles in the central zone of native tissue, as well as the reduction in the percentage of sphere forming ability of cultured lens epithelial cells in the cataractous lens, highlights the cellular changes in the central zone of cataract lens epithelium. Further studies are essential to explore the association of these changes with cataract pathogenesis.

5. Conclusions

In summary, this study identified four distinct zones in the human anterior lens epithelium and confirmed the location of the putative adult lens epithelial stem cells in the central zone and the functional loss of these stem cells in the cataractous condition.

Supplementary Materials: The following supporting information can be downloaded at: https://www.mdpi.com/article/10.3390/cells12232727/s1, Figure S1: Representative confocal microscopic image of cells in the central zone immunostained for SOX2 (green) and GJA1 (red), counterstained with DAPI (blue).

Author Contributions: Conceptualization, C.G.P. and P.S.; methodology, P.S.; validation, C.G.P., P.S. and V.M.; formal analysis, P.S.; investigation, C.G.P.; resources, C.G.P.; data curation, P.S.; writing—original draft preparation, P.S.; writing—review and editing, C.G.P., V.M., M.S. and A.H.; visualization, C.G.P., M.S. and P.S.; supervision, C.G.P., V.M., M.S. and A.H.; project administration, C.G.P. and M.S.; funding acquisition, C.G.P. and M.S. All authors have read and agreed to the published version of the manuscript.

Funding: The authors thank Science and Engineering Research Board, New Delhi, India (grant number CRG/2018/003921) for the financial support and Lady Tata Memorial trust, Mumbai, India for the Junior and Senior Research Scholarship (Pandi Saranya).

Institutional Review Board Statement: The study was conducted in accordance with the Declaration of Helsinki, and approved by the Institutional Review Board of Aravind Eye Care System, Madurai, Tamil Nadu, India (IRB number: IRB2018015BAS and date: 11 July 2018) for studies involving humans.

Informed Consent Statement: The donor eyes were procured by the eye bank after obtaining informed consent from the donors' families.

Data Availability Statement: Data are contained within the article and supplementary materials.

Acknowledgments: The authors thank D. Saravanan, Rotary Aravind International Eye Bank, Madurai, India for his help and support in collecting human donor tissues, M. Gowri, Aravind Communications, Aravind Eye Care System, Madurai, India for her help in preparing the figures, and Mohammed Sithiq Uduman, Biostatistician, Department of Biostatistics, Aravind Eye Hospital, Tirunelveli, India for help in the statistical analysis.

Conflicts of Interest: The authors declare no conflict of interest.

Abbreviations

SOX-2	SRY-Box transcription factor 2
GJA1	Connexin 43
LRCs	Label retaining cells
LESCs	Human lens epithelial stem cells

References

1. Muthukkaruppan, V. Inductive Tissue Interaction in the Development of the Mouse Lens in Vitro. *J. Exp. Zool.* **1965**, *159*, 269–287. [CrossRef] [PubMed]
2. Ong, M.D.; Payne, D.M.; Garner, M.H. Differential Protein Expression in Lens Epithelial Whole-Mounts and Lens Epithelial Cell Cultures. *Exp. Eye Res.* **2003**, *77*, 35–49. [CrossRef] [PubMed]
3. Shi, Y.; De Maria, A.; Lubura, S.; Šikić, H.; Bassnett, S. The penny pusher: A cellular model of lens growth. *Investig. Ophthalmol. Vis. Sci.* **2015**, *56*, 799–809. [CrossRef] [PubMed]
4. Zhou, M.; Leiberman, J.; Xu, J.; Lavker, R.M. A Hierarchy of Proliferative Cells Exists in Mouse Lens Epithelium: Implications for Lens Maintenance. *Investig. Ophthalmol. Vis. Sci.* **2006**, *47*, 2997–3003. [CrossRef] [PubMed]
5. Bassnett, S.; Šikić, H. The lens growth process. *Prog. Retin. Eye Res.* **2017**, *60*, 181–200. [CrossRef] [PubMed]
6. Tsonis, P.A.; Del Rio-Tsonis, K. Lens and retina regeneration: Transdifferentiation, stem cells and clinical applications. *Exp. Eye Res.* **2004**, *78*, 161–172. [CrossRef] [PubMed]
7. Gwon, A. Lens regeneration in mammals: A review. *Surv. Ophthalmol.* **2006**, *51*, 51–62. [CrossRef]
8. Lin, H.; Ouyang, H.; Zhu, J.; Huang, S.; Liu, Z.; Chen, S.; Cao, G.; Li, G.; Signer, R.A.J.; Xu, Y.; et al. Lens Regeneration Using Endogenous Stem Cells with Gain of Visual Function. *Nature* **2016**, *531*, 323–328. [CrossRef]
9. Arpitha, P.; Prajna, N.V.; Srinivasan, M.; Muthukkaruppan, V. A Method to Isolate Human Limbal Basal Cells Enriched for a Subset of Epithelial Cells with a Large Nucleus/Cytoplasm Ratio Expressing High Levels of P63. *Microsc. Res. Tech.* **2008**, *71*, 469–476. [CrossRef]
10. Yu, W.Y.; Grierson, I.; Sheridan, C.; Lo, A.C.-Y.; Wong, D.S.-H. Bovine Posterior Limbus: An Evaluation of an Alternative Source for Corneal Endothelial and Trabecular Meshwork Stem/Progenitor Cells. *Stem Cells Dev.* **2015**, *24*, 624–639. [CrossRef]
11. Fu, Q.; Qin, Z.; Yu, J.; Yu, Y.; Tang, Q.; Lyu, D.; Zhang, L.; Chen, Z.; Yao, K. Effects of Senescent Lens Epithelial Cells on the Severity of Age-Related Cortical Cataract in Humans: A Case-Control Study. *Medicine* **2016**, *95*, e3869. [CrossRef] [PubMed]
12. Yamamoto, N.; Majima, K.; Marunouchi, T. A Study of the Proliferating Activity in Lens Epithelium and the Identification of Tissue-Type Stem Cells. *Med. Mol. Morphol.* **2008**, *41*, 83–91. [CrossRef] [PubMed]
13. Oka, M.; Toyoda, C.; Kaneko, Y.; Nakazawa, Y.; Aizu-Yokota, E.; Takehana, M. Characterization and Localization of Side Population Cells in the Lens. *Mol. Vis.* **2010**, *16*, 945–953. [PubMed]
14. Stern, J.H.; Tian, Y.; Funderburgh, J.; Pellegrini, G.; Zhang, K.; Goldberg, J.L.; Ali, R.R.; Young, M.; Xie, Y.; Temple, S. Regenerating Eye Tissues to Preserve and Restore Vision. *Cell Stem Cell* **2018**, *22*, 834–849. [CrossRef]
15. Kamachi, Y.; Uchikawa, M.; Collignon, J.; Lovell-Badge, R.; Kondoh, H. Involvement of Sox1, 2 and 3 in the early and subsequent molecular events of lens induction. *Development* **1998**, *125*, 2521–2532. [CrossRef] [PubMed]
16. Arnold, K.; Sarkar, A.; Yram, M.A.; Polo, J.M.; Bronson, R.; Sengupta, S.; Seandel, M.; Geijsen, N.; Hochedlinger, K. Sox2$^+$ Adult Stem and Progenitor Cells Are Important for Tissue Regeneration and Survival of Mice. *Cell Stem Cell* **2011**, *9*, 317–329. [CrossRef]
17. Jaenisch, R.; Young, R. Stem cells, the molecular circuitry of pluripotency and nuclear reprogramming. *Cell* **2008**, *32*, 567–582. [CrossRef]
18. Matic, M.; Evans, W.H.; Brink, P.R.; Simon, M. Epidermal Stem Cells Do Not Communicate through Gap Junctions. *J. Investig. Dermatol.* **2002**, *118*, 110–116. [CrossRef]
19. Chen, Z.; Evans, W.H.; Pflugfelder, S.C.; Li, D.-Q. Gap Junction Protein Connexin 43 Serves as a Negative Marker for a Stem Cell-Containing Population of Human Limbal Epithelial Cells. *Stem Cells* **2006**, *24*, 1265–1273. [CrossRef]
20. West-Mays, J.A.; Pino, G.; Lovicu, F.J. Development and Use of the Lens Epithelial Explant System to Study Lens Differentiation and Cataractogenesis. *Prog. Retin. Eye Res.* **2010**, *29*, 135–143. [CrossRef]

21. Berthoud, V.M.; Minogue, P.J.; Osmolak, P.; Snabb, J.I.; Beyer, E.C. Roles and Regulation of Lens Epithelial Cell Connexins. *FEBS Lett.* **2014**, *588*, 1297–1303. [CrossRef] [PubMed]
22. McAvoy, J.W. Cell Division, Cell Elongation and Distribution of Alpha-, Beta- and Gamma-Crystallins in the Rat Lens. *J. Embryol. Exp. Morphol.* **1978**, *44*, 149–165. [PubMed]
23. Sundaresan, Y.; Veerappan, M.; Ramasamy, K.S.; Chidambaranathan, G.P. Identification, Quantification and Age-Related Changes of Human Trabecular Meshwork Stem Cells. *Eye Vis.* **2019**, *6*, 31. [CrossRef] [PubMed]
24. Sundaresan, Y.; Ramasamy, K.S.; Veerappan, M.; Chidambaranathan, G.P. Functional characterization of adult human trabecular meshwork stem cells. *Exp. Cell Res.* **2021**, *405*, 112709. [CrossRef] [PubMed]
25. Van Velthoven, C.T.J.; Rando, T.A. Stem Cell Quiescence: Dynamism, Restraint, and Cellular Idling. *Cell Stem Cell* **2019**, *24*, 213–225. [CrossRef] [PubMed]
26. Arpitha, P.; Prajna, N.V.; Srinivasan, M.; Muthukkaruppan, V. High Expression of P63 Combined with a Large N/C Ratio Defines a Subset of Human Limbal Epithelial Cells: Implications on Epithelial Stem Cells. *Investig. Ophthalmol. Vis. Sci.* **2005**, *46*, 3631–3636. [CrossRef]
27. Meyer-Blazejewska, E.A.; Kruse, F.E.; Bitterer, K.; Meyer, C.; Hofmann-Rummelt, C.; Wünsch, P.H.; Schlötzer-Schrehardt, U. Preservation of the limbal stem cell phenotype by appropriate culture techniques. *Investig. Ophthalmol. Vis. Sci.* **2010**, *51*, 765–774. [CrossRef] [PubMed]
28. Hayashi, R.; Yamato, M.; Saito, T.; Oshima, T.; Okano, T.; Tano, Y.; Nishida, K. Enrichment of corneal epithelial stem/progenitor cells using cell surface markers, integrin alpha6 and CD71. *Biochem. Biophys. Res. Commun.* **2008**. [CrossRef]
29. Shinin, V.; Gayraud-Morel, B.; Tajbakhsh, S. Template DNA-strand co-segregation and asymmetric cell division in skeletal muscle stem cells. In *Methods in Molecular Biology*; Humana Press: Totowa, NJ, USA, 2009; pp. 259–317. [CrossRef]
30. Pellegrini, G.; Golisano, O.; Paterna, P.; Lambiase, A.; Bonini, S.; Rama, P.; De Luca, M. Location and clonal analysis of stem cells and their differentiated progeny in the human ocular surface. *J. Cell Biol.* **1999**, *145*, 769–782. [CrossRef]
31. Sekiya, I.; Larson, B.L.; Smith, J.R.; Pochampally, R.; Cui, J.G.; Prockop, D.J. Expansion of human adult stem cells from bone marrow stroma: Conditions that maximize the yields of early progenitors and evaluate their quality. *Stem Cells* **2002**, *20*, 530–541. [CrossRef]
32. Isern, J.; Martín-Antonio, B.; Ghazanfari, R.; Martín, A.M.; López, J.A.; del Toro, R.; Sánchez-Aguilera, A.; Arranz, L.; Martín-Pérez, D.; Suárez-Lledó, M.; et al. Self-renewing human bone marrow mesenspheres promote hematopoietic stem cell expansion. *Cell Rep.* **2013**, *3*, 1714–1724. [CrossRef] [PubMed]
33. Goodell, M.A.; Brose, K.; Paradis, G.; Conner, A.S.; Mulligan, R.C. Isolation and functional properties of murine hematopoietic stem cells that are replicating in vivo. *J. Exp. Med.* **1996**, *183*, 1797–1806. [CrossRef] [PubMed]
34. Martin, J.; Helm, K.; Ruegg, P.; Varella-Garcia, M.; Burnham, E.; Majka, S. Adult lung side population cells have mesenchymal stem cell potential. *Cytotherapy* **2008**, *10*, 140–151. [CrossRef]
35. Watanabe, K.; Nishida, K.; Yamato, M.; Umemoto, T.; Sumide, T.; Yamamoto, K.; Maeda, N.; Watanabe, H.; Okano, T.; Tano, Y. Human limbal epithelium contains side population cells expressing the ATP-binding cassette transporter ABCG2. *FEBS Lett.* 2004. [CrossRef]
36. Rama, P.; Matuska, S.; Paganoni, G.; Spinelli, A.; De Luca, M.; Pellegrini, G. Limbal stem-cell therapy and long-term corneal regeneration. *N. Engl. J. Med.* **2010**, *363*, 147–155. [CrossRef]
37. Cheng, X.; Yu, Z.; Song, Y.; Zhang, Y.; Du, J.; Su, Y.; Ma, X. Hair follicle bulge-derived stem cells promote tissue regeneration during skin expansion. *Biomed. Pharmacother.* **2020**, *132*, 110805. [CrossRef]
38. Dorà, N.J.; Hill, R.E.; Collinson, J.M.; West, J.D. Lineage tracing in the adult mouse corneal epithelium supports the limbal epithelial stem cell hypothesis with intermittent periods of stem cell quiescence. *Stem Cell Res.* **2015**, *15*, 665–677. [CrossRef]
39. Konturek-Ciesla, A.; Bryder, D. Stem Cells, Hematopoiesis and Lineage Tracing: Transplantation-Centric Views and Beyond. *Front. Cell Dev. Biol.* **2022**, *10*, 903528. [CrossRef]
40. Kenmotsu, M.; Matsuzaka, K.; Kokubu, E.; Azuma, T.; Inoue, T. Analysis of side population cells derived from dental pulp tissue. *Int. Endod. J.* **2010**, *43*, 1132–1142. [CrossRef]
41. Liang, Y.; Van Zant, G.; Szilvassy, S.J. Effects of Aging on the Homing and Engraftment of Murine Hematopoietic Stem and Progenitor Cells. *Blood* **2005**, *106*, 1479–1487. [CrossRef]
42. Keyes, B.E.; Segal, J.P.; Heller, E.; Lien, W.-H.; Chang, C.-Y.; Guo, X.; Oristian, D.S.; Zheng, D.; Fuchs, E. Nfatc1 Orchestrates Aging in Hair Follicle Stem Cells. *Proc. Natl. Acad. Sci. USA* **2013**, *110*, E4950–E4959. [CrossRef] [PubMed]
43. Mikulicich, A.G.; Young, R.W. Cell proliferation and displacement in the lens epithelium of young rats injected with tritiated thymidine. *Investig. Ophthalmol. Vis. Sci.* **1963**, *2*, 344–354.
44. Rafferty, N.S.; Rafferty, K.A. Cell Population Kinetics of the Mouse Lens Epithelium. *J. Cell Physiol.* **1981**, *107*, 309–315. [CrossRef] [PubMed]
45. Griep, A.E. Cell Cycle Regulation in the Developing Lens. *Semin. Cell Dev. Biol.* **2006**, *17*, 686–697. [CrossRef] [PubMed]
46. Zhang, W.; Cveklova, K.; Oppermann, B.; Kantorow, M.; Cvekl, A. Quantitation of PAX6 and PAX6(5a) transcript levels in adult human lens, cornea, and monkey retina. *Mol. Vis.* **2001**, *7*, 1–5.
47. Bhattacharya, S.; Serror, L.; Nir, E.; Dhiraj, D.; Altshuler, A.; Khreish, M.; Tiosano, B.; Hasson, P.; Panman, L.; Luxenburg, C.; et al. SOX2 Regulates P63 and Stem/Progenitor Cell State in the Corneal Epithelium. *Stem Cells* **2019**, *37*, 417–429. [CrossRef] [PubMed]

48. Bhatia, B.; Singhal, S.; Lawrence, J.M.; Khaw, P.T.; Limb, G.A. Distribution of Müller Stem Cells within the Neural Retina: Evidence for the Existence of a Ciliary Margin-like Zone in the Adult Human Eye. *Exp. Eye Res.* **2009**, *89*, 373–382. [CrossRef]
49. Carrasco-Garcia, E.; Moreno-Cugnon, L.; Garcia, I.; Borras, C.; Revuelta, M.; Izeta, A.; Lopez-Lluch, G.; de Pancorbo, M.M.; Vergara, I.; Vina, J.; et al. SOX2 Expression Diminishes with Ageing in Several Tissues in Mice and Humans. *Mech. Ageing Dev.* **2019**, *177*, 30–36. [CrossRef]
50. Nishiguchi, S.; Wood, H.; Kondoh, H.; Lovell-Badge, R.; Episkopou, V. Sox1 directly regulates the gamma-crystallin genes and is essential for lens development in mice. *Genes Dev.* **1998**, *12*, 776–781. [CrossRef]
51. Priya, C.G.; Arpitha, P.; Vaishali, S.; Prajna, N.V.; Usha, K.; Sheetal, K.; Muthukkaruppan, V. Adult Human Buccal Epithelial Stem Cells: Identification, Ex-Vivo Expansion, and Transplantation for Corneal Surface Reconstruction. *Eye* **2011**, *25*, 1641–1649. [CrossRef]
52. Shortt, A.J.; Secker, G.A.; Munro, P.M.; Khaw, P.T.; Tuft, S.J.; Daniels, J.T. Characterization of the Limbal Epithelial Stem Cell Niche: Novel Imaging Techniques Permit in Vivo Observation and Targeted Biopsy of Limbal Epithelial Stem Cells. *Stem Cells* **2007**, *25*, 1402–1409. [CrossRef] [PubMed]
53. Di Iorio, E.; Barbaro, V.; Ruzza, A.; Ponzin, D.; Pellegrini, G.; De Luca, M. Isoforms of DeltaNp63 and the Migration of Ocular Limbal Cells in Human Corneal Regeneration. *Stem Cells* **2005**, *23*, 63–73.
54. Priya, C.G.; Prasad, T.; Prajna, N.V.; Muthukkaruppan, V. Identification of Human Corneal Epithelial Stem Cells on the Basis of High ABCG2 Expression Combined with a Large N/C Ratio. *Microsc. Res. Tech.* **2013**, *76*, 242–248. [CrossRef] [PubMed]
55. Priya, C.G.; Waseema, A.; Narendran, S.; Babu, K.N.; Kim, R.; Muthukkaruppan, V. Decline in the function of adult human retinal pigment epithelial stem cells with ageing. *Investig. Ophthalmol. Vis. Sci.* **2023**, *64*, 5387.
56. Turan, G.; Turan, M. The Evaluation of TUNEL, PCNA and SOX2 Expressions in Lens Epithelial Cells of Cataract Patients with Pseudoexfoliation Syndrome. *Curr. Eye Res.* **2020**, *45*, 12–16. [CrossRef]
57. Heslop, L.; Morgan, J.E.; Partridge, T.A. Evidence for a myogenic stem cell that is exhausted in dystrophic muscle. *J. Cell Sci.* **2000**, *113*, 2299–2308. [CrossRef]

Disclaimer/Publisher's Note: The statements, opinions and data contained in all publications are solely those of the individual author(s) and contributor(s) and not of MDPI and/or the editor(s). MDPI and/or the editor(s) disclaim responsibility for any injury to people or property resulting from any ideas, methods, instructions or products referred to in the content.

MDPI AG
Grosspeteranlage 5
4052 Basel
Switzerland
Tel.: +41 61 683 77 34

Cells Editorial Office
E-mail: cells@mdpi.com
www.mdpi.com/journal/cells

Disclaimer/Publisher's Note: The title and front matter of this reprint are at the discretion of the Guest Editor. The publisher is not responsible for their content or any associated concerns. The statements, opinions and data contained in all individual articles are solely those of the individual Editor and contributors and not of MDPI. MDPI disclaims responsibility for any injury to people or property resulting from any ideas, methods, instructions or products referred to in the content.

Academic Open
Access Publishing

mdpi.com

ISBN 978-3-7258-8488-9